JAERI-Review
2001-004

JP0150336

研究炉利用における研究成果集
(平成11年度)

2001年3月

(編) 豊田　政幸

日本原子力研究所
Japan Atomic Energy Research Institute

本レポートは、日本原子力研究所が不定期に公刊している研究報告書です。
入手の問合わせは、日本原子力研究所研究情報部研究情報課（〒319-1195　茨城県那珂郡東海村）あて、お申し越し下さい。なお、このほかに財団法人原子力弘済会資料センター（〒319-1195　茨城県那珂郡東海村日本原子力研究所内）で複写による実費頒布を行っております。

This report is issued irregularly.
Inquiries about availability of the reports should be addressed to Research Information Division, Department of Intellectual Resources, Japan Atomic Energy Research Institute, Tokai-mura, Naka-gun, Ibaraki-ken 〒319-1195, Japan.

© Japan Atomic Energy Research Institute, 2001
編集兼発行　日本原子力研究所

JAERI－Review 2001－004

研究炉利用における研究成果集（平成１１年度）

日本原子力研究所東海研究所研究炉部
（編）豊田　政幸

（2001年1月30日受理）

本報告書は、平成１１年度に研究炉で実験あるいは照射利用を行った利用者（原研外を含む）から成果の提出を受け、これを取りまとめたものである。

東海研究所：〒319-1195　茨城県那珂郡東海村白方白根2-4

JAERI－Review 2001－004

Activity Report on the Utilization of Research Reactors (Japanese Fiscal Year, 1999)

(Ed.) Masayuki TOYODA

Department of Research Reactor
Tokai Research Establishment
Japan Atomic Energy Research Institute
Tokai-mura, Naka-gun, Ibaraki-ken

(Received January 30, 2001)

This is the second issue of the activity report on the utilization of research reactors in the fields of neutron beam experiments, neutron activation analysis, radioisotope production, etc., performed during Japanese Fiscal Year 1999(April 1, 1999- March 31, 2000).

All reports in this volume were described by users from JAERI and also users from the other organizations, i.e., universities, national research institutes and private companies, who have utilized our research reactor utilization facilities for the purpose of the above studies.

Keywords: Research Reactor, Neutron Scattering, Neutron Radiography, Prompt Gamma-ray Analysis, Neutron Activation Analysis, Neutron Beam, Irradiation

目　次

はじめに 1
研究成果一覧 3
1. 中性子散乱 29
1) 構造・励磁 29
2) 磁　性 77
3) 超伝導現象 187
4) 非晶質・液体 199
5) 材料科学 229
6) 高分子 235
7) 生物学 271
8) 基礎物理学・中性子光学 289
9) 装　置 301
10) その他 317
2. 中性子ラジオグラフィ 329
3. 即発ガンマ線分析 337
4. 放射化分析 371
5. ＲＩの製造 429
6. 原子炉材料照射試験 433
7. その他 439
謝 辞 486
付 録 (1) 487
付 録 (2) 491

Contents

Preface 1
Research Reports 3
1. Neutron Scattering 29
1) Structure・Excitation 29
2) Magnetism 77
3) Superconductivity 187
4) Amorphous・Liquid 199
5) Material Science 229
6) Polymer 235
7) Biology 271
8) Fundamental Physics・Neutron Optics 289
9) Instrument 301
10) Others 317
2. Neutron Radiography 329
3. Prompt Gamma-ray Analysis 337
4. Neutron Activition Analysis 371
5. Produciton of Radio Isotopes 429
6. Irradiation Test of Reactor Materials 433
7. Others 439
Acknowledgments 486
Appendix (1) 487
Appendix (2) 491

はじめに

平成１１年度における研究炉の利用運転は、ＪＲＲ－３の８サイクルの共同利用運転と、ＪＲＲ－４の３７サイクルの共同利用運転があり、これに伴いさまざまな利用が行われた。

本報告書は、利用者（原研外利用者を含む）から当該利用の成果の提出を受け、取りまとめたものである。

提出して頂いた成果の件数は、中性子散乱２２３件、中性子ラジオグラフィ３件、即発γ線分析８件、放射化分析１６件、ＲＩの製造１件、原子炉材料２件、その他１３件で合計２６６件であった。事情により利用成果を提出して頂けなかった利用者については、その利用内容の一覧を付録に掲載した。なお、本報告書では下記の報告書の中から一部を転載させて頂いた。

最後に、原稿を提出して頂いた利用者の皆様の協力に感謝するとともに、今後も研究炉が有効に利用され、種々の研究がさらに進展されることを期待します。

研究炉利用課長
堀口　洋二

---

1) レポート番号：Vol.7（第７巻）
標　　題　：ACTIVITY REPORT ON NEUTRON SCATTERING RESEARCH issued by ISSP-NSL,University of Tokyo（東京大学物性研究所発行）
編　　者　：N.Aso and K.Kakurai（阿曽尚文，加倉井和久）
発 行 年　：２０００年

2) レポート番号：UTRCN-G-29
標　　題　：原研施設利用共同研究成果報告書（平成１１年度）
編　　者　：東京大学原子力研究総合センター
発 行 年　：２００１年（発行予定）

This is a blank page.

研 究 成 果 一 覧

Research Reports

This is a blank page.

No.	「 Title 」	Page
	Neutron Scattering - Structure · Excitation -	
1-1-1	**Neutron Powder Diffraction study on Thermal Expansion of UGe_2** K.Oikawa,M.Kohgi,H.Sagayama,K.Kuwahara,Y.Shimojo,Y.Morii,Y.Onuki	31
1-1-2	**Structural Study of High Ionic Conductor $Rb_4Cu_{16}I_{7.2}Cl_{12.8}$** K.Oikawa,T.Kamiyama,T.Ikeda,R.Kanno,T.Hata,F.Izumi,Y.Shimojyo,Y.Morii	33
1-1-3	**Crystal Structure of Charge Ordering State of $CuIr_2S_4$** K.Oikawa,T.Matsumoto,T.Furubayashi,N.Matsumoto,S.Nagata,Y.Shimojyo, Y.Morii	34
1-1-4	**Structural Phase Transition of Orthorhombic $LaCrO_3$** K.Oikawa,T.Kamiyama,T.Hashimoto,Y.Shimojyo,Y.Morii	35
1-1-5	**Nuclear-and Electron-Density Distribution in the Superconductor $HgBa_2CuO_{4+\delta}$** F.Izumi,S.Kumazawa,W.-Z.Hu,A.Yamamoto,K.Oikawa,T.Ikeda	37
1-1-6	**Neutron Powder Diffraction study of K_x@K-LTA using the MEM-based whole pattern fitting** T.Ikeda,T.Kodaira,F.Izumi	38
1-1-7	**Neutron Diffraction study of open tunnel oxide α -MnO_2** N.Kijima,T.Ikeda,K.Oikawa,F.Izumi,Y.Yoshimura	39
1-1-8	**Neutron diffraction study of $La_{1-x}Ca_xMnO_3$ with x=0.18 and 0.25** Y.Ono,S.Begum,H.Fujishiro,M.Ikebe,T.Fukase,T.Kajitani	40
1-1-9	**Structure of layered superconductor,$Li_{0.18}ZrNBr$,and the parent compound β -ZrNBr** S.Shamoto,Y.Kato,K.Oikawa,T.Kajitani	41
1-1-10	**Powder Neutron Diffraction study of the Crystalline-State 3-1 Photoisomerization of the 3-Cyanopropyl Cobaloxime Complex** T.Ohhara,H.Uekusa,T.Ozeki,Y.Ohashi,K.Oikawa,Y.Morii	42
1-1-11	**Single Crystal Neutron Diffraction Study of the Crystalline-State Photoracemization of Cobaloxime Complex with Bulky Alkyl Group by BIX-3 Diffractometer** H.Imura,T.Ohhara,H.Uekusa,T.Ozeki,Y.Ohashi,I.Tanaka,K.Kurihara,N.Niimura	43
1-1-12	**Lattice Dynamics of Lithium Oxide** Y.Ishii,Y.Morii	44
1-1-13	**Lattice dynamics of disordered Perovskite PZN ($Pb(Zn_{1/3}Nb_{2/3})O_3$)** I.Tomeno,S.Shimanuki,Y.Tsunoda,Y.Ishii	45
1-1-14	**Neutron Scattering Study of the Normal-Incommensurate Phase Transition in Rb_2CoCl_4** H.Shigematsu,Y.Kondo,Y.Kawamura,T.Matsui	46
1-1-15	**Lattice Dynamics in $CuGeO_3$ by Inelastic Neutron Scattering** M.Nishi,K.Kakurai,Y.Fujii,S.Katano,J.Akimitsu	47
1-1-16	**Anomalous Lattice Dynamics in the Magnetic Polaron States of CeSb** K.Iwasa,M.Kohgi,Y.Haga,M.Braden,J.-M.Mignot,T.Suzuki	49
1-1-17	**Investigation on charge stripe of $YBa_2Cu_3O_{6+x}$ single crystals** M.Arai,A.Garrett,T.Nishijima,Y.Endoh,K.Tomimoto,S.Tajima,Y.Shiohara	51

1－1－18	**Phonon Spectra of YB_4As_3 in the Critical Temperature Region of Charge Ordering** K.Iwasa,M.Kohgi,A.Ochiai,H.Aoki,T.Suzuki	52
1－1－19	**Stuctural Analysis on NiAs** T.Nozue,H.Kobayashi,T.Kamimura	54
1－1－20	**Ordering of Methylammonium in $CH_3NH_3PbBr_3$** H.Mashiyama,Y.Kawamura,K.Ohoyama	55
1－1－21	**Relation between the Property,Crystal Strucure and Electrode Characteristics of $Li_{1+x}Mn_{2-x}O_4$ as a Cathode Active Material for the Lithium Secondary Battery** Y.Idemoto,S.Ogawa,N.Koura	56
1－1－22	**Neutron diffraction study of layered oxides $Na_x(Co_{1-y}Mn_y)O_{2-\delta}$** Y.Ono,R.Ishikawa,Y.Miyazaki,T.Kajitani	58
1－1－23	**Orbital stability in the spin-ordered phase of bilayer manganites as investigated by neutron diffraction measurements** K.Hirota,A.Nakamura	59
1－1－24	**Reconsideration of the lattice effect on the charge-ordering transition of doped manganites** A.Machida,Y.Moritomo,K.Ohoyama,S.Okamoto,S.Ishihara,S.Maekawa A.Nakamura	60
1－1－25	**Pressure-induced insulator-metal transition in a bilayer manganite -Pressure-control of orbital stability-** Y.Moritomo,K.Hirota,H.Nakao,T.Kiyama,Y.Murakami,S.Okamoto,S.Ishihara S.Maekawa,M.Kubota,H.Yoshizawa	61
1－1－26	**Stuctural Changes of Thallium Pyrochlores Synthesized under High Pressure** T.Takeda,R.Kanno,K.Oyama,Y.Yamaguchi	62
1－1－27	**Residual Strain measurement of functionally gradient material by RESA** K.Inoue,T.Tsujikami,M.Kawagai,M.Ohyanagi,N.Minakawa,Y.Morii,T.Saitoh	63
1－1－28	**Neutron Diffraction study on Heusler-type Ni_2MnGa-based Alloys** K.Inoue,K.Enami,M.Igawa,Y.Yamaguchi,K.Ohoyama	65
1－1－29	**Diffuse Neutron Scattering from GaAs** M.Arai,K.Ohki,M.Mutou,T.Sakuma,H.Takahashi,Y.Ishii	67
1－1－30	**Neutron Diffraction study on Shape Memory Effect of Ni_2MnGa-based Alloys** K.Inoue,K.Enami,M.Igawa,Y.Yamaguchi,Y.Morii,Y.Matsuoka	68
1－1－31	**Neutron scattering study of $La_{1-x}Ca_xMnO_3$ with x=0.15** S.Begum,Y.Ono,Y.Miyazaki,Y.Tomioka,Y.Tokura,T.Kajitani	70
1－1－32	**Observation of Low Lying Phonons in $CuGeO_3$** M.Nishi,K.Kakurai,Y.Fujii,S.Katano,J.Akimitsu	71
1－1－33	**Neutron Incoherent Inelastic Scattering of Oriented Oleic Acid;Dynamics of a Hierarchic Structure Crystal** T.Yokoyama,N.Achiwa,M.Suzuki	73
1－1－34	**Characterization of Asphaltene Micelles and Their Interactions in Vacuum Residue of Crude Oil by Small-Angle Neutron Scattering** S.Kamei,K.Yogo,M.Ishikawa,J.Suzuki	75

1-1-35	**SANS Study of precipitation phenomena of electron-irradiated Fe-Cu alloy** K.Aizawa,A.Iwase,T.Tobita,M.Suzuki	76

No.	「 Title 」	Page
	Neutron Scattering - Magnetism -	
1-2-1	**Neutron Diffraction Study on Ordered Perovskite Ba_2NdRuO_6** Y.Izumiyama,Y.Hinatsu,K.Oikawa,Y.Shimojo,Y.Morii	79
1-2-2	**Neutron Diffraction Study on Ordered Perovskite Sr_2TbRuO_6** Y.Doi,Y.Hinatsu,K.Oikawa,Y.Shimojo,Y.Morii	80
1-2-3	**Magnetic Structure of the Ordered Perovskite Ba_2PrRuO_6 by Powder Neutron Diffraction Measurements** Y.Izumiyama,Y.Hinatsu,K.Oikawa,Y.Shimojo,Y.Morii	81
1-2-4	**Crystal Structure Magnetic Properties of Ordered Perovskite Ba_2PrIrO_6** M.Wakeshima,D.Harada,Y.Hinatsu,K.Oikawa,Y.Shimojo,Y.Morii	82
1-2-5	**Magnetic Structure of the Antiferromagnetic Manganese Sulfide $BaLa_2MnS_5$ by Powder Neutron Diffraction Measurements** M.Wakeshima,Y.Hinatsu,K.Oikawa,Y.Shimojo,Y.Morii	83
1-2-6	**Neutron Diffraction Study on $La_{0.95}Sr_{0.05}CrO_3$ and $La_{0.85}Sr_{0.15}CrO_3$** K.Tezuka,Y.Hinatsu,K.Oikawa,Y.Shimojo,Y.Morii	84
1-2-7	**Neutron Powder Diffraction Study of Ferroelectric Antiferromagnet YMn_2O_5** H.Kimura,Y.Noda,I.Kagomiya,K.Kohn K.Oikawa,Y.Morii	85
1-2-8	**Neutron Diffraction Study at 10K of the Spinel Compound $Co_{0.8}Mn_{0.2}Al_{1.6}Fe_2O_4$** S.M.Yunus,F.U.Ahmed	86
1-2-9	**Crystal distortion and magnetic structure of γ-Mn(Ru) alloys** T.Hori,Y.Tsuchiya,Y.Ishii,K.Hojou	88
1-2-10	**Study on the Crystal and Magnetic Structures of $(La,Tb)_{2/3}Ca_{1/3}MnO_3$ by Neutron Powder Diffraction** M.Watahiki,K.Oikawa,J.Suzuki	89
1-2-11	**Neutron-Scattering Study of the "17.5K Transition" in URu_2Si_2** H.Amitsuka,M.Yokoyama,K.Kuwahara,M.Sato,N.Metoki,S.Kawarazaki, Y.Miyako,J.A.Mydosh	91
1-2-12	**Magnetic properties of the ladder compound $(Sr,Ca)_{14}Cu_{24}O_{41}$** T.Nagata,H.Fujino,J.Akimitsu,S.Katano	92
1-2-13	**Magnetic Ordering in CeSb under Ultra-High Pressure** T.Osakabe,N.Tachi,M.Kohgi,H.Kitazawa	93
1-2-14	**Survey of long range magnetic order in YbAs under high pressure** T.Osakabe,K.Ohoyama,A.Oyamada	94
1-2-15	**Study of the Magnetic Ordering in $La_{2-x}Sr_xCuO_4$ with x=0.12 by Neutron Diffraction** M.Sato,S.Katano,K.Yamada,T.Suzuki,T.Hukase	95
1-2-16	**Field Induced Ferromagnetic Spin Fluctuation in a Heavy Fermion Compound $CeRu_2Si_2$** M.Sato,Y.Koike,S.Katano,N.Metoki,H.Kadowaki,S.Kawarazaki	97
1-2-17	**Neutron Scattering Study of Linear-Chain Haldane Compounds NDMAZ and NDMAP** Y.Koike,N.Metoki,Y.Matsuoka,T.Kobayashi,M.Yamashita	98

1-2-18	**Neutron Diffraction Study of the Magnetic Ordering of $CeCu_{1+x}Al_{3-x}$** Y.Oohara,G.Motoyama,T.Nishioka,M.Kontani	100
1-2-19	**Crystal and Magnetic Structure of $Rb(Co_{1-x}Mg_x)F_3$** K.Motoya,T.Kumazawa,J.Kikuchi,S.Itoh,Y.Kouchi	101
1-2-20	**Two kinds of magnetic excitations in reentrant spin-glasses** K.Motoya,T.Kumazawa,K.Hioki	102
1-2-21	**Crossover of electronic regime in long-range magnetic order of Kondo lattices** K.Watanabe,Y.Uwatoko,M.Miyamura,S.Kawarazaki	104
1-2-22	**Quasi-Bi-Stripe Charge Order in a Bilayer Manganite $La_{2-2x}Sr_{1+2x}Mn_2O_7$ [1]** M.Kubota,H.Yoshizawa,H.Fujioka,K.Shimizu,K.Hirota,Y.Moritomo,Y.Endoh	105
1-2-23	**Random-Field Effect on Spin Correlation in 2D Percolating Ising Antiferromanets** K.Iwasa,H.Ikeda	106
1-2-24	**Anisotropic groeth kinetics in the geometrically frustrated isosceles trangular Ising antiferromagnet $CoNb_2O_6$** S.Kobayashi,S.Mitsuda,T.Jogetsu,J.Miyamoto,H.Katagiri,K.Kohn	108
1-2-25	**Critical Neutron Scattering Study of the Compositional Phase Transition in Mg-Doped $CuGeO_3$** M.Nishi,H.Nakao,Y.Fujii,T.Matsuda,K.Uchinokura,G.Shirane	109
1-2-26	**Pseudogap of magnetic excitation in Kondo semiconductor CeNiSn** H.Kadowaki,G.Nakamoto,T.Takabatake	111
1-2-27	**Neutron Scattering Study on a single crystal of Pyrochlore Compound $Nd_2Mo_2O_7$** Y.Yasui,Y.Kondo,M.Ito,M.Kanada,H.Harashina,S.Iikubo,K.Oda,T.Kageyama,K.Murata,S.Yoshii,M.Sato,H.Okumura,K.Kakurai	112
1-2-28	**Studies on Geometrically Frustrated Pyrochlore System $R_2Ru_2O_7$ (R=Y and Nd)** M.Ito,Y.Yasui,M.Kanada,H.Harashima,S.Yoshii,K.Murata,M.Sato,H.Okumura,K.Kakurai	114
1-2-29	**Magnetic Excitations in the Spin Gap System $TlCuCl_3$** A.Oosawa,T.Kato,H.Tanaka,K.Nakajima,M.Nishi,K.Kakurai	116
1-2-30	**Dispersion Curves of the Magnetic Excitation of $KCuCl_3$** T.Kato,A.Oosawa,H.Tanaka,K.Nakajima,K.Kakurai	117
1-2-31	**Measurements of spin-wave in CoO** K.Tomiyasu,Y.Tsunoda	118
1-2-32	**Spin Correlations on an S=5/2 Heisenberg Antiferromagnet of Simple Quadratic Lattice** K.Takeda,M.Mito,K.Nakajima,K.Kakurai,K.Yamagata	119
1-2-33	**Magnetic phase transition in $(Sr,Ca)CuO_2$** M.Matsuda,K.Katsumata,K.Kakurai,G.Shirane	120
1-2-34	**Neutron scattering study of heavy fermion antiferromagnet Ce_7Ni_3** K.Motoya,T.Kawasaki,H.Kadowaki,T.Osakabe,H.Okumura,K.Kakurai,K.Umeo,T.Takabatake	121

1-2-35	**Magnetic Neutron Diffraction of $ZnCr_2O_4$** Y.Hata,E.Kita,I.Kagomiya,M.Toki,K.Kohn,K.Shiratori,K.Nakjima,K.Kakurai	123
1-2-36	**Inelastic Neutron Scattering Study of the Orthogonal Dimer System $SrCu_2(BO_3)_2$** H.Kageyama,M.Nishi,N.Aso,K.Onizuka,K.Nukui,K.Kodama,K.Kakurai,Y.Ueda	125
1-2-37	**Magnetic From Factor in UGe_2** H.Sagayama,K.Kuwahara,K.Iwasa,M.Kohgi,Y.Haga,Y.Onuki,M.Nishi, K.Nakajima,N.Aso,K.Kakurai	127
1-2-38	**Dynamics of magnetite particles in ferro-fluid by NES method** N.Achiwa,G.Shirozu,T.Yokoyama,K.Kakurai	128
1-2-39	**Study of orbital degrees of freedom in $La_{1-x}Sr_xMnO_3$ by x-ray and neutron scattering** K.Hirota,K.Takahashi,T.Fukuda,J.Mizuki,Y.Murakami,Y.Endoh	129
1-2-40	**Spin dynamical properties and orbital states of the layered perovskite $La_{2-2x}Sr_{1+2x}Mn_2O_7(0.3\leq x<0.5)$** K.Hirota,H.Fujioka,M.Kubota,S.Ishihara,H.Yoshizawa,Y.Moritomo,Y.Endoh	130
1-2-41	**Orbital State in Layered-Perovskite Manganite Compound** T.Arima,A.Nakazawa,K.Ohoyama,H.Ichikawa,J.Akimitsu,T.Matsumura,K.Hirota	131
1-2-42	**Direct observation of the spin gap in a S=1/2 alternating chain compound,high pressure phase of $(VO)_2P_2O_7$** M.Azuma,T.Saito,M.Fujita,M.Takano	132
1-2-43	**Spin Density Wave in Epitaxial Cr/Sn and Cr/Au Multilayers with Nonmagnetic Spacer Layers** M.Takeda,K.Mibu,K.Takanashi,K.Himi,Y.Endoh,T.Shinjo,H.Fujimori	133
1-2-44	**Magnetic excitations in antiferromagnetic phase of NiS_2** M.Matsuura,H.Hiraka,K.Hirota,K.Yamada,Y.Endoh	134
1-2-45	**Search for 3-d magnetic correlation in Yb_4As_3** M.Kogi,K.Iwasa,T.Takeuchi,N.Aso,A.Ochiai,H.Aoki	135
1-2-46	**Neutron Diffraction Studies on Tb_7Rh_3** T.Tsutaoka,M.Nagao,T.Tokunaga,T.Kosugi,S.Kawano,Y.Andoh,G.Nakamoto, M.Kurisu	136
1-2-47	**Neutron Diffraction Studies on TbPdSn** Y.Andoh,M.Kurisu,G.Nakamoto,T.Tsutaoka,S.Kawano	137
1-2-48	**Neutron Diffraction Study on HoNiSn** M.Kurisu,G.Nakamoto,T.Nobata,T.Ida,T.Tsutaoka,Y.Andoh,T.Kosugi,S.Kawano	138
1-2-49	**Neutron Diffraction Studies of Magnetic Structures on Mn Formate Di-Urea Single Crystal** T.Kosugi,S.Kawano,K.Yamagata	139
1-2-50	**Neutron Diffraction Study of Magnetic Structure in $Ca_3Co_2O_6$** S.Niitaka,K.Yoshimura,S.Kawano,H.Kageyama,N.Aso,K.Nakajima	140
1-2-51	**Magnetic Structure of α -Mn at High Pressure** A.Onodera,Y.Tsunoda,Y.Nakai	141
1-2-52	**Incommensurate Magnetic Structure of the Antiferromagnet Proximate to Magnetic Instability;$Ce(Ni_{0.65}Pd_{0.35})_2Ge_2$** T.Fukuhara,K.Maezawa,H.Kadowaki	142

1-2-53	**Modulated Magnetic Structure in Oxygen Doped $La_2CoO_{4.24}$** K.Nakajima,T.Sawada,K.Kakurai,Y.Endoh	143
1-2-54	**Magnetic Ordering in a Frustrated Antiferromagnet ZnV_2O_4** M.Mekata,T.Ishida,Y.Yamada,T.Fujii,H.Kikuchi	145
1-2-55	**Spin Correlation in Mn3Pt (High Temperature phase)** T.Ikeda,Y.Tsunoda	146
1-2-56	**Neutron Scattering Study of Pyrochlore Compound $Tb_2Ti_2O_7$ in Magnetic Fields** Y.Yasui,M.Kanada,M.Ito,H.Harashima,M.Sato,H.Okumura,K.Kakurai	147
1-2-57	**Neutron Scattering Study on Magnetically Frustrated Pyrochlore System $Tb_2Ti_2O_7$** M.Kanada,Y.Yasui,M.Ito,H.Harashina,M.Sato,H.Okumura,K.Kakurai	149
1-2-58	**Mössbauer spectroscopy and neutron scattering measurements in a 3D-frustrated system $ZnFe_2O_4$** T.Usa,K.Kamazawa,S.Nakamura,Y.Tsunoda,K.Kohn,M.Tanaka	151
1-2-59	**Magnetic Neutron Scattering Measurements in the Highly Frustrated $ZnFe_2O_4$ Single Crystal** K.Kamazawa,Y.Tsunoda,K.Odaka,K.Kohn	152
1-2-60	**Neutron Diffraction Studies of PtFe alloy in Magnetic Fields** D.Tsuchiya,Y.Tsunoda	153
1-2-61	**Neutron Scattering Studies of PtMn alloys** A.Harigae,T.Sunaga,Y.Tsunoda	154
1-2-62	**Neutron Scattering Study of the Spin Structure in ND_4CuCl_3** B.Kurniawan,H.Tanaka,A.Oosawa,N.Aso,K.Nakajima,Y.Oohara,K.Kakurai, T.Takeuchi,S.Kawarazaki	155
1-2-63	**Study of the Effect of Uniaxial Pressure on $CuGeO_3$ along the a-axis** M.Nishi,J.Akimitsu,O.Fujita,K.Kakurai,Y.Fujii	156
1-2-64	**Hysteretic behavior under magnetic fields in the competing anisotropy system $Fe_{0.50}Co_{0.50}TiO_3$** A.Fukaya,J.Satooka,A.Ito,K.Nakajima,K.Kakurai	158
1-2-65	**Magnetic Structure of $Y_{0.8}Tb_{0.2}Mn_6Sn_6$ alloy** T.Hori,H.Shiraishi,Y.Yamaguchi	159
1-2-66	**Magnetic properties of hp13 type TFe_6Ge_6 (T=Zr,Nb,Hf) alloys** T.Hori,R.Nishihara,M.Akimitsu,K.Ohoyama,H.Onodera,Y.Yamaguchi	160
1-2-67	**Magnetic and Neutron Diffraction Study on $(Mn_{1-x}Ni_x)_{65}Ga_{35}$** H.Shiraishi,T.Hori,H.Miki,H.Onodera,K.Ohoyama,Y.Yamaguchi	161
1-2-68	**Magnetic Structure of $Sr_3Fe_2O_{7-\delta}$** K.Mori,T.Kamiyama,H.Kobayashi,K.Ohoyama,S.Ikeda	162
1-2-69	**Magnetic Structure of Ce_3SnC** M.Kosaka,S.Koiwai,Y.Uwatoko,H.Onodera,K.Ohoyama,Y.Yamaguchi	163
1-2-70	**Magnetic Structure in the tetragonal compound $Er^{11}B_2C_2$** K.Ohoyama,A.Tobo,K.Indoh,H.Onodera,Y.Yamaguchi	164
1-2-71	**Characteristic magnetic structure due to antiferroquadrupole ordering in the tetragonal compound $Ho^{11}B_2C_2$** K.Ohoyama,H.Yamauchi,A.Tobo,H.Onodera,Y.Yamaguchi	165

1-2-72	**Magnetic Structure of Iridium (IV) Perovskites Sr_2LnIrO_6 (Ln=Ce,Tb)** D.Harada,M.Wakeshima,Y.Hinatsu,K.Ohoyama,Y.Yamaguchi	166
1-2-73	**Magnetic Structure in the antiferroquadrupolar ordering compound $Dy^{11}B_2C_2$** K.Ohoyama,H.Yamauchi,A.Tobo,H.Onodera,Y.Yamaguchi	167
1-2-74	**Y Dilution Effect on Antiferroquadrupolar Ordering in DyB_2C_2** A.Tobo,S.Sako,H.Onodera,H.Yamauchi,K.Indoh,K.Ohoyama,Y.Yamaguchi	168
1-2-75	**Neutron Diffraction on 1D Quantum Ferrimagnet,$Sr_3Cu_3(PO_4)_4$** Y.Ajiro,T.Asano,M.Yoshihara,K.Ohayama,Y.Yamaguchi,Y.Koike,Y.Morii	169
1-2-76	**Powder neutron diffraction study of SrV_6O_{11}** Y.Hata,E.Kita,K.Ohoyama,Y.Kanke	171
1-2-77	**Study of Magnetic Structure in Novel Layered Transition-Metal Oxysulfide by Neutron Diffraction Technique** M.Matoba,K.Ohoyama,S.Soyano,S.Fukumoto,Y.Yamaguchi	172
1-2-78	**Magnetic Phase transition in Heavy Fermion Compounds $Ce_2Fe_{17-x}Al_x$** K.Konishi,T.Kamimori,H.Tange	174
1-2-79	**Magnetic Field Effect on the Antiferromagnetic Ordering in $La_{2-x}Sr_xCuO_4$ with x=0.12** M.Sato,S.Katano,K.Yamada,T.Suzuki,T.Hukase	175
1-2-80	**Neutron Scattering Study of $Sr_2EuCu_2RuO_8$** T.Mochiku,Y.Matsuoka,N.Metoki,D.P.Hai,K.Kadowaki	176
1-2-81	**Neutron Scattering Study of the Two-Dimensional Spin Glass $K_2Cu_{0.7}Co_{0.3}F_4$** H.Kadowaki,R.Kajimoto,H.Yoshizawa,I.Yamada	177
1-2-82	**Magnetic excitations in the Zn-Mg-RE icosahedral quasicrystals** T.J.Sato,H.Takakura,A.P.Tsai,H.Kadowaki,K.Shibata	178
1-2-83	**Low-energy Neutron Diffraction and Scattering of $BaVS_3$** M.Shiga,H.Nakamura,T.Yamasaki,K.Kojima,M.Nishi,K.Kakurai	179
1-2-84	**Magnetic Ordering and Excitation in Triangulated Antiferromagnet $Cu_9Cl_2(cpa)_6 \cdot nH_2O$** M.Mekata,M.Abdulla,M.Kubota,Y.Oohara	180
1-2-85	**Critical Dynamics in Percolating Ising System,$Rb_2Co_cMg_{1-c}F_4$** S.Itoh,Y.Kouchi,S.Ikeda,K.Iwasa,H.Ikeda,M.A.Adams,R.Kajimoto	181
1-2-86	**Off Specular Neutron Reflection from Magnetic Interfacial Roughness in Fe/Cr Multilayers** M.Takeda,Y.Endoh	183
1-2-87	**Small-Angle Neutron Scattering Study on Magnetoresistance Effect in Sr_2FeMoO_6** M.Watahiki,J.Suzuki,Y.Tomioka	184
1-2-88	**SANS Study of Slow Dynamics in Concentrated Spin Glasses** K.Motoya,K.Hioki,J.Suzuki	186

No.	「 Title 」	Page
	Neutron Scattering - Superconductivity -	
1-3-1	**Spin-Wave Excitations Stripe Phase of La_2NiO_4** K.Nakajima,T.Sawada,H.Yoshizawa,Y.Endoh	189
1-3-2	**The magnetic excitation of $YBa_2(Cu_{1-x}Zn_x)_3O_{6+y}$ - the pseudo gap and the detailed momentum-energy structure -** H.Harashina,M.Kanda,Y.Yasui,M.Ito,M.Sato,H.Okumura,K.Kakurai,M.Nishi	190
1-3-3	**Incommensurate Elastic peaks in $La_{1.79}Sr_{0.21}Cu_{0.99}Zn_{0.01}O_4$** H.Kimura,K.Hirota,M.Aoyama,T.Kawamata,T.Adachi,Y.Koike,K.Yamada, Y.Endoh	192
1-3-4	**Spin Fluctuations in the Underdoped High-T_c Cuprate $La_{1.93}Sr_{0.07}CuO_4$** H.Hiraka,M.Fujita,K.Yamada,Y.Endoh	193
1-3-5	**Systematic Study of Elastic Spin Correlation near Insulator-Superconductor Phase Boundary** M.Fujita,K.Yamada,H.Hiraka,Y.Endoh,K.Hirota,P.M.Gehring,G.Shizane	194
1-3-6	**Dynamic spin correlations in lightly-doped $La_{2-x}Sr_xCuO_4$** M.Matsuda,R.J.Birgeneau,Y.Endoh,M.Fujita,H.Hiraka,M.A.Kastner,G.Shirane, S.Wakimoto,K.Yamada	195
1-3-7	**Mosaic Spread of Pressed ZrNCl and HfNCl Pellets** S.Shamoto,K.Iizawa,T.Kajitani	196
1-3-8	**Structure of β -HfNCl** S.Shamoto,K.Iizawa,Y.Kato,T.Koiwasaki,M.Yasukawa,S.Yamanaka, K.Ohoyama,Y.Yamaguchi,T.Kajitani	197
1-3-9	**Phonon of Novel 2D superconductor Na_xHfNCl** S.Shamoto,K.Iizawa,Y.Kato,T.Kajitani,T.Koiwasaki,M.Yasukawa,S.Yamanaka	198

No.	「 Title 」	Page
	Neutron Scattering -Amorphous・Liquid-	
1-4-1	**Temperature dependence of the structure of liquid Sn:Neutron scattering experiment and an ab initio molecular-dynamics simulation** S.Munejiri,T.Masaki,T.Itami,Y.Senda,F.Shimojo,K.Hoshino,T.Kamiyama, Y.Ishii	201
1-4-2	**Hydration Structure of Ammonium Ion in Concentrated Aqueous Ammonium Chloride Solutions** Y.Kameda,K.Sugawara,K.Abe,T.Usuki,O.Uemura	203
1-4-3	**Neutron Scattering Measurement on Liquid Ge-Chalcogen Mixtures** K.Maruyama,S.Takeda,M.Kanehira,M.Misawa	205
1-4-4	**Neutron diffraction study on M_2O-TeO_2 (M=Li,Na,$Li_{0.62}Na_{0.38}$) glasses** H.Munemura,M.Misawa,K.Maruyama,K.Ohyama	206
1-4-5	**Mechanisms of the Structural Formation in a Ternary Microemulsion System** M.Nagao,H.Seto,Y.Kawabata,T.Takeda	207
1-4-6	**Analysis of Small-Angle Neutron Scattering Profiles of Ternary Microemulsion Systems** M.Nagao,H.Seto	209
1-4-7	**Structural Study of a Phospholipid Microemulsion by Neutron Scattering** S.Ichikawa,Y.Sano,M.Nakajima,S.Mukataka	211
1-4-8	**Concentration fluctuation of 1-propanol-water solution at sub-critical salt composition** T.Omi,H.Munemura,M.Nagao,K.Maruyama,M.Misawa	212
1-4-9	**Temperature Dependence of Small-Angle Neutron Scattering of a Hexafluoroisopropanol-water mixture** T.Yamaguchi,K.Yoshida,M.Nagao	213
1-4-10	**Small-angle Neutron Scattering of Supercritical Methanol** T.Yamaguchi,K.Watanabe,K.Yoshida,M.Nagao	214
1-4-11	**Structure of a reentrant liquid crystal** O.Oishi,M.Nagao	215
1-4-12	**Neutron Spin Echo Study on the Dynamics of Wormlike Micelles** H.Seto,T.Kato,T.Takeda,M.Nagao,Y.Kawabata	216
1-4-13	**Neutron Spin Echo Investigations on the Slow Dynamics in Complex Fluids Involving Amphiphiles** T.Takeda,Y.Kawabata,H.Seto,S.G.Ghosh,S.Komura,M.Nagao	217
1-4-14	**Temperature and Pressure Effects on Dynamical Fluctuation of Amphiphilic Membrane in a Ternary Complex Fluids** Y.Kawabata,M.Nagao,H.Seto,T.Takeda	218
1-4-15	**Low-energy Excitation in Protonated Potassium Phosphate Glass** O.Yamamuro,Y.Madokoro,H.Yamasaki,K.Harabe,I.Tsukushi,T.Matsuo	220
1-4-16	**Low-energy Excitations in LiCl Aqueous Solution Glasses** O.Yamamuro,Y.Madokoro,H.Yamasaki,I.Tsukushi,T.Matsuo	221
1-4-17	**Dynamics of Liquid Selenium-Halogen Mixture** M.Yao,Y.Ohmasa,A.Chiba,Y.Hiejima,Y.Kawakita,H.Endo	223

1-4-18	**Slow-Dynamics in the Metal-nonmetal Transition Range of Liquid Chalcogens** M.Yao,Y.Ohmasa,A.Chiba,Y.Hiejima,Y.Kawakita,H.Endo	224
1-4-19	**Quasi-elastic neutron scattering study on 1-propanol-water solution** Y.Hosokawa,H.Munemura,K.Maruyama,T.Kajitani,M.Misawa	225
1-4-20	**Quasi Elastic Neutron Scattering Measurements on the Liquid Mixture Having Closed Two Phase Region** K.Maruyama,S.Kawase,M.Misawa	226
1-4-21	**Neutron Scattering Study on Dynamics of Benzene and Methanol Molecules in MCM-41** S.Kittaka,S.Takahara,Y.Kuroda,T.Mori,T.Yamaguchi	227

No.	「 Title 」	Page
Neutron Scattering - Materials Science-		
1-5-1	**In Situ Investigation of Structural Change of ZrO_2-15mol% $YO_{1.5}$ during Annealing at 1000℃** M.Yashima,Y.Hatoyama,S.Utsumi,M.Ohashi,K.Nemoto,K.Ohoyama, Y.Yamaguchi	231
1-5-2	**A New Furnace for High-Temperature Neutron-Diffraction Measurements under Nitrogen Gas Flow** M.Yashima,H.Doi,K.Nemoto,K.Ohoyama,Y.Yamaguchi	232
1-5-3	**High-temperature neutron-diffraction study of $La_{0.683}Ti_{0.95}Al_{0.05}O_3$ perovskite** R.Ali,M.Yashima,H.Yoshioka,K.Ohoyama,Y.Yamaguchi	233

No.	「 Title 」	Page
	Neutron Scattering - Polymer -	
1-6-1	**Scattering Studies on Hierarchical Structutes of Rubber/Filler Systems** T.Hashimoto,M.Takenaka,T.Koga,K.Aizawa	237
1-6-2	**PNO Study on Bovine Serum Albumin Gels 3** Y.Izumi,Y.Jinbo,T.Matsugi,K.Aizawa,H.Tomimitsu	238
1-6-3	**Attempts to measure the Dipersion Curve of Crystalline Polymers** Y.Takahashi	239
1-6-4	**Neutron Structure Analysis of Poly (p-phenylenebenzobisthiazole)** Y.Takahashi	240
1-6-5	**Shear-Induced Ordering of Lamellar and Gyroid Structures Observed in a Nonionic Surfactant / Water System** M.Imai,K.Nakaya,T.Kato	242
1-6-6	**Morphology and Dynamics of Microemulsion Droplet Confining Single Polymer Chain** K.Nakaya,M.Imai	243
1-6-7	**The Association Behavior of Amophiphilic Carbosilane Block Copolymer in Solution** K.Matsumoto,U.Mizuno,Y.Yamamoto,M.Shinohata,H.Matsuoka,H.Yamaoka	244
1-6-8	**Macrophase -and Macrophase- Separated Structures in Binary Mixtures of Diblock Copolymers** D.Yamaguchi,M.Takenaka,H.Hasegawa,T.Hashimoto,H.Nagao	245
1-6-9	**Complex Microphase Transitions in an ABC Triblock Copolymer** K.Yamauchi,H.Hasegawa,T.Hashimoto,M.Nagao	246
1-6-10	**Study on the Thermodynamic Interactions between Isotactic Polypropylene and Ethylene-1-hexene Random Copolymers by SANS** M.Seki,Y.Matsushita,M.Nagao	247
1-6-11	**Critical Phenomena in Complex Phase Transition of Poly (deutrated styrene-b-isoprene) / Polybutadiene mixture** M.Takenaka,H.Hasegawa,S.Saito,T.Hashimoto,M.Nagao	248
1-6-12	**SANS Measurement of Interface Thickness in Immiscible Polymer Blends** M.Hayashi,K.H.Hasegawa,M.Takenaka,T.Hashimoto,M.Nagao	249
1-6-13	**Observation of Microphase Separation Induced by Pressure Jump** H.Hasegawa,H.Takeno,N.Sakamoto,T.Hashimoto,M.Nagao	250
1-6-14	**Conformation of polypeptide chains in dodecyl sulfate micelles** Y.Watanabe	251
1-6-15	**Conformation of Sugar Ball in Aqueous Solutions** K.Funayama,T.Imae,K.Aoi,K.Tsutsumiuchi,M.Okada,M.Nagao	253
1-6-16	**Small-Angle Neutron Scattering Study of the Structure of Chitosan-Iodine Complex with Contrast Variation Method** H.Yajima,Y.Suzuki,T.Sakajiri,T.Ishii	254
1-6-17	**Comparison of Microscopic Structures for Chemically Cross-linked and γ -ray Irradiated Gels by Small-angle Neutron Scattering** T.Norisuye,M.Shibayama	256

1-6-18	**Effects of Shear Flow on the Structure of the Lamellar Phase Formed by Nonionic Surfactants** K.Minewaki,T.Kato,M.Imai	258
1-6-19	**Large Scale Structures in Gellan Gum Gels** Y.Izumi,Y.Jinbo,T.Matsugi,M.Hashimoto,T.Takahashi	259
1-6-20	**Ultra-Small-Angle Neutron Scattering Study of Colloidal Crystal Structure in Two-Component Colloidal Dispersion** H.Matsuoka,T.Harada,H.Yamaoka	260
1-6-21	**Development of Neutron Reflectometer for Air/Water Interface with Imaging Plate** H.Matsuoka,E.Mouri,R.Yoshitome,K.Kago,H.Yamaoka,K.Soyama	261
1-6-22	**Dynamics of Poly (amido amine) Dendrimer in Aqueous Solutions** K.Funayama,T.Imae,K.Aoi,K.Tsutsumiuchi,M.Okada,H.Seto	262
1-6-23	**Microscopic dynamics of ergodic and non-ergodic gels as studies by neutron spin echo technique** T.Kanaya,K.Kaji,Y.Kawabata,M.Nagao,H.Seto,T.Takeda	263
1-6-24	**Neutron Spin Echo Study of the Dynamics of Ionic Polymer Micelles in Aqueous Solution** H.Matsuoka,Y.Yamamoto,K.Matsumoto,H.Yamaoka	265
1-6-25	**Evaluation of Interdiffusion Behavior of (Polystyrene/Deuterated Polystyrene) Bilayer below the Bulk Glass Transiton Temperature by Neutron Reflectivity** T.Kajiyama,D.Kawaguchi,K.Tanaka,S.Sasaki,S.Tasaki,A.Takahara	266
1-6-26	**Analysis of the Distribution of Chain End Groups in End-functionalized Polymer Thin Film by Neutron Reflectivity** A.Takahara,Y.Yokoe,N.Satomi,K.Tanaka,S.Tasaki,T.Kajiyama	267
1-6-27	**Neutron reflectivity measurements of PS-d_8 thin films as a function of temperature Is glass transition temperature Tg of thin film different from surface Tg ?** T.Kanaya,I.Tsukushi,K.Kaji,S.Tasaki,T.Ebisawa	268
1-6-28	**Nanostructure of protein adsorbed layer at water/quartz interface by neutron reflactometry** H.Matsuoka,E.Mouri,K.Kago,H.Yamaoka	270

No.	「 Title 」	Page
	Neutron Scattering - Biology -	
1-7-1	**A Neutron Diffraction Analysis of Met-Myoglobin at 1.5 Å** A.Ostermann,I.Tanaka,N.Niimura,F.G.Parak	273
1-7-2	**Small-Angle Neutron Scattering Study of the Structure of Serum-Soluble Transferrin Receptor with Contrast Variation Method** H.Yajima,H.Tanaka,T.Sakajiri,T.Ishii,M.Umeda,Y.Kohgo	274
1-7-3	**Physicochemical characterization of a proteoglycan in solution by small-angle neutron scattering** Y.Watanabe,I.Tanaka,Y.Sanol,N.Niimura	276
1-7-4	**Small-Angle Neutron Scattering of Apolipophorin-III** C.Katagiri,M.Nagao,M.Sato,Y.Ito	278
1-7-5	**Small-Angle Neutron Scattering from Chymotrypsin Inhibitor 2 in Water-Ethanol Binary Solutions** J.Kawaguchi,S.Lee,K.Yoshida,H.Wakita,G.Sugihara,T.Yamaguchi,M.Nagao	279
1-7-6	**Geometric Structure for the Complex formed between Escherichia coil Outer Membrane Protein,OmpA and a nonionic surfactant Octylglucoside** K.Kameyama,M.Sato,S.Ohnishi,M.Nagao	280
1-7-7	**Protein-Protein Interactions between the DNA-Binding Protein HU:a Neutron Scattering Study** S.Fujiwara,Y.Yonezawa,M.Nagao	282
1-7-8	**Measurement of the micellar sizes of deterget used for solubilizing photosynthetic membrane protein** Z.-Y.Wang,Y.Muraoka,M.Shimonaga,T.Nozawa	283
1-7-9	**Dynamics of w/o AOT Microemulsions Occluding Proteins** M.Hirai,T.Hayakawa,H.Iwase,R.K.Hirai,H.Seto,Y.Kawabata,T.Takeda	284
1-7-10	**Neutron Diffraction Measurements of Single Crystals of Hen Egg-White Lysozyme Grown under Different pH Conditions** S.Fujiwara,M.Maeda,Y.Yonezawa,N.Niimura	285
1-7-11	**Neutron Diffraction Measurements of Live Frog Muscle Using the Contrast Variation Method** S.Fujiwara,Y.Takezawa,Y.Sugimoto,K.Wakabayashi	286
1-7-12	**Neutron scattering study on self-assembly of keratin molecules in water** S.Naito,F.Ikkai,T.Karino,M.Furusaka,S.Fujiwara,N.Niimura	287
1-7-13	**Orientatinal behavior of biological super-macromolecules under high magnetic field** M.Hirai,T.Hayakawa,H.Iwase,Y.Sano,J.Suzuki	288

No.	「 Title 」	Page
	Neutron Scattering - Fundamental Physics · Neutron Optics -	
1-8-1	**Neutron Interferometric Measurement of the Scattering Lengths of ^{202}Hg,Hg, ^{63}Cu,^{65}Cu,Cu and W** H.Tomimitsu,Y.Hasegawa,K.Aizawa	291
1-8-2	**Neutron Phase Strain measurement in SiC Particulate Reinforced Aluminum Alloy during Fatigue** Y.Akiniwa,K.Tanaka,H.Kimura,N.Minakawa,Y.Morii	292
1-8-3	**Tests of BGO ($Bi_{12}GeO_{20}$) perfect crystals using double crystal method for the preparation of neutron EDM (Electric Dipole Moment) search** Y.Otake,C.M.E Zeyen,H.M.Shimizu,H.Funahashi,T.Tabaru,D.Seki,M.Kitaguchi, K.Miyazaki,M.Miyabe,Y.Yasuda,T.Takahashi,M.Hashimoto	293
1-8-4	**Experiments to Detect the Phenomena in between Coherence and Decoherence using Interferometer for cold neutron (C3-1-2) with Mechanical Alloying ($Ni_{25}Ti_{75}$) Samples** Y.Otake,T.Fukunaga,T.Tasaki,T.Ebisawa,N.Achiwa,M.Hino	294
1-8-5	**Mieze Spin Echo Method Using RF Flippers** T.Ebisawa,S.Tasaki,N.Achiwa,G.Shirozu,D.Yamazaki,T.Kanaya,N.Torikai, M.Hino,T.Kawai,K.Soyama	295
1-8-6	**Study on Effects of the interface roughness on the neutron reflectivity/ transmissivity** S.Tasaki	297
1-8-7	**Time Beat Neutron Spin Interferometry before or after π / 2 Neutron Spin Flipper** N.Achiwa,G.Shirozu,T.Ebisawa,M.Hino,S.Tasaki,T.Kawai,D.Yamazaki	298
1-8-8	**Measurement of spin precession angle through Fabry-Perot magnetic resonator with absorption** M.Hino,S.Tasaki,T.Ebisawa,T.Kawai,M.Utsuro,N.Achiwa,D.Yamazaki	299

No.	「 Title 」	Page
	Neutron Scattering - Instrument -	
1-9-1	**Neutron cyrstallography of rubredoxin** K.Kurihara,I.Tanaka,M.W.W.Adams,N.Moiseeva,R.Rau,N.Niimura	303
1-9-2	**Application of a Stacked Elastically Bent Perfect Si Monochromator with Identical Crystallographic Planes at a Diffrcatometer for Bio-Macromolecules (BIX-3)** I.Tanaka,F.U.Ahmed,N.Niimura	304
1-9-3	**An Attempt to refrigerate Si-crystal optical component on a Double Crystal Diffractometer** K.Aizawa,H.Tomimitsu	305
1-9-4	**Single Crystal Neutron Diffraction of Cobaloxime Complexes by FONDER Diffractometer** T.Ohhara,H.Imura,H.Uekusa,Y.Ohashi,H.Kimura,N.Takesue,Y.Noda	306
1-9-5	**Development of Double-Focused Si Monochromator** H.Kimura,A.Kojima,R.Kiyanagi,Y.Noda,N.Minakawa,Y.Morii,N.Takesue, Y.Yoshizawa	307
1-9-6	**Characterization Study of a troidal bent pyloric graphite Neutron Condenser lens** N.Nishiki,N.Metoki,Y.Koike,K.Soyama,S.Fujiwara,Y.K.Haga,S.Koizumi	308
1-9-7	**Performance of a Multi-Wavelength Monochromator System for Neutron Single-Crystal and Powder Diffraction** F.U.Ahmed,I.Tanaka,N.Niimura	310
1-9-8	**Development of a high-frequency cold neutron pulser for producing a time-dependent optical potential** T.Kawai,M.Hino,S.Tasaki,T.Ebisawa,D.Yamazaki,Y.Otake,N.Achiwa	311
1-9-9	**Development of Wide Band Neutron Monochormator Consisting of a Stack of Multilayers** Y.Kawabata,K.Somemiya,S.Tasaki	312
1-9-10	**Development of Compound refractive optics and evaluation of a quadrupole magnet as a neutron prism** T.Oku,S.Morita,S.Moriyasu,Y.Yamagata,S.Ohmori,H.M.Shimizu,T.Hirota, Y.Kiyanagi,T.Ino,M.Furusaka,J.Suzuki	313
1-9-11	**Cold neutron imaging detector with two scintillator** F.Tokanai,T.Oku,K.Morimoto,H.M.Shimizu,J.Suzuki,T.Ino,T.Ikeda,W.Ootani, C.Otani,H.Sato,Y.Kiyanagi,T.Hirora,K.Kuroda,A.Riazantsev	315

No.	「 Title 」	Page
	Neutron Scattering - Others -	
1-10-1	**Neutron Stress Measurement using Neutron Image Plate** T.Sasaki,N.Minakawa,Y.Morii,N.Niimura,Y.Hirose	319
1-10-2	**Trial of Neutron Measurement of Stress in Cu Film Deposited on Glass Substrate** M.Nishida,T.Hanabusa,N.Minakawa	321
1-10-3	**Measurement of Elastic Constant of A7075 in Neutron Diffraction** T.Saito,N.Minakawa,Y.Morii	323
1-10-4	**Residual Stress measurement of friction welding boundary by neutron diffraction method** S.Okido,M.Hayashi,Y.Morii,N.Minakawa	324
1-10-5	**Measurement of Residual Stress Redistribution for Structural Material by Neutron Diffraction** Y.Tsuchiya,K.Kikuchi,N.Minakawa,Y.Morii,T.Kato,H.Nakajima,H.Tsuji	325
1-10-6	**Phonon Dispersion of $Ti_{50}Ni_{30}Cu_{20}$ Prior to B2-B19 Martensitic Transformation** X.Ren,K.Taniwaki,N.Miura,M.Inami,J.Zhang, K.Otsuka,Y.Morii, Yu.I.Chumlyakov	326
1-10-7	**Structural Investigation of Nanocrystalline Silicon by Small-Angle Scattering** J.Suzuki,T.Matsumoto,Y.Masumoto,M.Ohnuma	328

No.	「 Title 」	Page
	Neutron Radiography	
2-1	**Measurement error of the instantaneous and time-averaged void fraction measurement by dynamic neutron radiography** M.Kureta,H.Akimoto	331
2-2	**Visualization and Measurement of Plunging Water Jet Behavior into Molten Metal** Y.Shibamoto,H.Nakamura,Y.Anoda	332
2-3	**Development of high resolution imaging using a scintillator coated FOP coupled CCD camera** M.Matsubayashi,T.Hibiki,K.Mishima,Y.Saito	334

No.	「 Title 」	Page
	Prompt Gamma-ray Analysis	
3-1	**Study on Neutron Induced Prompt Gamma-Ray Analysis** C.Yonezawa,H.Matsue	339
3-2	**The boron concentration measurement of the BNCT patient's blood** N.Hori,T.Yamamoto,A.Matsumura,Y.Torii,K.Yamamoto,T.Kishi,J.Takada, S.Ohtake,K.Ohta	341
3-3	**Determination of Boron in Animal Materials by Reactor Neutron Induced Prompt Gamma-ray Analysis** S.Miyamoto,K.Nishimura,C.Yonezawa,H.Matsue,T.Adachi,M.Hoshi	343
3-4	**B Analysis in a Plant Sample** T.Nakanishi,J.Furukawa,T.Kataoka,H.Iikura	345
3-5	**Nuclear and Radiochemical Application of Neutron Absorption Reactions at the Neutron Beam Guides of JRR-3M (Ⅱ) : Development of the Precise Meassurement Method for Energy of Neutron Capture Prompt Gamma-ray －Photpeak profile** T.Kishikawa,J.Uemura,C.Yonezawa	349
3-6	**Prompt Gamma-ray Analysis of Large and Volumious Samples. Ⅱ** Y.Oura,K.Sueki,H.Nakahara,S.Enomoto,H.Matsue,C.Yonezawa	355
3-7	**Prompt γ-ray Analysis of Sludge from Electroplating** S.Morisaki,C.Yonezawa	364
3-8	**Action of zinc ion in the control of oocyte maturation of amphibian** K.Watanabe,K.Ishikawa	367

No.	「 Title 」	Page
	Neutron Activition Analysis	
4-1	**Determination of Sodium and copper in saltwater clam shell by activation analysis** H.Kamioki	373
4-2	**Content Levels and Dynamics of the Halogen Elements in the Soil Plant System of the World - Soils of the Neimenggu and Yunnan in China and Luzon island in Philipin -** K.Yuita,I.Taniyama,S.Nagatsuka	374
4-3	**Behavior of trace elements in the weathered products of sandstone** H.Kamioka,Y.Seki,K.Tsukimura,Y.Kanai,Y.Kanazawa,S.Hamasaki,T.Nakajima	376
4-4	**Study on Neutron Activation Analysis** C.Yonezawa,H.Matsue,A.Sirinuntavid,J A.Liyanage	377
4-5	**Neutron activation analysis of igneous standard rock samples by multidimensional spectrum analysis** Y.Hatsukawa,M.Ohshima,T.Hayakawa,Y.Fuji,N.Shinohara	379
4-6	**Uranium-content measurement of zircon by fission-track method** H.Iwano,T.Yoshioka,T.Danhara	381
4-7	**Source and Residence Time of Atmospheric Aerosols** S.Ohsaki,N.Momoshima,S.Sugihara	382
4-8	**Application of Carbon Fiber for Environmental Monitor** Y.Maeda,S.Sugihara,Y.Nakayama	386
4-9	**Variations in sex and age of organic halogen concentration in human serum** Y.Kashima,M.Matsui,H.Sakai	388
4-10	**Trace Element Analyses of Submarine Hydrothermal Deposits** K.Nakashima,A.Ogasawara	394
4-11	**Radiochemical Neutron Activation Analysis of Iridium in 300 m core samples from Lake Baikal** K.Toyoda,M.Shimada,Y.Shinozuka,S.Imai,N.Baba	399
4-12	**Extractable Organohalogens (EOX) in Grey - tailed Tattler (Heteroscelus Brevipes)** M.Kawano,M.Matsuda,T.Wakimoto	406
4-13	**Geochemlcal study of the high magnesian andesites in western Toki city,Gifu prefecture** H.Shinjoe	411
4-14	**Measurement of Al impurity content on quartzes for TL age determination** Y.Ganzawa	414
4-15	**Effects of Zn deficiency during the pregnant and lactaing period on growth of mice** M.Yanaga,T.Omori,M.Noguchi,M.Iwama,T.Yoshida,T.Ohyama,K.Inukai, M.Kamaya	421
4-16	**Development of neutron Activation analysis for ultra-trace elements in high purity materials (Ⅱ)** Y.Okada,S.Suzuki,S.Hirai	426

No.	「 Title 」	Page
	Irradiation Test of Reactor Materials	
5-1	**Aqueous chemistry of Rf in JAERI** H.Haba,K.Tsukada,I.Nishinaka,M.Asai,M.Hirata,S.Ichikawa,Y.Nagame, A.Yokoyama,A.Toyoshima,Y.Shoji,A.Shinohara,S.Goto,T.Kaneko,H.Kudo, M.Sakama,Y.Oura,M.Schädel	431

No.	「 Title 」	Page
	Irradiation Test of Reactor Materials	
6-1	**Electrical conductivity change under neutron irradiation in single crystal Al_2O_3 containing Cr_2O_3** T.Tanifuji,Y.Katano,T.Nakazawa,S.Jitsukawa	435
6-2	**Tritium release from neutron-irradiated Li_2O sintered pellets:porosity dependence** T.Tanifuji,D.Yamaki,T.Takahashi,A.Iwamoto	436

No.	「 Title 」	Page
	Others	
7-1	**Measurement of Axial Thermal Neutron Flux Distribution at SI-1 in JRR-3** T.Kumai,C.Akutsu	441
7-2	**Measurement of Axial Thermal Neutron Flux Distribution at N Pipe in JRR-4** J.Takada,C.Akutsu	442
7-3	**Evalution of JRR-4 Neutron Beam Using Tumor Cells in in vitro** K.Yamamoto,Y.Torii,T.Kishi,H.Kumada,J.Takada,S.Ohtake,T.Yamamoto, A.Matsumura,T.Nose	443
7-4	**Measurement of Thermal Neutron Distribution in Patient Head for BNCT** H.Kumada,K.Yamamoto,Y.Torii,T.Kishi,J.Takada,S.Ohtake	444
7-5	**A Quantitative Approach to the Characterization of Neutron Beam for Boron Neutron Capture Therapy (BNCT) Using In Vitro Cell Survival** T.Yamamoto,A.Matsumura,T.Nose,K.Yamamoto,H.Kumada,K.Ono,Y.Sakurai, T.Kobayashi	445
7-6	**Improved In Vitro Cytocidal Effect in Boron Neutron Capture Therapy (BNCT) Using Boronated Mn-Metalloporphyrins** T.Yamamoto,A.Matsumura,T.Nose,K.Yamamoto,H.Kumada	447
7-7	**Intraoperative Boron Neutron Capture Therapy for Malignant Gliomas: First Clinical Results of Tsukuba Phase Ⅰ/Ⅱ Trial Using Jaeri Mixed Thermal-Epithermal Beam** A.Matsumura,T.Yamamoto,Y.Shibata,H.Akutsu,S.Yasuda,A.Matsushita, K.Nakai,T.Yamada,S.Takano,T.Mizutani,H.Takahashi,H.Toyooka,K.Yamamoto, H.Kumada,Y.Torii,K.Ohara,Y.Nakagawa,K.Ono,T.Nose	449
7-8	**Basic and Clinical Studies for Application of Epithermal Neutron Beam for Neutron Capture Therapy** T.Nose,A.Matsumura,T.Yamamoto,Y.Shibata,F.Yoshida,H.Akutsu,S.Yasuda, A.Matsushita,K.Nakai,T.Yamada,S.Takano,T.Mizutani,H.Takahashi,H.Toyooka, K.Yamamoto,H.Kumada,Y.Torii,K.Ohara,Y.Nakagawa,K.Ono	452
7-9	**Study of metallofullerenes with neutron activation** K.Sueki,W.Sato,K.Akiyama,Yulang.Zhao,K.Kikuchi,M.Katada,H.Nakahara	462
7-10	**Mössbauer Spectroscopic Studies on Inorganic Compounds Part Ⅲ** M.Takahashi,M.Takeda,T.Kitazawa,J.Wang,A.Ishiguro,M.Maeda,H.Iwasaki, Y.Ito,H.Sawahata	465
7-11	**Synergistic Extraction of Lanthanoides (Ⅲ) with β - Diketones having Long Chain and Neutral Bidentate Amines** S.Takei,S.Nakamura,K.Akiba	474
7-12	**X-ray State Analysis by Means of Electron Capture Decay** Y.Tamaki	479
7-13	**The Production of Radiopharmaceuticals with short lived Radionuclides produced by Reactor** A.Ando,S.Oishi,I.Ando	482

1. 中性子散乱 1) 構造・励磁

1. Neutron Scattering 1) Structure・Excitation

This is a blank page.

研究テーマ：強相関電子系の中性子散乱による研究
表　題　：粉末中性子回折によるUGe_2の熱膨張測定

1-1-1 Neutron Powder Diffraction Study on Thermal Expansion of UGe_2

K. Oikawa*, M. Kohgi[1], H. Sagayama[1], K. Kuwahara[1], Y. Shimojyo, Y. Morii and Y. Onuki

Advanced Science Research Center, Japan Atomic Energy Research Institute, Tokai, Ibaraki 319-1195
[1] Tokyo Metropolitan University, Hachioji, Tokyo 192-0397
* Present address: National Institute of Materials and Chemical Research, 1-1 Higashi, Tsukuba, Ibaraki 305-8565

A heavy fermion compound, UGe_2 shows highly anisotropic ferromagnetism with Curie temperature, T_c = 52 K[1]. Crystal structure of UGe_2 is isomorphic with the orthorhombic $ThGe_2$[2,3], and uranium magnetic moment as large as 1.4 μ_B aligned along the *a*-axis.

Oomi et al.[4] measured thermal expansion of a single-crystalline UGe_2 by using a strain gauge, and showed anomalies at T_c and T' (≈ 25 K). The former is due to magnetostriction, but the origin of the later was not clarified. Kohgi et al.[5] measured thermal expansion of a single-crystalline UGe_2 with a capacitance bridge. The resultant values were, however, not coincident with Oomi's result, especially in the behavior of the *a*-axis.

To study the thermal expansion, Rietveld refinement of high-resolution neutron powder diffraction has several advantages, because

i) lattice constants can be obtained simultaneously,
ii) magnetic moment can be estimated,
iii) in addition, other structural parameters can be obtained.

On the other hand, disadvantages as compared with strain gauge method are that

iv) relative precision is worse,
v) temperature fluctuation and uniformity of the sample are not negligible, and
vi) a target material is restricted by the diffracted intensity.

In this work, we studied the anomalies in thermal expansion due to magnetostriction in UGe_2 using high-resolution neutron powder diffraction and compare the results with previous studies.

Neutron powder diffraction data were collected every 5 K from 10 K to 110 K and every 10 K from 110 K to 300 K. The 40 diffraction data were analyzed by the Rietveld refinement program RIETAN. The obtained lattice constants were fitted by Grueneisen-Einstein function between 55 K and 300 K, and the calculated line was extrapolated to 10 K. Figure 1a shows refined lattice parameters (lower), and resultant thermal expansion coefficients, $\alpha = \frac{1}{l}\frac{\Delta l}{\Delta T}$ (upper), of *a*-axis as a function of temperature. Figure 1b and 1c shows those of *b*- and *c*-axis, respectively.

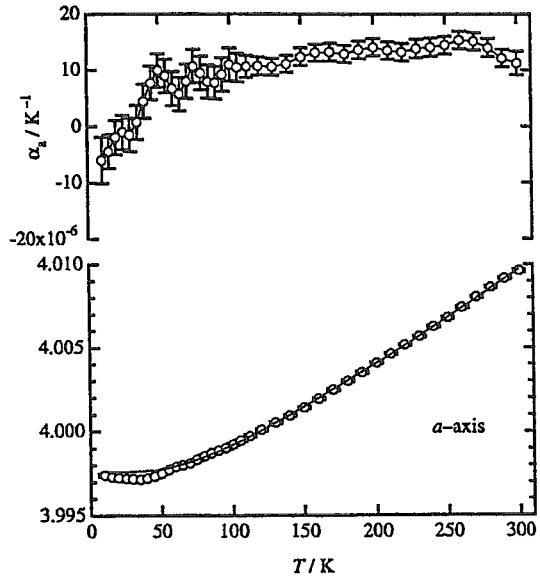

Fig. 1a. Temperature variation of the thermal expansion coefficient and the lattice constant (Å) along the *a*-axis.

The thermal expansion coefficients shows some spurious roughness around 80 K, but the behavior of the coefficients of *a*-axis under T_c is similar to Oomi's result. These spurious humps would come from limitation of the precision and the accuracy of the refined lattice prameters and its standard deviations. Typical values concerned with α in this region were, for example, l = 4.00000(6) Å, Δl = 16(8)×10^{-5}, ΔT = 5.0(5),

原子炉：JRR-3M　装置：HRPD（1）　分野：中性子散乱（構造）

thus deviation of Δl was worst. The relative deviation of Δl will be negligible if the temperature interval (which depends on the steepness of the variation of the phenomena) could be chosen to be large.

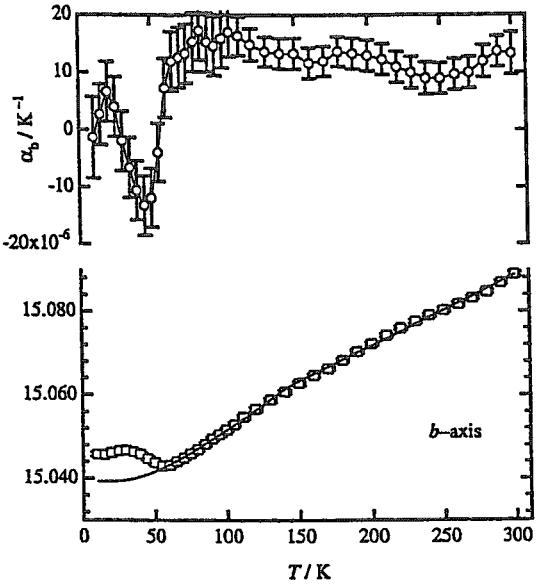

Fig. 1b. Temperature variation of the thermal expansion coefficient and the lattice constant (Å) along the *b*-axis

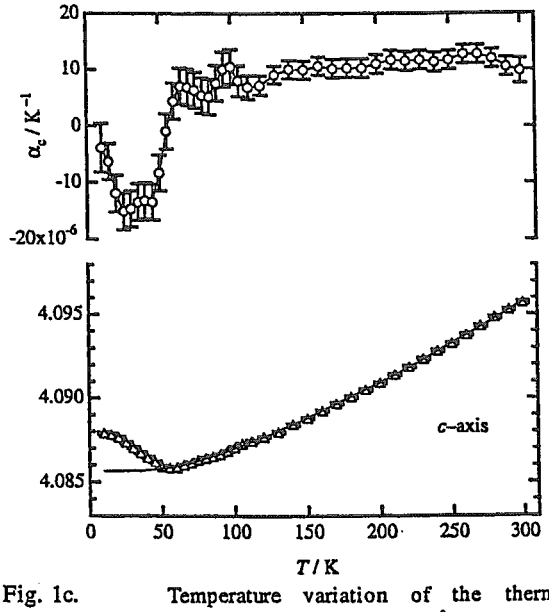

Fig. 1c. Temperature variation of the thermal expansion coefficient and the lattice constant (Å) along the *c*-axis

Figure 2 shows temperature dependence of refined magnetic moment. The value is much larger than reported value of 1.4 μ_B, but it would be attributed to that preferred orientation correction does not correct the magnetic component. The quantitative analysis between spontaneous magnetization and anomalies in thermal expansion under 55 K is in progress.

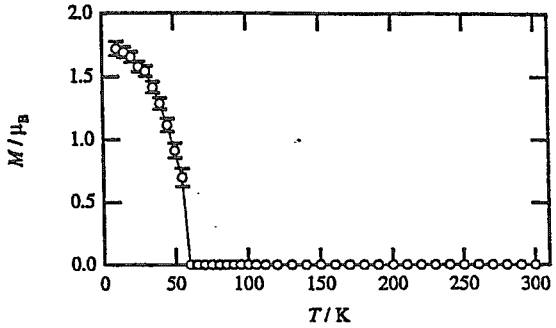

Fig. 2. Calculated ferromagnetic moment of Uranium, assuming magnetic formfactors of U^{3+}.

In conclusion, we showed that Rietveld refinement using high-resolution neutron powder diffraction is available for work on thermal expansion, and the temperature interval should be properly chosen to achieve reliable results.

References

1) Y. Onuki, I. Ukon, S. W. Yun, I. Umehara, K. Satoh, T. Fukuhara, H. Sato, S. Takayanagi, S. Shikama and A. Ochiai: J. Phys. Soc. Jpn. 61, (1992) 293.
2) K. Oikawa, T. Kamiyama, H. Asano, Y. Onuki and M. Kohgi: J. Phys. Soc. Jpn. 65, (1996) 3229.
3) P. Boulet, A. Daoudi, M. Potel, H. Noel, G. M. Gross, G. Andre and F. Bouree: J. Alloys Compd. 247, (1997) 104.
4) G. Oomi, K. Nishimura, Y. Onuki and S. W. Yun: Physica. B 186-188, (1993) 758.
5) T. Inamura, M. Kohgi, K. Iwasa, Y. Haga and Y. Onuki: Autumn Meeting of the Phys. Soc. Jpn. Abstract 25a-PS-12 (1998).

研究テーマ：強相関電子系の中性子散乱による研究
表　　題　：イオン伝導体$Rb_4Cu_{16}I_{7.2}Cl_{12.8}$の構造解析

1-1-2 Structural Study of High Ionic Conductor $Rb_4Cu_{16}I_{7.2}Cl_{12.8}$

K. Oikawa*, T. Kamiyama[1], T. Ikeda[2], R. Kanno[3], T. Hata[3], F. Izumi[2], Y. Shimojyo and Y. Morii

Advanced Science Research Center, Japan Atomic Energy Research Institute, Tokai, Ibaraki 319-1195
[1] Institute of Materials Structure Science, High Energy Accelerator Research Organization, Tsukuba, Ibaraki 305-0801
[2] National Institute for Research in Inorganic Materials, 1-1 Namiki, Tsukuba, Ibaraki 300-0047
[3] Department of Chemistry, Faculty of Science, Kobe University, Nada, Kobe, Hyogo, 657-8501
* Present address: National Institute of Materials and Chemical Research, 1-1 Higashi, Tsukuba, Ibaraki 305-8565

The high ionic conductor $Rb_4Cu_{16}I_7Cl_{13}$ has a room-temperature conductivity of 0.34 S/cm, which is the highest conductivity value of the ionic conductors so far prepared. The crystallographic study on the transition from a normal conduction state to a high conduction state at around 200 K is of particular importance for understanding the conduction mechanism of high ionic conductors. Geller et al.[1)] have determined the crystal structure of $RbCu_4I_2Cl_3$ ($Rb_4Cu_{16}I_8Cl_{12}$) at room temperature by single-crystal X-ray diffraction. Kanno et al.[2)] studied the structural changes of $Rb_4Cu_{16}I_{7.2}Cl_{12.8}$ using time-of-flight neutron powder diffraction at low temperatures. Their results are summarized as follows; no structural phase transition was detected, and a gradual migration of copper ions from the Cu(3) 'nonconducting' site into the Cu(2) 'conducting' site. However, their neutron diffraction study seems to be somewhat uncertain because the Rietveld refinements were carried out without reflections at large-d region (d-spacing > 3.4 Å) which are important for determination of the occupation factors.

In this study, we reinvestigate the structural change of $Rb_4Cu_{16}I_{7.2}Cl_{12.8}$ using angle dispersive neutron powder diffraction at low temperatures. The incident wavelength of 1.16 Å was chosen to collect as many reflections as possible, including lowest index. Figure 1 and 2 show temperature dependence of occupation factors × multiplicity and isotropic thermal displacement parameters of Cu sites, respectively. The isotropic thermal displacement parameters of Cu(3) site were converged to be larger than those of Kanno's, but the parameters were found to be strongly correlated with occupation factors of this site. The nuclear density distribution analysis using Maximum Entropy Method is in progress.

References

1) S. Geller, J. R. Akridge and S. A. Wilber, Phys. Rev. 19, 5396 (1993)
2) R. Kanno, K. Ohno, Y. Kawamoto, Y. Takeda, O. Yamamoto, T. Kamiyama, H. Asano, F. Izumi and S. Kondo, J. Solid State Chem. 102, 79 (1993)

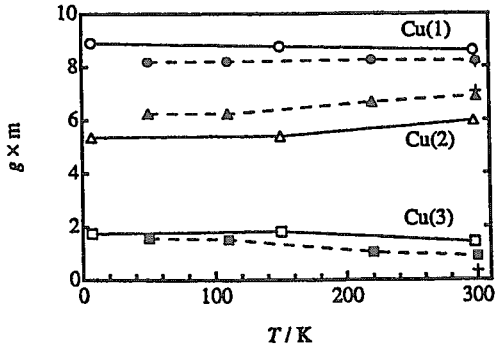

Fig. 1. Temperature dependence of occupation factor × multiplicity of each Cu(1), Cu(2) and Cu(3) sites: open marks; this work, closed; Kanno et al. and +; Geller et al.

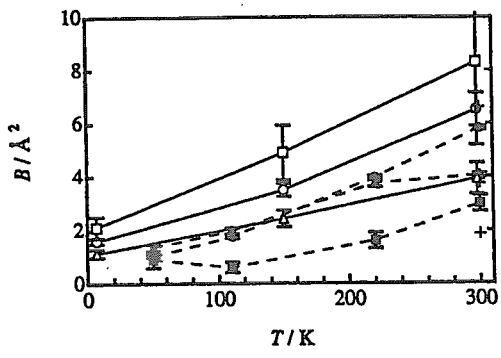

Fig. 2. Temperature dependence of the isotropic thermal displacement parameters of Cu(1), Cu(2) and Cu(3) sites. Marks are the same as in Fig. 1.

原子炉：JRR-3M　　装置：HRPD（1）　分野：中性子散乱（構造）

研究テーマ：強相関電子系の中性子散乱による研究
表　　題　：$CuIr_2S_4$の電荷整列相の結晶構造解析

1-1-3 Crystal Structure of Charge Ordering State of $CuIr_2S_4$

K. Oikawa*, T. Matsumoto[1], T. Furubayashi[1], N. Matsumoto[2], S. Nagata[2], Y. Shimojyo and Y. Morii

Advanced Science Research Center, Japan Atomic Energy Research Institute, Tokai, Ibaraki 319-1195
[1] National Research Institute for Metals, Tsukuba, Ibaraki 300-0047
[2] Department of Materials Science and Engineering, Muroran Institute of Technology, Mizumoto-cho, Muroran, 50-8585
* Present address: National Institute of Materials and Chemical Research, 1-1 Higashi, Tsukuba, Ibaraki 305-8565

The thiospinel compound $CuIr_2S_4$ exhibits a metal-insulator transition accompanied by a structural transition at T_{MI} ~ 230 K[1]. Superlattice reflections below T_{MI} were previously reported by the X-ray powder diffraction[1] and the electron diffraction[2]. A triclinic unit cell was recently proposed from the analysis of the high-resolution synchrotron powder diffraction at 50 K[3]. The details of the crystal structure at the low temperature (LT) phase, however, have not been clarified yet.

In this work, the crystal structure of the LT phase of $CuIr_2S_4$ was studied by neutron powder diffraction on HRPD. Two wavelengths were selected for the present study; the wavelength λ = 1.82299 Å (Ge 331 monochromator) was employed in order to obtain higher Q-resolution, and the wavelength λ = 1.16379 Å (Si 533 monochromator) was used to obtain precise structural parameters. The diffraction data taken at 50 K were analyzed on the basis of the triclinic unit cell (space group $P\bar{1}$) with lattice parameters a = 13.979(2), b = 11.954(2), c = 6.9880(5) Å, α = 91.1267(6), β = 88.201(5) and γ = 125.764(7)°. Figure 1 shows Rietveld refinement patterns of $CuIr_2S_4$ at 50 K. The possible ordered ionic configurations of Ir^{3+} and Ir^{4+}, which are deduced by calculating $[IrO_6]$ octahedral volumes, were consistent with the magnetic properties[1].

References

1) T. Furubayashi, T. Matsumoto, T. Hagino and S. Nagata, J. Phys. Sci. Jpn., 63 (1994) 3333.
2) H. Ishibashi, K. Tanioka, R. Oshima and K. Nakahigashi, Annual Meeting of the Phys. Soc. Jpn. Abstract 1p-YL-13 (1998).
3) H. Ishibashi, T. Sakai, R. Oshima and K. Nakahigashi, Autumn Meeting of the Phys. Soc. Jpn. Abstract 24aPS-92 (1999).

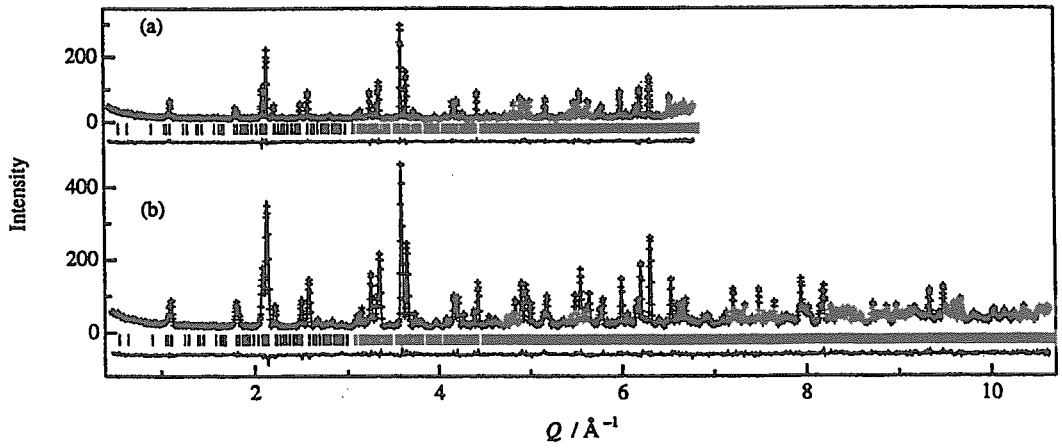

Fig. 1. Rietveld refinement patterns of $CuIr_2S_4$ at 50 K; (a) λ = 1.82299 Å, (b) λ = 1.16379 Å.

原子炉：JRR-3M　　装置：HRPD（1）　分野：中性子散乱（構造）

研究テーマ：強相関電子系の中性子散乱による研究
表　題　：$LaCrO_3$の構造相転移

1-1-4 Structural Phase Transition of Orthorhombic $LaCrO_3$

K. Oikawa*, T. Kamiyama[1], T. Hashimoto[2], Y. Shimojyo and Y. Morii

Advanced Science Research Center, Japan Atomic Energy Research Institute, Tokai, Ibaraki 319-1195
[1] Institute of Materials Structure Science, High Energy Accelerator Research Organization, Tsukuba, Ibaraki 305-0801
[2] Department of Applied Physics, College of Humanities and Sciences, Nihon University, Setagaya-ku, Tokyo 156-8550
* Present address: National Institute of Materials and Chemical Research, 1-1 Higashi, Tsukuba, Ibaraki 305-8565

$LaCrO_3$ and related oxides have been studied widely aiming at various industrial uses above room temperature (RT): for example, interconnects in solid-oxide fuel cells. It is well known that stoichiometric $LaCrO_3$ has phase transitions at around T = 15 and 260°C. The former is due to a magnetic order-disorder transition, while the latter to a structural phase transition, i.e., from an orthorhombic to a rhombohedral symmetry. Although the physical properties such as heat capacity and thermal conductivity of $LaCrO_3$–based perovskites at high temperatures have been measured widely, the crystal structure above room temperature has not been examined precisely.

By use of X-ray powder diffraction at high temperatures, several workers reported that $LaCrO_3$ showed the volume contraction at the structural phase transition. However, it remains open whether the large volume contraction arises from the deformation of $[LaO_{12}]$ and/or $[CrO_6]$ polyhedra. Then we carried out neutron diffraction experiments on $LaCrO_3$ at high temperatures and studied the structural phase transition from an orthorhombic to a rhombohedral phase. A geometrical relationship between polyhedral volumes and their tilts in perovskites developed by Thomas (1-3) was utilized to deduce polyhedral volume changes at the phase transition.

Neutron powder diffraction experiments were carried out on HRPD from RT to 740 °C with a high-temperature furnace. The sample was contained in a V holder. The temperature was monitored by a Chromel-Alumel thermocouple and was kept within ±0.5 K during the measurement. Two different wavelengths were selected depending on the requirement for the present study. The elastically-bent Si (533) monochromator which gives wavelength of 1.16251 Å was mainly used to obtain detailed structural information for the orthorhombic phase. The hot-pressed Ge (331) monochromator which gives 1.82340 Å was employed at around the phase transition region in order to obtain higher Q-resolution and at high temperature region. The 30 diffraction data were analyzed by the Rietveld method with RIETAN. Typical R_{WP} and R_B were ca. 7 % and 3 % respectively. The coefficients of volume thermal expansion, $-\frac{1}{V}\frac{\partial V}{\partial T}$, were estimated as 2.285(16) × 10^{-5} K^{-1} (between T = 295 K and T = 533 K) and 2.842(12) × 10^{-5} K^{-1} (between T = 533 K and T = 1013 K) for the orthorhombic and rhombohedral phases, respectively. The volume contraction at the phase transition was calculated to be about –0.138%, which is very close to the values reported by Sakai et al (4).

The relationship between polyhedral volumes and their shapes in orthorhombic and rhombohedral perovskites ABO_3 were discussed by Thomas. For orthorhombic perovskites, the volume of the $[AO_{12}]$ polyhedron, V_A, that of the $[BO_6]$ polyhedron, V_B, and their ratio V_A/V_B are given by

$$V_B = \frac{s_1 s_2 s_3}{6},$$

$$\frac{V_A}{V_B} = 6\cos^2\theta_m \cos\theta_z - 1,$$

where s_1, s_2 and s_3 are distances between diagonal vertices of an octahedron, and θ_m and θ_z the tilt angles of the $[BO_6]$ octahedra along [101] and [010] direction of the present setting, respectively.

For rhombohedral perovskites, V_A, V_B, V_A/V_B and octahedral tilt angle, ω, are given by

$$V_B = \frac{\sqrt{3}cs^2}{18},$$

$$V_A = \frac{\sqrt{3}a^2c}{12} - \frac{\sqrt{3}cs^2}{18},$$

原子炉：JRR-3M　装置：HRPD（1）　分野：中性子散乱（構造）

$$\cos\omega = \frac{a}{2s} \text{ and}$$

$$\frac{V_A}{V_B} = 6\cos^2\omega - 1$$

where a and c are the lattice constants in the hexagonal unit cell, and s the edge length of the $[BO_6]$ octahedra. From these equations given by Thomas et al., V_A, V_B and V_A/V_B for both the orthorhombic and rhombohedral phases were calculated and plotted in Fig. 1. We can clearly see the shrinking of V_B at the phase transition and almost linear expansion of V_A at whole temperature range. This figure unambiguously reveals that the volume contraction at the phase transition principally results from the shrinking of the $[BO_6]$ polyhedron.

Thomas introduced a parameter Φ to combine θ_m and θ_z in orthorhombic structure:

$$\Phi = 1 - \cos^2\theta_m \cos\theta_z.$$

Using Φ, V_A/V_B can be simply written as

$$\frac{V_A}{V_B} = 5 - 6\Phi$$

In order to extend Φ to the rhombohedral structure and to study the characteristics of the phase transition in the present system, the degree of tilt in rhombohedral structure is expressed as

$$\Phi = 1 - \cos^2\omega.$$

Using Φ, V_A/V_B is similarly written as

$$\frac{V_A}{V_B} = 5 - 6\Phi$$

V_A/V_B of both orthorhombic and rhombohedral phases in $LaCrO_3$ is plotted as a function of Φ in Fig. 2. V_A/V_B of various known samples having orthorhombic (space group Pnma) and rhombohedral (space group $R\bar{3}c$) structure are also included in the figure. The rhombohedral samples tend to have smaller tilts Φ and larger V_A/V_B values. It is emphasized in the case of $LaCrO_3$ that Φ decreases as the phase transition from the orthorhombic to rhombohedral proceeds, and its phase boundary is located near the limit of the reference values of rhombohedral samples.

It is curious that the $[BO_6]$ polyhedron contracts instead of the $[AO_{12}]$ polyhedron, because the V_B is much tighter than V_A. The same kind of contraction would occur in the structural phase transition of $La(Co_{1-t}Cr_t)O_3$, $(La_{1-t}A_t)CrO_3$ (A = Ca or Sr) system. Further investigations are required to clarify the origin of the V_B contraction.

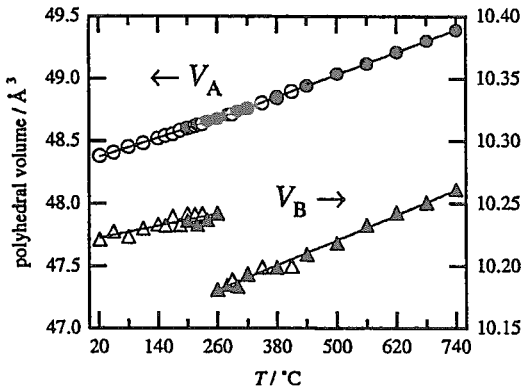

Fig. 1. Temperature variation of the volume of the $[LaO_{12}]$ polyhedron: V_A, and of the $[CrO_6]$ polyhedron: V_B. Circles and triangles express the volume for the orthorhombic and the rhombohedral phases respectively. Data points obtained from experiments with wavelength of 1.82340 Å are represented by filled symbols.

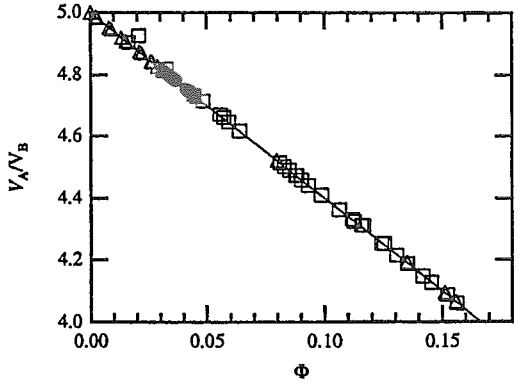

Fig. 2. Variation of V_A/V_B of $LaCrO_3$ with degree of tilt Φ (circles). Triangles and squares represent that of rhombohedral and orthorhombic structure.

References

1) N. W. Thomas and A. Beitollahi: *Acta Crystallogr.* B 50, (1994) 549.
2) N. W. Thomas: *Acta Crystallogr.* B 52, (1996) 16.
3) N. W. Thomas: *Acta Crystallogr.* B 52, (1996) 954.
4) N. Sakai, H. Fjellvag and B. C. Hauback: *J. Solid State Chem.*, 121 (1996) 202.

研究テーマ: 超低温の導入による中性子散乱の研究
表題：超伝導体 $HgBa_2CuO_{4+\delta}$中の核・電子密度分布

1-1-5

Nuclear- and Electron-Density Distribution in the Superconductor $HgBa_2CuO_{4+\delta}$

F. Izumi, S. Kumazawa[1], W.-Z. Hu[2,3], A. Yamamoto[2], K. Oikawa[4] and T. Ikeda

National Institute for Research in Inorganic Materials, 1-1 Namiki, Tsukuba, Ibaraki 305-0044, Japan
[1] Institute of Materials Structure Science, KEK, 1-1 Oho, Tsukuba, Ibaraki 305-0801, Japan
[2] Superconductivity Research Laboratory, 1-10-13 Shinonome, Koto-ku, Tokyo 135-0062, Japan
[3] Tokyo University of Mercantile Marine, 2-1-6 Etchujima, Koto-ku, Tokyo 135-8533, Japan
[4] Japan Atomic Energy Research Institute, Tokai, Naka-gun, Ibaraki 319-1195, Japan

We have recently developed a structure refinement system REMEDY [1] comprising RIETAN for angle-dispersive diffraction [2] and MEED for a maximum entropy method (MEM). MEM analysis and whole-powder-pattern fitting are repeated with REMEDY. In the latter, the diffraction pattern calculated from F_c(MEM) data derived by the Fourier transform of nuclear/electron densities is fit to the observed one to refine parameters irrelevant to the structure. This iterative procedure enables us to model disordered atomic arrangements, covalent bonds, nonlocalized electrons, and anharmonic thermal motion more adequately than the conventional Rietveld method.

We prepared a superconductor $HgBa_2CuO_{4+\delta}$ (Hg-1201; T_c = 97 K) where the content of carbonate ions substituting for O2−Hg−O2 groups was minimized to distribute excess oxygen atoms very uniformly by O_2 annealing for a relatively long time [3]. Neutron powder diffraction data of Hg-1201 were measured on HRPD with a wavelength of 1.823 Å. In structure refinements with both neutron and X-ray diffraction data, MEM-based whole-pattern fitting gave lower R factors than conventional Rietveld analysis [1,4]. Such improvements in profile fits are achieved by more sufficient representation of the real structure with nuclear/electron densities than with structure parameters in Rietveld analysis.

Figure 1 shows nuclear and electron densities on the (100) plane of Hg-1201. Interposition of bonding electrons between Hg and O2 and between Cu and O1 is clearly recognized in Fig. 1(b). The presence of a region where electron densities are negligibly low between the Cu and O2 atoms indicates nearly electrostatic interaction between them. Despite the assumption of harmonic thermal motion in the Rietveld analysis prior to the REMEDY cycles, the isosurface of nuclear densities for O2 considerably deviated from an ellipsoid. In fact, the analysis of anharmonic thermal vibration for O2 afforded significant cubic and quartic anharmonic terms.

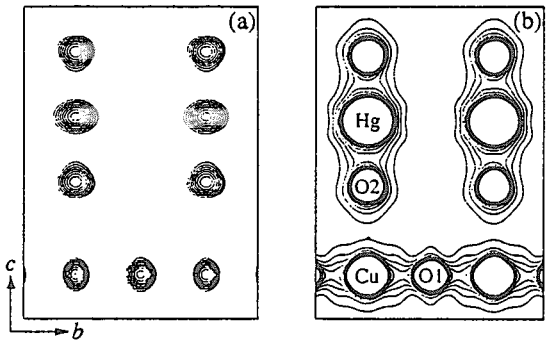

Fig. 1 (a) Nuclear- and (b) electron-density maps for the (100) plane in Hg-1201.

Interstitial oxygen defects, O3, at (1/2,1/2,0) are responsible for hole doping in Hg-1201. In Rietveld analysis, the isotropic atomic displacement parameter, B, of a slightly occupied site like O3 is often fixed arbitrarily at a typical value, *e.g.*, 1 Å^2, to refine only its occupancy, g, on account of very high correlation between B and g. We took more sophisticated approaches to get more reliable values of g(O3) and B(O3). That is, g(O3) was estimated at 0.14 by integrating nuclear densities of O3, and B(O3) at 1.5 Å^2 by evaluating mean square displacements. This technique is useful for determining B and g for partially occupied sites from nuclear densities obtained by the MEM.

References

[1] F. Izumi *et al.*: Mater. Sci. Forum, in press.
[2] F. Izumi and T. Ikeda: Mater. Sci. Forum, **321−324** (2000) 198.
[3] A. Yamamoto *et al.*: J. Low Temp. Phys. **117** (1999) 789.
[4] F. Izumi *et al.*: Physica C (Amsterdam), in press.

原子炉：JRR-3M　　装置：HRPD(1G)　　分野：構造

研究テーマ：超低温の導入による中性子散乱の研究

表題：粉末中性子回折による MEM-based Whole Pattern fitting を用いた K_x@K-LTA の研究

1-1-6

Neutron Powder Diffraction study of K_x@K-LTA using the MEM-based whole pattern fitting

T. Ikeda, T. Kodaira[1] and F. Izumi

National Institute for Research in Inorganic Materials, Tsukuba, Ibaraki 305-0044, Japan
[1]National Institute of Materials and Chemical Research, Tsukuba, Ibaraki 305-8565, Japan

Crystal structure of the K clusters in K_x-doped zeolite K-LTA (x = 4.9, 5.8) with ferromagnetic properties were studied by using neutron powder diffraction.

A detailed crystallographic study is indispensable for understanding the mechanism of the ferromagnetism because the mode of ordering in the clusters affects a magnetic ordering. Especially, nuclear density distribution gives us very important information to understand a spatial view of K clusters. Neutron powder diffraction data of x = 4.9 and 5.8 were collected at 11 K and 7 K, respectively, on the HRPD high-resolution powder diffractometer with λ = 1.824 Å at the JAERI JRR-3M [1,2].

The space group of K_x-doped zeolite K-LTA was determined F23 with lattice constant of twice α-cage size a = 24.7065(9) Å at x = 4.9 and 24.6573(3) Å at x = 5.8, which led to alternate ordering of two kind of K clusters of different K^+ ions location between adjacent α-cages in framework of LTA. All atom location is clearly shown by nuclear density distributions which were obtained using the MEM-based whole-pattern fitting method derived from combination the Rietveld refinement and the MEM calculation by REMEDY & RIETAN-98 [3] .

Preliminary Rietveld refinements revealed almost structural view and K^+ ions positions. However, disordering of K atoms cannot be sufficiently represented in these structure refinements. After one iteration of the MEM-based whole-pattern fitting, R_B slightly decreased from 2.82% to 2.32%, and R_F from 1.55% to 1.07% for $K_{4.9}$@K-LTA in Fig. 1, respectively. Figure 2 shows nuclear density map of (110) plane. K^+ ions are observed with different arrangements in adjacent α-cages.

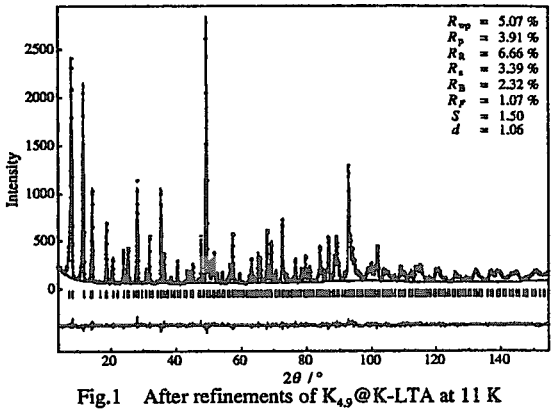

Fig.1 After refinements of $K_{4.9}$@K-LTA at 11 K

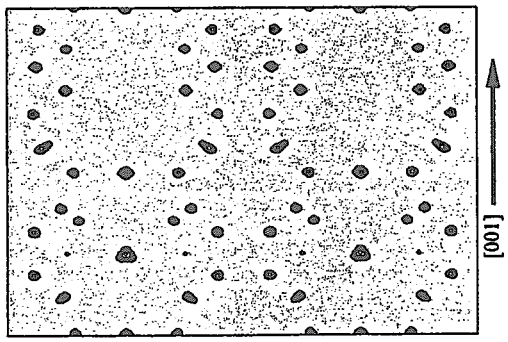

Fig.2 Nuclear density distributions of $K_{4.9}$@K-LTA.

The difference in the number of K atoms between the two types of the α-cages was ca. two in a sample with the highest degree of spontaneous magnetization, which will give rise to the ferromagnetism with antiferromagnetic components.

Reference

[1] T. Ikeda, T. Kodaira, F. Izumi and T. Kamiyama, Chem. Phys. Lett., 318, 93 (1999).
[2] T. Ikeda, T. Kodaira, F. Izumi and S. Kumazawa, Mol. Cryst. Liq. Cryst., in press.
[3] F. Izumi, T. Ikeda, Mater. Sci. Forum, 321-324 198-203 (2000).

原子炉：JRR-3M　　装置：HRPD　　分野：中性子散乱（構造）

研究テーマ：超低温の導入による中性子散乱の研究
表題：粉末中性子回折によるトンネル構造を持つ Mn 酸化物 α-MnO_2 の研究

1-1-7 Neutron diffraction study of open tunnel oxide α-MnO_2

N. Kijima*, T. Ikeda†, K. Oikawa‡, F. Izumi†, and Y. Yoshimura*

* *National Institute of Materials and Chemical Research, Tsukuba, Ibaraki 305-8565, Japan*
† *National Institute for Research in Inorganic Materials, Tsukuba, Ibaraki 305-0044, Japan*
‡ *Japan Atomic Energy Research Institute, Tokai, Ibaraki, 319-1195, Japan*

Introduction

Alminosilicates, including zeolites, clay minerals, and mesoporus silicates, are well known families of porous crystals. Recently, much attention has been focused on the porous materials of transition metal oxides.

It is known that α-MnO_2 alone has a tunnel structure without any large stabilizing cations in its tunnel, whereas almost of porous manganese oxides have some large stabilizing cations in its tunnels. Rossouw *et al.* [1] have synthesized the α-MnO_2 specimen without any large stabilizing cations for the first time, whereas it might contain H_3O^+ in its tunnel. They have also investigated the crystal structure of hydrated and dehydrated α-MnO_2 specimens by using the neutron diffraction technique. However, nature and locations of residual H_2O molecules in its tunnel remain unclear at present.

We have recently succeeded in synthesizing a well-crystallized α-MnO_2 specimen by a redox precipitation using ozone oxidation. To verify and clarify the nature of residual H_2O molecules in the tunnel structure, neutron diffraction investigations have been made in this work.

Experimental

A well-crystallized α-MnO_2 specimen was prepared by oxidation of $MnSO_4$ with ozone gas in H_2SO_4 solution at 353 K. Scanning electron microscope images indicated the particles of the α-MnO_2 have needle-like crystals. This α-MnO_2 specimen contained residual H_2O molecules in its tunnels on the based of a temperature-programmed desorption (TPD) analysis.

Neutron powder diffraction data were taken at room temperature on the high-resolution powder diffractometer (HRPD) equipped with Si (533) monochromator with a neutron wavelength of 1.16 Å. Data were collected between $2\theta = 5°$–$165°$ with a step interval of 0.05°. The deuterated specimen was located in a cylindrical vanadium can with an inner diameter 12 mm. The collected data were analyzed by a Rietveld-refinement program RIETAN-2000, and the technique of partial profile relaxation was applied to a few reflections.

Results and discussion

Figure 1 shows the preliminary result of the Rietveld-refinement pattern for the neutron powder diffraction data of the deuterated α-MnO_2·0.3D_2O specimen at room temperature. The lattice constants are a = 9.7387(10) Å and c = 2.8438(2) Å. The technique of partial profile relaxation considerably improves fits between observed and calculated profiles, although highly asymmetric reflections due to anisotropic broadening.

The amount of water in the tunnel is estimated to be 0.1 per α-MnO_2 molecule from the result of the Rietveld-refinement, which is consistent with a result of the TPD analysis. These detailed experimental results will be published elsewhere [2]

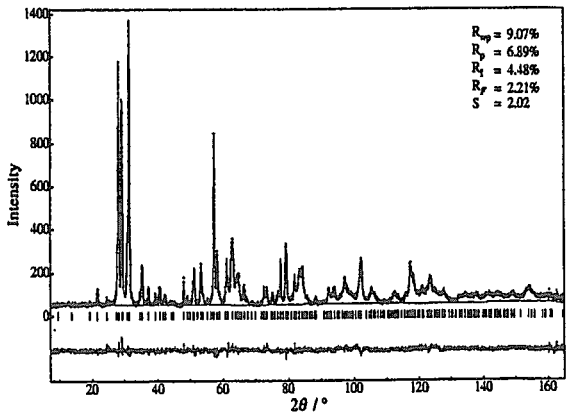

Fig. 1 Rietveld-refinement pattern for the neutron powder diffraction data of the deuterated α-MnO_2·0.3D_2O.

References

[1] M. H. Rossouw *et al. Mat. Res. Bull.* 27, 221 (1992).
[2] N. Kijima *et al.*, in preparation.

原子炉：JRR-3M　　装置：HRPD　　分野：中性子回折（構造）

研究テーマ：半磁性電気伝導体の磁性と化学構造
表題：$La_{1-x}Ca_xMnO_3$ x=0.18と0.25の中性子回折測定

1-1-8 Neutron diffraction study of $La_{1-x}Ca_xMnO_3$ with x= 0.18 and 0.25

Y. Ono[1], Shahnaz Begum[1], H. Fujishiro[2], M. Ikebe[2], T. Fukase[3] and T. Kajitani[1]
[1] Graduate School of Engineering, Tohoku University, Sendai, 980-8579
[2]Faculty of Engineering, Iwate University, Morioka, 020-8551
[3]IMR, Tohoku University, Sendai, 980-8577

Perovskite-based manganese oxides, $La_{1-x}A_xMnO_3$, where A refers to Ca or Sr, have attracted much attention since the discovery of colossal magnetoresistance [1]. The Sr-doped manganite undergoes successive phase transitions in the vicinity of x=1/8 [2]. We have studied deformation of MnO_6 octahedron and magnetic structure of $La_{1-x}Ca_xMnO_3$ with x～1/8 by means of neutron powder diffraction.

Powder samples of $La_{1-x}Ca_xMnO_3$ with x=0.18 and 0.25 were prepared by a conventional solid state reaction from stoichiometric mixture of La_2O_3, Mn_2O_3 and $CaCO_3$. Their magnetizations were measured by a SQUID magnetometer (Quantum design Co.) in the range from 4.2 K to 290 K. Neutron powder diffraction experiments were carried out using HRPD installed at JRR-3M (JAERI). The Pnma type space symmetry was assumed for both samples. Structure parameters and spin arrangement were determined using a Rietveld analysis program, GSAS [3]. Figure 1 shows observed, calculated and difference profiles of powder neutron diffraction intensities of $La_{0.75}Ca_{0.25}MnO_3$ at 8K. Figure 2 shows temperature variation of Mn-O bond lengths in the sample with x=0.18 (open circles). A large breathing-type *Jahn-Teller (J-T)* distortion was observed for the MnO_6 octahedron at low temperatures, i.e., in MnO_4 square plane, two equivalent Mn-O(2') bonds become short while others elongate. Mn-O(1) distance

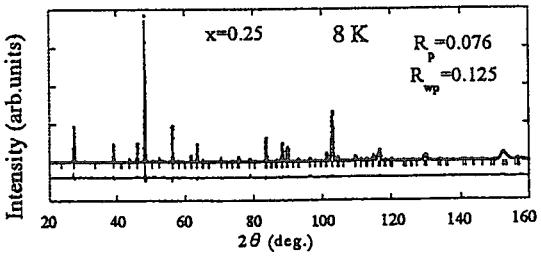

Figure 1 Observed, calculated and difference neutron diffraction profiles of $La_{0.75}Ca_{0.25}MnO_3$.

remains practically unchanged at low temperatures. As shown in Fig.2, the *J-T* distortion of this sample is comparable to that of $La_{1-x}Sr_xMnO_3$ with x=0.125 (filled circles) [4]. However, the sample with x=0.25 (open square) does not show such large

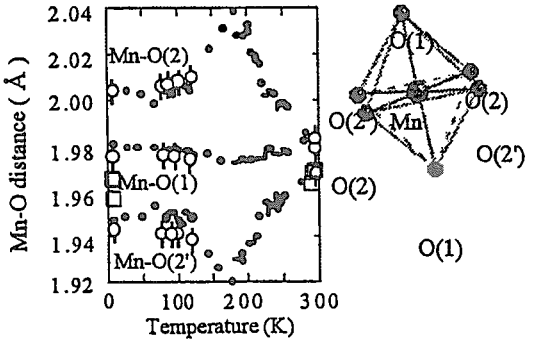

Fig.2 Temperature variations of Mn-O bond lengths in $La_{0.82}Ca_{0.18}MnO_3$ (open circles) and in $La_{0.875}Sr_{0.125}MnO_3$ (filled circles) [4]. Open squares represent Mn-O bond lengths of $La_{0.75}Ca_{0.25}MnO_3$ at 8 K and 293 K.

distortion at 8 K. The magnetic spins on Mn ions are almost colinearly oriented parallel to [001] direction in both samples at low temperatures. Figure 3 shows the calculated magnetic moments of Mn ion (x=0.18) and the magnetizations measured under an applied field of 0.5 T.

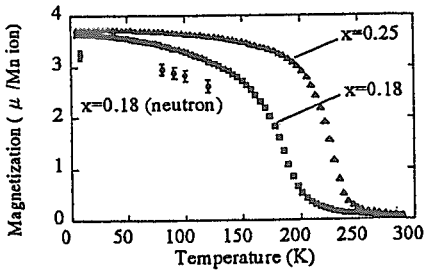

Fig.3 Magnetizations as a function of temperature. ● represents the neutron diffraction data. ▲ and ■ are SQUID data.

References

[1] Millis, A.J. Nature 392(1998)147.
[2] Yamada, Y. *et al.* Phys.Rev.Lett.77(1996)904.
[3] von Dreele, R.B. & Larson, A.C. General Structure Analysis System, University of California (1998).
[4] Argyriou, D.N. *et al.* Phys.Rev.Lett.76(1996)3826.

原子炉：JRR-3M　　装置：HRPD(1G)　　分野：磁性・構造

研究テーマ：半磁性電気伝導体の磁性と化学構造
表題：超伝導体、$Li_{0.18}ZrNBr$と母相β-ZrNBrの結晶構造

1-1-9 Structures of layered superconductor, $Li_{0.18}ZrNBr$, and the parent compound ß-ZrNBr

S. Shamoto[1], Y. Kato[1], K. Oikawa[2], T. Kajitani[1]
[1]*Department of Applied Physics, Faculty of Engineering, Tohoku University, Sendai 980-8579*
[2]*Advanced Science Research Center, Japan Atomic Energy Research Institute, Tokai-mura, 319-1195*

One of the novel honeycomb lattice superconductors, $Li_{0.18}ZrNBr$, and the parent compound, β-ZrNBr, have been studied from a structural point of view by means of Rietveld analysis technique using powder neutron diffraction data with the incident wave length of 1.1636 Å at T=8 K. In the ZrNBr-system, the sliding of $[ZrNBr]_2$ blocks by Li intercalation has not taken place unlike the other isostructual compounds, such as A_xHfNCl or A_xZrNCl (A; alkali metals) [1,2]. Structural parameters of ß-ZrNBr and $Li_{0.18}ZrNBr$ are shown in Table I. The ratio of electronic density of states for three superconductors, $Li_{0.18}ZrNBr$, $Li_{0.16}ZrNCl$, and $Na_{0.29}HfNCl$, has been estimated to be 1.00:1.05:1.23 from each bond length between the nearest neighbor transition metals. The ratio corresponds well to their superconducting transition temperatures, i.e., 12.6 K, 15.0 K and 20.0 K, respectively. This could be explained in terms of the simple BCS theory, indicating the importance of electronic density of states in the present novel layered superconductors.

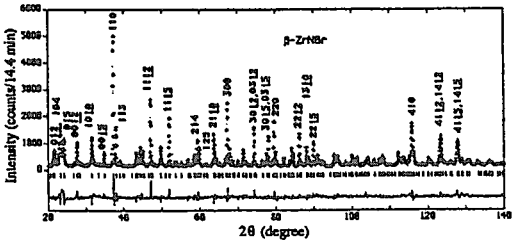

Fig. 1. Neutron diffraction pattern of ZrNBr.

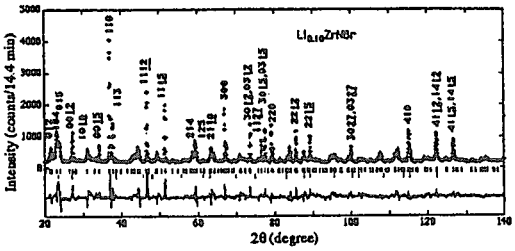

Fig. 2. Neutron diffraction pattern of $Li_{0.18}ZrNBr$.

Table I. Structural parameters, a. ß-ZrNBr, b. $Li_{0.18}ZrNBr$ [3].

a. R-3m; a=3.6341(2) Å, c=29.157(2) Å

atom	site	g	x	y	z
Zr	6c	1	0	0	0.12348(9)
N	6c	1(fixed)	0	0	0.19725(7)
Br	6c	1(fixed)	0	0	0.38847(9)

R_I=6.27%, R_p=10.88%, R_{wp}=13.69%, R_e=5.58%, B_{eq}^{all}=0.41(3) Å^2

b. R-3m; a=3.6504(3) Å, c=29.568(3) Å

atom	site	g	x	y	z
Zr	6c	1	0	0	0.1280(2)
N	6c	1(fixed)	0	0	0.2002(2)
Br	6c	1(fixed)	0	0	0.3882(2)
Li	3a	0.36(fixed)	0	0	0

R_I=12.32%, R_p=14.41%, R_{wp}=18.79%, R_e=5.58%, B_{eq}^{all}=0.03(5) Å^2

References

[1] S. Shamoto, T. Kato, Y. Ono, Y. Miyazaki, K. Ohoyama, M. Ohashi, Y. Yamaguchi and T. Kajitani, Physica C 306, 7 (1998).
[2] S. Shamoto, K. Iizawa, M. Yamada, K. Ohoyama, Y. Yamaguchi and T. Kajitani, J. Phys. Chem. Solids 60, 1431 (1999).
[3] S. Shamoto, Y. Kato, K. Oikawa and T. Kajitani, in preparation (ASR-2000).

原子炉：JRR-3M　　装置：HRPD(1G)　　分野：超伝導・構造

研究テーマ：コバロキシム錯体結晶の光異性化反応における水素移動
表題：3-シアノプロピルコバロキシムにおける 3-1 光異性化反応の粉末中性子回折による研究

1-1-10

Powder Neutron Diffraction Study of the Crystalline-State 3-1 Photoisomerization of the 3-Cyanopropyl Cobaloxime Complex

T. Ohhara, H. Uekusa, T. Ozeki, Y. Ohashi, K. Oikawa[1], Y. Morii[1]

Dept. of Chemistry and Materials Science, Tokyo Inst. of Tech., Meguro-ku, Tokyo 152-8551, Japan
[1]Japan Atomic Energy Research Institute, Tokai, Ibaraki 319-1195, Japan

In recently works[1-3], we showed that single crystal neutron diffraction became a powerful method to clarify the mechanism of crystalline-state reactions because the migration of deuterium atoms, which were introduced into the reactive part as markers, according to the crystalline-state reaction can be observed. However, a large single crystal (~2mm) is required for single crystal neutron diffraction. It is usually difficult to prepare such a large single crystal and to penetrate the light into the crystal. On the other hand, powder neutron diffraction can be carried out with small crystals, which is easier to prepare and penetrate the light. In this work, the migration of deuterium atoms according to the 3-1 photoisomerization of (3-cyanopropyl-$d_2^{\alpha,\alpha}$)[(*R*)-1-phenylethylamine-d_{11}]cobaloxime-d_{14} (*1* : Fig. 1) was studied by powder neutron diffraction.

In compound *1*, two deuterium atoms were introduced to the α-carbon of 3-cyanopropyl group as markers, and other deuterium atoms were in order to prevent the incoherent neutron scattering by hydrogen atoms. Two powder neutron diffraction measurements were carried out by HRPD at the 1G port of JRR-3M reactor. One was the compound *1* before irradiation (*1-ini*) and another was the *1* after 20 days exposure of visible light (*1-end*). The wavelength was 1.823Å, the temperature was 90K and the $2\theta_{max}$ was 162.5°.

The rietveld structure refinement was carried out for the *1-ini* with the initial model structure precedently determined by single crystal X-ray diffraction. The result of rietveld profile fitting is shown in Fig. 2. The positions of hydrogen and deuterium atoms in the obtained structure was consistent with the molecular structure of *1*, and there was no irregular bond lengths and angles. The structure of *1-end* is now under investigation.

References

[1] Y. Ohgo et al., Enantiomer 2 (1997) 241-248
[2] T. Ohhara et al., Chem. Lett. (1998) 365-366
[3] T. Ohhara et al., Acta. Cryst. B56 (2000) 245-253.

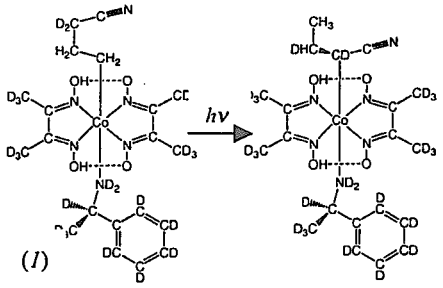

Fig. 1 Crystalline-state 3-1 photoisomerization of compound *1*.

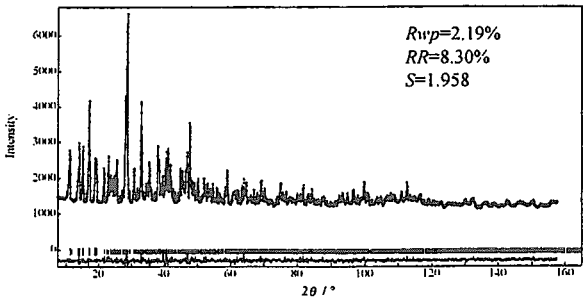

Fig.2 Result of the rietvled rifinement of *1-ini*.

原子炉：JRR-3M　　装置：HRPD(1G)　　分野：中性子散乱(構造)

研究テーマ：コバロキシム錯体結晶の光異性化反応における水素移動
表題：嵩高い置換基を持つコバロキシム錯体における光ラセミ化反応の BIX-3 による解析

1-1-11

Single Crystal Neutron Diffraction Study of the Crystalline-State Photoracemization of Cobaloxime Complex with Bulky Alkyl Group by BIX-3 Diffractometer

H. Imura, T. Ohhara, H. Uekusa, T.Ozeki, Y. Ohashi, I. Tanaka[1], K. Kurihara[1] and N. Niimura[1]

Dept. of Chemistry and Materials Science, Tokyo Inst. of Tech., Meguro-ku, Tokyo 152-8551, Japan
[1]Japan Atomic Energy Research Institute, Tokai, Ibaraki 319-1195, Japan

Crystalline-state photoreaction of cobaloxime complexes which have intramolecular Co-C bond have been greatly interested as a model reaction of the bioactivation of Vitamin B_{12}, and various reactions of cobaloximes have been investigated by X-rays. Recently, the crystalline-state photoracemization of [(*R*)-bis(ethoxycarbonyl)ethyl](pyridine)cobaloxime (*1a*) was reported[1]. This reaction was very interested because the bulky (*R*)-bis(ethoxycarbonyl)ethyl group was racemized in the restricted environment of crystal lattice, however, the mechanism of the racemization was obscure. In this work, the hydrogen atom bonded to the α-carbon atom of the reactive group was replaced with the deuterium atom and the migration of this deuterium atom according to the racemization was followed by single crystal neutron diffraction to clarify the mechanism of this photoracemization.

The crystal of partly deuterated *1a* (*1b*) was prepared. The hydrogen atoms of dimethylglyoximato and pyridine ligands were also replaced with deuterium atom to prevent the incoherent neutron scattering from hydrogen atoms. The near infrared light (>680nm) was irradiated to the crystal for 7 days. After irradiation, the single crystal neutron diffraction measurement was carried out by BIX-3 diffractometer at the 1G port of the JRR-3M reactor. The crystal size was 2.5x1.6x1.0mm, and the wavelength was 2.35Å. In the 3 days measurement at room temperature, 656 independent reflections were obtained.

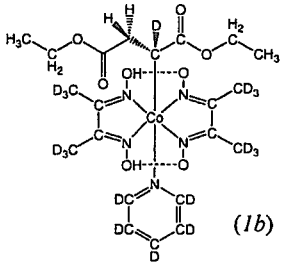
(*1b*)

As a result of structure refinement, the inverted (*S*)-bis(ethoxycarbonyl)ethyl group was observed with 35% occupancy. In this group, the deuterium atom was also bonded to the α-carbon atom. This result indicates that the crystalline-state photoracemization proceeds with the rotation of bis(ethoxycarbonyl)ethyl radical produced by irradiation as shown in Figure 1. The free rotation of the single bond between the α-carbon and its neighbor carbon atoms in alkyl radical would make such inversion mechanism possible.

Reference

[1] H. Sato and Y. Ohashi, Bull. Chem. Soc. Jpn. **72** (1999) 367-375.

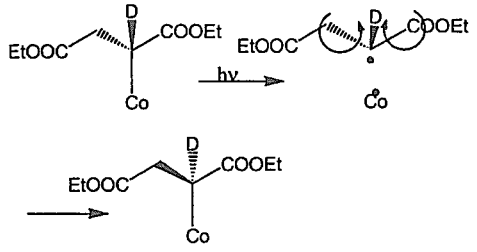

Fig. 1 Mechanism of the crystalline-state photo-inversion of bis(ethoxycarbonyl)ethyl group

原子炉：JRR-3M　　装置：BIX-3(1GA)　　分野：中性子散乱(構造)

研究テーマ：超低温の導入による中性子散乱の研究
表　　題　：酸化リチウムの格子力学

1-1-12 Lattice Dynamics of Lithium Oxide

Yoshinobu ISHII and Yukio MORII

Advanced Science Research Center, Japan Atomic Energy Research Institute
Tokai-mura, Naka-Gun, Ibaraki 319-1195, Japan

To clarify the fundamental properties of lithium oxide (Li_2O), measurements of phonon dispersion relations of Li_2O are very significant. The sample used in this measurements was a single crystal of $^7Li_2O$ and experiments were mainly carried out by the TAS-1 spectrometer installed at JRR-3M in JAERI. Measurements were conducted with fixed incident neutron energy by a constant-q method at 293 K and 700 K.

Figure 1 shows the phonon dispersion relations of Li_2O along three principal crystallographic axes. The open and solid circles indicate the transverse and longitudinal modes, respectively.

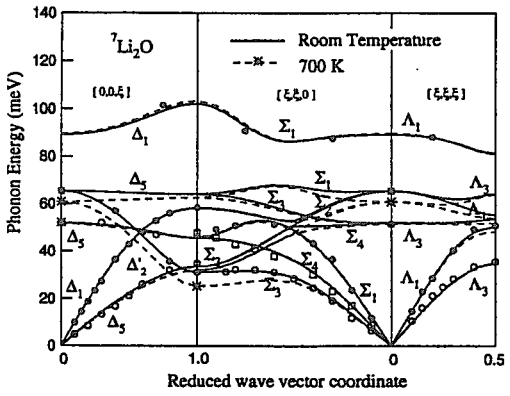

Fig.1. Phonon dispersion relations of Li_2O at 293 K and 700 K. Solid and broken lines indicate the calculated dispersion relations at 293 K and 700 K, respectively.

The motion of the ion is as follows in a matrix form[1)]

$$M\omega^2 U = (R + ZCZ)U + (T + ZCY)W,$$
$$0 = (\widetilde{T} + YCZ)U + (\vartheta + YCY)W.$$

The notations for the matrices in above equations are the same as defined by Cowley et al.[1)] The force constants acting between ions are as follows

$$\frac{e^2 A_i}{v} = \left(\frac{\partial^2 V}{\partial r^2}\right) \quad and \quad \frac{e^2 B_i}{v} = \left(\frac{1}{r}\frac{\partial V}{\partial r}\right).$$

We calculate the force constants using all measured data by a best fitting method. Obtained phonon dispersion relations are shown in Fig.1 by solid lines and the force constants are listed in Table 1. In this table the Farley's results are also listed as a reference.

TableI. Force constant of Li_2O at 293 K.

Force constants		Units	Present Cal.	Farley's result[2)]
A_1	O-Li^1	e^2/v	11.43	11.97
B_1	O-Li^1	e^2/v	-1.34	-1.46
A_2	Li^1-Li^2	e^2/v	0.16	-0.25
B_2	Li^1-Li^2	e^2/v	-0.005	-0.09
A_3	O-O	e^2/v	0.03	-0.89
B_3	O-O	e^2/v	-0.05	-0.05
A_4	Li^1-Li^1	e^2/v	0.11	0.15
B_4	Li^1-Li^1	e^2/v	-0.01	-0.08
Z_{Li}		e	0.95	1.0*
α_O		$10^{-30}m$	2.39	2.46
d_O		e	0.71	-0.76
α_{Li}		$10^{-30}m$	0.002	-0.05
d_{Li}		e	0.001	0.02

A frequency distribution for Li_2O was calculated using a mesh of 744299 q-vectors in the reducible 1/48 volume of the first Brillouin zone. The frequency distribution is shown in Fig.2 as a histogram.

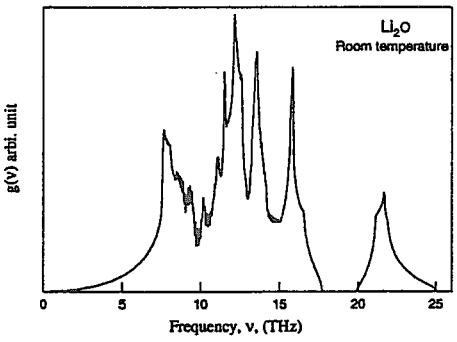

Fig.2. Frequency distribution of Li_2O at 293 K.

From this measurement, we obtained some fundamental knowledge for Li_2O and found that phonon energies for the Δ_2' mode drastically decreased with increasing temperature.

1) R.A. Cowley, W. Cochan, B.N.Brockhouse and A.D.B Woods, Phys. Rev. **131** (1963) 1020.
2) T.W.D. Farley, H. Hayes, S. Hull, R. Ward, M.T. Huchings and M. Alba, Solid State Ionics **28-30** (1988) 189.

原子炉：JRR-3M　　装置：TAS-1(2G)　　分野：中性子散乱（構造）

研究テーマ ： リラクサ-PZNの格子振動

表題 ： 無秩序ペロフスカイトPZN ($Pb(Zn_{1/3}Nb_{2/3})O_3$) の格子動力学

1-1-13 Lattice dynamics of disordered Perovskite PZN ($Pb(Zn_{1/3}Nb_{2/3})O_3$)

I. Tomeno, S. Shimanuki, Y. Tsunoda[1], and Y. Ishii[2]

Research and Development Center, Toshiba Corporation, Saiwai-ku, Kawasaki 210-8582
[1]School of Science and Engineering, Waseda University, Shinjuku-ku, Tokyo 169-8555
[2]Japan Atomic Energy Research Institute, Tokai, Ibaraki 319-11

Relaxor is the important industrial material which is applied to the ultrasonic devices, actuators and multi-layer capacitors due to its huge piezoelectric and dielectric response in wide temperature range. The microscopic mechanism of the properties, however, such as a glass-like phenomenon are still not well known. To study the essence of the phenomena microscopically, phonon dispersion relation of PZN ($Pb(Zn_{1/3}Nb_{2/3})O_3$) was measured by neutron inelastic scattering. The industrial PZN includes about 10% of Ti impurities, but we used pure PZN single crystal in order to avoid the effects of the impurities.

Phonon data were taken along the symmetric directions above and below the transition temperature (T_C～100 ° C). The dispersion relation curves obtained above the transition temperature (T=150° C) is given in Fig. 1. The dispersion curves for typical dielectric materials with the perovskite structure are also given for comparison. The [1 1 0] TA_2 phonon branch of the PZN is very special. The phonon frequency is very low at small q-region. In addition, another phonon mode which is not observed for other materials seems to exist. One of possible explanations of this feature is a resonance phonon mode around 5 meV; Zn and Nb are randomly distributed in B site of perovskite structure in PZN and the mass ratio of these elements is rather large (65 : 93). Thus, the resonance phonon mode is anticipated for this system as a mass-defect random system. In the [1 0 0] T branch phonon line width studied by the constant-q mode abruptly increases around q ～0.2. This is consistent with above discussion if we assume that the resonance phonon energy is about 5 meV. Further measurements are desired to confirm the resonance phonon mode.

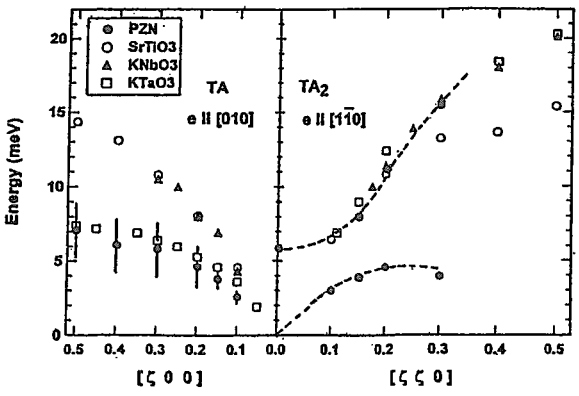

原子炉： JRR-3M　　装置： TAS-1(2G)　　分野： 中性子散乱(構造)

研究テーマ：A_2BX_4型強誘電体の整合-不整合相転移と相転移機構
表題：Rb_2CoCl_4の整合-不整合相転移における中性子散乱

1-1-14 Neutron Scattering Study of the Normal-Incommensurate Phase Transition in Rb_2CoCl_4

H. Shigematsu, Y. Kondo, Y. Kawamura[1] and T. Matsui

Department of Quantum Engineering, Nagoya University, Nagoya 464-8603, Japan
[1]Department of Physics, Yamaguchi University, Yamaguchi 753-8512, Japan

Rubidium tetrachlorocobaltate, Rb_2CoCl_4, belongs to a family of crystals with the β-K_2SO_4 type structure such as Rb_2ZnCl_4. Three phase transitions are observed at temperatures T_i = 294 K, T_C = 199 K and T_3 = 66 K.

Gesi pointed out an empirical law between the pressure coefficient of the transition temperature dT_i/dp and the mechanisms of the normal-incommensurate phase transition for various β-K_2SO_4 type ferroelectrics: a displacive type transition temperature has a negative coefficient, while an order-disorder type transition temperature has a positive coefficient.[1)] In Rb_2CoCl_4, although the absolute value of the pressure coefficient is small, the coefficient is negative. Therefore, we expect that the underdamped soft modes will be observable in the normal and low-temperature phases.

As the first step, in order to clarify the behavior of the phase and the amplitude modes below T_i (below room temperature), we performed inelastic neutron scattering experiments by using the triple-axis spectrometers (4G and C1-1) at JRR-3M of JASRI. Single crystals were grown from melt by the Bridgman method. Energy scans were done with the fixed incident neutron momentum k_i = 2.57 Å at 4G and k_i = 1.55 Å at C1-1. The data collections were carried out in the (a^*, c^*) scattering planes.

Figure 1 shows the neutron scattering spectra at Q = (2 0 4/3) at 30 K. Two excitation peaks can be seen at about 1.3 and 4.8 meV. These excitation peaks correspond to the phase mode and 37 cm^{-1} $a(cc)b$ Raman active mode (amplitude mode), respectively.[2)] In addition, the phonon dispersion curves, which were almost the same as K_2SeO_4, were confirmed at low-temperature.

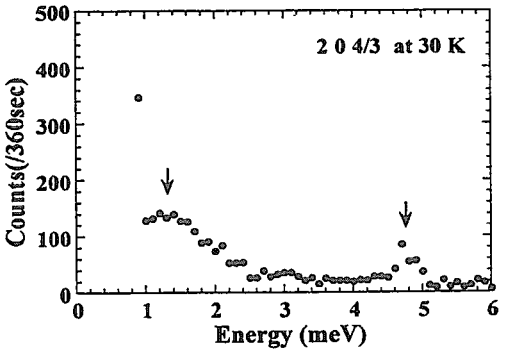

Fig. 1 Neutron scattering spectrum at 204/3 at 30 K. The excitation peaks of the phase and amplitude modes are indicated by arrows.

The phase and amplitude modes, which make a contribution to the normal-incommensurate phase transition, are clearly observable in the low-temperature phase. Therefore, the normal-incommensurate is considered to be a displacive type.

The behavior of phonons in the normal phase of Rb_2CoCl_4 will be investigated in our study.

References

1). K. Gesi: J. Phys. Soc. Jpn. **59** (1990) 1841.
2). V. I. Torgashev, Yu. I. Yuzyuk, F. Smutny, P. Vanek and B. Brezina: Phy. Stat. Sol. (b) **154** (1989) 777.

JRR-3M, GPTAS(4G) and HER(C1-1), 1. Structures & Excitations

研究テーマ：$CuGeO_3$の中性子非弾性散乱
表題：中性子非弾性散乱による$CuGeO_3$のフォノン分枝測定

1-1-15
Lattice Dynamics in $CuGeO_3$ by Inelastic Neutron Scattering

M. Nishi, K. Kakurai, Y. Fujii, S. Katano[1], and J. Akimitsu[2]

Neutron Scattering Laboratory, ISSP, University of Tokyo, Tokai, Ibaraki, 319-1106
[1]ASRC, JAERI, Tokai, Ibaraki, 319-1196
[2]Department of Physics, Aoyama-Gakuin University, Setagaya-ku, Tokyo, 157-8572,

The spin-Peierls transition is accompanied with an intrinsic lattice instability in a system of quantum mechanical antiferromagnetic chains, where the spins (S = 1/2) are interacting via a Heisenberg exchange interaction and are also coupled to a three-dimensional lattice. In the case of the first inorganic spin-Peierls compound $CuGeO_3$, the magnetic one-dimensionality is not better than that of $KCuF_3$, and hence the origin of the spin-Peierls transition may stem from the small deformation energy of the crystal lattice. Oxygen atoms play an important role for an alternation of exchange interaction in CuO_2 chain along *c*-axis. Phonon measurements have been performed on various phonon branches using a single crystal but phonon softening has not been observed so far [1]. Recently the longitudinal phonon propagating along *b**-direction was measured with high resolution by inelastic neutron scattering, and it was clarified that an optical phonon branch exists near the acoustic longitudinal phonon branch [2].

In this study the phonon measurement of $CuGeO_3$ has been performed in (*h*, *k*, 0) scattering plane in the reciprocal lattice space at RT by means of inelastic neutron scattering on ISSP-PONTA spectrometer installed at the research reactor JRR-3M, Japan Atomic Energy Research Institute (JAERI), in Tokai, Japan. Fig. 1 shows the raw data of inelastic neutron scattering taken at several *Q* positions of (*h*+*q*, *k*, 0) with E_f = 14.7 meV at RT (see Fig. 1). These phonon profiles are composed of two peaks which are corresponding to acoustic and optical dispersion branches propagating along the *a**-direction at lower and higher energy side, respectively. We can recognize that the phonon peaks are observed at almost identical energy values for each *q* point (*q*=0.2, 0.3, 0.4 *a**) in all three different zones around the Bragg points,

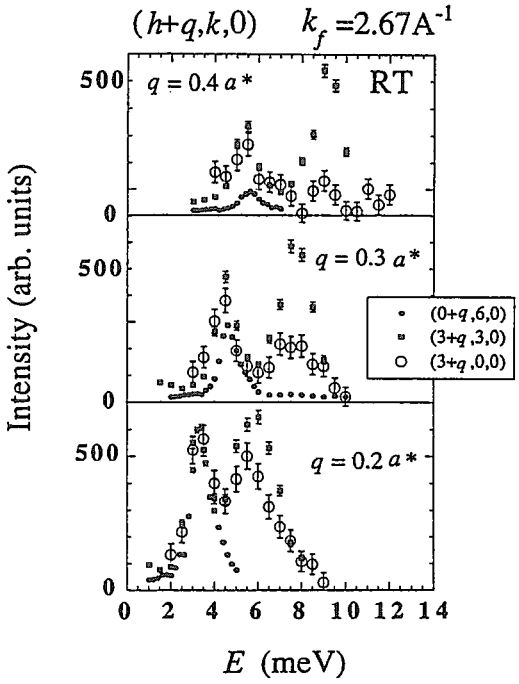

Fig. 1. Neutron scattering profiles at (*h*+*q*, *k*, 0) with E_f = 14.7 meV. Vertical bars show statistical errors.

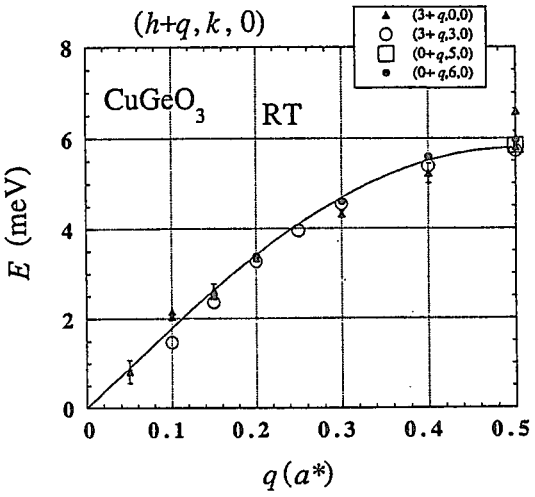

Fig. 2. The phonon dispersion along a^*-direction.

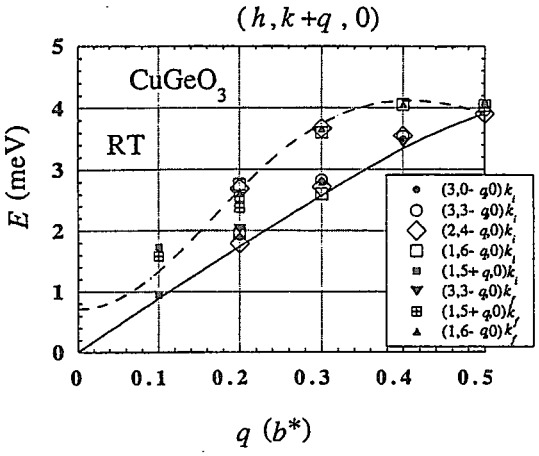

Fig. 3. The phonon dispersion along b^*-direction. The longitudinal and transverse modes have nearly the same energies in *ab* plane.

(0, 6, 0), (3, 3, 0), and (3, 0, 0). These energy values are plotted against q in Fig. 2 as the phonon dispersion propagating along the a^*-direction. These results indicates that the energy of transverse acoustic phonon which is propagating along the a^*-axis and polarized along b^*-axis (abbreviated by a^*-TA(b^*)), is equal to that of the longitudinal acoustic phonon which is propagating along the a^*-axis (abbreviated by a^*-LA). The phonon dispersion branch propagating along the b^*-direction has also the similar behavior as shown in Fig. 3. In the figure, the dispersion of a longitudinal optical phonon branch is also shown, for which the softening can clearly be observed.

The characteristic feature of phonon dispersion branches in (h, k, 0) surface is that the energy of b^*-TA(a^*) is equal to that of b^*-LA with the energy of 4 meV at zone boundary and that the energy of a^*-TA(b^*) is equal to that of a^*-LA with the energy of 6 meV at zone boundary. These results are very rare in solid state compounds. We speculate this phenomena may be caused by the special structure of the *ab* plane with hard chains of CuO_2 and GeO along *c*-axis and interacting very weakly with each other.

[1] M. Nishi, O. Fujita, and J. Akimitsu, Physica B **210** (1995) 149.
[2] M. Nishi *et al.*, J. Phys. Chem. Solid **60** (1999) 1109.

研究テーマ：CeSb の磁気ポーラロン状態における異常な格子ダイナミクス
表題：CeSb の磁気ポーラロン状態における異常な格子ダイナミクス

1-1-16 Anomalous Lattice Dynamics in the Magnetic Polaron States of CeSb

K. Iwasa, M. Kohgi, Y. Haga[1], M. Braden[2], J.-M. Mignot[2] and T. Suzuki[3]

Department of Physics, Tokyo Metropolitan University, Hachioji, Tokyo 192-0397, Japan
[1] ASRC, Japan Atomic Energy Research Institute, Tokai, Ibaraki 319-1195, Japan
[2] Laboratoire Léon Brillouin, CEA/Saclay, 91191 Gif-sur-Yvette Cedex, France
[3] Tsukuba Institute of Science and Technology, Tsukuba, Ibaraki 300-0819, Japan

Novel physical properties have been explored in cerium monopnictides (CeX, X = P, As, Sb and Bi), which have characteristic low carrier concentrations (< 10^{-2}/Ce^{3+}). [1] One of the typical phenomena is the formation of complex magnetic structures with various periods of stacking of ferromagnetic (001) planes of the NaCl-type crystal structure under high pressures or under magnetic fields at low temperatures. [2-4] Cerium ions with a larger magnetic moment of $M_L \sim 2\mu_B$ appear in the ordered phases, although the crystal-field ground state in the paramagnetic phase is Γ_7 with a magnetic moment of $M_S \sim 0.7\mu_B$. [2,5] Moreover, the magnetic phase diagram exhibits a consecutive change between CeX with different pnictogens. The magnetic structures of CeP and CeAs above about 2 GPa become similar to those of CeSb which consist of dominant M_L layers and paramagnetic layers of Γ_7 state. [3] Polarized-neutron studies on the magnetic form factors of CeP showed direct evidence that the form factor of the Ce ions with M_L is quite close to that calculated for the Γ_8 crystal-field state. [6] Thus, the heterogeneous appearance of Γ_8-like Ce ions among the normal Γ_7 Ce-ion lattice characterizes the common physics of CeX. The magnetically polarized Ce ions with M_L are considered to be due to the combined effect of strong *p-f* mixing and localization of low-density carriers (magnetic polaron effect).

The 4*f*-electron state providing the complex magnetic ordering also gives crystal lattice anomalies. Low-temperature x-ray diffraction study of CeSb shows the distinct superlattice structures in its magnetically ordered phases. [7] The observed satellite-peak patterns are well explained by a model in which the effective ionic size of the Γ_8-like Ce ions is smaller by the order of 10^{-3} than that of the Γ_7 Ce ions. We have also observed that the lattice constants of CeP and CeAs decrease anomalously with increasing temperature up to 120 K and 90 K, respectively. [8] This phenomenon is also interpreted as the result of the thermal excitation of the 4*f*-electron state to the excited Γ_8 level which has an effective ionic size smaller than that of the Γ_7 state. The contraction of ionic size is due to the *p-f* mixing effect between neighboring Ce and X ions.

The strong coupling between the crystal-field states and the interatomic distance due to the *p-f* mixing effect suggests that the lattice dynamics is also affected by the appearance of the unusual magnetic state. It can be said that dynamical properties mediated by the *p-f* mixing effect may show us a new kind of electron-phonon interaction. In order to study the effects of low-carrier density and *p-f* mixing on phonons, CeSb has been studied by inelastic neutron scattering performed at TOPAN (6G) installed in JRR-3M and at 1T in Orphée reactor of LLB.

The measured phonon branches of CeSb along the principal of the axes at room temperature are reproduced well by a model based on a screened Coulomb potential together with Born-von Kármán force constants. In

addition, the measured inelastic responses in the magnetically ordered phases shows quite unusual features. In Fig. 1, inelastic spectra at fixed Q = (4.0, -0.7, -0.7) measured at 4 K in the ordered phase and at 21 K in the paramagnetic region are shown. The data at 4 K shows three peaks at 4, 7 and 9 meV, in contrast to the data at 21 K showing no peak at 7 meV. The peak at 4 meV corresponds to the magnetic excitation reported by Rossat-Mignod *et al.*[9] The peak at 9 meV was detected even at 300 K and is attributed to a transverse acoustic phonon. However, the peak at 7 meV has not been explained yet. We found that the intensities at both 7 and 9 meV measured at a smaller Q = (2.0, -0.7, -0.7) were 1/3 of those at Q = (4.0, -0.7, -0.7), although the intensity of magnetic-excitation peak at 4 meV was almost same. This observation indicates that the new excitation observed at 7 meV has a phonon character. By the measurement along the [4, ζ, ζ] direction, energy of this new excitation is found to be less dispersive along the [011] direction. Thus, the excitation seems to be a localized one. In the measurement at Q = (0, 2.3, 2.3) as shown in Fig. 2, a new peak at 8 meV is seen at 4.4 K in addition to those by magnetic excitation at 4 meV and by longitudinal acoustic phonon at 11 meV. This new peak shifts to 7 meV at just above the magnetically ordering temperature (20 K). The mechanism of the new phonon excitation is quite intriguing. In order to obtain more detailed information on the new phonon peak, we have to continue the phonon study on CeX using thermal-neutron triple-axis spectrometers.

References

[1] T. Suzuki: Jpn. J. Appl. Phys. Series 8 (1993) 267.

[2] M. Kohgi *et al.*: Phys. Rev. B49 (1994) 7068, M. Kohgi *et al.*: J. Phys. Soc. Jpn. 65 (1996) Suppl. B 99, T. Osakabe *et al.*: Physica B 230-232 (1997) 645.

[3] T. Chattopadhyay *et al.*: Phys. Rev. B49 (1994) 15096, J. Rossat-Mignod *et al.*: Phys. Rev. B16 (1977) 440.

[4] H. Bartholin *et al.*: J. de Phys. C5-40 (1979) 130.

[5] T. Osakabe *et al.*: JJAP Series 11 (1999) 123.

[6] K. Iwasa *et al.*: Physica B 259-261 (1999) 285, K. Iwasa *et al.*: J. Phys. Chem. Solids 60 (1999) 1185.

[7] K. Iwasa *et al.*: J. Phys. Soc. Jpn. 68 (1999) 2498.

[8] K. Iwasa *et al.*: J. Magn. Magn. Mater. 177-181 (1998) 393, K. Iwasa *et al.*: J. Phys. Soc. Jpn. 68 (1999) 881.

[9] J. Rossat-Mignod *et al.*: J. Magn. Magn. Mater. 52 (1985) 111.

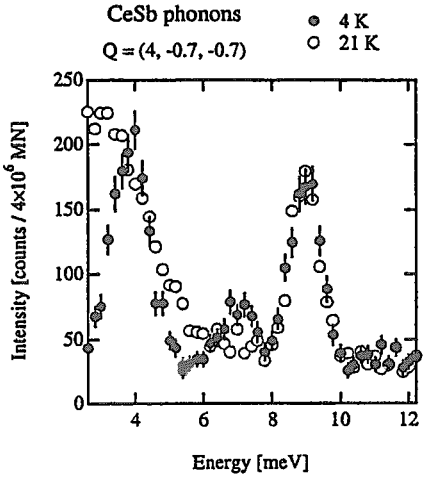

Fig. 1. Inelastic neutron data at Q = (4, -0.7, -0.7) by LLB.

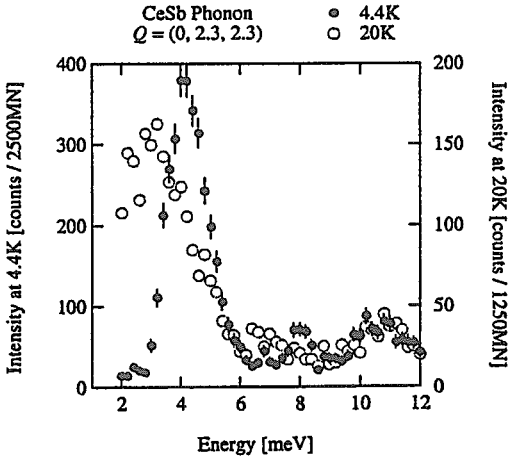

Fig. 2. Inelastic neutron data at Q = (0, 2.3, 2.3) by JAERI.

研究テーマ：酸化物高温超伝導物質の構造とダイナミクスの研究
表題：$YBa_2Cu_3O_{6+x}$(x=0.7,1)の非整合スピン揺動の研究

1-1-17 Investigation on charge stripe of $YBa_2Cu_3O_{6+x}$ single crystals

M. Arai, A. Garrett, T. Nishijima, Y.Endoh[1], K. Tomimoto[2], S. Tajima[2] and Y. Shiohara[2]

Institute of Materials Structure Science, KEK, Oho 1-1, Tsukuba, 305-0801, Japan
[1]*Institute for Materials Research, Tohoku Univ., Katahira, Sendai 980, Japnan*
[2]*Superconductivity Research Laboratory, ISTEC, Koto-ku, Tokyo, 135-0062, Japan*

It is well known that the spin fluctuation has a crucial role in the mechanism on high T_c cuprate superconductors. From the first discovery of a cuprate superconductor, the extensive experimental studies have been done in order to clarify the spin fluctuations by the neutron scattering technique. Recently we also study the spin fluctuations on the high quality single crystals of $YBa_2Cu_3O_{6+x}$ by using the MARI and HET spectrometer at Rutherford Appleton Laboratory. We found that magnetic incommensurate peaks appears at (1/2, 1/2±δ) and (1/2±δ, 1/2). The incommensurability $\delta = 0.11 r.l.u. \sim 1/8$ for the 60 K phase sample [1,2] and $\delta = 0.17 r.l.u. \sim 1/6$ for the 90 K phase sample. The hole content dependence of the incommensurability is quite similar as that of La-214 systems. The incommensurate spin fluctuation could be a common feature in cuprate superconductors and that may be derived from the spin and charge spatial modulation in CuO_2 plane.

However, it is still a controversial issue of the existence of charge and spin stripe domain structure in HTSC. It may be one of the reasonable explanation to the superlattice peak appeared at (1/2, 1/2±2δ) and (1/2±2δ, 1/2) along with magnetic incommensurate peaks at (1/2, 1/2±δ) and (1/2±δ, 1/2) in $La_{2-x-y}Nd_ySr_xCuO_4$ [3]. Hence we investigated the superlattice peaks associated with a formation of the charge stripe domain structure by MRP diffractometer at KENS Facility and TOPAN spectrometer at JAERI. As shown in the Figure 1, we found the very weak superlattice peak at (1+1/4,0,0), which is exactly the expected position from the incommensurability in the spin dynamics for the hole content of about 1/8. That intensity is about one millionth of that of the fundamental Bragg peaks. More surprisingly, the temperature dependence of the intensity showed a rapid development from much about T_c (inset of Fig.1). Then an evolution in the spin dynamics occurs below T_c. Analogous structural evolution was observed in $La_{2-x-y}Nd_ySr_xCuO_4$, and was understood that a charge ordering develops at first and triggers a spin stripe ordering at lower temperature at T_c. Therefore it is quite important if our observation in the superconductor has the same evolution as was expected for the formation of a stripe domain structure.

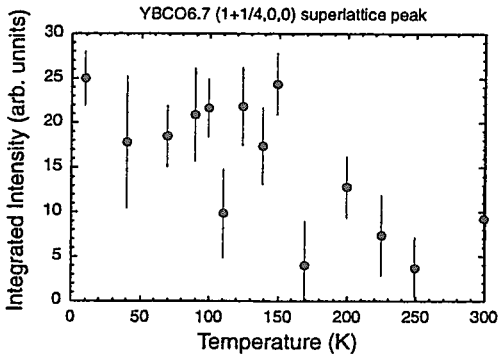

Fig. 1. Diffraction pattern along a-axis at 10 K and 300 K. Inset shows the temperature dependence of the integrated intensity of (1+1/4,0,0) peak.

References

[1] M. Arai *et al.*, Phys. Rev. Lett. **83**, 608 (1999).
[2] H. A. Mook *et al.*, Nature **395**, 580 (1998).
[3] J. M. Tranquada *et al.*, Nature **375**, 561 (1995).

Reactor : JRR-3M Facility : TOPAN(6G) Field : Structure and Excitation

研究テーマ：電荷秩序の臨界温度領域における Yb_4As_3 のフォノンスペクトル
表題：電荷秩序の臨界温度領域における Yb_4As_3 のフォノンスペクトル

1-1-18
Phonon Spectra of YB_4As_3 in the Critical Temperature Region of Charge Ordering

K.Iwasa,M.Kohgi,A.Ochiai[1],H.Aoki[2] and T.Suzuki[3]

Department of Physics, Tokyo Metropolitan University, Hachioji, Tokyo 192-0397, Japan
[1] Department of Material Science and Technology, Niigata University, Niigata 950-2181, Japan
[2] Graduate School of Science and Technology, Niigata University, Niigata 950-2181, Japan
[3] Tsukuba Institute of Science and Technology, Tsukuba, Ibaraki 300-0819, Japan

One of the typical low-carrier-concentration system Yb_4As_3 has been studied because of its unusual electronic properties like in heavy-fermion compounds.[1)] This behavior is observed in the charge ordered phase accompanied with a structural phase transition at T_C = 288 K. Its crystal structure is an anti-Th_3P_4-type cubic one above T_C, and transforms to a trigonal one below T_C with shrinking slightly along the [111] direction. The 4f-electron state is thought to be valence fluctuating in the cubic phase. Polarized-neutron diffraction experiments revealed that the charge ordered state appears with Yb^{3+} ions aligning along the shrinking [111] direction and the Yb^{2+} ions on the other lattice sites.[2)] Magnetic excitations within this one-dimensional Yb^{3+}-ion chain measured by inelastic neutron scattering are explained by the model of S = 1/2 Heisenberg antiferromagnet, and take important roles in the low-temperature properties in this system.[3)] Dynamical properties of crystal lattice of Yb_4As_3 were studied by ultrasonic measurement.[4)] The elastic constant, C_{44}, exhibits a strong decrease by 13% from 400 to 300 K in critical region near T_C, which may indicate a softening of phonons.

In order to obtain more information about the charge-ordering mechanism in this system, we have performed measurements of lower-energy phonons at 300 and 400 K in a temperature range around T_C using TOPAN (6G) and HER (C1-1) spectrometers. The temperatures are controlled with the furnace of Tohoku University.

In Fig. 1, inelastic neutron spectra at the reciprocal point Q = (2.2, 2.2, 3.8) are shown. The observed peak centered at 3.4 meV corresponds to transverse acoustic (TA) phonon excitation with wavevector q = (0.2, 0.2, 0.2). The peak position shows no distinct change between 300 K near T_C and 400 K. The observed temperature variation of intensity is explained by the temperature factor due to Bose distribution function; the scattering intensity at 3.4 meV and 300 K is evaluated as 76% of that at 400 K. Figure 2 shows spectra at the reciprocal point Q = (1.8, 1.8, 3.8), which corresponds to longitudinal acoustic (LA) phonon with q = (0.2, 0.2, 0.2). The observed peak energy is almost same as that of q = (0.2, 0.2, 0.2) TA phonon, in contrast to usual cases where LA modes take higher energies than those of TA mode. This fact is similar to that of typical valence fluctuating systems $Sm_{0.75}Y_{0.25}S$ and TmSe, whose LA phonons propagating along the cubic [111] direction show softening and their energies become slightly lower than those of the TA phonons propagating along the same direction.[5)] Another remarkable phenomenon in Yb_4As_3 is that the intensity of q = (0.2, 0.2, 0.2) TA phonon at 300 K is much less than that expected from the data at 400 K by correcting the temperature factor. In order to investigate anomalous properties of C_{44}, some TA phonons with q = (ξ, 0, 0) were measured. Spectra for the TA modes with q = (0.3, 0, 0) are shown in Fig. 3. As the data of q = (0.2, 0.2, 0.2) TA shown in Fig.

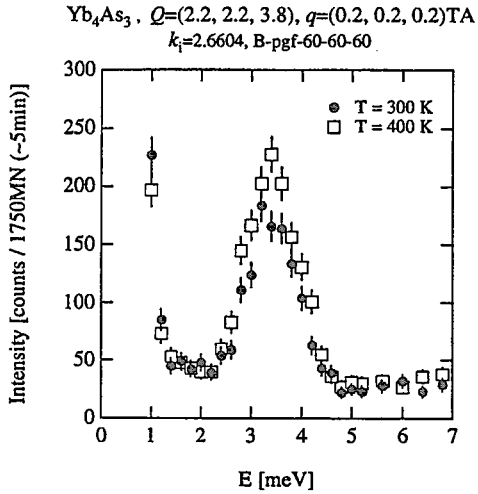

Figure 1. Phonon spectra at Q = (2.2, 2.2, 3.8).

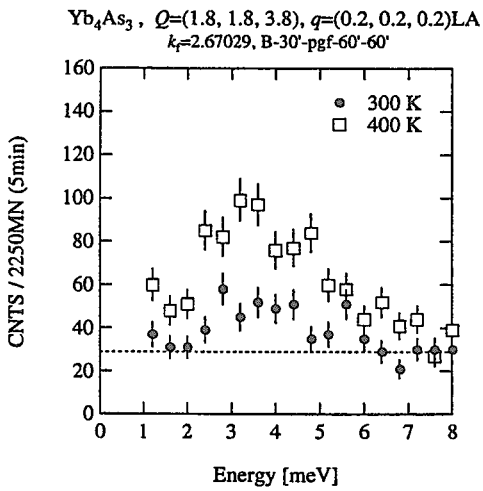

Figure 2. Phonon spectra at Q = (1.8, 1.8, 3.8). A dotted line indicates the background level.

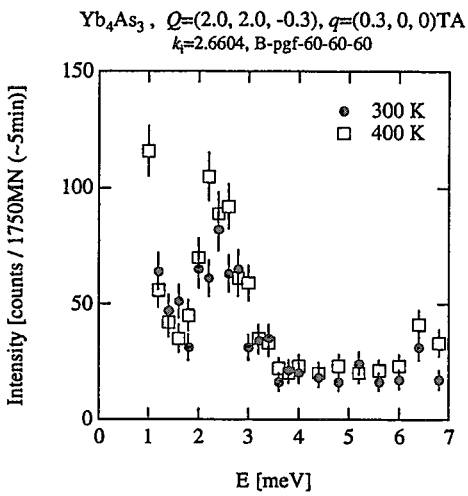

Figure 3. Phonon spectra at Q = (2.0, 2.0, -0.3).

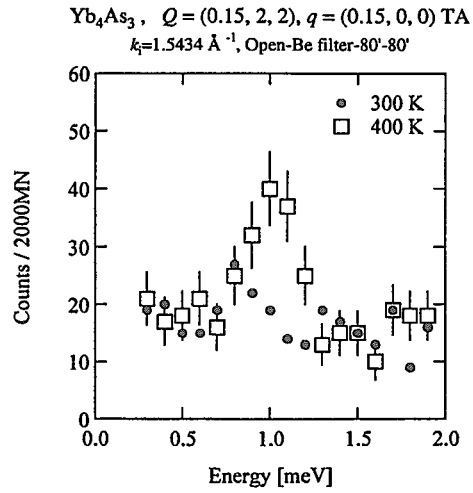

Figure 4. Phonon spectra at Q = (0.15, 2.0, 2.0).

1, the peak energy has no temperature dependence, and the intensity decrease from 400 K to 300 K is explained by the temperature factor. On the other hand, as shown in Fig. 4, the spectrum of q = (0.15, 0, 0) TA phonon at 300 K measured by HER is hardly seen in contrast to that at 400 K detected clearly.

The observed anomalies of phonon energies and neutron-scattering intensities are thought to be caused by the charge order coupling strongly with the lattice dynamics.

References

1) A. Ochiai *et al.*: J. Phys. Soc. Jpn. **59** (1990) 4129.
2) M. Kohgi *et al.*: Physica B **230-232** (1997) 638; K. Iwasa *et al.*: Physica B **281-282** (2000) 460.
3) M. Kohgi *et al.*: Phys. Rev. **B56** (1997) R11388.
4) T. Goto *et al.*: Physica B **230-232** (1997) 702.
5) H. A. Mook and R. M. Nicklow: Phys. Rev. **B20** (1979) 1656; H. A. Mook and F. Holtzberg: *Valence Fluctuations in Solids* (North Holland, 1981) p. 113.

研究テーマ:NiAs の結晶構造解析
表題:NiAs の結晶構造解析

1-1-19 Structural Analysis on NiAs

T. Nozue, H. Kobayashi and T. Kamimura

Department of Physics, Tohoku University,
Aramaki Aza–Aoba, Aoba–ku, Sendai, Miyagi, 980-8578 Japan

Among 3d transition metal arsenides, CrAs, MnAs and CoAs with an orthorhombic MnP–type structure transform to a hexagonal NiAs–type structure with increasing temperature. NiAs has a bottom–centered orthorhombic structure with the $Cmc2_1$ symmetry (*niccolite*–type) in which the Ni and As atoms form sinusoidal displacements from the atomic positions in the NiAs–type with $\vec{q} = \frac{1}{3}(11\bar{2}0)$. In this *niccolite*–type, the single crystal consists of three domain structures related to three possible directions of $\vec{q}$. The measurement of temperature dependence of the powder X-ray diffraction revealed that NiAs undergoes a structural transition to the NiAs–type at T_t =335K. In the previous experiment of neutron diffraction in the ($h0l$) plane at room temperature by T-1-2 KSD, we observed the weak reflections indexed as (001) and (003) which are not possible reflections in $Cmc2_1$. Thus, there are two possible reasons for this result, that is, (i) this sample have periodic defects, such as the random vacancies on every other Ni–layer and (ii) the crystal structure of NiAs does not have the $Cmc2_1$ symmetry.

In this experiment, we have measured the reflections in the ($0kl$) plane in a temperature range from 20 to 420K using the same sample as our previous measurement. The other extra reflection indexed as (012) was observed. Figure 1 shows the temperature dependence of the integrated intensities of the (001), (002) and (004) reflections. The intensities of the (002) and (004) reflections are almost independent of temperature and then show no anomalies around T_t. However, the intensity of the (001) reflection decreases with the temperature increasing up to 335K and is almost constant above T_t. The observation of (012) reflection and T–dependence of the (001) reflection were not explained by the random vacancies on the every other Ni–layer. The crystal structure were not determined from only these results. However, the extra reflections are connected with the structural transition. To investigate the origin of the extra reflections, the measurement of the temperature dedendence of the intensities of the reflections in the ($h0l$) plane is required.

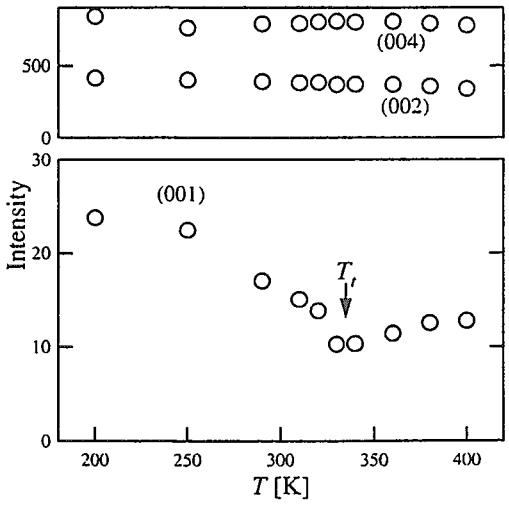

図 1: Temperature dependence of the integrated intensities of the (002) and (004) reflections and (001) reflection which is absent in the $Cmc2_1$ symmetry. The arrow indicates the temperature of the structural transition determined by the powder X-ray diffraction.

JRR-3M, T1-2 KSD, 1. Structrures&Excitations

研究テーマ:メチルアンモニウム基をもつペロブスカイト型誘電体の構造と相転移機構
表題:$CH_3NH_3PbBr_3$のメチルアンモニウムの秩序化

1-1-20 Ordering of Methylammonium in $CH_3NH_3PbBr_3$

H. Mashiyama, Y. Kawamura, K. Ohoyama[1]
Faculty of Science, Yamaguchi University, Yoshida 1677-1, Yamaguchi 753-8512
[1]Institute for Materials Research, Tohoku University, Sendai 980-8577

$CH_3NH_3PbBr_3$ takes the cubic perovskite structure in room temperature phase. Since methylammonium (abbreviated as MA, hereafter) takes C_{3v} symmetry, the MA ions should be disordered in the phase. At low temperatures, some transitions take place successively with accompanying ordering of MA ions, which has been studied by calorimetric measurement by Yamamuro *et al.*[1] They proposed three models of phase transition; MA ions point either <100>, <110> or <111> direction in cubic phase.

Our purpose is to inspect this in the view of analysis of the crystal structure. We have analyzed the cubic structure by the use of X-ray data.[2] But the high scattering factors Pb and Br prevented to analyse the MA orientation. Therefor we use neutron powder diffractmeter HERMES. Since we used the hydrogen compound, value of S/N isn't very well, however a profile fitting program system RIETAN-94[3] works to determine the structure.

Phase I is cubic Pm3m(Z=1), a_0=5.90 Å at 298K. Four-site disorder is assumed for Br.[2] The <110> orientation model seems to the best (R_f=9.5%, S=1.2, d=1.4), as shown in Fig.1. However, the difference between the <100> orientation model is tiny and MA ions may occupy the mixed state of <100> and <110> orientations.

Phase II is tetragonal I4/mcm(Z=4). Phase II shows a super structure and the unit cell parameter a_{II} and c_{II} are related $a_{II}\sim\sqrt{2}a_0$ and $c_{II}\sim 2a_0$. $PbBr_6$ octahedrons tilted about ±7.4 degree at 200K from the Pb–Pb line.

MA ions point the <111> direction. It seems that this result is different from Yamamuro's model for phase II, but this is a derivative of the <110> model. From Fig.2, the nitrogen atom occupies a short distance from the bromine atom.

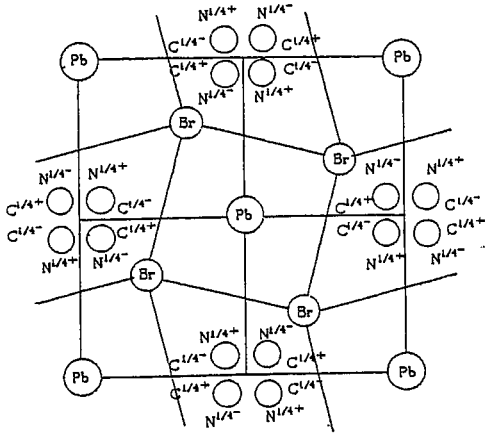

Fig.2 Phase II structure of $CH_3NH_3PbBr_3$.The half of the unit cell($0 \leqq Z < 1/2$) is projected on (001) plane.

Reference

[1] N. Onoda-Yamamuro, T. Matuso and H. Suga, J. Phys. Chem Solids., 51, 1383 (1992)
[2] H. Mashiyama, Y. Kurihara and T.Azetsu, J. Korean Phys. Soc., 32, S156(1998)
[3] F. Izumi : The Rietvelt Mothod, ed. By R. A. Young (Oxford Univ. Press, 1993, Oxford) chap.13.

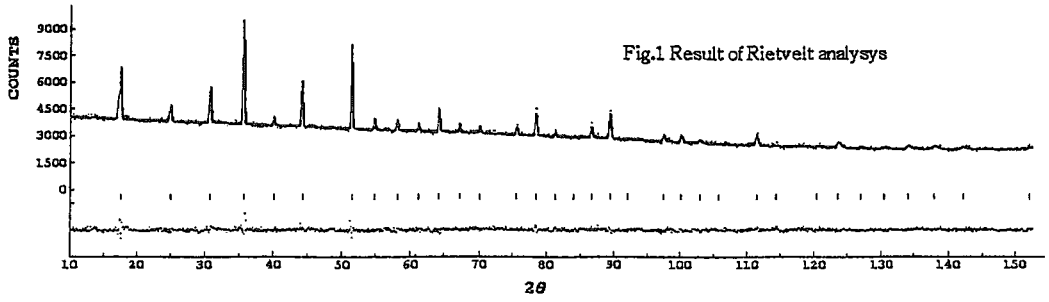

Fig.1 Result of Rietvelt analysys

JRR－3M、HERMES、1.Structure

研究テーマ：リチウム二次電池正極材料 $Li_{1+x}Mn_{2-x}O_4$ の結晶構造と電池特性

表題：リチウム二次電池正極活物質 $Li_{1+x}Mn_{2-x}O_4$ の物性、結晶構造と電極特性の関係

1-1-21 Relation between the Property, Crystal Strucure and Electrode Characteristics of $Li_{1+x}Mn_{2-x}O_4$ as a Cathode Active Material for the Lithium Secondary Battery

Y. Idemoto, S. Ogawa and N. Koura

Faculty of Science and Technology, Science University of Tokyo
2641 Yamazaki, Noda-shi, Chiba 278-8510, Japan

The relation between property, crystal structure, and electrode characteristics of the spinel $Li_{1+x}Mn_{2-x}O_4$ (x=0~0.1) was investigated.

The samples were prepared by mixing $^7Li_2CO_3$ and MnO_2 so as to avoid the high neutron absorption of ^6Li. The Mn valence was controlled by the annealed treatment or change of composition. Mn valence was determined by chemical analysis.

The phase transition of products was investigated by measurement of resistivity and DSC measurements. The peak of DSC decreased with increasing Li content or higher Po_2 anneal treatment. The substitution of Li^+ into the Mn(16d) site or higher Po_2 anneal treatment are accompanied by an oxidation of Mn^{3+} to Mn^{4+} resulting in an increase in the average valency of the manganese ions, and thereby a suppression of the Jahn-Teller distortion.

The neutron powder diffraction was performed using HERMES. Data were corrected at room temperature, 275K, and 200K. The crystal structure was refined with the Rietveld techniques(Rietan 97 β). First, analysis of the $Li_{1+x}Mn_{2-x}O_4$(x=0~0.1) diffraction data at room temperature were carried out using an initial cubic structure (space group:Fd3m) with oxygen deficiency. Second, the 200K and 275K data were analyzed starting from a cubic (Fd3m) phase or orthorhombic (Fddd) phase with oxygen deficiency. From these results, we compared the goodness-fit indicator, $S=R_{wp}/R_e$. The S value for the orthorhombic $^7LiMn_2O_4$(500°C, Po_2=2.02×10⁶Pa annealed) is lower than that of cubic one at 200K and 275K. G. Rousse, et al. reported that stoichiometric spinel $LiMn_2O_4$ undergoes a transition from orthorhombic (observed at 230K) to a cubic symmetry (observed at 350K) by indexing the neutron diffraction patterns[1]. Our results agree with Rousseís report. On the other hand, the S of cubic $^7Li_{1.1}Mn_{1.9}O_4$ (500°C, Po_2=2.02×10⁶Pa annealed) is lower than that of orthorhombic one at 200K. From the results, $^7LiMn_2O_4$ is orthorhombic at 200K whereas $^7Li_{1.1}Mn_{1.9}O_4$ retains its room-temperature cubic phase down to 200K. Hence, the crystal structure is more stable at low temperature by the substitution of Li for Mn. Figure 1 shows the relation between the selected bond lengths from structural parameter and the Mn valence of $Li_{1+x}Mn_{2-x}O_4$ at room temperature. The lattice parameter a, the bond lengths of Li-O and Mn(Li/Mn)-O decreased and Mn valence increased

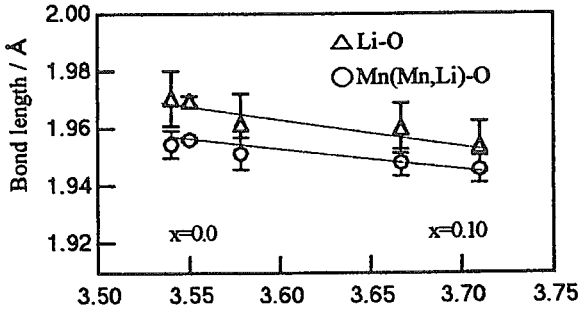

Figure 1 Relation between the selected bond lengths from structural parameter and the Mn valence of $Li_{1+x}Mn_{2-x}O_4$ at 298K.

with increasing Li content or higher Po_2 anneal treatment. Accordingly, the crystal structure is more stable by the substitution of a part of Mn with Li or increase of Mn valence.

The effect of electrode characteristics for the positive electrode active materials was investigated over the 4V range. Increase of Li content and higher Po_2 annealed treatment brought to a good cycle performance in spite of some decrease on the initial capacity, that is, the substitution a part of Mn with Li and increase of Mn valence brought to a good cycle performance.

Reference

[1] G. Rousse, C. Masquelier, J. R. Caravajal, and M. Hervieu, *Electrochem. and Solid- State Lett.*, 2, 6(1998).

研究テーマ：半磁性半導体 $Zn_{1-x}Mn_xTe$ の中性子回折
表題：層状酸化物 Na_x $(Co_{1-y}Mn_y)$ $O_{2-\delta}$ の中性子回折による研究

1-1-22

Neutron diffraction study of layered oxides $Na_x(Co_{1-y}Mn_y)O_{2-\delta}$

Y.Ono, R.Ishikawa, Y.Miyazaki and T.Kajitani
Department of Applied Physics, Graduate School of Engineering,
Tohoku University, Aobayama 08, Sendai, 980-8579 Japan

Layered cobalt oxide, Na_xCoO_2, is a promising thermoelectric material with unusually large thermopower (100 μ V/K), low electric resistivity (0.2 m Ω・cm) and low thermal conductivity (15 mW/cm・K) at 300 K [1]. In this compound, strong electron-electron correlation plays an important role in enhancement of the thermopower [2]. However, the mechanism of this enhancement is not fully understood yet. In order to get more insight into the origin of large thermopower, we have studied structure changes in the Mn substituted Na_xCoO_2.

Polycrystalline samples, $Na_x(Co_{1-y}Mn_y)O_2$ with y=0.0, 0.1, 0.3, 0.5 and 0.7, were prepared by a conventional solid state reaction. Nominal sodium content for each sample was fixed to 0.75. Neutron diffraction experiments were carried out at room temperature using double-axis diffractometer HERMES implemented with multi-counter detection system at JAERI. The $P6_322$ type space symmetry was assumed for $Na_x(Co_{1-y}Mn_y)O_2$ [3]. The structure parameters were refined using a Rietveld analysis program, RIETAN [4]. Figure 1 shows observed, calculated and difference profiles of powder neutron diffraction intensities of $Na_{0.75}CoO_2$. Lattice parameter, *c*, increases nonlinearly from 10.8920(3) Å at y=0 to 11.1810(9) Å at y=0.5. This is mainly ascribed to the increase of CoO_2 interlayer distance. For further substitution, the lattice parameter, *c*, does not increase. Sodium ions sit in two non-equivalent sites, namely, Na1(0 0 1/4) and Na2 (2/3 1/3 1/4) sites,

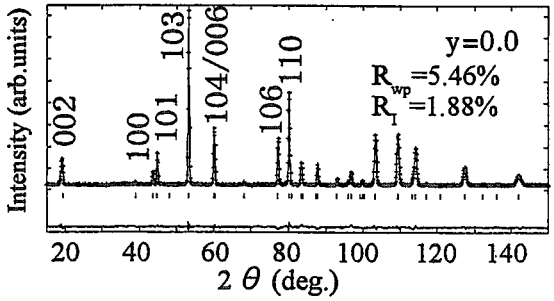

Figure 1 Observed, calculated and difference neutron diffraction profiles for $Na_{0.75}CoO_2$.

respectively. Occupancies of these sodium cations and oxygen atom were also successfully refined. The sodium content in this system continuously vary from 0.75 at y=0 to 0.39 at y=0.5 despite of the fixed nominal content, 0.75. The samples with y=0.0, 0.1 and 0.3 do not contain oxygen deficiency, while the samples with y=0.5 and 0.7 are highly oxygen-deficient. Average formal valence at Co-site was evaluated from the charge neutrality condition in the chemical formula, $Na_x(Co_{1-y}Mn_y)O_{2-\delta}$, where the valences of the sodium and the oxygen atoms were assumed to be +1 and -2, respectively. All samples except for y=0.5 have almost the same averaged valence at the Co-site (～3.30).

References

[1] I.Terasaki, Y.Sasago and K.Uchinokura: Phys.Rev.B56(1997)R12685.
[2] T.Kawata *et al.*:Phys.RevB60(1999)10584.
[3] M.Jansen and R.Hoppe:Z.anorg.allg.Chem. 408(1974)104.
[4] F.Izumi, in:R.A.Young(Ed.), *The Rietveld Method, Oxford University Press, Oxford, 1993 Chapter 13.*

研究テーマ: 層状マンガン酸化物の化学圧力効果
表題：層状マンガン酸化物の軌道の安定性と磁気秩序

1-1-23 Orbital stability in the spin-ordered phase of bilayer manganites as investigated by neutron diffraction measurements

T. Akimoto[1], Y. Moritomo[2], K. Ohoyama[3], S. Okamoto[3], S. Ishihara[3], S. Maekawa[3], K. Hirota[4] and A. Nakamura[2]

[1]Department of Crystalline Materials Science, Nagoya University, Nagoya 464-8601, Japan
[2]CIRSE, Nagoya University, Nagoya 464-8601, Japan
[3]IMR, Tohoku University, Sendai 980-8577, Japan
[4]Department of Physics, Tohoku University, Sendai 980-77, Japan

We have found that 20% Ca-doped manganite, $La(Sr_{0.8}Ca_{0.2})_2Mn_2O_{0.7}$, becomes FM below T_C = 100 K. Note that the mother material, $LaSr_2Mn_2O_7$, shows a charge-ordering (CO) transition at 210 K. In order to investigate the orbital state in the spin-ordered phase, we have performed neutron powder diffraction experiments on the F-type $La(Sr_{0.8}Ca_{0.2})_2Mn_2O_7$ and A-type $NdSr_2Mn_2O_7$. The relative stability of the $d_{3z2-r2}$and d_{x2-y2} orbitals has been estimated by difference in the Madelung potential ΔV between the two e_g-orbitals.

Melt-grown crystals of $La(Sr_{0.8}Ca_{0.2})_2Mn_2O_7$ and $NdSr_2Mn_2O_7$ has been used for the neutron diffraction measurement to reduce the impurity phase. Neutron-diffraction measurements were performed with the Kinken powder diffractometer for high efficiency and high-resolution measurements (HERMES) installed at the JRR-3M reactor at the Japan Atomic Energy Research Institute, Tokai, Japan. Melt-grown crystal ingots were crushed into fine powder and were sealed in a vanadium capsule with helium gas, and mounted at the cold head of a closed-cycle He-gas refrigerator. We have used RIETAN-97β program developed by Izumi, and analyzed the powder patterns with two phase model ("327" main phase and "214" impurity phase). The final refinement is satisfactory, in which R_{wp} and R_I (reliable factor based on the integrated intensity) are fairly typical of published structures

In the case of F-type $La(Sr_{0.8}Ca_{0.2})_2Mn_2O_7$, the c-value decreases below T_C. Such a behavior makes a sharp contrast with the case of $La_{1.2}Sr_{1.8}Mn_2O_7$., in which the c-value increases below T_C. In the A-type $NdSr_2Mn_2O_7$, both the lattice constants change below T_N, indicating a significant spin-lattice coupling.

Now, let us proceed to the relative stability of the e_g-orbitals. Based on the structural data obtained by the neutron-diffraction experiment, we have calculated temperature variation of difference of the Madelung potentials between two e_g-orbitals: $\Delta V = V(d_{3z2-r2}) - V(d_{x2-y2})$. The d_{x2-y2} orbital becomes stable as ΔV decreases. The results are plotted in Figure 1 together with the data points (closed squares) for the F-type $La_{1.2}Sr_{1.8}Mn_2O_7$. With decrease of temperature, the ΔV value (closed circles) of $La(Sr_{0.8}Ca_{0.2})_2Mn_2O_7$ gradually decreases, and hence the d_{x2-y2} orbital becomes stable. Oppositely to this case, the ΔV-value (closed squares) of A-type $NdSr_2Mn_2O_7$ rather increases (the d_{3z2-r2}-orbital becomes stable) at low temperature. Here, we should mention that ΔV -values for both the ferromagnetic systems converge at 0.06 - 0.07 eV at the lowest temperature. This suggests that the orbital state in the FM phase is a linear combination of the d_{3z2-r2}- and d_{x2-y2} orbitals.

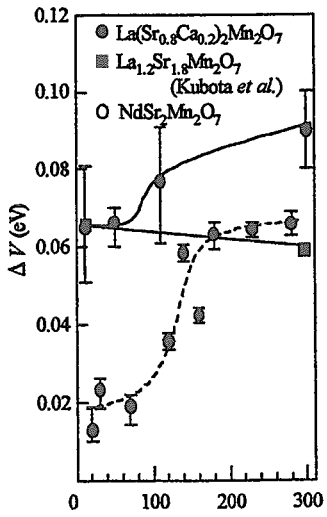

Figure 1: Temperature variation of difference of the Madelung potentials ΔV The d_{x2-y2} orbital becomes stable as ΔV decreases.

研究テーマ: $Nd_{1/2}Sr_{1/2}MnO_3$のフォノン分散
表題：$Nd_{1/2}Sr_{1/2}MnO_3$等の電荷整列における化学圧力効果

1-1-24

Reconsideration of the lattice effect on the charge-ordering transition of doped manganites

A.Machida[1], Y. Moritomo[2], K. Ohoyama[3], S. Okamoto[3], S. Ishihara[3], S. Maekawa[3], A. Nakamura[2]
[1]Department. of Crystalline Materials Science, Nagoya University, Nagoya 464-8601, Japan
[2]CIRSE, Nagoya University, Nagoya 464-8601, Japan
[3]IMR, Tohoku University, Sendai 980-8577, Japan

We have investigated stability of the respective e_g-orbitals by means of Madelung potential calculations based on the structural data obtained by neutron powder diffraction experiments. We have found a strong correlation between the orbital stability and charge-ordering transition, indicating that the orbital stability is another feature of the chemical pressure.

A series of ceramics compounds, $R_{1/2}A_{1/2}MnO_3$ (R=La, Nd, $Nd_{1/2}Tb_{1/2}$ and Tb, A=Sr and Ca), was synthesized by solid state reaction in air atmosphere. Rietveld analysi of neutron powder pattern indicate that investigated compounds were single phase without a detectable impurity. Neutron powder diffraction measurements were performed with the Kinken powder diffractometer for high efficiency and high resolution measurements (HERMES) installed at the JRR-3M reactor at the Japan Atomic Energy Research Institute, Tokai, Japan.

The charge-ordering temperature T_{CO} was determined from the maximal point of the activation energy E_{ac}. In the case of Ca-compounds, T_{CO} increases with decrease of the averaged ionic radius r_A This trend is consistent with the picture of the t-control by the chemical pressure. Curiously enough, there is no trace of the charge-ordering transition disappears for $Tb_{1/2}Sr_{1/2}MnO_3$ and $(Nd_{1/2}Tb_{1/2})_{1/2}Sr_{1/2}MnO_3$. Such an unexpected behavior suggests that there exists a hidden factor besides the variation of t.

Now, let proceed to the structural feature of $R_{1/2}A_{1/2}MnO_3$. We have used RIETAN-97 β program developed by Izumi, and have analyzed the neutron powder patterns at room temperature. Significant rare-earth dependence is observed in the bond length -values In the Pbnm setting, there are three kinds of Mn-O bonds, i.e., out-of-plane and two in-plane bonds. In the four Ca-compounds, the out-of-plane bond length is the shortest among the three bond. With this structure, the $d_{3z^2-r^2}$ orbitals are stable as compared with the $d_{x^2-y^2}$ orbital. Then, the e_g-electrons tend to occupy the $d_{3x^2-r^2}$ and $d_{3y^2-r^2}$ orbitals, and hence, are easy to form the orbital alternation at low temperatures to cause the charge-ordering transition. By contrast, in $Tb_{1/2}Sr_{1/2}MnO_3$ and $(Nd_{1/2}Tb_{1/2})_{1/2}Sr_{1/2}MnO_3$, Jahn-Teller-type distortion of the MnO_6 octahedra, i.e., two long and four short bonds, disturbs the charge/orbital-ordering.

To quantitatively estimate the stability of the respective e_g-orbital, we have calculated the Madelung potential V for each orbitals based on the structural data. The stability of the $d_{3x^2-r^2}/d_{3y^2-r^2}$ orbital alternation can be estimated by the difference of the Madelung potential Δ V. We plotted in Figure 1 T_{CO} against Δ V. Open and closed symbols stand for the Ca- and Sr-compounds, respectively. If one sees the phase diagram from left to right (the stability of the $d_{3x^2-r^2}/d_{3y^2-r^2}$ orbital alternation increases.), the CO state appears and T_{CO} increases.. Thus, the orbital stability is another factor at least on the charge-ordering transition of cubic manganites.

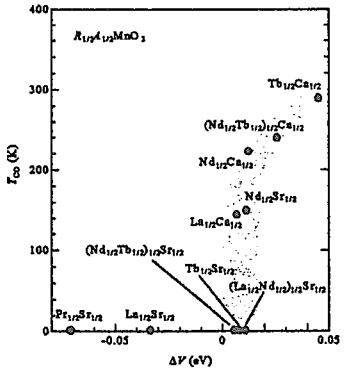

Figure 1: T_{CO} against the difference of the Madelung energies Δ V. Open and closed symbols stand for the Ca- and Sr-compounds, respectively. Hatching is a guide to the eye.

研究テーマ: LSMO327 の高圧下におけるスピン状態
表題 : LSMO327 の高圧下における絶縁体金属転移

1-1-25 Pressure-induced insulator-metal transition in a bilayer manganite - Pressure-control of orbital stability -

Y. Moritomo[1], K. Hirota[2], H. Nakao[3], T. Kiyama[3], Y. Murakami[3], S. Okamoto[4], S. Ishihara[4], S. Maekawa[4], M. Kubota[5] and H. Yoshizawa[5]

[1]CIRSE, Nagoya University, Nagoya 464-8601, Japan
[2]Department of Physics, Tohoku University, Sendai 980-8578, Japan
[3]PF, Institute of Materials Structure Science, Tsukuba 305-0801, Japan
[4]IMR, Tohoku University, Sendai 980-8577, Japan
[5]Neutron-Scattering Laboratory, ISSP, University of Tokyo, Tokai, Ibaraki 319-1106, Japan

We have investigated pressure effects on the transport as well as structural properties for a bilayer maganite, $La_{1.04}Sr_{1.96}Mn_2O_7$, which shows the A-type spin ordering below T_N = 200 K. Application of pressures is found to induce an insulator-metal (IM) transition. To comprehend the pressure-induced IM transition, we further have estimated the orbital stability through difference in the Madelung potential ΔV between the $d_{3z^2-r^2}$ and $d_{x^2-y^2}$ orbitals.

Single crystals of $La_{1.04}Sr_{1.96}Mn_2O_7$ were grown by the floating-zone method at a feeding speed of 10 - 20 mm/h. The crystal symmetry is tetragonal (I4/mmm; Z =2) at ambient pressure without detectable impurities.

A hydrostatic pressure was obtained with a clamp-type piston cylinder cell . The in-plane component of resistivity was measured by the four-probe method using heat-treatment-type silver paint as electrodes. At ambient pressure, the insulating behavior is fairly suppressed at around T_N (= 200 K), reflecting the long-range ferromagnetic spin ordering in the respective MnO_2-sheets (A-type structure).At 1.44 GPa (1.08 GPa), the resistivity curve shows a sharp drop below 130 K (120 K) and then monotonously decreases. The resistivity curve at P > 0.7 GPa is reminiscent of that of FM $La_{1.2}Sr_{1.8}Mn_2O_7$.

To determine the variation of structural parameters under pressures, we have performed high-pressure x-ray experiments using a specially designed diamond anvil cell (DAC) at room temperature. Synchrotron radiation (SR) x-ray source at Photon factory BL-1B was used with a cylindrical imaging plate as a detector, to obtain powder data of good counting statistics. Melt-grown crystal ingots were crushed into fine powder and were sealed in a gasket hole of the DAC, 0.1mm in thickness and 0.3mm in diameter, which was filled with ethanol/methanol mixture as a pressure-transmitting medium. We have analyzed thus obtained x-ray patterns with RIETAN-97 β program The final refinements are satisfactory, in which R_{wp} is fairly typical of the published one (2 - 3 %).

Based on the structural parameters, we have calculated pressure variation of difference in the Madelung potentials ΔV between two e_g-orbitals. The results are plotted in Figure 1 against applied pressures. With increase of pressure, the ΔV value (closed circles) gradually increases, and hence the $d_{3z^2-r^2}$ orbital becomes stable. Such a pressure variation of the ΔV-value qualitatively explains the pressure-induced IM transition, because the stabilized $d_{x^2-y^2}$ orbital favors the FM state. We plan to confirm the pressure-induced A-type to F-type transition using a single crystal sample.

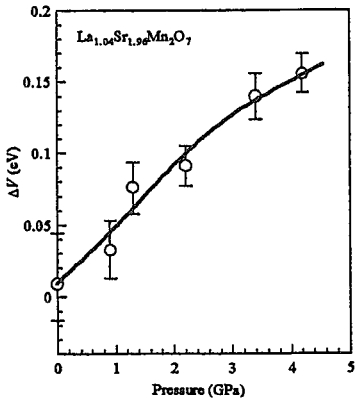

Figure 1: Pressure variation of difference in the Madelung potentials ΔV. The $d_{3z^2-r^2}$ orbital becomes stable as ΔV

研究テーマ：高圧下で合成したタリウムパイロクロア固溶体の構造変化
表題：高圧下で合成したタリウムパイロクロアの構造変化

1-1-26
Structural Changes of Thallium Pyrochlores Synthesized under High Pressure

T. Takeda, R. Kanno, K. Oyama[1], Y. Yamaguchi[1]

[s]*Department of Chemistry, Faculty of Science, Kobe University, Nada, Kobe, Hyogo 657-8501, Japan*
[1]*Institute for materials Research, Tohoku University, Sendai, Miyagi 980-8577, Japan*

Thallium pyrochlore $Tl_2Ru_2O_7$ synthesized under high oxygen pressure shows metal-semiconducting transition at 120 K. The amount of oxygen vacancies in $Tl_2Ru_2O_{7-\delta}$ affects on the electrical property[1]. Crystal structure also varies according to the electrical property. As well as the amount of oxygen vacancy, the substitution of Tl site also affects on the electrical property. Figure 1 shows the temperature dependence of the electrical resistivity for $Tl_{1.8}A_{0.2}Ru_2O_7$ (A = In, Y, Bi, Hg, Pb). The electrical resistivity varied depending on the substitutions. In the present study, the structural changes with the substitution was determined.

The Neutron diffraction data were taken on a T1-3 neutron powder diffractometer at JRR-3M at Tokai Establishment of JAERI. The diffraction data were collected at each 0.1° step width over a 2θ range 3° to 150°.

The structural parameters were refined by Rietveld method with space group $Fd\bar{3}m$ using a structure model, Tl(A) at 16d (0.5, 0.5, 0.5), Ru at 16c (0, 0, 0), O1 at 48f (x, 0.125, 0.125) with x~0.325, O2 at 8b (0.375, 0.375, 0.375). Figure 2 shows the relationship between the Ru-O distance and Ru-O-Ru angle. The changes from the metallic to semiconducting regions corresponded to the distances and angles variations. Longer Ru-O distances and smaller Ru-O-Ru angles lead to semiconducting properties which correspond to weaker Ru-O interactions.

1) T. Takeda *et al.*, *J. Solid State Chem.*, **140**, 182 (1998)

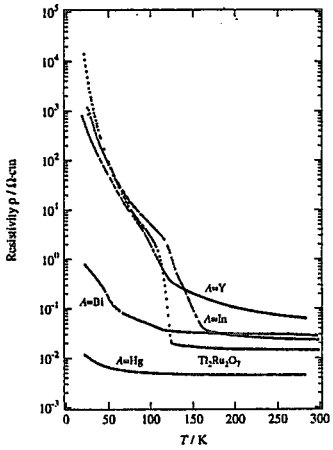

Fig. 1 Temperature dependence of the electrtical resistivity for $Tl_{1.8}A_{0.2}Ru_2O_7$ (A = In, Y, Bi, Hg, Pb).

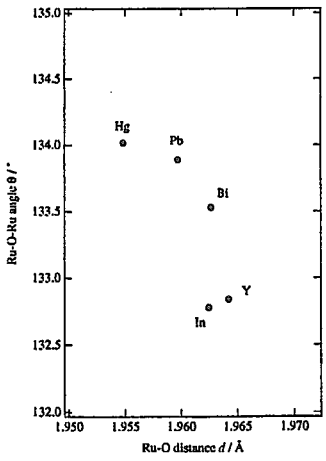

Fig. 2 Relationship between the Ru-O distance and Ru-O-Ru angle.

研究テーマ：構造材料の残留応力と疲労損傷の評価
表題：傾斜機能材料の RESA による残留ひずみ測定

1-1-27
Residual strain measurement of functionally gradient material by RESA

K. Inoue, T.Tsujikami, M. Kawagai, M.Ohyanagi, N.Minakawa[1], Y. Morii[1] and T.Saitoh[1]

Fac. Sci & Tech. Ryukoku Univ. Seta, Otsu 520-2194, Japan
[1]Japan Atomic Energy Research Institute, Tokai, Ibaraki 319-1195, Japan

An internal residual strain of the three-layer functionally gradient material, [WC-10Wt%Ni]-[Ni]-[WC-10Wt%Ni], made by combustion synthesis was measured by neutron diffraction with a detection system, RESA, which is installed at JRR-3M reactor at JAERI. The material [WC-10Wt%Ni] is a super hard alloy. The results obtained by the measurements are discussed in comparison with those calculated by finite element method.

The material was made by self-propagating high temperature synthesis with the ignition by the induction heating. The synthesis was done by the static pseudo isostatic compaction method under 25MPa. The obtained three layers material and the SEM image of [WC-10Wt%Ni] layer is shown in Figs.1(a) and (b). The diameter of this material is about 37.8 mm and the thickness is about 12.4mm. In Fig.1 (b), the white particle is composed of WC, of which size is several μm, and the black region is composed of Ni.

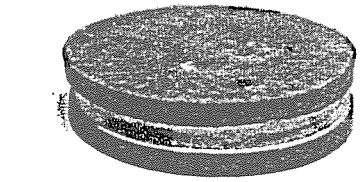

(a)

(b)

Fig.1. (a) the shape of the three layers sample and (b) the SEM image of the [WC-10Wt%Ni] layer.

The residual strain was measured for radial and axial directions. As the size of the slits for both incident and reflected beams was 2mm×10mm, the area including three layers was observed simultaneously. Some typical peaks versus 2θ angle are shown in Figs.2 and 3.

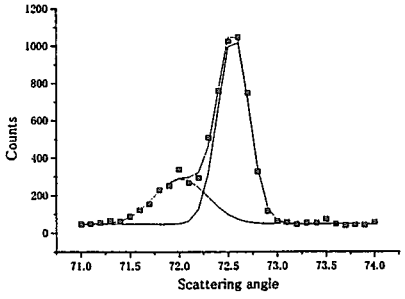

(a)

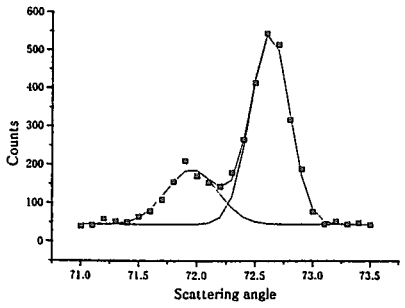

(b)

Fig.2. Ni (200) reflection (a)for radial direction at 14mm position from the center of the diameter and (b)for axial direction at 10mm position from the center.

In Fig.2, a large peak from the middle [Ni] layer and a small peak from the Ni region in both side

原子炉：JRR-3M　　装置：RESA(T2-1)　　分野：中性子散乱（構造）

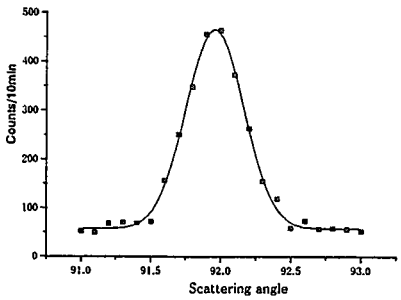

Fig.3. WC (110) reflection for radial direction at 14mm position from the center of the sample.

[WC-10Wt%Ni] layers are observed. We can estimate each strain of Ni region, comparing with the Ni (200) reflection from the [Ni] single layer material. The strain of WC in both side [WC-10Wt%Ni] layers is estimated, using the general lattice constant of WC at room temperature, a=2.9065 Å, as a standard. The strain of Ni (200) plane and that of WC (110) plane in [WC-10Wt%Ni] layers for radial direction are shown in Figs.4 (a) and (b). There is no explicit difference according to each position of the sample. The Ni region in [WC-10Wt%Ni] layer both for single layer material and for three layers material is exposed to large tensile strain of 0.7～0.8%, whereas WC particles are exposed to small compressive strain between 0 and –0.2%.

The strain obtained by the measurements for the axial direction does not show any explicit difference from that for the radial direction.

The obtained strain values of Ni and WC in [WC-10Wt%Ni] layer show good coincidence with those calculated by finite element method. This fact indicates that as the Ni melted in [WC-10Wt%Ni] layer joins tightly with WC particles, it is elongated in the cooling process under the influence of the small coefficient of

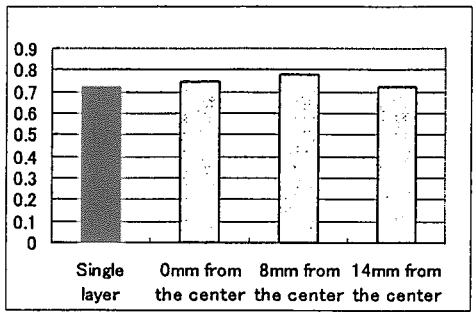

(a)

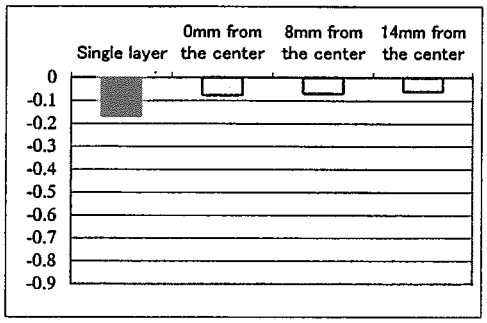

(b)

Fig.4. Strain (%) of (a) Ni (200) and (b)WC (110) in [WC-10Wt%Ni] layer for radial direction. Black bar shows the strain of single layer [WC-10Wt%Ni] material and gray bars show those of three layers [WC-10Wt%Ni]-[Ni]-[WC-10Wt%Ni] material.

contraction of WC. This tensile strain is not released at room temperature. On the other hand, a large amount of WC is hardly influenced by the contraction of Ni region.

It was found that the middle [Ni] layer experiences almost no strain. This experimental result suggests that the [Ni] layer shrinks freely in the process of cooling, because the joint between the [Ni] layer and the [WC-10Wt%Ni] layer seems to be loose.

研究テーマ：ホイスラー型 Ni_2MnGa 系合金の中性子回折
表題：ホイスラー型 Ni_2MnGa 系合金の中性子回折

1-1-28
Neutron Diffraction Study on Heusler-type Ni_2MnGa-based Alloys

K. Inoue, K. Enami, M.Igawa, Y. Yamaguchi[1] and K. Ohoyama[1]

Fac. Sci & Tech. Ryukoku Univ. Seta, Otsu. 520-2194 Japan
[1]IMR, Tohoku Univ. Aoba-ku, Sendai, 980-8577 Japan

The Heusler-type Ni_2MnGa alloy shows a thermoelastic martensitic transformation at a temperature, M_S, of about 200K[1]. Both the martensitic phase below M_S point and the Heusler phase above M_S point show ferromagnetism. The Curie temperature, T_C, of the Heusler phase is around 370K[1]. We intend to control the shape memory effect caused by this martensitic transformation, using the external magnetic field instead of temperature change. For this purpose, we tried to bring the temperature, M_S, closes to the temperature, T_C, by changing the composition of the alloy off-stoichiometrically or by replacing some atoms with the other kind of atoms.

The effect of replacing Ni atoms with Pd, or Ga with Ge, is already reported [2].

In this paper, we report the effect of changing the concentration of Ni and Mn atoms off-stoichiometrically. By the measurements of temperature dependence of electrical resistivity and magnetization, it was found that the coincident transformation temperatures are 340K for $Ni_{2.18}Mn_{0.82}Ga$ and 350K for $Ni_{2.19}Mn_{0.81}Ga$. This result is consistent with that obtained by A.N.Vasil'ev et al [3]. The temperature dependence of magnetization is shown in Figs.1 (a) and (b).

We have made the powder neutron diffraction of $Ni_{2.18}Mn_{0.82}Ga$ at 100K and of $Ni_{2.19}Mn_{0.81}Ga$ at 297K, using HERMES diffractometer installed at JRR-3M reactor at JAERI. The neutron wave length was 1.8196Å.

The results are shown in Figs.2 (a) and (b). The diffraction patterns are similar to that of

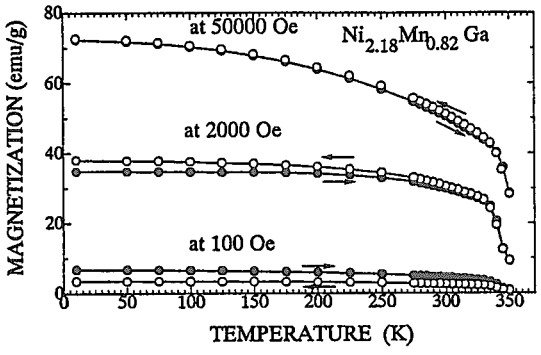

(a)

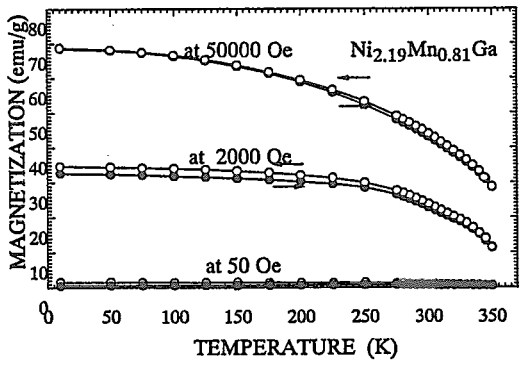

(b)

Fig.1. Magnetization versus temperature for (a) $Ni_{2.18}Mn_{0.82}Ga$ and (b) for $Ni_{2.19}Mn_{0.81}Ga$

$Ni_2(Pd_{0.16}Mn_{0.84})Ga$ at 16K[2] for both compounds. This fact indicates that the martensitic structure for these two compositions is the same as that of $Ni_2(Pd_{0.16}Mn_{0.84})Ga$, that is, two crystal structures coexist. One is an orthorhombic structure distorted from the cubic Heusler one and the other is a monoclinic one with the shuffling of 6 layers of (220) planes of this orthorhombic structure [2].

To investigate whether the martensitic transformation is affected by an external

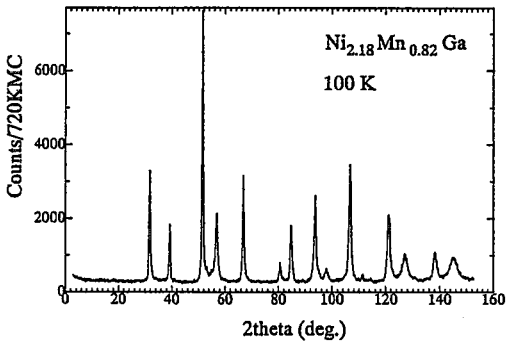

(a)

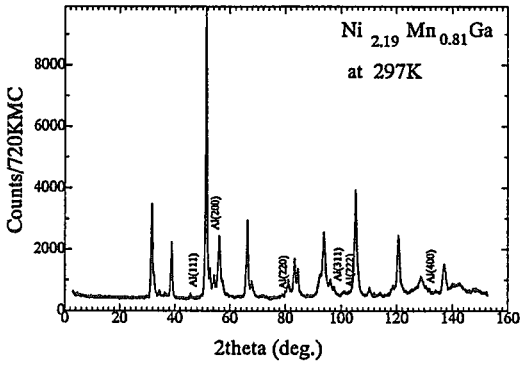

(b)

Fig.2. Neutron diffraction pattern (a)for $Ni_{2.18}Mn_{0.82}Ga$ at 100K (b) for $Ni_{2.19}Mn_{0.81}Ga$ at 297K.

magnetic field or not, we have made the neutron diffraction of $Ni_{2.19}Mn_{0.81}Ga$ at M_S temperature of 350K under the external magnetic field. The TAS-2 diffractometer installed at JRR-3M reactor at JAERI was used. The neutron wave length was 1.6498Å. We have observed the peaks in the region of $2\theta = 67^\circ \sim 96^\circ$. There are split nuclear peaks for both martensitic phase and Heusler phase, and the effect of magnetic scattering does not appear in this high 2θ region. The diffraction pattern under the magnetic field of 5T is shown in Fig.3. The mass fraction of each structure under each magnetic field, calculated by Rietveld analysis, is shown in Fig.4. We explicitly observe that the application of magnetic field of 5T reduces the mass fraction of cubic Hesler phase to almost half.

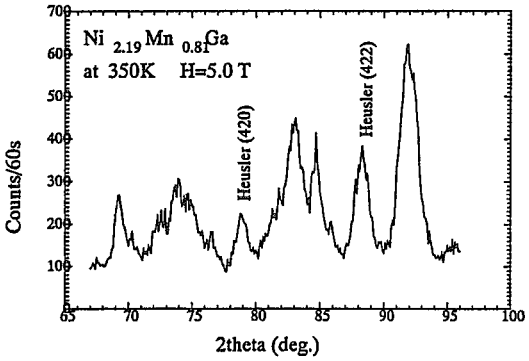

Fig.3. Diffraction pattern of $Ni_{2.19}Mn_{0.81}Ga$ at 350K under the magnetic field of 5T. Two peaks of Heusler phase and the other peaks of martensitic phase are observed.

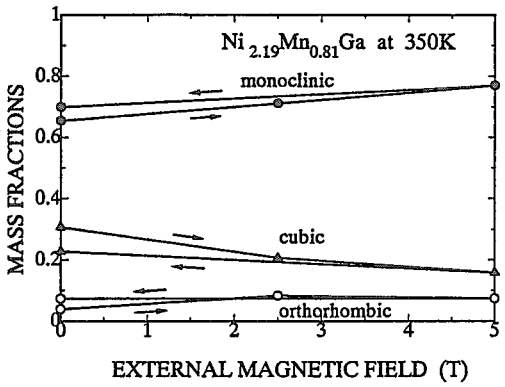

Fig.4. Mass fraction of each structure for $Ni_{2.19}Mn_{0.81}Ga$ at 350K.

This phenomenon suggests that there is a possibility that we can control the martensitic transformation by external magnetic field.

References

[1]P.J.Webster, K.R.A.Ziebeck, S.L.Town and M.S.Peak: Philos.Mag. 49 (1984) 295.

[2]Kazuko Inoue, K.Enami, M.Igawa, Kanryu Inoue, Y.Yamaguchi and K.Ohoyama: Proceedings of the International Conference on Solid-Solid Phase Transformations '99 (1999) 1120.

[3]A.N.Vasil'ev, A.D.Bozhko, V.V.Khovailo, I.E.Dikshtein, V.G.Shavrov, V.D.Buchelnikov, M.Matsumoto, S.Suzuki, T.Takagi and J.Tani: Phys.Rev.B 59 (1999) 1113.

研究テーマ：超イオン導電体における構造不規則性と動的性質
表　　題：GaAsの中性子散漫散乱

1-1-29 Diffuse Neutron Scattering from GaAs

M. Arai, K. Ohki, M. Mutou, T. Sakuma, H. Takahashi[1], Y. Ishii[2]

Faculty of Science, Ibaraki University, Mito 310-8512, Japan
[1]Faculty of Engineering, Ibaraki University, Hitachi 316-8511, Japan
[2]Japan Atomic Energy Research Institute, Tokai 319-1195, Japan

Correlation effects between the thermal displacements of atoms[1)] play an important role to explain the oscillatory diffuse scattering in solid electrolytes, CuI and AgBr. The correlation effect would not be specific in solid electrolytes. In order to inspect the existence of the oscillatory diffuse scattering in semiconductor, diffuse neutron background intensity of GaAs has been measured at 290 K and 8 K using a neutron diffractometer TAS-2 installed at JRR-3 in JAERI. A powder sample of GaAs in a vanadium container with 8 mm in diameter was used. The incident neutron wave length of 1.443 Å was used. Neutron diffraction data were collected for 60 sec per step at 0.1° intervals over the 2θ range of 5° to 118° by a step-scan mode. Fig. 1 shows the result of the double-axis measurement of GaAs at 8 K and 290 K. Several sharp Bragg lines and a

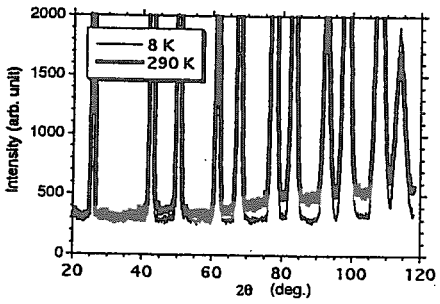

Fig.1 Observed neutron powder diffraction intensity for GaAs at 8 K and 290 K.

large diffuse scattering were observed at 290 K. The first and second peak of the oscillatory diffuse scattering appear at 2θ~45° and 85°, respectively. The oscillatory characteristic in the diffuse scattering of GaAs at 8 K is not clear. The temperature dependence of the oscillatory diffuse scattering from GaAs crystals, which was predicted with the correlation effect between the thermal displacements of atoms, was confirmed by the measurement.

Numerical calculations of the diffuse background have been made based on zinc blende type structure of GaAs including the correlation between the thermal displacements of atoms. The peak positions of the first and second peak in diffuse scattering of GaAs in fig. 1 are greater than those of super ionic conductor CuI which belongs to zinc blende type structure. They are related to the reciprocal of the distance between nearest neighbor atoms; the distances in CuI and GaAs are 2.60 and 2.45 Å at 290 K, respectively. The main contribution to the oscillatory diffuse scattering of super ionic conductors was from the correlation among the displacements of cation and anion atoms. It is suggested that the main contribution of GaAs would be from the correlation among the displacements of gallium and arsenic atoms.

Expected contributions from Ga-Ga, Ga-As and As-As pairs to the diffuse scattering were calculated. The contribution from the correlation among Ga-Ga and As-As atoms was very weak to produce the observed oscillating scheme. The main contribution to the observed oscillatory diffuse scattering is from the correlation between the thermal displacements of gallium and arsenic atoms. The background function including the correlation effect between the thermal displacements of atoms is very effective to treat the diffuse scattering from crystals with the measurement by X-rays and neutrons.

Reference

[1] T. Sakuma: J. Phys Soc. Jpn, 42(1993), 4150

原子炉：JRR-3M　　装置：TAS-2(T2-4)　　分野：中性子散乱 (構造)

研究テーマ：形状記憶効果の磁場による制御
表題： Ni_2MnGa 系合金の形状記憶効果の中性子回折による研究

1-1-30

Neutron Diffraction Study on Shape Memory Effect of Ni_2MnGa-based Alloys

K. Inoue, K. Enami, M. Igawa, Y. Yamaguchi[1], Y. Morii[2] and Y. Matsuoka[2]

Fac. Sci & Tech. Ryukoku Univ. Seta, Otsu 520-2194, Japan
[1]IMR, Tohoku Univ. Aoba-ku, Sendai 980-8577, Japan
[2]Japan Atomic Energy Research Institute, Tokai, Ibaraki 319-1195, Japan

We intend to control the shape memory effect originated from the thermoelastic martensitic transformation of the Heusler-type Ni_2MnGa-based alloy, using the external magnetic field instead of temperature change. The martensitic transformation temperature, M_S, of stoichiometric Ni_2MnGa is about 200K[1]. The alloy is ferromagnetic below and above this M_S point. The Curie temperature, T_C, of the Heusler structure above M_S point is around 370K[1]. For our intention, we tried to bring the temperature, M_S, closes to the temperature, T_C, by changing the concentration of composite atoms off-stoichiometrically. As a result, the magnetic energy under the magnetic field of the ferromagnetic martensitic phase is smaller than that of the paramagnetic Heusler phase.

In this paper, we report the effect of magnetic field on the transformation of Heusler-type $Ni_{2.19}Mn_{0.81}Ga$, of which the M_S and T_C temperatures coincide to be about 350K.

We have made the powder neutron diffraction of this $Ni_{2.19}Mn_{0.81}Ga$ at 297K with no magnetic field, using HERMES diffractometer installed at JRR-3M reactor at JAERI. The neutron wave length was 1.8196Å. The result is shown in Fig.1. The diffraction pattern is similar to that of $Ni_2(Pd_{0.16}Mn_{0.84})Ga$ at 16K [2]. This fact indicates that the martensitic structure of this $Ni_{2.19}Mn_{0.81}Ga$ is the same as that of $Ni_2(Pd_{0.16}Mn_{0.84})Ga$, that is, two structures coexist. One is an orthorhombic structure distorted from the cubic Heusler one and the other is a monoclinic one with the shuffling of 6 layers of

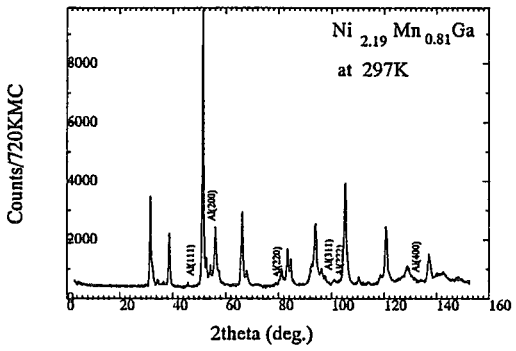

Fig.1. Neutron diffraction pattern of $Ni_{2.19}Mn_{0.81}Ga$ at 297K with no external magnetic field.

(220) planes of this orthorhombic structure [2].

To investigate whether the martensitic transformation is affected by external magnetic field or not, we have observed the powder neutron diffraction patterns of $Ni_{2.19}Mn_{0.81}Ga$ at M_S temperature of 350K under the external magnetic field. The TAS-2 diffractometer installed at JRR-3M reactor at JAERI, equipped with a superconductor magnet, was used. The neutron wave length was 1.6498Å. We have observed the change of the peak intensity in the region of 2θ =67° ～96° , which corresponds 2θ =75° ～ 110° in the case of HERMES measurement. In this 2θ region at 350K, two nuclear peaks of Heusler phase and the other peaks of martensitic phase are observed simultaneously. The effect of magnetic scattering disappears in this high 2θ region.

The experimentally obtained diffraction patterns of the alloy under each magnetic field and the result of Rietveld analysis with the computer program, RIETAN [3], are shown in

原子炉：JRR-3M　　装置：TAS-2(T2-4)　　分野：中性子散乱（構造）

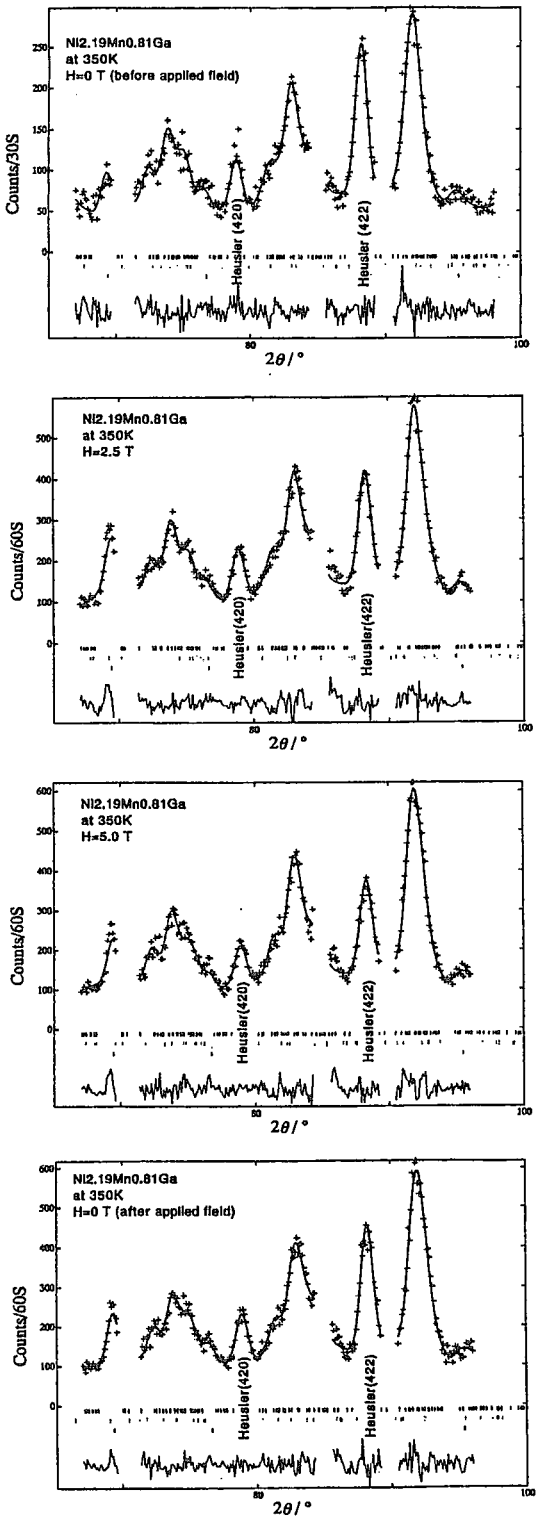

Fig.2. Change of diffraction pattern due to external magnetic field and the result of Rietveld analysis.

Fig.2. The magnetic field was applied in the order 0T, 2.5T, 5.0T and then 0T. The results are shown from upward to downward in the figure. We explicitly observe that the application of magnetic field reduces the peak intensity of the Heusler phase. The mass fraction of each phase versus each magnetic field, obtained by Rietveld analysis, is shown in Fig.3.

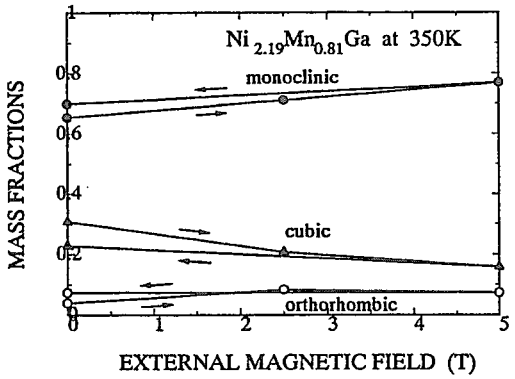

Fig.3. Mass fraction of each phase versus external magnetic field for $Ni_{2.19}Mn_{0.81}Ga$ at 350K.

The mass fraction of cubic Heusler phase under the magnetic field of 5T decreases to be half as much as that under the first field of 0T. This result suggests the possibility that the application of magnetic field onto the cubic Heusler phase just above the transformation temperature changes the Heusler phase to martensitic one.

References

[1]P.J.Webster, K.R.A.Ziebeck, S.L.Town and M.S.Peak: Philos.Mag. 49 (1984) 295.

[2]Kazuko Inoue, K.Enami, M.Igawa, Kanryu Inoue, Y.Yamaguchi and K.Ohoyama: Proceedings of the International Conference on Solid-Solid Phase Transformations '99 (1999) 1120.

[3]F.Izumi: *The Rietveld Method*, ed. R.A.Young (Oxford Univ. Press, Oxford, 1993) Chap.13.

研究テーマ：半磁性半導体 $Zn_{1-x}Mn_xTe$ の非弾性中性子散乱
表題：層状酸化物 $La_{1-x}Ca_xMnO_3$ (x=0.15) の中性子散乱による研究

1-1-31 Neutron scattering study of $La_{1-x}Ca_xMnO_3$ with x= 0.15

Shahnaz Begum[1], Y. Ono[1], Y. Miyazaki[1], Y. Tomioka[2]
Y.Tokura[2,3] and T. Kajitani[1]
[1] Department of Applied Physics, Graduate School of Engineering,
Tohoku University, Sendai 980-8579, Japan
[2]Joint Research Centre for Atom Technology (JRCAT), Tsukuba, 305, Japan
[3] Department of Applied Physics, University of Tokyo, Tokyo 113-0033.

Hole doped perovskite manganites are now one of the most important subject to the researchers since the discovery of colossal magnetoresistance (CMR) near Curie temperature T_c. The appearance of the ferromagnetic (FM) metallic state has been qualitatively explained by the double-exchange (DE) mechanism [1]. It has been pointed out that the DE model is not suffucient to fully explain the CMR phenomena in this system. Strong electron-lattice coupling plays an important role in order to perceive the nature of the interaction between the transport properties and magnetism of this system [2]. This system shows strong FM spin fluctuations in the paramagnetic (PM) state [4]. We performed elastic and inelastic neutron scattering experiments on $La_{0.85}Ca_{0.15}MnO_3$ in both powder and single crystal samples to confirm the FM spin fluctuations in the PM state. Neutron diffraction and scattering experiments were carried out using double-axis neutron spectrometer HERMES and the TOF-type cold neutron spectrometer AGNES respectively, both installed at JRR-3M reactor in JAERI.

Figure 1 shows the contour maps of the neutron diffraction intensities in h0l plane at 15 and 293 K. Forbidden peaks are observed at the reciprocal lattice points (100), (001) and (1/201/2) , indication of the doubling of lattice parameters by the slight residual distortion [3]. The diffuse scattering intensities observed in the vicinity of 101 point exhibit strong FM spin fluctuations in the PM phase [4].

Figure 2 shows the temperature dependent change of the inelastic scattering intensities obtained by AGNES for powder sample in the counter group situated at 2-theta = 57-64 degree (close to 101 Bragg peak) at temperatures from 17 to 220 K. An anomalous peak at -1.0 meV is observed only at 17 and 98 K, being in the FM region meaning that the excitation at -1.0 meV is highly temperature dependent and smearing in the PM region, whose origin also may be the spin fluctuations characterized by the hopping of small polarons [4].

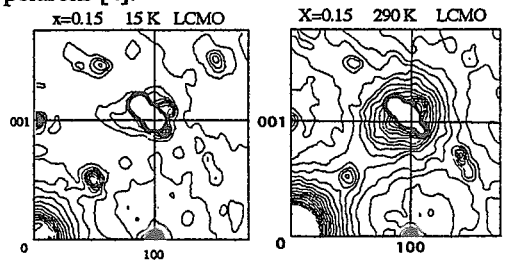

Figure 1 : Contour maps of neutron diffraction intensities for $La_{0.85}Ca_{0.15}MnO_3$ (single crystal) at 15 and 293 K.

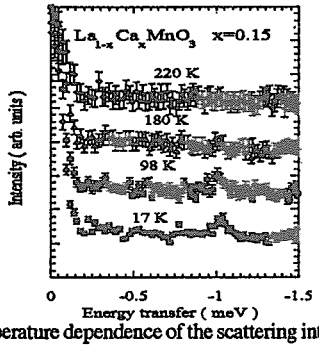

Figure 2 : Temperature dependence of the scattering intensities observed at the counter group situated at 2-theta=57-64 degree.

References :
[1] C. Zener, Phys. Rev., 82 (1951) 403.
[2] A.J. Millis et al., Phys. Rev. Lett. 74 (1995) 5144, ibid 77 (1996) 175.
[3] K.N. Clausen et al. J. Phys. Cond. Matt. 1 (1989) 2721-2726.
[4] R. Kajimoto et al., Activity report on Neutron Scattering Research, vol. 5, (1998) 84.

研究テーマ：$CuGeO_3$の中性子非弾性散乱
表題：$CuGeO_3$の低エネルギーフォノン分枝

1-1-32 Observation of Low Lying Phonons in $CuGeO_3$

M. Nishi, K. Kakurai, Y. Fujii, S. Katano[1], and J. Akimitsu[2]

Neutron Scattering Laboratory, ISSP, University of Tokyo, Tokai, Ibaraki, 319-1106
[1]ASRC, JAERI, Tokai, Ibaraki, 319-1196
[2]Department of Physics, Aoyama-Gakuin University, Setagaya-ku, Tokyo, 157-8572,

The spin-Peierls (SP) transition is accompanied with an intrinsic lattice instability in a system of quantum mechanical antiferromagnetic chains, where the spins (S = 1/2) are interacting via a Heisenberg exchange interaction and are also coupled to a three-dimensional lattice. In the case of the first inorganic SP compound $CuGeO_3$, the transition temperature T_{sP}, the exchange interaction J, spin-Peierls gap Δ, and spin-lattice coupling constant η are the intermediate values among the organic SP substances discovered until now. Moncton *et al.* [1] observed the soft phonon in TTF-CuBDT and van Bodegom *et al.* did also in MEM-$(TCNQ)_2$ [2] that is observed below the characteristic temperature higher than J and has the energy of about 1 meV. Recently the longitudinal phonon propagating along b*-direction was measured with high energy resolution by inelastic neutron scattering, and it was clarified that an optical phonon branch exists near the acoustic longitudinal phonon branch [3]. We got the low lying phonon dispersion around k = odd number of b*-LO branch that has about 0.76 meV as the minimum energy at (0, 3.05, 0). In this study the phonon measurement of $CuGeO_3$ has been performed in (h, k, 0) scattering plane in the reciprocal lattice space at room temperature (RT) by means of inelastic neutron scattering on ISSP-HER (C11) spectrometer installed at the research reactor JRR-3M, Japan Atomic Energy Research Institute (JAERI), in Tokai, Japan. Fig. 1 shows the raw data of inelastic neutron scattering taken at (0, 3.05, 0) with E_f = 3.1 meV at RT (see Fig. 1). We could observed the phonon peaks at several q points (q = 0.0, 0.025, 0.05, 0.075, 0.1 (b*)) around the Bragg point, (0, 3, 0) that are plotted in Fig. 2. These phonons are plotted in the optical branch near Γ point but correspond to zone boundary in extended Brillouin zone (see Fig. 3) which means the out of phase motion between the two chains occupied each other within the half distance of lattice constant b . We speculate that the oxygen atoms play important role for the alternation of the exchange interaction of Cu spins, and they shift also in ab-plane at T_{sP}. It may be thought as one origin of SP transition that oxygen-atoms motion has very low frequency and shift very easily in *ab*-plane.

[1] D.E. Moncton, R.J. Birgeneau, L.V. Interrante, and F. Wudl, Phys. Rev. Lett. **39** (1977) 507.
[2] B. van Bodegom, B.C. Larsen, and H.A. Mook, Phys. Rev. **B 24** (1981) 1520.
[3] M. Nishi *et al.*, J. Phys. Chem. Solid **60** (1999) 1109.

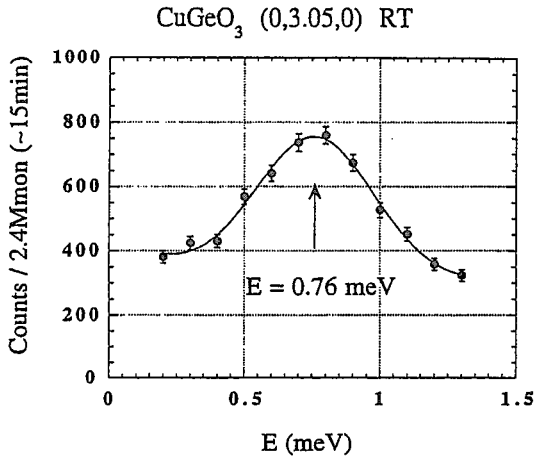

Fig. 1. Neutron scattering profiles at (0, 3.05, 0) with E_f = 3.1 meV. Vertical bars show statistical errors.

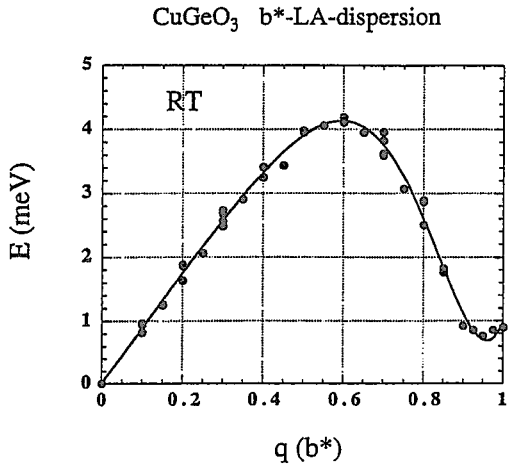

Fig. 3. Extended Brillouin zone of the phonon dispersion along b*-direction. (0, 3, 0) position corresponds to zone boundary of k = 1.

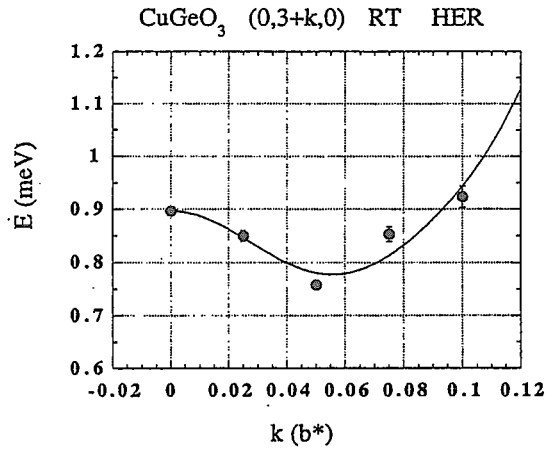

Fig. 2. Optical phonon dispersion along b*-direction near (0, 3, 0).

研究課題：非弾性中性子散乱法によるオレイン酸の分子運動の研究
表題：非弾性中性子散乱法によるオレイン酸の分子運動の研究：階層モード Reactor:JRR-3M

1-1-33 NEUTRON INCOHERENT INELASTIC SCATTERING OF ORIENTED OLEIC ACID; DYNAMICS OF A HIERARCHIC STRUCTURE CRYSTAL

Tomoyuki YOKOYAMA, Norio ACHIWA and Masao SUZUKI[A]
Department of Physics, Kyushu University, Fukuoka, 8128581, Japan
[A]Nippon Oil and Fat Co.ltd.,Amagasaki, Hyougo, 580, Japan

May 31, 2000

1 INTRODUCTION

Lattice vibrational modes of infinite polymethylene chain -C(CH_2)$_n$C- of phonon and internal molecular modes of CH_2 bending mode were observed by means of neutron incoherent inelastic scattering method and infrared absorption and Raman scattering methods[1,2].

On the other hand in the case of finite zigzag chain compound hierarchic spectra of local vibrational accordion modes are expected owing to its hierarchic structure.

Oleic acid is a typical finite zigzag molecular compound. Oleic acid molecule consists of a couple of finite polymethylene chains connected by ethylene double bond carbon and makes dimer along the chain axis connected by hydrogen bonds between carboxyl groups in liquid and crystal phases; molecular formula is $CH_3(CH_2)_7CH{=}CH(CH_2)_7COOH$. Oleic acid crystal consists of two dimers in the unit cell; so a hierarchic bonding structure of polymethylene chain exists in the crystal. Then it is expected that it should exist a hierarchic vibrational accordion modes. We planed to observe these hierarchic excitation of local modes by using neutron incoherent inelastic scattering of oriented oleic acid in oriented crystal and in liquid phases.

It is interesting to show that these internal molecular, coupled molecular and lattice vibrational modes exist in low frequency region. In liquid phase if any periodic structure does not exist then lattice vibrational modes should not exist. So we are interesting how these three kind modes behavior in liquid phase. In our previous study low energy region spectra of oriented oleic acid were observed by mean of TOF neutron spectrometer[3,4]. But their bands were broad because of inharmonisity of thermal vibration. Then in order to lower the inharmonisity of thermal vibration, spectra have been observed at lower temperature.

2 EXPERIMENTS

In order to get an oriented crystal, a field cooling technique was adopted for ferrofluid solution of oleic acid. The ferrofluid was prepared by solventing 1 weight percent of oleic acid covered-magnetite(Fe_3O_4) particle to ultra pure oleic acid liquid(99.9 %, supplied by M.Suzuki on Nippon Oil and Fat Co.ltd.). A strong magnetic field tends to align the magnetic particles along the magnetic field in liquid crystal phase. Then the sample was cooled down below the melting point, 286K of oleic acid, under applied magnetic field 0.6T. The solvent oleic acid is crystallized as β phase with the direction of the hydrocarbon chain perpendicular to the applied field but in the horizontal plane. In this experiment the magnetic field was applied in the horizontal scattering plane of neutron.

The inelastic incoherent neutron spectra of the oriented oleic acid were measured with time-of-flight neutron spectrometer AGNES with an incident neutron energy 4.59meV, installed at the cold neutron guide, C3-1-1, in JRR-3M[5]. 118 detectors of the spectrometer cover the angle region from 9° to 130° per 1°. After the magnetic field cooling in the horizontal scattering plane, the solid oriented sample can be freely rotated in the scattering plane. The spectra were measured at one temperature along two different directions angled 45 degrees, step by step. In the time-of-flight experiment the direction of scattering vector varied according to the time channel of each counter. So the direction dependence of phonon scattering function is obtained by summing up the data in the range of 10 degrees of each Q direction.

3 RESULTS AND DISCUSSIONS

Figure 1 shows the anisotropic phonon scattering function, which is normalized as follows for the neu-

tron energy gain case,

$$G(Q,\omega) = \frac{4\pi m_n}{Q^2\hbar^2}\frac{\omega}{e^{2W(Q)}n(\omega)}S(Q,\omega) \qquad (1)$$

This shows anisotropic phonon contribution to the phonon density of state.

Molecular formula of oleic acid is $CH_3(CH_2)_7CH{=}CH(CH_2)_7COOH$ and it makes dimer in the crystal. The crystal constants of β phase is a=9.3Å b=5.5Å c=35.3Å α=87.9° β=82.8° γ=86.2°. The c-axis is approximately parallel to the molecular chain.

Oleic acid molecule has two finite polymethylene carbon chain $CH(CH_2)_7C$ which has nine carbon atoms. It is expected that $CH(CH_2)_7C$ of which number called m is a unit of accordion mode. Then oleic acid molecule is 2m and dimer is 4m and zone boundary mode along the c-axis is 8m. Energy of accordion mode is inversely proportional to number of carbon atoms. Then it is expected that these accordion modes reflect this hierarchic structure. Accordion mode of polymethylene chain of nine carbon atoms is estimated 31.1meV by Shaufele[6]. Then bands around 33.1meV and 31.5meV were assigned to accordion modes of $CH(CH_2)_7CH_3$ and $CH(CH_2)_7COOH$, respectively in a crystal. Then it is estimated that energy of accordion modes of oleic acid molecule(2m), dimer(4m) and zone boundary mode(8m) are 15.6meV, 7.8meV and 3.9meV. Then bands around 15.7meV, 7.3meV and 3.6meV were assigned to accordion modes of 2m and 4m and zone boundary mode, respectively. These bands show maximum parallel to the c-axis in crystal phase. In liquid phase long range structure and orientation is extinguished. Then accordion mode of 8m is extinguished in liquid phase and that of m, 2m and 4m show all **Q** direction.

Accordion modes should be that of m, 2m, 4m and 8m in perfect crystal. But band correspond to accordion modes of 1.5m, 2.5m, 3m, 3.5m, 5m, 6m, 7m, 12m and 16m were observed and their energy were 21.5meV, 12.5meV, 10.2meV, 8.8meV, 6.1meV, 5.2meV, 4.4meV, 2.7meV and 1.7meV, respectively. The oriented oleic acid crystal is not perfect single crystal, but it contained a lot of miss match in molecular packing. Then pinning was occurred at the lattice defects and new periodic structure of just as 1.5m,2.5m,3m,$\cdots$ or those several times occurs. So these anomalous modes appeared. In liquid phase these anomalous modes are extinguish because long range structure is extinguished.

Bands around 6.8meV, 9.3meV, 13.1meV, 17.6meV and 21.8meV of which polarization vector is perpendicular to the chain c-axis were assigned to $\nu_9^b(0)$, $\nu_5^a(\pi)$, $\nu_5^b(\pi)$, $\nu_5^b(0)$ and $\nu_5^a(0)$, respectively. These modes were only observed **Q** perpendicular to the c-axis in crystal phase. These modes are extinguished in liquid crystal because long range structure perpendicular to the c-axis is extinguished.

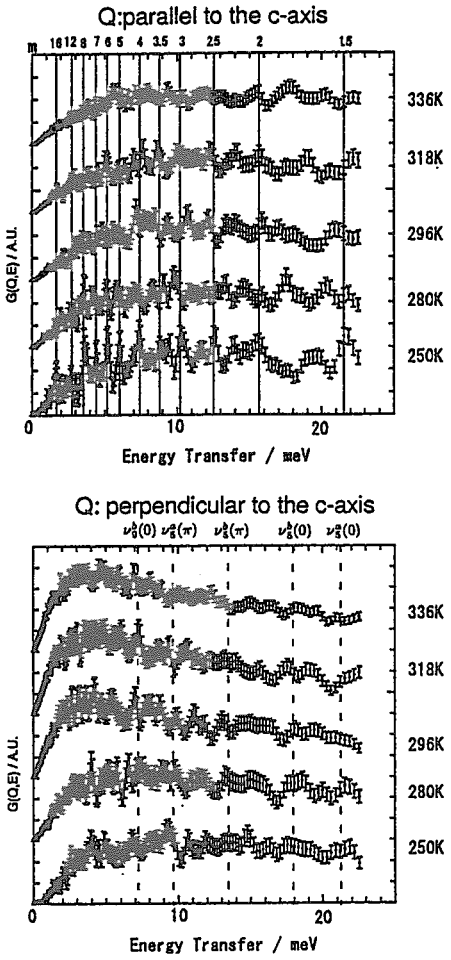

Figure 1: Normalized phonon scattering function at several temperature for the scattering Q vector parallel and perpendicular to the chain axis c of oleic acid. The mode assignments are given at the top row where m times these numeral means the length of accordion modes.

REFERENCES

1. Jobic H, J.Chem.Phys. **76**, 2693(1982).
2. M.Tasumi and T.Shimanouchi, J.Chem.Phys. **43**, 1245(1965)
3. T.Yokoyama, N.Achiwa and M.Suzuki,J.Phys.Chem.Solids **60**, 1519(1999)
4. T.Yokoyama and N.Achiwa, Activity Report on Neutron Scattering Research, **6**, 153(1999)
5. Kajitani T., Shibata K., Ikeda S., Kohgi M., Yoshizawa H., Nemoto K. and Suzuki K., Phisica **B213&214**, 872(1995).
6. Schaufele R.F. and Shimanouchi T., J.Chem.Phys. **47**, 3605(1967).

研究テーマ：重質油の改質を目的とした小角中性子散乱法によるアスファルテンミセルの解析（黎明研究）
表題：重質油の改質を目的とした小角中性子散乱法によるアスファルテンミセルの解析

1-1-34

Characterization of Asphaltene Micelles and Their Interactions in Vacuum Residue of Crude Oil by Small-Angle Neutron Scattering

S. Kamei, K. Yogo, M. Ishikawa and J. Suzuki[1]

Mitsubishi Research Institute, Inc., 2-3-6 Otemachi Chiyoda-ku Tokyo 100-8141, Japan
[1]Japan Atomic Energy Research Institute, Tokai, Ibaraki 319-1195, Japan

Recently, the development of better refining technology of heavy oil is becoming more important in the field of oil industry, because available crude oils become heavier and more concentrated in sulfur and metals. Asphalten, which is the n-heptane insoluble fraction of petroleum, strongly affects the property of crude oil, though its content is slightly several % in weight.

Experimental study on the micellar structure of asphaltenes and their interaction in Arabian heavy vacuum residue was performed utilizing small-angle neutron scattering (SANS) techniques. Since asphaltenes are mainly composed of poly-condensed aromatics, they intend to form micelles in the heavy oils by interacting each other. It is, therefore, very important to clarify the precise micellar structure of asphalten for the oil industry.

Samples used were Arabian Heavy Vacuum Residue (AH-VR) and VR fractions of the hydrotreated oil from AH atmospheric residue. Asphaltene was prepared from VR with addition of n-heptane. Hydrotreatment was performed in a fixed bed continuos flow reactor system, in which hydrodemetallization (HDM) and hydrodesulfurization (HDS) catalysts were installed, respectively.

SANS was measured as a function of concentration (0.5%, 1.0%, 2.0%) and temperature (13C°, 100C°, 200C°, 250C°). d-toluene was used as a solvent. Fig.1 shows the q-I(q) plot of asphalten. R_G of AR-AH-VR, -HDM and HDS are shown in Table1, respectively. R_G of HDM and HDS were 2times larger than that of VR. This strongly suggests the existence of molecular association of asphalten micelles by hydrodemetallization.

Based on the more precise analysis of SANS, we found that the core of micelles had prelate structure with a 29Å, 7Å and 7Ådiameter and that the thickness of polar region was 8Å.

SANS is very powerful tool to understand the micellar structure of asphaltens.

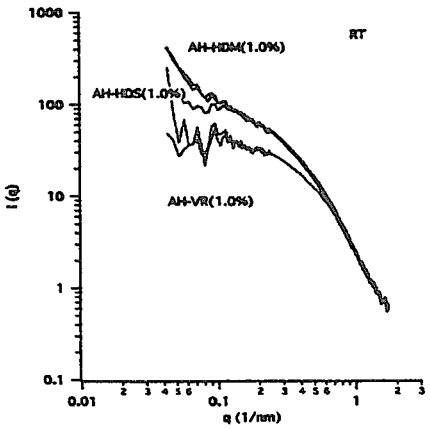

Fig.1 q-I(q) plot of Asphalten

Table1 R_G of Asphalten

	Concentration	R_G(nm)
AR-AH-VR	2.0%	3.728
	1.0%	3.730
	0.5%	3.666
AR-AH-HDM	2.0%	4.428
	1.0%	4.417
	0.5%	4.332
AR-AH-HDS	2.0%	4.494
	1.0%	4.513
	0.5%	4.468

Acknowledgement

We thank Prof. M. Frusaka of KEK and Y. Matsushita of Nagoya Univ. for useful discussion. The samples were provides by Petroleum Energy Center (PEC).

Reference

[1] M.Scarsella, D. Mastorofini, L. Barre, D. Espinat, and D. Fenistein, Energy and Fuels, 13 (1999) 739.
[2] D. A. Storm, E. Y. Sheu, Fuel, 74 (1995) 1140.

原子炉：ＪＲＲ-3M　装置：SANS-J (C3-2)　　分野：中性子散乱（構造）

研究テーマ：超低温の導入による中性子散乱の研究

表題：電子線照射されたFe-Cu合金の析出現象の中性子小角散乱による研究

1-1-35

SANS Study of precipitation phenomena of electron-irradiated Fe-Cu alloy

K. Aizawa, A. Iwase, T. Tobita and M. Suzuki

Japan Atomic Energy Research Institute, Tokai, Ibaraki 319-1195, Japan

In order to understand the relation of precipitation and hardening of electron irradiated Fe-Cu alloy system, we studied Fe-0.53at%Cu and Fe-0.0018at%Cu alloys by small-angle neutron scattering (SANS). Electron irradiations were carried out at the ACCELERATOR NO.2 at Takasaki establishment of JAERI. The electron irradiation dose is ranged from 8×10^{-5} to 8.55×10^{-4} dpa. SANS measurements were performed using SANS-J instrument at JRR-3M in JAERI. The covered q-range ($q=2\pi\theta/\lambda$, θ : scattering angle, λ : neutron wavelength) was from 0.2 to $2nm^{-1}$.

Figure 1 shows the evolution of SANS cross-section of electron irradiated samples evaluated by subtracting intensity from unirradiated sample. As increasing electron irradiation dose, SANS cross-section increased and shifted to lower q-value in the case of Fe-0.53at%Cu alloy. On the other hand, SANS cross-section of Fe-0.0018at%Cu alloy, which is low copper concentration sample, is rather lower than that of Fe-0.53at%Cu alloy corresponding to electron irradiation dose. This means that SANS cross-section arise from copper precipitation due to electron irradiation but not irradiation damage such as vacancy clusters. We assumed that the shape of the precipitation is spherical and performed least square fittings. Solid lines are fitted curves in Fig. 1. The fitting is quite well. We performed Guinier analysis also and Guinier plots showed straight regions in all data. These mean that polydispersibility of precipitate is low.

Figure 2 shows the evolution of the radius of copper precipitate obtained from model fitting and Guinier analysis. Copper precipitated even very low electron irradiation dose in the case of Fe-0.53at%Cu alloy. And we can see a tendency of saturating of the radius in high electron irradiation dose.

The hardness curve obtained from the Vickers hardness measurement behaves as a curve of evolution of radius. This means that the radius or volume of precipitation is strongly correlated to the hardness.

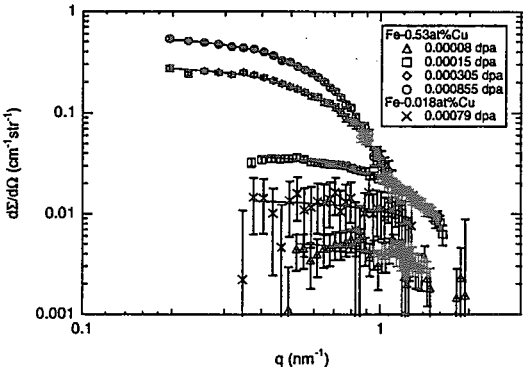

Fig. 1 SANS cross-section for copper precipitate of electron irradiated Fe-0.53at%Cu and Fe-0.0018at%Cu alloys.

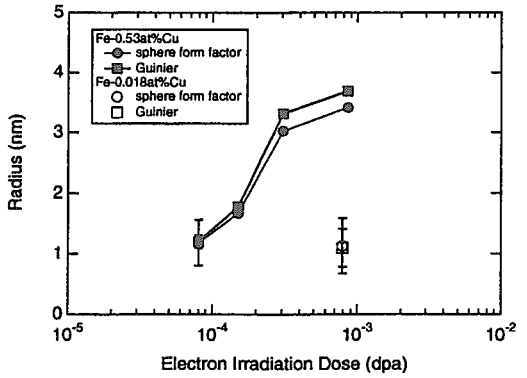

Fig. 2 Evolution of radius of copper precipitate obtained from sphere-particle model fitting and Guinier analysis.

1. 中性子散乱 2) 磁　性

1. Neutron Scattering　2) Magnetism

This is a blank page.

研究テーマ:f, d 混合電子系複合酸化物の磁気構造
表題:秩序化ペロブスカイトBa_2NdRuO_6の中性子回折

1-2-1 Neutron Diffraction Study on Ordered Perovskite Ba_2NdRuO_6

Y. Izumiyama, Y. Hinatsu, K. Oikawa[1], Y. Shimojo[1] and Y. Morii[1]

Division of Chemistry, Graduate School of Science, Hokkaido University, Sapporo 060-0810, Japan
[1] Japan Atomic Energy Research Institute, Tokai-mura, Ibaraki 319-1195, Japan

Magnetic properties of an ordered perovskite compound Ba_2NdRuO_6 have been reported. The temperature dependence of the magnetic susceptibility was measured in the temperature range of 2 - 300K. Two magnetic anomalies have been found in the susceptibility vs. temperature curve, i.e., one maximum of the susceptibility appears at ca.27K and an inflection of the susceptibility occurs at ca. 58K.

In order to determine the crystal structure and magnetic properties, powder neutron diffraction measurements were performed at 100, 35 and 7K using the high resolution powder diffractometer (HRPD) in the JRR-3M reactor, with a Ge (331) monochromator ($\lambda = 1.8230$ Å).

Figure 1 shows the powder neutron diffraction profiles for Ba_2NdRuO_6 and the Rietveld analysis at 100, 35 and 7K. The refinement of the data collected at 100K showed that this compound has a monoclinic symmetry with space group $P2_1/n$ (No.14), and that the structure is a perovskite with a 1:1 ordered arrangement of Ru^{5+} and Nd^{3+} over the 6-coordinate sites.

The magnetic structure determined is illustrated in Fig. 2, i.e., the magnetic type is Type I. Both the magnetic moments are found to be in the same direction from the analysis, therefore the *ab* plane would be ferromagnetic plane. On the *ab* plane, there exist both the Nd^{3+} and Ru^{5+} ions. Unfortunately, there is no difference between the profiles measured between at 35K and at 7K except for the variation of the intensity of their magnetic peaks, which indicates that two kinds of magnetic ions (Nd^{3+} ion and Ru^{5+} ion) magnetically order at the same temperature, 58K.

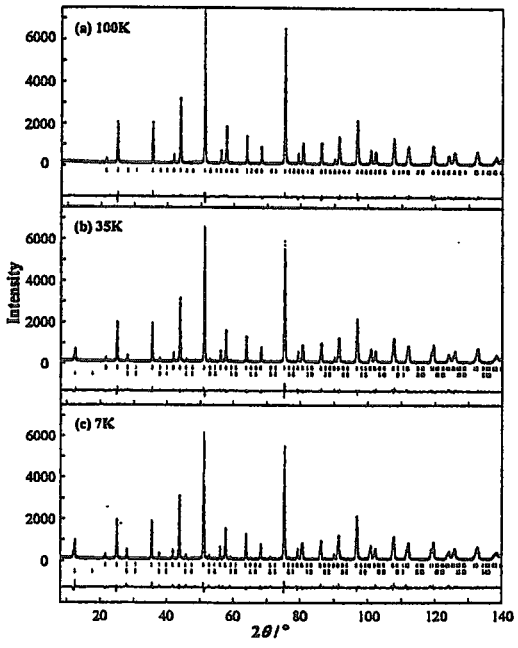

Figure 1 Powder neutron diffraction profiles for Ba_2NdRuO_6 at 100K (a), 35K (b) and 7K (c).

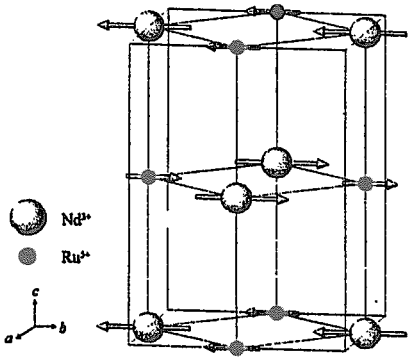

Figure 2 The magnetic structure of Ba_2NdRuO_6. Diamagnetic ions are omitted. Larger circles Nd^{3+}; smaller circles Ru^{5+}.

原子炉:JRR-3M　　装置:HRPD(1G)　　分野:中性子散乱(磁性)

研究テーマ:f, d 混合電子系複合酸化物の磁気構造
表題:秩序化ペロブスカイト Sr_2TbRuO_6 の中性子回折

1-2-2 Neutron Diffraction Study on Ordered Perovskite Sr_2TbRuO_6

Y. Doi, Y. Hinatsu, K. Oikawa[1], Y. Shimojo[1] and Y. Morii[1]

Division of Chemistry, Graduate School of Science, Hokkaido University, Sapporo 060-0810, Japan
[1] *Japan Atomic Energy Research Institute, Tokai-mura, Ibaraki 319-1195, Japan*

Magnetic properties of ordered perovskite-type compound Sr_2TbRuO_6 have been reported. The magnetic susceptibility and specific heat measurements show the existence of magnetic transitions at 32K and 41K.

In order to determine the magnetic structures, powder neutron diffraction measurements were performed at room temperature and 10K with a High Resolution Powder Diffractometer (HRPD) in the JRR-3M reactor with a neutron incident wave length ($\lambda = 1.8230$Å).

Powder neutron diffraction patterns of Sr_2TbRuO_6 and the Rietveld analysis are shown in Fig.1. The crystal structure at room temperature is monoclinic with space group $P2_1/n$ (No.14), and the Tb^{3+} and Ru^{5+} ions are structurally ordered at the *B* sites of the ABO_3 perovskite-type structure.

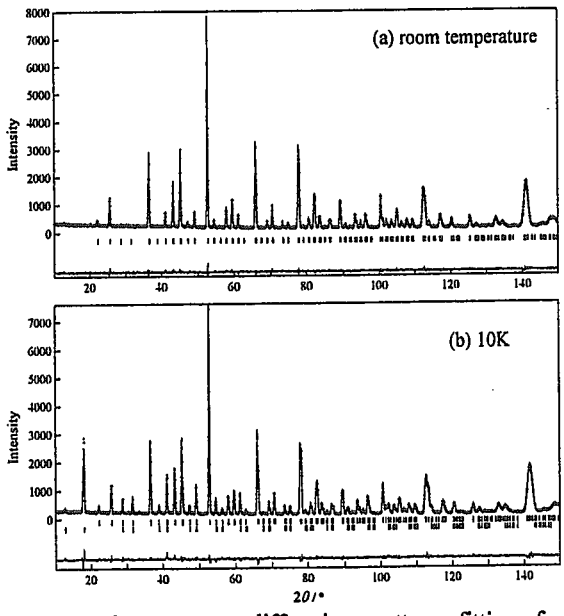

Fig.1 Powder neutron diffraction pattern fitting for Sr_2TbRuO_6.

The magnetic structure of Sr_2TbRuO_6 at 10K is illustrated in Fig.2. The magnetic moment of the Tb^{3+} and Ru^{5+} are ordered antiferromagnetically, respectively. Each of these orders in a type I arrangement. The gradient of the magnetic moments against the *c* axis is about 20°. The ordered magnetic moments are $2.99(11)\mu_B$ for Ru^{5+} and $4.98(12)\mu_B$ for Tb^{3+}. The ordered moment for Tb^{3+} is much smaller than the value of g_JJ ($9\mu_B$). This may be due to the fact that the magnetic moments of Tb^{3+} ions do not saturate at 10K.

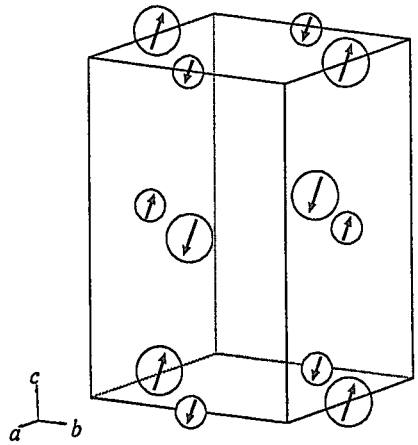

Fig.2 The magnetic structure of Sr_2TbRuO_6. Diamagnetic ions are omitted. Larger circles Tb^{3+}; smaller circles Ru^{5+}.

原子炉:JRR-3M　　装置:HRPD(1G)　　分野:中性子散乱(磁性)

研究テーマ:f, d 混合電子系複合酸化物の磁気構造
表題:秩序化ペロブスカイトBa_2PrRuO_6の磁気構造

1-2-3 Magnetic Structure of the Ordered Perovskite Ba_2PrRuO_6 by Powder Neutron Diffraction Measurements

Y. Izumiyama, Y. Hinatsu, K. Oikawa[1], Y. Shimojo[1] and Y. Morii[1]

Division of Chemistry, Graduate School of Science, Hokkaido University, Sapporo 060-0810, Japan
[1] Japan Atomic Energy Research Institute, Tokai-mura, Ibaraki 319-1195, Japan

Magnetic properties of an ordered perovskite compound Ba_2PrRuO_6 have been reported. The temperature dependence of the magnetic susceptibility was measured in the temperature range of 2 - 300K, which is shown in Figure 1. A magnetic anomaly has been found at ca.112K.

In order to study the crystal and magnetic structures in detail, powder neutron diffraction measurements were performed at 150 and 7K using the high resolution powder diffractometer (HRPD) at the JRR-3M reactor, with a Ge (331) monochromator ($\lambda = 1.8230$ Å).

The RIETAN program was used for the analysis of the crystal and magnetic structures. The structural refinements of the neutron data collected at 150K showed that this compound has a monoclinic symmetry with space group $P2_1/n$ (No.14), $a = 6.0062(5)$, $b = 5.9863(4)$, $c = 8.4679(8)$ Å and $\beta = 90.03(2)°$, and that the structure is a perovskite with a 1:1 ordered arrangement of Ru^{5+} and Pr^{3+} over the 6-coordinate sites.

Magnetic peaks have been observed from the 7K neutron diffraction data. The magnetic structure we determined is Type I (Fig. 2), in which both the magnetic moments of Pr^{3+} and Ru^{5+} ions in the *ab* plane are parallel and the moments of adjacent planes are antiparallel each other. The strong magnetic reflections of (100) and (010) planes suggest that these moments are along the *c* axis. The ordered magnetic moments at 7K are 2.2(1) μ_B for Pr^{3+} and 2.0(2) μ_B for Ru^{5+}.

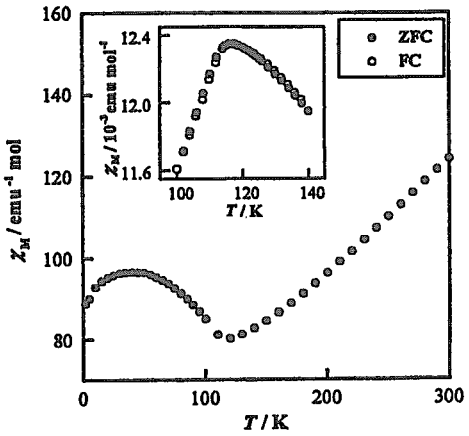

Figure 1 Temperature dependence of the magnetic susceptibility of Ba_2PrRuO_6.

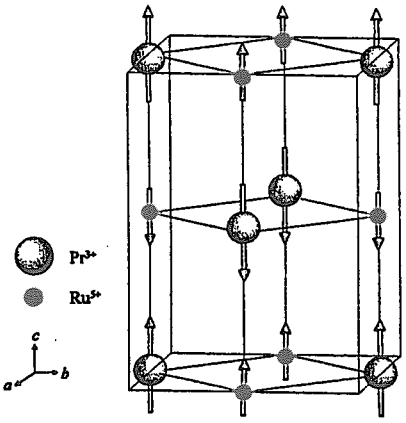

Figure 2 The magnetic structure of Ba_2PrRuO_6. Diamagnetic ions are omitted. Larger circles Nd^{3+}; smaller circles Ru^{5+}.

原子炉:JRR-3M　　装置:HRPD(1G)　　分野:中性子散乱(磁性)

研究テーマ：*f, d* 混合電子系複合酸化物の磁気構造
複合ペロブスカイト Ba_2PrIrO_6 の結晶構造と磁気的性質

1-2-4 Crystal Structure and Magnetic Properties of Ordered Perovskite Ba_2PrIrO_6

M. Wakeshima, D. Harada, Y. Hinatsu, K. Oikawa[1], Y. Shimojo[1] and Y. Morii[1]

Division of Chemistry, Graduate School of Science, Hokkaido University, Sapporo 060-0810, Japan
[1] *Japan Atomic Energy Research Institute, Tokai-mura, Ibaraki 319-1195, Japan*

For a series of ordered perovskites Ba_2RIrO_6 (R = rare earths) except for R = Ce and Pr, the rare earth and iridium ions are in the trivalent and pentavalent states, respectively. These compounds show paramagnetic behavior above 2 K. On the other hand, for the case of R = Ce and Pr, both R and Ir ions are in the tetravalent states and the antiferromagnetic transitions occur at 17 K for Ba_2CeIrO_6 and at 71 K for Ba_2PrIrO_6. [1)]

Specific heat of Ba_2PrIrO_6 was measured using the commercial specific heat measurement system (Quantum Design, PPMS) in the temperature range 2-120 K. Powder neutron diffraction measurements of Ba_2PrIrO_6 were carried out at 7 and 100 K using a High Resolution Powder Diffractometer (HRPD) in the JRR-3M reactor with a neutron incident wave length (λ = 1.82263 Å). The Rietveld analyses were performed with the neutron diffraction data.

Figure 1 shows the temperature dependence of specific heat for Ba_2PrIrO_6. It has a λ-type anomaly at 71 K. This result reveals that both Ir^{4+} and Pr^{4+} ions are in the antiferromagnetic states below 71 K. In comparison with T_N of Ba_2CeIrO_6, high T_N of Ba_2PrIrO_6 is supposed to result from the participation of f electron of Pr^{4+} in the superexchange interaction

Figure 2 shows the observed and calculated diffraction patterns for Ba_2PrIrO_6 at 10 and 100 K. No magnetic reflection is found. This is caused by small magnetic moments of Ir^{4+} and Pr^{4+}. Their diffraction patterns were fitted with perovskite-type monoclinic structure (space group $P2_1/n$). The average Ir-O and Pr-O bond lengths at 100 K are calculated to be 2.004 and 2.192 Å. These values also suggest that the Ir and Pr ions are in the tetravalent states.

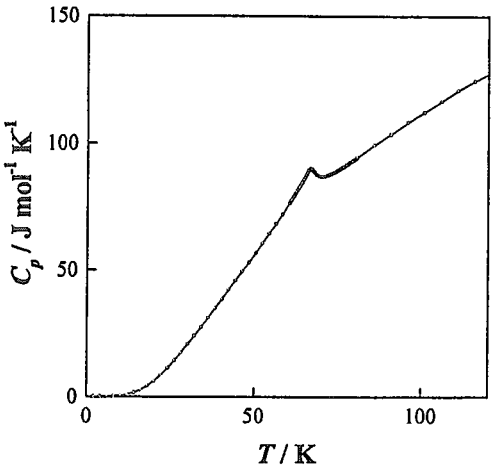

Fig. 1 Specific heat of Ba_2PrIrO_6.

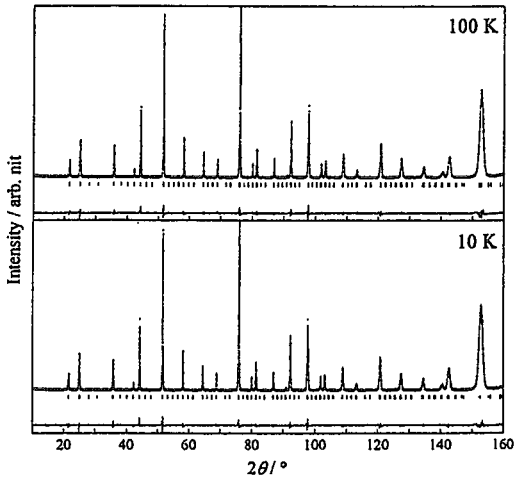

Fig. 2 Powder neutron diffraction patterns fitting for Ba_2PrIrO_6.

Reference

1) M. Wakeshima D. Harada and Y. Hinatsu, J Mater. Chem., 419, **10** (2000).

原子炉：JRR-3M　　装置：HRPD　　分野：磁性

研究テーマ：*f, d* 混合電子系複合酸化物の磁気構造
反強磁性マンガン硫化物 $BaLa_2MnS_5$ の磁気構造

1-2-5 Magnetic Structure of the Antiferromagnetic Manganese Sulfide $BaLa_2MnS_5$ by Powder Neutron Diffraction Measurements

M. Wakeshima, Y. Hinatsu, K. Oikawa[1], Y. Shimojo[1] and Y. Morii[1]

Division of Chemistry, Graduate School of Science, Hokkaido University, Sapporo 060-0810, Japan
[1] Japan Atomic Energy Research Institute, Tokai-mura, Ibaraki 319-1195, Japan

A quaternary manganese sulfide $BaLa_2MnS_5$ has a tetragonal structure with space group *I*4/*mcm*. Its magnetic susceptibility and specific heat showed that the Mn^{2+} ions were in the antiferromagnetic state below 58.5 K [1].

Powder neutron diffraction patterns of $BaLa_2MnS_5$ were measured at 7 and 100 K using a High Resolution Powder Diffractometer (HRPD) in the JRR-3M reactor with a neutron incident wave length (λ = 1.82263 Å). The Rietveld analyses were performed with the neutron diffraction data.

Figure 1 shows the observed and calculated diffraction patterns for $BaLa_2MnS_5$ at 7 and 100 K. The calculated pattern at 100 K is in good agreement with the observed one (R_{wp} = 10.37 %, R_I / % = 2.39). Compared with the pattern at 100 K, no additional peaks appear, but some peaks are observed to be much stronger in intensity at 7 K. This result indicates that $BaLa_2MnS_5$ has a collinear antiferromagnetic structure (space group $I\bar{4}$) with a propagation vector $\boldsymbol{k}$ = (1/2, 1/2, 1/2) at 7 K. The magnetic moment of Mn^{2+} is estimated to be 4.21 μ_B and determined to lie in a parallel direction with the *c*-axis. The reliability factors R_{wp} and R_I for 7 K are 11.29 and 2.43 %, respectively. The magnetic structure of $BaLa_2MnS_5$ is shown in Fig. 2.

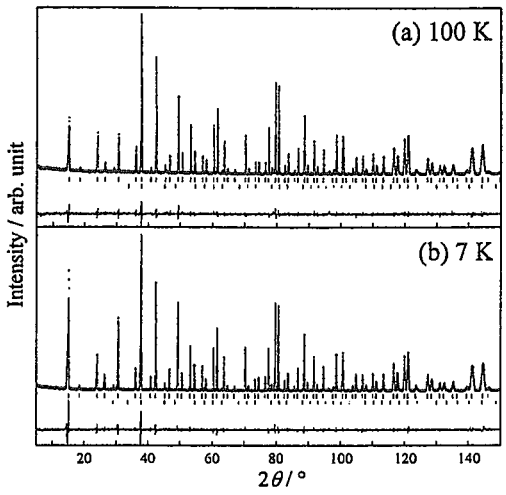

Fig. 1 Powder neutron diffraction patterns fitting for $BaLa_2MnS_5$.

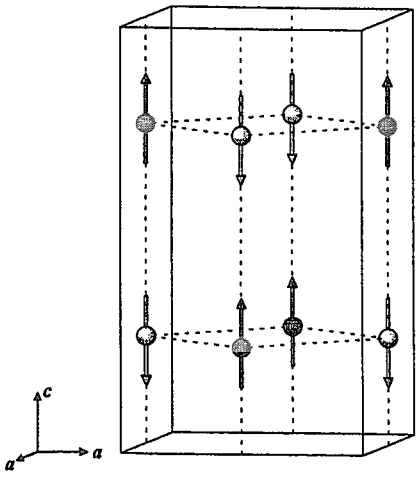

Fig. 2 Magnetic structure for $BaLa_2MnS_5$.

Reference

1) M. Wakeshima and Y. Hinatsu, J Solid State Chem., submitted.

研究テーマ： *f, d* 混合電子系複合酸化物の磁気構造

表題：$La_{0.95}Sr_{0.05}CrO_3$ 及び $La_{0.85}Sr_{0.15}CrO_3$ の中性子回折

1-2-6 Neutron Diffraction Study on $La_{0.95}Sr_{0.05}CrO_3$ and $La_{0.85}Sr_{0.15}CrO_3$

K. Tezuka, Y. Hinatsu, K. Oikawa[1], Y. Shimojo[1] and Y. Morii[1]

Division of Chemistry, Graduate School of Science, Hokkaido University, Sapporo 060-0810, Japan
[1] Japan Atomic Energy Research Institute, Tokai-mura, Ibaraki 319-1195, Japan

Magnetic properties on perovskite-type compounds $La_{1-x}Sr_xCrO_3$ (x = 0.05 and 0.15) have been investigated. From the magnetic susceptibility measurements, three magnetic anomalies have been observed for $La_{0.95}Sr_{0.05}CrO_3$ (at 21K, 85K and 280K) and for $La_{0.85}Sr_{0.15}CrO_3$ (at 26K, 160K and 267K) as shown in Fig. 1.

Powder neutron diffraction measurements on these two compounds indicate that the anomaly found at *ca.* 20K in their susceptibility vs. temperature curves is not ascribable to the magnetic transition. Heat capacity measurements also show that two anomalies have been found at 90K and 280K for $La_{0.95}Sr_{0.05}CrO_3$ and at 160K, 190K and 266K for $La_{0.85}Sr_{0.15}CrO_3$, and no anomaly has been found at *ca.* 20K. The anomaly observed at *ca.* 20K in the susceptibility vs. temperature curve may be due to the weakness of the magnetic anisotropy with increasing temperature.

The magnetic structures for both the compounds have been determined to be the G-type, in which Cr atoms are antiferromagnetically coupled with the six neighboring Cr atoms at any of the temperatures. The magnetic moments of Cr atoms are directed to the *z*-axis of an orthorhombic unit cell for $La_{0.95}Sr_{0.05}CrO_3$ at 10K and 50K, and for $La_{0.85}Sr_{0.15}CrO_3$ at 10K and 50K; the G_z mode dominates. The G_y mode dominates for $La_{0.95}Sr_{0.05}CrO_3$ at 125K, *i.e.*, a spin reorientation has occurred between 50K and 125K. Table 1 summarizes the results of the magnetic structures for $La_{1-x}Sr_xCrO_3$ (x = 0, 0.05, 0.15).

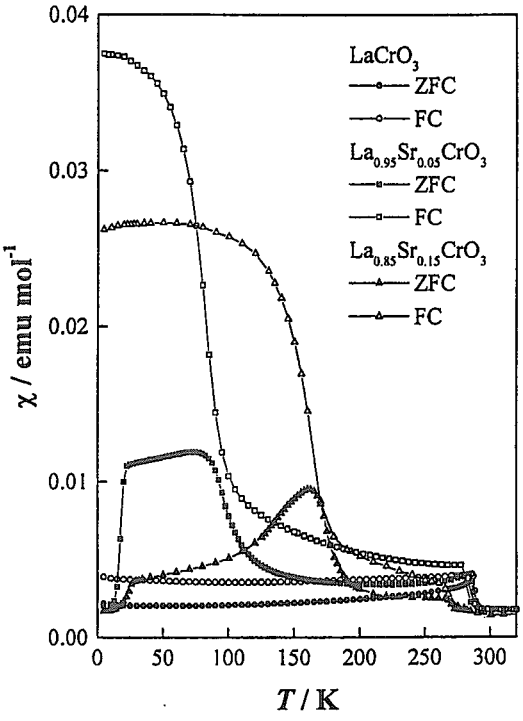

Figure 1 Temperature dependence of magnetic susceptibilities for $La_{1-x}Sr_xCrO_3$ (x = 0, 0.05 and 0.15) measured after zero field cooling (ZFC) and field cooling (FC).

Table 1
The magnetic structures for $La_{1-x}Sr_xCrO_3$ (x = 0, 0.05 and 0.15) at various temperatures.

	10K	50K	125K(250K)	r.t.
$LaCrO_3$	G_x			paramag.
$La_{0.95}Sr_{0.05}CrO_3$	G_z	G_z	G_y (125K)	paramag.
$La_{0.85}Sr_{0.15}CrO_3$	G_z	G_z	G* (250K)	paramag.

* The magnetic moment is directed to [111] of the rhombohedral unit cell.

原子炉：JRR-3M　　装置：HRPD(1G)　　分野：中性子散乱（磁性）

研究テーマ：誘電体の低温での構造相転移の研究
表題：強誘電反強磁性体YMn_2O_5の中性子粉末構造解析

1-2-7 Neutron Powder Diffraction Study of Ferroelectric Antiferromagnet YMn_2O_5

H. Kimura[1], Y. Noda[1], I. Kagomiya[2], K. Kohn[2], K. Oikawa[3], and Y. Morii[3]

[1]*Research Institute for Scientific Measurements, Tohoku University*
[2]*Department of Physics, Waseda University*
[3]*Advanced Science Research Center, Japan Atomic Energy Research Institute*

In manganites of RMn_2O_5 (R; rare-earth or Y) system, ferroelectric transitions ($\equiv T_{CE} \sim 35$ K) occur under the Néel state ($T_N \sim 45$ K), indicating the coexistence of ferroelectricity and antiferromagnetism due to a strong spin–lattice interaction. Furthermore, some compounds in this system show anomalous behavior below T_{CE}, where the spontaneous polarization has a large jump ($\equiv T_2$)[1]. However, no structural information associated with the phase transition around T_{CE} and T_2 have been reported yet in Xray- and neutron- diffraction studies. In the present work, we studied the structure below and above T_N for YMn_2O_5, which has simple properties comparing with the other rare-earth manganites.

The neutron powder diffraction experiments were performed at HRPD in JRR-3M. The diffraction patterns were taken at 60 K ($> T_N$) and 7 K ($< T_2$) with incident neutron wavelength 1.163 Å. Figure 1(a) and (b) show the results of Rietvelt analyses for the 60 K and 7 K data, respectively. Fitting result at 60 K well reproduces the observed powder pattern. The reliable factor for profile fit R_{wp} was 6.29 % and that for intensities R_I was 1.02 %. The obtained atomic positional parameters well agree with the other rare-earth compounds[2]. As for the data at 7 K, we have analyzed the data with the high temperature structure parameters at the moment so that magnetic and ferroelectric characters were not included. Since then all the reliable factors were worse than those at 60 K, particularly because the extra magnetic reflections due to Néel order were observed at low-Q region (Figure 1(c)). It was cleared recently by our measurements of the YMn_2O_5 single crystal that the magnetic ordering has an incommensurate propagation wave vector $Q_{AF} \sim (1/2+\delta\ 0\ t)$ with $\delta \sim 0, t \sim 0.28$. No extra reflections suggesting structural change were found from the powder pattern taken at 7 K. In order to clarify the detailed magnetic and lattice structure at the lowest temperature phase, neutron- and Xray-diffraction studies by using single crystals are required.

References

[1] K. Kohn and I. Kagomiya, (in Japanese) J. Cryst. Soc. Jpn. **41**, 342 (1999).

[2] J. A. Alonso *et al.*, J. Phys. Cond. Matt. **9**, 8515 (1997).

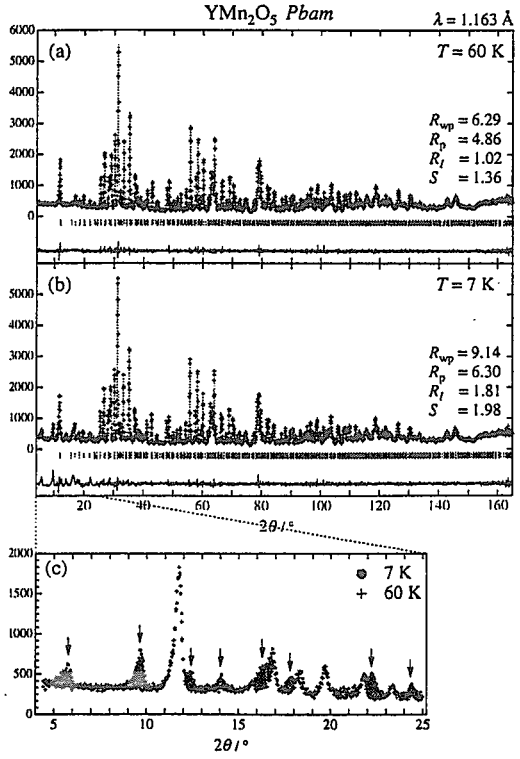

Figure 1: (a) and (b); Observed and calculated diffraction profiles at 60 K and 7 K, respectively. (c); Detailed diffraction patterns of low-Q region at 7 K (gray circle) and 60 K (cross). Hatched peaks indicate magnetic Bragg reflections.

原子炉：JRR-3M　　装置：HRPD (1G)　　分野：2. 磁性

研究テーマ:超低温の導入による中性子散乱の研究
表　　題:スピネル化合物$Co_{0.8}Mn_{0.2}Al_{1.6}Fe_2O_4$の10Kにおける中性子結晶構造解析

1-2-8 NEUTRON DIFFRACTION STUDY AT 10K OF THE SPINEL COMPOUND $Co_{0.8}Mn_{0.2}Al_{1.6}Fe_2O_4$

S. M. Yunus[1], F. U. Ahmed[1,2]

[1] Institute of Nuclear Science and Technology, Atomic Energy Research Establishment, PO Box 3787, Dhaka 1000, Bangladesh. e-mail: inst@bangla.net, aere@bangla.net

[2] ASRC, Japan Atomic Energy Research Institute, Tokai, Ibaraki 319-1195, Japan.

In spinel oxides there are two sublattices namely tetrahedral or A site and octahedral or B site. The interaction between the magnetic moments of ions in A and B sites takes place via the neighboring anions (oxygen ions) in the super-exchange mechanism. The two intra-sublattice interactions J_{AA} and J_{BB} are much weaker than the inter-sublattice interaction J_{AB}. Therefore, the inter-sublattice interaction dominates over the intra-sublattice interaction resulting into anti-parallel alignments of the moment of one sublattice to that of the other. Thus, there are unsatisfied bonds in the ferrimagnetic phase and with the introduction of nonmagnetic impurities a competition arises between the various exchange interactions which gives rise to a variety of magnetic behavior. Changing the concentration of magnetic ions in different sublattices by introducing nonmagnetic atoms one can induce interesting magnetic properties in spinel oxides [1-3]. In the present work we have studied magnetic properties of one such diluted spinel oxide sample $Co_{0.8}Mn_{0.2}Al_{1.6}Fe_2O_4$ at a temperature of 10K.

Neutron diffraction data from the sample have been collected at the JRR-3M reactor of JAERI using the High resolution Powder Diffractometer (HRPD). A neutron wavelength of 1.16Å reflected from a Si (5 3 3) monochromator set at an angle 89 deg. was used in the experiment. For this measurement a close circuit refrigerator was used to maintain the sample temperature at 10K. From our previous works on the spinel compound $Co_{0.8}Mn_{0.2}Al_{1.6}Fe_2O_4$ [4] we found a diffuse signal below the (111) Bragg diffraction peak. This signal arose at about 200K and showed a general trend of enhancement with the lowering of temperature up to 15K. We suggested that this diffuse signal was an indication of the formation of magnetic spin clusters and the evolution of the diffuse signal with lowering of temperature was due to the freezing of this clusters. The principal aim of the present work was to find how this diffuse signal behave at further low temperature. Fig. 1 shows the diffraction pattern limited to low-Q region taken at 10K. It is seen from the figure that the diffuse signal around (111) Bragg reflection is also present in this diffraction pattern. The diffuse signal appears to be rather stronger in this case than it was in the previous patterns taken up to 15K [4]. This means that at this temperature the magnetic spin clusters which are frozen in random directions, have been enhanced considerably. This feature provides a further support to our previous conclusion of a semi-spin glass transition at low temperature for this sample.

References

[1] Kanul B. Modi, V. T. Thanki and H. H. Joshi, Indian J. Phys., **70A** (4), 497, (1996).
[2] K. Muraleedharan, J. K. Srivastava, V. R. Marathe and R. Vijayaraghavan, J. Magn. Magn. Mater., **54-57**, 66, (1986).

原子炉:JRR-3M　　装置:HRPD(1G)　　分野:磁性

[3] R. V. Upadhyay, R. B. Jotania and R. G. Kulkarni, Physica B **190**, 183, (1993).

[4] S. M. Yunus, J. A. Fernandez-Baca, M. A. Asgar and F. U. Ahmed, J. Alloys and Comp., **298**, 9, (2000).

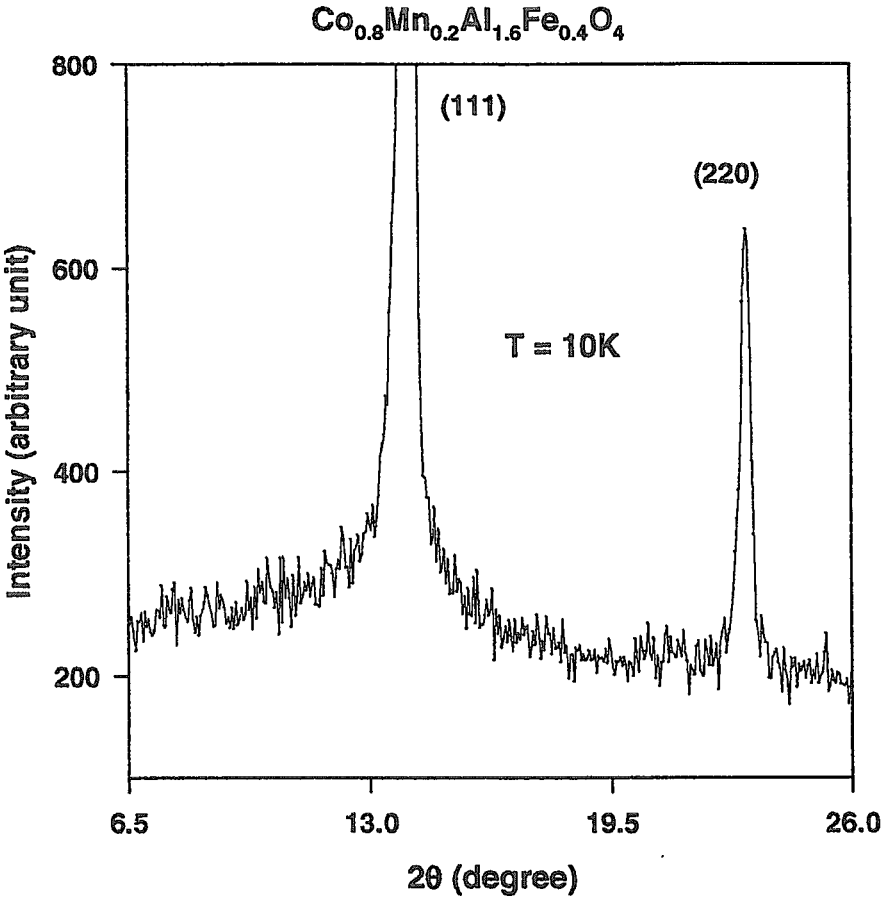

Fig. 1 Neutron diffraction pattern limited to low scattering angle of the spinel oxide sample $Co_{0.8}Mn_{0.2}Al_{1.6}Fe_2O_4$ taken at 10K with λ. = 1.16 Å.

研究テーマ：γ-Mn 合金の結晶変態と磁性
表題：γ-MnRu 合金の結晶変態と磁気構造

1-2-9 Crystal distortion and magnetic structure of γ−Mn(Ru) alloys

T. Hori[1], Y. Tsuchiya[2], Y. Ishii[2] and K. Hojou[2]

Shibaura Institute of Technology, Oomiya, Saitama 330-8570
[1]Japan Atomic Energy Research Institute, Tokai, Ibaraki 319-1106

As is well known, most Mn-rich γ−Mn alloys undergo a distortion from the face centered cubic structure to a face centered tetragonal (f.c.t.) structure with $c/a < 1$ below the Néel temperature. In some cases a distortion to a f.c.t. with $c/a > 1$ is also observed. In the γ−Mn(Ni) alloys, there is a face centered orthorhombic (f.c.o.) region in addition to the f.c.t. regions with $c/a < 1$ and $c/a > 1$ [1]. Recently, the present authors [2] have found that these three regions exist in the γ−Mn(Ga) alloys, and determined a non-collinear magnetic structure with 4 sublattices for the f.c.o. phase. The a, b and c-axis components of the magnetic moments, μ_a, μ_b and μ_c are as follows: $\mu_c^2 > \mu_b^2 > \mu_a^2 = 0$ in the f.c.o. structure with $a > b > c$. We have also found that there is the f.c.o. phase in γ−MnRu alloys with a small amount of Cu. Neutron diffraction experiments were made by using the HRPD and TAS II diffractometers in the JRR-3M reactor at JAERI. The HRPD has a higher resolution than the TAS II.

Fig. 1 shows a neutron diffraction pattern for the γ−Mn Alloy with 14 at % Ru and 5 at % Cu at 10 K obtained by the HRPD diffractometer (wave length λ=1.823 Å). The pattern can be indexed by assuming the f.c.o. structure with a = 3.566, b = 3.525 and c = 3.456 A and a non-collinear antiferromagnetic structure similar to that of the γ-Mn(Ga) alloy [2]. The components of the magnetic moments, $\mu_a = 0$, μ_b =1.33 and μ_c = 2.47μ_B/ Mn atom. We also measured the temperature dependence of these lines using the TAS II diffractometer (λ = 2.376 Å). Although the 110 and 101 reflections were not resolved, we obtained the intensities, I_{110} and I_{101}, by a curve fitting analysis using the double Gaussian functions. The results are shown in Fig. 2.

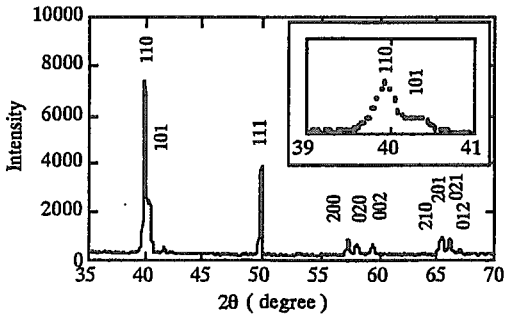

Fig. 1. Neutron diffraction pattern for the γ−Mn Alloy with 14 at % Ru and 5 at % Cu at 10 K.

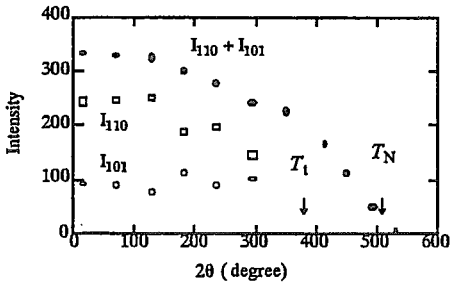

Fig. 2. Temperature dependence of the 110 and 101 intensities of the neutron diffraction for the γ−Mn Alloy with 14 at % Ru and 5 at % Cu at 10 K

From X-ray diffraction experiments, we have made confirmed that the alloy has the orthorhombic structure below T_o (= 380 K), the tetragonal structure with c/a <1 between T_t and T_N (= 510 K) and the cubic structure above T_N corresponding the Néel temperature. Jo et al. [7] have proposed a theoretical phase diagram and magnetic structures for various γ - Mn alloys on the basis of Landau expansion of the free energy. For example, the components of the magnetic moments along the three crystallographic axes μ_a, μ_b and μ_c in the f.c.o. structure with $a > b > c$ are as follows; $\mu_c^2 > \mu_b^2 > \mu_a^2$. The results of the present experiments are consistent with this theory.

[1] T. Hori, Y. Morii, S. Funahashi, H. Niida, M. Akimitsu and Y. Nakagawa; Physica B 213&214 (1995) 354.
[2] T. Jo and K. Hirai, J. Phys. Soc. Jpn 55 (1986) 1614.

原子炉：JRR-3M　装置：HRPD (1G), TAS 2 (T2-4)　分野：中性子散乱（磁性）

研究テーマ：強相関電子系の中性子散乱による研究
表題：$(La,Tb)_{2/3}Ca_{1/3}MnO_3$ の中性子粉末回折

1-2-10

Study on the Crystal and Magnetic Structures of $(La,Tb)_{2/3}Ca_{1/3}MnO_3$ by Neutron Powder Diffraction

M. Watahiki[1,2], K. Oikawa[3], J. Suzuki[1]

[1]Advanced Science Research Center, JAERI, Tokai-mura, Ibaraki 319-1195, Japan
[2]Japan Science and Technology Corporation, Kawaguchi, Saitama 332-0012, Japan
[3]National Institute of Materials and Chemical Research, Tsukuba, Ibaraki 305-8565, Japan

Much interest is devoted to the manganese perovskite $La_{1-y}A_yMnO_3$ (A : divalent alkali ion), since the discovery of colossal magnetoresistance (CMR). A series of studies has been carried out on the systems expressed as $(La_{1-x}Tb_x)_{2/3}Ca_{1/3}MnO_3$ in which the average ionic radius of the La site is systematically varied by substituting Tb ions[1]. The motivation of the study is that by varying the x-value, one can control the band width of the e_g-band, while the carrier density is kept constant. Polycrystalline samples of $(La_{1-x}Tb_x)_{2/3}Ca_{1/3}MnO_3$ were prepared by solid-state reaction processing[2].

The neutron powder diffraction experiments were carried out using a high resolution powder diffractometer HRPD and a triple-axis spectrometer TAS-2 constructed in JRR-3M. For HRPD experiments the incident beam was monochromatized with a vertically focused Ge(331) monochrometer for the wave length λ = 0.182 nm. The collimation 6'-20'-6' gives the resolution of typically 0.15 degrees. For TAS-2 experiments a vertically bent pyrolitic graphite (PG) monochrometer was used to obtain the incident beam with λ = 0.237 nm. Higher order contaminations were removed by a 10 cm thick PG filter. The collimation was 40'-40'-40', giving higher intensity at the sacrifice of the q-resolution.

The temperature dependence of resistivity ($\rho(T)$) curves with x = 0.1 and 0.3 exhibited cusp like behavior in the absence of magnetic field. These cusps appeared close to the Curie temperature (T_c) determined by ac susceptibility measurement. An application of external magnetic field of 5 T suppressed the $\rho(T)$ for both samples. The sample of x = 0.3 shows remarkable CMR effect of the order of 10^4 below T = 50 K. The sample of x = 0.1 suppressed the $\rho(T)$ close to T_c by one order of magnitude, indicating that the CMR effect is correlated with the paramagnetic-ferromagnetic transition. Figure 1 shows the Rietveld refinement pattern at room temperature for the sample of x = 0.1 measured on HRPD. From the Rietveld analysis we found that this profile can be explained in terms of a single phase of $(La_{1-x}Tb_x)_{2/3}Ca_{1/3}MnO_3$ with homogeneous Tb substitution into (La,Ca) sites. The lattice parameters were determined to be a = 0.545 nm, b = 0.77063(3) nm, and c = 0.54628(3) nm for x = 0.1 and a = 0.54577(3) nm, b = 0.76789(4) nm, and c = 0.54364(3) nm for x = 0.3. From the definition $t = d_{A\text{-}O}/\sqrt{2}\,d_{Mn\text{-}O}$, where $d_{A\text{-}O}$ and $d_{Mn\text{-}O}$ are the distances between the metallic ions and the neighbor oxygen atom, we calculated the tolerance factor t = 0.913 and 0.907 for x = 0.1 and 0.3, respectively. The bond angles of Mn-O-Mn becomes close to θ = 180 deg when the tolerance factor increases up to t = 1. The tolerance factor t = 0.9128 and 0.9071 for x = 0.1 and 0.3 obtained from the present work are consistent with the calculation.

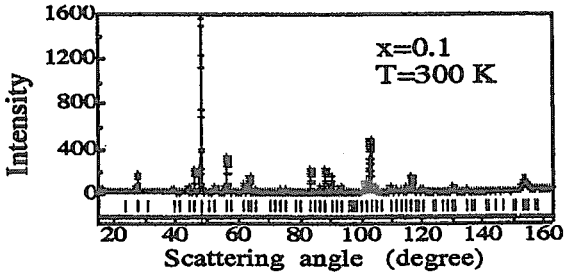

Fig. 1. The Rietveld refinement pattern at room temperature for the sample of x = 0.1.

原子炉：JRR-3M　　HRPD(1G)　TAS-2(T2-4)　　分野：磁性

Figure 2 shows the temperature dependence of the neutron powder diffraction patterns for the system of (a) $x = 0.1$ and (b) $x = 0.3$ measured on TAS-2. In the system of $x = 0.1$, it is clearly seen that at lower temperature there are extra contributions in each fundamental Bragg reflection. The integrated intensity of extra component at each indexed Bragg reflection was indexed by the ferromagnetic ordering of Mn spins with the moment of 1.45 μ_B parallel to the a- or c-axis at $T = 7$ K. On the other hand, for $x = 0.3$, a new superlattice reflection appears in the pattern taken below T = 50 K in addition to the ferromagnetic component similar to that for x = 0.1. The new peak can be indexed as (1/2,0,1/2) or (0,1,0). These two indices can not be distinguished from our experiments with rather low resolution using a triple-axis spectrometer. Since the new reflection is observed only in the low angle region, we infer that the reflection is of magnetic origin (antiferromagnetic reflection).

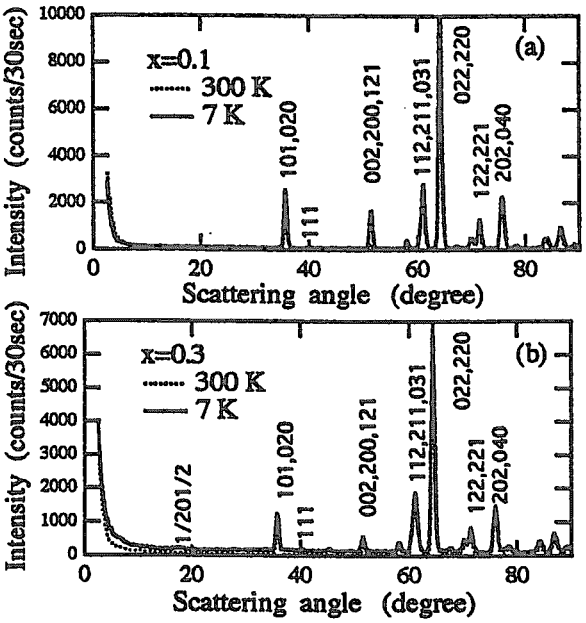

Fig. 2. The neutron powder diffraction patterns at T= 300 K and 7 K for the system of (a) $x = 0.1$ and (b) $x = 0.3$.

Figure 3 shows the temperature dependence of the three characteristic reflections (0,0,2)/(1,2,1) (x = 0.1 and 0.3), and (1/2,0,1/2)/(0,1,0) (x = 0.3). Since the intensity of (0,0,2)/(1,2,1) (x = 0.1) reflection develops exactly at T_c = 190 K, this reflection is due to the ferromagnetic ordering. The behavior of the magnetic reflections is similar to the one for $La_{0.7}Ca_{0.3}MnO_3$ in which double exchange interaction plays an important role for the magnetic transition. In contrast, for $x = 0.3$ the intensity of (0,0,2)/(1,2,1) reflection increases below about 100 K but does not show a clear transition to characterize the ordinary three dimensional cooperative ordering. This gradual temperature variation in the ferromagnetic order parameter is consistent with the result of the magnetization measurement. The intensity of (1/2,01/2)/(0,1,0) reflections (x = 0.3) sharply increases with decreasing temperature below 100 K. This temperature dependence of the antiferromagnetic intensity is different from the usual ordering process. Notice the intensity does not show any indication of saturation even at $T = 7$ K. The results for the system of $x = 0.3$ suggest that at T < 100 K, ferromagnetic and antiferromagnetic order coexist either in microscopic level (single canted antiferromagnetic phase) or in macroscopic level (segregated ferromagnetic and antiferromagnetic phases). Our result exhibited that the CMR effect appeared conspicuously with the excess doping of Tb ions since the substitution of Tb ions suppresses the growth of homogeneous ferromagnetic order.

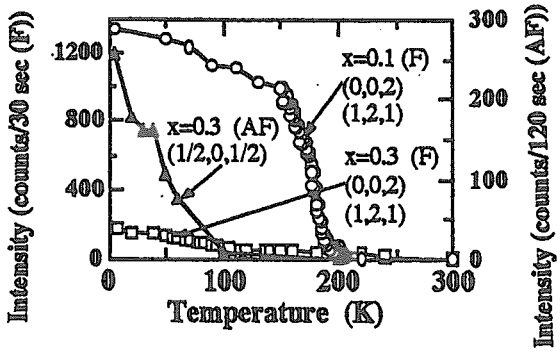

Fig. 3. Tthe temperature dependence of the three characteristic reflections (0,0,2)/(1,2,1) and (1/2,0,1/2).

References

[1] H.Y. Hwang *et al.*, Phys. Rev. Lett. **75** (1995) 914.
[2] J. Nie *et al.*, J. Magn. Mater. **192** (1999) 379

研究テーマ：強相関電子系の中性子散乱による研究
表題：URu_2Si_2における“17.5K転移”に関する研究

1-2-11
Neutron-Scattering Study of the "17.5 K Transition" in URu_2Si_2

H. Amitsuka, M. Yokoyama, K. Kuwahara[1], M. Sato[2], N. Metoki[2],
S. Kawarazaki[3], Y. Miyako[3], and J.A. Mydosh[4]

Graduate School of Science, Hokkaido University, Sapporo 060-0810, Japan
[1]Department of Physics, Tokyo Metropolitan University, Hachioji, Tokyo 192-0397, Japan
[2]Advanced Science Research Center, JAERI, Ibaraki 319-1195, Japan
[3]Graduate School of Science, Osaka University, Toyonaka 560-0043, Japan
[4]Kamerlingh Onnes Laboratory, Leiden University, 2300 RA Leiden, The Netherlands

A puzzling phase transition at $T_o \sim 17.5$ K of the heavy-electron 5f system URu_2Si_2 is characterized by development of an unusually small staggered moment μ_o accompanied by large bulk anomalies and sharp magnon excitations. Through elastic and inelastic neutron scattering for a high quality single crystal, we have studied the influence of pressure P up to ~ 2.8 GPa on this phase transition. The experiments were performed on a triple-axis spectrometer TAS-1 at the JRR-3M reactor. Pressure was applied by means of a barrel-shaped piston cylinder and monitored by measuring the lattice constant of NaCl. Elastic scans were performed in the $(hk0)$ scattering plane, particularly on the antiferromagnetic Bragg reflections (100) and (210), and on the nuclear ones (200), (020) and (110). For inelastic scattering measurements, we made constant-Q scans at $Q = (1,0,0)$ and $(1,0.4,0)$, using neutrons with a fixed incident energy of $E_0 = 14.7$ meV. The energy resolution determined from the vanadium incoherent scattering was ~ 0.95 meV (FWHM).

We have found URu_2Si_2 to undergo a new phase transition under high pressure, at $P_c \sim 1.5$ GPa (Fig.1)[1-3]. Below P_c, the sublattice magnetization associated with the 17.5 K transition is strongly enhanced from $\sim 0.017(3)\ \mu_B$ to $\sim 0.25(2)\ \mu_B$, where the unusual T-linear behavior is conserved. In contrast to the ten-times increase in the saturation moment, the transition temperature rises only ten percent with pressure. These results for $P < P_c$ indicate that the tiny dipole moments are intrinsically induced by the 17.5 K transition, but that they are not the primary order parameter. A simple analysis based on the Landau's theory supports the hidden (non-dipolar) order scenarios[1]. Above P_c, on the other hand, the T variations of the staggered moment are well described by a 3D-Ising model, where we also found that the sharp magnon excitations below P_c disappear[3]. We suggest that the magnetic instabilities at P_c as well as the exotic phase below P_c could be ascribed to the competitions between the quadrupolar and dipolar degrees of freedom in the Γ_5 non-Kramers doublet[2,3]. In this context the low-pressure phase will be described as a staggered quadrupolar ordered state concomitant with dynamical spin fluctuations[4].

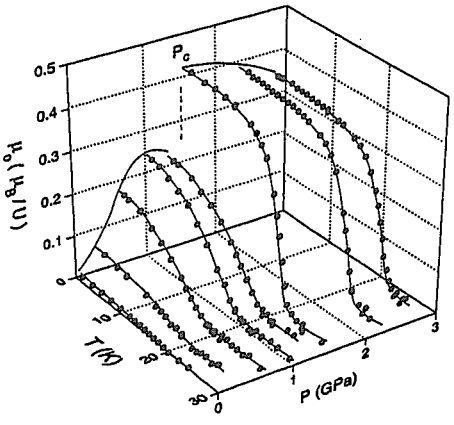

Fig.1 Temperature variations of the antiferromagnetic staggered moment μ_o of single-crystalline URu_2Si_2 under hydrostatic pressures.

References

[1] H. Amitsuka et al., Phys. Rev. Lett. **83**(1999), 5114.
[2] H. Amitsuka et al., Physica B **281&282** (2000), 326.
[3] H. Amitsuka et al., to be published in J. Phys. Soc. Jpn.
[4] F.J. Ohkawa and H. Shimizu, J. Phys.: Condens. Matter **11** (1999), L519.

原子炉：JRR-3M　　装置：TAS-1(2G)　　分野：中性子散乱（磁性）

研究テーマ：強相関電子系の中性子散乱による研究
表　題　　：梯子格子系物質 $(Sr,Co)_{14}Cu_{24}O_{41}$の磁気的性質

1-2-12 Magnetic properties of the ladder compound $(Sr,Ca)_{14}Cu_{24}O_{41}$

T. NAGATA, H. FUJINO, J. AKIMITSU, and S. KATANO[1]

Department of Physics, Aoyama-Gakuin University, Setagaya-ku, Tokyo 157-8572
[1]Neutron Scattering Group, Advanced Science Research Center, Japan Atomic Energy Research Institute, Tokai, Ibaraki 319-1195

The ground state of hole-doped spin ladder system $Sr_{14-x}Ca_xCu_{24}O_{41}$ has been believed to be spin gap state from the NMR[1)] and neutron scattering experiments.[2)] However, magnetic long range ordering was observed by the specific heat and magnetic susceptibility measurements.[3,4)] The magnetic susceptibility measurements reported that the magnetic long range order is antiferromagnetic and the direction of magnetic moments at x=10 is different from that at x=11.5. To examine the difference of magnetic structure between x=10 and 11.5, neutron scattering experiment was performed for x=10 samples.

The experiments have been carried out using TAS-1 (2G) triple-axis spectrometers in JRR-3M at JAERI with a collimation of 40′-40′-S-80′-80′. In these experiments, we used the neutron wavelength of 2.44 Å and placed the pyrolytic graphite and sapphire filters in front of the sample to eliminate the higher order contamination. $Sr_4Ca_{10}Cu_{24}O_{41}$ single crystals were mounted on a dilution refrigerator. The lattice constants along chain direction were determined to be c_L(ladder unit) = 3.902 Å and c_C(chain unit) = 2.749 Å for x=10 (at 1 K) from the neutron scattering measurements. In these lattice units, the lattice constant c becomes more commensurate at $c = 12\times c_L \approx 17\times c_C$ rather than at $c = 7\times c_L \approx 10\times c_C$. For this reason, in this report, we regard the lattice constant c as the length of $12\times c_L \approx 17\times c_C$.

Figure 1 shows the temperature dependence of the neutron scattering intensities from (3 0 12) at x=10 and (1 0 12) at x=11.5.[3)] Bragg peak intensity at x=10 gradually increases below 1.1 K with decreasing temperature,

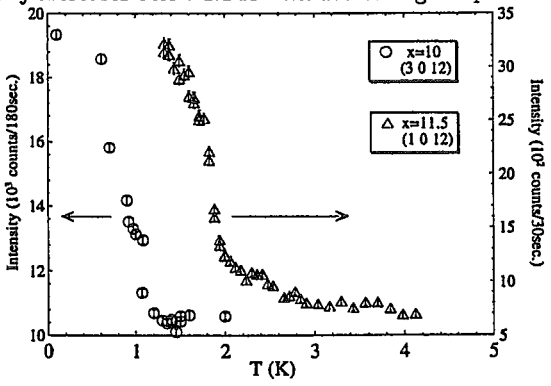

Fig. 1. Temperature dependence of magnetic Bragg peak intensities from (3 0 12) at x=10 and (1 0 12) at x=11.5.

Table I. Observed integrated intensities (I_{obs}) and calculated intensities (I_{calc}) of magnetic Bragg reflections on $Sr_4Ca_{10}Cu_{24}O_{41}$. I_{obs} was measured at T=0.1 K.

(h k l)	I_{obs}	I_{calc}
(1 0 2)	44	440
(3 0 2)	18	161
(1 0 12)	151	150
(3 0 12)	687	460
(5 0 12)	345	366
(1 0 22)	8	19

which is corresponding to the T_N confirmed in the specific heat and susceptibility measurements, so this Bragg peaks must be magnetic in origin. In fact, the polarized neutron scattering experiments were performed for one of the Bragg peaks, (1 0 12) at x=11.5, and the results clearly showed that the Bragg peak, (1 0 12), is purely magnetic.[3)]

Table I summarizes the observed Bragg peak positions and intensities (I_{obs}) at x=10. I_{obs} is integrated intensity after subtracting the intensity at 1.5 K from at 0.1 K. We confirmed that the FWHM of the observed Bragg peaks is nearly resolution limited.

The magnetic structure factors (I_{calc}) were calculated with using the magnetic structure at x=11.5 reported in Ref.3. In this calculation, the direction of magnetic moments are supposed to be directed along c-axis and distributed uniformly at only chain sites. The magnetic moments at ladder site are ignored. Because neutron elastic scattering experiments in b-c plane were not performed for x=10, we could not determine the magnetic structure at ladder site. The magnetic form factors at chain site were evaluated by comparing with the magnetic peak intensity at (1 0 12) and nuclear Bragg peak intensity at (0 0 24). The estimated value of μ_{eff} at x=10 is about μ_{eff}(chain) $\sim$ 0.378 μ_B/Cu in chain layer at 0.1 K.

From this experiment, we found that the antiferromangnetic structure at x=10 is basically same with that at x=11.5 except for the direction of magnetic moments. A more detailed study is required to completely clarify the magnetic structure both at chain and ladder planes.

1) K. Magishi *et al.*, Phys. Rev. B **57** (1998) 11533.
2) S. Katano *et al.*, Phys. Rev. Lett. **82** (1999) 636.
3) T. Nagata *et al.*, J. Phys. Soc. Jpn. **68** (1999) 2206.
4) T. Nagata *et al.*, unpublished.

原子炉：JRR-3M　　装置：2G (TAS-1)　　分野：中性子散乱（磁性）

研究テーマ名：強相関電子系の中性子散乱による研究
表題　　：超高圧下における CeSb の磁気秩序

1-2-13 Magnetic Ordering in CeSb under Ultra-High Pressure

T. Osakabe, N. Tachi[1], M. Kohgi[1], H. Kitazawa[2]

ASRC, Japan Atomic Energy Research Institute, Ibaraki 319-1195, Japan
[1]Dep. of Physics, Tokyo Metropolitan University, Tokyo 192-0397, Japan
[2]National Research Institute for Metals, Ibaraki 305-0047, Japan

It is well known that CeSb shows the complicated magnetic (H-T and P-T) phase diagrams in spite of the simple NaCl-type crystal structure. The magnetic structures of CeSb in the phase diagram under magnetic field below about 11 T or under high pressure below about 2 GPa have been investigated so far by the neutron diffraction experiments [1]. Their magnetic structures are composed of ferromagnetic Ce layers with Γ_8 state Ce ions and paramagnetic layers with Γ_7 state Ce ions.

On the other hand, above about 2.5 GPa, it was reported that enormous enhancement of the resistivity appears at around 35 K and at the pressure of about 7 GPa the peak value of resistivity reaches a value nearly 20 times as large as that at ambient pressure [2].

In order to investigate the magnetic ordering of CeSb in the pressure – temperature range where huge peak of resistivity appears, we carried out the neutron diffraction experiments above 3 GPa on the triple axis spectrometer TAS-1 installed at the 2G beam hole of JRR-3M reactor in JAERI, Tokai. The high pressure was generated by a newly-developed sapphire anvil-type high pressure cell. The pressure was monitored by the measuring the positions of two fluorescence lines from a splinter ruby placed next to the sample.

Fig. 1 shows the temperature dependence of the (1 –2 0) and (1/2 –2 0) magnetic Bragg peaks which correspond to the type-I and type-IA antifferomagnetic order of Γ_8 state Ce ions, respectively. The results clearly show that the enormous enhancement of resistivity is accompanied by the type-I antiferromagnetic ordering and that the development of type-IA antiferromagnetic ordering below about 35 K leads to the rapid decrease of the resistivity. This may be explaned by the difference of mechanism in carrier-scattering or the difference of carrier number itself between two kinds of the magnetic phases.

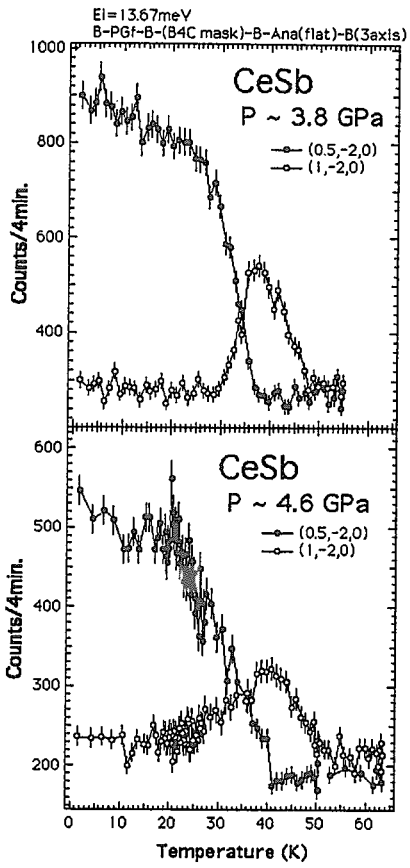

Fig. 1 Temperature dependence of the (1 –2 0) and (1/2 –2 0) magnetic Bragg peaks at 3.8 and 4.6 GPa.

References

[1] T. Chattopadhyay et al., Phys. Rev. B 49 (1994) 15096 and references therein.
[2] N. Môri et al., JJAP Series 8 (1993) pp.182-194

原子炉：JRR-3M 、装置名：TAS-1 、分野　：中性子散乱（磁性）

研究テーマ名 ：強相関電子系の中性子散乱による研究
表題 ：高圧下における YbAs の磁気秩序探索

1-2-14 Survey of long range magnetic order in YbAs under high pressure

T. Osakabe, K. Ohoyama[1], A. Oyamada[2]

ASRC, Japan Atomic Energy Research Institute, Ibaraki 319-1195, Japan
[1] Institute for Materials Research, Tohoku University, Sendai 980-77, Japan
[2]Graduate School of Human and Environmental Studies, Kyoto University, Kyoto 606-01, Japan

YbAs is a semi-metallic compound with NaCl type crystal structure and shows heavy fermion behavior in spite of the low carrier concentration (~0.01 per Yb atom). This compound shows the type-III antiferromagnetic long range order below T_N = 0.49 K, whose propagation vector is [0.5, 0, 1]. The saturation magnetic moment in the ordered state is about $0.6\mu_B$, which is considerably smaller than the expected value of 1.3 μ_B for the crystal electric field ground state Γ_6. Furthermore, the short range magnetic correlation exists far above T_N [1].

Recently, Okayama et al. measured the electrical resistivity under high pressure up to 2 GPa. They found an anomalous bend in ρ(T) curve around 10 K at 0.75 GPa. They infer that the clear bend is attributed to an anomalous enhancement of T_N by applying pressure [2].

To confirm this point directory, we carried out neutron diffraction experiments under high pressure of 0.75 GPa and 0.95 GPa for single crystal sample of YbAs . The experiments were carried out using triple-axis spectrometer TAS-1, installed 2G beam hole of JRR-3M reactor. The pressure is generated by the clamp-type high pressure cell. The sample size is about 4×4×3 mm^3.

Fig. 1 show the diffraction patterns along [H 0 1] and [H 0 2] directions at 0.75 GPa. The patterns show the difference between data taken at 1.4 K and 16 K. The (200) nuclear Bragg peak at 0.75 GPa is shown in an inset of fig. 1. The intensity of the (200) peak is about 43000 counts/5sec. If the magnetic structure and the value of the magnetic moment of Yb ion under pressure are same as those under ambient pressure, the intensity at (0.5 0 1) is estimated to be about 200 counts/90sec because of the magnetic Bragg peak of a type-III antiferromagnetic order. We also carried out the mesh scan at around (0.5 0 1) at 0.75 GPa. However, as seen in fig. 1, there is no change

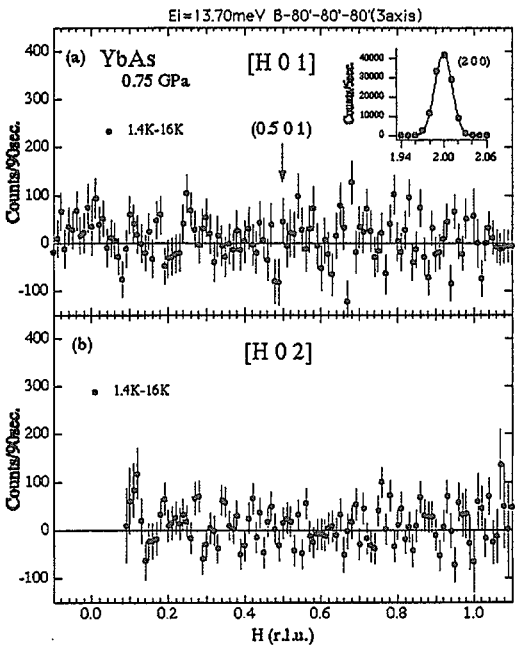

Fig. 1 The diffraction patterns along (a) [H 0 1] and (b) [H 0 2] directions at 0.75 GPa. The patterns show the difference between data taken at 1.4 K and 16 K.

from 1.4 K to 16 K in the diffraction patterns and no extra peak at around (0.5 0 1) in the mesh scan within the experimental error. Under pressure of 0.95 GPa, the experimental results are same as those at 0.75 GPa. These results imply that the origin of the anomalous bend in ρ(T) curve is not the static long range magnetic order. In order to investigate the origin of the anomaly seen in ρ(T) curve, we intend to carry out inelastic neutron scattering experiments under high pressure.

References

[1] K. Ohoyama et al., J. Magn. Magn. Mater.177-181 (1998) 339 and references therein.
[2] Y. Okayama et al., Physica B 259-261 (1999) 148

原子炉： JRR-3M 、装置名： TAS-1 、分野 ： 中性子散乱（磁性）

研究テーマ：強相関電子系の中性子散乱による研究
表題：中性子回折による $La_{2-x}Sr_xCuO_4$ x=0.12 における磁気秩序の研究

1-2-15

Study of the Magnetic Ordering in $La_{2-x}Sr_xCuO_4$ with x=0.12 by Neutron Diffraction

M. Sato, S. Katano, K. Yamada[A], T. Suzuki[B,*] and T. Hukase[B]

ASRC, JAERI, Tokai, Ibaraki 319-1195
[A]Institute for Chemical Research, Kyoto University, Uji, Kyoto 611-0011
[B]Insititute for Materials Research, Tohoku University, Sendai, Miyagi 980-8577

One of the attractive features of the high-T_C superconductor $La_{2-x}Sr_xCuO_4$ (LSCO) is the suppression of the superconductivity observed in the compounds with x of around 0.12, which is called the 1/8 problem. In the recent neutron diffraction studies on these compounds, it has been discovered that a static antiferromagnetic long range order coexists with the superconductivity.[1,2] The relationship between this magnetic ordering and the superconductivity is considered to be important to understand the mechanism of the high-T_C superconductivity. For the samples of LSCO with x=0.12, T_C is ordinarily around 32 ~ 34 K, and shows a small dip in the bell-shaped curve which represents T_C vs. x. These samples were grown and annealed at the oxygen atmosphere. Quite recently, we have grown a sample with T_C of 12 K for x=0.12, which was grown under the air and then annealed at the oxygen atmosphere. This T_C is fairly lower than that of the samples described above. In the present work, we investigate the magnetic ordering in this new sample with T_C=12 K and that with T_C=32 K by neutron diffraction.

At first, we compared the magnetic structures in these two compounds. Similar to the previous results [2,3], the Bragg peaks due to the magnetic ordering are observed at the reciprocal lattice points of $(1/2\pm\varepsilon, 1/2\mp\delta, 0)$ and $(1/2\mp\delta, 1/2\pm\varepsilon, 0)$, as shown schematically in Fig.1. As can be seen in the figure, the direction of the incommensurability is slightly shifted by δ from the direction pararell to the crystal axis for the tetragonal structure in which this compounds crystallize at high temperature. In both samples, ε and δ take almost the same values, respectivly; ε=0.12 ± 0.002, δ=0.004±0.001.

Secondly, Fig.2 shows the temperature-dependence of the intensity of the magnetic Bragg peaks. In this figure, the intensities are normalized by the value at 10 K. The ordering temperatures T_m are about 25 K for the sample with T_C=12 K, and about 35 K for that with T_C=32 K, respectively. This sample dependence of T_m seems to suggest that T_m has a correlation with T_C. However, in the studies on the x-dependence of the magnetic ordering in $(La_{1-y}Nd_y)_{2-x}Sr_xCuO_4$ with x of around 0.12, a competition between T_m and T_C is clear.

Furthermore, we investigate the temperature-dependence of δ in the sample with T_C=12 K. The results are shown in Fig.3. As shown in this figure, we found that δ decreases above T_C and disappears around T_m. It, however, needs more investigations to clarify whether this phenomenon is related with the

原子炉：JRR-3M　　装置：TAS-1(2G),HER(C1-1)　　分野：中性子散乱（磁性）

superconductivity or not.

*Present Address : Department of Physics, Sophia University, 7-1 Kioi-cho, Chiyodaku 102-8554

Refereces

[1] T. Suzuki et al., Phys. Rev. B57 (1998) R3229
[2] H. Kimura et al., Rhys. Rev. B59 (1999) 6517
[3] Y. S. Lee et al. Phys. Rev. B60 (1999) 3643

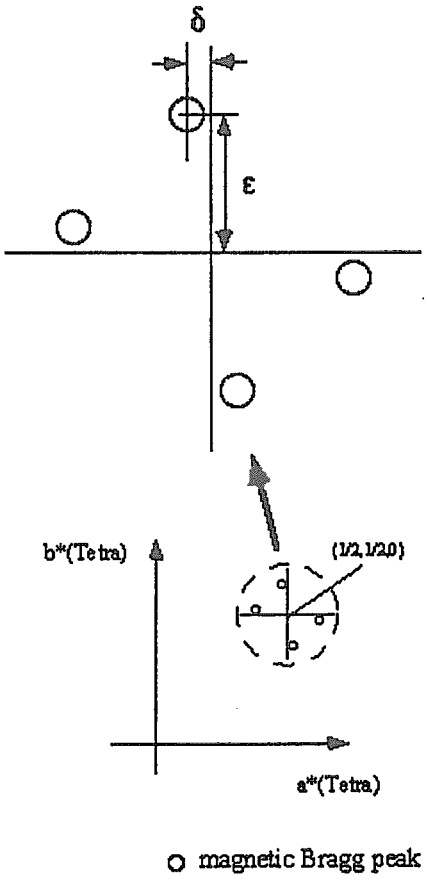

Fig.1 Positions of the magnetic Bragg peaks in the reciprocal lattice space.

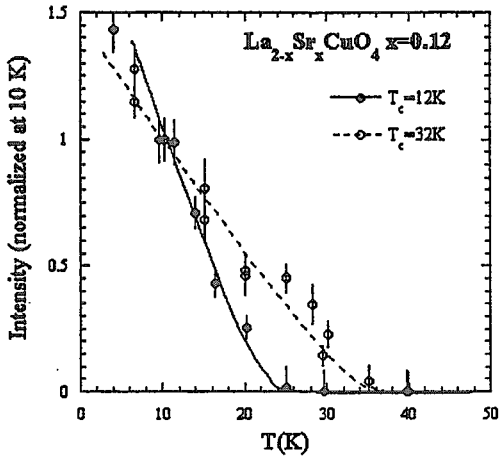

Fig.2 Temperature dependence of the intensity of the magnetic Bragg peaks.

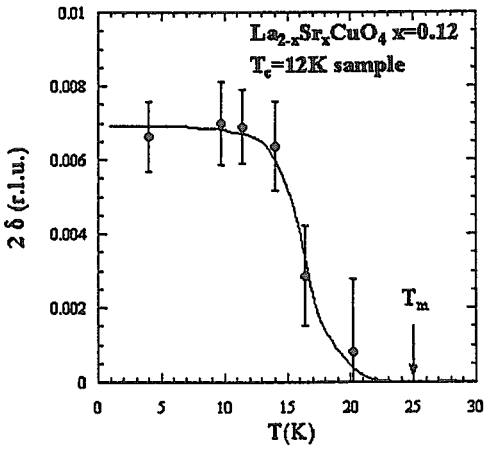

Fig.3 Temperature dependence of δ of the sample with T_C=12 K.

研究テーマ：強相関電子系の中性子散乱による研究
表題：重い電子系物質$CeRu_2Si_2$における磁場誘起強磁性スピン揺らぎ

1-2-16

Field Induced Ferromagnetic Spin Fluctuation in a Heavy Fermion Compound $CeRu_2Si_2$

M. Sato[A] Y. Koike[AB] S. Katano[A] N. Metoki[A] H. Kadowaki[C] S. Kawarazaki[D]

[A]ASRC, JAERI, Tokai 319-1195
[B]JST Corporation, Kawaguchi, Saitama 332-0012
[C]Department of Physics, Tokyo Metropolitan University, Hachioji, Tokyo 192-0397
[D]Department of Earth and Space Science, Osaka University, Toyonaka, Osaka 560-0043

$CeRu_2Si_2$ is a paramagnetic heavy fermion compound. In this compound, antiferromagnetic (AFM) correlations grow into three dynamical spin fluctuations below 60 K.[1,2] Applying field along its magnetic easy axis, the magnetization jumps up around 7.7 T ($=H_m$) below 10 K, which is called as the metamagnetic-like-behavior.[3] We investigated the change of the spin fluctuations around H_m by inelastic neutron scattering under high magnetic field. As the result, we have discovered that a ferromagnetic (FM) fluctuation develops around H_m.

In Fig.1 are shown the results of constant E-scans with energy transfer ΔE=0.4 meV along [h,1,0] (in r.l.u.). These scans are carried out at T=0.45 K under H=0, 7.7 and 10 T. (110) is a Brillouin zone center. The peak at (0.7,1,0) under H=0 T corresponds to one of the AFM fluctuations. As applying field, this peak disappears, which is consistent with the previous studies.[4] In addition, the intensity around the zone center grows up at 7.7 T. In Fig.2 is shown the field dependence of the scattering intensity with ΔE=0.4 meV at (0.9,1,0) (T=0.45 K). This point is located near the zone center. As can be seen in this figure, the intensity peaks around H_m. This result indicates that the metamagnetic behavior must be associated with field-induced FM correlation, and this is consistent with the recent theoretical prediction by Satoh and Ohkawa[5] based on the quasi-particle band spectrum considerations.

References

[1]L. P. Regnault et al., Phys. Rev. B **38** (1988) 4481
[2]M. Sato et al., J. Phys. Chem. Solids **60** (1999) 1203
[3]P. Haen et al., J. Low Temp. Phys. **67** (1987) 391
[4]J. Rossat-Mignod et al., J. Magn. Magn. Matter. **76&77** (1988) 376
[5]H. Satoh and F. J. Ohkawa, preprint.

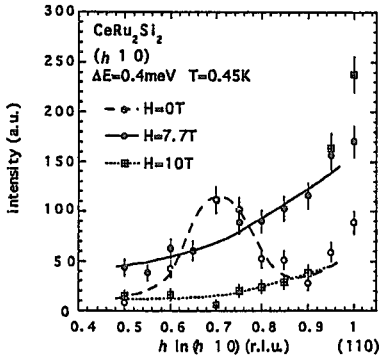

Fig.1. Field dependence of constant E-scans with ΔE=0.4 meV along [h,1,0] (in r.l.u.) at T=0.45 K.

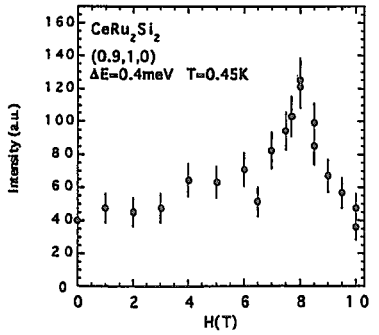

Fig.2. Field dependence of the scattering intensity with ΔE=0.4 meV at (0.9,1,0) (T=0.45 K).

原子炉：JRR-3M 装置：LTAS(C2-1),TAS-1(2G),HER(C1-1) 分野：中性子散乱（磁性）

研究テーマ：量子凝縮相の研究
表題：直鎖型ハルデン物質NDMAZとNDMAPの中性子散乱による研究

1-2-17

Neutron Scattering Study of Linear-Chain Haldane Compounds NDMAZ and NDMAP

Y. Koike[a,b], N. Metoki[a], Y. Matsuoka[a], T. Kobayashi[c], M. Yamashita[d]

a- Advanced Science Research Center, Atomic Energy Research Institute, Tokai, Naka, Ibaraki 319-1195, Japan

b- Japan Science and Technology Corporation, Kawaguchi, Saitama 332-0012, Japan

c- KYOKUGEN Osaka University, Toyonaka, Osaka 560-8531, Japan

d- Faculty of Science, Toyko Metroplitan University, Hachioji, Tokyo 192-0397, Japan

The low dimensional quantum spin gap systems attract much interest. Haldane conjectured that one-dimensional Heisenberg antiferromagnet (1D HAF) with an integer spin number has a spin singlet ground state with spin excitation gap (Haldane gap) [1]. Recently the field induced long range order has been reported in new Haldane compounds $Ni(C_5H_{14}N_2)_2N_3(ClO_4)$ (NDMAZ) [2] and $Ni(C_5H_{14}N_2)_2N_3(PF_6)$ (NDMAP) [3]. We carried out neutron scattering experiments in order to investigate the antiferromagnetic (AFM) order and spin excitaion for these new Haldane compounds.

Neutron scattering experiments were carried out using thermal neutron triple-axis spectrometers (TAS1, TAS2) and a cold neutron triple-axis spectrometer (LTAS). Low temperature and high field experiments were carried out by using a liquid-He-free dilution refrigerator and liquid-He-free 10 T split-pair magnet for neutron scattering.

In NDMAZ and NDMAP we observed clear Haldane gap at zero field. Figure 1 shows the constant-Q scan profiles for NDMAZ. Inelastic responses were observed at about 1.7 meV and 3.2 meV. From our systematic measurements we obtained the gap energies Δ_X = 1.61 meV, Δ_Y = 1.76 meV, Δ_Z = 3.2 meV, the intra-chain coupling J = 4.3 meV, and the anisotropy parameters D = 0.76 meV, E = 0.038 meV for NDMAZ. In NDMAP the gap energies were Δ_X = 0.48 meV and Δ_Y = 0.64 meV.

Figure 2 shows the field dependence of the constant-Q profile at Q = (0 0 0.5) for NDMAZ as applying the field parallel to the b-axis (perpendicular to the chain axis). The splitting of the 1.7 meV peak was observed in the magnetic field. The behaviors of these peaks were completely different. With increasing field, 1.6 meV peak shifted to low energy, while we observed no change of the high energy peak at about 1.76 meV. The lowest energy gap decreased to 0.87 meV at H = 10 T. The field dependence of the gaps is well explained by the fermionic field-theory treatment of the 1D HAF Hamiltonian [4] with obtained gap energies and g-value, 2.3.

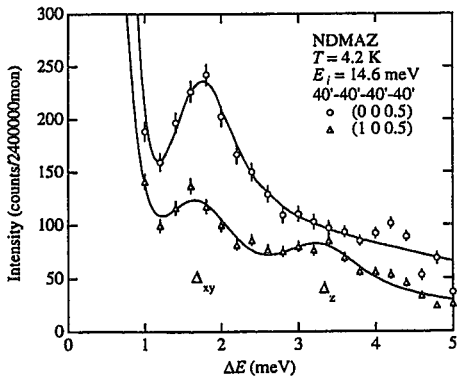

Fig. 1 Constant-Q profilse of NDMAZ measured at Q = (0 0 0.5) and (1 0 0.5).

原子炉：JRR-3M　装置：TAS-1 (2G), TAS-2 (T2-4), LTAS (C2-1)　分野：中性子散乱(磁性)

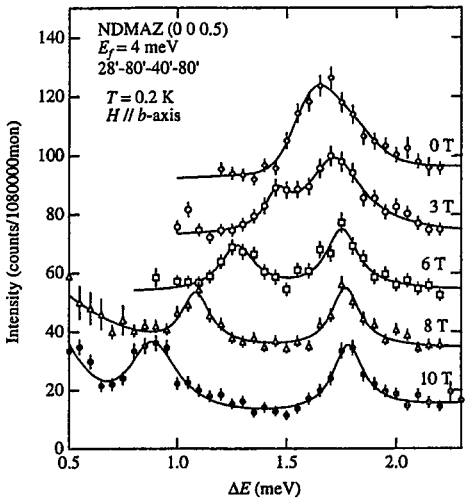

Fig. 2 The external field dependence of the constant-Q profiles at (0 0 0.5). Each profile is shifted by 20 counts in the ordinate.

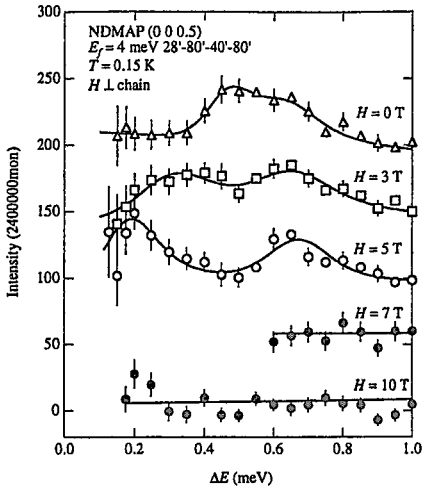

Fig. 3 Field dependence of the constant-Q profiles o NDMAP. Each profile is shifted by 50 counts.

Figure 3 shows the field dependence of the constant-Q profiles for NDMAP. The field was applied perpendicular to the chain direction. In Fig. 3 the data are plotted after the subtraction of the background measured at Q=(0 0 0.56) and T = 0.15 K in zero field. The inelastic signal observed at about 0.55 meV clearly splits into two peaks, and the low energy peak showed remarkable shift with applying field. At H = 5 T, the existence of the Haldane gap becomes unclear from the excitation profile, because the peak maximum would be smaller than 0.13 meV which is comparable to the resolution of our spectrometer. This result indicates that the Haldane gap is almost closed at this field. Above the critical field ~ 6 T, we found drastic change in the scattering profile. The low energy excitation and 0.64 meV peak became unobservably week. This change would be interpreted by the level crossing of this system.

We carried out the elastic neutron scatting experiments for NDMAP at H = 10 T and T = 0.2 K. However so far no trace of the magnetic Bragg peak has been observed around the antiferromagnetic scattering vector, (0 0 0.5), (0 0.5 0.5), (0 1 0.5), (1 0 0.5) beyond the statistical error about 10^{-4} of the (002) nuclear Bragg intensity. The most probable reason for the absence of the Bragg peak is the small magnetic moment induced by magnetic field. Another possibility is that the magnetic peak may appear the different wave vector because of the magnetic structure factor or incommensurate structure under magnetic field.

Further studies using deutrized sample are necessary to understand the nature of the Haldane system under magnetic field.

References

[1] F.D.M. Haldane, Phys. Lett A93 (1983) 464.

[2] Z. Honda, K. Katsumata, H. Aruga Katori, K. Yamada, T. Ohishi, T. Manabe and M. Yamashita, J. Phys. Condens. Matter. 9 (1997) L83.

[3] Z. Honda, H. Asakawa and K. Katsumata, Phys. Rev. Lett. 81 (1998) 2566.

[4] I. Affleck, Phys. Rev. B41 (1990) 6697, *ibid.* B46 (1992) 9002.

研究テーマ: $CeCu_{1+x}Al_{3-x}$の磁気構造
表題:中性子回折による$CeCu_{1+x}Al_{3-x}$の磁気構造

1-2-18 Neutron Diffraction Study of the Magnetic Ordering of $CeCu_{1+x}Al_{3-x}$

Y. Oohara, G. Motoyama,[1] T. Nishioka[1] and M. Kontani[1]

ISSP, University of Tokyo, Tokai, 319-11
Department of Physics, Nagoya University, Nagoya, 464-01

$CeCuAl_3$ is a heavy fermion compound of $BaNiSn_3$ structure. The magnetic ions, Ce^{3+}, form the body-centred tetragonal lattice. The tetragonal crystal field splits the $^2F_{5/2}$ of the 4f electron into the three doublet states. At the low temperature, it exhibits antiferromagnetic ordering. This antiferromagnetic ordering can be easily destroyed by applying the magnetic field, particularly when Al is substituted by Cu.[1)] To explore the vulnerability of the antiferromagnetism in $CeCu_{1+x}Al_{3-x}$, we have performed the neutron diffraction measurements.

Neutron diffraction measurements were carried out on the ISSP triple-axis spectrometer GPTAS installed at the 4G experimental port in JRR-3M in JAERI (Tokai). At 1.5 K, magnetic signals were observed in every samples. The magnetic structure in all the systems is constructed by the antiferromagnetic c-plane. The stacking, however, depends on x; the propagation wave vector is (0.5 0.5 0) for the x=-0.2 and the x=0 and (0.5 0.5 0.4) for the x=0.1 sample. The ordered moment drastically changes with x. We made a rough estimation as follows; 1 μ_B/Ce^{3+} for x=-0.2, 0.2 μ_B/Ce^{3+} for x=0 and 0.4 μ_B/Ce^{3+} for x=0.1. At x=0, the moment becomes minimum value and the ordering becomes short ranged.(Fig. 1) It indicates that the Neel state is highly suppressed at x=0.

Reference

1) G. Motoyama *et.al.*: Jpn. J. Appl. Phys. Series 11(1999)257.

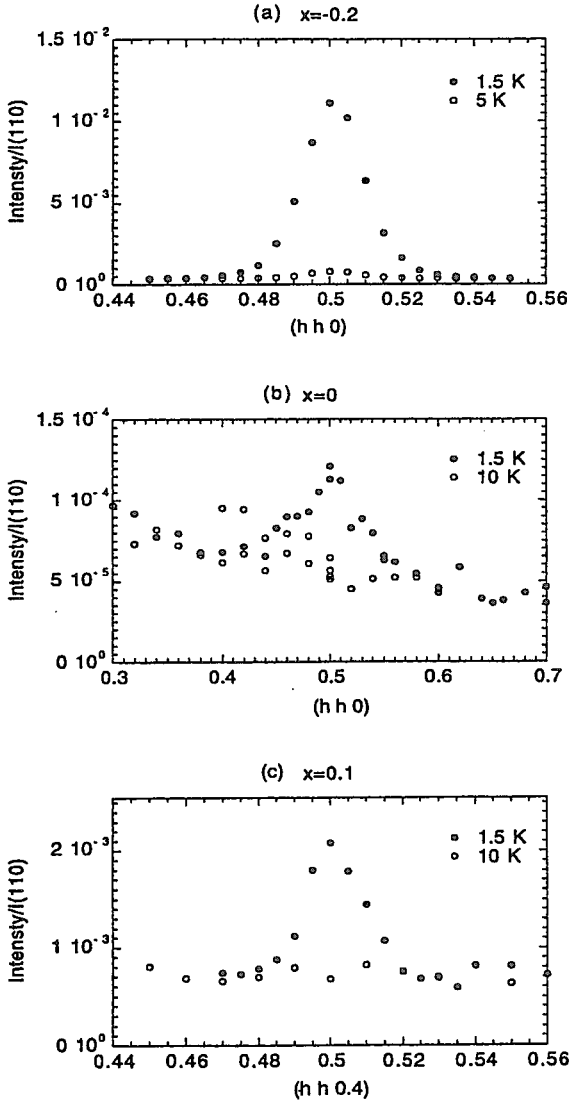

Figure. 1 The line scans along the (h h 0) line for (a)x=-0.2, (b) x=0 and the line scan along the (h h 0.4) line for (c)x=0.1.

研究テーマ：$Rb(Co_{1-x}Mg_x)F_3$ の原子秩序、磁気秩序、磁気励起
表題：$Rb(Co_{1-x}Mg_x)F_3$ の原子秩序、磁気秩序、磁気励起

1-2-19 Crystal and Magnetic Structure of $Rb(Co_{1-x}Mg_x)F_3$

K. Motoya, T. Kumazawa, J. Kikuchi, S. Itoh[1] and Y. Kouchi[1]

Faculty of Science and Technology, Science University of Tokyo, Noda 278-8510
[1]Neutron Scattering Laboratory, KEK, Tsukuba, Ibaraki 305-0801

Although the crystal and magnetic structure of a group of fluoride, ABF_3, have extensively been studied in the past, the number of reports on $RbCoF_3$ and $Rb(Co\text{-}Mg)F_3$ system is small and also inconsistent each other.

We made a systematic study of magnetic properties of $Rb(Co\text{-}Mg)F_3$ system by means of susceptibility and neutron diffraction measurements. In this report, we present the results of powder and single crystal neutron diffraction experiments on $RbCoF_3$, $Rb(Co_{0.7}Mg_{0.3})F_3$ and $Rb(Co_{0.5}Mg_{0.5})F_3$.
The crystal structure of $RbCoF_3$ and $Rb(Co_{0.7}Mg_{0.3})F_3$ is determined to be the cubic perovskite structure (Pm3m). These compounds order antiferromagnetically with G-type structure below T_N=99.0±0.2K and 54.0±0.3K, respectively. The result for $RbCoF_3$ is much different from the previous report (T_N=32K).[1] The amplitude of the ordered moment for $RbCoF_3$ and $Rb(Co_{0.7}Mg_{0.3})F_3$ are 2.9±0.2 and 2.7±0.5 μ_B/Co atom, respectively.

The crystal structure of $Rb(Co_{0.5}Mg_{0.5})F_3$ is determined to be the hexagonal $BaTiO_3$-type ($P6_3/mmc$). Temperature variations of neutron scattering intensity for $(1/2, 1/2, 1/2)_c = (1, 0, 1)_h$ and $(2/3, 1/3, 1/3)_c = (1, 0, 0)_h$ Bragg peaks (c and h denote the cubic and hexagonal notations) is shown in Fig.1. The result indicates that $Rb(Co_{0.5}Mg_{0.5})F_3$ orders ferrimagnetically below T_N=12.6K, which is consistent with the previous report.[2] Detailed structure analysis concerning the possibility of partial atomic order between Co and Mg is now in progress.

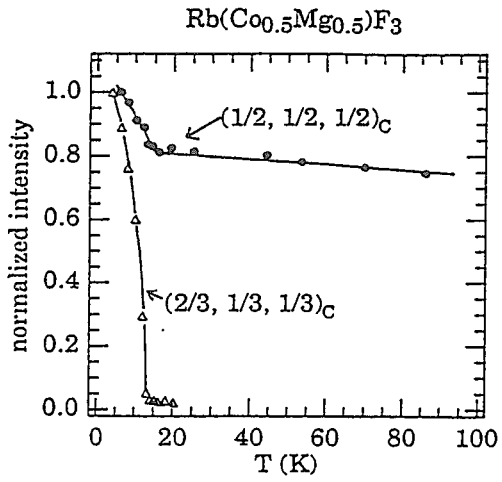

Fig.1. Temperature variations of neutron scattering intensity for $(1/2, 1/2, 1/2)_c$ and $(2/3, 1/3, 1/3)_c$ Bragg peaks.

References

1) F. F. Y. Wang and M. Kestigian: Bull. Am. Phys. Soc. 10 (1965) 352.

2) M. W. Shafer and T. R. McGuire: J. Phys. Chem. Solids 30 (1969) 1989.

研究テーマ：リエントラントスピングラスにおける異なる磁気励起の共存
表題：リエントラントスピングラスにおける異なる磁気励起の共存

1-2-20
Two kinds of magnetic excitations in reentrant spin-glasses

K. Motoya, T. Kumazawa and K. Hioki

Department of Physics, Faculty of Science and Technology,
Science University of Tokyo, Noda 278-8510

There are marked differences among reentrant spin-glass materials in the temperature variation behavior of the spin-wave excitations. The spin-wave stiffness constant D increases as the temperature decreases below ~70K (~$1.8T_{S.G.}$) in $Ni_{0.784}Mn_{0.216}$ alloy.[1] On the other hand in other RSG alloys such as $Fe_{0.26}Cr_{0.74}$,[2] $Fe_{0.70}Al_{0.30}$[3], D decreases gradually in the ferromagnetic phase as the temperature decreases toward $T_{S.G.}$. In the $Ni_{0.784}Mn_{0.216}$ and $Fe_{0.26}Cr_{0.74}$ alloys, spin-wave amplitude (corrected for thermal factor) increases at low temperature, whereas in the $Fe_{0.70}Al_{0.30}$ alloy it decreases at low temperature. Moreover at the lowest temperature in the RSG phase, spin-wave excitations are observed for the $Ni_{0.784}Mn_{0.216}$ and the $Fe_{0.26}Cr_{0.74}$ alloys. On the other hand, for the $Fe_{0.70}Al_{0.30}$ alloy, no propagating magnetic excitation has been observed at the lowest temperature.

In order to clarify the origin of the wide variety in spin dynamics, we reexamined spin-wave excitations in a typical RSG, $Fe_{65}(Ni_{0.866}Mn_{0.134})_{35}$ alloy, in wide range of wave-length. We observed two kinds of spin-wave excitations. In this alloy, *spin-wave* excitations, of which amplitude increases at low temperatures, have previously been observed in relatively large q region.[4] On the other hand, the new spin-wave excitation is observed only for small q range and in the ferromagnetic phase. Figure 1 shows the temperature variations of (a) the spin-wave amplitude, (b) the spin-wave stiffness constant D and (c) the spin-wave line-width Γ measured at q=0.06Å^{-1} and 0.243Å^{-1}. Temperature variations of the spin-wave parameters obtained from the measurements at q=0.06Å^{-1} are essentially same as the cases for $Fe_{0.26}Cr_{0.74}$. On the other hand parameters for q=0.243Å^{-1} are essentially same as the cases for $Ni_{0.784}Mn_{0.216}$. We interpret this observation as due to the coexistence of two kinds of spin-waves in the finite magnetic clusters and in the infinite ferromagnetic network. The co-existence of two kinds of magnetic excitations in different q region has also been observed in the $Fe_{0.7}Al_{0.3}$ alloy.[5] We conclude that the apparent

difference in the temperature variation of the spin-wave property among RSG materials is due to the coexistence of two kinds of magnetic excitations. Each excitation can exist only in a limited q range and/or in a limited life time because of a finite size of media or the presence of large number of obstacles. One might observe only one kind of excitation in certain q range depending on the size and number of magnetic clusters. In this sense the key parameter which determines the spin-wave property in RSG's is the size of magnetic clusters.

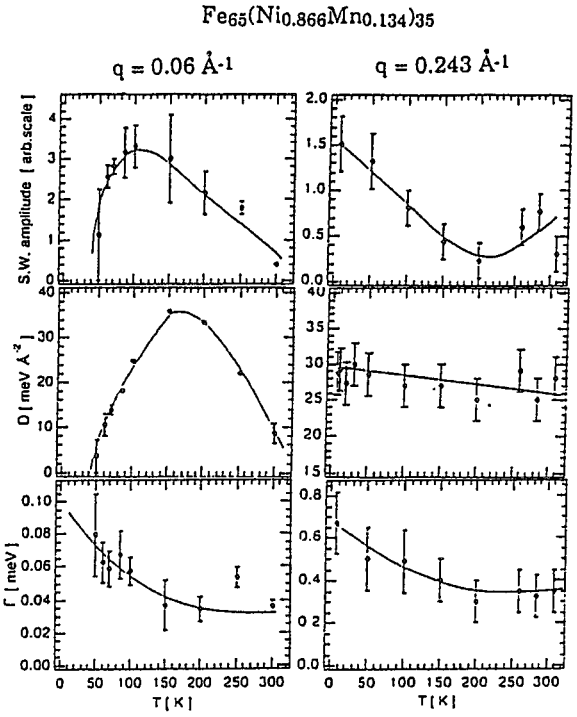

Fig. 1. Temperature variations of (a) the spin-wave amplitude, (b) the spin-wave stiffness constant D and (c) the spin-wave line-width Γ measured at q=0.06Å^{-1} and 0.243Å^{-1}.

References

1) B. Hennion, M. Hennion, F. Hippert and A. P. Murani: J. Phys. F **14** (1984) 489.
2) S. M. Shapiro, C. R. Fincher, Jr., A. C. Palumbo and R. D. Parks: Phys. Rev. B **24** (1981) 6661.
3) K. Motoya, S. M. Shapiro and Y. Muraoka: Phys. Rev. B **28** (1983) 6183.
4) K. Motoya and Y. Muraoka: J. Phys. Soc. Jpn. **62** (1993) 2819.
5) S. Raymond, W. Bao, S. M. Shapiro and K. Motoya: physica B **241-243** (1998) 597.

研究テーマ：近藤格子上の磁気秩序の研究
表題：近藤格子上の磁気秩序における電子レジームのクロスオーバー

1-2-21 Crossover of electronic regime in long-range magnetic order of Kondo lattices

K. Watanabe, [A]Y. Uwatoko, M. Miyamura and S. Kawarazaki

Graduate School of Earth and Space science, Osaka University, Toyonaka, Osaka 560-0043
[A]Faculty of Science, Saitama University, Urawa, Saitama, 338

Previously, we have reported[1] the experimental results of the effects of hydrostatic pressure on the amplitude of the antiferromagnetic staggered moment, μ, and on the transition temperature,TN, of the Kondo-lattice antiferromagnet CeRh2Si2. The relation between μ and TN is such that μ is proportional to TN when pressure is relatively low but decreases more rapidly with increasing pressure than TN does around the critical pressure to destroy the antiferromagnetism thoroughly. We consider that this behavior of μ and TN originates from a crossover of the regime of long-range order, that is, from the RKKY-regime at low pressure to the quasi-particle band regime. We also consider that this crossover phenomenon is rather common through the Kondo-lattice antiferromagnets.

In order to test the validity of this idea, we have measured μ and TN of the Kondo-lattice SDW magnet $Ce(Ru_{0.85}Rh_{0.15})_2Si_2$ as functions of hydrostatic pressure. The result is shown in a form of μ as a function of TN. In the figure, one can see again a linear dependence of μ on TN at small pressure, the region is rather narrow though, followed by a rapid decrease. In another experiment using another crystal with nominally the same composition, we have observed that μ again depends on TN linearly after this rapid reduction. The broken curve in the figure is drawn taking this fact into account. We regard the present result as a manifestation of the crossover in the electronic regime in long range ordering of Kondo-lattices.

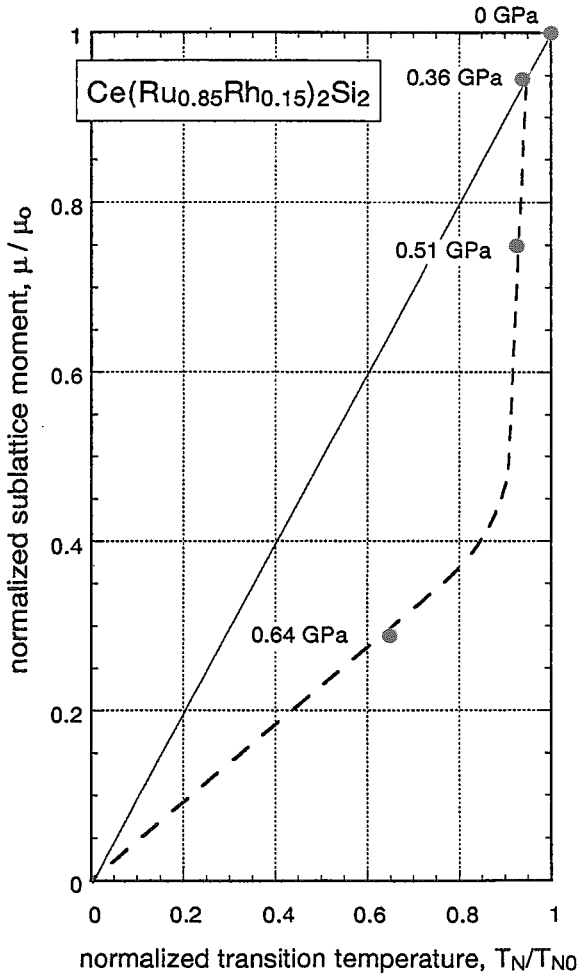

References :

[1]S. Kawarazaki et al., Phys. Rev. B 61 (2000) 4167

JRR-3M, 4G-T11, 2.magnetism

研究テーマ; ストライプ構造　表題; $La_{2-2x}Sr_{1+2x}Mn_2O_7$の擬バイストライプ電荷秩序

1-2-22 Quasi-Bi-Stripe Charge Order in a Bilayer Manganite $La_{2-2x}Sr_{1+2x}Mn_2O_7$[1]

M. Kubota[1], H. Yoshizawa[1], H. Fujioka[2], K. Shimizu[2], K. Hirota[2], Y. Moritomo[3], Y. Endoh[4]

[1]Neutron Scattering Laboratory, I.S.S.P., University of Tokyo, Tokai, 319-1106
[2]CREST, Department of Physics, Tohoku University, Aoba-ku, Sendai, 980-8578
[3]CIRSE, Nagoya University, Nagoya, 464-8601
[4]Institute for Materials Research, Tohoku University, Aoba-ku, Sendai 980-8577

The A-type antiferromagnetic (AFM) spin order consists of antiferromagnetically stacked ferromagnetic (FM) layers in manganites. Although the A-type spin ordering appears in the two-dimensional bilayer manganite $La_{2-2x}Sr_{1+2x}Mn_2O_7$ ($0.39 \leq x \leq 0.48$) system[2,3], the resistivities exhibit an insulating behavior within the FM MnO_2 plane, unlike three-dimensional manganite such as $Nd_{0.45}Sr_{0.55}MnO_3$[4].

Very recently, Vasiliu-Doloc *et al.* have observed diffuse scattering in the paramagnetic phase of the $x = 0.40$ sample which is possibly originated from a charge ordering[5]. Stimulated by this work, we have carried out systematic neutron diffraction studies on the 2D bilayer system $La_{2-2x}Sr_{1+2x}Mn_2O_7$ with $0.30 \leq x \leq 0.50$, using triple-axis spectrometers GPTAS, TOPAN, and KSD in the JRR-3M of JAERI, Tokai. The $(h0l)$ and $(hk0)$ reciprocal planes were aligned as the scattering planes.

Figure 1 shows typical profiles of the diffuse scattering observed in the paramagnetic, A-type AFM, and canted AFM phase for the $x = 0.40, 0.45$ and 0.48 samples, respectively. The scans were made along the [100] direction, and the diffuse scattering was observed around $Q = (2 \pm q_o, 0, 1)$. The peak position of the diffuse scattering is located near $q_o \sim 0.3a^*$ for given three concentrations, but q_o is slightly smaller and close to $\sim 0.25a^*$ for $0.30 \leq x < 0.40$ (not shown).

We also measured profiles in the $(hk0)$ zone and demonstrated that holes are aligned in a stripe way.

The temperature dependence of the bistripe order accounts well for that of the resistivity for each hole concentration x. The quasi-bistripe order is stable within the FM MnO_2 layers in the A-type AFM order, but is instabilized by the three-dimensional FM order.

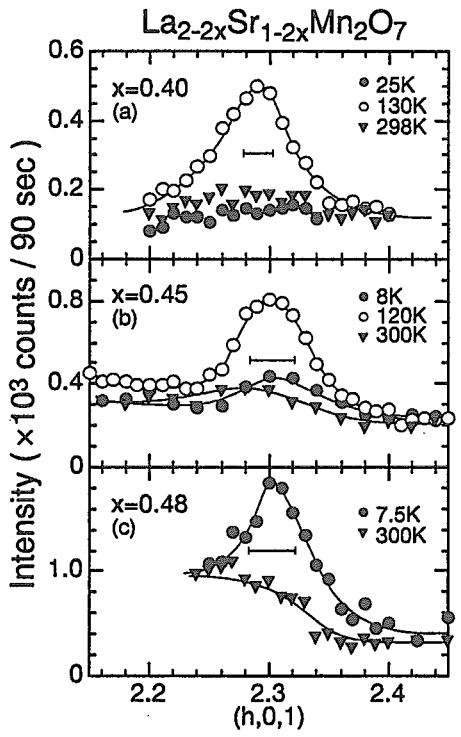

Fig.1 Profiles of the diffuse scattering from charge ordering for $x = 0.40, 0.45$ and 0.48. Horizontal bars indicate the instrumental resolution.

[1]M. Kubota *et al.*: J. Phys. Soc. Jpn. **70** (2000) in press july issue.
[2]K. Hirota, *et al.*; J. Phys. Soc. Jpn. **67** (1998) 3380.
[3]M. Kubota, *et al.*; J. Phys. Chem. Solids **60** (1999) 1161; J. Phys. Soc. Jpn. **69** (2000) 1606.
[4]H. Kuwahara *et al.*: Phys. Rev. Lett. **82** (1999) 4316.
[5]L. Vasiliu-Doloc *et al.*: Phys. Rev. Lett. **83** (1999) 4393.

JRR-3M GPTAS, TOPAN, KSD, 2 Magnetism

研究テーマ：二次元パーコレーションイジング反強磁性体におけるスピン相関へのランダム磁場効果
課題：二次元パーコレーションイジング反強磁性体におけるスピン相関へのランダム磁場効果

1-2-23 Radom-Field Effect on Spin Correlation in 2D Percolating Ising Antiferromanets

K. Iwasa and H. Ikeda[1]

Department of Physics, Tokyo Metropolitan University, Hachioji, Tokyo 192-0397, Japan
[1] Neutron Science Laboratory, Institute of Materials Structure Science, High Energy Accelerator Research Organization, Tsukuba, Ibaraki 305-0801, Japan

Percolating networks have been attractive, because a concept of fractal structures can describe them. They are found in diluted magnets with inter-spin connectivity mediated with exchange interaction. The fractal structures in two-dimensional (2D) diluted Ising-type antiferromagnets (AFM) $Rb_2Co_cMg_{1-c}F_4$ have been investigated by neutron experiments,[1] where c corresponds to a magnetic concentration on a 2D square lattice. Their exchange interaction dominates within the 2D plane and is limited to the nearest neighbors. An infinite spin cluster appears in the system with c above c_p = 0.593 (percolation threshold), and it orders in long range. Magnetic neutron Bragg scattering from the near-percolating system with c = 0.60 shows a peak profile broader than that of a Gaussian profile which is given by a δ-function convoluted by the resolution function for the long-range order in a uniform system. The diffraction intensity in the q range outside the inverse of geometrical correlation length is reproduced well by a power-law function q^{-D_f}, where q is a reduced wave number in the 2D square lattice and D_f = 1.896 is a fractal dimension. This fact reveals that the long-range ordered percolating cluster is considered to hold self-similar fractal characters.

Another interesting physics is random-field effect. A spin system has a lower spatial dimensionality below which long-range order does not occur. Under random fields, this lower dimensionality should increase. Fishman and Aharony proposed that the random field can be obtained by applying a uniform field to diluted Ising-type AFM.[2] The long-range order in $Rb_2Co_{0.70}Mg_{0.30}F_4$ is destroyed by cooling the sample under applied magnetic field, as observed in the neutron-scattering profile with large width in reciprocal space even at the lowest temperature.[3] In the state without long-range order due to random fields, magnetic domains are considered to appear. In this case, the spin-correlation function is proposed to be a squared Lorentzian (LSQ), not a conventional Lorentzian (LRZ). The validity of LSQ has been checked for some diluted magnets. However, the self-similar structure of percolating network has not been explicitly considered in the previous studies. The purpose of this study to elucidate spin correlation in percolation network under random field by neutron scattering measurements.

The experiments were performed for two samples, $Rb_2Co_cMg_{1-c}F_4$ with c = 0.60 and 0.65, at GPTAS (4G) spectrometer controlled to measure elastic scattering by triple-axis mode. The samples are installed in the superconducting magnet producing a vertical filed parallel to the favor direction of spin ordering. The profiles of scattering within the 2D-squared lattice were obtained by detecting intensities around the AF ordering point in the reciprocal space.

Figure 1 shows a profile around the magnetic zone center of the c = 0.60 sample at 0 T and 2.6 K as represented by open squares. We analyzed this profile by fitting the function composed of a LRZ and a LSQ with a common width parameter, as used in the previous report for the c = 0.70 system.[3] The result is shown by lines. It is

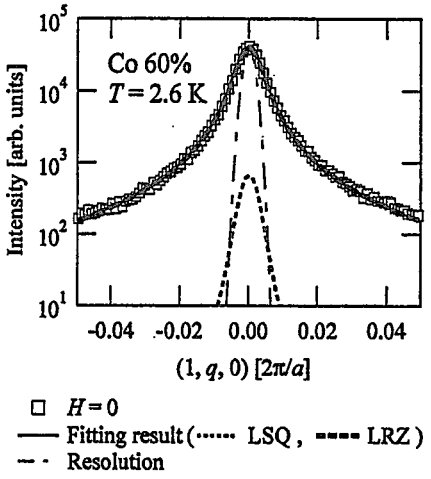

Figure 1. Magnetic scattering profile of the c = 0.60 sample at 0 T and 2.6 K.

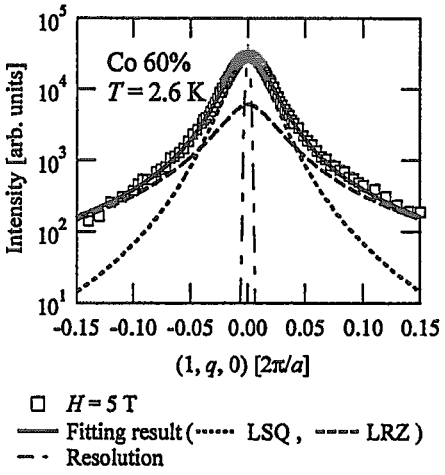

Figure 2. Magnetic scattering profile of the c = 0.60 sample after cooling down to 2.6 K with field of 5 T.

reasonable that the dominant function is LRZ, which can be considered as an approximate function for the above-mentioned power-law function of q. Figure 2 shows the profile of the c = 0.60 sample at 5 T and 2.6 K. It is clear that the peak is much broader than that at 0 T. Therefore, the random-field effect destroys the long-range order. By the fitting the sum of LRZ and LSQ, we found that the LRZ component still exists and is dominant in the q-range far from the zone center. The ratio of LRZ component to the total intensity at q = 0 is 20%, and it is much larger than 5% for the c = 0.70 system. The measurement at 5 T and 10.2 K was also performed. The scattering intensity is independent of the temperature, and the ratio of LRZ component is 21%. Thus, the LRZ component is not caused by the critical spin fluctuation, but by fractal structure of percolating network. The result for the c = 0.65 system at 5 T and 2.5 K is shown in Fig. 3. The same analysis is applied to the observed broad peak due to random-field effect, and resultant ratio of LRZ component is 11% which is just middle value between those of c = 0.60 and c = 0.70 systems.

It is concluded that the profile function contains a LRZ representing the fractal structure near c_p. The spin correlation cannot be interpreted only by the simple magnetic domain.

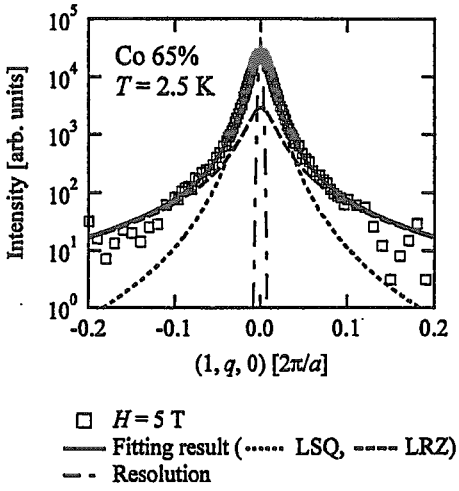

Figure 3. Magnetic scattering profile of the c = 0.65 sample after cooling down to 2.5 K with field of 5 T.

References

1) H. Ikeda *et al*: J. Phys. Soc. Jpn. 62 (1993) 3832.
2) S. Fishman and A. Aharony: J. Phys. C: Solid State Phys. 12 (1979) L729.
3) R. J. Birgeneau *et al.*: Phys. Rev. B 28 (1983) 1428.

研究テーマ: 縮退度の高い非ランダム磁性体におけるスローダイナミックス
表題 : 幾何学的フラストレーション系イジング二等辺三角格子反強磁性体 $CoNb_2O_6$ における異方的なドメイン成長のキネティクス

1-2-24 Anisotropic growth kinetics in the geometrically frustrated isosceles triangular Ising antiferromagnet $CoNb_2O_6$

S. Kobayashi, S. Mitsuda, T. Jogetsu, J. Miyamoto, H. Katagiri, and K. Kohn[1]

Department of Physics, Science University of Tokyo, Kagurazaka, Shinjuku-ku, Tokyo 162-8601, Japan

[1]School of Science and Engineering, Waseda University, Tokyo 169-8555, Japan

Triangular antiferromagnet with a partially released geometrical frustration have been attracting particular attention because of a possibility for appearing an unusual magnetic order absent in both frustrated and unfrustrated magnets. As one of model materials, we have studied a quasi-1D Ising magnet $CoNb_2O_6$ where zigzag chains along the *c* axis form *isosceles triangular lattice* in the *a*-*b* plane.[1-2] Previous neutron scattering under zero field [1] has revealed that a rapid cooling produces anisotropic interchain magnetic correlations in the antiferromagnetic (AF) phase below $T_2 \sim 1.9$ K, where the correlation length along the *b* axis is much larger than that along the *a* axis. Nevertheless, the domain-growth law as well as magnetic-field effect on the domain growth in the AF phase was not studied in detail.

We have performed single-crystal neutron scattering experiments at T = 1.5 K under magnetic field up to $H_{//c} \sim 600$ Oe, using the triple-axis spectrometer (4G) in a two-axis mode, installed at JRR-3M. The wave number of incident neutrons was 2.57 $Å^{-1}$ and the collimation with 40'-20'-20'-open was employed. To obtain non-equilibrium AF state, the magnetic field was rapidly removed from a field-induced ferrimagnetic state at $H_{//c} \sim 600$ Oe with a sweep rate of –100 Oe / sec. After reaching the zero field, the magnetic field was applied up to each measuring field.

In Fig. 1, we show the time evolution of the correlation length along the *a* and *b* axes, $\xi_a(t)$ and $\xi_b(t)$, obtained from the (h 1/2 0) and (3 k 0) transverse scans, respectively. For a comparison, near-equilibrium field-independent correlation length obtained after slow cooling is also shown: ξ_a^{SC} and ξ_b^{SC}. For all measuring fields, $\xi_b(t)$ is already close to ξ_b^{SC} at $t \sim 0$ and slowly increases with time. By contrast, $\xi_a(t)$ is rather smaller than $\xi_b(t)$ and is far from ξ_a^{SC} even at $t \sim 2\times10^4$ sec. With increasing magnetic field, $\xi_b(t)$ at a fixed time systematically decreases, while $\xi_a(t)$ is almost magnetic-field independent. These results clearly show anisotropic domain-growth kinetics in the AF phase, where the domain growth along the *b* axis proceeds much faster than along the *a* axis and is strongly suppressed by the magnetic field. We found that $\xi_a(t)$ well fits to the power law with the field-independent growth exponent $n \simeq 0.20$. This value is anomalously low compared with 1/2 of the conventional Ising magnet, indicating the extremely slow growth kinetics in this geometrically frustrated system.[2]

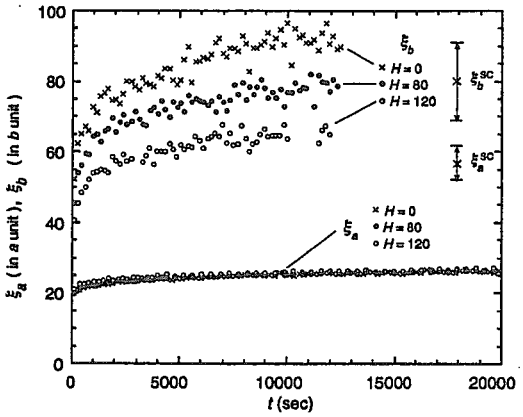

Fig. 1. Time evolution of $\xi_a(t)$ and $\xi_b(t)$ at several magnetic fields at T = 1.5 K.

References

[1] S. Kobayashi, S. Mitsuda, M. Ishikawa, K. Miyatani, and K. Kohn, Phys. Rev. B **60**, 3331 (1999).

[2] S. Kobayashi, S. Mitsuda, T. Jogetsu *et al.*, Phys. Rev. B **60**, R9908 (1999).

JRR-3M, 4G, 2. Magnetism

研究テーマ：Mg 置換 $CuGeO_3$ の中性子臨界散乱
表題：Mg 置換 $CuGeO_3$ の中性子臨界散乱

1-2-25

Critical Neutron Scattering Study of the Compositional Phase Transition in Mg-Doped $CuGeO_3$

M. Nishi, H. Nakao*, Y. Fujii, T. Masuda[1], K. Uchinokura[1], and G. Shirane[2]

Neutron Scattering Laboratory, Institute for Solid State Physics, The University of Tokyo, 106-1 Shirakata, Tokai, Ibaraki, 319-1106
[1] Department of Advanced Materials Science, The University of Tokyo, Hongo, Bunkyo-ku, Tokyo, 113-8656
[2] Department of Physics, Brookhaven National Laboratory, Upton, NY, 11973-5000, USA

The first inorganic spin-Peierls (SP) compound $CuGeO_3$[1] with T_{SP} = 14 K has offered a great opportunity to study doping effects on its SP state[2]. Regnault *et al.*[3] reported a striking fact that the SP state coexists with antiferromagnetic (AF) state using $CuGe_{1-x}Si_xO_3$ below T_N ($<T_{SP}$). Fukuyama *et al.*[4] proposed a theoretical model to understand such a coexistence by a unique phase in which both magnetic moments and lattice dimerization are spatially modulated. This AF state stabilized on the dimerized lattice is called D-AF, *i.e.* coexistence of AF and SP order parameters. Recently, Masuda *et al.*[5] reported a first-order phase transition from such a D-AF to a regular AF state on an undistorted uniform lattice (called U-AF) at a critical composition x_c = 0.023 in $Cu_{1-x}Mg_xGeO_3$ by magnetic susceptibility measurements. While recently Nakao *et al.*[7] reporteded x_c = 0.027 ± 0.001 by neutron scattering study. By using three high-quality single crystals with different concentration in the vicinity of x_c, *i.e.* x = 0.024, 0.0266 and 0.029, we have carried out critical neutron scattering experiments to settle such an inconsistent value of x_c. Neutron scattering experiments were carried out with an ISSP-owned triple-axis spectrometer (ISSP-GPTAS) installed at JRR-3M of JAERI in Tokai, Japan. A single crystal of Mg-doped $CuGeO_3$ with the mosaicness of 0.2 degrees FWHM was mounted with the (0, k, l) scattering plane in an ILL-type orange cryostat. Magnetic critical scattering was measured by a triple-axis configuration to significantly reduce background. In Fig. 1 the diverging behavior of the critical scattering was clearly observed at T_N for Q = (0, 0.99, 0.5). The peak positions of the previous heat capacity data[8] are shown by vertical arrows in the figure. Each transition temperature is determined as T_N =3.22 ± 0.02 K for x = 0.024 and 3.54 ± 0.05 K for x = 0.0266 much more unambiguously than a conventional method to measure a superlattice intensity. On the x = 0.029 sample, on the other hand, a small shoulder peak was observed near the lower T_N (3.39 ± 0.09 K) while a dominant peak corresponds to the higher T_N (4.01 ± 0.02 K). These experimental results are consistent with the T-x phase diagram of $Cu_{1-x}Mg_xGeO_3$ previously obtained by Nakao *et al.*[7] as displayed in Fig. 2 (bottom). Therefore, the compositional phase boundary at T_N = 3.4 ~ 4 K can be determined unambiguously as x_c = 0.028 ± 0.001 in confirming the two AF transition temperatures which was not observed by the temperature dependence of the AF Bragg intensity. An effective magnetic moment of Cu atoms obtained at T = 1.5 K is shown also in top of Fig. 2 where one can see the maximum value of the moment just at the phase boundary.

This study was supported in part by the US-Japan Cooperative Program on Neutron Scattering between USDOE and MONBUSHO. Work at Brookhaven National Laboratory was carried out under contract No. DE-AC02-98CH10886, Division of Material Science, U. S. Department of Energy.

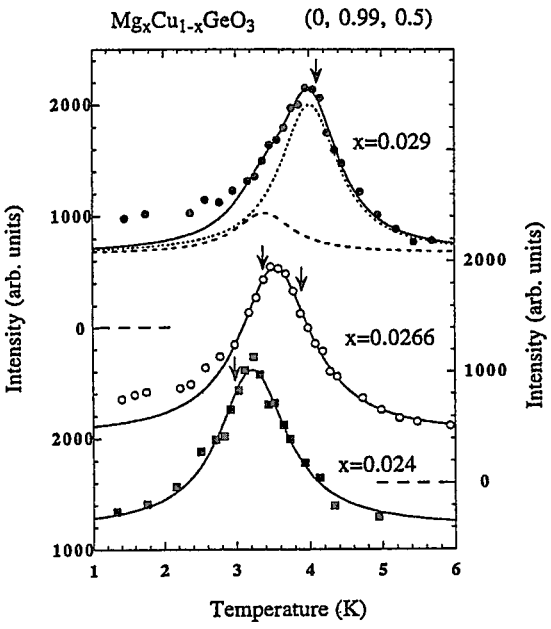

Fig. 1. Critical neutron scattering observed at (0, 0.99, 0.5) near the AF Néel points. Intensity differences from solid line at low temperature side of x = 0.0266 and 0.029 are contributed by the foot of Bragg peak (0, 1, 0.5).

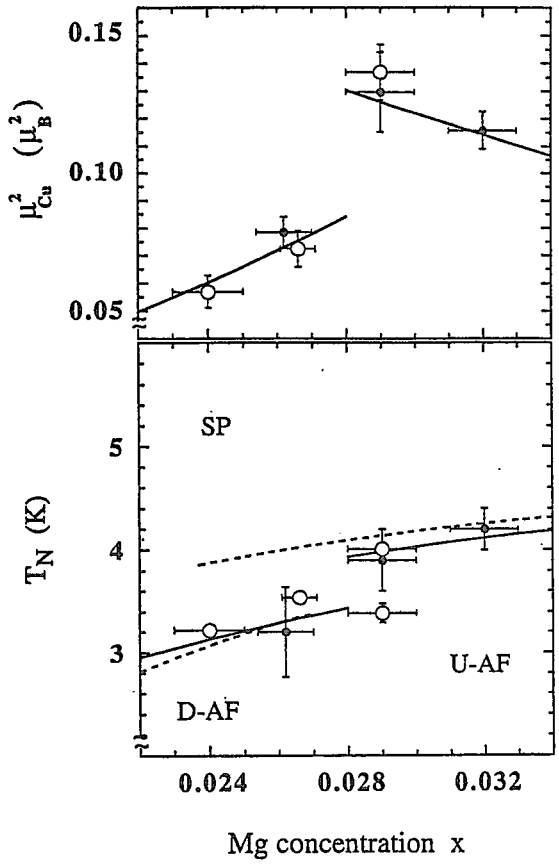

Fig. 2. (a) The Mg concentration dependence of the square of magnetic moment of Cu atom $(\mu_{Cu})^2$ at 1.3 K. Closed circles are referred from Nakao *et al.* [6] and open circles are present data. Solid curves are guides for eye.
(b) The T-x magnetic phase diagram based on Mg concentration x. At $x < x_c$ SP state coexists with AF Néel state. At $x > x_c$ SP state disappears at T = 0 K. The phase boundary between two kinds of Néel states exists at x_c= 0.028. Broken curves are referred from Masuda *et al.*[7].

References

1) M. Hase, I. Terasaki and K. Uchinokura: Phys. Rev. Lett. 70 (1993) 3651.
2) M. Hase *et al.* : Phys. Rev. Lett. 71 (1993) 4059.
3) L. P. Regnault *et al.* : Europhys. Lett. 32 (1995) 579.
4) H. Fukuyama, T. Tanimoto and M. Saito: J. Phys. Soc. Jpn. 65 (1996) 1182.
5) T. Masuda *et al.* : Phys. Rev. Lett. 80 (1998) 4566.
6) H. Nakao *et al.* : J. Phys. Soc. Jpn. 68 (1999) 3662.
7) T. Masuda *et al.* : Phys. Rev. B 61 (2000) 4103.
8) T. Masuda *et al.* : in preparation.

** present address; Photon Factory, Institute of Materials Structure Science, High Energy Accelerator Research Organization (KEK), 1-1 Ooho, Tsukuba, Ibaraki, 305-0801*

研究テーマ：CeNiSnの擬スピンギャップの構造
表題：近藤半導体CeNiSnにおける磁気励起の擬ギャップ

1-2-26
Pseudogap of magnetic excitation in Kondo semiconductor CeNiSn

H. Kadowaki, G. Nakamoto[1], and T. Takabatake[2]

Department of Physics, Tokyo Metropolitan University, Hachioji-shi, Tokyo 192-0397
[1]School of Materials Science, Japan Advanced Institute of Science and Technology, Ishikawa 923-1292
[2]Department of Quantum Matter, ADSM, Hiroshima University, Higashi-Hiroshima 739-8526

The pseudogap formation of the Kondo semiconductor CeNiSn was clearly observed by specific heat and NMR [1] experiments. The partial disappearance of the density of state at the Fermi energy brings about decrease of C/T or $1/(T_1T)$ with lowering temperature below 10 K. From this observation, one can naturally expect a certain gap-type energy spectrum for neutron inelastic scattering. However, in the low energy range of 10 K = 1 meV neutron scattering had failed to detect the pseudogap. In a higher energy range, neutron scattering showed interesting excitation peaks with E = 2 and 4 meV at specific wave vectors. These excitation peaks show increase of intensity with lowering temperature, and thus qualitatively differ from the gap-type spectrum. To investigate the low energy range more carefully, we have performed high-energy-resolution neutron experiments using an isotope ^{58}Ni sample, which reduces the incoherent elastic scattering and ensures low background. The pseudogap spectrum of the order 10 K have been proved to exist in $\mathrm{Im}\chi(Q,E)$ [2].

Neutron scattering experiments were performed on the cold-guide triple-axis spectrometer ISSP-HER. The spectrometer was operated with the final energy fixed to 3.1 meV. The vertically and horizontally focusing analyzer were employed. The typical energy resolution with collimations guide-40'-open-open was 0.1 meV (FWHM) at the elastic position.

The development of the pseudogap formation was measured by temperature dependence of $\mathrm{Im}[\chi(Q, E)]$ with $0.88 < Q < 1.03$ Å^{-1} at a small energy of 1.3 meV, which is a good choice in view of small background. The result is shown in Fig. 1. The decrease of $\mathrm{Im}[\chi(Q, E)]$ below 10 K demonstrates the gap formation. This neutron result is consistent with $1/(T_1T)$ data of NMR [1], except for the discrepancy below 5 K caused by a finite value of E. The pseudogap formation has been theoretically explained as a hybridization gap, which becomes a pseudogap type because of an anisotropic hybridization matrix determined by the crystal field and symmetry. To compare the experimental temperature dependence with this model, we calculated $\mathrm{Im}\chi(Q, E)$ and show it in Fig. 1. One can see that the theory qualitatively account for the experiment, but discrepancy at the lowest temperature suggests a certain modification of the theory.

Magnetic ordering induced by uniaxial stress along the c-axis was also studied, but no magnetic reflection was observed in the (h,k,0) scattering plane.

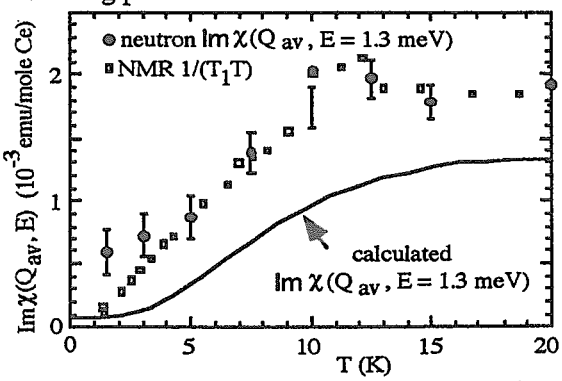

Fig. 1 $\mathrm{Im}\chi(Q_{av},E=1.3\mathrm{meV})$ is plotted as a function of temperature. To compare with NMR [1] $1/(T_1T)$ is also shown. The solid line is calculated $\mathrm{Im}\chi(Q_{av},E=1.3\mathrm{meV})$ using the anisotropic hybridization model [3].

[1] K. Nakamura et al., J. Phys. Soc. Jpn. 63 (1994) 433. [2] H. Kadowaki et al.: Physica B 281-282 (2000) 288. [3] H. Ikeda and K. Miyake, J. Phys. Soc. Jpn. 65 (1996) 1769.

研究テーマ：フラストレーションのある強相関電子系の磁性
表題：パイロクロア型化合物$Nd_2Mo_2O_7$の中性子散乱

1-2-27

Neutron Scattering Study on a single crystal of Pyrochlore Compound $Nd_2Mo_2O_7$

Y. Yasui[1,2], Y. Kondo[1], M. Ito[1], M. Kanada[1,2], H. Harashina[1,2], S. Iikubo[1], K. Oda[1], T. Kageyama[1], K. Murata[1], S. Yoshii[2], M. Sato[1,2], H. Okumura[3] and K. Kakurai[2,3],

[1]*Department of Physics, Division of Material Science, Nagoya University, Furo-cho, Chikusa-ku, Nagoya 464-8602*

[2]*CREST, Japan Science and Technology Corporation (JST)*

[3]*Neutron Scattering Laboratory, ISSP, The University of Tokyo, Shirakata 106-1, Tokai, Ibaraki 319-1195*

$R_2Mo_2O_7$ (R=Y and various rare earth elements) belongs to a series of molybdenum pyrochlore system. It consists of two kinds of three-dimensional networks individually formed by corner-sharing tetrahedra of R^{3+} or Mo^{4+}. Such an arrangement leads to geometrical frustration and therefore, strong magnetic fluctuation, if at least one kind of ions has the antiferromagnetic nearest neighbor coupling. The magnetic moments are also frustrated even for the ferromagnetic coupling, if they have local easy axes. Both the transport and magnetic properties depend on the species of R or on the ionic radius of R^{3+}: For R=Nd, Sm and Gd, the system exhibits the ferromagnetic transition, whereas for R=Dy, Y and relatively smaller rare earth elements, it exhibits the spin-glass-like behavior.[1)] With decreasing the ionic radius of R^{3+}, the transport nature also exhibits the metallic to the insulating crossover. The spin-glass behavior is considered to originate from the geometrical frustration. Mo 4d electron are presumed to play the principal role for the ferromagnetism and the electrical conduction, because these characters do not basically depend on the value of the magnetic moment of R^{3+} ions but the their ionic radii. Then this metal-insulator transition is considered to be due to the correlation effect of Mo4d electrons. Here, we report results of neutron diffraction study carried out with ISSP-PONTA spectrometer at JRR-3M on a single crystal of $Nd_2Mo_2O_7$ together with those of transport and magnetic measurements on another crystal and a polycrystalline sample prepared from the molten system.

Figure 1 shows the temperature (T) - dependence of the magnetic susceptibility χ ($\equiv M/H$, M and H being the magnetization and the magnetic field, respectively) on

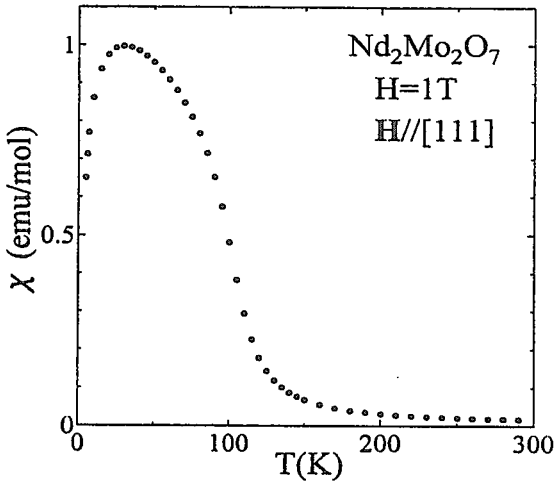

Fig. 1. Temperature dependence of the magnetic susceptibility $\chi(\equiv M/N)$ of a single crystal of $Nd_2Mo_2O_7$ measured in the magnetic field H=1 T along the [111] direction.

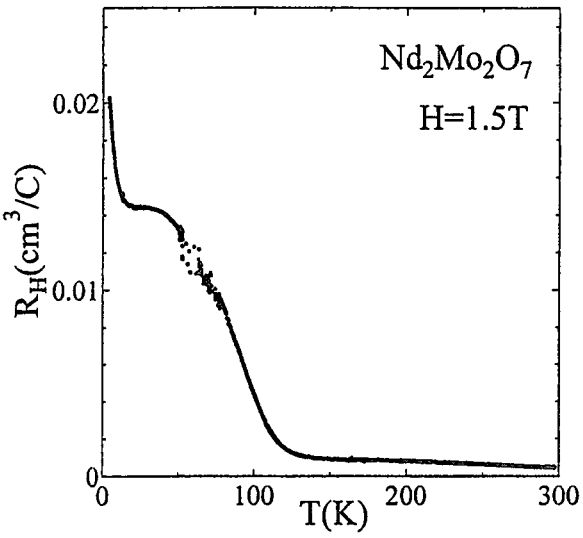

Fig. 2. Temperature dependence of the Hall coefficients R_H of a polycrystalline sample of $Nd_2Mo_2O_7$

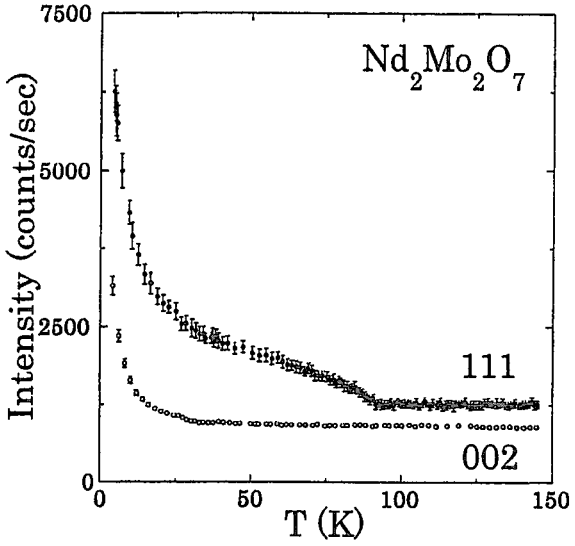

Fig. 3. Temperature dependence of the neutron intensities of the 111 and 002 reflections taken for a single crystal of $Nd_2Mo_2O_7$

the single crystal of $Nd_2Mo_2O_7$ measured under the field H=1 T along the [111] direction. The magnetic susceptibility exhibits an anomalous increase with decreasing T, reflecting the ferromagnetic transition at T_C ~95 K(determined by the using the Allot plot). With further decreasing T, the decrease of the magnetic susceptibility is observed below ~ 20 K, possibly due to the effect of the ordering of Nd moments.

Figure 2 shows the Hall coefficients R_H of $Nd_2Mo_2O_7$ as a function of T, where we can easily recognize that the change of the magnetic state at T_C and at 20 K significantly affect the T-dependence of R_H, indicating the rather strong coupling between the transport and magnetic properties.

The T-dependence of the neutron intensities of the 111 and 002 reflections of $Nd_2Mo_2O_7$ is shown in Fig. 3, where T_C-value of ~ 93 K is roughly consistent with the one determined by the magnetic measurements. Below ~ 20 K, intensities of both the 111 and 002 reflections remarkably increase with decreasing T, indicating the beginning of the significant contribution of the Nd^{3+} moments. Detailed measurements of the integrated intensities of magnetic Bragg points have been carried out at 40 K and 4 K. Based on these results and the behavior of the $\chi - T$ curve, the spin state of $Nd_2Mo_2O_7$ is understood as follows. A spontaneous magnetization in the T-region between 50 K and T_C is primarily due to the ferromagnetic ordering of the moments at Mo sites. Below 20 K, the moments at Nd sites exhibit the ordering, which partially cancel the spontaneous moment of Mo atoms. The rapid increase of R_H with decreasing T observed in the lowest T-region studied here indicates that the coupling between conducting Mo4d electrons with the Nd-moments is also significant. The detailed spin structure (of primarily Mo-moments) at 40 K and that of both Mo and Nd moments at 4 K will be reported in the near future.

References

1) N. Ali *et al.*, J. Solid State Chem. **83** (1989) 178.

研究テーマ ： フラストレーションのある強相関電子系の磁性

表題 ： フラストレーションのある系 $R_2Ru_2O_7$ (R=Y,Nd) の粉末中性子散乱

1-2-28 Studies on Geometrically Frustrated Pyrochlore System $R_2Ru_2O_7$(R=Y and Nd)

M. Ito[A], Y. Yasui[A,C], M. Kanada[A,C], H. Harashina[A,C], S. Yoshii[C], K. Murata[A], M. Sato[A,C], H. Okumura[B], K. Kakurai[B,C]

[A]*Department of Physics, Division of Material Science, Nagoya University, Furo-cho, Chikusa-ku, Nagoya 464-8602*
[B]*Neutron Scattering Laboratory, ISSP, The University of Tokyo, 106-1 Shirakata, Tokai 319-1195*
[C]*CREST, Japan Science and Technology Corporation (JST)*

Neutron scattering studies have been carried out on powder samples of pyrochlore ruthenates $R_2Ru_2O_7$ with R= Y and Nd, in which 3-dimensional (3D) networks of corner-sharing tetrahedra of R_4 and Ru_4 are individually formed. Because of this structural characteristic, just like a 3D version of the triangular lattice, magnetic moments at Ru sites (and also at R sites if R carries a magnetic moment) are expected to be highly frustrated, if they have antiferromagnetic nearest-neighbor interaction. The spin-glass-like transition observed at temperature $T=T_G$ in the magnetic susceptibility (χ) data of $Y_2Ru_2O_7$ and those observed at T_G and T_G' ($T_G > T_G'$) for $Nd_2Ru_2O_7$ are considered to be due to this kind of geometrical frustration (For the latter system, the two transition temperatures T_G and T_G' correspond to the networks of Ru_4- and R_4-tetrahedra, respectively).

However, specific-heat (C) measurements carried out by the present authors' group have revealed that the C-T curve exhibits a sharp jump at T_G, which is typical for second order transitions but not for spin-glass transitions. The behavior of the specific heat is not affected by the external magnetic field of H=5 T.

In order to clarify the nature of the transition at T_G, two models were considered. The first one is that the transition is caused by a structural distortion which stabilizes the glassy state. The second is that the transition is purely magnetic and almost antiferromagnetic long-range order is realized in the microscopic sense, even if the macroscopic quantity χ indicates the glass-like behavior. To clarify which model is appropriate, we carried out neutron powder diffraction. For $Y_2Ru_2O_7$, the measurements were on the spectrometer at T1-1 of the thermal guide of JRR-3M of JAERI in Tokai. The wavelength was 2.459 Å. A Pyrolytic graphite (PG) monochromater was used. Horizontal collimations were open-20'-20'. To remove the higher order beam, PG filter was put in front of the sample. Measurements on $Nd_2Ru_2O_7$ were carried out on the spectrometer ISSP-PONTA at JRR-3M. The horizontal collimations were 40'-80'-40', and we used a PG monochromater and a PG filter as in the case of $Y_2Ru_2O_7$. The wavelength was 2.353 Å. Samples packed in a V-can were put in an Al cell filled with the He gas. The packing factors of $Y_2Ru_2O_7$ and $Nd_2Ru_2O_7$ were about 0.4 and 0.3, respectively. Structural analyses were carried out by the Rietveld method.

We collected the data for both compounds above and below T_G ($T > T_G'$ for $Nd_2Ru_2O_7$). Above T_G, we have found that the Rietveld fittings to the observed powder patterns by using the well-known space group of pyrochlore systems ($Fd\bar{3}m$) are satisfactory (In Fig.1, the result only in a region around the 111 reflection is shown, for example). In the fittings of $Y_2Ru_2O_7$, a reflection peak from an Al cell and two unidentified peaks at the scattering angles $2\theta \sim 66°$ are omitted. In the case of $Nd_2Ru_2O_7$, reflections which indicate the existence of Nd_3RuO_7 as an impurity phase were observed. Then, the fitting was carried out for the mixture of $Nd_2Ru_2O_7$ and Nd_3RuO_7. With decreasing T, the intensities of several reflections begin to increase at T_G (Fig.2). At temperatures $T \ll T_G$,

we cannot reproduce the powder patterns by adopting the space group $Fd\bar{3}\,m$ (Fig.1). Even for the maximal subgroups of $Fd\bar{3}\,m$ which can be realized by second-order type structural distortion, we cannot reproduce the observed patterns, either. Therefore, the increase of the reflection intensities observed with decreasing T below T_G cannot be explained by adopting the structural transition model.

Then, we examine the second model. Assuming that the almost long range ordered state is realized below T_G, even though the macroscopic quantity χ exhibits the spin-glass-like transition, we have found that the spin arrangement shown in the inset of Fig.2 (note that it is not the true long range order) can reproduce the observed increase of the intensities below T_G with decreasing T, where each spin is in the plane perpendicular to the line which connects the center of the tetrahedron and the spin site, and total magnetization of the four spins is zero. In Table I, the absorption corrected integrated intensities of the magnetic reflections are shown together with those calculated by the spin arrangement. The estimated moment values μ per Ru in $Y_2Ru_2O_7$ and $Nd_2Ru_2O_7$ are about 1.36 μ_B and 1.18μ_B, respectively. These reasonable values suggest that the model is correct. It may also indicate that lattice system is not participating the transition. The correlation length of the Ru spins is found to be so large that we cannot distinguish the intrinsic broadening of the reflections by the present experimental resolution, confirming that the initial assumption is reasonable.

In summary, experimental results indicate that the lattice system does not participate in the transition at T_G. Ru spins at the corners of the tetrahedron undergo with decreasing T, the almost long range antiferromagnetic order at T_G, though the transition is, in the macroscopic sense, to the glassy state.

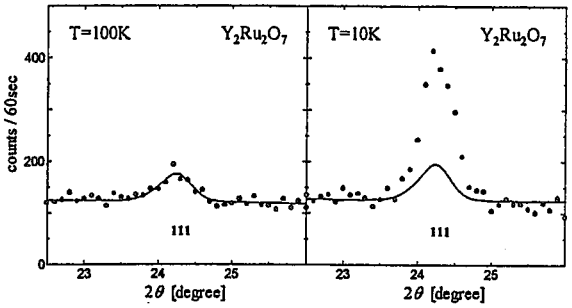

Fig. 1: Results of the Rietveld fittings around the 111 reflection of $Y_2Ru_2O_7$ obtained for $Fd\bar{3}\,m$ at 100K and at 10K.

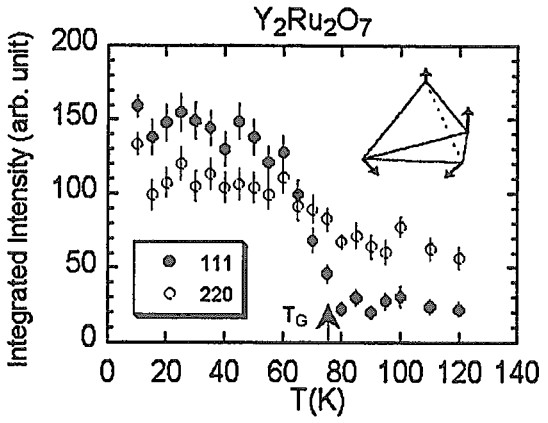

Fig. 2: The temperature dependence of the integrated intensities of the 111 and 220 reflections of $Y_2Ru_2O_7$. The T_G value (76.5K) is indicated by the arrow. The inset shows the spin structure which can explain the intensities of the magnetic reflections observed for both compounds. Spins of different tetrahedra are aligned in-phase.

Table I : Integrated intensities of the magnetic reflections after the absorption correction for both compounds are shown together with the calculated values.

	$Y_2Ru_2O_7$		$Nd_2Ru_2O_7$	
	exp.	calc.+	exp.	calc.*
111	165 ± 13	165	737 ± 58	737
220	60 ± 13	76	407 ± 69	344
113	39 ± 20	32	155 ± 19	147
331	< 26	13	38 ± 52	58

+ for $\mu = 1.36\mu_B$, * for $\mu = 1.18\mu_B$

研究テーマ：２重鎖構造をもつスピンギャップ系$TlCuCl_3$における磁気励起と磁場誘起相転移
表題：２重鎖構造をもつスピンギャップ系$TlCuCl_3$における磁気励起と磁場誘起相転移

1-2-29 Magnetic Excitations in the Spin Gap System $TlCuCl_3$

A. Oosawa, T. Kato, H. Tanaka, K. Nakajima[1], M. Nishi[1] and K. Kakurai[1]

Department of Physics, Tokyo Institute of Technology, Oh-okayama, Meguro-ku, Tokyo 152-8551

[1]Neutron Scattering Laboratory, Institute for Solid State Physics, The University of Tokyo, Tokai, Naka-gun, Ibaraki 319-1106

$TlCuCl_3$ is isostructual with $KCuCl_3$ which belongs to the monoclinic space group $P2_1/c$. The main feature of the crystal structure is double chain structure of edge-sharing octahedral $CuCl_6$ along a-axis. The double chains are located at the corners and center of the unit cell in the bc-plane, and are separated by Tl^+ ions. From the magnetization measurements, it is found that the ground state of $TlCuCl_3$ is spin singlet with an excitation gap Δ~0.65meV.

The single crystal neutron inelastic scattering was performed in order to investigate the magnetic excitations in the spin gap system $TlCuCl_3$ using the ISSP-PONTA spectrometer installed at JRR-3M, Tokai. The constant-k_f mode was taken with fixed final neutron energy of E_f=14.7meV. In order to gain intensity, collimations were set as open – monochromater - 80' – sample - 80'- analyzer -80' – detector. Excitation data were mainly collected at T=1.5K. All excitation spectra were taken by the constant-Q energy scan in the energy range of 2~15 meV. In order to obtain the dispersion relation $\omega(Q)$, we collected scan along (h,0,0), (h,0,1), (1.0,l), (1.5,0,l) and (h,0,2h-1) for $1 \leqq l \leqq 1.5$ and $0 \leqq h \leqq 1$.

From the constant-Q energy scan, three excitations are observed. Thus, there are three branches in the dispersion relations for the wavevector along (1,0,l), as shown in Fig.1. The lowest magnetic excitation with E_{min} ~ 0.5meV occurs at Q=(1,0,1). The lowest excitation energy was estimated as E_{min} ~ 0.5meV by the Gaussian fit using the data for E > 2meV. The value of E_{min} is compatible with the gap energy Δ~0.65meV evaluated from the magnetization measurements.

From the results, it is found that the highest ω_3 branch observed at E ~ 12meV in Fig.1 is not dispersive. In isostructual $KCuCl_3$, we observed a dispersionless excitation with E ~ 13meV, which is attributed to the phonon excitation. Therefore we infer that the dispersionless ω_3 excitation E ~ 12meV in $TlCuCl_3$ may also be attributed to the phonon excitation.

From the temperature dependence of the intensity of the lowest ω_1 excitation, its origin was confirmed to be magnetic. In isostructual $KCuCl_3$, the magnetic excitations are well described by the weakly coupled dimer model. Suzuki *et al.* argued that there exist two excitation modes in $KCuCl_3$, because there are two kinds of dimers, which are located in the corner and the center of the chemical unit cell in the b-c plane. The excitation modes are expressed as

$$\omega_{\pm}(\mathbf{Q}) = \sqrt{J^2 - JJ_{\pm}(\mathbf{Q})} \qquad (1)$$

with

$$J_{\pm}(\mathbf{Q}) = 2[J_a \cos(2\pi h) + J_{2a} \cos(4\pi h) + J_{2ac} \cos\{2\pi(2h+l)\}] \pm 4[J_{abc} \cos\{\pi(2h+k+l)\} + J_{bc} \cos\{\pi(k+l)\}]$$

where J is the interaction in the dimer and J_a, J_{2a}, J_{2ac}, J_{abc} and J_{bc} are the effective interactions between a dimer and those located at $\mathbf{r} = \pm\mathbf{a}$, $\pm 2\mathbf{a}$, $\pm(2\mathbf{a}+\mathbf{c})$, $\pm(\mathbf{a} \pm 1/2\ \mathbf{b} + 1/2\ \mathbf{c})$ and $\pm(\pm 1/2\ \mathbf{b} + 1/2\ \mathbf{c})$, respectively. We try to fit eq. (1) for $\omega_+(Q)$ to the lowest ω_1 branch in $TlCuCl_3$, and obtain J=5.23, J_a = 0.21, J_{2a} = -0.06, J_{2ac} = 1.56, J_{abc} = -0.34 and J_{bc} = -0.09 meV. In $TlCuCl_3$ the value of J_{2ac} is large. Therefore, it is suggested that in $TlCuCl_3$ the hopping of excited triplets is strong along the [2,0,1] direction.

Since the intensity of the $\omega_-(Q)$ excitation should be zero in a^*-c^* plane, the origin of the dispersive ω_2 excitation is unclear.

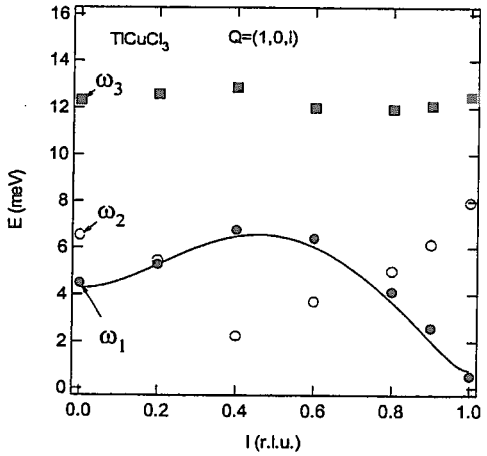

Fig.1 The dispersion relation $\omega(Q)$ in $TlCuCl_3$ for Q=(1,0,1). Closed and open circles and rectangles denote the ω_1, ω_2 and ω_3 modes, respectively. Solid line are the fits for ω_1 mode using eq. (1) for $\omega_+(Q)$. See text for the fitting parameters.

Reference

[1] N. Suzuki *et al.*: Physica B in press.

研究テーマ：スピンギャップ系$KCuCl_3$における磁気励起と次元性
表題：スピンギャップ系$KCuCl_3$における磁気励起と次元性

1-2-30 Dispersion Curves of the Magnetic Excitation of $KCuCl_3$

T. Kato[1], A. Oosawa[2], H. Tanaka[2], K. Nakajima[3], K. Kakurai[3]

[1]*Faculty of Education, Chiba Univ., Chiba 263-8522, Japan*
[2]*Dept. of Physics, Tokyo Institute of Technology, Tokyo 158-8551, Japan*
[3]*Neutron Scattering Lab., ISSP, the Univ. of Tokyo, Ibaraki 319-1106, Japan*

The magnetic excitation of the spin gap system $KCuCl_3$ was studied using the neutron inelastic scattering technique. The ground state of this spin system were known to be the spin singlet state with a finite spin gap energy 2.74 meV. Previous inelastic neutron scattering studies revealed that the three-dimensional network of the super-exchange interactions between dimers in $KCuCl_3$ made difficult to analyze the dispersion data. Especially in the *a*-*c* plane, on which the double-chain sub-structure is lying (along the *a*-axis), the inelastic scattering data only along the *a*- and *c*-axes were found to be insufficient because of the arbitrariness of choice of the fitting functions for the dispersion curves.

The experimental set-up was the same to the previous measurements: The spectrometer PONTA in JRR-3M at Tokai was used with the initial neutron energy fixed at E_i = 14.7 meV. The collimations 40'-M-40'-S-40'-A-80'-D were used and a PRG filter was inserted behind the sample. The sample temperature was fixed at 7 K.

The profiles of the constant-Q energy scans for Q along the diagonal lines (h, 0, $2h\pm1$), (h, 0, 1-$2h$), (h, 0, 1.4-$2h$) and (h, 0, 3-$2h$) were measured. Some of them were shown in Fig.1. Recorded dispersion was large for Q changing along the directions (h, 0, $2h\pm1$), but small for Q scanning along the other (perpendicular) directions. From these results, we can choose the function for the best fitting uniquely and obtain highly reliable fitting parameters, *i.e.*, the ratio of the inter-dimer interactions in $KCuCl_3$ in the random phase approximation. The (10-2) plane, which coincides with the first cleavage plane in $KCuCl_3$, was found to be important for the exchange network as much as the double-chain direction.

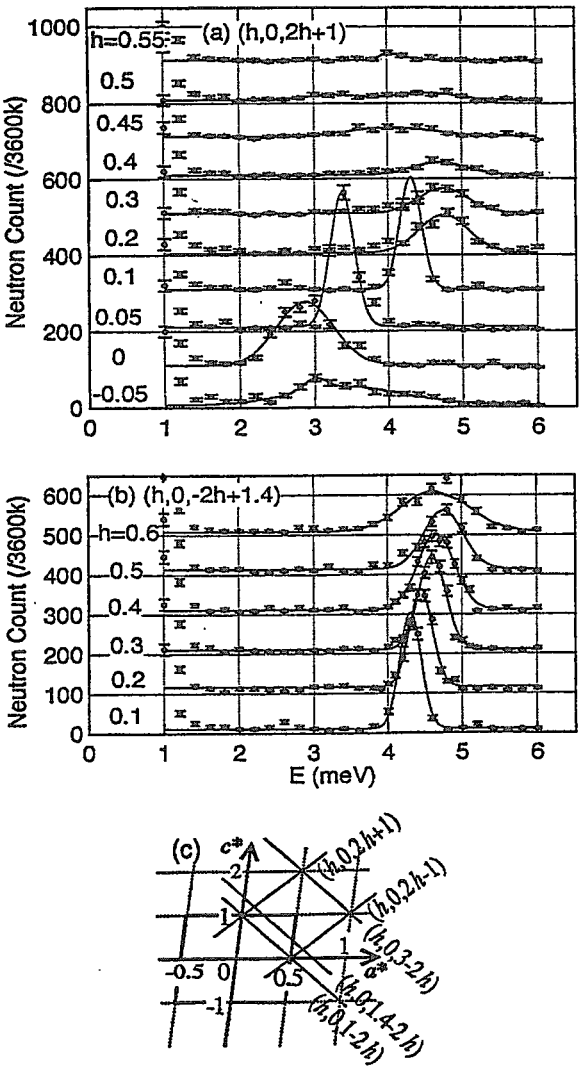

Fig.1 The profiles of the constant-Q energy-scans along the lines of (h, 0, $2h$+1) (a) and (h, 0, 1.4-$2h$) (b). An additional drawing (c) indicates the scan directions for this study in the a^*-c^* plane of the reciprocal space.

JRR-3M, PONTA, 2.Magnetism

研究テーマ：CoOのスピン構造とスピンダイナミクス
表題：CoOのスピン波測定

1-2-31 Measurements of spin-wave in CoO

Keisuke Tomiyasu and Yorihiko Tsunoda

School fo science and engineering, Waseda University,
3-4-1 Ohkubo, Shinjuku-ku, Tokyo 169-8555 Japan

The cobalt monoxide CoO belongs to a group of the antiferromagnetic monoxides with the rocksalt structure in the paramagnetic phases like MnO, FeO and NiO. All of their magnetic structures are the type-Ⅱ fcc, that is, the ferromagnetic sheets of the spins in the (111) planes, antiferromagnetically stacked along the <111> directions. The spin waves in these substances were meseaured by means of inelastic neutron scattering about 30 years ago, however, it was reported that the dispersion curves were flat only in CoO in spite of their very similar structures.

We performed the inelastic neutron scatterting experiments for a single crystal of CoO at the T1-1 and 5G PONTA triple axis spectrometer installed at JRR-3M.

We observed normal spin-wave scattering at 260[K] (T/T_N～0.9) by scanning along the <111> direction in the reciprocal lattice space. The line profile observed by a constant-E scan mode at 20 and 40 [meV] are shown in Fig.1. In Fig.2, the data points are plotted as the dispersion curve. The solid straight line represents the linear dispersion relation determined from the data at 3, 5, 8 and 10[meV] after the corrections of the resolution function. Quantitatively, the initial slope is estimated to be 97.9[meV Å] and the energy gap is $1.58*10^{-2}$[meV] at 260[K]. One may therefore say that CoO lies between metal-like NiO and typical insulators MnO and FeO.

We have to pay attention to the fact that the orbital moment of Co^{2+} is not quenched and the data analysis for this point is now in progress.

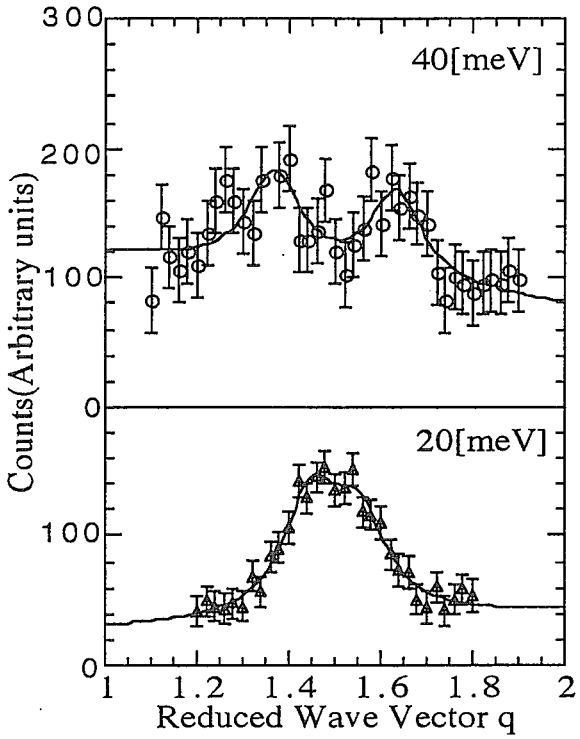

Fig.1 Magnon line profiles observed in CoO at 260K along the [q-1,q,q] directions by a constant-E operation at 20[meV] and 40[meV] .

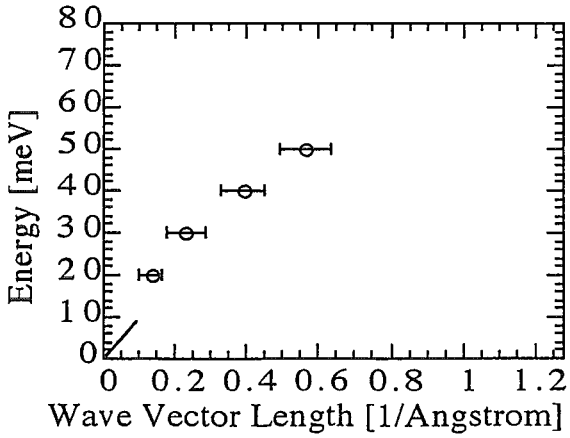

Fig.2 Spin-wave dispersion relation along the <111> direction at 260[K].

JRR-3M, T1-1 and 5G, 2.Magnetism

研究テーマ：S=5/2 反強磁性ハイゼンベルグ正方格子上のスピン相関
表題：S=5/2 反強磁性ハイゼンベルグ正方格子上のスピン相関

1-2-32

Spin Correlations on an $S = 5/2$ Heisenberg Antiferromagnet of Simple Quadratic Lattice

K. Takeda, M. Mito, K. Nakajima[1], K. Kakurai[1], and K. Yamagata[2]
Faculty of Engineering, Kyushu University, Fukuoka 812-8581,Japan
[1]Neutron Scattering Laboratory, The Institute of Solid State Physics, The University of Tokyo, Tokaimura, Naka-gun, Ibaragi 319-1106, Japan
[2]College of Science and Engineering, Iwaki Meisei University, Iwaki, Fukushima 970-8551

We have checked the spin correlations in an $S = 5/2$ Heisenberg antiferromagnet $Mn(HCOO)_2{\cdot}2(ND_2)_2CO$ (MF2U) with a simple quadratic lattice, which has the low magnetic ordering temperature $T_N = 3.77$ K and the exchange constant $J/k_B = 0.68$ K supposedly being free from the effects of larger thermal fractuations at higher temperatures.

For the present neutron scattering experiment, a single crystal of the deuterated urea compound MF2U of the averaged size of $(0.7\ \mathrm{cm})^3$ was prepared. The neutron scattering experiments were performed by the spectrometer PONTA, installed at JRR-3M at the Tokai Establishment of JAERI. The (002) reflection of pyrolytic graphite (PG) was used as a monochromator. A PG filter was employed to eliminate the higher-order reflections from the monochromator. The spectrometer was operated in the two-axis mode without the analyzer. The incident neutron energy E_i was fixed at $E_i = 14.8$ meV. The crystal was set into an *Orange*-type ^{4}He cryostat. Depending on the intensity and the temperature, ranging $T_N < T < 8.52$ K$(= 2.5\ T_N)$, two sets of collimator sequence for the spectrometer, 15'-20'-20' open and 40'-40'-40' open were employed,and the gate time was chosen as 200, 400 and 600 sec for the former set and 106, 162 and 216 sec for the latter one.

In the recent theory of the pure quantum self-consistent harmonic approximation (PQSCHA), both the spin correlation length and the magnetic heat capacity are given against the scale $t = T/2J\tilde{S}^2$, where $\tilde{S}$ is the effective spin length. With this temperature scale t, we express the thermal development of the correlation length ξ of MF2U within the same theory, as shown in Fig. 1.

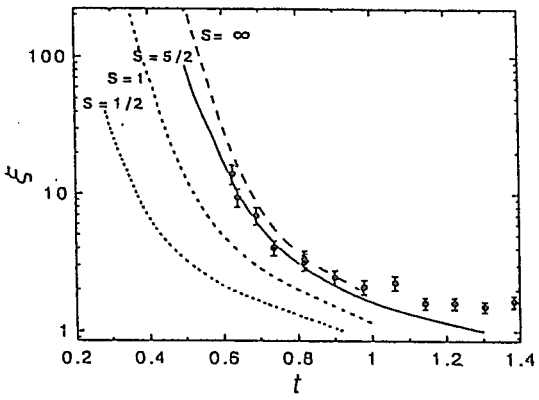

Figure 1: The theoretical magnetic correlation length ξ plotted against the reduced temperature $t = T/2J\tilde{S}^2$ and the experimental results for MF2U. The curves correspond to the values for $S = 1/2$, 1, 5/2 and the classical limit, respectively from the left side.

In summary, the dependence of the spin correlations on the spin quantum number in the simple quadratic lattice has been studied for the case of $S = 5/2$ employing the neutron scattering and thermal experiments on MF2U. By the use of the common reduced temperature scale, both the thermal developement of the spin correlations and magnetic heat capacity are well described by the theory of PQSCHA for $S = 5/2$, without an indication of approaching to the results by the QNLσM method, which one would expect for a higher spin value.

JRR-3M, PONTA, 2.Magnetism

研究テーマ: (Sr,Ca)CuO_2の磁気構造の研究
表題: (Sr,Ca)CuO_2の磁気構造の研究

1-2-33 Magnetic phase transition in (Sr,Ca)CuO_2

M. Matsuda, K. Katsumata, K. Kakurai[1], and G. Shirane[2]

The Institute of Physical and Chemical Research (RIKEN), Wako, Saitama 351-0198, Japan
[1]NSL-ISSP, University of Tokyo, Tokai, Ibaraki 319-1195, Japan
[2]Physics Department, Brookhaven National Laboratory, Upton, New York 11973, USA

The compound $SrCuO_2$ has a unique structure consisting of zigzag chains of Cu ions. Copper spins are coupled by the nearly 180° Cu-O-Cu interaction (J_2) and also by the nearly 90° Cu-O-Cu interaction (J_1). Judging from the exchange interactions in similar copper oxides such as La_2CuO_4 J_2 is expected to be strongly antiferromagnetic. In this case, there exists a competition between J_1 and J_2 irrespective of the sign of J_1.

Matsuda *et al.* performed magnetic susceptibility, heat capacity, muon spin relaxation, and neutron scattering experiments in $SrCuO_2$ [1] and observed a static magnetic ordering below T_c~2 K from the results of magnetic susceptibility, heat capacity, and muon spin relaxation experiments. However, no magnetic Bragg peak is observed down to 0.3 K. This result suggests that the Cu^{2+} moments are largely reduced probably due to the quantum fluctuation, which is consistent with the weak internal field in the μSR spectra.

Very recently, Zaliznyak *et al.* performed detailed neutron scattering experiments in $SrCuO_2$ [2] and found an anomalous spin frozen state below 5 K. Interestingly, the magnetic correlation length is fairy long along *c* (chain) but extremely short along *b* (2.2*b*) which is the direction of the frustrated interaction.

Since the transition temperature is very sensitive to oxygen concentration in $SrCuO_2$, the difference of the two results probably comes from the difference of oxygen concentration in the two crystals. In order to clarify the ground state in $SrCuO_2$ we performed neutron elastic scattering measurements on the triple-axis spectrometer PONTA using a new crystal of $SrCuO_2$, which has a transition temperature of 2.2 K determined from a heat capacity measurement. We tried to find magnetic Bragg peak around (0.5,0,0.5), where a well-defined magnetic peak is observed by Zaliznyak *et al.* However, no temperature dependent peak is observed as shown in Fig. 1. We plan to perform further measurements in the future.

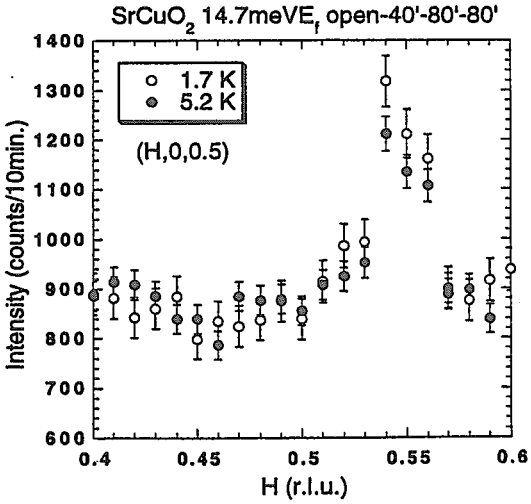

Figure 1 Elastic scans along *H* around (0.5,0,0.5) at *T*=1.7 and 5.2 K.

References

[1] M. Matsuda *et al.*, Phys. Rev. B 55, (1999) 11953-11956.
[2] I. A. Zaliznyak *et al.*, Phys. Rev. Lett. 83, (1999) 5370-5373.

研究テーマ：非フェルミ流体状態における Ce7Ni3 の磁気励起
表題：非フェルミ流体状態における Ce7Ni3 の磁気励起

1-2-34

Neutron scattering study of heavy fermion antiferromagnet Ce_7Ni_3

K. Motoya , T. Kawasaki , H. Kadowaki[1], T. Osakabe[2], H. Okumura[3], K. Kakurai[3], K. Umeo[4] and T. Takabatake[4]

Faculty of Science and Technology, Science University of Tokyo, Noda
[1] Department of Physics, Tokyo Metropolitan University, Hachioji, Tokyo
[2] Japan Atomic Energy Research Institute, Tokai, Ibaraki
[3] Institute for Solid State Physics, The University of Tokyo, Tokai, Ibaraki
[4] ADSM, HiroshimaUniversity, Higashi-Hiroshima

Ce_7Ni_3 crystallizes in the Th_7Fe_3-type hexagonal structure with three non-equivalent Ce sites. Specific heat and magnetic susceptibility measurements showed that an antiferromagnetic order (T_N=1.8K) coexists with a heavy Fermion state (γ=9J/K^2 mol f.u.) in this compound. The antiferromagnetic order is suppressed by extremely low pressure (P_c=0.33GPa) and non-fermi-liquid (NFL) behavior appears around P=0.4GPa in specific heat and magnetic susceptibility. Above P=0.62GPa, the normal FL state recovers. Taking advantage of the low P_c and the absence of lattice disorder introduced by the alloying, we made neutron scattering study of magnetic excitations of Ce_7Ni_3 under pressure around the magnetic instability and NFL/FL crossover.

Magnetic structure of Ce_7Ni_3 under the ambient pressure was studied by neutron diffraction using a single crystal. It was shown that the two successive phase transitions at T_{N1}= 1.8 K and T_{N2}= 0.7 K take place in zero field. At T_{N1} ordering of a single-k type magnetic structure with an incommensurate modulation vector $\mathbf{k}_{ic}$= 0.22 $\mathbf{c}^*$ takes place. This structure is approximately a sinusoidally modulated structure of c-axis moments, which belongs to the Γ_2 and Γ_3 irreducible representations of the space group. The root mean squares of the moments at T= 1.4 K are 0.46± 0.07, 0.70±0.03 and 0.10±0.05 μ_B for the Ce-1 (2(b)), the Ce-2 (6(c)) and the Ce-3 (6(c)) sites, respectively. Below T_{N2} the incommensurate modulation vector $\mathbf{k}_{ic}$ becomes temperature independent, and a commensurate ordering with $\mathbf{k}_c$=(1/4)$\mathbf{c}^*$ appears in addition to the incommensurate structure. The metamagnetic transition under magnetic field of H_c= 0.16T applied parallel to the c-axis at T= 1.5K was shown to be the first order transition to a ferromagnetic state. Inelastic neutron scattering measurements were made on a high energy-resolution triple-axis spectrometer utilizing a horizontally focused analyzer. The energy resolution is 95μeV (FWHM) at the elastic position. A single-crystal

sample (7mm diameter x 20 mm length) was mounted in a clamp-type piston-cylinder pressure cell attached to a dilution refrigerator. Magnetic excitation spectra in the antiferromagnetic and the pressure-induced paramagnetic phase up to P=0.79GPa were taken with constant-q scans.

Figure 1 shows the excitation spectra under various pressure at T=0.22~0.35K measured at Q=(100). Subtraction of the background noise mainly caused by the pressure cell, pressure media (Fluorinert) and large incoherent scattering from Ni atoms was made by measuring the scattering intensity with mounting a standard incoherent scatterer (vanadium metal) in the pressure cell instead of the sample.

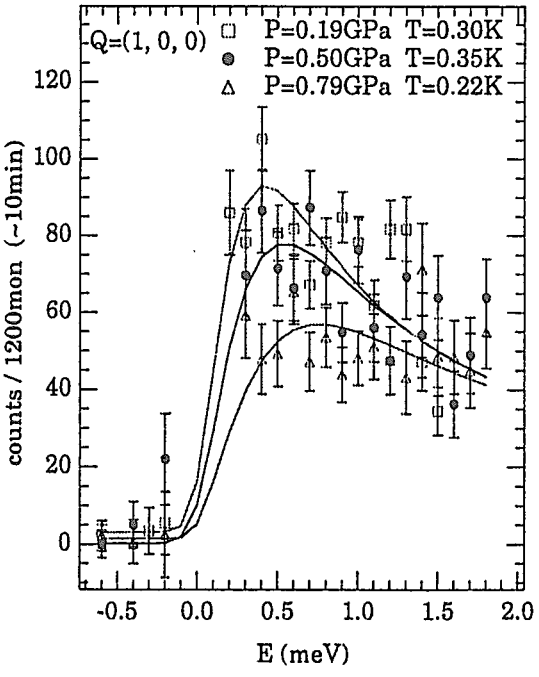

Fig.1 Inelastic neutron scattering spectra of Ce_7Ni_3 under various applied pressure.

Qualitative aspect of the inelastic scattering spectra observed in the antiferromagnetic (P=0.19GPa), the NFL (P=0.5GPa) and the FL states (P=0.79GPa) is quite similar in the present energy range. The scattering intensity decreases whereas the peak energy increases as the applied pressure is increased. The analysis of the excitation spectra was made based on the self-consistent renormalization (SCR) theory for spin fluctuations around the antiferromagnetic instability of heavy fermions proposed by Moriya and Takimoto. Following their theory we used a simplified form of the imaginary part of the dynamical susceptibility,

$$\mathrm{Im}\,\chi(Q_0+q, \omega) = \chi(q)\,\omega\,\Gamma(q) / (\omega^2 + \Gamma^2(q))$$

, where $\chi(q)$, $\Gamma(q)$ and Q_0 are the static susceptibility, the specific energy scale of spin fluctuations and the antiferromagnetic wave vector, respectively. The solid curves in Fig. 1 are the results of the least squares fit to the observed excitation spectra including the instrumental resolution function. Quantitative analysis of spin fluctuation parameters, together with the comparison with the results of macroscopic measurements, will be presented in the forthcoming paper.

研究テーマ: $ZnCr_2O_4$の中性子散乱
表題: $ZnCr_2O_4$の中性子磁気散乱

1-2-35 Magnetic Neutron Diffraction of $ZnCr_2O_4$

Y. Hata, E. Kita, I. Kagomiya[1], M. Toki[1], K. Kohn[1], K. Siratori[2], K. Nakajima[3] and K. Kakurai[3]

Institute of Applied Physics, Tsukuba University, Tsukuba, Ibaraki 305-8557, Japan,
[1]Department of Physics, Waseda University, Shinjyuku-ku, Tokyo 169-8555, Japan,
[2]Department of Physics, Kyushu University, Fukuoka, 812-8581, Japan,
[3]Institute for Solid State Physics, University of Tokyo,Kashiwa, Chiba 277-8581, Japan

$ZnCr_2O_4$ is a typical example of normal spinels with magnetic ions (Cr^{3+}) only at the B-sites.[1] The network of the B-sites in spinel structure is composed of tetrahedra sharing their corners with the four neighbors. Consequently, magnetic ions are frustrated with respect to the antiferromagnetic interaction between the nearest neighbors. In this connection, it is interesting to know what magnetic structure is realized in $ZnCr_2O_4$ and how it transforms into an ordered state.

The aim of this study is to determine the magnetic structure of $ZnCr_2O_4$ and to clarify the features of its magnetic transition. In such a study, it is desirable to use a single crystal sample composed of a single antiferromagnetic domain.

Neutron scattering data (at wavelength 1.63763 Å) were collected between 2 K and 15 K with the PONTA diffractometer installed at JRR-3M in JAERI. A single crystal sample was set in such a way as the [001] or [011] direction of high temperature cubic phase was vertical to the horizontal plane.

In a few experimental runs the sample was cooled down from about 30 K to 2 K in magnetic field of 50 kOe applied along the [100] or [010] direction. If this magnetic field cooling produces a change of domain structure , it will result in the difference of the intensity of a pair of peaks such as (1, 3/2, 0) and (3/2, 1, 0). So, we shall be able to estimate how the magnetic field cooling is effective in obtaining a single domain sample.

Figure 1 shows the position of the magnetic Bragg reflections observed at 2 K as well as the region of relatively high diffuse scattering. Generally, magnetic Bragg peaks of the (*h*/2, *k*, *l*), and the (*h*/2, *k*/2, *l*) types were observed.

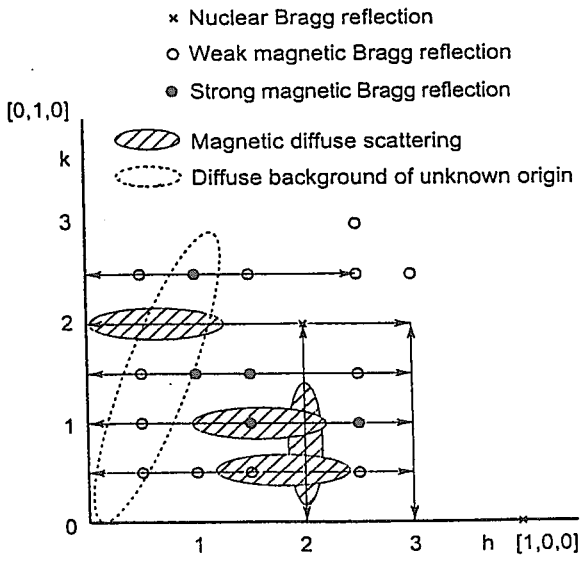

Figure 1 Position of magnetic Bragg reflections and magnetic diffuse scattering.

JRR-3M, PONTA, 2. Magnetism

Figure 2(a) depicts the temperature dependence of the height of the two Bragg peaks (3/2, 1, 0) and (3/2, 3/2, 0). Both had a similar temperature dependence and vanished at 10±1 K, which was identified as the Néel temperature T_N. Thus, two successive magnetic transitions claimed on isomorphous $MgCr_2O_4$ [2] is denied in the case of $ZnCr_2O_4$. Recently, dielectric anomaly [3] and development of tetragonal distortion were detected at T_N.[4]

Magnetic diffuse scattering was observed in the range indicated in Fig. 1. Its intensity increased gradually from temperatures around 100 K with decreasing temperature down to T_N. Figure 2(b) shows the temperature dependence of diffuse scattering intensity around the reciprocal lattice point (2, 1, 0) in the temperature range around T_N.

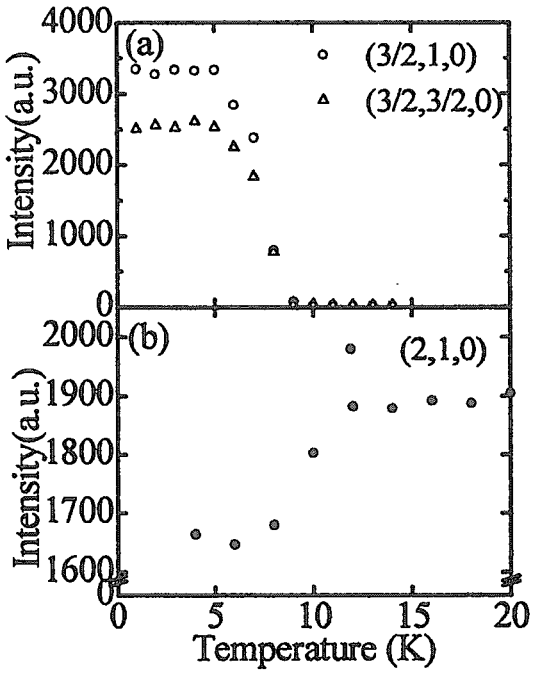

Figure 2 Temperature dependence of magnetic Bragg peaks (3/2, 1, 0) and (3/2, 3/2, 0) (a), and a magnetic diffuse scattering around (2,1,0) (b).

These results indicate the presence of a remarkable magnetic short-range order in the temperature much higher than T_N. A deviation of susceptibility from the Curie-Weiss behavior and remarkable low-frequency dielectric dispersion were observed in the same temperature range. The diffuse scattering intensity made a remarkable drop around T_N, and remained at a finite level in the magnetically ordered state. The intensity of the diffuse scattering was widely distributed in the reciprocal space. The distribution seemed independent of temperature.

The effect of magnetic field cooling was not observed within the accuracy of the experiment. If the ordered phase below T_N has a certain magnetic symmetry, a single domain state will be obtained by cooling a single crystal sample within both magnetic and electric fields applied simultaneously. We are preparing for neutron diffraction experiment of a sample after such magnetoelectric field cooling.

References

[1] R. Plumier, M. Lecomte and M. Sougi, J. de Phys. Lett. 38(1977) L-149.

[2] H. Shaked, J. M. Hastings and L. M. Corliss, Phys. Rev. B1 (1970) 3116.

[3] I. Kagomiya, K. Kohn, Y. Hata, E. Kita and K. Siratori, unpublished.

[4] S. -H. Lee, C. Broholm, T. H. Kim, W. Ratcliff II and S-W. Cheong, Phys. Rev. Lett. 84(2000) 3718.

研究テーマ：２次元量子スピン系SrCu2(BO3)2の中性子非弾性散乱
表題：２次元量子スピン系SrCu2(BO3)2の中性子非弾性散乱

1-2-36
Inelastic Neutron Scattering Study of the Orthogonal Dimer System $SrCu_2(BO_3)_2$

H. Kageyama, M. Nishi[1], N. Aso[1], K. Onizuka, K. Nukui[1], K. Kodama[2], K. Kakurai[1], and Y. Ueda

Material Design and Characterization Laboratory, Institute for Solid State Physics, University of Tokyo, Kashiwanoha, Kashiwa, Chiba 277-8581, Japan

[1] *Neutron Scattering Laboratory, Institute for Solid State Physics, University of Tokyo, 106-1 Shirakata, Tokai, Ibaraki 319-1106, Japan*

[2] *Division of New Materials Science, Institute for Solid State Physics, University of Tokyo, Roppongi, Kashiwanoha, Kashiwa, Chiba 277-8581, Japan*

$SrCu_2(BO_3)_2$, which has an orthogonal dimer network of one-half spins, is a 2D spin gap system with the known ground state, i.e., correspondence of the Shastry-Sutherland model [1]. In this study, we performed inelastic neutron scattering to investigate the dynamical properties of the dimer system [2].

Inelastic neutron scattering experiments were carried out on ISSP-PONTA spectrometer installed at 5G beam port of the Japan Research Reactor 3M (JRR-3M) in Japan Atomic Energy Research Institute, Tokai Establishment. The spectrometer was operated in the unpolarized neutron mode with pyrolytic graphite (PG) monochromator and analyzer. The inelastic scans were performed with fixed final energy Ef=14.7 meV (kf=2.67 -1) and horizontal collimations of open(40')-40' -sample-80' -80' . A PG filter was placed after the sample to suppress the higher order contaminations. In order to minimize the neutron absorption by the natural abundance of ^{10}B, ^{11}B-enriched (99.6%) bulk single crystals of $SrCu_2(^{11}BO_3)_2$ were prepared by the traveling solvent floating zone method using $Li^{11}BO_2$ flux [11]. The neutron scattering sample consisted of two single crystals with a total volume of $\sim$1.5 cm^3 aligned within 20' and it was oriented with its a- and b-axes in the scattering plane.

Shown in Fig. 1 are typical energy scans obtained at 1.7 K and 24 K for a scattering vector of Q=(2, 0). An abrupt growth in intensity below 2 meV is due to the elastic incoherent scattering from the sample. The 1.7 K spectrum consists of three peaks centered at 3.0 meV, 5.0 meV and 9.7 meV (transitions I, II and III, respectively), while that for 24 K no longer has any appreciable peak, indicating that all excitations are of magnetic origin. As already confirmed by other measurements, transition I at 3.0 meV is the excitation of a single triplet from the singlet ground state. Transition II arises from two-triplet excitations and transition III from three- or multitriplet excitations.

The dispersion relation of band I is shown in Fig. 2. Most importantly, the excitation energies are almost Q independent. Namely, the magnitude of the dispersion, the difference between the maximum and minimum of the excitation energy, is 0.2 meV at most. This width is significantly small in contrast to conventional low-dimensional quantum spin systems. As theoretically shown by Miyahara and Ueda, the key to the dispersionless band in $SrCu_2(BO_3)_2$ lies not in the spatial isolation of the spin clusters but in the orthogonality of the neighboring dimers: They proved that a hopping of the single triplet from one site to another within each plane is possible only from the sixth order in the perturbation calculations, leading to an exceedingly weak dispersion of band I.

We also shown in Fig. 2 the Q dependence of band II and III. The striking difference between band I and band II is that the latter shows more

dispersive behavior with a bandwidth of 1.5 meV. This observation may indicate that the propagation of correlated two triplets is much easier than that of the single triplet. The newly observed transition III may be interpreted within the framework of correlated three or multitriplets. Compared with the transition II, the observed profile of the transition III is considerably broader (see Figs. 1 and 2), which may result from a much wider spin continuum and/or a much shorter lifetime of the bound state.

References

[1] H. Kageyama et al., Phys. Rev. Lett. 82, 3168 (1999).

[2] H. Kageyama et al., to appear in Phys. Rev. Lett.

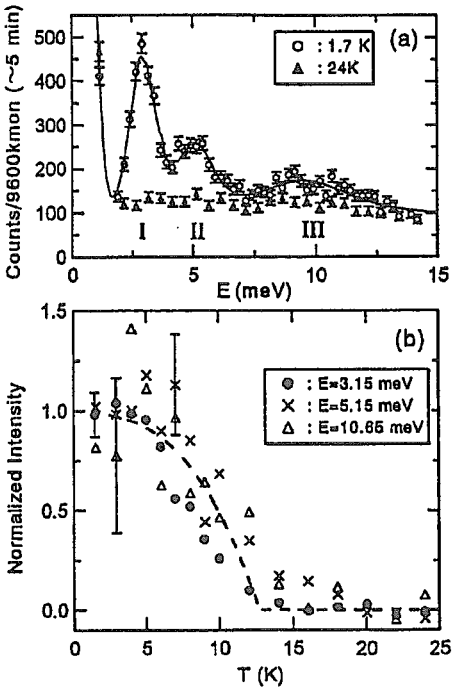

Fig.1 Energy scans at Q=(2, 0) obtained at T=1.7 K (circles) and 24 K (triangles).

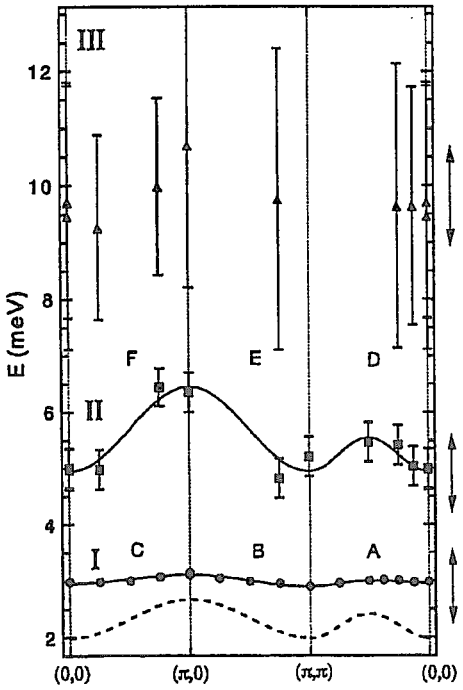

Fig. 2 Q-dependence of the excitation energies of bands I, II and III obtained at 1.7 K. The arrows represent the energy resolutions of the instrument (FWHM). The solid curves are guides to the eye. The bars represent the intrinsic line width (FWHM) of bands II and III. The theoretical dispersion curve for the single-triplet excitations by Weihong *et al.* with J=100 K and J' =68 K is given by the broken line.

研究テーマ：UX_2 (X=Ga,Ge)の 5f 電子状態
表題：UGe_2の磁気形状因子

1-2-37 Magnetic Form Factor in UGe_2

H. Sagayama, K. Kuwahara, K. Iwasa, M. Kohgi, Y. Haga[1], Y. Ōnuki[1,2], M. Nishi[3], K. Nakajima[3], N. Aso[3] and K. Kakurai[3]

Department of Physics, Tokyo Metropolitan University, Hachioji, Tokyo 192-0397, Japan
[1]Asvanced Science Research Center, Japan Atomic Energy Research Institute, Tokai 319-1195, Japan
[2]Division of Physics, Graduate School of Science, Osaka University, Toyonaka 560-0043, Japan
[3]Neutron Scattering Laboratory, ISSP, University of Tokyo, Tokai, Ibaraki 319-1195, Japan

In the actinides and their compounds, there has been interest because of the variety of physical properties. One of fundamental questions is whether 5f electrons are itinerant or localized. In most cases, 5f electrons exhibit both the itinerant and localized features. It is very difficult to describe their ground states experimentally.

In this study, we have investigated an orthorhombic uranium compound UGe_2, in which 5f electrons have been considered itinerant. It crystallizes in the orthorhombic structure (space group Cmmm) with lattice parameters, a = 4.01Å, b = 15.09Å, c = 4.10Å. This material exhibits the ferromagnetic phase transition at T_C = 52 K. There is a strong uniaxial anisotropy with the a-axis as an easy magnetization direction. The strong anisotropy might indicate that 5f electrons are localized under strong crystal field. However, the spontaneous magnetic moment (μ =1.43μ_B/U ion) is smaller than half that of the localized free ion U^{3+} or U^{4+}. Our neutron inelastic scattering measurements have failed to detect any definite magnetic excitation in this material. Furthermore the Fermi surface and transport properties strongly suggest that 5f electrons are itinerant. In order to clarify the extent of 5f electrons of UGe_2, therefore, we have measured the magnetic form factor with polarized neutrons.

Single crystal of UGe_2 was grown in a triarc furnace using the Czochralski method. It was cut into two different shapes: a cylinder (~3.5mm diameter and ~40mm in length) and rectangular parallelepipeds (10.0×~3.5×1.35 mm and 10.0×~3.5×0.5 mm). The polarized neutron experiment has been done using the triple axis spectrometer PONTA (5G) at the JRR-3M, Tokai. Polarized neutrons of wavelength λ = 1.01Å, produced by a Heusler alloy monochromator, were used. Measurements were performed at 2 K in a magnetic field of 2 T, applied parallel to the a- axis.

Figure 1 shows the observed magnetic amplitude μf of UGe_2. In spite of the 5f itinerant features of this material, the magnetic form factor f is similar to that of the free ion of U^{3+} or U^{4+}. The reason of its discrepancy is not clear at present. Further detailed investigations are needed to understand 5f states in this material.

Recently a pressure-induced superconductivity of UGe_2 has been reported. If its superconductivity is intrinsic, the form factor measurements under high pressure may be interesting.

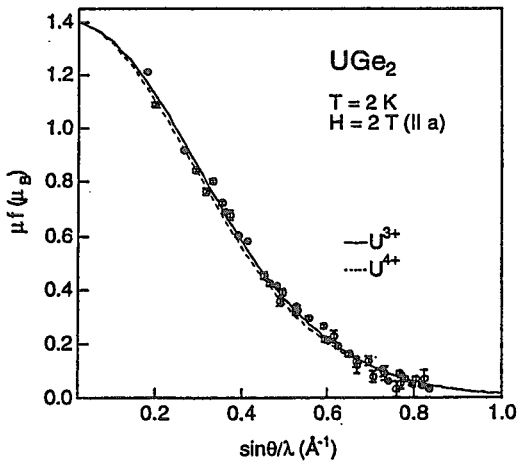

Figure 1 The magnetic amplitude μf as a function of $\sin\theta/\lambda$ for ferromagnetic UGe_2 at 2 K in the field of 2 T, applied parallel to the easy magnetization axis. The solid line and dashed line represent the calculated values for U^{3+} and U^{4+} form factors in the dipole approximation, respectively.

研究テーマ: 中性子ラーモア回転による動力学回折位相
表題: 中性子スピンエコー法によるオレイン酸磁性流体マグネタイト微粒子の運動

1-2-38 Dynamics of magnetite particles in ferro-fluid by NSE method

N. Achiwa, G. Shirozu, T. Yokoyama, K. Kakurai[1]

Graduate school of Sciences, Kyushu University, Hakozaki, Fukuoka 812-8581, Japan
[1]Neutron scattering Laboratory, ISSP, University of Tokyo, Tokai, Ibaraki, 319-11, Japan

1 Introduction

We have tried to observe dynamics of magnetite fine particle clothed by oleic acid dispersed in light water by neutron spin echo (NSE) technique at the Bragg angles of the magnetite. The Bragg reflection is quasi-elastic when the magnetite particles are dancing Brownian motion in colloidal state. From theoretical estimation the quasi-elastic energy spread by the Brownian motiis order of $10\mu eV$ for the magnetite particles with 100Åradius. On the other hand, since the size of magnetic particle is the order of 100Å, the magnetization of such fine particle is thermally fluctuated showing superparamagnetism. This fluctuation of magnetization also gives energy broadening for magnetic Bragg reflection. Since two origens of quasi-elastic Bragg scattering can be proposed, it is interesting to compare NSE visibility for various indices of Bragg reflections from magnetite particle in ferro-fluid as functions of spin echo time and temperature. In this case, the difference of NSE visibilities in Bragg reflections with magnetic and nonmagnetic contributions of structure factor is expected.

2 Experimental Results

Measurements of spin echo experiment were carried out by using PONT at JRR-3M with polarized neutron of 2.353Å. Ferrofluid containing 40 weight % magnetite is closed in rectangular cell with the thickness of 2mm. Preliminary spin echo experiment with Al(111) Bragg reflection (2θ = 60°) of a thin aluminum container including ferro-fluid shows the echo vibibility around 0.85 at 298 K for around spin echo time of $10^{-10}sec$ as shown in Fig.1. But the visibility decreases of to 0.75 at 333 K. This means that the depolarization due to magnetic fluctuations through ferro-fluid contributes. For (311) Bragg reflection (2θ = 55°) of magnetite, visibility is order of 0.1 at room temperature as shown in Fig. 1. This small visivility is due to large back ground of hydrogen incoherent scattering. At 333 K the visibility clearly increases. Further, the changes of visibility with spin echo time were observed.

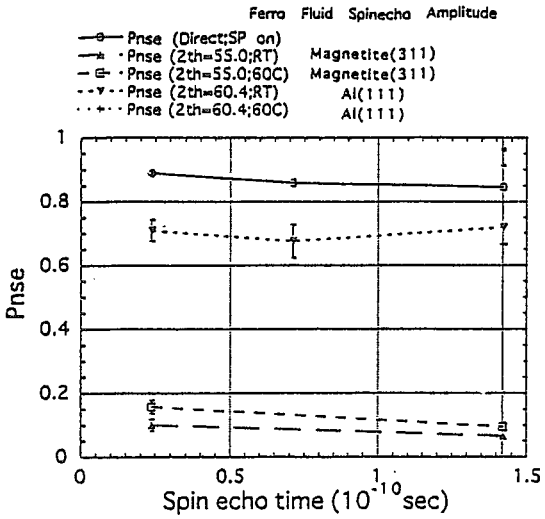

Figure 1: Spin echo amplitude for (311) Bragg reflection of magnetite fine particles in ferro-fluid oleinic acid as a function of spin echo time. Similar results for Al(111) reflection of a thin aliminun container showing reference NSE amplitude through the ferro-fluid.

In order to improve the intensity of Bragg reflection from magnetite in ferr-fluid it should be dispersed in heavy water.
At the present stage though the experimental results are preliminary, we have shown the effectiveness of spin echo technique for the system of moving fine crystal particle such as magnetite in ferro-fluid.

[1] JRR-3M, PONTA, 2, Magnetism

研究課題：$(La,Sr)_{n+1}Mn_nO_{3n+1}$のスピン・電荷ダイナミクス
標題：層状Mn酸化物$La_{2-2x}Sr_{1+2x}Mn_2O_7$のスピンダイナミクスと軌道状態

1-2-39
Study of orbital degrees of freedom in $La_{1-x}Sr_xMnO_3$ by x-ray and neutron scattering

[1]K. Hirota, [1]K. Takahashi, [2]T. Fukuda, [2]J. Mizuki, [3]Y. Murakami and [4]Y. Endoh

[1]*Department of Physics, Tohoku University*
[2]*Department of Synchrotron Radiation Facility Project, JAERI*
[3]*Photon Factory, Institute of Materials Structure Science, KEK*
[4]*Institute for Materials Research, Tohoku University*

$La_{1-x}Sr_xMnO_3$ is a prototype of colossal magneto resistive materials and an ideal platform to study the orbital degrees of freedom in $3d$ electron systems. A resonant x-ray scattering study shows that $LaMnO_3$ undergoes orbital ordering associated with cooperative Jahn-Teller (JT) ordering. The orbital ordering, most likely $3x^2 - r^2/3y^2 - r^2$ type, result in two-dimensional anisotropy of the spin wave dispersion, though the crystal structure is close to a cubic perovskite. Recently, it was found that $La_{0.88}Sr_{0.12}MnO_3$ exhibits a phase transition at $T_{OO} = 145$ K from a ferromagnetic metal to a novel ferromagnetic insulator, where orbital ordering occurs in spite of significant *diminution* of the cooperative JT distortion. This finding indicates that the orbital ordering at $x = 0.12$ is not realized by the conventional JT-driven mechanism.

We have carried out a systematic investigation of the orbital ordering and structural transition of $x = 0.08 - 0.13$ single crystals by resonant x-ray scattering, neutron scattering and high-resolution powder diffraction. We have established a new phase diagram of lightly doped $La_{1-x}Sr_xMnO_3$ and found that there exists a clear phase boundary between $x = 0.10$ and 0.11 and the following differences:

Structure Ortho* (Pseudo cubic) → Ortho′ (JT) at $x \leq 0.10$. Ortho* → Monoclinic (JT) → Triclinic (small JT) at $x \geq 0.11$.

Orbital ordering Orbital orders in Ortho′ (JT) at $x \leq 0.10$. At $x \geq 0.11$, cooperative JT distortion diminishes upon orbital ordering and the structure changes to Triclinic.

Spin wave Anisotropic
$x \leq 0.10$ ($D_{[100]}/D_{[001]} \sim 0.5$). Isotropic at $x \geq 0.11$.

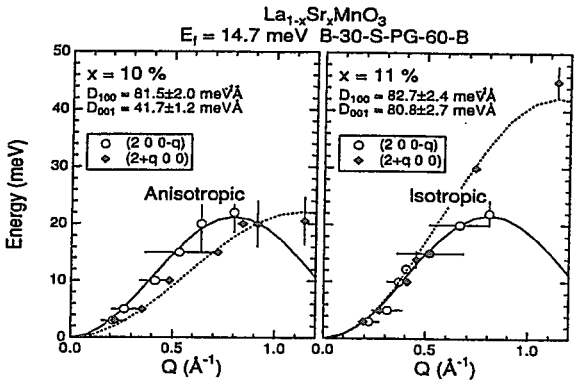

Figure 1: Spin wave dispersions measured at $(2+q\ 0\ 0)$ and $(2\ 0\ q)$ for $x = 0.10$, and 0.11. Error bar indicates FWHM of a peak profile.

These experimental results unambiguously show that there are two different types of orbital ordering states, which we speculate correspond to $3x^2 - r^2/3y^2 - r^2$ in the lower doped region and $x^2 - z^2/y^2 - z^2$ in the higher doped region. A recent theoretical work suggests that the novel orbital ordering found at $x = 0.11$ and 0.12 is driven by a strong correlation between electrons.

Reactor: JRR-3M　　Facility: TOPAN(6G)　　Field: 2 磁性 Magnetism

研究課題：$La_{1-x}Sr_xMnO_3$の軌道自由度とスピン・格子ダイナミクス
標題：X線と中性子散乱による$La_{1-x}Sr_xMnO_3$の軌道自由度の研究

1-2-40
Spin dynamical properties and orbital states of the layered perovskite $La_{2-2x}Sr_{1+2x}Mn_2O_7$ $(0.3 \leq x < 0.5)$

K. Hirota,[1] H. Fujioka,[1] M. Kubota,[2] S. Ishihara,[3], H. Yoshizawa,[2] Y. Moritomo[4] and Y. Endoh[3]

[1] *CREST, Department of Physics, Tohoku University*
[2] *Neutron Scattering Laboratory, Institute for Solid State Physics, University of Tokyo*
[3] *Institute for Materials Research, Tohoku University*
[4] *CIRSE and Department of Applied Physics, Nagoya University*

Series of inelastic neutron-scattering measurements were performed on single crystals of the layered perovskite $La_{2-2x}Sr_{1+2x}Mn_2O_7$ (LSMO327) in the range of $0.3 \leq x < 0.5$. We found that the spin-wave dispersion is almost perfectly two-dimensional and has two branches due to a coupling between layers within a double-layer, and that both the in-plane spin stiffness constant and the gap between the two branches strongly depend on the hole concentration x. To study the magnetic interactions in LSMO327, we have calculated the spin-wave dispersion and the differential scattering cross section by applying the Holstein-Primakov approximation and the Bogoliubov transformation to a Heisenberg model with the in-plane ($J_\parallel$), *intra*-bilayer ($J_\perp$) and *inter*-bilayer (J') interactions assuming three different magnetic structures proposed by Kubota *et al.* [J. Phys. Chem. Solids **60** (1999) 1161.] In addition to noticing difference among the dispersion curves belonging to different magnetic structures, we found that the calculated cross-section has a characteristic oscillation along the c-axis and is very sensitive to J'. We have then determined the $J_\parallel$, $J_\perp$ and J' values at $x = 0.30, 0.35, 0.40$, and 0.48 by fitting the data with the theoretical calculations. At $x = 0.30$, we found that $J_\parallel$ is -4 meV, which is slightly smaller than $J_\perp = -5$ meV. With increasing x, the absolute value of $J_\parallel$ gradually increases and that of $J_\perp$ decreases. At $x = 0.48$, $J_\parallel$ reaches -9 meV, while $J_\perp$ turns to $+1$ meV indicating the antiferromagnetic interaction. This drastic change can be only explained by the change of the e_g orbital state upon doping, namely $d_{3z^2-r^2}$, which is dominant at $x = 0.30$, is gradually taken over by $d_{x^2-y^2}$ with increasing x. This is consistent with the x dependence of the ratio of the apical and equatorial Mn-O bond lengths $\langle \mathrm{Mn-O}_{ap} \rangle / \mathrm{Mn-O}_{eq}$, which decreases 1.03 at $x = 0.30$ and 1.00 at $x = 1.00$. We have also theoretically determined the e_g orbital state at a give x by comparing the theoretical model and the neutron scattering result.

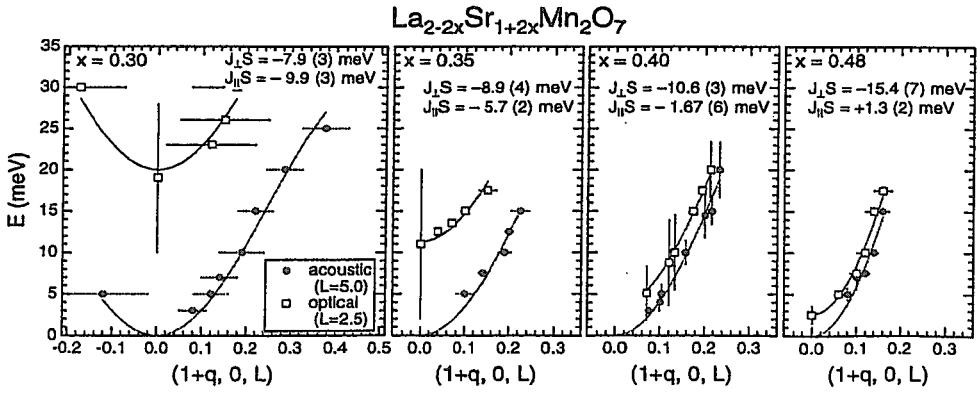

Reactor: JRR-3M　　Facility: TOPAN(6G)　　Field: 2 磁性 Magnetism

研究テーマ：層状マンガン酸化物の軌道秩序
表題：層状ペロブスカイト型マンガン酸化物の軌道状態

1-2-41 Orbital State in Layered-Perovskite Manganite Compound

T. Arima, A. Nakazawa, K. Ohoyama[1], H. Ichikawa[2], J. Akimitsu[2], T. Matsumura[3], K. Hirota[3]

Institute of Materials Science, University of Tsukuba, Tsukuba 305-8573, Japan
[1]Institute for Materials Research, Tohoku University, Sendai 980-8577, Japan
[2]Department of Physics, Aoyama-Gakuin University, Tokyo 157-8572, Japan
[3]Department of Physics, Tohoku University, Sendai 980-8573, Japan

Recently, orbital states in strongly-correlated-electron systems have attracted a great deal of attention. We are studying the orbital state in a layered-perovskite manganese oxide compound $La_{1.2}Sr_{1.8}Mn_2O_7$ using a polarized-neutron scattering technique. The spin density distribution should be equivalent to the density distribution of 3*d* electrons, because the manganite compound is half-metallic. The magnetic structure factor obtained by elastic neutron scattering is the Fourier series of the spin density distribution.

A crystal of $La_{2-2x}Sr_{1+2x}Mn_2O_7$ (x=0.40) was melt-grown using a floating-zone furnace. The ratios of magnetic structure factor, F_M, to nuclear structure factor, F_N, for various scattering vectors, Q=($h0l$), were obtained by polarized-neutron scattering measurements using the triple-axis spectrometer TOPAN in JRR-3M of the Japan Atomic Energy Research Institute (JAERI). The measurement was carried out in a magnetic field of 1 T along the *b*-axis. The absolute values of $|F_M|^2 + C|F_M|^2$ were obtained by Rietveld analysis of powder neutron diffraction data, where C is the factor dependent on the angle between the scattering vector and the spin moment. The powder diffraction measurement was carried out using the powder neutron diffractometer, HERMES, which is equipped with multi-detectors with the Ge (331) monochromator (λ=1.819 A) in JRR-3M of JAERI. Magnetic structure factors, $F_M(h0l)$, were calculated from the data of F_M/F_N and $|F_N|^2 + C|F_M|^2$.

In Figure 1 we plot the magnetic form factor of a manganese ion, f_{Mn}, as a function of $|Q|$. Here we neglect the contribution of other ions to the spin polarization. If the two e_g orbitals, d_{x2-y2} and d_{3z2-r2}, would be occupied with the same probability, the form factor would decrease almost monotonically. Contrary to the expectation, the f_{Mn} values are significantly scattered. This should be related with possible orbital ordering and the hybridization between Mn and O. Further analysis is now on the way.

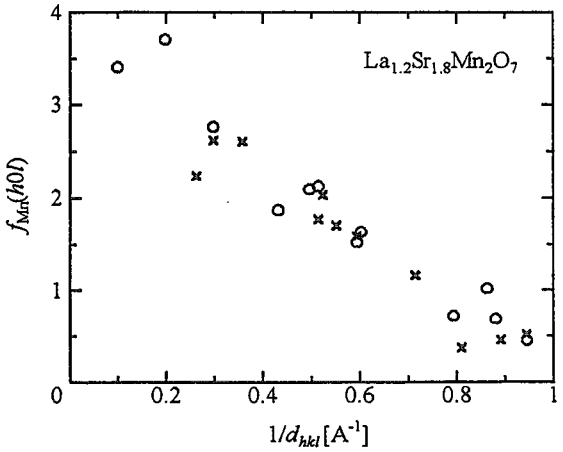

Figure 1 Magnetic form factor of a Mn ion plotted against $|Q|$. Circles: for Q with $ha^*<lc^*$, crosses: for Q with $ha^*>lc^*$.

JRR-3M, HERMES TOPAN, 2. Magnetism

研究テーマ：$(VO)_2P_2O_7$高圧相のスピンギャップの研究
表題：スピン 1/2 ボンド交代化合物 $(VO)_2P_2O_7$ 高圧相のスピンギャップ直接観察

1-2-42
Direct observation of the spin gap in a S=1/2 alternating chain compound, high pressure phase of $(VO)_2P_2O_7$

M. Azuma, T. Saito, M. Fujita and M. Takano
Institute for Chemical Research, Kyoto University, Uji Kyoto-fu, 611-0011 Japan

Recently one dimensional antiferromagnets with spin gaps attract much attentions. $(VO)_2P_2O_7$ (VOPO) comprises vanadium ions in the 4+ oxidation state with spin-1/2. A recent neutron scattering study on single crystals showed the validity of the alternating chain model for this compound. Interestingly, the data also revealed the existence of a second energy gap of about twice as large as the first one as predicted theoretically. However, this compound comprises two slightly different chains making it difficult to determine whether these chains have single but different spin gaps or have the same double gaps.

We found that this compound undergoes a pressure-induced transition to a similar but simplified structure with a unique kind of chain. The crystal structures of the high-pressure (HP) and the ambient-pressure (AP) phases are illustrated in Fig. 1. Both these are made of edge-sharing pairs of VO_5 pyramids and PO_4 tetrahedra, while the arrangement is simpler in the HP phase. The AP phase has two major AF interactions along the c axis, one mediated by the two V-O-(P)-O-V paths (J_1) and the other through the almost orthogonal V-O-V paths (J_2) where J_2 / J_1 ~ 0.8. The alternation of these interactions seems to survive in the HP phase as marked in Fig. 1 (b) with solid (J_1) and dashed (J_2) lines. Note that the HP phase has only one V^{4+} site while the AP phase with multiple sites. Therefore, the HP phase comprises a unique kind of chain, in contrast with the ambient pressure phase containing two crystallographically different chains. This high pressure (HP) phase seems to be a good example of spin-1/2 Heisenberg AF chain with a weak alternation (J_2 / J_1 ~ 1).

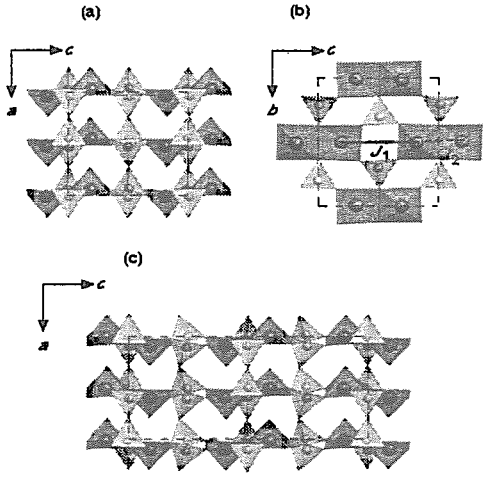

Figure 1 Crystal structures of HP $(VO)_2P_2O_7$ illustrated along the a-axis (a) and the b-axis (b). The large and small spheres represent V and P ions, respectively. Crystal structure of the AP phase along the b axis is also shown for comparison (c)

The inelastic neutron scattering data were collected on the TOPAN triple axis spectrometer at the JRR3M reactor, Japan Atomic Energy Research Institute to observe the spin gap of this compound directly. Figure 2 shows the scattering from the powder sample of HP-VOPO collected at 1.5 and 40 K. The data were taken with the incident energy of 14.7 meV and collimations 30'-30'-S-30'-30' at fixed Q = 0.83 Å^{-1}. The data at 1.5 K clearly showed a peak at 2.15 meV (25.5 K) in the scattering. The peak vanished in the 40 K data, indicating that this scattering was magnetic in nature and the spin gap size was 25.5 K.

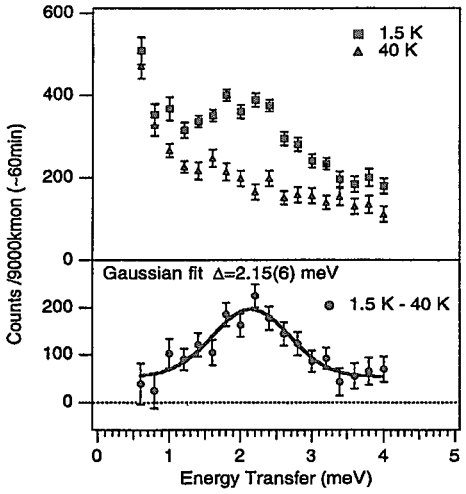

figure 2 Inelastic neutron scattering from HP $(VO)_2P_2O_7$ at Q = 0.83 with the incident ener gy of 14.7 meV. Squares show the data collected at 1.5 K while the triangles corresponds to the data at 40 K.

JRR-3M, TOPAN, 2.Magnetism

研究テーマ: Cr薄膜の磁性
表題 : 非磁性スペーサーを持つエピタキシャルCr/Sn, Cr/Au人工格子のスピン密度波

1-2-43
Spin Density Wave in Epitaxial Cr/Sn and Cr/Au Multilayers with Nonmagnetic Spacer Layers

M. Takeda, K. Mibu[1], K. Takanashi[2], K. Himi[2], Y. Endoh, T. Shinjo[1], and H. Fujimori[2]

Physics Department, Graduate School of Science, Tohoku University, Sendai 980-8578, Japan
[1]Institute for Chemical Research, Kyoto University, Uji 611-0011, Japan
[2]Institute for Material Research, Tohoku University, Katahira Sendai 980-8577, Japan

Chrominium (Cr) in thin films and multilayers exhibits a variety of magnetic properties different to those of bulk Cr.[1] For examples, in bulk Cr, the nesting vector which connects the Fermi surface of electrons with that of holes is responsible for the wave vector of spin density wave (SDW). In Fe/Cr multilayers, however, it has been theoretically noted that the SDW wave vector is not simply determined by the nesting of the Fermi surface but the number of atomic layers of Cr [2] Neutron scattering experiments of Fe/Cr multilayers have been already done by several groups. [3 - 4]

In order to elucidate the influence of ferromagnetic spacer layers on SDW of thin film Cr in multilayer systems, we have investigated [Cr(8.0 nm)/Sn(0.2 nm)] × 30 and [Cr(8.0 nm)/Au(0.2 nm)] × 30 multilayers on MgO substrate by using TOPAN(6G) installed at JAERI in Tokai.

Samples are prepared by ultrahigh-vacuum deposition. Scans are performed along the axis normal to the sample plane (L direction). The incident neutron energy was fixed at 14.7 meV using a PG(002) monochromator and the PG filter before the samples.

Figure 1(a) and 1(b) show L scans of the Cr/Sn multilayer through bcc (001) reciprocal point at 300 K and 20 K, respectively. This figures indicate that the commensurate antiferromagnetic (CAF) phase at 300 K changed into coexistence phase of CAF and SDW at 20 K. From the separation of SDW separation , δ, we fined the SDW period (16 nm) was twice as large as that of the multilayer (8 nm). The period is much longer than that of bulk Cr at the same temperature (6 nm). The antinode of the SDW are probably pinned at the Cr/Sn interfaces, and consequently the SDW whose wave vector is determined not by the nesting vector but by the boundary condition was formed in this multilayer. The coexistence of CAF and the long-period SDW was also observed in the Cr/Au multilayer. Details of the experiments will be appeared in ref 5.

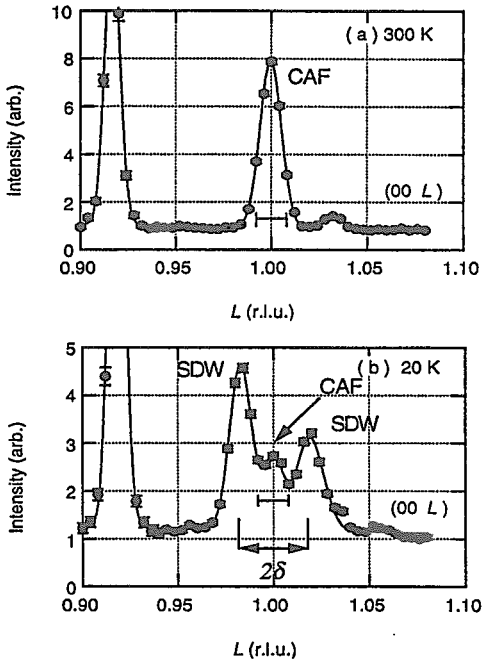

Fig. 1 L scans of [Cr(8.0 nm)/Sn(0.2 nm)] × 30 on a MgO(001) substrate through the (001) positions at (a) 300 K and at (b) 20 K . The horizontal line represents the instrumental resolution.

References

[1] H. Zabel: J. Phys.: Condens. Matter **11** (1999) 9303.
[2] K. Hirai: Phys. Rev. B **59** (1999) R6612.
[3] E. E. Fullerton, S. D. Bader and J. L. Robertson: Phys. Rev. Lett. **77** (1996) 1382.
[4] A. Schreyer, C. F. Majkrzak, Th. Zeidler, T. Schmitte, P. Bödeker, K. Their-Bröhl, A. Abromeit, J. A. Dura and T. Watanabe: Phys. Rev. Lett. **79** (1997) 4914.
[5] M. Takeda, K. Mibu, K. Takanashi, K. Himi, Y. Endoh, T. Shinjo and H. Fujimori: J. Phys. Soc. Jpn **69** (2000) in press

研究テーマ：TOPAN-IMT
表題：NiS_2反強磁性相の磁気励起

1-2-44 Magnetic excitations in antiferromagnetic phase of NiS_2

[1]Masato MATSUURA, [1]Haruhiro HIRAKA, [1]Kazuma HIROTA, [2]Kazuyoshi YAMADA, [3]Yasuo ENDOH

[1]*Department of Physics, Tohoku University, Sendai 980-8578*
[2]*Institute of Chemical Research, Gokasho, Uji, Kyoto 610-0011*
[3]*Institute for Materials Research, Tohoku University, Katahira, Aoba-ku,* Sendai 980-8577

A prototype of the transition metal pyrite, NiS_2 has long been recognized to be a Mott-Hubbard insulator. The magnetic properties, however, are not simply antiferromagnetic (AF), but it is little complicated due mainly to the effect of the face centered cubic (fcc) geometrical frustration. The AF type I long range ordering (LRO) exists below 39.6 K (T_{N1}), and the AF type II LRO appears at 30.6 K (T_{N2}) in first order transition with a small rhombohedral crystal-deformation. A weak ferromagnetism occurs with AF type II LRO, which comes from a cant in spin direction towards [100]. The magnetic ground state showing the simultaneous existence of type I and type II AF long range order (LRO) seemed to be solved by introducing the four spin exchange interactions besides usual two spin interactions.

Here, we report an important feature of spin fluctuations in the intermediate phase of NiS_2, where the Ni magnetic moments have a type I LRO. Our recent magnetic neutron scattering studies revealed the first direct evidence of spin frustration in NiS_2.

Single crystals were grown by chemical vapor transport method using Cl_2 and Br_2 gas. They have (100) and (111) facets as grown state. 9 single crystals with total volume of 0.9 cm^3 were aligned in the (hkk) reciprocal lattice zone using those facets. Neutron scattering measurements were performed on the triple-axis spectrometer TOPAN installed at the JRR-3M Reactor of JAERI.

We investigated the magnetic excitation at 32K, where only AF type I LRO exists. Fig.1 shows the constant-energy scan with $\hbar\omega = 2and10$ meV around AF type I Bragg reflection (011) along [100] direction. At $\hbar\omega = 2$ meV, single peak was observed at $h = 0$ for $0 \leq k \leq 0.25$ with (hkk) and double peaks for $0.25 < k \leq 0.5$. These peaks are situated on the zone boundary of fcc lattice. We confirmed that it comes from magnetic origin by Q-dependence in the intensity of these peaks. Such magnetic excitation has never been observed in any material.

At $\hbar\omega = 10$ meV, the double peak for $0.25 \leq k \leq 0.5$ almost disappears, while it still exists for $0 \leq k < 0.25$. For $k = 0$ and 0.5, the peak position corresponds to the AF type I and II Bragg position; (011) and $(\frac{1}{2}, \frac{3}{2}, \frac{3}{2})$, respectively. The peak at AF type I Bragg position ($k = 0$) was observed up to $\hbar\omega = 16$ meV with no change in the peak width; 0.11 $Å^{-1}$, which reminds the magnetic excitation in itinerant antiferromagnet, Cr and V_2O_3.

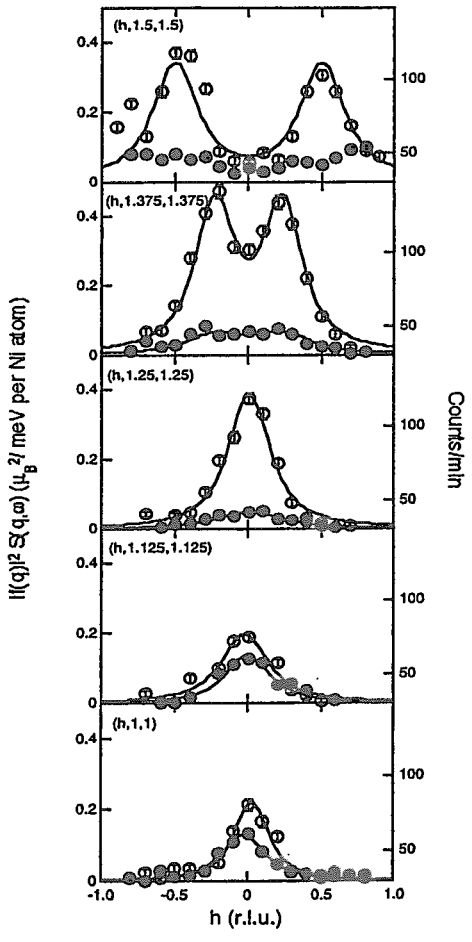

Figure 1: Constant-enrgy scan along [100] direction on NiS_2 at 32 K. Open and closed circle represents the data at $\hbar\omega = 2$ and 10 meV,respectively. The horizontal collimator is B-30'-60'-B with $E_f = 14.7meV$. Absolute units for S(q,ω) were obtained from an intensity of transverse acoustic phonon.

研究テーマ：Yb_4As_3のチャージオーダーと重い電子異常
表題： Yb_4As_3における３次元磁気相関の探査

1-2-45 Search for 3-d magnetic correlation in Yb_4As_3

M. Kohgi,[a] K. Iwasa,[a] T. Takeuchi,[b] N. Aso,[c] A. Ochiai,[d] and H. Aoki[d]

[a]*Tokyo Metropolitan University, Hachioji, Tokyo 192-0397, Japan*
[b] *Osaka University, Toyonaka 560-0043*
[c]*Neutron Scattering Laboratory, ISSP, The University of Tokyo, Tokai, Ibaraki 319-1106, Japan*
[d]*Niigata University, Niigata 950-2181, Japan*

Yb_4As_3 is known with its typical heavy-electron-like anomalies at low temperatures in spite that the compound is semimetallic with extremely low carrier density [1]. On the other hand, our neutron scattering experiments revealed that this material exhibits one-dimensional quantum spin behaviors of Yb^{3+} chains caused by the charge ordering with the exchange interaction value of J= 2.2 meV, and that the "heavy-electron" behaviors in Yb_4As_3 except for the resistivity anomaly originate from the spin excitations of the one-dimensional Yb^{3+} chains [2,3].

However, the material shows no long range magnetic ordering even at very low temperatures down to 45 mK. It is puzzling because existing "one-dimensional" magnetic materials show usually three-dimensional (3-d) long range ordering at a certain temperature due to inter-chain interaction. On the other hand, the material shows unusual enhancement of specific heat below about 0.5 K which is superimposed on the large T-linear term and suppressed (together with the T-linear term) by applying a magnetic field [4]. So, there is some possibility of appearance of 3-d magnetic short range ordering around that temperature. In order to check this point, neutron scattering experiment on Yb_4As_3 were performed at very low temperatures.

The experiment was carried out on the 6G spectrometer using a single crystal sample of about 2 g. The crystal, which was sandwiched by a couple of copper plates to get a single domain sample below the charge ordering temperature, was set inside a cryostat with dilution-refrigerator. The incident neutron energy of E_i = 13.7 meV was used in the experiment.

We have done elastic scattering scans along the principal axes ([100], [011], [111]) and along the ridge of one-dimensional wavevector q = 1 (by the unit of π/d, where d is the atomic distance in the Yb^{3+} chain) around (200) reciprocal lattice point at T = 0.1 K with and without magnetic field (H = 4 T). Constant-E scans with $\hbar\omega$ = 2 meV along the q = 1 ridge and constant-Q scans at q = 1, 0.7, and 0.4 at T = 1.3 and 0.1 K were also done. However, no evidence for the appearance of magnetic short range order nor visible change of the spectra was observed even at 0.1 K in these scans. Considering the fact of the imperfection of the charge ordering [2], a possible scenario for the present result may be that the effective inter-chain interaction in this material is weakened due to existence of some randomness of inter-chain interaction giving no long range ordering. However, more study is necessary to get a definite conclusion.

References

[1] A. Ochiai et al., Phys. Soc. Jpn. 59 (1990) 4129.
[2] M. Kohgi et al., Physica B 230-232 (1997) 638; K. Iwasa et al., Physica B 281-282 (2000) 460.
[3] M. Kohgi et al., Phys. Rev. B 56 (1997) R11388; M. Kohgi et al., Physica B 259-261(1999)269.
[4] R. Helfrich et al., J. Magn. Magn. Mater., 177-181 (1998) 309.

研究テーマ：金属間化合物 R_7Rh_3(R=Nd, Tb, Ho)の磁気構造
表題：Tb_7Rh_3の中性子回折

1-2-46 Neutron Diffraction Studies on Tb_7Rh_3

T. Tsutaoka, M. Nagao, T. Tokunaga, T. Kosugi[1], S. Kawano[2], Y. Andoh[3],
G. Nakamoto[4] and M. Kurisu[4]

Faculty of School Education, Hiroshima University, Higashi-Hiroshima 739-8524, Japan
[1]Graduate School of Human and Environmental Studies , Kyoto University, Sakyo-Ku, Kyoto 606-8501, Japan
[2]Reearch Reactor Institute, Kyoto University, Kumatori, Osaka 590-0494, Japan
[3]Faculty of Education and Regional Sciences, Tottori University, Tottori 680-8551, Japan
[4]Japan Advanced Institute of Science and Technology, Ishikawa 923-1292, Japan

The rare earth intermetallic compound Tb_7Rh_3 crystallizes in the hexagonal ($P6_3mc$) Th_7Fe_3 type structure. From precise magnetic measurements, it was found that there are three magnetic phase transitions, paramagnetic (P.M.) to antiferromagnetic (A.F.) at T_N = 91 K, the A.F. to ferrimagnetic (Ferri.) at T_C = 73 K and Ferri. to another A.F. phase at T_t = 27 K [1]. We have made neutron diffraction studies to determine the magnetic structure of Tb_7Rh_3.

Samples were prepared by arc melting of constituent elements of 99.9 % Tb, and 99.96 % Rh using tri-arc furnace. Neutron diffraction measurements were made by using the HQR spectrometer of JRR-3M of JAERI at Tokai in the temperature range from 1.5 K to 100 K.

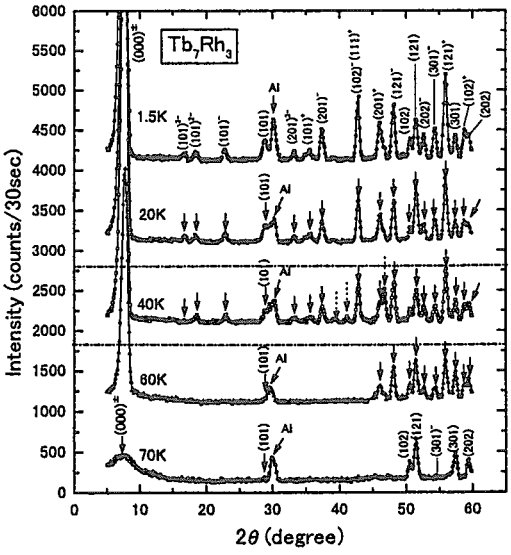

Fig. 1 Neutron diffraction patterns at several temperatures.

Figure 1 shows the neutron diffraction patterns at several temperatures. The strong (000) $^{\pm}$ reflection is observed at 2θ = 7.51° at 1.5K. The magnetization measurements suggest the antiferromagnetic component is in the basal plane below T_t. Thus, we assume that the Tb moment in the basal plane is helically modulated at 1.5 K. The propagation vector of this helical component is determined to be k = (0, 0, 1/3) from the position of the (0 0 0) reflection. Using this helical model, we have indexed the magnetic reflections, as shown in Fig. 1 and summarized them in Table 1. The other peaks can be assigned to nuclear Bragg reflections of the Th_7Fe_3 structure. Lattice constants using this calculation are a = 9.789 Å and c = 6.158 Å, respectively. With increasing temperature, the (0 0 0) reflection peak intensity decreases and vanishes at around T_N. The changes of diffraction pattern can be seen at 40 K, 60 K and 70 K. Thus, it is considered that the magnetic configuration changes in ferrimagnetic phase, in which the basic propagation vector remains. Since Tb_7Rh_3 has three non-equivalent Tb sites, more precise investigation using single crystals are required.

Table 1 Observed and calculated values of 2θ at 1.5

$h\ k\ l$	$2\theta_{obs}$	$2\theta_{calc}$	$diff$
(000)*	7.51	7.63	-0.12
(101)$^{3-}$	16.66	16.69	0.03
(101)$^{2-}$	18.41	18.38	-0.03
(101)$^{-}$	22.78	22.71	-0.06
(101)$^{+}$	35.44	35.31	-0.13
(201)$^{-}$	37.40	37.25	-0.14
(201)$^{+}$	46.09	46.40	0.31
(102)$^{-}$	42.83	42.58	-0.24
(102)$^{+}$	58.87	58.42	-0.44
(121)$^{-}$	48.12	47.97	-0.15
(121)$^{+}$	55.95	55.72	-0.22
(301)$^{-}$	54.33	54.18	-0.16
(202)$^{-}$	52.63	52.42	-0.21
(201)$^{3-}$	33.76	33.20	-0.55

[1] Y. Nakamori et. al., Meeting Abstract of Phys. Soc. Jpn. 54, 1 Part 3 (1999) 386.

研究課題：ＲＰｄＳｎ（Ｒ＝Ｔｂ，Ｄｙ，Ｈｏ，Ｅｒ）化合物の磁性
表題：　ＴｂＰｄＳｎの中性子回折

1-2-47 Neutron Diffraction Studies on TbPdSn

Y. Andoh, M. Kurisu[1], G. Nakamoto[1], T. Tsutaoka[2] and S. Kawano[3]

Department of Environmental Sciences, Tottori University, Tottori 680-8551, Japan
[1]Japan Advanced Institute of Science and Technology, Ishikawa 923-1292, Japan
[2]Faculty of School Education, Hiroshima University, Higashi-Hiroshima 739-8524, Japan
[3]Reearch Reactor Institute, Kyoto University, Kumatori, Osaka 590-0494, Japan

TbPdSn is one of the equiatomic ternary compounds RPdSn which crystallize in the orthorhombic TiNiSi type. Recently, we have presented the detailed magnetic properties of TbPdSn single crystal [1]. TbPdSn is characterized by three successive magnetic transitions (T_N, T_1 and T_2) and the multistep metamagnetic transition along the *b*-axis at 1.8 K [1]. Powder neutron diffraction of TbPdSn by Andre *et. al.* reported that its magnetic structure is a sine-wave-modulated type with propagation vector k=(0,0.25,0) at T_N and with k=(0,0.25,0.075) below 10K. In the present work, we have performed the neutron diffraction study on single crystalline samples. Single crystals of TbPdSn were grown by a Czochralski method. Neutron diffraction measurements were carried out in the b^*-c^* and a^*-c^* reciplacal planes at the $T_{1\text{-}1}$ beam hole of the JRR-3M reactor of JAERI.

Figure 1 shows the neutron reflections in the a^*-c^* reciprocal plane at 1.8K. The strong magnetic reflections appear at the positions

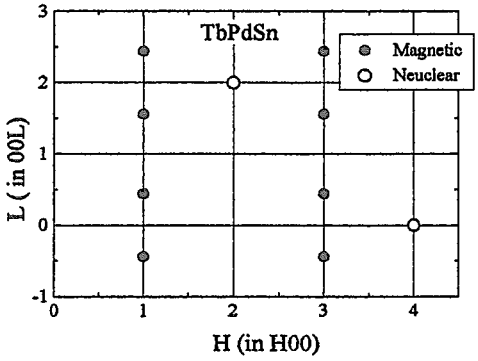

Fig. 1 Neutron reflections in the b*-c* reciprocal plane at 1.8 K.

indexed with the propagation vector k_1=(1,0,0.44). Absence of the higher order satellites has been confirmed in this plane. Figure 2 shows the peak height intensities of the Q_1 =(000)$^+$ as a function of temperature. The z-component changes abruptly from 0.44 to 0.40 at T_1 and the magnetic reflection vanishes at T_N.

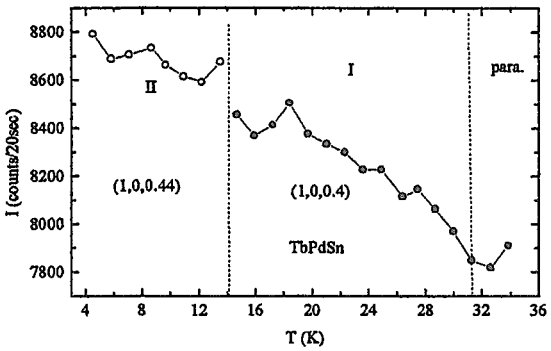

Fig. 2 Temperature variation of the peak height intensities for (1,0,L) reflection.

In the b^*-c^* reciprocal plane, on the other hand, a weak magnetic reflection is observed only at the Q_2=(0,~0.4,1). Figure 3 shows the temperature dependence of the peak intensities of the Q_2. The Q_2 is not corresponding to the higher order reflection of the propagation vector k_1. Therefore, it seems that the TbPdSn has two kind of magnetic reflections with different propagation vectors.

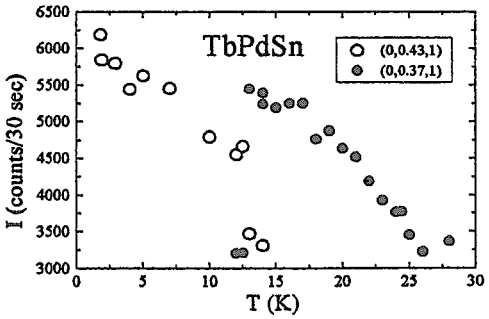

Fig. 3 Temperature variation of the peak integrated intensities for (0,L,1) reflection.

References

[1] Y. Andoh et. al., Meeting Abstract of Phys. Soc. Jpn. 54, 2 Part 3 (1999) 365.
[2] G. Andre et. al., J. Magn. Magn. Mater., 125 (1993) 303.

JRR-3M, HQR(T1-1), 2. magnetism

研究課題：HoNiSn 単結晶の中性子回折
表題：HoNiSn の中性子回折

1-2-48 Neutron Diffraction Study on HoNiSn

M.Kurisu, G.Nakamoto, T.Nobata, T.Ida, T.Tsutaoka[1], Y.Andoh[2], T.Kosugi[3] and S.Kawano[4]

Japan Advanced Institute of Science and Technology, Ishikawa 923-1292, Japan
[1]*Faculty of School Education, Hiroshima University, Higashi-Hiroshima 739-8524, Japan*
[2]*Department of Environmental Sciences, Tottori University, Tottori 680-8551, Japan*
[3]*Graduate School of Human and Environmental Studies, Kyoto University, Kyoto 606-8501, Japan*
[4]*Research Reactor Institute, Kyoto University, Kumatori, 590-0494, Japan*

HoNiSn is one of equiatomic ternary compounds RNiSn of nickel and tin with rare earths which crystallize in the orthorhombic TiNiSi type structure. Powder neutron diffraction by Yakinthos *et. al.* reported that HoNiSn is in antiferromagnetic ordered state at 1.4 K [1]. We have recently studied the magnetic properties of RNiSn ternary compounds with heavy R elements from precise magnetic measurements and neutron diffraction study on single crystalline samples [2-5]. Most recently, we have elucidated that HoNiSn orders antiferromagnetically below T_N = 3.0 K and exhibits a metamagnetic transition along the *b*-axis [4]. A strong magnetic anisotropy observed in magnetization process as well as temperature dependence of susceptibility is ascribed to the effects of crystal field in the compounds. In the present report, we present the neutron diffraction study on HoNiSn single crystalline sample.

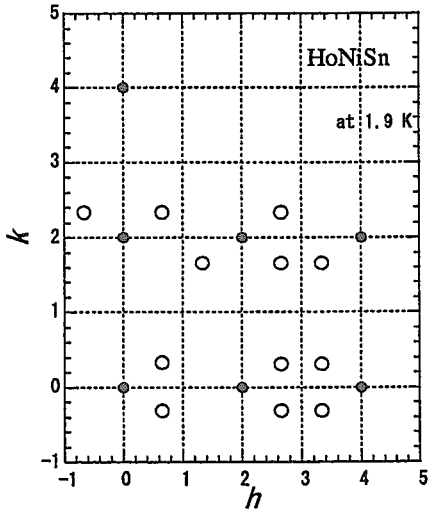

Fig.1 Magnetic reflections at 1.9 K in the *a**-*b** reciprocal plane. The magnetic peaks are indexed with a propagation vector q = (0.661,0.341,0). Open circles for magnetic reflections; closed circles for nuclear reflections.

Single crystals of HoNiSn were grown by a Czochralski method. Neutron diffraction measurements were performed at the T_{1-1} beam hole of the JRR-3M reactor of JAERI.

Figure 1 gives the magnetic Bragg reflections at 1.9 K in the *a**-*b** reciprocal plane. It is derived that magnetic Bragg reflections are indexed by ($h\pm\tau_1$, $k\pm\tau_2$ 0) with τ_1= 0.661 and τ_2=0.341 for $h+k$ = even in the *a**-*b** reciprocal plane. Absence of the higher order satellites has been confirmed. No magnetic reflections are observed in *a**-*c** plane. It should be noted that the components of the wave vector to represent the magnetic modulation in HoNiSn is almost the same as that of DyNiSn in which the structure is of a square incommensurate type [5]. The magnetic structure of HoNiSn should be a sine-modulated amplitude one.

Figure 2 shows the temperature dependence of the magnetic (0.661,0.341,0) peak height intensities. T_N is estimated at 3.0 K.

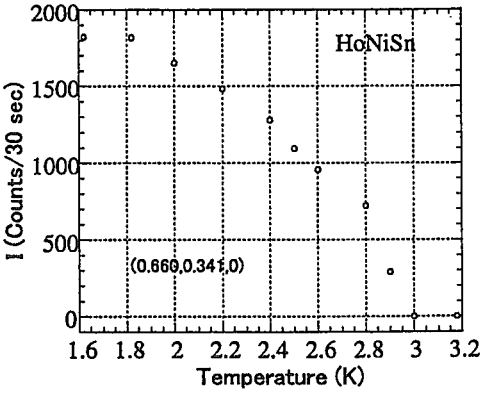

Fig.2 Temperature dependence of the magnetic (0.661,0.341,0) peak height intensities.

References

[1] J.K.Yakinthos *et. al.*, J. Magn. Magn. Mater. **136** (1992) 65.
[2] M.Kurisu *et al.*, Physica B **201** (1994) 107.
[3] Y.Andoh *et al.*, Physica B **237-238** (1997) 575.
[4] Y.Andoh *et al.*, J. Magn. Magn. Mater. **177-181** (1998) 1063.
[5] S.Kawano *et al.*, J. Phys. Chem. Solids. **60** (1999) 1205.

研究課題：2 次元スピン格子 $Mn(HCOO)_2 \cdot 2(NH_2)_2CO$ の磁気構造と磁気転移　　表題：蟻酸 Mn2 尿素塩の中性子回折

1-2-49

Neutron Diffraction Studies of Magnetic Structures on Mn Formate Di-Urea Single Crystal

T. Kosugi[1], S. Kawano[2] and K. Yamagata[3]

[1]*Graduate School of Human and Environmental Studies, Kyoto University, Kyoto 606-8501, Japan*
[2]*Research Reactor Institute, Kyoto University, Osaka 590-0494, Japan*
[3]*College of Science and Engineering, Iwaki Meisei University, Iwaki 970-8044, Japan*

Manganese formate di-urea, $Mn(HCOO)_2 \cdot 2(NH_2)_2CO$, is a compound belonging to tetragonal $P4_12_12$ symmetry and the magnetic Mn ions form a two dimensional layer network. Magnetization measurements of this material show antiferromagnetic order below a Neel temperature of T_N = 3.8 K. Recently, Kubo *et al.* have reported from proton NMR measurements that the Mn moments within a layer point to the direction rotating 15° around the c-axis from the middle direction between the [001] and [-100] directions [1]. The details of the spin arrangement are still unclear. To determine the magnetic structure we have carried out neutron diffraction measurements of the partially-deuterated manganese formate di-urea $Mn(HCOO)_2 \cdot 2(ND_2)_2CO$ single crystal.

Neutron diffraction measurements were performed in the temperature range from 1.5 K to 7.0 K using the HQR installed at the $T_{1\text{-}1}$ beam hole of JRR-3M in JAERI (Tokai). The data were collected for the (*hhl*) and (*h*0*l*) type reflections.

Figure 1 gives neutron diffraction patterns scanning around (11*l*) and (22*l*) along the *c**-directions at 1.5 K and 7.0 K, well above T_N. In the case of h = 1, the magnetic reflections are observed in every l position. On the other hand, there is no magnetic reflection in the case of h = 2. Similarly to the cases above mentioned, there exist no magnetic reflections for l = 0, while magnetic reflections are found for l = 3. Thus, magnetic reflections appear only for h =odd in the (*hhl*) plane. The nuclear reflections from the Mn ions position appear only where h is an even number for the (*hhl*) type reflections. This indicates that the magnetic reflections on the (11*l*) line are attributable to the Mn moments positioned on the (00*l*) and (22*l*) line, and then the magnetic scattering vector can be expressed as $\boldsymbol{k}$ = (110). As for the (*h*0*l*) type reflections, no magnetic reflection has been observed. The results obtained in this experiment are consistent with a possible spin arrangement proposed by Kubo *et al.*.

References

[1] H. Kubo *et al.*, J. Phys. Soc. Jpn. **68** (1999) 263.

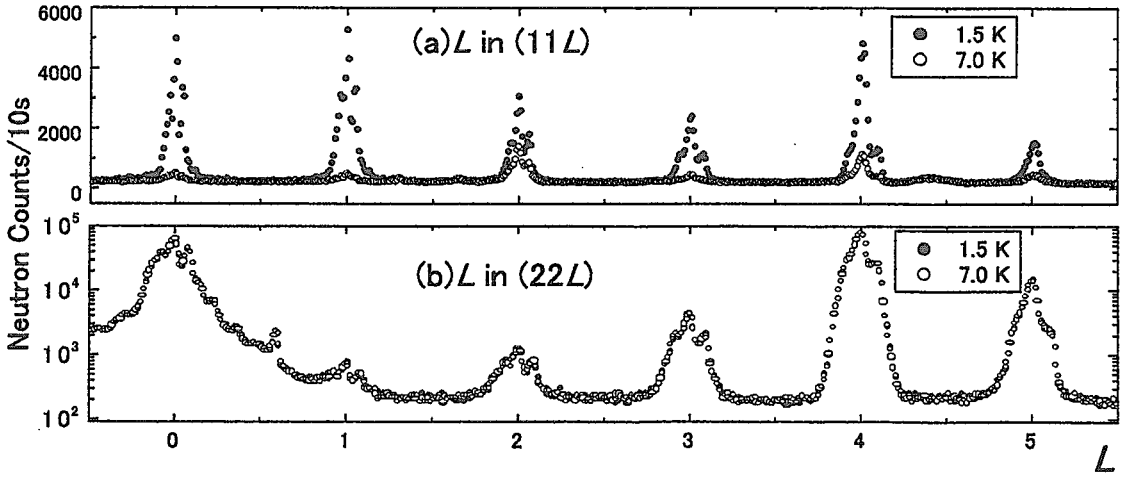

Fig. 1. Neutron diffraction patterns scanning along the (1,1,*l*) and the (2,2,*l*) directions at 1.5 K and 7.0 K.

Reactor: JRR-3M　　Facilities: HQR($T_{1\text{-}1}$)　　Research Field: Magnetism

研究テーマ：Ca3Co2O6 の低温および低磁場の磁気構造
表題：中性子回折による Ca3Co2O6 の磁気構造

1-2-50 Neutron Diffraction Study of Magnetic Structure in $Ca_3Co_2O_6$

S. Niitaka, K. Yoshimura, S. Kawano[1], H. Kageyama[2], N. Aso[3] and K. Nakajima[3]

Department of Chemistry, Graduate School of Science, Kyoto University, Kyoto 606-8502, Japan
[1]Research Reactor Institute, Kyoto University, Kumatori, Sennan, Osaka 590-0494, Japan
[2]Institute for Solid State Physics, University of Tokyo, Kashiwanoha, Kashiwa, Chiba 277-8581, Japan
[3]Neutron Scattering Laboratory, Institute for Solid State Physics, University of Tokyo, Shirakata, Tokai 319-1195, Japan

$Ca_3Co_2O_6$ with the rombohedaral K_4CdCl_6-type structure contains the 1-D chains consisting of alternating faced-sharing CoO_6 trigonal prisms and CoO_6 octahedra. These chains form a triangular lattice in c-plane. $Ca_3Co_2O_6$ exhibits a ferrimagnetic ordering of the ferromagnetic chains below 25K, which has been confirmed by a 1/3 plateau in the magnetization curves and also by neutron diffraction peaks. However in the magnetization curves below 5K, three plateaus accompanied with the large hysteresis were observed, suggesting the presence of other magnetic structures at lower temperature. Since the previous neutron diffraction measurement was carried out only above 10K, the magnetic structure below 5K is not clear. In order to clarify the magnetic structure of $Ca_3Co_2O_6$ at lower temperature, we performed the neutron diffraction experiments at 2.5K using a powdered sample of $Ca_3Co_2O_6$. We also measured at 4K the neutron diffraction pattern of Ca_3CoRhO_6 which has the same structure as $Ca_3Co_2O_6$.

The neutron diffraction experiments were carried out using the HQR diffractometer (T1-1) installed at JRR-3M Guide Hall in JAERI (Tokai).

Figure 1 shows the powder neutron diffraction patterns of $Ca_3Co_2O_6$ at 2.5K and 100K and of Ca_3CoRhO_6 at 4K. With regard to $Ca_3Co_2O_6$, four additional magnetic Bragg reflections were observed at 2.5K. The Miller indices of these magnetic reflection peaks are (100), (200), (112), and (210). The observed magnetic peaks at 2.5K are the same as those at 10K, indicating that the ferrimagnetic ordering still occurs at 2.5K. The magnetic structure of $Ca_3Co_2O_6$ at 2.5K has become clear, although the origin of the multisteps remains an open question. The magnetic Bragg reflections in the powder neutron diffraction patterns of Ca_3CoRhO_6 at 4K are same as that of $Ca_3Co_2O_6$ at 2.5K, suggesting that Ca_3CoRhO_6 is ferrimagnetically ordered at 4K.

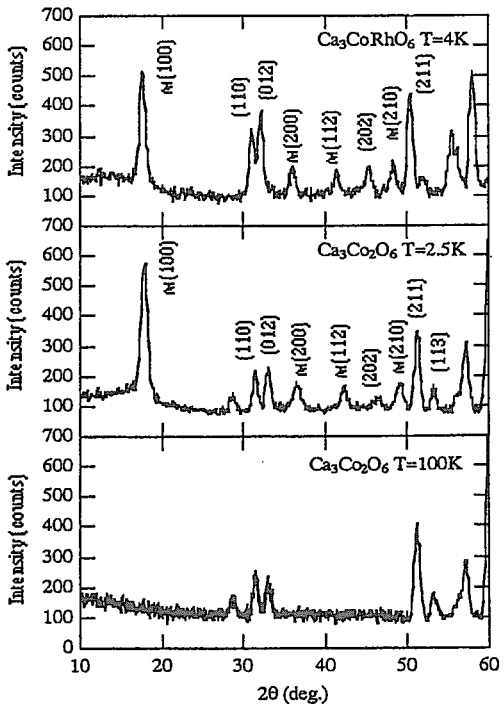

Fig.1 Neutron powder diffraction patterns of $Ca_3Co_2O_6$ at 2.5K and 100K and of Ca_3CoRhO_6 at 4K. The peak at 28.7° corresponds to the sample holder.

研究テーマ：高圧力による合金の秩序変数の制御
表題：高圧下における α-Mn の磁気構造

1-2-51 Magnetic Structure of α-Mn at High Pressure

A. Onodera, Y. Tsunoda[1], and Y. Nakai[2]

School of Engineering Science, Osaka University, Toyonaka, Osaka 560-8531, Japan
(Now at University of Marketing and Distribution Sciences, Nishi, Kobe 651-2188, Japan)
[1]School of Science and Engineering, Waseda University, Shinjuku, Tokyo 169-8555, Japan
[2]Shizuoka Intitute of Science and Technology, Fukuroi, Shizuoka 437-0032, Japan

Among the four polymorphic forms of Mn, α-form is the most stable at ambient conditions. It has 58 atoms that are nonequivaent with four different coordination numbers in the unit cell. Neutron scattering experiments have shown that, in the antiferromagnetic phase appearing below T_N=95 K, the atoms at different sites have different magnetic moments. Likewise, it is expected that such atoms can behave in different manners under high pressure. The present study was undertaken to see the presence or absence of this expected difference by measuring the neutron magnetic scattering peaks of α-Mn at high static pressure.

An ingot of polycrystalline α-Mn was enclosed in a micro capsule made of an Al-alloy, together with a pressure-transmitting medium, Fluorinert. A single crystal of NaCl as a pressure marker was placed next to the α-Mn sample. The micro capsule was pressurized within a supported-cylinder type high-pressure cell. The cylinder was made of sapphire, instead of sintered alumina in the standard design. After pressure was generated at room temperature, the cell was cooled to 3.5 K at which neutron scattering measuremet was carried out at $T_{1\text{-}1}$ of JRR-3M.

Figure 1 shows neutron scattering pattern of α-Mn at high pressure and low temperature. No appreciable change was observed in the relative intensities of magnetic peaks of α-Mn in Fig. 1 from those at ambient pressure (not shown). It should, however, be noted that the intensity of (422) nuclear peak increases upon application of pressure relative to that of (322) peak.

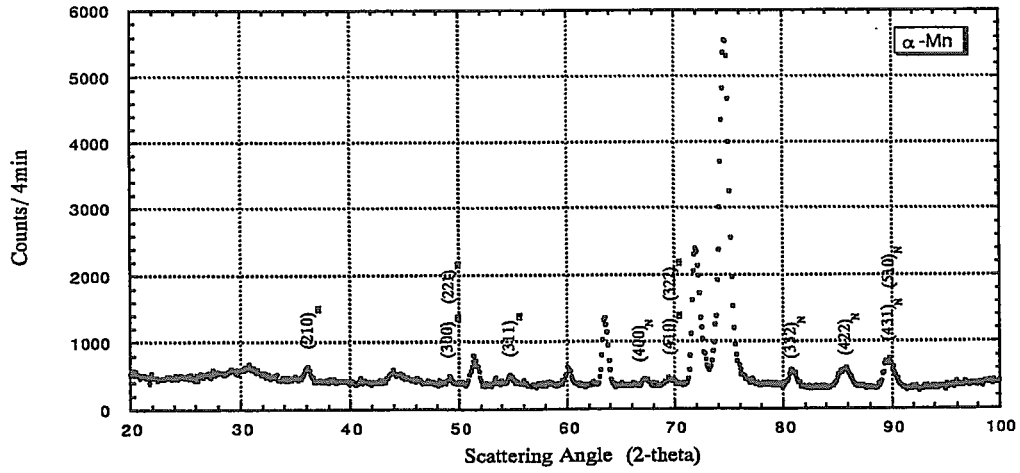

Figure 1 Neutron scattering pattern of α-Mn at high pressure and low temperature. Suffices m and N denote magnetic and nuclear peaks, respectively.

JRR-3M, T1-1, 2. Magnetism

研究テーマ：磁気不安定点近傍の反強磁性体 $Ce(Ni_{1-x}Pd_x)_2Ge_2$ の磁気構造
表題：磁気不安定点近傍の反強磁性体 $Ce(Ni_{1-x}Pd_x)_2Ge_2$ の不整合磁気構造

1-2-52 Incommensurate Magnetic Structure of the Antiferromagnet Proximate to Magnetic Instability; $Ce(Ni_{0.65}Pd_{0.35})_2Ge_2$

T. Fukuhara, K. Maezawa and H. Kadowaki[1]

Department of Liberal Arts and Science, Toyama Prefectural University, Kosugi, Toyama, 939-0398 Japan
[1]Department of Physics, Tokyo Metropolitan University, Hachioji-shi, Tokyo 192-0397 Japan

Magnetic and crystal structures of $Ce(Ni_{1-x}Pd_x)_2Ge_2$ proximate to magnetic instability were studied by elastic neutron scattering experiments.

A single crystal of $Ce(Ni_{0.65}Pd_{0.35})_2Ge_2$ was grown by pulling up method by a tetra-arc furnace. An ingot of polycrystalline $Ce(Ni_{0.77}Pd_{0.23})_2Ge_2$ was prepared by arc melting, and homogenized by annealing in purified Ar atmosphere at around 1200°C for 6 hours. The ingot was crushed into small pellets for powder-neutron-diffraction experiments. Concentration of Pd in the samples was determined by the energy dependence x-ray (EDX) analysis. The Néel temperature (T_N) of these samples was determined beforehand by magnetic and thermal measurements as T_N~3.5K and T_N~2.2K for single crystal and polycrystal samples, respectively. Neutron diffraction experiments were performed using the triple-axis spectrometer T11-HQR installed at JRR-3M JAERI (Tokai). Neutron energy was fixed at 13.6meV.

The powder diffraction pattern was measured at 2K. Since this tempeture is just below T_N, we did not observed any magnetic peak within experimenal error. The powder pattern consists of nuclear reflections was analyzed by the Rietveld method using RIETAN-97, and was well fitted based on the $ThCr_2Si_2$-structure (I4/mmm) with the atomic positions of Ce in 2a : (0,0,0), Ni/Pd in 4d : (0,1/2,1/4) and Ge in 4e : (0,0, 0.370).

Fig.1 indicates the temperature dependence of the magnetic peak around Q= (0.5,0.5,0.84) measured on the single-crystal sample. The magnetic peak disappears at 3.5K. The integrated intensity of 18 magnetic reflections in (kkl) the scattering plane were measured by the θ-2θ scan at T=1.8K. Those magnetic reflections are consistent with $\mathbf{Q}=\boldsymbol{\tau}\pm\mathbf{q}$ with an ordering vector $\mathbf{q}$~(0.5,0.5,0.16) where $\boldsymbol{\tau}$ is a reciprocal lattice vector. We could not detect a third-order harmonic at 1.8K, suggesting sine-wave-modulated structures. Detailed analysis of the magnetic structure is in progress.

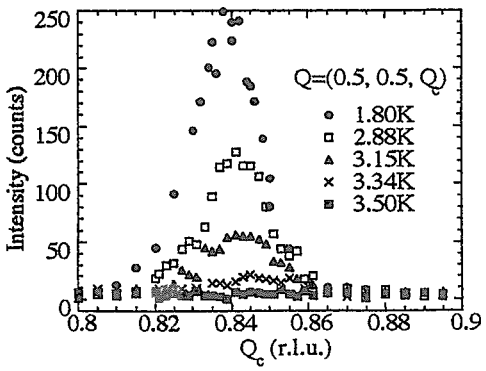

Fig.1 Q-scans at various temperatures. The ordering vector **q** changes slightly with increasing temperature.

JRR-3M, T1-1-HQR, 2. Magnetism

研究テーマ：La_2CoO_4のスピンダイナミクスとそのホールドープの効果の研究
表題：酸素ドープした$La_2CoO_{4.24}$の磁気構造の変調

1-2-53 Modulated Magnetic Structure in Oxygen Doped $La_2CoO_{4.24}$

K. Nakajima, T. Sawada, K. Kakurai, Y. Endoh[1]
Neutron Scattering Laboratory, Institute for Solid State Physics, University of Tokyo,
106-1 Shirakata, Tokai, Naka, Ibaraki 319-1106 Japan
[1] Institute for Materials Research, Tohoku University,
Katahira, Aoba-ku, Sendai 980-8577, Japan

Charge ordering is widely observed in layered transition metal oxides, La_2MO_4 (M: 3d metal). In La_2NiO_4, induced holes develop long range ordering in a stripe fashion in the NiO_2 plane and a hole stripe changes the in-plane magnetic correlation from commensurate to incommensurate [1]. The hole stripe has been found also in $La_{1.48}Nd_{0.4}Sr_{0.12}CuO_4$ [2], which has stimulated controversial arguments on the origin of incommensurate magnetic fluctuations and the mechanism of the superconductivity observed in cuprates. Soon after the finding a stripe in cuprates and nickelate, charge ordering and related modulated magnetic structure have been reported in $La_{0.5}Sr_{1.5}MnO_4$ [3]. Since it seems rather common properties in La_2MO_4, charge ordering and modulated magnetic structure caused by charge ordering are expected also in La_2CoO_4. Actually, the magnetization and electrical resistively measurements on $La_{2-x}Sr_xCoO_4$ suggest that charge ordering occurs at x=0.5 [4], which should be examined by neutron scattering experiments.

We have prepared the single crystal of $La_2CoO_{4+\delta}$ (0.5 cm^3). We loaded the excessive oxygen by heat-treatment in O_2 gas flow and resulted δ was determined to be 0.24 by the weight loss measurement in H_2 gas flow using TG-DTA. The value of δ is almost 0.25, which corresponds to x=0.5 of $La_{2-x}Sr_xCoO_4$ in the

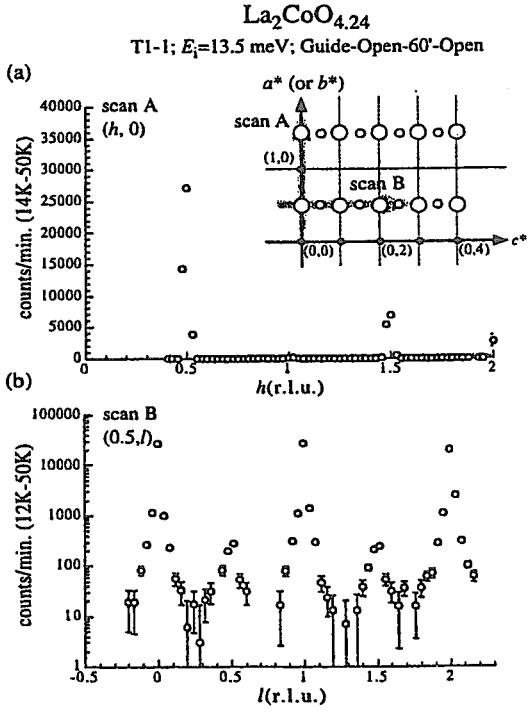

FIG 1. Neutron diffraction spectra at low tempearture. Scans were performed along a) (h, 0) and b) (0.5, l). Background was subtracted using 50 K data in the plots.

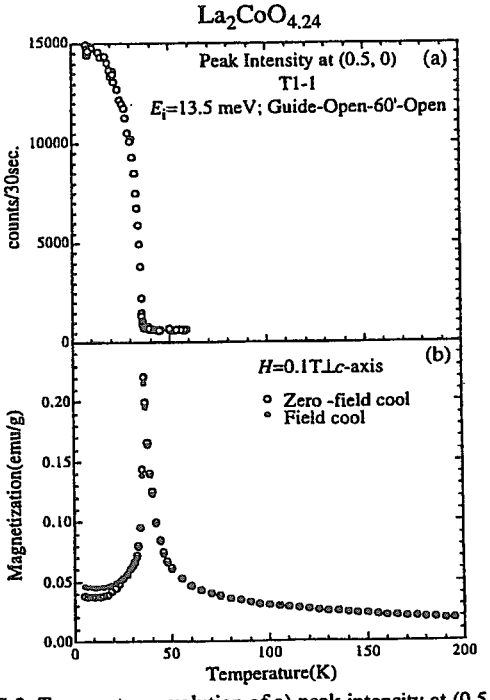

FIG 2. Temperature evolution of a) peak intensity at (0.5, 0) and b) magnetization with magnetic field palarell to the CoO_2 plane.

JRR-3M, HQR(T1-1), 2.Magnetism

amount of introduced holes. Neutron scattering experiment was carried out on HQR (T1-1). The crystal was set into a ^{4}He closed cycle refrigerator so as a^* (or b^* due to the twining of the crystal) -c^* plane to be in the scattering plane.

In Fig. 1, typical results of elastic scans are shown. Below 36 K, we observed superlattice reflections at (h±0.5, l±0.5) (h, l: integer). It should be noted that because of crystal twinning, we can not distinguish scattering from a^*-c^* ((h, 0, l)) plane from that from b^*-c^*((0, k, l)) plane. Since a sharp anomaly is observed in the magnetization measurement at 36 K (Fig. 2), we conclude these peaks are magnetic origin. In pure La_2CoO_4, magnetic Bragg reflections are observed at (h, l) (h: odd, l: integer). Therefore, the magnetic unit cell is enlarged double in a^* (or b^*) and c^* direction in $La_2CoO_{4.24}$. It is considered that induced holes are localized at Co sites. [4] In $La_2CoO_{4.24}$, half of Co^{2+} spins become Co^{3+} spins. One of possible magnetic structure is shown in Fig. 3. (At this moment, we do not determine which site corresponds to Co^{2+} or Co^{3+} spin.) To determine the unique magnetic structure of $La_2CoO_{4.25}$, further experiments are required.

[1] J. M. Tranquada *et al.*: Phys. Rev. Lett. 73 (1994) 1003
[2] J. M. Tranquada *et al.*: Nature 375 (1995) 561
[3] B. J. Sternlieb *et al.*: Phys. Rev. Lett. 76 (1996) 2169
[4] Y. Moritomo *et al.*: Phys. Rev. B 55 (1997) R14725

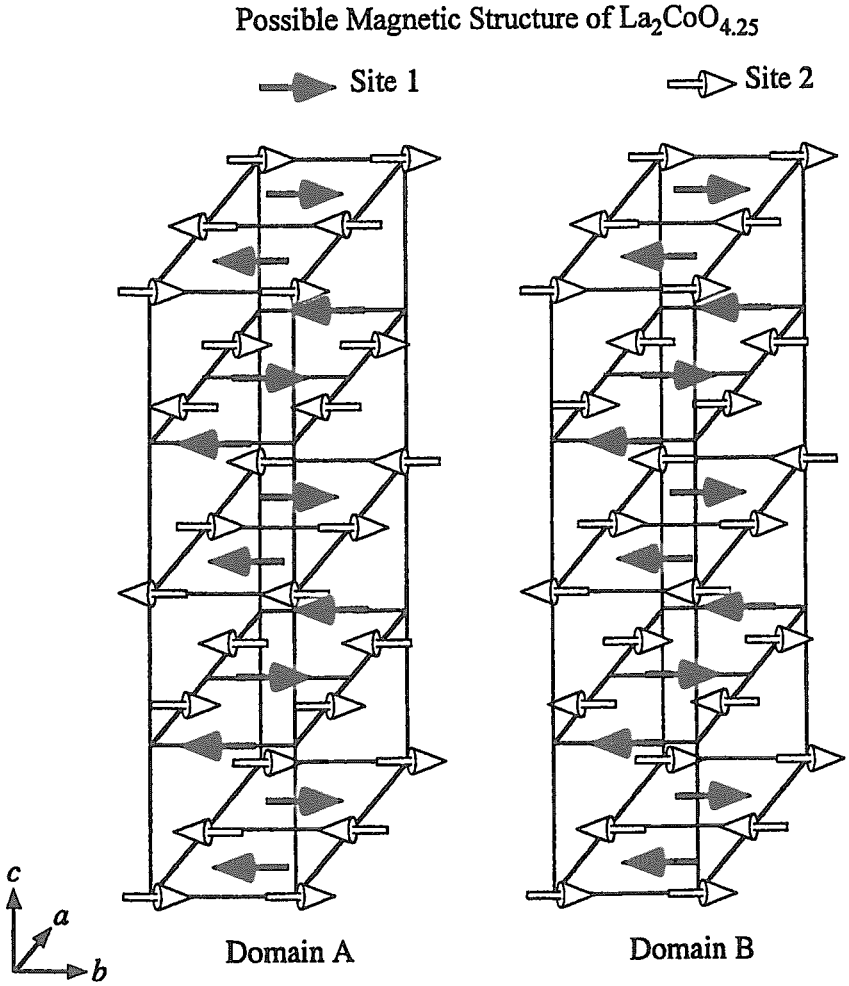

FIG 3. Possible magnetic structure in $La_2CoO_{4.25}$.

研究テーマ：磁気競合系における磁気的秩序化過程
表題：フラストレーションをもつZnV_2O_4の磁気秩序

1-2-54

MAGNETIC ORDERING IN A FRUSTRATED ANTIFERROMAGNET ZnV_2O_4

M. Mekata, T. Ishida, Y. Yamada, T. Fujii, and H. Kikuchi

Department of Applied Physics, Fukui University, Bunkyo, Fukui, 910-8507 Japan

The magnetic ions at the octahedral B sites of the spinel structure form a corner-sharing tetrahedral lattice which is known to have strong frustration if the predominant nearest neighbor interaction is antiferromagnetic. ZnV_2O_4 is one of the normal spinel with magnetic B sites occupied by V^{3+} ions. In spite of the large negative value of Weiss temperature -990K, ZnV_2O_4 shows no indication of ordering down to 80K due to the spin frustration [1]. Below 80K a field cooling effect is observed in magnetic susceptibility. Low temperature X-ray diffraction revealed that a tetragonal distortion occurs at T_t=50K.

The magnetic susceptibility measured in a field of 3mT shows a distinct effect of field cooling in 3mT below T_f=80K although the magnetization curve at 4.2K is linear to the applied field up to 1T without appreciable remanent magnetization. The Weiss temperature and effective Bohr magneton evaluated from the inverse magnetic susceptibility above 100K amount to -1121K and 3.5μ_B, respectively, in agreement with the reported values. An anomaly in the magnetic susceptibility may be attributed to the lattice distortion at T_t=50K.

The width of ESR line increases gradually with decreasing temperature below 80K without g-shift.

Powder neutron diffraction was measured with the T1-1 spectrometer installed at JRR3A of JAERI Tokai. Magnetic Bragg reflections are observed at (110) and (210). This result can be interpreted in terms of a tetragonal collinear spin arrangement with alternative ferromagnetic *c*-planes in accordance with the lattice symmetry. The magnetic moment of 2.5μ_B was deduced from the magnetic structure. The temperature dependence of the peak intensity of (1 1 0) shown in Fig. 1 indicates that the long range ordering occurs at T_N=40K which is lower than T_f or T_t.

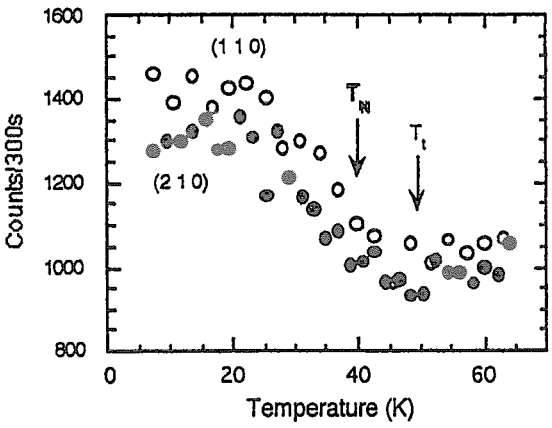

Fig.1 Tempertature dependence of peak intensity of magnetic reflection of ZnV_2O_4.

The observed field cooling effect implies that spins are frozen into short range ordered state below 80K. It should be noted that the long range ordering occurs at a lower temperature than the lattice distortion due to the spin frustration and that the field cooling effect persists even in the long range ordered state. This implies the coexistence of the long range order and the short range order inherent of strong spin frustration.

In conclusion we have determined the magnetic structure in highly frustrated ZnV_2O_4 and the long range ordering temperature to be 40K by powder neutron diffraction.

Reference

[1] Y. Ueda, N. Fujiwara and H. Yasuoka: J. Phys. Soc. Jpn. 66, 778 (1997).

研究テーマ：合金の遮蔽効果とフェルミ面
表題：Mn_3PTのスピン相関（高温相）

1-2-55 Spin Correlation in Mn3Pt (High Temperature phase)

Takashi Ikeda and Yorihiko Tsunoda

School of science and engineering, Waseda University,
Okubo3-4-1,Shinjuku-ku,Tokyo169-8555,Japan.

The ordered alloy Mn_3Pt is an antiferromagnet but shows a first order AF-AF transition at T_{SF}=400K below Néel temperature (T_N=475K) .The magnetic structure is triangular (D-phase) below T_{SF} and collinear (F-phase) above T_{SF}. At T_{SF}, the crystal structure transforms from cubic to tetragonal and the unit cell volume changes at the same temperature. The similar alloys ,Mn_3Ir and Mn_3Rh, do not have the collinear structure below T_N. It is considered that one third of Mn atoms has no moment in the F phase.

At first we assumed that the one third of Mn atoms is paramagnetic. To check this point, the experiments were performed using powder specimen to investigate the behavior of spins in the F phase at T1-1 triple axis spectrometer installed at thermal guide, JRR-3M , JAERI, Tokai. Diffuse scattering around the Bragg peaks at 100 and 11/20 was observed in the measurement of off Bragg setting of the analyzer (Fig.1).

Thus, we started inelastic neutron scattering measurements by means of single crystal sample. Then, diffuse scattering with low excitation energies was observed along the line from 100 to 110.

Intensity contour map of inelastic diffuse scattering studied at low excitation energy (3meV) on the 001 scattering plane in the temperature between T_{SF} and T_N is given in Fig.2. The inelastic scattering intensities were distributed along the direction of <010>.

From these experimental data, we can propose following models for the spins in the F-phase, The Mn spins which is located at the zero molecular field will couple ferromagnetically in the direction of <100>. But this configuration would be inconsistent with the nearest neighbor AF coupling in the direction of <010>. Thus, the Mn spins feel strong frustrations with nearest neighbor spins, although they have rather strong parallel coupling with second neighbor spins.

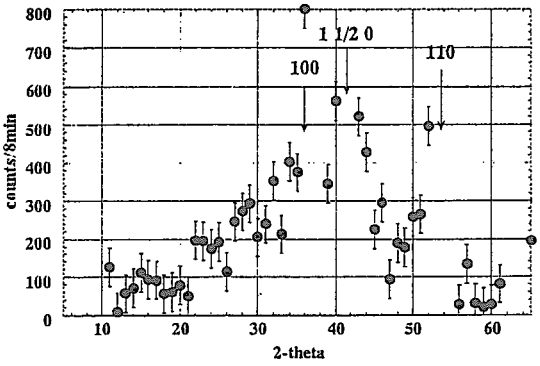

Figure1, Measured with analyzer off-setting in powdersample .Intensity of D-phase was subtracted from that of F-phase.

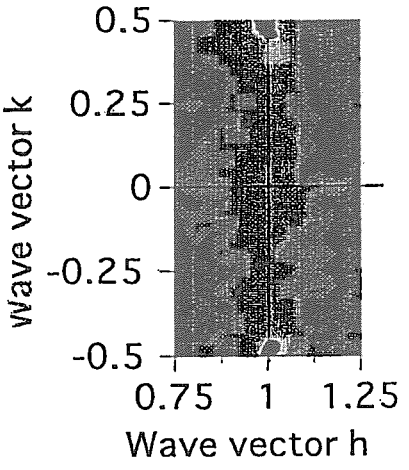

Figure2, Intensity contour Map of inelastic diffuse scattering (T=423K)

JRR-3M, T1-1 2.Magnetism

研究テーマ：フラストレーションのある強相関電子系の磁性
表題：パイロクロア型化合物$Tb_2Ti_2O_7$の磁場下の中性子散乱

1-2-56

Neutron Scattering Study of Pyrochlore Compound $Tb_2Ti_2O_7$ in Magnetic Fields

Y. Yasui[1,2], M. Kanada[1,2], M. Ito[1], H. Harashina[1,2], M. Sato[1,2], H. Okumura[3] and K. Kakurai[2,3],

[1]*Department of Physics, Division of Material Science, Nagoya University, Furo-cho, Chikusa-ku, Nagoya 464-8602*

[2]*CREST, Japan Science and Technology Corporation (JST)*

[3]*Neutron Scattering Laboratory, ISSP, The University of Tokyo, Shirakata 106-1, Tokai, Ibaraki 319-1195*

Pyrochlore compound $Tb_2Ti_2O_7$ consists of two kinds of three-dimensional networks individually formed of corner-sharing tetrahedra of Tb^{3+} or Ti^{4+}. Because the lattice is not bipartite, the magnetic moments of Tb^{3+} ions with the antiferromagnetic (AF) nearest neighbor interaction are expected to be geometrically frustrated and to have strong magnetic fluctuation. Actually it has been reported that magnetic ordering has not been found down to 70 mK, even though the Weiss temperature Θ estimated by fitting the magnetic susceptibility is as large as 19 K[1)].

Neutron inelastic scattering studies have been carried out on a single crystal of $Tb_2Ti_2O_7$. Based on the results, the correlation pattern of the observed magnetic excitations has been identified. The dispersion curves and its T-dependence have also been determined.[2,3)] The isotropic (Heisenberg-like) exchange interaction and the single-ion anisotropy energy of the system are presumed to have comparable strength.

It is interesting to study the magnetic properties of this system in the magnetic field, because it is expected that its magnetic ground state is dramatically changed by the external magnetic field H. In the field H along the $[1\bar{1}1]$ direction, which corresponds to the local principal direction of one of four spin sites at the corners of a tetrahedron (we label it site A as shown in Fig. 1(a)), the magnetic energy at A is different from those of the remaining three sites. The sites except A form, as shown in Fig. 1(b), the *kagomé*-lattice type network, which is well-known to be geometrically frustrated, too. We have studied what kind of ground state is realized in the magnetic field along the $[1\bar{1}1]$ direction by means of neutron scattering.

T1-1 spectrometer installed at a thermal guide of JRR-3M at JAERI in Tokai was used in the present work, where the measurements were carried out in the field H //

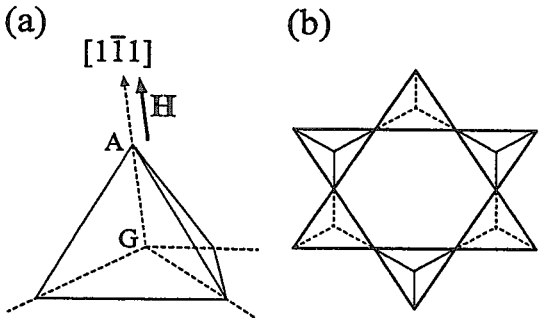

Fig. 1. (a)Direction of the applied magnetic field is shown schematically. G indicates the center of the gravity. (b)Projection of the atom sites onto the $(1\bar{1}1)$ plane.

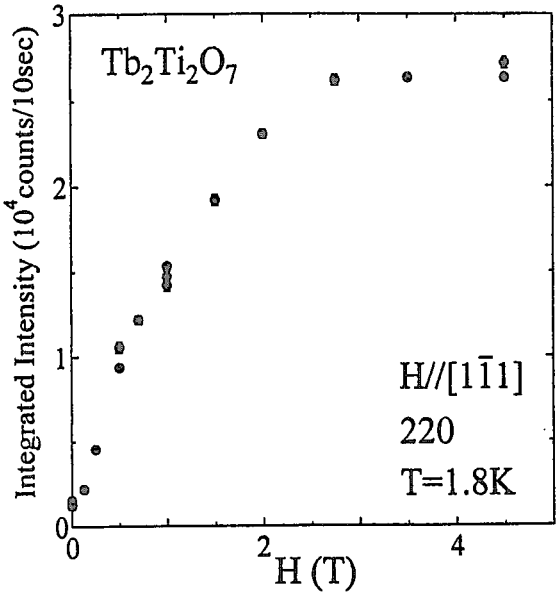

Fig. 2. H-dependence of the integrated intensity of the 220 reflection (H//[1$\bar{1}$1]) taken at T=1.8K.

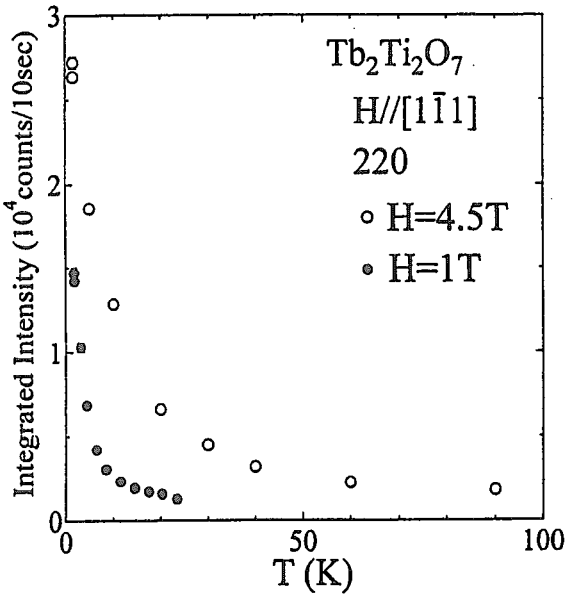

Fig. 3. Temperature dependence of the integrated intensity of the 220 reflection taken at H=1.0 (solid circles) and 4.5 T (open circles).

[1$\bar{1}$1] up to 4.5 T at T=1.8 K. With increasing magnetic field, the neutron scattering intensity measured at the elastic position (E=0) increases at several nuclear Bragg points. As an example, the integrated intensity of 220 reflection taken at 1.8K is shown

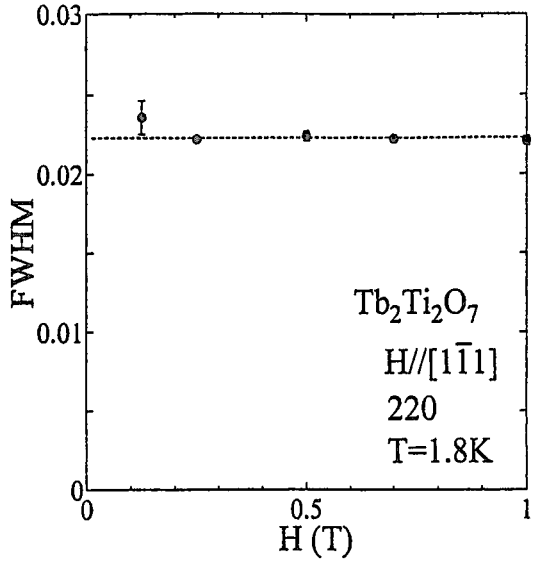

Fig. 4. H-dependence of the profile width of the 220 reflection. The instrumental resolution width is shown by the horizontal dashed line.

in Fig. 2 as a function of H. Its T-dependence taken at H=1.0 and 4.5 T is also shown in Fig. 3. The scattering intensity increases with decreasing T without any anomalous T-dependence. Figure 4 shows the H-dependence of the profile width of the reflection, which is found to be almost equal to the instrumental resolution even for H smaller than 0.2 T, that is, the almost long-range order is induced by applying the relatively small magnetic field. However, we have not obtained an unambiguous ordering pattern yet.

References

1) J. S. Gardner *et al.*, Phys. Rev. Lett. 82 (1999) 1012.

2) M. Kanada *et al.*, J. Phys. Soc. Jpn. 68 (1999) 3802.

3) Y. Yasui *et al.*, J. Phys. Chem. Solids, to be published.

研究テーマ：フラストレーションのある強相関電子系の磁性

表題：磁気フラストレーションを持つパイロクロア化合物 $Tb_2Ti_2O_7$ の中性子散乱

1-2-57

Neutron Scattering Study on Magnetically Frustrated Pyrochlore System $Tb_2Ti_2O_7$

M. Kanada[1], Y. Yasui[1,3], M. Ito[1], H. Harashina[1,3], M. Sato[1,3], H. Okumura[2] and K. Kakurai[2,3]

[1]Department of Physics, Division of Material Science, Nagoya University, Furo-cho, Chikusa-ku, Nagoya 464-8602

[2]Neutron Scattering Laboratory, ISSP, The University of Tokyo, 106-1 Shirakata, Tokai 319-1195

[3]CREST, Japan Science and Technology Corporation (JST)

Pyrochlore compounds $Tb_2Ti_2O_7$ consists of two kinds of 3D-networks, each of which is formed by corner-sharing tetrahedra of Tb_4 or Ti_4. Tb^{3+} ions have antiferromagnetic nearest neighbor interaction and the system is expected to have geometrical frustration. For this system, it has been reported that magnetic ordering is not observed down to 70 mK,[1)] even though the Weiss temperature Θ obtained from the magnetic susceptibility χ is as large as 19 K.

Neutron inelastic measurements on this compound have been carried out with T1-1 spectrometer at JRR-3M of JAERI in Tokai, where the incident energy Ei=12.54 meV and the collimations are open-open-40'-40'. The incoherent resolution width is about 0.7 meV. A typical example of the observed spectra is shown in Fig.1, where beside the peak around the elastic position, the inelastic scattering peak can be observed. Here, we first measured the Q-dependence of the scattering intensity at the energy E=0.8 meV along several directions, and from the results, the correlation pattern of the magnetic excitation has been determined as shown in

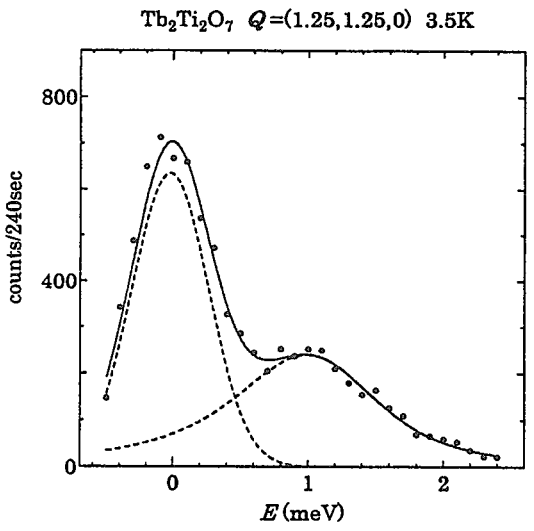

Fig.1 Scattering profiles observed at Q =(1.25,1.25,0) at 3.5K. The broken lines separately show the inelastic contribution and that at around E =0. The latter contains the nuclear incoherent scattering.

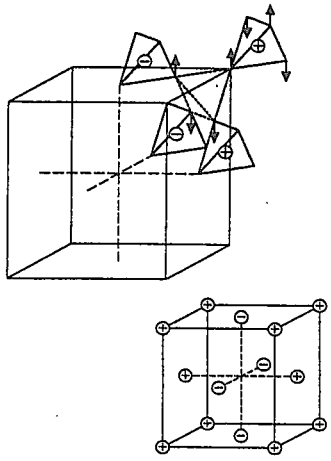

Fig.2 Schematic figure of the correlation pattern of the magnetic excitation. The bottom figure shows its inter-tetrahedra phase correlation.

JRR-3M, HQR, 2. magnetism

Fig.2. The spins within a tetrahedron are aligned antiferromagnetically with a collinear structure and the inter-tetrahedra phase correlation is also shown by the signs.

We express the intensity profile of magnetic excitation by using the damped oscillator-type form of the excitation as

$$I(Q,\omega) \sim \frac{1}{1-e^{-\beta\omega}} \times \chi(Q) \frac{\Gamma_Q \omega}{(\omega^2-\omega_Q^2)^2+\Gamma_Q^2\omega^2}$$

where ω_Q and Γ_Q are the energy and the broadening of the excitation, respectively.

Fig.3 shows the dispersion relations along $(h,h,0)$ obtained in the present analyses at 3.5 K. We presume from the data that Heisenberg-like exchange interaction and the anisotropy energy of the system are comparable. The dispersion curve at 30 K is also shown. Even at this temperature higher than Θ, the slight softening can be observed.

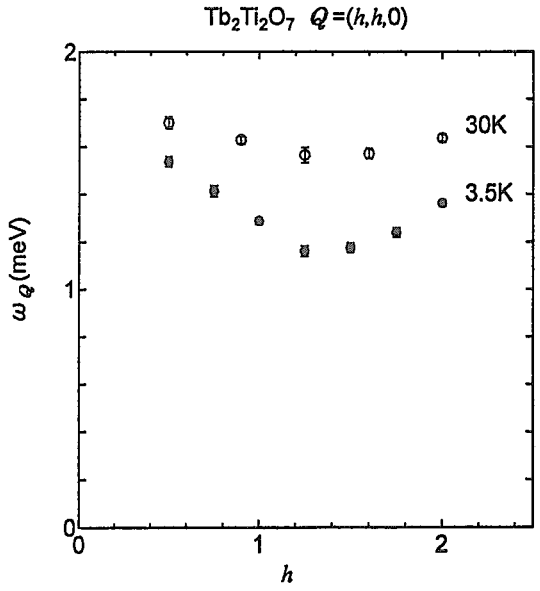

Fig.3 The dispersion curves along $(h,h,0)$ at 3.5 K and 30 K.

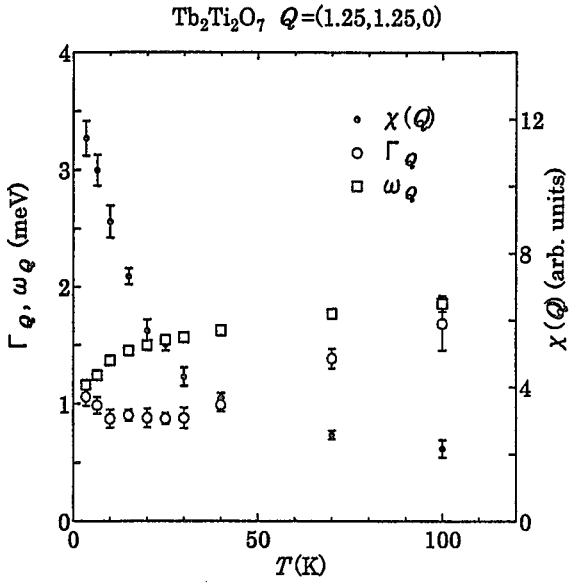

Fig.4 T-dependence of Γ_Q, ω_Q and $\chi(Q)$ at $Q=(1.25,1.25,0)$.

In Fig.4, we summarize the T-dependence of the parameters obtained at $Q=(1.25,1.25,0)$. $\chi(Q)$ grows with decreasing T.

We have also found that there exists significant amount of magnetic scattering contribution in the peak at $E\sim 0$. The Q-dependence of the intensity at $E\sim 0$ seems to be similar to that of the inelastic excitation presented here. A whole physical picture of the dynamics of the Tb^{3+}-moments will be presented after experimentally studying the magnetic scattering with much higher energy resolution.

Reference

1) J. S. Gardner, S. R. Dunsiger, B. D. Gaulin, M. J. P. Gingras, J. E. Greedan, R. F. Kiefl, M. D. Lumsden, W. A. McFarlane, N. P. Raju, J. E. Sonier, I. Swainson and Z. Tun, Phys. Rev. Lett. 82 (1999) 1012.

研究テーマ ： 3 次元フラストレーション系 $ZnFe_2O_4$ のスピン液体

表題 ： 3 次元フラストレーション系 $ZnFe_2O_4$ のメスバウアー分光及び中性子散乱

1-2-58
Mössbauer spectroscopy and neutron scattering measurements in a 3D-frustrated system $ZnFe_2O_4$

T.Usa, K.Kamazawa, S.Nakamura[1], Y.Tsunoda, K.Kohn, M.Tanaka[2]

School of Science and Engineering, Waseda University, Ohkubo, Shinjuku, Tokyo 169-8555, Japan
[1]School of Science and Engineering, Teikyo University, Toyosatodai, Utsunomiya, Tochigi 320-8551, Japan
[2]Advance Research Center for Science and Engineering, Waseda University, Ohkubo, Shinjuku, Tokyo 169-8555, Japan

$ZnFe_2O_4$ takes a normal spinel structure and contains Fe^{3+} magnetic ions only in the B-site. The magnetic moments couple antiferromagnetically through oxide and for this reason the strong geometrical frustration is induced. Several authors have investigated the magnetism of $ZnFe_2O_4$ by means of powder neutron diffraction. W.Schiessl reported a strong and sharp magnetic peak at (1 0 1/2) at 4.2K. On the other hand, Yu.G.Chukalkin observed two peaks, rather weak with broad line width and strong diffuse peak, coexist at (1 0 1/2) at 4.2K. Scattering intensities and line profiles of the (1 0 1/2) magnetic peaks reported by these authors are inconsistent.

These data suggest that the magnetic features of the samples are sensitive to the heat treatment. We investigate the magnetic character of the best quality specimen among the samples prepared for different heat treatments by using neutron powder diffraction, Mössbauer spectroscopy and susceptibility measurements.

Fig.1 shows the patterns of neutron powder diffraction for various samples studied at 7K. The nuclear peaks at (111) are normalized to compare the relative magnetic peak intensities at (1 0 1/2). The sample Ⅱ shows no Bragg peak. Fig.2 indicates the Mössbauer spectra for the same samples as those for neutron diffraction data. The line width in the Mössbauer spectra has strong correlation with the magnetic peak intensity at (1 0 1/2). The sample Ⅱ has the broadest line width. Fig.3 shows magnetization data. The data of $ZnFe_{1.98}Ga_{0.02}O_4$ are included in order to show the effect of artificial defect. Thus, the sample Ⅰ-a seems to include some defects, such as oxygen deficits. In the sample Ⅱ, the zero field cooled path and the field cooled one are the same. The sample Ⅱ seems to include the minimal defects.

We can conclude that the best quality specimen among these four samples is the Sample Ⅱ which was prepared by crushing single crystals.

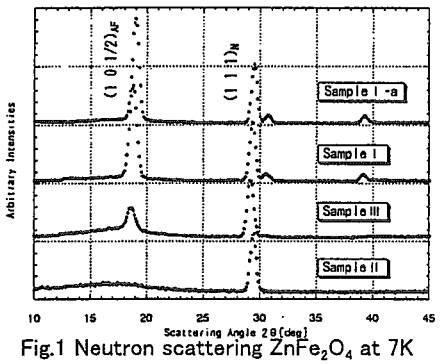

Fig.1 Neutron scattering $ZnFe_2O_4$ at 7K

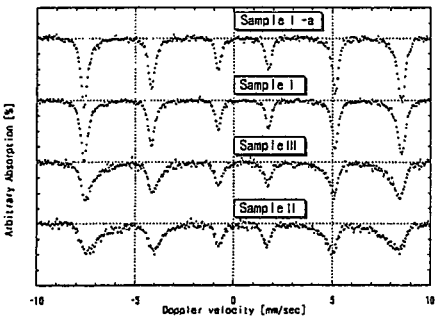

Fig.2 Mössbauer spectra of $ZnFe_2O_4$ at 4.2K

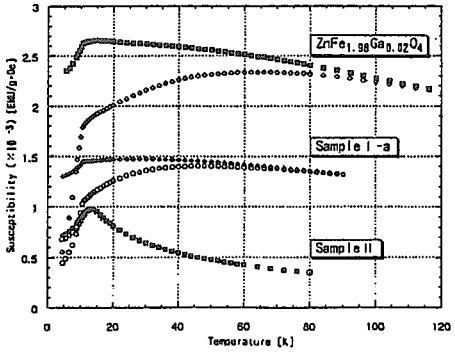

Fig.3 Magnetization of $ZnFe_2O_4$ Sample Ⅰ-a, Ⅱ, $ZnFe_{1.98}Ga_{0.02}O_4$

研究テーマ：3次元フラストレーション系 $ZnFe_2O_4$ のスピン液体
表題：フラストレートしたスピン系－$ZnFe_2O_4$ 単結晶の中性子磁気散乱

1-2-59

Magnetic Neutron Scattering Measurements in the Highly Frustrated $ZnFe_2O_4$ Single Crystal

K. Kamazawa, Y. Tsunoda, K. Odaka*, and K. Kohn*

Department of applied physics, School of Science and Engineering, Waseda University
3-4-1 Ohkubo, Shinjuku-ku, Tokyo 169-8555, Japan
Department of physics, School of Science and Engineering, Waseda University
3-4-1 Ohkubo, Shinjuku-ku, Tokyo 169-8555, Japan

$ZnFe_2O_4$ has a normal spinel structure with A site occupied by Zn^{2+} and B site by Fe^{3+}. If we take the magnetic Fe^{3+} ions, they construct a three dimensional network of corner-sharing tetrahedra. One can also regard it as a fcc configuration of the tetrahedra. These network of tetrahedra is just the same as that for various pyrochlores and C15 intermetallic Laves phase compounds $Y(Sc)Mn_2$, which are limelight systems as a 3D-frustration system. Thus, the strong frustration is expected for $ZnFe_2O_4$, because the Fe^{3+}-Fe^{3+} interaction is considered to be antiferromagnetic. Previously, we reported neutron elastic scattering data for $ZnFe_2O_4$ single crystal. The magnetic diffuse peaks extend along the fcc Brillouin zone boundary. We can explain the data that the each tetrahedron has a net magnetic moment and it fluctuates dùe to the frustration, because the net moment couples antiferromagnetically on a fcc configuration of the tetrahedra .

This time, we present the neutron inelastic scattering data studied at the diffuse peak position. The measurements were performed at the $T_{1\text{-}1}$ and $C_{1\text{-}1}$ triple axis spectrometer installed at the guide hall of JRR-3M. The energy spectrum is almost like quasielastic as shown in Figure 1 and the relaxation time of spin correlation is estimated to be less than $\sim 10^{-11}$ sec at T=7K. In addition, we observed different type energy spectrum at the point where the diffuse scattering shows the minimum intensity. The latter extends to a few meV as shown in Figure 2. We are considering that it comes from the dynamical motion of each Fe^{3+} spin which composes of a tetrahedron.

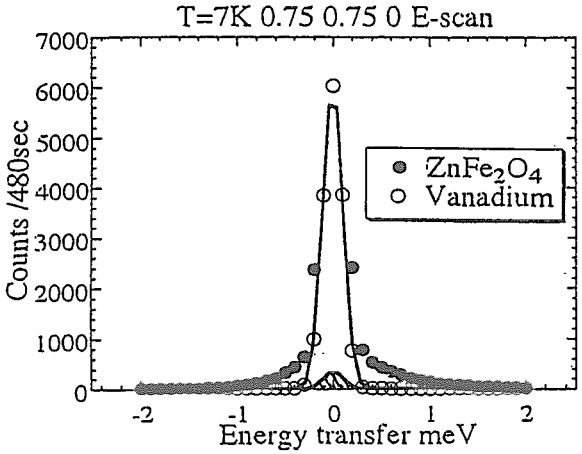

Figure 1 The data show the energy spectrum studied at 0.75 0.75 0 . The hatch indicates incoherent scattering component of $ZnFe_2O_4$ determined from background counts at high temperature. Open circles represent the incident neutron energy spectrum determined using vanadium incoherent scattering.

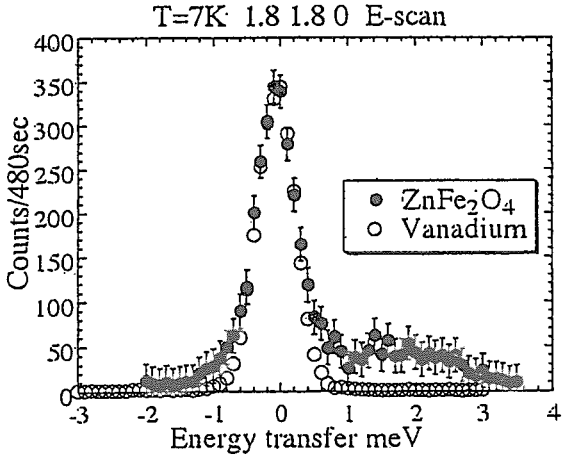

Figure 2 The data show the energy spectrum obtained at the reciprocal lattice point at 1.8 1.8 0. Open circles represent the vanadium incoherent scattering.

研究テーマ：合金の遮蔽効果とフェルミ面
表題：PtFe合金の磁場中における中性子散乱

1-2-60 Neutron Diffraction Studies of PtFe alloy in Magnetic Fields

Daisuke Tsuchiya and Yorihiko Tsunoda

**School of Science and Engineering,Waseda University,
3-4-1,Okubo,Shinjuku,Tokyo,169-8555,Japan**

Pt is well known as nearly ferromagnetic substance. An introduction of less than 1 at. % of Fe induces ferromagnetic long-range order (LRO) . For disordered PtFe alloys with Fe concentrations around 10 at. % , diffuse satellite reflections are observed around 1 0 0 reciprocal-lattice point (RLP) , indicating that these alloys possess an antiferromagnetic spin correlation. The antiferromagnetic spin component is periodically modulated and incommensurate with the lattice. The wave vector of the spin modulation varies with Fe concentration. An incommensurate-commensurate transition takes place around 14 at. % Fe

On the other hand, another magnetic peak is observed at the 1/2 1/2 0 RLP for more Fe concentrated alloys. This peak comes from the Pt_3Fe-type antiferromagnetic atomic short range order (ASRO). Thus, the two magnetic states, one is ferromagnetic with antiferromagnetic spin correlation and another is pure antiferromagnetic, coexist in the PtFe alloys with 15~20 at. % Fe concentration.

The purpose of this study is to investigate the correlation between ferromagnetic regions and antiferromagnetic regions in magnetic fields. For this aim, therefore we selected the PtFe alloy with Fe concentration of 16 at. % . The data were taken at the T1-1 triple axis spectrometer installed at a thermal guide of JRR-3M.

Practically, we measured both the 1 0 0 ferromagnetic peak intensities (strictly speaking, the antiferromagnetic spin component) and the 1/2 -1/2 0 antiferromagnetic peak intensities under the various magnetic field. The magnetic field is applied first up to 3000 Gauss and then down to 0 G .

The results are given in Fig.1 and Fig.2 for the ferromagnetic peak intensities and antiferromagnetic peak intensities, respectively. When the magnetic field returns to 0 G, the ferromagnetic peak intensity doesn't recover its original value because of hysteresis. While the antiferromagnetic peak intensity also doesn't recover, but the antiferromagnetic region shows no hysteresis. This means antiferromagnetic regions decreases because of the existence of ferromagnetic regions. Similar experiments were performed on the ordered Pt_3Fe alloy and 1/2 1/2 0 antiferromagnetic peak intensity didn't vary. A detailed investigation is now in progress.

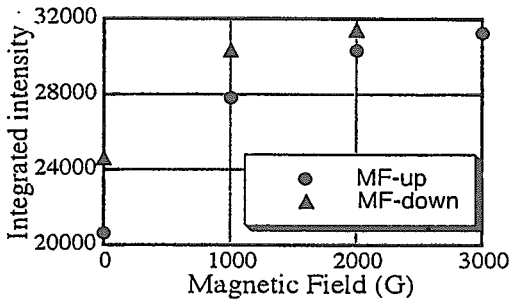

Fig.1 Intensity variation vs. magnetic field at the 1 0 0 ferromagnetic peak

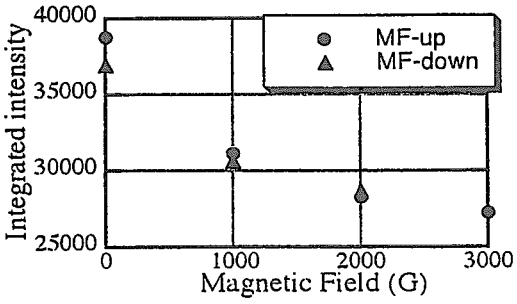

Fig.2 Intensity variation vs. magnetic field at the 0.5 -0.5 0 antiferromagnetic peak

研究テーマ：PdMn, PtMn 希薄合金の磁性
表題：PtMn 合金の中性子散乱

1-2-61 Neutron Scattering Studies of PtMn alloys

A.Harigae,T.Sunaga and Y.Tsunoda
School of Science and Engineering,Waseda University
3-4-1 Ohkubo,Shinjuku-ku Tokyo 169-8555 Japan

Most of PdM and PtM (M=3d transition metal) alloys show the same magnetism because Fermi surfaces of Pd and Pt are very similar. In the case of Mn impurity, however, the magnetism of PdMn is not the same as that of PtMn; PdMn alloy with Mn concentration below 3 at. % shows ferromagnetism and with more than 5 at. % behaves as a spin glass. PtMn alloy with low Mn concentration is already a spin glass. Searching for the origin of the different magnetic behaviors, we carried out the neutron scattering experiments on single crystal of PtMn alloys. The data were taken at the T1-1 triple axis spectrometer installed at a thermal guide of JRR-3M. Prior to the neutron scattering measurements, all samples were comfirmed to show spin-glass-like behavior by magnetic susceptibility measurements.

Figs.1 and 2 show the data obtained by scanning along the [1 0 0] axis on Pt-3% and 13%Mn alloys respectively. We also studied Pt-6% and 9%Mn alloys. In order to examine the magnetic scattering, high temperature data were subtracted from low temperature data. Subtracted data show satellite peaks at the $1\pm\delta$ 0 0 postions (δ=0.5) on all samples. The data indicate that the spin density wave (SDW) clusters play an important role as the origin of spin-glass-like behavior. The wave length of SDW is independent of Mn concentration. Invariability of the wave length is a unique property on PtMn alloy. For all other PdM and PtM alloys except for PtMn alloy, the wave length of modulated structure which comes from special shape of Fermi surfaces varies with M concentration. This difference may be related to the difference of the magnetism between PdMn and PtMn.

The peaks of the nuclear diffuse scattering were observed at the same positions as the magnetic dffuse scattering in Fig.1 for Pt-3%Mn. That means the existence of the concentration wave reflecting the shape of Fermi surface, which was observed for PdV, PtV, etc. and not for PdMn. In Fig.2, the peak of the nuclear diffuse scattering on Pt-13%Mn was observed at the 1 0 0 RLP probably due to the atomic short range order (ASRO) of the superlattice structure Pt_3Mn. We comfirmed that these two kinds of ASRO coexist in Pt-6% and 9%Mn alloys.

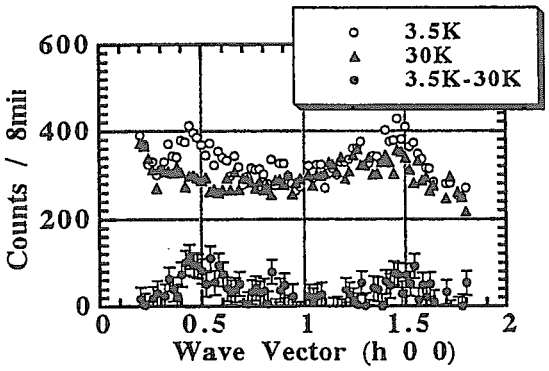

Fig.1 The data for Pt-3%Mn obtained by scanning along the [1 0 0] axis at higher and lower temperature than 16K at which the magnetic scattering disappears.

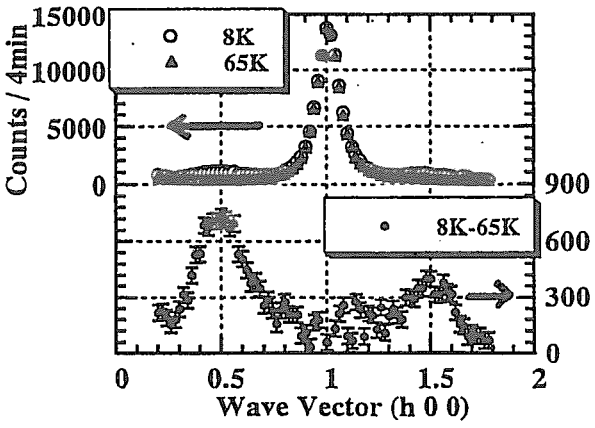

Fig.2 The data for Pt-13%Mn observed at higher and lower temperature than 55K at which the magnetic scattering disappeares.

研究テーマ：NH_4CuCl_3における磁化の量子化とスピン状態
表題：NH_4CuCl_3における磁化の量子化とスピン状態

1-2-62 Neutron Scattering Study of the Spin Structure in ND_4CuCl_3

B. Kurniawan, H. Tanaka, A. Oosawa, N. Aso[1], K. Nakajima[1], Y. Oohara[1], K. Kakurai[1], T. Takeuchi[2] and S. Kawarazaki[3]

Department of Physics, Tokyo Institute of Technology, Meguro-ku, Tokyo 152-8551
[1]Neutron Scattering Laboratory, ISSP, The University of Tokyo, Tokai, Naka, Ibaraki, 319-1195
[2]Low Temperature Center, Osaka University, Osaka University, Toyonaka, Osaka 560-0043
[3]Department of Earth and Space Science, Osaka University, Toyonaka, Osaka 560-0043

The quantum spin system NH_4CuCl_3 is isostructural with $KCuCl_3$ which belongs to the monoclinic space group $P2_1/c$. The crystal structure is composed of chains of planar dimer Cu_2Cl_6 along the a-axis. The chains are located at the corners and center of the unit cell in the bc-plane, and are separated by NH^{4+} ions. The spin-spin interactions can be described by the S=1/2 Heisenberg model. NH_4CuCl_3 exhibits well defined magnetization plateaus at one-quarter and three-quarters of the saturation magnetization, irrespective of the external field direction. In the gapless slope regions in the magnetization curve, the three-dimensional ordering can occur. Recently it was found that NH_4CuCl_3 undergoes the 3d ordering at T_N=1.3 K at zero field. Although several mechanisms leading to the plateaus have been proposed theoretically, the microscopic mechanism is still unclear. The key to solving the problem is to determine the spin. In order to investigate the spin structure, we carried out neutron elastic scattering experiment on ND_4CuCl_3 structure in magnetic fields up to 4 T.

The experiments were performed on the triple-axis spectrometer HQR installed at JRR-3 in Japan Atomic Energy Research Institute (JAERI), Tokai using a vertical field cryomagnet and a dilution refrigerator. The neutron energy was fixed at 13.5 meV. The collimation sequence was chosen as Open-40'-40'.

Figure 1(a) shows the profiles of the omega-scan above and below T_N=1.3 K at around Q=(1, 0, -3). We can see the presence of the magnetic Bragg peak at (1, 0, -3). Below T_N, magnetic Bragg peaks were observed at not only commensurate but also incommensurate positions for $H \leq 4$ T, e.g., Q=(1, 0, 2.58). Thus it is deduced that the spin structure for $H \leq H_{c1}$ is incommensurate, where H_{c1}=5 T is the lower edge field of the first magnetization plateau. Figure 1(b) shows the field dependence of the Bragg peak intensity at Q=(1, 0, -3) measured at 0.05 K. With increasing external field, the intensity increases.

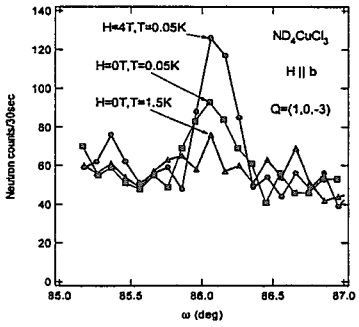

(a)

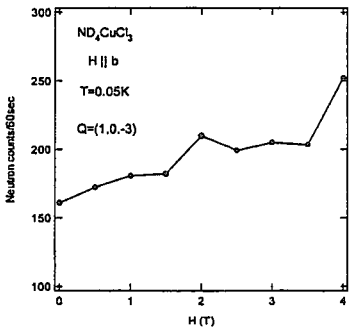

(b)

Fig. 1. (a) Profiles of the omega-scan at around Q=(1,0,-3) at 1.5 and 0.05 K, and at zero field and 4 T, and (b) the field dependence of the magnetic Bragg peak intensity at Q=(1,0,-3).

研究テーマ：一軸性圧力による$CuGeO_3$の物性研究
表題：一軸性圧力による$CuGeO_3$の物性研究

1-2-63
Study of the Effect of Uniaxial Pressure on $CuGeO_3$ along the *a*-axis

M. Nishi, J. Akimitsu[1], O. Fujita[1], K. Kakurai, and Y. Fujii

Neutron Scattering Laboratory, ISSP, University of Tokyo, Tokai, Ibaraki, 319-1106, Japan
[1]Department of Physics, Aoyama-Gakuin University, Setagaya-ku, Tokyo, 157-8572, Japan

The anisotropic thermal expansion coefficients of $CuGeO_3$ were measured along the three orthorhombic axes and the extremely anomalous temperature dependence of them was observed by Winkelmann *et al.* [1]. The uniaxial pressure of the spin-Peierls transition temperature (T_{SP}) was calculated also from the thermal expansion coefficients and the specific heat via the Ehrenfest relation. According to these results the uniaxial pressure along the *a*-axis strongly suppress T_{SP} with dT_{SP}/dp = -4.2 K/GPa [1]. $CuGeO_3$ has a cleavage surface including *b* and *c*-axes. A single crystal of $CuGeO_3$ ($3x7x8mm^3$) was pressed along *a*-axis using a spring to keep constant pressure. Neutron diffraction measurements were performed on a high *Q* resolution spectrometer (HQR) installed in the guide hall (T1-1 port) of the JRR-3M at JAERI. The pressure cell with a sample was set on the cold tip of a helium-gas circular type 4K-cryostat and cooled down to 4 K. The temperature dependence of superlattice peak (1.5, 1, 1.5) was measured in thermal equilibrium using a step by step method. The thermal hysteresis was not observed between the cooling and heating process. As shown in Fig.1 applying the uniaxial pressure of 5 and 128 MPa along the *a*-axis T_{SP} shifts to 13.55 (5) K and 14.21 (5) K, respectively from 14.06 (10) K at ambient pressure. The uniaxial pressure dependence of T_{SP} is plotted in Fig. 2 with a logarithmic absica. Above 40 MPa our experimental results are consistent with the estimated line with -4.2 K/GPa as shown by the solid curve, but below 20 MPa T_{SP} is higher than the calculated value by about 0.2 K as shown by the dotted area. This behavior is very unique and unusual. We speculate that the unharmonic potential of the atomic positions perhaps increases T_{SP} because of the low-energy phonon excitation at the Γ point observed near 1 meV at ambient pressure by Nishi *et al.*

[1] Winkelmann *et al.*, Phys. Rev. **B51** (1995) 12884.

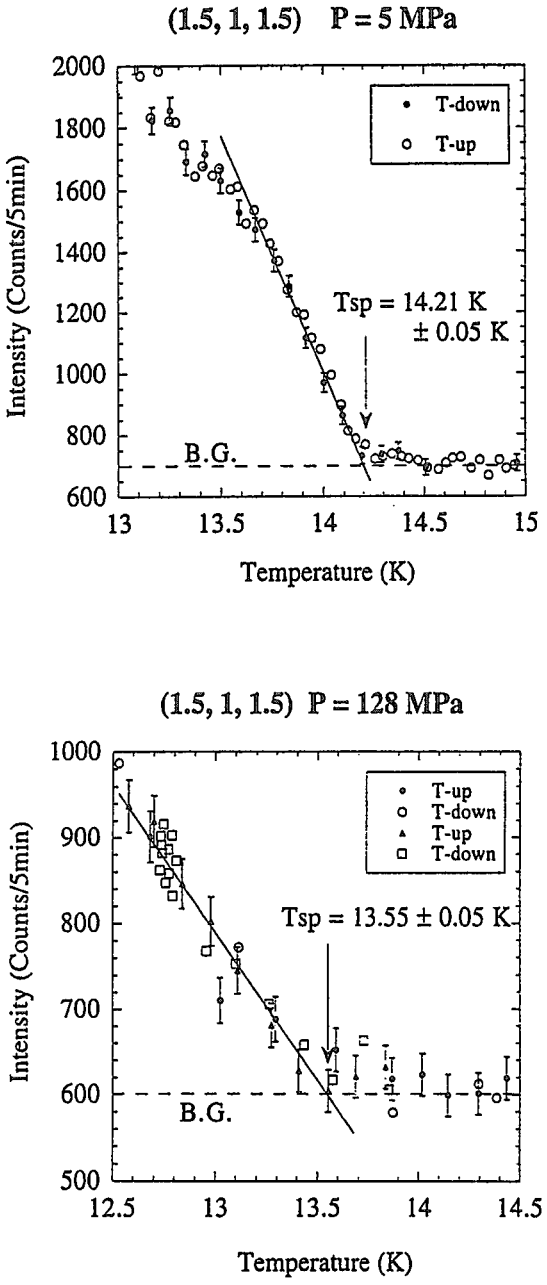

Fig. 1 The temperature dependence of superlattice reflection (1.5, 1, 1.5) at 5 MPa (top) and 128 MPa (bottom). Background was estimated from the data above T_{SP}.

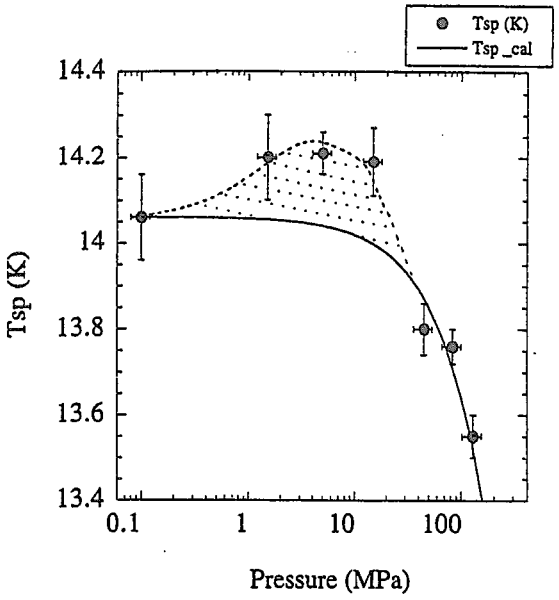

Fig. 2 The temperature-pressure phase diagram of the uniaxial pressure along a-axis of $CuGeO_3$. The dotted area shows the deviation from the Ehrenfest relation.

研究テーマ：異方性競合系 $Fe_xCo_{1-x}TiO_3$ の磁場中での新しい相転移の研究
表題：異方性競合系 $Fe_xCo_{1-x}TiO_3$ の磁場中における履歴現象

1-2-64

Hysteretic behavior under magnetic fields in the competing anisotropy system $Fe_{0.50}Co_{0.50}TiO_3$

A. Fukaya, J. Satooka, A. Ito, K. Nakajima[1] and K. Kakurai[1]

The Institute of Physical and Chemical Research (RIKEN), Hirosawa 2-1, Wako, Saitama, 351-0198 Japan

[1]*Neutron Scattering Laboratory, The Institute for Solid State Physics The University of Tokyo, Shirakata, Naka, Ibaraki,319-11 Japan*

The mixed compound $Fe_xCo_{1-x}TiO_3$ is well-known as one of competing anisotropy systems.[1] For $Fe_{0.50}Co_{0.50}TiO_3$, it is clarified from the magnetization measurement that, when the temperature is lowered, the spin component perpendicular to the c-axis of the ilmenite structure and that parallel to c-axis form the order (not real long range order but domain state [3]) successively at T_N=36 K and T_L=31 K in H=0. Recently, we found that the temperature variations of magnetizations of $Fe_{0.50}Co_{0.50}TiO_3$ show anomalous hysteresis between those under zero-field-cooled(ZFC) and those of field-cooled(FC) condition in fields parallel to b-axis. In order to clarify the origin of the anomalous hysteretic behavior, we have performed neutron scattering measurements under fields. We have briefly reported the result in Ref. 2. In this report, we describe the behavior of magnetic scattering intensities only at a (1 0 -0.5) reciprocal lattice position.

In Fig. 1, we show magnetic scattering intensity at (1 0 -0.5) as a function of the temperature under various fields. For comparison, we also show that in H=0. A notable point seen in Fig. 1 is that hysteresis between the intensity under ZFC and that under FC condition is observed in H=3 kG and 10 kG. In H=3 kG, weak hysteresis is observed below T_L=31 K and no other anomaly is observed down to 2 K. In 10 kG, the intensity under ZFC condition suddenly decreases at 6.5 K and collapses to that under FC condition which exhibits no anomaly. In both of H=3 kG and 10 kG, any diffuse scattering was not observed around (1 0 -0.5) in FC condition, which suggests that the direction of spin or magnetic structure strongly depends on cooling condition. In a higher field of 25 kG, no hysteresis is observed. By the magnetization measurements, it is clarified that, at T=4.5 K, a spin-flop transition occurs at H=13 kG. Thus, we consider that the hysteretic behaviors observed in the temperature dependence of the scattering intensity strongly relate to the spin-flop transition.

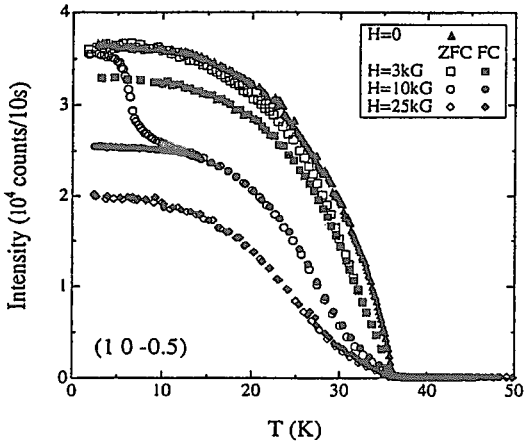

Fig. 1 Magnetic scattering intensity at (1 0 -0.5) as a function of temperature under various fields.

[1] A. Ito, S. Morimoto, Y. Someya, Y. Syono and H. Takei, J. Phys. Soc. Jpn. 51 (1982) 3173.

[2] A. Ito, C. Uchikosi, A. Fukaya, S. Morimoto, K. Nakajima and K. Kakurai, J. Phys. Chem. Sol. 60 (1999) 1233.

[3] Q. J. Harris, Q. Feng, Y. S. Lee, R. J. Birgeneau and A. Ito, Phys. Rev. Lett. 78 (1997) 346.

研究テーマ：強磁性と反強磁性の共存する Fe, Mn 合金の磁性
表題： $Y_{0.8}Tb_{0.2}Mn_6Sn_6$ 合金の磁気構造

1-2-65 Magnetic structure of $Y_{0.8}Tb_{0.2}Mn_6Sn_6$ alloy

T. Hori[a], H. Shiraishi and Y. Yamaguchi[b]
[a]Shibaura Institute of Technology, Oomiya, Saitama 330-8570, Japan
[b]Institute for Materials Research, Tohoku University, Sendai 980-8577, Japan

It has been reported that the alloy YMn_6Sn_6 having a hp13 type ($MgFe_6Ge_6$ type) layer structure shows an inhomogeneous helical antiferromagnetism with the Néel temperature T_N = 333 K [1]. It should be noticed that Mn atom layers on 6i (1/2,0,z_2) and (1/2,0,1−z_2) site are well separated by Sn atom layers on 2c (1/3,2/3,0), 2d (1/3,2/3,1/2) and 2e (0,0,z_1) sites. The magnetic moments of Mn are ferromagnetically arranged in the same *c*-plane. Y atom layers on 1a (0,0,1/2) site are non-magnetic. The isotypic alloy $TbMn_6Sn_6$ having magnetic Tb atom layers shows a simple ferrimagnetism with the Curie temperature T_C = 423 K [2]. We have extended the studies to $Y_{1-x}Tb_xMn_6Sn_6$ alloys, which are found to have the hp13 type structure in the whole composition range ($0 \le x \le 1$). In the present paper, we have reported the results of magnetization measurements and neutron diffraction experiments for $Y_{0.8}Tb_{0.2}Mn_6Sn_6$. Neutron diffraction experiments were made using the HERMES of IMR installed in the JRR-3M reactor at JAERI.

Fig. 1 shows neutron diffraction patterns for $Y_{0.8}Tb_{0.2}Mn_6Sn_6$ at 12 K and 460 K. It has been confirmed from the Rietveld analysis of the data at 460 K (higher than T_C) that Sn occupies 2c, 2d and 2e with z_1=0.163, Y and Tb occupy randomly 1a and Mn occupies 6i with z_2 = 0.253. The existence of 100 satellite reflections and the absence of 001 reflection at 12 K suggest following magnetic structure: all the magnetic moments of Mn (= 2.0 μ_B/ Mn atom) are ferromagnetic and antiparallel to the magnetic moments of Tb (= 9.0 μ_B/Tb atom); the direction of the moments slightly deviates form the *c*-axis, and the small components on the *c*-plane shows a helical arrangement with a propagation vector parallel to the *a*-axis having a period of 7.5 *a*. The magnetic contribution in the pattern above 160 K is quite different form that of 12 K, and similar to the pattern of YMn_6Sn_6 in reference [1], suggesting that the magnetic moments lie on the *c*-plane, and the propagation vector is parallel to the *c*-axis.

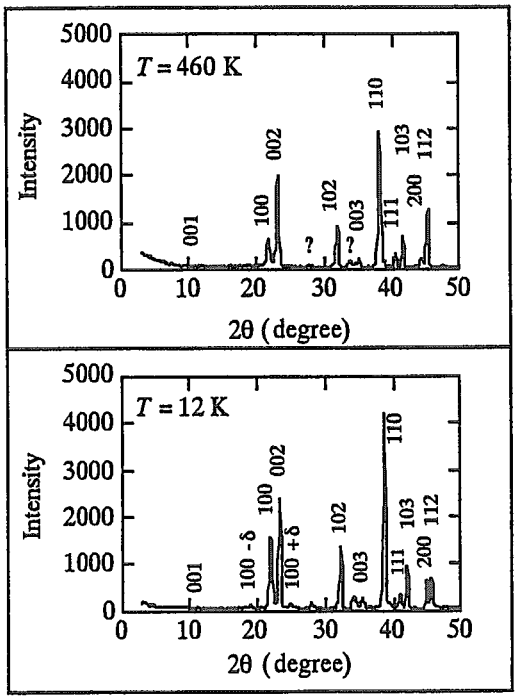

Fig.1. Neutron diffraction patterns for $Y_{0.8}Tb_{0.2}Mn_6Sn_6$ at 460 K and 12 K.

References
[1] G. Ventrurini, D. Fruchart, B. Malaman, J. Alloys and Compounds **236** (1996) 102.
[2] G. Venturini, B. Chafik El Idrissi and B. Malaman, J. Alloys and Compounds **200** (1993) 51

JRR-3M, HERMES, 2. Magnetism

研究テーマ：強磁性と反強磁性の共存する Fe, Mn 合金の磁性
表題：hp13 型 TFe_6Ge_6 (T=Zr, Nb, Hf) 合金の磁性

1-2-66 Magnetic properties of hp13 type TFe_6Ge_6 (T=Zr, Nb, Hf) alloys

T. Hori[a], R. Nishihara[a], M. Akimitsu[a], K.Ohoyama[b], H. Onodera[b], Y. Yamaguchi[b]

[a]Shibaura Institute of Technology, Oomiya, Saitama 330-8570, Japan
[b]Institute for Materials Research, Tohoku University, Sendai 980-8577, Japan

Recently, we made magnetization measurements and neutron diffraction experiments on $M_{7-x}Mn_xGe_6$ (M = Co, Fe) alloys[1], which have a hexagonal layer structure (P6/mmm) of hp13 type (Pearson symbol), in which transition element layers consisting of 1a and 6i sites are well separated by Ge layers of 2c and 2e sites. The $Mn_4Fe_3Ge_6$ alloy is antiferromagnetic; the paramagnetic Curie temperature θ_P is positive and close to the Néel temperature T_N of 528 K. More recently, we reported that the isotypic alloy $TiFe_6Ge_6$ exhibits simpler antiferrmagnetic behaviors [2]; θ_P (= 70 K) is much lower than T_N (= 510 K). We have determined the Néel temperature T_N and the paramagnetic Cuire temperature θ_P also by the magnetization measurements for $TFe_6Ge_{6.2}$; T_N = 495 K and θ_P = 70 K for T = Zr, T_N = 462 K and θ_P = 62 K for T = Hf and T_N = 554 K and θ_P = 71 K for T =Nb. We have made neutron diffraction experiments for $TFe_6Ge_{6.2}$ alloys at room temperature using the HERMES (wave length λ = 1.817 Å) of IMR installed in the JRR-3M reactor at JAERI. For a typical example, Fig. 1 shows the neutron diffraction pattern of $ZrFe_6Ge_{6.2}$ in a lower Bragg angle range. The pattern is almost identical to that of $TiFe_6Ge_{6.1}$[2]; the 001 line is absent. It is that the magnetic structure of $TFe_6Ge_{6.2}$, (T = Zr, Nb and Hf) is similar to that of $TiFe_6Ge_{6.1}$, i.e. magnetic moments of Fe atom are ferromagnetically arrangement in the same *c*-plane and antiferromagnetically arranged between adjacent *c*-planes, and the direction of the magnetic moment is parallel to the *c*-axis. We determined the atomic site occupation from a Rietveld analysis using the neutron diffraction intensities in which the data around the 101 and 201 reflections containing some magnetic contributions were removed. The results are as follows: Ge on 2c (1/3,2/3,0), 2d (1/3,2/3,1/2) and 2e (0, 0, z_1), T on (0, 0, 1/2) and Fe on (1/2, 0, z_2) with z_1 = 0.158 and z_2 = 0.251 for T = Zr; z_1 = 0.159 and z_2 = 0.251 for T = Hf; z_1 = 0.164 and z_2 = 0.250 for T = Nb. We also estimated the magnetic moment of about 1 μ_B / Fe atom from the 101 and 201 reflections.

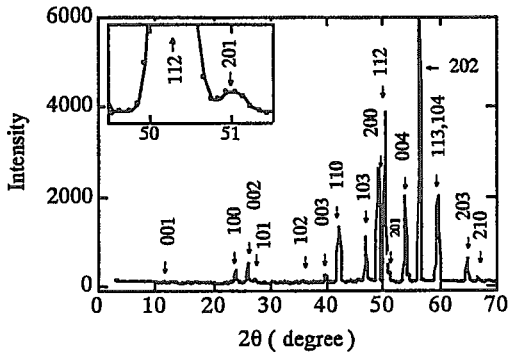

Fig. 1. Neutron diffraction pattern for $ZrFe_6Ge_{6.2}$ at 295 K.

References

[1] T. Hori, Y. Tuchiya, S. Funahashi, M. Akimitsu, Y. Shimojo, H. Shiraishi and Y. Nakagawa, J. Magn. Magn. Matter. 177-181 (1998) 1425.

[1] R. Nishihara, M. Akimitsu, T. Hori, H. Niida, K. Ohoyama, M. Ohashi, Y. Yamaguchi and Y. Nakagawa, J. Magn. Magn. Matter. 196-197 (1999) 665.

JRR-3M, HERMES, 2. Magnetism

研究テーマ：強磁性と反強磁性相互作用の共存する Fe,Mn 合金の磁性
表題：磁性と中性子回折による $(Mn_{1-x}Ni_x)_{65}Ga_{35}$ の研究

1-2-67
Magnetic and Neutron Diffraction Study on $(Mn_{1-x}Ni_x)_{65}Ga_{35}$

H.Shiraishi, T.Hori, H.Miki [a], H.Onodera [a], K.Ohoyama [a], Y.Yamaguchi [a]

Shibaura Institute of Technology, Oomiya, Saitama 330-8570, Japan
[a] *Institute of Materials Research, Tohoku University, Sendai 980-8577, Japan*

New intermetallic compounds $(Mn_{1-x}Ni_x)_{65}Ga_{35}$ of Ni_2In type structure are found in the range of $0.15 \leqq x \leqq 0.45$. In the higher x range $x \geqq 0.4$, the temperature dependence of magnetization σ exhibit ferromagnetism and a Curie-Weiss type behaviors in the paramagnetic region, but those with $x \leqq 0.35$ suggest another type ferromagnet as shown in Fig.1.

We have carried out the neutron diffraction experiments to determine the magnetic structure of $(Mn_{1-x}Ni_x)_{65}Ga_{35}$ with x=0.275 using HERMES installed in the JRR-3M in JAERI. The atom arrangement corresponding to minimum values of disagreement factor R is as follows: in the Ni_2In type structure, the 2(a) site is entirely occupied by Mn, the 2(d) site by Ni and residual Mn randomly and 2(c) site by Ga. A preferred occupation of Ni on the 2(d) site is observed. We observed the neutron diffraction patterns for x=0.275 at several temperatures. Fig2 shows a part of the diffraction patterns in the low Bragg angle region. The pattern at T=165 and 200K, the (001) magnetic reflection is observed, indicating the presence of antiferromagnetic component lying in the basal plane. As the magnetic contribution to the (002) reflection is negligible, the ferromagnetic component is parallel to the c axis. From these consideration, the spins at the 2(a) site are thought to be a canted one. The spins at the 2(d) site are antiparallel to the ferromagnetic component. This model is the same as for CoMnSn[1]. In the patterns for T<140K, satellite lines of (001) and (101) are observed, suggesting the appearance of helical spin structure. The pitch of helix changes $5.78c(T$=15K) ~ $8.47c$(140K), where c is lattice constant.

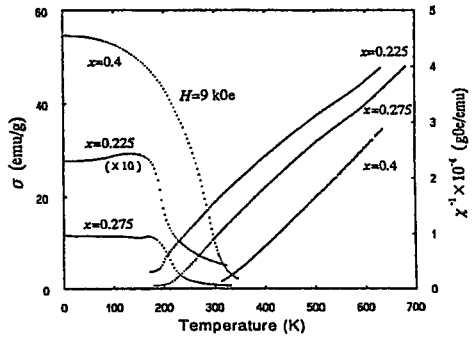

Fig.1. The σ-T and χ^{-1}-T curve for x=0.225, x=0.275 and x= 0.4

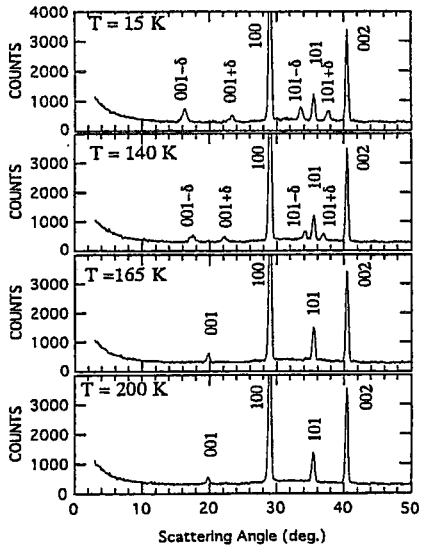

Fig.2. Neutron diffraction patterns in the low Bragg angle region for x=0.275

Reference

[1] W.Bazela, A.Szytula, J.Todorovic, Z.Tomkowicz and A.Zieba, Phys.Stat. Sol.(a) 38(1976)721

研究テーマ：Fe^{4+}酸化物の電荷不均化反応

表題：$Sr_3Fe_2O_{7-\delta}$の磁気構造

1-2-68 Magnetic Structure of $Sr_3Fe_2O_{7-\delta}$

K. Mori[1], T. Kamiyama[1], H. Kobayashi[2], K. Ohoyama[3] and S. Ikeda[1]

[1]*Institute of Material Structure Science, High Energy Accelerator Research Organization, Tsukuba, Ibaraki 305-0801, Japan*
[2]*Department of Physics, Tohoku University, Sendai 980-8578, Japan*
[3]*Institute of Materials Research, Tohoku University, Katahira, Sendai 980-8577, Japan*

Recently, iron oxides with an average oxidation state +4 have arose much interest, because some of these oxides show charge disproportionation ($2Fe^{4+} \rightarrow Fe^{3+} + Fe^{5+}$) while others do not. In the case of $Sr_3Fe_2O_{7-\delta}$ the Mössbauer spectra measured at 4.2 K indicate charge disproportionation [1,2], while in the case of $SrFeO_3$, such phenomenon is not observed between 4 K and room temperature (RT).

$Sr_3Fe_2O_{7-\delta}$ which is a polycrystalline sample has been studied using a neutron powder diffraction [2,3]. Consequently, diffraction data at low temperature showed no sign of any structure distortion arising from charge disproportionation.

In this study, we investigated the magnetic structure of $Sr_3Fe_2O_{7-\delta}$ at low temperature with a neutron powder diffractometer.

$Sr_3Fe_2O_{7-\delta}$ was synthesized by conventional processing from Fe_2O_3 (99.999%) and $SrCO_3$ (99.999%). The mixture was fired at 1100°C for 36h in air, pressed into disks, and heated at 1200°C for 30h. Finally, the product was annealed at oxygen pressures of 2000atm at 450°C for 96h. The diffraction data of $Sr_3Fe_2O_{7-\delta}$ were collected between 10K and 250K on a neutron powder diffractometer HERMES installed at T-3 port of JRR-3M reactor of JAERI.

Figure 1 shows three diffraction patterns. A number of magnetic peaks (indexed as M and m) are observed below the Néel temperature ($T_N \approx 90$ K). We guess that lattice parameters for the magnetic structure of $Sr_3Fe_2O_{7-\delta}$ are $a \approx 2a_0$ and $c \approx 4c_0$, respectively, where a_0 and c_0 are lattice parameters for the chemical unit cell. However, it was not easy to determine the magnetic structure, because such a magnetic unit cell was very large and intensity of several magnetic peaks (indexed as m) were very week.

On the other hand the large diffuse scattering was observed at low angle regions above T_N. As Figure 1 indicates, the diffuse scattering remains even at 250K. We have carried out the experiment of small angle neutron scattering (SANS) for this sample. From the SWAN data, we conclude that the diffuse scattering mainly consists of two components; one is the nuclear diffuse scattering, the other the magnetic one.

More detailed investigations are necessary in order to clarify the relation between the magnetic structure and the diffuse scattering.

Acknowledge

We wish to acknowledge for Mr. Tokuno the help in the preparation of the high oxygen-doped sample.

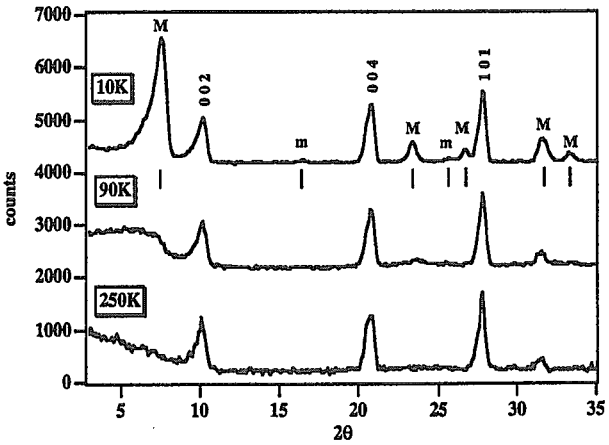

Figure 1

References

[1] P.Adler, *J. Solid State Chem.* **130** (1997) 129
[2] S. E. Dann, M. T. Weller, D. B. Currie, M. F. Thomas and A. D. Al-Rawwas, *J. Mater. Chem.* **3** (1993) 1231
[3] K. Mori, T. Kamiyama, H. Kobayashi, S. Torii, F. Izumi and H. Asano, *J. Phys.Chem. Solids* **60** (1999) 1443

研究テーマ：中性子回折による Ce_3SnC の磁気構造の決定
表題：Ce_3SnC の磁気構造

1-2-69 Magnetic structure of Ce_3SnC

M. Kosaka, S. Koiwai, Y. Uwatoko, H. Onodera[1], K. Ohoyama[1] and Y. Yamaguchi[1]
Department of Physics, Saitama University, Urawa 338-8570, Japan
[1] Institute for Materials Research, Tohoku University, Sendai 980-8577, Japan

New ternary compound Ce_3SnC has a simple face-centered cubic $CaTiO_3$-type structure. This crystal structure features that Ce atoms are situated on a face-centered position of an unit cell which occupies 3c tetragonal symmetry site (4/mmm) while the crystal structure is cubic. Ce_3SnC undergoes a transition to an antiferromagnetic state at T_N = 6.9 K and the magnetization process shows multi-step metamagnetic transitions at T = 1.5 K. This behavior is called a devil's staircase [1].

For sample preparation we used Ce of 99.99%, Sn of 99.999% and C of 99.9995% purity. The compounds are synthesized by a conventional argon arc technique and annealed at 1100 ℃ for a week in tantalum foil, which was sealed in an evacuated quartz tube. Neutron powder diffraction measurements were carried out using the high efficiency and resolution powder diffractometer (HERMES) installed at JRR-3M reactor in the Japan Atomic Energy Research Institute.

Figure 1 shows the neutron diffraction patterns of Ce_3SnC at T = 2.2 K. In the pattern, magnetic reflections are clearly observed (a character N denotes a nuclear reflection) and propagation vector is determined to be q = [½, 0, 0]. Abcence of magnetic (½, 0, 0) reflection suggests that a magnetic moment lies along the a-axis. We calculate intensities of magnetic reflections which the reliability factor $R(\sum|Iobs-Ical|/\sum|Iobs|)$ = 7.5%, the determined magnetic structure of Ce_3SnC shows in fig. 2. It is noticed that there are two kind Ce atoms, one has magnetic moment of 2.0 μ_B (Ce-I) and the other has no magnetic moment (Ce-II) while Ce atoms occupy the same crystallographic site. The reason is because Ce atoms are affected by the tetragonal symmetry crystalline electric field (CEF). Accordingly, Ce-I atoms are situated on the easy plane which has tetragonal symmetry, but Ce-II atoms can not generate a magnetic moment toward Sn which is hard direction. Therefore, the results reveal that the strange magnetic structure of Ce_3SnC is due to the tetragonal CEF and the magnetic exchange interaction.

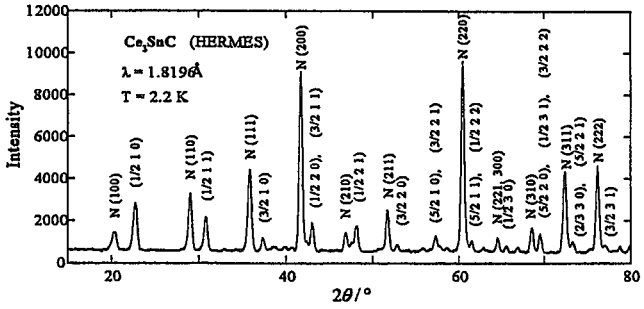

Fig. 1 Neutron powder diffraction pattern of Ce_3SnC at 2.2 K.

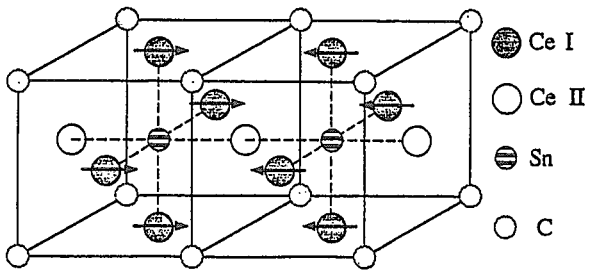

Fig. 2 Magnetic structure model of Ce_3SnC.

[1] M. Kosaka et al., Physica B 284 (2000) 1323.

研究テーマ：$Tb^{11}B_2C_2$および$Ho^{11}B_2C_2$における四重極相互作用と磁気構造
表題：正方晶化合物$Er^{11}B_2C_2$の磁気構造

1-2-70 Magnetic structure in the tetragonal compound $Er^{11}B_2C_2$

K. Ohoyama, A. Tobo, K. Indoh, H. Onodera, Y. Yamaguchi,

Institute for Materials Research, Tohoku University, Sendai 980-8577

Magnetic properties in REB_2C_2 compounds (RE= rare earth) with the tetragonal LaB_2C_2 type crystal structure[1] attract our interest recently. In particular, DyB_2C_2 undergoes an antiferroquadrupolar (AFQ) ordering at T_Q=24.7K and a further transition to an antiferromagnetic (AFM) ordered state at 15.3K[2]. It should be pointed out that T_Q of DyB_2C_2 is nearly ten times higher than those of other AFQ ordering materials. Moreover, HoB_2C_2 shows a complicated phase diagram which indicates existence of an AFQ ordered state below the magnetic ordering temperature[3]. To understand the mechanism of AFQ interactions in DyB_2C_2 and HoB_2C_2, it is also important to make clear magnetic behaviour in other RB_2C_2 compounds as a whole. This work aims, therefore, of determining magnetic structures in the isostructural compound ErB_2C_2. The temperature dependence of magnetic susceptibility of ErB_2C_2 shows an apparent anomaly at T_N=15.9K and a small anomaly at T_t=13K. The magnetic easy axis is the [001] direction in the whole measured temperature range.

Figs.1 show powder patterns of a polycrystalline sample of $Er^{11}B_2C_2$ on Kinken powder diffractometer HERMES(T1-3) at JRR-3M. Natural boron was replaced by ^{11}B, to avoid the strong neutron absorption effect. As shown in Fig.1(a), strong magnetic peaks denoted with M were observed. The magnetic Bragg reflections can be indexed with the propagation vector k=[100]. Since the magnetic moments is parallel to the [001] direction because of the magnetic anisotropy, the result indicates that the magnetic structure in the ground state is a simple antiferromagnetic one which is the same as that of an isostructural compound NdB_2C_2[4]. The magnetic moment in the ground state is determined as about $8\mu_B$, which is well consistent with the saturation magnetisation at 1.5 K.

Fig.1(b) indicates the pattern in the intermediate state between T_N and T_t. Apparent satellite peaks were observed. The propagation vector is determined as k=[1+δ,δ,0] where δ=0.12. This means that the structure in the intermediated state is based on the AFQ coupling with k=[100] which is the same as that in the ground state. Anti-phase domain structure based on k=[100] AFM structure is hardly accepted as a origin of the satellite peaks because of intensity estimation of higher order satellite peaks by anti-phase domain structure within experimental error of neutron powder diffraction experiments. Thus, in spite of well locarised 4f state, the magnetic structure in the intermediated state of ErB_2C_2 may be a long period one with magnetic moments parallel to [001] direction. For discussion of the magnetic structure in the intermediate state, however, neutron diffraction experiments with a single crystal sample are seriously needed.

References

[1] T. Onimaret al.: J. Phys. Soc. Jpn. 68(1999) 2287.
[2] H. Yamauchi et al. J. Phys. Soc. Jpn 68 (1999) 205.7
[3] H. Onodera et al.: J. Phys. Soc. Jpn. 68(1999) 2526.
[4]K. Ohoyama et al.: J. Phys. Soc. Jpn. 69(2000) in press

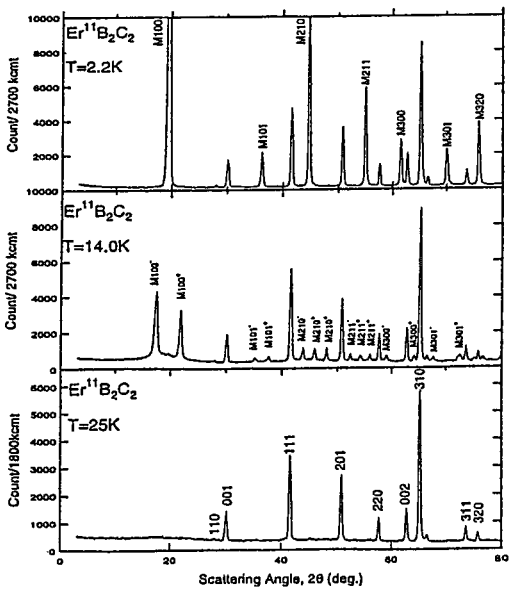

Fig.1 Powder patterns of the antiferroquadrup ordering compound $Ho^{11}B_2C_2$. at (a)1.4K (<T, (b)5.3K(T_0<T<T_N) (c)9.2K(>T_N)

JRR-3M,HERMES(T 1-3) 2:Magnetism

研究テーマ：$Tb^{11}B_2C_2$および$Ho^{11}B_2C_2$における四重極相互作用と磁気構造
表題：正方晶化合物$Ho^{11}B_2C_2$における反強四重極秩序による特異な磁気構造

1-2-71
Characteristic magnetic structure due to antiferroquadrupole ordering in the tetragonal compound $Ho^{11}B_2C_2$

K. Ohoyama, H. Yamauchi, A. Tobo, H. Onodera, Y. Yamaguchi,

Institute for Materials Research, Tohoku University, Sendai 980-8577

Recently, Yamauchi et al. found that DyB_2C_2 with the tetragonal LaB_2C_2 type crystal structure[1] is the first compound which undergoes an antiferroquadrupolar (AFQ) ordering among tetragonal compounds with well-localised 4f states[2]. DyB_2C_2 undergoes the AFQ ordering at T_Q=24.7K and a further transition to an antiferromagnetic (AFM) state with a weak ferromagnetic component at T_N =15.3K[2]. It should be pointed out that T_Q of DyB_2C_2 is nearly ten times higher than those in other AFQ compounds. Moreover, HoB_2C_2 shows a complicated phase diagram which indicates the existence of a AFQ ordered state below the magnetic ordering temperature[3].

This work aims of determining detailed magnetic structures of $Ho_{11}B_2C_2$ by neutron powder diffraction technique on HERMES. Natural boron was replaced by ^{11}B isotope to minimise the absorption effect.

Figs.1 show powder patterns of $Ho^{11}B_2C_2$ at (a)1.4K($<T_Q$), (b)5.3K($T_Q<T<T_N$) and (c)9.2K($>T_N$). As shown in Fig.1(a), we observed magnetic Bragg reflections with propagation vectors k_1=[100], k_2=[011/2], k_3=[001/2]. These reflections indicate that the ground state of HoB_2C_2 shows a characteristic magnetic structure which is basically the same as the other tetragonal antiferroquadrupole ordering compound DyB_2C_2, which is caused by competitive coexistence of AFQ and AFM interactions. The angle between adjacent magnetic moments along [001] is slightly smaller than that of DyB_2C_2. This means that ferromagnetic coupling along[001] is relatively dominant in comparison with the case of DyB_2C_2.

Moreover, magnetic satellite peaks at 5.3K in Fig.1(b) mean the intermediate phase between T_Q and T_N exhibits a long period magnetic structure. The propagation vector is determined as k=[1+d,d,d'] within experimental error of powder diffraction. It should be emphasise that the long period structure is based on the [100] AFM coupling which is the same as those in the ordered states of other isostructural compounds[3]. Because of broadness of the magnetic satellite peaks, the intermediate phase is a short range ordering state. The results of the experiments indicate that the AFQ ordering in HoB_2C_2 is quite rare case which is realised in the magnetic ordered state. Detail results of this work are reported in elsewhere[4].

References

[1] T. Onimaret al.: J. Phys. Soc. Jpn. 68(1999) 2287.
[2] H. Yamauchi et al. J. Phys. Soc. Jpn 68 (1999) 2057
[3] K. Ohoyama et al.: J. Phys. Soc. Jpn. 69(2000) in press
[4] K. Ohoyama et al.:submitted to J. Phys. Soc. Jpn.

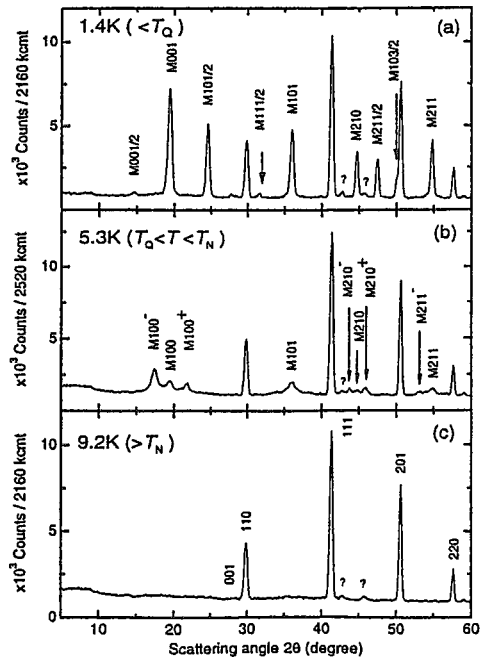

Fig.1 Powder patterns of th antiferroquadrupole ordering compound $Ho^{11}B_2C$ at (a)1.4K ($<T_Q$) , (b)5.3K($T_Q<T<T_N$) (c)9.2K($>T_N$) o HERMES

JRR-3M, HERMES(T-13), 2:Magnetism

研究テーマ：希土類ーイリジウム複合酸化物の磁気構造
表題：イリジウムペロブスカイト Sr_2LnIrO_6(Ln=Ce,Tb)の磁気構造

1-2-72 Magnetic Structure of Iridium(IV) Perovskites Sr_2LnIrO_6(Ln=Ce,Tb)

Daijitsu Harada, Makoto Wakeshima, Yukio Hinatsu, Kenji Ohoyama[1] and Yasuo Yamaguchi[1]

Division of Chemistry, Graduate School of Science, Hokkaido University, Sapporo 060-0810, Japan
[1]Institute for Materials Research, Tohoku University, Sendai 980-8577, Japan

We have reported crystal structures and magnetic properties of iridium perovskites Sr_2CeIrO_6 and Sr_2TbIrO_6. From their magnetic susceptibility measurements, Sr_2CeIrO_6 and Sr_2TbIrO_6 show the antiferromagntic transition at 21K and 51K, respectively. In addition to the magnetic transition at 51K, Sr_2TbIrO_6 shows another anomaly at 27K in its magnetic susceptibility vs temperature curve.

To elucidate their magnetic structures in the antiferromagentic state, we have performed powder neutron diffraction measurements for both the compounds by HERMES of the Institute for Materials Research, Tohoku University, installed at the JRR-3M reactor at wavelength of 1.819Å at 2K, 28K, and 60K.

All the diffraction peaks of Sr_2TbIrO_6 measured at 60K can be indexed in a monoclinic unit cell with space group $P2_1/n$ and the Ln^{4+} and Ir^{4+} ions are structurally ordered at the B sites of the ABO_3 perovskite-type structure. In the profiles measured at 28K and at 2K, magnetic Bragg reflections in addition to the nuclear Bragg reflections appear (see Fig.1). These magnetic Bragg peaks are only due to the alignment of the Tb^{4+} ions. The magnetic Bragg peaks indicates that the magnetic moments are aligned almost along c-axis, and that the magnetic structure is of the type I (Fig. 2). The ordered magnetic moments at 28K and at 2K are calculated to be 4.94μ_B and 6.60 μ_B, respectively. The saturated magnetic moment for the Tb^{4+} ion ($4f^7$) is 7.0 μ_B. For Sr_2CeIrO_6 no difference between the neutron diffraction profiles measured at 2K and at 28K was observed. We consider that this is due to the very small magnetic moment of Ir^{4+} ion which is the only magnetic ion in this Sr_2CeIrO_6, which is the same as the case of Sr_2TbIrO_6.

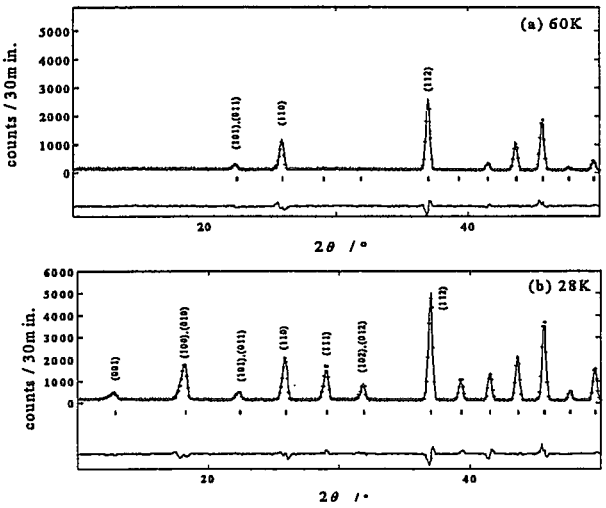

Fig.1 Neutron diffraction profiles for Sr_2TbIrO_6 at (a)60K and (b)28K.

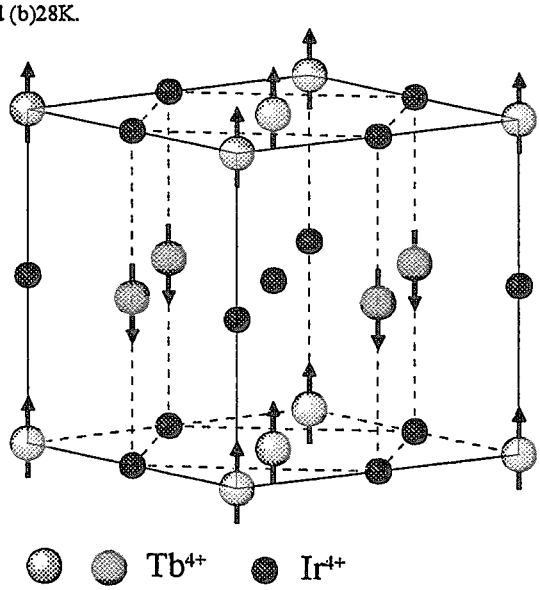

Fig.2 The Type I magnetic structure of Sr_2TbIrO_6. Only terbium and iridium ions are depicted.

原子炉：JRR-3M　　装置：HERMES　　分野：2. Magnetism

研究テーマ：反強四極子秩序化合物$Dy^{11}B_2C_2$における中性子回折
表題：反強四極子秩序化合物$Dy^{11}B_2C_2$の磁気構造

1-2-73
Magnetic structure in the antifferoquadrupolar ordering compound $Dy^{11}B_2C_2$

K. Ohoyama, H. Yamauchi, A. Tobo, H. Onodera, Y. Yamaguchi,

Institute for Materials Research, Tohoku University, Sendai 980-8577

DyB_2C_2 with the tetragonal LaB_2C_2 type crystal structure[1] undergoes an antiferroquadrupolar (AFQ) ordering at T_Q=24.7K and a further transition to a antiferromagnetic (AFM) ordered state at 15.3K[2]. It should be pointed out that T_Q of DyB_2C_2 is nearly ten times higher than those of other AFQ ordering materials. From the experimental point of view, the AFQ ordering was confirmed from the characteristic magnetic structure in the ground state which is caused by effects of competitive coexistence of AFQ and AFM interactions; the magnetic moments which lie in the c-plane are fixed to be perpendicular to those of adjacent Dy atoms along the [001] direction, and are canted from the [110] direction to the [100] direction in the c-plane by a canting angle of 28°[2]. The conclusion was, however, obtained from the data of neutron powder diffraction experiments of DyB_2C_2 on HERMES. Since absorption effect of DyB_2C_2 was seriously strong, quality of the data was not very high. This work aims, therefore, of determining detailed magnetic structures of DyB_2C_2 from powder patterns of $Dy^{11}B_2C_2$. Natural boron was replaced by ^{11}B isotope to minimise the absorption effect.

Figs.1 show powder patterns of polycrystalline samples of $Dy^{11}B_2C_2$ on Kinken powder diffractometer HERMES(T1-3) at JRR-3M. As shown in Fig.1(a), some magnetic peaks denoted with M were observed. These magnetic Bragg reflections can be indexed with propagation vectors k_1=[100], k_2=[011/2], k_3=[001/2]. k=[000] type reflections are not observed because of strong nuclear Bragg peaks. Results of Rietveld refinement analysis by means of FullProf, we can conclude that the magnetic structure is basically consistent with that in ref.[2]. The angle between adjacent magnetic moments along [001], however, was determined as about 75° instead of 90° from the data in Fig.1. Consequently, the magnetic structure of DyB_2C_2 has lower symmetry than that reported in ref.2 which has two. It should be pointed out that the angle between adjacent magnetic moments along [001] indicates that the coupling along [001] is mainly ferromagnetic one with k=[100]. In fact, some isostructural compounds RB_2C_2 show a simple antiferromagnetic structure with a propagation vector of k=[100][3]. Therefore, we can concluded that the characteristic magnetic structure in the ground state of the AFQ compound is mainly caused by the AFM. structure with k=[100] which is strongly affected by the AFQ ordering.

References

[1] T. Onimaret al.: J. Phys. Soc. Jpn. 68(1999) 2287.
[2] H. Yamauchi et al. J. Phys. Soc. Jpn 68 (1999) 2057
[3]K. Ohoyama et al.: J. Phys. Soc. Jpn. 69(2000) in press

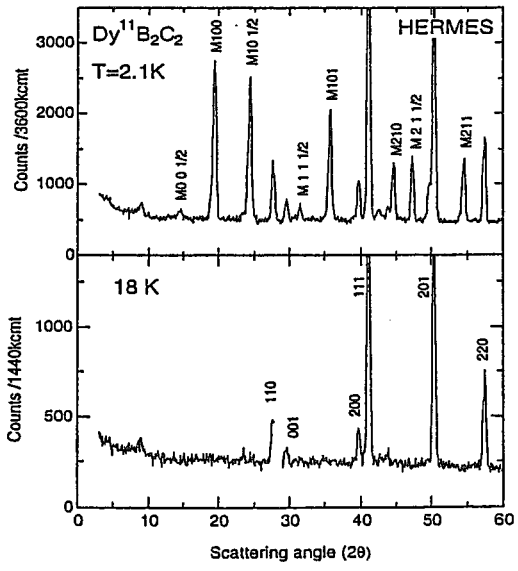

Fig.1 Powder patterns of the antiferroquadrupole ordering compound $Dy^{11}B_2C_2$ at 2.1K ($<T_N$) and 18K($>T_N$). Letters M denote magnetic Bragg reflections.

JRR-3M,HERMES(T 1-3) 2:Magnetism

研究テーマ：$Dy_{1-x}Y_x{}^{11}B_2C_2$における反強四重極と反強磁性相互作用の競合と磁気構造
表題：DyB_2C_2の反強四重極秩序における Y 希釈の効果

1-2-74

Y Dilution Effect on Antiferroquadrupolar Ordering in DyB_2C_2

A. Tobo, S. Sako, H. Onodera, H. Yamauchi, K. Indoh, K. Ohoyama and Y. Yamaguchi

Institute for Materials Research, Tohoku University, Sendai, 980-8577 Japan

The systems showing both of an antiferroquadrupolar (AFQ) ordering and an antiferromagnetic (AFM) ordering have been attracting many interests because of their complicated magnetic behavior. DyB_2C_2 is one of those materials, which crystallize in the tetragonal LaB_2C_2-type structure (the space group P4/mbm).[1, 2] In order to investigate the nature of AFQ ordering, we try changing the strength of interactions in DyB_2C_2 by substituting nonmagnetic Y^{3+} ion for Dy^{3+} ion. The transition temperatures of $Dy_{1-x}Y_xB_2C_2$ have been investigated by magnetization and specific heat measurements.[3] As the Y concentration increases, the magnetic transition temperature decreases from 15.3 K at x=0 to 4.5 K at x=0.6. The AFQ transition temperature also decreases from 24.7 K at x=0 to 7.4 K at x=0.6. In this report, we show the results of neutron powder diffraction measurements of $Dy_{1-x}Y_xB_2C_2$.

Neutron powder diffraction experiments were performed using the high efficiency and resolution powder diffractometer (HERMES) installed at JRR-3M in Japan Atomic Energy Research Institute. For the measurements, we prepared the powder sample using 99.5 % enriched ^{11}B, since the natural B atoms strongly absorb neutrons.

In fig. 1, we show the neutron powder diffraction patterns of $Dy_{1-x}Y_xB_2C_2$ at zero field. Each diffraction pattern was measured at the temperature well below the transition temperatures. The magnetic reflections are clearly observed where they are denoted by the letter M. From these reflection patterns, we consider that the basic magnetic structure of all the sample shown here can be described by

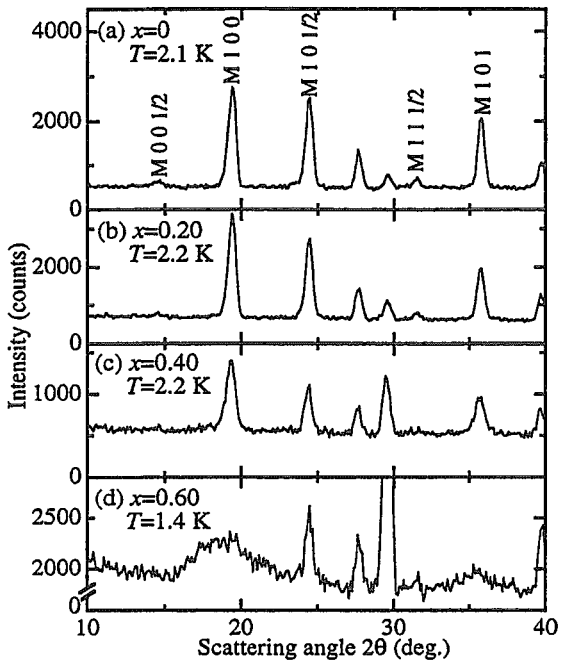

Fig. 1. Neutron powder diffraction patterns of $Dy_{1-x}Y_xB_2C_2$ at zero field.

two propagation vectors of k_1=[1 0 0] and k_2=[0 1 1/2] as in the case of DyB_2C_2. The magnetic 1 0 0 and 1 0 1 reflections become broad as the Y concentration x increases, although the width of the magnetic 1 0 1/2 and 1 1 1/2 reflections are almost independent of x. It implies that the magnetic moments between c-plains maintain antiferromagnetic periodicity fairly well, but that the periodicity of antiferromagnetic coupling in the c-plain easily disturbed by the Y dilution. In order to investigate the dilution effect on the magnetic structure further, neutron diffraction measurements on the single crystal samples are needed.

[1] H. Yamauchi et al.,J. Phys. Soc. Jpn. 68 (1999) 2057.
[2] T. Onimaru et al., J. Phys. Soc. Jpn. 68 (1999) 2287.
[3] S. Sako et al., J. Phys. Soc. Jpn., in press.

JRR-3M, HERMES (T1-3), 2 magnetism

研究テーマ：構造を持つ一次元量子スピン系の磁性
表題：一次元量子フェリ磁性体$Sr_3Cu_3(PO_4)_4$の中性子回折

1-2-75 Neutron Diffraction on 1D Quantum Ferrimagnet, $Sr_3Cu_3(PO_4)_4$

Y. Ajiro, T. Asano, M. Yoshihara, K. Ohayama[1], Y. Yamaguchi[1], Y. Koike[2], Y. Morii[2]

Department of Physics, Kyushu University, Fukuoka 812-8581, Japan
[1]*Insutitute for Materials Research, Tohoku University, Sendai 980-8577, Japan*
[2]*Advanced Science Research Center, JAERI, Tokai 319-1195, Japan*

Quantum antiferromagnetism in low dimensional systems has been a subject of intense study in recent years. Much of the recent interest in this field has been focused on the magnetic properties of generalized (not regular and non-uniform) one-dimensional magnets with peculiar topologies of the exchange pathways, giving rise to interesting quantum and spin frustration effects.

The crystal structure of $A_3Cu_3(PO_4)_4$ with A = Ca, Sr is monoclinic and the metal network is characterized by intertwining double chains of Cu(II) ions as shown in Fig. 1(a) [1]. As a result, the system may be viewed as S = 1/2 zig-zag chains of triangular units with relevant exchange interactions J_1, J_2 and J_3 by focusing on the metal ions and bridging oxygen network, as sketched in Fig. 1(b). For instance, a highly frustrated situation occurs due to competing exchange interactions in the triangular units of the chain. Interesting enough, it is known that the system is characterized by a 1D ferrimagnet due to peculiar topologies, although only one kind of metal is involved and all the couplings are antiferromagnetic. Magnetic susceptibility measurements, reported by Drillon *et al.* [2], show the clear signature of 1D ferrimagnets,

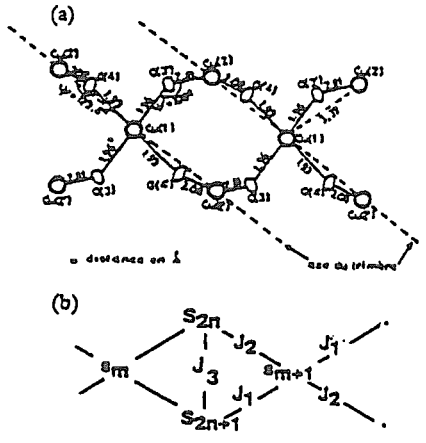

Fig. 1 (a) Metal network characterized by intertwining double chains of Cu(II) ions. (b) Relevant exchange pathways denoted by J_1, J_2 and J_3.

i.e. a characteristic minimum of χT around 25 K and a strong divergence upon cooling down. At very low temperature, $Ca_3Cu_3(PO_4)_4$ orders ferromagnetically at T_C = 0.8 K, while $Sr_3Cu_3(PO_4)_4$ exhibits an antiferromagnetic ordering at T_N = 0.9 K, due to the effect of inevitable interchain interactions. In order to interpret the susceptibility results, Drillon *et al.* have proposed the interesting 1D ferrimagnetic model based on the antiferromagnetically coupled trimers (the largest interaction being J_1).

High field magnetization for $Sr_3Cu_3(PO_4)_4$ and $Ca_3Cu_3(PO_4)_4$ increases steeply and saturates around 20 T for Sr-compound and around 10 T for Ca-compound, respectively [3]. It should be noted that the absolute value of 0.35 μ_B/Cu^{2+} for the saturated magnetization is far from the expected of 1.15 μ_B for S = 1/2 and g = 2.3 but just 1/3 of the fully aligned ferromagnetic state. The observed saturated state, therefore, should be regarded as an intermediate quantum state with a so-called 1/3 magnetization plateau. Unfortunately, the fully aligned ferromagnetic state is not able to observe in our available field up to 40 T but the observation of the fully saturated state is our future challenging task for more intense magnetic field.

Neutron diffraction was performed on powder samples of $Sr_3Cu_3(PO_4)_4$ at 3.5 K above T_N and 70 mK well below T_N = 0.9 K, using the Kinken powder neutron diffractometer HERMES for high efficiency and high resolution measurements installed at the T1-3 beam port of JRR-3M, JAERI, Tokai. This multi-detector system has a large solid angle of detectors of 0.13 sr and gives quite high counting efficiency. Instrumental details of HERMES is given in Ref. [4]. Figure 2 shows a powder pattern of $Sr_3Cu_3(PO_4)_4$ at 3.5 K above T_N and at 70 mK well below T_N = 0.9 K at low-angles up to 2θ = 60°. Observed powder pattern above T_N was best fitted by Rietveld refinement procedure by means of RIETAIN-97β. Since we used accurate positional parameters of the heavy atoms determined by X-ray diffraction as the initial values of the fitting procedure, we were able to obtain quite good results of Rietveld analysis, although almost all of the peaks are overlapped in the pattern. (There exist about 1000 Bragg peaks.) This result indicates that it is possible to refine rather complicated structures with low symmetry using HERMES, when

JRR-3M, HERMES, 2.Magnetism

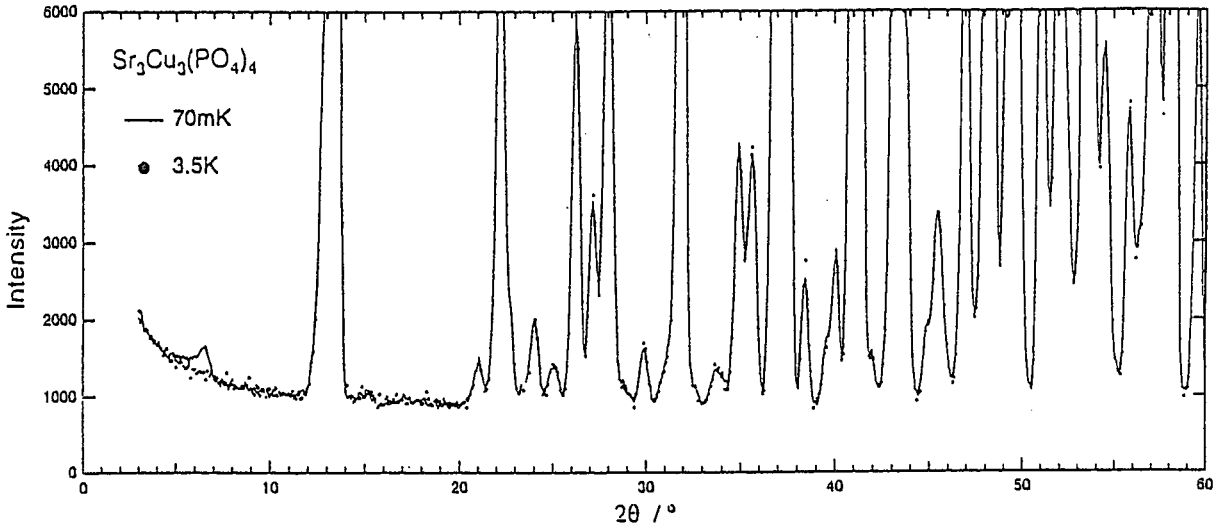

Fig. 2 Neutron diffraction patterns of $Sr_3Cu_3(PO_4)_4$ at 70 mK and 3.5 K.

reliable initial values are given, as has been noticed already by Ohoyama [5]. Very few magnetic peaks are observed around $2\theta \approx 7.5°$. However, it is not easy to give their indices. The magnetic structure is considered to be not so simple from the fact that the intensity of the magnetic peaks are very weak, compared with those of the nuclear peaks. From the present work, we were not able to deduce a meaningful result of ordered magnetic structure below T_N. Detailed investigations are necessary in order to determine the magnetic structure and the magnitude of the magnetic moment.

We thank to H. Aruga-Katori, K. Kamishima and T. Goto at ISSP and K. Nakaya and M. Mekata at Fukui University for their collaboration on magnetization measurements. This work was partly supported by a Grand-in-Aid for Science Research from the Japanese Ministry of Education, Science, Sport and Culture.

[1] J.B. Anderson *et al.*, J. Solid State Chem. 39 (1981) 29.
[2] M. Drillon *et al.*, J. Appl. Phys. 63 (1988) 3551.
[3] Y. Ajiro *et al.*, unpublished.
[4] K. Ohoyama *et al.*, Jpn. J. Appl. Phys. 37 (1998) 3319.
[5] K. Ohoyama, Activity Report on Neutron Scattering Research 6 (1999) 30.

研究テーマ：AV_6O_{11}(A=Na,Sr,Pb,K)化合物の中性子回折による磁気構造の研究
表題：SrV_6O_{11}化合物の粉末中性子回折

1-2-76 Powder neutron diffraction study of SrV_6O_{11}

Y. Hata, E. Kita, K.Ohoyama[1] and Y. Kanke[2]

Institute of Applied Physics, University of Tsukuba, Tsukuba 305-8573, Japan
[1]Institute for Materials Research, Tohoku University, Sendai 980-8577, Japan
[2]National Institute for Research in Inorganic Materials, Tsukuba, Ibaraki 305-0044, JAPAN

A series of AV_6O_{11} (A=Na, K, Pb, Sr, Ba) compound systems is known as mixed valence compounds and is intensively studied in a research group of NIRIM. The structure of AV_6O_{11} is close related to a magnetoplumbite structure and consists of only R-blocks of this structure. Vanadium sites are categorized in three octahedral V(1), two octahedral V(2) and one trigonal-bypyramidal V(3) sites. The V(1) sites form hexagonal Kagome lattices. In the SrV_6O_{11} case, metal-insulator transition takes place at 80 K and antiferromagnetic order is established below the same temperature. Details of magnetic structures are unknown for these compounds.

In order to investigate structure and magnetic properties, powder neutron scattering study was carried out on SrV_6O_{11}. Poly-crystalline SrV_6O_{11} samples were prepared with a solid reaction technique.

Powder neutron diffraction (ND) studies were employed with a high-resolution powder ND spectrometer (HERMES) installed at beam line T1-3 in the JAERI JRR-3. The wave length was 1.82 Å and sample temperature was changed between room temperature and 2.2 K. Data were analyzed with a Rietvelt fitting program, Rietan97 β.

Figure 1 shows temperature dependence of ND patterns of SrV_6O_{11}. In the patterns, major strong peaks did not change in peak height and position, however some weak peaks became stronger or appeared clearly when the sample was cooled down from room temperature to 50 K. Corresponding peaks are depicted by bold typed indices, for instance (1,0,2) and (0,0,4), in the figure. These satisfy the extinction role of room symmetry, $P6_3mc$ and can be seen even at high angles above 100 deg. From this result, these changes are considered to originate in the transition related to the structure. The other extra peak appeared at lower angle around 4° and the peak position is coincident with the (0,0,1/2) reflection. No more peaks with half integer indices were observed in the pattern and then this peak is possibly due to the magnetic origin. From the preliminary small angle XRD study, the corresponding reflection was not detected at 15 K. This result suggests the presence of change in magnetic structure between 50K and 2.2.K.

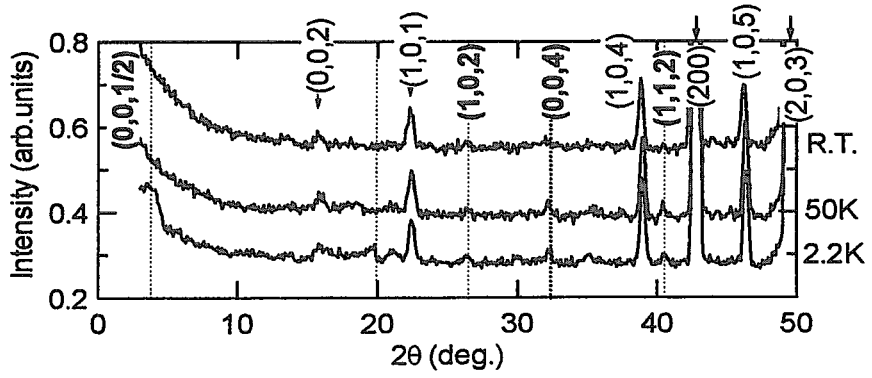

Fig.1 Temperature variation of powder neutron diffraction patterns of SrV_6O_{11}

JRR-3M, HERMES, 2. Magnetism

研究テーマ：中性子回折による新規な層状遷移金属オキシ硫化物の磁気構造の研究
表題：中性子回折による新規な層状遷移金属オキシ硫化物の磁気構造の研究

1-2-77

Study of Magnetic Structure in Novel Layered Transition-Metal Oxysulfide by Neutron Diffraction Technique

M. Matoba[1], K. Ohoyama[2], S. Soyano[1], S. Fukumoto[1], and Y. Yamaguchi[2]

[1]*Faculty of Science and Technology, Keio University*
3-14-1 Hiyoshi, Yokohama 223-8522, Japan
[2]*Institute for Materials Research, Tohoku University*
2-1-1 Katahira, Sendai 980-8577,

Layered transition-metal oxysulfide $Sr_2Cu_2CoO_2S_2$ crystallizes in an unusual intergrowth structure with alternating square-planar CoO_2 sheets and anti-PbO type Cu_2S_2 layers (space group *I/4mmm*)[1-3], as schematically depicted in Fig.1.

The novel layered oxysulfide is an antiferromagnetic semiconductor with magnetic anomalies and exhibits a spin-glass like behaviour at low temperatures[1]. At low spin-freezing temperatures, the long time decay of the magnetization are observed and it can be well described by the typical stretched exponential form.[4]

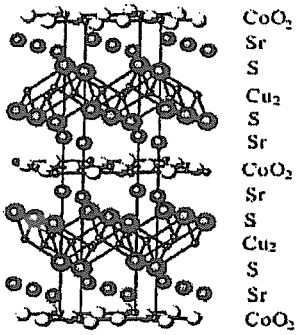

Fig.1 Crystal structure of $Sr_2Cu_2CoO_2S_2$. Outline shows the crystallographic unit cell. The layers are indentified on the side of figure.

In this study, we have measured neutron powder diffraction (NPD) patterns for $Sr_2Cu_2CoO_2S_2$ at various temperatures in order to reveal the unknown magnetic structure of novel layered cobalt oxysulfide $Sr_2Cu_2CoO_2S_2$. The polycrystalline sample was prepared in an evacuated quartz tube containing pellets with appropriate mixture of SrS, Co, Cu, and CuO at 825℃ for 2 days.[3]

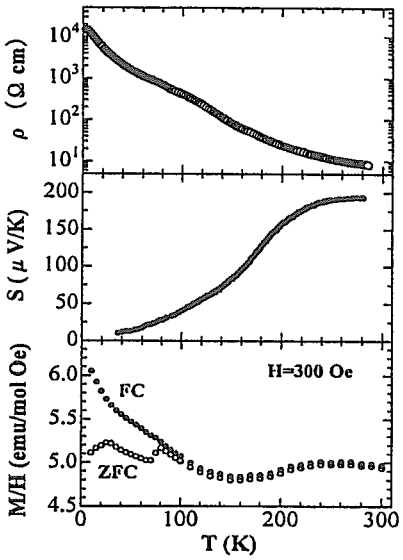

Fig.2 Temperature dependence of electrical resistivity, thermopower, and field-cooled (FC) and zero-field-cooled (ZFC) magnetic susceptivilities of $Sr_2Cu_2CoO_2S_2$.

Obtained black samples were characterized as shown in Fig.2. The magnetic behavior of $Sr_2Cu_2CoO_2S_2$ above 80K is similar to that of La_2CuO_4[5] which also shows successive antiferromagnetic transitions. The NPD patterns were obtained with Kinken powder diffractometer[6] for high efficiency and high resolution measurements (HERMES) installed at the T1-3 beam hole of the guide hall at the Japan Research Reactor 3M (JRR-3M) in Japan Atomic Energy Research Institute (JAERI). Neutrons with wave length 1.819 Å were obtained by the (331) reflection of Germanium monochromater, and a combination of 12'－∞－sample－18' collimator. The sample was put into a cylindrical aluminum with a thickness of 60 μ m and a diameter of 15mm and was mounted in a closed cycle refrigerator.

Figure 3 shows the NPD patterns measured at various temperatures (75K-300K). At 75K, below the spin-freezing temperatures, the long time decay of the magnetization are observed.[4] If layered cobalt oxysulfide $Sr_2Cu_2CoO_2S_2$ is a usual spin-glass, one can expect that it have no magnetic reflections peaks in the spin-frozen state. However, magnetic reflections peaks (indexed A and B) are clearly seen. This feature suggests that $Sr_2Cu_2CoO_2S_2$ is an unusual spin-glass in which some component of magnetic moments are only frozen. Furthermore, the A-peak disappears above 190K, while the B-peak disappears above 290K. At this time, we assume that the A and B peaks come from the ordered magnetic moments in the Cu_2S_2 layer and the CoO_2 sheet.

The HERMES experiment below 75K and the Rietveld refinement of NPD patterns are now in progress in order to determine the spin structure of novel layered cobalt oxysulfide $Sr_2Cu_2CoO_2S_2$ at various temperatures.

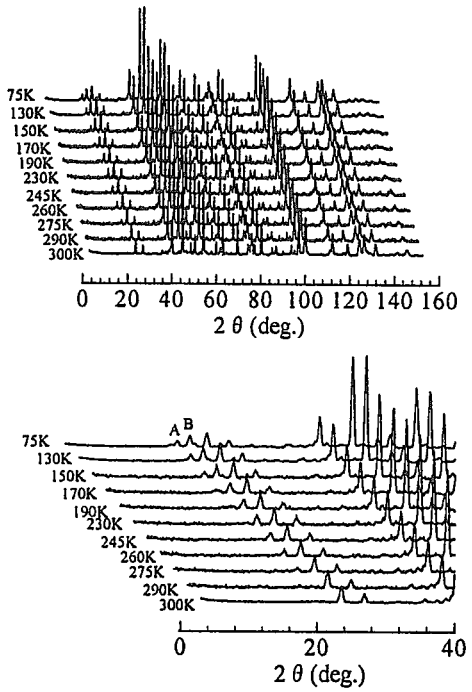

Fig.3 The neutron powder diffraction patterns of $Sr_2Cu_2CoO_2S_2$ at various temperatures (75K-300K).

1) Zhu et al.: J. Am. Chem. Soc. **119** (1997) 12398.
2) H. Kito: J. Crystallogr. Soc. Jpn. **41** (1999) 245 [in Japanese].
3) M.Matoba et al.: Jpn. J. Appl. Phys., in press.
4) M.Matoba et al.: to be submitted.
5) K. Yamada et al.: Phys. Rev. B**39** (1989) 2336.
6) K. Ohoyama et al.: Jpn. J. Appl. Phys. **37** (1998) 3319.

研究テーマ：$Ce_2Fe_{17-x}Al_x$ の磁性と伝導
表題：重い電子系化合物 $Ce_2Fe_{17-x}Al_x$ の磁気相転移

1-2-78
Magnetic Phase transition in Heavy Fermion Compounds $Ce_2Fe_{17-x}Al_x$

K. Konishi, T. Kamimori and H. Tange

Department of Physics, Faculty of Science, Ehime University, Bunkyo-cho, Matsuyama 790-8577, Japan

Cerium-based intermetallic compounds are characteristic representatives for systems with competition between the Kondo and RKKY interactions at low temperatures. Iron-based compounds with rhombohedral Th_2Zn_{17} structure have high saturation magnetization. Recently, many investigations have been performed on the magnetic properties of Ce_2Fe_{17} and its solid solutions, $Ce_2Fe_{17-x}Al_x$ and $Ce_2Fe_{17-x}Si_x$, as permanent ferromagnetic materials [1, 2, 3, 4]. We have previously reported magnetic properties and phase transition of $Ce_2Fe_{17-x}Al_x$ ($x > 7$) as a function of Al content x [5]. Susceptibility and heat capacity studies for $8 \leq x \leq 13$ indicate that two magnetic ordered phases are newly found besides spin-glass phase. The Weiss temperature turns from positive to negative for $x \geq 12$. The number of Fe atoms at each crystallographic site was obtained from neutron diffraction below x=11 at 295K [4]. According to that result, Fe atoms on 6c and 18f site are almost replaced by Al atoms, but Fe atoms of 9d site are in themselves. Because of the preferential site occupation of Al, these compounds for $x \gtrsim 10$ consist of Ce(6c)-Al(6c, 18f) and Fe(9d, 18h)-Al(18h) layers alternatively stacked along c axis. As a continuing part of the investigation of the effect of nonmagnetic substitutional atoms on the microscopic properties of Ce_2Fe_{17} compounds, we perform neutron diffraction measurement at low temperature phases.

The nascent compounds were prepared by inert atmosphere arc melting technique, and remelted several times to ensure homogeneity. After shaved surface of the pellet to remove impurity, the samples were vacuum annealed at 800 $\sim$ 1000 °C for two or more weeks, and were subsequently quenched into water. Their purities and structure were checked by powder X-ray diffraction. Neutron powder diffraction experiments were performed on HERMES of Institute for Materials Research(IMR), Tohoku University, installed at the JRR-3M reactor. The sample was sealed in a vanadium cylinder with helium gas, and mounted at the cold head of a closed cycle He-gas refrigerator.

Unfortunately, we didn't use finely powdered samples, so it is difficult to carry out the Rietvelt-refinements of neutron diffraction data. Analysis of data is in progress.

References

[1] J. M. Coey *et al.*, J. Appl. Phys. **73** (1993) 5430

[2] Y. Janssen *et al.*, Phys. Rev. B **56** (1997) 13716.

[3] D. Vandormael *et al.*, J. Appl. Phys. **81** (1997) 2643.

[4] S. R Mishra *et al.*, J. Appl. Phys. **79** (1996) 3145.

[5] K. Konishi *et al.*, Physica B **284–288** (2000) 1275.

JRR-3M, HERMES, 2.Magnetism

研究テーマ：強相関電子系の中性子散乱による研究
表題：$La_{2-x}Sr_xCuO_4$ x=0.12 における反強磁性秩序の磁場効果

1-2-79

Magnetic Field Effect on the Antiferromagnetic Ordering in $La_{2-x}Sr_xCuO_4$ with x=0.12

M. Sato, S. Katano, K. Yamada[A], T. Suzuki[B,*] and T. Hukase[B]

ASRC, JAERI, Tokai, Ibaraki, 319-1195
[A]Institute for Chemical Research, Kyoto University, Uji, Kyoto, 611-0011
[B]Institute for Materials Research, Tohoku University, Sendai, Miyagi, 980-8577

In the recent studies on the high-T_C superconductor $La_{2-x}Sr_xCuO_4$ (LSCO), it has been discovered that antiferromagentic ordering coexists with the superconductivity in the compounds with x of around 0.12.[1,2] In these compounds, the superconductivity is suppressed, which is related with the "1/8 problem". The relationship between the antiferromagnetic order and the superconductivity is attracting much attention to understand the mechanism of the high-T_C superconductivity. Quite recently, for LSCO with x=0.12, we have grown a sample with T_C=12 K. In this sample, the critical magnetic field H_C of the superconductivity is estimated to be around 8 T. In order to investigate the field-dependence of the antiferromagnetic order in this sample, we carried out neutron diffraction experiments under high magnetic field using Liquid He Free Type 10T Magnet developed by the neutron scattering group of JAERI.

Figure 1 shows the field dependence of the magnetic Bragg peaks around (0.5,0.62,0) and (0.5,0.38,0) at T=4.2 K. As can be seen in this figure, applying filed of 10 T, the integrated intensities of the peaks increase significantly by about 40 % of that under 0 T. This result suggests that the destruction of the superconductivity enhances the antiferromagnetic order.

* Present Address : Department of Physics, Sophia University, 7-1 Kioi-cho, Chiyodaku 102-8554

References

[1] T. Suzuki et al. Phys. Rev. B57,R3229 (1998)

[2] H. Kimura et al. Rhys. Rev. B59, 6517 (1999)

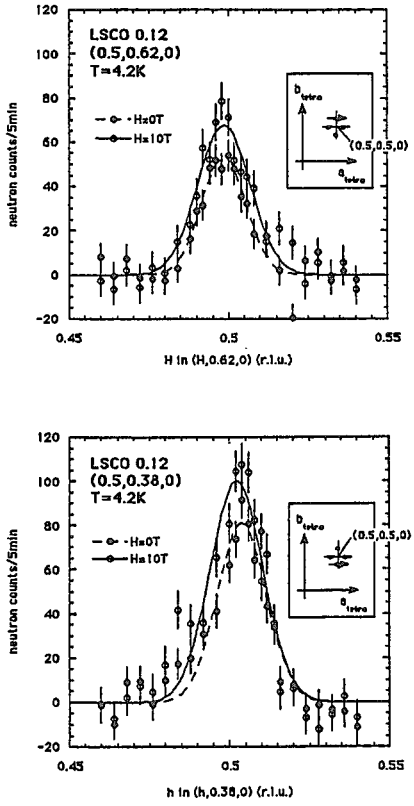

Fig.1 Field dependence of the magnetic Bragg peaks at T=4.2 K.

原子炉：JRR-3M　　装置：TAS-2(T2-4)　　分野：中性子散乱（磁性）

研究テーマ：強相関電子系の中性子散乱による研究
表題：$Sr_2EuCu_2RuO_8$の中性子散乱による研究

1-2-80 Neutron Scattering Study of $Sr_2EuCu_2RuO_8$

T. Mochiku, Y. Matsuoka[1,*], N. Metoki[1], D.P. Hai[2] and K. Kadowaki[2]

National Research Institute for Metals, Tsukuba, Ibaraki 305-0047, Japan
[1]Japan Atomic Energy Research Institute, Tokai, Ibaraki 319-1195, Japan
[2]Institute of Materials Science, University of Tskuba, Tsukuba 305-8573, Japan

Coexistence of ferromagnetism and superconductivity has been discovered in $Sr_2GdCu_2RuO_8$ which has a Curie transition around 135 K and a superconducting transition around 15-40 K [1]. A recent study [2] using a zero-field muon spin rotation experiments shows that this compound is microscopically single phase with no evidence of spatial separation of ferromagnetic and superconducting phases. We report neutron scattering results for a $Sr_2EuCu_2RuO_8$ sample exhibiting a magnetic transition at 135 K and without superconductivity, which compound has the same structure as $Sr_2GdCu_2RuO_8$.

Sample was prepared by the solid state reaction of stoichiometric amount of $SrCO_3$, Eu_2O_3, CuO and RuO_2 powder. Isotope Eu153 with powder form of Eu_2O_3 was used in stead of natural Eu_2O_3, because the natural Eu has strong absorption for neutron. Neutron powder scattering experiments were carried out using a triple-axis spectrometer, TAS-2, installed in the research reactor, JRR-3M at the Japan Atomic Energy Research Institute. Intensity data of 101, 004 and 113 Bragg reflections were collected at room temperature, 150 K, 75 K and 7 K. Fig. 1 shows temperature dependence of 113 Bragg reflection. The intensity increases with decreasing temperature, although we observed no change of the intensity of other reflections within the deviation. More detailed experiments are required to discuss magnetism in this system.

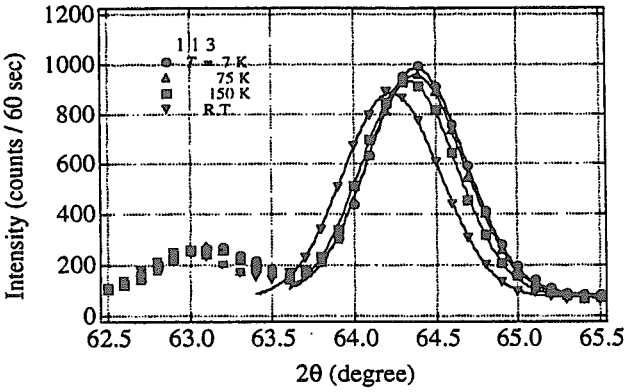

Fig. 1 Temperature dependence of 113 Bragg reflection.

References

[1] J.L. Tallon, C. Bernhard, M.E. Bowden, P.W. Gilberd, T.M. Stoto and D.J. Pringle: IEEE Trans. Appl. Supercond. 9 (1999) 1696.
[2] C. Bernhard, J.L. Tallon, Ch. Niedermayer, Th. Blasius, A. Golnik, E. Brucher, R.K. Kremer, D.R. Noaks, C.E. Stronach and E.J. Ansaldo: Phys. Rev. B 59 (1999) 14099.

* Present address: Nara Women's University, Nara, Nara 630-8506, Japan

原子炉：JRR-3M　　装置：TAS-2(T2-4)　　分野：中性子散乱(磁性)

研究テーマ：二次元スピングラス$K_2Cu_{0.7}Co_{0.3}F_4$のスピン凍結と量子揺らぎ
表題：二次元スピングラス$K_2Cu_{0.7}Co_{0.3}F_4$の中性子散乱による研究

1-2-81

Neutron Scattering Study of the Two-Dimensional Spin Glass $K_2Cu_{0.7}Co_{0.3}F_4$

H. Kadowaki, R. Kajimoto[1], H. Yoshizawa[1] and I. Yamada[2]

Department of Physics, Tokyo Metropolitan University, Hachioji-shi, Tokyo 192-0397
[1]Institute for Solid State Physics, University of Tokyo, Shirakata 106-1, Tokai, Ibaraki 319-1106
[2]Department of Physics, Chiba University, Yayoi-cho, Chiba 260, Japan

Spin freezing process of the two-dimensional Ising spin-glass $K_2Cu_{0.7}Co_{0.3}F_4$ was studied using neutron scattering techniques. This compound is a mixture of the two-dimensional XY ferromagnet K_2CuF_4 with T_C = 6 K and the two-dimensional Ising antiferromagnet K_2CoF_4 with T_N = 110 K, and has been regarded as one of a few archetypal two-dimensional spin-glass systems.

Neutron scattering experiments were performed on the cold-guide triple-axis spectrometer ISSP-HER. The spectrometer was operated with the final energy fixed to 3.1 meV. The vertically and horizontally focusing analyzer were employed. The typical energy resolution with collimations guide-40'-open-open was 0.1 meV (FWHM) at the elastic position.

As temperature is lowered below 80 K, the stronger antiferromagnetic and Ising interactions bring about development of two-dimensional antiferromagnetic short-range-order of spins parallel to the c-axis. Fig. 1 shows a typical scan across the antiferromagnetic ridge at k = (1/2, 1/2, L). The peak intensity of the ridge as a function of temperature is plotted in Fig. 2. The correlation length of this short-range order ceases to increase slightly above the freezing temperature of $T_{f//}$ = 4 K [1], where the magnetic susceptibility shows standard spin-glass freezing behavior. At this temperature range, the majority Cu^{2+} spins with the weak XY-like anisotropy form two-dimensional ferromagnetic short-range-order showing another ridge at k = (1, 0, L). Its peak intensity is shown in Fig. 3. An intriguing point of these spins are that they are substantially canted from the c-axis, which suggests that a certain mechanism such as formation of local non-collinear structure play leading role in the freezing process. It should be noted that the XY component of ferromagnetic short-range-order was shown to freezes at a lower $T_{f\perp}$ = 0.5 K by susceptibility measurements [1]. The spin dynamics of the freezing process are also investigated by the inelastic scattering method.

[1] M. Itoh et al.: J. Phys. Soc. Jpn. 59 (1990) 1792.

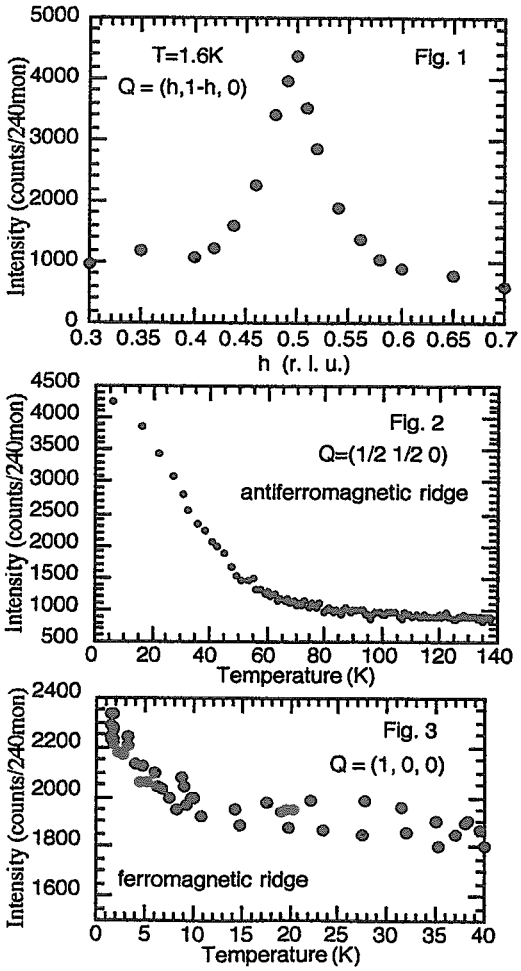

研究テーマ: Zn-Mg-Ho 単準結晶の準弾性散乱
表題: Zn-Mg-RE 系正20面体準結晶の磁気励起

1-2-82
Magnetic excitations in the Zn-Mg-RE icosahedral quasicrystals

T. J. SATO[1], H. TAKAKURA[1], A. P. TSAI[1], H. KADOWAKI[2], and K. SHIBATA[3]
[1]*NRIM and CREST-JST, Tsukuba 305-0047, JAPAN*
[2]*Department of Physics, Tokyo Metropolitan University, Hachioji, JAPAN*
[3]*Institute for Materials Research, Tohoku University, Sendai, JAPAN*

The Zn-Mg-*RE* (*RE*: rare earth) icosahedral quasicrystals have localized $4f$ magnetic moments on the RE sites. Therefore, it provides an opportunity to study magnetism on the quasiperiodic lattice. Recently, we performed neutron scattering experiments, and observed development of short-range spin correlations at low temperatures which were well described by a six-dimensional (6D) modulation vector [1]. Since the 6D spin correlations are quite unique and special to the quasicrystals, it should be very interesting to study their spin dynamics.

In the present study, we have performed neutron inelastic scattering experiments using single-crystalline samples of the Zn-Mg-Ho quasicrystal. Neutron scattering experiments were performed at the triple-axis spectrometer HER installed at JRR-3M, JAERI (Tokai). The spectrometer is operated with the final-energy fixed to 3.1 meV. Since the magnetic scattering peaks are broad in $\boldsymbol{Q}$-space, we used the horizontally-focusing analyzer. The higher harmonics is eliminated by a Be filter.

Typical inelastic scattering spectrum is shown in Fig. 1(a). As seen in the figure, the magnetic scattering consists of a resolution limited elastic peak and a broad possibly-quasielastic peak. Note that the energy scale of the possibly-quasielastic peak is considerably larger than the observed temperature $T \simeq 1.5$ K. It suggests the existence of anomalously large magnetic fluctuations (or some kind of inelastic modes if not quasielastic) at the lowest temperatures in this quasicrystal. The $\boldsymbol{Q}$-dependence of the magnetic scattering are studied by several constant-E scans. Typical results are shown in Fig. 1(b), which are for $E = 0$ meV (elastic) and for $E = 0.8$ meV (peak energy in the constant-$\boldsymbol{Q}$ scan). The elastic scattering shows large $\boldsymbol{Q}$-dependence, confirming the static short range spin correlations reported earlier [1]. On the other hand, the scattering at $E = 0.8$ meV has little $\boldsymbol{Q}$-dependence, indicating that corresponding magnetic fluctuations are rather spatially localized. Further study is apparently necessary to elucidate the nature of the localized fluctuations in the icosahedral quasicrystals.

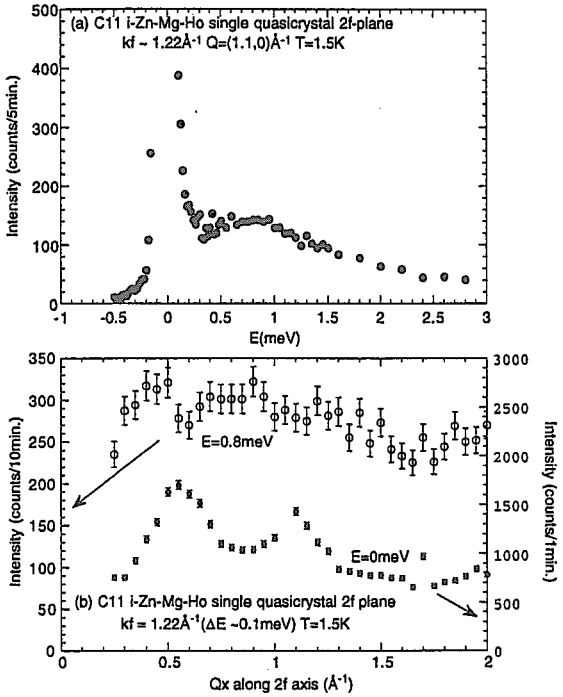

Figure 1: Constant-$\boldsymbol{Q}$ scan at $\boldsymbol{Q} = (1.1, 0)\text{Å}^{-1}$. (b) Constant-$E$ scans at $E = 0$ meV (filled circles) and $E = 0.8$ meV (open circles).

References

[1] T. J. Sato *et al.*, Phys. Rev. Lett 81 (1998) 2364; T. J. Sato *et al.*, Phys. Rev. B61 (2000) 476.

テーマ：スピンギャップ系 $BaVS_3$ 化合物の非弾性散乱
表題：$BaVS_3$ の低エネルギー中性子回折・散乱

1-2-83 Low-energy Neutron Diffraction and Scattering of $BaVS_3$

M. Shiga, H. Nakamura, T. Yamasaki, K. Kojima[1], M. Nishi[2], and K. Kakurai[2]

Department of Materials Science and Engineering, Kyoto University, Kyoto 606-8501 Japan
[1] Department of Superconductivity, The University of Tokyo, Tokyo 113-8656 Japan
[2] Neutron Scattering Laboratory, ISSP, The University of Tokyo, Tokai 319-1106 Japan

Low-energy powder neutron diffraction and scattering experiments of the S = 1/2 triangular lattice system $BaVS_3$, which shows a metal-insulator transition at T_{MI} = 70 K, were performed to investigate magnetic ground-state and excited properties.

The experiments were performed using the triple axis spectrometer ISSP-HER installed at the C1-1 cold-neutron beam port of a reactor JRR-3M. All the measurements were made with a fixed incident energy k_i = 1.55 Å^{-1} (E_i = 5.0 meV, λ_i = 4.05 Å) with a collimation sequence of open-open-80'-80' and with a Be filter before the sample.

Figure 1 shows neutron diffraction pattern of $BaVS_3$ measured at 4 K. Besides nuclear reflections, extra magnetic peaks were found. The observation of magnetic reflections is rather unexpected since it was denied in a previous experiment [1]. However, it is likely that these low-Q peaks were out of the range of measurements in the previous measurement made with thermal neutrons. Assuming ferromagnetic coupling in the c-axis spin chain, the modulation vector is determined as incommensurate (0.226 0.226 0) in the hexagonal index. The ordered moment is roughly estimated as ~ 0.5 μ_B/V.

The static magnetic reflections disappear above T_X = 30 K, which is different from T_{MI} (the maximum of the susceptibility). Interestingly, however, we observed magnetic scattering at finite energy transfer at around the magnetic Bragg points in $T_X < T < T_{MI}$. The scattering shows a continuous Q-ω dispersion, suggesting spin-wave-like excitations with a small gap, i.e., dynamic spin fluctuations with antiferromagnetic correlation. In other words, a spin-liquid-like state, which reduces the macroscopic susceptibility as average, is formed below T_{MI} and condenced into static ordering below T_X.

These anomalous properties may be caused by the charge (or orbital) instability and/or characteristic spin dynamics of geometrically frustrated triangular-lattice chains. The observation of zero-field nuclear resonance signals, which were interpreted as nuclear quadrupole resonance [2], remains to be explained consistently with the present results.

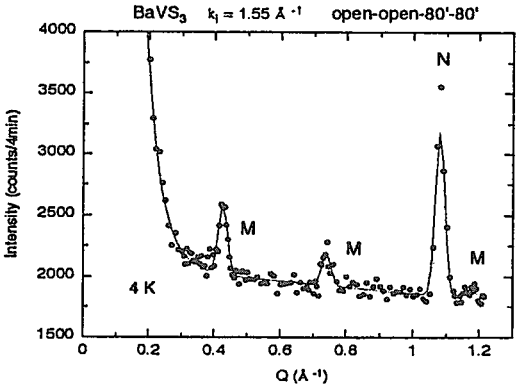

Figure 1 Neutron diffraction pattern of $BaVS_3$ measured at 4 K. N and M mean nuclear and magnetic reflections, respectively.

References

[1] M. Ghedira et al, J. Phys. C 19 (1986) 6489.
[2] H. Nakamura et al, Phys. Rev. Lett. 79 (1997) 3779.

研究テーマ：磁気競合系における磁気的秩序化と励起
表題：三角カゴメ格子における$Cu_9Cl_2(cpa)_6 \cdot nH_2O$磁気秩序と励起

1-2-84

MAGNETIC ORDERING AND EXCITATION IN TRIANGULATED ANTIFERROMAGNET $Cu_9Cl_2(cpa)_6 \cdot nH_2O$

M. Mekata, M. Abdulla, M. Kubota[1] and Y. Oohara[1]

Department of Applied Physics, Fukui University, Bunkyo, Fukui, 910-8507 Japan
[1]Neutron Scattering Laboratory., ISSP, University of Tokyo, Tokai 319-1195, Japan

The Cu^{2+} ions in $Cu_9Cl_2(cpa)_6 \cdot nH_2O$ (H_3cpa : 2-carboxy pentonic acid, $n \approx 41$) form a Kagomé lattice with a smaller triangle in each triangle of Kagomé lattice showing strong frustration. A number of water molecules separate the two- dimensional magnetic planes from each other.

The magnetic susceptibility reveals that the number of the magnetic moments decreases to about 1/3 below 50 K. This is confirmed also by high field magnetization measurements up to 100T. These compounds exhibit no long range order down to 1.5 K, but below 10 K prominent nonlinear susceptibility is observed implying freezing of moments. The partial disappearance of magnetic moments implies that some of Cu^{2+} moments order in each plaquette below 50K [1].

To detect energy gap due to the plaquette ordering, we performed inelastic neutron scattering measurements on powder of $Cu_9Cl_2(cpa)_6 \cdot nH_2O$ and $Cu_9Cl_2(cpa)_6 \cdot nD_2O$ with the 4G spectrometer installed to the JRR3A of JAERI Tokai using unpolarized neutron beams with incident momenta of 2.670Å^{-1} and 3.837Å^{-1}. In spite of the heavy water substitution, sizable incoherent scattering spoils the s/n ratio of the spectrum due to hydrogen atoms in cpa and fine grain size of the specimen in addition to small quantity. Consequently, the measurements were carried out mainly on the light water specimen using a high momentum incident beam.

The q-scan spectrum with zero energy transfer observed at 2K shows no appreciable change from those at higher temperatures indicating the absence of the long range order. We observed a dispersionless inelastic scattering peak with a Lorentzian line shape at 6.5 meV with full width of about 8 meV indicating single site excitation with $E/k_B \approx 70$K. as illustrated in Fig.1. The scattering is hardly observed above 50K and merged into the incoherent quasielastic component.

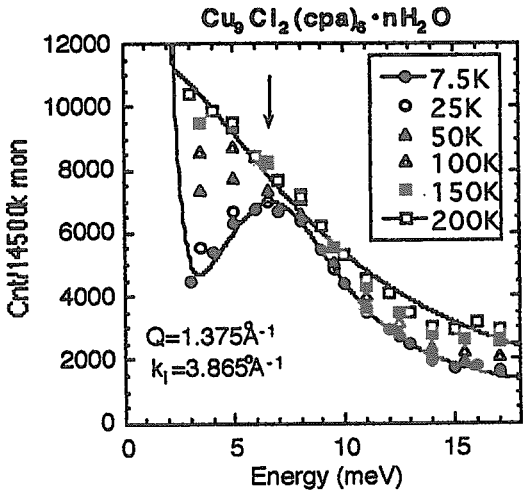

Fig. 1 Temperature dependence of magnetic excitation spectrum.

Evidently this inelastic scattering is associated with a local magnetic excitation and may be attributed to the plaquette ordering at low temperatures. Although singlet formation of each triangle gives a reasonable account for the ordering process, it is not plausible that three moments in a triangular plaquette form a quantum singlet. The model consistent with these experimental results is under investigation.

Reference

[1] M. Mekata et al.: J. Magn. Magn. Mater. 177-181 (1998) 731.

JRR-3M, C1-1, 2. magnetism

研究テーマ：二次元希釈イジング型反強磁性体の臨界散乱における不純物効果
表題：パーコレーションイジング系$Rb_2Co_cMg_{1-c}F_4$における動的臨界現象

1-2-85

Critical Dynamics in Percolating Ising System, $Rb_2Co_cMg_{1-c}F_4$

S.Itoh, Y.Kouchi,[1] S.Ikeda, K.Iwasa,[2] H.Ikeda, M.A.Adams[3] and R.Kajimoto[4]

Neutron Science Laboratory, High Energy Accelerator Research Organization, Tsukuba
[1]The Graduate University for Advanced Studies, Tsukuba
[2]Tokyo Metropolitan University, Hachioji
[3]Rutherford Appleton Laboratory, Didcot, Oxox OX11 0QX, UK
[4]Neutron Scattering Laboratory, ISSP, The University of Tokyo, Tokai

A two-dimensional (2D) antiferromagnet, Rb_2CoF_4, has been reported to be well described by the 2D Ising model, and it has been experimentally confirmed that its critical dynamics obeys the dynamical scaling, $\Gamma=\kappa^z$, where Γ is the damping constant, κ is the inverse correlation length, and z is the dynamical critical exponent [1]. On the other hand, recent theoretical developments have revealed that the critical dynamics in a percolating 2D Ising system does not obey the standard dynamical scaling. It has been reported that $\kappa(T)$ in a percolating system can be described by a power of that in a 1D Ising system,

$$\kappa(T) \sim \exp(-2\nu_p J/T), \qquad (1)$$

with the exchange constant J and the exponent ν_p, because magnetic order propagates through essentially 1D paths in the percolating network [2]. The spin dynamics is determined by thermal activation over energy barriers resulting from the non-uniform geometry of the percolating network, and the damping constant is presented as follows:

$$\Gamma(T) \sim \exp(-2\nu_p J^2/(T^2 \ln b)), \qquad (2)$$

where b is a constant related to the geometrical structure of the percolating network [3]. Thus, $\Gamma(T)$ drops faster than any power of $\kappa(T)$ with decreasing T, or, in terms of the dynamical scaling, the effective dynamical exponent diverges at the critical point.

In order to observe the singular critical dynamics, we performed neutron scattering experiments on $Rb_2Co_cMg_{1-c}F_4$ (c=0.6 and 0.65) of which magnetic concentration c is close to the percolation threshold of the 2D square lattice (c_p=0.593). We measured the energy-integrated scattering function, $S(q)$, above T_N, on the triple-axis spectrometer installed at the C1-1 beam hole at the JRR-3M reactor with E_i=4meV, to determine $\kappa(T)$. The spectrometer was operated with the double-axis mode, and the single-crystal sample was mounted with [100] and [001] in the scattering plane. The scan was performed keeping the 2D reciprocal lattice rod parallel to k_f in order to realize the geometrical condition of the energy-integration at each q. Also, we performed inelastic neutron scattering experiments with high energy resolution on IRIS at ISIS and LAM-80ET at KENS, in order to measure $\Gamma(T)$. The single-crystal sample was mounted with [100] and [010] in the scattering plane, and the inelastic spectrum, $I(E)$, at (100) above T_N was measured with the energy resolution of 4μeV and 6μeV on IRIS and LAM-80ET, respectively. T_N was determined to be 23K and 32K and 45K for the c=0.6 and 0.65 samples,

respectively, by measuring the intensity of the (100) magnetic Bragg reflection. The resolution functions for $S(q)$ and $I(E)$ were measured below T_N at each measurement.

$S(q)$ was well fitted to the correlation function, $(q^2+\kappa^2)^{-1+\eta/2}$, convoluted with the resolution function. It has been reported that the exponent η for $c\geq 0.7$ takes the same value as that in the homogeneous system, $\eta=0.25$ [4]. At present, we obtained $\eta=0.66\pm0.05$ for $c=0.6$ and 0.25 ± 0.10 for $c=0.65$ by the fit, thus we found that η increases drastically toward c_p. $I(E)$ was well fitted to the scattering function, $A/(E^2+\Gamma^2)+B\delta(E)$, convoluted with the resolution function, where the δ-function, $\delta(E)$, represents the elastic incoherent scattering and A and B are adjustable parameters.

As shown in Fig.1, the observed $\kappa(T)$ and $\Gamma(T)$ were well fitted to the functional forms in eqs. (1) and (2). $\kappa(T)$ for $c=0.6$ was almost identical to that for $c=0.65$ except for the T-range near T_N, and ν_p was obtained to be 1.3 by the fit, using the value of $J=7$meV [5]. The value of ν_p well agreed with the theoretical value 4/3 for the 2D square lattice. Using the obtained value of ν_p, b was obtained to be 3.4 ± 0.3 for $c=0.6$ and 2.8 ± 0.6 for $c=0.65$. The fractal dimension (D_f) of the 2D square lattice is 1.896. On the fractal structure composing a pieces of the similar figure which is reduced to $1/b$ of the whole, D_f is defined as $\ln a / \ln b$. An analytical model for the percolating clusters on the 2D square lattice can be described with $a=8$ and $b=3$, and in this case, $D_f=1.893$, thus this model is believed to be a good model for the percolating 2D square lattice. The value of b obtained in the present experiment was very close to $b=3$. In conclusion, at the first time, we demonstrated that the critical dynamics in 2D Ising antiferromagnets, $Rb_2Co_cMg_{1-c}F_4$, with c very close to c_p can be well described by the percolation model.

References

[1] M. T. Hatchings, Phys. Rev. Lett. 49 (1982) 386.

[2] R. A. Cowley et al., Phys. Rev. B 21 (1980) 4038.

[3] C.L.Henley, Phys.Rev.Lett.54(1985)2030.

[4] H.Ikeda, J.Phys.Soc.Jpn. 50 (1981) 3215.

[5] H. Ikeda and K. Ohoyama, Phys. Rev. B 45 (1992) 7484.

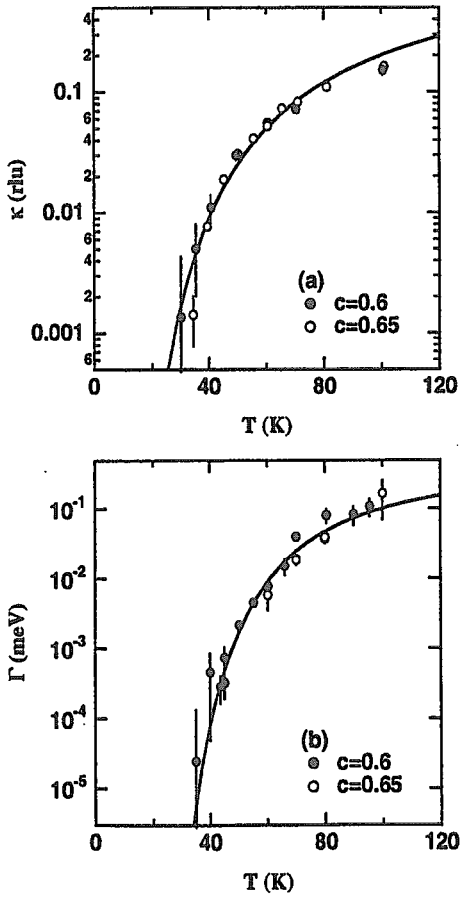

Fig.1 Temperature dependence of the inverse correlation length $\kappa(T)$ (a) and the damping constant $\Gamma(T)$ (b) in $Rb_2Co_cMg_{1-c}F_4$. The solid lines are the fitted curves.

表題：Fe/Cr 人工格子の界面の磁気的な乱れによる中性子非鏡面反射

1-2-86
Off Specular Neutron Reflection from Magnetic Interfacial Roughness in Fe/Cr Multilayers

M. Takeda and Y. Endoh

Physics Department, Graduate School of Science, Tohoku University, Sendai 980-8578, Japan

Atomic disorder at the interface between a ferromagnetic Fe layer and a nonmagnetic Cr one plays an important role in the giant magnetoresistance (GMR) effect of Fe/Cr multilayer. The interfacial roughness is expected to induce the magnetic disorder at the interfaces. Such magnetic disorder is likely to affect on the GMR effect directly because the spin-dependent scattering of conduction electrons at the interface plays an important role in the GMR effect. However, little attention has been paid to such a magnetic disorder. We have done the neutron off specular reflectivity measurements of Fe/Cr multilayers with different interfacial roughness in order to clarify the role of the magnetic disorder in the GMR effect by using HER (C1-1) in JRR3-M.

An epitaxial multilayer of [Fe(3.0 nm)/Cr(1.0 nm)] × 50 on an $Al_2O_3(1\bar{1}02)$ substrate was prepared by a molecular beam epitaxy. The interfacial roughness was changed by annealing time and temperature, as grown, 1 hour at 623 K, 1 hour at 723 K and 7 hours at 723 K in vacuum chamber. The MR ratio, $(\rho\ (0)\ -\rho\ (\mu_0 H >>1))/\rho\ (0)$, of these samples are 11.5%, 9.8%, 7.0% and 0.9 %.

Figures 1(a) shows scan along the direction normal to the sample plane (H) of the sample annealed at 723 K for 7 hours. A peak at $H = 0.5$ is the antiferromagnetic Bragg peak from antiferromagnetic structure of the Fe/Cr bilayer and a peak at 1.0 from the bilayer itself. Figures 1(b) and (c) are the transverse scan, normal to the H direction, at the fixed H of 0.5 and 1.0, respectively. In these figures the direction normal to the H is denoted as K which is the in-plain component of scattering vector. The ridge at $K = 0$ is specular reflection, and intensity at $K \neq 0$ is off specular reflection which indicate the interfacial roughness of the sample. It is noted that the off specular reflection in Fig. 2(c) indicates the magnetic disorder at the interfaces because the peak at $K = 0$ arises

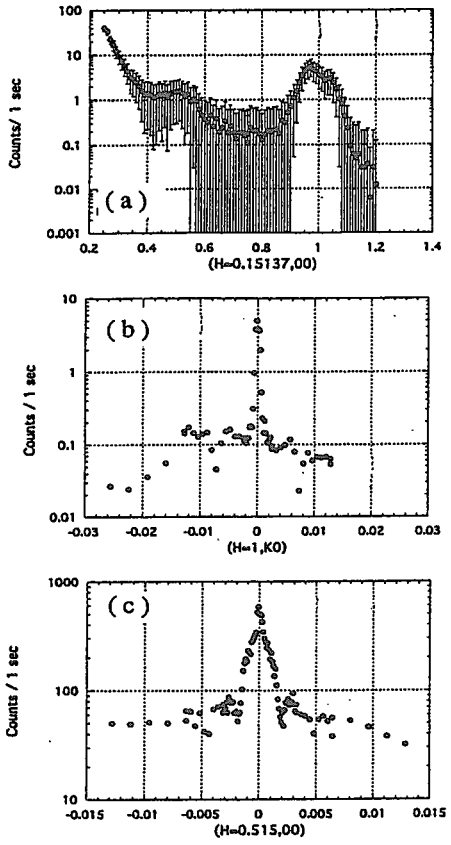

Fig. 1 H scans of Fe/Cr multilayer annealed at 723 K for 7 hours (a) and the transverse scans at H = 1.0 (b) and 0.5 (c).

from the antiferromagnetic structure of Fe/Cr bilayer. These data clearly show that the atomic disorder at the interfaces is different to magnetic disorder. Off specular profile at H = 1.0 is less sensitive to the annealing condition, i.e. the MR ratio. On the other hand, the profile at $H = 0.5$ is strongly affected by the condition, which suggests that the magnetic disorder at the interface plays an important role in the GMR effect. Detailed analysis is currently in progress.

We would like to express our thanks to Dr. A. Kamijo of NEC corp., for sample preparation.

研究テーマ：強相関電子系の中性子散乱による研究
表題：Sr_2FeMoO_6の磁気抵抗効果に関する中性子小角散乱実験

1-2-87

Small-Angle Neutron Scattering Study on Magnetoresistance Effect in Sr_2FeMoO_6

M. Watahiki[1,2], J. Suzuki[1], Y. Tomioka[3]

[1]Advanced Science Research Center, Japan Atomic Energy Research Institute, Tokai-mura, Ibaraki 319-1195, Japan
[2]Japan Science and Technology Corporation, Kawaguchi, Saitama 332-0012, Japan
[3]Joint Research Center for Atom Technology (JRCAT), Tsukuba, Ibaraki 305-8568, Japan

In order to investigate the origin of the negative magnetoresistance (MR) for the layered perovskite Sr_2FeMoO_6, both the single and polycrystalline samples have been studied by small-angle neutron scattering (SANS) under magnetic field. Sr_2FeMoO_6 has been known as a conducting ferrimagnet with a transition temperature T_N of 410 ~ 450 K[1]. It is composed of the ordered perovskites forming alternating Sr-O layer and transition-metal-O layer where Fe^{+3} (spin quantum number S=5/2) and Mo^{+5} (S=1/2) ions order alternately and the respective spins couple anitferromagnetically. Many groups have reported that negative MR effect of polycrystalline sample is larger than that of single crystalline sample. The SANS spectrum give the information on the spatial distribution of ferromagnetic correlation length and grain size with mesoscopic length scale (1 ~ 100 nm). The present study exhibited the difference appearing in SANS spectrum in both systems.

We performed measurements for the single crystalline sample prepared by floating zone-melting method and the polycrystalline sample prepared by solid-state reaction processing. Magnetoresistivity measurements have been performed under magnetic field by conventional four-probe method. The magnetic properties have been investigated by using the dc magnetization measurements. The small-angle scattering (SANS) experiments were performed by SANS-J of the research reactor JRR-3M installed at Japan Atomic Energy Research Institute (JAERI).

Figure 1 shows the temperature dependences of the resistivity $\rho(T)$ for both the samples of Sr_2FeMoO_6. Though the $\rho(T)$ curve for single crystalline sample shows the metallic behavior at zero magnetic field, the $\rho(T)$ curve for polycrystalline sample shows a gradual increase with decreasing temperature and tends to leave a large residual resistance. An application of magnetic fields suppressed the ρ for both the samples below T = 300 K. It is noted that a negative MR effect of polycrystalline sample is an order of magnitude larger than that of single crystalline sample at lowest temperature.

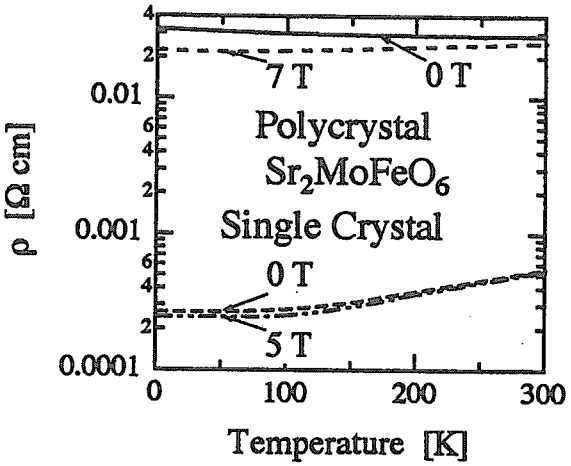

Fig. 1. The temperature dependences of the resistivity $\rho(T)$ for both the samples of Sr_2FeMoO_6.

The SANS profiles at T = 10 K where the negative MR effect was becoming more conspicuous are summarized in Fig.2 for both samples, respectively. In this figure the azimuthally averaged scattering intensities are transferred to the scattering cross-sections per unit volume, $d\Sigma(q)/d\Omega(q)$. It is clearly seen that at zero

magnetic field there are diffused component of $d\Sigma(q)/d\Omega(q)$ in the SANS profile around q = 0.1 nm^{-1}. An application of magnetic field suppressed the diffused component of $d\Sigma(q)/d\Omega(q)$. This diffused scaterring around q = 0.1 nm^{-1} indicates the existence of magnetic domains with the size of several tens nm. An application of external magnetic field forces the ferromagnetic domains to grow into long range order. In the case of single crystalline sample the diffused scattering due to magnetic contribution shifts below q range used in these experiments. In comparison between the resistivity and SANS measurements, we notice that the ρ for both the samples increases with appearance of ferrimagnetic cluster.

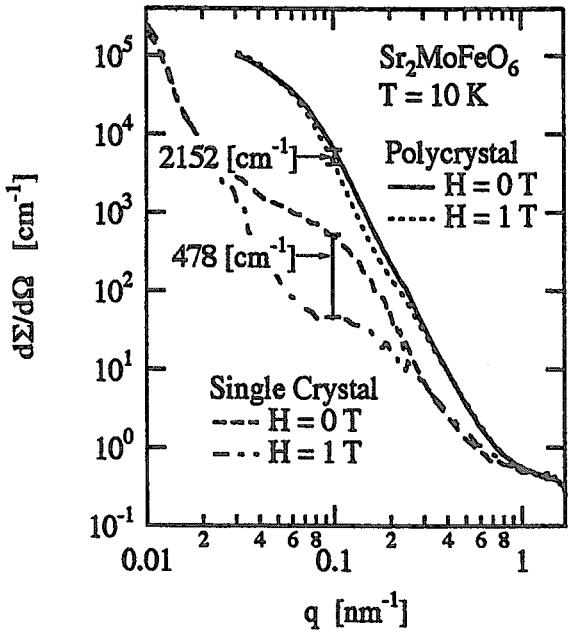

Fig.2. The SANS profiles at T = 10 K are summarized for both the single crystal and polycrystalline samples.

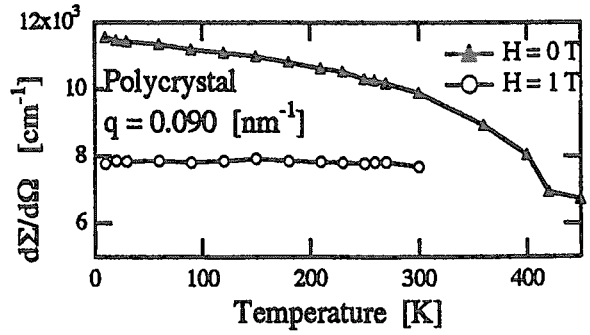

Fig. 3. The temperature dependences of $d\Sigma(q)/d\Omega(q)$ for the polycrystalline sample at q = 0.09 nm^{-1}

Figure 3 shows the temperature dependences of $d\Sigma(q)/d\Omega(q)$ for the polycrystalline sample at q = 0.09 nm^{-1} where the diffuse scattering due to magnetic contribution appeases conspicuously. At zero magnetic field, the $d\Sigma(q)/d\Omega(q)$ rises suddenly at T = 420 K and increased gradually with decreasing temperature. This behavior is consistent with the result that the negative MR effect was becoming more conspicuous on the lower temperature side. This result indicates that the negative MR for both samples are correlated with mesoscopic ferrimagnetic clusters. In the case of polycrystalline samples, we need to take notice of the effect of supplementary scattering from a grain boundary. The $d\Sigma(q)/d\Omega(q)$ for polycrystalline sample is larger than that for single crystalline sample within the q range up to 0.6 nm^{-1} (see Fig.2). It is a specious interpretation that this supplementary component of $d\Sigma(q)/d\Omega(q)$ which appeared in the low-q range is assigned to the scattering from a grain boundary. The grain size in polycrystalline sample is nearly one order of magnitude larger than the size of domains. Though the negative MR effect of polycrystalline sample is larger than that of single crystalline sample, we need to take notice of the influence of grain boundary in the case of polycrystalline sample. The ferrimagnetic domains in the polycrystalline sample grow into long range order comparable with grain size under magnetic field. The number of ferrimagnetic domains influences the negative MR effect. Figure 3 shows the differences between the $d\Sigma(q)/d\Omega(q)$ under H = 0 T and the $d\Sigma(q)/d\Omega(q)$ under H = 1 T at q = 0.09 nm^{-1} for both samples. The differences are proportional to the number of ferrimagnetic domains whose radius is corresponding to several tens nm. This value of polycrystalline sample is five times as large as that of the single crystalline sample. This result is comparable with the result that the negative MR effect of polycrystalline sample is larger than that of single crystalline sample. An application of magnetic field contributed to growing microscopic domains into a large domains, resulting in the suppresses of ρ.

References

[1] K. Kobayashi *et al.*, nature 395 (1998) 677.

研究テーマ：高濃度スピングラスにおけるスローダイナミックスの機構
表題：中性子小角散乱法による高濃度スピングラスのスローダイナミックス研究

1-2-88

SANS Study of Slow Dynamics in Concentrated Spin Glasses

K. Motoya, K. Hioki, J. Suzuki[1]

Department of Physics, Science University of Tokyo, Noda 278-8510 Japan
[1]Japan Atomic Energy Research Institute, Tokai, Ibaraki 319-1195 Japan

Previous neutron scattering studies on $Fe_{65}(Ni_{1-x}Mn_x)_{35}$ and $Cu_2(Mn_{1-x}Ti_x)Al$ alloys showed that magnetic clusters play an important role for the reentrant spin-glass (RSG) transition, and that a wide variety of spin dynamics observed by inelastic neutron scattering studies can be attributed to differences in the size and number of the magnetic clusters.[1-3] Based on these studies, we speculate that the mechanism of slow dynamics might be probed by an observation of the time evolution of the magnetic diffuse scattering arising from magnetic clusters.

Small-angle neutron scattering measurements on two kinds of single crystal alloys, $Fe_{65}(Ni_{0.866}Mn_{0.134})_{35}$ and $Cu_2(Mn_{0.7}Ti_{0.3})Al$ were made utilizing the SANS-J spectrometer. The incident-neutron wave length and band-width are $\lambda = 0.65$nm and $\Delta\lambda/\lambda = 10\%$, respectively. The momentum-transfer range of $0.03 < Q < 2$ nm^{-1} was covered with the sample-detector lengths of 1.35 and 10m. The time-resolved scattering patterns were taken with a time window of 10min. at low temperature RSG phase after being rapidly cooled from the ferromagnetic phase under various magnetic field. The magnetic part of the scattering patterns were well traced by the sum of Lorentzian (LOR) and squared Lorentzian (SQL) functions in the momentum space as

$$I(q) = A_L / (q^2 + \kappa_L^2) + A_S / (q^2 + \kappa_S^2)^2 ,$$

where A_L (A_S) and κ_L (κ_S) are the amplitude and the width (inverse correlation length) for the LOR (SQL) component, respectively. The goal of the present study is to determine the time evolution of these parameters from sequentially taken scattering patterns, and then to construct a real-time image of magnetic clusters. However, the statistics of the present data are not sufficient to definitely determine the time-variations of these parameters. We show in Fig.1 the time-variation of the magnetic scattering intensity from $Fe_{65}(Ni_{0.866}Mn_{0.134})_{35}$ at representative values of q. The measurement was made under the field of 120Oe and the scattering intensity for $q \perp H$ was obtained. The time variation persists up to 20 hours, as was observed in low-field susceptibility measurements. The present observation showed that the sensitivity of the present experimental method satisfies the condition to detect the slow dynamics of RSG. A quantitative analysis together with an improvement of the counting statistics by repetition of same heat cycles is under way.

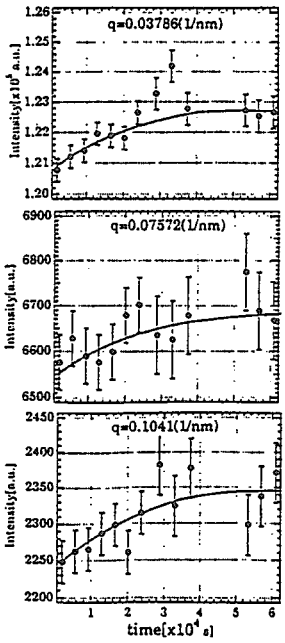

Fig. 1. Time-variation of the magnetic scattering intensity from $Fe_{65}(Ni_{0.866}Mn_{0.134})_{35}$ at representative values of q.

References

[1] K. Motoya and Y. Muraoka: J.Phys. Soc.Jpn. **62** (1993) 2819-2831.
[2] K. Motoya et al.: J.Mag.Mag.Mater. **140-144** (1995) 75-76.
[3] K. Motoya et al.: J.Phys.Soc.Jpn. **68** (1999) 2351-2360.

原子炉：JRR-3M　装置：SANS-J (C3-2)　分野：中性子散乱（磁性）

1. 中性子散乱 3) 超伝導現象

1. Neutron Scattering 3) Superconductivity

This is a blank page.

研究テーマ：電荷秩序相の La_2NiO_4 のスピンダイナミクスの研究
表題：ストライプ相の La_2NiO_4 のスピン波励起

1-3-1 Spin-Wave Excitations in Stripe Phase of La_2NiO_4

K. Nakajima, T. Sawada, H. Yoshizawa, Y. Endoh[1]
NSL-ISSP, University of Tokyo, Tokai, Ibaraki 319-1106 Japan
[1]Institute for Materials Research, Tohoku University, Sendai 980-8577, Japan

Introduced holes in La_2NiO_4 develop long range ordering in a 1D fashion, which is known as a 'hole stripe.' Since a hole stripe has been also found in the cuprate [1], numerous works have been devoted on this issue. Since a hole stripe affects the spin fluctuations in the system, spin dynamics in a stripe phase of La_2MO_4 is of great interest. In this context, we have measured the spin-wave excitations in a stripe phase of La_2NiO_4.

We have prepared single crystals of stripe phase of La_2NiO_4 ($La_2NiO_{4.125}$ (0.5 cm^3), $La_{1.68}Sr_{0.32}NiO_4$ (1 cm^3), $La_{1.65}Sr_{0.35}NiO_4$ (1 cm^3)). Experiments were carried out on GPTAS (4G). Each of crystals was set into a ^{4}He closed cycle refrigerator.

In $La_2NiO_{4.125}$, at low energy region ($\Delta E \leq 10$ meV), well-defined spin-wave excitations at the incommensurate zone center are observed (Fig. 1(a)). Observed spin-wave velocity is consistent to the previously reported result. [2] However, above $\Delta E > 10$ meV, intensity decreases rapidly and we could not observe magnetic signal in the higher energy region (Fig. 1(b)). At the intermediate region, broad excitations, which are considered to be phonon excitations, prohibited to detail inspection of the magnetic excitations at this region. The spin-wave excitations in Sr doped samples, $La_{1.68}Sr_{0.32}NiO_4$ and $La_{1.65}Sr_{0.35}NiO_4$ are qualitatively same as those observed in the oxygen doped system.

Still we could not get the full picture of the magnetic excitations in a stripe phase of La_2NiO_4. One of the problems is low intensity of the magnetic signal. We are preparing further experiments with increasing sample volume.

[1] J. M. Tranquada *et al.*: Nature 375 (1995) 561
[2] J. M. Tranquada *et al.*: Phys. Rev Lett. 79 (1997) 2133

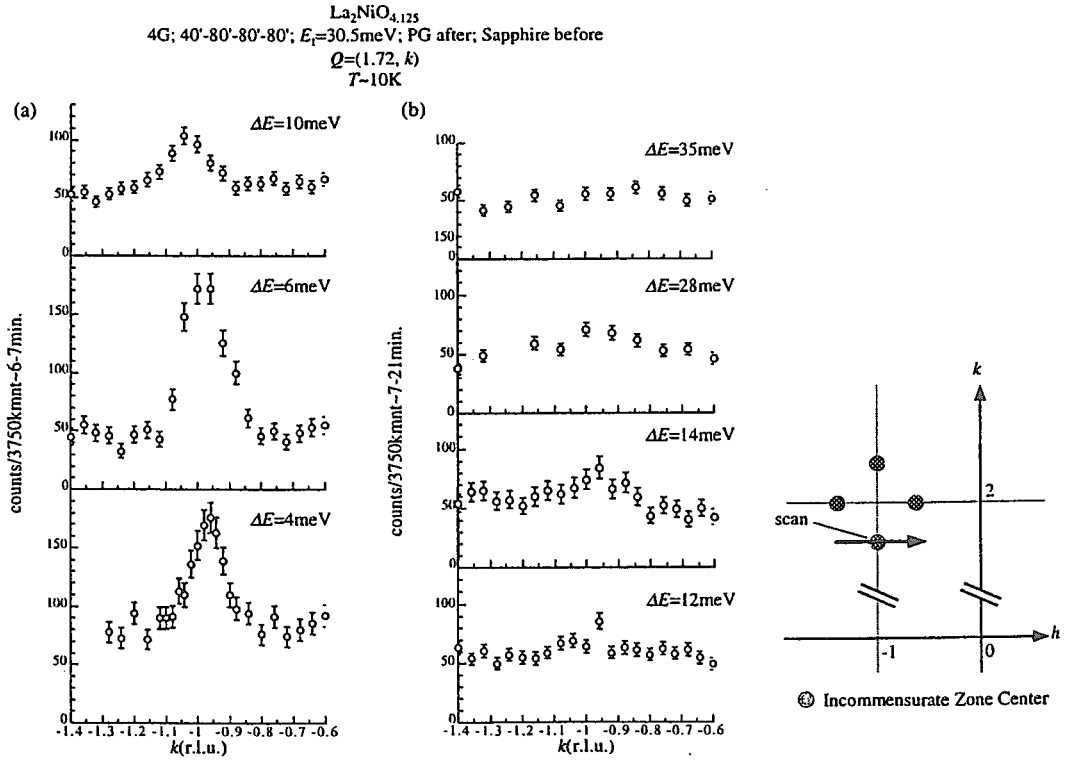

Figure 1: Typical results of constant energy-transfer scans across the incommensurate zone center.

JRR-3M, GPTAS(4G), 3.Superconductivity

研究テーマ：$YBa_2Cu_3O_{6+x}$の磁気励起研究
表題：$YBa_2(Cu_{1-x}Zn_x)_3O_{6+y}$の磁気励起

1-3-2 The magnetic excitation of $YBa_2(Cu_{1-x}Zn_x)_3O_{6+y}$ —the pseudo gap and the detailed momentum-energy structure—

H. Harashina[1,3], M. Kanada[1,3], Y. Yasui[1,3], M. Ito[1], M. Sato[1,3], H. Okumura[2], K. Kakurai[2,3], M. Nishi[2]

[1]Department of Physics, Nagoya University, Furo-cho, Chikusa-ku, Nagoya 464-8602
[2]Neutron Scattering Laboratory, ISSP, The university of Tokyo, Shirakata 106-1, Tokai 319-1195
[3]CREST Japan Science and Technology (JST)

Pseudo gap (or spin gap) which appears in the electronic (or magnetic) excitation spectra of high-T_c Cu oxides is a key issue to understand their "anomalous" normal state. By neutron inelastic measurements of a *c*-polarized B_{2u} phonon (the pattern of the atomic motions of the mode is shown in the inset of Fig. 1) of $YBa_2Cu_3O_{6+y}$ (YBCO or $YBCO_{6+y}$) system,[1] we have found that the pseudo-gap structure originates from the fluctuating singlet pairs with the same symmetry as that of the Cooper pairs.

In the magnetic excitation spectra $\chi''(q, \omega)$ of optimally doped $YBCO_7$, a sharp peak, so-called resonance peak rapidly grows at the energy $\omega = \omega_0 \sim 41$ meV at around the point $q = q_{AF} \equiv (\pi, \pi)$ in the 2-dimensional reciprocal space below the superconducting transition temperature T_c with decreasing T. The peak has often been argued in relation to the existence of the order parameter Δ. Fong *et al.*[2] have recently reported that the peak at (π, π) can also be observed even far above T_c in a 0.5% Zn-doped sample of $YBCO_7$, which should be contrasted to the case of the Zn-free $YBCO_7$. Because the observed T-dependence is similar to that for YBCO samples with smaller oxygen numbers (underdoped samples), the doping of very small amount of Zn might be considered to enhance the fluctuating singlet correlation (or the pseudo gap) above T_c even in the optimally carrier doped system ($YBCO_7$).

In order to see whether the Zn-doped $YBCO_7$ really exhibits pseudo-gap behavior, we have measured the B_{2u} phonon which are sensitive to the existence of the singlet pairs. The B_{2u} phonon was measured by means of neutron inelastic scattering with use of a large single crystal (~2.6 cm^3) of $YBa_2(Cu_{0.995}Zn_{0.005})_3O_7$ ($T_c \sim 86$ K). Neutron

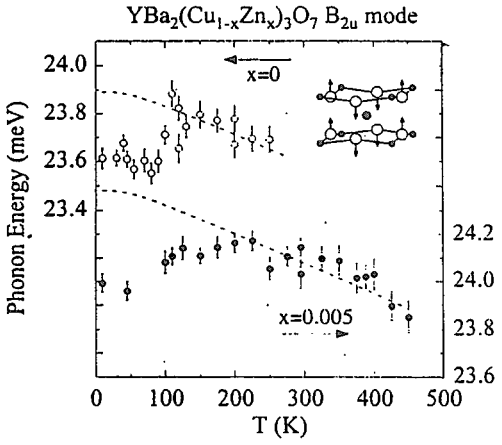

Fig. 1 Energy of the B_{2u} mode is plotted against T for $YBa_2(Cu_{0.995}Zn_{0.005})_3O_7$ together with the results for $YBCO_7$. Dashed lines show the T-dependence expected from the ordinary anharmonic effect.

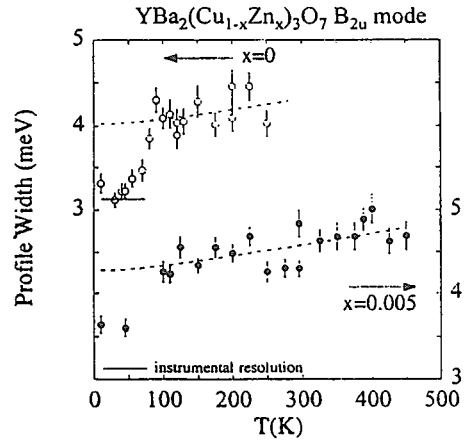

Fig. 2 Profile width of the B_{2u} mode is plotted against T for $YBa_2(Cu_{0.995}Zn_{0.005})_3O_7$ together with the results for $YBCO_7$. Dashed lines show the T-dependence expected from the ordinary anharmonic effect.

measurements were carried out with the ISSP-PONTA spectrometer at JRR-3M at JAERI in Tokai.

Values of the energy $\hbar\omega$ and the profile width w of the B_{2u} mode obtained for $YBa_2(Cu_{0.995}Zn_{0.005})_3O_7$ are plotted against T in Figs. 1 and 2, respectively, together with those for $YBCO_7$. For the Zn-doped crystal no appreciable anomaly appears above T_c in the T-dependence of w. In the T-dependence of the phonon energy, the Zn doping, at first glance, seems to induce anomalous downward deviation from the ordinary T-dependence estimated for the pure $YBCO_{6.7}$.[1] The difference between results for the pure and Zn-doped $YBCO_7$ samples, however, is insignificant and may be due to trivial broadening effects by the Zn doping. The T-dependences of the NMR Knight shift, the longitudinal relaxation rate and the in-plane resistivity, which are also sensitive to the existence of Δ, have been measured for similar Zn-doped samples by our group[3] and no appreciable anomaly have been found.

Then, for the complete understanding of the Zn-doping effects on $\chi''(q,\omega)$, we have to see the detailed structure of $\chi''(q,\omega)$ or to clarify the detailed relationship between the resonance peak centered at q_{AF} and the remaining part which has a peak at the incommensurate q-point.

We are now studying on the detailed q-ω structure of magnetic excitation spectra. Figure 3 shows examples of the profiles obtained for $YBa_2Cu_3O_{6.7}$ ($T_c \sim 62$K). In this experiment, a velocity selector for thermal neutrons constructed at the PONTA spectrometer were used as a higher order filter. Although we cannot distinguish if $\chi''(q,\omega)$ has the incommensurate peak or not because of the large q-resolution width of the present experiment (the double peak structure found for ω = 25 meV has turned out to be extrinsic), the results of the preliminary analyses are roughly consistent with the results obtained by a theory[4] based on the band picture which naturally explain the characteristic ω-dependence of the (q, ω) structure of χ'', where we can see the incommensurate peak at $\omega \sim$ 25 meV, the resonance peak at $\omega \sim$ 30 meV and again the incommensurate peak at $\omega >$ 45 meV.

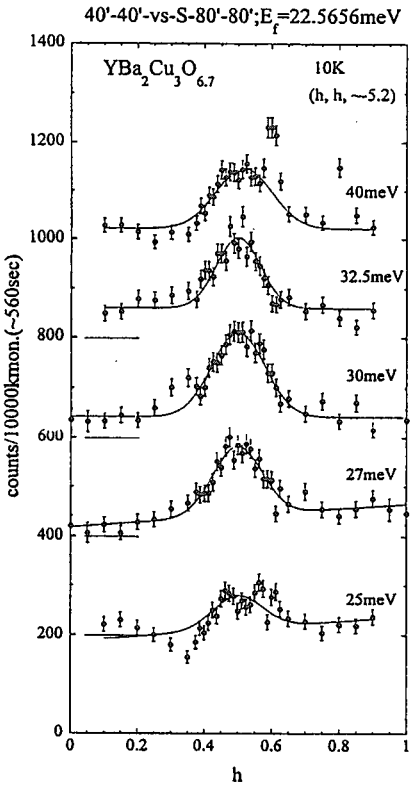

Fig. 3 Profiles obtained by the q-scans around (1/2. 1/2, -5.2) are shown for various energy transfer

References

1. H. Harashina *et al.*: J. Phys. Soc. Jpn. 67 (1998) 3216.
2. H. F. Fong *et al.*: Phys Rev. Lett. 82 (1999) 1939.
3. H. Harashina et al.: J. Phys. Chem. Solid (2000) to be published.
4. Y.-J. Kao et al.: cond-mat/9908302

研究テーマ：TOPAN IMT課題
表題：$La_{1.79}Sr_{0.21}Cu_{0.99}Zn_{0.01}O_4$の格子不整合磁気弾性ピーク

1-3-3 Incommensurate Elastic peaks in $La_{1.79}Sr_{0.21}Cu_{0.99}Zn_{0.01}O_4$

H. Kimura[1], K. Hirota[2], M. Aoyama[3], T. Kawamata[3], T. Adachi[3], Y. Koike[3]
K. Yamada[4], and Y. Endoh[5]

[1]*Research Institute for Scientific Measurements, Tohoku University*
[2]*Department of Physics, Tohoku University*
[3]*Department of Applied Physics, Tohoku University*
[4]*Institute for Chemical Research, Kyoto University*
[5]*Institute for Material Research, Tohoku University*

Transport and T_c anomalies in over-doped $La_{2-x}Sr_xCuO_4$ (LSCO) have been investigated by Koike *et al.*[1]. They found that the suppression of superconductivity is strongly enhanced around $x = 0.21$ with a partial substitution of Zn (~ 1 %) at the Cu site, of which T_c is below 4 K. Furthermore, at $x = 0.21$, a resistivity in the normal state also exhibits anomalous upturn with decreasing temperature. Since there is a possibility that the ordering of holes or spins develops in the vicinity of $x = 0.21$, we carried out comprehensive neutron-scattering studies of $La_{1.79}Sr_{0.21}Cu_{0.99}Zn_{0.01}O_4$ (LSCZO) single crystal by TOPAN triple-axis-spectrometer. As shown in Figure 1 (a), elastic magnetic peaks were clearly observed at the incommensurate position $(\frac{1}{2}\ \frac{1}{2} \pm \varepsilon\ 0)$. The incommensurability ε was estimated to be 0.135 ± 0.002 r.l.u., which is much smaller than the hole concentration ($x = 0.21$). Temperature dependence of the elastic peak intensity is shown in Figure 1 (b), suggesting that the static antiferromagnetic correlations starts developing around 20 K. Note that the overall properties of the elastic peaks are almost identical to that of $La_{1.86}Sr_{0.14}Cu_{0.988}Zn_{0.012}O_4$ studied by Hirota *et al*[2]. Quite remarkably, the exact position of elastic peak shifts away from the tetragonal [100]/[010] axes (*Y-shift*), which is very similar to that of underdoped LSCO[3] and stage-4 La_2CuO_{4+y}[4]. As for the charge order peaks, all the elastic scattering were below the detectable limit.

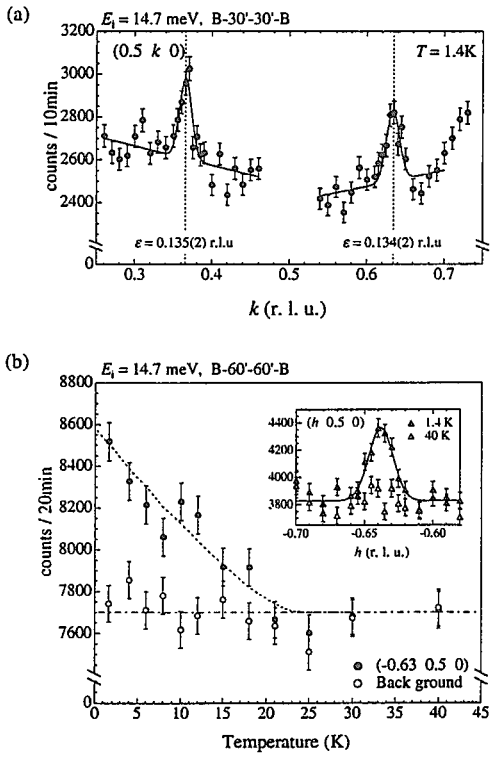

Figure 1: (a); (1/2 k 0) scans at $T = 1.4$ K. (b); Temperature dependences of (-0.63 1/2 0) peak intensity (filled circle) and background one (open circle). Inset shows the peak profiles at 1.4 K and 40 K.

References

[1] Y. Koike *et al.*, private communication.

[2] K. Hirota *et al.*, Physica B **241**, 817 (1998).

[3] H. Kimura *et al.*, submitted to Phys. Rev. B.

[4] Y. S. Lee *et al.*, Phys. Rev. B **60**, 3643 (1999).

原子炉：JRR-3M　　装置：TOPAN (6G)　　分野：3. 超伝導

研究テーマ：TOPAN IMT課題
表題：酸化物高温超伝導体$La_{1.93}Sr_{0.07}CuO_4$のアンダードープ領域におけるスピン揺らぎ

1-3-4
Spin Fluctuations in the Underdoped High-T_c Cuprate $La_{1.93}Sr_{0.07}CuO_4$

H. Hiraka[1], M. Fujita[2], K. Yamada[2], and Y. Endoh[3]

[1]*Core Research for Evolutional Science and Technology, JST, Kawaguchi 332-0012*
[2]*The Institute for Chemical Research, Kyoto University, Uji 611-0011*
[3]*Institute for Material Research, Tohoku University, Sendai 980-8577*

Inelastic neutron scattering (INS) technique has been giving invaluable information about the connection between magnetism and high-Tc superconductivity. It is well known that characteristic low-frequency fluctuations exist in LSCO system, which result in the missing of energy gap except for the optimal hole-doping phase. We report here the T- and ω-dependence of gapless-type spin excitations in the underdoped LSCO.

Single crystals were grown by means of TSFZ technique and the sample had 1.3 c.c. in volume. The scattering plane was chosen to be (*hk*0) or (*h*0*l*) in *Bmab* notation. The INS experiments were carried out at TOPAN under q-scan mode with final neutron energy of 14.7 meV.

Our findings are displayed in Figs. 1 and 2. One is the enhanced $\chi''(\omega)$ below 20 meV, which is remarkably suppressed with T at low energies (< 10 meV). In the high transferred energy region, the spectral weight is nearly even, or tends to increase slightly with ω. No sharp salient resonance-peak was observed in the ω- and T-range measured, in contrast with optimal doping YBCO. Other significant feature appears in the scaling behavior of $\chi''(\omega)$ with a functional form of $\tan^{-1}(\omega/T)$. To our surprise, the above experimental facts qualitatively agree with those from insulating spin-glass LSCO compounds[1,2] which show a different stripe pattern. We conjecture that a common type of spin excitations exists in the underdoped superconductor and insulator for LSCO.

Reference

1) B.Keimer, *et.al.* : Phys. Rev. B **46**, 14034 (1992).
2) M.Matsuda, *et.al.*: J. Phys. Soc. Jpn. **62**, 1702 (1993).

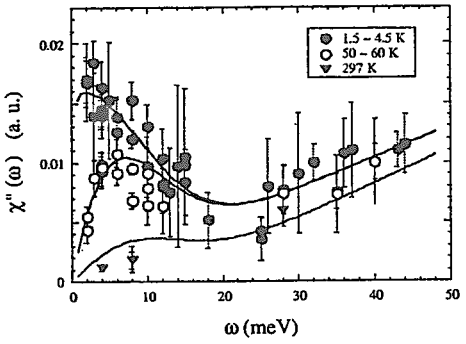

Fig. 1 T-variation of energy spectrum $\chi''(\omega)$.

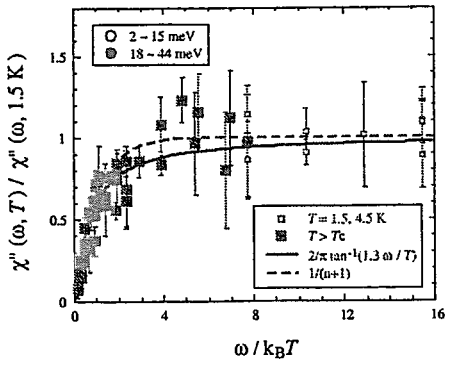

Fig. 2 Conventional Scaling of $\chi''(\omega)$.

研究テーマ:TOPAN IMT 課題
表題:絶縁体-超伝導体相境界付近の静的スピン相関の系統的研究

1-3-5 Systematic Study of Elastic Spin Correlation near Insulator- Superconductor Phase Boundary

M. Fujita,[1] K. Yamada,[1] H. Hiraka,[2] Y. Endoh,[2] K. Hirota,[3] P.M. Gehring,[4] and G.Shirane,[5]

[1] *Institute for Chemical Research, Kyoto University*
[2] *Institute for Materials Research, Tohoku University*
[3] *Department of Physics, Tohoku University*
[4] *National Institute of Standards and Technology*
[5] *Department of Physics, Brookhaven National Laboratory*

We investigated the elastic spin correlation in $La_{2-x}Sr_xCuO_4$ focusing on the qualitative change in the direction of spin modulation near the insulator-superconductor phase boundary. Systematic elastic neutron scattering measurements were performed on several single crystals with $0.053 \leq x \leq 0.07$ at the HER and the TOPAN triple-axis spectrometers. The single crystals are grown by a traveling-solvent floating-zone method.

In the insulating sample (x=0.053), we observed so-called diagonal magnetic component corresponding to the magnetic correlation modulated along the diagonal direction of the CuO_2 square lattice, consistent with our recent work on x=0.05. [1] On the other hand, all the superconducting samples (x=0.056,0.06,0.07) show so-called vertical magnetic component corresponding to the modulation vertical to Cu-O-Cu line. [2] As a remarkable feature, the superconducting sample in narrow concentration range above the insulator-superconductor boundary exhibits the diagonal component in addition to the vertical one, if the isotropic peaks for both components are assumed. For both the diagonal and vertical components, the incommensurability parameter δ, defined in the Fig.1(a), approximately follows a linear relation of δ=x, however, δ's are smaller than those expected from the relation around the phase boundary. Furthermore, as seen in Fig.1(b), it is found that the intrinsic peak width as a function of Sr concentration x broadens around the phase boundary.

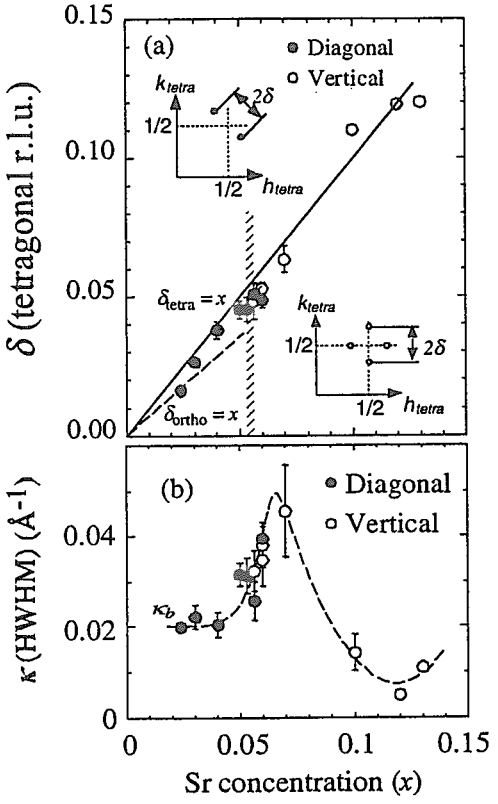

Figure 1: Sr condentration x dependence of (a) the incommensurability δ and (b) the peak width. In both figures, solid and open circles represent the results of diagonal and vertical component.

Reference
[1] S. Wakimoto et al, Phys. Rev. B **60**, R769 (1999)
[2] T. Suzuki et al, Phys. Rev. B **57**, 3229 (1998)

研究テーマ: TOPAN IMT課題
表題: TOPAN IMT課題

1-3-6 Dynamic spin correlations in lightly-doped $La_{2-x}Sr_xCuO_4$

M. Matsuda[1], R. J. Birgeneau[2], Y. Endoh[3], M. Fujita[4], H. Hiraka[3], M. A. Kastner[2], G. Shirane[5], S. Wakimoto[2], and K. Yamada[4]

[1]*The Institute of Physical and Chemical Research (RIKEN), Wako, Saitama 351-0198, Japan*
[2]*Department of Physics and Center for Materials Science and Engineering, MIT, Cambridge, Massachusetts 02139, USA*
[3]*Institute for Materials Research, Katahira, Sendai 980-8577, Japan*
[4]*Institute for Chemical Research, Kyoto University, Gokasho, Uji, 610-0011, Japan*
[5]*Department of Physics, BNL, Upton, New York 11973, USA*

The lightly-doped $La_{2-x}Sr_xCuO_4$ shows a static one-dimensional spin modulation, which is rotated by 45° from that in the superconducting phase, across the entire spin-glass phase. This is consistent with the diagonal spin modulation.

The next step is to understand how the inelastic magnetic correlations behave in the spin-glass phase of $La_{2-x}Sr_xCuO_4$. Neutron inelastic scattering experiments were performed in $La_{1.976}Sr_{0.024}CuO_4$ using the triple-axis spectrometer TOPAN. Figure 1 shows constant-ω scans at the energies 3 and 7.5 meV measured at 10 K. A sharp excitation peak is centered at H=1 at 3 meV. On the other hand, the peak position is shifted to lower H (~0.99) at 7.5 meV.

We speculate that this behavior is explained as follows. At 3 meV, the magnetic peaks exist at diagonal incommensurate (DIC) positions. Since the instrumental resolution elongated vertically integrates the magnetic signal around H=1 very effectively, the sharp and intense peak is centered at H=1. On the other hand, the magnetic correlations are considered to be commensurate (C) and isotropic at 7.5 meV. In this case, there exist two equi-intense peaks at H =0.985 and 1 so that one broad peak is located at H~0.99. From this result, it is considered that a DIC-C transition occurs between 3 and 7.5 meV. Further measurements are needed to clarify the DIC-C transition in more detail.

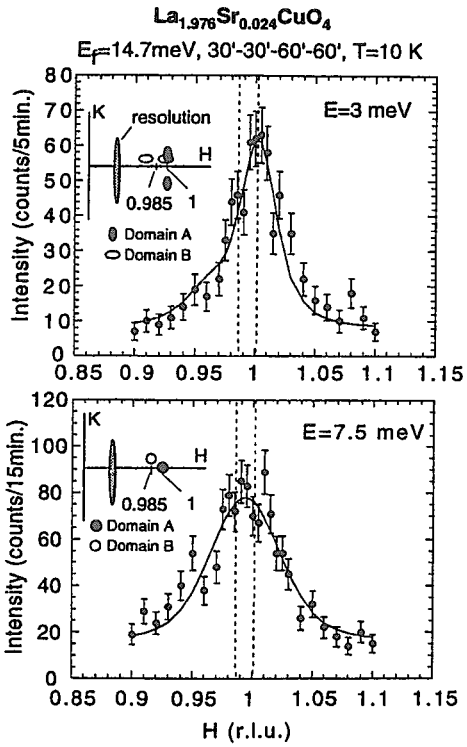

Figure 1 Inelastic scans along (H,0,-0.6) at 10 K as a function of energy in $La_{1.976}Sr_{0.024}CuO_4$. The solid lines are guides to the eye. The broken lines show the centers of the peaks (1,0,-0.6) and (0,1,-0.6) determined from the nuclear Bragg peak positions. Insets show the schematic configurations of the magnetic peaks in the (H0L) scattering zones. The instrumental resolution is elongated perpendicular to the scattering plane. The ellipsoids and circles represent magnetic peaks.

研究テーマ：新2次元高温超伝導体 $Na_x(Zr_{1-y}Hf_y)NCl$ の配向度
表題：ZrNClとHfNClペレットのモザイク巾

1-3-7 Mosaic Spread of Pressed ZrNCl and HfNCl Pellets

S. Shamoto, K. Iizawa, and T. Kajitani

Dept. of Applied Physics, Grad. Sch. of Engineering, Tohoku University, Sendai 980-8579

Since the superconductivity on layered halide nitrides Li_xZrNCl with T_c=15 K and $Li_x(THF)_yHfNCl$ with T_c=25 K has been discovered by S. Yamanaka et al. [1,2], the single crystal growth has never been reported. The difficulty on growing single crystals prevents us from extend research about these novel interesting compounds, especially neutron scattering study. However, the flaky morphology of their crystallites might enable us to orient their c-axes. Here, we have carried out neutron diffraction study on pressed pellets of these compounds. In addition, this work may give us a chance to study the anisotropy of their physical properties.

Neutron scattering measurement was carried out using KINKEN Single Crystal Diffractometer (KSD) at T1-2 thermal guide of JAERI-JRR3M in Tokai. Each pellet was pressed by a piston cylinder with 12 mm diameter at 0.44 GPa. Note that the original densities of ZrNCl and HfNCl are about 4.5 and 6.8 g/cm^3, respectively.

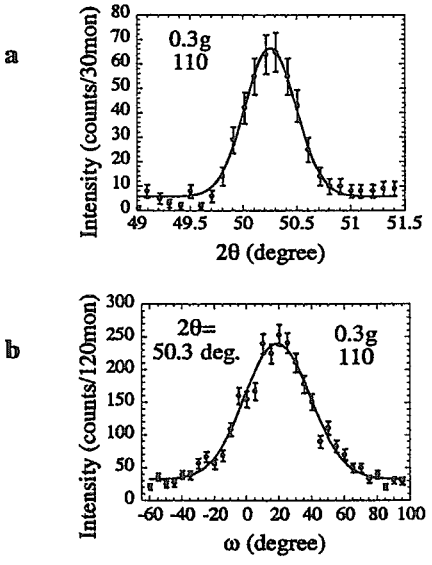

Figure 1. Typical diffraction patterns of a ZrNCl pellet at room temperature. a. θ-2θ scan. b. ω scan

Typical diffraction patterns for θ-2θ scan and ω scan are shown in Fig. 1. FWHM values of ω scan, i.e., mosaic spread, are summarized as a function of sample weight in Fig. 2. Since the ω scan for 110 peak was performed along the direction normal to pellet plane, the FWHM value corresponds to the distribution of c-axis of crystallites. We have checked the FWHM values by measuring different peaks, e.g., 003, giving us consistent results. Although this alignment can be achieved only about c-axis, it might help us with measuring neutron scattering at specific Q points.

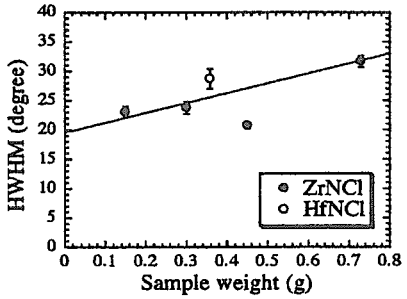

Figure 2. Half width of half maximum (FWHM) of pressed pellets obtained by ω scan [3]. The line is a guide for the eye.

References

[1] S. Yamanaka, H. Kawaji, K. Hotehama and M. Ohashi, Adv. Mater. **8**, 771 (1996).
[2] S. Yamanaka, K. Hotehama and H. Kawaji, Nature **392** (1998) 580.
[3] S. Shamoto, K. Iizawa, Y. Asano, K. Ohoyama, and T. Kajitani, Molecular Crystals and Liquid Crystals (1999) in press.

研究テーマ：新2次元高温超伝導体 HfNCl 系関連物質の構造
表題：HfNClの構造

1-3-8 Structure of ß-HfNCl

S. Shamoto[a)], K. Iizawa[a)], Y. Kato[a)], T. Koiwasaki[b)], M. Yasukawa[b)], S. Yamanaka[b)], K. Ohoyama[c)], Y. Yamaguchi[c)], and T. Kajitani[a)]

[a)]*Department of Applied Physics, Faculty of Engineering, Tohoku University, Sendai 980-8579*

[b)]*Department of Applied Chemistry, Faculty of Engineering, Hiroshima University, Higashi-hiroshima 739-8527*

[c)]*Institute for Materials Research, Tohoku University, Sendai 980-8577.*

Novel layered superconductor, $Li_x(THF)_yHfNCl$ (T_c~25.5 K), was discovered by Yamanaka et al. [1]. The crystal structures of related compounds, $Li_{0.2}ZrNCl$ (T_c~15 K) and $Na_{0.3}HfNCl$ (T_c~20 K), determined by Rietveld analysis using powder neutron diffraction data, have a fairly flat double honeycomb lattice as a conducting plane [2,3]. The electronic density of states for A_xHfNCl (A;alkali metals and organic molecules) is estimated to be larger than that for A_xZrNCl based on the nearest neighbor bond length between Zr or Hf atoms [3], which must be one of the reasons of the high transition temperature in A_xHfNCl system. However, the origin of this structural difference is unknown. Therefore, we have carried out neutron diffraction measurement of the parent compound, ß-HfNCl. Neutron diffraction enables us to avoid the preferred orientation problem of the present powder sample which consists of thin plate-like crystallites. Neutron scattering measurement was carried out at room temperature using KINKEN Powder diffractometer (KPD, HERMES) at T1-3 thermal guide of JAERI-JRR3M in Tokai. Powder sample was prepared as in ref. 1. In contrast to the structures of superconducting compounds, there is almost no difference of the pristine

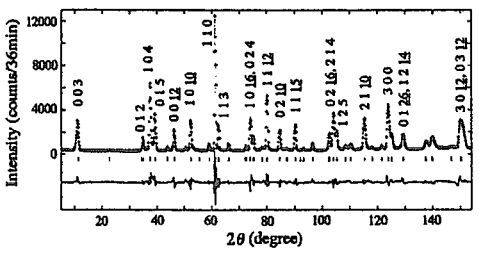

Fig. 1. Neutron diffraction pattern of HfNCl.

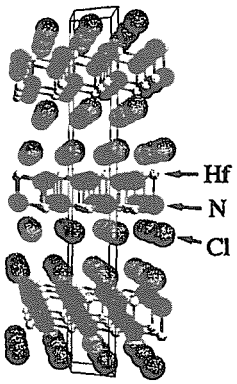

Fig. 2. Determined structure of ß-HfNCl.

Table 1. Structural parameters of HfNCl [4].
R-3*m*; *a*=3.5712(2) Å, *c*=27.682(3) Å

atom	site	*g*	*x*	*y*	*z*	B_{eq}/Å^2
Hf	6*c*	1	0	0	0.1210(7)	0.2(4)
N	6*c*	1	0	0	0.1979(7)	0.2(5)
Cl	6*c*	1	0	0	0.3879(7)	0.3(5)

R_I=4.2%, R_p=9.7%, R_{wp}=13.0%, R_e=3.5%

structures between ß-ZrNCl and ß-HfNCl. This result suggests the rigidness of ß-HfNCl lattice, or the different character of conduction bands between ß-ZrNCl and ß-HfNCl that can be filled by electrons upon alkali metal intercalation.

References

[1] S. Yamanaka, K. Hotehama and H. Kawaji, Nature 392, 580 (1998).

[2] S. Shamoto, T. Kato, Y. Ono, Y. Miyazaki, K. Ohoyama, M. Ohashi, Y. Yamaguchi and T. Kajitani, Physica C 306, 7 (1998).

[3] S. Shamoto, K. Iizawa, M. Yamada, K. Ohoyama, Y. Yamaguchi and T. Kajitani, J. Phys. Chem. Solids 60, 1431 (1999).

[4] S. Shamoto, K. Iizawa, T. Koiwasaki, M. Yasukawa, S. Yamanaka, K. Ohoyama, Y. Yamaguchi, and T. Kajitani, in preparation (CGCT-1, 2000).

研究テーマ：新2次元高温超伝導体 $Li_x(Zr_{1-y}Hf_y)NCl$ のフォノン
表題：新2次元高温超伝導体 Na_xHfNCl のフォノン

1-3-9 Phonon of Novel 2D superconductor Na_xHfNCl

S. Shamoto[a)], K. Iizawa[a)], Y. Kato[a)], T. Kajitani[a)],
T. Koiwasaki[b)], M. Yasukawa[b)], and S. Yamanaka[b)],

[a)]*Department of Applied Physics, Faculty of Engineering, Tohoku University, Sendai 980-8579*
[b)]*Department of Applied Chemistry, Faculty of Engineering, Hiroshima University, Higashi-hiroshima 739-8527*

Novel layered superconductors, Li_xZrNCl (T_c~15 K) and $Li_x(THF)_yHfNCl$ (T_c~25.5 K), was discovered by Yamanaka et al. [1]. The electronic density of states (EDOS) for A_xHfNCl (A;alkali metals and organic molecules) is estimated to be larger than that for A_xZrNCl based on the nearest neighbor bond length between Zr or Hf atoms [2], which must be one of the reasons of the high transition temperature in A_xHfNCl system. However, EDOS also suggests that other factor, e.g., phonon, must also play an important role. Therefore, we have carried out neutron scattering measurement on Na_xHfNCl with typical x values, i.e., x=0, 0.27, and 0.75. Diffraction patterns of Na_xHfNCl with x>0.5 and x<0.5 are known to be different with each other, probably because Na atoms occupy 3*a* site that can be filled at x=0.5. Note that the superconducting transition temperature does not change at the boundary. Neutron scattering measurement was carried out using a TOF-type spectrometer AGNES at C3-1-1 cold guide of JAERI-JRR3M in Tokai. Figure 1 shows phonon density of states, GPDOS, of Na_xHfNCl with x=0, 0.27, and 0.75. The c-axis parameters at x=0, 0.27, and 0.75 were 27.7 A, 29.7 A, 30.1 and 33.1 A (two phase mixture), respectively. The elongation of c-axis upon Na intercalation is somewhat larger than that expected from the case of Li_xZrNCl, although it is much smaller than that of $Li_x(THF)_yHfNCl$. Not only the intensity around E=10 meV but also total intensity increased with increasing x. Unknown weight gain estimated by inductively coupled plasma analysis also increased with increasing x. Therefore, we may conclude that this gain is due to the intercalation of THF, where the amount, y, of THF in $Na_x(THF)_yHfNCl$ is estimated to be 0.11 and 0.23 for x=0.27 and 0.75, respectively. Note that both of experimental conditions for HfNCl and $Na_{0.75}HfNCl$, e.g., sample cans and sample weight were the same. These two data normalized by their measuring time can be compared quantitatively.

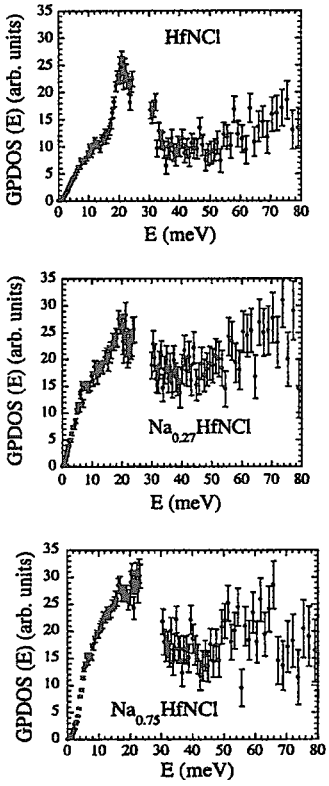

Figure 1. Observed phonon density of states (GPDOS) of Na_xHfNCl at about 270K [3].

References

[1] S. Yamanaka, K. Hotehama and H. Kawaji, Nature 392, 580 (1998), and a reference therein.

[2] S. Shamoto, K. Iizawa, M. Yamada, K. Ohoyama, Y. Yamaguchi and T. Kajitani, J. Phys. Chem. Solids 60, 1431 (1999), for example.

[3] S. Shamoto, Y. Kato, K. Iizawa, T. Koiwasaki, M. Yasukawa, S. Yamanaka, and T. Kajitani, in preparation (ASR-2000).

1. 中性子散乱 4) 非晶質・液体

1. Neutron Scattering 4) Amorphous・Liquid

This is a blank page.

研究テーマ：拡散現象のモデル化および高精度拡散係数測定
表題：液体スズの構造の温度依存性－中性子散乱実験および第一原理分子動力学シミュレーション

1-4-1

Temperature dependence of the structure of liquid Sn: Neutron scattering experiment and an *ab initio* molecular-dynamics simulation

S. Munejiri, T. Masaki, T. Itami, Y. Senda[1], F. Shimojo[1], K. Hoshino[1], T. Kamiyama and Y. Ishii[2]

Space Development Agency of Japan (NASDA), 2-1-1 Sengen, Tsukuba 305-8505, Japan
[1]*Hiroshima University, Higashi-Hiroshima 739-8521, Japan*
[2]*Japan Atomic Energy Research Institute, Tokai, Ibaraki, 319-1195, Japan*

The measurements of the self-diffusion coefficient D of liquid tin for a wide range of temperature have been made under a microgravity environment and rather accurate data compared with those measured on the ground have been obtained owing to the absence of convection [1,2]. Several models to try to explain the temperature dependence of D of liquid metals have been proposed so far. However, to clarify the mechanism of the self-diffusion and to construct a reliable model for a wide range of temperature, it is crucial not only to measure D accurately but also to understand the microscopic liquid structure.

It is known that though the structure factor $S(Q)$ of liquid tin has a shoulder on the high-Q side of the first peak near the melting point[3], the shoulder becomes less clear with increasing temperature[4]. Since the shoulder is probably related to a complex local structure, it is expected that the disappearance of the shoulder makes an effect on the diffusion mechanism. In this sense, the liquid tin is a suitable liquid to investigate the relation between the structure and the self-diffusion systematically. In this paper, to investigate a correlation between the microscopic structure and the self-diffusion of liquid tin for a wide range of temperature, we have performed a neutron scattering experiment and an *ab initio* molecular-dynamics (AIMD) simulation.

The neutron scattering measurements for liquid tin have been performed on JRR-3M, using the TAS-1 (2G) spectrometer. The data of scattering intensity were measured in a Q-range from 0.2 to 12.1 $Å^{-1}$ with the steps 0.05 and 0.1 $Å^{-1}$ for $Q < 6.0$ $Å^{-1}$ and $Q > 6.0$ $Å^{-1}$, respectively at the temperatures of 573, 773 and 1073 K. For almost whole Q region, $0.5 < Q < 10.3$ $Å^{-1}$ the wavelength 0.95 Å was used and the data at high and low angle regions were obtained with the wavelengths of 0.85 and 2.44 Å, respectively. The sample was sealed in a thin quartz glass tube, 8.0 mm inner diameter with 0.3 mm thickness and 30 mm height. The accumulated counts of scattering intensity were of the order of 10^4 and those of empty quartz glass cell were about 10^3.

The AIMD was performed using the supercomputer VPP500 at the Center for Promotion of Computational Science and Engineering(CCSE). Our method of the AIMD calculation[5] is based on density functional theory with the local density approximation. The norm-conserving pseudopotential by Troullier and Martins was employed for the interaction between valence and core electrons. The MD simulation was carried out with 64 atoms from 773 to 1473 K with Nosé-Hoover thermostat.

In Fig.1, the data of $S(Q)$ obtained in the present study from 573 to 1473 K are shown. The solid and circles show the results obtained from AIMD simulation and from the neutron scattering, respectively. The calculated results

原子炉：JRR-3M　装置：TAS-1(2G)　分野：中性子散乱（液体・不規則物質）

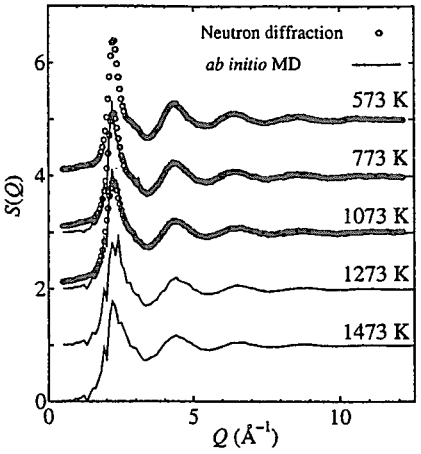

Fig 1: Structure factors pf liquid tin from 523 to 1473 K.

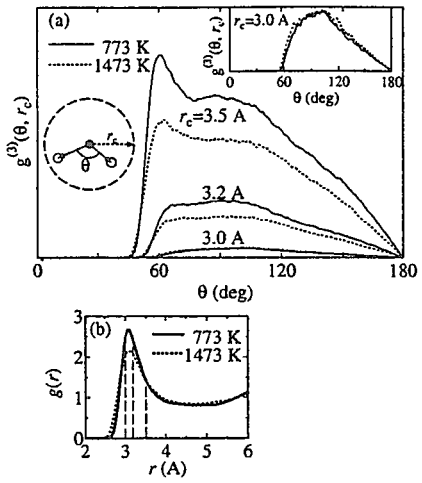

Fig 2: Bond angle distribution functions (a) and Radial distribution functions (b).

are in excellent agreement with the experiments. In both the calculated and the experimental $S(Q)$, the shoulders are observed clearly at high-Q side of main peak, around $Q = 2.8$ Å^{-1} at low temperatures. With increasing temperature, the first peak becomes lower and broader and the shoulder seems to disappear. However since the values of $S(Q)$ around the shoulder stay almost constant and even at highest temperature 1473 K the shape of the first peak in $S(Q)$ is unsymmetrical, it is considered that at high temperature the shoulder dose not disappear but is merely covered by the broadened first peak. From these results we conclude that the some local structures still remain at 1473 K in the liquid tin.

To study the microscopic structure more detail, we calculated bond angle distribution functions from the atomic configuration obtained by the AIMD simulation; the bond angle is formed by a pair of vectors drawn from a reference atom to any other two atoms within a cutoff radius r_c. In Fig.2(a) the result of the bond angle distribution functions $g^{(3)}(\theta, r_c)$ at 773 and 1473 K are shown. When the cutoff radius r_c is 3.0 Å, which is shorter than the average nearest neighbor distance, $g^{(3)}(\theta, r_c)$ shows one broad peak centered at 100°. This peak suggests that some fragments of a tetrahedral structure persist in a short period even in the liquid state. With increasing the cutoff radius r_c, a new peak appears around 60°. Since when an interatomic interaction is isotropic and the atoms are in closed-packed, the peak distributed near 60° occurs, the latter peak means a typical metallic interaction. With increasing temperature the distribution function $g^{(3)}(\theta, r_c)$ becomes broad for $r_c = 3.2$ and 3.5 Å while that for $r_c = 3.0$ Å is almost unchanged. This means that the short-range structure within 3 Å dose not so much depend on the temperature.

References

[1] G. Frohberg *et al.*, Proc. 6th Europ. Symp. on Material Sciences under microgravity conditions, Bordeaux, 2-5 Dec. 1986.

[2] T. Itami *et al.*, J. Jpn. Soc. Microgravity Appl. **15** (1998) 225-232.

[3] S. Takeda *et al.*, J. Phys. Soc. Jpn. **53** (1984) 3447-3456

[4] Y. Waseda, The Structure of Non-Crystalline Materials, Liquid and Amorphous Solid, McGraw-Hill, New York 1980

[5] F. Shimojo *et al.*, Phys. Rev. B **52** (1995) 9320-9329

研究テーマ：濃厚塩化アンモニウム水溶液中の分子間水素結合

表題：濃厚塩化アンモニウム水溶液中におけるアンモニウムイオンの水和構造

1-4-2
Hydration Structure of Ammonium Ion in Concentrated Aqueous Ammonium Chloride Solutions

Y. Kameda, K. Sugawara, K. Abe, T. Usuki, and O. Uemura

Department of Material and Biological Chemistry, Faculty of Science, Yamagata University, Yamagata, 990-8560 Japan

The hydration structure of NH_4^+ has long been a matter of interest in extended fields of chemical and biological sciences. Despite considerable efforts for elucidating the hydration property of hydrated NH_4^+ in aqueous solutions, there still remain some ambiguities concerning both the hydration number and intermolecular distance between NH_4^+ and the nearest neighbor water molecules.[1] The neutron diffraction with the isotopic substitution technique is one of the most suitable experimental techniques to obtain detailed structural information on hydrated NH_4^+.

In this report, we describe results of neutron diffraction measurements on aqueous 8 mol% $*N*H_4Cl$ solutions in which isotopic compositions of both nitrogen and hydrogen atoms have been changed. The weighed amount of ^{14}N- and ^{15}N-enriched ammonium chlorides were dissolved into D_2O or D_2O-H_2O mixtures to prepare four kinds of aqueous 8 mol% $*N*H_4Cl$ solutions with different isotopic compositions,

1) $(^{14}ND_4Cl)_{0.08}(D_2O)_{0.92}$,
2) $(^{15}ND_4Cl)_{0.08}(D_2O)_{0.92}$,
3) $(^{14}N^0H_4Cl)_{0.08}(^0H_2O)_{0.92}$,
4) $(^{15}N^0H_4Cl)_{0.08}(^0H_2O)_{0.92}$.

The superscript "0" on the hydrogen nucleus denotes an isotopic mixture with the mean scattering length of b_H=0. Sample solutions were sealed into a cylindrical quartz sample cell with 11.4 mm in inner diameter and 1.2 mm in thickness, respectively. Neutron diffraction measurements were carried out at 25 °C using the ISSP 4G diffractometer installed at the JRR-3M reactor of JAERI. The incident neutron wavelength of $\lambda = 1.105 \pm 0.003$ Å was employed. The collimation used were 40'-80'-80' in going from the reactor to detector. Scattered neutrons from the sample solution were collected over the angular range of $3 \leqq 2\theta \leqq 115$ °, which corresponds to $0.30 \leqq Q \leqq 9.59$ Å^{-1}. Measurements of scattering intensities were also made for a vanadium rod, an empty cell and a background, respectively. After corrections for absorption and multiple scatterings, the observed count rates were converted to the normalized scattering cross section.

The first-order difference function,[2] $\Delta_N(Q)$, between corrected scattering cross sections for the sample solutions with the same isotopic state for hydrogen atoms and different one for nitrogen atoms, can be expressed as follows,

$$\Delta_N(Q) = A[a_{NO}(Q)\text{-}1] + B[a_{NH}(Q)\text{-}1] + C[a_{NCl}(Q)\text{-}1] + D[a_{NN}(Q)\text{-}1], \quad (1)$$

where,

$A = 2x(1\text{-}x)b_O(b_{^{14}N} - b_{^{15}N})$,
$B = 4x(1+x)b_H(b_{^{14}N} - b_{^{15}N})$,
$C = 2x^2b_{Cl}(b_{^{14}N} - b_{^{15}N})$, and
$D = x^2(b_{^{14}N}^2 - b_{^{15}N}^2)$, respectively.

x denotes the mole fraction of $*N*H_4Cl$ in the solution. Numerical values of the coefficients A—D in eq. 1 are listed in Table 1. Since magnitudes of coefficients A and B are much larger than those of C and D in the present experimental condition, $\Delta_N(Q)$ is dominated by the contribution from the ammonium ion - water correlation. The Fourier transform of $\Delta_N(Q)$ gives the distribution function around the nitrogen atom, $G_N(r)$, that is,

Table 1 Values of coefficients A-D in eq. 1

	A/mbarn	B/mbarn	C/mbarn	D/mbarn
$^D\Delta_N(Q)$	24.4	65.8	3.5	2.9
$^{0H}\Delta_N(Q)$	24.4	0	3.5	2.9

$$G_N(r) = 1 + (2\pi^2\rho r)^{-1}(A+B+C+D)^{-1} \times \int_0^{Q_{max}} Q\Delta_N(Q)\sin(Qr)\,dQ . \quad (2)$$

The observed $\Delta_N(Q)$ functions for D_2O and ${}^0H_2O$ solutions are shown in Fig. 1. In the present ${}^D\Delta_N(Q)$ function for the D_2O solution (Fig. 1a), the intramolecular N-D contribution within ND_4^+ has already been subtracted. A significant difference in the oscillational phase and amplitude between ${}^D\Delta_N(Q)$ and ${}^0H\Delta_N(Q)$, due to the difference in the N-H contribution, can clearly be observed.

The Fourier transform of the observed $\Delta_N(Q)$ gives the distribution function around the nitrogen atom, $G_N(r)$, as shown in Fig. 2. Since there is no contribution from N-H pair in the present ${}^0HG_N(r)$ (Fig. 2b), the function can be regarded to describe the distribution of water-oxygen atoms around the nitrogen atom within NH_4^+. A predominant first peak located at r = 2.8 Å in ${}^0HG_N(r)$ is attributable to the nearest neighbor hydrogen-bonded N···O interaction. The coordination number, $n_{NO} \approx$ 4 obtained from the integration over the first peak, indicates that NH_4^+ is tetrahedrally coordinated by nearest neighbor water molecules in the aqueous solution. The broadened second peak in ${}^0HG_N(r)$ suggests the existence of the stable second hydration shell of NH_4^+.

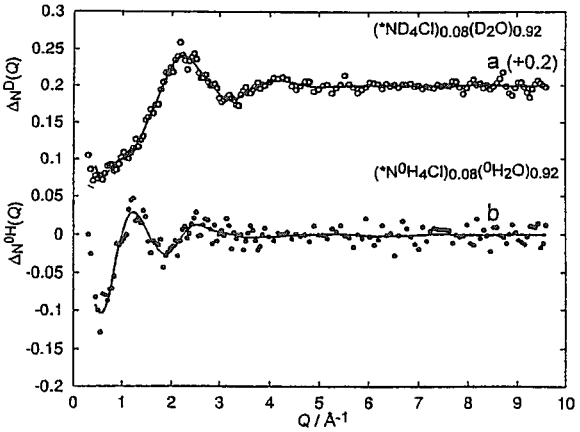

Fig. 1 First-order difference functions concerning the nitrogen atom within NH_4^+, ${}^D\Delta_N(Q)$ (a) and ${}^0H\Delta_N(Q)$ (b), observed for aqueous 8 mol% *N*H_4Cl solutions in D_2O and ${}^0H_2O$, respectively.

The present ${}^DG_N(r)$ is characterized by the first peak located at r = 3.3 Å with small humps at both lower- and higher-sides of the peak. This first peak position can be attributed to the nearest neighbor N···H distance between NH_4^+ and the nearest neighbor water molecules. The functional form of the present ${}^DG_N(r)$ is quite similar to that for the 9.1 mol% ND_4Cl solution in D_2O reported by Hewish and Neilson.[3] They have obtained 10—11 water molecules in the first hydration shell of ND_4^+ from the integration of the observed $G_N(r)$ in the range of 2.60—4.35 Å. Obviously, contributions from the longer-range interaction should be overlapped with the first peak in ${}^DG_N(r)$, in which N-O and N-H contributions are both involved. The present result of the hydration number for NH_4^+ is therefore considered to be more reliable. In order to obtain detailed structural parameters concerning the NH_4^+ hydration, the least squares fitting analysis is in progress.

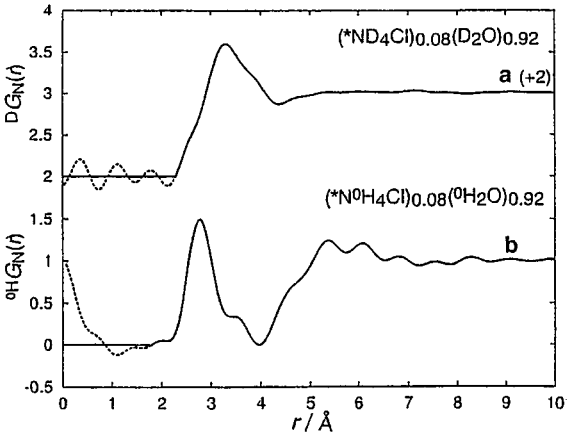

Fig. 2 Distribution functions around the nitrogen atom within NH_4^+, ${}^DG_N(r)$ (a) and ${}^0HG_N(r)$ (b), observed for aqueous 8 mol% *N*H_4Cl solutions in D_2O and ${}^0H_2O$, respectively.

References

1. H. Ohtaki and T. Radnai, *Chem. Rev.*, 93, 1157 (1993).
2. J. E. Enderby, *Chem. Soc. Rev.*, 24, 159 (1995).
3. N. A. Hewish and G. W. Neilson, *Chem. Phys. Lett.*, 83, 425 (1981).

研究テーマ: Ge-カルコゲン混合液体のネットワーク構造
標題: 液体Ge-カルコゲン混合系の中性子散乱

1-4-3 Neutron Scattering Measurements on Liquid Ge-Chalcogen Mixtures

K. Maruyama, S. Takeda[1], M. Kanehira[1], and M. Misawa

Faculty of Science, Niigata University, Niigata 950-2181, Japan
[1]Faculty of Science, Kyushu University, Ropponmatsu, Fukuoka 810-8560, Japan

The liquid Ge-Se mixtures show the change of electronic conductivity over the magnitude of six with changing their composition. The conductivity at the stoichiometric composition, $GeSe_2$, depends on temperature largely as well. These phenomena suggest that the bonds between atoms change the properties with both composition and temperature changes.

We have carried out neutron scattering measurements for liquid Ge-Se mixtures[1]. The results show that the local structure for Ge rich mixtures is metallic one and the network structure appears at about the composition of $Ge_{50}Se_{50}$. For the stoichiometric composition, vary large prepeak was found, which becomes smaller quickly with increasing temperature. This means that the network structure is destroyed at high temperature.

In order to investigate the effect of exchange of chalcogen element and to study the prepeak precisely with neutron beam with longer wave length of 1.82 Å, we have performed the neutron scattering measurement for liquid Ge-S mixtures by using HERMES spectrometer equipped at JRR-3M in JAERI Tokai. The samples were sealed in cylindrical fused silica tube with an inner diameter of 8mm. To decrease the scattering from air and to avoid the damage of the heater, the sample environment was exchanged with He gas.

At the measurement time, the electric heater was unfortunately down. Hence the sufficient statistics was not achieved. However we can compare the structure factor $S(Q)$ for liquid Ge-S mixtures with those obtained from the HIT spectrometer using pulsed neutron beam.

Figure 1 shows the $S(Q)$ for liquid $Ge_{33}S_{67}$ at 900 °C and $Ge_{50}S_{50}$ at 730 °C. The quality of former spectrum is not good but the very large prepeak, which is larger than that of liquid $Ge_{33}Se_{67}$, is clearly seen. The another spectrum has good statistics. The quality of this spectrum can be compared with the spectra for Ge-Se mixtures obtained from HIT spectrometer. Hence the use of HERMES spectrometer is effective for investigation of the $S(Q)$ of liquid semiconductors in the low Q region especially in the region around the prepeak.

In order to obtain more infomation about the the prepeak in $S(Q)$ more measurements using HERMES is in progress.

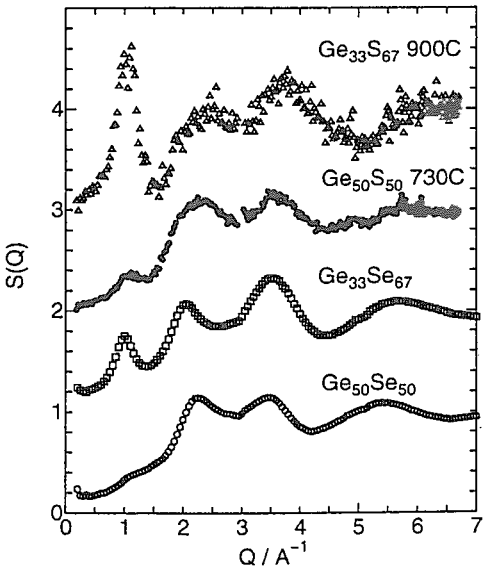

Figure 1. The $S(Q)$ obtained from HERMES spectrometer (upper two spectra) and from HIT spectrometer (lower two spectra).

Reference

1) K. Maruyama, et al., J. Non-Cryst. Solids **250-252** (1999) 483.

研究テーマ：TeO_2ガラスにおける網目構造の null-matrix 法による観測
表題：中性子回折実験による M_2O-TeO_2 (M=Li, Na, $Li_{0.62}Na_{0.38}$) ガラスの構造

1-4-4 Neutron diffraction study on M_2O-TeO_2 (M=Li, Na, $Li_{0.62}Na_{0.38}$) glasses

H. Munemura, M. Misawa[1] and K. Maruyama[1] and K. Ohyama[2]

Graduate School of Science and Technology, Niigata University, Niigata 950-2181, Japan
[1]Department of Chemistry, Niigata University, Niigata 950-2181, Japan
[2]Institute for Materials Research, Tohoku University, Sendai 980-8577, Japan

It is well known that tellurite glasses form a network structure composed of Te-O. By the melt quenching method, the tellurite (TeO_2) glass can be easily obtained when the modifier such as alkalioxide is added to TeO_2. In the glassy state, it is suggested that there are two main structural units which are TeO_3 trigonal pyramid (tp) and TeO_4 trigonal bipyramid (tbp). However the network structure is not clear yet.

In order to decide exact structure factor S(Q), neutron diffraction measurements were performed on $25(Li_{0.62}Na_{0.38})_2O$-$75TeO_2$ and $20M_2O$-$80TeO_2$ (M=Li, Na, $Li_{0.62}Na_{0.38}$) glasses. For the blended alkalioxide $(Li_{0.62}Na_{0.38})_2O$, Li and Na were mixed at the ratio where the neutron scattering length averaged for alkali cations became null. All glass samples were prepared by melting the component oxides in platinum crucible at 550-600°C for 30-60min in air. The melt was quenched by putting the bottom of the crucible into the water.

Neutron diffraction measurements were carried out by using the Kinken powder diffractometer for high efficiency and high resolution measurements, HERMES, of Institute for Materials Research(IMR), Tohoku University, installed at the JRR-3M reactor in JAERI, Tokai. A wavelength 1.8196 Å was employed.

Fig. 1 shows the comparison of the S(Q) obtained by HERMES and HIT, the High Intensity Total scattering spectrometer installed in KEK. Those are in good agreement with each other. Fig. 2 shows S(Q) obtained by HERMES for $20M_2O$-$80TeO_2$ glasses.

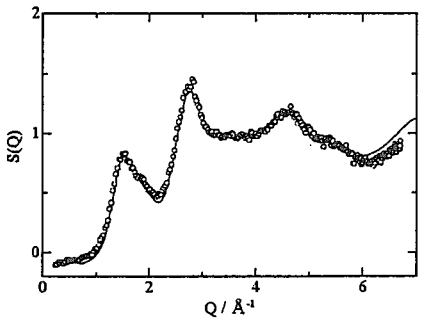

Fig. 1 The Structure factors S(Q) of $25LiNa_2O$- $75TeO_2$ glass. Dots show the result by HERMES and line shows one by HIT-II.

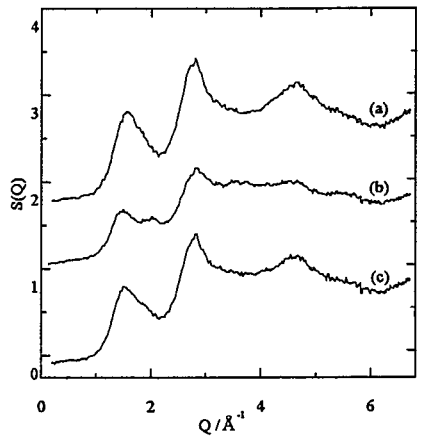

Fig. 2 The structure factors S(Q) from HERMES; (a) $20Li_2O$-$80TeO_2$ glass (b) $20Na_2O$-$80TeO_2$ glass (c) 20 $(Li_{0.62}Na_{0.38})_2O$-$80TeO_2$ glass

研究テーマ：温度圧力による droplet→lamellar 構造相転移のメカニズムの解明
表題：三元系マイクロエマルジョンにおける構造形成のメカニズム

1-4-5

Mechanisms of the Structural Formation in a Ternary Microemulsion System

M. Nagao*, H. Seto†, Y. Kawabata† and T. Takeda†

Institute for Solid State Physics, The University of Tokyo, 106-1 Shirakata, Tokai 319-1106, Japan, †Faculty of Integrated Arts and Sciences, Hiroshima University, 1-7-1 Kagamiyama, Higashihiroshima 739-8521, Japan

Ternary microemulsion systems consisting of water, oil and amphiphile have been investigated by many researchers, since the systems form various self-assemble structures under various external conditions such as composition of samples, temperature or pressure. We have focused on an AOT (dioctyl sulfosuccinate sodium salt), D_2O and *n*-decane ternary microemulsion system with AOT volume fraction ϕ_s being about 0.2 and the same volume of D_2O and *n*-decane. This mixture is known to form a dense water-in-oil droplet structure at ambient temperature and pressure. We have investigated the structural phase transitions with increasing temperature and/or pressure by means of small angle neutron scattering (SANS) and neutron spin echo (NSE). It has been clarified that the system transformed from the one-phase dense water-in-oil droplet to two-phase coexistence of the lamellar phase and the disordered phase, which includes both the possibilities of the droplet structure and the bicontinuous [1,2]. From the NSE measurement [2,3], however, it was suggested that mechanisms of the structural formation were different between the high temperature phase and the high pressure one. In this report, we introduce normalized temperature ($\hat{T}$) and pressure ($\hat{P}$) and characterize the temperature and the pressure effects on structural formation.

In Figure 1, temperature and pressure dependence of SANS profile for the sample ϕ_s=0.230 is shown. At ambient temperature and pressure a broad single peak profile due to the one-phase dense droplet structure was observed. At both the conditions of

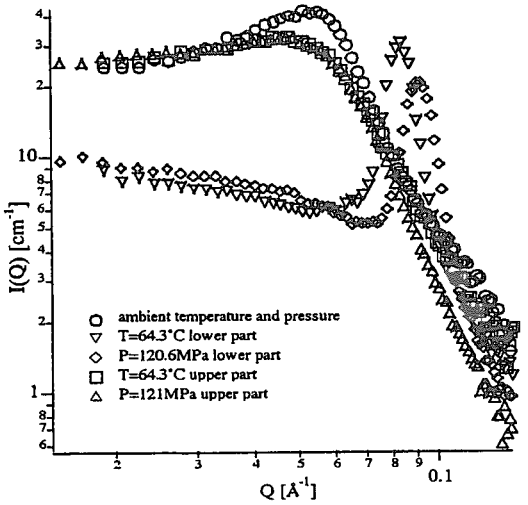

Figure 1: SANS profiles at ambient temperature and pressure (○), T=64.3°C and P=0.1MPa (lower part of sample ▽ and upper part □) and T=25°C and P=121MPa (lower part of sample ◇ and upper part △). The lamellar structure appeared only at the lower part of sample at high temperature or high pressure region.

T=64.3°C, P=0.1MPa and of T=25°C, P=121MPa, single peak profile from the lamellar structure was observed at the lower part of sample. Detailed description of temperature and pressure dependence of SANS profiles and the data analysis has already been published [1,2].

The characteristic mean repeat distances of water domains for the disordered phase, d_m^T and d_m^P, and that of lamellar structure, d_l^T and d_l^P, were derived from the SANS profile and their temperature and pressure dependences are shown in Fig. 2. The horizontal axis is the normalized temperature $\hat{T} = (T - T_s)/|T_c - T_0|$ and the normalized pressure $\hat{P} = (P - P_f)/|P_f - P_0|$ for ϕ_s=0.209, 0.224 and 0.230. Here, T_0, T_c, P_0 and P_f are room temperature, transition crossover temperature, ambient pressure and transition finish pressure, respectively.

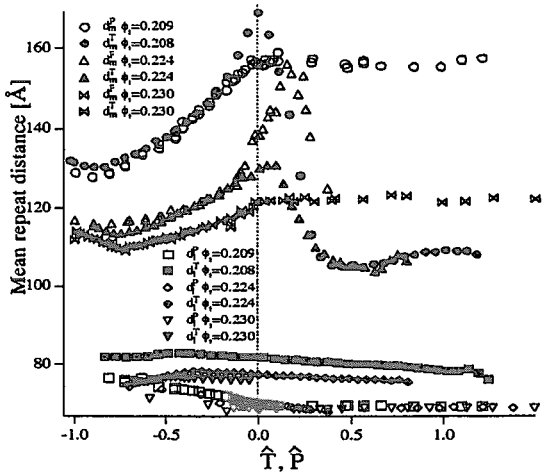

Figure 2: Mean repeat distance d of the disordered phase (d_m^T for temperature variation and d_m^P for pressure) and of the lamellar phase (d_l^T for temperature and d_l^P for pressure). At $\hat{T} < 0$ and $\hat{P} < 0$, d_m^T and d_m^P depended on $\hat{T}$, $\hat{P}$ and ϕ_s. Above $\hat{T} = 0$, d_m^T decreased drastically because of subsequent phase transition to the high temperature single phase, while above $\hat{P} = 0$ d_m^P kept constant for each ϕ_s. The d_l^T depended on $\hat{T}$ and ϕ_s at the covered temperature range, while d_l^P depended on $\hat{P}$ at $\hat{P} < 0$ and constant at $\hat{P} > 0$.

With increasing temperature and pressure at $\hat{T}<0$ and $\hat{P}<0$ temperature and pressure dependences of d were the same. At $\hat{T}>0$, the d_m^T drastically decreased with increasing temperature because there exists another structural phase transition to high temperature single phase, while d_m^P kept constant at $\hat{P}>0$. This implies that there is no subsequent phase transition at high pressure, like the temperature case. In order to estimate the polydispersity of water or oil domains, Chen and co-workers [4] proposed the disorder parameter, $\Delta=d/2\pi\xi$, where ξ is the correlation length of the system. They suggested that when $\Delta\leq0.446$ the system should be the droplet structure and $\Delta>0.446$ the bicontinuous. In Fig. 3 $\hat{T}$ and $\hat{P}$ dependences of Δ are shown. It indicated that the system became more disordered with increasing temperature or pressure below $\hat{T}=0$ or $\hat{P}=0$, and the lamellar phase was highly ordered and the degree of the order did not change through the covered temperature and pressure range. Above $\hat{T}=0$ or $\hat{P}=0$, the disordered phase became more ordered with increasing temperature, while it stayed disordered with increasing pressure.

The successive phase transition with increasing temperature showed that the electrostatic interaction, due to the dissociation of counter ion from the head group of AOT molecules, increased and the spontaneous curvature of membranes were changed even above $\hat{T}=0$. On the contrary, the result suggested that the spontaneous curvature changed below $\hat{P}=0$, while it did not changed above $\hat{P}=0$ with increasing pressure. This result could be interpreted that the hydrophobic interaction between AOT tails and oil molecules are important to understand the structural formation in case of pressure.

[1] M. Nagao and H. Seto, *Phys. Rev. E* **59** (1999) 3169-3176.

[2] M. Nagao, H. Seto, Y. Kawabata and T. Takeda, *J. Appl. Cryst.* **33** (2000) 653-656.

[3] M. Nagao, H. Seto, Y. Kawabata, T. Takeda and S. Komura, *AIP Conference Series* **461** (1999) 154-155.

[4] S. H. Chen, S. L. Chang and R. Strey, *Col. Polym. Sci.* **81** (1990) 30-35.; S. H. Chen, S. L. Chang, R. Strey, J. Samseth and K. Mortensen, *J. Phys. Chem.* **95** (1991) 7427-7432.

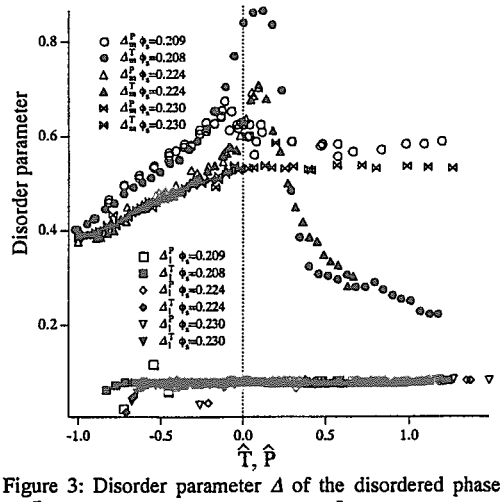

Figure 3: Disorder parameter Δ of the disordered phase (Δ_m^T for temperature variation and Δ_m^P for pressure) and of the lamellar phase (Δ_l^T for temperature and Δ_l^P for pressure). At $\hat{T}<0$ and $\hat{P}<0$, the disordered phase became more disordered and at $\hat{T}=0$ another phase transition occurred and the system became ordered, while above $\hat{P}=0$, Δ_m^P kept constant. Δ_l^T and Δ_l^P stayed at almost constant value. This implies that the static feature of the lamellar stacking is almost the same between temperature and pressure.

研究テーマ：マイクロエマルジョンにおける油分子と界面活性剤炭化水素鎖の相互作用の解明
表題：三元系マイクロエマルジョンから得られる小角散乱関数の解析

1-4-6

Analysis of Small-Angle Neutron Scattering Profiles of Ternary Microemulsion Systems

M. Nagao* and H. Seto†

Institute for Solid State Physics, The University of Tokyo, 106-1 Shirakata, Tokai 319-1106, Japan, †Faculty of Integrated Arts and Sciences, Hiroshima University, 1-7-1 Kagamiyama, Higashihiroshima 739-8521, Japan

As discussed in a previous article in this issue [1], the hydrophobic interaction between amphiphile tails and oil molecules has a decisive role for the structural formation of microemulsion systems as well as the electrostatic interaction between head groups of amphiphile and water molecules. In order to clarify the effects of oil molecules, we performed small angle neutron scattering (SANS) experiments on AOT (dioctyl sulfosuccinate sodium salt), D_2O and 3 different kinds of *n*-alkane (*n*-hexane, *n*-octane, and *n*-decane) systems. The effects of a kind of *n*-alkane have been investigated in the dilute droplet region by Eastoe et al [2,3]. However, the dense droplet system could be more interesting because such the systems have a phase transition to the lamellar structure with increasing temperature or pressure. From such the viewpoint, 3 mixtures of ϕ_s (volume fraction of AOT) =0.2 with the same volume of water and *n*-alkane were prepared and the SANS profiles were observed at SANS-U. In order to explain observed SANS profiles, two types of model were compared.

For the *n*-decane system, we have analyzed SANS data using Teubner and Strey's (TS) model [4] so far. This model assumes a periodic distribution of water and oil domains, and their correlation decays exponentially with distance. In Fig. 1, observed SANS profiles of the microemulsions with various *n*-alkanes are shown. The lines indicate the fitting results to the TS model. This model can explain the data observed from the *n*-decane system, however, can not explain the scattering

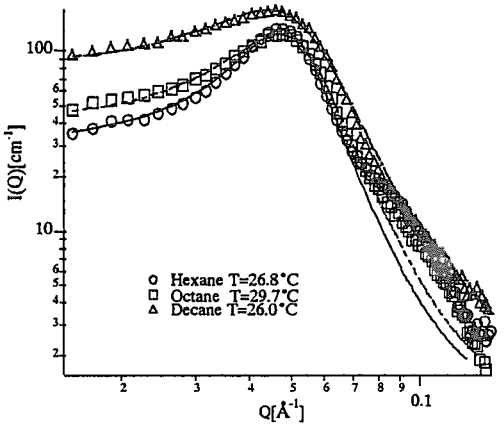

Figure 1: Observed SANS profiles of AOT / D_2O / *n*-hexane (○), *n*-octane (□) and *n*-decane (△). The temperature conditions were 26.8, 29.7 and 26.0°C, respectively. Lines are fitting result to TS model [3].

profiles for the system with shorter *n*-alkanes at high Q region. Therefore, we introduced another model which is a product of the particle form factor, $P(Q)$, and the structure factor, $S(Q)$. The form factor is assumed to be the one of spherical particle with Schultz size distribution [5] and the structure factor is of a hard sphere adhesive potential case [6]. The $P(Q)$ includes the mean radius of droplet R_s and a droplet radius distribution width Z as fit parameters. The $S(Q)$ includes the number density of the hard sphere particles ϕ, adhesive potential parameter Ω with the fractional surface thickness ε, and a hard sphere diameter R_h. The stickiness between droplets, $1/\tau$, was determined as $1/\tau=12\varepsilon\exp(-\Omega)$. The fitting results were much better than the TS model as depicted in Fig. 2.

This model was successfully used to explain small angle x-ray scattering (SAXS) profiles of the AOT / D_2O / *n*-decane system

by Seto et al [7]. The differences of SAXS and SANS are a scattering length distribution of each ingredient and the instrumental resolution. The Q-resolution of SANS is worse than SAXS at SOR in general, and smearing effects in SANS should be corrected with valid resolution function. We convoluted the theoretical prediction with assuming a 12% Q-resolution. The result indicated that the smearing effects mainly affected the value of ε, and $1/\tau_s$ was decreased about 17% after considering smearing effects. The carbon number dependence of $1/\tau$ and of the other parameters, however, did not change after the convolution was considered.

The computed $P(Q)$ and $S(Q)$ are shown in Fig. 3 with obtained fit parameters as shown in Table 1. Here, we fixed some parameters for simplicity, Z=10, ε=0.02 and ϕ=0.4. With increasing carbon number of n-alkane, the adhesive potential parameter between droplets decreased and, therefore, the stickiness between droplets increased. This fact might imply that the oil penetration to AOT tail region decreases with increasing carbon number of n-alkane and the tail-tail interaction increase. This result supported the result obtained by Eastoe et al [2,3].

[1] M. Nagao, H. Seto, Y. Kawabata and T. Takeda, *ISSP-NSL Activity Report* 7 (2000) previous article in this issue.

[2] J. Eastoe, B. H. Robinson and D. C. Steytler, *J. Chem. Soc. Faraday Trans.* **86** (1990) 511-517.

[3] J. Eastoe, W. K. Young, B. H. Robinson and D. C. Steytler, *J. Chem. Soc. Faraday Trans.* **86** (1990) 2883-2889.

[4] M. Teubner and R. Strey, *J. Chem. Phys.* **87** (1987) 3195-3200.

[5] M. Kotlarchyk and S. H. Chen, *J. Chem. Phys.* **79** (1983) 2461-2469.

[6] Y. C. Liu, S. H. Chen and J. S. Huang, *Phys. Rev. E* **54** (1996) 1698-1708.

[7] H. Seto, D. Okuhara, Y. Kawabata, T. Takeda, M. Nagao, H. Kamikubo and Y. Amemiya, *J. Chem. Phys.* in press.

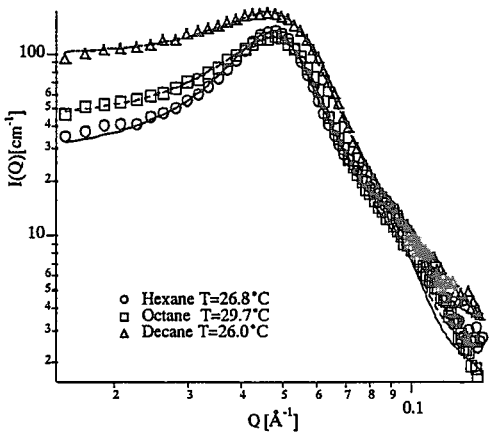

Figure 2: Observed SANS profiles of AOT / D_2O / n-hexane (○), n-octane (□) and n-decane (△). The fitted data are the same as shown in Fig. 1. Solid, dashed and dotted lines are fitting result to the model consisting of $P(Q)$ for spherical particle form factor with Schultz distribution [5] and $S(Q)$ for hard sphere adhesive potential [6].

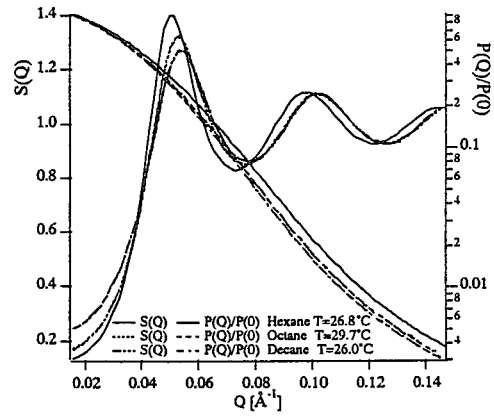

Figure 3: Calculated $S(Q)$ and $P(Q)$ / $P(0)$. The first peak intensity of $S(Q)$ became larger and the adhesive potential increased with decreasing alkane chain length. Calculated $P(Q)$ was shown as normalized value at Q=0.

	R_s[Å]	Ω	R_h[Å]	$1/\tau$	$1/\tau_s$
hexane	30.6±0.3	-0.42±0.02	136.6±0.4	0.36±0.02	0.29
octane	32.0±0.2	-0.67±0.01	134.0±0.3	0.47±0.01	0.39
decane	32.6±0.4	-0.91±0.02	136.1±1.0	0.60±0.01	0.52

Table 1: Obtained fit parameters. The observed value of $1/\tau_s$, after considering the smearing effects, is also shown in the last column.

研究テーマ：リン脂質マイクロエマルションの構造解析
表題：中性子散乱法によるリン脂質マイクロエマルションの構造解析

1-4-7 Structural Study of a Phospholipid Microemulsion by Neutron Scattering

S. Ichikawa, Y. Sano[1], M. Nakajima[2], S. Mukataka

Institute of Applied Biochemistry, University of Tsukuba, Tennodai 1-1-1 Tsukuba, Ibaraki 305-8572 Japan
[1] Faculty of Pharmaceutical Sciences, Setsunan University, Nagaotoge-cho 45-1, Hirakata, Osaka 573-0101, Japan
[2] National Food Research Institute, Ministry of Agriculture, Forestry and Fisheries Kannondai 2-1-2, Tsukuba, Ibaraki 305-8642, Japan

Biocompatible microemulsion system will expand its application field to the food and pharmaceutical industries. Recently, we found the formation of biocompatible W/O microemulsion system by the significant increase of water content in the organic phase for the combination of phosphatidylcholine (PC) / water/ oleic acid. In this study, small-angle neutron scattering experiments were carried out in order to characterize the structure of this W/O microemulsion system composed of PC, D_2O and oleic acid.

Microemulsion systems having different water (D_2O) volume fraction were prepared at constant PC concentration (200g/L). All samples were clear even the maximum water volume fraction was 4.6%, then seemed to be identical visually. Small-angle neutron scattering experiments were performed with SANS-U spectrometer in the guide hall of the reactor JRR-3M. A wavelength was 7.0 Å. Multiple samples were mounted on a sample changer at 25℃.

Scattering profiles remarkably changed by the water volume fraction as shown in Fig. 1. It suggests the structural change of microemulsion system. The analysis is in progress to clarify the way of structural change of microemulsion.

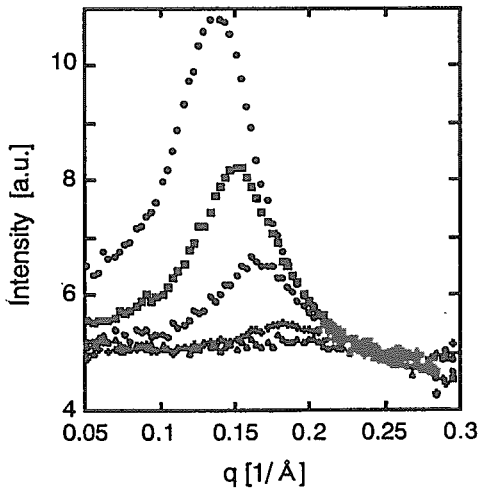

Figure 1 Effect of water volume fraction on the small-angle neutron scattering profiles of PC / water (D_2O) / oleic acid microemulsion system. PC concentration was constant at 200 g/L. Water volume fraction was 0.3% (▲), 1.6% (+), 2.5% (◆), 3.7% (■) and 4.6% (●), respectively.

研究テーマ：水－プロパノール－KCl 系の亜臨界組成におけるクラスターの不完全凝集構造の観察
表題：水－1 -プロパノール溶液の亜臨界塩組成における濃度ゆらぎ

1-4-8 Concentration fluctuation of 1-propanol-water solution at sub-critical salt composition

T. Omi, H. Munemura[1], M. Nagao[2], K. Maruyama and M. Misawa

Department of Chemistry, Faculty of Science, Niigata University, Niigata 950-2181 Japan
[1]Graduate School of Science and Technology, Niigata University, Niigata 950-2181 Japan
[2]Institute for Solid State Physics, The University of Tokyo, Tokai 319-1106 Japan

1-propanol and water mix in any proportion. However, when the concentration of salt such as KCl, C_{KCl}, added into the solution exceeds a critical concentration C_0, the reentrant type phase separation occurs. We have reported the structural evolution of concentration fluctuation of the solution including KCl in excess of C_0 ($C_{KCl}>C_0$) as a function of temperature[1]. In the present study we intend to measure the concentration fluctuation of the same solution at sub-critical concentration of KCl ($C_{KCl}< C_0$).

The solution of 1-propanol (C_3H_7OH) and heavy water (D_2O) with the molar ratio of 1-propanol/water of 1/5 including sub-critical concentration of KCl, C_{KCl}=0.0197 in mole fraction, was examined by using SANS-U. Figure 1 compares the scattering intensities I(Q) observed at temperatures from 28 to 77℃. Each curve was obtained by combining two data measured at different camera lengths of 8m and 2m. The fractal nature of the concentration fluctuation with a fractal dimension of 1.92 is obtained by fitting the I(Q) curves to the theoretical formula proposed for fractal structure[2]. The value of 1.92 is the same as that obtained for the solution with KCl in excess of C_0, C_{KCl}=0.0208, reported previously[1]. The temperature dependence of the correlation length ξ obtained for the current solution is, however, quite different from that for the solution with excess KCl[1] as shown in Fig.2.

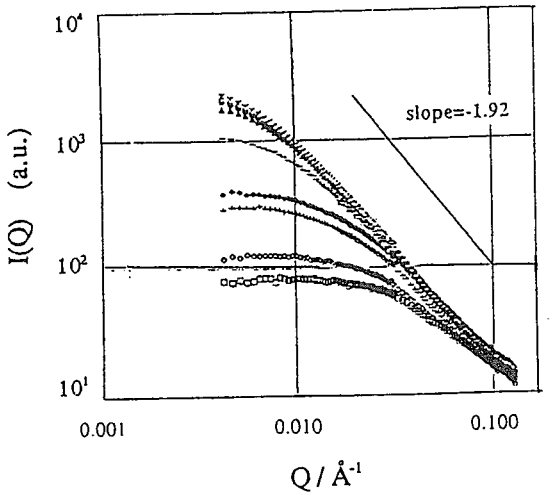

Fig. 1 Small angle neutron scattering intensity I(Q) measured for 1-propanol-water solution $(C_3H_7OH)_1$-$(D_2O)_5$ including KCl of 0.0197 in mole fraction by using SANS-U.

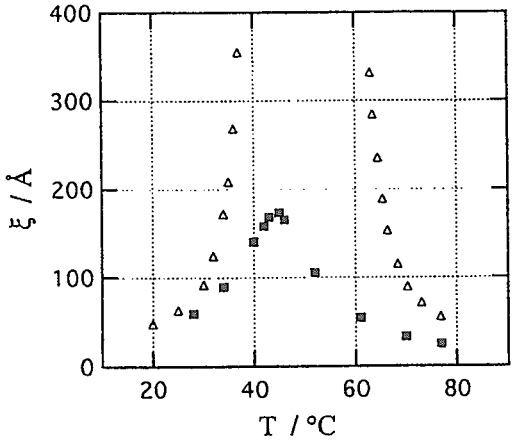

Fig. 2 Correlation length ξ for sub-critical solution $(C_3H_7OH)_1$-$(D_2O)_5$ of C_{KCl}=0.0197 (solid squares) and that for the solution with excess KCl, C_{KCl}=0.0208 (open triangles).

References
1) K. Yoshida, M. Misawa, K. Maruyama, M. Imai and M. Furusaka, J. Chem. Phys. (in press).
2) T. Flertoft, K. Kjems and S. K. Sinha, Phys. Rev. B33 (1986) 269.

研究テーマ：ヘキサフルオロイソプロパノール/水混合溶液の中性子小角散乱の温度依存性
表題：ヘキサフルオロイソプロパノール/水混合溶液の中性子小角散乱の温度依存性

1-4-9
Temperature Dependence of Small-angle Neutron Scattering of a Hexafluoroisopropanol-water mixture

T. Yamaguchi, K. Yoshida, and M. Nagao[1]

Department of Chemistry, Faculty of Science, Fukuoka University, Johnan-ku, Fukuoka, 814-0180 Japan
[1]Neutron Scattering laboratory, The Institute for Solid State Physics, The University of Tokyo, Tokai, Ibaraki, 319-1106 Japan

Hexafluoroisopropanol(HFIP) is widely used in biochemistry field because it is the most powerful reagent for denaturation of protein. In our previous work, we found that alcohol-induced denaturation of protein is closely related to cluster formation in HFIP-water mixture solvent. To extend this study, it is necessary to investigate temperature dependence of correlation length of a HFIP-water mixture to elucidate the driving force of cluster formation in it. Small-angle scattering is a useful probe of observing the cluster.

We carried out small-angle neutron scattering (SANS) measurements of 8.9 mol% HFIP-water mixture at 12, 25, and 37°C. SANS measurements were performed on the SANS-U spectrometer of the Institute for Solid State Physics, the University of Tokyo, installed at the beamline of a cold source in JRR-3M. The camera length was 2 m, where Q range obtained is from 0.03 to 0.15 Å^{-1}. The scattering intensities $I(Q)$ were obtained after subtraction of background of a quartz cell of thickness 2 mm and absorption correction of the sample.

The Ornstein-Zernike plots, $I(Q) = I(0)[1+\xi^2Q^2]^{-1}$, of HFIP-water at various temperatures are shown in Figure 1. The correlation length ξ are 6.5, 9.6, and, 11.6 Å at 12, 25, and 37°C, respectively. The ξ values of HFIP-water monotonously increase with increasing of temperature, although those of aliphatic alcohols, *e.g.* ethanol and 1- and 2-propanol, have a minimum at around 25°C.[1] The different temperature dependence indicates that cluster formation in HFIP-water mixture does not arise from the hydrophobic hydration as shown in aliphatic alcohol–water mixtures. The generated cluster in HFIP-water seems to be not micell-like one where the hydrophobic groups of HFIP aggregates inside, but a composite one composed of HFIP and water molecules due to hydrogen bonding.

[1] G. D'Arrigo *et al.*, *J. Chem. Soc. FARADAY Trans.*, **86**, 1503 (1990).

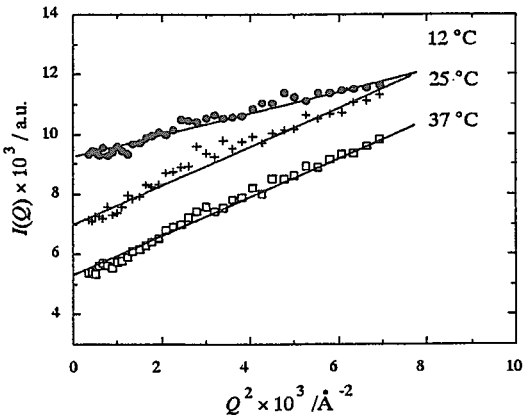

Figure 1. Ornstein-Zernike plots of 8.9 mol% HFIP-water mixture at 12, 25, and 37 °C.

研究テーマ：超臨界メタノールの中性子小角散乱
表題：超臨界メタノールの中性子小角散乱

1-4-10
Small－angle Neutron Scattering of Supercritical Methanol

T. Yamaguchi, K. Watanabe, K. Yoshida, and M. Nagao[1]

Department of Chemistry, Faculty of Science, Fukuoka University, Johnan-ku, Fukuoka, 814-0180 Japan

[1]Neutron Scattering laboratory, The Institute for Solid State Physics, The University of Tokyo, Tokai, Ibaraki, 319-1106 Japan

Supercritical methanol (SCM; T_c = 513K, P_c = 8.1 MPa) is a novel solvent in recovery of useful chemicals from plastic wastes *e.g.* PET. The characteristic chemical reaction in SCM originates from the degree of hydrogen bonding and cluster formation in it. Small-angle neutron scattering (SANS) measurement is a useful probe to elucidate the cluster formation.

We designed a high-temperature high-pressure SANS cell and carried out SANS measurements on SCM at 8.28 ~ 11.1 MPa and 521K. The HTHP cell is made of Inconel 718 to prevent corrosion and we used sapphire as windows. SANS measurements were performed on the SANS-U spectrometer of the Institute for Solid State Physics, the University of Tokyo, installed at the beamline of a cold source in JRR-3M. The camera lengths were 2 m and 8 m, where the Q range obtained was from 0.008 to 0.15 Å^{-1}. The intensities $I(Q)$ were obtained after subtraction of background of empty cell and absorption correction of the sample.

Figure 1 shows Q (= $4\pi\lambda^{-1}\sin\theta$) dependence of the scattering intensity $I(Q)$ of SCM at various pressures. The scattering intensities of SCM drastically changed depending on pressure, *i.e.* density of SCM, and had a maximum at 8.69 MPa. The thermodynamical condition where density fluctuation has a maximum locates on the extended line of vapor-liquid equilibrium line as in the case of other supercritical fluids. The correlation lengths of SCM obtained from the Ornstein-Zernick plot applied to the SANS data are smaller than those of supercritical carbon dioxide, but resemble the values of supercritical water (SCW) at the same reduced densities.[1] The hydrogen bonding in SCM and SCW appears to shorten the correlation length in the hydrogen bonded liquids.

[1] T. Morita *et al.*, *J. Chem. Phys.* **112**, 4203 (2000).

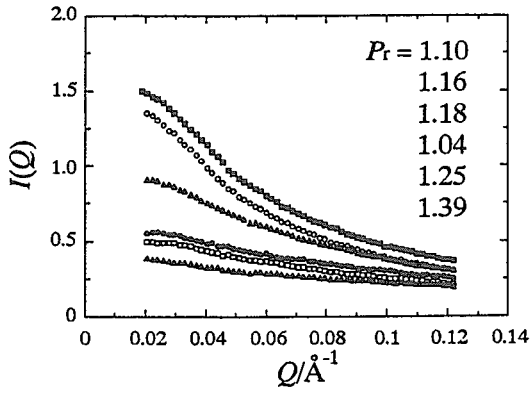

Figure 1. Q dependence of scattering intensity $I(Q)$ of SCM at various reduced pressure ($P_r = P/P_c$) and at 521 K.

研究テーマ：リエントラント液晶の構造
表題：リエントラント液晶の構造

1-4-11 Structure of a reentrant liquid crystal

O. Oishi, M. Nagao[1]

Institute for Molecular Science, Myodaiji, Okazaki 444-8585, Japan

[1] *Neutron Scattering Laboratory, The Institute for Solid State Physics, the University of Tokyo, Shirakata, Tokai, Naka, Ibaraki, 319-11, Japan*

When conventional liquid loses its isotropic (I) symmetry and assumes uniaxial orientational order, the nematic (N) liquid crystalline state is formed. The smectic A (S_A) state is characterized by its one-dimensional translational order in addition to the nematic order. It is therefor natural that the phase transition sequence be I-N-S_A on lowering the temperature. However, the present compound, CBOBP (4-cyanobenzoyloxy-[4-octylbenzoyloxy]-p-phenylene), exhibits a transition sequence, I-510-N-458-S_{Ad}-431-N-415-S_{A1}-398-crystal(The transition temperatures are shown in K.) (doubly reentrance sequence) on lowering the temperature. The second N phase is called reentrant nematic (RN), and the S_{Ad} to RN transition means that 1-D translational lattice melts on lowering the temperature. Due to this peculiarity, the nature of this transition sequence has been one of the interesting topics in recent liquid crystal research[1].

We made neutron diffraction study to clarify the structure of the liquid crystalline phases and hence to clarify the microscopic mechanism of this phenomenon. For this purpose a compound with perdeuterated chain, CBOBP-d17 was prepared. SANS-U instrument was used at an wavelength of 7Åwith a velocity selector.

Figure 1 shows the magnitudes of the scattering vectors of the diffraction peaks. The two data points at lowest temperatures correspond to the supercooled S_A1 phase. It is revealed that two peaks coexist in the RN phase.

[1] S. Miyajima and T. Hosokawa, Phys. Rev. B, 52, 4060(1995)

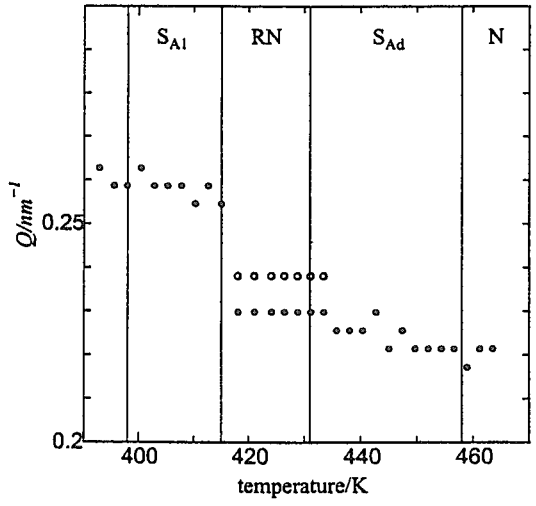

Figure 1. Magnitudes of the scattering vectors in the liquid crystalline phases.

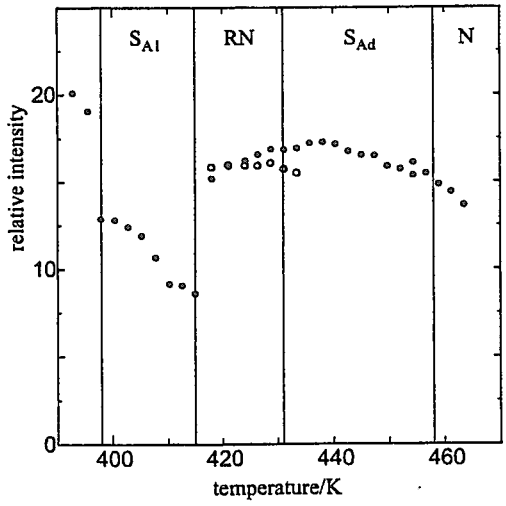

Figure 2. Relative intensities of the diffraction peaks.

研究テーマ：紐状ミセルの集団運動
表題：紐状ミセルのダイナミクスの中性子スピンエコー法による実験

1-4-12
Neutron Spin Echo Study on the Dynamics of Wormlike Micelles

H. Seto, T. Kato[1], T. Takeda, M. Nagao[2], Y. Kawabata

Faculty of Integrated Arts and Sciences, Hiroshima University, Higashihiroshima 739-8521, Japan
[1]Department of Chemistry, Tokyo Metropolitan University, Hachioji, 192-0397, Japan
[2]Institute for Solid State Physics, The University of Tokyo, Tokai 319-1106, Japan

Aqueous solution of non-ionic surfactant $C_{16}E_7$ (= $C_{16}H_{33}$ $(OC_2H_4)_7OH$) forms network of wormlike micelles at proper temperature and concentration. Static properties of this system were known to be the same as those of entangled solutions of flexible polymers, however, their dynamic properties are different form those of polymers.

Neutron spin echo experiments were performed in order to investigate the collective motion of the wormlike micelles at T = 35°C and 45°C. In this experiment, 3 mixtures with $C_{16}E_7$ contents C being 3.2%, 9.6%, and 15.8% were prepared in order to complement the data obtained preveously. [1] All the intermediate structure factor could be explained using the stretched exponential form proposed by Zilman and Granek[2],

$$I(Q,t)/I(Q,0) = \exp(-(\Gamma t)^{\beta}),$$

where β = 0.75 for the "1-dimensional membrane" case, i. e., polymers and wormlike micelles.

By their model, the decay rate Γ is proportional to $Q^{2/\beta}$ and the coefficient is interpreted to be the proportionality factor D_G which has a direct relation with an effective diffusion constant D_{eff} of micelles. Figure 1 shows the concentration dependence of the observed D_G at T = 35°C. The values at C = 1.6, 6.4%, 12.8% and 20% were those depicted in ref. 1. It is noticed that the present values were somewhat larger than the ones preveously obtained. The reason is not yet clear. The experimental conditions of the NSE spectrometer at C2-2, especially the counter system, were changed last year. Therefore, the present values may be calibrated using inappropriate resolution function and the discrepancy should not be essential.

References

[1] H. Seto, et al., J. Phys. Chem. Sol. **60** (1999) 1371.
[2] A. G. Zilman, R. Granek, Phys. Rev. Lett. 77 (1996) 4788.

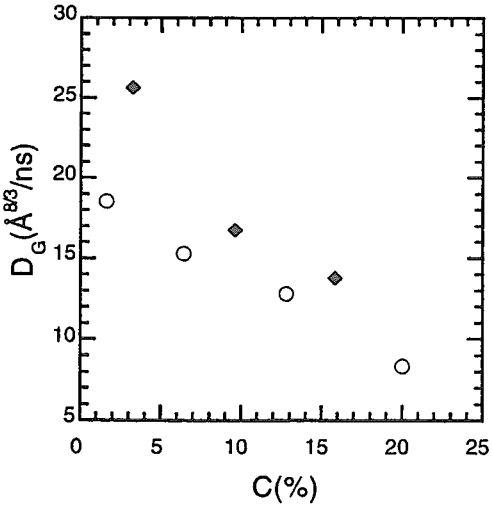

Fig.1 The effective diffusion constant comparing with the preveous values. The open circles are the data obtained at Jülich and the full diamonds at ISSP.

JRR-3M, C2-2 (NSE), 4. Amorphous & Liquid

研究課題：両親媒子系複雑液体のスローダイナミックス

表題：中性子スピンエコー法による両親媒子系複雑液体のスローダイナミクス

1-4-13 Neutron Spin Echo Investigations on the Slow Dynamics in Complex Fluids Involving Amphiphiles

T. Takeda*, Y. Kawabata†, H. Seto*, S. K. Ghosh*, S. Komura‡ and M. Nagao§

*Faculty of Integrated Arts and Sciences and †Graduate School of Bio-Sphere Science, Hiroshima University, Higashi-Hiroshima 739-8521, Japan

‡Department of Physics, ChuoUniversity, Bunkyo-ku, Tokyo 112-8551, Japan

§Institute for Solid State Physics, University of Tokyo, Tokai, Naka Ibaraki 319-1106, Japan

We have studied slow dynamics in complex fluid systems such as the shape fluctuation of microemulsion droplets, membrane undulation in lipid-bilayers and bicontinuous micro-emulsions using neutron spin echo (NSE) spectrometer at C2-2 port of JRR-3M[1]. In the dipalmitoylphosphatidyl-choline (= DPPC) - water system, the lamellar repeat distance d_1 varies greatly with an addition of salt in DPPC - water system. In order to study the dynamics in undulation of lipid bilayers, NSE experiments were carried out on the dilute lamellar phase of the DPPC / water / $CaCl_2$ system with longer d_1 than 300 Å in order to avoid the interactions from neighbouring sheets of membranes.

Figure 1 shows a SANS pattern for a lipid sample (7.7wt% DPPC dispersed in D_2O solutions with 6.8mM $CaCl_2$) with the peak corresponding to d_1 = 430 Å at 52°C. As shown in Fig. 2, the intermediate correlation functions $I(Q, t)$ obtained from the NSE experiments for the lipid samples were well fitted to the following equation,

$$I(Q,t) = I(Q,0)\exp[-(\Gamma t)^{2/3}]. \quad (1)$$

The relaxation rate Γ obtained from the fitting to Eq.(1) increased as Q^3. These results support the theory presented by Zilman and Granek[2]. We have estimated the bending modulus of the lipid membrane κ as a function of the temperature and d_1 using the similar procedure to the case of the non-ionic surfactant $H(CH_2)_{12}(OCH_2CH_2)_5OH$ ($C_{12}E_5$)/n-octane /D_2O system[3,4,5].

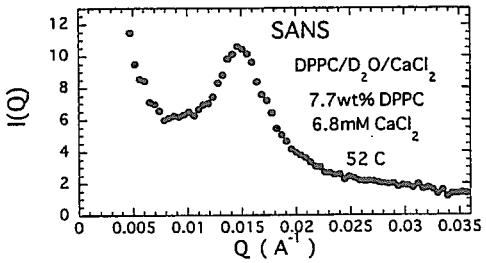

Fig. 1 SANS pattern obtained using SANS-U.

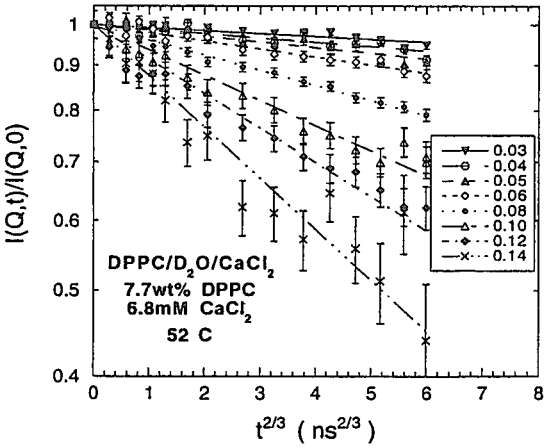

Fig. 2 Intermediate correlation functions $I(Q, t)$ obtained from the NSE experiment for a lipid sample (7.7wt% DPPC dispersed in D_2O solutions with 6.8mM $CaCl_2$) at 52°C.

References

1. T. Takeda et al: J. Phys. Soc. Jpn. 65 Suppl.A, (1996) 189.
2. A. G. Zilman and R. Granek: Phys. Rev. Letters 77, 4788 (1996).
3. T. Takeda et al, AIP CP-469 (1999) 148.
4. T.Takeda et al, J. Phys. Chem. Solids 60 (1999) 1375.
5. T. Takeda et al, AIP CP (2000) in press.

Facilities and Instruments

JRR-3M NSE (C2-2)

Research field

4. Amorphous & Liquid

研究テーマ：温度及び圧力による droplet－lamellar 転移のメカニズムの解明
表題：３元系複雑液体における両親媒子膜の動的ゆらぎについての温度圧力効果の実験

1-4-14

Temperature and Pressure Effects on Dynamical Fluctuation of Amphiphilic Membrane in a Ternary Complex Fluids

Y.Kawabata*,M.Nagao†,H.Seto‡, and T.Takeda‡

*Graduate School of Bio-Sphere Science, Hiroshima University,Faculty of Integrated Arts and Sciences, Hiroshima University1-7-1 Kagamiyama, Higashi-Hiroshima 739-8521 †Institute for Solid State Physics,The University of Tokyo,106-1 Shirakata,Tokai 319-1106, ‡

A ternary complex fluids consisting of water, oil, and amphiphile forms various structures depending on its composition, temperature, and/or pressure. We have investigated temperature– and pressure–induced phase transitions in AOT/D_2O/$C_{10}H_{22}$ system from one-phase dense droplet to two-phase coexistence by means of Small Angle X-ray(SAXS) and Neutron Scattering (SANS), and Neutron Spin Echo(NSE) so far[1]-[5]. Our results indicated that the static features of the high–temperature and the high–pressure phases were similar, however, the dynamical features were different. We concluded that the membrane became flexible with increasing temperature, while rigid with increasing pressure.

In this study, we focused on the dynamical features of the dilute droplet system ($\phi \sim 0.1$, where ϕ is the droplet density). In this system, observed dynamics were successfully explained in terms of the shape and size fluctuation and the translational diffusion of droplets as shown by Huang et al experimentally[6]. Therefore, this system is suitable to check the temperature and the pressure effects on the shape fluctuation of droplets.

The NSE experiments were performed using the ISSP-NSE at JRR-3M in JAERI, Tokai. The measured q ranged over $0.04 \leq q \leq 0.14$ [Å^{-1}] and Fourie time t over $0.15 \leq t \leq 15$[ns]. A mixture of 5.4% AOT, 4.6% D_2O and 90% $C_{10}D_{22}$ was used for the present study. The structure of this system was characterized to be dilute water–in–oil droplet structure with the droplet radius being about 30Å at ambient temperature and pressure. The experiments were carried out at 25°C under ambient pressure (RTP), at 43°C and 0.1MPa (HT) and at 25°C and 45MPa (HP).

The intermediate correlation function $I(q,t)/I(q,0)$ obtained from the NSE experiments decayed with single exponential function as follows,

$$I(q,t)/I(q,0) = \exp(-D_{eff}q^2t), \qquad (1)$$

where D_{eff} was the effective diffusion coefficient. The D_{eff} is a sum of two terms,

$$D_{eff} = D_{tr} + D_{def}, \qquad (2)$$

where D_{tr} is the translational diffusion coefficient and D_{def} the shape deformation diffusion coefficient. The D_{def} could be written as,

$$D_{def} = \frac{5\lambda_2 f_2(qr_0)\langle|a_2|^2\rangle}{q^2[4\pi r_0^2 f_0(qr_0)+5f_2(qr_0)\langle|a_2|^2\rangle]} \qquad (3)$$

up to the lowest mode($n = 2$) of the shape deformation, where λ_2 is the damping frequency of the second mode, $\langle|a_2|^2\rangle$ the mean square of the second mode fluctuation amplitude, q the scattering vector, r_0 the radius of droplet, and f_n the n–th form factor of the spherical shell. The λ_2 can be ex-

pressed as,

$$\lambda_2 = \frac{\kappa}{\eta r_0^3}\frac{96}{55}w, \qquad (4)$$

where η is the average of the viscosity inside and outside the droplet, κ the bending modulus of amphiphilic membrane, $w = r_0/r_s$, and r_s the spontaneous radius of membrane.

The obtained $D_{eff}(q)$ is shown in Fig.1 with fitting results to the Eq.(2). The peak position, q_{max}, corresponds to the characteristic wave number of the droplet radius ($q_{max} = \pi/r_0$). At RTP, the peak position was observed at $q_{max}^{RTP} \sim 0.08\text{Å}^{-1}$, shifted to $q_{max}^{HT} \sim q_{max}^{HP} \sim 0.1\text{Å}^{-1}$ with increasing temperature and/or pressure, and the value of D_{eff}^{HT} and D_{eff}^{HP} became larger than D_{eff}^{RTP}. This result indicated that the radius of droplets became smaller and the shape deformation of droplets became faster with increasing temperature or pressure. The κ and $\langle|a_2|^2\rangle/r_0^2$ could be obtained from Eq.(4) and were showen in Table1. The κ at HP was larger, and that at HT was smaller than that at RTP. This result indicated that the membranes became rigid with applying pressure, while flexible with increasing temperature. The $\langle|a_2|^2\rangle/r_0^2$ decreased with increasing pressure and increased with increasing temperature. It indicated that the shape fluctuation was suppressed at HP, on the other hand, the shape fluctuation became larger at HT. These results were consistent with the results of "dense droplet" system[2, 4]. Therefore, we could conclud that the effects of temperature and pressure played opposite roles although the apparent structures of high temperature and high pressure phases were similar. This fact suggested that the mechanism of the structural formation with increasing temperature is different from that with increasing pressure.

Table 1: The bending modulus κ and $\langle|a_2|^2\rangle$ for each phase obtained from the NSE experiments.

	RTP	HP	HT
$\kappa_{\phi\sim0.1}[k_BT]$	0.18	0.22	0.14
$\frac{\langle\|a_2\|^2\rangle}{r_0^2}_{\phi\sim0.1}$	0.12	0.14	0.16

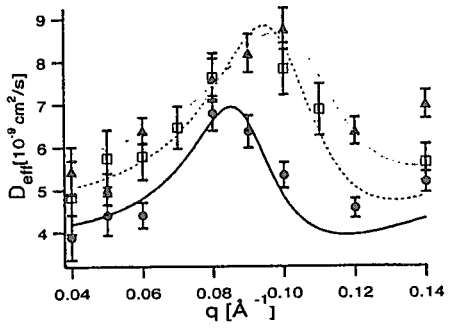

Figure 1: Derived diffusion coefficient D_{eff} from the NSE experiments. Full circles correspond to the RTP phase, full triangles the HT phase and squares the HP phase. Lines are fitting results to Eq.(2)

References

[1] Nagao, M., and Seto, H., *Phys. Rev. E* **59**, 3169-3176 (1999).

[2] Nagao, M. et al., *J. Appl. Cryst* **33**, 653-656 (2000),

[3] Seto, H. et al., *J. Chem. Phys.* in press,

[4] Nagao, M. et al., *AIP Conference Proceedings* **469** 154 (1999).

[5] Kawabata, Y. et al., *AIP Conference Proceedings* in press.

[6] Huang, J. S. et al., *Phys. Rev. Lett.* **59**, 2600 (1987).

研究テーマ：リン酸２水素カリウム結晶より生成する非晶質の低エネルギー振動
表題：水素化リン酸カリウムガラスの低エネルギー励起

1-4-15

Low-energy Excitation in Protonated Potassium Phosphate Glass

O. Yamamuro, Y. Madokoro, H. Yamasaki, K. Harabe, I. Tsukushi [1], and T. Matsuo

Department of Chemistry, Graduate School of Science, Osaka University, 1-1 Machikaneyama-cho, Toyonaka, Osaka 560-0043, Japan
[1] Department of Physics, Chiba Institute of Technology, Narashino, Chiba 275-0023, Japan.

Introduction

KH_2PO_4 (KDP) is a well-known hydrogen-bonded crystal undergoing a ferroelectric phase transition at T_c = 123 K. The ferroelectricity of KDP is due to the ordering of protons on O-H···O hydrogen-bonds. A number of studies have been done to investigate this transition with interesting properties such as a large isotope effect (T_c (DKDP) = 213 K). Recently we found that glassy KDP can be obtained by quenching KDP melt. Our calorimetric study showed that the ferroelectric transition completely disappeared, and a glass transition occurred at 323 K [1]. The purpose of this study is to investigate the boson peak of glassy KDP. It is of interest to compare glassy KDP with other hydrogen bonding glasses such as glycerol.

Experimental

The INS experiments were performed using a TOF spectrometer AGNES [2] installed at JRR-3M (Tokai, Japan). The energy resolution was 0.1 meV and the energy window was < 20 meV on the side of neutron energy gain. The scattering vector region was 0.23—2.70 Å^{-1} for elastic scattering.

KDP crystals purchased from Wako Pure Chemical Industries, Ltd. were melted (T_{fus} ≈ 553 K) and then press-cooled between a pair of copper plates at room temperature. Vitrification of the sample was checked by X-ray diffraction. The composition of the glassy sample was determined to be $KH_{1.34}PO_{3.67}$ by thermogravimetry. The sample (transparent slabs) was crushed into smaller pieces and confined in a concentric double-cylinder aluminum can sealed with an indium gasket. The effective thickness of the samples considering the packing factor was 0.9 mm corresponding to the transmission of neutron beam of about 94 %. The measurement was performed at room temperature (298 K). The duration of the measurement was 41 h.

Results and Discussion

Figure 1 shows the $S(Q_{av},E)$ spectra of glassy KDP and glycerol [3]. These spectra were obtained by summing up the data from the counters positioned at scattering angles of 89—120°; the average Q value for elastic scattering was 2.35 Å^{-1}. The glassy KDP was measured at 298 K, while glassy glycerol at 180 K. For comparison, therefore, the data of glassy KDP was bose-scaled to 180 K and then both data were divided by the integrated intensity of each spectrum. A boson peak appeared at 4 meV in glassy KDP. We found that the boson peak intensity of glassy KDP is much smaller than that of glassy glycerol.

Glassy KDP may have a chain or ring structure of phosphate groups by the analogy with alkali meta-phosphate glasses. The hydrogen bonds may interconnect such chains. Glassy glycerol has a network structure formed by intermolecular hydrogen bonds which are weaker than O-P-O covalent bonds. Hence the network structure in glassy KDP is stronger than that in glassy glycerol. The present result is consistent with our model [3]; the stronger the network connectivity is, the weaker the boson peak intensity becomes.

References

[1] H. Obara et al., J. Korean Phys. Soc. **32**, S821 (1998). [2] T. Kajitani et al., Physica B **213&214**, 872 (1995). [3] O. Yamamuro et al., J. Phys.: Cond. Matter **12**, 5143 (2000).

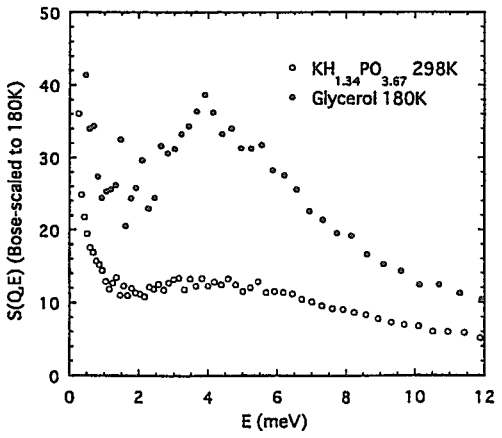

Fig. 1 $S(Q,E)$ of glassy KDP and glycerol.

研究テーマ：LiCl および $BeCl_2$ 水溶液ガラスの低エネルギー励起
表題：LiCl 水溶液ガラスの低エネルギー励起

1-4-16

Low-energy Excitations in LiCl Aqueous Solution Glasses

O. Yamamuro, Y. Madokoro, H. Yamasaki, I. Tsukushi [1], and T. Matsuo

Department of Chemistry, Graduate School of Science, Osaka University, 1-1 Machikaneyama-cho, Toyonaka, Osaka 560-0043, Japan
[1] Department of Physics, Chiba Institute of Technology, Narashino, Chiba 275-0023, Japan.

Introduction

The glasses formed from aqueous solutions of salts are typical disordered hydrogen-bond network systems. They can be prepared easily, and are good approximations to amorphous ice which can be prepared by difficult methods such as vapor deposition. They are also of interest because of the variation of the dynamical properties caused by different type and concentration of the salt species. The neutron diffraction studies by Ansell et al [1] and Tromp et al. [2] showed that Li ions were strongly coordinated by water molecules and the hydrogen-bond network was broken by the added ions. In spite of the large structural change, it has been reported that the glass transition temperature (ca. 140 K) [3] and the vibrational density of states [4] are not changed much by addition of the ions. No extra peak assignable to a "boson peak" was found in the INS and Raman spectra of $LiCl{\cdot}4H_2O$ glass [5]. This was the same as in amorphous ice [6].

The purpose of the present experiments was to show that there does exist the low-energy excitation (boson peak) in aqueous solution glasses. We have performed the incoherent neutron scattering measurements of $LiCl{\cdot}nH_2O$ (n = 4, 6) glasses and ice on the same spectrometer and the same conditions (temperature, sample thickness, etc.) to make a comparison as exactly as possible.

Experimental

The INS experiments were performed using a direct geometry chopper-type TOF spectrometer AGNES [7] installed at the cold neutron guide (C3) of JRR-3M (Tokai, Japan). The wavelength of the incident neutron (selected by PG(002) monochromaters) was 4.22 Å (4.59 meV). The energy resolution was 0.1 meV and the energy window was $E <$ 20 meV on the side of neutron energy gain. In our experiments, 122 ^{3}He tube counters were installed at 2θ = 9—130° at steps of 1°, covering the scattering vector Q region of 0.23—2.70 $Å^{-1}$ for elastic scattering.

LiCl powder (purity: 99.99 %) was purchased from Aldrich Chemical Company, Inc. and dried at 403 K in vacuo. The dried LiCl was dissolved in purified water (conductivity: 16.5 $M\Omega^{-1}$) to prepare the solutions with the composition of $LiCl{\cdot}4H_2O$ and $LiCl{\cdot}6H_2O$. The liquid samples were confined in a concentric double-cylinder aluminum can (35 mm in height, 14.5 mm in outer diameter of the outer cylinder, 12 mm in outer diameter of the inner cylinder, 0.25 mm in thickness of both cylinders) using an indium gasket. The thickness of the samples was 0.5 mm corresponding to the transmission of neutron beam of about 80 %. All of the samples were measured at 100 K. The duration of the measurement was 40—45 h for each sample.

The raw scattering data, neutron counts (I) against time-of-flight (t_f), were processed into the dynamic structure factor $S(Q,E)$ by correcting for the effects of the background, counter efficiency, Jacobian dt_f/dE, etc. in the standard way.

Results and Discussion

Figures 1 shows the $S(Q_{av},E)$ spectra of $LiCl{\cdot}4H_2O$ glass, $LiCl{\cdot}6H_2O$ glass and hexagonal ice. These spectra were obtained by summing up the data from the counters at scattering angles of 89—120°; the average Q value for elastic scattering was 2.35 $Å^{-1}$. The data were scaled by dividing by the integrated intensity for each sample. These spectra arise essentially from hydrogen atoms since the cross section of the incoherent scattering from hydrogen atoms is much lager than those from all of other atoms. A boson peak appeared at around 4 meV in both LiCl aqueous solution glasses. The data of $LiCl{\cdot}4H_2O$ and $LiCl{\cdot}6H_2O$ are similar to each other. The peak of the curve for ice at 7 meV is due to the TA mode [8]. The present data are the first and clear evidence for the boson peak in the aqueous solution glasses.

Figure 2 shows the heat capacities of $LiCl{\cdot}nH_2O$ (n = 4, 6, 7.5) glasses and hexagonal ice divided by T^3. All of the data

are plotted as quantities per H_2O-mole by assuming the additivity of the heat capacities of H_2O and LiCl. The heat capacities of the three solution glasses are much larger than those of crystalline $LiCl{\cdot}4H_2O$ and ice. The effect of the concentration was small. These heat capacity data are quite consistent with the INS data shown above.

Figure 3 shows the density of states calculated from the INS data by assuming one phonon scattering process. The scale factor of each substance was determined by fitting to the experimental heat capacity data in the temperature range 5—15 K. The data by Achibat et al. [5] are also plotted for comparison. The low energy excitations of $LiCl{\cdot}nH_2O$ glasses appeared as excess density of states over a broad region below 7 meV. The excess density of states integrated over 0—7 meV was 0.3 degrees of freedom per water molecule.

From the above data, we may relate the boson peaks of the hydrogen-bond network glasses with the broken or weakly connected hydrogen bonds. The same model explains our recent results on alcohol glasses [9]. The present result, combined with further INS and C_p experiments on other solution glasses (e.g., $MCl_2{\cdot}nH_2O$ (M = Be, Mg, Ca)) now in progress will give a comprehensive overview of the low-energy excitations in hydrogen-bonded glasses.

References

[1] S. Ansell et al., J. Phys.: Cond. Matter **9**, 8835 (1997). [2] R. H. Tromp et al., J. Chem. Phys. **96**, 8460 (1992). [3] A, Elarby-Aouizerat et al., J. Non-Cryst. Solids **104**, 203 (1988). [4] J. Dupuy et al., J. Mol. Struct. 250, 315 (1991). [5] T. Achibat et al., J. Chem. Phys. **102**, 8114 (1995). [6] H. Schober et al., Physica B **241-243**, 897 (1998). [7] T. Kajitani et al., Physica B **213&214**, 872 (1995). [8] D. D. Klug et al., Phys. Rev. B **44**, 841 (1991). [9] O. Yamamuro et al., J. Phys.: Cond. Matter **12**, 5143 (2000).

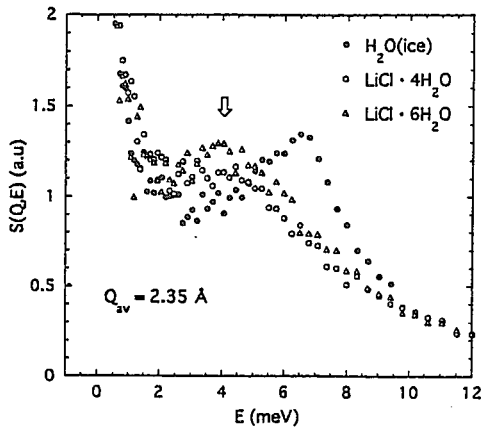

Fig. 1 $S(Q,E)$ spectra of $LiCl{\cdot}nH_2O$ glasses and hexagonal ice measured at 100 K.

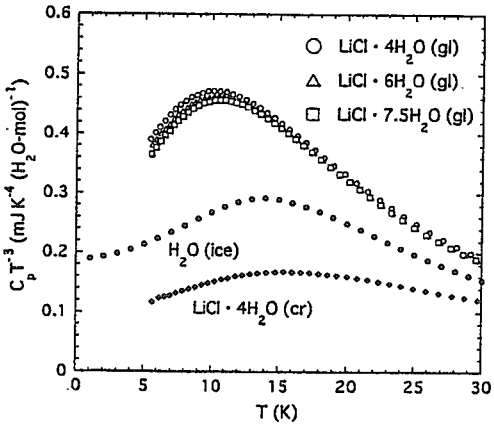

Fig. 2 Heat capacities of glassy and crystalline $LiCl{\cdot}nH_2O$ and hexagonal ice.

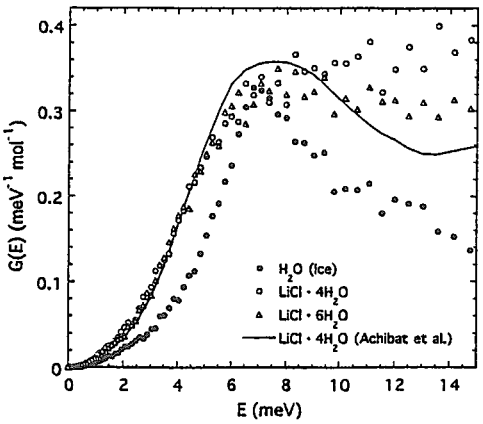

Fig. 3 Vibrational density of states of $LiCl{\cdot}nH_2O$ glasses and hexagonal ice.

研究テーマ:セレン-ハロゲン混合系のダイナミクス
表題:セレン-ハロゲン混合系のダイナミクス

1-4-17 Dynamics of Liquid Selenium-Halogen Mixture

M. Yao, Y. Ohmasa, A. Chiba, Y. Hiejima, Y. Kawakita[1], H. Endo[2]

Department of Physics, Graduate School of Science, Kyoto University, Sakyo-ku, Kyoto 606-8502
[1]Department of Physics, Faculty of Science, Kyushu University, Ropponmatsu, Fukuoka 810-8560
[2]Faculty of Engineering, Fukui Institute of Technology, Fukui 910-8505

Liquid selenium is composed of chains in which each atom is bonded to two adjacent atoms by covalent bonds. When halogens are added, they act as chain terminators and the length of Se chain molecules shortens. Liquid Se-Br mixture with equiatomic concentration is composed of molecular unit, Se_2Br_2. It is very interesting to study the dynamic structures of liquid Se_2Br_2, having the most shortest Se chain unit, Br-Se-Se-Br. It is known that the structures in these liquids depend not only on the intramolecular but also on the intermolecular correlation. Besides its interest from a scientific point of view, the Se-Br mixture is a very favourable compound to measure the dynamic structure factor $S(Q,E)$ by a neutron scattering experiment, because of the high coherency.

The measurement were performed for liquid Se_2Br_2 at room temperature using the direct geometry neutron spectrometer AGNES installed in the research reactor JRR-3M. Figure 1 shows a three-dimensional representation of the experimental dynamic structure factor $S(Q,E)$ of Se_2Br_2 at room temperature. A prominent peak is seen near $2Å^{-1}$, where the first peak of $S(Q)$ exists. Figure 2 shows the dispersion obtained from the maxima of the longitudinal current-current correlation function $J_l(Q,E) \propto E^2S(Q,E)$. The vibrational density of states $G(E)$ obtained by integrating $S(Q,E)$ over Q is also shown in Fig.2. The molecular vibrations such as torsional, bond-bending and bond-stretching modes are observed. We found that each mode is nearly flat but has a little change with momentum transfer, Q. The analysis of the structure of the quasielastic peak is now in progress.

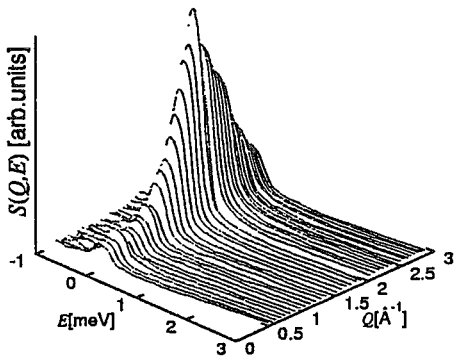

Fig.1: The dynamic structure factor $S(Q,E)$ of Se_2Br_2 measured at room temperature.

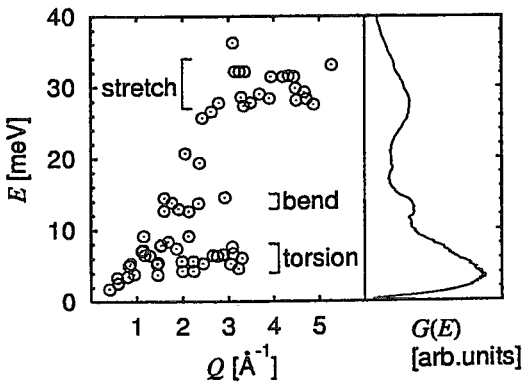

Fig.2: The dispersion obtained from the maxima of the longitudinal current-current correlation function of Se_2Br_2 (left), and the vibrational density of states $G(E)$ (right).

研究テーマ:液体カルコゲン系の金属-非金属転移領域におけるスロー・ダイナミクス
表題:液体カルコゲン系の金属-非金属転移領域におけるスロー・ダイナミクス

1-4-18
Slow Dynamics in the Metal-nonmetal Transition Range of Liquid Chalcogens

M. Yao, Y. Ohmasa, A. Chiba, Y. Hiejima, Y. Kawakita[1], H. Endo[2]

Department of Physics, Graduate School of Science, Kyoto University, Sakyo-ku, Kyoto 606-8502
[1]Department of Physics, Faculty of Science, Kyushu University, Ropponmatsu, Fukuoka 810-8560
[2]Faculty of Engineering, Fukui Institute of Technology, Fukui 910-8505

In the solid state, both Se and Te are semiconductors composed of helical chains in which each atom is bonded to two adjacent atoms by covalent bonds. When Te is melted by heating, it exhibits metallic properties in contrast to Se in which the helical chain structure is more or less preserved even in the liquid state. It is well known that in liquid Se-Te mixtures a semiconductor-to-metal(S-M) transition occur by raisig temperature and that the transition region shifts towards higher temperature as the Se concentration increases. Recently, based upon observations of anomalous sound attenuation, we have suggested that there may occur a slow dynamics with a nanosecond time scale in the S-M transition range. It is interesting to consider how the structural properties correlate with the electronic properties and how the dynamic properties are influenced by the S-M transitions.

Neutron scattering experiments for liquid $Se_{30}Te_{70}$ at 410 ℃(slightly above the melting point, semiconducting regime), 490 ℃ and 580 ℃(metallic regime) were performed using the direct geometry neutron spectrometer AGNES installed in the JRR-3M. The dynamic structure factor $S(Q,E)$ obtained from the measurements were analyzed by curve fitting with a Lorentzian function. An example of the fit for Q=2.1Å^{-1} is given in Fig.1. Figure 2 shows the half-width at half-maximum(HWHM) of the quasielastic scattering peaks as a function of Q. We found that the width of the quasielastic peak increases monotonously with the wave-number in the semiconducting regime, while it exhibits a de Gennes narrowing at the first peak position of the static structure factor $S(Q)$ in the metallic regime. Since the first peak of $S(Q)$ in this system mostly associated with the interchain correlation, the narrowing is consistent with a view that the electrons are transferred towards the interchain direction in the metallic state. In the next step, the method of the fitting should be improved.

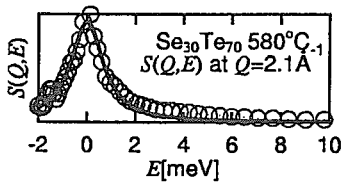

Fig.1: Fit of the Lorentzian function to the $S(Q,E)$ for $Se_{30}Te_{70}$ at 580 ℃ and at Q=2.1Å^{-1}.

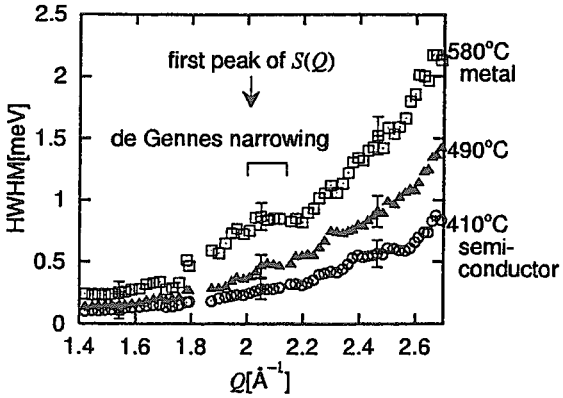

Fig.2: HWHM of the quasielastic peaks for $Se_{30}Te_{70}$ at 410 ℃, 490 ℃ and 580 ℃ are plotted as a function of Q.

研究テーマ：水ープロパノール系における水分子の運動性

表題：水－1-プロパノール溶液の中性子準弾性散乱

1-4-19
Quasi-elastic neutron scattering study on 1-propanol-water solution

Y. Hosokawa, H. Munemura, K. Maruyama[1], T. Kajitani[2] and M. Misawa[1]

Graduate School of Science and Technology, Niigata University, Niigata 950-2181 Japan
[1]Department of Chemistry, Faculty of Science, Niigata University, Niigata 950-2181 Japan
[2]Department of Applied Physics, Graduate School of Engineering, Tohoku University, Sendai, Japan

Quasi-elastic neutron scattering (QENS) measurements were carried out on the solution of 1-propanol and water as a function of 1-propanol concentration at ambient temperature by using AGNES. The two solutions differently substituted in D/H were examined; one was xC_3H_7OD-$(1-x)D_2O$ solution (solution A) and another was xC_3H_7OH-$(1-x)H_2O$ solution (solution B). The motion of propyl chains is obtained directly from the QENS data of the solution A, while that of water molecules or -(OH) groups is obtained from the difference in spectrum between the solution A and B.

Figure 1 shows the QENS spectra summed over 8 counters at $\overline{Q}_e$=0.67Å^{-1} for the solution A. The FWHM of the spectrum seems not to depend on concentration x studied, suggesting that the motion of propyl chains is rather insensitive to water concentration.

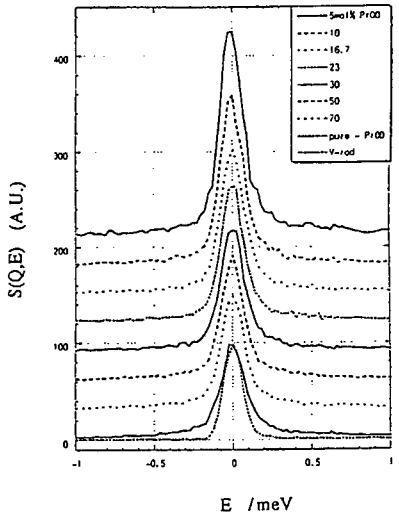

Fig. 1 Quasi-elastic neutron scattering spectra for 1-propanol-water solution A, xC_3H_7OD-$(1-x)D_2O$, measured by using AGNES.

Figure 2 shows the difference in spectra of solution A and B at $\overline{Q}_e$=1.26Å^{-1}, *i.e.* B-A. Before subtraction, each spectrum was corrected for self absorption. Since the raw spectrum has large values at quasi-elastic region, the subtracted one scatters as shown in Fig.2. Nevertheless we can see that the FWHM of the subtracted spectrum decreases with increasing x, suggesting that the motion of water molecules depends strongly on x. This tendency is in good agreement with that observed directly on the solution of xC_3D_7OH-$(1-x)H_2O$ for the limited range of x, i.e. x=0, 0.075 and 0.167[1].

The detailed analysis of the data is in progress.

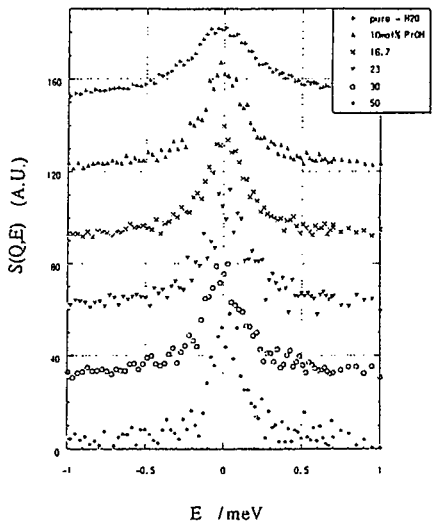

Fig. 2 Residual spectrum after subtracting spectrum of solution A from that of B.

Reference

1) M. Misawa, K. Yoshida, K. Maruyama, H. Munemura, Y. Hosokawa, J. Phys. Chem. Solids, 60 (1999) 1310.

研究テーマ: 上部および下部臨界温度を持つ混合液体の動的構造
標題: 閉環2相分離領域を持つ液体混合系の準弾性散乱

1-4-20 Quasi Elastic Neutron Scattering Measurements on the Liquid Mixture Having Closed Two Phase Region

K. Maruyama, S. Kawase[1], M. Misawa

Faculty of Science, Niigata University, Niigata 950-2181, Japan
[1]*Faculty of Medicine, Niigata University, Niigata 951-8518, Japan*

The mixture of glycerol ($CH_2OH - CHOH - CH_2OH$) and guaiacol (o-methoxy phenol $C_6H_4OHOCH_3$) has a closed two phase region in its concentration-temperature phase diagram and has lower and higher critical points at 45°C and about 35 mol % guaiacol, and at 81°C and about 40 mol % guaiacol, respectively. The existence of lower critical point is peculiar phenomenon according to the usual thermodynamic rules.

Recently we have measured the thermodynamic quantities, such as the concentration-concentration fluctuation, the Gibbs free energy of mixing, the entropy of mixing etc., by using Rayleigh-Brillouin scattering measurements and the relation between the thermodynamic quantities and the long wavelength limit of the Faber-Ziman type structure factors. Those studies shown the very small entropy of mixing compared to the ideal mixing in lower temperature region, which suggests the formation of clusters of glycerol or guaiacol molecules.

In order to confirm the existence of the clusters, we have performed quasi elastic neutron scattering measurements of the glycerol-guaiacol mixtures by using AGNES spectrometer equipped at JRR-3M in JAERI Tokai. The used sample cell was aluminum double cylindrical cell with 0.5mm spacing to avoid multiple scattering by hydrogen atoms. The measurements were carried out in the higher and lower one phase region, at 30 °C and 85°C, respectively, for three samples with concentration of 20, 35, and 100 mol% guaiacol.

Figure 1 shows the obtained dynamic structure factor $S(Q,\omega)$ as a function of energy transfer ω. The width of quasi elastic peak at higher temperature is wider than that at lower temperature, which means slower motion of molecules in lower temperature region and is consistent with the cluster formation. The change of the peak width becomes larger with increasing guaiacol composition.

The Q dependence of peak width is small for lower temperature, which suggests the small diffusion constant. In the higher temperature region, on the other hand, the peak width changes drastically.

We are planning farther experiments with samples of other concentration in order to analyze the molecular motion near the critical region precisely.

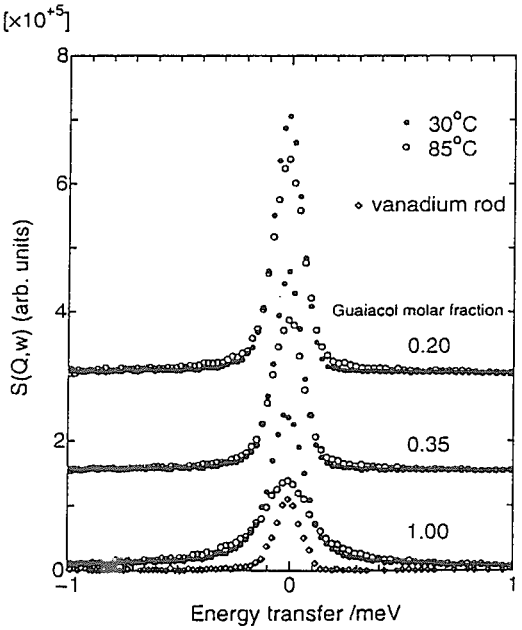

Figure 1. The obtained $S(Q,\omega)$ for glycerol guaiacol mixtures.

研究テーマ：種々の細孔次元を有する多孔体中の吸着分子の動力学
表題：中性子散乱による MCM-41 メソ孔内のベンゼンおよびメタノール分子のダイナミクスに関する研究

1-4-21

Neutron Scattering Study on Dynamics of Benzene and Methanol Molecules in MCM-41

Shigeharu Kittaka,[a] Shuichi Takahara,[a] Yasushige Kuroda,[b] Toshinori Mori,[b] and Toshio Yamaguchi[c]

[a] *Department of Chemistry, Faculty of Science, Okayama University of Science, 1-1 Ridaicho, Okayama 700-0005, Japan*
[b] *Department of Chemistry, Faculty of Science, Okayama University, Tsushima, Okayama 700-8530, Japan*
[c] *Department of Chemistry, Faculty of Science, Fukuoka University, Nanakuma, Jyonan-ku, Fukuoka 814-0180, Japan*

We have investigated dynamics of water molecules in mesopores of MCM-41 by using neutron scattering,[1] and found that the water molecules in MCM-41 at room temperature are less mobile than those in bulk liquid water, but more mobile below ~ 250 K. This crossover phenomenon is probably due to distortion of hydrogen-bond network in the confined space. In the present study, dynamics of benzene and methanol molecules in MCM-41 were investigated by using quasi-elastic neutron scattering (QENS). Benzene molecule is non-polar and the dispersion force is predominant when interacting with neighbor molecules. Methanol molecules form one-dimensional hydrogen-bond chains, which is different from water molecules in dimensionality, i.e. water molecules form three-dimensional hydrogen-bond network. Comparative study of dynamic properties of these molecules should lead to present principal factors governing dynamics of small molecules in the confined space. Dependence of the dynamics of the molecules on pore sizes is also important problem in this study.

MCM-41, which were developed by Beck *et al.* in 1992,[2] are one of the most suitable samples for studying properties of confined liquid, because they contain highly controlled cylindrical channels with very narrow pore size distribution. In this study, three kinds of siliceous MCM-41 samples (C10, C14 and C18) were prepared by the method of Beck *et al.*[2] using alkyltrimethylanmmonium bromide with alkyl chains of 10, 14 and 18 carbon atoms, respectively. The pore diameters determined from the N_2 adsorption isotherms were 2.14 (C10), 2.84 (C14) and 3.74 nm (C18). C10 and C18 samples were used in benzene experiments, while C10 and C14 samples in methanol experiments.

The dynamics of molecules in confined space depends not only on pore size, but also on adsorbed amount. To investigate this effect, we prepared three kinds of samples having different amounts of adsorption for every MCM-41. (1) pore-filled sample: the mesopores were filled with the adsorbed molecules; (2) monolayer sample: the pore walls are covered with monolayer of the adsorbed molecules; (3) dry sample: MCM-41 samples were evacuated at room temperature to remove physisorbed molecules but chemisorbed species, for example the surface hydroxyls, remained.

QENS measurements were carried out by using time-of-flight type spectrometer AGNES[3] installed at the JRR-3M reactor of Japan Atomic Energy Research Institute. The wavelength of neutron beam was 4.22 Å, the momentum transfer (Q) range 0.41-2.46 Å^{-1}, and the temperature range 50-300 K. A resolution function of the instrument was determined with a vanadium rod.

Typical examples of the QENS spectra of the pore-filled samples at 298 K are shown in Figures 1 (the benzene system) and 2 (the methanol system). For both benzene and methanol systems, elastic peak intensities were decreased remarkably

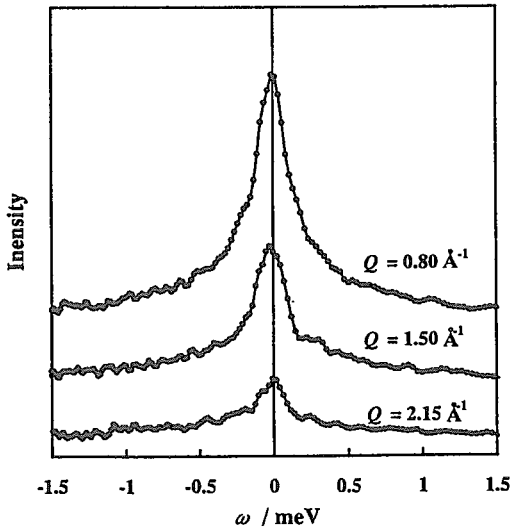

Figure 1. QENS spectra of the pore-filled C10 sample for the benzene system at 298 K.

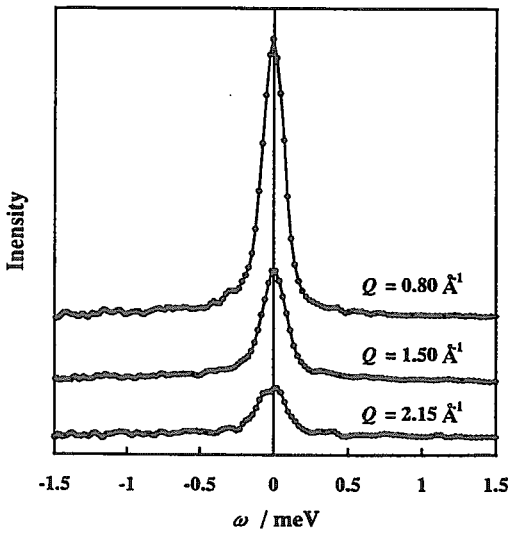

Figure 2. QENS spectra of the pore-filled C14 samples for the methanol system at 298 K.

with increasing in Q values. This implies that the quasi-elastic wings of these spectra are not ascribable to translations but to rotations of the molecules.

Pore size dependences of the QENS spectra for benzene and methanol at 298 K are shown in Figures 3 and 4, respectively. Here, the displayed

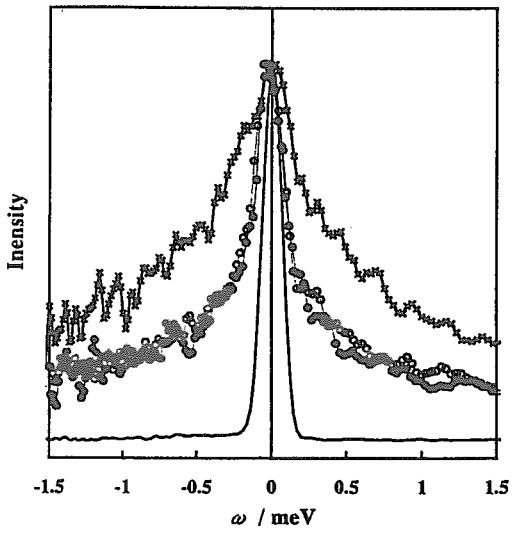

Figure 3. QENS spectra of the pore-filled samples (C10: ○, C18: ●) and bulk (×) for the benzene system at Q = 1.50 Å^{-1} and 298 K. Solid line represents the vanadium spectrum.

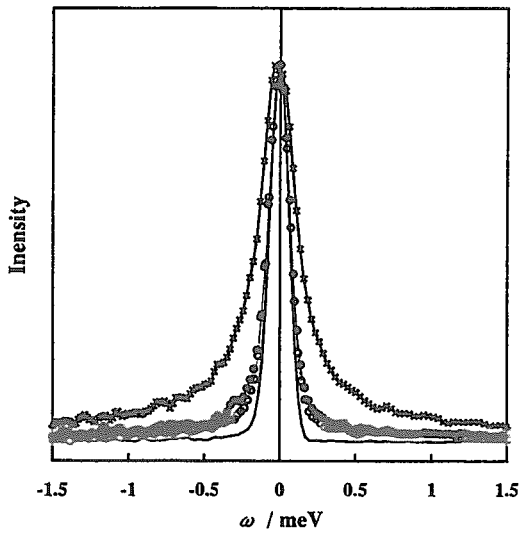

Figure 4. QENS spectra of the pore-filled samples (C10: ○, C14: ●) and bulk (×) for the methanol system at Q = 0.80 Å^{-1} and 298 K. Solid line represents the vanadium spectrum.

spectra of the pore-filled samples are the difference between raw spectra of the pore-filled samples and spectra of the dry sample, and thus contain the contributions only from the physisorbed molecules. All the spectra are normalized ones, in which peak maxima were coincided with each other to emphasize the change in quasi-elastic wings of the spectra. For both benzene and methanol systems, the molecules in MCM-41 are less mobile than those of bulk liquid and no significant pore size effects were observed in this range. Quantitative analysis is now in progress.

References

1 Takahara, S.; Nakano, M.; Kittaka, S.; Kuroda, Y.; Mori, T.; Hamano, H.; Yamaguchi, T. *J. Phys. Chem. B*, **1999**, *103*,5814-5819.

2 Beck, J. S.; Vartuli, J. C.; Roth, W. J.; Leonowicz, M. E.; Kresge, C. T.; Schmitt, K. D.; Chu, C. T-U.; Olson, D. H.; Sheppard, E. W.; McCullen, S. B.; Higgins, J. B.; Schlenker, J. L. *J. Am. Chem. Soc.* **1992**, *114*, 10834.

3 Kajitani, T.; Shibata, K.; Ikeda, S.; Kohgi, M.; Yoshizawa, H.; Nemoto, K.; Suzuki, K. *Physica B* **1995**, *213&214*, 872.

1. 中性子散乱 5) 材料科学

1. Neutron Scattering 5) Material Science

This is a blank page.

研究テーマ：螢石関連固溶体の構造変化
表題：ZrO_2-15mol%$YO_{1.5}$を1000℃でアニールしている間の構造変化のその場観察

1-5-1 *In Situ Investigation of Structural Change of* ZrO_2-15mol%$YO_{1.5}$ *during Annealing at* 1000°C

M. Yashima, Y. Hatoyama, S. Utsumi,
M. Ohashi[1], K. Nemoto[1], K. Ohoyama[1], and Y. Yamaguchi[1]

Department of Materials Science and Engineering, Interdisciplinary Graduate School of Science and Engineering, Tokyo Institute of Technology, Nagatsuta, Midori, Yokohama, 226-8502, Japan.
[1]*Institute for Materials Research, Tohoku University, Katahira, Aoba, Sendai, 980-8577, Japan.*

A ceramic fuel cell is an all solid-state energy conversion device that produces electricity by electrochemically combining fuel and oxidant gases across an ionic conducting oxide. The ceramic fuel cells, commonly referred to as solid-oxide fuel cells (SOFCs), are presently under development for a variety of power generation applications. The most advanced SOFCs are those based on oxygen-ion-conducting stabilized zirconia electrolyte, because the material possesses an adequate level of oxygen-ion conductivity and exhibits desirable mechanical properties and chemical stability in both oxidizing and reducing atmospheres. The conductivity of zirconia-yttria solid solutions as a function of yttria content exhibits a maximum around the tetragonal-cubic phase boundary. Degradation of the conductivity during working at 1000°C is a major problem of SOFCs. Here we report *in situ* investigation of structural change of ZrO_2-15mol%$YO_{1.5}$ during annealing at 1000°C.

The neutron diffraction measurements were done in air at KSD (T1-2) using a high-temperature furnace (λ=1.53Å). The ZrO_2-15mol%$YO_{1.5}$ sample was heated up to 1000°C and the sample temperature was kept constant during neutron-diffraction measurements for 5000 min. Figure 1 shows a typical 112 reflection peak profile which is forbidden for ideal fluorite structure. From the integrated intensities of 111 and 112 peaks, the atomic coordinate z of oxygen was calculated. The z parameter was almost independent of annealing time at 1000°C within the estimated standard deviations (Fig.2).

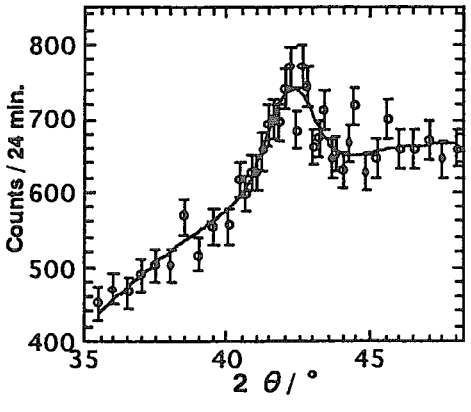

Fig.1: A typical neutron diffraction profile for 112 reflection measured at 1000℃.

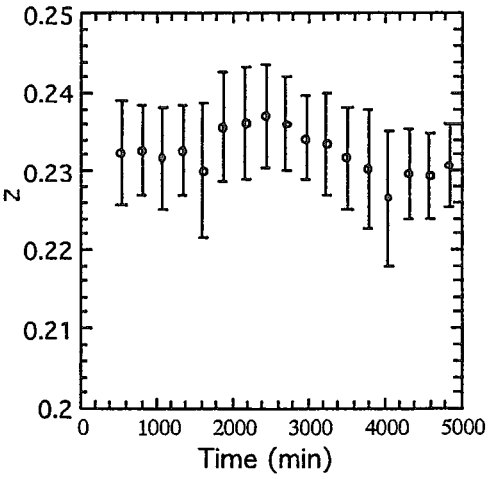

Fig. 2 Time dependence of z atomic coordinate in tetragonal zirconia during annealing at 1000℃.

Reactor: (JRR-3M) Facility: KSD (T1-2) Field: (materials)

研究テーマ：中性子粉末回折用高温電気炉の開発
表題：窒素ガス気流中での高温中性子回折測定のための新しい電気炉

1-5-2

A New Furnace for High-Temperature Neutron-Diffraction Measurements under Nitrogen Gas Flow

M. Yashima, H. Doi[1], K. Nemoto[2], K. Ohoyama[2], and Y. Yamaguchi[2]

Department of Materials Science and Engineering, Interdisciplinary Graduate School of Science and Engineering, Tokyo Institute of Technology, 4259, Nagatsuta-cho, Midori, Yokohama, 226-8502, Japan.

[1]*San-Rikou-Denki Co, Soka, Saitama, 340, Japan.*

[2]*Institute for Materials Research, Tohoku University, Katahira, Aoba, Sendai, 980-8577, Japan.*

Structural investigation at high temperatures is of vital importance for materials science and engineering, physics, chemistry and geoscience. Neutron diffraction is very effective tool to investigate crystal structures at high temperatures. So, we have devised and constructed furnaces for neutron-diffraction measurements in air at high-temperatures at T1-2 and T1-3 sites, JRR-3M in Japan Atomic Energy Research Institute. Here we report a new furnace that can work at higher temperatures under nitrogen atmosphere.

We have designed and fabricated a new electric furnace for neutron diffraction measurements under nitrogen gas flow at high temperatures up to 1600°C. The instrument has been designed as effectively as possible to maximize the neutron-diffraction intensity as well as to suppress the background level and neutron-diffraction intensity from outside the sample. This furnace was also designed to have both a temperature homogeneity and ease for use. This furnace uses carbon heater, so it can work at 2000°C or at higher temperatures under nitrogen gas flow. The

Figure 1 shows Rietveld pattern for ZrO_2-12 mol% $YO_{1.5}$ specimen placed in the new furnace. The reliability factors were Rwp = 13.5 %, Rp = 9.8 %, and RI = 4.9 %. Goodness of fit S was 1.27. It should be noted that no significant peaks from heaters, refractories and sample holder are observed. Therefore we can investigate weak reflection peaks and diffuse scattering from samples. We succeeded in measurements up to 1600°C under nitrogen gas flow. We are now improving this furnace to measure at higher temperatures.

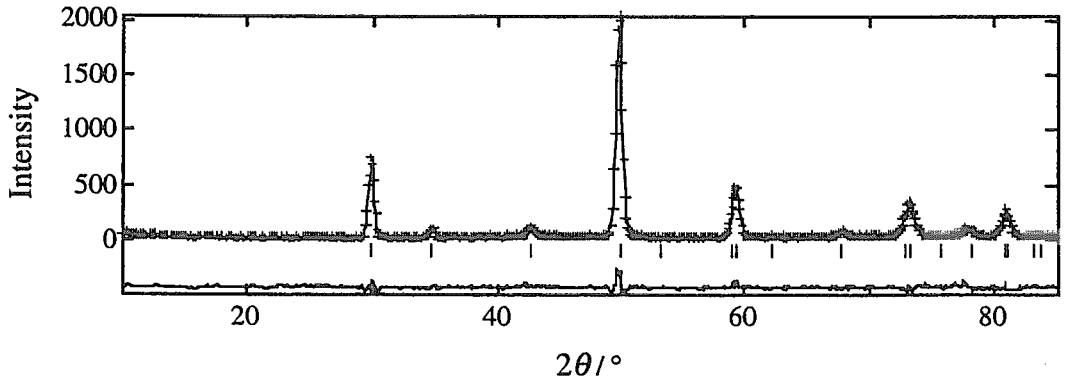

Fig. 1 Rietveld pattern of for ZrO_2-12 mol% $YO_{1.5}$ specimen placed in the new furnace.

Reactor: (JRR-3M) Facility: KSD (T1-2)Field: (materials)

研究テーマ：ペロブスカイト関連化合物の構造変化
表題：高温中性子回折による$La_{0.683}Ti_{0.95}Al_{0.05}O_3$ペロブスカイトの研究

1-5-3
High-temperature neutron diffraction study of $La_{0.683}Ti_{0.95}Al_{0.05}O_3$ perovskite

Roushown Ali, Masatomo Yashima, Hideki Yoshioka[1], Kenji Ohoyama[2] and Yasuo Yamaguchi[2]

Department of Materials Science and Engineering, Interdisciplinary Graduate School of Science and Engineering, Tokyo Institute of Technology, 4259, Nagatsuta-cho, Midori, Yokohama, 226-8502, Japan

[1]Hyogo Prefectural Institute of Industrial Research, Suma, Kobe 654-0037, Japan

[2]Institute for Materials Research, Tohoku University, Katahira, Aoba, Sendai, 980-8577, Japan

$La_{0.683}Ti_{0.95}Al_{0.05}O_3$ is an ion conducting material. At room temperature $La_{0.683}Ti_{0.95}Al_{0.05}O_3$ has an orthorhombic structure and exhibits a phase transition to tetragonal symmetry between 192°C and 392°C [1]. $La_{0.683}Ti_{0.95}Al_{0.05}O_3$ perovskite has been studied by some researchers, but temperature dependence of atomic coordinates has not been studied yet. Therefore, neutron diffraction experiments of $La_{0.683}Ti_{0.95}Al_{0.05}O_3$ perovskite have been performed in the temperature range from 25°C to 592°C and subsequently structural refinements were carried out by Rietveld analysis.

The sample was prepared by solid state reactions from La_2O_3, TiO_2 and Al_2O_3 powders. Neutron-diffraction data were collected in the temperature range from 25°C to 592°C using the powder diffractometer HERMES installed at JRR-3M in JAERI [2]. The data collections were done over the 2θ range from 20.0 to 152.0 with the step width 0.1°. The powder diffraction data were analyzed using the Rietveld analysis method RIETAN [3].

Figure 1 shows the profile fit and difference patterns of Rietveld analysis for the powder neutron data of $La_{0.683}Ti_{0.95}Al_{0.05}O_3$ measured at 388°C. The profile fitting results obtained from the analyses were, *R*wp=7.31, 8.43, 8.49, 8.69(%); *R*p=5.42, 6.04, 6.26, 6.36 (%) and *S*=1.60, 1.61, 1.60, 1.64 for 25°, 182°, 388° and 592°C, respectively.

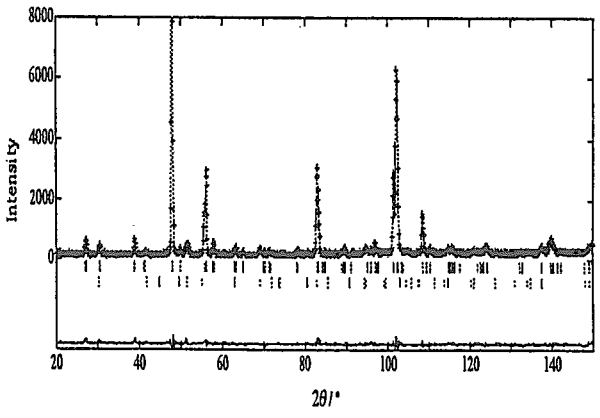

Fig. 1 Observed (crosses), calculated (solid) and difference (solid, lower) profiles for tetragonal phase of $La_{0.683}Ti_{0.95}Al_{0.05}O_3$. Positions of the Bragg reflections are marked with vertical lines.

Reactor: (JRR-3M) Facility: HERMES(T1-3) Field: (materials)

The R-factors, goodness of fit values and Fig.1 show good agreements between observed and calculated profiles.

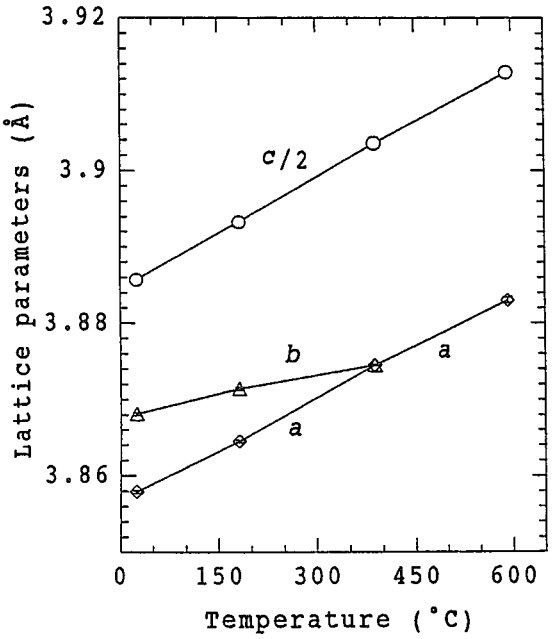

Fig. 2 Relationship between lattice parameters and temperature (error bars are smaller than the size of the symbols).

The variation of lattice parameters of this compound is shown in Fig. 2. The *a* and *b* parameters approached each other and coincided at 388°C, resulting in the orthorhombic-to-tetragonal phase transition. As shown in Fig. 3, the *z* parameters of Ti/Al and O(2,3) atoms were constant within the estimated error bars in the temperature range measured, while other atomic coordinates were fixed. These results suggest that the orthorhombic phase transforms to tetragonal structure by changing only lattice parameters.

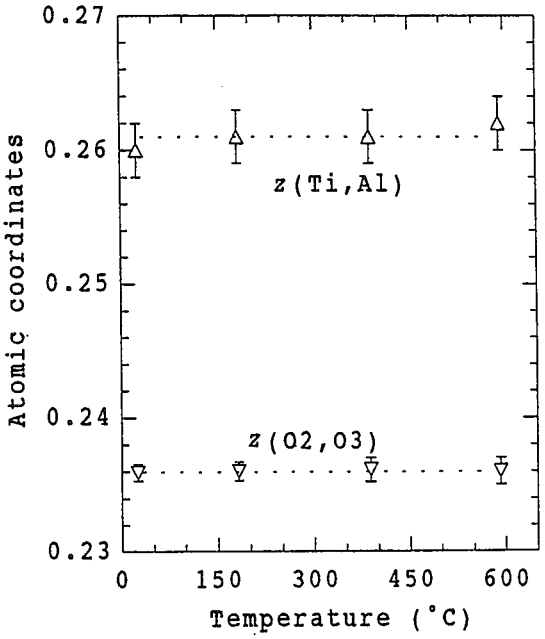

Fig. 3 Relationship between *z* coordinate and temperature.

References

1) M. Yashima, R. Ali and H. Yoshioka, *Solid State Ionics*, **128**, 105-110 (2000).
2) K. Ohoyama, T. Kanouchi, K. Nemoto, M. Ohashi, T. Kanitani and Y. Yamaguchi, *Jpn. J. Appl. Phys.* **37**, 3319-3329 (1998).
3) F. Izumi, "*The Rietveld Method*", Oxford University Press, Oxford (1993), Chapter. 13.

1. 中性子散乱 6) 高分子

1. Neutron Scattering 6) Polymer

This is a blank page.

研究テーマ：高分子多成分系のパターン形成に関する研究
表題：散乱法を用いたゴム充填系の階層構造の研究

1-6-1 Scattering Studies on Hierarchical Structures of Rubber/Filler Systems

T.Hashimoto, M.Takenaka, T.Koga[1], and K.Aizawa[2]

Department of Polymer Chemistry, Graduate School of Engineering,
Kyoto University, Kyoto, 606-8501-,Japan
[1]Hashimoto Polymer Phasing Project, Department of Polymer Chemistry,
Graduate School of Engineering,, Kyoto University, Kyoto, 606-8501-,Japan
[2]Japan Atomic Energy Research Institute, Tokai, Ibaraki 319-1195, Japan

The incorporation of fillers, such as carbon black or sillica particles, in rubber imporves the mechnical properties of the rubbers. The inprovement depends on the aggregation structures formed by prticles of the fillers in the rubbers. The aggregation structures is expected to have hierarchical structures so that we have to obsertve the wide range of length scale from 1 nm to 10 μm to explore the structure. In this study, we, thus aim to explore the hierarchical structures of the rubber/carbon black system by combining very small angle neutron scattering (VSANS), ultra small angle small x-ray scattering (USAXS), and small angle x-ray scattering (SAXS).

The rubber used in this study was polyisoprene (PI) and poly(styrene-r-butadiene) (SBR). Carbon black (CB) were used as the fillers. The weight fraction of the fillerss in each system is 0.2. VSANS was performed at PNO (3G) in JRR-3M, Tokai. USAXS, SAXS was performed at Hashimoto Polymer Phasing Project, Kyoto. Figure 1 shows VSANS, USAXS, and SAXS profiles of the PI/CB system. Each profile can be well superimposed so that we obtained the scattered intensity distribution over 4 decade in length scale. This superimposed profile indicates that the PI/CB system ahs the folowing hierarchical structure: (i) the carbon black particle with an averaged diameter 13 nm forms the elipsoidal primary aggregation structure where the length of minor axis and the axis raito are, respectively, 32 nm and 5.3. (ii) the primary aggregation structure forms the mass-fractal sturcture with its exponent being 2.1.

Though we do not show the profiles here, we obateind the well-superimposed VSANS, USAXS, and SAXS profiles for the SBR/CB system. Similar to the PI/CB system, SBR/CB system has the following hierarchical structure: (i) the carbon black forms the elipsoidal primary aggregation structure where the length of minor axis and the axis raito are, respectively, 28 nm and 2.8. (ii) the primary aggregation structure forms the mass-fractal sturcture with its exponent being 2.2 and the upper limit can be observed at q=0.001 nm^{-1}.

Acknowkedgment: We are grateful to the material research department , Yokohama Rubber Co., Ltd. for their help in perparing samples the experimental samples used in this work.

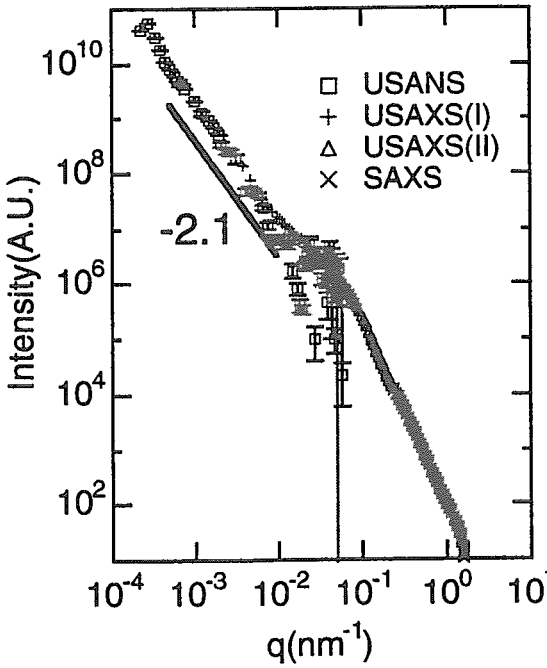

Fig.1 VSANS,USAXS, and SAXS Profiles of PI/CB system

原子炉：JRR-3M　　装置：PNO(3G)　　分野：中性子散乱（高分子）

研究テーマ：極小角散乱法用高分子温度調節器の開発
表　題　　：高分子多成分系の静的階層構造の研究「牛血清アルブミンゲルのPNO研究3」

1-6-2 PNO Study on Bovine Serum Albumin Gels 3

Y. IZUMI, Y.JINBO, T.MATSUGI, K.AIZAWA[1] AND H.TOMIMITSU[1]

Graduate School of Science and Engineering, Yamagata University, Yonezawa, Yamagata 992-8510
[1]Advanced Science Research Center, JAERI, Tokai, Ibaraki 319-1195

Globular protein gels have been extensively investigated over many years. Most of the studies concentrated on examining structural and rhelogical properties of fully cured gels. Protein gelation is known to be promoted by several kinds of treatments. Among them, gelation induced by temperature, the so-called heat-induced or thermally induced gelation, has received insufficient attention.

In previous reviews[1], we reported the large scale structures of bovine serum albumin (BSA) gel revealed by Precise Neutron Optics (PNO) measurements. The previous results are summarized as follows. The transparent BSA gel (C_p, the concentration of BSA, 15wt% and no added salt) gave too very small excess intensity to detect, indicating a structure with a very small contrast or very small junction point. On the other hand, the opaque gels (C_p= 15wt% and C_s, the concentration of NaCl, 0.05, 0.1, 0.2 and 0.3mol NaCl) gave a clear difference between the intensity of the gel and that of the solvent. The excess intensity for the gel prepared at 0.05M NaCl indicated the exponent value of 4.0 as the fractal dimension. On the other hand, that for the gel prepared at $C_s \geqq 0.1$ indicated the exponent value of 3.0 as the fractral dimension. The crossover between these exponents indicates a change in the surface structure of the gels. The exponent value of 4.0 indicates the smooth surface of the junction zones, while the exponent value of 3.0 indicates a very rough surface. The crossover occurs at a concentration between 0.05M and 0.10M NaCl. Furthermore, the structures of the opaque gels, i.e., the size of the junction zone and the size distribution strongly depend on the gelation temperature. However, it is still unknown whether the exponent-value is continually changing or not at the crossover point.

In present work, we intended to reveal whether the surface structure was continually changing or not at the crossover point. The BSA gel of 20 wt% was prepared to obtain a higher contrast. The measurements have been carried out by PNO spectrometer. The details of measurements and the analysis are described elsewhere[2]. Four gels with different Cs (0, 0.05, 0.075 and 0.1M NaCl) were prepared by heating during 6min at 70℃.

The results gave very small excess intensities. As the changes of the surface structures of junction zones reflect in the rheological properties, further studies should be needed. As the gels accumulate the influences of many factors which cannot be controlled, it is very difficult to specify the main factor which determins the gel structures. However, the PNO technique is still useful to characterize the surface structure and the size of the junction zone of micron order in fully cured gels and also gels around a crossover point.

References

1) Y.Izumi, K.Soma, K.Aizawa, S.Koizumi, and H.Tomimitsu, JAERI-Rev. 99-003, p.27(1999); ibid., 2000-005, p15(2000).
2) K.Aizawa & H.Tomimitsu, Physica B 213&214(1995)884-886.

原子炉：JRR-3M　　装置：PNO(3G)　　分野：中性子散乱（高分子）

結晶性高分子の分散曲線を求める試み
高分子の結晶構造とダイナミックス

1-6-3 Attempts to measure the Dipersion Curves of Crystalline Polymers

Yasuhiro Takahashi
Department of Macromolecular Science, Graduate School of Science, Osaka University, Toyonaka, Osaka 560, Japan

Dispersion relation contains rich informations of the vibrational states of the crystal. Especially, the acoustic branch can not be measured by the methods other than the neutron inelastic scattering. During past several years, the attempts to measure the accoustic mode of the crystalline polymers have been made by neutron inelastic scattering with a triple axis spectrometer T1-1.

Two commercially supplied fiber samples, poly(p-phenylene benzobisoxazole) and poly(p-phenylene sulfide) were used. Two polymers were adopted because a large amount of fibers can be easily obtained and a small amount of hydrogen atoms are contained in the chemical structures. The crystallinity of two polymers are very high. Especially, the crystallinity of poly(p-phenylene benzobisoxazole) is almost 100 %. First, the fibers were arranged in a cylindrical bundle with 1.0 cm diameter and 3 cm long, and subsequently, five bundles were arranged in a plate with size 3 x 5 cm.

In Fig. 1, the results for poly(p-phenylene sulfide) is shown. Unfortunately, no clear peaks can be observed. Almost the same results were obtained in the case of poly(p-phenylene benzobisoxazole).

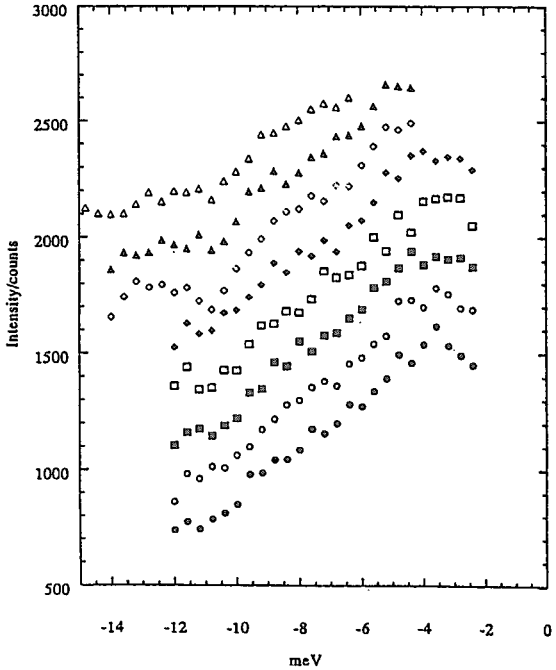

Fig. 1

JRR-3M, T 1 — 1 , Polymer

ポリ（p－フェニレンベンゾビスチアゾール）の中性子構造解析
高分子の結晶構造とダイナミックス

1-6-4 Neutron Structure Analysis of Poly(p-phenylenebenzobisthiazole)

Yasuhiro Takahashi
Department of Macromolecular Science, Graduate School of Science, Osaka University, Toyonaka, Osaka 560, Japan

Poly(p-phenylenebenzobisthiazol) (PBZT) is known to be a strongest polymer and a polymer with the highest modulus, which is frequently discussed in comparison with poly(p-phenylene benzooxazole)(PBO). Neutron diffraction has several advantages in comparison with X-ray diffraction as discussed before.[1] The purpose of the present study is to determine the crystal structure of PBZT more accurately than the X-ray crystal structure analysis[2] and the temperature dependence of the crystal structure.

The fiber sample of PBZT was kindly supplied by Dr. Chyi-Shan Wang of the University of Dayton Research Institute. The specimen for neutron diffraction was prepared by arranging the fibers in a cylindrical bundle of about 1 cm in diameter.

Neutron measurements were carried out on the equator at 17, 60, 120, 180, 240, 295K by using HERMES. The h0l and -h0l reflections cannot separated. Therefore, the unit cell dimension cannot be determined only by neutron diffraction. The unit cell dimensions with parameters, a = 11.60 Å, b = 3.588 Å, and γ = 92.0° which were determined by X-ray work[2], was adopted.

The constrained least-squares refinements were carried out by fixing the bond lengths and bond angles to the values proposed by Fratini et al.[3] The crystal structure of PBZT at 295K is shown in Fig, 1, which is somewhat different from the structure determined by X-ray.[2] In Fig. 2, the temperature dependences of the spacings of the reflection 200 and the overlapped reflection of 010, 110 and -110 are shown. The temperature dependences are very small in comparison with the tendencies of the flexible polymers, polyethylene[1] and poly(vinyl alcohol)[1]. In Fig. 3, temperature dependence of the azimuthal angle between phenyl and benzobisthiazole rings is shown. The angle slightly increases as temperature decreases in contrast with the dependence of PBO.[4] In Fig. 4, the temperature dependence of the temperature parameter B is shown.

1) Y. Takahashi, "Neutron Diffraction by Crystalline Polymers", Chapter 5, p74, ACS Symposium Series 739 "Scattering from Polymers" edited by P. Cebe et al., 2000.
2) Y. Takahashi and H. Sul, *J. Polym. Sci.: Part B: Polym. Phys.*, **38**, 376 (2000).
3) A. V. Fratini et al., *Mater. Res., Soc. Symp. Proc.*, **134**, 431 (1989).
4) Y. Takahashi, *Macromolecules*, **32**, 4010 (1999).

JRR-3M, HERMES, Polymer

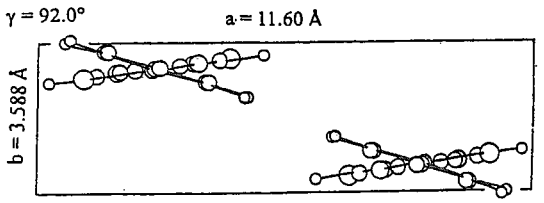

Fig. 1

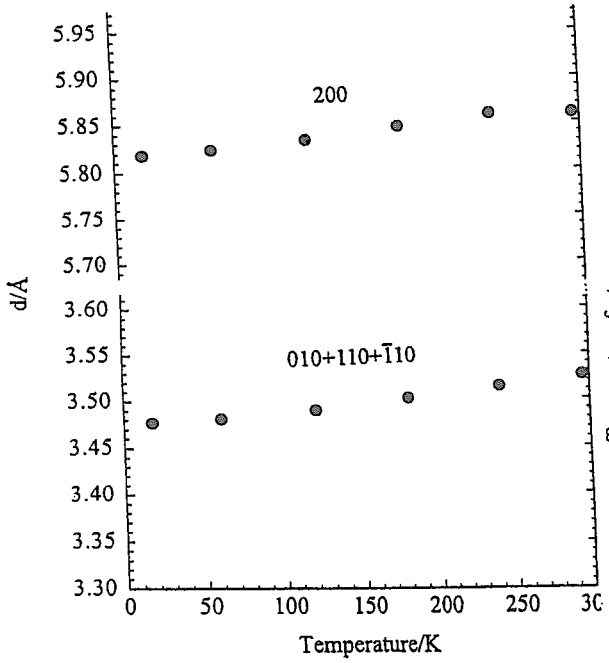

Fig. 2

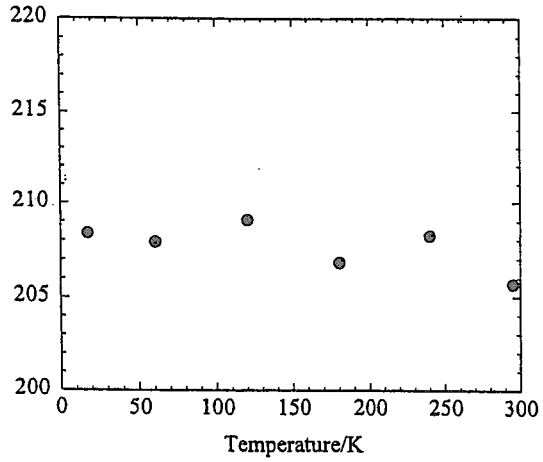

Fig. 3

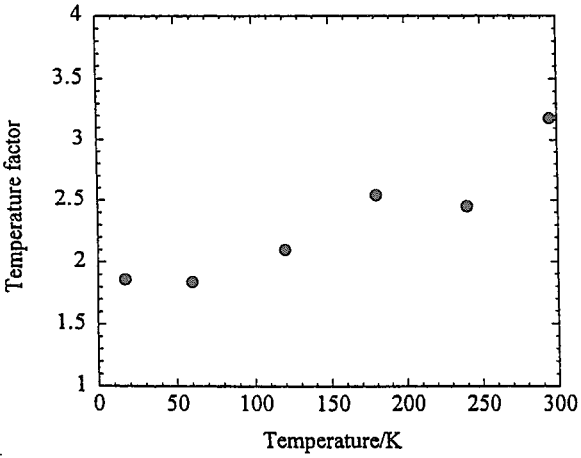

Fig. 4

表題：界面活性剤／水系におけるラメラとジャイロイド構造の流動場による秩序化
研究テーマ：両親媒性分子・水系におけるモルフォロジー転移に及ぼす流動場の影響

1-6-5 Shear-Induced Ordering of Lamellar and Gyroid Structures Observed in a Nonionic Surfactant/Water System

M.Imai, K. Nakaya, and T. Kato[1]

Department of Physics, Ochanomizu University, Bunkyo, Tokyo 112-0012, Japan
[1]Faculty of Science, Tokyo Metropolitan University, Hachioji, Tokyo 192-03, Japan

One of the most fascinating properties of surfactant/water systems and block copolymers is their ability to form a variety of ordered mesophases, such as hexagonally ordered cylinders (C), lamellae (L), and a gyroid (G) structure having a bicontinuous cubic network with Ia3d symmetry. The ordered mesophases have unique spatial geometry and are expected to show characteristic behaviors under anisotropic external fields such as shear flow. The purpose of this study is to elucidate roles of the elastic nature of the membrane in the shear ordering of mosophases observed in a nonionic surfactant/water system.

We examined the shear ordering pathway of L and G phases of a C16E7/D2O system. Measurements of SANS under shear flow were carried out on the SANS-U instrument with a Coutte shear cell.

In the radial configuration, intensity of an isotropic lamellar ring decreased with increasing of shear rate until $\dot{\gamma} \sim 0.1$ s^{-1} and then scattering peaks appeared at q_{VXV}=±0.1 Å^{-1} as shown in Figure 1(a). The scattering pattern observed $\dot{\gamma}$=1.0 s^{-1} denotes the perpendicular orientation. On the other hand, in the tangential configuration (Figure 1(b)), the dominant scattering peaks appeared at q_{VV}=±0.1 Å^{-1}, indicating parallel orientation lamellae and the scattering peak intensity increased with increasing the shear rate. With increasing of shear rate in the lamellar phase, undulation fluctuations of lamellae are suppressed and simultaneously lamellae are ordered to the parallel orientation. When shear rate exceeds a critical value (~0.3s^{-1}), parallel-to-perpendicular orientation transition starts.

We also found the shear-induced G→L transition. With increasing of shear rate in the gyroid phase, the gyroid structure transforms to the parallel oriented lamellae through isotropic disordered structure at the critical shear rate.

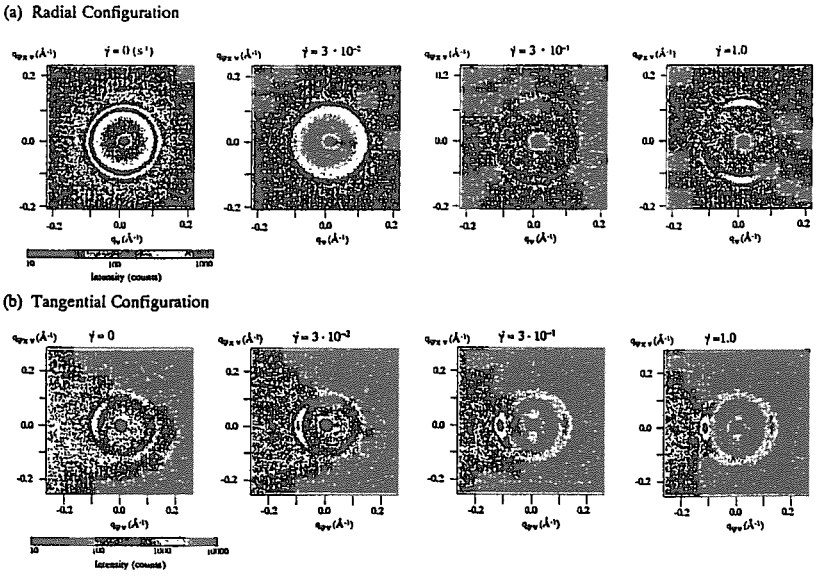

Fig. 1 Evolution of SANS patterns with increasing of shear rate from 0 to 1.0 s^{-1} at 55°C for radial (a) and tangential (b) configurations.

JRR-3M, SANS-U, 6 Polymer

表題：高分子を拘束したマイクロエマルションの形態とダイナミクス
研究テーマ：マイクロエマルションにおける高分子誘起モルフォロジー転移

1-6-6 Morphology and Dynamics of Microemulsion Droplet Confining Single Polymer Chain

K. Nakaya, and M.Imai

Department of Physics, Ochanomizu University, Bunkyo, Tokyo 112-0012, Japan

Microemulsions (ME) consisting of water/oil/ /surfactant show a variety of meso-phases, such as lamellar, droplet, due to amphiphilic nature of the surfactant molecule. We can control these morphologies by changing temperature and composition of systems. Among these morphologies, water-in-oil droplets provide isolated meso-scale space separated by continuous oil phase. When we introduced water soluble polymer which is insoluble to oil, into the water-in-oil droplet system, a polymer chain confined in the spherical meso-space surrounded by the surfactant membrane. In this study we have investigated the morphology and dynamics of the surfactant membrane of ME droplet confining single polymer chain using a small angle neutron scattering (SANS) and neutron spin echo (NSE) techniques.

This study was performed with water-in-oil ME consisting of iso-octane, Aerosol-OT. We varied the droplet radius R (determined by the water to surfactant ratio [water] /[AOT]=ω_0), and kept the relative water-to-oil volume fraction, α=0.05 at 30°C. As the confined polymer, we used gelatin having radius of gyration, Rg=89Å. We controlled the polymer concentration so as to obtain the average number of the polymer chain per droplet, n=1. SANS and NSE measurements were performed using SANS-U and ISSP-NSE instruments at JRR-3M reactor in Tokai, respectively. SANS and NSE experiments were carried out under the film contrast condition, which provided detail information regarding the morphology of the membrane.

The SANS profiles for the ME droplets could be described by a shell structure model without the structure factor contribution, indicating dilute droplet system. The droplet sizes obtained from fitting of the scattering profiles were in the range of about 50 to100Å. The SANS profiles for the droplets confining polymer chains showed smearing of the characteristic peak observed for ME droplets (Figure 1), indicating increase of the polydispersity of droplets. Furthermore from fitting of the scattering profiles, it was revealed that the confined gelatin brought change of the ME droplet size. We explained this behavior on the basis of total free energy of the system consisting of the confinement entropy of the chain, the droplet elastic energy, and osmotic pressure. We'll elucidate what governs the morphology of the ME droplets confining of the polymer chain.

Normalized intermediate scattering functions $I(Q,t)/I(Q,0)$ for the ME droplets and ME droplets confining a gelatin chain are shown in Figures 2 and 3 at Q=0.03 and 0.06 Å^{-1}. Both relaxation curves show monotonic decay profiles, which may be described by stretched exponential decay functions. However, in order to find significant feature in dynamics of the membrane confining a polymer chain, we need more precise measurements.

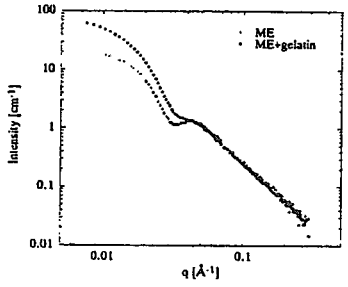

Fig. 1 SANS profiles for water/AOT/iso-octane ME droplet and the droplets confining a polymer chain.

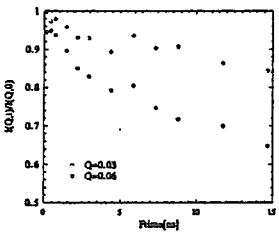

Fig. 2 Normalized intermediate scattering functions for ME droplets.

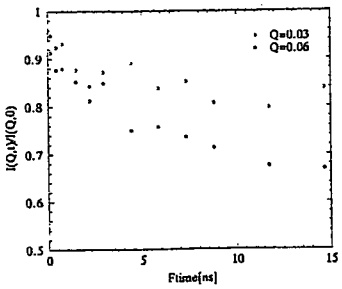

Fig. 3 Normalized intermediate scattering functions for ME droplets confining a gelatin chain.

JRR-3M, SANS-U, 6 Polymer

研究テーマ：両親媒性ポリマー溶液の溶媒組成変化に伴う会合体構造変化
表題：両親媒性カルボシランブロック共重合体の溶液中での会合挙動

1-6-7
The Association Behavior of Amphiphilic Carbosilane Block Copolymer in Solution

Kozo Matsumoto, Utako Mizuno, Yusuke Yamamoto, Masaaki Shinohata, Hideki Matuoka and Hitoshi Yamaoka

Department of Polymer Chemistry, Kyoto University, Kyoto 606-8501, Japan

Polycarbosilanes are expected as a new series of functional material because of their unique properties such as high stability, flexibility, and hydrophobicity. The self-assembly of amphiphilic block copolymers consisting of hydrophobic polycarbosilane segment and hydrophilic polymer segment are of particular interest. We have already reported the micelle formation of poly(1,1-diethylsilacyclobutane)-*b*-poly(2-hydroxyethyl methacrylate), poly(DESB-*b*-HEMA), in methanol or toluene by small-angle X-ray scattering.[1] We have also reported the analysis of monolayer structure of the polymer at the water surface by X-ray reflectivity measurement.[2]

In this research, we examined the structure of micelles formed by amphiphilic block copolymers composed of poly(1,1-dimethylsilacyclobutane) and poly(HEMA) (poly(DMSB-*b*-HEMA)) in methanol by small angle neutron scattering (SANS).

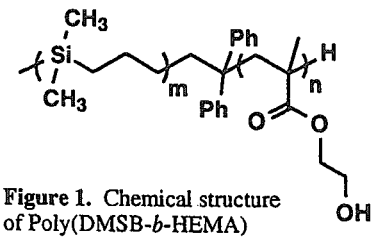

Figure 1. Chemical structure of Poly(DMSB-*b*-HEMA)

Since DMSB homopolymer exhibits melt-crystallization transition around the room temperature, the effect of this transition on the polymer association can be evaluated. Figure 2 shows SANS profiles for the block copolymer (m:n = 19:21) at 25 °C and 13 °C in CD_3OD. The scattering curve at 25 °C was well reproduced by the theoretical curve for a coexistence model of core-shelled spheres and sandwivh disks (0.85 / 0.15 v/v). To the contrary, the scattering curve at 13 °C was reproduced by the curve for a model of core-shelled spheres and disks (0.25 / 0.75). This implies that the block copolymer forms disk-like aggregates when polyDMSB segment is in the crystalline state, while it forms spherical micelles when the polyDMSB segment is in the liquid state.

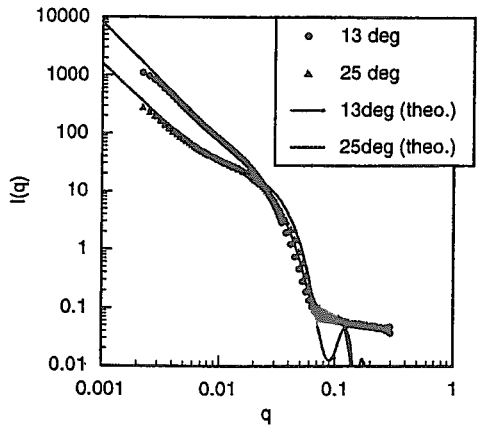

Figure 2. SANS profiles of poly(DMSB-*b*-HEMA) (m:n = 19:21) at 13 °C and 25 °C. The solid lines are the theoretical curves.

References

1) Nakano, M.; Deguchi, M.; Matsumoto, K.; Matsuoka, H.; Yamaoka, H. *Macromolecules*, **1999**, *32*, 7437.
2) Nakano, M.; Deguchi, M.; Endo, H.; Matsumoto, K.; Matsuoka, H.; Yamaoka, H. *macromolecules*, **1999**, *32*, 6088.

研究テーマ：2種類のブロック共重合体を混合した系の秩序構造に関する研究
表題：2種類のブロック共重合体を混合した系の秩序構造に関する研究

1-6-8
Macrophase- and Microphase- Separated Structures in Binary Mixtures of Diblock Copolymers

D. Yamaguchi, M. Takenaka, H. Hasegawa T. Hashimoto , and H. Nagao [1]

Department of Polymer Chemistry, Graduate School of Engineering, Kyoto University, Kyoto 606-8501, Japan
[1]Neutron Scattering Laboratory, The Institute for Solid State Physics, The University of Tokyo, Shirakata, Tokai, Naka, Ibaraki, 319-11 Japan

It is well known that the AB diblock copolymers show microphase-separated structures. Recently it has been elucidated that the binary mixture of diblock copolymers where the constituent copolymers have nearly symmetric compositions but rather different molecular weights, shows not only microphase-separated structure between A- and B-block chains but also macrophase-separated structure between constituent copolymers. The criterion of the miscibility of two nearly symmetric diblock copolymers has already been revealed experimentally and theoretically as follow: when the molecular weight ratio of long block copolymer to short block copolymer is smaller than 5 to 1, two copolmers are completely miscible, whereas the molecular weight ratio is larger than 5 to 1, they become partially miscible and the macrophase separation takes place. In this study, we employed the long (protonated) polystyrene (PS)-*block*-(protonated) polyisoprene (PI) copolymer with number-average molecular weight (M_n) of 6.3×10^4 and volume fraction of PS block (f_{PS}) of 0.44, and the short deuterated PS (dPS)-*block*-PI copolymer with $M_n = 1.0 \times 10^4$ and $f_{PS} = 0.52$ where the molecular weight ratio of long copolymer to short copolymer is 6.3, and investigated the macrophase-separated structure of long and short copolymers as well as microphase-separated structure of each copolymer by small-angle neutron scattering (SANS) and small-angle X-ray scattering (SAXS) for the blend specimen whose weight ratio of long : short = 1 : 4. In Figure 1 we show the SAXS profiles of the blend specimen measured at 40, 160, and 200°C. From Figure 1 we discern that at high temperatures, i.e., 200 and 160°C, the SAXS profile has single scattering peak, suggesting that two copolymers are completely miscible and macrophase separation does not occur, whereas at 40°C there are two peaks (at $q \approx 0.2$ and $q \approx 0.5$ nm^{-1}) on the SAXS profile, indicating that the macrophase separation between long and short copolymers occurs. In Figure 2 we show the SANS profiles of the blend specimen taken at 30, 100, and 150°C. By using SANS we can access the lower q region than that of SAXS (the arrows both in Figures 1 and 2 denote the position $q = 0.2$ nm^{-1}). The SANS results shown in Figure 2 seem consistent with the SAXS results, namely, the excess scattering at $q \leq 0.1$ nm^{-1} increases at low temperature (30°C) indicating that the macrophase separation progresses at lower temperatures.

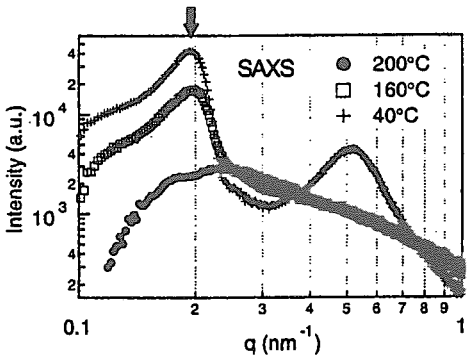

Figure 1. SAXS profiles for the blend specimen

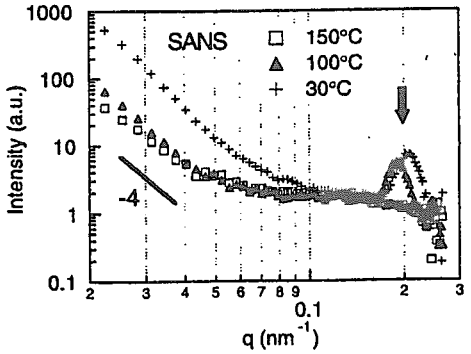

Figure 2. SANS profiles for the blend specimen

研究テーマ：高分子のナノ拘束空間における相転移の研究
表題：ABCトリブロック共重合体の複雑相転移

1-6-9
Complex Microphase Transitions in an ABC Triblock Copolymer

K. Yamauchi, H. Hasegawa, T. Hashimoto and M. Nagao[1]

Department of Polymer Chemistry, Graduate School of Engineering, Kyoto University, Sakyo-ku, Kyoto, 606-8501 Japan
[1] Neutron Scattering Laboratory, The Institute for Solid State Physics, The University of Tokyo, Shirakata, Tokai, Naka, Ibaraki, 319-1106 Japan

Introduction Complex microphase transitions of a polyisoprene-b-poly(D6-styrene)-b-poly(vinyl methyl ether) triblock copolymer (abbreviated to PI-DPS-PVME) were investigated by small-angle neutron scattering (SANS) and small-angle X-ray scattering (SAXS). At room temperature DPS and PVME are miscible but PI is immiscible with both DPS and PVME so that the copolymer is separated into two microphases, PI phase and the mixed phase of DPS and PVME. With increasing temperature the segregation power between PI and DPS decreases and DPS tends to mix with PI. However, PVME is still immiscible with PI while miscibility between DPS and PVME decreases with temperature. Therefore, it is quite interesting to investigate the phase behavior of the copolymer.

Experiment A PI-DPS-PVME (M_n=1.4×10^4, 3×10^3 and 3×10^3 for each block, respectively) triblock copolymer sample cast from benzene solution and thoroughly dried was served for the measurements. SANS-U (l=7.0.Å, SDD=4.0m) equipped with a heating stage controlled by TEMCON was used. The SANS data were obtained for a heating and a cooling cycle by 5-20 K step for each between room temperature and 425 K. The SAXS measurement was performed for the cooling cycle from 450 to 300 K.

Results The figure shows the temperature change of the SANS profiles on cooling. At temperatures above 350 K only a single scattering peak is seen in each profile. However, the scattering peak is not so broad suggesting the copolymer is still in the ordered state. At 345 K higher-order peaks start to appear at $(3)^{1/2}$ and $(7)^{1/2}$ positions with respect to the first-order peak position suggesting that cylindrical microdomains of DPS/PVME mixed phase are hexagonally packed in the matrix of PI phase. A discontinuous change in the half width at half maximum of the first-order peak with temperature was also observed between 345 and 350 K. Above 350 K DPS may become miscible with PI. However, since PI is still immiscible with PVME, DPS in PI phase may be localized near the PI/PVME interface. On the other hand, the SAXS data showed a transition at a different temperature requiring further analysis.

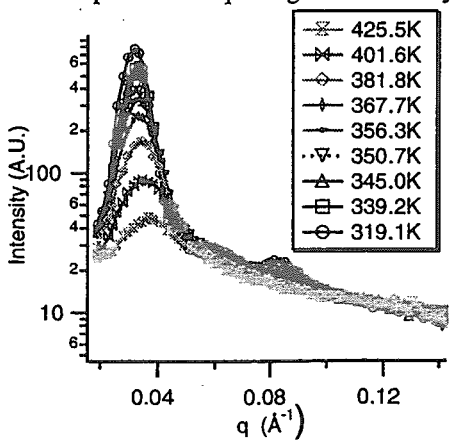

Temperature dependence of SANS profiles

JRR-3M, SANS-U, 6. Polymer

研究テーマ：ポリオレフィンブレンドの相構造解析
表題:ポリプロピレンとエチレンヘキセンランダム共重合体ブレンドの熱力学的相互作用の研究

1-6-10 Study on the Thermodynamic Interactions between Isotactic Polypropylene and Ethylene-1-hexene Random Copolymers by SANS

Motohiro Seki, Yushu Matsushita, Michihiro Nagao [1]
Department of Applied Chemistry, Graduate School of Engineering, Nagoya University,
Furo-Cho, Chikusa-ku, Nagoya, 464-8603 Japan
1 Neutron Scattering Laboratory, The Institute for Solid Sate Physics,
The University of Tokyo, Shirakata, Tokai, Naka, Ibaraki, 319-1106 Japan

Miscibility of perdeuterated isotactic polypropylene(d-PP) and ethylene-1-hexene random copolymer(EHR) blends were investigated by small angle neutron scattering(SANS) with changing hexene content in EHR and temperature above the melting point of d-PP. Flory-Huggins interaction parameter($\chi_{d\text{-}PP/EHR}$) between two polymers was determined based on random phase approximation.

d-PP were obtained by the polymerization of perdeuterated propylene(C_3D_6) with metallocene catalyst. Four copolymers with different hexene content ranging from 26 to 46 mol% were obtained by copolymerization of regular ethylene with n-hexene and they have been named EHR-m, where m indicates the hexene content in mol%. Two kinds of poly(1-hexene)(PH) i.e., isotactic-PH and atactic-PH were also prepared by using two different catalysts. All of these random copolymers and PHs were fractionated by GPC.

SANS measurements were performed at SANS-U spectrometer of the Institute for Solid State Physics(ISSP) the University of Tokyo in JRR-3M at Tokai. The form factor of d-PP was evaluated from the SANS coherent cross section($d\Sigma/d\Omega$) for d-PP/h-PP, while those for EHR and PH were obtained from ($d\Sigma/d\Omega$) for dilute solutions with various polymer concentrations in deuterated poor solvent at room temperature.

It is revealed that $\chi_{d\text{-}PP/EHR}$ decreases with increasing hexene content in EHR up to 46mol%, and with increasing temperature, however, the $\chi_{d\text{-}PP/a\text{-}PH}$ is larger than expected and decreases with increasing temperature as shown in Figure 1. This behaviour was explained by the Lattice Cluster Theory considering contact energy among component polymers and molecular topology. Scattering intensities from d-PP/isotactic-PH blend revealed q^{-4} dependence, being concluded that these two polymers are immiscible.

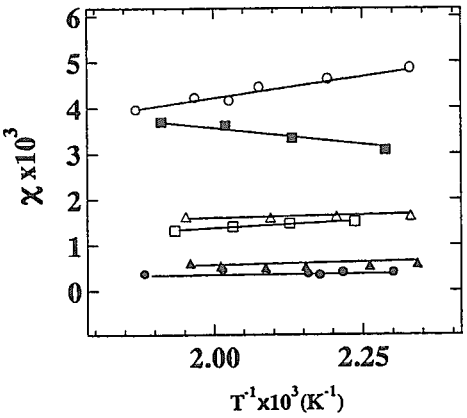

Figure 1. $\chi_{d\text{-}PP/EHR}$ for d-PP/EHR and d-PP/a-PH blends plotted against inverse of the absolute temperature. (○); d-PP/EHR-26(55:45), (△); d-PP/EHR-35(52:48), (□); d-PP/EHR-40(54:46), (●);d-PP/EHR-46(52:48), (▲); d-PP/EHR-46(62:38), (■); d-PP/a-PH(53:47).

JRR-3M, SANS-U, 6. Polymer

研究テーマ：ホモポリマー／ブロックコポリマー混合系のミクロ・マクロ複合相転移に関する研究
表題：重水素化スチレン－イソプレン／ポリブタジエン混合系の複合相転移における臨界現象

1-6-11

Critical Phenomena in Complex Phase Transition of Poly(deutrated styrene-*b*-isoprene)/Polybutadiene mixture

M.Takenaka, H.Hasegawa, S.Saito, T.Hashimoto, and M.Nagao[1]

Department of Polymer Chemistry, Graduate School of Engineering, Kyoto University, Sakyo-ku, Kyoto 606-8501, Japan

[1]Neutron Scattering Laboratory, The Institute of Solid State Physics, The Universty of Tokyo, Tokai, Naka, Obaraki, 319-1106, Japan

We investigated the critical concentration fluctuations induced by macrophase separation in nano-collidal system, where spherical microdomain structures of poly(deutrated styrene-*b*-isoprene) (dS-I) are dispersed in polybutadiene (PB) matrix, using samm-angle neutron scattering (SANS).

The nano-colloidal system is obtained by solvent cast of the homogeneous solution of the dS-I/B=70/30 wt/wt/ mixture. We measured the temeprature dependence of SANS intensity of the dS-I/B mixture with the SANS-U spectrometer of the Institute for Solid State Physics of the University of Tokyo in JRR-3M at Tokai.

We found that the scattered intensity increases with temperature at small qregion since the miscibility between isoprene in dS-I and B becomes worse with temeprature. We applied Ornstein-Zernike plot to the scattered intensity and obtained the temperature dependencies of the correlation length ξ and I(0) as shown in Fig.1. The drastic changes in $I(0)^{-1}$ and ξ^{-2} were found at 1/T=0.00275 (T=353K) after graddualdecreases during 0.0028 <1/T< 0.0031. This facts indicate that the macrophase separation occurs at 1/Tc= 0.00275 (Tc=353K). We obtained the spinodal temperature of the nano-colloidal system by extrapolating the plots of $I(0)^{-1}$ and ξ^{-2} vs 1/T. We can estimated Ts= 598K from the plots and Ts was found to be much higer than Tc.

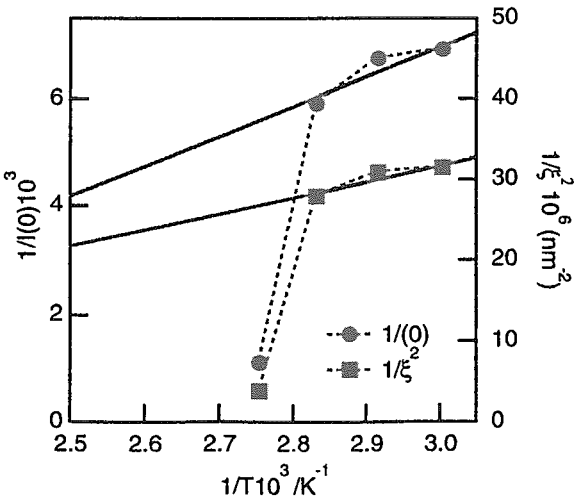

Fig.1 1/I(0) and $1/\xi^2$ plotted as a function of 1/T

JRR-3M, SANS-U, 6. Polymer

研究テーマ：反応性末端基を有する非相溶な高分子ブレンドの相挙動に関する研究
表題：SANSによる非相溶な高分子ブレンドの界面厚の測定

1-6-12 SANS Measurement of Interface Thickness in Immiscible Polymer Blends

M. Hayashi, K. H. Hasegawa, M. Takenaka, T. Hashimoto and M. Nagao[1]

Department of Polymer Chemistry, Graduate School of Engineering, Kyoto University, Sakyo-ku, Kyoto, 606-8501 Japan
[1] Neutron Scattering Laboratory, The Institute for Solid State Physics, The University of Tokyo, Shirakata, Tokai, Naka, Ibaraki, 319-1106 Japan

Introduction The overall physical properties of immiscible polymer blends critically depend on the interfacial adhesion between two phases. Therefore, it is very important to evaluate interfacial mixing of two components. In this study we measured interfaces between the two phases formed in immiscible polymer pairs by means of small-angle neutron scattering (SANS) and compared the results with those obtained by neutron reflectivity (NR) measurements.

Experiment SANS-U (λ=7.0Å, SDD=4.0m or 8.0m) was used. The polymer samples used in this study, deuterated polysulfone (dPSU) and amorphous aromatic polyamide (PA) were supplied by BASF AG. The 50/50 wt%/wt% blend sample was prepared by precipitating from solution and annealed above the glass transition temperature.

Results The SANS profiles obtained for the blend sample annealed at 240 °C for 2 min are shown in Figures a and b. In Fig. a the net scattering $S_t(q)$ (○) was corrected only for incoherent scattering S_{incoh} (solid line). The corrected profile $S_c(q)$ (■) has an asymptote with a slope > -4. This leads to an errant interpretation about the interface. In Fig. b $S_t(q)$ (○) was corrected for the frozen density heterogeneities within each phase $S_h(q)$ (solid curve) evaluated from the SANS profile of pure PSU. The corrected profile $S_c(q)$ (■) has an asymptote with a slope < -4. In the Porod region

$$S_c(q)=2\pi\Delta\rho^2\Sigma q^{-4}\exp(-\sigma^2q^2)$$

The intrinsic interfacial widths, W_I is given by $(2\pi)^{1/2}\sigma$. W_I thus obtained agreed well with those evaluated by NR at NIST after the correction for the contribution of capillary wave fluctuations to a net (or observed) interfacial width.

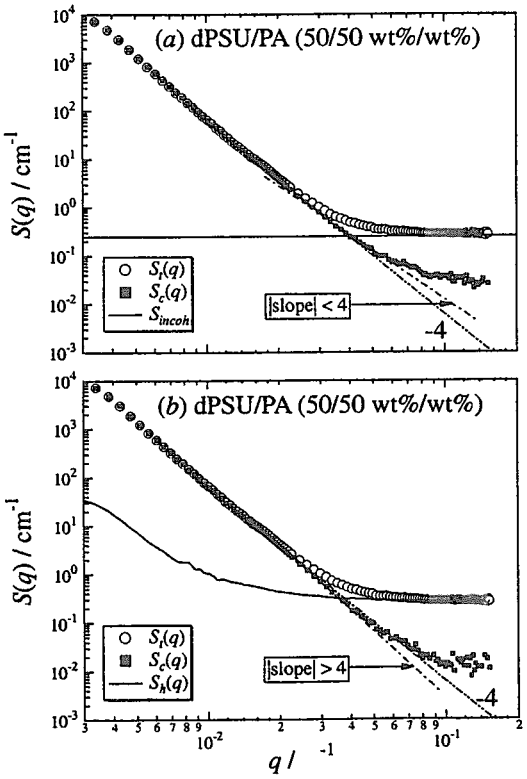

Comparison of the corrections for (a) incoherent scattering and (b) density heterogeneities.

研究テーマ：SANSによる高分子多成分系の相溶性におよぼす圧力効果研究
表題：圧力ジャンプによるミクロ相分離の観察

1-6-13

Observation of Microphase Separation Induced by Pressure Jump

H. Hasegawa, H. Takeno, N. Sakamoto, T. Hashimoto and M. Nagao[1]

Department of Polymer Chemistry, Graduate School of Engineering, Kyoto University, Sakyo-ku, Kyoto, 606-8501 Japan
[1] Neutron Scattering Laboratory, The Institute for Solid State Physics, The University of Tokyo, Shirakata, Tokai, Naka, Ibaraki, 319-1106 Japan

Introduction We have found that a block copolymer composed of perdeuterated polybutadiene (DPB) and polyisoprene (HPI) undergoes microphase separation by increasing temperature and that pressure decreases the miscibility. The copolymer keept in the disordered state at high temperature and high pressure may undergo microphase separation by pressure drop that can be done much faster than temperature jump. Thus the microphase separation process can be observed by SANS.

Experiment SANS-U (λ=7.0Å, SDD= 8.0m) equipped with the high-pressure cell was used. The scattering data were obtained for a perdeuterated polybutadiene-*block*-polyisoprene diblock copolymers (B-11, DPB/HPI=47/53wt%/wt%, M_n=4.9×10^5) as a function of time after pressure drop from 80 MPa to 0.1 MPa at 341K. The counting time was 30 sec until 989 sec and 120 sec afterward.

Results The time evolution of the SANS profiles is shown in Fig. 1. At 80 MPa (before the pressure drop) the profile shows a broad scattering peak with low intensity typical for the disordered state. After the pressure drop to 0.1 MPa the peak intensity I_m increases with time and half width at half maximum s_q decreases with time dramatically suggesting the onset of microphase separation. The dependences of I_m and s_q on logarithm of time t after the pressure drop are plotted in Fig. 2. I_m almost linearly increases with log t. It should be noted that the scattering peak shifted to lower q immediately after the pressure jump (t = 31 sec) but moved back to the higher q shortly (t = 77 sec).

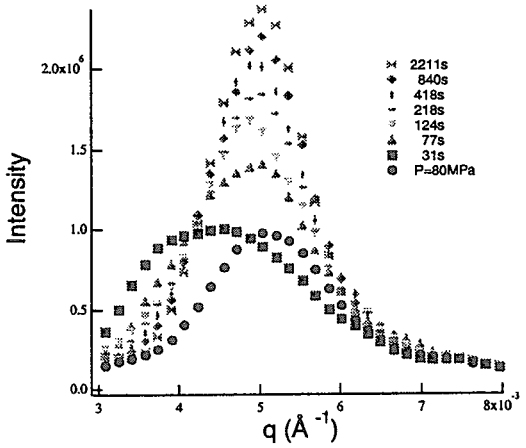

Fig. 1 Time evolution of SANS profiles after pressure drop from 80 to 0.1 MPa at 341K.

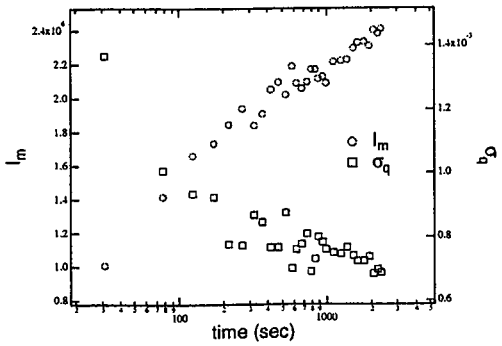

Fig. 2 Time dependence of I_m and σ_q.

研究テーマ：ドデシル硫酸ミセル中のポリペプチド鎖の構造
表題：ドデシル硫酸ミセル中のポリペプチド鎖の構造

1-6-14
Conformation of polypeptide chains in dodecyl sulfate micelles

Yasushi Watanabe
National Food Research Institute. Tsnkuba. lbaraki 305-8642. Japan

The most popular analytical method for estimating the relative molecular weight of a polypeptide chain in every area of biochemistry and molecular biology is by its mobility in polyacrylamide gel electrophoresis in the presence of dodecyl sulfate (1). The electrophoretic mobility of a protein is determined not only by its molecular weight but also by its net charge and its shape. Proteins that interact in the typical manner with dodecyl sulfate also appear to produce complexes with similar shapes and net charge densities on these chains. The original conformations of the protein are disrupted by the surfactant, but the nature of the conformation they adopt in dodecyl sulfate is not known.

A variety of models such as "rodlike-particle model"(2) and "necklace-model"(3) have been proposed and usefully summarized by Ibel et al. (4). Despite the relatively extensive investigations that have been carried out on the structure of protein-surfactant complexes, definitive results have yet to be obtained. In this study, the perdeuterated dodecyl sulfate in neutron scattering experiments was used to determine the configuration of the protein-polypeptide in the dodecyl sulfate micelles.

Neutron scattering measurements were made a SANS-U spectrometer installed at the C I -2 port of the cold-neutron beam line in the research reactor JRR-3M of the Japan Atomic Energy Research Institute (JAERI). The solution samples were contained in flat square-shaped quartz cells of window thickness 1 mm and path length 4 mm. Multiple samples were mounted on a sample changer at 25℃. The wavelength was 7.0 Å and the sample to detector distance was 100 cm. Sample transmission was taken before and after each measurement to check the material conditions and to correct for absorption of the sample. A buffer solution consisting of 99.8% D_2O, 10 mM MOPS, pD 7.0, 200 mM LiCl, 3.5 mM (above the critical micelle concentration) perdeuterated dodecyl sulfate was used as a reference solution for scattering experiments.

Figure 1 shows the Kratky plot (Q vs. Q^2I) which reveals clearly the transition region for the typical scattering patterns of reduced carboxymethylated lysozyme (egg white), ovalbumin, bovine serum albumin in

perdeuterated dodecyl sulfate. From intersection of the straight line (not shown) corresponding to a rod conformation, Q*, the persistence length Lp may easily be estimated by the equation $Lp=6/(\pi Q^*)$. In this case, since Q* is 0.12 $Å^{-1}$, Lp is found to be 16 Å. From these results it is found that the protein polypeptide chain was partially expanded. In the case of protein denatured in dodecyl sulfate, the hydrophobic residues and hydrophilic charged residues, half of which may form helix, are localized in the interior and the interface of the dodecyl sulfate micelle, respectively. In conclusion, by using the perdeuterated dodecyl sulfate, it was found that the protein polypeptide (molecular weight range: 14,000-66,300) chain in the complex is a wormlike chain with a persistence length of about 16 Å. Further investigations are in progress to characterize the surfactant-protein complex by small-angle neutron and X-ray scattering because the structural model remains to be established.

References

1. van Holde K. E., Johnson W. C., and Hon P. S., Principles of Physical Biochemistry, p222, Prentice-Hall Inc., New Jersey (1998).

2. Reynolds J. A., and Tanford C., J. Biol. Chem. 245, 5161(1970).

3. Shirahama K., Tsujii K., and Takagi T., J. Biochem. 75, 309(1974).

4. Ibel K., May R. P., Kirschner K., Szadkowski H., Mascher E., and Lundahl P., Eur. J. Biochem. 190, 311(1990).

Acknowledgements : The encouragement and support of SANS-U IMT members is greatly appreciated. This work was supported in part by a grant of Rice Genome Project PR-2102, MAFF, JAPAN.

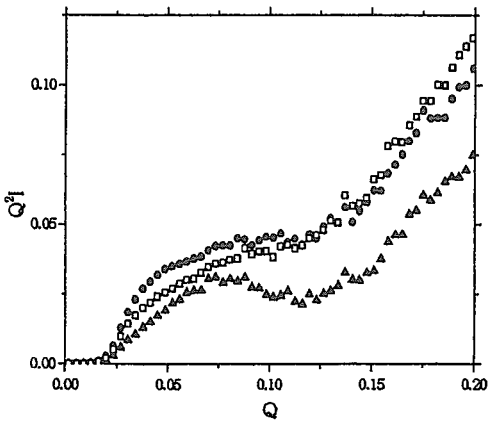

Figure 1 Kratky plots for the typical scattering patterns of reduced carboxymethylated hen egg lysozyme (▲), ovalbumin (●), bovine serum albumin (□) in perdeuterated dodecyl sulfate.

研究テーマ：水溶液中におけるシュガーボールの構造
表題：水溶液中におけるシュガーボールの構造

1-6-15 Conformation of Sugar Ball in Aqueous Solutions

K. Funayama[1], T. Imae[1,2], K. Aoi[3], K. Tsutsumiuchi[3], M. Okada[3], and M. Nagao[4]

[1]Graduate School of Science and [2]Research Center for Materials Science, Nagoya University, Nagoya, Aichi 464-8602,
[3]Graduate School of Bioagricultural Sciences, Nagoya University, Nagoya, Aichi 464-8601,
[4]The Institute for Solid State Physics, The University of Tokyo, Tokai, Ibaraki 319-1106, Japan

The interior or exterior chemical structure of dendrimer is expected to effect on the segment profile and solvent-penetration in dendrimer. We have before reported structure analysis of poly(amido amine) (PAMAM) dendrimer with OH end groups and poly(trimethyleneimine) /mono(amido amine) (PTMIN) layer-block dendrimer with OH end groups by small-angle neutron scattering (SANS).[1,2] In this study, we performed the external contrast variation experiments of SANS on the solutions of fifth (G5) and sixth (G6) generation poly(amido amine) dendrimers with galactose-having glycopeptide end groups (Sugar Ball, SB).

The dendrimer was dissolved at 1 wt% of dendrimer concentration in the mix solvent of D_2O/H_2O. The mixing ratio, $\%D_2O$ (=v/v%), was varied from 75 to 100. SANS measurements were performed at room temperature with the SANS-U spectrometer of JRR-3M in Tokai.

The apparent radius of gyration $R_{g,app}$ was estimated from Guinier region of SANS intensity profile at each $\%D_2O$. Figure 1 shows $R_{g,app}$ of four dendrimers; two generation SBs, PAMAM, and PTMIN, as a function of $\%D_2O$. The $\%D_2O$-dependence of $R_{g,app}$ on SBs is different from those on the other dendrimers, indicating different segment profile and solvent-penetration among dendrimers. The difference could be demonstrated using the theory of five layer model applied before.[2]

Refferences

[1] Imae et al. *Langmuir* **1999**, 15, 4076.
[2] Funayama et al. *J. Phys. Chem. Solid* **1999**, 60, 1355.

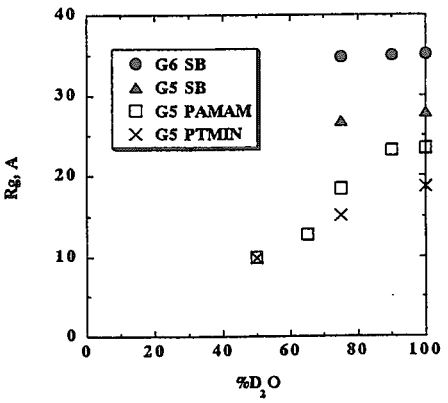

Figure 1 Apparent radius of gyration $R_{g,app}$ from Guinier region for four dendrimers as a function of mixing ratio of solvent $\%D_2O$.

研究テーマ：中性子小角散乱によるキトサン・ヨウ素錯体の構造解析
表題：中性子小角散乱コントラスト変調法によるキトサン・ヨウ素錯体の構造研究

1-6-16

Small-Angle Neutron Scattering Study of the Structure of Chitosan-Iodine Complex with Contrast Variation Method

H. Yajima, Y. Suzuki, T. Sakajiri, and T. Ishii

Department of Applied Chemistry, Faculty of Science, Science University of Tokyo, 1-3 Kagurazaka Shinjuku-ku, Tokyo 162-8601, Japan

Chitosan, a linear polysaccharide of β-(1,4) linked D-glucosamine, obtained primarily as a by-product of the seafood industry, has recently attracted a great deal of attention as a multifunctional biopolymer because of its unique properties including a variety of complexation and biological activities etc. For improvement and further development of the potential applications of chitosan, it is necessary to gain a great information of its molecular characteristics based on extensive physicochemical studies. We have so far investigated the physicochemical properties, in particular, the spectral and structural properties of chitosan-iodine (CI) complexes in solution. As a result, we have obtained the findings that thermal hysteresis, i.e., an irreversible reaction process, is involved in complexation and molecular assembly of chitosan chains plays an important role in CI complexation [1]. No clear pictures have yet established with regard to the structural characteristics of the CI complexes. The objective of this study is to characterize the CI complex structure by means of small-angle neutron scattering (SANS) with contrast variation method.

The CI complex solutions containing [chitosan] = 0.05 uM (u: one D-glucosamine residue), $[I_2]$ = 0.003 M, and [KI] = 0.03 M were prepared by freezing mixtures of chitosan (M_w = 11,000, degree of deacetylation = 98%) with KI-I_2 solutions and thawing them at 4°C using the mixed solvents of D_2O/0.3M deuterated acetate buffer and H_2O/0.3M acetate buffer with different D_2O contents (ϕ_D) = 0, 20, 80, and 100%. SANS measurements were carried out at 20°C using a SANS spectrometer (SANS-U) installed at the C1-2 port of the cold-neutron beam line in the research reactor JRR-3M of the Japan Atomic Energy Research Institute (JAERI), Tokai, Japan. The wavelength (λ) used was 7.0 Å with a fractional spread ($\Delta\lambda/\lambda$) of 10% and the sample-to-detector distance was 4m (8×10^{-3} Å^{-1} < q < 7×10^{-2} Å^{-1}) mainly for the CI

JRR-3M, SANS-U, 6. Polymer

complex and 1m ($4x10^{-2}$ Å^{-1} < q < 0.25 Å^{-1}) mainly for mere chitosan. Structural analyses were performed based on the Stuhrmann plot from the SANS data. This procedure was described in detail elsewhere [2].

Figure 1 shows the Stuhrmann plots for intact chitosan and the CI complex, where $\overline{\rho}$ refers to the contrast. It should be noted that the contrast matching points of the chitosan and CI complex were determined to be 45% and 44% D_2O, respectively. The Rg value at infinite contrast (Rg,c), the radial second moment of the mean scattering length density (SD), α, and the derivation of the center of the SD distribution, β, were estimated to be Rg,c = 91.6 Å, α = -74.2 and β = 0 Å^{-2}, respectively. For intact chitosan, these values were Rg,c = 40.4 Å, α = -10.0, and β = 29.6 x 10^{-10} Å^{-2}. SANS structural analyses suggested that the CI complex forms an aggregate with a cylindrical structure composed of an inner polyiodide chain surrounded by an assembly of crystalline-like extended chitosan chains involving intermolecular hydrogen bonds network. For intact chitosan, it was conceived that chitosan takes a compactly folded conformation involving intramolecular hydrogen bonds.

References

1. H. Yajima et al., *Polym. Prepr. Jpn.* **46** (1997) 382; **46** (1997) 2489-2490; **47** (1998) 3520-3521.
2. H. Yajima et al., *Biochim. Biophys. Acta* **1381** (1998) 68-76.

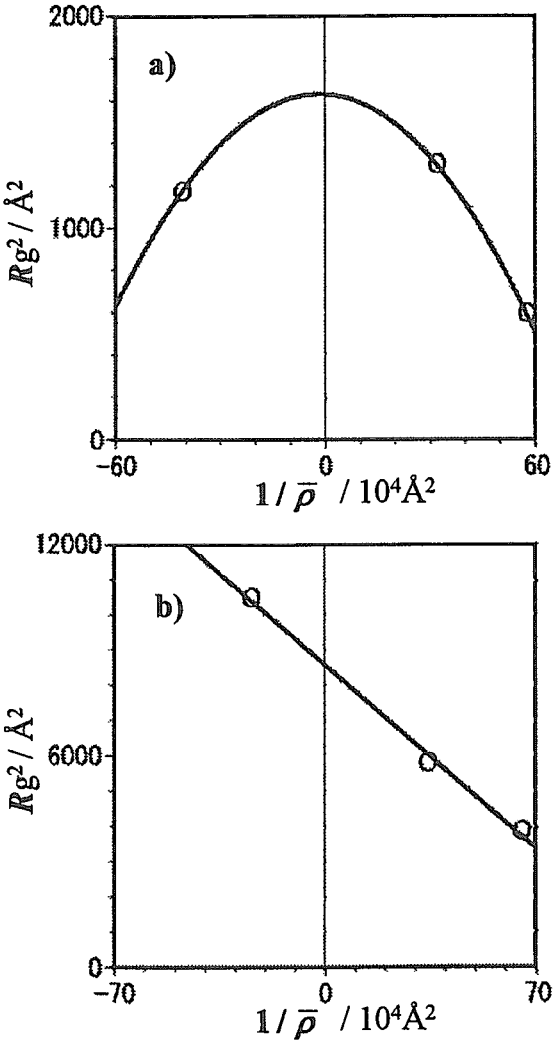

Fig.1 Stuhrmann plots for intact chitosan (a) and the CI complex (b).

小角中性子散乱による化学架橋ゲル及びγ線架橋ゲルの微視的構造の比較に関する研究

1-6-17
Comparison of Microscopic Structures for Chemically Cross-linked and γ-ray Irradiated Gels by Small-angle Neutron Scattering

T. Norisuye and M. Shibayama

Department of Polymer Science and Engineering,
Kyoto Institute of Technology, Matsugasaki, Sakyo-ku, Kyoto 606-8585, JAPAN

Introduction

It is well known that polymer gels have structural inhomogeneities due to restriction of local chain mobility. The inhomogeneities have been extensively studied in terms of light and neutron scattering experiments by taking into account the fact that gels have two types of concentration fluctuations, i.e., thermal fluctuations and frozen inhomogeneities.[1,2] In our previous work, we evaluated a degree of inhomogeneities for chemically cross-linked gels (BIS gel) as a function of cross-linking density by dynamic light scattering (DLS).[3] Spatial distribution of cross-links, however, depends on the reactivity ratio of chemical constituents and may affect the frozen inhomogeneities. In order to elucidate the nature of structural inhomogeneities, we made a comparison between chemically cross-linked gels and γ-ray irradiated gels (γ-ray gels), whose cross-linking points are expected to be randomly distributed in the space.

Experimental

Poly(*N*-isopropylacrylamide)(NIPAm) gels having different cross-link densities were prepared by polymerizing NIPAm monomer with cross-linker, methylene-bisacrylamide (BIS) in water at 20°C. The concentrations of BIS, C_{BIS} were varied from 0 to 3.25mM, while the that of NIPAm (C_{NIPA}) was kept to 690mM. The cross-linking density for γ-ray irradiated gels was controlled by varying the radiation time (0 ~ 3 Mrad).

Small angle neutron scattering (SANS) measurements were carried out with SANS-U spectrometer of the Institute for Solid Sate Physics, University of Tokyo in Tokai. The wavelength of neutron beam was 7Å.

Theory

Theoretical scattering functions for polymer gels with excluded volume effect were proposed by Panyukov and Rabin.[4] According to the theory, the scattered intensity consists of two contributions, i.e., thermal fluctuations, $G(q)$ and frozen inhomogeneities, $C(q)$,

$$S(q) = G(q) + C(q) \tag{1}$$

$$G(q) = \frac{\phi N g(q)}{1 + w(q)g(q)} \tag{2}$$

$$C(q) = \frac{\phi N}{[1 + w(q)g(q)]^2 (1 + Q^2)^2} \times \left[6 + \frac{9}{w_0(q) - 1 + (1/2)Q^2 (\phi_0/\phi)^{2/3} \phi_0^{-1/4}} \right] \tag{3}$$

where ϕ is the volume fraction of a gel and Q is the reduced wave vector defined by

$$Q = aN^{1/2}q \tag{4}$$

with a, N, q being the segment length, the degree of polymerization between cross-links and the wave vector, respectively. w and w_0 are the excluded volume parameters at observation

and at sample preparation, respectively. Mean field approach gives the following expression for w and w_o,

$$w = (1-2\chi+\phi)\phi N \quad (5)$$

$$w_0 = (1-2\chi_0+\phi_0)\phi_0 N \quad (6)$$

where χ is the Flory's interaction parameter. $g(q)$ is the thermal correlation function without excluded volume effect,

$$g(q) = \frac{1}{Q^2/2+(4Q^2)^{-1}+1} + \frac{2}{(1+Q^2)^2(\phi_0/\phi)^{2/3}\phi_0^{-1/4}} \quad (7)$$

Results and Discussion

Figure 1 shows double logarithmic plots of scattered intensity, $I(q)$, having different cross-linking densities for a series of (a) BIS gels and (b) γ-ray gels. For the BIS gel, $I(q)$ increased and became a power law function with increasing the cross-linking density. On the other hand, any significant cross-linking density dependence or a power-law behavior was not observed for the γ-ray gels, although $I(q)$ slightly increased with cross-linking density. The solid lines inserted in the figure indicate theoretical curves obtained by fitting with eq (1) - (7). The evaluated values of N by the analysis systematically increased by decreasing C_{BIS} from 142 to 289 for the BIS gels whereas the value of N for the γ-ray gels was around 110 irrespective of the cross-linking densities except for that of the highest cross-linking density. The constant N for the γ-ray gels may be due to competition of cross-linking and chain scission as reported in the literature.[5] Thus, the cross-linking density dependence for the BIS gels and the γ-ray gels were examined by SANS and a significant difference in the gel structure was observed. The experimental results were well reproduced by the PR theory and the values of N were quantitatively obtained. The detail of the results will be unveiled in the forthcoming paper with DLS data.

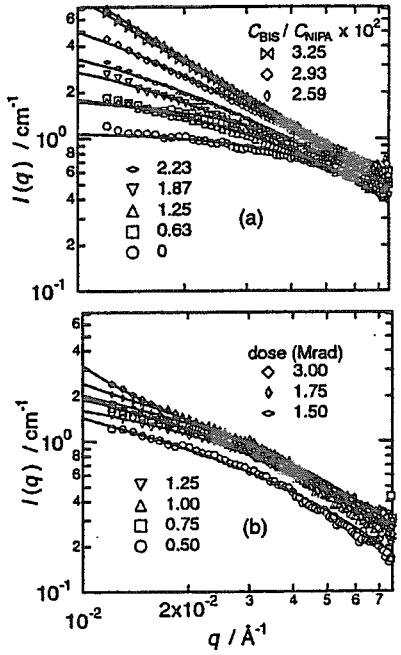

Figure 1. Double logarithmic plots of $I(q)$ having different cross-linking densities for (a) chemically cross-linked gels (BIS gels) and (b) γ-ray gel.

Reference

1) Pusey, P. N.; van Megen, W. *Physica A* **1989**, *157*, 705.

2) Shibayama, M. *Macromol. Chem. Phys.* **1998**, *199*, 1.

3) Shibayama, M.; Norisuye, T.; Nomura, S. *Macromolecules* **1996**, *29*, 8746.

4) Panyukov, S.; Rabin, Y. *Macromolecules* **1996**, *29*, 7960.

5) O'Donnell, J. H.; Winzor, C. L.; Winzor, D. J. *Macromolecules* **1990**, *23*, 167.

研究テーマ：ずり流動場による分子組織体再構成過程の追跡
表題：非イオン界面活性剤が作るラメラ相の構造に対するずり流動場の効果

1-6-18
Effects of Shear Flow on the Structure of the Lamellar Phase Formed by Nonionic Surfactants

K. Minewaki, T. Kato, and M. Imai[1]

Department of Chemistry, Tokyo Metropolitan University
[1] Department of Physics, Ochanomizu University

In recent years, much attention has been paid to the effects of shear flow on the structure of a lamellar phase formed by surfactants. In the present study, we have measured small-angle neutron scattering (SANS) on a nonionic surfactant $C_{16}H_{33}(OC_2H_4)_7OH$ ($C_{16}E_7$)-water system under shear flow for the shear rates $\dot{\gamma}$ = 10^{-3}-10^{2} s^{-1} much lower than those for other studies reported so far. This system was chosen because phase behaviors and results of SAXS measurements have been reported by us.

Measurements of SANS were carried out at the instrument SANS-U of Institute for Solid State Physics of University of Tokyo in JRR-3M at Tokai with a Couette shear cell. All the measurements were made for the sample containing 55 wt% of $C_{16}E_7$ at 55°C and 70°C.

Figure 1 shows shear rate dependence of the position and the peak intensity of the first reflection (20° sector) at 70°C in flow and neutral directions. At lower shear rates less than $0.1s^{-1}$, the peak intensities for both directions decrease with increasing shear rate without change in the peak position, q_{max}.

At the shear rates 0.1-1 s^{-1} (depending on the history of the sample) the peak position suddenly shifts to higher scattering angles, which may correspond to an appearance of a new peak because we sometimes observed coexistence of two peaks in 10 minutes. As $\dot{\gamma}$ increases further, q_{max} decreases towards the initial value. At the same time, the peak intensity in neutral direction increases with the increase of $\dot{\gamma}$ while that in flow direction continues to decrease.

At 55°C, we have measured SANS in gradient direction in addition to other two directions. The minimum of the peak intensity was observed also in gradient direction around $1s^{-1}$ (in this case the intensity takes a maximum around $0.1s^{-1}$). These results indicate that the minimum of the peak intensity is not due to the ordering of the lamellae along a certain direction.

Taking into account the results of SAXS measurements reported before, we can infer the following scenario. As the shear rate increases from 10^{-3} up to 0.1-1 s^{-1}, the lamellar domain contracts into smaller domains. At the shear rate of 0.1-1 s^{-1}, a new domain is formed composed of disrupted bilayer sheets with random orientations. As the shear rate increases further, such a domain grows accompanying the reduction of defects until the original microstructure is reconstructed.

We are indebted to Prof. Yoshihiko Takahashi of Nogoya University and Prof. Toshiharu Kanaya of Kyoto University for their cooperation.

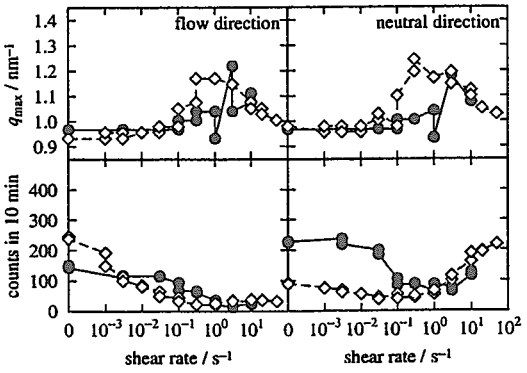

Figure 1 Shear rate dependence of the position (q_{max}) and the peak intensity of the first reflection in flow and neutral directions at 70°C. Different symbols indicate independent runs.

研究テーマ：多糖/水系の高次構造形成と機能発現
表題：ULSによるジェランガムゲルの構造研究

1-6-19 Large Scale Structures in Gellan Gum Gels

Y. Izumi, Y.Jinbo, T.Matsugi, M. Hashimoto[1] and T. Takahashi[1]

Graduate School of Science and Engineering, Yamagata University, Yonezawa, Yamagata 992-8510 Japan
[1]Institute for Solid State Physics, University of Tokyo, Kashiwa, Chiba 277-8581 Japan

Small-angle scattering (SAS) studies were performed in order to specify the intermediate scale structures of gellan gum gels in the absence of added salts. The SAS results revealed that an ordered structure presented in the gels in a concentration range above 4 wt %, the ordered structures were lamellae and the junction zone was formed by such a lamellar stack[1]. Furthermore, ultra-low angle scattering (ULS) studies were performed in order to clarify the large scale structure of the gels and revealed that in the q range between 3×10^{-5} and 5×10^{-4} A^{-1}, the gel with the concentration of 15wt% at 30°C had a fractal structure with the dimension of 2.6[2].

The present work aimes to clarify the concentration dependence of the large scale structures in the gels without added salts. The sample of sodium-salt-type gellan gum (NaGG-3) was used[2]. The weight average molecular weights were 21.7×10^{4} at 25°C and 9.47×10^{4} at 40°C, respectively[3].

The neutron scattering experiments were performed with the ISSP C1-3 ULS spectrometers installed at JRR-3M reactor of JAERI (Tokai) in the concentration range from 7.9 to 19.7wt% at 25°C.

Figure 1 shows the excess ULS profiles for the NaGG-3 gels in the double-logarithmic scale. As can be seen, a power-law decay is observed in the concentration above 15wt%. We obtained about 3.0 as the fractral dimension, suggesting that the gel structures are characterized by large aggregates with a very rough interface boundary. On the other hand, the behavior of the profiles in the concentration below 12.5wt% are different from those above 15wt%, suggesting the presence of a two population-system. Thus, large scale structures in the present gels are different at a concentration across 13-14wt%. In addition, there is no peak indicating the ordering in such a large scale structure of gels, i.e., there is no ordered structure between the aggregates in the gels.

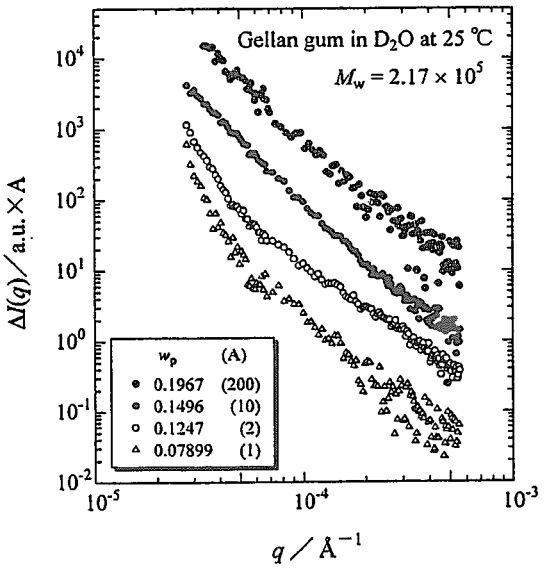

Fig. 1. Excess ULS profiles for the gellan gum gel in D_2O at the concentrations of 7.9wt% (△), 12.5wt%(○), 15.0wt%(●) and 19.7wt% (◎).

Reference
1. Y.Izumi, S.Saito, K.Soma, *Prog. Coll. Polym. Sci.* 114 (1999) 48-55.
2. Y.Izumi, Y.Jinbo, K.Soma, S.Saito, M.Nagao, M.Hashimoto anf T.Takahashi, *Activity Rep. Neutron Scattering Res.* 6 (1999) 195.
3. M.Akutu,K.Kubota and K.Nakamura, *Prog.Coll. Polym. Sci.* 114 (1999) 56-61.

JRR-3M, ULS, 6. polymer

研究テーマ：超小角中性子散乱法によるコロイド分散液中における合金様結晶構造と相転移の解析
表題：超小角中性子散乱法による２成分コロイド分散液中のコロイド結晶構造解析

1-6-20 Ultra-Small-Angle Neutron Scattering Study of Colloidal Crystal Structure in Two-Component Colloidal Dispersion

H. Matsuoka, T. Harada, H. Yamaoka

Department of Polymer Chemistry, Kyoto University, Kyoto 606-8501, JAPAN

Highly charged colloidal particles form colloidal crystals in dispersions by electrostatic interparticle interaction. The mechanism of the colloidal crystal formation still has mysterious aspects.[1] Therefore, to clarify the origin of this phenomenon is one of hot topics in colloid science. We have performed ultra-small-angle neutron scattering (USANS) study of the mixture of colloidal dispersions to investigate the colloidal crystal formation in two-component system. In our previous study, it was revealed that the scattering from each component could be obtained separately by USANS with the contrast variation method.

In this study, we performed the USANS study of colloidal crystals in the mixture of polystyrene latex (*d*PS02: diameter = 1560Å, surface charge density = 1.1μC/cm^2) and silica colloidal (KEP10W: diameter = 1060Å, surface charge density = 0.06μC/cm^2) dispersions. The mixing number ratio was 36:64. USANS measurement was carried out using the ultra-small-angle (ULS) instrument at the Institute for Solid Sate Physics, University of Tokyo, located at the C-1-3 beam line of the JRR-3M reactor in Tokai, Ibaragi, Japan. The optical system was based on the Bonse-Hart type.

Figure 1 shows USANS curve of *d*PS02 particles dispersed in water (profile A). Clear Bragg peaks, which indicate the existence of colloidal crystals in the dispersion, were observed. USANS curve for the binary colloidal dispersion (profile B) was also shown in Figure 1. Since the scattering length density of the medium was nearly equal to that of KEP10W, USANS scattering intensity corresponds to the scattering intensity from *d*PS02 particles only. Profile C in Figure 2 shows the USANS curve of KEP10W particles dispersed in water, while profile D shows the USANS curve of the binary colloidal dispersion. Since the medium of the binary dispersion was D_2O, its scattering length density is equal to that of *d*PS02, we can estimate the distribution of only KEP10W particles in the binary dispersion. In both Figures 1 and 2, the clear difference between USANS profile for the one-component system and that for the two-component was observed. The relative peak position obtained for the two-component system indicates that colloidal crystals in the binary dispersion have complicated structure – like colloidal alloy structure.

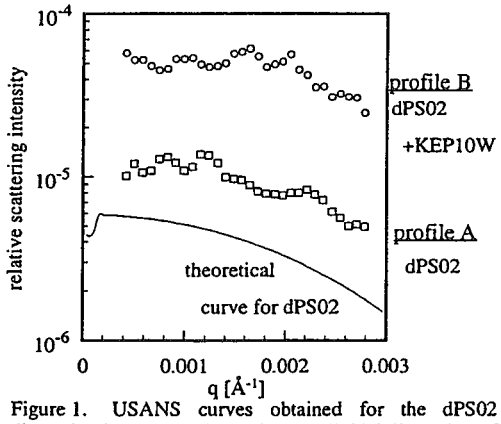

Figure 1. USANS curves obtained for the dPS02 dispersion in water and the binary colloidal dispersion of dPS02 and KEP10W. The medium of the binary dispersion was the mixture of H_2O and D_2O (H_2O/D_2O=42/58).

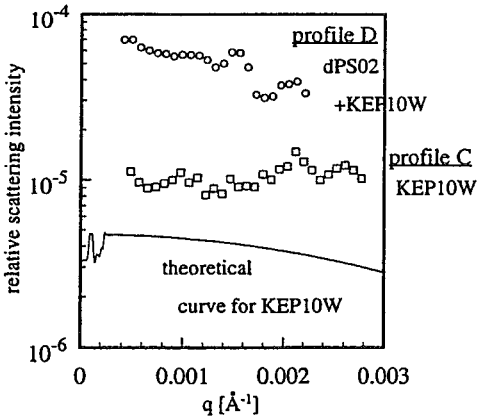

Figure 2. USANS curves for the KEP10W dispersed in water and the binary colloidal dispersion of dPS02 and KEP10W. The medium of the binary dispersion was D_2O.

(1) T. Harada, H. Matsuoka, T. Ikeda, H. Yamaoka, *Colloids Surfaces A*, in press.

JRR-3M, ULS(C1-3), Polymer

研究テーマ：イメージングプレートを用いた気液界面測定用水平型中性子反射率計の開発
表題：イメージングプレートを用いた気液界面測定用水平型中性子反射率計の開発

1-6-21 Development of Neutron Reflectometer for Air/Water Interface with Imaging Plate

H.Matsuoka, E.Mouri, R.Yoshitome, K.Kago, H.Yamaoka and K.Soyama[1]

Department of Polymer Chemistry, Kyoto University, Kyoto 606-8501, Japan
[1]Japan Atomic Energy Research Institute, Tokai, Ibaraki 319-1195, Japan

Reflectivity measurement is a powerful tool for the structural study of surfaces and interfaces in nanometer scale. X-ray and neutron reflectivity (XR, NR) measurements have been applied to solid surfaces and thin films on solid substrates, and significant information has been coming out. One of the recent hot topic in surface and interface science is the structure of monolayers on water surface. Such a system is quite important for novel functional devices and also from biological point of view. The structure of monolayer has been investigated by XR, NR and atomic force microscope (AFM) *after* deposited on solid substrate in dried state. However, it has been found that the nanostructure of monolayer after deposition is largely different from that on water surface. The horizontal type XR and NR are the only the technique to investigate the monolayer structure on water directly.

In this study, we have developed the horizontal type NR instrument. In addition to 1D PSD, the imaging plate(IP) was also used as a detector. By IP, the off-specular reflection and in-plane information can be obtained in addition to depth-profile.

The C2-1 port (LTAS) in JRR-3M, Tokai, was used. We have developed a new device to control the tilting angle of the monochrometer of LTAS. By this mechanism, the incident angle of neutron to water surface can be changed. For the water surface measurement, the specially designed Langmuir-Brodgett (LB) rough was constructed. By the position of the barrier of the LB trough, the surface pressure of the monolayer on water can be controlled.

Figure 1 shows the NR profile for pure water surface and DPPC (a kind of lipid) monolayer on water. The intensity of reflected neutron can be clearly detected as a function of incident/reflection angle (specular reflection). This is the first NR data for water surface in Japan. The detailed analysis is now in progress.

Figure 2 shows the IP image. The off-specular reflection is excellently observed. Modification and improvement of this NR apparatus are now going on.

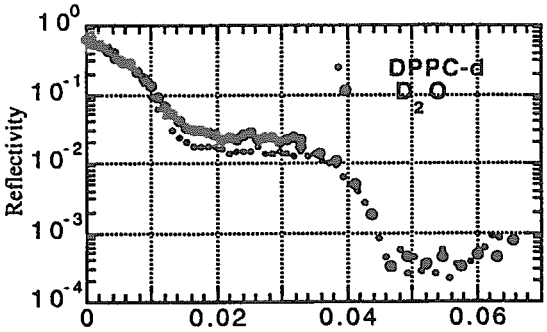

Figure 1 NR profiles for pure D_2O surface and DPPC monolayer on D_2O surface.

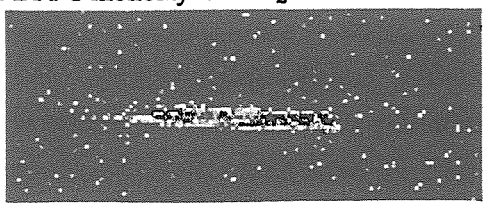

Figure 2 IP image of NR for D_2O surface. θ=0.24 degree.

原子炉：JRR-3M　　装置：LTAS(C2-1)　　分野：中性子散乱（高分子）

研究テーマ：水溶液中のポリアミドアミンデンドリマーのダイナミックス
表題：水溶液中のポリアミドアミンデンドリマーのダイナミックス

1-6-22

Dynamics of Poly(amido amine) Dendrimer in Aqueous Solutions

K. Funayama[1], T. Imae[1,2], K. Aoi[3], K. Tsutsumiuchi[3], M. Okada[3], and H. Seto[4]

[1]Graduate School of Science and [2]Research Center for Materials Science, Nagoya University, Chikusa, Nagoya, Aichi 464-8602,

[3]Graduate School of Bioagricultural Sciences, Nagoya University, Chikusa, Nagoya, Aichi 464-8601,

[4]Faculty of Integrated Arts and Sciences, Hiroshima University, Higashihiroshima 739-8521, Japan

Dendrimers, which are one of highly branched polymers, have recently been focused as novel materials. In this work, dynamics of the fifth generation poly(amido amine) (PAMAM) dendrimer with hydroxyl end groups in D_2O were studied by neutron spin echo (NSE).

PAMAM dendrimer D_2O solutions were prepared at 1 and 10wt% of dendrimer concentration. NSE measurements were carried out using NSE spectrometer of JRR-3M in Tokai at room temperature. The scattering vector Q range covered in the experiments was 0.02 to 0.1A^{-1}. The intermediate correlation functions I(Q,t)/I(Q,0) were obtained by the normalization of elastic scattering from standard sample Grafoil.

There were obvious difference between the dynamics behavior for two dendrimer concentrations. I(Q,t)/I(Q,0) at 10wt% could be fitted with single exponential function (Fig. 1a). On the contrary, one at 1wt% was well fitted with the double exponential function (Fig. 1b), including fast and slow relaxation modes. The diffusion coefficient of the slow mode corresponds to the translational diffusion coefficient estimated by dynamic light scattering. That of the fast mode may be originated by the motion of segments or solvents in dendrimer.

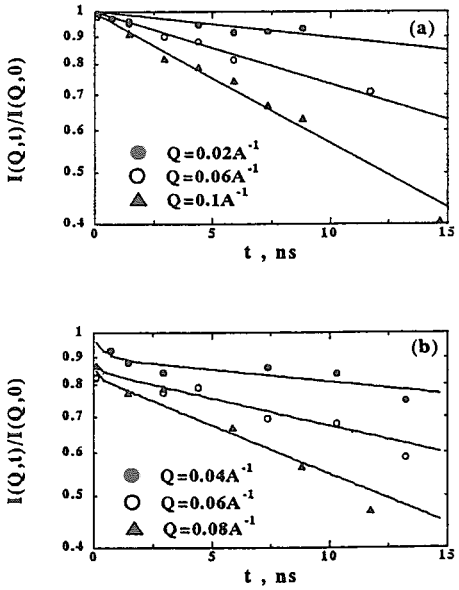

Figure 1 I(Q,t)/I(Q,0) functions as a function of Fourier time t for 10wt% (a) and 1wt% (b) solutions of PAMAM dendrimer. The solid lines are theoretical ones with single (a) and double (b) exponential functions.

JRR-3M, NSE, 6. Polymer

研究テーマ：中性子スピンエコー法によるPVAゲルのダイナミクス
表題：中性子スピンエコー法による エルゴードゲルと非エルゴードゲルの微視的ダイナミクス

1-6-23 Microscopic dynamics of ergodic and non-ergodic gels as studied by neutron spin echo technique

T. Kanaya, K. Kaji, Y. Kawabata[2], M. Nagao[1], H. Seto[2] T. Takeda[2]
Institute for Chemical Research, Kyoto University
Institute for Solid State Physics, University of Tokyo[1]
Faculty of Integrated Arts and Science, Hiroshima University[2]

Polymer gels are three dimensional networks of polymer chains swollen with solvents. From a viewpoint of lifetime of crosslinking points, polymer gels can be classified into two classes: one is a class of gels with *infinite* lifetime of crosslinking points. Chemical gels and some physical gels belong to this class and such gels cannot flow even in an infinite period because the network structure is permanent. Some other physical gels with *finite* lifetime of crosslinking points belong to another class. Such physical gels can flow extremely slowly through exchanges of crosslinking points between different polymer chains. Its viscosity is usually very high, e. g., more than 10^3 Pa s.

In the previous paper [1] we have studied dynamics of poly(vinyl alcohol) (PVA) gels whose crosslinking points (crystallites) have *infinite* lifetime and found that the normalized intermediate function $I(Q,t)/I(Q,0)$ has a non-decaying component, suggesting that the system is non-ergodic. In contrast to the PVA gels, it is known that PVA gels in an aqueous borax solution have crosslinking points with a *finite* lifetime. It is therefore expected that the intermediate scattering function decays to zero at a finite time due to the ergodicity of the system.

In this experiment, we used poly(vinyl alcohol) (PVA) in an aqueous borax solution. The crosslinking points of the gel are a complex of PVA-BO_4-PVA and exchangeable one another between different chains. The molecular weights and the degree of saponification are 600 and 87.5 %, respectively.

NSE measurements were carried out on NSE spectrometer at a beam port (C2-2) of JRR-3M reactor. Using neutron wavelength 7.7 Å, we can cover a Fourier time range from 0.08 to 15 ns. The Q range covered by the NSE spectrometer is 0.02 to 0.15 $Å^{-1}$.

Small-angle neutron scattering were observed with SNAS-U spectrometer installed at a cold neutron guide C1-2.

In Fig. 1, the normalized intermediate scattering functions $I(Q,t)/I(Q,0)$ of the PVA gel in DMSO/D_2O (60/40) are shown at Q = 0.03, 0.07 and 0.1 $Å^{-1}$. This Q range corresponds to the so-called Porod's region.[1] $I(Q,t)/I(Q,0)$ shows a very rapid decay in the time region shorter than about 2 ns while it is almost constant in the time region longer than about 2 ns. This non-ergodic behavior has been assigned to *infinite* lifetime of the crosslinking points in the previous paper.

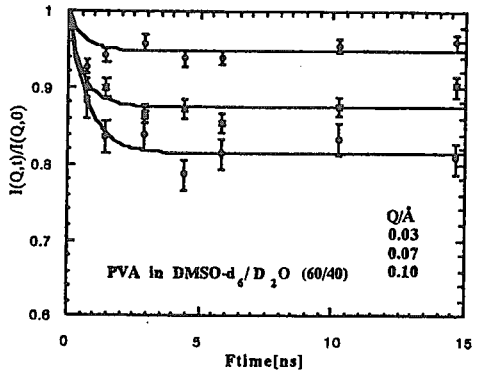

Fig. 1. $I(Q,t)/I(Q,0)$ of PVA gel in DMSO/D_2O (60/40), showing a typical non-ergodic behavior.

The normalized intermediate scattering functions $I(Q,t)/I(Q,0)$ of the PVA gels in an aqueous borax solution are plotted for the sols (C_p = 2. 4%) and the gel (C_p = 4.8%) in Fig. 2 and Fig. 3, respectively, in a Q range of 0.03 to 0.13 $Å^{-1}$. It should be emphasized

that the $I(Q,t)/I(Q,0)$ seems to decay to 0 at a finite time for both the sol and gel.

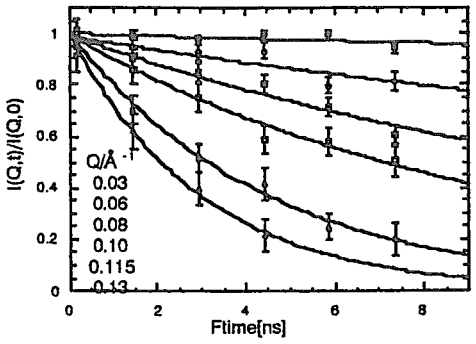

Fig. 2. $I(Q,t)/I(Q,0)$ of PVA in an aqueous borax solution. $C_p = 2.4$ wt% (sol).

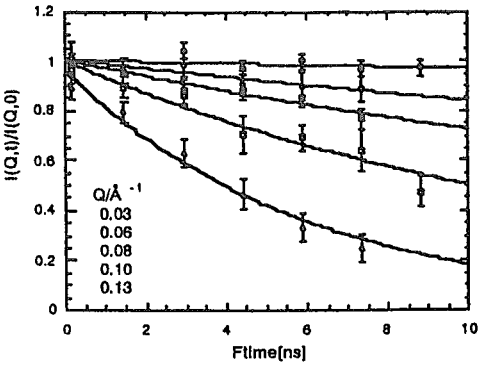

Fig. 3. $I(Q,t)/I(Q,0)$ of PVA in an aqueous borax solution. C_p = 4.8 wt% (gel), showing a typical ergodic behavior.

In the case of the sol, such ergodic behavior is obvious because the sol can flow and molecules move anywhere in the system. In the PVA gel in an aqueous borax solution the crosslinking points are exchangeable between different polymer chains and hence the gel can flow and molecules can move anywhere even in the gel although the flow rate or the relaxation time is very slow. Assuming that the decay function can be described by an exponential function, we fitted it to the observed $I(Q,t)/I(Q,0)$. The results of the fit are shown by solid curves in Figs 2 and 3 for the sol and gels, respectively. The agreements are good, suggesting that the relaxation observed here is described by a single exponential function.

The decay rate Γ estimated from the fit are plotted as a function of Q in Fig. 4 for both the sol and gel in a double logarithmic form. The Q dependence of the decay rate is approximately described by a power low $\Gamma \sim Q^3$ for the sol and gel. It is very surprising that the decay rate of the gel is less than two times of that for the sol although the macroscopic viscosity of the gel is more than 6 order of magnitude larger than that of the sol. This result suggests that the relaxation process observed in the NSE measurements is not related to the flow process. In the non-ergodic PVA gels the non-decaying component is observed in the corresponding Q range (see Fig. 1) and related to the motion of crosslinking points. If we observed the relaxation of the crosslinking points in the ergodic PVA gels in an aqueous borax solution, the decay rate Γ must correspond to the inverse of the lifetime of the crosslinking points. It is expected that the lifetime of the PVA gels do no depend on the concentration of PVA whether it is sol or gel because it is determined by local structure and not related to the flow relaxation. This picture explains the present observation well.

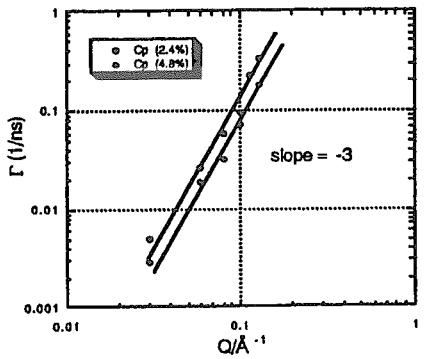

Fig. 4. Decay rate Γ for PVA sol (C_p =2 .4 wt%) and gel (C_p=4.8 wt%) as a function of Q.

[1] T. Kanaya et al., Activity Report on Neutron Scattering, 6, 183 (1999).

研究テーマ：中性子スピンエコー法による両親媒性およびイオン性高分子溶液中における特異的単独・協同運動の解析
表題：中性子スピンエコー法による水溶液中におけるイオン性高分子ミセルのダイナミクス

1-6-24 Neutron Spin Echo Study of the Dynamics of Ionic Polymer Micelles in Aqueous Solution.

Hideki Matsuoka, Yusuke Yamamoto, Kozo Matsumoto, Hitoshi Yamaoka

Department of Polymer Chemistry, Kyoto University, Kyoto 606-01, Japan

We have been systematically studying the micellization behavior, micelle strucuture, and functions of micellar systems of amphiphilic block copolymers in aqueous solution. Although the characterisitcs of amphiphilic copolymer micelles is recently extensively investigated, most of them are for organic solvent systems: not so many studies for aqueous systems have been reported. From the biological point of view, the inportance of the study on aqueous system is obvious. The structure of the polymer micelles can be examined by utilization of SAXS and SANS.1,2 Our next interest is the dynamics in polymer micelle systems. For this porpose, the neutron spin echo (NSE) technique is one of themost probably technique due to its suitable Q-range and time-scale for polymer micelle study.

We have reported the NSE results for non-ionic polymer micelle systems.3 By NSE we have found two dynamic modes in the system. The slow mode was assigned to be the translational diffusion of the whole micelle and the fast mode was concluded to be the corona dynamics, which is a flucutuation of hairly hydrophilic chains in the micelle shell. In this study, we examined the ionic amphiphilic diblock copolymer. The polymer used in this study is shown in Fig.1.

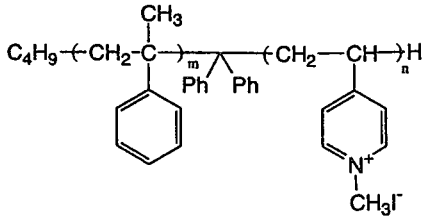

Figure 1 Structure of S2550 ionic amphiphilic diblock copolymer.

SANS profiles of two polymers (S3075, S2550), which have different segment length, in heavy water (1wt.%) obtained by SANS-U showed a strong scattering at small-angle regions, indicating that these polymers form micelle in water. Base on SANS data, NSE experiments were performed at Q positions of 0.06, 0.08, 0.10, and 0.12Å^{-1}.

Figure 2 shows the time-correlation function for S2550 thus obtained. These decay behavior were well fitted by the function

$$P_{nse}=\exp(-\Gamma_{slow}t)\{(1-A_{fast})+A_{fast}\exp(-\Gamma_{fast}t)\}$$

and two dynamic modes were quantitatively evaluated. The slow mode corresponds to the translational motion of the whole micelle as was the case of non-ionic system. The fast mode is also consideted to be the corona dyanmics. The characteristic for ionic system is much faster diffusion coefficient for the fast mode compared to the non-ionic ones. This is thought to be a collective behavior of ionic chains and countersions.

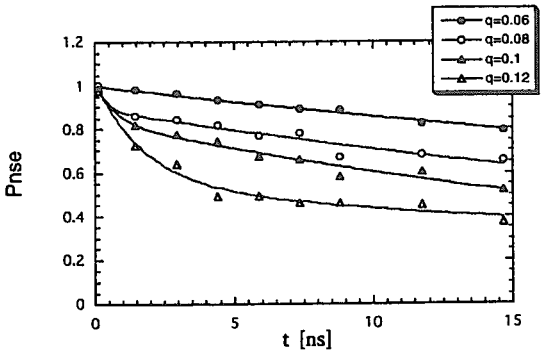

Figure 2 The time correlation function for S2550 polymer micelles in heavy water (1wt.%) obtained by NSE.

References

1) M.Nakano et al. Macromolecules,32, 697-703 (1999).
2) M.Nakano et al. Macromolecules, 32(12), 4023-4029 (1999).
3) H.Matsuoka et al. submitted.

テーマ：中性子反射率測定による高分子界面での分子拡散挙動評価
表題：中性子反射率測定による（ポリスチレン/重水素化ポリスチレン）二層膜界面における分子鎖拡散挙動評価

1-6-25

Evaluation of Interdiffusion Behavior of (Polystyrene/Deuterated Polystyrene) Bilayer below the Bulk Glass Transition Temperature by Neutron Reflectivity

T. Kajiyama, D. Kawaguchi, K. Tanaka, S. Sasaki, S. Tasaki*[1], and A. Takahara*[2]

Graduate School of Engineering, Kyushu University, 6-10-1 Hakozaki, Higashi-ku, Fukuoka 812-8581, Japan
[1]Research Reactor Institute, Kyoto University, Kumatori-cho, Sennan-gun, Osaka 590-0494, Japan
[2]Institute for Fundamental Research of Organic Chemistry, Kyushu University, 6-10-1, Hakozaki, Higashi-ku, Fukuoka 812-8581, Japan

Molecular motion at polymer surfaces is quite different from that in the bulk region due to the free energy difference between surface and bulk. The purpose of this study is to investigate surface molecular motion based on the polymer interdiffusion behavior at the [hydrogenated PS/deuterated PS] (h-PS/d-PS) interfaces at a temperature above the surface glass transition temperature, T_g^s and below the bulk glass transition temperature, T_g^b by neutron reflectivity (NR) measurement.

The samples used in this study were monodisperse h-PS and d-PS with M_n of 190k and 185k, respectively. The thin films were prepared by the spin-coating method on silicon wafers. Then, (h-PS/d-PS) bilayers were prepared by floating technique as follows. The perimeter of the h-PS film was scored with a blade, and then floated off onto the surface of distilled water. Then, the h-PS film was picked up onto the d-PS film by attaching the d-PS film from the air side. For the interdiffusion experiment, the bilayers were annealed at 365 K, which was above T_g^s and below T_g^b for 96 hrs.

NR measurement was carried out by using the multilayer interferometer for neutrons (C3-1-2, MINE) at the Institute for Solid State Physics, University of Tokyo. The incident neutrons had the long wavelength resolution of 3.5 %. The reflectivity was calculated based on the scattering length density profile along the depth direction by using Spread Environmental Reflectivity Sheets.

Figure 1 shows the neutron reflectivity profiles of the as-prepared (h-PS/d-PS) bilayer and annealed one at 365 K for 96 hrs. The solid and dotted lines denote the calculated reflectivity on the basis of the scattering length density, b/V profile along the depth direction as shown in Figure 2. The magnitudes of b/V for h-PS and d-PS were 1.41 x 10^{-4} and 6.46 x 10^{-4} nm^{-2}, respectively. The Kiessig interference fringes shown in Figure 1 were mainly determined by the d-PS thickness because a contrast of b/V at the (air/h-PS) interface was trivial. Since the calculated reflectivity curves were in good agreement with the experimental ones as shown in Figure 1, it is considered that the modeled interfacial structure at the (h-PS/d-PS) interface shown in Figure 2 reflects the real structure. The interfacial width discernibly increased by annealing at 365 K, which was below T_g^b for 96 hrs. Thus, it seems reasonable to conclude that the molecular mobility of polymer chains at the surface is much enhanced in comparison with its bulk phase.

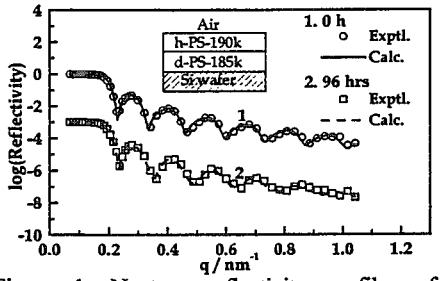

Figure 1. Neutron reflectivity profiles of the as-prepared (h-PS/d-PS) bilayer and annealed one at 365 K for 96 hrs.

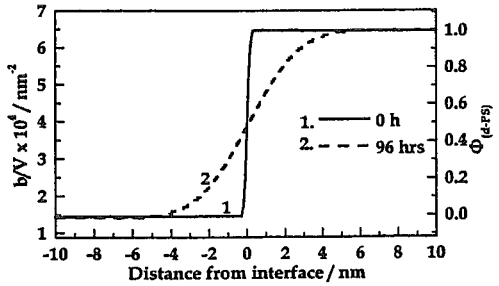

Figure 2. Scattering length density profiles at the as-prepared (h-PS/d-PS) interface and annealed one at 365 K for 96 hrs.

テーマ：中性子反射率測定に基づく分子鎖の主鎖末端構造を制御した高分子薄膜中での末端基の空間分布評価
表題　：中性子反射率測定に基づく分子鎖末端構造を制御した高分子薄膜中での末端基の空間分布評価

1-6-26

Analysis of the Distribution of Chain End Groups in End-functionalized Polymer Thin Film by Neutron Reflectivity

A. Takahara*[1], Y. Yokoe, N. Satomi, K. Tanaka, S. Tasaki*[2] and T. Kajiyama

Graduate School of Engineering, Kyushu University, Higashi-ku, Fukuoka 812-8581, Japan
*[1] Institute for Fundamental Research of Organic Chemistry, Kyushu University, Higashi-ku, Fukuoka 812-8581, Japan
*[2] Research Rector Institute, Kyoto University, Osaka 590-04, Japan

The manifestation of surface functions for polymeric materials are closely related to its surface aggregation structure and thermal molecular motion. The purpose of this study is to investigate the distribution of chain end groups through the polymer film by NR measurements.

The polymer used in this study was symmetric (tridecafluoro-1,1,2,2-tetrahydrooctyl) dimethylsilyl-terminated poly(styrene-d_8–*block*–styrene–*block*–styrene-d_8) triblock copolymer [R_f-P(dSt-St-dSt)-R_f] synthesized via living anionic polymerization. Figure 1 shows the chemical structure of R_f-P(dSt-St-dSt)-R_f. The number average molecular weight (M_n), the molecular weight dispersity (M_w/M_n), PS weight fraction, and functionality was 25.7k, 1.09, 0.744, 2.02, respectively. The R_f-P(dSt-St-dSt)-R_f film was coated from toluene solution onto a silicon wafer with native oxide layer by a spin-coated method and then annealed at 423 K for 24 hrs under vacuum in order to remove any sample preparation history. The surface aggregation structure of the R_f-P(dSt-St-dSt)-R_f film was evaluated by NR measurements. The NR measurement was carried out with the multilayer interferometer for neutrons (C-3-1-2, MINE). The incident neutrons have a long wavelength of 1.26 nm with wavelength resolution of 3.5 %. The reflectivity was calculated based on the model scattering length density profile along the depth direction by using spreadsheet environment reflectivity fitting (SERF).

Figure 2 shows the scattering vector, q [$=(4\pi/\lambda)\sin\theta$ where λ and θ are the wavelength and the incident angle of the neutron beam] dependence of neutron reflectivity for the R_f-P(dSt-St-dSt)-R_f film. The solid curve denotes the best-fitted reflectivity profile calculated on the basis of model scattering length density, (b/V) profile along the direction normal to the surface shown in the inset of Figure 2. The model (b/V) profile in the depth range from the outermost surface to ca. 10 nm was drawn on the basis of angular dependent X-ray photoelectron spectroscopic results. Since the magnitude of (b/V) at the air/polymer interface was 6.03×10^{-4} nm^{-2}, and was sufficiently high compared with that of its interior region, 2.64×10^{-4} nm^{-2}, it can be claimed that fluoroalkylsilyl end groups are preferentially segregated at the air/polymer interface to minimize the surface free energy. Also, the magnitude of (b/V) at slightly deeper region from the air/polymer interface, ranging from 1.7– 8.7 nm, was 2.34×10^{-4} nm^{-2}, which was a little smaller than that of the internal region. This result apparently indicates that fluoroalkylsilyl end groups are depleted at this region due to the number density conservation of chain end groups. On the other hand, the magnitude of (b/V) at the polymer/substrate interface was 1.50×10^{-4} nm^{-2} and was remarkably smaller than that of the internal region. Therefore, it seems reasonable to conclude that fluoroalkylsilyl end groups are depleted at polymer/substrate interface.

$$R_f\text{—(d-PS)}_{28.6}\text{—(PS)}_{178.8}\text{—(d-PS)}_{28.6}\text{—}R_f$$

$$R_f = \text{—Si(CH}_3\text{)}_2\text{—(CH}_2\text{)}_2\text{(CF}_2\text{)}_5\text{CF}_3$$

Figure 1 Chemical structure of symmetric (tridecafluoro -1,1,2,2-tetrahydrooctyl) dimethylsilyl-terminated poly(styrene-d_8 – *block* –styrene –*block* -styrene-d_8) triblock copolymer.

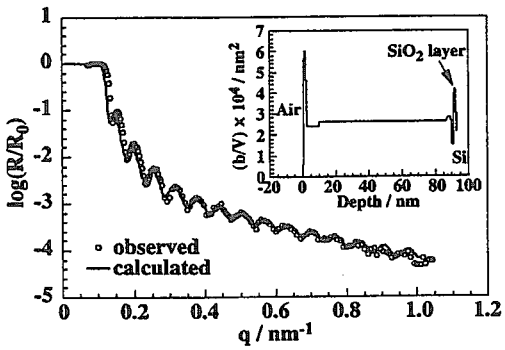

Figure 2 The scattering vector, q dependence of neutron reflectivity for the R_f-P(dSt-St-dSt)-R_f film. The inset shows the model scattering length density, (b/V) profile along the direction perpendicular to the film surface.

研究テーマ：中性子反射率測定による高分子薄膜のガラス転移
表題：PS-d_8薄膜の中性子反射率測定。薄膜の Tg は表面 Tg とは異なるか？

1-6-27

Neutron reflectivity measurements of PS-*d*8 thin films as a function of temperature. Is glass transition temperature Tg of thin film different from surface Tg ?

T. Kanaya, I. Tsukushi[1], K. Kaji, S. Tasaki[2] and T. Ebisawa[2]
Institute for Chemical Research, Kyoto University
Department of Physics, Chiba Institute of Technology[1]
Research Reactor Institute, Kyoto University[2]

Dynamics of glass-forming polymers near Tg have been extensively studied in the last decade. Many of them suggested that there are some domains in glass-forming materials near Tg where molecules (or segments) must move cooperatively, i. e., the so-called cooperatively rearranging region (CRR). Although many researchers tried to find CRR in static measurements using small angle X-ray, small angle neutron and light scattering techniques, there are still no direct evidences of CRR. On the other hand, dynamic measurements have directly and indirectly provided evidences of inhomogeneity indicating existence of CRR. It is believed that another way to show CRR is an experiment on glass-forming materials confined in a micro-domains such as thin films and micropores. In such systems, it is considered that the size of CRR cannot exceed the size of system, and hence the cooperativity of motions is suppressed, leading to the decrease of Tg. According to such idea, some experimental works have been done. Some found decrease of Tg, but others increase of Tg. Such experimental contradiction is not strange because in confined systems effects of surface (or interface) are relatively large compared with in bulk. In order to extract the size effects on Tg, therefore, we have to separately evaluate the effects of surface on Tg and those of size (or thickness) on Tg.

According to the idea, we have been doing neutron reflectivity measurements on thin polystyrene films (50 - 400 Å) as a function of temperature below and above Tg to evaluate film thickness d and surface roughness σ. From the temperature dependence of the film thickness and the surface roughness, we have estimated Tg of the films as well as Tg of the surface.

In this experiment on MINE we focused on films ~200 and ~400 Å thick.

Deuterated polystyrene (PS-d8) with molecular weight Mw 350,000 and polydispersity Mw/Mn 1.03 was spin coated on Si wafer. The coated films were annealed at 80 °C for about 12 h. Bulk glass transition temperature Tg is 104°C. Neutron reflectivity measurements were done on MINE reflectometer at C-3-2 beam port of JRR-3M reactor, Tokai, from 25 °C t0 125 °C.

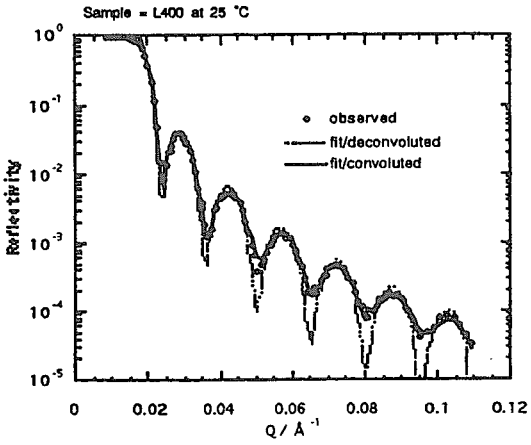

Fig. 1. Neutron reflectivity from PS-d8 film spin coated on Si wafer at 25 °C. Solid line is the result of fit with theoretical function convoluted with the resolution function of MINE. Dashed line is a deconvoluted one.

Fig. 1 shows an example of reflectivity of PS-*d*8 film coated on Si wafer at 25 °C. Theoretical expression of reflectivity R_0 is easily obtained for such a simple system. The

surface roughness σ was introduced in the theoretical expression through a form of exp(-σ^2Q^2) where Q is length of scattering vector. The observed reflectivity was fitted to the theoretical one $R = R_0\exp(-\sigma^2Q^2)$ after convoluting with the resolution function of the spectrometer to evaluate the thickness d and the surface roughness σ. The solid line in Fig. 1 is the result of fit, showing a good agreement, and the dashed line is the deconvoluted reflectivity.

The temperature dependence of the thickness d is shown in Figs. 2 for a film with the initial thickness of 401 Å at 25 °C. It is clearly observed that the thickness increases with temperature and the expansivity suddenly changes at about 105°C, showing a clear glass transition. The estimated Tg (~ 105 °C) is almost same as Tg in bulk. In the case of a film with an initial thickness of !79 Å at 25 C, it was found that the glass transition temperature is 104°C, suggesting that the glass transition temperature does not depend on film thickness in the present thickness range.

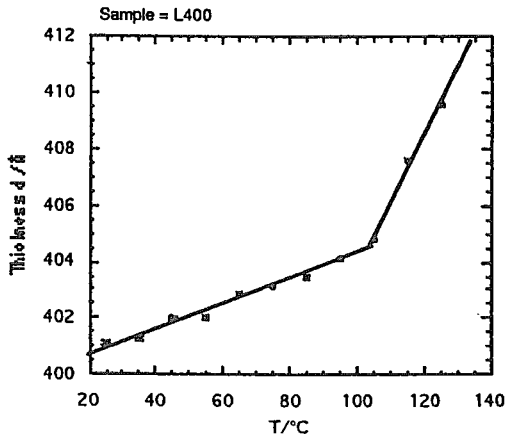

Fig. 2. Temperature dependence of the thickness of PS-d8 film wit initial thickness of 401 Å at 25 °C as function of temperature. Glass transition temperature Tg is located at ~ 105 K.

The surface roughness σ of the 401 Å film is plotted in Fig. 3 as a function temperature. The roughness at 25 °C is about 7.5 Å which is in good agreement with root mean surface roughness evaluated by a laser interferometer. As increases temperature, it continuously decreases until about 70 °C, being about 35 °C below Tg. Although the reason of the decrease is not clear at the moment, one possible reason is that structural relaxation below Tg, i. e., the so-called annealing effect, which must reduce surface roughness. Above 70 °C, the roughness begins to increase with temperature. It is no double that something happens at 70 °C, which must be glass transition at the surface. The surface Tg is 35 °C lower than the bulk Tg. The lower surface Tg than bulk Tg was also observed in a tapping mode of AFM measurements on PS [1]. The increase of σ above 70 °C may be attributable to capillary wave above Tg.

The film with an initial thickness of 179 ° at 25 °C also showed the surface glass transition tenperature is about 70 °C.

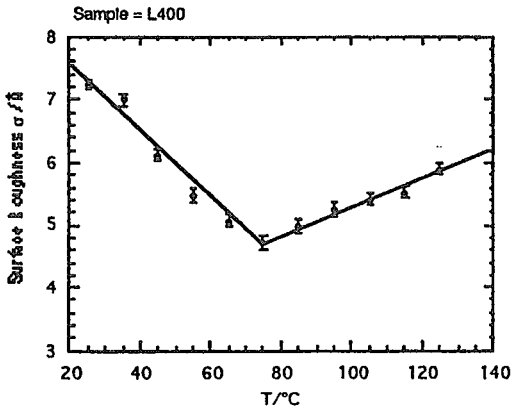

Fig. 3. Temperature dependence of the surface roughness of PS-d_8 film with an initial thickness of ~401 Å at 25 °C as a function of temperature. Temperature dependence of surface roughness suddenly changes at around 70 °C, which has been assigned to the surface glass transition temperature.

[1] K. Takahara et al., *Macromolecules*, 29, 3040 (1996).

研究テーマ：中性子反射率測定による固-気界面への蛋白質吸着のナノ構造解析

表題：中性子反射率測定による固-気界面への蛋白質吸着のナノ構造解析

1-6-28 Nanostructure of protein adsorbed layer at water/quartz interface by neutron reflactometry

Hideki Matsuoka, Emiko Mouri, Keitaro Kago, Hitoshi Yamaoka

Department of Polymer Chemistry, Kyoto University, Kyoto, 606-8501, Japan

Neutron reflectivity (NR) measurements were performed by MINE at JRR-3 for protein BSA (bovine serum albumin) solution - quartz interface as a function of solution pH. Isoelectric point of BSA is about 6, at which BSA molecules are apparently neutral. Below pI, BSA is positively charged, hence it is expected to be adsorbed at quartz surface since it is negatively charged. As NR gives us the scattering length density profile normal to the surface, thickness and roughness of adsorbed BSA layer can be estimated.

Sample was prepared as follows. 1 mg/ml BSA/D_2O solution was prepared. pH was adjusted by addition of HCl aq. or NaOH aq. Solution was kept in Teflon cell with quartz block for about 12h to reach absorption equilibrium.

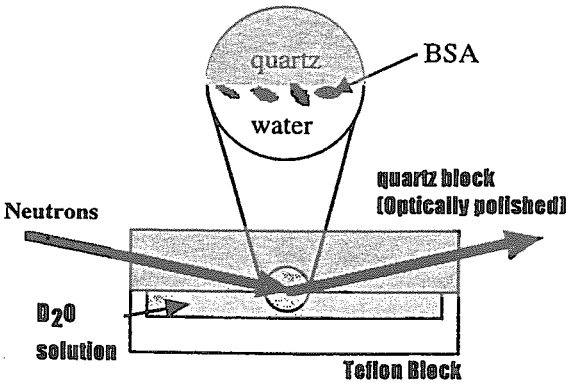

Figure 1 Sample arrangement.

NR experiments were performed from incident/reflection angle 0° to 6° by the step ranged from 0.02° to 0.2° . The wavelength of neutron was 12.6Å. Corresponding wave vector q ($q=4\pi\sin\theta/\lambda$) was 0 to 0.1 $Å^{-1}$. Background intensity was estimated by the reflection intensity by 0.5 ° -off-specular measurement. Direct beam intensity was about 25cps with 0.02mm slit width and the accumulation time was from 100s to 2000s depending on q.

The NR curves for quartz/BSA aq. interface and for quartz/D_2O are shown in Figure 2. Kiessig fringe was observed clearly only for the curve of pH=3.8 condition which is well below isoelectric point, while the profiles for pH=6.0 and 9.8 were similar to that for pure D_2O. The fringe at pH=3.8 indicates the existence of BSA adsorbed layer at the interface. By simulation program *mlayer*[1], the thickness and roughness of the layer were estimated. The line on data of pH=3.8 in Figure 2 is the best fit, and it gives 280 Å thickness for adsorbed BSA layer and 120 Å roughness for layer surfaces. BSA molecule has the shape of prolate ellipsoid with the major and minor axes of 140 Å and 40 Å, respectively. Hence, multi-layer adsorption is the possible explanation for this result at this stage. More detailed analysis is now going on.

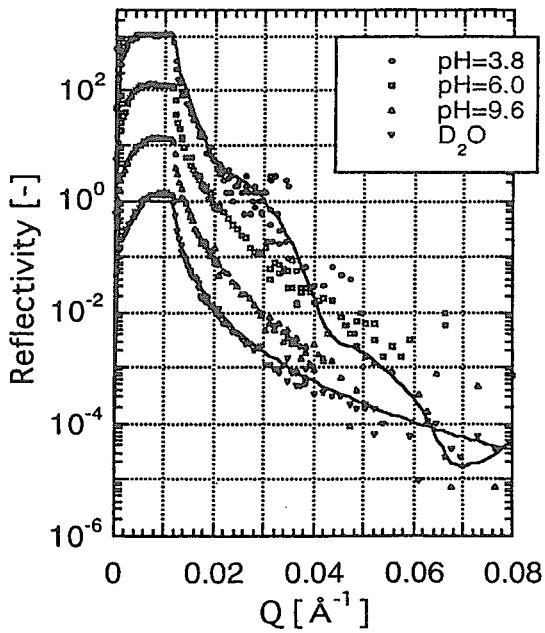

Figure 2 NR curves for quartz/BSA solution interface as pH varied. Curves are separated by factor of 10 for clarity. Lines are obtained by simulation for adsorbed BSA and for D_2O.

1) developed by John Ankner

JRR-3M, MINE(C3-1-2), Polymer

1. 中性子散乱 7) 生物学

1. Neutron Scattering 7) Biology

This is a blank page.

研究テーマ：生体物質の中性子回折による研究
表　　題：酸化ミオグロビンの 1.5Å分解能中性子結晶構造解析

1-7-1

A NEUTRON DIFFRACTION ANALYSIS OF MET-MYOGLOBIN AT 1.5Å

A. Ostermann[1], I. Tanaka[2], N. Niimura[2], F.G. Parak[1]

[1]Physik-Department E17, Technische Universität München, 85747 Garching, Germany
[2]Advanced Science Research Center, JAERI, Tokai, Ibaraki 319-1195, Japan

Hydrogen bonds are essential interactions for stabilizing the 3-dimensional structures of proteins and thus play an essential role for protein dynamics. So far, there exists only a small number of structures determined by neutron crystallography to high resolution with a satisfying completeness and redundancy. A high resolution and data completeness are needed because the number of free parameters in the crystallographic refinement is approximately twice as high as in a conventional X-ray structure determination due to the visibility of deuterium and hydrogen atoms. In this study we used the respiratory heme protein myoglobin from sperm whale. Myoglobin consists of 153 amino acids which form 8 α-helices. Myoglobin serves as a „model-protein" in biophysics. It is investigated by many research groups with a wide range of physical and biochemical methods. Thus much complementary information is available. We determined the neutron structure of met-myoglobin up to 1.5Å resolution. The myoglobin crystal (2.5 x 2.5 x 1.0 mm^3) used in this study was soaked in deuterated mother liquor for years. The space group is $P2_1$ with the lattice constants a = 64.8Å, b = 31.1Å, c = 35.0Å and β = 105.8°. Neutron diffraction data were collected at room temperature at the neutron single crystal diffractometer BIX3 at the JAERI equipped with a neutron imaging plate.[1)] The following values refer to a resolution range from 10.0 – 1.5Å. The values in parentheses refer to the highest resolution shell (1.55-1.50Å). 88.6% (67.7%) of the possible reflections have been collected with an overall redundancy of 3.1 (2.3). The overall R_{merge} value of the data set is 10.2% (24.7%) with an overall $\langle I \rangle / \langle \sigma(I) \rangle$ of 6.9 (3.0). At the present refinement stage 62 of the exchangeable back bone hydrogen atoms (amid protons) were assigned as deuterium atoms. 9 exchangeable back bone hydrogen atoms were assigned as hydrogen atoms. Fig.1 shows an example for a strong deuterium position as well as for a strong hydrogen position in the back bone hydrogen bonds. Up to now 31 water molecules are included in the model whereas 13 of this water molecules show distinct deuterium positions. This high resolution data set provides the possibility to analyze hydrogen bridges as well as the extent of exchange of hydrogen atoms by deuterium within the protein. The obtained patterns can be interpreted in terms of different degrees of flexibility in the different parts of the protein structure.

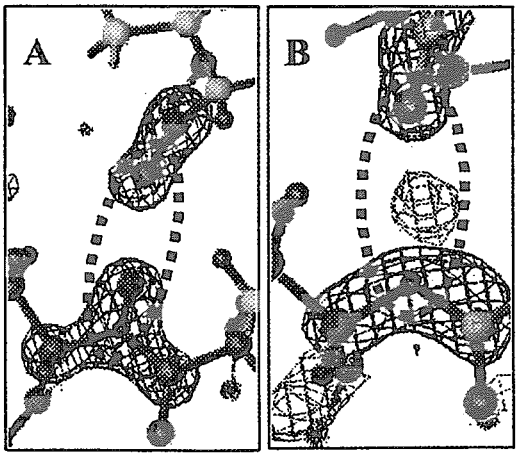

Fig.1 **(A)** Deuterium position in a back bone hydrogen bond. F_o-F_c-omit-map at +3σ in black. Omitted atoms: C_α-N-C and D of amino acid #71 (C of #70) and carbonyl C and O of #67. **(B)** Hydrogen position in a back bone hydrogen bond. F_o-F_c-omit-map at +3σ in black and -3σ in gray. Omitted atoms: C_α-N-C, H and the C_α-hydrogen of #76 (C of #75) and carbonyl C and O of #62. The dotted area marks the hydrogen bond atoms N-D···O and N-H···O.

References

[1] I. Tanaka, K. Kurihara, Y. Haga, Y. Minezaki, S. Fujiwara, S. Kumazawa, and N. Niimura, J. Phys. & Chem. Solids **60** (1999) 1623.

原子炉：JRR-3M　　装置：BIX-3（1GA）　　分野：生物

研究テーマ：中性子小角散乱による血中可溶性トランスフェリンの構造解析
表題：中性子小角散乱コントラスト変調法による血中可溶性トランスフェリンの構造研究

1-7-2

Small-Angle Neutron Scattering Study of the Structure of Serum-Soluble Transferrin Receptor with Contrast Variation Method

H. Yajima, H. Tanaka, T. Sakajiri, T. Ishii, M. Umeda[†], and Y. Kohgo[††]

Department of Applied Chemistry, Faculty of Science, Science University of Tokyo, 1-3 Kagurazaka, Shinjuku-ku, Tokyo 162-8601, Japan

[†] *Research Laboratory, Nissui Pharmaceutical Co., Ltd., 1075-2 Hokunanmoro, Yuki-shi, Ibaraki 307-0036, Japan*

[††] *Third Department of Internal Medicine, Asahikawa Medical College, 4-5 Nishikagura, Asahikawa 078-8510, Japan*

Transferrin receptor (TfR) in serum exists as a soluble form (sTfR, 85 kDa) that arises from proteolysis of TfR at a specific site (at Arg_{100}-Leu_{101}) in the extracellular domain, and the measurement of sTfR is used for monitoring of total erythropoiesis and iron deficiency, especially for patients with concurrent chronic disease, where standard tests of iron status are compromised by the inflammatory condition. A number of studies have been reported with regard to the development of immunoassays for sTfR [1-3]. Recently, Tanaka et al. [4] developed a new method by latex immunoturbidimetric assay (LIA) for sTfR, in which the LIA system is based on the increase of the turbidity induced by the reaction of anti-sTfR antibody-immobilized latex with sTfR in serum. LIA is a rapid and sensitive assay compared to conventional immunological methods such as enzyme-linked immunosorbent assays (ELISA) and radio immunoassays (RIA). The sTfR intrinsically exists in the form of a complex with transferrin (STf) in serum [2,4]. Tanaka et al. [4] reported the molecular weight of the intrinsic sTfR was determined by GPC to be approximately 230kDa This objective of this study is to characterize the structure of the intrinsic sTfR by means of small-angle neutron scattering (SANS) with contrast variation method.

The sTfR was prepared from human sera according to the following procedure: Pooled human sera were passed through a Sepharose-4B column coated with mouse monoclonal anti-sTfR antibody supplied from Nissui Pharmaceutical Co., Ltd. The sTfR-rich fraction eluted with ammonia solution (pH11) was further purified by ion-exchange

JRR-3M, SANS-U, 5. Biology

chromatography equilibrated with 10mM Tris-HCl buffer using a linear gradient from 0 to 0.5 M NaCl, and the fractions eluted in the range of 0.1 - 0.2 M NaCl were collected. The sTfR solutions (total protein conc. 1 mg/mL) were prepared with 10 mM Tris-HCl buffer (pH7.4), using D_2O/H_2O solvents with different D_2O contents (ϕ_D) = 0, 80, 100%. SANS measurements were carried out at 20°C using a SANS spectrometer (SANS-U) installed at the C1-2 port of the cold-neutron beam line in the research reactor JRR-3M of the Japan Atomic Energy Research Institute (JAERI), Tokai, Japan. The wavelength (λ) used was 7.0 Å with a fractional spread ($\lambda/\Delta\lambda$) of 10% and the sample-to-detector distance was 4m (8×10^{-3} Å^{-1} < q < 7×10^{-2} Å^{-1}). Structural analyses were performed based on the Stuhrmann plot from the SANS data. This procedure was described in detail elsewhere [5].

Figure 1 shows the Stuhrmann plots for the sTfR, where $\overline{\rho}$ refers to the contrast. It should be noted that the contrast matching points of the sTfR was determined to be 46.8 % D_2O. The Rg value at infinite contrast (Rg,c), the radial second moment of the mean scattering length density (SD), α, and the derivation of the center of the SD distribution, β, were estimated to be Rg,c = 50.3 Å, α = -20.1 and β = 1.31×10^{-10} Å^{-2}, respectively. At present, the molecular simulation study is in progress on the basis of the SANS data.

References

1. Y. Kohgo et al., *Blood* 70 (1987) 1955-1958..
2. A. Hikawa et al., *Clin. Chim. Acta* 254 (1996) 159-172.
3. P. Suominen et al., *Clin. Chem.* 43 (1997) 1641-1646.
4. S. Tanaka et al., *American Association for Clinical Chemistry/Protein/Enzymes* (New Orleans, LA), 1999.
5. H. Yajima et al., *Biochim. Biophys. Acta* 1381 (1998) 68-76.

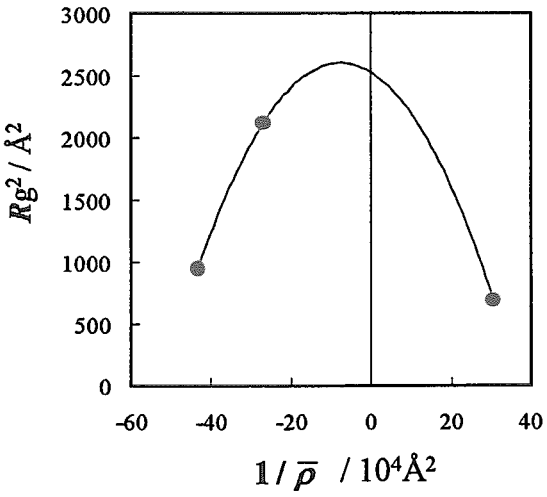

Fig.1 Stuhrmann plot for the sTfR.

研究テーマ：小角中性子散乱による溶液状態のプロテオグリカンの物理化学的特性評価
表題：小角中性子散乱による溶液状態のプロテオグリカンの物理化学的特性評価

1-7-3 Physicochemical characterization of a proteoglycan in solution by small-angle neutron scattering

Yasushi Watanabel. Ichiro Tanaka2. Yoh Sanol and Nobuo Niimura2
1National Food Research Institute. Tsnkuba. lbaraki 305-8642. Japan
2Advanced Science Research Center, JAERI. Tokai. lbaraki 319- 1195. Japan

Proteoglycans are important constituents of the extracellular matrix of multicellular organisms. They are associated with most cells on their surface and inside intracellular storage granules. The bulk of their structure is usually the large amount (95 % or more) of carbohydrate that is attached to the polypeptide chain at very many sites. The carbohydrates consequently dominate the physical and biological properties of proteoglycans. Furthermore, their food functional properties for health have recently received increased attention. In order to characterize the structure of the proteoglycan that purified from shark-fin cartilage, we have been studied by small-angle neutron scattering (SANS) method.

Proteoglycans were purified from shark-fin cartilages and soluble in 10mM sodium phosphate buffer, pH 7.0, in O %, 20 %, 80 % and 100 % D_2O. Small-angle neutron scattering experiments were performed by using a SANS-U spectrometer installed at the C I -2 port of the cold-neutron beam line in the research reactor JRR-3M of the Japan Atomic Energy Research Institute (JAERI). The wavelength was 7.0 Å and the sample to detector distance was 1200 cm. The temperature of samples was kept at 24 ℃.

In the previous studies (1, 2), the averaged radius of gyration in 100 % D_2O was found to be 250- ± 15 Å without concentration dependence ranging from 8 to 20 mg/ml. The contrast mating point was estimated to be 47 % D_2O. The Stuhmrann plots indicated that the protein is the core of the proteoglycan molecule with symmetrical distribution of neutron scattering density. This result consists with the observation that proteoglycans consist of many glycosaminoglycan chains covalently linked to a protein polypeptide chain. The result of a shape analysis suggested that the proteoglycan molecule could bc described to a first approximation by a simple elongated ellipsoid with a main axial ratio 1:1:120. In this study, we reconfirmed the results for the scattering curves of O %, 20 %, 80 % and 100 % D_2O as shown in Figure 1.

References

1 .Y. Watanabe et al., Activity report on neutron scattering research. Vol. 3 (1996) .

2. .Y. Watanabe et al., Activity report on neutron scattering research. Vol. 6 (1999) .

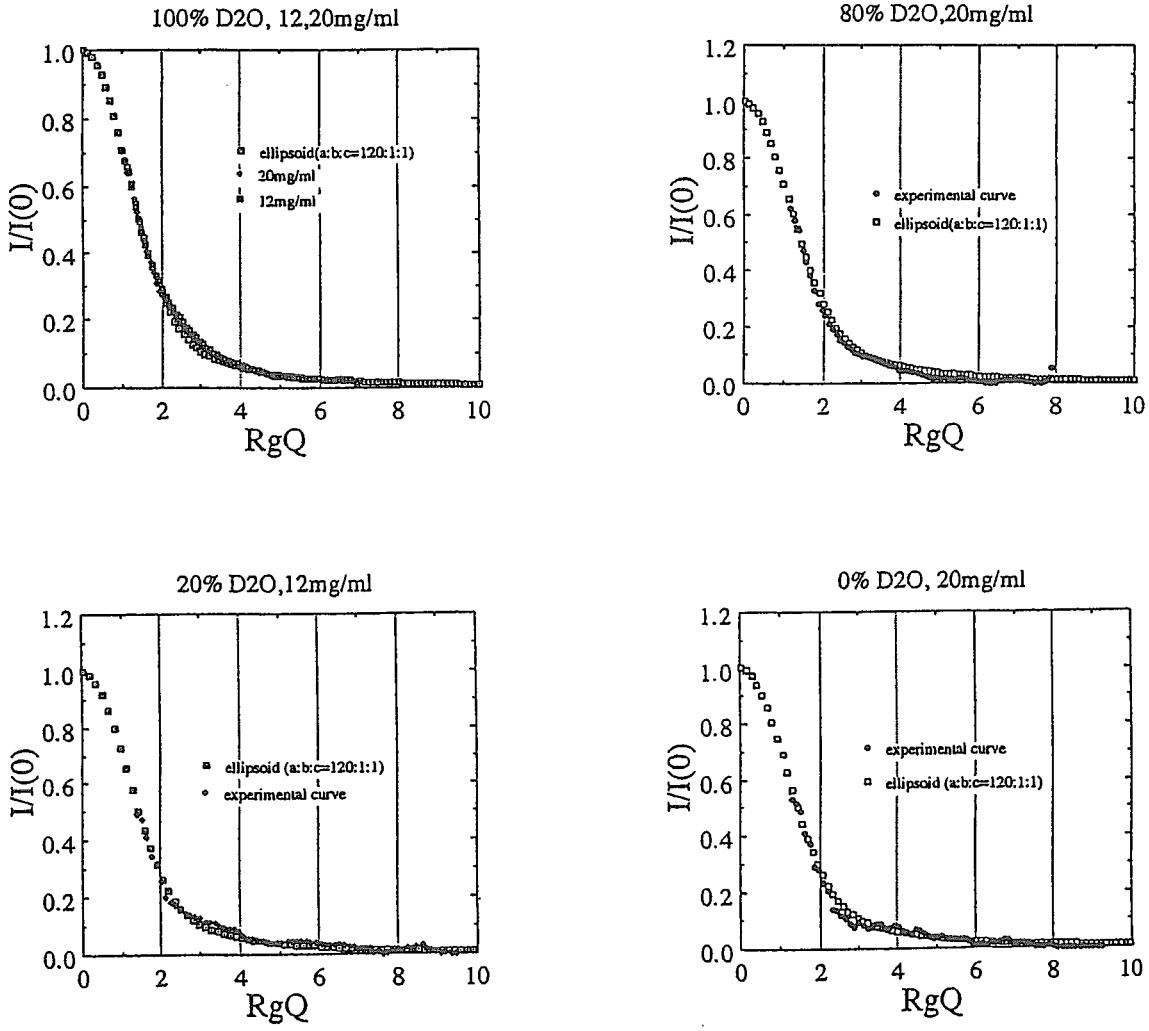

Figure 1 Comparison of the experimental curves with theoretical curves for ellipsoids of revolution of the axial ratio 1 : 1 : 120.

研究テーマ：中性子小角散乱法による昆虫リポホリンの構造解析

表題：中性子小角散乱法によるアポリポホリン－Ⅲの構造解析

1-7-4 Small-Angle Neutron Scattering of Apolipophorin-III

C. KATAGIRI, M. NAGAO*, M. SATO† and Y. ITO§

Institute of Low Temperature Science, Hokkaido University, Sapporo 060-0819
**Institute for Solid State Physics, University of Tokyo, Tokai, Naka, Ibaraki 319-1106*
†Graduate School of Integrated Science, Yokohama City University, Yokohama, Kanagawa 236-0027
§Faculty of Education and Human Sciences, Yamanashi University, Kofu 400-8510

Lipophorin is a spherelike particle and contributes to lipid transport in insect blood. Apolipophorin-III (apoLp-III) is a 20k apoprotein of the lipophorin with a five helix bundle; each of the amphipathic helices orients with its hydrophobic face directed toward the interior of the bundle[1]. In the blood, normally, apoLp-III is not associated to lipophorin. Upon long-distance flight, lipophorin (high-density lipophorin, HDLp, ρ=1.10g/ml, diameter=170Å) starts to load flight fuel, diacylglycerol, from the fat body to the flight muscle by the stimulation of a neurosecretary hormone. This induces association of apoLp-III molecules to the outer phospholipid-monolayer surface of the lipophorin, which results in the transformation of HDLp to low-density lipophorin (LDLp, ρ=1.05g/ml, diameter=230Å)[2,3,4]. The LDLp contains about five times more diacylglycerol than HDLp. It has been hypothesized that the association of apoLp-III to the outer surface requires a dramatic conformational change wherein the helix bundle opens about putative hinge domains located in the loops between hellices[5]. To examine this hypothesis, the small-angle neutron scattering study with H_2O/D_2O contrast variation was performed on the 70-80% deuterated apoLp-III located in the liposome made of dimyristoyl-phosphatidylcholine (Fig.1).

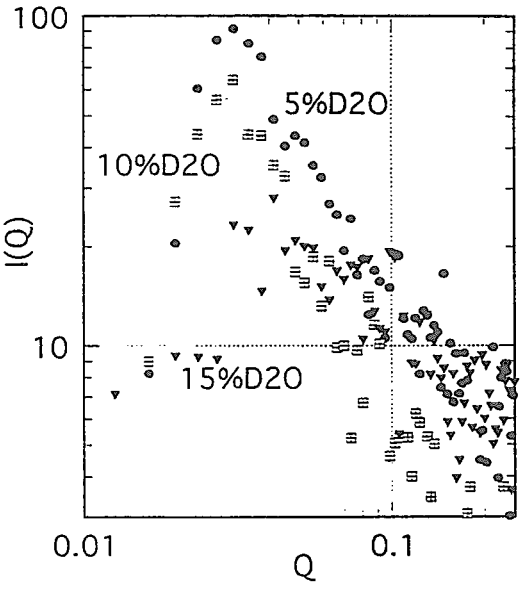

Fig.1 Small-angle neutron scattering curves of the deuterated apoLp-III incorporated into liposomes.

References

1)D. R. Breiter *et al.*, *Biochem.* **30** (1991) 603.
2)C. Katagiri *et al.*, *Biochem.* **30** (1991) 9675.
3)C. Katagiri, *J. Crystallographic Soc. Jpn.* **36** (1994) 162 [in Japanese].
4)C. Katagiri *et al.*, *Activity Report on Neutron Scattering Research* **3** (1996) 208.
5)M. Wientzek *et al.*, *J. Biol. Chem.* **269** (1994) 4605.

研究テーマ：水/エタノール二成分溶液中のキモトリプシン・インヒビター2の中性子小角散乱
表題：水/エタノール二成分溶液中のキモトリプシン・インヒビター2の中性子小角散乱

1-7-5

Small-Angle Neutron Scattering from Chymotrypsin Inhibitor 2 in Water-Ethanol Binary Solutions

Junko Kawaguchi, Sannamu Lee, Koji Yoshida, Hisanobu Wakita, Gohsuke Sugihara, Toshio Yamaguchi, Michihiro Nagao*

Department of Chemistry, Faculty of Science, Fukuoka University, Nanakuma, Jonan-ku, Fukuoka, 814-0180, Japan
** Neutron Division, Institute of Solid State Physics, University of Tokyo, Shirakata, Tokai, Naka, Ibaraki, 319-1195, Japan*

An alcohol is known to destabilize the tertiary structure of a protein, but to stabilize its helical structure. Recently, we have found that the structure of clusters in water-ethanol solutions changes at the ethanol mole fraction X_E ~ 0.2, where their various properties show anomaly. In the present study, chymotrypsin inhibitor 2 (CI-2) was chosen as a probe to examine whether or not the solvent cluster influences protein folding. CI-2 consisting of 64 amino acid residues has one α-helix and six β-sheets. Small-angle neutron scattering (SANS) measurement was made to characterize the overall shape and size of the protein as a function of X_E.

CI-2 was synthesized according to the Fmoc method starting from Fmoc-Gly-PEG [poly (ethylene glycol)] resin with a Pioneer automatic peptide synthesizer (PE Biosystems). The crude peptide obtained was purified by high performance liquid chromatography. SANS spectra were measured with the SANS-U spectrometer of the Institute for Solid State Physics (ISSP) of the University of Tokyo in JRR-3M at Tokai. The sample to detector distance was 2 m. The wavelength of neutrons was 8 Å. Approximately 250 μl of each sample was placed into a quartz cell with a path length of 2 mm and wall thickness of 1mm; the cell was sealed with a plug. The protein was dissolved in various D_2O/C_2D_5OD solutions. The sample concentration was 400 μM. The measurement time was 90 min. The binary solutions without CI-2 were also measured as background.

The Guinier plot gives the radius of gyration (R_g), characteristic for size or compactness of the protein. Figure 1 shows the R_g values obtained by the Guinier plots as a function of X_E. With increasing X_E the R_g values increased and had a maximum ~ 36.4 Å at X_E = ~ 0.1, and then gradually decreased. The ethanol mole fraction on X_E ~ 0.1 where the maximum of R_g appeared is slightly lower than the value (~ 0.2) expected from our previous results. This might be caused by the complexity of CI-2 structure, i.e. a balance between hydrophobicity and hydrophilicity of CI-2. A further detailed study is in progress.

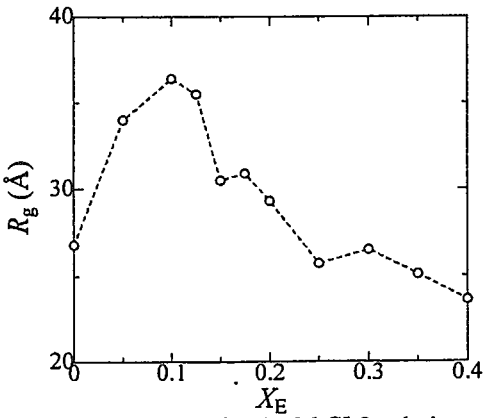

Figure 1. R_g of 400 μM CI-2 solutions in various C_2D_5OD mole fractions.

JRR-3M, SANS-U, 5. Biology

研究テーマ：大腸菌外膜蛋白質ＯｍｐＡの構造変化ならびに
両親媒性分子との相互作用の研究
表題　　：大腸菌外膜蛋白質ＯｍｐＡとオクチルグルコシド
との間に形成される複合体の形状

1-7-6

Geometric Structure for the Complex formed between *Escherichia coli* Outer Membrane Protein, OmpA and a nonionic surfactant Octylglucoside

K.Kameyama, M.Sato[1], S.Ohnishi[2], and M.Nagao[3]

Faculty of Engineering, Gifu University, Yanagido, Gifu, 501-1193 Japan
[1] *Graduate School of Integrated Science, Yokohama City University*
[2] *Department of Biochemistry abd Biophysics, University of Rochester, 601 Elmwood Ave. Box 712, Rochester, NY, USA*
[3] *Newtron Scattering Laboratory, The Institute for Solid State Physics, The University of Tokyo, Shirakata, Tokai, Naka, Ibaraki, 319-1106*

Gross structure of a complex formed between outer membrane protein A (OmpA) from *Escherichia coli* solubilized in the prsence of a nonionic surfactant, *n*-octyl-β-glucoside (OG) was investigated according to the results of small angle neutron scattering (SANS) using the contrast variation method [1] and related properties.

Experimental

The membrane protein was solubilized from the envelope fraction of a strain of *E.coli* K-12, TNE001 and purified as described previously [2]. The purified protein was equlibrated against 50mM Na-phosphate buffer (pH 6.9) containing 22mM of OG and concentrated. A couple of aliquots of the solution were dialysed against the buffer with the same composition as above prepared with defined contents of heavy water.

SANS measurements were carried out by the use of the SANS-U instrument installed at the C1-2 beam port of JAERI JRR-3M reactor. Scattering intensity was collected as described previously[2].

Results

The mean neutron scattering length density, $\bar{\rho}$, for the complex was determined to be $1.21 \times 10^{10}\mathrm{cm}^{-2}$. This value lower than those for simple proteins (around $1.8 \times 10^{10}\mathrm{cm}^{-2}$) implies that 0.99 g of OG is bound to 1g of OmpA, by using the calculated value of $\bar{\rho}$ for the surfactant, $0.694 \times 10^{10}\mathrm{cm}^{-2}$. The amount of OG bound to OmpA was lower than the value, 1.6(g/g) measured by chromatographic method[1] in the presence of 27.4mM of OG. The level of surfactant binding in this system seems to depend on the surfactant concentration.

The results can be analyzed according to the Stuhrmann plot,

$$r_g^2(\Delta\rho) = a\Delta\rho^{-2} + b\Delta\rho^{-1} + r_V^2$$

where $\Delta\rho$ is the difference in ρ between the complex and solvent. The r_V, the r_g of the particle shape for the complex, was etimated to be 31.2Å. The plot gave a non-zero negative value for a. This result strongly suggests that the surfactant moiety in the complex distributes asymmetrically on the surface of the membrane protein. Provided that the bound surfactant molecules form a cluster, the center of the surfactant cluster is separated by 2.3nm from that of the neat peptide body.

Discussion

We can evaluate the geometry and the dimension of the complex formed by OmpA and OG. OmpA molecule is considered to have a couple of domains: N-terminal and C-terminal ones. While the structure of its N-terminal fragment was revealed crystallographically [3], the whole structure of OmpA have not been reported. The present SANS studies are significant to provide physicochemical properties as well as geometric dimension for intact OmpA.

For a object consists of two units, namely the protein unit and the surfactant unit, its radius of

[1] K.Kameyama, M.Sato, S.Ohnishi, and M.Nagao *Act.Rep.Neutron scattering Res.*, **6**, 205 (1999)
[2] Ohnishi, S., Kameyama, K., and Takagi, T. *Biochim. Biophys. Acta*, **1375**, 101-109 (1998)
[3] Pautsch, A. and Schulz, G.E. *Nature Struc. Biol.*, **5**, 1013-1017 (1998)

gyration of the whole complex can be calculated by the following equation [4].

$$R_v^2 = \frac{V_p(R_{g,p}^2 + \Delta x_p^2) + V_s(R_{g,s}^2 + \Delta x_s^2)}{V_p + V_s}$$

Here, V_p and V_s are volumes for the protein part and to the surfactant part respectively, and $R_{g,p}$ and $R_{g,s}$ are radii of gyration of the respective units. In this equation, Δx_p and Δx_s are the distance between the center of mass of the whole body and the respective parts.

For the present system, we may reasonably assume the shape of whole peptide part of OmpA as cyrindrical, since the N-terminal domain of OmpA can be regarded as a cylinder with dimensions around 3nm in radius and 6nm in length. In the complex, the surfactant molecules should bind to perimeter of the N-terminal domain to form a cluster with low scattering length density. The shape of the cluster may assumed to be a cyrinder carrying a hollow inside. The parameters in the model consisting the two cyrindrical units should be chosen so that each of the empirically determined values, the volume ratio between surfactant to peptide, the separition of center of gravity between the units, and the radius of gyration for the whole structure should be consistent with each other.

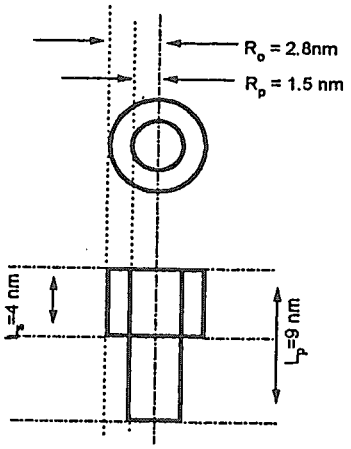

Figure 1. The model for the complex between OmpA and octylglucoside.

The model shown in Figure 1 is one of the best possible models among the models tested with various sets of parameters. The parameters and resulting properties for the model are described in Table 1.

Table 1. Dimension of the model for OmpA-OG complex

For protein unit

Parameters	L_p	R_p	V_p	$R_{g,p}$
values	9	1.5	63.6	2.67

For surfactant unit

Parameters	L_s	R_s	V_s	$R_{g,s}$
Values	4	2.8	70.2	1.74

The lengths and the volumes are given in nm and nm^3, respectively.

To determining the dimension of the model, the D_{max} estimated to be 8.5nm by small angle X-ray scattering can be also taken into account. This set of the parameters yields the amount of OG bound to OmpA, R_v and the separation of the two units to be 0.95(g/g), 3.2nm, and 2.5nm, respectively. Although it is restricted to reproduce all the quantities accurately, the compromising properties could be obtained with the above construction of the model, and they seem fairly consistent with each other.

For the dimensions of the surfactant unit, L_s is consistent with the thickness of hydrophobic layer of lipid membrane. The thickness of the surfactant "torus" being 1.4 nm ($R_s - R_p$) appears significantly smaller than the hydrodynamic radius of neat OG micelle [5], but is consistent rather with the extended length of the OG molecule. The present model thus seems quite reasonable to show the gross properties of the complex formed between OmpA and OG.

Concluding Remarks

In the present study, SANS technique has been applied to solutions of a membrane protein-surfactant comlex formed by OmpA and OG. The possible geometric model which consistently accounts for various properties of the complex indicates that the whole protein has elongated rod-like shape, and the surfactants bind to the limited surface of the protein and their distribution is asymmetric. This indicates that the surfactant molecules do not bind to the C-terminal domain of the protein.

[4] Yoshimura, T., Kameyama, K., Maezawa, S. and Takagi, T., *Biochemistry*, **30**, 4528-4534 (1991)

[5] Kameyama, K., and Takagi, T., *J. Colloid Interface Sci.*, **137**, 1-10 (1990)

研究テーマ：中性子溶液散乱による原核生物核様体構造の研究
表題：DNA結合蛋白質HUにおける蛋白質間相互作用：中性子小角散乱による研究

1-7-7

Protein-Protein Interactions between the DNA-Binding Protein HU: a Neutron Scattering Study

S. Fujiwara, Y. Yonezawa[1], and M. Nagao[2]

Advanced Science Research Center, Japan Atomic Energy Research Institute, Tokai, Ibaraki 319-1195, Japan
[1]Tsukuba College of Technology, Tsukuba, Ibaraki 305-0821, Japan
[2]Neutron Scattering Laboratory, The Institute for Solid State Physics, The University of Tokyo, Tokai, Ibaraki 319-1196, Japan

The DNA-binding protein of bacteria, HU, plays an important role in the condensation of the bacterial DNA as well as in a variety of DNA metabolic events such as replication, transcription, and site-specific recombination. Understanding how the long DNA molecule is condensed in the HU-DNA complex should give valuable insight into the molecular mechanism of these events. As a first step towards understanding the structure of the HU-DNA complex, we did the small-angle neutron scattering experiments of HU in solution. It was shown that HU is in equilibrium between the dimers (the structural unit of HU) and the tetramers [1,2]. Since HU-HU interactions may play some role in the HU-DNA complex formation, it is important to understand how the tetramer is formed. Here, in order to gain insight into the driving force of the tetramer formation, we have done the small-angle neutron scattering experiments of HU in solution of various salt concentration.

HU dimers were expressed in *E. coli*., purified, and suspended in 10 mM Imidazole (pH 7.0) in 100% D_2O. The salt concentration of the HU solutions was adjusted to be 50 mM, 150 mM, and 300 mM NaCl. For each NaCl concentration, a series of solutions with different HU concentration was prepared. Small-angle neutron scattering experiments on these HU solutions were done with the SANS-U spectrometer in the guide hall of the reactor JRR-3M. A wavelength (l) of 7.0 Å was used with a fractional spread (Dl/l) of 10%. A sample-to-detector distance was 200 cm. The temperature of the samples was kept at 10℃.

The Guinier analysis of the scattering curves yields the radius of gyration (R_g) and the extrapolated scattering intensity at zero scattering angle (I(0)). In Figure 1 the R_g values of HU at various NaCl concentrations are plotted against HU concentration. It was shown that while at 50 mM NaCl the R_g value is increased with increasing the HU concentration, at above 150 mM NaCl such a dependence of the R_g value is not observed. This indicates that the tetramer formation is a function of the salt concentration. It is concluded from these results that the primary interaction between the HU dimers during the tetramer formation is electrostatic.

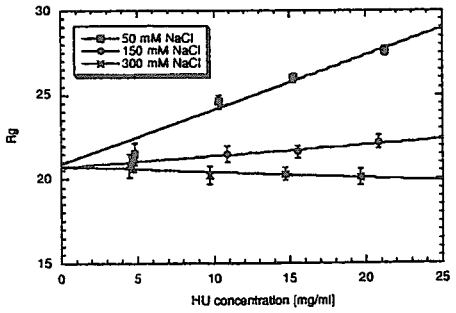

Figure 1 Dependence of the radius of gyration of HU under various NaCl concentration on HU concentration.

References

[1] S. Fujiwara, Y. Yonezawa & M. Nagao, Activity Report on Neutron Scattering Research (1999) **6**, 206.
[2] S. Fujiwara & Y. Yonezawa, J. Phys. Chem. Solids (1999) **60**, 1393-1395.

研究テーマ：光合成細菌由来光捕集系の構造解析
表題：光合成膜蛋白質を可溶化する界面活性剤のミセルサイズの測定

1-7-8 Measurement of the micellar sizes of detergent used for solubilizing photosynthetic membrane protein

Z.-Y. Wang, Y. Muraoka, M. Shimonaga, and T. Nozawa

Department of Biochemistry and Engineering, Faculty of Engineering, Tohoku University, Sendai 980-8579 Japan

Detergent solubilization is a common procedure in investigations of membrane proteins and peptides through methods designed for soluble biopolymers. The light-harvesting (LH) complex in purple photosynthetic bacterium *Rhodospirillum rubrum* is an integral membrane protein comprising two small polypeptides, α and β, along with bacteriochlorophyll (BChl) and carotenoid molecules. A structural subunit (B820), characterized by a near-infrared absorption at 820 nm, can be formed by dissociation of the LH complex with non-ionic detergent *n*-Octyl β-D-glucopyranoside (OG) and be reconstituted by its individual components. The B20 subunit is considered to be made up in either αβ·2BChl or 2α2β·4BChl form. As a step towards estimating the size of B820 subunit, we first investigated the micellar sizes of OG at various concentrations by SANS and compared with the previously reported results using other techniques.

Measurements were conducted at room temperature (~24°C) with SANS-U(C1-2) at JRR-3M. Neutron wavelength was 7Å. Commercial OG samples (purity > 98%) were dissolved in D_2O. The SANS data were analyzed by using standard Guinier analysis

Figure 1 shows the results of OG micelles in a range of concentrations 2~4% obtained from Guinier plots. Radius of gyration (*Rg*) was found around 25Å, only slightly smaller than the hydrodynamic radius determined by dynamic light scattering. The value of *Rg* increased with increasing the concentration (bottom). The aggregation number determined from *I*(0) increased from 85 at 2% OG to 105 at 4% OG (middle). The micellar molecular weight varied over a range of 24,800 ~ 30,700 (top), compatible with the results of diffusion and sedimentation velocity. The data of this study have provided a lower limit of overall dimension and molecular weight for the OG-solubilized membrane protein complex, which are crucial for precisely evaluating the size of B820 subunit.

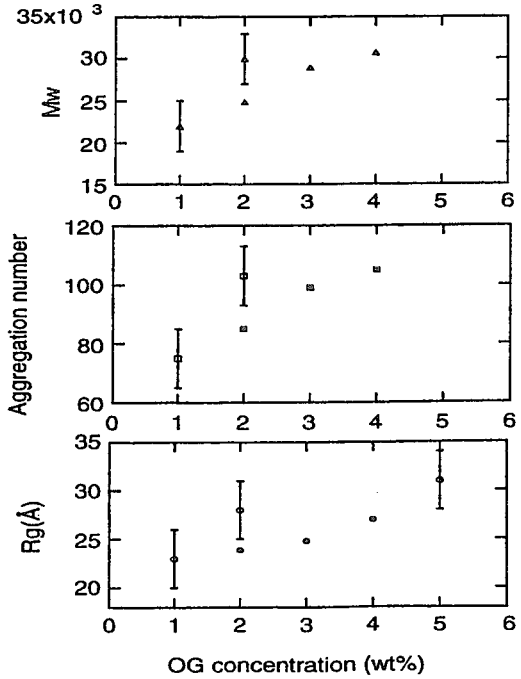

Figure 1. Concentration dependences of Rg, aggregation number and molecular weight of OG micelles. Filled symbols: from SANS. Symbols with error bars: from DLS, sedimentation and velocity

JRR-3M SANS-U(C1-2) 生物 Biology

研究課題：非極性溶媒／AOT／水／酵素マイクロエマルジョン系の構造と超酵素活性
表題：含蛋白質 w/o AOTマイクロエマルジョンのダイナミックス

1-7-9 Dynamics of w/o AOT Microemulsions Occluding Proteins

M. Hirai,[1] T. Hayakawa,[1] H. Iwase,[1] R. K. Hirai,[2] H. Seto,[3] Y. Kawabata,[3] and T. Takeda.[3]
[1] *Department of Physics, Gunma University, Maebashi 371, Japan.*
[2] *Meiwa Women's Junior College, Maebashi, Gunma 371, Japan*
[3] *Faculty of Integrated Arts and Science, Hiroshima University, Higashi-Hiroshima 739, Japan,*

Generally, enzymes entrapped in w/o microemulsions are known to show so-called "super-activity", which has attracted significant interest concerning not only with the biophysical catalytic properties of enzymes but also with possible future practical applications such as microreactors.

Previously, by using small-angle X-ray scattering and enzymatic activity measurements we showed that the hydrolysis of some esters catalyzed by α-chymotrypsins entrapped in w/o sodium bis(2-ethylhexyl)sulfosuccinate (AOT) microemulsions is greatly enhanced at low water/surfactant molar ratio w_0 (= [water]/[AOT]) and that at this low w_0 range the appearance the oligomeric phase of the reversed micelle would play an important role for the acceleration of the metabolic turnover. In addition our previous neutron spin echo (NSE) study of water/AOT/heptane system showed that the effective diffusion coefficient D_{eff} relating to bending fluctuation of the AOT microemulsion is significantly enhanced at low w_0 value. These previous studies suggest that the structure and dynamics of the AOT microemulsion would play an essentially important role on the appearance of super activity of enzymes entrapped in the microemulsion.

However, the physicochemical mechanism of appearance of "super-activity" of enzymes has still been ambiguous. The aim of the present study is to clarify this mechanism from the point of view of dynamics. In the present experiments using NSE, we have measured the dynamics of α-chymotripsin/water/AOT/ d_{16}-*n*-heptane. In the present NSE experiments, we have studied the effect of the presence of proteins on the dynamics of the AOT microemulsion by varying the protein concentration in the microemulsion at constant water content (w_0 =20). NSE experiments have been carried out at the film-contrast condition ($\rho_{water\ (98.5\%D2O)} = \rho_{d16\text{-}n\text{-}heptane}$) by using a NSE spectrometer installed at C2-2 beam port at the research reactor JRR-3M of JAERI. In Figure 1 we show preliminary results obtained by the present NSE measurements. We can recognize the change of the effective diffusion coefficient D_{eff} depending on the protein concentration, namely the shift and height of the peak of D_{eff} around q ~0.06-0.07 Å^{-1} which originates from the bending fluctuation of the microemulsion. Further experiments and analyses are in progress.

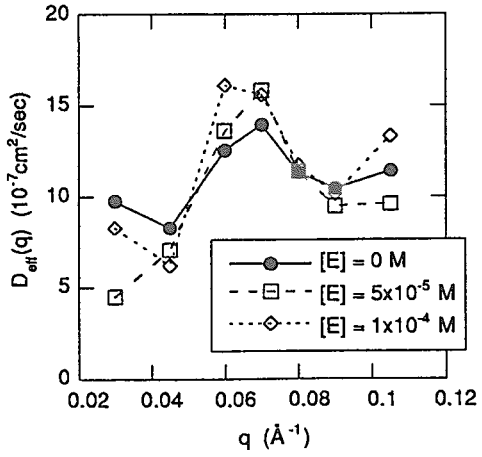

Figure 1 q and protein concentration [E] dependence of effective diffusion coefficient D_{eff} of w/o AOT microemulsion.

JRR-3M, NSE, 5, Biology

研究テーマ：生体物質の中性子回折法による研究
表題：異なったpHで調製したニワトリ卵白リゾチーム単結晶の中性子回折測定

1-7-10
Neutron Diffraction Measurements of Single Crystals of Hen Egg-White Lysozyme Grown under Different pH Conditions

S. Fujiwara, M. Maeda, Y. Yonezawa[1], and N. Niimura

Japan Atomic Energy Research Institute, Tokai, Ibaraki 319-1195, Japan
[1]Tsukuba College of Technology, Tsukuba, Ibaraki 305-0821, Japan

In various aspects of functions of proteins, hydrogen atoms play essential roles. Moreover, hydrogen bonds between the atoms in the protein as well as hydration are important in the stability of the protein. Locating the positions of hydrogens and hydrated water is therefore important in considering the molecular mechanism of the protein function and the stability of the proteins. Neutron crystallography, which can locate the hydrogens, is one of the important methods to investigate these problems. We have started a project which explore the protonation state of amino acid residues in the protein at various pH, since the charge distribution of the protein, which can be different in different pH, may have important effect on thermodynamic characterization of the protein. As a first step, we had been collecting the neutron diffraction data of the single crystal of hen egg-white (HEW) lysozyme grown in pH 4.9[1-2].

We finished collecting the data of the crystal under this condition in this fiscal year (1999). The space group of the crystals was $P4_32_12$, and the cell parameters were a=b=7.91 nm, c=3.66 nm. After data reduction by MAC-DENZO and SCALEPACK[3] was done, the obtained number of independent reflections ($I/\sigma>1$) was 5692, completeness of the data was 74.3% at 0.2 nm resolution, and the overall R_{merge} was 0.228. We have started structure analysis using X-plor[4]. Figure 1 shows a density map around Lys33 obtained by the structure analysis. Although the analysis is preliminary, hydrated waters around the residue are clearly detected.

In parallel with the structure analysis, we have started collecting the data from the crystal grown in different pH. Crystals of HEW lysozyme were grown in D_2O at pH 3.4. The crystals with the same space group and the same cell parameters as those at pH 4.9 were obtained. Neutron diffraction patterns of the crystal have been measured with BIX-II[5]. The oscillation method of 0.4 degrees has been employed. Exposure time per one frame has been 11 hours. Diffraction spots of at least 0.2 nm resolution have been observed. So far, the crystal has been rotated about 60 degrees.

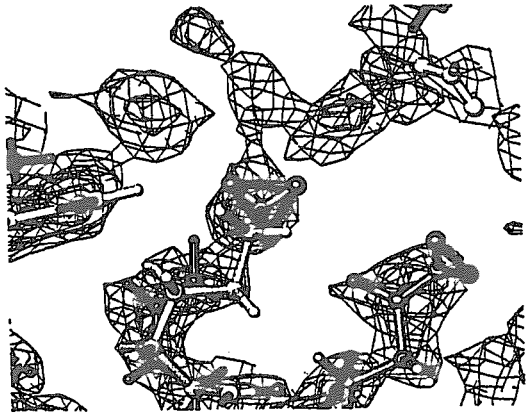

Figure 1. An example of the neutron density map of HEW lysozyme at pH 4.9

References

[1] S. Fujiwara et al.: JAERI Review **99-003** (1999) 13.
[2] S. Fujiwara et al.: JAERI Review **2000-005** (2000) 7.
[3] Z. Otwinowski and W. Minor: Methods Enzym. 276 (1997) 307-326
[4] A. T. Brünger: X-PLOR Version 3.1 (1993) (Yale Univ., New Haven, CT)
[5] S. Fujiwara et al.: Physica B 241-243 (1998) 207-209.

原子炉：JRR-3M　　装置：SANS-J (C3-2)　　分野：中性子散乱（生物）

研究テーマ：中性子回折法による筋肉の研究（協力研究）
表題：コントラスト変調法を用いた“生きた”カエル筋肉の中性子回折測定

1-7-11

Neutron Diffraction Measurements of Live Frog Muscle Using the Contrast Variation Method

S. Fujiwara, Y. Takezawa[1], Y. Sugimoto[1], and K. Wakabayashi[1]

Japan Atomic Energy Research Institute, Tokai, Ibaraki 319-1195, Japan
[1]Grad. School of Engineering Science, Osaka University, Toyonaka, Osaka 560-8531, Japan

Neutron scattering/diffraction has a unique ability that information on the internal structure of a particle can be obtained with contrast variation measurements. This type of measurements is widely used in the area of solution scattering[1]. This method is, however, not restricted to solution scattering, but applicable to all type of low-resolution measurements. Low-resolution neutron crystallography has been, for example, successfully applied to extract information on the detergent region in single crystals of membrane protein-detergent complexes[2]. Here we applied this method to neutron fiber diffraction.

Sartorius muscle, dissected from a live frog, was perfused with Ringer's solution containing 115 mM NaCl, 2.5 mM KCl, 1.8 mM $CaCl_2$, 3 mM HEPES/NaOH (pH 7.2) in various D_2O concentrations (0%, 18.7%, 57.7%, 72.3%, and 92.9%). The neutron fiber diffraction patterns of these samples were measured with the Small-Angle Neutron Scattering Instrument (SANS-J) at the guide hall of the reactor JRR-3M in Japan Atomic Energy Research Institute. Neutrons with the wavelength of 0.653 nm ($\Delta\lambda/\lambda$=13.8%) were employed.

Figure 1 shows the neutron diffraction patterns of muscle in 92.9% D_2O and 0% D_2O (H_2O). In these measurements, the fiber axis of the muscles was set horizontally. Reflections on the equator and the meridian were clearly observed. The off-meridional myosin first layer line was also observed. Analysis of the contrast dependence of the scattering amplitudes of these reflections showed that there were reflections with the different contrast-matching points. This indicated that there was localization of the distribution of the scattering length density in the unit cell of the muscle. The detailed analysis using Fourier synthesis is in progress.

References

[1] L. A. Feigin and D. I. Svergun: Structure Analysis by Small-Angle X-Ray and Neutron Scattering (1987) Plenum Press, New York.
[2] E. Pebay-Peyroula et al.: Structure 3 (1995) 1051-1059.

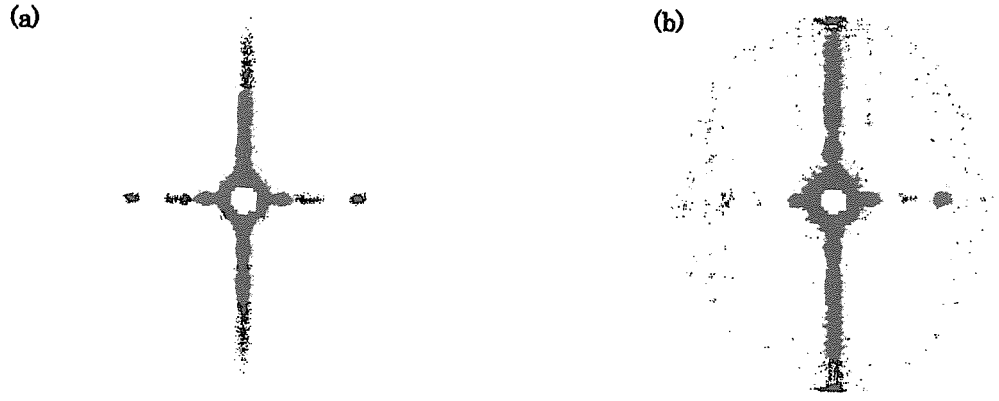

Figure 1. Neutron fiber diffraction patterns of the frog sartorius muscle (a) in D_2O, and (b) in H_2O.

原子炉：JRR-3M　　装置：SANS-J (C3-2)　　分野：中性子散乱（生物）

研究テーマ：細胞における蛋白質の高次構造化不全と細胞の異常死に関する研究
表題：水中におけるケラチンタンパク質の自己集合に関する中性子散乱研究

1-7-12 Neutron scattering study on self-assembly of keratin molecules in water

Sachio Naito, Fumiyoshi Ikkai , Takeshi Karino[1], Michihiro Furusaka[1], Satoru Fujiwara[2], and Nobuo Niimura[2],

The Institute of Advanced Science Research, L'ORÉAL Tsukuba Center, Tsukuba, Ibaraki 300-2635, Japan
[1]High Energy Accelerator Research Organization, Tsukuba, Ibaraki 305-0801, Japan
[2] Japan Atomic Energy Research Institute, Ibaraki 319-11, Japan

The aim of this study is to clarify structural changes of proteins in apoptosis. Once apoptotic trigger is pulled in a hair cell, the cell begins to produce enormous amount of keratin proteins (Figure 1). Then, SS cross-linking is induced between the molecules and keratin proteins are finally gelated. This type of apoptosis is unusual in normal body but often occurs in cancer, AIDS, etc,. In this study, we have employed small-angle neutron scattering (SANS) and static light scattering (SLS) techniques for characterizing the early organization process of hair formation as a model of abnormal apoptosis.

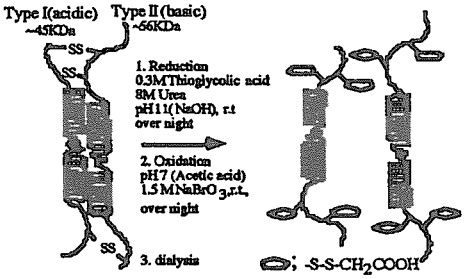

Figure 1. Structure of keratin (protofibril) and preparation of water soluble S-carbomymethyl alanyl disulfide keratin (CMADK).[1]

Protofibril consist of a pair of type I(acidic) and type II(basic). We have estimated the cross-sectional dimensions of CMADK in D_2O by wide-angle neutron scattering measurement (WINK). The radius of $CMADK_{monome}$ and $CMADK_{dimer}$ are estimated to be 9.6 Å for monomer and 20.4 Å for dimer, respectively. We confirmed the scattering profile corresponding to the $CMADK_{dimer}$ disappeared in 8 M urea solution. Figure 2 shows the least-squares fitting by Guinier equation (1) to the scaled SLS and SANS (by SANS-J, PSD located L = 7 m) data of 0.75 % CMADK in the buffer (pH 7) and pH11 D_2O in the q range 0.00068 – 0.0027 $Å^{-1}$.

$$I(q) = I(0)_{monomer} \exp(-q^2 \langle Rg_{monomer} \rangle^{2\beta}) + I(0)_{dimer} \exp(-q^2 \langle Rg_{dimer} \rangle^{2\beta}) \quad (1)$$

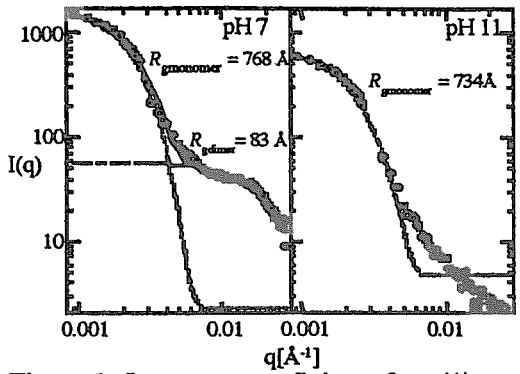

Figure 2. Least-squares fitting of eq (1) to the SANS and and scaled SLS $I(q)$ vs q curves.

The theoretical curve for scattering profile of whole CMADK particles reproduces well the experimental data. It is clearly shown two kinds of CMADK particles whose sizes are quite different disperse in the buffer (pH 7). In the q range 0.01 - 0.02 $Å^{-1}$, however, a shoulder profile observed on the scattering curve in the buffer (pH7) disappears in the pH 11 solution. We confirmed that about 40% of α-helical structure remained in CMADK even in the pH 11 solution. On the base of the CMADK molecular weight, $\langle R_{gmonomer} = 768 Å \rangle$ is too large for a monomeric $CMADK_{monomer}$. It is suggested that two $CMADK_{monomer}$ molecules exist as a long rod-like complex by head (N-terminal)-to-tail (C-terminal) overlap mode. This like decomposition of $CMADK_{dimer}$ could be observed in 0.8 M urea solution. These results suggest that the $CMADK_{dimer}$ structure is stabilized by very weak inter-molecular hydrophobic interaction. Consequently, in the early organization process, type I and II keratin molecules recognizes each other, and self-assembles without SS cross-linking formation. Then, the assembly forms parallel or anti-parallel dimer but not coiled-coil.

Reference

[1] Y. Miyauchi, S. Naito, K. Kurita, and M. Furusaka, KENS Report-XI, 107 (1997).

原子炉：JRR-3M　　装置：SANSJ(C3-2)　　分野：生物

研究テーマ：磁場下における生体高分子系の構造形成
表題：生体超分子の高磁場下における配向挙動

1-7-13
Orientatinal behavior of biological super-macromolecules under high magnetic field

M. Hirai,[1] T. Hayakawa,[1] H. Iwase,[1] Y. Sano,[2] and J. Suzuki.[3]

[1] *Department of Physics, Gunma University, Maebashi 371, Japan.*
[2] *Department of Pharmacy, Setsunan University, Maikata 573-1010, Japan.*
[3] *Japan Atomic Energy Reseach Institute, Tokai, Ibaraki 319-1195, Japan.*

Introduction The behavior of a biological supermacromolecular suspension under magnetic field is a very attractive scientific concern from the viewpoint relating to cooperative phenomena in liquid crystal phase transition. Many theoretical works have been done to predict and explain the self-ordering mechanism of liquid crystals rod-shaped colloidal particles by assuming some repulsive or attractive interaction between them. Tobacco mosaic virus (TMV) is a rod-shaped virus that consists of coat protein subunits and RNA (180Å in diameter and 3000 Å in height). Previously, by using synchrotron radiation SAXS method we showed the presence of critical magnetic-field strength and the phase diagram of TMV liquid crystal depending on both magnetic-field strength (up to 1.8 tesla) and molecular concentration [1]. In the present study using SANS method we measured the phase behabior and the orientational processes of TMV under a hgih magnetic field strength.

Experimental The sample was TMV from Japanese common strain OM. The virus was suspended in 10 mM sodium phosphate buffer adjusted at pH 7.2, and the concentrations of the TMV suspensions were 25-176 mg/ml, respectively. SANS experiments were carried out by using a small-angle neutron scattering spectrometer called SANS-J at JRR-3M, Tokai, Japan. The wave length was 10 Å and the sample-to-detector distances were 10 m and 1.5 m. The exposure time for one time frame was 50 minutes. A helium-free super-conducting magnet HF10-100VT-20H-1 by SUMITOMO Heavy Ind.was used. The applied magnetic field strength was varied from 2.5 tesla to 10 tesla.

Results In the previous studies we found that the TMV suspensions under magnetic field of 1.8 tesla do not show an evidential orientational behavior at lower concentration below the isotropic-to-nematic lyotropic phase transition concentration of ~67 mg/ml. Fig. 1(a) and (b) show the 2-D scattering patterns of 25 mg/ml TMV isotropic phase suspensions under magnetic field of 0 tesla, and 10 tesla, respectively. The inserts show the 2-D contour maps of those scattering patterns. Fig. 1 (a) and (b) show a partial orientation of the long axis of TMV particle along the magnetic field. In comparison with the scattering pattern and contour map of 110 mg/ml TMV nematic phase suspension under magnetic field 10 tesla in Fig. 1 (c), the observed orientation of 25 mg/ml TMV suspension can be understood as a creation of small polynematic domains in isotropic phase induced by high-magnetic field. Further experiments and analyses are in progress.

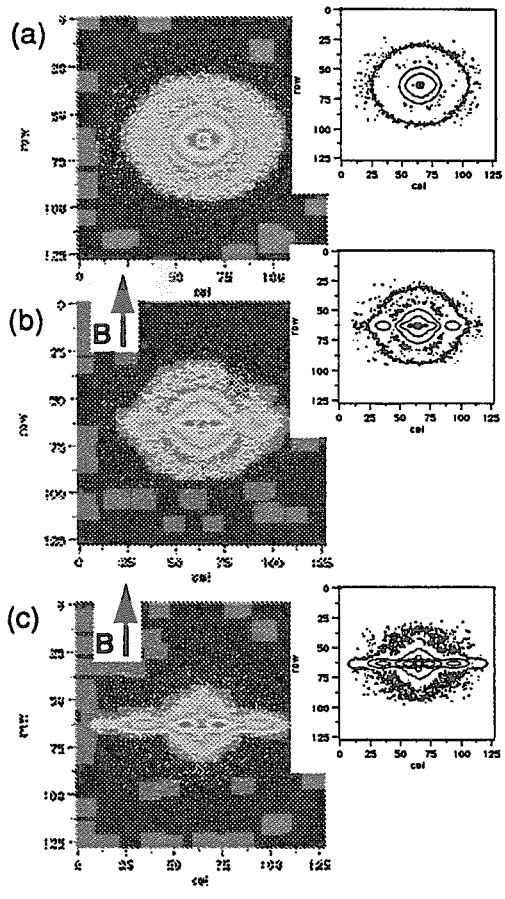

Fig. 1. 2-D scattering patterns and contour maps of TMV suspensions in log-scale. (a), 25 mg/ml, B = 0; (b), 25 mg/ml, B = 10 tesla; (c), 110 mg/ml, B = 10 tesla.

Reference
M. Hirai et. al., Phys. Rev. B, 1997, 3490.

原子炉：JRR-3M　　装置：SANS-J(C3-2)　　分野：中性子散乱（生物）

1. 中性子散乱 8) 基礎物理学・中性子光学

1. Neutron Scattering 8) Fundamental Physics Neutron Optics

This is a blank page.

研究テーマ：超低温の導入による中性子散乱の研究
標　　題：干渉計による ^{202}Hg, ^{63}Cu, ^{65}Cu, natural W, Cu, Hg 等の散乱半径の測定

1-8-1 Neutron Interferometric Measurement of the Scattering Lengths of ^{202}Hg, Hg, ^{63}Cu, ^{65}Cu, Cu and W

Hiroshi TOMIMITSU[a], Yuji HASEGAWA[b] and Kazuya AIZAWA[a]

[a]Advanced Science Research Center, JAERI, Tokai-mura, Ibaraki-ken, 319-1195 Japan
[b]Department of Applied Physics, University of Tokyo, Hongo, Bunkyo-ku, Tokyo113-8656, Japan

We successfully determined the coherent neutron scattering lengths for ^{202}Hg, first in the world, and for several elements and isotopes, with very high accuracies.

Measurements were carried out with a Si LLL-type interferometer at the special apparatus "PNO" implemented at JRR-3M. Temperature at the interferometer was kept around the RT +/-0.005deg. Wavelength, 0.15784nm, was selected so as to realize the best visibility of the interference oscillation curve of a reference Al plate, in combination with the position of the interferometer. The best visibility, thus surveyed, was more than 50%, while it was around 40% in the previous experiment[1].

Every sample was set so as to receive only the reflected beam only between the 1'st(splitter) and the 2'nd(mirror) reflecting plate of the interferometer, as shown in Fig.1.

Compared with the previous experiment[1], samples in the present experiment were rotated much wider, which also improved the quality of the final data.

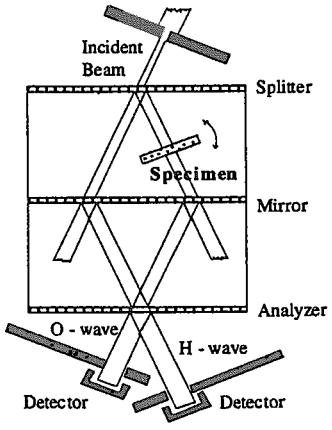

Fig. 1. Drawing of the experiment with the beam paths.

With the fitting parameters A~E, the intensity I for O-wave is analyzed by the following function[1];

$$I = A*\cos(B/(\cos(\alpha+C))+D)+E. \quad .....(1)$$

The coherent scattering length, b, is then derived through the relation below, with N: atomic number density, t: thickness and λ: wavelength;

$$B = N*b*\lambda*t. \quad .....(2)$$

Example of the interference oscillation is shown below (Fig.2); for the case of ^{202}Hg, with a least squares fit.

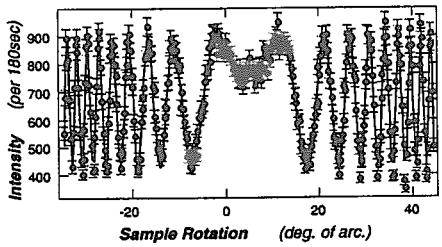

Results for b's are summarized below, comparing with the tabulated values[2].

Specimen	b(derived, fm)	b(Table, fm)
nat. W	4.7300(0.0271)	4.77~5.1
^{63}Cu	6.5033(0.0103)	6.40, 6.72
^{63}Cu	10.1694(0.0167)	10.57, 11.09
nat. Cu	7.7093(0.0044)	7.35 ~7.90
^{202}Hg	11.0019(0.0440)	*none*
nat. Hg	12.5951(0.0461)	12.66~13.10

References

[1] H.Tomimitsu, Y.Hasegawa, K.Aizawa and S.Kikuta: Nucl. Instr. Meth. in Phys.Res. **A420** (1999) 435.

[2] L.Koester, H.Rauch and E.Seymann: *Atomic Data and Nuclear Data Tables* **49** (1991), pp 65-120.

研究テーマ：構造材料の残留応力と疲労損傷の評価
表題：疲労過程におけるSiC粒子強化アルミ合金の中性子相ひずみ測定

1-8-2 Neutron Phase Strain measurement in SiC Particulate Reinforced Aluminum Alloy during Fatigue

Yoshiaki AKINIWA, Keisuke TANAKA, Hidehiko KIMURA,
Noriaki MINAKAWA[1], and Yukio MORII[1]

Nagoya University, Nagoya 464-8603, Japan
[1]Japan Atomic Energy Research Institute, Tokai, Ibaragi 319, Japan

Aluminum alloys reinforced with silicon carbide particles (SiCp) are currently being considered for use as new structural materials in automobile and aerospace industries because of their low weight, high strength and high wear resistance. In metal matrix composites, the residual stress will be developed due to a mismatch of the coefficients of thermal expansion between the reinforcing particles and the matrix[1]. The thermal residual stress has a significant effect on the mechanical properties and fatigue strength of the composites.

Structural materials fracture when they are subjected to cyclic loading, even if the load is less than the static strength. This phenomenon is known as fatigue failure. For engineering components, clarification of fatigue properties and development in inspection procedures to detect fatigue damage are very important to obtain a good reliability.

In this study, silicon carbide particulate reinforced aluminum alloy was fatigued. The neutron diffraction method was used to measure the change of the phase strains of the composite during the fatigue process.

The experimental materials used were aluminum alloy reinforced by silicon carbide particles (SiCp/Al2024). The volume fraction of SiC particles of the composite is 20% and their average size is 3 μ m. The composite was fabricated by powder metallurgical processing. An extruded rod of the composite was heat-treated under T6 conditions. The grain size of the matrix is about 5 μ m. The Young's modulus is E=114 GPa, the 0.2% proof strength is $\sigma_{0.2}$=465 MPa and the tensile strength is σ_B=625 MPa.

The loading axis of the specimen is taken along the extrusion direction. Specimen with a thickness of 3 mm and a height of 6 mm was used.

Fatigue tests were conducted using a specially designed mechanical tensile testing equipped machine under a constant amplitude of stress cycling. The loading frequency was about 4/1000 Hz. The stress ratio is R=0.1. The maximum applied stress and the maximum strain were 465 MPa and 6600×10^{-6}, respectively.

The neutron diffractions from Al 200 and SiC 116 were used for stress measurement with the RESA (REsidual Stress Analyze equipment) at JAERI. The specimen was uniaxially strained with a tensile testing equipment. The wave length used was 2.068140 Å. The direction of the lattice strain measured was parallel and perpendicular to the loading axis. The phase strains were measured at σ=46.5, 200 and 465 MPa. The strain was calculated on the basis of the lattice spacing of monolithic aluminum alloy and silicone carbide in stress free condition.

For the case of the first loading, both phase strains of composite increased with applied stress. When the plastic deformation occurred, the measured phase strain of aluminum alloy was less than that evaluated from the elastic relation. The strain decreased with number of stress cycles. On the other hand, the phase strain of SiC particles increased with number of stress cycles. In this fatigue condition, fatigue life expected was 7.5×10^3 cycles. The final number of stress cycles was 450 in this study. Further fatigue loading was necessary to detect the fatigue damage of the composite.

References

[1] Y. Akiniwa, K. Tanaka, T. Takezono, M. Hayashi, N. Minakawa and Y. Morii, J. Soc. Mater. Sci, Japan, 47 (1998), 755-761.

原子炉：JRR-3M　　装置：RESA(T2-1)　　分野：中性子散乱（基礎物理）

研究テーマ：時間反転の直接検証のための準備実験

表題：結晶を用いた中性子電気双極子モーメント測定のための二結晶法による決勝評価実験

1-8-3

Tests of BGO ($Bi_{12}GeO_{20}$) perfect crystals using double crystal method for the preparation of neutron EDM (Electric Dipole Moment) search

Y. Otake, C.M.E Zeyen[1], H.M.Shimizu[2], H.Funahashi[3], T.Tabaru[3], D.Seki[3], M.Kitaguchi[3], K.Miyazaki[3], M. Miyabe[3], Y.Yasuda[3], T.Takahashi[4] and M.Hashimoto[4]

Riken Harima Institute, 1-1-1 Kouto, Mikazuki, Sayo, Hyogo, 679-5148, Japan
1 Institut Laue-Langevin BP156 F-38042, Grenoble, Cedex9 France
2 RIKEN, Imaging lab. Wako, Saitama, 351-0198 Japan
3 Dept. of Phys. Kyoto Univ. Kyoto 606-8502 Japan,
4 ISSP Kashiwa, Chiba, Japan

We appraised four sets of Bismuth German. Oxide ($Bi_{12}GeO_{20}$) perfect crystals fabricated by different companies, using double crystal method with 4.71 Å neutrons at ULS. These non-centrosymmetric crystals have strong internal electric fields (10^9 to 10^{10} V/cm). Its magnitude is much larger than the electric field we can apply in vacuum. The novel dual polarised beam technique enables us to measure very small anti-symmetric optical spin rotations. It has been shown that anti-symmetric imaginary spin dependent scattering amplitudes related to atomic effects such as spin-orbit (S-O) coupling [1]. Nuclear effects such as parity violating weak forces, or neutron EDM, create such spin rotations in perfect crystals. From the recent experimental result of CPREAR [3], direct measurement of time reversal non-invariance is quite encouraging result for us to detect n-EDM using crystal method. Until now, it is the most important point for us to find by collaborating and to fabricate as good BGO crystal as possible. It means the crystal FWHM is very close to the theoretical value. Based on recent super-symmetry theoretical research [4] the neutron EDM value should be in the range of our experiment.

Experiment: We have measured FWHM to judge the quality of the crystals for neutron using (222) lattice surface, with BGO crystals whose cutting surfaces are also parallel to (222). This time, we have two crystals whose cutting surface are (100) and (110). Some crystals are smaller than that we usually used. Under this different cutting lattice face, there may be certain effects of inclined measurement into the FWHM values. For these crystals we normally use normal (222) cutting surface crystal as the first crystal, which is already measured whose FWHM value. For BGO, progress to grow better perfect big crystals is underway. The theoretical value of FWHM of rocking curve of BGO crystals from double crystal method is about 2.6 sec for 4.71 Å neutron.

Table 1. Measured and Theoretical FWHM

Crystal, BGO	Measured FWHM
A(French)	21.0 sec
B(Japanese-(100)->(222))	38.3 sec
C(Japanese-(100)->(222))	39.8sec
D	Not completely measured yet

ULS environment: We have changed computers, and control program system with Laboview system, which makes measuring time shorter than before, at least half. There is a Dos-V machine, and I-Mac with which we can make graphs during the experiment at the same time. So, intensity does not change but measuring time becomes shorter, it gives you more or less the same effect with the double intensity in ULS facility.

[1] M. Forte and C. M. E. Zeyen; Nucl. Instr. and Meth. **A284**, 147 (1989) [2] C. M. E. Zeyen, Y. Otake, T. Tabaru, and B. Toperverg; J.Phys.Soc.Jpn. **65**, 177 (1996) [3]Cern-EP/98-153 [4]M.Aoki and N.Ohshimo Nuc.Phys.B 531 (1998)49-64

研究テーマ：量子力学基礎分野波動関数のコヒーレンシーとでコヒーレンシー検出実験
表題：メカニカルアロイ試料（$Ni_{25}Ti_{75}$）を用いた冷中性子スピン干渉実験による干渉、非干渉間現象の検出実験

1-8-4

Experiments to Detect the Phenomena in between Coherence and Decoherence using Interferometer for cold neutron (c3-1-2) with Mechanical Alloying ($Ni_{25}Ti_{75}$) Samples

Y.Otake, T.Fukunaga[1] T.Tasaki[1], T.Ebisawa[1], N.Achiwa[2], M.Hino[1]

RIKEN Harima Institute, Coherence X-ray laboratory, Kouto, Sayo-gun, 679-5148 Japan
1 Kyoto Univ. Research Reactor Institute, Kumatori, Sen'nangun, Japan
2 Kyushu Univ. Condensed Matter, Dept. of Phys. Hakozaki, Fukuoka, Japan

An observation of the phenomena between the coherence and decoherence, which had been known as one part of the QM measurement problems, has been discussed much theoretically without experimental verification. Matter wave interferometry, such as neutron interferometers have been widely known as a sensitive and powerful method and tools to detect very small values of the interactions for last two decades[1]. We have done experiments with spin interference experiment at C3-1-2 Cold neutron multilayer interferometer, to try to detect certain signal of this phenomena. We focus on the Mechanical Alloying samples, which are made by Fukunaga. $Ni_{25}Ti_{75}$ powder sample with 50μm diameter was chosen as a sample. From the previous researches by Fukunaga, et al this sample becomes complete alloy after 800hours milling. They also clear up after it becomes complete alloy of $Ni_{25}Ti_{75}$, whose potential for neutron becomes zero, concentration fluctuation and density fluctuation remain. We prepared such four samples with different milling time as 0 hour, 360,370, 460, 480, 880 hours, milling time of NiTi powder samples. The experimental set-up is spin interferometer, which is the same as spin-echo experiments in principle. The two position were chosen to measure the interference. One is a transmission position(Q=0) called here as position "A", while another is diffuse scattered position, called as position "B" where the neutron direct beam does not come without any samples. The clear interference fringes are measured except 0hour sample at position A.

The visibility and the polarisation at position A and B are shown in Fig. 2. We observed unexpected quite interesting result. The visibility at the position B is that of the scattered beam from MA samples once improve but after about six hundred hours of milling, it decreases. This tendency appears only in the scattered beam.

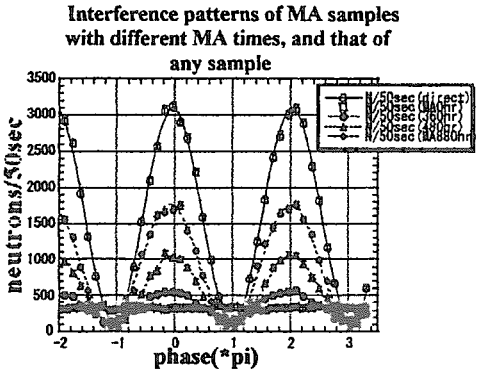

Fig.1 The interference at position A

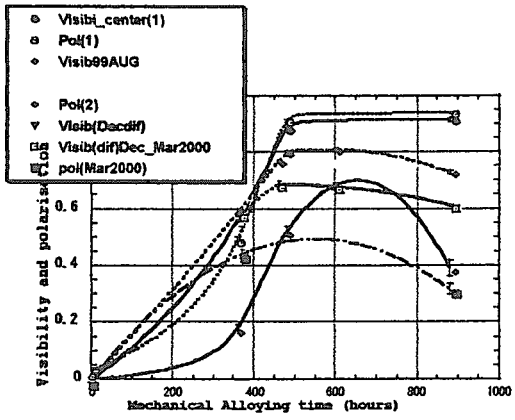

Fig.2 Visibility and polarisation of MA samples

Discussion: The loss of the visibility of the complete alloy sample, which contains density and concentration fluctuation, might indicate certain degree of the phenomenon between the coherence and decoherence. This is the first experiment to measure the phase correlation between the diffuse scattering beams.

研究課題: 冷中性子スピン干渉計の開発とその応用
表題: RF flipperによる冷中性子スピン干渉を用いた分光法の開発

1-8-5 Mieze Spin Echo Method Using RF Flippers

T.Ebisawa, S.Tasaki, N. Achiwa[1], G.Shirozu[1], D.Yamazaki[2], T.Kanaya[3], N.Torikai[4], M.Hino, T.Kawai, K.Soyama[5]

Research Reactor Institute Kyoto University
Department of Physics, Kyushu University[1]
Department of Nuclear Engineering Kyoto University[2]
Institute for Chemical Research, Kyoto University[3]
Neutron Science Laboratory, High Energy Accelerator Research Organization[4]
Japan Atomic Energy Research Institute[5]

We have been developing a Mieze spin echo method [3, 4] using RF flippers)[1, 2]. We have made two preliminary applications of this spin echo method to two scattering phenomena including inelastic reflection from a polymer with lamelar structure and incoherent inelastic scattering by hydregen atoms.

The structure of the modified spin echo method is shown in Fig.1(a). Satisfing the time focusing condition, a measured time spectrum corresponding to a phase shift, $\Phi_t = 2\omega_z t$, is shown in Fig.1(b) for a frequency of 100KHz by RF-flippers with frequency ω_z=50 KHz and neutron detection time t. This spin echo method is featured by the sample position after the analyzer mirror and the time dependent interference (time beat) in time spectrum.

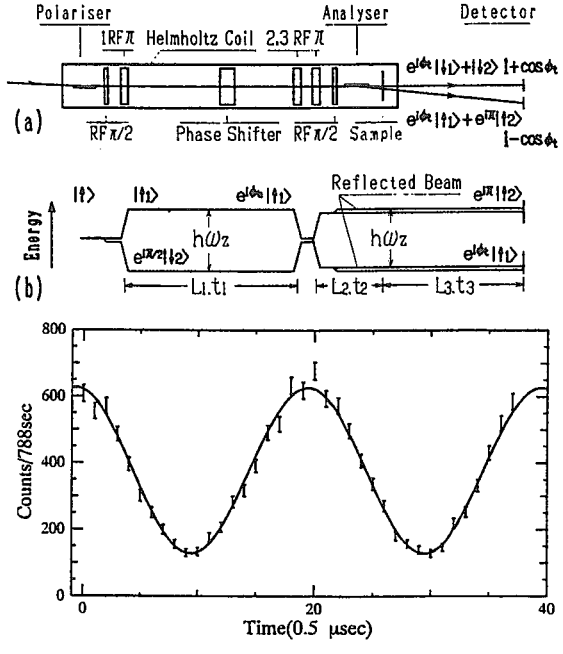

Figure 1: (a) An arrangement of a Mieze type spin echo method with RF flippers. (b) Time beat measured for a frequency of 100 KHz.

Expressing the neutron velicity and the velocity change as v and Δv, respectively, the change of the phase shift $\Delta\Phi$ are given as follows,

$$\Delta\Phi = -\omega_z L_3 \frac{\Delta v}{v^2} \quad (1)$$

$$= -\omega\tau_{nse} \quad (2)$$

ω and τ_{nse} are the energy transfer corresponding to the velocity change and the spin echo time, respectively. They are given by,

$$\omega = \frac{m}{\hbar} v\Delta v \quad (3)$$

$$\tau_{nse} = \frac{\hbar\omega_z L_3}{mv^3} \quad (4)$$

These equations show that this spectroscopy is similar to conventional spin echo method inspite of different spin interferometry. The typical characteristics of this system as a spin echo method can be evaluated from these equations and are shown in Table 1.

Table 1: Energy resolution and τ_{nse} of a modified spin echo method using RF flippers as a function of neutron wavelength for three frequencies of the time interference, assuming L_3 = 1m. The energy range corresponds to phase shift of 2π.

wavelength(Å)	6	12	24
Frequency : 10KHz			
energy range(μeV)	267	33	4.2
τ_{nse}(nsec)	0.0155	0.124	0.99
Frequency : 100 KHz			
energy range (μeV)	26.7	3.3	0.42
τ_{nse}(nsec)	0.155	1.24	9.93
Frequency : 1 MHz			
energy range(μeV)	2.67	0.33	0.04
τ_{nse}(nsec)	1.55	12.4	99.2

* In the previous paper[1, 2] the values of the energy range and τ_{nse} in this Table were mistaken by factor 8.

Now we present very briefly two preliminary applications of this spin echo method. A polymer film of "DP26" has a measurable component of off-specular around a big peak of 1.2 deg in the neutron reflectivity[5]. A preliminary analysis shows this off-specular component would have an inelasticity. Measured time beats are given in Fig. 2 for specular reflection of 1.2 deg. by dashed line, off-specular of 1.19 deg. by dotted line and off-specular of 1.93 deg. by solid line. The statistics of the data are very bad, because the neutron intensity was very low of 100 counts/sec. Measured phase shifts are 1.50±0.40 and 0.66±0.26 rad. for off-specular of 1.93 deg. and 1.19 deg., respectively. The net phase shifts by the inelasticity is evaluated to be 1.38 ± 0.40 and 0.88 ± 0.26 rad., taking account of the path difference between the two cases. These phase shifts correspond to an energy transfer of $1.0 \pm 0.29\mu$ eV and 0.63 ± 0.19, which are comparable with $0.7\ \mu$ eV and $0.43\ \mu$ eV, respectively, predicted by a simple consideration[6]. We should note that we need much more measurements with much larger neutron intensity in order to confirm the above result.

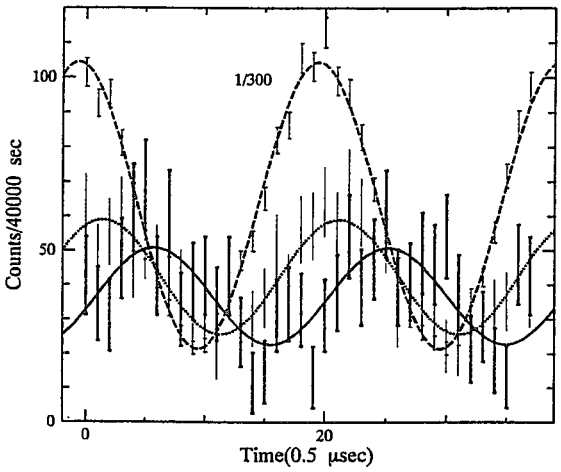

Figure 2: Time beats measured for specular reflection and two off-specular reflections. Dashued, dotted and solid lines indicate time beats for the specular, off-specular reflections of 1.19 deg. and 1.93 deg. The reductions showed in the off-specular data are due to the wider beam acceptance of 10mm in contrast with specular beam width of 3mm.

Another is an application of this spin echo method to incoherent inelastic scattering. Figure 3 shows time beat data for neutrons scattered by vanadium in a direction of 90 deg. The data showed that the contrast of the time beat did not changed by the incoherent elastic scattering. Vanadium is a typical atom with large incoherent elastic scattering cross section based on spin incoherent. Contrast of the time beat profile will be reduced for the conventional method owing to the neutron spin flip in the incoherent scattering. In this modified method, however, the time beat was not kept unchanged for the neutron spin flip process[6]. This situation have been verified in case of depolarized neutron beam transmitted through a thin iron plate[7]. This method, therefore, will bring us a spin echo method applicable to a condense matter including hydrogen atoms which have a large incoherent inelastic scattering[4].

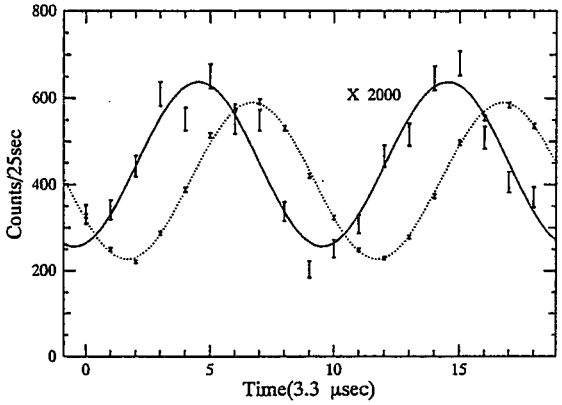

Figure 3: Time beats measured for non sample by dotted line and incoherent elastic scattering by vanadium by solid line. Both data with frequency of 30 KHz show the same contrast.

We have a plan to install more two beam ports with much more intensity in this year. This plan will be promising for the development of the new spin echo methods.

References

[1] T.Ebisawa, S.Tasaki, M.Hino, T.Kawai, Y.Iwata, D.Yamazaki, N.Achiwa, Y.Otake, T.Kanaya, K.Soyama, Journal of Physics and Chemistry of Solids 60,(1999) 1569-1572.

[2] T.Ebisawa, S.Tasaki, D.Yamazaki, G.Shirozu, M.Hino, T.Kawai, T.Kanaya, K.Soyama, N.Achiwa. Physica B,276-278(2000),144-145.

[3] W.Besenböck, P.Hank, M.Köppe, R.Gähler, T.Keller, R.Golub, J. Phys. Soc. Jpn. **65** Suppl.A (1996) 215.

[4] M.Köppe, M.Bleuel, R.Gähler, R.Golub, P.Hank, T.Keller, Physica B **266** (1999) 75.

[5] N.Torikai et al., private comunications.

[6] T.Ebisawa, S.Tasaki, D.Yamazaki, N.Achiwa, G.Shirozu, M.Hino, T.Kawai, T.Kanaya, K.Soyama, to be published.

[7] N.Achiwa, G.Shirozu, T.Ebisawa, S.Tasaki, M.Hino, T.Kawai, D.Yamazaki, in this proceedings.

研究課題: 多層膜の界面粗さによる中性子反射率・透過率への影響
表題: 多層膜の界面粗さによる中性子反射率・透過率への影響

1-8-6 Study on Effects of the interface roughness on the neutron reflectivity/transmissivity

S.Tasaki
Research Reactor Institute Kyoto University

Interface roughness is one of the main cause of reduction of neutron reflectivity and transissivity from multilayer mirrors. Usually reflectivity reduction due to the interface roughness is taken into account to the calculated reflectivity by multiplying the ideal reflectivity by a Debye-Waller type reduction factor. The calculation is based on a model that reflected wave is scattered by the interface roughness. This model gives us the result that the sum of the reflectivity and the transmissivity becomes less than unity at the Bragg angle. On the other hand, there is another explanation for the reduction of reflectivity that the optical potential which neutrons 'see' in the multilayer is effectively lowered due to the roughness and/or density reduction of the evaporated materials. This latter model gives us that the sum of neutron reflectivity and transmissivity is unity except for the absorption and incoherent scattering by the materials.

In this study, we made measurements on reflectivity and transmissivity of neutron from a multilayer mirror.

The multilayer, fabricated using the vaccum evaporation in Research Reactor Institute Kyoto University[1], consists of Ni and Ti with d-spacing of 100Å, and the number of layers of 100. The multilayer is evaporated on a 130mm×60mm×0.6mm-Si wafer. The measurements were performed with the neutron reflectometer installed at C3-1-2 beam port of JRR-3M reactor in Japan Atomic Energy Research Institute.

For the transmissivity data, absorption by the Si substrate should be corrected by the factor

$$f = \exp\left(\frac{\sigma_a}{\lambda_0}\lambda N_{\mathrm{Si}}\frac{T}{\sin\theta}\right), \qquad (1)$$

where $\sigma_a(=\ 0.2091 \pm 0.0005\mathrm{b})$, $N_{\mathrm{Si}}(= 5.0175 \times 10^{22}/\mathrm{cm}^3)$, $T(=\ 0.6\mathrm{mm})$ are absorption cross section, atomic number density of Si, and the thickness of the substrate. $\lambda_0(=\ 1.79\text{Å})$ is the neutron wavelength at which absorption cross section is given by σ_a. $\lambda(=\ 6\text{Å})$ and θ are neutron wavelength and incident angle of neutron to the substrate. The absorption cross section is about 40% larger than the reported value[2]. The difference might be due to the error in substrate thickness and the absorption cross section itself.

The results are shown in Fig.1. The transmissivity T in the figure is Si absorption corrected. In the ordinal roughness scattering model, the sum (R+T) should be less than unity at the Bragg position ($\theta \approx 1.1$deg) and very close to unity else where. The figure shows, however, that there is no such reduction of the sum around Bragg condition. The results are quite similar to those obtained using the reflectometer at C2-1 beam port, which is repoted last year. This result implies that neutrons 'see' mean structure of the multilayer and the scattering induced by the roughness is very weak.

Moreover,
the sum is about 5% higher than unity at Bragg peak($Q = 0.64\mathrm{nm}^{-1}$. The amount corresponds to the Si-absorption correction for the transmitted beam. There will requre more study to explain this phenomenon.

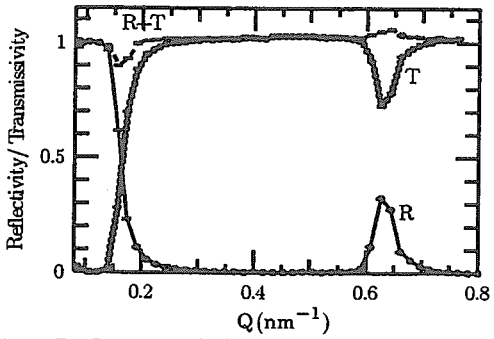

Fig.1 Reflectivity(R) and transmissivity(T) and their sum(R+T) from a Ni/Ti multilayer.

References

[1] S.Tasaki, T.Ebisawa, T.Akiyoshi, T.Kawai, and S.Okamoto, *Nucl. Inst. Meth. Phys. Res.*, A**355** (1995) 501

[2] Kurt Sköld and David L.Price ed., *Mthods of Experimental Physics*, vol.23 'Neutron Scattering', 1986, Academic Press.

研究課題：ラーモア回転による中性子波束のスピン干渉
表題：時間ビート中性子スピン干渉における$\pi/2$中性子スピンフリッパー前後のスピン干渉状態

1-8-7

Time Beat Neutron Spin Interferometry before or after $\pi/2$ Neutron Spin Flipper

N. Achiwa, G. Shirozu, T. Ebisawa[A], M. Hino[A], S. Tasaki[A], T. Kawai[A], D. Yamazaki[A]
Department of Physics, Graduate School of Sciences, Kyushu University, Fukuoka, 8128581, Japan
[A]Res. React. Inst. Kyoto Univ.[A], Kyoto Univ. Kumatori, Osaka, 5900494, Japan

1 INTRODUCTION

We have developed neutron spin interferometry using RF flippers[1]. Time beat of neutron intensity is observed at detector position if the time echo condition is satisfied. This time beat of neutron intensity can be understood as the superpostion of ↑ neutron spin wave functions with different total energies produced by magnetic resonance of neutron.

The time beat interferometry will operate as spin interferometer or classical shift time measurement depending on sample position before or after $\pi/2$ flipper. by a similar principle of resonance spin echo developed by Gähler et al.[2].

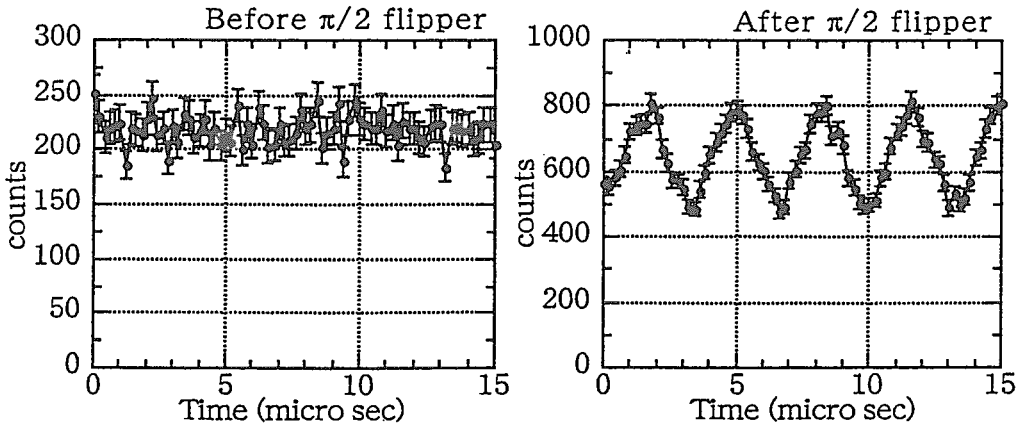

Figure 1: a)The time beat signal when unmagnetized iron depolarizer of 1mm is inserted before the second $\pi/2$ spin flipper. The time beat signal of 320 KHz frequency is vanished. b)When the same depolarizer is inserted after the polarization analyser. The time beat signal of 320 KHz frequency is unchanged comparing with the case without inserting depolarizer.

Then, if we put in depolarizing unmagnetized iron sheet after the $\pi/2$, neutron time beat will not be influenced by the depolarizing Fe sheet. Of course, through the depolarizing Fe sheet, spin flip of neutron happens. But this spin flip happens for the both ↑ neutron spin states with different total energies. The situation is very different comparing the case when the depolarizer is inserted before the second $\pi/2$ spin flipper. This time, the time beat at the detector position was destroyed because the depolarizing field destroyed the coherency of wave functions between ↑ and ↓ spins.

When the sample is inserted after the analyser, the time phase is influenced by the change of classical arrival time at the detector; the velocity change of neutron by inelastic scattering or a path length delay due to multiple scattering process and so on.

This new priciple opens new applications of the time beat spectrometer for magnetic scattering as well as incoherent spin scattering. The incoherent elestic scattering of vanadium sheet was recently tried by one of our group and the time beat was also unchanged by the elastic incoherent scattering process[3].

REFERENCES

1. T.Ebisawa, S. Tasaki, M. Hino, T. Kawai, Y.Iwata, D.Yamazaki, N. Achiwa, Y.Otake, T. Kanay and K. Soyama, J. Phys. Chem. Solids **60**(1999) 1569-1572., J, Phys. Soc. Japan, **67**(1998) 1569-1573.
2. R. Gähler and R. Golub, J. Phys. **49** (1988) 1195.
3. Ebisawa et al., private communication

研究テーマ:中性子ラーモア歳差回転によるトンネル時間とラーモア時計の研究
表題:吸収の強いファブリペロー磁気膜を透過する中性子のスピン回転

1-8-8
Measurement of spin precession angle through Fabry-Perot magnetic resonator with absorption

M. Hino, S. Tasaki, T. Ebisawa, T. Kawai, M. Utsuro, N. Achiwa[1], D. Yamazaki[2]

Research Reactor Institute, Kyoto University, Osaka, 590-0494, Japan
[1]Department of Physics, Kyushu University, Fukuoka, 812-8581, Japan
[2]Department of Nuclear Engineering, Kyoto University, Kyoto, 606-8501, Japan

We have measured precisely spin precession angles and transmission probability of neutrons through Fabry-Perot magnetic absorber, Supersendust(SSD)-(Ge/Gd)-SSD Fabry-Perot magnetic resonator, where thickness of both SSD($Fe_{86.8}Ni_{3.2}Si_6Al_4$) layers is 20 nm. The Ge/Gd film consists of germanium and gadolinium elements, the total thickness of Ge/Gd film is 26.0nm and the ratio of Ge and Gd is 7:3. The film were evaporated on a polished silicon wafer in an applied magnetic field of 14mT in order to saturate the magnetic film under lower magnetic field[1]. A value of potential barrier in the magnetic absorber can be represented as $V = V_{\rm nucl} \pm \mu B + iV_{\rm ab}$ for ↑ and ↓ spin, respectively, where $V_{\rm nucl}, V_{\rm ab}$ and μB is the average coherent nuclear potential, absorption one, magnetic one, respectively. The purpose of this study is to determine whether the optical potential model is adequate or not.

By inserting the Fabry-Perot resonator into the second spin precession field of a neutron spin interferometer(NSI)[2], we observe quasi-bound states of ↑ spin neutron in the Fabry-Perot resonator using spin precession, which is shown by the shift of neutron spin echo(NSE) signals. The NSI is a miniature of a transverse NSE instrument and installed at the cold neutron guide tube(C3-1-2) of the JRR-3M reactor at JAERI. For the NSI, the wavelength resolution and the divergent angle are 12.6Å±0.44Å(FWHM) and 0.7×10^{-3}rad, respectively.

We measured transmission probabilities of ↑ and ↓ spin neutrons, and which are well reproduced by the theoretical lines. The theoretical lines are calculated from one-dimensional Schrödinger equation using the optical potential barrier with absorption including effects of the incident wavelength distribution [3]. Here the nuclear and the magnetic potential values of the SSD were assumed to be 190neV and 78.4neV, respectively, and the nuclear[$V_{\rm nucl}$(Ge/Gd)] and absorption one of Ge/Gd film were 80neV and 30neV, respectively. The critical angle of total reflection of ↑ spin neutron for the SSD films at wavelength of 1.26nm was calculated to be 1.31°.

The angles of additional spin precession are directly observed as a shift of NSE signals by inserting the film in one of the spin precession fields of a transverse NSE spectrometer. As shown in Fig.1, the additional spin precession angles were reproduced by the relative phase difference between ↑ and ↓ spin neutron wave functions which were derived with solving one-dimensional Schrödinger equation for the optical potential with absorption. The result of our experiment clearly shows that the optical potential model with absorption is suitable except for tunneling case.

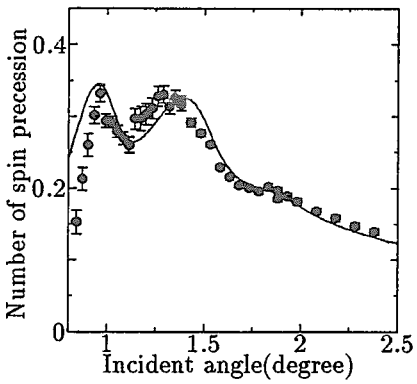

Figure 1: The spin precession of neutron transmitted through the SSD-(Ge/Gd)-SSD Fabry-Perot resonator.

References

[1] M. Hino, T.Kawai, T.Ebisawa, S.Tasaki and N.Achiwa, Physica B **267-268**, 360(1999).

[2] T. Ebisawa, S.Tasaki, T. Kawai, M. Hino, N. Achiwa, Y.Otake, H. Funahashi, D. Yamazaki and T. Akiyoshi, Phys. Rev. A57, 4720(1998).

[3] T. Ebisawa, T. Akiyoshi, N. Achiwa, S. Yamada and S. Okamoto, Annu. Rep. Res. Reactor Inst. Kyoto Univ., **14**, 10(1981).

This is a blank page.

1. 中性子散乱 9) 装　置

1. Neutron Scattering　9) Instrument

This is a blank page.

研究テーマ：機能性生体物質の水和構造研究
表題：ルブレドキシンの中性子結晶構造解析

1-9-1 Neutron crystallography of rubredoxin.

K. Kurihara, I. Tanaka, M.W.W. Adams[a], N.Moiseeva[b], R. Bau[b], N. Niimura

Advanced Science Research Center, Japan Atomic Energy Research Institute, Tokai, Ibaraki 319-1195
[a] University of Georgia, Athens, GA 30602, USA
[b] University of Southern California, Los Angels, CA 90089, USA

A single-crystal diffractometer (BIX-3) dedicated to neutron protein crystallography has been successfully constructed at JRR-3M reactor of JAERI. This instrument features a new type of elastically-bent perfect-Si crystal (EBP-Si) monochromator and neutron imaging plates (NIP).

With this BIX-3 a single-crystal neutron diffraction analysis of the structure of small protein rubredoxin from the hyperthermophile *Pyrococcus furiosus* is currently under way. Rubredoxins are small protein containing an iron atom coordinated by sulfur atoms of four cysteine side chains. Although the physiological role for rubredoxins have not been definitively established, it is likely that they function as electron transfer proteins. Despite the uncertainty of its function in most species, rubredoxins from different organisms have been extensively studied by structural and spectroscopic methodologies, owing to their small size, stability, and ease of isolation.

Data are being collected at room temperature up to a resolution of 1.5 Å (so far the highest resolution neutron data set), using wavelength λ=2.35 Å. A single crystal of dimension 2 x 2 x 1 mm, grown via vapor diffusion from 3.6 M NaK phosphate, is being used in this project. Two sets of data from the same crystal, roughly corresponding to the crystal being mounted along the a and c axes, are being collected and merged. Data collection is by the step-scan method, with 0.3° intervals in φ and exposure times ranging from 60 to 75 minutes per frame. The completeness factor of the 1.5- Å resolution data set is currently at 78.2%. 301 hydrogen atoms and 49 deuterium atoms are included in the refinement of the structure of rubredoxin. 26 water molecules are also identified. In the present model R factor and R-free are 0.254 and 0.279, respectively.

Space group	$P2_12_12_1$ (Z=4)
Unit cell parameters	
a(Å)	34.3
b(Å)	35.3
c(Å)	44.2
Resolution	1.5 Å
Observed reflections	17,432
Unique reflections	7,297
Overall completeness	78.2 %

Table 1 Data collection statistics.

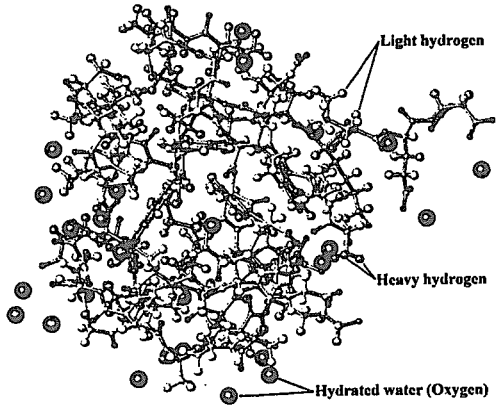

Figure 1 3-dimensional structure of rubredoxin determined by neutron diffraction.

原子炉：JRR-3M　　装置：BIX 3(1GA)　　分野：中性子散乱（装置）

研究テーマ：生体物質の中性子回折による研究

表　　題：生体高分子用回折計（BIX-3)における同一および異種結晶面の重ね合せ弾性湾曲完全結晶シリコンモノクロメータの応用

1-9-2 APPLICATION OF A STACKED ELASTICALLY BENT PERFECT SI MONOCHROMATOR WITH IDENTICAL CRYSTALLOGRAPHIC PLANES AT A DIFFRCATOMETER FOR BIO-MACROMOLECULES (BIX-3)

I. Tanaka[1], F.U. Ahmed[1,2], N. Niimura[1]

[1]ASRC, Japan Atomic Energy Research Institute, Tokai, Ibaraki 319-1195, Japan
[2]On leave from Inst. of Nucl. Science and Tech., Atomic Energy Res. Est., Bangladesh Atomic Energy Commission, Dhaka-1000, Bangladesh

Neutrons have a great potential as a probe to investigate soft and hard materials, but the low intensity of incident neutrons is always a big obstacle compared to the intensity of X-rays. In order to overcome this, elastically bent perfect silicon(EBP-Si) monochromator was used to increase the flux. The merit of using EBP-Si has been already reported by authers and by others. The high-transmission property of EBP-Si for 1-3 Å thermal neutrons is specially noted here. Up to the present some investigators installed stacked identical crystal planes of EBP-Si as a monochromator and an analyzer in a TAS machine at ILL, France to increase the supplementary gains in intensity.

The intensity at the sample position of a diffractometer for studies of biological macromolecules (BIX-3) for two identical (*hkl*) planes stacked EBP-Si monochromator was compared with that for single EBP-Si. A single plate of EBP-Si with 250 x 40 mm^2 surfaces of (111) and 5 mm in thickness, was setup in the monochromator housing of a TAS at JAERI, Japan (TAS-2). The optimum curvature of this monochromator was determined using a neutron imaging plate (NIP), by placing it at the same distance as MtoS (2.3 m) of BIX-3, in open geometry (no soller slits) when the maximum peak intensity was observed at -350 μ deformation strain on the scale of a strain gauge connected to the concave side of the monochromator crystal, which corresponded to a radius of curvature of 10 m. It should be noted that the difference in the peak intensity of EBP-Si for the deformation strain from -350 to -400 μ was within 2%, i.e. intensity gain was almost saturated. Then, two 5 mm thick identical Si (111) plates, the total 10 mm, were stacked, bent and aligned. When the deformation strain reached to -350 μ, the peak intensity increased by a factor of 1.61 compared to that of a single plate. The aligning step sizes for ω, Rx and X were 0.1°, 0.2° and 1.0 mm, respectively.

The optimized EBP-Si was installed in the monochromator housing of BIX-3 without any modification. The experiments were carried out for the single plate EBP-Si (5 mm thickness) and the stacked plates EBP-Si (2 times 5 mm thickness) with a strain of -400 and -350 μ, respectively. The neutron wavelength was 2.35 Å with $2\theta_M = 44°$ for these experiments. The flux measurements were carried out by using an NIP at the sample position of BIX-3. The improved ratios of peak and integrated intensities were 1.60 and 1.59, respectively, when a single EBP-Si (5 mm thick) plate was replaced with stacked EBP-Si plate (2 times 5 mm thick). Fig. 1 shows the result of profiles at each peak. The abscissa is the position on the NIP and the ordinate is the linear intensity. The diffraction spots on the detector were found well separated to determine the indices of protein diffraction[1].

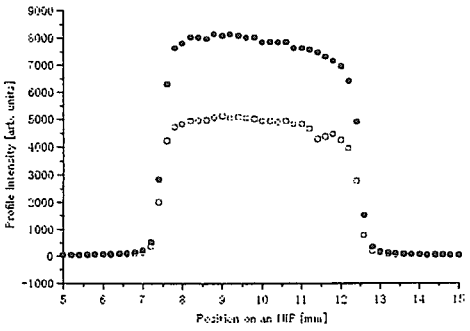

Fig.1. Profile intensity comparison between the two (111) planes stacked EBP-Si monochromator (solid circles) and a single one (open circles).

Reference

[1] I. Tanaka, F. U. Ahmed and N. Niimura, Physica B **283** (2000) 295.

原子炉：JRR-3M　　装置：TAS-2（T2-4)および BIX-3（1GA)　　分野：装置

研究テーマ：超低温の導入による中性子散乱の研究
表題：2結晶回折計におけるSi光学素子の冷却化の試み

1-9-3

An Attempt to refrigerate Si-crystal optical component on a Double Crystal Diffractometer

K. Aizawa and H. Tomimitsu
Advanced Science Research Center, Japan Atomic Energy Research Institute, Tokai,Ibaraki 319-1195, Japan

It is well known that a deviation from the theoretical rocking curve in the region where intensities are less than ~1/100 of peak is observed in a double crystal diffractometer using perfect Si single crystals of non-dispersive setting. There are several possibilities to explain this situation. For example, imperfections of the lattice planes or roughness of surface of Si crystals are conceivable. On the other hand, another possible explanation would be the influence of thermal diffuse scattering of Si crystals. For this reason we attempted to refrigerate the Si crystals to reduce thermal diffuse scattering to compare with the theoretical rocking curve.

Experiments were performed at the PNO apparatus at the JRR3-M research reactor in JAERI. The configuration of the double crystal diffractometer was (5,-5) setting of (111) symmetrical reflection. The wavelength used of this study was 0.25nm. Because of the difficulty of setting up a double crystal diffractometer refrigerating both first and second crystals, we started by refrigerating only the second crystal. Because the lattice constant of Si is almost constant to temperature under 50 K and it is better to refrigerate to lower temperature to remove thermal diffuse scattering, we attempted to refrigerate the second crystal about 10 K. We used CRYODYINE® REFRIGERATION SYSTEM produced by CTI-CRYOGENICS Helix Technology Corporation. The second crystal was isolated from vibration generated by a compressor. Figure 1 shows rocking curves at room temperature and 14.78K together with theoretical curve (Ewald curve) in log-log scale. Peak intensities for both refrigerated and theoretical rocking curves are scaled to peak intensity of rocking curve at room temperature. Broadening of the full width at half maximum (FWHM) of the second crystal rocking curve was observed in Fig.1. We think that this effect may be attributed to the breaking of non-dispersive condition due to small lattice-parameter change in the second crystal at 14.78K. Calculation of this effect is in progress. As for tail of the rocking curve, it seems to be reduced. Now, we are planning to refrigerate both 1st and second crystals.

From the viewpoint of very small-angle neutron scattering (VSANS) method, the broadening of FWHM of rocking curve of second crystal corresponds to extend to measurable q-range toward higher q-values. So, refrigerating a second crystal seems to be useful option for VSANS.

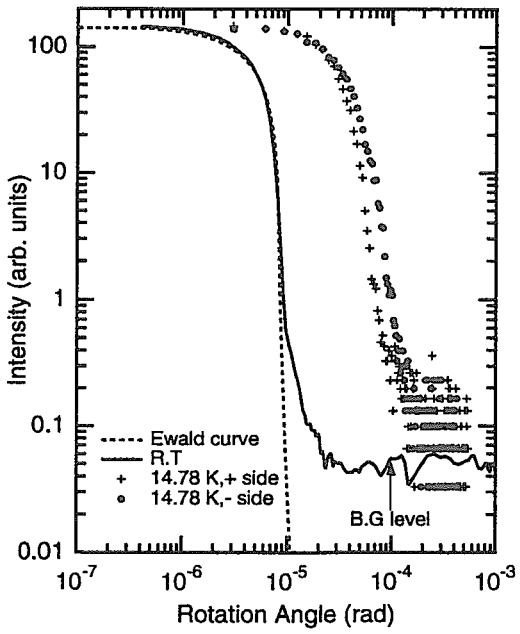

Fig. 1 Ewald curve, rocking curve at room temperature and 14.78K

原子炉：JRR-3M　　装置：PNO (3G)　　分野：中性子散乱（装置）

研究テーマ：コバロキシム錯体結晶の光異性化反応における水素移動
表題：FONDER 回折計によるコバロキシム錯体の単結晶中性子回折

1-9-4

Single Crystal Neutron Diffraction of Cobaloxime Complexes by FONDER Diffractometer

T. Ohhara, H. Imura, H. Uekusa, Y. Ohashi, H. Kimura[1], N. Takesue[2], and Y. Noda[1]

Department of Chemistry and Materials Science, Tokyo Institute of Technology, Meguro-ku, Tokyo, 152-8551 Japan; [1]Research Institute for Science Measurements, Tohoku University, Aoba-ku, Sendai, 980-8577 Japan; [2]Neutron Scattering Laboratory, The Institute for Solid State Physics, University of Tokyo, Tokai, Ibaraki, 319-1106 Japan

The crystalline-state reaction means the solid-state reaction which proceeds with retention of single crystal form, and it is possible to follow the reaction in detail by single crystal structure analysis. Recently, we proposed to use single crystal neutron diffraction for the analysis of crystalline-state reactions. Neutron diffraction can not only determine the position of hydrogen atoms exactly but also distinguish hydrogen and deuterium atoms clearly. So, the process and mechanism of the reaction would be obtained by replacing the hydrogen atoms in the reactive part with the deuterium atoms and observing the deuterium-transfer process in the reaction by single crystal neutron diffraction. Recently, a new four-circle single crystal neutron diffractometer FONDER was installed at the T2-2 port of JRR-3M reactor. In this work, some cobaloxime complexes which show crystalline-state photoreactivity were measured by FONDER and the performance of this new diffractometer was examined.

Measured cobaloxime complexes were as follows; [(*R*)-bis(ethoxycarbonyl)ethyl](pyridine)cobaloxime before and after irradiation (*DEP-ini* and *DEP–end*, respectively) and photoirradiated (3-cyanopropyl-$d_2^{\alpha,\alpha}$) [(*R*)-1-phenylethylamine-d_{11}]cobaloxime-d_{14} (*GCP-end*) which had been measured by BIX-I previously. The wavelength of incident beam was 2.435Å and $2\theta_{max}$ was 80°. Lorentz and absorption corrections were carried out for the diffraction data. The results were shown in Table 1. In addition, the measured reflection intensities were compared with the values calculated from the model structures, the *R* values were also shown in Table 1. The model structure of *DEP-ini* and *DEP–end* were constructed by X-rays with fixing the distance of C-H and N-H at the value on the *International Table*. On *GCP-end*, the previous result of single crystal neutron diffraction was adopted. The values of R_{int} and *R* were sufficiently small and it showed that the FONDER has sufficient accuracy for analysis of crystalline-state reactions of organometallic complexes. And, from the values of measuring time and measured reflections in Table1, it can be expected that the structure of one or two crystals would be determined in one beam-time (4 weeks) when the measuring wavelength shortened and collection of enough reflections for structure analysis become possible in near future.

	DEP-ini	*DEP-end*	*GCP-end*
a/Å	16.800(1)	16.95(1)	9.055(3)
b/Å	16.775(4)	16.76(1)	13.840(3)
c/Å	9.142(3)	9.113(5)	9.196(3)
β/°	-	-	100.12(3)
space group	$P2_12_12_1$	$P2_12_12_1$	$P2_1$
measuring time	34hours	59hours	32.5hours
measured refl.	413	574	168
crystal size/*mm*	5.7x4.2x1.5	11.0x6.0x2.0	3.5x3.5x0.6
R_{int}	0.0281	0.0298	0.0424
R	0.1479	0.1207	0.1267

Table 1

研究テーマ：誘電体の低温での構造相転移の研究
表題：水平・垂直集光型Siモノクロメータの開発

1-9-5 Development of Double-Focused Si Monochromator

H. Kimura[1], A. Kojima[1], R. Kiyanagi[1], Y. Noda[1], N. Minakawa[2], Y. Morii[2], N. Takesue[3], and Y. Yoshizawa[3]

[1]*Research Institute for Scientific Measurements, Tohoku University*
[2]*Advanced Science Research Center, Japan Atomic Energy Research Institute*
[3]*Institute for Solid State Physics, the University of Tokyo*

We have developed Four circle Off-centered Neutron DiffractometER (FONDER) at T_{2-2} beam port to carry out single crystal structural studies. Since before the incident neutron wavelength was fixed at 2.435 Å by using PG(002) monochromator, measurements at high-Q region had not been available. In order to obtain much shorter wavelength, a double-focused monochromator using Si single crystals has been developed. As shown in Figure 1, nine-Si single crystal plates are aligned vertically, and they can be rotated by the horizontal rod with a pulse motor. In addition, the each single crystal can be bent horizontally on the monochromator. Thus the monochromatized beam can be focused vertically and horizontally at a sample position.

In the present work, we optimized the amplitude of horizontal bend and assembled the Bragg reflection planes as a nine-vertically aligned crystal. (4 2 2) reflection was chosen as a monochromator in order to obtain $\lambda = 1.5$ Å neutrons at $2\theta_M = 90°$. The experiments were carried out with TAS-2 spectrometer at T_{2-4} beam port. Incident neutron wavelength was fixed at 1.567 Å where the flux of neutron in T_2 thermal guide is maximum. (4 2 2) peak intensity as a function of strain inside the bent crystal is shown in Figure 2. The peak intensity increases with increasing the strain because the extinction effect is reduced. The intensity starts saturating around 300 μ strain (indicated with an arrow in the Figure 2), of which value corresponds to 70 % of strain where the Si single crystal was broken. Therefore we applied the same strain (300 μ) for nine crystals. All the bent crystals mounted in the monochromator (Figure 1) was assembled along $< 4\ 2\ 2 >$ axis. As shown in Figure 3, rocking curves of (4 2 2) reflections for all the crystals are perfectly identical, which means that all of the vertically aligned crystals have the same line-widths, intensities, and peak positions.

At this moment, the double-focused monochromator tuned at the present work is installed at T_{2-2} port for further tuning at this beam port. The neutron intensity monochromatized by the new monochromator is a half comparing with that by PG(002) monochromator.

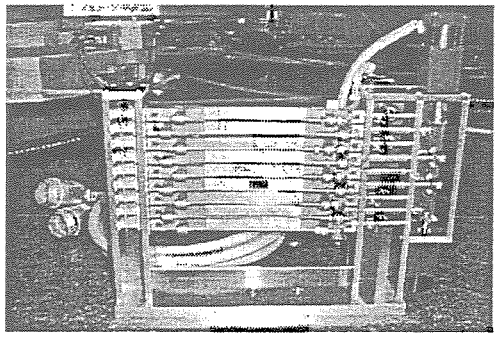

Figure 1: Horizontally and vertically focused monochromator.

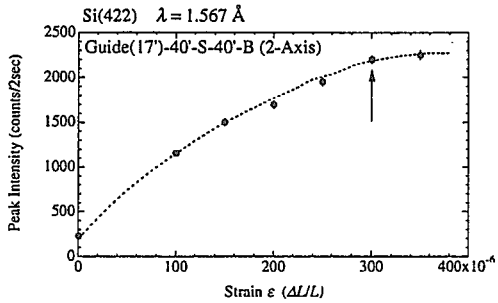

Figure 2: Strain dependence of the (4 2 2) Bragg peak intensity.

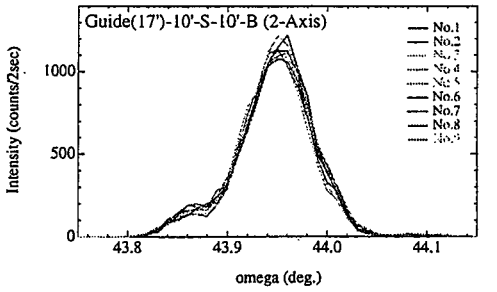

Figure 3: Rocking curves of (4 2 2) Bragg peak for vertically aligned crystals.

原子炉：JRR-3M　　装置：TAS-2 (T2-4)　　分野：中性子散乱（装置）

研究テーマ：黎明研究
表題　　：トロイダル黒鉛結晶による中性子集光光学デバイスの評価
1-9-6

Characterization Study of a troidal bent pyloric graphite Neutron Condenser lens

N. Nishiki, N. Metoki[1], Y. Koike[1], K. Soyama[3], S. Fujiwara[1], Y. K. Haga[1], S. Koizumi[1]

Matsushita Electric Industrial Co., Ltd. 1006 Kadoma, Kadoma 571, Japan
[1]ASRC-JAERI, Tokai, Naka, Ibaraki 319-1195, Japan
[2]Japan Science and Technology Corporation, Kawaguchi, Saitama 332-0012, Japan
[3]Center for Neutron Science, JAERI, Tokai, Naka, Ibaraki 319-1195, Japan

There is strong demand to obtain high flux neutron which is an inevitable probe for the fundamental research as well as industrial use. Especially neutron imaging attracts strong interest in addition to the traditional method like scattering technique or activation analysis. For these purposes sophisticated neutron optical device has to be developed and used with a high-density neutron storage media like neutron image plate.

Very recently double bent pyloric graphite (PG) along the troidal surface is developed in Matsushita electric Industrial Co. A very good focusing with large flux gain more than 200 times as strong as primary intensity has been reported using Cu-$K\alpha$ radiation. The purpose of this study is to characterize the imaging and magnification of the neutron flux of this troidal PG crystal as a neutron condenser lens.

The troidal double bent pyloric graphite is made of polyimide sheets. The glassy carbon sheets obtained from the polyimide sheets annealed at 1000 ℃ can be easily bent along any two-dimensionally curved surface. After the forming an ideal troidal surface, the carbon sheet is annealed about 2800℃ under pressure in order to crystallize graphite, then heated at 3100 ℃ in argon atmosphere to improve the quality of the graphite crystal. This cylindrical PG has a large size typically 60 mm in diameter and 80 mm in length with 120 mm focal length.

The characterization study with neutron has been carried out using triple axis spectrometer TAS-2. The incident beam was monochromated at the wave length of 1.54 Åwith a flat PG monochromator. The small sample rod was exposed , and the incoherent scattering from the sample was collimated and stored on a neutron image plate. A Cd disk was mounted on the optical axis to prevent the incoherent scattering from hitting directly onto the image plate. The forcus was roughly adjusted by minimizing the image size of a polyethylene disk with 3 mm diameter with changing the distances between sample tube, double troidal PG, and image plate. After that focusing was finely tuned with 1mm diameter paraffin tube. This sample was also used to check the imaging and the magnification of the neutron flux. The experimental set up is schematically shown in Fig. 1.

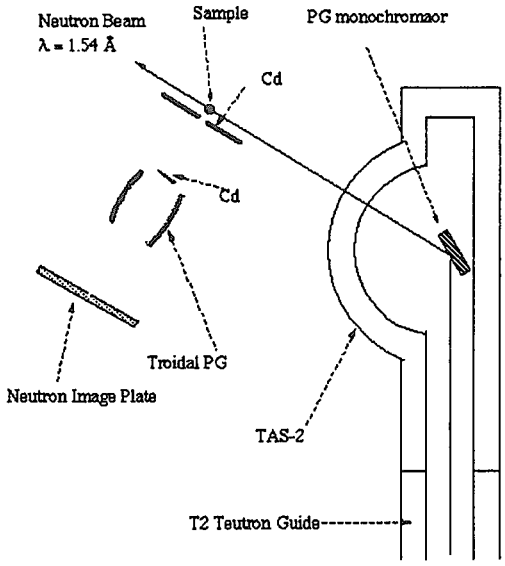

Fig. 1 The experimental set up for characterization of the troidal PG.

原子炉：JRR-3M　　装置　TAS-2(T2-4)　　分野：中性子散乱（装置）

Figure 2 shows the profile of the image of polyethylene disk (3 mmϕ) as a function of the distance between the troidal PG and image plate. The linewidth of the profile changes with distance and shows a minimum at the focusing point. This result indicates that the neutron stored on the image plate is diffracted and collimated by troidal PG.

After determined the focusing point, the image from a paraffin tube has been stored. Figure 3 is the image of the sample. Surprisingly we obtained well collimated image on image plate which is 250 mm apart from the sample. Figure 4 shows the profile of the image. We found that the width of the profile was about 1.5 mm which is very sharp compare to the size of the sample, 1 mm in diameter. In addition we estimated magnification of the flux by comparing the intensity of the collimated beam and the background due to direct incoherent scattering. We found that the magnification would be 150, which is in our knowledge, the world record for the magnification of a neutron flux by reflective neutron optical device. Therefore we conclude that this double bent PG has an ideal troidal surface and it can be used as a condenser lens for high flux neutron beam. By improving the mosaic spread and the error of the curvature, we hope that the increase of the flux of the troidal PG, which is a powerful tool as a neutron device for imaging as well as focusing of neutron

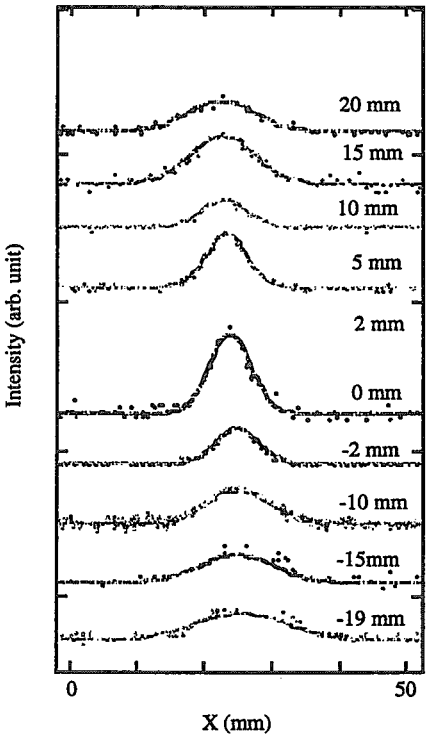

Fig. 2 The image profile of a polyethylene disk (3 mmϕ) as a function of the distance between the troidal PG and image plate.

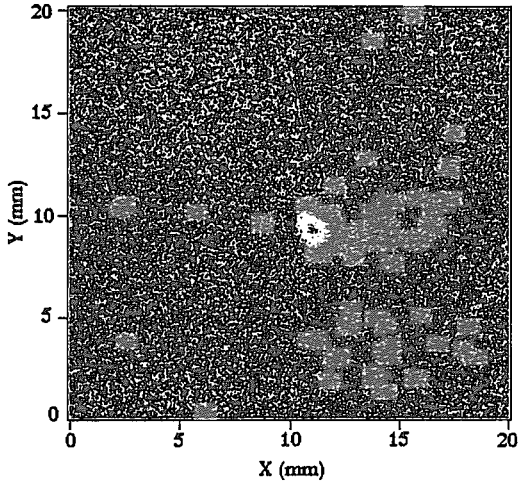

Fig. 3 The image of a paraffin tube with 1 mm diameter.

研究テーマ:生体物質の中性子回折による研究
表　　題:単結晶および粉末中性子回折用多波長モノクロメータシステムの性能

1-9-7

PERFORMANCE OF A MULTI-WAVELENGTH MONOCHROMATOR SYSTEM FOR NEUTRON SINGLE-CRYSTAL AND POWDER DIFFRACTION

F. U. Ahmed[1,2], I. Tanaka[1], N. Niimura[1]

[1]Advanced Science Research Center, JAERI, Tokai, Ibaraki 319-1195, Japan
[2]On leave from Inst. of Nucl. Science and Tech., Atomic Energy Res. Est., Bangladesh Atomic Energy Commission, Dhaka-1000, Bangladesh

Elastically bent Si crystals have been developed and used in diffractometers to increase the neutron flux density at the sample position. It was reported by authers that the intensity gain for a bent crystal was about 30 times that of a flat perfect crystal. This result must encourage the use of low/medium flux reactors for diffraction experiments by developing bent monochromators with optimum curvature. The focusing principle enables diffraction experiments with a signifcantly higher angular resolution and a broader wavelength distribution without using flux-reducing Soller collimators. Recently, it is reported that a two-wavelength sandwich monochromator to investigate stress/strain of polycrystalline materials had successfully been used. Previously, one of the authers also proposed using a curved monochromator assembly composed of several different types and segments of crystals to diffract and focus neutrons of different wavelengths onto the sample. When multi-wavelength and quasi-Laue methods are applied to crystallography dealing with larger unit cells (for example, proteins), the multi-wavelength methods produce better quality data, although data collection times are a little longer. Higher signal to background ratios can be achieved with multi-wavelength methods than with quasi-Laue methods owing to the different way of scanning the lattice points in reciprocal space. It is therefore preferable to obtain better quality data though expending a little more time in the case of multi-wavelength methods. Major aims of the present study were to employ the neutron imaging plate (NIP) detector and elastically bent perfect crystals for a multi-wavelength monochromator system to improve the data collection efficiency and improve the reliability of the experiments.

In order to improve significantly data collection efficiency, the advantages of using multi-wavelengths in single-crystal neutron diffraction as well as in powder neutron diffraction were established by experiments using a stacked monochromator assembly of two elastically bent perfect Si(111) and Si(220) crystals. Each crystal was elastically bent in order to increase the flux density at the sample position. Two wavelengths, λ_1 = 1.80 Å for Si(220) and λ_2 = 2.94 Å for Si(111), were selected. The alignment of the stacked monochromator was successful and a well defined rocking curve of approximately 0.3° full width at half-maximum (FWHM) was obtained. Diffraction patterns of Si powder were collected using the TAS-2 point detector as well as a neutron imaging plate (NIP) detector to compare the relative performance of the two detector systems (Fig.1). With the NIP detector, it was possible to acquire multiple reflections simultaneously with better intensity, better statistics and higher spatial resolution with an open geometry. The NIP detector was used to obtain the diffraction pattern of a single crystal of the organic compound piperidine cobaloxime. For the systems investigated in this study, it was possible to assign unambiguously rings or spots to diffraction by λ_1 or by λ_2 in the case of powder and single-crystal diffraction [1].

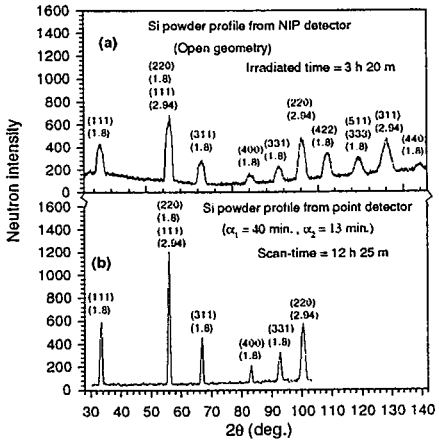

Fig.1. The powder diffraction profiles of Si powder for the multi-wavelength monochromator system obtained using (a) the NIP detector, (b) the point detector of TAS-2.

Reference

[1] F. U. Ahemd, I. Tanaka and N. Niimura, J. Appl. Cryst. **33** (2000) 291.

原子炉:JRR-3M　　装置:TAS-2(T2-4)　　分野:装置

研究課題: 低磁場制御冷中性子偏極パルサーの開発
表題: 時間依存ポテンシャル生成のための高周波冷中性子パルサーの開発

1-9-8

Development of a high-frequency cold neutron pulser for producing a time-dependent optical potential

T.Kawai, M.Hino, S.Tasaki, T.Ebisawa, D.Yamazaki, Y.Otake[1] and N.Achiwa[2]
Research Reactor Institute Kyoto University
SPring8 The Institute of Physical and Chemical Research[1] Physics Department, Kyushu University[2]

The development of a device for producing a time-dependent optical potential is now important in observing time-dependent phenomena of a neutron matter wave [1, 2, 3]. If an induction magnitude in a neutron magnetic mirror can be changed in a direction parallel to the neutron polarization by an oscillating external field, a polarized neutron feels the oscillating potential while the neutrons are inside the mirror. The magnetic neutron mirror with such a function is called a cold neutron pulser(CNP). The CNP made of Permalloy has been applied successfully to the delayed choice experiment[4].

A Supersendust/Ge multilayer($2d$ = 330Å), evaporated on a Si wafer in a magnetic field of 140 gauss, was used as a magnetic mirror for a high-frequency CNP(hf-CNP). The schematic experimental setup is shown in Fig.1. 12.6 Å neutrons with a FWHM bandwidth of 3.5 % polarized in a direction parallel to the guide field(6 gauss) by a polarizing mirror is incident on a hf-CNP after passing through a π-flipper and a slit with 5 mm in the opening width. Neutrons reflected from the hf-CNP are detected by the Li-glass scintillator of 0.3 mm in thickness. The distance between the hf-CNP and the detector is 75 mm. Using this arrangement, we can investigate the performance of the CNP up to the 10 kHz. Above this value, a frame overlap due to the wavelength dispersion of the neutron beam occurs and it is difficult to use TOF method.

The two-channel function generator and the power amplifier are used to provide an oscillating current supplied to the magnetic coil for the hf-CNP. The trigger signal to the time analyzer is sent synchronously from the same function generator. The signal for producing the oscillating magnetic field for the $rf-\pi$-flipper is also provided from the function generator.

The time spectra of neutrons reflected from the hf-CNP at 5 kHz are shown in Fig. 2. The close circle indicates the case of of π-flipper on and the open circle the case of π-flipper off. The figure shows that the polarization efficiency is 91 % at 5 kHz. The hf-CNP can work as a chopper for providing a polarized neutron pulse and has such a good property that the intensity loss is small.

A hf-CNP could also split the two spin eigenstates longitudinally in time when the neutron polarized in xy plane is incident on it. A hf-CNP could be applicable to the measurement of the longitudinal coherence length using time resolving method, if a CNP works in the range of MHz. We are now developing such a device.

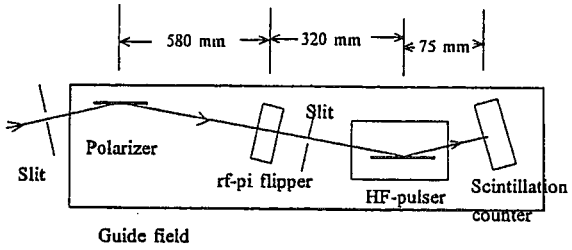

Figure 1: Schematic experimental setup. A frequency cold neutron pulser(hf-CNP) imposes a time structure on neutrons reflected from the CNP mirror.

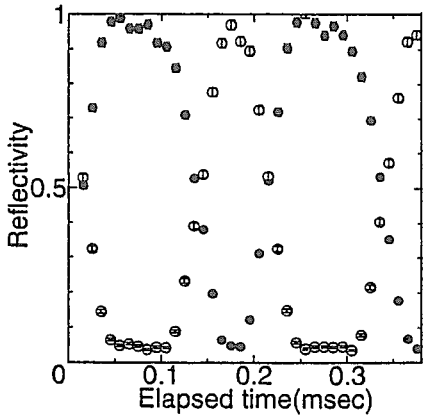

Figure 2: Time spectra of the neutron beam reflected from the hf-CNP at 5 kHz. The close circle indicates the case case of π-flipper on and the open circle the case of π-flipper off.

References

[1] Th.Hils et al., *Phys. Rev.* **A58** (1998) 4784.

[2] D.L.Haavig, R.Reifenberger, *Phys. Rev.* **B26** (1982) 6408.

[3] H.Rauch, H.Wölwitsch, *Phys. Rev.* **A46** (1992) 49.

[4] T.Kawai et al., *Nucl. Instr. Methods* **A410** (1998) 259.

研究テーマ：繰り返し加熱のレプリカスーパミラー中性子反射率に及ぼす影響
表題：多層膜積層による広帯域中性子モノクロメータの開発

1-9-9

Development of Wide Band Neutron Monochormator Consisting of a Stack Of Multilayers

Y. Kawabata[1], K.Somemiya[2] and S. Tasaki[1]

[1] *Research Reactor Institute, Kyoto University, Kumatori, Osaka 590-0494, Japan*
[2] *Faculty of Engineering, Kyoto University, Sakyo-ku, Kyoto, Japan*

Neutron scattering experiments demand the neutron beam control technique which requires multilayers for the shorter neutron wavelength with a large number of thin layers. Wide band neutron monochromators which consist of a stack of multilayers have been developed.

To extend the neutron reflection wavelength range with high reflectivity, it is essential to increase the number of thin layers without deteriorating the layer structure. Here, two new trials were carried out. First, the multilayers were formed in both sides of a Si wafer. The number of layers per substrate is doubled than a usual monochromator on which a multilayer is deposited only on one side. Second, monochromators with two multilayers on both sides of the substrate were piled up as shown in Fig.1. In the case of piling up two monochromators, this stacked one has four multilayers. The stacking of Si wafers is easy but does not raise a problem to the contact between them, because they have very good surface flatness and uniformity of thickness. The layer thickness distribution in this monochromator is gradually thin like a supermirror from the upper surface to the back side.

Multilayer monochromators were manufactured by the evaporation method. They had 201 Ni/Ti multilayers on each side of Si wafers of which thickness was 225 μm.

The neutron reflectivity of a wide band monochromator was measured by the reflectometer at C3-1-2 in JRR-3M, JAERI. The measured and calculated results are shown in Fig.2. A monochromator consisted of four multilayers could enhance widely the reflective neutron wavelength to 19 - 40 nm with proper reflectivity from 26 - 40 nm of one multilayer. The effectiveness of this multilayer fabrication is established with the wide reflective neutron wavelength and the high reflectivity.

References

[1] Y.Kawabata et al., J. Nucl. Sci. Technol., 37(2000)102-106.

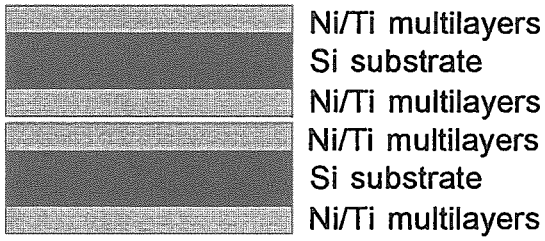

Figure1 Whole structure of a wide band monochromator

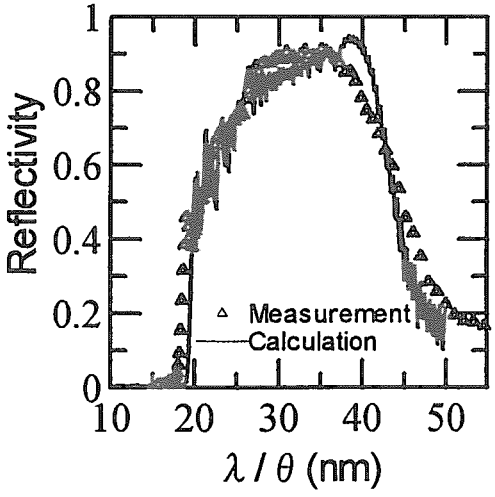

Figure 2 Measured and calculated neutron reflectivities

研究テーマ：冷中性子磁気光学系の基礎研究

表題：化合物レンズの開発と四重極磁石の磁気プリズム機能の評価

1-9-10

Development of Compound refractive optics and evaluation of a quadrupole magnet as a neutron prism.

T. Oku, S. Morita, S. Moriyasu, Y. Yamagata, S. Ohmori, H.M. Shimizu, T. Hirota[1], Y. Kiyanagi[1], T. Ino[2], M. Furusaka[2], and J. Suzuki[3]

RIKEN, 2-1 Hirosawa, Wako, Saitama 351-0198, Japan
[1]Hokkaido University, Sapporo 060-8628, Japan
[2]Inst. of Mater. Struct. Sci., High Energy Accel. Organ., 1-1 Oho, Tsukuba, Ibaraki 305-0801, Japan
[3]Japan Atomic Energy Research Institute, Tokai, Ibaraki 319-1195, Japan

Neutron scattering method is essential in a study of internal structure and dynamics of material due to the exclusive nature of a neutron. However, owing to the extremely low intensity of the neutron beam compared with the synchrotron-radiation photoemission, it can be restrictedly applied. To improve this situation, we have been developing neutron optical devices based on neutron refractive optics, such as a neutron lens and a neutron prism. In this study, we have developed compound refractive lens for cold neutrons and evaluated the function of a quadrupole magnet as a neutron prism.

So far, the result of a neutron beam focusing experiment using MgF_2 compound refractive lens (CRL) which has symmetric concave shape was reported [1]. In their experiment, the neutron intensity gain of over 30 was obtained. However, the neutron transmission is drastically decreased with increasing the neutron beam size due to the lens shape, i.e., the effective lens thickness increases with the neutron beam size. To overcome this problem, we have developed a fresnel lens for neutrons which is made from vitreous silica with effective potential of $(90.1–2.7\times10^{-4}i)$ neV. This lens was grinded out from a vitreous silica disk using Electrolytic In-Process Dressing (ELID) Grinding Technique [2]. The cross section of the lens is depicted in Fig.1. The surface roughness R_y of the lens was measured to be less than 0.1μm. The lens was investigated with cold neutrons using a neutron spectrometer SANS-J installed at JRR-3M of JAERI. The experimental setup is shown in Fig.2. To evaluate performance of the lens accurately, the neutron beam collimated by a slit with 1mmϕ pinhole was employed, and the neutron intensity distribution on the surface of the 2d-PSD was measured with shifting the lens position, X_{lens}, perpendicular to the neutron beam. Fig.3 shows the intensity distribution along the x-axis on the surface of 2d-PSD. The peak shifts of the intensity distribution was observed as the lens shifts away from the center position. This indicates that the neutron beam is refracted by the passage through the lenses, and

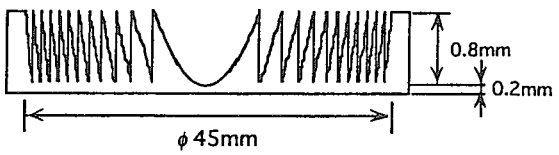

Fig. 1 Cross section of vitreous silica fresnel lens.

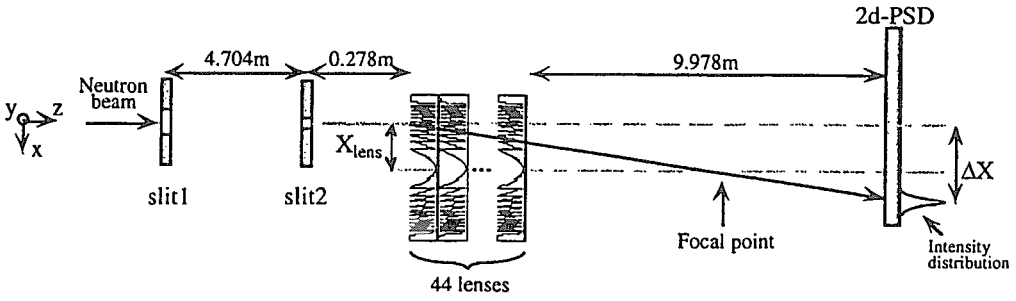

Fig. 2 Experimental setup: Slit 1 and 2 have pinholes with 7 and 1 mmϕ, respectively.

原子炉：JRR-3M　　装置：SANS-J(C3-2)　　分野：中性子散乱(装置)

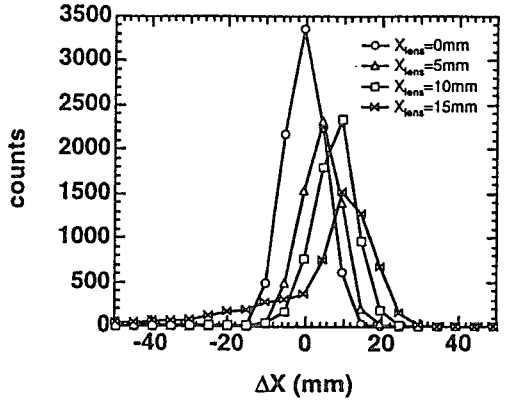

Fig.3. Horizontal intensity distribution on the surface of the 2d-PSD.

the focal length was estimated to be 14m for 10Å neutrons. Also, relatively large neutron transmission of 64% is obtained even for 40mm beam size at neutron wavelength λ=10Å resulting from the shape. It is expected that the compound refractive lens which has aperture and refracting power large enough for practical use can be realized by selecting the lens shape and material.

In the quadrupole field given by $|B|=C_Q(x^2+y^2)^{1/2}$, neutrons are accelerated following the equations: $d^2x/d\theta^2=\mp x\rho_0/(x^2+y^2)^{1/2}$, $d^2y/d\theta^2=\mp y\rho_0/(x^2+y^2)^{1/2}$ for positive and negative spin polarity, where $\theta=\omega t$, $\omega^2=|C_Q\mu/ml/\rho_0$ and ρ_0 is the radius of the quadrupole magnet aperture. In the special case of y=0, the equation is simplified as $d^2x/d\theta^2=\mp\rho_0$, which clearly visualizes a prism function according to the constant acceleration.

We have constructed a permanent quadrupole magnet with ρ_0 = 3.5 mm[3]. The strength of the magnetic field was $\omega \sim 480\ s^{-1}$. We measured

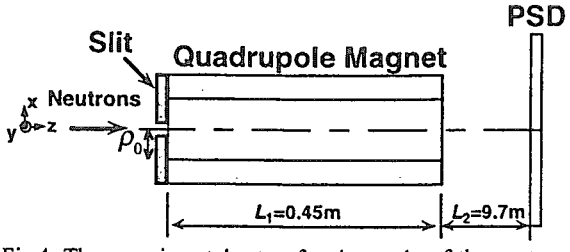

Fig.4. The experimental setup for the study of the neutron prism.

the prism function of the quadrupole magnet using cold neutrons from a reactor neutron source JRR-3M of JAERI. The neutron has the wavelength resolution of $\Delta\lambda/\lambda=0.129$. The length of the quadrupole magnet was L_1 = 0.45m and the distance between the magnet and the position sensitive detector (PSD) was L_2 = 9.7 m as shown in Fig.4. A two-dimensional neutron image obtained by the PSD is shown in Fig.5 (a) and (b). The neutrons are split into two regions due to the spin selectivity of the prism. The experimental image was well reproduced by the numerical calculation with a collimator misalignment of (x, y)=(-1.0 mm, -0.45 mm) as shown in Fig.5(c) and (d).

The prism with PSD is capable to analyze the neutron energy and is applicable to inelastic scattering instruments using pulsed neutrons. With a non-monochromatic neutron beam, all components of incident and scattered momentum vectors can be measured by tracing back the arrival time of incident neutrons from the timing of PSD signals. A favorable energy resolution can be achieved in a wide range of energy transfers using a highly collimated incoming beam and a PSD with good position and time resolution.

References

[1] M.R. Eskildsen et al., Nature 391 (1998) 563.
[2] H. Ohmori, Int. J. Japan Soc. Prec. Eng., Vol.26, No.4 (1992) 273.
[3] T. Oku et al., Physica B, 276-278 (2000) 112.

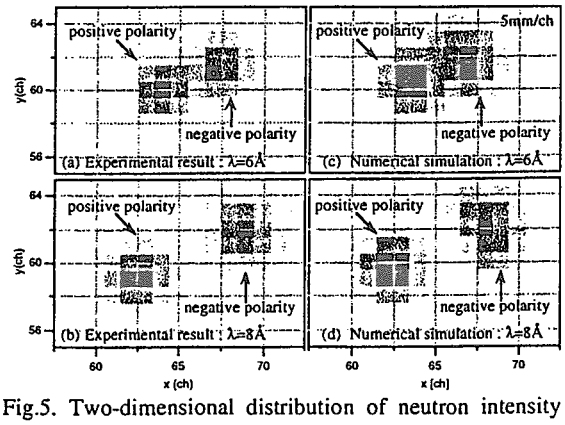

Fig.5. Two-dimensional distribution of neutron intensity at the surface of the 2d-PSD:(a),(b):experimental result, (c),(d):numerical simulation

研究テーマ:冷中性子磁気光学系の基礎研究
表題:冷中性子シンチレーション画像検出器

1-9-11 Cold neutron imaging detector with two scintillator

F. Tokanai, T. Oku, K. Morimoto, H. M. Shimizu, J. Suzuki[1], T. Ino[2], T. Ikeda, W. Ootani, C. Otani, H. Sato, Y. Kiyanagi[3], T. Hirora[3], K. Kuroda[4], A. Riazantsev[3]

RIKEN , Hirosawa, Wako, Saitama 351-0198, Japan.
[1]Japan Atomic Energy Research Institute, Shirane, Tokai, Naka, Ibaraki 319-1195, Japan
[2]Institute of Materials Structure Science High Energy Accelerator Research Organization
KEK, Oho, Tsukuba, Ibaraki 305 -0801, Japan
[3]Faculty of Engineering, Hokkaido University, Sapporo 060-8628, Japan
[4]CERN Div. EP, 1277 Geneva 23 Switzerland

Recently, the project of spallation neutron source has been started in Japan, Europe and the United States aiming at starting operations at the beginning of the 21st century. Neutron imaging detector for the spallation neutron source will be required large area with good position information, high detection efficiency, and fast response for timing information on individual neutron signals or for counting neutrons at a high counting rate. We are currently developing two cold neutron imaging detector based on GSO scintillator and ZnS scintillator coupled to wave-length shifting fiber. In this report, the progress of these detector will be presented.

Cerium-doped Gd_2SiO_5 (GSO) [1] contains Gd in the compound and has potential application as an efficient neutron detector due to the very large neutron absorption cross section of Gd amounting to 49700 b. The absorption cross section of Gd comprises 61100 b for ^{155}Gd (14.8% abundance) and 259000 b for ^{157}Gd (15.7%). The neutron absorption reactions by ^{155}Gd and ^{157}Gd produce conversion electrons with energy ranging from 30 keV to 250 keV and γ-rays up to 2 MeV through the cascade of deexcitation of the excited ^{156}Gd and ^{158}Gd. Thus, Gd and the its compounds have been applied to neutron radiography as a versatile neutron converter for neutron imaging plates and as a Si-based neutron detector. Therefore, a thin GSO crystal is sufficient to absorb slow neutrons which enables the influence of background γ-ray signals to be suppressed. In addition, GSO has a short decay time constant of 60 nsec which are suitable for measuring the arrival time of individual neutrons from a pulsed neutron source at a high counting rate and with a good signal-to-noise ratio. However, only a few attempts have been reported on the detection of cold neutrons with a GSO scintillator.

We investigated the characteristics of a GSO scintillator by using a cold neutron beam at the C3−2 beamline of the JRR-3M research reactor of JAERI. The wavelength of incident cold neutrons was 6 Å with a wavelength resolution of 13.5% (FWHM). A GSO crystal of 50 mm × 50 mm × 0.5 mm was attached with optical grease to a 2 inch diameter Hamamatsu H1949-50 photomultiplier tube (PMT). The GSO crystal had a Ce concentration of 0.5%mol provided by Hitachi Chemical Co. Ltd. The obtained pulse height spectrum of 0.5 mm thick GSO scintillator is indicated as 'Neutron On' in Fig. 1. The 31 keV and 81 keV peaks resulting from neutron absorption by Gd nuclei were identified in the pulse height spectrum by using a photomultiplier tube.

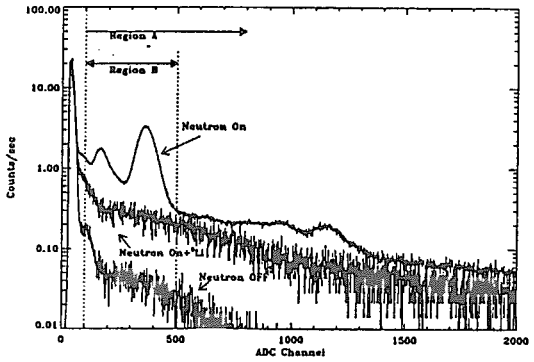

Figure 1: Pulse height spectrum of GSO for 6Å cold neutrons which is labeled as 'Neutron On'. he background spectrum from the beam line and the intrinsic background spectrum are respectively labeled as 'Neutron On + ^6Li' and 'Neutron Off'.

Imaging capability was studied by using an image intensifier with a CCD camera H4693FCCD). Figure 2 shows the neutron image obtained for neutron beams defined by LiF collimator of 1 mm with an image intensifier and viewed by a CCD camera. Image of 1.5 mm in diameter were observed for 1 mm diameter incident beams with corresponding to a position resolution of 1.3 mm (FWHM). A better position resolution can be achieved by employing a thinner GSO scintillator (see more detail reference 2).

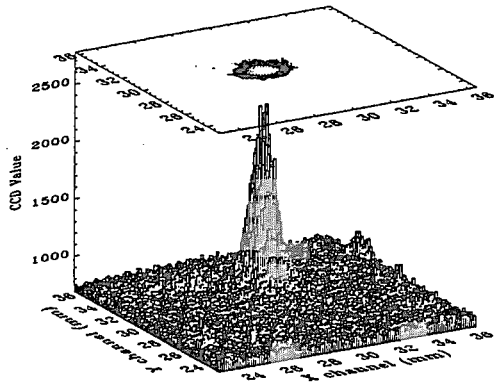

Figure 2: Two-dimensional image of the 1 mm diameter neutron beam obtained with a 0.5 mm thick GSO and an image intensifier with a CCD camera.

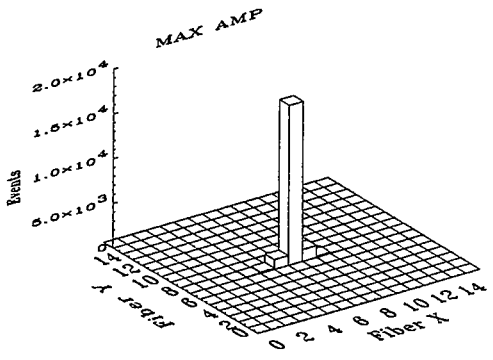

Figure 4: Two-dimensional image of the 1 mm diameter neutron beam obtained with a WLS fiber + ZnS scintillator detector. 1 bin is corresponding to 1mm.

Other neutron imaging detector was firstly developed by Kuroda[3]. It consists of a ZnS(Ag)^{6}Li scintillator of 20 mm × 20 mm × 0.5 mm (Bicron BC-704) and 16 wave-length shifting (WLS) fibers optically glued onto the up- and down-sides. The arrays were placed in orthogonal directions to supply two dimensional readout. The WLS fibers (Kuraray Y11) cross-section are 1 mm × 1mm , far ends were covered with Al mirror. The WLS fibers were attached with optical grease to a Hamamatsu H6568 16-channel multi-anode photomultiplier tube (MAPMT). Figures 3 shows the imaging detector.

The performance of the neutron imager was investigated by using a cold neutron beam at the C3−2 beamline of the JRR-3M research reactor of JAERI. The wavelength of incident cold neutrons was 10 Å with a wavelength resolution of 12.9% (FWHM). The last dynode signals from MAPMTs in X and Y planes were sent to standard discriminators with a threshold low enough to recored single photoelectrons. The total charge of the individual output signals from the MAPMT was analyzed with a charge-sensitive ADC device (LeCroy 2249W) with a logic gate of 400 nsec width, and data were accumulated event by event through a CAMAC bus in a personal computer. Total number of the readout channels was 34 (X:16 anodes, Y:16 anodes, 2 last dynodes). The dead time of the data acquisition system was 400 μs on average.

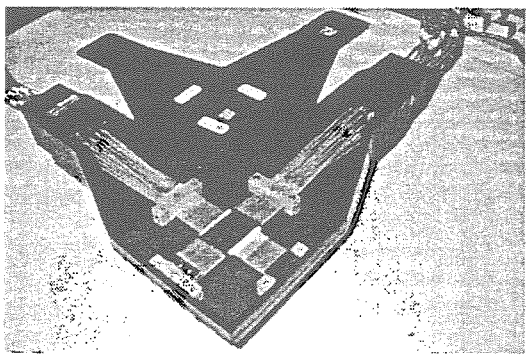

Figure 3: Neutron imaging detector with WLS fiber + ZnS scintillator.

Figure 4 shows the neutron image obtained for neutron beams defined by a 1 mm diameter cadmium collimator. Hit position of a cold neutron was determined by the applying the maximum amplitude algorithm on the anode signals. We obtained the position resolution of 1 mm (FWHM). The measured detection efficiency was about 56%. In order to estimate the neutron absorption in a fiber array, we measured the count rates with and without the fiber layer in front of a conventional ^{3}He proportional counter. The measured neutron absorption was about 38%. Taking into account the neutron absorption, the measured detection efficiency is almost consistent with the calculated efficiency.

We are developing a very large neutron imaging detector with a ZnS(Ag)^{6}Li scintillator of 100 mm × 100 mm × 0.5 mm and 256 WLS fiber (cross sectuion of 0.5 mm × 0.5 mm).

References

1) K. Takagi and T. Fukazawa, Appl. Phys. Lett., 42, (1983), 43

2) F. Tokanai, K. Morimoto, T. Oku, J. Suzuki, T. Ino, W. Ootani, C. Otani, H. Sato, H.M. Shimizu, Y. Kiyanagi, T. Hirota, Nucl. Instr. and Meth. A to be published.

3) K. Kuroda and I. Manuilov., Nucl. Instr. and Meth. A, 430, (1999), 311

1. 中性子散乱 10) その他

1. Neutron Scattering 10) Others

This is a blank page.

研究テーマ：中性子回折による残留応力測定
表題：中性子イメージングプレートを用いた中性子応力測定

1-10-1 Neutron Stress Measurement using Neutron Image Plate

T.Sasaki[1], N.Minakawa[2], Y.Morii[2], N.Niimura[2] and Y.Hirose[1]

[1]Kanazawa University, Kanazawa, Ishikawa 920-1192, Japan
[2]Japan Atomic Energy Research Institute, Tokai, Ibaraki 319-1195, Japan

A neutron image plate (NIP) was developed recently as an area detector for the neutron experiment. It is possible to obtain strains along the line in the material where neutron beams penetrate analyzing a Debye-Scherrer ring recorded on a NIP. The diffraction ring contains continuous strains with different orientations, so that the depth profile of stress can be determined more correctly as well as quickly than the ordinary method. In this study, we investigate the fundamental possibility of the NIP for the stress measurement.

The neutron experiment was conducted using the reactor named JRR-3M at the Japan Atomic Energy Research Institute (JAERI). Thermal neutrons derived from the reactor pass through the guide tube which is made from glass coated with nickel thin film, and was monochromated by 002 diffraction of pyrolytic graphite to the wave length of 0.20888 nm. There is a 2000 mm length flight tube made from aluminum after the monochrometer. A slit made from B_4C rubber having a hole of the diameter of 10 mm was put at the entrance of the flight tube, and another slit made from cadmium of the diameter of 3 mm was put at the exit. The NIP enwrapped in black paper was put into a cassette which was covered with both an aluminum plate (1 mm thickness) and a lead plate (1 mm thickness). The cassette, placed normal to the beam, has a hole at its center so the neutron beam can pass through. The specimen was put after the NIP. The distance between the NIP and the specimen was 65 mm. The incidence angle of the neutron beams to the specimen was 20 degree.

The specimen used for the neutron experiment was steel (JIS S50C) with a thickness of 2 mm. Mean grain size of the specimen was 10 μm. Main neutron diffraction conditions were as follows: wave length of neutron 0.20888 nm, diffraction plane Fe-211, diffraction angle 2θ =127 deg., incident angle of neutron beam to the specimen 24 deg, diameter of neutron beam about 3 mm, exposure time 2 hours. The specimen was applied tensile strains of 0, 400 and 800 ($\times 10^{-6}$) respectively. Strain in the specimen was monitored with a strain gauge attached. Applied stress was calculated by multiplying the Young's modulus (206 GPa) to the strain.

The NIP used had a rectangular shape with the dimensions of 250 mm×200 mm. The intensity of the diffracted neutron stored in NIP was read out under the condition of 100 μm for space resolution and 8 bit for intensity resolution, and saved in the computer. The fundamental image processing was conducted using the software made by Fuji Film Co., which was however not sufficient for the stress analysis. So new software was developed for the stress analysis in this study.

A steel plate was used for determining the position of the incident neutron beams on NIP, assuming its Debye-Scherrer ring as a circle. The diffraction pattern of the plate was double exposed on NIP by putting the plate at the position between NIP and the specimen. The distance between the plate and NIP was 35 mm.

Since the diffraction profile obtained from NIP is a superposition of diffracted neutron beams from a wide range of the depth, the stress calculation should be conducted considering the effect of the neutron beams diffracted inside of the specimen. However, such a method has not been proposed yet. So the method which has been used for the X-ray image plate (XIP) was used in this study (ref [1][2]). The result will show limits and effectiveness of the theory used in the X-ray stress analysis.

The diffraction image data was analyzed on the computer with the diffraction profile in the direction of the radius of the ring calculated for the whole ring, from which the radii of the ring and the strain were

determined. This calculation was conducted by 1 degree step of the central angle, and 360 strains were obtained from each Debye-Scherrer ring. Finally, the stress was calculated according to the method shown in the previous section. The stress which was obtained from the specimen was compared with the theoretical one which was calculated with applied strain and Young's modulus. It was seen that the stress obtained by the present method almost agrees with the theoretical value. The result shows that it is possible to determine mean stress in the material with neutron diffraction using a NIP. Fig.1 shows the distribution of radii obtained from the Debye-Scherrer ring as a function of the central angle. Plots in the figure indicate the result obtained with NIP, and the curved line indicates the result recalculated by the present method using the stress obtained from the experiment. The result shows a similar tendency in macroscopic view in case of the applied strain of 800×10^{-6}, but a larger difference can be seen at the other strain levels. Since the calculation of the stress and the recalculation of the radius on the diffraction ring were conducted using the equations based on the X-ray stress measurement, the effect of the beams diffracted at the deeper place in the specimen was not considered. As the neutron diffracted beams can emerge from deeper in the specimen than X-rays, the diffraction profile is influenced by them more severely. In the case of the small specimen, a part of the diffracted beam can pass through the side face of the specimen. Since these beams are absorbed by the material slightly, they deform the shape of the diffraction profile on NIP, which leads to the shift of the peak position as shown in Fig.6. A similar phenomena can occur in the Cu plate, which results in the error at the determination of the center position of the diffraction ring on NIP images. This error can have influence on the determination of the radius of the diffraction ring.

Another new experiment has been conducted after this experiment by improving some experimental conditions used in this study. Although the data has not yet been analyzed completely, some good results have been seen.

Though the experiment was performed in a uniaxial and uniform stress state, most materials

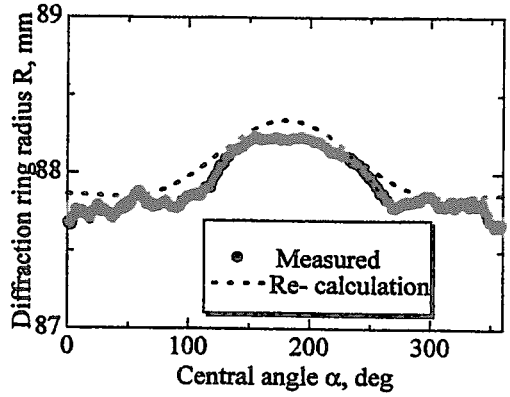

Fig.1 Plots of radius of the Debye-Scherre ring vs. central angle. Curved line indicates recalculated results using stress measured.

have generally a multiaxial stress state as well as nonlinear depth profile inside the body. So the method need to be modified to cope with these situation at the next stage. The theoretical proposal and the verification for this problem have already been done in the X-ray range using XIP. (see ref[1]-[3])

References

[1] T. Sasaki and Y. Hirose, J. Soc. Mat. Sci., Japan, vol.44, No.504 (1995) 1138-1143.
[2] T. Sasaki and Y. Hirose, Trans. Japan Soc. Mech. Eng., vol.61, No.590, A, (1995) 2288-2295.
[3] T. Sasaki, Y. Hirose and S. Yasukawa, Trans. Japan Soc. Mech. Eng., vol.63, No.607, A, (1997) 533-541.
[4] T. Sasaki and Y. Hirose, Trans. Japan Soc. Mech. Eng., vol.63, No.606, A, (1995) 370-377.
[5] T. Sasaki and Y. Hirose, Trans. Japan Soc. Mech. Eng., vol.63, No.614, A, (1997) 2196-2204.

研究テーマ：中性子回折による残留応力測定研究
表題：ガラス基盤上に蒸着したCu薄膜における中性子応力測定の試み

1-10-2

Trial of Neutron Measurement of Stress in Cu Film Deposited on Glass Substrate

M. Nishida , T. Hanabusa[1] and N. Minakawa[2]

Kobe City College of Technology, Kobe 651-2194, Japan
[1] Faculty of Engineering, Tokushima University, Tokushima 770-8506, Japan
[2] Japan Atomic Energy Research Institute, Tokai, Ibaraki 319-1195, Japan

Recently, a variety of functional materials are vigorously developing in industrial fields. In mechanical as well as electrical field, diverse thin solid films are built on several kind of substrates. Multi-layer structure is also developed so as to bring out several functions. In these cases, development of residual stresses in the films is essential because of different mechanical and physical properties between the substrate and the film as well as among the layers. If residual stress becomes very large, the film may be destroyed and/or the characteristics of the film may change by the residual stress itself. Therefore, it is important to evaluate the behavior of residual stresses in the films in order to ensure a reliable function of the film structurs. The X-ray stress measurement technique has been applied to measure residual stresses in thin films. However, in the case of laminated films, residual stresses may not be able to measure because of a shallow penetration depth of X-rays. On the other hand, the penetration depth of neutron is much higher than X-rays. Therefore, the stresses in the sub-surface layers might be possible to meaure.

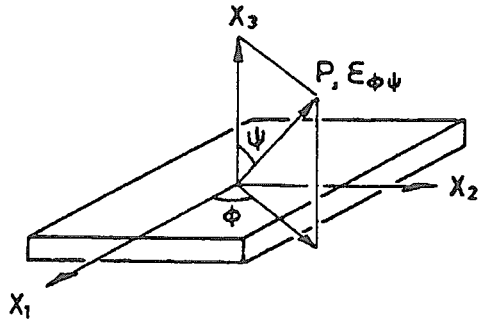

Fig. 1 Coordinate system for neutron stress measurement.

The present investigation is the first trial of measuring the stress in thin films by neutron diffraction.

This investigation made the measurement of residual stress in the Cu film deposited on a glass substrate and confirmed a possibility of the stress mesurement by neutron diffraction.

Cu thin films spattered on glass substrate were used in this investigation. Figure 1 shows a specimen coordinate system. We assume in this experiment that the state of residual stress in Cu film is an equi-biaxial, because the film is a mono-layered thin structure. In this case, the stress strain relation is considered as follows. The normal lattice strain $\varepsilon_{\phi\psi}$ in the direction defined by the angles ϕ and ψ is written as folows:

$$\varepsilon_{\phi\psi} = \frac{1+\nu}{E}\sigma \sin^2\psi - \frac{2\nu}{E}\sigma . \qquad (1)$$

Since $\varepsilon_{\phi\psi}$ is linearly related to $\sin^2\psi$, residual stress σ can be calculated from the slope of the straight line in $\varepsilon_{\phi\psi}$ - $\sin^2\psi$ relation. However, the present Cu film exhibits a high {111} preffered orientation so that the conventional $\sin^2\psi$ method cannot be applied. Therefore, the following equation[1)] is used to evaluate stress in the film, i.e., the two-exposure measurement (ψ=0°, 70.53°) was applied:

$$\sigma = \frac{E}{1+\nu}\,\frac{\varepsilon(\psi_1) - \varepsilon(\psi_2)}{\sin^2\psi_1 - \sin^2\psi_2} \qquad (2)$$

From the results of neutron measurement, the measurable peak was 111 diffraction appeared at 2θ =60.1° in the "RESA" system. For the diffraction of low Bragg angle, the Ψ

原子炉：ＪＲＲ－３Ｍ　　装置：RESA（T2-1）　　分野：中性子散乱（その他）

- diffractometer method must be used in order to get the diffraction at large ϕ - angle. However, in a case of neutron diffraction, the glass substrate transmits the neutron beam very easily. Therefore, the Ω -diffractometer method can be used in the neutron stress measurement. Table 1 shows material parameters of Cu and measurement conditions.

Table1 Material parameters and measurement conditions.

Diffraction plate	Cu 111
Diffraction angle (deg.)	$2\theta = 60.1$
ϕ angle (deg.)	0, 70.53
Young's modulus E (GPa)	136
Poison's ratio ν	0.3
Neutron wave length λ (nm)	0.2091102

Before the stress measurement, the neutron diffraction pattern from 111 plane of Cu powder was measured. From this profile, a lattice spacing in stress free state is determined as do = 0.20869 nm. Since this value agrees very well with the hand book data, a considerable precision is expected in this investigation.

Figure 2 shows the rocking curve of 111 diffraction for the Cu film. This measurement was made of θ -scanning under the conditions of fixed 2θ angle at 60.149° . It can be seen from this result that the diffraction peak exists in the range of ± 10 degrees. Furthermore, it was identified that a orientation gap of about +3° exists against the normal of the substrate surface.

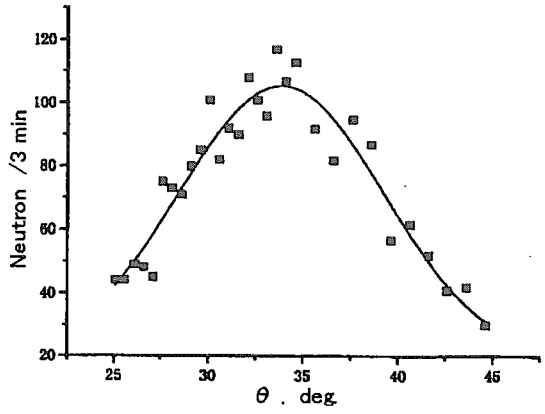

Fig. 2 Rocking curve of 111 plane in Cu film.

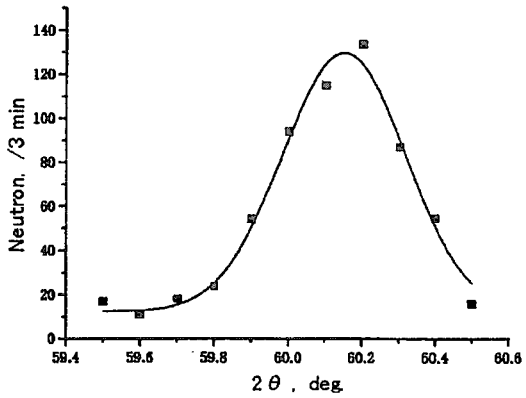

Fig. 3 Diffraction pattern of Cu film (ϕ =0).

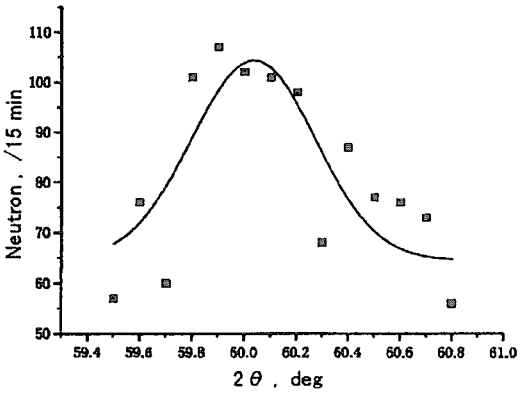

Fig. 4 Diffraction pattern of Cu film (ϕ =70.53°).

Figures 3 and 4 show the neutron diffraction patterns measured from the Cu 111 at the angles ϕ =0° and 70.53°, respectively. From these diffraction profiles the 2θ values were determined as:

$$2\theta_{(\phi=0^\circ)} = 60.150^\circ$$
$$2\theta_{(\phi=70.53^\circ)} = 60.034^\circ$$

and the stress in the film was evaluated by Eq. (2) as:

$$\sigma = 206 \text{ (MPa)}.$$

Form the above discussion, the neutron stress measurement method can be applied for the stress measurement of thin Cu film.

Reference

[1] T.Matsue et al., J. Soc. Mat. Sci., Japan, Vol. 44, No.504 (1995) 1121-1126.

研究テーマ：中性子回折による残留応力測定
表題：中性子回折による A7075 の弾性定数測定

1-10-3 Measurement of Elastic Constant of A7075 in Neutron Diffraction

T.Saito[1,2], N.Minakawa[2], Y.Morii[2]

[1]Department of Material Science & Engineering, Kanazawa University, Kanazawa, Ishikawa 920-1192, Japan
[2]Japan Atomic Energy Research Institute, Tokai, Ibaraki 319-1195, Japan

Residual stress in material has been frequently measured by neutron diffraction method. In the residual stress measurement by the neutron diffraction method, the strain on various diffraction planes should be measured. The stress can be obtained by using Hooke's law from the strain arises when material is deformed. In the neutron diffraction method, the stress can be calculated from the strain for three axial directions.

$$\sigma_{R,H,A} = \frac{E}{1+\nu}\left[\varepsilon_{R,H,A} + \frac{\nu}{1-2\nu}\left(\varepsilon_R + \varepsilon_H + \varepsilon_A\right)\right]$$

The elastic constant is necessary to convert this strain into the stress. E is Young's modulus, and ν is Poison's ratio.

Purposing of this experiment is to make the data bank of this elastic constant. Then, the elastic constant for Al(111), (200) and (220) of A7075 was calculated in this experiment. In the measurement a small tensile specimen was loaded in the tensile test rig specially designed for a neutron diffractometer. To calculate the elastic constant, the strain on two kinds of diffraction planes should be measured. That is, when the load is given to the sample, the strain of the expanding lattice spacing and the shrinking lattice spacing should be measured. This state is shown in Fig.1(a) and (b). The expanding lattice spacing is measured in (a). Fig.2 shows the peak position of the diffraction profile against the stress. The peak position shifts to the low angle in the lattice spacing of the expansion. The peak position shifts to the high angle in the lattice spacing of shrinking. The shrinking lattice spacing is measured in (b). Fig.3 shows the strain against each load for A7075. The slope of the approximation straight line of the expanding strain is E in these graphs. Moreover, ν is a ratio for the slope of the approximation straight line of the expansion and shrinking.

The elastic constant in each diffraction plane which had been as mentioned above calculated by the neutron diffraction method was able to be calculated.

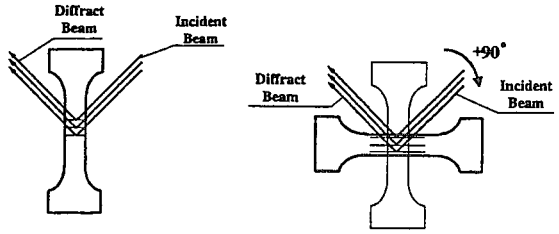

(a) expanding (b) shrinking

Fig. 1. Scattering geometries for measurement of two components of lattice strain

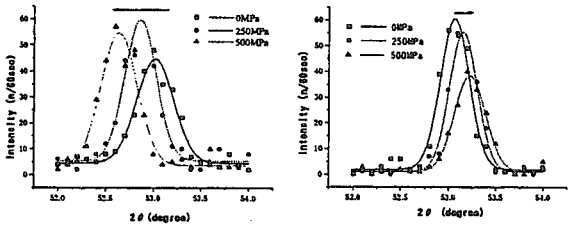

(a) expanding (b) shrinking

Fig. 2. Peak position of diffraction profile against stress for Al(111).

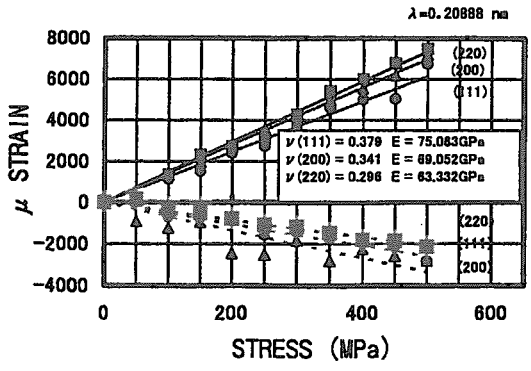

Fig. 3. Relation between stress and strain for A7075.

研究テーマ：中性子回折による構造物の残留応力測定
表　　題：中性子回折法による摩擦圧接界面の残留応力測定

1-10-4 Residual stress measurement of friction welding boundary by neutron diffraction method

S.Okido, M.Hayashi, Y.Morii[1], N.Minakawa[1]

Mechanical Engineering Research Laboratory, Hitachi Ltd. Hitachi, Ibaraki 317-8511
[1]ASRC, JAERI, Tokai, Ibaraki 319-1195

The friction welding is the bonding method which uses the friction heat generating in the rotation of two contacted components under the load. This method is used widely in the fields of automobile, industrial machine and so on, since it can weld the different materials. However, high residual stress is expected to generate at the welding boundary through the heat history in the welding process. In this study, the neutron diffraction method is applied to measure the residual stress, and the mechanism of residual stress initiation at the bonding boundary is discussed.

SS400 carbon steel bar and Type 304 stainless steel one were bonded by friction welding. The diameter and length of each bar were 25mm and 100mm. The welding was performed in the conditions that the rotating velocity was 1200 rpm, the friction pressure was 59 MPa, and the upset pressure and time was 118 MPa and 10 sec.

RESA (REsidual Stress Analyzer) at JRR-3M, which is operated by JAERI (Japan Atomic Energy Research Institute), was used for the measurement of the lattice strain. The 110 diffraction for SS400 and the 111 diffraction for type 304 were measured. The wavelength λ of the used monochromatic neutron beam was 0.208872nm. The measurement was performed at 1, 3, 5, 8, 15 and 30 mm from the welding boundary in the center and at the surface of bar. The sampling volume in each measurement was a 2mm width and 4mm height in parallel to the boundary. The strain measured by neutron diffraction was converted to the stress using E=165GPa, Poisson's ratio=0.16 for SS400 obtained from the calculation for the mono-crystal model, and E=231 GPa, Poisson's ratio=0.19 for Type 304 obtained by literature quotation.

The obtained residual stresses in the vicinity of the boundary for both materials were shown in Fig.1. The residual stress showed compressive about 300 MPa at the surface and tensile about 200 MPa in the center of the specimen. The difference of circumferential velocity makes the higher temperature rise at the surface than in the center. However the heat radiation in the cooling process makes the temperature at surface lower rather than that of the center. The result of neutron diffraction measurement means that the residual stresses generate in the cooling process after up-set process.

The residual stresses abruptly decrease in the 5mm region from the boundary for SS400 and 10 mm for type 304. These differences of residual stress distribution are attributed to the effects of the heat conductivity, since the heat conductivity is 47.2 W/m/K for SS400, and is 19.0 W/m/K for Type 304 stainless Steel.

In this report, the mechanism of residual stress generation at the bonding boundary is discussed. The residual stresses generate in the cooling process after up-set process, and the differences of residual stress distribution are attributed to the effects of the heat conductivity.

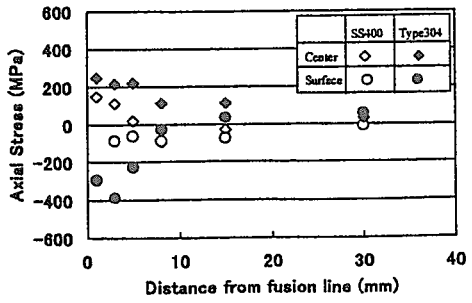

Fig.1 Residual stress distribution around the friction welding.

原子炉：JRR-3M　　装置：RESA(T2-1)　　分野：中性子散乱（その他）

研究テーマ：超電導磁石に関する研究

表　題　：構造材料における残留応力再分配挙動の中性子回折測定

1-10-5

Measurement of Residual Stress Redistribution for Structural Material by Neutron Diffraction

Y. Tsuchiya, K. Kikuchi[1], N. Minakawa[2], Y. Morii[2], T. Kato, H. Nakajima and H. Tsuji

Naka Fusion Research Establishment, Japan Atomic Energy Research Institute, Ibaraki 311-0193 Japan
[1] Center for Neutron Science, Japan Atomic Energy Research Institute, Ibaraki 319-1195 Japan
[2]Advanced Science Research Center, Japan Atomic Energy Research Institute, Ibaraki 319-1195 Japan

A machining introduces a residual stress and produces a redistribution of the residual stress to a material. Estimation of the residual stress for industrial material at each step of processes is required for preventing some problems such as stress-induced cracking. In this study, the residual stress redistribution that was brought by a bending processing of a conduit material was measured by neutron diffraction using a neutron diffractometer for the residual stress analysis, RESA, installed at the research reactor JRR-3M guide hall.

The sample is a round-hollowed conduit of INCOLOY908 alloy for a superconducting coil. INCOLOY908 is a nickel-iron based alloy and it shows fcc single phase. The conduit has been compressed by 5% to the radial direction by cold rolling. After the rolling, the conduit has a square cross section of 46 × 46 mm^2 and an inner diameter of 37 mm. For the neutron diffraction measurement, the conduit was cut in length of 150 mm. Then the compressed conduit was bent in radius of 500 mm by a triple-roll bender at room temperature. A sampling volume was adjusted for the size of 2 × 2 × 4 mm^3 by the cadmium slits. The sampling volume was located at every 1 mm in depth from the sample surface to the radial direction. The measurement position was the center of the conduit sample as illustrated in figure 1. The thickness of the conduit is 4.5 mm at the measurement position. The wavelength of the incident neutron beam used was 2.07 - 2.08 Å. The reflection of (111) plane was used for the measurement. The data acquisition time was set 2 to 8 hours for a spectrum. The elastic constants that were evaluated by the neutron diffraction measurement under tension load were used for a calculation of the residual stress. The Young's modulus was 195 GPa and the Poisson's ratio was 0.26 for the (111) plane of INCOLOY 908 alloy.

Figure 1 shows the axial residual stress distribution at the inside position of the bent conduit as a function of the depth from the outer surface of the conduit. The triangles indicate the residual stress and the solid line shows the distribution of the as-compressed straight sample in the figure. The axial residual stresses were observed tension on the all measurement point at the inside of bent sample. The axial residual stress reveals the largest value of 220 MPa of tension at the outer surface. The tensile stress decreases gently with the depth of sample and became 65 MPa at 3 mm in depth.

While, the residual stress of the as-compressed straight sample shows a large distribution from tension to compression. These result shows that the initial large residual stress tends to relax by the bending processing of the conduit.

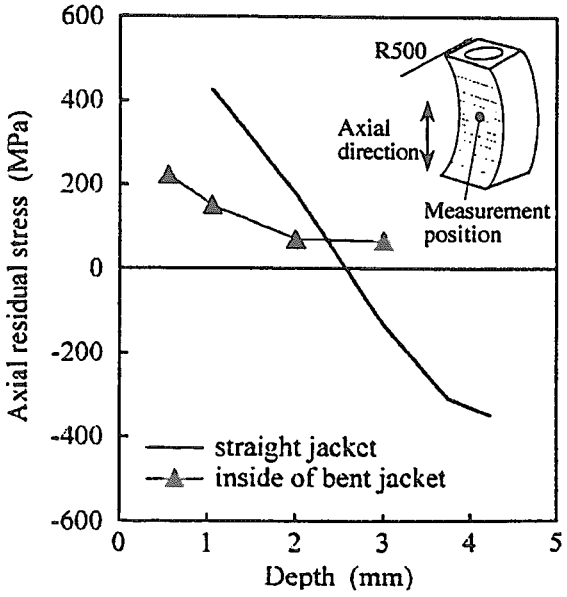

Fig 1. The redistribution of the axial residual stress of the conduit material after bending process.

原子炉：JRR-3M　　装置：RESA(T2-1)　　分野：中性子散乱（その他）

研究テーマ：超低温の導入による中性子散乱の研究

表題：$Ti_{50}Ni_{30}Cu_{20}$合金におけるマルテンサイト変態の前駆段階の phonon 分散関係

1-10-6

Phonon Dispersion of $Ti_{50}Ni_{30}Cu_{20}$ Prior to B2-B19 Martensitic Transformation

X. Ren, K. Taniwaki, N. Miura, M. Inami, J. Zhang, K. Otsuka, Y. Morii[1], Yu.I. Chumlyakov[2]

Institute of Materials Science, University of Tsukuba, Tsukuba, Ibaraki 305-8573, Japan

1. Japan Atomic Energy Research Institute, Tokai, Ibaraki 319-1195, Japan

2. Siberian Physical Technical Institute, Tomsk 634050, Russia

Point defects and alloying elements can greatly alter many aspects of martensitic transformation. The most well known effect is the great change in transition temperature and even in the structure of transformation product with alloying addition or quench (which introduces point defects). Another effect is the martensite aging effect, which causes interesting rubber-like pseudo-elasticity [1] and two-way shape memory [2]. The latter effect has attained a fairly clear understanding [1,2]; however, the former effect is far from being well understood. To understand these effects, a study of lattice dynamics as a function of composition is most desirable, because martensitic transformation is closely related to lattice dynamics. Our recent work on TiNi-based alloys [3-5] revealed some interesting aspects of the composition dependence of elastic constants prior to martensitic transformation. These results provided some new insight into the central question about how martensitic transformation is altered by alloying addition or composition change.

Nevertheless, elastic constant measurement provides only incomplete information about lattice dynamics, because it is related only to the initial slop of the phonon dispersion curve. To obtain complete information about lattice dynamics, measurement of the whole phonon dispersion curve, especially the TA2 [110](e//[1 $\bar{1}$ 0] acoustic branch is most desirable.

In the present study, we measured the phonon dispersion relation of $Ti_{50}Ni_{30}Cu_{20}$ alloy prior to B2-B19 (cubic-orthorhombic) transformation with neutron inelastic scattering. The result is compared with the phonon dispersion of $Ti_{50}Ni_{50}$ alloys. Such a comparison may provide important insight into the nature of the composition effect on martensitic transformation.

Single crystal sample with a size of $9*9*6mm^3$ was mounted on a triple axis spectrometer TAS-2 with a temperature controlling system. The incident neutron energy was 14.7mV (wavelength 2.35A) , a PG filter was used to reduce higher order reflection, the collimations were 17'-40'-40'-40'. It should be pointed out that Ti-Ni based alloys appear to exhibit strong incoherent scattering, which makes the background very high, thus the accurate determination of peak position is difficult, especially around BZ boundary. We tried to solve this problem by sampling over a wide ΔE range for several times and determined peak position with Guassian fitting.

The main results are as follows:

(1) TA2 phonon branch exhibits a very broad dip around $0.375q_{max}$, being neither 1/3 nor 1/2 position. This dip deepens with lowering temperature toward Ms. However, it seems that it will not go to zero even at Ms temperature.

(2) The position of the dip also exhibits strong temperature dependence. It shifts towards $(1/2)q_{max}$ position with approaching Ms temperature.

(3) TA1 [100][001] branch is also low for this system, having the same feature as the binary TiNi alloy. Due to the limitation in

原子炉：JRR-3M　　装置： TAS-2 (T2-4)　　分野：中性子散乱（相転移）

machine time, we were not able to measure the temperature dependence of this branch. Nevertheless, from the elastic constant measurement, we can indirectly conclude that this branch also softens with lowering temperature [5].

Compared with the phonon dispersion of binary TiNi alloys, $Ti_{50}Ni_{30}Cu_{20}$ alloy show some similarities and dissimilarities. TiNi alloys exhibit a clear 1/3 TA2 dip and a shallow 1/2 TA2 dip [6]. The 1/3 dip is related to the trigonal R phase, while to 1/2 dip is related to the B19 phase. However, this alloy does not transform to B19 phase due to the coupling of 1/2 mode with the low TA1. The initial slope of the TA1 branch of TiNi is lower than that of $Ti_{50}Ni_{30}Cu_{20}$ alloy. This is responsible for the fact why TiNi transforms into the B19' martensite (which requires a softening in TA1 BZ center mode), while $Ti_{50}Ni_{30}Cu_{20}$ alloy transforms into B19' at much lower temperature.

From the above information, we can clearly understand why $Ti_{50}Ni_{30}Cu_{20}$ alloy does not transform into R phase. This is due to the absence of the 1/3TA2 dip. We can also understand why B19 martensite appears (which does not appear in TiNi alloys. This is due to the significant softening around 1/2 position, as well as the hardening of the TA1 BZ center mode; the first factor promotes the condensation of 1/2[110](e//[1 $\bar{1}$ 0] mode (which leads to B19) and the second factor prevents the coupling of the TA1 BZ center mode with the 1/2 TA2 mode (such a coupling leads to B19' formation). As a result, Cu addition changes the transformation path from B2-(R)-B19' for TiNi into B2-B19-B19' for $Ti_{50}Ni_{30}Cu_{20}$.

References:

1. X. Ren and K. Otsuka, Nature, 389 (1997), 6651.
2. X. Ren and K. Otsuka, Phys. Rev. Lett., 2000, in press.
3. X. Ren and K. Otsuka, Scripta Mater., 38(1998), 1669.
4. X. Ren, K. Taniwaki, K. Otsuka, T. Suzuki, K. Tanaka, Yu.I. Chumlyakow, and T. Ueki, Philo. Mag. A, 79(1999), 31.
5. X. Ren, N. Miura, J. Zhang, K. Otsuka, K. Tanaka, M. Koiwa, T. Suzuki, Yu.I. Chumlyakov, M. Asai, submitted to Mater. Sci. Eng. A, 2000.
6. P. Moine, J. Allain, and B. Renker, J. Phys. F: Met. Phys. 14 (1984), 2517.

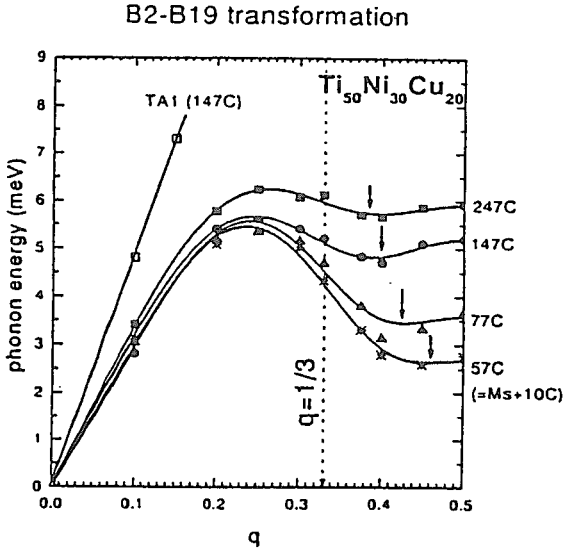

Figure 1. TA2 and TA1 phonon branch of $Ti_{50}Ni_{30}Cu_{20}$ alloy prior to B2-B19 martensitic transformation.

研究テーマ：中性子散乱による強相関電子系の研究
表題：小角散乱によるナノ結晶シリコンの構造解析

1-10-7 Structural Investigation of Nanocrystalline Silicon by Small-Angle Scattering

J. Suzuki[1], T. Matsumoto[2], Y. Masumoto[2], and M. Ohnuma[3]

[1]Advanced Science Research Center, JAERI, Tokai 319-1195, Japan
[2]Single Quantum Dot Project, ERATO, Japan Science and Technology Corporation, Tsukuba 300-2635, Japan
[3]National Research Institute for Metals Tsukuba 305-0047, Japan

Nanocrystalline porous silicon fabricated by electrochemical anodization has attracted much interest because it exhibits strong photoluminescence (PL) at room temperature [1,2]. Although a great deal of effort has been made to elucidate the origin of the PL, much uncertainty still remains due to the difficulty of physical characterization of silicon nanostructures.

We studied the nanostructures of porous silicon using small-angle scattering. Figure 1 shows scattering intensities $I(q)$ obtained from silicon nanocrystals with the porosity of p = 0.63, 0.79, and 0.87. The scattering profiles give qualitatively similar features and they can be divided into two q regions characterized by clear humps around 0.1 nm^{-1}. In the lower q region the scattering intensities gradually increase toward 0 nm^{-1}, which indicates that silicon nanocystals correlate with each other. In the higher q region, the scattering intensities obey the Porod law, *i.e.*, $I(q) \propto q^{-4}$. This well-known q dependence implies that the interface between the silicon nanocrystal and the pore shows a sharp boundary like a step function. Furthermore, we observed the porosity dependence of the scattering intensity. The decrease of the scattering volume fraction with increasing the porosity leads to the reduction of the scattering intensity in the whole q region. However, the reduction is not uniform for the whole q region. Especially, in the lower q region, the reduction is remarkable. This result suggests that in the higher porosity sample the correlation between silicon nanocrystals becomes lost.

According to a correlating polydisperse hard spherical nanocrystalline model, we determined the size distribution of nanocrystals (Fig. 2). The size distribution shifts toward the smaller radius of the silicon nanocrystal with increasing the porosity. The mean radius become 1.8, 1.36, and 1.18 nm for the porosity of p = 0.63, 0.79, and 0.87, respectively. The size estimated here is much smaller than the values determined by the Raman scattering [3] but shows similar value determined by silicon K-edge X-ray absorption measurements [4]. We report the effect of nanocrystal size on the photoluminescence elsewhere.

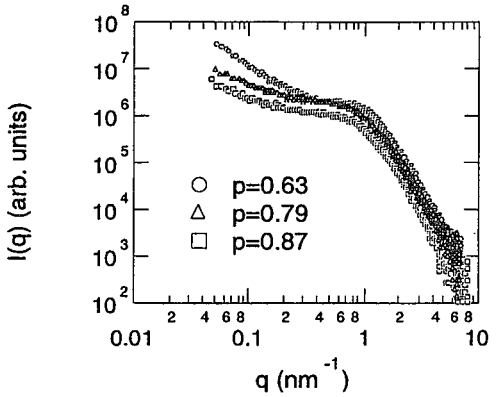

Fig. 1 Small-angle scattering from porous silicon.

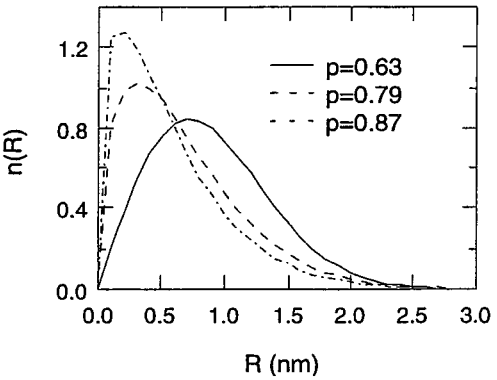

Fig. 2 Normalized size distribution function of nanocrystals in porous silicon samples.

References

[1] S. S. Iyer and Y. -H. Xie, Science **260** (1993) 40.
[2] Z. H. Lu, D. J. Lockwood, and J. –M. Baribeau, Nature **378** (1995) 258.
[3] Y. Kanemitsu, Phys. Reports 263 (1995) 15.
[4] S. Schuppler *et al.*, Phys. Rev. Lett. **72** (1994) 2648.

原子炉：JRR-3M　装置：SANS-J（C3-2）　分野：半導体

2. 中性子ラジオグラフィ

2. Neutron Radiography

This is a blank page.

研究テーマ：中性子ラジオグラフィによる沸騰二相流のボイド率計測（計測誤差評価）
表　題　　：中性子ラジオグラフィ動画法による瞬間および時間平均ボイド率の計測誤差

2-1　中性子ラジオグラフィ動画法による瞬間および時間平均ボイド率の計測誤差

呉田 昌俊、 秋本 肇
日本原子力研究所
エネルギーシステム研究部
熱流体研究グループ

当研究グループでは、中性子ラジオグラフィ（NRG）を用いて狭い流路内を流れる熱的に非平衡な沸騰流（サブクール沸騰流）を高時間分解能で可視化し、瞬間ボイド率分布および時間平均ボイド率分布を計測してきた。今年度は、NRGを熱流体計測に応用し計測されるボイド率の計測誤差を実験的、また解析的に評価する目的で基礎実験を実施した。計測誤差実験は、厚さが既知のポリスチレン板を沸騰二相流の模擬体として使用し、計測誤差を評価した。

実験は、JRR-3M 熱中性子ラジオグラフィ実験施設（TNRF-2）を利用した。計測誤差評価実験は、図1に示す沸騰二相流 NRG 実験用矩形流路（流路間隙が3mmおよび5mm、加熱長100mm、流路幅30mm、加熱幅20mm）を用い、この流路内の発熱部に厚さの異なるポリスチレン板を挿入し、NRG法で求まる厚さやボイド率と実厚さとの比較を行い、誤差を計測した。画像は、沸騰流実験と同じ条件で記録した（約1 msecの時間分解能）。

図2に計測誤差評価実験を実施し、NRG法で計測した瞬間ボイド率と設計値（既知のポリスチレン厚さから求まるボイド率）とを比較した結果を示す。図2条件は誤差が最大となる条件での結果であり、計測誤差は17%であった。また、図2から計測値は設計値とよく一致することが確認できた。なお、右端で計測値が高い値となっているのは、ポリスチレン板と流路側壁の間にわずかな隙間が生じた事に起因している。実際に沸騰する領域は、d_{CL}<10mmの領域であり、真のボイド率は計測誤差の範囲内にあることが実験により確認できた。

本計測誤差評価実験と解析的に誤差原因を評価した結果とを比較し、誤差の主原因は計測時間内に透過する中性子数の低下に起因する中性子束の統計的変動誤差に起因すること

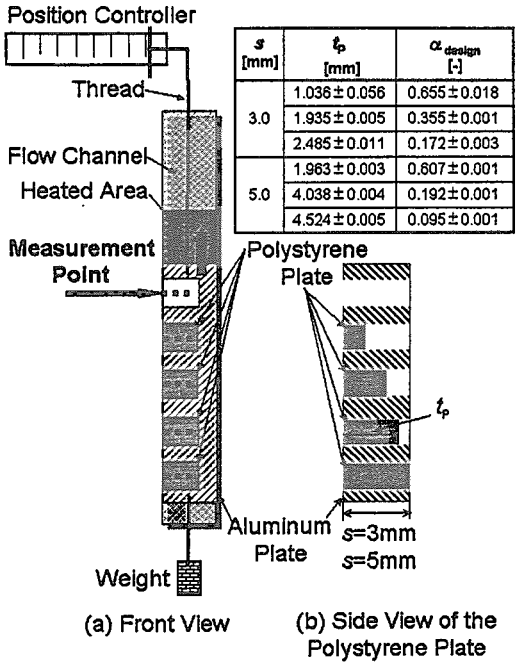

s [mm]	t_p [mm]	α_{design} [-]
3.0	1.036±0.056	0.655±0.018
	1.935±0.005	0.355±0.001
	2.485±0.011	0.172±0.003
5.0	1.963±0.003	0.607±0.001
	4.038±0.004	0.192±0.001
	4.524±0.005	0.095±0.001

図1　ボイド率の計測誤差評価実験の概要

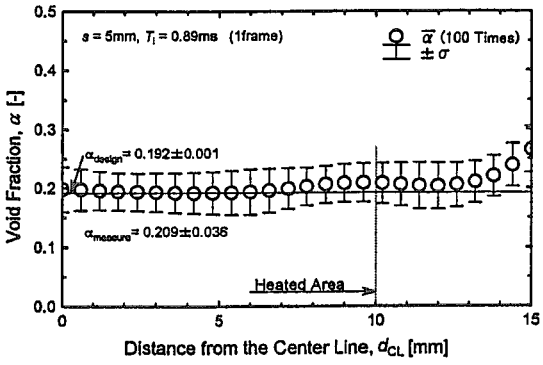

図2　瞬時ボイド率の計測誤差

が推定された。その他、画像増幅ノイズや気泡の移動に起因する不鮮明さに起因する誤差、デジタル化に起因する誤差等も評価した。

原子炉：JRR-3　装置：熱中性子ラジオグラフィ施設　分野：中性子ラジオグラフィフィ（熱水力）

研究テーマ：原子炉シビアアクシデント時の溶融炉心冷却に関する基礎研究
表　　題：溶融燃料／冷却材相互作用の可視化実験

2-2　溶融金属中に注入する水ジェット挙動の可視化と計測

柴本　泰照、　　中村　秀夫、　　安濃田　良成、　　久木田　豊[1]
日本原子力研究所　東海研究所　原子炉安全工学部
[1]名古屋大学　大学院工学研究科　エネルギー理工学専攻

低温低沸点液体と高温高沸点液体が接触すると低沸点液体が激しく蒸発することがある。その際、蒸発速度が大きく、蒸気圧力の増加速度が周囲の液体中での圧力緩和速度より大きい場合には蒸気爆発と呼ばれる爆発的反応となり、例えば原子炉シビアアクシデント時の溶融炉心冷却過程において最も過酷な現象として知られている。この溶融燃料と冷却材の相互作用（Molten Fuel and Coolant Interactions; MFCIs）時には、冷却材の蒸気が大量に発生するのであるが、蒸気生成速度によって蒸気爆発になる場合と爆発に至らない場合がある。後者は穏やかな MFCI 事象と呼ばれ、本研究ではその現象解明研究の一環として、高温の溶融金属中に水をジェット状に落下させた体系（Coolant Injection mode; CI mode）についての基礎研究を行っている。

従来の研究では、水などの透明な液体に注入される水ジェットの挙動については数々の研究例があるものの[1]、高温金属中に注水するといった沸騰を伴う両者の相互作用について論じられた例は限られていた。特に、多くの溶融金属は可視光には不透明であり、その中の水の挙動を可視化することは非常に困難であった。そこで本研究では、原研 3 号炉の中性子ラジオグラフィ施設を用いた実験を行い、可視化に対する問題を解決するとともに、発生蒸気量やジェット貫入深さなどの混合パラメータを画像処理により定量計測を試みている。[2,3]

実験は、試験部としてギャップ 10mm ・半径 85mm の扁平半円形容器を用い、模擬溶融燃料として Pb-Bi 合金（融点 398K）を満たしたところに、流速約 7.4m/s の水（室温）をジェット状（直径 D_j = 6mm）に注入した。実験パラメータである溶融金属の初期温度は、水と溶融金属の界面接触温度を考慮し、446K(#1)と 687K（#2）となる 2 ケースを選択した。界面接触温度は熱伝導理論による近似式[4]、

$$T_i = \frac{T_M + \beta T_j}{1+\beta}, \text{ ここで } \beta = \left[\frac{(\lambda\rho c_p)_j}{(\lambda\rho c_p)_M}\right]^{0.5},$$

から見積もった。これは、本実験条件における均質核生成温度（594K）を境界とした二種類の沸騰状態の比較を意味する。撮像系には、高速減衰のイメージインテンシファイア（I.I.）を用いた高速度のビデオ撮影（FASTCAM-Ultima、撮影速度＝1125 fps）を採用し、沸騰を伴う高

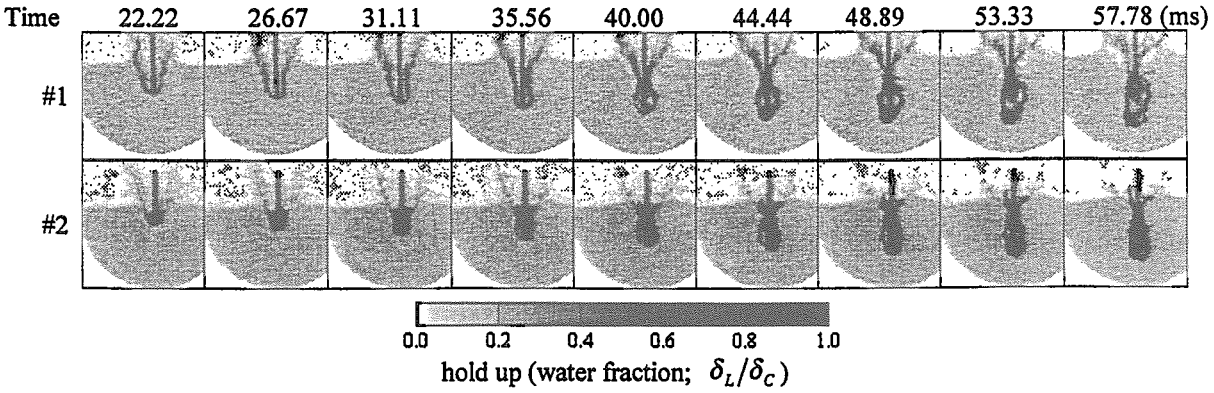

図 1　　溶融金属中に落下する水ジェットのホールドアップ分布時間変化

原子炉：JRR3-M　　装置：7R(TNRF)　　分野：中性子ラジオグラフィ（熱水力）

速現象に対応した。

図 1 に、NRG 原画像から画像処理により得られた水ジェットのホールドアップ分布の時間変化を示す。液膜分布は NRG 画像の輝度情報より、次式で求めることができる。

$$\frac{\delta_L}{\delta_C}=\ln\left(\frac{G_G-G_0}{G_{MP}-G_0}\right)\Big/\ln\left(\frac{G_G-G_0}{G_L-G_0}\right),$$

ここで、δ_Lは液膜厚さ、δ_Cは流路ギャップ（＝10 mm）、Gは各画素の輝度（256 階調）で、添字G, L, MPは、気相、液相、混相を表す。G_0はオフセット画像である。

図 1 において、半円容器を満たす灰色部分はメルトプールを表している。上段の経過時間は、水ジェットがメルトプール表面に到達した瞬間を 0.0 ms としている。同図から計測した、貫入ジェットにより形成される cavity 内の蒸気体積変化を図 2 に示す。注入初期（t < 30ms）において、#1 では水ジェットの沸騰がなく、周囲の空気を巻き込みながら貫入するため、形成される cavity が比較的大きくなったが、#2 では、両者の接触と同時に水の蒸発が開始し、形成 cavity も小さい。しかし、その後の蒸気発生量については図 2 に示すように、高温メルトに落下させた#2 の方が蒸気の発生量が少ない結果となった。本実験のような高サブクール条件下（サブクール度=70K）では、最小膜沸騰温度が過熱限界温度（自発核生成温度の理論上限値）となる Sakurai ら—の報告に従うと、#2 においては、注入直後から水／メルトの界面上に安定な蒸気膜が形成され、伝熱の阻害に寄与したことが予想される。図 3 に、水ジェット貫入深さの時間変化を示す。縦軸はジェット径で規格化している。#2 では、先述の膜沸騰による蒸気発生量の減少によりジェットの吹上がり開始の時間が#1 よりも遅れており、長時間かつ深く貫入する結果となっている。また、従来の等温実験では貫入深さが Froude 数の関数として整理されていたが、沸騰に関するパラメータについても考慮する必要があることがわかる。

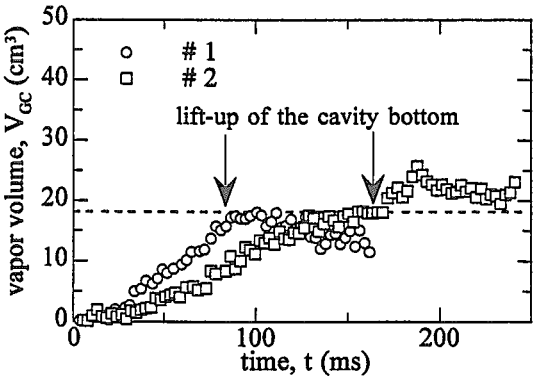

図 2　形成 cavity 内の発生蒸気量

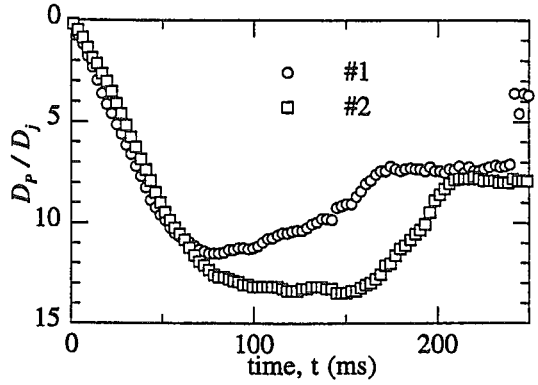

図 3　水ジェット貫入深さ

以上、MFCI／CI に関して、高速度撮影 NRG を用いて、沸騰を伴う冷却水侵入挙動の撮影に成功した。蒸気発生量の見積もりから、高温条件では、伝熱量が少なく、注入ジェットが長時間かつ深く貫入する安定な挙動を示すことがわかった。これは水／液体金属表面での膜沸騰条件が主要な原因であることが予想される。

参考文献

(1) Oguz, H.N., et al., Journal of Fluid Mechanics, 294, (2000), 181-207.
(2) Park, H.S., et al., Proc. of 7th International Conference on Nuclear Engineering (ICONE-7), (1999), ICONE-7254.
(3) Sibamoto, Y., et al., Proc. of ICONE-8, (2000), ICONE-8246.
(4) Corradini, M.L., et al., Topics in Two-Phase Heat Transfer and Flow, Proc. of ASME Winter Meeting, (1978), 17-28.
(5) 日本機械学会編、「沸騰熱伝達と冷却」、(1989)、121.

原子炉：JRR3-M　装置：7R(TNRF)　分野：中性子ラジオグラフィ（熱水力）

研究テーマ：中性子ビーム利用技術に関する開発研究
表　　題：シンチレータ付きFOPカプリングCCDカメラによる高解像度撮像法の開発

2-3 シンチレータ付きFOPカプリングCCDカメラによる高解像度撮像法の開発

松林政仁，日引俊[1]，三島嘉一郎[1]，齊藤泰司[1]
日本原子力研究所　東海研究所　中性子科学研究センター
[1]京都大学　原子炉実験所　核エネルギー基礎研究部門

1. 研究の背景及び目的

中性子ラジオグラフィではこれまで蛍光コンバータと撮像デバイス(CCDカメラ)を暗箱の中で光学レンズによりカプリングした撮像システムが広く用いられてきた。このシステムの特徴は光学レンズを変更することにより可視化したい領域を変更可能なこと及び実験の目的に応じて撮像デバイスを変更できることである。

高解像度撮像に伴う問題点の一つに撮像デバイスの単位画素当たりの入射光量低下が挙げられる。コンバータ面での発光は等方的であり、その一部がレンズによりCCD上に結像される。一方、FOP(Fiber Optic Plate)を用いたカプリングでは、蛍光体はFOP上に直接塗布されており、FOPの残りの一端がCCDチップに直付けされている。FOPは光ファイバを束ねて融着させた形状をしており、屈折率の高いコアガラス及び屈折率の低いクラッドガラスから構成される。両ガラスの屈折率の違いによりFOP端面における最大受光角が決定される。

本研究では中性子を用いた微細構造物の３次元非破壊計測を可能とするため、分解能数μmを目標とした撮像系を開発する。対象となる微細構造物の例としては、1) 植物の地上部(茎及び花)及び根(成長過程観察、水分動態確認)、2) リチウム電池、水素吸蔵合金(充・放電に伴うLiイオンの移動，Hの拡散状況観察)が挙げられる。

2. 実　験

実験はJRR-3M 7R (TNRF-2)及びJRR-3M C2-3 (CNRF)で実施した。FOPカプリングのシステム構成は以下のとおりである。

a) シンチレータ: $Gd_2O_2S(Tb)$, 5, 10, 15, 20 mg/cm^2
b) FOP：コアサイズ3μm, NA 1.0
c) CCD :セルサイズ 11.0μm(H) x 13.0μm(V),
有効画素数768(H) x 493(V)

3. 結　果

1) 発光輝度

Fig. 1にシンチレータの塗布重量に対する発光輝度の測定結果を示す。冷中性子の場合10mg/cm^{2}で最大となるが、熱中性子の場合では20mg/cm^{2}が最大であり、曲線の傾向から30mg/cm^{2}程度で飽和するものと考えられる。冷中性子と熱中性子の結果の相違はGdの吸収断面積の違いによるものと考えられる。つまり、シンチレータ内での光の単位塗布重量当たりの減衰割合が一定であるとすれば、発光点がCCDから遠いほど減衰距離が長くなる。冷中性子の場合、熱中性子と比較してGdの吸収断面積増加により発光点の中心がシンチレータ表面部分に近くなりより減衰を受けることになる。

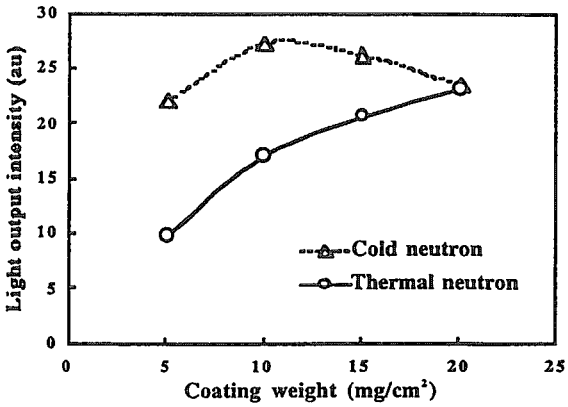

Fig. 1 Light output intensity of different coating weight scintillator

2) Edge spread function

Fig. 2及びFig. 3にそれぞれ、熱中性子及び冷中性子を用いて測定したCd製ナイフエッヂのEdge spread function(ESF)測定結果を示す。どちらの結果も塗布重量が少ない5mg/cm^{2}の場合に最適値（熱中性子：35μm, 冷中性子：37μm）

原子炉：JRR-3M　　装　置：TNRF, CNRF　　分　野：中性子ラジオグラフィ（その他）

が得られている。塗布重量に対するESFの変化は冷中性子の場合が大きく、発光輝度の違いと同様の原因によるものと考えられる。

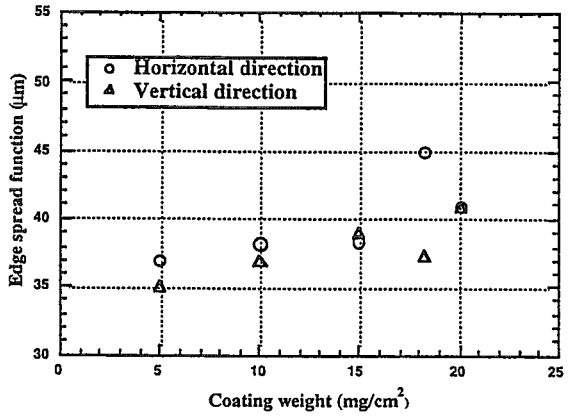

Fig. 2 ESF of different coating weight scintillator for thermal neutron

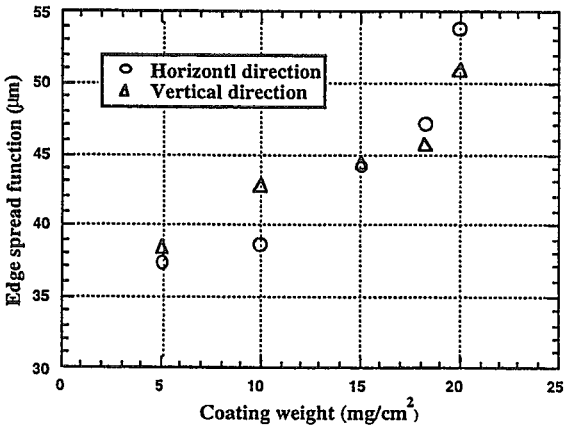

Fig. 3 ESF of different coating weight scintillator for cold neutron

3) 微細構造試料の可視化

高解像度撮像を必要とする試料は一般的に小さいため中性子の透過長も短くなり、透過画像のコントラストが低くなる。リチウムは比較的断面積が大きいことから微細な試料の場合でも可視化が良好に行える。ここではリチウム電池としては比較的小さなBR435の可視化を行い、併せてCT(Computed Tomography)も行った。本電池はアルミニウム製のケース内にリチウムがメタルの状態で中心部にあるマイナス端子のまわりにコーティングされており、これをセパレーターを介して正極（フッ化黒鉛）が取り巻いている。

Fig. 4に試料の投影画像及び各断層位置におけるCT画像を示す。CT像は1度ずつ回転して撮影した180枚の投影画像よりフィルタ逆投影法により計算した。さらにこれらのCT像を用いてレンダリングによって3次元可視化した画像をFig. 5に示す。CT像で観察される回転鋸刃のような部分はメッシュ状であることが容易に観察できる。

4. まとめ

シンチレータを$Gd_2O_2S(Tb)$とした場合の高輝度化及び高解像度化についてデータが得られ、さらに試験的に行ったCTで応用研究に十分な画像が得られた。

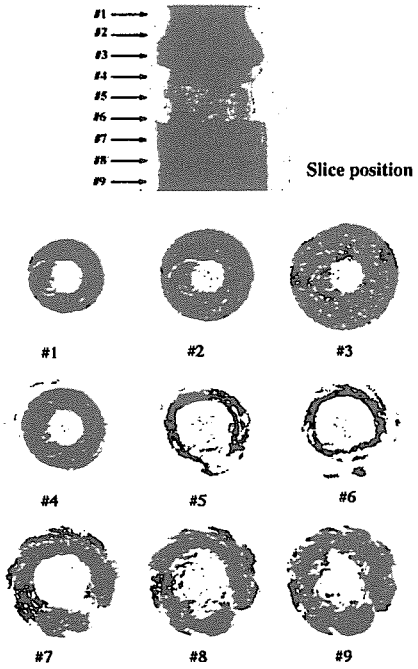

Fig. 4 Projection image and computed tomograms of BR435

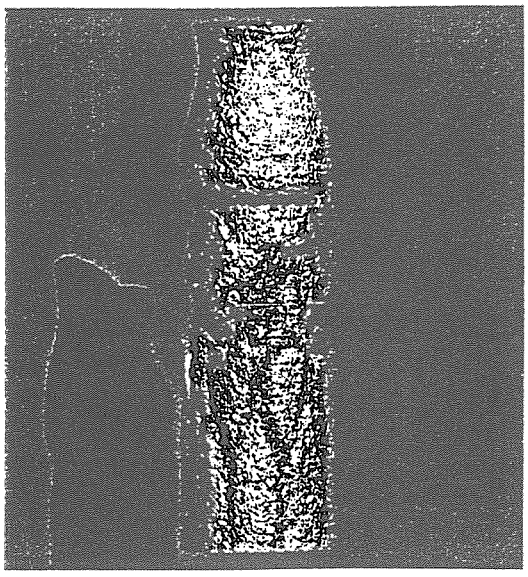

Fig. 5 Rendering image of BR435.

This is a blank page.

3. 即発ガンマ線分析

3. Prompt Gamma-ray Analysis

This is a blank page.

研究テーマ：環境関連物質の分析高度化研究
表　　題：中性子即発γ線分析の研究

3-1　中性子即発γ線分析の研究

米沢仲四郎，松江秀明
環境科学研究部 分析科学研究グループ

1.　はじめに

報告者らはこれまでにJRR-3Mの冷及び熱中性子ビームを使用する中性子即発γ線分析法(PGA)を開発し，各種分野の試料分析に応用してきた。本年度は，熱中性子ビーム(第 1～5 サイクル)と冷中性子ビーム(第 6～8 サイクル)を使用し，1) k_0 法による標準物質の多元素定量，2) 即発荷電粒子測定装置の導入，3) 大学及び国立研究所との協力研究及び共同研究を実施した。

2.　k_0法による標準物質の多元素定量

PGA は，他の方法では分析が困難な軽元素を含む多元素を非破壊で同時定量することができるという特長を持つ。また，内標準法に基づく k_0-PGA は各元素の k_0 係数を使用することで比較標準試料を使用しないで多元素の相対濃度を正確に定量できる。現在，国立環境研究所では日本人の代表的な食事の標準物質(Typical Japanese Diet)が，また，日本分析化学会では土壌標準物質(金属添加森林土壌(JSAC401)，火山灰土壌(JSAC411))が調製され，その共同分析が行われている。報告者らはこの共同研究に参加し，k_0-PGA で軽元素を中心にその多元素定量を行った。k_0-PGA では元素の絶対濃度を求めることができないため，標準添加法により食事試料中の Cl 及び土壌試料中の Ti の絶対濃度を定量し，それらの値から各元素の絶対濃度を求めた。

各標準物質は定められた方法で乾燥し，水分含量を測定後分析に使用した。標準添加法では，各標準物質をはかり取り，食事試料の場合には NH_4Cl(5～30 mg)を，また，土壌の場合は TiO_2(5～30 mg)を添加し，良く混合し，錠剤成型器により 13 mmφのディスク試料とした。各試料は FEP フィルムに熔封し，即発γ線スペクトルを冷及び熱中性子ビームで，He 雰囲気中 5000 ～ 100000 秒間測定した。定量には他の元素の妨害が少なく，放出率の大きなγ線ピークを使用し，そのピーク計数率，k_0 計数及びγ線検出効率から各元素の相対濃度を求めた。

本分析により，Typical Japanese Diet では H, B, N, Na, S, Cl, K の軽元素を中心とした 8 元素，JASC401 及び JASC411 では H, B, Na, Al, Si, K, Ca, Ti, Mn, Fe, Sm Gd の 12 元素，JASC401 ではこれらの 12 元素に加え Cd の定量を行うことができた。標準添加法による Typical Japanese Diet 中の Cl の定量結果は 1.67 ± 0.07%，土壌標準物質中の Ti の定量結果はそれぞれ，0.411 ± 0.006%(JASC401)，0.354 ± 0.005%(JASC411)であった。定量値の正確さを評価するために，NIST の標準物質，食事試料(SRM 1548a)，脱脂粉乳試料(SRM 1549)，河川堆積物(SRM 1645)，コールフライアッシュ(SRM 1645)の分析を行った。本方法による各元素の定量値は認証値と 6%以内で一致した。

3.　中性子深さ方向分析

B と Li に中性子を照射した場合，$^{10}B(n,\alpha)^7Li$ 及び $^6Li(n,\alpha)^3H$ 反応によりα粒子等の荷電粒子が放出される。これらの反応の断面積は 3837 バーン(^{10}B)，940 バーン(^6Li)と大きい。α粒子等の荷電粒子は，物質との相互作用によりエネルギーを失い

原子炉: JRR-3M　　装置：即発γ線分析装置線　　分野:即発γ線分析(分析化学一般)

ながら物質中を透過する。この荷電粒子のエネルギー損失を利用し，そのエネルギースペクトルと透過する物質の荷電粒子阻止能から，BとLiの数μm程度までの濃度分布を高感度で求めることができる。この方法は中性子深さ方向分析（Neutron Depth Profiling, NDP）と呼ばれ，米国及び欧州を中心に研究が行われている。しかしながら，我が国では研究例は少ない。報告者らは即発γ線分析装置内に即発荷電粒子測定用チェンバーを設置し，NDPの検討を開始した。

装置は，荷電粒子測定用の真空チェンバー（Al製 20×20×30 mm^3）とそのスペクトル測定用の電子回路部から構成される。真空チェンバーには表面障壁型Si検出器（EG&G製BU-017-450-100型）が取り付けられ，減圧下で，冷又は熱中性子ビームを試料に照射しながら，発生する荷電粒子を測定することができる。

荷電粒子スペクトロメーターのエネルギー校正には^{241}Amと^{235,238}Uのα線スペクトルを用いた。NISTのBの深さ方向分析用標準物質（SRM 2137）を測定し，本装置の深さ方向の分解能等の基本特性を測定した。その結果，SIMSによる深さ方向分析結果と5%以内で一致した。また，シリコン単結晶上にスパッタリング法によりBを蒸着した試料及びそれを真空中で960℃10時間加熱し，Bを深さ方向に熱拡散させた試料を測定し，その深さ分布からBの熱拡散挙動を観察した。更に，シリコン単結晶上にLiを蒸着した試料を作成し，その深さ方向分析も測定した。それらの結果，本法による深さ方向分析の分解能はB 0.08μm以下，Li 0.2μm以下であった。

4. 協力及び共同研究

JRR-3Mの即発γ線分析装置を使用し，大学との協力研究（3件）及び国立研究所（1件）を実施した。協力研究としては，PGA法による高エネルギー荷電粒子の物質中での挙動の研究（大同工業大学工学部），X線・低エネルギーγ線検出による即発γ線分析（Ⅱ）（武蔵大学人文学部），内部起源粒子線による石英中の常磁性格子欠陥の生成効率の研究（岡山理科大学 理学部）を行った。また，共同研究としては，廃棄物埋立地浸出水中ホウ素の起源に関する研究（国立環境研究所 化学環境部）を実施した。

5. 成果の公表

1. Yonezawa, "Prompt Gamma-Ray Analysis Using Cold and Thermal Guided Neutron Beams at JAERI", Biological Trace Element Research 71 (1999) 407.
2. C. Yonezawa, H. Matsue, "Usefulness of prompt gamma-ray analysis with guided neutron beams comparing to neutron activation analysis", J. Radioanal. Nucl. Chem., 244 (2000) 373.
3. H. Matsue, C. Yonezawa, "k_0 Standardization approach in neutron-induced prompt gamma-ray analysis at JAERI", J. Radioanal. Nucl. Chem., 245 (2000) 189.
4. 松江秀明，米沢仲四郎，「k_0-中性子即発γ線分析法によるTypical Japanese Diet標準物質の多元素定量」、第43回放射化学討論会予稿集、p.83 (1999).
5. 松江秀明，米沢仲四郎，「中性子即発γ線分析法による食事及び土壌標準物質中の多元素定量」，第61回分析化学討論会講演要旨集，p. 75 (2000).
6. 米沢仲四郎，松江秀明，「中性子によるホウ素及びリチウムの深さ方向分析」，第61回分析化学討論会講演要旨集，p. 74 (2000).

研究テーマ:研究炉利用高度化の技術開発
表題:BNCT 患者血液中のボロン濃度測定

3-2 BNCT 患者血液中のボロン濃度測定

堀 直彦、山本哲哉[1]、松村 明[1]、鳥居義也、山本和喜、岸 敏明、高田準太郎、大竹真一、太田一昭

日本原子力研究所 研究炉部
[1]筑波大学

1.概要

即発γ線分析装置(PGA)を使ったボロン中性子捕捉療法(BNCT)患者血液中のボロン(^{10}B)濃度測定のメリットは、化学的分析手法では短い時間の中で血液中のボロン濃度(30ppm 程度)を高い精度で測定することは困難であるが、PGA を用いれば短い時間の中で高い精度のボロン濃度測定を行うことができるということである。

BNCT 患者の血液においては、必要なボロン濃度は総量中のボロン(^{10}B)重量であり、総量に対する比で表せればよいことから、総量に比例すると考えられる水素の即発γ線の量(ピーク面積)とボロンのピーク面積の比をとることにより測定するものとした。従って測定試料の量、中性子強度、検出器感度等のパラメータは相殺されて、それらの補正の必要が無くなるものである。

2.校正定数

ボロン濃度は、測定したスペクトルデータからボロンのピーク面積と水素のピーク面積を求め、その比(B/H 比)と校正定数から求めることとした。

まず、測定により得られたスペクトルデータからボロンピーク面積及び水素ピーク面積を計算し、B/H 比を得る。ボロンピークは即発γ線が運動中の ^{7}Li 粒子から放出されるためドップラーシフトにより台形状となっている。このため、台形状のピーク面積を正確に積分できるように分布関数を定義し、この関数(誤差関数)への非線形フィッティングプログラムを開発した。同様にこのプログラムは水素ピークのガウス曲線へのフィッティングを行い、その面積を計算するようにしている。フィッティングプログラムの画面を図1に示す。

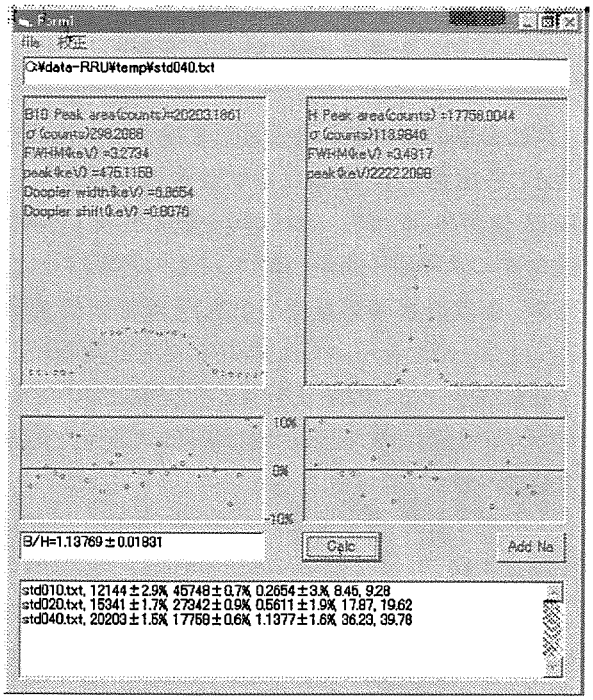

図1 フィッティングプログラム画面

ホウ酸水及びBSHを添加した血液を標準試料として使用し、ボロン濃度測定の校正を行った。 なお、ホウ酸水に含まれるボロンは天然同位体比(^{10}B:19.6～19.8%)のものであり、BNCT で患者に投与されるボロン化合物であるBSHのボロンは^{10}B 濃縮ボロンである。

まず、ホウ酸水の標準試料(測定に用いた試料の^{10}B 濃度は、1, 5, 10, 20, 40, 60, 80, 100ppm の8種類)を使用してボロン濃度とB/H 比の検量線を作成した。その結果、直線性を有することを確認した。検量線を図2に示す。

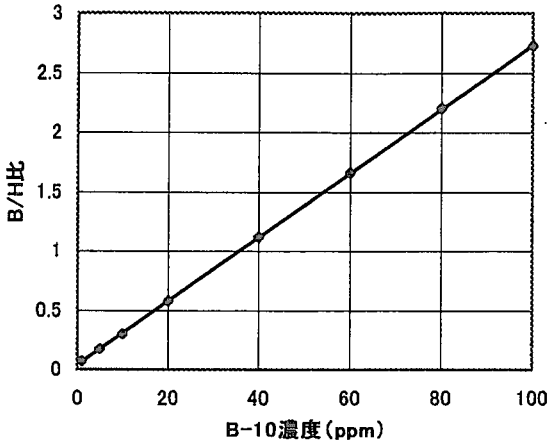

図2 ホウ酸水の標準試料による検量線

次に血液の標準試料を使用して検量線を作成したところ血液の検量線はホウ酸水のものに比べB/H 比が高くなった。これは同一量の血液中とホウ酸水中の水素原子の量の差によるものと考えられたため、血液の水素重量比(10.2%)と水の水素重量比(11.2%)の比を用いて血液中の校正定数を補正するものとした。この補正を加えることによりいずれのボロン濃度も同じ校正定数を基にして測定できるようになった。

3.測定方法

BNCT 患者の血液は点滴による希釈，手術時の出血による血液の希釈などの影響があり、健康な人の血液より分離しやすい傾向がある。医療照射当日の血液はもちろん、後日行われる再測定においても注意が必要である。このため、短時間測定による予備測定であらかじめその血液に含まれるボロン濃度を予想し、ボロンと水素の計数から必要十分な測定時間を決め、本測定を行うこととした。これは測定時間が短かすぎることによる統計誤差が大きくなること及び測定時間が長すぎることにより血液の分離が始まり測定値が真値から離れることを防ぐためである。また、血液の分離による測定値の変化をできる限り減らすため、試料の攪拌を十分に行い、その直後に測定を開始できるようにしている。

しかし、医療照射当日の測定は JRR-4 の運転時間が短いこともあり、事前に行っている BNCT 患者の薬物動態学的検査結果や医療照射当日に行われたICP発光分光分析装置による血液の測定結果を参考にして、測定時間を決定している。後日、十分時間をかけて事後測定を行い、その結果を最終的な線量評価に用いている。

また、測定に際しては、複数の濃度の標準試料も測定することにより、校正されていること確認している。

4.測定結果

平成11年度に行われた5回のBNCT当日は医療照射直前に採取した血液をはじめ、医師側から提出されたすべての血液サンプルについて測定を行った。また、後日には医療照射直後の血液サンプルを含め、すべての血液サンプルの再測定を行った。再測定の結果は3回測定の平均値とし、測定値は5%未満の精度になっている。

第1回(平成11年10月25日実施)、第2回(平成12年1月7日実施)及び第4回(平成12年3月10日実施)の3回の BNCT については、医療照射に先立ち患者の BSH に対する薬物動態学的検査のため血液中のボロン濃度の変化を測定した。薬物動態学的検査時の BSH 投与量を医療照射時の投与量に換算した曲線と実際の医療照射時のボロン濃度曲線はほぼ相似であり、事前に行う薬物動態学的検査は患者の照射当日のボロン濃度を予測する上で有効な手段であると思われる。

参考文献

1.岸、他、スーパーミラーを利用した即発ガンマ線分析装置の開発、日本原子力学会 1999 春の年会
2.日本原子力研究所 研究炉部、平成10年度研究炉部年報(運転・利用と研究・技術開発)、JAERI-Review 99-032、(1999)、124-127

原子炉 : JRR-4　装置名 : 即発γ線分析装置　　分野 : 即発γ線放射化分析(医学)

研究テーマ：畜産研究における原子炉中性子即発ガンマ線分析法の利用
表　　題：中性子即発ガンマ線分析法による畜産関係試料中のホウ素の定量

3-3 中性子即発ガンマ線分析法による畜産関係試料中のホウ素の定量

宮本進，西村宏一，米沢仲四郎[1]，松江秀明[1]，安達武雄[1]，星三千男[1]
農林水産省畜産試験場
[2]*日本原子力研究所*

1．目的

畜産研究分野においては、近年、分析対象とする環境および生体中の元素、成分が増加し、さらに対象とする試料の形状も多様化しているので、高感度で迅速かつ簡便な分析法の導入が望まれている。本研究では、即発ガンマ線分析法（ＰＧＡ）を畜産試料に適用し、家畜体内における元素の動態明らかにし、畜産における生産性の向上を図ることを目的とし、日本原子力研究所で開発、所有しているＪＲＲ－３Ｍの中性子ガイドビームを利用した中性子即発ガンマ線分析装置を利用して実験を行った。

今までに、即発ガンマ線分析法による植物及び動物海洋性試料中の元素分析法の基礎データを得るため、感度の高いホウ素を対象元素として、国際標準試料（植物、動物）を用い、測定時における試料形状、試料量、ホウ素の測定限界等について検討すると共に、畜産関連試料中のＢ等の測定をＰＧＡにより行った。

また、家畜への応用として、体内のミネラル（無機物）代謝と関連の深いホウ素を羊に連続投与しホウ素の血液濃度の推移、体外排泄（尿、糞）臓器への蓄積等の動態を調べた。

2．試験研究の概要

今回は、羊３頭にルーサンヘイキューブ（1，５００ｇ/日/頭）とホウ素添加水（ホウ酸ナトリウム：Ｂとして100ppm）を１回投与し、その後１０日間にわたり、得られた血液（血漿）糞、尿および実験終了後得られた臓器（肝臓、腎臓、筋肉等）を供試試料とした（ホウ素投与区(T)）。なお、対照区(C)の羊３頭（Ｂ非添加水を給与）から得られた試料についても同様に処理した。

各試料は、血漿および尿については1mlをテフロン製容器に入れ、糞は乾燥後、臓器は凍結乾燥後粉末とし錠剤成形器を用いてペレット状に成形（直径：13mm、重量：0.3g程度）FEPフィルム（厚さ25μm）で二重に溶着した。試料はPTFE製保持具の中央にPTFE製糸で固定し、原研ＪＲＲ－３M熱あるいは冷中性子ガイドビームに設置された即発ガンマ線分析装置を用い、ヘリウムふんい気中でガンマ線スペクトル測定を行った（測定時間、1，000～18，000秒/試料）。ホウ素の検量線は、スズ板にHBO_3標準溶液を滴下乾固した試料、血漿あるいは尿にホウ素を添加した試料を用い478 keVのホウ素のピークの面積を求める方法により作成した。

血漿のＢ濃度はＢ添加水給与開始後上昇し６時間及び１２時間後にピークを示し、以後、減少した（図１）。糞のホウ素濃度はホウ素添加水投与開始後、急上昇し、２４時間後にピークを示し、以後減少した（図２）。尿のホウ素濃度はホウ素添加水投与開始後、急上昇し、１２時間後にピークを示し、以後、減少した（図３）。

ホウ素非添加水を投与した対照区の羊では血漿、糞、尿、におけるホウ素の濃度は低レベルで推移した。実験終了後、と殺して得られた臓器（肝臓、腎臓等）中のホウ素濃度はホウ素投与区、対照区共、ほぼ、同レベルであった。

これらの結果から、羊の体内に入った飲料水中のホウ素は速やかに吸収され、血漿および尿、糞中のホウ素の濃度は急上昇した後、減少し、尿および糞を経由して体外排泄されることが明らかになった。ホウ素添加飲料水を１回、投与した今回の試験におけるホウ素の臓器における蓄積については、既に実施した連続投与のデータと併せ検討すると、１度は臓器に蓄積されたものの、と殺時（ホウ素添加水投与開始後１０日間経過している）までに、臓器外に移行したものと考えられる。

原子炉：ＪＲＲ－３Ｍ　　装置：即発γ線分析装置　　分野：即発γ線分析（農・水産物）

参考文献

1)理工学における同位元素発表会講演要旨集
（34, 34, 35回）（1995, 1997, 1998）
2)国立機関原子力試験研究成果報告書
（平成5, 6, 7, 8, 9, 10年度）（科学技術庁）
3)日本畜産学会講演要旨（８８，９１回）
（1994, 1996）
4)日本土壌肥料科学会誌、６７（１９９６）、
PP、６７２－６７６
5)Journal of Radioanalytical and Nuclear
Chemistry 244 (No. 2) (2000) PP. 307～309

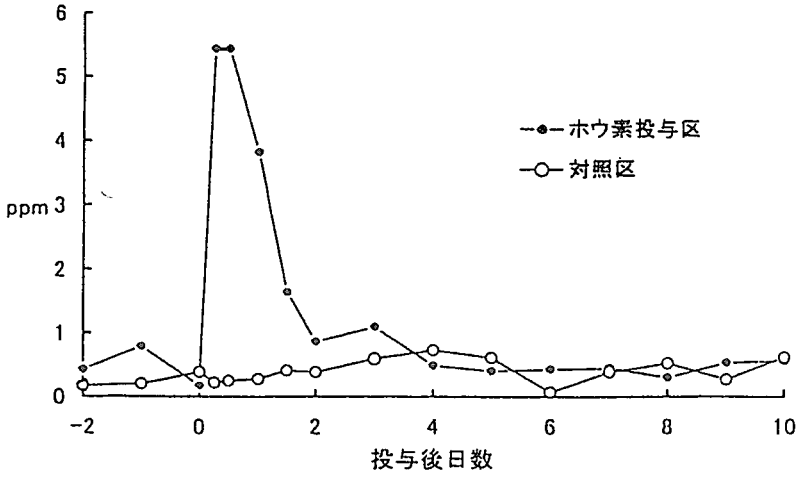

図1. 羊血漿におけるホウ素濃度の推移(各値は平均値)

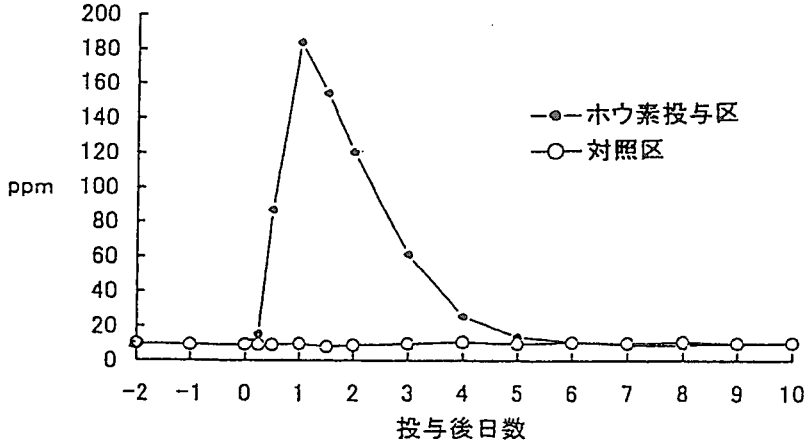

図2. 羊におけるホウ素の糞への排泄(各値は平均値)

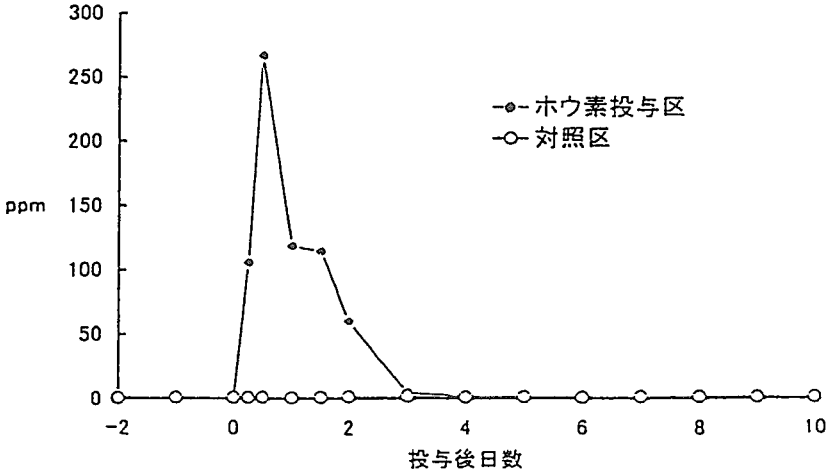

図3. 羊におけるホウ素の尿への排泄(各値は平均値)

B Analysis in a Plant Sample
3-4 植物試料中のBの分析

T.M.Nakanishi , J.Furukawa , T.Kataoka, H.Iikura
中西友子、古川純、片岡達彦、飯倉寛
Graduate School of Agricultural and Life Sciences, The University of Tokyo
東京大学大学院農学生命科学研究科

1. Introduction

Generally, inductively coupled plasma atomic emission spectrometry (ICP-AES), ICP Mass spectrometry (ICP-MS) and spectrophotometric measurement have been used for boron (B) determination in plant tissues. However, sample preparation to digest sample materials into solution involves time and contributes to errors. Since a suitable radioisotope for B does not exist, the radio-tracer work cannot be carried out. The prompt-gamma analysis (PGA) using thermal neutrons has been used for B determination in biological materials by several workers. However, thermal neutrons induce a high background in gamma-ray measurement, especially in the presence of H. Since the conventional PGA system has suffered from poor beam quality and low counter sensitivity, the method has lower sensitivity than ICP-AES or ICP-MS. Recently, PGA system at an atomic reactor, JRR-3M with cold neutron has been developed, therefore, we tried to use this system to determine B amount in a cultured cells. The sensitivity to detect B with this method was as high as those by ICP-AES or ICP-MS or spectrophotometric measurement.

In this study, we present B content in tobacco cultured cells collected from different stages of the cell cycle by PGA.

2. Materials and Methods

Cells and Culture Condition

Suspension cell line of tobacco (*Nicotiana tabacum*) cv. Bright Yellow 2 (BY-2) was cultured in a modified LS (Linsmaier and Skoog) medium at pH 5.6. The concentration of B in the medium was 1 mg B L^{-1} as boric acid. Cells were grown at 26 ℃ in 100mL of liquid medium in 300-mL Erlenmeyer flasks and shaken at 135 rpm on a rotary shaker in the dark. Subcultures were performed every 7 days with a 5-mL inoculum.

Synchronization of the Cells

To synchronize the cells, 20mL of 7-day-old suspension culture was transferred to 80 mL of modified LS medium containing 5 mg aphidicolin L^{-1}. After 24 hr of the treatment, cells were collected and washed 3 times with 0.4M mannnitol. Then the cells were resuspended in a fresh medium and cultured. During the cell growth, cells were collected every hour and washed with 0.4M mannnitol to get the cells at different cell cycle stages. On the other hand, treatment with propyzamide was also performed to synchronize the cells again at G_2/M phase. After 4 hr, when the cells began to grow, cells were treated with 3mM propyzamide and resuspended in a fresh medium. Then the cells were collected and divided into two samples, one for flow cytometry (FCM) and another for B analysis. Stock solutions of aphidicolin and propyzamide were 15mM and 6mM in DMSO, respectively, and stored at 0-4 ℃.

研究施設・装置
日本原子力研究所東海研究所、JRR-3M

研究分野
生物化学

Prompt Gamma-Ray Analysis

Cells were washed 3 times with 0.4 M mannnitol and dried at 60 ℃. The dried samples were milled in a mortar and 300 mg of the powder was pressed to form a small disk (1cm in diameter) by a tablet maker and hydraulic pump. Each tablet was prepared and then analysed for B by PGA.

Flow Cytometry

When the cells started to grow after the synchronizing treatment, cells were collected every hour and protoplasts were prepared. One hundred mg fresh weight samples of cells were washed twice with 0.4 M mannitol and treated with 1% (w/v) Cellulase Onozuka RS, 0.2% Macerozyme R10 (Yakult Co.) and 0.01% Pectolizse Y23 (Seishin Co.) in 0.7 M mannnitol at 30 ℃ for 6 hr, with gentle shaking. The protoplasts were filtrated through the nylon mesh (50 μm), and washed twice with 0.4 M mannitol. The same quantity of 0.4 M mannitol was added to the protoplast suspension. Then PI (propidium iodide)-staining solution was added to the 1mL of the cell suspension. The FCM was carried out right after DNA staining by an Epics Elite ver. 4.02 equipped with argon ion laser (488 nm). Data were analysed using the software, Multicycle. Twenty thousand protoplasts were analysed in each fraction.

3. Results and Discussion

When the cells are treated with aphidicolin, DNA synthesis is inhibited and the cells are synchronized at G_1/S phase. With the treatment of propyzamide, cells are synchronized at G_2/M phase because of the inhibition of microtubule formation. By synchronizing the cells with the treatments by aphidicolin and propyzamide, the cells at each cell cycle stage (Stage 1-6) were able to be collected (Fig. 1 B-G, J-O). When the cells started to grow again after removal of aphidicoloin, the cells were at G_1/S phase for 1 hr (Stage 1), and proceeded to S/G_2 phase in 3 hr (Stage 2). After 4 hr, more than 60% of the cells was found to be a G_2+M phase (Stage 3). Five hr after the treatment with aphidicolin, the stage of the cells was the same as those when propyzamide was removed, i.e. 50% and 20% of the cells were at G_2+M and G1 phase, respectively (Stage 4). In 2 hr after removal of propyzamide, about 30% of the cells went through the cell cycle again to G_1 phase (Stage 5), and more than 50% of the cells proceeded to G_1 phase after 3 hr (Stage 6). Two-day-old and 8-day-old cells in suspension culture without any treatments were used as control (Fig.1 H, P) and G_0/G1 phase (Stage 0; Fig. 1 A, I) samples, respectively. Figure 2 shows the proportion of cell cycle phase at each stage of cell harvest.

As is shown in Fig. 3, B content decreased gradually as the cells proceeded through the stages of the cell cycle. However, when cell division was finished, B content increased dramatically. It might be correlated with a change in density of the cell wall where most tissue B is localized. Indeed B content at Stage 0 (almost G_0/G_1 phase) was more than twice that in the proliferating phase (Stage 1-6). At present we cannot explain shy the cells at G_0/G_1 phase contained higher amount of B.

The improvement of PGA with cold neutrons made it possible to measure trace amounts of B in cells. Therefore this is the first report to determine B content in cells with respect to the cell cycle. We hope that the kinetics of B in cells during the cell cycle will be clarified and study of B in plant will become more active in future.

(List of Papers in this Study)

1.T.M.Nakanishi et al. Analysis by prompt gamma-ray method with cold neutrons of boron and other elements in soybean. Boron in Soils and Plants (R.W.Bell and B.Rerkasem eds.) pp69-72, 1997

2. H.Iikura et al. Boron analysis at different stages of the cell cycle in cultured tobacco cells. *ibid*, pp 63-67, 1997

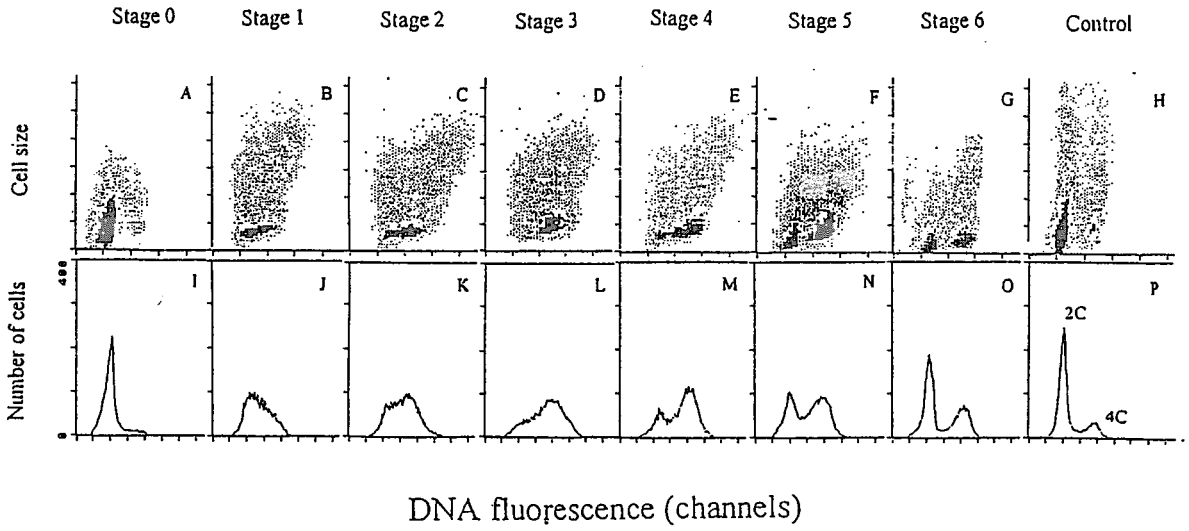

Fig.1. Flow cytometric analysis of the cells stained with PI.

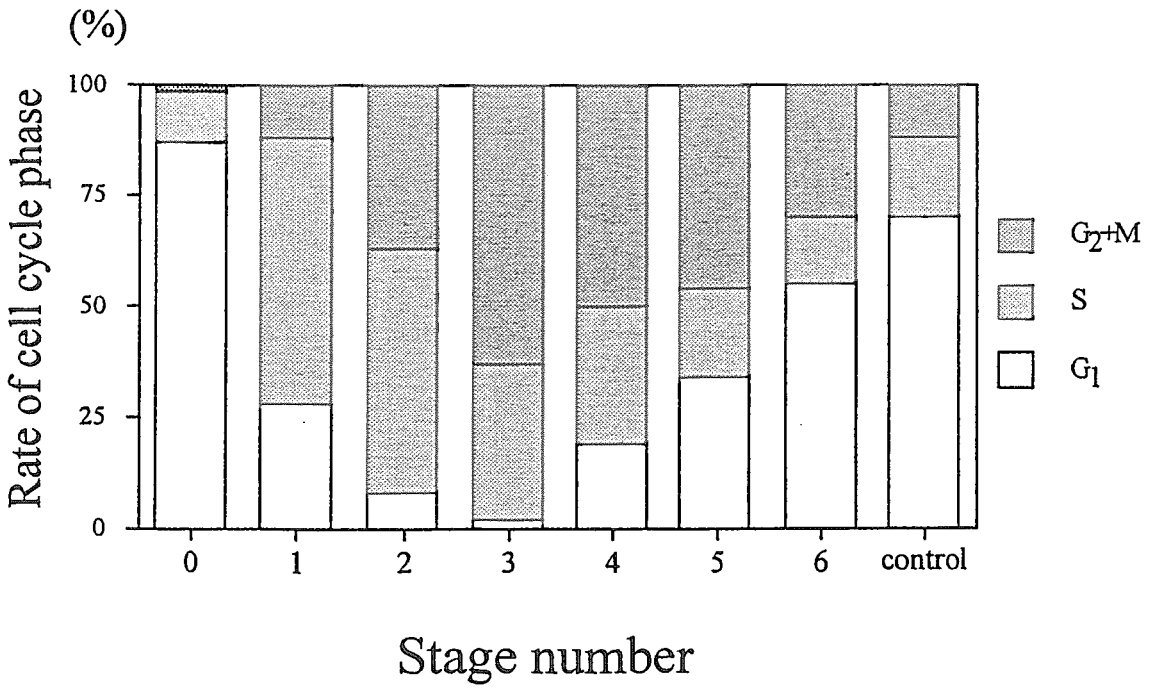

Fig. 2. Percentage of cell cycle phase at each synchronized stage.

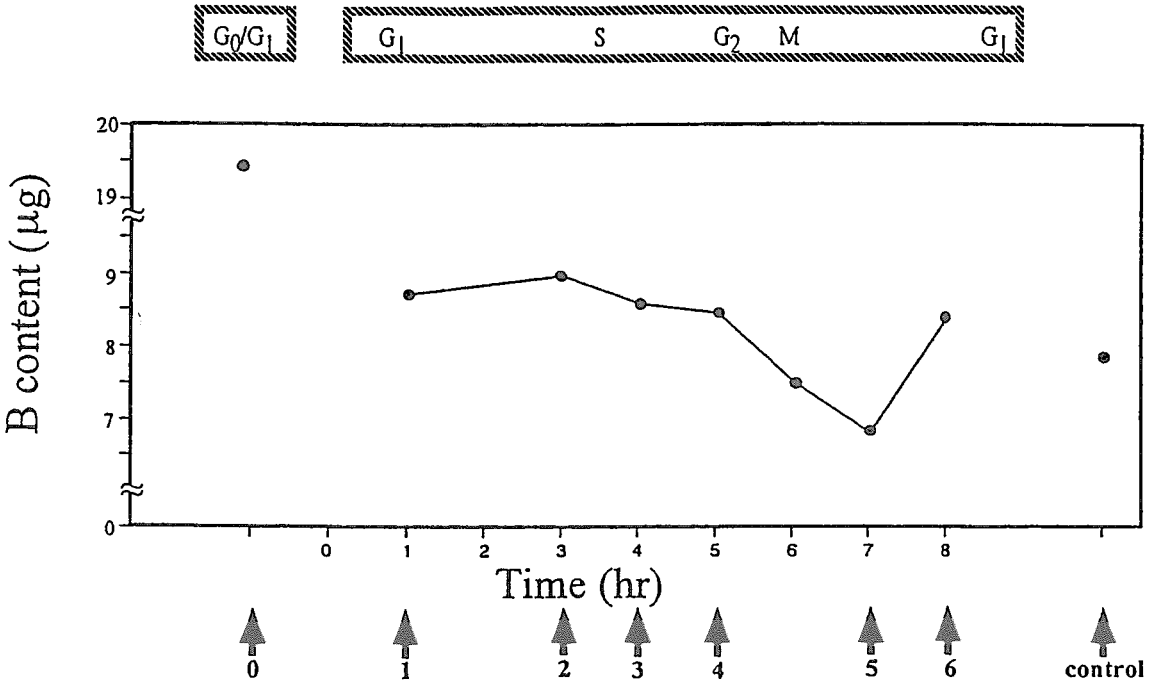

Fig.3. Boron content in 1 g cells (dry wt.) during the cell cycle.
The number under the arrow shows each growth stage number.

Nuclear and Radiochemical Applications of Neutron Absorption Reactions at the Neutron Beam Guides of JRR-3M (II): Developement of the Precise Meassurement Method for Energy 3-5 of Neutron Capture Prompt Gamma-Ray - Photpeak profile

中性子ビームガイドを用いた中性子吸収反応の核・放射化学への応用 (II)：即発ガンマ線エネルギー精密測定法の開発－光電ピーク形状

KISHIKAWA, Toshiaki and UEMURA, Jitsuya,
Kumamoto University Faculty of Engineering
YONEZAWA, Chushiro
JAERI
熊本大学工学部　岸川俊明，上村実也
原研物質科学研究部　米沢仲四郎

Abstract

This paper describes effect of base profile for precise measurement of photon energy in prompt gamma-ray analysis (PGA). The base profile has been examined in the vicinity of full energy (FE), single escape and double escape peaks. Major origins of step-wise base profiles are single and double escape events for triple photon annihilation and single and double Compton escape events for double photon annihilation in the detector in addition to general events for the FE peak. A formula has been proposed for the quantitative characterization of the base profile.

1. Introduction

Deviation of photon energy values between data obtained by photon spectrometry, i.e., the prompt-gamma ray analysis (PGA) and the decay gamma-ray analysis with Ge or Ge(Li) detectors, and those obtained by crystal diffraction spectrometry, has led that the "conventional" method of energy calibration for the photon spectrometry is not adequate to the precise energy assignment. A "new" method has solved this problem by introducing the concept of an instrument function, which is the transfer function between an input signal-shape function, as summarized in ref. 1.

General relationship of the input signal-shape function E(E,x), the instrument function I(x) and the output (measured) signal-shape function M(E,x) can be described as follows based on convolution nature of these functions:

$$M(E,x) = \int I(x)\, H(E,x-u)\, du = I(x)*H(E,x) \quad (1)$$

where x is the channel number appeared in the spectrometer and the symbol ' indicates the convolution integral. Equation (1) implies that if the input signal-shape function is the delta function, then the output (measured) signal-shape indicates the same shape as the instrument functional shape. If the input signal-shape function is, on the other hand, the step function, then the output (measured) signal-shape shows the sigmoid shape. Detailed description of the instrument function can be seen elsewhere [1].

The instrument function is different from the normal distribution (ND) due to distortion caused by the random losses of charge carriers in a Ge detector. The instrument function is a probability density distribution function in which the ND function is convoluted by the random escape probability density distribution (REPDED). The ND folded in the instrument function never appears in the spectrum, though it is the key function in the peak shape analysis. General

研究施設と装置名
JRR-3M 即発ガンマ線分析装置

研究分野
放射化学

prospects of the instrument function are as follows: (1) precise measurement of incident photon energy, because of the centroid of ND being the energy reflecting parameter, and (2) precise measurement of photopeak intensity, because of an integration of the instrument function multiplied by the frequency (i.e., the count rate) giving the intensity of photopeak.

For these prospects, however, it is indispensable to examine the feasibility of base profile subtraction from overall photopeak profile. Commonly used, pre-base profile subtraction methods for spectral analysis are insufficient for the precise measurement of both the photon energy and intensity. The general profile of a measured, full energy (FE) photopeak is an overall function of the individual input-signal shape functions convoluted with the instrument function:

(FE peak profile) = (Fe peak shape)
+ (base profile)
= (FE peak shape)
+ (SAS + LE + RS + CO shapes)

where SAS is the small angle scattering, LE is the edge loss, RS is the random summing and CO is the continuum (which is the shape due to photons coming from sources and Compton events produced by the more energetic photons). Schematic diagram of the FE peak profile is shown in Reference 3. By the method of pre-base subtraction, definite quantity of the base components is remained in the subtracted photopeak shape which cause one of origins of the deviation of the precise energy, as well as the uncertainty of precise photopeak counts. Therefore, non-base subtraction method [3] for the spectral analysis is the promising way of parameter estimation to obtain the centroid of ND. The key signal shapes are those of the single escape (SE) peak and the double escape (DE) peak, besides the FE peak shape, for the precise energy measurement by the PGA with photon energy higher than 1.02 MeV, because the energy difference of both the FE and SE and the SE and DE are 0.511 MeV and that of the FE and DE is 1.02 MeV. However, the profiles of the SE and the DE are both completely different from that of the FE, as shown in Fig, 1. While the base profile of the Fe indicates a step-down profile, that of the SE seems to show no step-wise profile and that of the DE, a step-up profile. The goal of the peak shape analysis (with prompt as well as decay and transition photons) [1] is, essentially, to estimate the parameters of the instrument function. This paper aims at describing interaction events in the Ge detector, formulating the relative energy spectrum functions of the base components in the vicinity of both the SE and the DE for either- analytical shape parameter estimation or Monte Carlo simulation of the spectral response.

2. Theoretical

2.1. Gamma-ray interactions in the detector

Here, we consider higher energy photon with energy E > 1.022 MeV. Major processes in the detector are the photoelectric absorption process, the Compton scattering process and the pair production process.

The input signal function for the full energy photopeak has the delta functional distribution function which is resulted from the following three processes: (1) the direct photoelectric absorption, (2) the photoelectric absorption of Compton scattered photon with diffused Compton electron in the detector, and (3) the photoelectric absorption of annihilation photons generated from pair creation partner of a positron with diffused, counter pair of an electron.

The input signal function for the Compton electron can be given by the probability density distribution function with E_c being the Compton electron energy. The differential cross section of Compton scattering is given by the Clein-Nishina equation.

The pair production occurs in the detector, if E is higher than twice of the electron rest mass energy (= 1.022 MeV).

2.2 Interaction of positron in a medium

When an energetic positron (create by the pair production) transmits in an appropriate medium, then it loses its kinetic energy by successive collisions with orbital electrons. Finally the positron forms a positron-electron pair. Then it undergoes either the double-photon annihilation (DPA) or the triple-photon annihilation (TPA). If the positron-electron pair forms a positronium, the DPA or the TPA is allowed according to the state being singlet or triplet. Ore and Powell [2] derived the energy spectrum function of the TPA based on the QED (quantum elcctrodynamic) theory with E_{3A} being the TPA photon energy.

The TPA relative energy spectrum is a continuously rising distribution in the energy range from zero to Ee (: = 0.511 MeV), because of the multiple character of the three-photon process.

2.3. Escape events of annihilation photon(s) from the detector

In the case of DPA the single escape peak (SE/2A) and the double escape peak (DE/2A) appears at energy of respectively, $E_{SE/2A} = E - E_{2A}$ and $E_{DE/2A} = E - 2E_{2A}$. Both the relative energy spectrum functions of SE/2A and DE/2A processes, i.e., $P_{SE/2A}(E_{SE/2A})$ and $P_{DE/2A}(E_{DE/2A})$, respectively, are in the form of delta function, because both the incident photon and annihilation photon are monoenergetic.

In the escape event with the TPA process, on ~he other hand, there are three types of escape processes: the single escape with energy $E_{1/3A}$, the double escape with energy $E_{3A,1} + E_{3A,2}$ and the triple escape with energy $E_{3A,1} + E_{3A,2} + E_{3A,3} \cong E_{TE/3A} = 2E_{e}$, where suffixes 3A,1, 3A,2 and 3A,3 are the first, the second and the third TPA photons, respectively. Figure 2 shows schematic diagrams of relevant photon interactions with the TPA in ~he detector. The relative energy spectra for the TPA escape processes are rather complicated as follows:

(I) Relative energy spectrum function of single escape for the TAP process (SE/3A):

In the case of single photon escape as a result of event coming after positron-electron pair creation, the two TPA photons undergo the photoelectric absorption. The photoelectrons marked 3A,2 and 3A,3 in Fig. 2(A) generates change carriers in the detector to give the input signal function. As three body nature of TPA process, the absorbed photon energy has continuous energy spectrum with the detected energy:

$$E_{detec} = E - 2E_{e} + E_{D/3A}$$
$$= E - 2E_{e} + E_{3A,2} + E_{3A,3} \quad (3)$$

where $E_{D/3A}$ is the sum energy of the second (3A,2) and third (3A,3) TPA photons.

According to the well known probability theory, on the other hand, if two probability variables have linear combination and two probability density distribution functions with those of the variables independent each other, then the overall function of these two functions can be obtained by the convolution integration of these functions. Therefore we obtain the relative energy spectrum function of single escape for the TPA, $P_{SE/3A}(E_{detec})$:

$$P_{SE/3A}(E_{detec}) = P_{3A,2}(E_{3A,2}) * P_{3A,3}(E_{3A,3}) \quad (4)$$

(2) Relative energy spectrum function of double escape for the TPA process (DE/3A):

Contrary to the case (1) in the previous paragraph, the double escape for the TPA process undergoes photoelectric absorption with the single TPA photon. Therefore, the shape of relative energy spectrum function is identical with that TPA probability density function:

$$P_{DE/3A}(E_{detec}) \cong P_{S/3A}(E_{S/3A})$$
$$\cong P_{3A}(E_{3A}) \quad (5)$$

with $E_{detec} = E - 2E_{e} + E_{3A}$, where $E_{S/3A}$ is the energy of absorbed TPA photon in the detector.

(3) Relative energy spectrum function of triple escape

for the TPA process (DE/3A):

Since the sum energy of the triple escape photons for the TPA is the same quantity as that of the double escape photons for the DPA, the observed energy is:

$$Edetec = E \sim ETE/3A = E - 2Ee \quad (6)$$

and, therefore, the shape of relative energy spectrum function, PTE/3A(Edetec) is identical with that of double escape signal of the DPA.

Figure 3 shows the relative energy spectrum functions of single, double and triple escape for the TPA process..

2.4. Compton escape events with double photon annihilation in the detector

Since the Compton scattering happen for the annihilation radiation as a result of interaction of annihilation photon with the detector material, escape events of the scattered annihilation photon takes place in the detector. In the DPA process there are three types of escape events concerning the Compton scattering.

(1) Relative energy spectrum function of single Compton escape and single annihilation absorption with the DPA (SCE/SA/2A):

In this process a Compton scattered DPA photon escapes from the detector while the counter part of DPA photon undergoes the photoelectric absorption. So we obtain the relative energy spectrum function: $P_{SCE/SA/2A}(E_{detec})$ with $E_{ditec} = E + E_a + E_C$.

(2) Relative energy spectrum function (if single Compton escape and single annihilation escape with the DPA (SCE/SE/2A):

In this process a Compton scattered DPA photon escapes form the detector while the counter part of DPA photon also escapes from the detector. So we obtain the relative energy spectrum function PSCE/SE/2A (Edetec) with Editec = E + 2Ee + Ec.

(3) Relative energy spectrum function of double Compton escape with the DPA (DCE/2A):

In this process, a similar probability relation to the former section (1) can be established, since these two Compton processes are independent each other. Therefore we obtain the folded relative energy spectrum function as:

$$P_{DCE/2A}(E_{detec}) = P_{C,1}(E_{C/2A,1}) * P_{C,2}(E_{C/2A,2}) \quad (7)$$

with $E_{detec} = E - 2Ee + E_{C/2A,1} + E_{C/2A,2}$.

(4) Compton escape with the TPA photons:

Similarly the Compton escape with the TPA photons happen with the TPA photon. The relative energy spectrum of both single and double Compton escape with the TPA are complicated, because the relative energy spectrum of single and double escape for the TPA processes, respectively, $P_{SE/3A}(E_{detec})$ and $P_{DE/3A}(E_{detec})$, have continuous spectrum. We omit to consider these events, here. Figures 4 and 5 shows, respectively, the interactions events of ~*rays and the relative energy spectrum function with these processes SCE/SA/2A, SCE/SE/2A and DCE/2A in the detector.

3. Experimental

PGA measurements were performed at the JRR-3M thermal (port T1-4-1) and cold (port C2-3-2) neutron beam guides in Tokai Establishment, JAERI. The PGA system

consist of a closed-end high purity (HP) germanium detector (HPGe) surrounded by bismuth-germanium oxide (BGO) scintillation crystals and a multi mode-operation spectrometer. A precision pulser, BNC PB-4 was used for non-proportionality correction.

4. Results and discussion

General input signal function. $H(E_{detec})$, of the corresponding relative energy spectrum function, P(detec), described in the previous subsections can be given by introducing frequency term n to the relative energy spectrum function:

$$H(E_{detec}) = n\, P(E_{detec}) \quad (8)$$

Overall input signal function for the detection events described in the former sections (3) and (4) are the summation of all the individual input signal functions:

$$H_{sum}(E_{detec}) = n_{FE}P_{FE}(E_{detec}) + n_{DE}P_{SE}(E_{detec}) + n_{DE}P_{DE}(E_{detec}) + n_{SCE/SA/2A}P_{SCE/SA/2A}(E_{detec}) + n_{SCE/SE/2A}P_{SCE/SE/2A}(E_{detec}) + n_{SE/3A}P_{SE/3A}(E_{detec}) + n_{DE/3A}P_{DE/3A}(E_{detec}) + n_{TE/3A}P_{TE/3A}(E_{detec}) \quad (9)$$

where n's are the frequency term (i.e., the count rate) or individual processes. Ore and Powell [2] derived the cross section ratio of the DPA to TPA being sDPA/sTPA=1/370 for free positron-electrons annihilation. However, if the annihilation undergoes via positronium formation, then the fraction of TPA depends on physicochemical nature of the material (i.e., Ge of the HPGe detector in operation). Therefore the n's should be treated as estimation variables when the output peaks for FE, SE and DE are subjected for the parameter estimation. Typical example of a heaping up pattern of the overall input signal function with appropriate n's values (n = 1 for every n) for the single mode operation of the Ge/BGO detectors is shown in Fig. 6. All of the FE, SE and DE peaks accompany the SAS, the LE, the RS and the CO shapes in their vicinity as quoted in the introducing section. Therefore we have to add up these terms for the practical cases. Even if we take these shapes into account, the partial spectrum of input signal functions remarkably demonstrates the step-wise base profiles around the FE and DE peak regions, and the non-step wise base profile around the SE peak region. According to the instrument function, the distortion of ND is caused by the trapping event of charge carriers forming the REPDED. That is, the position reflecting energy is not the position of peak maximum, namely, the peak position x [channel, but the centroid x_c Of the ND. If the peak position of energy E (keV), the $x_p(E)$ is proportional ~o energy then the quantity $x_p(E)\ c_w/E$ must be unity [i.e. = 1, with c_w being the channel width in units of (keV/channel)]. If the peak position, on the other hand, is not the energy reflecting position, then the quantity would be $x_p(E)\ c_w/E = 1 + \delta_{peak}(E)$ where $\delta_{peak}(E)$ ($\neq 0$) is the deviation indicating term (which is [to be the peak index). The variation of the peak position with energy has been remarkably demonstrated by the $^{nat}Fe(n,\gamma)$ prompt photons. Therefore, the energy differences of $E_{SE} - E_{FE}$, $E_{DE} - E_{SE}$ or $E_{DE} - E_{FE}$ should be adjusted for the centroid of ND convoluted in the instrument function. The energy differences of annihilation photons are, essentially, the self containing, intrinsic measure of energy in every samples. For this reason, the formulation of base profile provides strong tool for the de-convolution of Eq. (1) in the measurement of photon energy.

5. Conclusion

This work clearly demonstrates the importance of formulating input base-shape signal functions in the vicinity of full-energy, single-escape and double-escape peaks, particularly when they are subjected for the precise energy analysis. The result of this study demonstrate that major origins of the base profiles are (1) the escape of photons for the triple photon annihilation, (2) the escape of Compton scattered photons for the double photon annihilation and (3) the escape of Compton scattered photons for the triple photon annihilation.

References

[1] T. Kishikawa, K. Nishimura, S. Noguchi, Nucl. Instrum. Meth. A353 (1994) 285.

[2] A. Ore, J.L. Powell, Phys. Rev., 75 (1949) 1696.

Publications

[1] T. Kishikawa, S. Noguchi, C. Yonezawa, H. Matsue, A. Nakamura, H. Sawahata "Photopeak profile of full energy and escape peaks in neutron capture prompt-gamma ray spectra", J. Radioanal. Nucl. Chemistry,

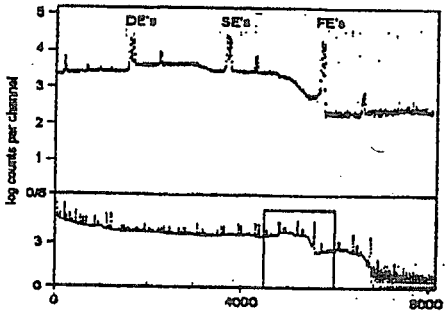

Fig. 1. Typical example of neutron capture gamma-ray spectra obtained by activation of natural iron plate at the single mode operation of BGO/Ge spectrometer installed at the JRR-3M neutron beam guide hall. Doublet peaks of 7631- and 7645-keV Fe capture gamma-rays are shown; FE: full energy peak, SE: single escape peak, DE: double escape peak

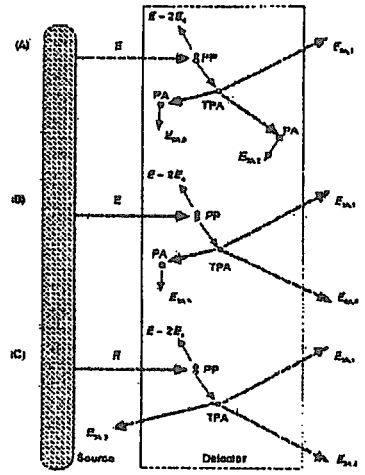

Fig. 2. Escape of photons after the triple photon annihilation (TPA) in the Ge detector. (A) single photon escape of TPA, (B) double photon escape of TPA, (c) triple photon escape of TPA, PP: pair production, PA: photoelectric absorption

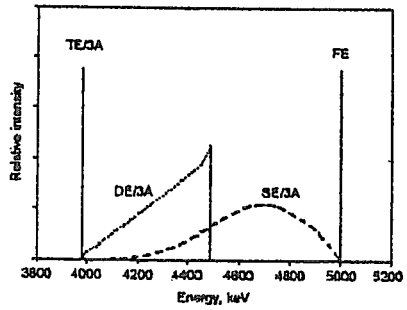

Fig. 3. Energy spectra of triple photon annihilation (TPA) in a Ge detector. TE/3A: triple escape of TPA. FE: full energy peak of photon energy 5000 keV, DE/3A: double escape of TPA, SE/3A: single escape of TPA

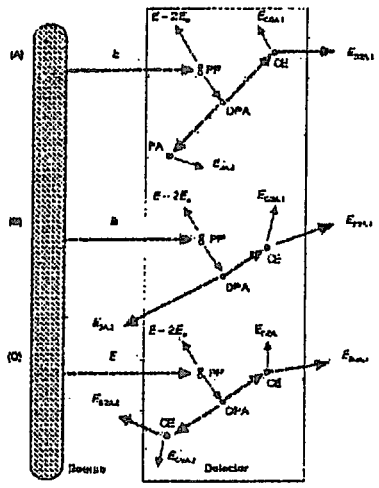

Fig. 4. Escape of photons after the double photon annihilation (DPA) in the Ge detector, (A) single Comnpton escape - single photoelectric absorption of DPA, (B) single Compton effect - singleescape of DPA, (C) double Ccmpton escape of DPA, PP: pair production, PA: photoelectric absorption

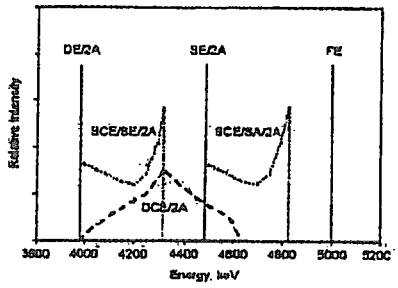

Fig. 5. Energy spectra of double photon annihilation (DPA) in a Ge detector, DE/2A: double escape of DPA, SE/2A: single escape of DPA, FE: fun energy peak of photon energy 5000 keV, SCE/SE/2A: single Compton escape with single escape of DPA, SCE/SA/2A: single Compton escape with single absorption of DPA, DCE/2A: double Compton escape of DPA

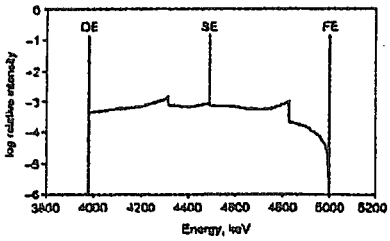

Fig. 6. Calculated overall input signal function with appropreate k's-values (= 1 for every k) of the BGO/Ge spectrometer at the single mode operation. Aoconlpanying SAS, LE, RS and CO for the FE, SE and DE peaks, together with the Compton spectrum of FE are not considered (see text). The photon energy is 5000 keV

3-6 即発γ線分析の大型試料への適用 (II)

Prompt Gamma-Ray Analysis of Large and Volumious Samples. II

東京都立大学大学院理学研究科
Graduate School of Science, Tokyo Metropolitan University
大浦 泰嗣・末木 啓介・中原 弘道
Yasuji Oura, Keisuke Sueki, Hiromichi Nakahara
理化学研究所
The Institute of Physical and Chemical Research (RIKEN)
榎本秀一
Shuichi Enomoto
日本原子力研究所
Japan Atomic Energy Research Institute
松江秀明・米澤仲四郎
Hideaki Matsue, Chushiro Yonezawa

1. はじめに

ガイドビーム型PGA装置は，原子炉外へ中性子を導き照射・測定を行うという構造から二次的特徴を持つ．すなわち，中性子束が小さいため，照射試料中の誘導放射能がごくわずかであること，また，原子炉内へ挿入する必要がないため，試料の大きさの制限が緩いことである．我々はこの特徴に特に注目し，PGAを大型試料(ここでの「大型」とは，ビームサイズより大きく，厚みのある不定形ということ)に適用するための内標準法を考案した[Sueki96]．そして，都内で出土した江戸時代に製作された肥前系ならびに瀬戸・美濃系陶磁器の元素分析に応用し，PGA法によりこれらの判別が可能であること示した[Sueki98]．

本研究では，さらに銅鏡と須恵器の分析を行い，考古学的試料に対するPGA法の有効性を探った．さらに，生物学分野への大型試料PGA法の有効性を調べた．近年，動物や植物中の微量元素濃度が生体内分布や特定器官での役割解明のため，様々な方法で定量されている．一般的に，動物の臓器中の元素濃度を定量するためには屠殺し，摘出された臓器を粉末化あるいは溶液化する必要がある．したがって，例えば，同じ個体を使って臓器中の投与した元素濃度の時間変化を追うことはむずかしい．もし，同じ生きている個体を使ってこの元素分布の時間変化や代謝研究が行うことができれば，個体差による変動のない何かおもしろい情報が得られるに違いない．そこで，大型試料PGA法を生体試料に応用した．PGA法は試料の物理的状態の制限が緩いので，摘出した臓器をそのまま分析に供せられる．また，ラット1個体をそのまま照射することも可能である．最終目標は，動物を生かしたまま中性子照射し，各臓器中の元素濃度の時間変化を得ることであるが，残念ながらまだこの目標までは到達しなかった．

2. 実験方法

中性子照射は日本原子力研究所JRR-3M実験ホールに設置されている即発γ線分析装置で行った．四フッ化エチレン六フッ化プロピレン共重合樹脂フィルムで包んだ試料をビームに対して45°傾けて設置し，He雰囲気下でビームサイズ20mm×20mmの熱中性子または冷中性子を照射した．即発γ線は，BGO検出器で取り囲まれたGe半導体検出器を用いて，コンプトンサプレッションモードで測定を行った．

誘導放射能がわずかであることがPGA法特徴の一つであるが，これは比放射能が小さいということであり，大型試料のようにある程度量があると全体の放射能，特に短半減期核種による放射能は

JRR-3M 即発γ線分析装置 放射化分析

無視できない．我々はこれを積極的に利用することにし，即発γ線測定後，(n, γ)反応により生成した試料中の放射性核種のγ線スペクトロメトリーをオフラインでGe半導体検出器をもちいて行った(ここではこれを便宜上INAAと呼ぶ)．

PGA，INAAともに定量は内標準法により元素濃度比として求めた．

3. 中性子透過度

大型試料を照射した場合，どの程度中性子が試料内を透過しているのかを調べた．試料として，須恵器・陶磁器の模擬試料としてセラミック板(いわゆるタイル，97mm×97mm×5mm)4枚のスタック，銅鏡の模擬として銅板(48mm×48mm×1mm)30枚のスタック，生体試料の模擬としてロースハム(48mm×48mm×1.8mm×15枚[熱中性子]，48mm×48mm×2.5mm×18枚[冷中性子])のスタックを用意した．これらを熱中性子および冷中性子で照射した後，各板中に生成した中性子捕獲放射性核種をイメージングプレートにて測定した．

図1に20mm×20mm領域での平均感光強度の相対値を深さに対してプロットした．セラミックと銅では熱中性子と冷中性子の透過度にはほとんど差は見られない．セラミック板では厚さ2cmまでは中性子はほとんど減衰することなく透過するが，銅板では2cmの深さまでで，約30%が吸収または散乱される．一方，H原子を多く含むハムでは1.5cmの厚さで中性子束はほぼ50%まで減少する．この厚さ付近までは，冷中性子と熱中性子の透過度に大きな違いは見られないが，これよりも深いところでは冷中性子の方が熱中性子よりもより透過度が大きく，より深くまで中性子が進行する．水素を多く含むハムでは冷中性子が熱中性子になりやすいことがこの一因ではないかと考えている．我々が分析してきた考古学的試料の厚さは最大で2～3cm程度であるので，中性子はほとんど透過しており，試料全体の，または，中性子照射部の平均組成が得られていることが確かめられた．ただし，生体試料においては，元素分布に不均一性があると誤った元素濃度比が得られ可能性があることに注意する必要がある．

4. 須恵器の分析

須恵器は，5世紀ごろ朝鮮半島から伝えられた高度な技術を使って製作された硬い土器で，古代全期間にわたって日本各地で生産された．日本各地に数千基の須恵器窯跡が残っており，発見されていないのは，北海道，山梨県，神奈川県，長崎県だけである．須恵器は，鋳型にはめられて作られておらず，全く同じ形式の須恵器はないと言っても過言ではない．また，工人集団の移動に伴い幾つかの場所で類似した形式の須恵器が製作されていた．そのため，形式による須恵器の産地推定は非常に困難であり，自然科学的手法による産地推定が必要である．

本研究では，宮城県六郎館窯群・大吉山窯・須江関の入窯群，新潟県日向窯群，愛知県皿山窯・山茶器，兵庫県久留美薮谷窯，島根県池の奥4号窯，香川県赤瀬山2号窯で出土した須恵器片，計79片を分析した．試料は小さいもので約1g，大きいものでは約40gであった．冷中性子または熱中性子で1～2時間測定を行い，一部の試料について照射終了約5分後よりオフラインにて試料中の中性子捕獲生成放射性核種の壊変γ線を約2時間測定した．Siを内標準元素として元素濃度比を定量した．

INAAでは，^{24}Na，^{28}Al，^{42}K，^{52}V，^{56}Mn，ならびに^{152m}Euを検出することができた．このうち，VとEuはINAAのみで検出でき，その他はPGAとINAAの両方で検出できた．MnとNaの検出感度はINAAの方がPGAよりもそれぞれ約200倍と約50倍高かった．

奈良教育大学の三辻先生は，約20年かけて約6万点の須恵器片の分析を粉末試料による蛍光X線分析法で行い，K，Ca，Rb，Srが産地推定の指標となることを見いだした[三辻96]．そこで，PGA法で得られたCa/SiとK/Siの二次元分布図を作成してみた(図2(a))．測定値は各窯ごとにまとまっていることがわかる．六郎館と日向は，Ca/Si比には差が見られないがK/Si比で区別でき，一方，大吉山と久留美柳谷はその反対でCa/Si比が異なっている．試料数の少ない赤瀬山，池の奥，皿山，須江関の入は柳谷の領域とほぼ重なっている．RbとSrの定量が

できなかったので，PGA法が得意とするBが指標にならないか調べた．図2(b)にB/Si-K/Si分布図を示す．皿山と池の奥，須江関の入がCa/Siのかわりに B/Siを用いることにより久留美柳谷と区別することができた．また，K/Si，Ca/Si，B/Siの3因子によるマハラノビスの汎距離による2群間判別を行ってみた．日向一久留美柳谷と大吉山一久留美柳谷の判別はK/SiとCa/Siの2因子の場合よりもはっきりと行えたが，それ以外は重複領域に分布する試料が多くこれら3因子による判別は思わしくなかった．

5. 銅鏡の分析

銅鏡の化学分析は1930年代より行われ，主としてCu，Sn，ならびにPbからできており，微量成分としてAs, Sb, Ni, Fe, Znなどが含まれていることが報告されている．高感度な分析法の発達により銅鏡から一部(数mg程度)を採取して分析を行うこともあり，この微量な試料が銅鏡全体の組成を反映するか問題が生ずる．腐食が進んだ銅鏡の分析結果は酸化物の影響で全成分の合計が100%に満たないことが多く，100%になるように換算されている．また，蛍光X線分析では表面のさびが定量値に影響をあたえるという報告もある．一方，中性子ビームをプローブとするPGAは，20mm×30mmの範囲を銅鏡内部まで分析できるため，これらの問題が生じにくい．

中国産の銅鏡87面を分析に供した．これらのほとんどは丸形で，一部は八角形をしており，直径5～21cm，重さ18～1700gで，裏面(鏡面が表)の文様により以下の製作時代が鑑定された：前漢(B.C.206 - A.D.8)，後漢(A.D.25 - A.D.220)，三国六朝(A.D.220 - A.D.589)，唐(A.D.618 - A.D.907)，宋(A.D.1127 - A.D.1279)，現代(つまり偽物)．これらのほぼ中心部を表面側より熱中性子で照射し，約1時間即発γ線測定した．一部の試料については照射終了5～7時間後から中性子捕獲放射性核種の壊変γ線の測定を2～3時間行った．

観測された即発γ線のほとんどはCuからのもので，Snの即発γ線がわずかに検出された．残念ながら，主成分の一つであるPbはPGAでは低感度のため検出できなかった．壊変γ線の測定により，(n, γ)生成物として^{64}Cu，^{76}As，^{122}Sb，^{198g}Auを確認した．Cuを内標準元素に選び，Sn/Cu，Au/Cu，As/Cu,ならびにSb/Cu比を定量した．

中性子照射は銅鏡の一部にのみ行うが，これにより得られた値が銅鏡全体の組成を代表するのか，以下の方法でまず調べた：1) AとBの2面の銅鏡で，表面側から照射したときと裏面側から照射したときの定量値を比較した．この際，Bには裏面のみさびている銅鏡を用いた．2) 同じ1面の銅鏡で異なるa，b，cの3箇所を照射し定量値を比較した．表1に結果を示す．1)，2)とも各定量値は誤差範囲内でよく一致している．1)の検討より中性子ビームは銅鏡を透過しており，表面のさびの影響は無視できることがわかる．また，2)の検討よりPGAの分析精度では銅鏡の組成に偏りは見られず，任意の一ヶ所を照射すればよいことが確認できた．

図3に各定量値を上から製作時代の古い順に示した．Sn/Cu比は5%から40%の範囲で変動している．図から明らかなように，前漢から唐までの約1100年間にわたりSn/Cu比はほぼ一定で，平均値は30%である．ところが，宋になるとSn/Cu比は小さくなり，平均13%であった．前漢から唐にかけてSn/Cu比がほぼ一定であることは，1937年と1940年の小松らの報告[小松37，小松40]ですでに明らかであったが，彼らの平均値は30%であった．また，宋になるとSn/Cu比が小さくなることは系統的な分析が行われておらずはっきりしていなかったが，本実

表1 銅鏡のSn/Cu分析値の検討

1			2	
	A	B	a (上部)	25.8±2.4%
表面	30.7±1.5%	31.9±4.6%	b (中央)	28.0±2.7%
裏面	30.6±1.4%	29.2±2.5%	c (下部)	26.9±1.8%

験により明かとなった．微量成分であるSb，As，AuのCuに対する濃度比は製作年代による明らかな特徴は見られなかった．

偽物は後漢式，唐式，戦国式の文様をしており，Sn/Cu比は30%よりも小さかった．試料によるばらつきの範囲をわずかに越えている程度であり，元素濃度比による真贋の判別は難しそうである．

6. ラットの分析

PGA法で感度の高いB(0.3mg)，Cd(1.5mg)，またはHg(3mg)を含んだ生理食塩水をWistar系7週令のオスのラットに腹腔内投与した．投与3時間後，22時間後，ならびに65時間後に脳，肝臓，腎臓，筋肉の一部，骨の一部を摘出した．摘出した臓器は何の処理も施すことなくそのままただちに冷凍し，中性子照射直前に解凍した．臓器は，冷中性子または熱中性子でそれぞれ約60分または約100分照射し，即発γ線を測定した．

投与したCdのピークとともに生体での主要元素であるNa，Cl，K，S，Hの即発γ線が観測された．しかしながら，自然に含まれている微量金属元素の即発γ線は検出されず，これらの定量は困難であることがわかった．主要元素であるCl/H, K/H, Na/H，S/Hは1%程度，B/H，Cd/H，Hg/Hは50ppm程度まで検出可能である．INAAでのγ線測定では^{56}Mn，^{24}Na，^{42}K，^{38}Clが観測された．即発γ線スペクトルでは観測されなかったMnを検出することができ，照射後に壊変γ線を測定することによりさらにMnの定量が可能であることがわかった．これら放射性核種の半減期は15時間以下であり，1週間後には照射試料中の放射能は無視し得る程度にまで減衰する．

図4に各臓器中のCd/H比とB/H比の経時変化を示した．Cdは脳では検出されなかった．また，骨や筋肉には腎臓と肝臓に比べてCdが蓄積しにくいようである．脳には有害な元素の侵入を防ぐ関門があることが知られているが，この結果はこの関門の作用を示している．Cd/H比は本研究の経過時間内では常に腎臓より肝臓の方が大きかった．腎臓のCd/H比は経過時間とともに徐々に増加しているが，肝臓ではほぼ一定値となった．投与されたCdの大部分はまず肝臓に蓄積し，肝臓から腎臓へゆっくり移っていき，約40日後に肝臓内と腎臓内のCd濃度が等しくなることが報告されている[桜井94]．本研究の結果はこの報告と矛盾しない．Bは投与3時間後に摘出した臓器と22時間後と65時間後の腎臓で検出された．BはCdと異なり，脳でも検出された．生理食塩水のみ投与したラットの腎臓でもBが検出され，そのB/H比の範囲を斜線でグラフ上に示した．22時間後，65時間後の腎臓のB/H比はこの範囲内であるから，Bは3時間後の臓器にのみ残留していたと考えられる．Bは吸収後すぐに尿へ排泄されるという報告[桜井94]と矛盾しない経時変化が得られた．Hgは投与3時間後の臓器のみ分析を行った(図5)．Hg/H比は腎臓が一番大きく，脳と骨では検出できなかった．無機イオン型Hgを投与すると主に腎臓に蓄積されることが知られており[桜井94]，Hg/H比でも同じ傾向が得られた．

内標準法では元素濃度比しか定量できないため，絶対濃度を得るには異なる方法でどれか一つの元素の絶対濃度を測定する必要がある．ここでは，H濃度を10%(人体での平均濃度)と仮定して，臓器中でのCd，B，Hg濃度を見積もった．Cdは投与した0.3mgのうち肝臓と腎臓に投与65時間後にはそれぞれ70%と6%蓄積していた．ラットに腹腔内投与されたCdは24時間後にはその40～50%が肝臓に蓄積されるという報告[桜井94]とほぼ一致する．Bは投与した1.5mgのうち，投与3時間後には肝臓，腎臓，脳にそれぞれ59%，34%，17%蓄積していた．また，Hgは腎臓と肝臓にそれぞれ13%と3%蓄積していた．

本方法で試料に特別な処理を施さずに，非常に簡単にB/H，Cd/H，Hg/H比を定量することができ，さらに濃度の経時変化を得ることもできた．揮発性の高いHgは試料処理，とくに灰化中の揮発に注意する必要があるが，本法は前処理が不要のため揮発することがなく，非常に有効な方法である．

生きたラットのPGA

摘出した臓器の分析にPGA法は有効であること

が確認された．しかし，摘出法を用いると元素濃度の経時変化を測定するには異なる固体を用いる必要があり，同一個体での経時変化を得ることができない．そこで，臓器を摘出することなく経時変化を測定するために，麻酔状態のラットをそのまま中性子照射し，即発γ線を測定することを試みた．

既存の中性子ビームサイズは20mm×20mmであり，ラット体内の臓器を直接照射するには大きすぎる(ねらった臓器以外も照射されてしまう)ので，厚さ20mmの^{nat}LiFブロックでコリメータを製作し，10mm×10mmのビームサイズにした．ビームサイズはイメージングプレートを用いて確認した．Cdを投与したラットに麻酔をかけた後，開腹し，一端を開封してあるFEPフィルム製袋に入れた(即発γ線分析装置内の汚染を防ぐため)．これを新たに製作したテフロン製架台上にテフロン製糸にて固定し，He+O_2雰囲気(分圧比 7：3)中で肝臓に熱中性子を約1時間照射した．1時間の照射でラットが死亡することはなかった．照射後，肝臓を摘出し，もう一度即発γ線測定を行い，同じCd/H比が得られるかどうか確認した．その結果は，体内照射の場合が$(2.08\pm0.13)\times10^{-4}$で，摘出照射のときが$(3.46\pm0.06)\times10^{-4}$であり，同じ定量値がえられず，体内照射の方が相対的にHが多いという結果となった．この原因と一つとして，肝臓で散乱された中性子の寄与が考えられる．中性子はとくにH原子により散乱されやすいことがわかっている．散乱中性子が肝臓周辺の臓器に入射し，その部分の即発γ線も検出されたと考えられる．投与されたCdの70%は肝臓に蓄積されており，その周辺の臓器にはわずかしか含まれていないはずである．しかし，H濃度は体内ではほぼ一定であるから，肝臓以外からのHの即発γ線を同時に測定したため，Cd/H比が小さくなってしまったのであろう．また，肝臓を透過した中性子が肝臓の後の組織を照射する影響も考えられる．そこで，摘出した肝臓を用いて中性子の透過度を測定した．Co試薬をのみを照射したときと，摘出した肝臓の後ろに同じCo試薬をおいて照射した時でのCoからの556keVの即発γ線の計数率を比較したところ，後者の計数率は前者の約3%であった．この差がすべて中性子束に由来すると考えると，肝臓を透過する中性子の割合は約3%である．体内法と摘出法で定量値が異なる原因は，散乱中性子の影響が透過中性子より大きいと推測される．当初，散乱中性子の影響は小さいと考えていたが，実際はその影響は大きく，その影響を最小限にする工夫およびその補正法を開発する必要があることがわかった．

7. まとめ

内標準法により考古学的試料である須恵器と銅鏡，ならびに生物学的試料であるラットの臓器を分析した．定量可能な元素の種類は多くはないが，どの試料もPGAの特徴をよくいかすことができ，PGA法は非常に有効であることがわかった．麻酔をかけたラットを開腹し，そのまま照射して即発γ線測定を試みたが，正確な定量値を得ることができなかった．散乱中性子による影響が大きいと考えられ，これを補正する方法を開発する必要がある．また，希望する部位に正確に照射できる様にする工夫も必要である．今後も，PGAの特徴を充分活かした分析法の開発や応用を続けていく予定である．

試料の選定や入手に関して，富沢威博士，西川寿勝氏，三辻利一博士の協力を得た．また，その専門分野についていろいろ教授していただいた．生きたラットの照射に対し，東京大学原子力研究総合センター大学開放研究室，ならびに日本原子力研究所研究炉利用課の方々に便宜をはかっていただいた．ここに記して謝意を表す．

参考文献

小松37：小松茂他，東方学報(京都) 8, 11 (1937).
小松40：小松茂他，東方学報(京都) 11, 161 (1937).
三辻96：三辻利一，放射化分析 No.3, 18 (1996).
桜井94：桜井弘，田中英彦編，「生体微量元素」(廣川書店，1994).

Sueki96 : K.Sueki et al., *Anal. Chem.* **68**, 2203 (1996).
Sueki98 : K.Sueki at el., *J .Radioanal. Nucl. Chem.* **234**, 27 (1998).

成果の公表

・"Prompt Gamma Ray Analysis of Archaeological Bronze" Y.Oura, K.Sueki, H.Nakahara, T.Tomizawa, and T.Nishikawa. Asia-Pasific Symposium on Radiochemistry '97 (1997)

・"中性子ビーム放射化分析法による須恵器の元素分析" 大浦泰嗣，齋藤綾子，末木啓介，中原弘道，三辻利一，松江秀明，米澤仲四郎．第42回放射化学討論会(1998)

・"Prompt Gamma Ray Analysis of Rat" Y.Oura, S.Enomoto, H.Nakahara, H.Matsue, and C.Yonezawa. Tenth International Conference on Modern Trends in Activation Analysis (1999)

・"Some Basic Studies on Non-Destructive Elemental Analysis of Bulky Samples by PGA" H.Nakahara, Y.Oura, K.Sueki, M.Ebihara, W.Sato, Sk.A.LAtif, T.Tomizawa, S.Enomoto, C.Yonezawa, Y.Ito. Tenth International Conference on Modern Trends in Activation Analysis (1999)

・"ラットの即発ガンマ線分析" 大浦泰嗣，榎本秀一，中原弘道．第43回放射化学討論会(1999)

・"即発γ線分析法による大型試料の元素分布測定" 大浦泰嗣，Sk.A.Latif，海老原充，中原弘道．日本化学会第78春季年会 (2000)

・"Prompt Gamma Ray Analysis of Archaeological Bronze" Y.Oura, A.Saito, K.Sueki, H.Nakahara, T.Tomizawa, T.Nishikawa, C.Yonezawa, H.Matsue, and H.Sawahata. *J. Radioanal. Nucl. Chem.* **239**, 581-585 (1999)

・"Completely Non-destructive Elemental Analysis of Bulky Samples by PGAA" Y.Oura, H.Nakahara, K.Sueki, W.Sato, A.Saito, T.Tomizawa,and T.Nishikawa. *Czechoslovak J. Phys.* **49/S1**, 311-321 (1999)

・"Prompt Gamma Ray Analysis of Rat" Y.Oura, S.Enomoto, H.Nakahara, H.Matsue, C.Yonezawa. *J. Radioanal. Nucl. Chem.* **244**, 311-315 (2000)

・"Some Basic Studies on Non-Destructive Elemental Analysis of Bulky Samples by PGA" H.Nakahara, Y.Oura, K.Sueki, M.Ebihara, W.Sato, Sk.A.LAtif, T.Tomizawa, S.Enomoto, C.Yonezawa, Y.Ito. *J. Radioanal. Nucl. Chem.* **244**, 405-412 (2000)

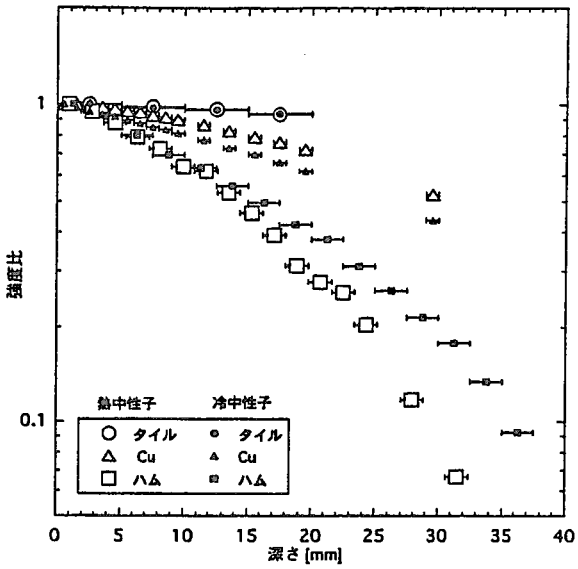

図1　中性子透過度

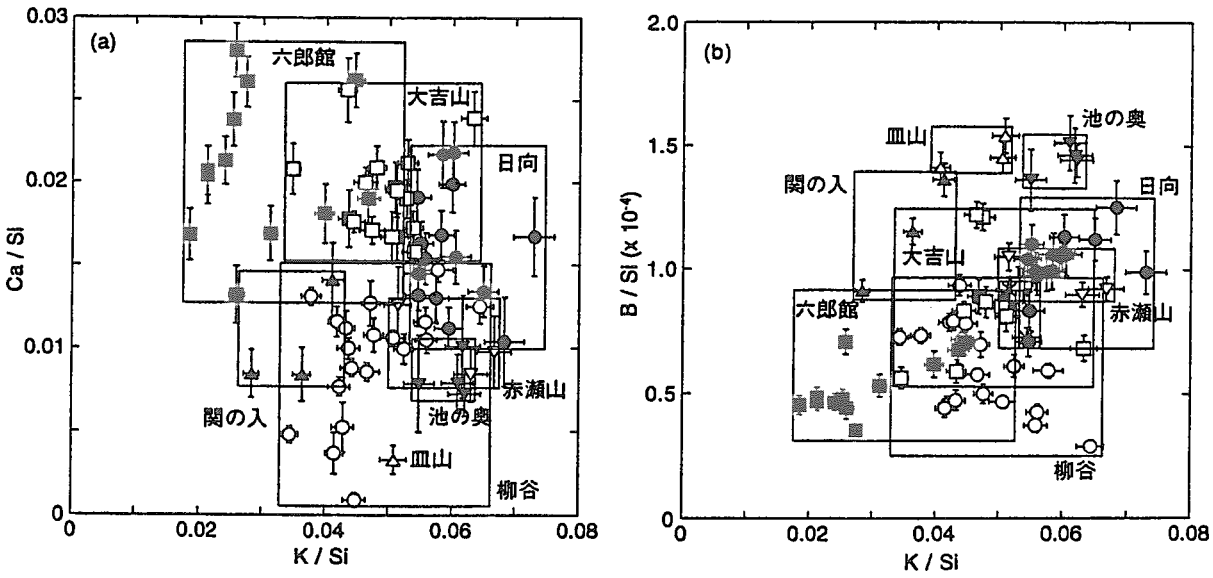

図2　須恵器の元素濃度比の二次元分布．(a)Ca/Si vs K/Si (b) B/Si vs K/Si
日向:●，久留美柳谷:○，六郎館:■，大吉山:□，須江関の入:▲，皿山:△，山茶器:×，
池の奥:▼，赤瀬山:▽．

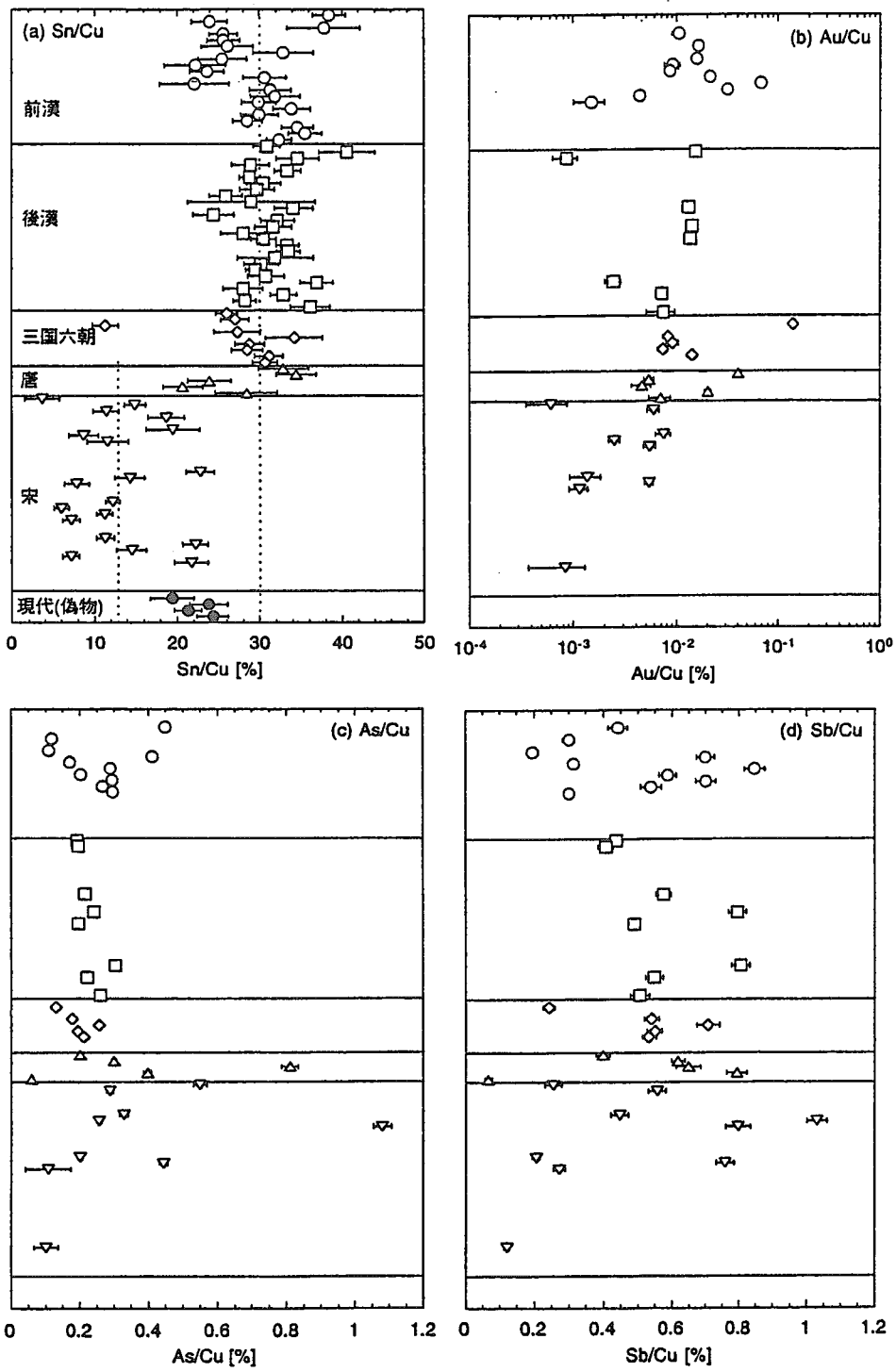

図3　銅鏡の元素濃度比．(a)Sn/Cu, (b)Au/Cu, (c)As/Cu, (d)Sb/Cu.
上から製作年代の古い物から順に並べた．

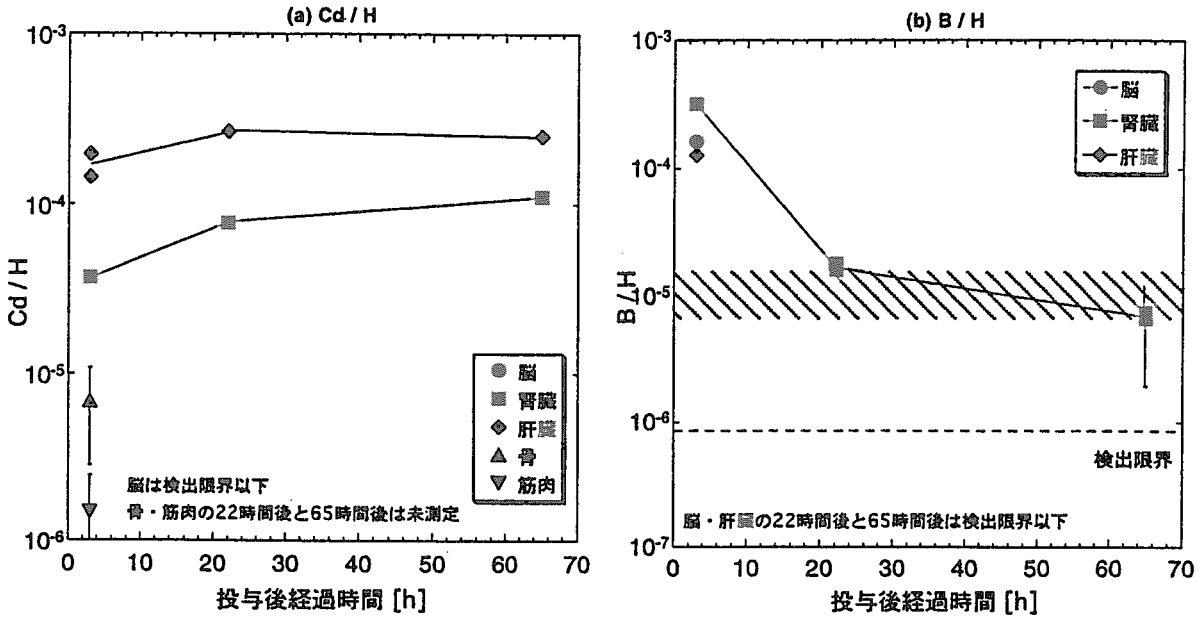

図4　(a)Cd/H と(b)B/H の経時変化

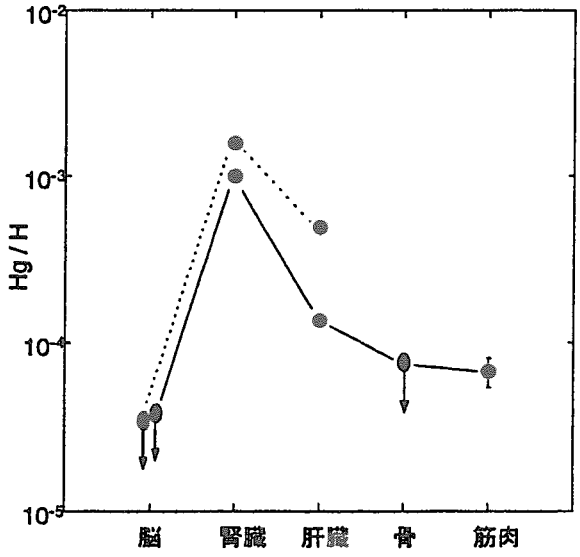

図5　投与3時間後のHgの体内分布．脳，腎臓，肝臓は2個体分析した．

3-7 電気めっきスラッジの即発γ線分析

Prompt γ-Ray Analysis of Sludge from Electroplating

森崎 重喜（東京都立大学 理学研究科 ＲＩ研究施設）
S. Morisaki (RI Center、tokyo Metropolitan University)
米沢 仲四郎（日本原子力研究所 東海研究所）
T. Yonezawa (Tokai Establishment、Japan Atomic Energy Research Institute)

1. はじめに

電気めっき業ほど多くの有害物質を扱う都市型の業種はあまり例を見ない。電気めっきの加工に付随する排水処理は多量のスラッジを発生させ、その処理，処分は大きな課題として関係業界において取り上げられてきた。廃棄物である約 8 万トン（東京都）の金属混合スラッジは有価金属を多量に含んでいるにもかかわらず，有効利用されることなく、海洋投棄、埋立処分されている。しかしながら、処理コストの高騰，埋立処分場の不足等に加えて，新たな環境規制などが生じ、また地球規模での環境保全意識の高まりとともに限られた資源・エネルギーの有効利用が強く要請されてきている。これらの再資源化（たとえば、山元還元による金属回収、コンクリート、タイル等の原材料）において常に問題になるのは金属成分以外の非金属成分（S, Cl, P, B）や添加剤に由来する種々の不純物元素である。これらの成分は再資源化を目的とする各種実試験では毎回指摘されるが、系統的な定量分析は行われていない。ここでは東京都地場産業対策の一環として，電気めっき混合スラッジの減容化と再資源化を実施するにあたり、非金属成分（H, S, Cl, B 等）と金属成分（Cu, Ni, Cr, Zn, Fe その他微量成分）の同時分析の方策を検討する。

2. 研究目的

電気めっき用電解液には，電気めっきの種類に応じてそれぞれ数種類の化学薬品が含まれている上に，前処理，後処理，排水処理でも多くの化学薬品が使用される。従って，電気めっき混合スラッジ中には多くの元素が含まれることになる。これらの成分元素のうち金属元素は必要に応じて定量されてきたが非金属元素の定量はほとんど行われていなかった。本研究では水素とホウ素の定量分析に優れている PGA 法を用いて混合スラッジ中の金属成分(S, H, B, Cl)と金属成分(Cu, Ni, Cr, Fe, Zn)の同時分析の可能性を検討する。

3. 実験

分析用試料は電気めっき事業所 5 箇所から採取した。それぞれの試料を(1)未処理、(2)110℃、3 日間熱処理、(3)900℃、1 時間熱処理したものについてビーム型中性子即発ガ

研究施設、 装置
JRR-3M，即発γ線分析

研究分野
環境、電気めっきスラッジの成分分析

ンマ線分析を行った。測定対象元素の定量値はいずれも標準試料による検量線の直線性を確認後求めた。

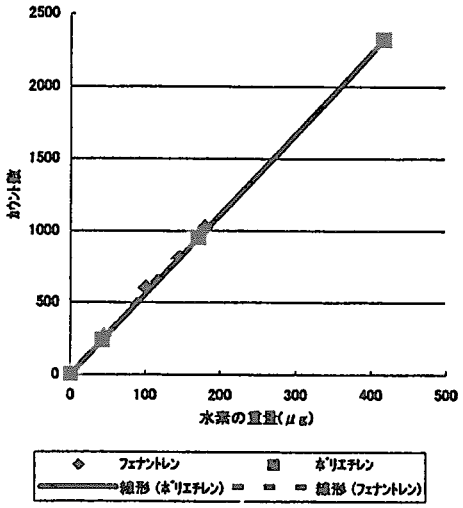

冷中性子照射時間：2000 秒

図１　水素の検量線

4. 結果

測定対象元素 Cu, Ni, Fe, Cr, Zn, S, B, H, Cl の検量線の一例として、撥水性のアントラセンとポリエチレン（分子量十万以上の微粉末）を標準物質とした場合の水素の検量線を図１に示す。両者は原点を通る同一の直線上にのる。照射時間は文献１の検出感度を参照した。試料の重さ 0.1~1.0 g の範囲でいずれの元素も測定可能であった。電気めっき混合スラッジの定量結果の一例を表１に示す。未処理スラッジと 110℃熱処理スラッジでは多量の水素が検出されたので金属の水酸化物に割り振り，残りを水とした。900℃熱処理スラッジでは水素が検出されなかったので金属化合物を酸化物とした。これらの元素は銅めっき（主成分：$CuSO_4+H_2SO_4$, $KCu(CN)_2+KCN$）、ニッケルめっき（$NiSO_4+NiCl_2+H_3BO_3$）、クロムめっき（$CrO_3+H_2SO_4$）、亜鉛めっき（ZnO+NaOH）の各めっき液の汲み出し，前処理工程での被めっき素材の溶解（Fe, Zn, Cu）に由来する。この外電気めっきの各工程と排水処理工程で使用される薬品に由来する Na, K, Ca, Cl, N（NO_3^-），S（SO_4^{2-}），C（有機化合物）は固形物として混合スラッジ中には移行しないで，事業所外へ排出されると考えられる。

表１　混合スラッジのＰＧＡ分析結果

（１）未処理

元素名	元素の割合 (%)	化合物	化合物の割合 (%)
Cu	0.080	$Cu(OH)_2$	0.124
Fe	1.03	$Fe(OH)_3$	1.97
Ni	21.2	$Ni(OH)_2$	2.00
B	0.024	BO_3^{3-}	0.128
Cl	0.221	Cl^-	0.221
Cr	1.19	$Cr(OH)_3$	2.36
Zn	5.20	$Zn(OH)_2$	7.91
H	7.21	H_2O	61.9
S	0.465	SO_4^{2-}	1.39
その他	63.3	その他	13.9

（２）110℃、３日間熱処理

元素名	元素の割合 (%)	化合物	化合物の割合 (%)
Cu	0.800	$Cu(OH)_2$	1.23
Fe	3.85	$Fe(OH)_3$	7.38
Ni	5.53	$Ni(OH)_2$	8.74
B	0.120	BO_3^{3-}	0.648
Cl	0.938	Cl^-	0.938
Cr	7.67	$Cr(OH)_3$	15.2
Zn	23.1	$Zn(OH)_2$	35.1
H	3.77	H_2O	19.8
S	2.75	SO_4^{2-}	8.23
その他	51.5	その他	2.38

(3)900℃、1時間熱処理

元素名	元素の割合 (%)	化合物	化合物の割合 (%)
Cu	2.32	CuO	2.90
Fe	9.07	Fe_2O_3	12.9
Ni	20.0	NiO	25.5
B	0.130	B_2O_3	0.420
Cl	0	Cl^-	0
Cr	7.55	Cr_2O_3	11.1
Zn	36.05	ZnO	44.9
H	0.030	H_2O	0.268
S	0.880	SO_4^{2-}	0.640
その他	23.9	その他	0

5. まとめ

電気めっき専業5社の混合スラッジのPGA分析を試みた結果、Cu, Ni, Cr, Zn, Fe, S, H, B, Clの同時分析が可能であることが判明した。特に非金属成分（S, H, B)の同時分析ができることにより，スラッジ組成比の信頼性を高め、山元還元等の再資源化に有用な情報を提供することになる。本実験の成果は、引き続いて実施予定の再資源化(建材等の原材料)に関する試験研究の基礎データとして重要である。

謝辞

研究の一部は東京都鍍金工業組合の助成を受けて実施したものであり、ここに記して感謝する。

引用文献

1.C.Yonezawa:Analytical Sciences,Vol.9,
185(1993).

3-8 カエル卵成熟における亜鉛イオンの作用

Action of zinc ion in the control of oocyte maturation of amphibian

渡辺健一、石川勝利（静岡大学理学部生物地球環境科学科）
Ken-ichi WATANABE and Katsutoshi ISHIKAWA
Faculty of Science, Shizuoka University

1. 研究の目的と意義

カエル卵を含めた多細胞動物における新しい個体の誕生は、卵と精子が合体することに始まる。卵が精子との反応に備えるステップのことを、ホルモン(プロゲステロン)によって誘起される卵成熟過程という。 当研究室では最近、カエル卵をZn イオンのキレート剤オルトーフェナンスロリンで予め処理すると、ホルモンによる卵成熟が阻害されることを見出した。他方、ホルモンの代わりに Zn イオンそのものが卵成熟を引き起こすことも分かった。この際、Zn イオンを必須とするプロテアーゼ(タンパク分解酵素)が卵成熟活性を制御していることが示唆された。 これらの知見から、カエル卵成熟における Zn イオンの役割を明らかにすることは重要なことと考え、本研究の目的とした。しかし、研究を進める過程で、k_0標準化法による多元素同時定量が可能な放射化分析法の有用なことを知った。カエル卵内の Zn のみではなく、それ以外の生体微量元素にも注目して研究を進めることは、この分野が欠落しているだけに非常に意義あることと考えた。具体的には、カエル卵のほかに、肝臓および血清を試料として放射化分析法の導入の可能性について検討した。

2．材料と方法

アフリカツメガエル卵、肝臓および血清：アフリカツメガエル雌成体を低温麻酔下に屠殺し血清を分取したほか、卵巣および肝臓を摘出した。

研究施設と装置名
ＪＲＲ－３Ｍ，γ線分析装置

研究分野
分子細胞生物学

卵については、卵巣を0.05%コラゲナーゼで2－3時間（20℃下）処理したあと遊離した卵を回収し、そのうち十分に成長した卵（直径 1.0－1.2mm）のみを実体顕微鏡下で選別した。

乾燥および秤量：一定数（10、20、40、80）の卵、肝臓断片の一部および血清の一定量を、風袋として予め精秤した石英管（信越石英：φ8mm、肉厚1mm）内に入れ、それぞれを凍結乾燥後再び精秤した。そのあと石英管の口をガスバーナーで封じ、照射用試料とした。必要な場合には、照射後に粉砕された試料を石英管から掻き出し、再度精秤して試料重量とした。

k_0標準化放射化分析：試料を封入した石英管を東海研究所JRR－3M原子炉（照射設備：HR－2)で中性子照射した。照射時間はS管で6時間行い、2週間冷却後ガンマ線で60,000秒間測定した。データはk_0標準化法により解析した。

3．分析結果

卵のほかに肝臓および血清を試料として元素分析し、Zn、Se、Co、Fe、AgおよびCsの6種の結果を表にまとめた。卵では、6種のうち求めた3種の元素存在量比 Zn：Se：Co は 2222：44：1で、Zn量が最大であった。SeおよびCoが見出されたことは非常に興味を与えた。肝臓の場合は6種全てを求めたが、存在量比 Fe：Zn：Se：Ag：Co：Cs は 6.5×10^4：3.1×10^2：2.8×10^2：2.2×10^2：1.2×10：1であった。ここで見られたZnの存在量はマウスなどほ乳類の肝臓で報告されている値に近いことが分かった。また、血清においては2種だけを求めたが、存在量比 Zn：Co は 239：1でZn量は有意であった。

表　主なる元素分析値（ng/g 乾燥重量：平均値±SE)

	Zn	Se	Co	Fe	Ag	Cs
卵（6）	1.0×10^5 ±4.4×10^3	2.1×10^3 ±1.4×10^2	4.5×10 ±2.2	NE	NE	NE
肝臓（1）	3.1×10^4	2.8×10^3	1.2×10^2	6.5×10^5	2.2×10^3	1.0×10
血清（1）	1.7×10^5	NE	7.1×10^2	NE	NE	NE

（　）内の数値：用いた個体数、NE：not estimated

4．考察

本研究は当初、カエル卵成熟における Zn イオンの作用に限定して計画したが、実験を進めていくうえで k_0 標準化放射化分析法が多元素の分析法として、我々にとって非常に有用なことを知り、Zn 以外の微量元素にも注目して分析した。

カエル卵内に微量金属元素として Zn のほかに Fe や Cu の存在が報告されていたものの、Se や Co が無視できない量存在していることが初めて分かった。 なかでも、卵に存在する Zn に加えて Se に興味を持ったが、それは Se の存在形がフリーの状態で遊離しているもののほかに、セレン含有アミノ酸としてセレノシステインやセレン含有タンパク質などを考えたとき、この研究分野の領域に新たな突破口となり得る鍵を握るからである。

導入を検討した k_0 標準化放射化分析法は多元素を同時に分析することが可能なだけに、カエル卵成熟の制御機構を明らかにするうえで、新しい観点から非常に意義を与え得る解析法であろう。つまり、カエル卵成熟は、核酸、タンパク質そして脂質分子に焦点をあてた分子生物学的な解析が主流で、微量元素に注目した研究はほとんどないからである。

なお、中性子照射用試料作製時に石英管を用いる場合、試料の重量の正確な測定法を見出すことが定量的な実験を実施するうえで急務であり、本研究で採用した方法とは違う改善法を検討する必要がある。

5. 本研究課題に関連した研究成果

1）渡辺健一、徳元俊伸、石川勝利（1999. 7）：カエル卵成熟調節因子としての亜鉛イオンの役割：第 24 回日本比較内分泌学会大会、P-44.

2）Ken-ichi Watanabe, Toshinobu Tokumoto and Katsutoshi Ishikawa : The role of zinc in the control of oocyte maturation of *Xenopus* : Biomedical Research (accepted).

6. 謝辞

本研究を実施するにあたって、東京大学原子力研究総合センター全国共同部門 伊藤泰男教授並びに澤幡浩之技官にご指導を賜わりました。 ここに、深く御礼申し上げます。

This is a blank page.

4. 放射化分析

4. Neutron Activition Analysis

This is a blank page.

研究テーマ:ラジオアイソトープ技術者の養成
表　　題 :実習　放射化分析

4-1　貝殻中の銅・ナトリウムの放射化分析

上沖　寛
国際原子力総合技術センター（東京研修センター）

本研究は、ＲＩ技術者の養成を目的とする研修コースの中で実習教科として行うものである。本報告では、平成11年度の研究炉をもちいた成果として、国内原子力技術および放射線利用に関係する人材養成を行った基礎課程およびアジア・太平洋地域開発途上国の原子力分野人材養成への国際援助としてＪＩＣＡと協力して行った原子力基礎技術コースにおいての実習教科としての放射化分析について報告する。

原子力の基礎として中性子核反応の理論や応用を理解させることは重要である。放射化分析の実際を経験させることはこれらの知識の理解を深めるのに大変重要であり、結果としてガンマ線スペクトル解析による放射能測定法および非密封ＲＩの安全取扱法を習得させることになる。

平成11年度は基礎課程とＪＩＣＡ原子力基礎技術コースの中で5回の放射化分析実習を行った。分析試料は海水産の大アサリであり、炭酸カルシウムをマトリックスにして微量元素を含有する。分析目的核種は、放射化生成核種のガンマ線スペクトルで主成分となるナトリウム24、放射化生成物が陽電子壊変を伴い陽電子消滅ピークを主要放射線ピークとする銅64である。照射条件は研究炉の気送管で2～5分間照射とし、ナトリウムと銅の標準試料と共に大アサリ貝殻の照射を5回行った。

銅の分析：

銅64の陽電子消滅放射線は、他の放射化生成核種からの高エネルギーガンマ線や宇宙線が物質にもたらす電子対生成による放射線と同一放射線であるから、銅64の分析には化学分離を必要とした。簡単な銅の化学分離法として金属亜鉛により銅イオンを還元させて銅の沈殿分離を行った。この化学分離の操作は、30分間の所用時間で0.1ppm Cu 濃度に対して5%の精度で分析された。本実習は、生成核種を同定および定量することにより核反応の理解を深め、ＲＩ実験における放射線被ばくに対する工夫、除染、サーベイ等の一連の安全取扱いの基礎を習得させるものとして有効であった。

本実験による研修生の被ばく線量は、線源が10^6Bq位に対し最大1μSv程度であった。

原子炉：JRR－3M、JRR－4　　装置：気送管　　分野：放射化分析（環境）

研究テーマ：農林生態系におけるハロゲン元素の動態
表　　題：世界の土壌・植物系におけるハロゲン元素の含量レベルと動態の解明

4-2　中国・内蒙古自治区，中国・雲南省及びフィリピン・ルソン島の土壌

結田康一[1)]、谷山一郎[1)]、永塚鎭男[2)]
1）農業環境技術研究所
2）筑波大学

ハロゲン元素(ヨウ素、臭素、塩素)の環境中での易動性は大きく、動植物での欠乏・過剰・汚染問題が生じやすい。

本研究では、これらの元素の高感度・高精度分析法である化学分離操作を伴う放射化分析法を用いて、世界各地の土壌・植物系における含量・分布と動態を明らかにする。その中で特に気候や地形条件、土壌や植物の種類、土地利用・農業活動等人為的作用との関連を解析する。

前年度は東・中央シベリア地方の土壌を対象にしたが、本報では中国の内蒙古自治区と雲南省及びフィリピン・ルソン島の土壌を対象とした。

対象土壌と分析法：1)半乾燥地域(年平均降水量約 400 ㎜；年平均気温 6.1 ～ 6.4 ℃)で内陸部(海岸より 240 ㎞以上)の中国内蒙古(モンゴル)自治区奈曼(ナイマン)旗地方の 5 地点。2）暖温帯照葉樹林地帯(年平均降水量 1000 ～ 2000 ㎜；年平均気温 8 ～ 18 ℃)で内陸部(海岸より 600 ㎞以上)の標高が高い雲南省の昆明とその周辺の 11 地点。3)熱帯モンスーン気候下(年平均降水量 1800 ㎜；年平均気温 27.4 ℃)で海岸より 20 ㎞のフィリピン・ルソン島バイ湖周辺地方の 2 地点。計 1 8 地点の層位別土壌を供試(図 1)。土壌中ヨウ素、臭素、塩素の定量：化学分離を伴う放射化分析法によった。

結果：〈前年度まで〉：世界各地の土壌・植物系におけるヨウ素、臭素、塩素の存在量・分布を明らかにしてきた。その中で降水量、土壌水分、気温(地温)などの環境要因が土壌中ハロゲン元素の存在量や土層分布に大きな影響を及ぼすことを示唆した。〈本年度〉：1)表層土壌中 3 ハロゲン元素含量が最も低いのはナイマン旗の風積砂質土(C層 0 ～ 82 ㎝)で、I 0.12, Br 0.059, Cl 1.7mg/kg 乾土と、いわゆる砂漠土壌のレベルであった。同じナイマン旗の地下水の地表面上昇がある沖積土(A 0 ～ 21 ㎝)は I 2.0, Br 7.2, Cl 505mg/kg 乾土で、Cl が地表面に高濃度に集積しているが、I, Br は低くヨウ素欠乏症が発現するレベルである。2) I, Br が最も高いのはルソン島の黄色土で、I は B 層、Br, Cl は A 層に最高集積層が存在し、I 71, Br 34, Cl 86mg/kg 乾土であった。世界最高濃度レベルの日本の平均値と比べて、腐植と関係が深い Br, Cl は約 1/3、2/3 と低かったが、I は逆に約 1.6 倍と高かった。3) 雲南土壌は全体としては 3 元素共ナイマン旗よりやや高い程度で、雲南と同じく乾期が存在する他地域の土壌と同じレベルであった。日本と気候的条件が似たアイラオ山中腹(平均気温 10 ℃、年平均降水量 1840 ㎜)の黄褐色森林土(A 層)では I 26, Br 39, Cl 56mg/kg 乾土で I、Br は他の雲南土壌より 1 桁高く、特に臭素は全供試土壌の最高値を示した。

参考文献

1)日本土壌肥料学会で発表予定，2001.4 上旬

原子炉：JRR-3M　　装置：気送管　　分野：放射化分析（環境、農・水産物）

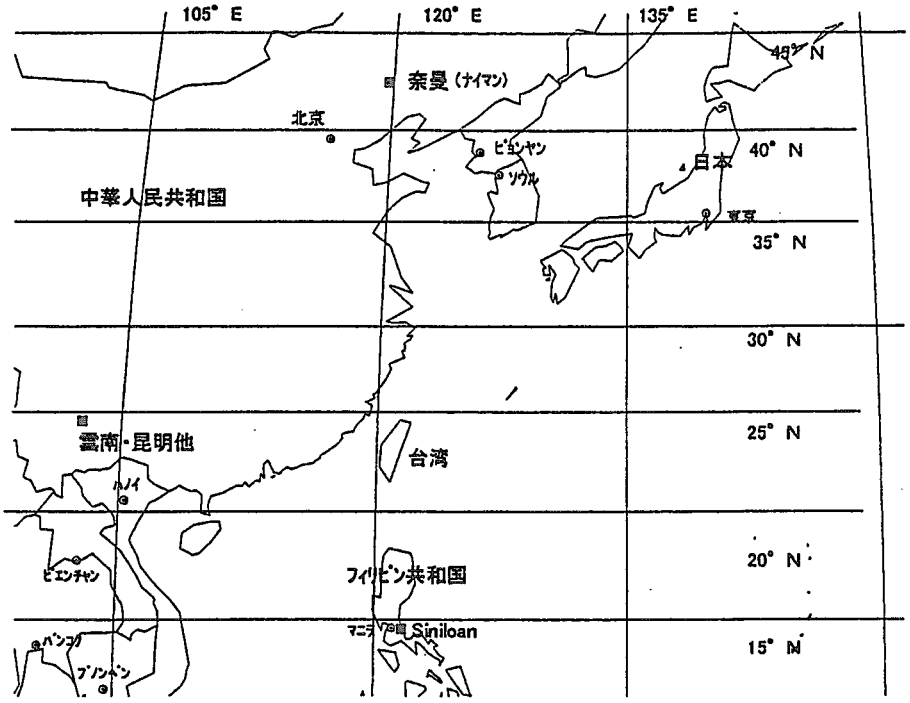

図１　土壌採取地（奈曼、雲南、フィリピン）

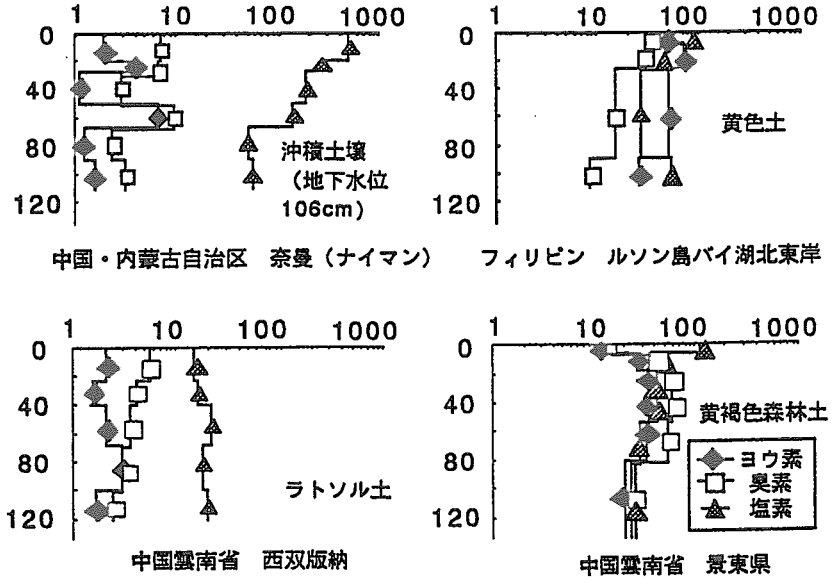

図２　中国（内蒙古・雲南）、フィリピン土常駐ヨウ素、臭素、塩素の深度分布事例（mg/kg乾土）

研究テーマ：惑星物質における元素の移動・濃集機構の研究
表　　題：堆積岩中の微量元素の挙動

4-3　砂岩風化土壌中の微量元素の挙動

上岡　晃、関　陽児、月村勝宏、金井　豊、金沢康夫、濱崎聡志、中嶋輝允

地質調査所

茨城、栃木、福島県にまたがる八溝山地には、八溝層群と呼ばれる中・古生代の堆積岩が分布する。本研究では、八溝山地南部の茨城県常北町において、砂岩の風化土壌を採取、粒度分離し、中性子放射化法によって微量元素を中心とする分析を行った。

試料採取場所は、標高約200mの山地斜面、沢の最上流部付近であり、地表から約50ｃｍは、黒褐色の腐植質土壌に覆われる。試料は、地表面からの深さそれぞれ0.3m、0.6m、1.2ｍの３箇所から採取した。採取した試料は風乾後ふるいによって、それぞれLL（1～2mm）、L（1/4～1mm）、M（1/16～1/4mm）、さらに水中での沈降速度の差によりS（1/64～1/16mm）、SS（2μm～1/64mm）、CLAY（2μm以下）の６つの粒度フラクションに分離した。これらの試料約100mgずつを、原研JRR-3のHR-2照射孔で１時間中性子照射し、１週間後および１カ月後の２回、γ線測定を行った。

図１に、深さ1.2mから採取した試料について、Mフラクション中の濃度で規格化した各粒度ごとの元素含有量を示す。粒度ごとの特徴は、他の試料でもほぼ同様である。Fe、Sc、Cr、Co、Znなどは、花崗岩風化土壌[1)]と同様に、SSやCLAYなどの細かい粒度で高濃度となっている。一方、LLフラクションは、花崗岩が大部分石英からなり、ほとんどの元素が他の粒度より低濃度であったのに対し、砂岩では石英以外にも長石、イライトなど、鉱物種が比較的豊富であり、元素濃度も他の粒度と比べて必ずしも低くない。Hfは、Sフラクションで顕著に濃度が高い。これは花崗岩土壌にも見られ、この粒度区分にジルコンが存在することを反映するものと思われる（X線回折では未検出）。またCsは、特定粒度への濃集が見られなかった花崗岩土壌と異なり、SSおよびCLAYのほかLLでも高濃度となっているのが特徴的である。

REEパターン（図２）は、花崗岩ではCeの正アノーマリーがSSやCLAYなどの細かいフラクションで見られたのに対し、砂岩では顕著なアノーマリーは見られない。またパターンそのものやREE濃度も各フラクション間の差が小さく、砂岩生成過程での均質化が示唆される。

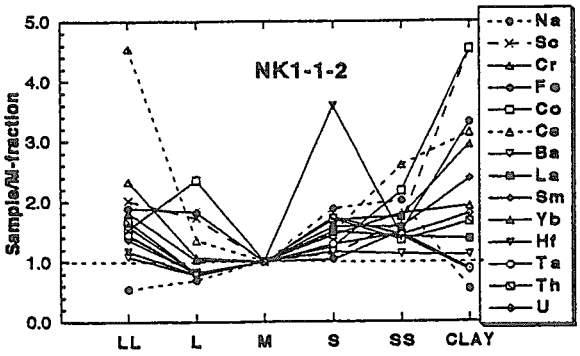

図１　粒度別化学組成

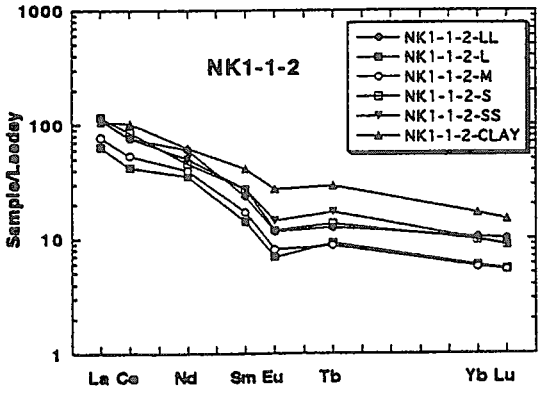

図２　粒度別希土類元素存在度パターン

参考文献

1) 1998年度日本地球化学会年会講演要旨集，(1998)，pp.196

原子炉：ＪＲＲ－３　　装置：ＨＲ－２　　分野：放射化分析（地球化学・宇宙化学）

研究テーマ： 環境関連物質の分析高度化研究
表　　題： 中性子放射化分析の研究

4-4 中性子放射化分析の研究

米沢仲四郎，松江秀明，Alice Sirinuntavid，Janitha A. Liyanage
環境科学研究部 分析科学研究グループ

１．はじめに

今年度は，JRR-3M，JRR-4 の気送管及び水力照射設備を使用し，原研内からの依頼分析に基づく中性子検出器用人工ダイヤモンド中の不純物定量，並びに IAEA 及び STA 原子力交流制度による研究者の研究テーマとして，k_0 法による多元素定量とリンの放射化学分析を実施した。

２．人工ダイヤモンド中の不純物定量

核融合炉の中性子検出器として人工ダイヤモンドが検討されている。人工ダイヤモンド中に含まれる微量金属不純物がエネルギー分解能及び動作特性等に影響するため，不純物の定量が必要とされている。しかし，ダイヤモンドは化学的に安定なため，分解が困難であり，更に不純物含量が ppb レベルと低いことから他の分析法では分析が困難である。このため，化学分解操作を必要としない機器中性子放射化分析法によりその分析を試みた。

高温高圧法によって合成された２種類の高純度人工ダイヤモンドを比較標準試料とともに JRR-3M の気送管（PN-1,-3）及び水力照射設備（HR-2）で 10 sec～166.5 hr 照射し，対象核種の半減期に応じた冷却及び測定時間で試料のγ線スペクトルを Ge 検出器で測定した。

半減期が秒～時間オーダーの短半減期核種は検出限界以下であったが，日のオーダーの長寿命核種 ^{51}Cr, ^{59}Fe, ^{60}Co, ^{58}Co, ^{76}As, ^{122}Sb, ^{187}W, ^{198}Au, ^{199}Au等が検出された。^{51}Cr (Cr), ^{59}Fe (Fe), ^{60}Co (Co), ^{58}Co (Ni) は，高温高圧法による合成の際に使用する溶媒の構成元素又はその不純物元素で，その含量は高品位ダイヤモンドでは 1～50 ppb，低品位ダイヤモンドでは 3～1600 ppb であった。また，Sb と As 含量は，低品位及び高品位ダイヤモンドで 0.8～500 ppt の範囲であった。本分析により人工ダイヤモンド中の金属不純物濃度が初めて明らかにされ，これらの金属不純物によるダイヤモンドの電気特性への影響は N, B 等の軽元素に比べて無視できることが分った。

３．k_0 法による多元素定量

比較標準試料を使用せずに多元素を定量することができる k_0 法による石炭，原子炉用黒鉛及び食餌標準試料中の多元素定量を行った。

試料（0.1～0.25g）と中性子モニター（Zr 板，Al-Au 合金線）をポリエチレン袋に封入し，JRR-3M 気送管（PN-1）で 10 min 照射し，約１日間冷却後試料とモニターのγ線スペクトルを Ge 検出器で測定した。得られたγ線スペクトルをγ線スペクトル解析プログラム HYPERMET-PC で解析し，更に k_0 法の解析プログラム KAYZERO/SOLCOI で解析して，試料中の元素含量を求めた。

石炭標準試料（NIST SRM1632a, 1635,）中の 10～15 元素の定量結果は，NIST の認証値及び他の研究者による分析値とほぼ 10%以内で一致した。原子炉黒鉛標準試料（JAERI-G5, -G6），食餌標準試

原子炉: JRR-3M, -4　　装置：気送管，水力照射設備　　分野：中性子放射化分析（分析化学一般）

料（NIES/NIRS, Typical Japanese Diet）中の6～11元素も定量した。

4．リンの放射化学分析

生命科学，材料及び環境科学等に於て重要な役割をする微量リンを中性子放射化分析法によって定量するため，^{32}P の放射化学分析法の検討を行った。リンの中性子照射によって生成する ^{32}P（半減期14.26日）は純ベータ線放出核種のである。このため，計数効率の大きな液体シンチレーション計数法によって ^{32}P の放射能を測定することにした。更に共存する他の放射性核種から分離するため，リンモリブデン酸アンモニウムのトリノルマルオクチルアミン(TNOA)ーキシレンによる溶媒抽出分離法の検討を行った。

JRR-3，JRR-4 の気送管及び水力照射設備でリンを照射して作製した ^{32}P をトレーサーとして使用し，抽出条件の検討を行った結果，^{32}P を抽出するための塩酸，モリブデン及び TNOA 濃度は，塩酸 0.01～0.05 M，Mo 20.mg/10 ml，TNOA 0.1 M が最適であることを明らかにした。更に，抽出液の液体シンチレーション測定法についても検討を行った結果，^{32}P の放出する β 線エネルギーが高いため，クエンチングの影響が少なく，87%以上の計数効率で測定できることが分った。今後更に検討を重ね，生体試料及び各種材料中の微量リンの放射化分析に適用する予定である。本分析法は，リンの放射化分析のみならず，^{32}S (n, p) 及び ^{35}Cl (n, α) 反応で生成する ^{32}P の放射能分析に使用することも可能であり，これにより広いエネルギー範囲の中性子照射線量を求めることができる。

5．成果の公表

1 J. Kaneko, C. Yonezawa, Y. Kasugai, H. Sumiya, T. Nishitani , "Determination of metallic impurities in high-purity type IIa diamond grown by high-pressure and high-temprature synthesis using neutron activation analysis", Diamond and Related Materials, in press, (2000).

2 Janitha A. Liyanage, 米沢仲四郎，「溶媒抽出分離と液体シンチレーション計数法による ^{32}P の放射化学分析」，第44回放射化学討論会（2000年9月，神戸市）で発表予定。

研究テーマ： 多重ガンマ線スペクトルの分析科学への応用
表題：多重ガンマ線測定装置の中性子放射化分析への応用

4-5 多重ガンマ線分析によるの標準岩石試料の中性子放射化分析

初川雄一、大島真澄、早川岳人[1]、藤暢輔、篠原伸夫、
物質科学研究部原子核科学研究グループ
[1]光量子科学センター自由電子レーザー研究グループ

多重ガンマ線測定装置を分析化学、特に中性子放射化分析法に応用して岩石試料中の微量元素の検出を試みた。 一般に地質学的試料の中性子放射化分析では主要成分からの放射線が強く微量成分の検出には化学分離などが必要であるが、クリスタルボールによって得られた２次元スペクトルにより非破壊で微量成分の検出に成功した。 さらに得られたピーク面積より元素の定量を行い分析手法として利用可能である事を示した。

実験は地質調査所から配布[1)]され微量成分の定量がなされている標準岩石試料ＪＢ－１ａ（玄武岩）とＪｐ－１（かんらん石）を用いて行った。 原研原子炉ＪＲＲ－４気送管で標準岩石試料約１００ｍｇを１０分間照射した後に多重ガンマ線測定装置ＧＥＭＩＮＩ[2)]を用いてガンマ線測定を行った。 地質学的試料の中性子放射化分析では主要成分であるナトリウムやマンガンから生成される^{24}Ｎａ（半減期１４．９５ｈ）や^{56}Ｍｎ（半減期２．５７ｈ）からのガンマ線が強いが多重ガンマ線分析法の高い分析感度を用いて化学分離する事無く微量成分からのガンマ線を測定する事ができた。 得られたガンマ線の強度からガンマ線の分岐、反応断面積、半減期などの補正を行って各元素の定量を行った。本研究では照射試料を非破壊で測定して微量成分の検出を試みた。

得られた結果を Table１および２に示す。JP-1,JB-1a 中の２４元素が同時に化学分離を行う事無く観測された。 得られた結果を文献値と比較してみると概ね良く一致している事が分かる。 臭素については文献値と比較すると２から４倍大きな値になっているが、これは本研究では以前の結果と違い化学分離を行っていないためにであると考えられる。 また Sm と Ta についても文献値との大きな相違が見られる。 これは観測したガンマ線の内部転換の大きな遷移であるが、この内部転換係数の不確かさによるものと思われる。

今回観測された最小の成分は JP-1 中の Eu で含有量は 3.3ppb(文献値は 4ppb)であった。

引用文献

1) N. Imai, et al., Geochemical Journal 29, 91(1995).
2) K. Furuno, et al., Nucl. Instr. and Meth. A 421 211(1999).

原子炉：JRR-4　　装置：気送管　　分野：放射化分析（その他）

Table 1.
Elements determined in JP-1

Element	This work (ppm)	Reference (ppm)*
Sc	9.2±0.7	7.24
Co	204±10	116
Ni	2460±230	2460
Ga	0.64±0.14	0.7
Br	1.1±0.2	0.28
Eu	0.0033±0.0003	0.004
W	0.52±0.06	0.85

*) 文献 1

Table 2.
Elements determined in JB-1a

Element	This work (ppm)	Reference (ppm)*
K	9590±410	11600
Sc	33.4±0.3	27.6
Ca	49600±4100	67800
Ti	8800±1000	8000
Fe	63300±1900	63300
Co	53.6±2.6	38.6
Ga	18.3±0.6	17.9
As	3.17±0.34	2.3
Br	1.0±0.1	0.4
Ba	432±15	505
Cs	1.0±0.1	1.32
La	39.8±2.9	37.6
Ce	49.6±22	65.6
Eu	0.83±0.03	1.46
Sm	2.3±0.4	5.07
Tb	0.58±0.09	0.69
Yb	1.18±0.36	2.1
Lu	0.38±0.03	0.33
Hf	2.43±0.19	3.41
Ta	5.51±0.27	1.93
W	1.99±0.13	1.83
Th	19±8	9.0
U	1.82±0.16	1.57

*)文献 1

研究テーマ：フィッション・トラック年代測定
表　　題：標準ガラスによる熱中性子線量の絶対測定

4-6　フィッション・トラック法によるジルコンのウラン濃度測定

岩野英樹・吉岡　哲・檀原　徹
(株)京都フィッション・トラック　京都市北区大宮南田尻町44-4

フィッション・トラック(FT)法によるウラン濃度測定は、鉱物内の ^{235}U を熱中性子照射により誘導核分裂をさせ、その際できた核分裂飛跡の密度(誘導トラック密度)と熱中性子線量、および ^{235}U の同位体存在度から求められる[1]。FT 法は結晶単位、或いはもっと微小領域の分析ができる有効な手法であるが、ウラン濃度の確度を左右する誘導トラック密度測定と熱中性子線量測定には問題もあった。近年これらについて再検討され、前者は、汎用的に用いられる外部ディテクター法の計数効率補正の定量化[2]、後者は、正確な熱中性子線量モニター用標準ガラス IRMM-540 の開発[3]が達成された。また、この基盤に従った FT 法のウラン濃度算出式も再定義された[1]。今回、中性子放射化分析(NAA)によるウラン濃度既知の標準試料について、再構築された FT 法での測定例を報告する。

試料には群馬県富岡地域の中新統馬場凝灰岩のジルコンを用いた。結晶外部面と研磨内部面を対象とし、無作為に選んだ各 50 粒子ずつを測定した。誘導トラック測定は白雲母外部ディテクター上で行い、熱中性子照射は日本原子力研究所(東海)の JRR4 気送管で 15 秒間行った。熱中性子線量モニターは上述の IRMM-540 ガラスを用いた。

ウラン濃度測定結果(粒子毎のヒストグラム)を図 1 に示した。結晶外部面と内部面に大きなウラン濃度差がなかったためまとめて示している。粒子毎のウラン濃度は最大 1595ppm から最小 106ppm までのばらつきを示し、平均で 480ppm という値が得られた。この値は NAA 値(535±8ppm)[4]と比べるとやや小さいが、個体毎のばらつきを考慮すれば NAA によるウラン濃度値と調和的である。

結晶毎に大きなウラン濃度のばらつきを持つ試料を比較する場合、1 結晶毎の比較が不可欠であるため、今後同一結晶・同一部位でウラン濃度比較を検討したい。

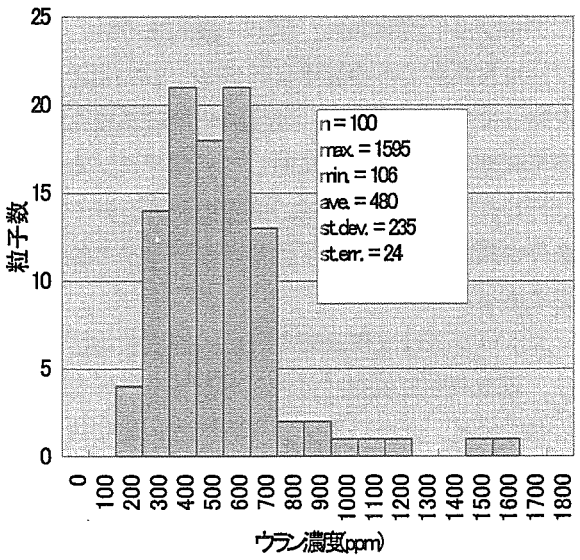

図 1. 馬場凝灰岩ジルコンのウラン濃度

参考文献

1)岩野英樹・吉岡哲・檀原徹 (2000) ﾌｨｯｼｮﾝ・ﾄﾗｯｸﾆｭｰｽﾚﾀｰ, 第 13 号, (印刷中).
2) Iwano, H. and Danhara, T, Advances in Fission Track Geochronology, (1998), 47-66.
3) De Corte, F., Bellemans, F., Van den haute, P., Ingelbrecht C. and Nicholl, C. Advances in Fission Track Geochronology, (1998), 67-78.
4)本多照幸・檀原徹・野崎徹也 (1990) ﾌｨｯｼｮﾝ・ﾄﾗｯｸﾆｭｰｽﾚﾀｰ, 第 3 号, 28-35.

原子炉：JRR-4　　装置：気送管　　分野：その他（放射年代学）

4-7 大気中エアロゾルの起源と滞留時間

Source and Residence Time of Atmospheric Aerosols

九州大学アイソトープ総合センター　大崎 進
九州大学理学部　百島則幸、杉原真司

1．はじめに

環境における元素の挙動を把握するために、大気中エアロゾルの測定を開始した。大気中に放出された汚染物質や放射性物質は、その拡散過程において、エアロゾルに捕捉され、沈降・移動を行い、エアロゾルは大気中での物質の移動媒体として大きな役割を持っている。近年は、酸性雨や地球温暖化などの環境変動の影響研究と関連して、エアロゾルの研究は行われているが、地域、気候により分布や移動の条件が異なり、各条件下におけるデータの蓄積が必要である。

エアロゾルは太陽放射を散乱・吸収することにより、地球の放射収支に大きな影響を及ぼすことが知られている。また、エアロゾルは雲の凝結核として働くために、雲の消長にも大きな影響を与え、その事が結果として、地球の放射収支に大きな影響を与えている。

アジア地域は、アジア大陸に発生源を持つ土壌粒子及びこの地域の工業化に伴って増加している人為起源のエアロゾル粒子のために、相対的に高いアルベドを持つ地域になっていると考えられる。福岡においてエアロゾルを測定することにより、大陸起源のエアロゾルの寄与を見積もることが可能であり、また滞留時間を知ることができる。エアロゾルは、種々の発生源を持ち、季節や気象条件によってその寄与の割合も異なると考えられ長期間に渡る観測が必要である。

本課題では、エアロゾルの発生源と滞留時間を見積もる事を目的としているが、降下した放射性核種であるBe-7,Pb-210についても同時に測定し、その季節変動や年変動を観測した。これらの放射性核種の変動は、対流圏大気の移動・混合を表すものであり、放射化分析で求めた元素の分布パターンと併せて考察することにする。

2．実験

（試料採取）

福岡市東区の九州大学アイソトープ総合センター及び篠栗町の九州大学農学部附属演習林に、採取面積約0.5平方メートルの水盤を設置し、月間の降下物（降水と大気浮遊塵）を採取した。採取地点の福岡市は海岸沿いの市街地で九州大学は国道沿いにあり、一方篠栗町は約８ｋｍ内陸に入った地点であり、標高約７０ｍの丘陵地で採取した。試料の採取期間は、1995年から1999年までである。降下物は、蒸発乾固させた。

（照射・測定）

照射は3時間照射と気送管による１０秒照射の２種類行った。それぞれ、約３０～４０ｍｇを石英管とポリエチレン袋に封入して照射した。３時間照射分は、１０日程度冷却し、１０秒照射分は直後に原研のGe半導体検出器でガンマ線を測定した。測定時間は、各１０００秒及び１００秒である。標準としては、JB-1を利用した。

（天然放射性核種の測定）

蒸発乾固した試料は、そのままプラスチック容器にいれ、Ge半導体検出器で測定した。対象核種は宇宙線生成核種であるBe-7と地殻起源のPb-210である。測定時間は約１日である。測定値は、採取時期に半減期補正した。

3．結果と考察

図１に、降下物中のBe-7,Pb-210の単位面積当たりの一日降下量と降水量を示す。両核種の降下量の

季節変動は、冬から春にかけて高く、特に Be-7 は春までその降下量の増加が見られ、スプリングピークと呼ばれる。

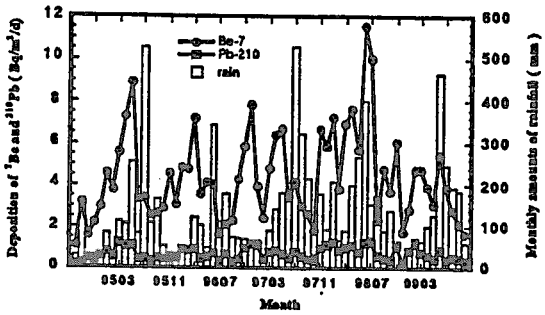

Fig. 1. Depositions of ^{7}Be and ^{210}Pb and monthy amounts of rainfall at Fukuoka.

発生源を考慮に入れて、土壌起源の Al、海塩粒子起源の Na、人為的起源の Cr、化石燃料起源の V を代表とする。 図２に福岡市における Al の１平方m当たりの月別降下量を平均降水量と伴に示した。

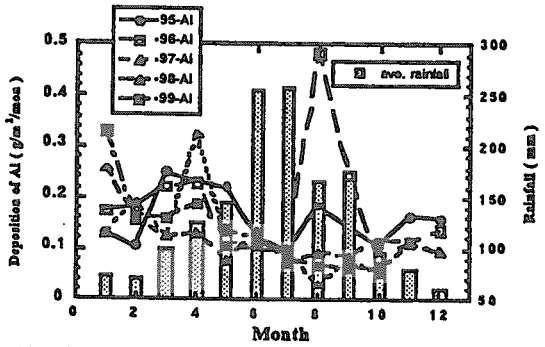

図２ 福岡市におけるAl降下量、平均降水量

1996 年８月に異常に高い値が見られるがこの原因ははっきりしない、この点を除けばほぼ平均して、夏場に低い傾向がある。Na についても同様な傾向が見られた。５年分の平均を取って、元素間の変動の違いを見ると、福岡においては、８月に Al,Na の高い値が見られ、１１月～３月の冬場では、Na,Cr が上昇しているのに対して、Al,V ではその傾向が少ない。Cr は、冬場 Na と同様に降下量が増加しているが、８月は増加していない。このことは、明らかにエアロゾルの組成が季節によって異なる事を示している。また、V は季節によって大きな変動は見られないが、４月、８月に小さいピークがみられ、Al と相関していることから、黄砂等の大陸起源の影響ではないかと考えられる。一方、篠栗町のデータでは、７月と９月にピークが Na で見られる。１１月～２月の冬場は、福岡市と同様に Na,Cr が増加しているのに対して、Al,V はその傾向がない。Cr については、福岡より変動が大きく、４、７、９月にピークが見られ、各元素の変化に同一性が少ないため、地点間の違いがあることが判る。

放射化分析によって定量できた元素の内、含有量が多い元素から順に１２元素を選び、相関を取ると共に、季節変動を見た。表１、２に福岡市と篠栗町での濃度相関を示す。まず、福岡市において Na が他のどの元素とも相関が低い。土壌起源の Al は、Cr,Cs,Na を除いてほぼ相関が高く、これらの多くの元素が土壌起源であるか、土壌起源のエアロゾルと挙動を伴にしていると考えられる。また、Cr は Na と相関が高く、海塩粒子と大きく関係していると考えられる。一方、篠栗町は、福岡市と同じ相関の傾向を示すが、Cr,Na の相関値が大きく低下していることから、発生源が明らかに異なることを示し、福岡市と比較して顕著に地点差が現れている。

今回は、月間の降下物試料であるため、種々の発生源を持つエアロゾルを混合した季節変動を観測しているので、発生源別のエアロゾルの寄与を見積もることは困難であったが、代表的な元素で、４つの発生源をみたところ、主に土壌起源のエアロゾルであり、その中には春先の大陸起源の部分も含まれている。また、海塩粒子起源のエアロゾルは、土壌起源とは異なった動きをしているが、発生地点までは予測できなかった。

これらの元素について、主成分分析を適用し、季節変動のパターンと各成分への元素分布の違いから発生源の寄与の推定を試みた。図３は、福岡市における、各成分の季節変動を示す。季節変動を３成分に分け、この３成分の組み合わせによって約９４％

表1　福岡市における元素間濃度相関

	Al	Ca	Co	Cr	Cs	Eu	Fe	La	Mn	Na	Sc
Ca	0.62										
Co	0.78	0.91									
Cr	0.54	0.78	0.79								
Cs	0.32	0.75	0.74	0.52							
Eu	0.81	0.82	0.91	0.57	0.67						
Fe	0.73	0.85	0.92	0.78	0.59	0.82					
La	0.83	0.90	0.96	0.71	0.75	0.96	0.86				
Mn	0.79	0.83	0.87	0.69	0.67	0.88	0.86	0.95			
Na	0.38	0.18	0.16	0.83	0.15	0.25	0.53	0.36	0.37		
Sc	0.90	0.88	0.93	0.68	0.62	0.92	0.85	0.97	0.92	0.32	
V	0.95	0.67	0.79	0.65	0.39	0.79	0.70	0.86	0.85	0.44	0.91

表2　篠栗町における元素間濃度相関

	Al	Ca	Co	Cr	Cs	Eu	Fe	La	Mn	Na	Sc
Ca	0.56										
Co	0.46	0.70									
Cr	-0.14	0.54	0.45								
Cs	0.80	0.51	0.26	0.13							
Eu	0.67	0.75	0.63	0.06	0.37						
Fe	0.82	0.41	0.52	-0.01	0.72	0.41					
La	0.78	0.82	0.46	0.19	0.69	0.80	0.50				
Mn	0.59	0.87	0.80	0.60	0.50	0.70	0.59	0.73			
Na	0.13	0.62	0.23	0.78	0.45	0.03	0.27	0.39	0.61		
Sc	0.92	0.60	0.38	-0.16	0.67	0.79	0.58	0.89	0.55	0.05	
V	0.94	0.72	0.52	0.12	0.85	0.73	0.75	0.90	0.74	0.36	0.92

の変動が表現できる。Z1 が第１主成分、Z2 が第２主成分、Z3 が第３主成分を示す。また、標準化した Al,Na 濃度を併せてプロットしている。縦軸は、変動の様子を見るため、平均値を０として、偏差で規格化している。第１主成分がほぼ全体の季節変動を示しているが、第２主成分では、夏と冬にピークがみられ、特に夏場の上昇が顕著に Na の増加に寄与している。

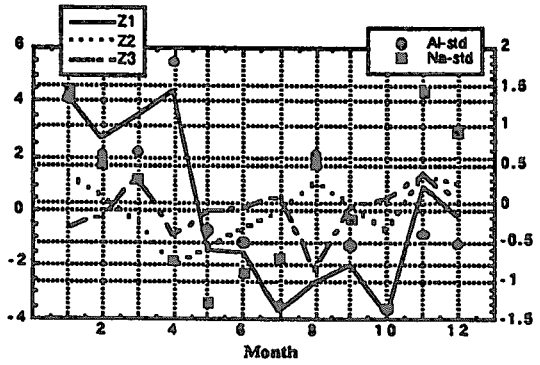

図３　福岡市におけるAl, Na濃度と各成分の季節変動

各成分への元素の寄与をみると、第１成分は、Cr,Cs,Na を除いて全元素がほぼ均一に含まれているのに対して、第２成分は Cr,Na の寄与が大きい海塩粒子起源の成分と考えられ、第３成分は、Al,V が少なく、Cs が比較的多く含まれる成分であることが判った。これを考慮にいれて月別変化をみると、Al を土壌起源と考えた場合、春の Al 降下量の増加は第１成分の寄与が大きいが、冬の増加は Na 降下量の増加も見られることから海塩粒子の寄与が大きくなり、大陸方向からの風に海塩粒子が取り込まれてきていると考えられる。

一方、篠栗町の季節変動は、各成分への元素の寄与が大きく異なり、第１成分が夏の Al の増加を表していて、第３成分までで約８９％を表現できる。元素の寄与は、第１成分は福岡と同様に Cr,Na の寄与が少なくなる傾向にあるが、第２成分は Cr,Na の寄与が顕著に多く、明らかに海塩起源と考えられる。また第３成分は、各元素間で変動が大きい。月別変化では、Al の変化は、第１成分でほぼ表す事ができるが、Na の変化の内、７月のピークには第２成分が、９月のピークには第１成分が寄与している事がわかる。海塩粒子の中で第２成分で表される部分は、第１成分中の海塩起源粒子とことなり、移動中にエアロゾルの組成が変化したことが、地点間の差異によって予測される。

４．今後の展開

主成分分析によって、降下物の成分を大きく３成分に分割して、季節変動を再現したが、成分にしめる発生源の寄与の割合については、まだはっきりと判っていない。ある程度の、発生源が特定できる試料を採取して、比較検討する事が必要である。

また、滞留時間については、大陸からの影響を考慮することと、２地点においても成分組成に変化が生じていたためこの原因を求める事が必要であろう。

５．成果の公表

学会発表

１）杉原真司、百島則幸、大崎　進、前田米蔵：「福岡におけるエアロゾル降下量の季節変動」第３７回理工学における同位元素研究発表会（２０００）

4-8 炭素材料による環境モニターの開発と応用

Application of Carbon Fiber for Environmental Monitor

九州大学理学部　前田米蔵、杉原真司
愛媛大学工学部　中山祐輔

1．はじめに

環境中に存在する有害元素、有害物質の分析定量を正確、迅速に行うことは現在重要な問題の一つである。環境中におけるこれらの有害元素はその多くが微量であるため、測定は困難な場合が多く、試料の採取時点或いは分析時点での測定値を得るためには多量の試料を利用するか、濃縮等の前処理が必要である。そこで、元素の濃縮法の一つとして、炭素材料の吸着、収着性を利用して、新しい環境指針として利用できる環境モニターの開発を目的としている。この環境モニターは、環境濃度の積算値又は平均値を求めることになり、瞬間の濃度は測定できないが、環境への影響を考える場合は、微量元素の定常時の変動を観測する必要があり、採取操作等が簡便であることも考慮しなければならない。

炭素繊維は、様々な用途に使用されている。材料としての利用が主な用途であるが、樹脂や金属などと混ぜ合わせて使用される複合材料である。これは炭素繊維が軽くて強度が大きいという点を活用したものである。一方、炭素繊維には微生物が大量に集まる現象があることがわかり、水質浄化、下水処理や、魚の藻場や漁礁、砂漠の緑化材等に利用されつつある。これは、炭素繊維の高い生物親和性を活用したものである。

炭素繊維のこの２番目の特性を利用して、環境モニターとしての応用のための基礎的実験を行った。本年度は、炭素材料への環境中の微量元素の吸着の様子や生物親和性による微生物の生育状況を探るために、数種類の元素を溶かした実験水と実際の河川水につけた炭素繊維を試料として、放射化分析で定量できる元素の探査を行った。

2．実験

混合溶液（イオン交換水に V,Zn,Fe,Cd,Sr,As,Cr の各標準溶液を２０ｍｌ混合）に２０日間、河川水に３０日間、炭素繊維を浸けた。炭素繊維を取り出しそのまま風乾させ、放射化分析用の試料とした。未処理の炭素繊維をブランク試料とした。

（照射・測定）

照射は６時間照射と気送管による１０秒照射の２種類行った。それぞれ、約３０～４０ｍｇを石英管とポリエチレン袋に封入して照射した。６ 時間照射分は、６ 日程度冷却し、１０秒照射分は直後に原研の Ge 半導体検出器でガンマ線を測定した。測定時間は、各１０００秒及び１００秒である。標準としては、JB-1 を利用した。

3．結果と考察

河川水に浸けた炭素繊維には、多量の藻が生成したが、混合溶液には発生しなかった。炭素の微生物増殖促進効果の作用により河川水中に存在していた微生物が増殖したが、混合溶液には微生物が存在していなかったためである。

放射化分析の結果、約３３種類の核種が検出できた。混合溶液に添加した７元素は検出でき、微生物等が存在しなくても、炭素繊維自体がこれらの元素を吸着する事が判った。標準の関係で、すべて定量できなかったが、定量できた元素では、吸着量は添加量の最大５０％であり、元素により吸着量は異なる。今後、炭素繊維自体の吸着量の定量や液浸時間との関係も調べる必要がある。

ブランク試料に検出された核種と比較して、１５元素が新たに検出できた。これらの内、河川水試料でのみ検出された元素は、Ca,Mn,Mg,Rb,Ti のみで

あり、その他の元素は混合溶液においても、程度は異なるが検出できたので、実験系で存在している元素の可能性があり、指標元素としては使用できない。さらに、照射・測定の条件を決め、測定元素数を増やすことも必要である。

4．今後の展望

今回は、炭素繊維の利用法として、環境モニターの1種として利用の可能性を探る年度であったため、定量的な実験ができなかった。今度、炭素繊維の吸着能等の基礎データと藻状物質の生成条件等の考察を行い、定量的に実験を開始し、実際の河川水への応用をはかる予定である。また、他の炭素材料である活性炭や活性炭素繊維等との比較検討を行う。

実験の結果、炭素繊維への高い生物親和性による河川水試料には多量の藻状物質の生成が見られたため、有機物と金属元素の関係を明らかにする予定である。また、実際の河川水（上流、中流、下流）での違いや、河川間の違いについて測定し、環境モニターとしての利用法開発を行う予定である。

5．成果の公表

なし

4-9 ヒト血清中有機態ハロゲン（Cl, Br, I）の性および年齢による変動

Variations in sex and age of organic halogen concentration in human serum

鹿島勇治，松井三明，堺 温哉（横浜市立大学医学部衛生学講座）
KASHIMA Yuji , MATSUI Mitsuaki and SAKAI Haruya
(Department of Hygiene, Yokohama City University School of Medicine)

【はじめに】近年，塩化ビニルやプラスチック製材を含むゴミの焼却過程でダイオキシンやPCBsを含む様々な有機ハロゲン化合物が生成されることが明らかにされ[1]，これらの有機ハロゲン化合物による複合的な環境汚染および生体影響が懸念されている．特に，これらの有機ハロゲン化合物はホルモン様の作用からヒトや野生生物の内分泌系を撹乱する危険性が指摘されてきている[2,3]．

ダイオキシンやPCBsには多くの同族体，異性体が存在し，また，これらの化合物の塩素の一部が臭素に置換した化合物も焼却過程で生成されることが確認されている．このような臭素置換化合物は，塩素置換化合物と類似した物理化学性，毒性を有すため[4]，これらの汚染状況も，既知の塩素系化合物と同様に監視が必要と思われる．しかし，これらの種々の有機ハロゲン化合物全てを個別に定量，監視することは，現時点では技術的にかなり難しく，また多くの時間とコストを必要とする．

水道水や排水などの汚染指標として用いられているTOX（全有機ハロゲン量）やAOX（吸着可能な有機態ハロゲン量）は，有機ハロゲン化合物を各ハロゲンの総量として評価する指標であり，パルプ・製紙業界では，AOXが工場排水中のダイオキシン量と正の相関関係があることに着目して,測定の容易なAOX量を指標にダイオキシン類の生成低減を図り成功している[5]．これらのことから，TOXなど有機態ハロゲンは，都市ゴミ焼却炉で生成するダイオキシン類の発生量を知る一次スクリーニングとして，また，ヒトへの都市ゴミ焼却炉から発生する種々の有機ハロゲン化合物や農薬などの暴露指標としても有効であるかもしれない．しかし，焼却灰，焼却炉排ガス，人体試料などの有機態ハロゲンの計測例は非常に限られており[6-8]，その暴露指標としての有効性については未だ明らかにされていない．

そこで，我々は，比較的入手可能なヒト血液を対象試料として，ダイオキシン類などの有機ハロゲン化合物の総曝露量指標とし有機態ハロゲン(extractable organic halogen, EOX）が有効であるかどうかを検討するために，中性子放射化分析法（INAA)によるEOXの測定条件の検討を行う一方,ヒトへの汚染源として重要と考えられる焼却灰の有機態ハロゲン濃度およびその化学特性について検討した．

1．ヒト血清中有機態ハロゲンの測定方法の検討

【目的】PCBsなどは生体内で代謝され，一部フェノール体となり，ヒトではその代謝物が未代謝物と同程度蓄積されることが報告されている[9]．またこれらの代謝物の中には親化合物と同じようにホルモン様の活性を示す物質も知られている[10]．これまでINAAを用いた人体試料及び生物試料によるEOXの分析例は[7,8]，脂肪や肝臓組織などをヘキサンにより抽出しているが，ヘキサン抽出法ではこれらの極性代謝物は十分に回収できない．これらの代謝物も含めて抽出する方法として，ヘキサン：ジエチルエーテル（1：1）溶液やヘキサン：*tert*-ブチルメチルエーテル（1：1）溶液による抽出法が広く使用されている[9,11]．しかし，これらの極性溶媒を使用すると，抽出過程で含水し易く，ヘキサンなどの無極性溶媒抽出よりも無機態ハロゲンの汚染が問題となる．ヘキサン抽出法では有効な無機態ハロゲンの除去法として水洗法が確立されているが，これらの極性溶媒による抽出液の水洗法の有効性については十分に検討されていない．また，中性子照射試料は，ポリエチレン管に有機溶媒抽出液として封入し，ドライアイス存在下で照射するが，試料をポリエチレン管に溶封してから照射当日までは室温で保存されることが多く，これらの溶媒で抽出されるクロロフェノール

研究施設・装置：原子炉JRR-3およびJRR-4（東海研究所）
研究分野：環境化学，環境衛生学

類のような中揮発性物質がポリエチレン管から揮発消失する可能性がある．

本研究では，これらの点を明らかにするために以下の検討を行った．

1）ポリエチレン管からの中揮発性有機塩素化合物の消失試験

2）無機態ハロゲン除去方法の検討

3）中揮発性有機塩素化合物の添加回収試験

4）ヒト血清中有機態ハロゲンの測定

【試料と方法】

1）ポリエチレン管からの中揮発性有機塩素化合物の消失試験： 4,5-dichlorophenol (2ClPhOH)，*o*-dichlorobenzene (2ClBz)，2,4,5-trichlorophenol (3ClPhOH) の3種の化合物をエタノール(100%)，オクタノール：エタノール（9：1），ヘキサン：エタノール（9：1）の各種の有機溶媒で1.0μg/m l の濃度に調製した．各々の溶液0.5m l をポリエチレン管に添加・溶封し，ポリエチレン袋で2重にシームした後に，室温で約3週間放置し，INAA に供した．

2）無機態ハロゲン除去方法の検討： 50ml ねじ栓付遠沈管に，ハロゲン化アンモニウム水溶液（NH_4Cl：1.0%，NH_4Br：150ppm， NH_4I：50 ppm ）7ml，中性（あるいは 0.5M硫酸酸性）のヘキサン洗浄水 7m l，メタノール 7m l を順次加え，この混合溶液に，ヘキサン：ジエチルエーテル［1：1］（あるいはヘキサン：tert-ブチルメチルエーテル［1：1］）20m l を加え，振とう抽出後，遠心分離し，上層を 200m l 分液ロートに移した．抽出操作を全部で3回繰り返した後に，中性（あるいは 0.5M硫酸酸性）ヘキサン洗浄水 60m l で3回洗浄，或いは無水硫酸ナトリウムで脱水後に，KD濃縮器により 5m l 程度に濃縮し，さらに窒素吹き飛ばし法により少量濃縮し，全量をポリエチレン管に添加・溶封し，INAA によりハロゲン量を測定した．

3）添加回収試験：2ClPhOH，2ClBz，3ClPhOH 各々 100 μg を血清 7m l に添加し，無機態ハロゲン除去方法の検討と同じ前処理を行い HPLC で定量した．また 2,3,4,6-tetrachlorophenol (4ClPhOH) 2μg を血清7m l に添加し，同様に処理し， INAA で塩素量を測定した．

4）血清あるいは血漿中有機態ハロゲンの測定：数名の成人男性および女性から 20～100m l の血液を提供頂き，血清或いは血漿を分離後，それらの 7～50m l を無機態ハロゲン除去方法の検討と同じ前処理を行い，INAA でハロゲン量を測定した．

5）照射および測定条件：試料あるいは標準溶液を添加・溶封したポリエチレン管を，蒸留水，アセトン，ヘキサンで順次洗浄後，ドライヤーで乾燥した後，ポリエチレン袋で2重にシームし，照射当日まで室温で保存した．INAA による照射は，試料を入れたポリエチレン容器2個と標準溶液を封入したポリエチレン容器1個を照射用の標準キャプセル（ポリエチレン製）にドライアイスと共に装填し，原子炉内で熱中性子を照射した．ＩＮＡＡの中性子源として，日本原子力研究所・研究用原子炉 JRR-3 あるいは JRR-4 を用い，単寿命核種照射装置に敷設されている気送管により熱中性子束下（JRR-3：5.0×10^{13}，JRR-4：3.2×10^{13}n/cm^2・sec）で2分間の照射を行った．照射後，直ちに外側のポリエチレン袋を取り替えて， γ線スペクトロメーターを用いて，^{38}Cl（1634 keV，2168 keV ），^{80}Br（617 keV ），^{128}I（443 keV）のγ線を測定した．

【結果と考察】

1) ポリエチレン管からの中揮発性有機塩素化合物の消失試験（表1）：3種の化合物いずれもエタノール溶液で保存した場合に回収率がよく，2ClPhOH： 128%，2ClBz：66%，3ClPhOH：119%の回収率を得た．これに対して，オクタノールおよびヘキサン溶液で保存した試料は，全ての化合物で約 80～95%がポリエチレン管から消失した．これらの結果より，血液粗抽出液をエタノール溶液へ置換するか，あるいはエタノールを保持溶液として添加することにより，ポリエチレン管封入後の汚染物質の消失を低減できることがわかった．

2）無機態ハロゲン除去方法の検討（表 2）： 血清試料のヘキサン：ジエチルエーテル（1：1）あるいはヘキサン：*tert*-ブチルメチルエーテル（1：1）抽出液中に混入した無機態ハロゲンの除去方法として，水洗あ

表1 中揮発性有機塩素化合物のポリエチレン管からの消失試験

Chemical	Solvent	Recovery (%)
2ClPhOH	ethanol	128
	octanol:ethanol (9:1)	7.5
	hexane:ethanol (9:1)	10.1
2ClBz	ethanol	66.1
	octanol:ethanol (9:1)	17.1
	hexane:ethanol (9:1)	5.0
3ClPhOH	ethanol	119

るいは無水硫酸ナトリウム脱水法の２つの方法について検討を行った結果，血液１ｍｌに換算した無機態塩素の汚染量は，約 0.03～0.05μg/ml 程度であった.予想される血清中の有機態塩素量が 0.01～0.05μg/ml 程度で無機態塩素の汚染量と同程度であることから，血清の測定に対しては，既存の無機態ハロゲン除去方法では不十分であることがわかった．今後，ゲル浸透カラムを用いるなど別の方法で，無機態ハロゲンの汚染量をさらに低減できるか検討する予定である．

表２ 種々の抽出法による無機態ハロゲンの残存量
（血清1 mlあたりに換算）

Solvent used to extract / procedure for eliminating inorganic halogen	Halogen	n	Mean (μg/ml)
hexane / dehydrated with anhydrous Na_2SO_4	Cl	2	0.005
	Br	2	ND
	I	2	ND
hexane / rinsed with distilled water	Cl	2	0.013
	Br	2	ND
	I	2	ND
hexane-diethyl ether (1:1) / dehydrated with anhydrous Na_2SO_4	Cl	2	0.026
	Br	2	0.003
	I	2	0.044
hexane-diethyl ether (1:1) / rinsed with 0.5 M H_2SO_4 aq.	Cl	2	0.024
	Br	2	ND
	I	2	0.004
hexane : *t* -butyl methyl ether (1:1) / rinsed with distilled water or 0.5 M H_2SO_4 aq.	Cl	6	0.046
	Br	6	0.004
	I	6	0.010

３）添加回収試験（表３）：血清あるいは血漿に中揮発性有機塩素化合物を添加し，回収試験を行った結果，2ClPhOH（66%）を除き，85%以上の回収率を得た．2ClPhOH は添加回収試験を行った４種の物質中最も水溶解度が高いため，他の物質よりも水洗過程での消失が大きかったものと考えられた．

表3 添加回収試験成績

Solvent used to extract /procedure for eliminating inorganic halogen	Added Chemical	n	Recovery (%) Mean ± SD
hexane: diethyl ether (1:1) / rinsed with 0.5 M H_2SO_4 aq.	2ClBz	3	85.0 ± 28.5
	2ClPhOH	3	66.0 ± 8.3
	3ClPhOH	3	89.6 ± 5.1
	4ClPhOH	3	85.8 ± 4.5
hexane: *t* -butyl methyl ether (1:1) / rinsed with distilled water / 0.5 M H_2SO_4 aq.	4ClPhOH	6	92.3 ± 21.1*

*: determined by INAA

４）ヒトの血清あるいは血漿中有機態ハロゲン量の測定（表４）：ヒト血清或いは血漿 7～8ｍｌ中の EOX 量は，分析行程のブランク試験値（表２）と同レベルであり，信頼できる分析値を得られなかった.これらの結果より,血清 10ｍｌ程度の有機態ハロゲン量を正確に測定するためには，無機態ハロゲンの有効な除去方法を新たに導入する必要があると考えられた．血清あるいは血漿 30～50ｍｌ程度を用いた場合には，ヨウ素を除き，ブランク試験値の 5～10 倍程度のハロゲン量を検出できたが，分析試料量の増加に伴い，無機態ハロゲンの汚染量も増加する可能性があり，今後，ゲル浸透カラムで分子量分画し，これらのハロゲン全てが有機態であるのか確認が必要と思われる．

表 4 有機態ハロゲン抽出法によるヒト血清あるいは血漿中ハロゲン量

	Sample	Halogen	n	concentration (μg/ml) Mean ± SD (Min - Max)
hexane-diethyl ether (1:1)	plasma (50ml)	Cl	3	0.306 ± 0.259 (0.137 - 0.604)
		Br	3	0.023 ± 0.010 (0.012 - 0.029)
		I	3	0.016 ± 0.023 (0.002 - 0.043)
	plasma (7ml)	Cl	3	0.201 ± 0.110 (0.069 - 0.345)
		Br	3	0.036 ± 0.019 (0.022 - 0.058)
		I	3	0.009 ± 0.007 (0.005 - 0.017)
hexane : *t* -butyl methyl ether (1:1)	serum (33 - 48 ml)	Cl	4	0.214 ± 0.134 (0.017 - 0.309)
		Br	4	0.064 ± 0.047 (0.004 - 0.113)
		I	4	0.006 ± 0.005 (0.001 - 0.012)
	serum (7 ml)	Cl	6	0.060 ± 0.017 (0.042 - 0.106)
		Br	6	0.046 ± 0.034 (0.010 - 0.105)
		I	6	0.022 ± 0.009 (0.010 - 0.039)

2．廃棄物焼却灰中有機態ハロゲンの化学特性

【目的】廃棄物焼却灰中のダイオキシン類分析行程で使用されるカラムクロマトグラフィーの分画画分中の有機態ハロゲン（EOX，有機態塩素：EOCl，有機態臭素：EOBr，有機態ヨウ素：EOI）およびPCDDs，PCDFs，塩素化ナフタレン（PCNs），none-*ortho* PCBsの個別定量を行い，ＥＯＸの化学特性について比較検討した．

【試料と方法】

1）灰試料：試料としてバッチ燃焼式焼却炉から採取した医療廃棄物あるいは一般廃棄物の残灰あるいは飛灰を用いた．

2）PCDDs，PCDFs，PCNs，none-*ortho* PCBsの定量：灰試料をトルエンでSohxlet抽出し，その抽出液（粗抽出液）を濃縮後，一部をEOXの測定に供した．残液は，濃硫酸処理，シリカゲルカラム，アルミナカラム，活性炭カラムクリーンナップに順次供した．GC-MS分析は，HRGC-HRMS（JEOL SX102A-HP589011）で行い，4～6塩素のPCDD/DFsに対しては，CHROMPACK CP-Sil88キャピラリーカラムを，7，8塩素のPCDD/DFsおよびnon-*ortho* PCBs, PCNsに対してはJ&W DB-5キャピラリーカラムを用い分析した．

3）EOXの定量：EOXを測定した画分は，粗抽出液（CE），硫酸処理抽出液(SE)，10%ジクロロメタン-ヘキサン溶液で溶出したシリカゲルカラム第2画分（Sil-2 Fr.），100%ヘキサン溶液で溶出したアルミナカラム第1画分（Al-1 Fr.），50%ジクロロメタン-ヘキサン溶液で溶出したアルミナカラム第2画分（Al-2 Fr.）である．全ての画分はINAA前に，KD濃縮し，ヘキサンに転溶後，MILL-Q SP reagent water systemによって精製した蒸留水5倍容で3回水洗し，無機態ハロゲンを除去した．

INAA条件は前述した血清の条件に従った．

【結果】CE中のEOCl，EOBr，EOI濃度は，各々150-1200, 0.8－25, 0.3－38 nmol/g ashでEOBrは残灰（-BA）に比較して，飛灰（-FA）で高値を示した．またEOIは一般廃棄物焼却灰（MSW，DSW）に比較して，医療廃棄物焼却灰（MedSW）で高値を示した（図1）．

ハロゲン別に，CE及び各画分中のEOX濃度の関係を見ると，EOClおよびEOBr濃度については，全ての画分間で有意な相関関係はなかった．EOI濃度に

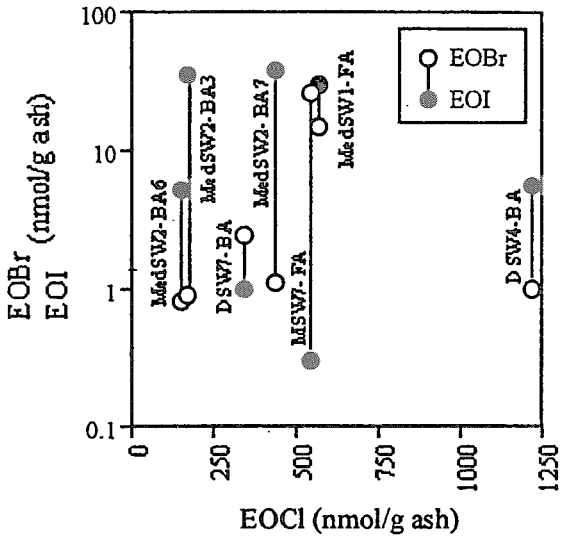

図1　粗抽出液中EOCl濃度とEOIまたはEOBr濃度との関係

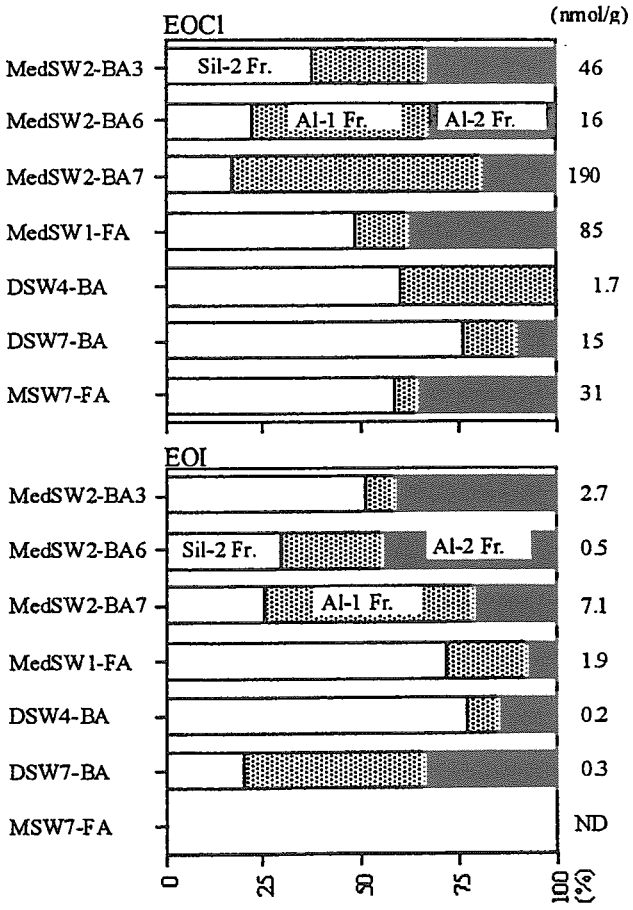

図2　カラムクロマトグラフィー分画画分におけるEOClとEOIの存在割合(%)

ついては，CE と Sil-2 Fr との間に有意な相関関係が認められた（図示していない，$p<0.0001$）．

Sil-2 Fr, Al-1, Al-2 Fr の合計を100%としたとき，ハロゲン別の各画分存在割合は，EOCl では Sil-2：17-60%，Al-1：7-65%，Al-2：ND－37%であった．EOI では Sil-2：20-77%，Al-1：8-54%，Al-2：ND－43%であった（図2）．EOBr では，Sil-2：85-100%，Al-1：ND，Al-2：14－19%であった（図示していない）．EOCl と EOI のこれらの画分中存在割合は，医療廃棄物焼却炉から得た同一試料中で類似していた．しかし，画分別に各 EOX 濃度間の関係を見ると，Sil-2 Fr.および Al-1 Fr.中の EOCl および EOI 濃度に各々相関関係が認められたが（Sil-2 Fr.: $p<0.05$, Al-1: $p<0.0001$），Al-2 Fr.では有意な関係は認められなかった（図示していない）．

Al-2 Fr. 中の EOCl 濃度は PCDFs，PCNs，non-*ortho* PCBs 濃度との間に各々有意な相関関係が認められ（PCDFs: $p<0.0001$, PCNs and non-*ortho* PCBs: $p<0.005$），同様に EOI と PCDDs との間に有意な相関関係が認められた（$p<0.05$，図3）．

【考察】EOI は一般廃棄物の焼却灰に比較して，医療廃棄物焼却灰で高値を示した（図1）．これは，医療廃棄物には殺菌剤などに使用されたヨウ素が含まれることから，焼却前の廃棄物中ヨウ素含有量が一般廃棄物よりも多いと考えられ，その差が EOI 濃度に影響を及ぼしたものと推察される．また，ダイオキシン類分析行程のカラムクロマトグラフィーで溶出される各画分中の EOI 存在割合が同一試料中の EOCl 存在割合と類似し（図2），さらにダイオキシン類溶出画分である Al-2 Fr.中の EOI 濃度と PCDDs 濃度との間に相関関係が認められたことから（図3），ダイオキシン類と同様な物理化学的性質を有する EOI が PCDDs と類似した生成メカニズムで廃棄物焼却過程中に生成されている可能性が示唆された． また Sil-2 Fr.および Al-1 Fr. 中の EOCl および EOI 濃度にも各々相関関係が認められたことから，ダイオキシン類以外にも種々の有機ヨウ素化合物が，有機塩素化合物と同様に生成されていると推察される．臭素化ダイオキシンや臭素化ビフェニールは，塩素化ダイオキシン類と同様に，焼却過程で生成し，またその毒性も類似していることが報告されている[4]．しかし，これまで，焼却灰や排ガス中のヨウ素化ダイオキシンやヨウ素化ビフェニールについて分析例はなく，今後，これらの化合物について，その汚染レベルを把握する必要があろう．

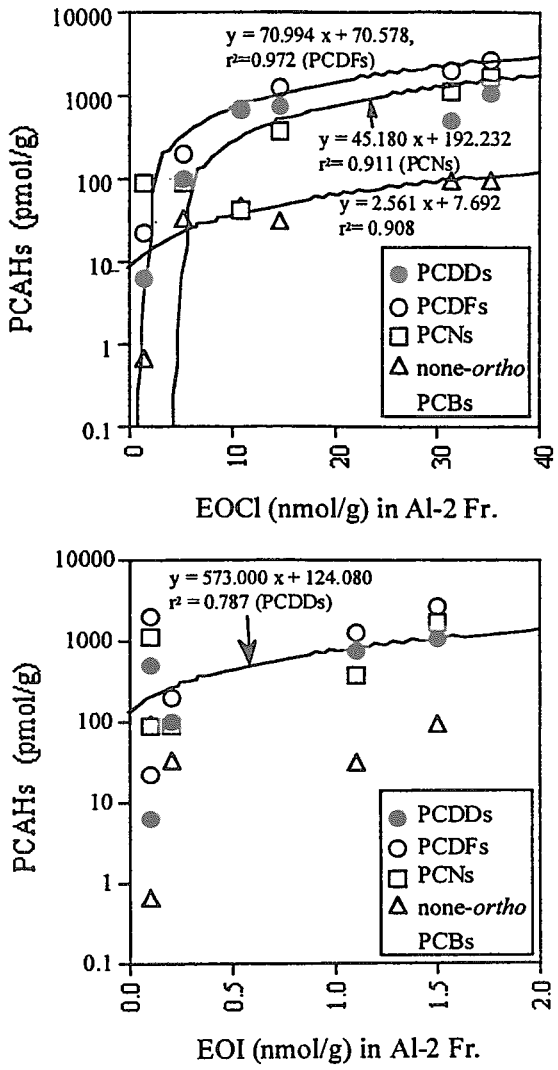

図3　アルミナカラム第2画分における種々の塩素化芳香族炭化水素（PCAHs）濃度と EOCl 或いは EOI 濃度との関係

【おわりに】ヒト血清中有機態ハロゲンの測定方法を3年間で確立することはできなかったが，今後,ゲル浸透カラム等,新たな無機態ハロゲンの除去方法を導入・検討し，測定方法の確立を目指す．

焼却灰中の有機態ハロゲンについては，粗抽出液の有機態塩素量とダイオキシン類の間には，有意な相関関係は認められず，ダイオキシン類の発生量を知る一次スクリーニングとして有機態ハロゲンは適当ではないと考えられた.しかし，未同定の汚染物質を探索する手段として，有機態ハロゲンの測定が有用であること

を本研究で示すことができた．今後は，同様な手法を用い，未同定物質の探索および同定を行い，それらの汚染物質の毒性評価へと発展させたい．

【謝辞】本研究の実施にあたり，中性子線の照射にご協力を頂いた澤幡浩之及び川手稔技官に感謝致します．

【参考文献】

1) Takasuga, T., Inoue, T., Ohi, E., Irelamd, P. Suzuki, T. and Takeda, N. (1994) *Organohalogen Compounds*, 19: 41-44

2) EPA (1997) *Special report on environmental endocrine disruption: An effects assessment and analysis*, risk assessment forum, U.S. Environmental Protection Agency, Washington DC., pp.111

3) Ahlborg, U.G., Lipworth, L., Titus-Ernstoff, L., Hsieh, C.-C., Hanberg, A., Baron, J., Trichopoulos, D., and Adami, H.-O. (1995) Organochlorine compounds in relation to breast cancer, endometrial cancer, and endometriosis: An Assessment of the biological and epidemio-logical evidence, *Crit. Rev.Toxicol.*, 25: 463-531

4) 立川　涼，渡部　功（1990）有機臭素系難燃剤の環境問題，*公害と対策*，26: 44-48

5) 尾崎史彦（1992）第3節　製紙産業界におけるダイオキシン問題とその対策，*ダイオキシン汚染問題解決への展望*，工業技術会，東京，p．188-202

6) Kawano, M., Ueda, M., Matsui, M., Kashima, Y., Matsuda, M., and Wakimoto, T. (1998) *Organohalogen Compounds*, 36: 221-224

7) Watanabe, I. , Kashimoto, T. , Kawano, M. and Tatsukawa, R. (1987) A study of organic bound halogens in human adipose, marine organisms and sediment by neutron activation and gas chro matographic analysis, *Chemosphere*, 16: 849-857

8) Bjorseth, A., Lunde, G. and Dybing, E. (1977) Residues of Persistent Chlorinated Hydrocarbons in human tissues as studied by neutron activation analysis and gas chromatography, *Bull. Environ. Contam. Toxicol.*, 18: 581-587

9) Bergman A., Klasson-Wehler, E., Kuroki, H . (1994) Selective retention of hydroxylated PCB metabolites in blood, *Environ. Health Perspect.*, 102: 464-469

10) Brouwer, A., Morse, D.C., Lans, M.C., Schuur, A.G., Murk, A.J., Klasson-Wehler, E., Bergman, A. and Visser, T.J. (1998) Interactions of persistent environmental organohalogens with the thyroid hormons system: Mechanisms and possible consequences for animal and human health, *Toxicol. Indust. Health*, 14: 59-84

11) Burse, V.W., Head, S.L., Korver, M.P., McClure, P.C., Donahue, J.F., and Needham, L.L. (1990) Determination of selected organochlorine pesticides and polychlorinated biphenyls in human serum, *J. Anal. Toxicol.*, 14: 137-142

【成果の公表】

1．学会発表

1)河野公栄,鹿島勇治，松井三明，上田守男，松田宗明，脇本忠明：焼却灰中の有機態ハロゲン，環境科学会，筑波，1998年9月

2)鹿島勇治，松井三明，河野公栄，上田守男，松田宗明，安倍和則，脇本忠明：ゴミ焼却灰中の有機態ハロゲン（EOX）とその化学特性．日本内分泌撹乱化学物質学会第1回研究発表会,京都,1998年12月

2．学術雑誌

1) Kawano M, Ueda M, Matsui M, Kashima Y, Matsuda M, Wakimoto T　(1998) Extractable organic halogens, polychlorinated naphthalenes and polychlorinated dibenzo-p-dioxins and dibenzo-furans in ashes from incinerators located in Japan. *Organohalogen Compounda*, 36: 221-224

2) Kashima Y., Matsui M., Kawano M., Ueda M., Tojo T., Takahashi G., Matsuda M., Anbe K., Doi R., and Wakimoto T. (1999) Characteristics of extractable organic halogens in ash samples from medical solid waste incinerator, *Organohalogen Compounds* 41: 191-194

3．その他

1)鹿島勇治，松井三明，岡部とし子，土井陸雄，河野公栄，松田宗明，脇本忠明（1999）廃棄物焼却灰の有機態ハロゲン，ダイオキシン様およびエストロゲン様作用．環境と測定技術，26：122-1

4-10 海底熱水沈殿物の微量元素分析

Trace Element Analyses of Submarine Hydrothermal Deposits

山形大学理学部 中島和夫・小笠原篤子

Faculty of Science, Yamagata University Kazuo Nakashima and Atsuko Ogasawara

1．研究の目的と意義

東太平洋中央海膨 (EPR) の様な拡大の速い海嶺や大西洋中央海嶺 (MAR) の様な拡大の遅い海嶺、沖縄トラフのような背弧海盆など様々な環境で熱水循環が起こっている。これまで海底熱水系に関するいくつかの研究がなされ、母岩の性質、地下構造、堆積物の有無、水/岩石比、熱水の温度と組成、pH などに違いがあり、沈殿物にもそれぞれの海嶺に特徴があることがわかっている [1]。中央海嶺の中で最も拡大速度の遅い拡大軸として知られている TAG (Trans Atlantic Geotraverse) 熱水マウンドは、1985 年に発見された硫化金属鉱床を伴う活動的海底熱水系である [2]。ブラックスモーカーから約 365℃の高温の熱水を噴出し [3]、熱水活動は現在知られている地球上の海底熱水系では最大規模のものである [4]。

1994 年 7 月 29 日から 8 月 27 日にかけて、海洋技術センターと米国ウッズホール海洋研究所の共同研究として、「しんかい 6500」による TAG マウンド地域の 15 回の潜航調査〈MODE'94 Leg2〉が行われ、チムニーなどの硫化物や玄武岩など多数の試料が得られた。本研究ではこの時に得られた熱水性沈殿物について、主要および微量元素組成を放射化分析により分析することを試みた。TAG 熱水マウンドの熱水性沈殿物の化学的特徴を明らかにすることは、TAG のみならず各地の海底熱水系の成因を考える上でも非常に重要である。

2．研究の方法

(1)分析試料

本研究で用いた試料は、MODE'94 Leg2 で得られたブラックスモーカーチムニー 6 個と硫化物ブロック 2 個である。試料は蒸留水で数回洗浄し、海水をできるだけ取り除いて保存した。

試料の肉眼的および鉱物学的特徴から次の 4 つに分類した：

A グループ (225R004, 219R001, 219R013)：チムニーの壁が 2cm 以下と薄く、筒状で熱水の通った跡があり、非常にもろい。外側から順に硬石膏、黄鉄鉱、黄銅鉱のゾーンが確認される。

B グループ (219R004, 225R002, 225R003)：チムニーの壁が厚く、熱水の通った跡は硫化物でふさがれていて、硬い。外側から順に黄鉄鉱、黄銅鉱のゾーンが確認される。

C グループ (23000202)：鉱物の分帯が識別できず、白っぽくて非常に硬い。全体が黄鉄鉱で鉱物の分帯がなく、黄銅鉱が非常に少ない。閃亜鉛鉱と非晶質シリカが少量存在する。

D グループ (2280301)：鉱物分帯があいまいで、硬いところと軟らかいところがある。外側から順に黄鉄鉱、黄銅鉱のゾーンが確認され、閃亜鉛鉱が多く非晶質シリカがない。

東海研究所、 JRR-3、 放射化分析

(2)中性子放射化分析

中性子放射化分析法（NAA: Neutron Activation Analysis)は、高感度、非破壊、多元素同時分析という 3 つの利点があるため、希少価値が高く様々な元素が含まれている熱水性硫化物の分析に適している。本研究の分析は茨城県東海村の日本原子力研究所東海研究所内にある東京大学原子力研究総合センター全国共同利用部門大学開放研究室で行った。試料は蒸留水でよく洗い粉末にして、60℃で 24 時間乾燥した bulk 試料を用い、マイクロ天秤で短寿命照射用は 5 ㎎、長寿命照射用は 10 ㎎秤量した。試料重量による誤差を軽減するため、ライトの光をあてて水分をとばしながら秤量し、薬包紙は粒子が付着してしまうので代わりに小さく切ったアルミホイルを使用した。短寿命照射用は高純度ポリエチレンに試料を入れ、内側のポリエチレンに手を触れないようにポリシーラーで二重封入する。長寿命照射用は石英管に試料を入れてガスバーナーで両端を閉じたものをアルミ箔でつつみ、まとめてさらにアルミ箔で包む。照射の条件を以下に記す。

短寿命照射

原子炉：JRR-4

照射孔：Pn(気相管)

熱中性子束：4.0×1013 □・ sec

照射容器：ポリエチレンカプセル(S)1 個

照射時間：5 分

クーリング時間：24 時間

測定時間：10000 秒

長寿命照射

原子炉：JRR-4

照射孔：T パイプ

熱中性子束：6.0×1013 □・ sec

照射容器：PEN(L)1 個

照射時間：90 分

クーリング時間：72 時間

測定時間：20000 秒

測定の条件を以下に記す。

Detector：ORTEC(Hp-Ge)

Model1112-16180- s

FWHM 2.3KeV at 1.33MeV

MCA：CAMMBERA Series 35plus

H. V Supply：Model459

Bias 3500volts

Linear Amp：Model 572

Time constant 3 μ sec

Geometry：短時間照射=0cm,

長時間照射=10cm

解析はヨーロッパを中心に行われている k_0（ケイゼロ）標準化法で行った。k_0 標準化法は、不正確なデータを k_0 因子という包括的な確定数で置き換えて濃度計算を行う。次の 3 つのソフトウェアー構成からなる。

SAMPO90：核種同定、データ取り込み

SOLCOI：同時係数補正、立体角計算

KAYZERO：濃度計算、半減期補正

3．結果とその評価

全ての試料の全岩化学組成を表 1 に示す。

放射化分析は多くの元素のガンマ線ピークを同時に測定することができるが、半減期の違いやバックグラウンドの影響でピークが重なり、計算ができない場合がある。今回の分析では Fe のピークが大きすぎるためバックグラウンドが持ち上げら

表1 TAG熱水マウンド、沈殿物の分析結果

元素	irradiate time	225R004	219R001	219R013	219R004	225R002	225R003	23000202	2280301
Ca	Long	20.21%	13.31%						
Fe	Long	18.3%	22.44%	35.31%	43.44%	42.47%	38.78%	47.94%	43.54%
Co	Long	191.9	262.5	559.7	285.2	278.2	31.24	60.39	3.696
Cu	Middle	17.84%	23.31%	23.38%	16.89%	18.68%	14.97%		3.137%
Zn	Middle	0.119%	0.161%	0.424%	592.6	578.4	865.6	0.107%	0.252%
Ga	Middle	2.416	1.87	4.084	5.582	7.314	8.138	9.225	17.17
As	Middle,Long	7.339	11.72	38.64	64.22	80.65	87.67	150.7	208.4
Se	Long	367.4	706.9	605.2					
Br	Middle.Long	14.65	18.6	9.623	6.738	7.471	15.82	5.428	20.79
Sr	Long							1.427%	
Mo	Long	138.1			311.5	341.7	375.8	0.362%	0.185%
Ag	Long	29.35	39.14				40.93	64.01	243.8
Sb	Middle,Long	1.37	1.358	2.097	3.583	3.441	7.709	11	41.64
La	Long	357.1ng/g						282.3ng/g	
Ce	Long							0.444%	0.220%
Re	Long	174	251	263.3					
Au	Middle,Long	242.6ng/g	241.9ng/g	390.1ng/g	2.75	3.346	2.12	2.091	5.442
U	Middle,Long				151.1	169.1		110.7	

れ、読みとれないピークが多数あった。表中で濃度の記入がないものは、実際に試料中には存在するがピークが正確に読めず、計算不可能だったものである。例えば顕微鏡観察で A グループの 219013 と B グループの 219R004 に硬石膏が観察されたが、中性子放射化分析でカルシウムが検出されなかった。これは実際には試料中にカルシウムが存在するが、正確なピークが読みとれないため誤差が大きくなり計算ができなかったことを表している。

図 1 は 23000202(C グループ)のγ線スペクトルである。Fe のピークのバックグラウンドで全体が持ち上げられいる。Co, Mo, As, Ga, Sb, Zn のピークの大きさの違いがわかる。

この 23000202 は、全体が黄鉄鉱からなり、少量の黄銅鉱、閃亜鉛鉱、非晶質シリカが少量存在する。黄鉄鉱(FeS_2)の Fe 量は 46.55 wt.%であるから、Fe 含有量としては 45%前後が予想されるが分析結果の 47.94%はそれを少し越えている（表1）。誤差の原因の主なものとしては、試料重量の不正確さとピークの読取り誤差が考えられる。試料には硫黄分が多く、準安定な鉱物相が多量に含まれるため、秤量中に誤差を生じる可能性がある。また、照射用のポリエチレンや石英管に封入するときの試料漏れの可能性も否定できない。これらの誤差を防ぐためには試料を十分に乾燥させることと重量を数倍にする必要があろう。今回は正確な評価ができるような標準試料を加えていなかったので明確ではないが、Fe のように結果として得られた絶対値の数%以内の誤差ではないかと思われる。

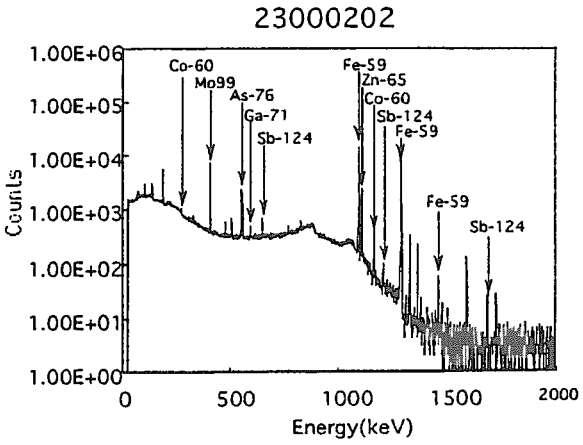

図1 23000202 試料のγ線スペクトル

4．他の海域との比較

全岩中の Fe と Cu の含有量を他の熱水域と比較すると、TAG 熱水マウンドは Fe の濃度が高く Cu の濃度も高い（図 2A)。これは同海域の Rona ほかの分析でも同様の結果が得られており、TAG あるいは大西洋中央海嶺(MAR)全体としても Fe と Cu 量が多いことが分かる。また、Rona ほかの分析値と類似していることからも今回の分析結果が妥当なものと判断される。

全岩中の Au と Ag の含有量を他の熱水域と比較すると（図 2B)、TAG 熱水マウンドを含め中央海嶺に少なく、BARC と NEPR に多いことが判明した。これらの原因については、海底下の岩石の種類、特に堆積物の有無と、地下構造の違いなどが考えられるが、詳細は別稿に議論する予定である。

5．今後の方針

まず実験手順として、試料重量を増やして照射した場合の照射および測定条件を探りたい。それから今回はできなかったが類似のサンプルで組成の分かっている標準試料を作成し、正確な評価を行う必要がある。これらの基礎実験に加えて、沖縄トラフの熱水性沈殿物について、Sb や As などに注目しながら分析を行いたい。

謝辞

本研究の実施にあたり、中性子線の照射、測定、解析の全ての面でご協力をいただいた澤幡浩之博士、川手稔氏、小野寺司史氏をはじめ大学共同利用解放研究室のスタッフの皆様に感謝いたします。

参考文献

1) Hannington, M.D., Jonasson, I.R., Herzig, P.M. and Peterson, S. , 1995: Physical and chemical precesses of seafloor mineralization at Mid-Ocena Ridges. In Seafloor Hydrothermal Systems (S.E. Humphris et al., eds.), Geophisical Monograph 91, 115-157

2) Rona, P.A., 1985: Black smoker and massive sulfides at the TAG hydrothermal field, Mid-Atlantic Ridge 26° N. EOS, 26, 431-465.

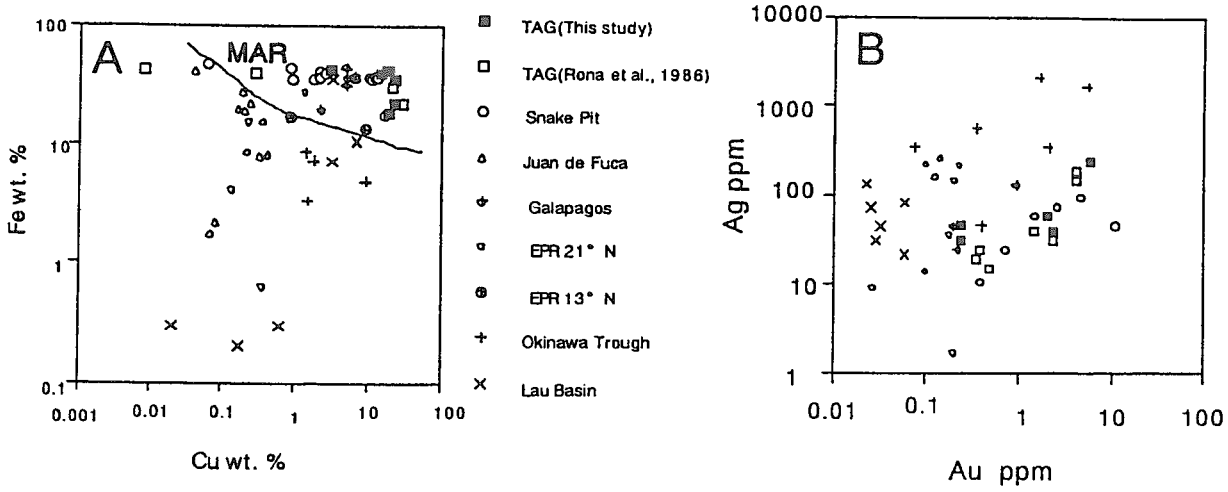

図 2　各地の海底熱水沈殿物の Fe/Cu 量 (A)と Ag/Au 量 (B) の比較

3) Humphris, S. ・ Herzig, P. ・千葉仁・中村光一・宮崎英剛, 1997：Leg 158: 大西洋中央海嶺 TAG マウンド―堆積物のない拡大速度の遅い海嶺の活動的海底熱水系の掘削―. 月刊地球, 号外(19), 89-93.

4) 益田晴恵・千葉仁・蒲生俊敬・藤岡換太郎・中村正和, 1995：TAG マウンドにおける熱水変質鉱物の分布と化学組成. JAMSTEC 深海研究, 第 11 号, 111-124.

6．成果の発表

(1)小笠原篤子・中島和夫・加藤和浩・藤岡換太郎(1997) 「TAG 熱水マウンド(MAR)における熱水性沈殿物の鉱物学的特徴」資源地質学会第 46 会年会講演会.

(2)中島和夫・小笠原篤子・加藤和浩・藤岡換太郎・澤幡浩之（1999）「大西洋中央海嶺 TAG 熱水マウンドの化学的特徴」資源地質学会第 48 会年会講演会

4-11
バイカル湖300mコア中のイリジウムの放射化分析

Radiochemical Neutron Activation Analysis of Iridium in 300 m core samples from Lake Baikal

豊田和弘・嶋田光雄・篠塚良嗣・今井志保・馬場直歩
（北海道大学・大学院地球環境科学研究科）
Kazuhiro Toyoda, Mistuo Shimada,Yoshistugu Shinozuka, Shiho.Imai, Naoho Baba
(Graduate school of Environmental Earth Science, Hokkaido Univ.)

1.巨大隕石衝突によるキューバ津波堆積物中のイリジウムの定量

人類は新しいミレニアムを迎えたが、次の千年間に直径１ｋｍ以上の小天体が地球に衝突する確率は0.5％と見積もられているそうだ。直径１ｋｍの巨大隕石が地球に衝突した場合、人類が保有している核爆弾を全部一度に爆発させたのに等しいエネルギーが放出されるものと考えられており、その場合に予想される全地球規模での環境破壊についても、現在まじめに検討されている。

特に６千５百万年前にメキシコのユカタン半島に落下して、恐竜などを絶滅させた巨大隕石は直径約１０ｋｍと推定されている。深海底のような静かな場所においてその時にゆっくりと堆積した１ｃｍほどの薄い粘土層中には、地球上の通常の堆積物には数ppt(1ppt=0.000001ppm)しか存在しないイリジウムという元素が、最高で十数ｐｐｂ(1ppb=0.001ppm)も濃縮していることが、世界各地から報告されている。その巨大隕石は衝突の衝撃により、隕石の大部分は蒸発して数μｍ（1μm=0.001mm）以下の微粒子として世界中に飛び散ったと考えられている。なお、このような新生代と中生代との境の地層を両者のスペルの頭文字を取って、ＫＴ境界と呼ばれている。さらに中央北太平洋の深海底堆積コアからは、その巨大隕石の一部と推定される2.5ｍｍほどの大きさの隕石片が１粒発見されており、その試料中のイリジウムの含有量は690ppbと報告されている。

約300メートルの高さの津波がニューヨークを襲う場面が印象的な映画「ディープ・インパクト」では、巨大隕石衝突により絶滅の危機に直面した人類の一部がミズーリ州の地下の鍾乳洞に２年間ほど潜んで生活して、人類が生存できる状態に地球環境が戻るのを待つという設定になっていた。しかし、そのような巨大隕石衝突後に地球の生態系や環境がどのように破壊されて、どれくらいの速度で回復するのだろうかという事についてはまだ不明な点が多く、それを明らかにする一つの手段として、６千５百万年前のような過去の巨大隕石衝突直後に、比較的早い速度で連続的に堆積した地層から、高い時間分解能で多数の試料について採取して、環境指標となる各項目の経時変化について解析する方法がある。

松井孝典教授（東大院・新領域創成科学）を代表とするグループは、ユカタン半島に近いキューバで大規模な野外調査をおこない、巨大隕石衝突による生じたと推測される何百ｍという厚い津波堆積物層の存在を数カ所で確認した。この層の下の方は大きな石がごろごろしているが、上に行くほど粒径が細かくなって最上部は粘土層になる。ちなみにこのプロジェクトには、クレーターの地球物理探査以外に、テクトニクス、堆積学、古生物の専門家が参加しており、本代表者は堆積物中のイリジウム含有量の分析を担当している。化学分離を伴う中性子放射化分析法でイリジウムは約十pptの含有量まで検出できる。

まず、初年度はペニャルベル層という160ｍほどの津波堆積物の全層の内から分取した14箇所について分析した。いずれも濃度は数十pptで、一試料だけ約100ppt示したが、これは塩基性岩由来のものが混じっているからで、ＫＴ境界の証拠は得られなかった。次年度にはそのペニャルベル層の

JRR-3M HR・PN、γ線スペクトロメトリー、堆積物の放射化分析

さらに上部にあたる２m厚の粘土層が採取され、分析したところ、その粘土層（モンカダ層）上部の約６ｃm厚の層中にイリジウムが0.2～0.9ppbと濃縮しており、確かにこの津波堆積物は巨大隕石衝突により引き起こされたものであることが証明できた。

巨大な津波により海中に巻き上げられた礫・土壌粒子は何十日かで海底に粗い粒度から沈殿して静かになった後に、隕石衝突で高度約10ｋm以上の上空の成層圏まで巻き上げられた、イリジウムに富んだ隕石微粒子が恐らく２～3年ほどかかってゆっくりと降下して、海中の沈降粒子と混じって堆積したために、このようなイリジウム濃度の高い層が生じたのだと解釈できる。この２～3年という数値は、1980年の米国西岸のセントヘレンズ火山の噴火など、火山の大爆発により成層圏に舞上げられた塵が対流圏に沈降するのに要すると観測された時間である。するとこの場所での堆積速度は、まだ私見ではあるが、１年間に2～３ｃmと推定できて、事件後の環境変動を数カ月単位で記憶している貴重な試料と考えられる。

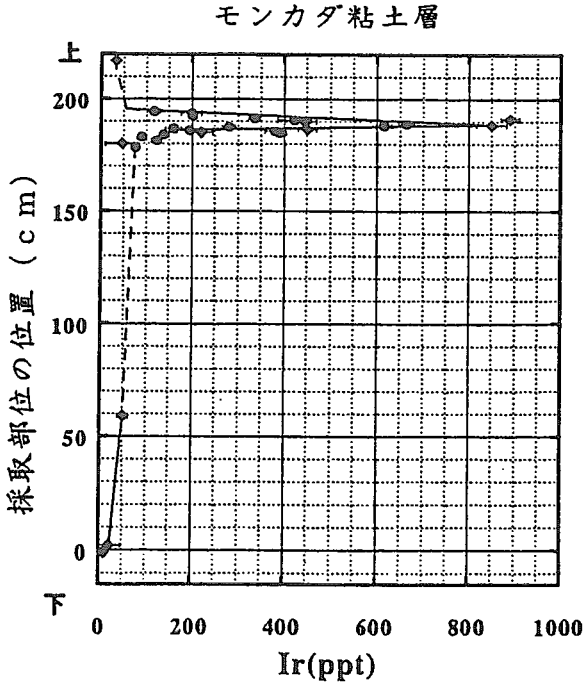

図１.キューバのモンカダ粘土層中のイリジウムの濃度垂直分布

ただし、本プロジェクトは現在進行中であり、各分析項目の解析作業やそれに基づいた精密な考察はこれからという段階である。もう一カ所の同様な地層についても、その最上部の粘土層試料中のイリジウムの定量を平成12年度中に予定している。

2.過去１万年～１万数千年前における琵琶湖と水月湖のコアによる近畿日本の堆積環境の変化

1990年代前半にｸﾞﾘｰﾝﾗﾝﾄﾞ各地の氷床コアの分析から地球の年平均気温がわずか50年で７度も上昇した記録が報告されるに従い、気候の変動メカニズムやその因果関係や地域的なずれが大変興味が持たれている。特に晩氷期から後氷期へと移行する時期には、地球の気候が何度も激変した。

本研究では、湖底堆積物及び周辺河口域から採取した堆積物中の主要元素と微量元素、計18元素をICP発光分析と機器中性子放射化分析を併用して測定し、1万数千年前から1万年前までの近畿地方での堆積環境の変動について化学組成から考察した。

まず、水月湖で1993年に採取された年縞堆積物コアのうち、湖底から深さ約17ｍの部分（約1.6万年前；以後年代はすべて暦年代）から深さ約12ｍの鬱陵沖火山灰層の部分（約1万年前)までの110試料（約4cm間隔）と、水月湖周辺河口域から採取した堆積物（17試料）を対象として分析した。その結果、TiO_2/Al_2O_3比とTh/Sc比のコア中の垂直分布の変動と、ｸﾞﾘｰﾝﾗﾝﾄﾞ氷床コア中の酸素同位体比の変動とは、よい対応関係を示していることが明らかとなった（図2）。

但し、300～1000年程度の時間差があり、およそ14.2～12.6千年前までがﾍﾞｰﾘﾝｸﾞからｱﾚﾚｰﾄﾞに、およそ12.6～10.6千年前までがﾔﾝｶﾞｰﾄﾞﾗｲｱｽに対応していると仮定した。水月湖周辺には花崗岩と古生層が主に分布しており、その仮定では気候が寒冷化すると花崗岩の寄与の割合が増加し、また逆に温暖化すると古生層の寄与の割合の増加があったと解釈される（図3・4）。

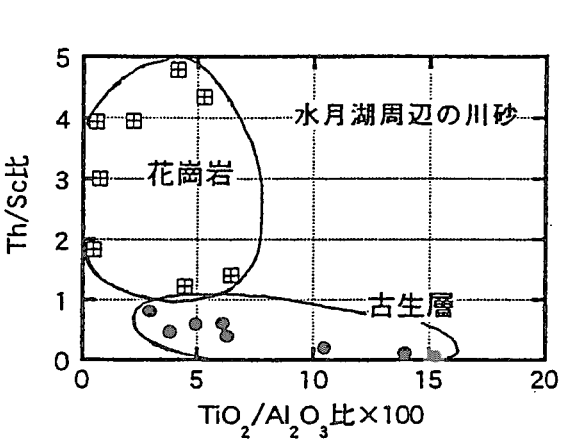

図２． 水月湖周辺に分布する花崗岩と古生層の化学組成

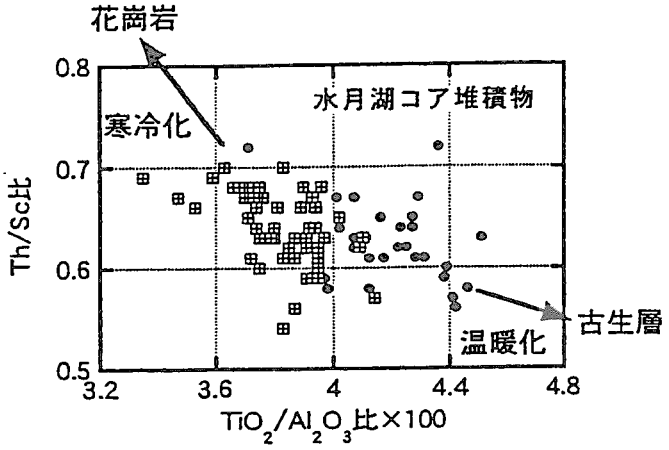

図３.水月湖コア堆積物の化学組成

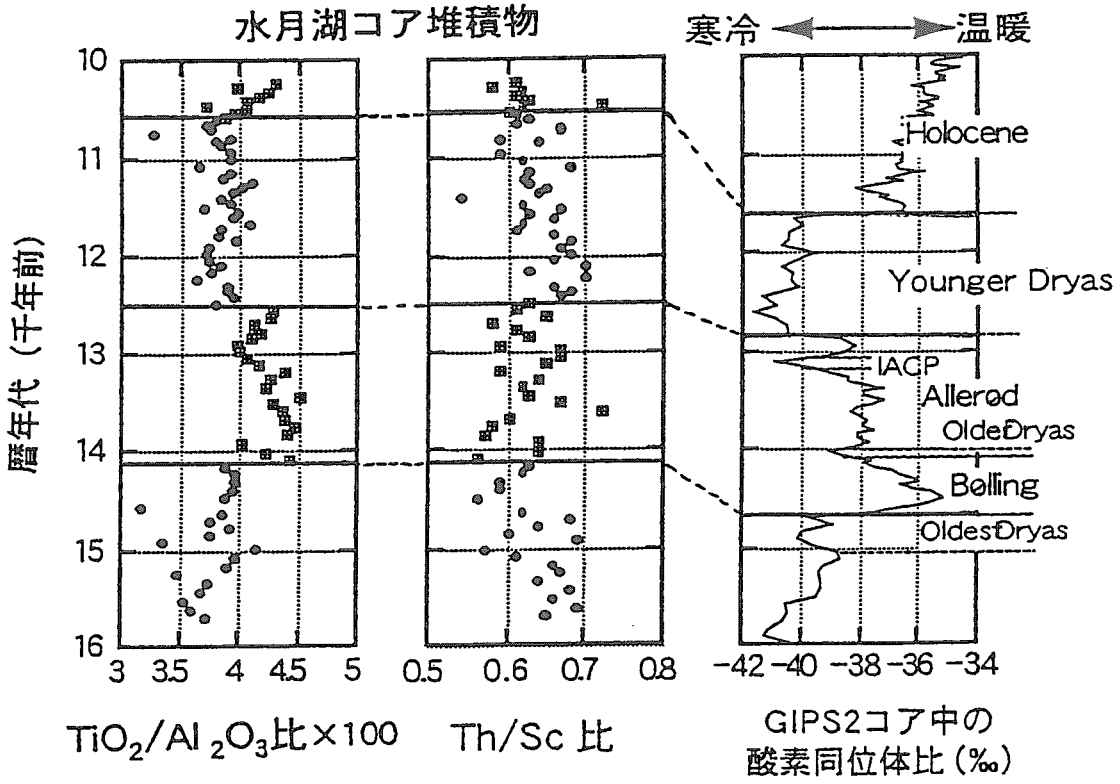

図４.水月湖コアの堆積年代による化学組成の変動とクリーンランド氷床コアでの酸素同位体比の変動との比較。

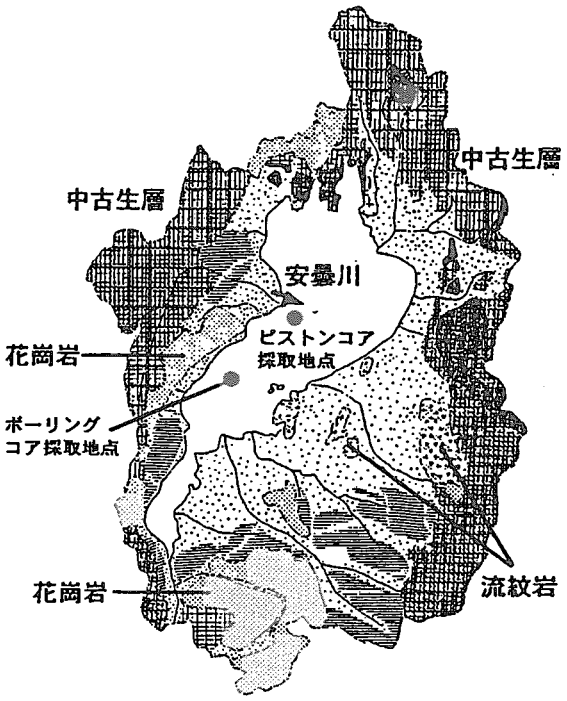

図5. 琵琶湖の地質図と高島沖ピストンコアと1400mボーリングコアの採掘位置

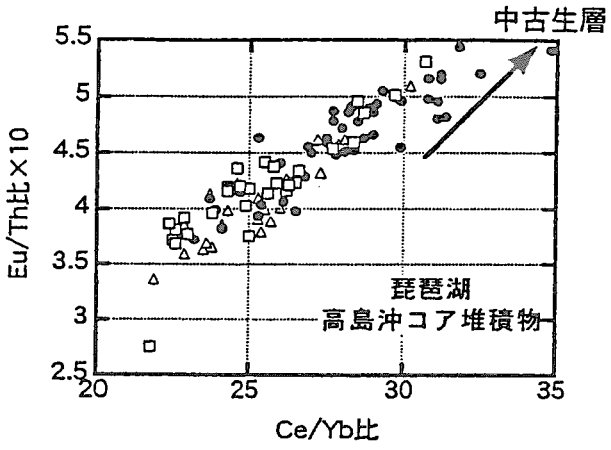

図6.琵琶湖高島沖の琵琶湖堆積物コア試料のEu/Th比とCe/Yb比との相関図

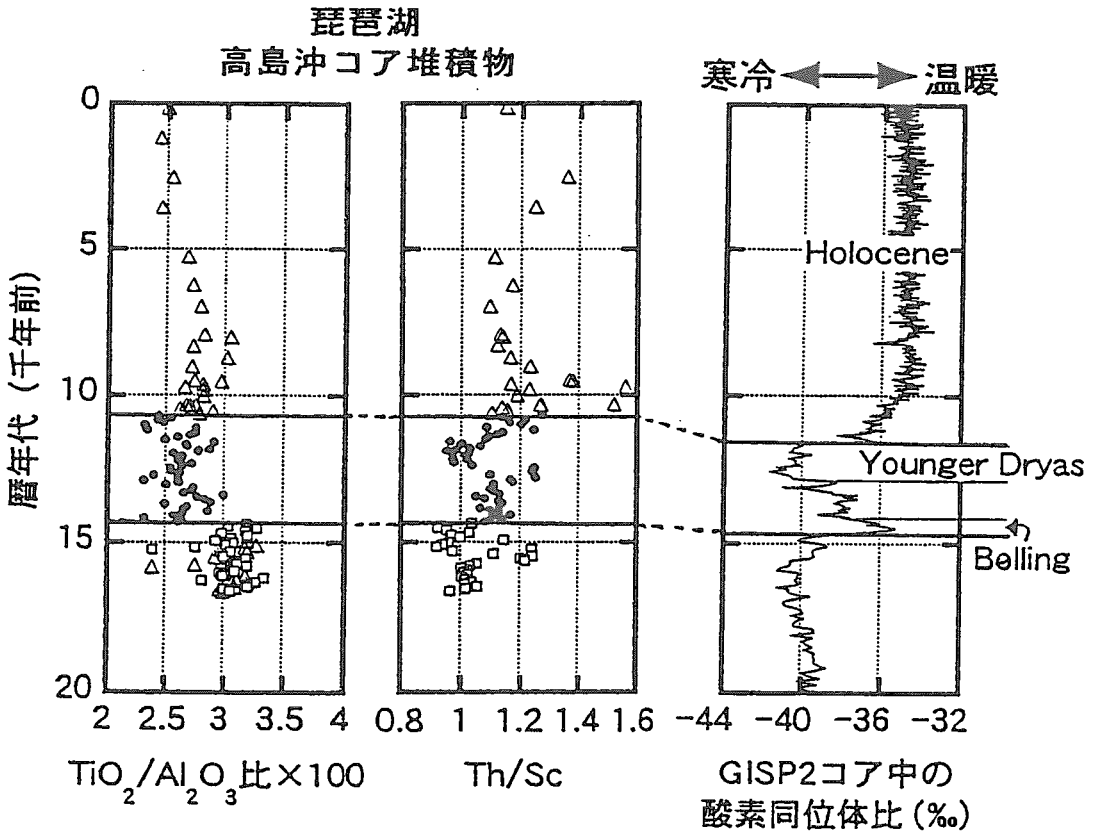

図7.琵琶湖高島沖の堆積物コア試料の化学組成変動と氷床コアの酸素同位体比の変動との比較。

なお、この水月湖コアの研究は国際日本文化研究センターの安田研究室との共同研究として行っている。

次に、中古生層を分水嶺域としてもつ安曇川河口付近の琵琶湖湖底（図5）で1995年に採取された高島沖コア（約10m長さで約1.7万年間分）から、約8cm間隔で採取した約100試料を、今回分析した。その結果、試料中のCe/Yb比とEu/Th比の間に相関係数が0.95と非常によい正の相関が見られ、これらの比が相対的に高い値を示す部分（およそ14.2～10.6千年前）と低い値を示す部分（およそ17～14.2千年前、およそ10.3千年前～現在）に分けるとができた（図6）。

この変動と気候変動曲線とを対応させると、1000年程度の時間差はあるが、比が高い値を示す時期は、ﾍﾞｰﾘﾝｸﾞからﾔﾝｶﾞｰﾄﾞﾗｲｱｽに対応しているように見える（図7）。また、琵琶湖周辺河口域から採取した堆積物（25試料）の分析から、Ce/Yb比とEu/Th比がコア試料より大きな値を持つ供給源は中古生層であることが明らかとなっており、この時期には安曇川からの流出物の影響の割合が増加したと推定される（図8）。また、同時期にTiO_2/Al_2O_3比とTh/Sc比からも同様な結果が得られた（図9・10）。

以上のことから、日本の近畿地方でもおよそ14.2～10.6千年前に大きな堆積環境の変動があったことが検出され、また300～1000年程度の時間差は、ｸﾞﾘｰﾝﾗﾝﾄﾞと日本との間の気候変動の起こった時間のズレと、気候変動の影響が湖底堆積物の化学組成にまで及ぶために必要な時間によるものと考えている。

以上の研究から水月湖コア試料中の化学組成の変動とｸﾞﾘｰﾝﾗﾝﾄﾞでの気候変動曲線との間にはよい対応関係が見られたが、まだ断定するには不十分な精度である。そこで現在は、コアから約1cm間隔で採取した約400試料のうち、今回分析した試料を除いた約300試料の分析を、現在機器中性子放射化分析とICP発光分析を併用して行っており、約10年単位の高精度で対応関係について明確に議論できるようにする予定である。

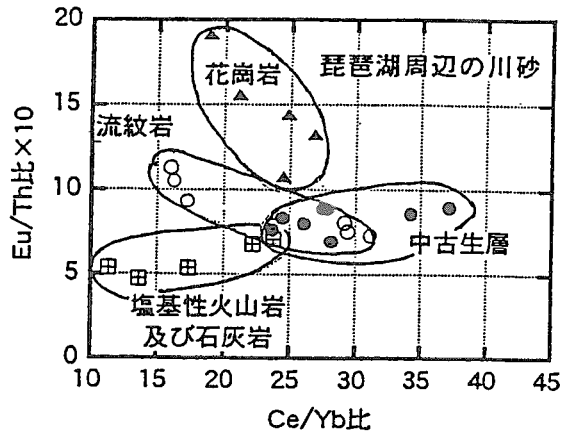

図8.琵琶湖周辺の川砂のEu/Th比とCe/Yb比との相関図

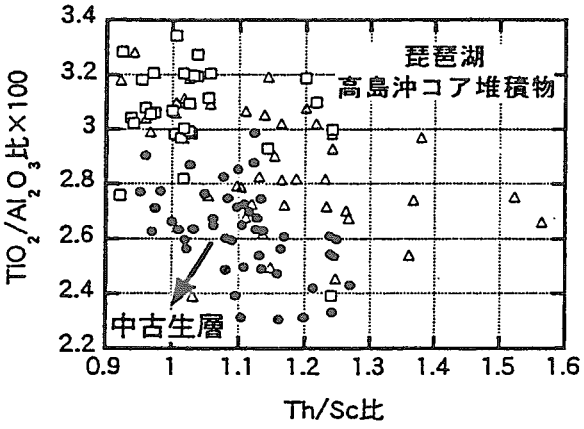

図9.琵琶湖高島沖の琵琶湖堆積物コア試料Th/Sc比とTi/Al比との相関図

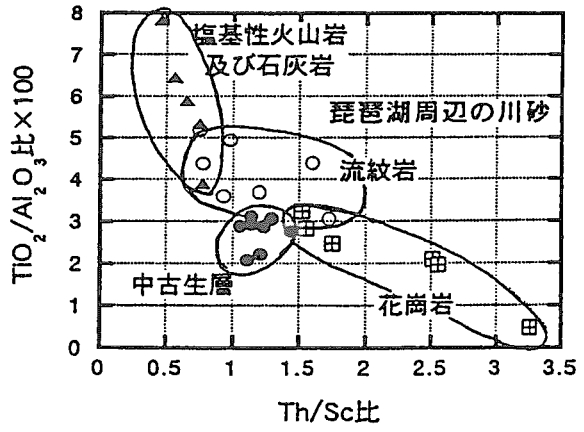

図10.琵琶湖周辺の川砂のTh/Sc比とTi/Al比との相関図

3.琵琶湖ボーリングコアによる過去43万年間の堆積環境の変化

琵琶湖の中央部には均質な粘土層が湖底から深度250mまで連続的に続いており、過去４３万年間の堆積環境を保存している（竹村1990）。第四紀の高精度な古環境変動を考察することを目的として、そこでの無機化学組成の垂直分布を測定しており、その一部は既に前回の報告書で報告した。今回、1982-83年掘削コア（図5）（水深68m）上部250mの粘土層コアから１～２m間隔に採取した試料について、機器中性子放射化分析をさらに行った。

まず、Hf/Th比及びHf/Sc比の垂直分布から、Hfの含有量が４３万年から現在まで徐々に増加している事がわかった。コアの採取地点の東岸には湖東流紋岩、南西岸には花崗岩、北西岸には中古生層、北東岸には塩基性岩がが分布している。特に掘削地点に近接して西側に存在する比良花崗岩はHfの含有量が高いことから、過去４３万年間の比良花崗岩体の琵琶湖湖底に対しての相対的な上昇運動が、掘削コア中のHfの含有量の増加として現れていると推測した（図11）。

また、約17万年前（深度約105m）に、Hfの含有量が多い物質の相対的な寄与が急に増加している事も検出された。一方、Na/Sm比とNa/La比の垂直分布から、約15万年前（深度約95m）にNa含有量が相対的に急に減ったことが観測されており、これは琵琶湖の北堆積盆の沈降速度が急に増えたため、北西岸に存在するNa含有量の比較的低い中古生層からの供給量が減ったためと考えた（図12）。２万年ほどの時間のずれがあるが、このようなテクトニックな変動がHfの含有量に反映しているかもしれない。

さらに、Th/Sc比の垂直分布は特異的な増減を繰り返しており、氷河き-間氷期サイクルの気候変動と連動しているようにも見えるが、その是非については検討中である。

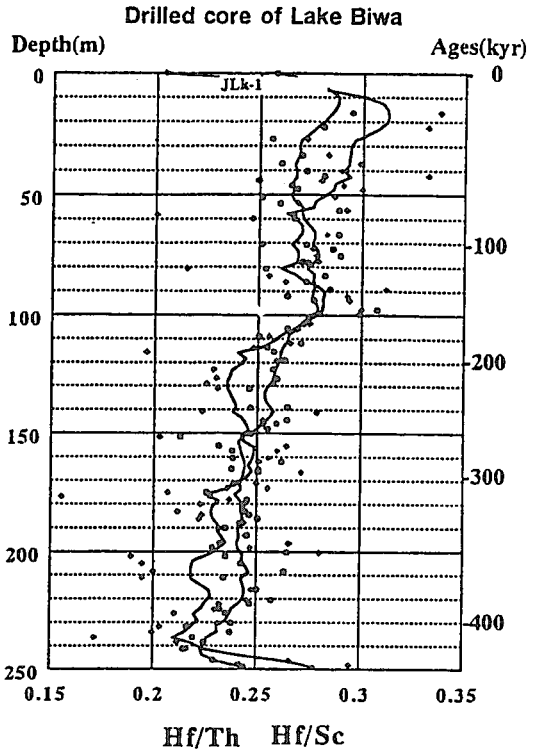

図11.琵琶湖掘削コアのHf/Th比及びHf/Sc比の垂直分布

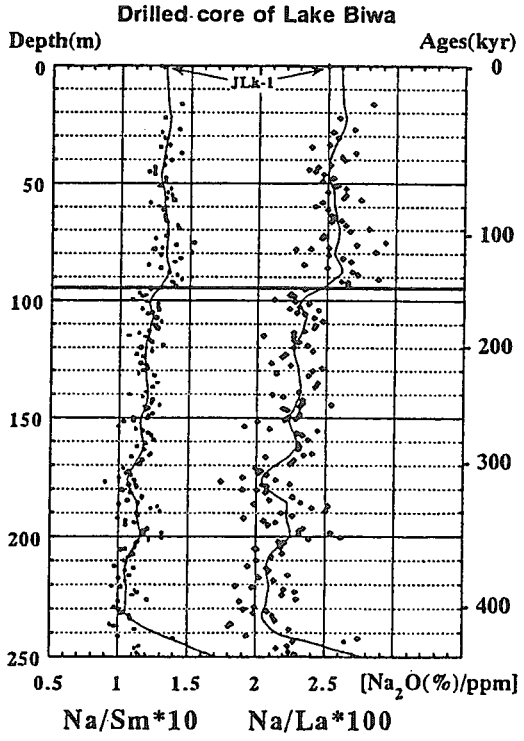

図12.琵琶湖掘削コアのNa/Sm比とNa/La比の垂直分布

成果の報告

○学会発表
琵琶湖コア試料中の無機化学組成の高分解能垂直分布（課題講演　地球環境変動史の解明に向けて）、
豊田和弘、
日本地球化学会年会、
1997年9月17日、東京都立大学

現世環境の深海底堆積物・生物源燐酸塩の希土類元素、
豊田和弘、
シンポジウム炭酸塩の希土類元素地球化学
1998年3月5日、東京大学海洋研究所

琵琶湖堆積物コア中の元素の高分解能垂直分布と過去三万年間の堆積環境の変遷
篠塚良嗣・豊田和弘
地球惑星科学関連学会1998年合同学会
1998年5月

BW95コア中の無機元素の高分解能垂直分布、篠塚良嗣・豊田和弘、日産科学振興財団研究助成　一般研究「最終氷期以降の堆積物に記録された環境変動と人間活動の歴史」研究集会1998年11月1日、京都大学

水月湖年縞堆積物の化学分析から検出された晩氷期の高分解能な環境変動の復元
篠塚良嗣・豊田和弘・安田喜憲
地球惑星科学関連合同学会1999年度年会
1999年6月

水月湖年縞堆積物の化学分析から検出された晩氷期の高分解能な環境変動の復元
篠塚良嗣・豊田和弘・安田喜憲
放射化分析研究会、1999年8月23日

高分解能な環境変動と関連した堆積物の機器放射化分析
豊田和弘
放射化分析研究会、1999年8月24日

中国蘭州の黄土及びカシュガル、ホタンのレス堆積物のAl-Fe-Mg-Scの化学組成
嶋田光雄・小野有五・豊田和弘
日本地球化学会1999年度年会、1999年9月

Sedimentary Palaeo-environments and chemical compositions from Lake Biwa in Japan
Kazuhiro Toyoda
The first joint meeting of the ADLP (Asian Lake Drilling Programme) and ELDP (European Lake Drilling Programme)国際シンポジウム
2000年3月23日

キューバＫＴ境界試料におけるイリジウムの分析結果
豊田和弘
キューバＫＴプロジェクト・ワークショップ
2000年6月3日

中国・遼寧省大連市のレス堆積物の化学組成
村田拓自・豊田和弘・安田喜憲
地球惑星科学関連合同学会2000年度年会
2000年6月26日

A Giant tsunami deposit at Cretaceous-Tertiary boundary in Cuba
R.Tada, H.Takayama, T.matsui, M.Iturade Venent, E.Tajika, T.Oji, S.Kiyokawa, D.Garcia, H.Okada, K.Toyoda, T.Hasegawa,
Impact 2000国際シンポジウム
2000年7月ウイーン

○学術雑誌

「天然の石英・長石粒の光励起ルミネッセンス現象を利用した埋没年代測定法の発展」
豊田和弘、ぶんせき、1997、No.5, 401-403,1997

「堆積物コア試料の機器中性子放射化分析」
豊田和弘、放射化分析、9号、6-13,1999

「堆積物中のヒ素の定量について」
豊田和弘・篠塚良嗣、放射化分析、9号、32-35,1999

Origin of the Penyiver Formation of northwestern Cuba and its relation to K/T boundary impact event.
R.Tada, H.Takayama, T.matsui, M.Iturade Venent, E.Tajika, T.Oji, S.Kiyokawa, D.Garcia, H.Okada, T.Hasegawa, K.Toyoda,
Sedimentary Geology (in press)
2000

4-12
キアシシギ (*Heteroscelus brevipes*)の有機態ハロゲン (Cl, Br, I)

Extractable Organohalogens (EOX) in Grey-tailed Tattler (*Heteroscelus brevipes*)

河野公栄、松田宗明、脇本忠明
M. Kawano, M. Matsuda and T. Wakimoto
愛媛大学農学部
Faculty of Agriculture, Ehime University

1. はじめに

今日、多種類の化学物質が大量に生産・使用され、それらによる環境汚染が懸念される。環境汚染物質の中でもPCBsやダイオキシン類など有機ハロゲン化合物は環境残留性を有し、生物に毒性影響を及ぼすことから特に注目されている。特に近年これらの化合物の新たな毒性影響として内分泌系の撹乱を導くことが明らかにされているが、毒性の強い未知有機ハロゲン化合物による環境汚染が懸念される。

そこで本研究では、機器中性子放射化分析法を用い環境中に残留する未だ検討されていない未知有機ハロゲン化合物の存在を明らかにすると共にそれらの蓄積性など環境挙動について検討を行った。なお有機態ハロゲン Extractable organic halogens (EOX)を放射化分析法で測定し、別途GC-MSで定量した個別ハロゲン化合物(PCBs, DDTs, HCHs, CHLs, HCB等、200種以上)の濃度との比較により未知有機ハロゲン化合物濃度を求めた。

本研究ではキアシシギ(*Heteroscelus brevipes*)を用いた。本種は、シベリアから日本を経てオーストラリア等の南方へ長距離移動する渡り鳥であるが、本種は河口等の干潟を摂餌域とする生態系の高次生物であり、餌生物を通じて未知有機ハロゲン化合物を高濃縮することが考えられる。また、干潟は陸域由来の汚染物質が集積する場でもある。

2. 試料と方法

分析対象のキアシシギは、千葉県・小櫃川河口で渡り途中の個体を許可の下に1989年から1992年の間、捕獲した。分析は、脂肪組織中の有機態ハロゲンを有機溶媒により抽出し、無機ハロゲンを水洗、ゲル浸透クロマトグラフィーにより除去した後、放射化分析によりハロゲン濃度を測定した。放射化分析には日本原子力研究所の研究用原子炉JRR-3,4を用い、放射化の条件は中性子束3.7x10^{13}n/cm^2・秒、2分間照射後、生成した核種 ^{38}Cl (1643keV、2168keV)、^{80}Br(617keV、666keV)、^{128}I (443keV)をγ-スペクトロメトリーにより定量した。γ-スペクトロメトリーには、高純度Ge同軸型検出器(EG&G ORTEC MODEL GEN-15180)及び多重波高分析器(CANBERA SERIES 35 PLUS)を用いた。また人工有機塩素化合物としてDDTs, HCHs, クロルデン化合物(CHLs), PCBs及びHCBの分析を行った。これらの化合物の分析は、有機溶媒による抽出後、フロリジルカラムクロマトグラフィーによる分画の後、GC-ECDまたはGC-MSを用い定量した。

3. 結果と考察

有機態塩素(EOCl)、有機態臭素(EOBr)及び有機態ヨウ素(EOI)が、全ての試料から検出された。試料中のEOCl濃度は1.3-62mg/g(湿重)，またEOBrはND-2.2mg/g, EOIではND-1.9mg/g、濃度順位はEOCl>EOBr>EOIであった。一方、既知の有機塩素化合物ではPCBsについて150-2,100 ng/g, DDTs

研究施設と装置名
JRR-3, 4 気送管

研究分野
放射化分析

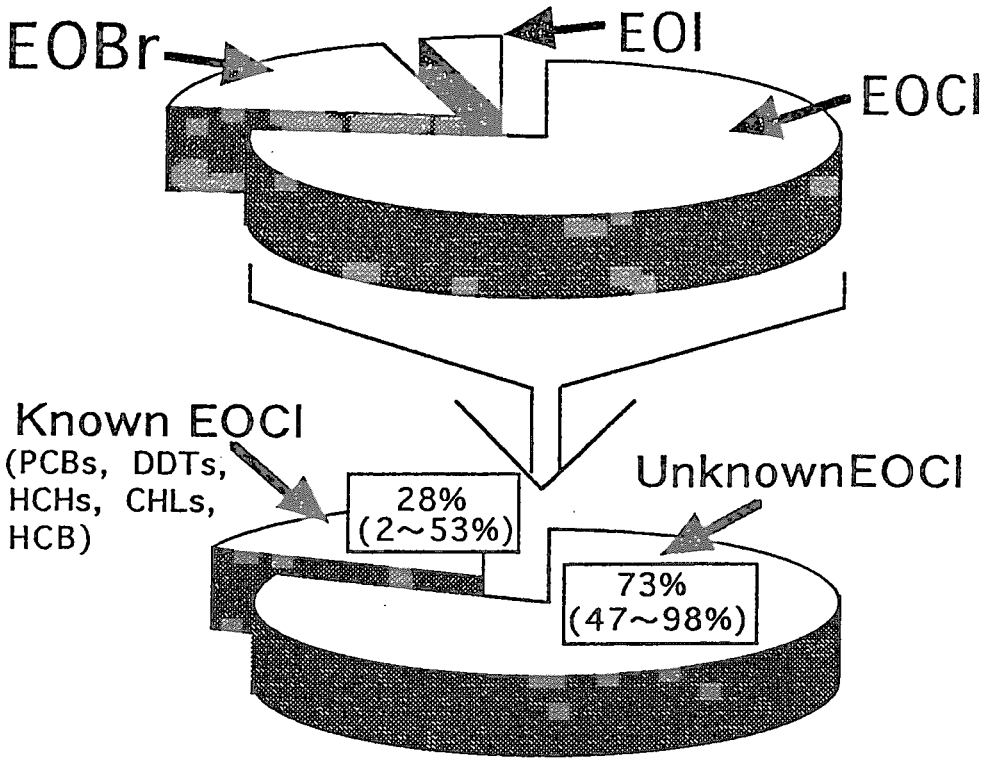

Fig.1 Compositions of EOX in Adipose Tissues of Grey-tailed Tattler.

は38-760ng/g, HCHsについては1.7-74ng/g,さらにCHLsは6.7-200ng/g,またHCBは1.6-28ng/gが検出された。EOXの中でEOClが最も高濃度で、EOClに占める上記の既知の総有機塩素化合物の割合は、2-53%であり、キアシシギ体内に存在する有機態塩素の47ないし98%が未検討の有機塩素化合物に由来する有機態塩素であることが示唆された(図1)。

既知有機塩素化合物は脂溶性であることから、EOXも脂溶性で体内の脂肪組織に蓄積していることが考えられる。従って、渡りの期間中の体脂肪の消長(消耗と蓄積)に伴いキアシシギ体内のEOXも変動することが推定される。そこで、EOXの体内総負荷量と体脂肪率(体重に占める脂肪組織の割合)の関係を検討した。その結果、EOClおよびEOBrについて、体内総負荷量と体脂肪率の間に相関関係が見られ、体脂肪の増加にともなって体内総負荷量も上昇する傾向が見られた。さらにEOClから既知人工有機塩素化合物(PCBs, DDTs, HCHs, CHLs およびHCB)の有機態塩素濃度を差し引いた未知の有機塩素化合物に由来する有機態塩素濃度について既知有機塩素化合物ほど顕著でないが、図2に示すように体脂肪率の上昇に伴い体内総負荷量が増加する傾向を示した。以上の結果は、キアシシギはシベリアからオーストラリアへ渡る途中で日本の干潟において休息し摂餌するが、その際、塩素及び臭素を含む未検討の有機ハロゲン化合物を餌生物を介して取り込んでいることを示唆している。

さらに未知有機塩素化合物と既知有機塩素化合物間の相関関係について検討したところ、未知有機塩素化合物とHCHs及びPCBsとの間に比較的良好な相関関係が見られた(表1)。このことは、キアシシギ体内に取り込まれている未知の有機塩素化合物はPCBsやDDTsなどと同様に極めて安定で蓄積性が強いことが考えられる。

以上、キアシシギは汚染物質が集積する河口域の干潟において、摂餌によって比較的残留性の強い未知の有機ハロゲン化合物を取り込んでいることが懸念される。

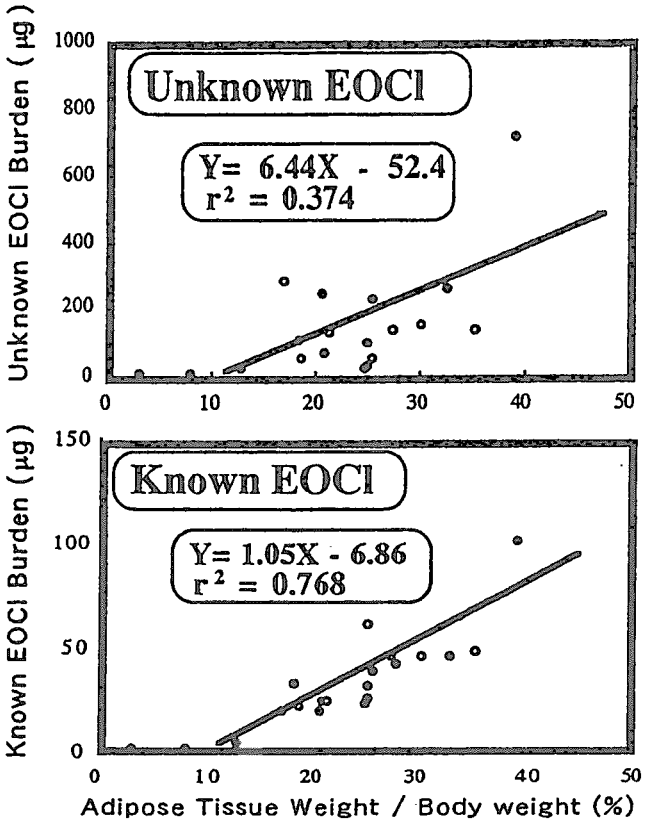

Fig.2 Relationship between Fat Content and EOCl Burden of Grey-tailed Tattler.

Table1 Correlation Coefficients among Burden of Unknown EOCl and Organochlorine Compounds Residued in Grey-tailed Tattler.

Compound / Compound	Unknown EOCl	PCBs	DDTs	HCHs	CHLs	HCB
Unknown EOCl						
PCBs	* 0.563					
DDTs	0.297	0.330				
HCHs	** 0.653	*** 0.777	0.378			
CHLs	0.019	0.146	0.305	0.216		
HCB	0.390	** 0.638	0.245	0.714	0.171	

* Significant at 1% level
** Significant at 0.5% level
*** Significant at 0.1% level

4. 成果の公表

学会誌等

1) M. Kawano, M. Ueda, M. Matsui, Y. Kashima, M. Matsuda and T. Wakimoto: Extractable organic halogens, polychlorinated naphthalenes and polychlorinated dibenzo-p-dioxins and dibenzofurans in ashes from incinerators located in Japan, Organohalogen Compounds, 36, 221-224 (1998).

2) M. Kawano, K. Yamamoto, Y. Shigeta, R. Tatsukawa and T. Wakimoto: Accumulation of Extractable Organic Halogens (EOX) and Persistent Man-Made Organochlorine Compounds by Grey-Tailed Tattler (*Heteroscelus brevipes*), Organohalogen Compounds, 43, 67-71 (1999).

3) Y. Kashima, M. Matsui, M. Kawano, M. Ueda, T. Tojo, Ge. Takahashi, M. Matsuda, K. Anbe, R. Doi, and T. Wakimoto: Characteristics of Extractable Organic Halogens in Ash Samples from Medical Solid Waste Incinerator, Organohalogen Compounds, 41, 191-194 (1999).

4) M. Matsui, Y. Kashima, M. Kawano, M. Ueda, T. Tojo, G. Takahashi, M. Mastuda, R. Doi, T. Wakimoto: Assessment of Dioxin-Like Effects of Ash Extracts -Comparison of Chemical Analysis and In Vitro Bioassay-. Organohalogen Compounds, 44: 475-478 (1999).

5) K. Kannan, M. Kawano, Y. Kashima, M. Matsui and J. P. Giesy: Extractable Organohalogens (EOX) in Sediment and Biota Collected at an Estuarine Marsh near a Former Chloralkali Facility, Environmental Science and Technology, 33, 1004-1008 (1999).

学会講演等

6)河野公栄、山本恭資、茂田良光、脇本忠明、立川 涼、キアシシギ(*Heteroscelus brevipes*)に蓄積する残留性の人工有機塩素化合物と有機態ハロゲン(EOX)、第42回放射化学討論会講演予稿集、p149、仙台、1998年9月16～18日.

7)河野公栄、脇本忠明、環境化学分野における放射化分析の利用 -生物、土壌中の有機ハロゲン化合物-、Jerzy Falandysz、第7回東京大学原子力研究総合センターシンポジウム、東京大学、p261-262、東京、1998年11月16,17日.

8)河野公栄、鹿島勇治、松井三明、上田守男、松田宗明、脇本忠明、焼却灰中の有機態ハロゲン、環境科学会1998年会講演要旨集、p186-187、つくば、1998年9月30～10月2日.

9)松井三明、鹿島勇治、河野公栄、上田守男、松田宗明、脇本忠明、医療廃棄物焼却灰のエストロジェン様活性、日本内分泌撹乱化学物質学会第一回研究発表会要旨集、p41、京都、平成10年12月11-12日.

10)鹿島勇治、松井三明、河野公栄、上田守男、松田宗明、安部和則、脇本忠明、ゴミ焼却灰中の有機態ハロゲン(EOX)とその化学的特性、日本内分泌撹乱化学物質学会第一回研究発表会要旨集、p42、京都、平成10年12月11,12日.

11)松井三明・鹿島勇治・小林智恵・河野公栄・上田守男・東條秀樹・高橋玄太・松田宗明・脇本忠明: ダイオキシン類分析行程諸画分の生物検定法によるダイオキシン様活性. 第8回環境化学討論会、北九州、7月、講演要旨集、p220-221 (1999).

12)河野公栄・Kannan, K.・鹿島勇治・松井三明・Giesy, J. P. ・脇本忠明: クロロアルカリ工場跡地付近の環境に残留する有機態ハロゲン(EOX). 日本放射化学会誌別冊 (第43回放射化学討論会講演要旨集)、Vol. 1、p 145、つくば市、平成11年10月13-15日.

13)河野公栄: 未知環境汚染物質への挑戦 - 環境中に残留する有機態ハロゲンについて、我々はどれだけ把握しているか?. 第一回放射化分析研究会・夏の学校、横須賀市、平成11年8月23-24日.

14)河野公栄: クロージングレクチャー(特別講演)・環境中に存在する有機態ハロゲンと人工有機塩素化合物. 第一回放射化分析・夏の学校、横須賀市、平成11年8月23-24日.

招待講演

15)河野公栄: 環境中の有機態ハロゲンと人工有機塩素化合物. 第一回生物資源開発学公開講演会、広

島県立大学「21世紀の生物資源開発 - 現状と未来」要旨集、p 14-15, 広島、平成11年6月15日.
16)河野公栄: 化学物質による環境汚染. 平成11年度高等学校総合理科教育講座、愛媛県総合教育センター、愛媛、平成11年8月19日.
17)Masahide Kawano, Distribution of extractable organic halogen (EOX) in soils and sediments, Lecture at Maejo University, Chiang Mai, Thailand, December 11, 1998.
18)Kawano, M.: Special lecture -Global distribution of extractable organic halogens (EOX) in marine mammals-. China Institute of Atomic Energy, Chinese Academy of Sciences, Beijing, China, December 7, 1999.
19)Kawano, M.: Special lecture -Global distribution of extractable organic halogens (EOX) in soils and sediments-. China Institute of Atomic Energy, Chinese Academy of Sciences, Beijing, China, December 9, 1999.

<u>その他</u>

20)鹿島勇治・松井三明・土井陸雄・河野公栄・松田宗明・脇本忠明・安倍和則: 廃棄物焼却灰中有機態ヨウ素の化学特性. 横浜市立大学環境ホルモン共同研究プロジェクト平成１１年度報告書、横浜、p.61-64, 1999.
21)松井三明・鹿島勇治・土井陸雄・河野公栄・松田宗明・脇本忠明: 廃棄物焼却灰のダイオキシン類分析とバイオアッセイによる毒性およびホルモン様作用評価. 横浜市立大学環境ホルモン共同研究プロジェクト平成１１年度報告書、横浜、p.65-68, 1999.

4-13

岐阜県土岐市西方に分布する高マグネシア安山岩の地球化学的研究

新正裕尚（東京経済大学経営学部）

Geochemlcal study of the high magnesian andesites in western Toki city, Gifu prefecture

Hironao SHINJOE (Department of Business Administration, Tokyo Keizai University)

1. はじめに

西南日本弧には中新世に活動した多様な火成岩類が分布する。その中でとりわけ特徴的なものとして1300-1500万年前を中心として海溝に近い場所で起こった、集中的な火成活動が挙げられる。その主な構成要素は、（1）西南日本弧の伸長方向に平行に走る中央構造線付近からその北側にかけて分布する瀬戸内火山帯、（2）中央構造線より海溝寄りに分布し珪長質の貫入岩体からなる外帯酸性岩、（3）海溝に最も近い部分に分布する、ソレアイト質玄武岩/はんれい岩、あるいはアルカリはんれい岩～花こう岩・閃緑岩からなる火成岩体である。さらに上記3者の活動に若干先立つ火成活動がいくつかの場所で知られている。このような火成活動は、日本海の拡大による西南日本弧の時計まわり回転、さらにそれに関連しておこった若く、熱いフィリピン海プレート（四国海盆）の沈み込みといった、大きなテクトニックな出来事に関連して起こったものである。従って西南日本の地史を議論する上でも、この火成活動は大きな鍵の一つとなるものである。これら西南日本中新世火成活動の中で、従来より多くの興味を惹きつけて来たのは主に瀬戸内火山帯のメンバーとして出現する高マグネシア安山岩である。この岩石に興味が集中した理由としては、その低い鉄/マグネシウム比、高いNi、Cr量などから、マントルに由来する「初生的」安山岩であると考えられたことが大きい。この考えは1980年代前半にTatumi(1982)などによる高温・高圧実験により、瀬戸内火山帯の高マグネシア安山岩マグマがマントルかんらん岩と平衡に存在し得ることが確認されたことで概ね確立した。しかし高マグネシア安山岩マグマがどのようなメカニズムで発生したかについては、その後も様々な議論がなされた。そして1990年代終わり頃にもっとも支持されている成因論としては、西南日本弧に沈み込んだ若く、熱いフィリピン海プレート（四国海盆）の表面が部分融解し、それによって発生した珪長質メルトがマントルウェッジを構成するかんらん岩と反応し化学組成を変じた、と言うものである（Shimonda et al, 1998）。

このように成因論についての変遷にもかかわらず、高マグネシア安山岩質マグマがマントルに由来すると言うことから、その存在はその地域の地史の組み立てについて重要な拘束条件を与えることに変わりはない。

西南日本弧の高マグネシア安山岩は1300-1500万年前を中心を中心とする、瀬戸内火山帯のみならずそれに若干先行する火成岩の中にも知られるようになってきた。例えば岐阜県の中濃～東濃地

域に分布する瑞浪層群の最下部を占め、美濃加茂市周辺に分布する蜂屋累層の火成岩（およそ1800-2000万年前）の中からも高マグネシア安山岩が見いだされている（白木・野村、1989）。今回報告するものは、蜂屋累層の分布域よりもおよそ15km南東方に位置する土岐市西方の土岐川沿いに主に岩脈として産する高マグネシア安山岩についての分析結果である。この岩脈群については未だ放射年代測定が行われていないため、これまで述べてきた中新世の火成活動の一員として捉えて良いか否かは明らかではない。ただし、先に述べたように極めて近接して、中新世の高マグネシア安山岩が見いだされていることから、関連する活動である可能性が大きいと考えている。

先に述べたような高マグネシア安山岩の成因論に対して、その微量元素全岩組成やSr-Nd-Pb系の同位体組成などの地球化学的データが果たした役割は極めて大きい。そこで今回土岐市西方地域の高マグネシア安山岩について研究する上で、希土類元素を含む多くの微量元素について非破壊で感度よく測定できる中性子放射化分析を試みた。

2. 試料の概要と研究方法

分析試料は土岐市西方の土岐川沿いの露出から得られたものである。この地域は美濃帯のシェールや砂岩を主体としチャートをともなう堆積岩類に7200万年前の放射年代が報告されている土岐花こう岩が貫入している。高マグネシア安山岩はこの花こう岩、堆積岩の両者をほぼ東西性に貫く岩脈として多数存在する（図1）。また岩脈が多数集中して分布する場所の数百メートル下流に、角閃石閃緑岩の厚さ数メートルのシート状岩体があるが主成分元素組成の分析によると、他の岩脈とほぼ同様の化学組成を持つ事が判明した。

現地で9試料を採取し、薄片観察を行った。そして、新鮮な部分およそ数十グラムを微粉に粉砕し全岩化学組成分析用の試料とした。その全てについて、蛍光X線分析により主成分元素組成を測定した。また一部試料は蛍光X線分析により微量元素組成の分析も行った。薄片を鏡下で観察して、岩石組織のバリエーションと試料の新鮮さを勘案して3試料を選び中性子放射化分析に供することにした。およそ100mgの粉末試料を石英管に封入後、JRR4原子炉Tパイプで40分間照射した。そして大学開放研究室のγ線検出器を用いてγ線測定を行った。γ線の測定は照射後およそ1週間冷却した後4000秒、1カ月冷却した後約6時間と2回に分けて行った。分析は地質調査所のJB-1、JR-2を同時に照射しこれらを標準試料として相対法により行った。

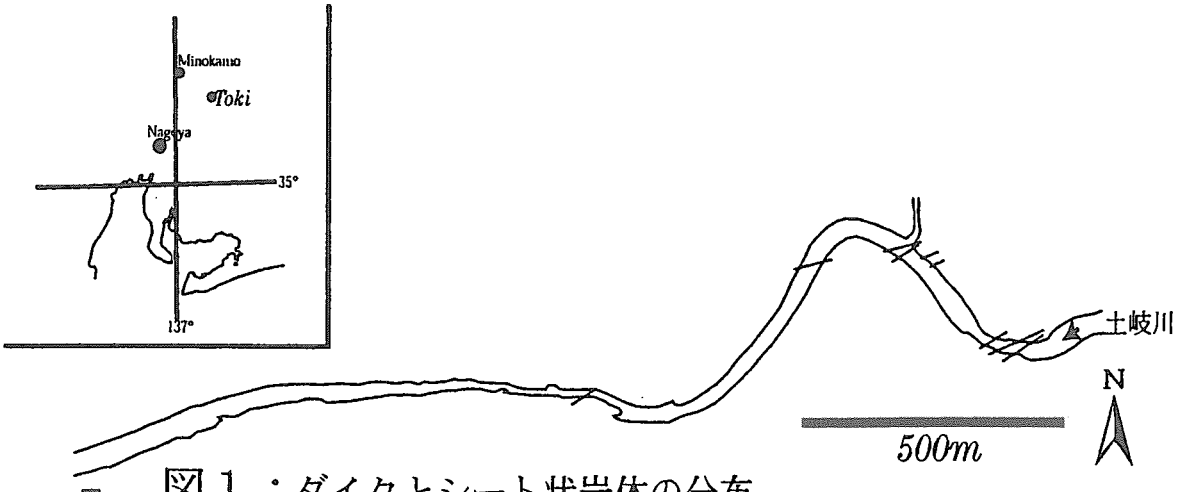

図1：ダイクとシート状岩体の分布

3. 結果

以下に蛍光X線分析による主成分元素組成の分析結果とともに、中性子放射化分析による微量元素組成の分析結果を掲げる。主成分元素組成についてはTotal=100%に再計算して表示した。

	Toki1	Toki4	Toki9
SiO2	55.57	56.10	54.69
TiO2	0.89	0.82	0.92
Al2O3	15.63	15.14	15.61
Fe2O3	8.03	8.30	8.11
MnO	0.18	0.20	0.18
MgO	8.24	8.59	8.62
CaO	8.56	7.29	8.89
Na2O	1.44	2.18	1.72
K2O	1.27	1.20	1.05
P2O5	0.21	0.19	0.21
total	100.00	100.00	100.00
FeO*/MgO	0.97	0.97	0.94
Cr	304	361	317
As	2.9	3.2	2.1
La	13.3	15.2	11.9
Ce	30.5	32.0	25.9
Sm	3.13	3.41	3.02
Eu	1.16	1.27	1.36
Tb	0.39	0.43	0.40
Yb	1.37	1.29	1.28
Lu	0.21	0.18	0.20
Th	4.3	5.0	3.4
Zn	86.7	95.9	105.4
Sc	25.7	26.5	28.3
Cs	4.3	3.8	2.5
Hf	2.5	2.7	2.3

主成分元素を見るとSiO2=55-56 wt%で安山岩組成でありFeO*/MgO<1であり高マグネシア安山岩である。またこの3試料は斑晶の粒度など岩石組織からはなるべくバリエーションの広いものを選択したが、それでも主成分元素組成の相互の違いは小さい。中性子放射化分析による微量元素測定結果から見られる特徴としては、高いCr量が挙げられる。これはマントルと共存し得る高マグネシア安山岩マグマに特徴的なものである。図2にコンドライトで規格化した希土類元素パターンを示す。やや軽希土に富み重希土に枯渇する希土類パターンは、従来瀬戸内火山帯の高マグネシア安山岩について報告されているもの（例えば石坂・巽、1985など）と極めて類似する。これらについても3つの試料相互にパターンはよく一致する。ここで特徴的なのは3試料に共通して、Euの正異常が見られることである。これは分析した3試料に斜長石斑晶の集積があったことを示唆するものと解釈される。

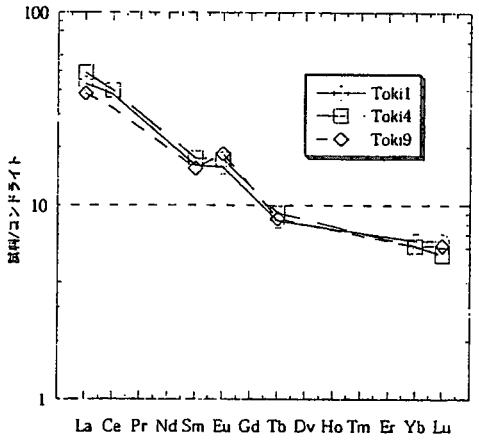

図2：高マグネシア安山岩試料の希土類パターン

4. さいごに

今回分析した試料については希土類元素組成なども含めて瀬戸内火山帯に産するものと類似した高マグネシア安山岩であることがわかった。今後放射年代測定を行い、これらの岩石群のテクトニックな位置づけを明解にする必要がある。

今回報告したもの以外に中期中新世のものと思われる玄武岩質岩脈などについても同様に中性子放射化分析で微量元素組成を求め良好な結果を得ている。今回これらの岩石の成因を検討する上で中性子放射化分析の有効性がはっきりしたので、測定対象をより広げて、中性子放射化分析による微量元素組成分析を継続して行くべく、研究課題を改めて共同研究を新規申請し採択されている。

5. 成果の公表

今回報告した分析結果を含めて、土岐市西方の高マグネシア安山岩岩脈群についてその岩石記載・地質記載を現在投稿準備中である（新正裕尚・尾崎淳・角井朝昭「岐阜県土岐川沿いの高Mg安山岩岩脈」）。

4-14 熱蛍光年代測定のための石英中のAl量の測定

Measurement of Al impurity content on quartzes for TL age determination

鴈澤 好博
Yoshihiro Ganzawa
北海道教育大学函館校
Hokkaido University of Education, Hakodate College

はじめに

石英は微弱なルミネセンス（熱蛍光）を発することが知られ，岩石に含まれる石英には地質年代とともに蓄積したルミネセンスが蓄積されている．石英花崗岩や火山岩などの地球大陸地殻中にごく普通に見出される鉱物であるだけに，このルミネセンスを利用した年代測定が試みられている．最近になって，石英の熱蛍光の波長解析から，従来から知られてきた青熱蛍光（450nm前後）に加え，赤熱蛍光（600nm前後）が存在することが明らかになってきた(Hashimoto,1987)．また，Hashimoto(1994)の研究から，青熱蛍光は石英の晶出温度が低かった深成岩マグマ起源のα石英に，青熱蛍光はマグマ温度が高い火山岩起源のβ石英に由来することが明らかにされている．

石英が熱蛍光を発する原因の一要素として不純物としてのAlの存在が指摘されている．Hashimoto（1994）によれば青色熱蛍光にはAl不純物が関与しているとされている．また，加熱に伴う赤熱蛍光センターの生成にもAl不純物が関わっていることが指摘された．これはがAl量が0から200ppmの範囲においての指摘である．

しかし，これまで様々な産出状況を示す天然石英がどの程度のAl含有量を持つものかほとんど検討された事がない．本論ではこのような視点に立ち，各種の岩石から分離された石英を用いて，Al含有量を定量しその赤および青熱蛍光の強度を検討することを目的とした．

実験方法

約20mgの石英試料をJRR-3MのPN-3において約10秒間の照射を行った．試料に応じて1分から5分の冷却後，γ線測定を200秒行った．カリミョウバンを用い，検量線を作成し，標準試料（JG1a）による測定精度のチェックを行った．実験は都合3回行い，約60試料の測定を行った．

実験結果

A. 石英中のAl濃度について

石英中のAl含有量を表-1にまとめた．全体では10^2ppmから10^5ppmオーダーまで，予想をはるかに上回る大きなばらつきを示した．最小含有量は試料番号；90102510で163ppm，最大含有量は試料番号OK-perで62376ppmであった．前者は日高山脈に分布する変成岩類，後者は奥尻島に分布す

JRR-3MPN-3・PN-3室，地球科学試料放射化分析

るパーライトから産する石英である．
これらの石英を岩石種に区分して Al 含有量を比較した（図－1）．Al 含有量は赤熱蛍光を示す火山灰(tephra)や火山岩(volcanic)で高い傾向があり，10^2ppm～10^5ppm の範囲にある．青熱蛍光を示す深成岩類(plutonic)はそれらより低く，最大でも 10^4ppm 程度である．堆積岩類起源(sedimentary)の石英は 10^3～10^4ppm の範囲にあり，変成岩類(metamorphic)は最も分布が広い 10ppm～10^5ppm の範囲にある．

この結果を岩石の生成条件から見れば，次のような解釈が可能である．つまり，高温マグマから晶出した火山灰や火山岩起源の石英は結晶晶出の際，不純物としての Al を排除する時間がないままで結晶化したのに対し，深成岩起源の石英は結晶晶出の過程で余分な Al を排除しながら結晶化したと推定される．一方，変成岩類の石英は源岩が多様性に富むため，幅広い Al 量を示すのであろう．

B．熱蛍光強度測定

前項で Al の測定を行った石英粒子について，熱蛍光測定装置により自然に赤熱蛍光と青熱蛍光の測定を行った．測定には光電子増倍管（赤測定には R－649，青測定には R－585，いずれも浜松フォトニクス社製）とフォトカウンター(C5410，同)を用い，加熱温度は 50℃から 400℃まで 1℃/秒の上昇率で試料を加熱した．また用いたフィルターはケンコー製の O－56（赤熱蛍光）

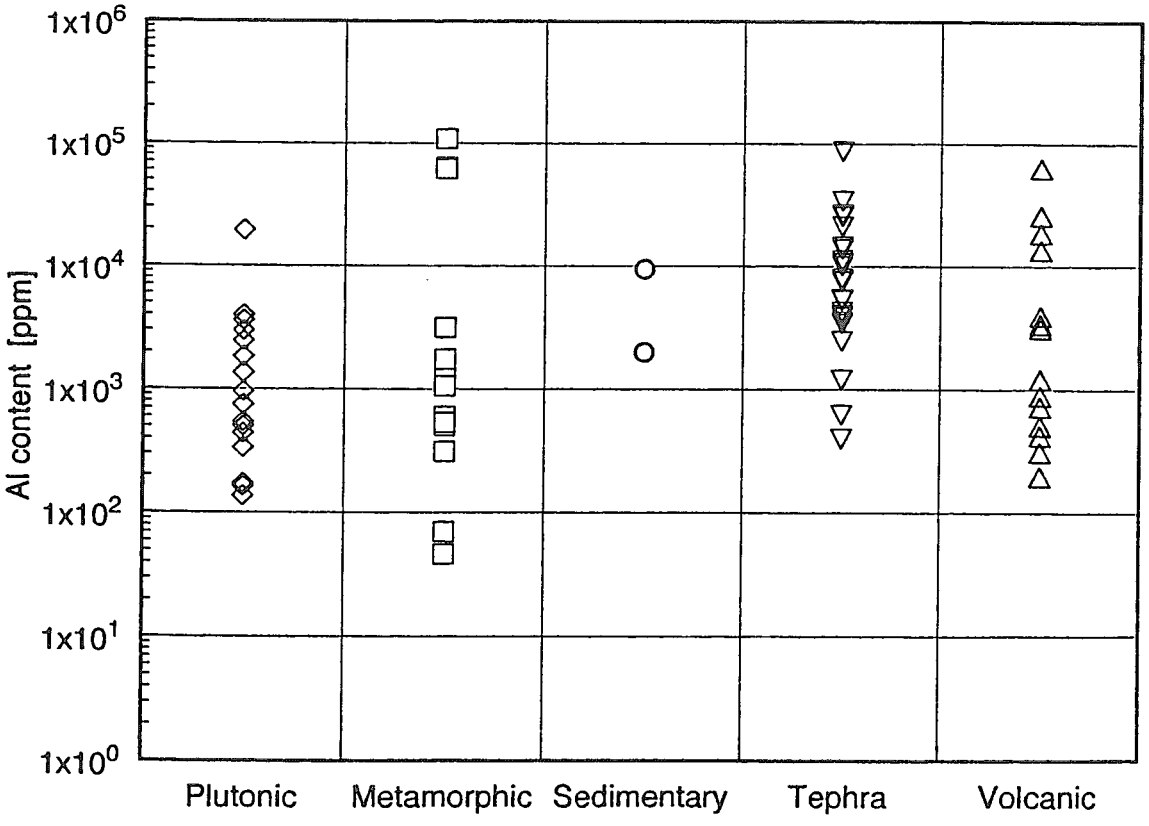

図－1　岩石種の分類による Al 含有量の比較

表－1　石英の源岩リスト，Al含有量および赤および青の熱蛍光強度

sample code	material	Al cont. [ppm]	TL intensity
BTL intensity			
AKE04	tonalite (650° C)	600	10999
OKE18	tonalite mylonitic	3578	2172958
90102510	tonalite	163	2742890
Hanawa	granodiorite	172	6167
Australia	granite	539	14779
Cab2	charnockite (800° C)	334	10809
AKE08	mylonitic gneiss (600° C)	600	56150
OKE01	mylonitic granulite (650° C)	61451	3662492
SKV	granulite (810° C)	3122	27112
SKV19	granulite (810° C)	500	5156
SKV25	granulite (810° C)	310	8507
Cab5	schist (350-400° C)	1056	2409
Cab6	hydrothermal vein (200-250° C)	9382	4694
Shz-lim	limestone	1980	7464
RTL intensity			
Z-M	pyroclastic flow	395	466233
Kt-1	pyroclastic flow	7504	182300
Dr-T	pyroclastic flow	7449	304100
Nf-T	pyroclastic flow	5360	273994
Esan lava	lava flow	725	123468
Ok-per	perlite	62376	19019
FR	pyloclastic flow	18337	562499
Tate-ptf	pumice tuff	25695	570957
YZ-5	quartz diorite - 'hypabyssal'	420	137532
Es2-da	dacite	1200	259694
Kts-gd	granodiorite - 'hypabyssal'	197	119828
NS-and	dacitic andesite	3363	150877
moonstone	moonstone rhyolite	3913	23956
HA-wtf	welded tuff	508	348553
SA-wtf	welded tuff	310	155718

material の温度は岩石の推定形成温度

BTL integrated range: 250-300 ° C
RTL integrated range: 325-375 ° C

とB－390（青熱蛍光）である．これら測定系全体はパソコンで制御されている．測定試料は400℃，5分間加熱することによって，地質時代に蓄積された天然ルミネセンスを予め消去した．その後，γ線500Gyを照射し2週間以上冷暗所で放置した．熱蛍光測定は堆積岩，変成岩および深成岩石英については青，火山灰および火山岩いついては

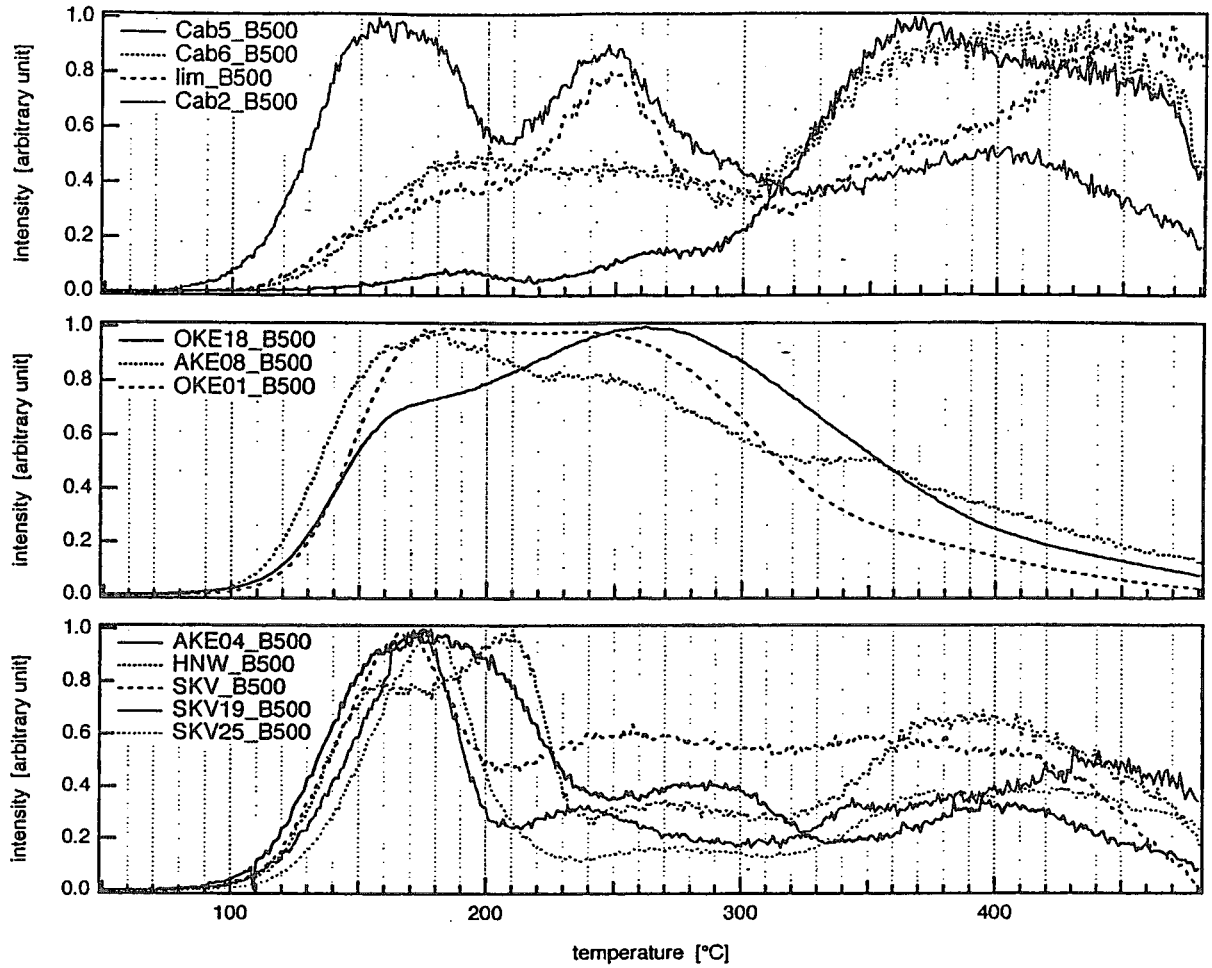

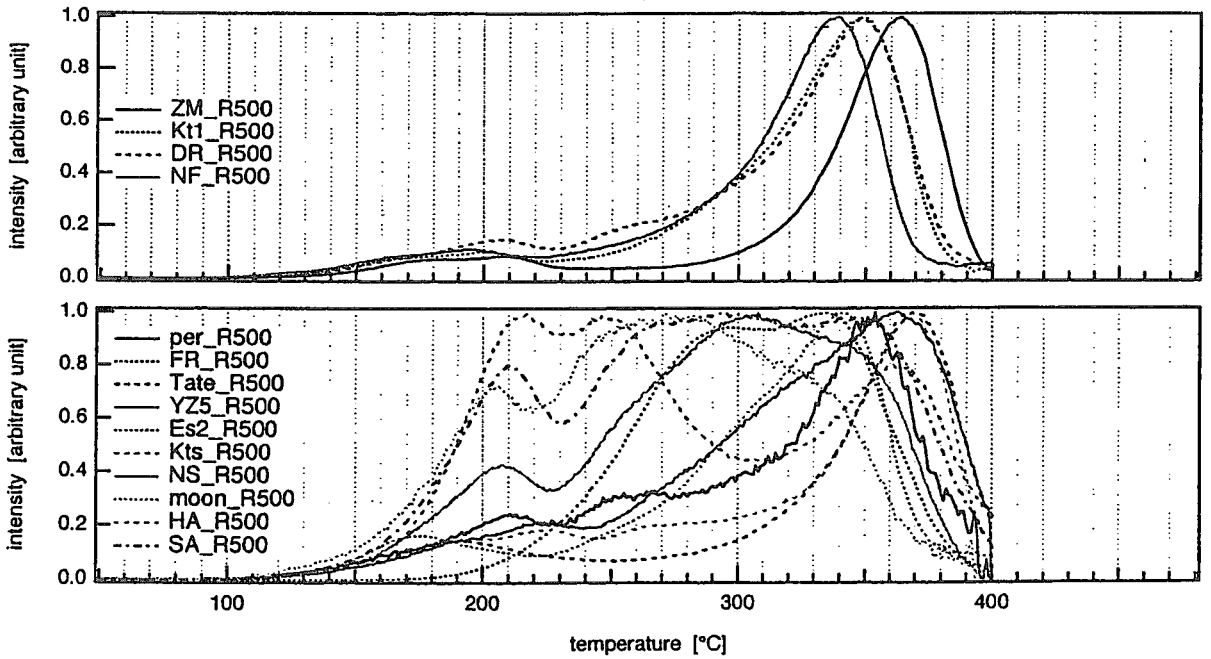

図－2　石英の青熱蛍光と赤熱蛍光の温度に対する発光パターン

上３図：堆積岩，変成岩，深成岩類の青熱蛍光パンターン，下２図：火山灰および火山岩の赤熱蛍光パターン

BTL side Total Data(500Gy:Anneal cond.400℃ 5min)

sample code	Al cont.[ppm]	peak intensity	peak temp.	material	location
90102510	163	55864	262	tonalite	Hidaka metamorphic belt,Hokkaido
SKV-25	310	1078	177	granulite	Skarvsnes,Antarctica
Hanawa	343	379	210	granodiorite	Hanawa,Fukushima pref.
SKV-19	500	468	174	granulite	Skarvsnes,Antarctica
Australia	539	1234	350	granite	Australia
AKE04	600	558	175	tonalite	Hidaka metamorphic belt,Hokkaido
Cab2	669	345	157	charnockite	Kazachiyi par,Ukraine
Cab5	1056	310	370	schist	Nishi-sonogi,Nagasaki pref.
AKE08	1201	1552	175	mylonitic gneiss	Hidaka metamorphic belt,Hokkaido
SKV	3122	915	170	granulite	Skarvsnes,Antarctica
Shz-lim	3959	283	453	limestone	Shiyazaki cape,Aomori pref.
OKE18	7155	44317	262	tonalite mylonitic	Hidaka metamorphic belt,Hokkaido
Cab6	9382	229	435	hydrothermal vein	Hishikari-mine,Kagoshima pref.
OKE01	122903	84586	187	mylonitic granulite	Hidaka metamorphic belt,Hokkaido
OK-gd	2638				

RTL side Total Data(500Gy:Anneal cond.400℃ 5min)

sample code	Al cont.[ppm]	peak intensity	peak temp.	material	location
FR	36674	6927	335	pyloclastic flow	Furano,Hokkaido
Kts-gd	394	2803	217	granodiorite-'hypabyssal'	Otsuki,Kochi pref.
Esan lava	725	3275	305	lava flow	Esan, Hokkaido
Moonstone	3913	1010	270	moonstone rhyolite	Usunaka,Toyama pref.
Kt-1	790	4602	348	Kuttara flow 1	Noboribetu
HA-wtf	1017	9925	367	welded tuff	Hamada,Shimane pref.
Es2-da	2400	7213	340	dacite	Toi,Hokkaido
Dr-t	14897	7756	347	Toya	Date along root230
YZ-5	840	2992	363	quartz diorite-'hypabyss	Yuzawa Niigata pref.
Tate - pt†	51390	16278	369	pumice tuff	Otobe Sunasaka,hokkaido
Nf-t	5360	8498	339	Toya	Nifushinai
SA-wtf	619	3392	292	welded tuff	the Maritime,Russia
OK-per	124752	490	354	perlite	Okushiri I.,Hokkaido
NS-and	6727	3916	266	dacitic andesite	Ninohe,Aomori pref.
ZM	7504	12880	364	Z-M	Esan along root

OK-gd

Cab 1

Cab 4

C2103

C2305

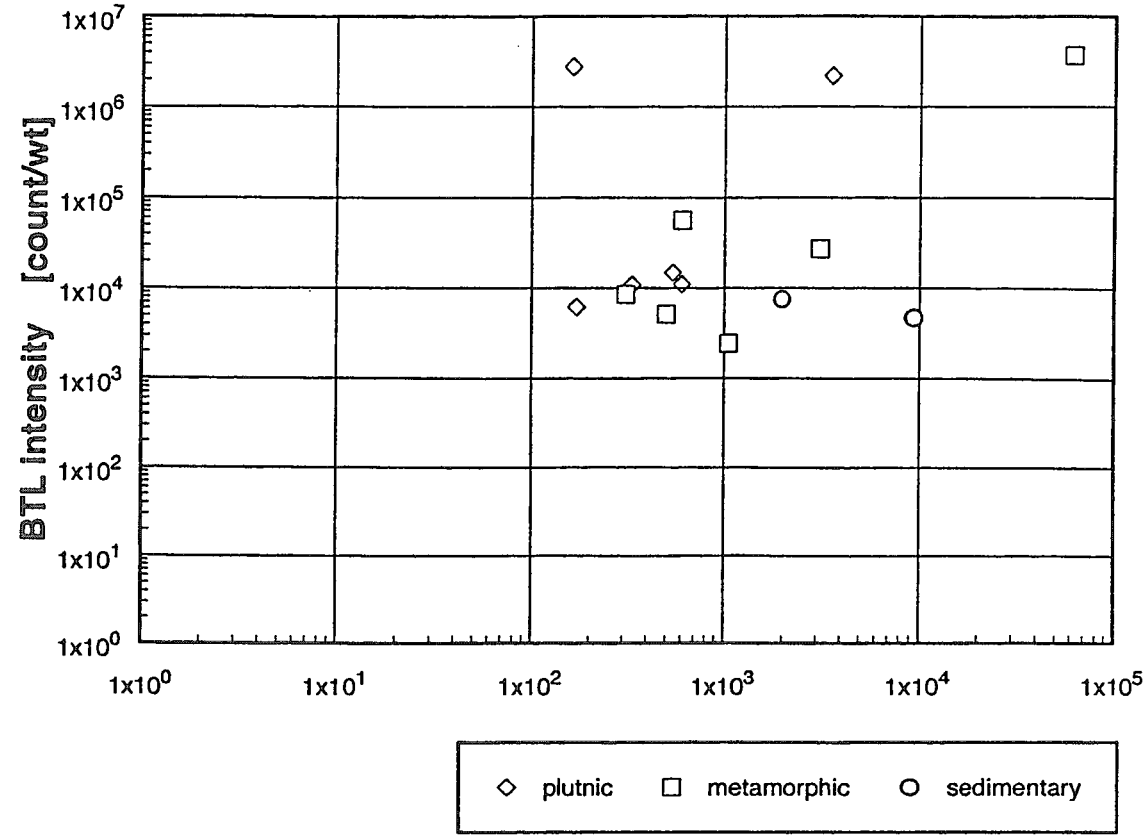

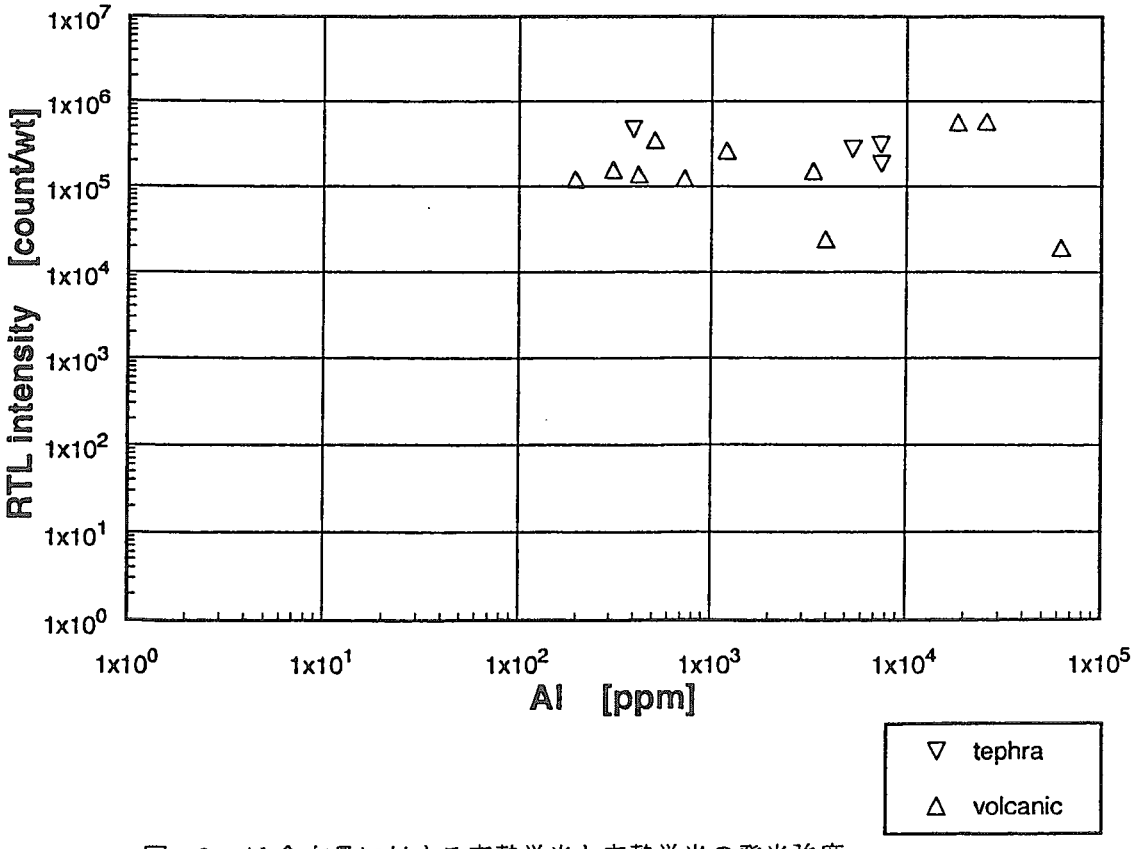

図－3　Al 含有量に対する青熱蛍光と赤熱蛍光の発光強度

赤の測定を行った.

測定結果の代表例を図－2 に示した. 図の上 3 図（堆積岩, 変成岩起源および深成岩）が青石英の青熱蛍光パターンである. また, 下 2 図（火山灰および火山岩）は赤石英の赤熱蛍光パターンである. カウント数の総計は赤熱蛍光カウント(RTL)の場合ピークにあたる 325℃～375℃の範囲で, 青熱蛍光カウント(BTL)の場合 250℃～300℃の範囲で積算した. 最終実験で測定されたカウント数を表－1 に示した. その値は RTL で 10^2 から 10^4 オーダーである. また, 深成岩類では 10^2 から 10^4 オーダーであるが, 10^3 オーダーを示すものが多い.

C. Al 含有量と熱蛍光強度

上記の Al 含有量と熱蛍光との測定の基づいて, 両者の相関について検討を加えた. 図－3 に今回の測定結果を示した. BTL で見た場合, Al 量 10^2ppm から 10^4ppm まで変化するが, BTL 強度が Al 量に相関がある傾向は見出されない. 一方, 赤熱蛍光では Al 量は 10^2ppm から 10^5ppm までの間にあるが, RTL 強度は BTL 強度と同様 Al 量に対しての相関は見られない.

Hashimoto(1994)は天然においては比較的小さな Al 量（200ppm 以下）を持つ大きな単結晶を利用して, 結晶内の Al 量変化に対応して, BTL 強度は減衰し, これを 1000℃100 時間でアニールした場合, RTL 強度は増加することを示した. 今回実験に用いた試料はこれよりはるかに大きい Al 量を示す石英粒子である. したがって, 1000ppm 以上の高い Al 量の変化が熱蛍光にどのような影響を与えるかさらに追求が必要と思われる. また, 今回の実験は晶出条件が異なる石英を用いているので, 単純な Al 量と熱蛍光強度との比較に限界があると言える.

参考文献

T. Hashimoto, S.Sakaue, H. Aoki and M.Ichino (1994) Dependence of TL-property changes of natural quartzes on aluminum contents accompanied by thermal annealing treatment. Rad. Meas., 23, 293-299

T. Hashimoto, A.Koyanagi, k.yokosaka, Y. Hyashi and T. Sotobayashi (1986) Thermoluminescence color images from quartzes of beach sands. Geochem.J.20, 111-118

成果の公表

窪北 耕治, 鴈澤 好博, TL 特性から見たレス起源石英の特徴, 第 14 回 ESR 応用計測研究会（1999 年 11 月）

窪北 耕治, 鴈澤 好博, 伊藤記子, 火山灰石英の TL 特性－洞爺火山灰を例として－第 14 回 ESR 応用計測研究会（1998 年 11 月）

鴈澤 好博, Naomi Porat, Luminescence dating of loess deposits from Kamikita Plane, Northern Japan, 第 14 回 ESR 応用計測研究会（1998 年 11 月）

4-15
胎児期および成長期における亜鉛欠乏がその後の発育に与える影響
Effects of Zn deficiency during the pregnant and lactating period on growth of mice

矢永誠人、大森 巍、野口基子、岩間基訓、吉田 努、大山拓也、犬飼桂子、釜谷恵実
(静岡大学理学部)
Makoto YANAGA, Takashi OMORI, Motoko NOGUCHI, Motonori IWAMA,
Tsutomu YOSHIDA, Takuya OHYAMA, Keiko INUKAI and Megumi KAMAYA
(Faculty of Science, Shizuoka University)

1．はじめに

近年、我々は、生体微量元素の一つである亜鉛に注目し、その欠乏が他の微量元素の挙動に与える影響、すなわち、微量元素間の相互作用について検討している。その手段として、亜鉛欠乏餌および対照餌(亜鉛添加餌)で飼育したマウスの各臓器・組織について、機器中性子放射化分析法による種々の微量元素の定量・比較検討を行っている。

亜鉛欠乏症としては、成長障害、性腺機能低下、味覚・嗅覚障害、皮膚障害、脱毛、免疫不全、胎児への催奇性などが知られている。亜鉛欠乏状態に陥る原因として、遺伝的要因と食生活が考えられるが、本研究では、食餌中の亜鉛不足に伴う亜鉛欠乏を対象としている。

食餌中の亜鉛欠乏の影響および亜鉛投与による欠乏状態からの回復の様子は、亜鉛欠乏餌を摂取した期間やマウスの週齢(成長期にある場合と成獣の場合)によっても異なることが考えられるため、様々な飼育条件下のマウスを分析対象としている。本報告では、生後３日目から６週間にわたって、すなわち、授乳期から離乳後の成長期にかけて、亜鉛を欠乏させたマウスについての結果を中心に述べることとする。

2．実験

2－1　供試動物および分析試料

妊娠 13 ～ 14 日目のＩＣＲ系マウス(14 週齢) 16 頭を(株)日本クレアより購入した。これらマウスを、動物飼育施設内において、同社より購入した実験動物用一般飼料(CE-2)を用いて飼育した。各マウスより、12 ～ 20 頭の仔マウスが出生した。出生３日後に、これら仔マウスの頭数を各母マウスにつき 10 頭に調整するとともに、亜鉛欠乏群 12 家族および対照群４家族の２群に分け、亜鉛欠乏群には亜鉛欠乏餌およびミリポア水を、また、対照群には対照餌(亜鉛欠乏餌に塩基性炭酸亜鉛を添加した飼料)およびミリポア水を与えた。各飼料は、(株)日本クレアに調製を依頼したものを使用した。３週間後、各仔マウス(オス)を母マウスから離し、同条件にてさらに３週間の飼育を行った。したがって、各仔マウスは、生後３日目から３週間は、亜鉛欠乏餌あるいは対照餌を摂取した母マウスの母乳によって育ち、その後は仔マウス自身が各飼料を摂取したことになる。この延べ６週間の亜鉛欠乏餌あるいは対照餌による飼育の後、エーテル麻酔下において、各仔マウスより主な臓器および組織を摘出した。なお、妊娠中(購入時)から臓器の摘出までの期間、各ケージの中にステンレス製ネットを二重に敷き、いずれの場合も飼料および水以外の敷き藁あるいは排泄物等を摂取できない条件とした。

摘出した各臓器・組織を直ちに秤量し、凍結乾燥後、再度、乾燥状態において精秤した。本研究では、摘出した臓器・組織のうち、肝臓、腎臓、すい臓、精巣および骨について分析を行った。

研究施設・装置
JRR-3 気送照射設備(PN-1, PN-3)

研究分野
生体試料の放射化分析

2－2　照射および測定

凍結乾燥した試料のうち、各マウスのすい臓および精巣については全量を、また、肝臓、腎臓および骨についてはその一部を分析試料とした。各試料(20～100 mg)をポリエチレンで二重封入し、照射試料とした。標準試料には、NIST SRM 1577b Bovine Liver および $CaCO_3$ の一定量を、また、原子吸光分析用 Mg 標準溶液および同 Co 標準溶液の一定量をろ紙上に滴下し乾燥させたもののそれぞれを、ポリエチレンで二重封入したものを用いた。

熱中性子照射は、JRR-3M において、目的元素に応じて2種類の照射を行った。短寿命核種により定量する元素については、放射化分析用照射設備(PN-3)にて 10 秒間の照射を行った。まず、Mg、Cl、Ca の定量を目的として、照射2～8分後に高純度 Ge 半導体検出器にて 100～150 秒間のγ線スペクトロメトリーを行い、次に、Na、K および Mn の定量のため、1回目の測定から 40～90 分後に、再度、200～250 秒間の測定を行った。

また、長寿命核種により定量する元素(Fe、Co、Zn、Se および Rb)の放射化のために、気送照射設備(PN-1)にて 20 分間の照射を行い、8～60 日後に1～24 時間のγ線測定を行った。

なお、一部の試料についての分析は、立教大学原子力研究所 TRIGA-MarkII 原子炉を利用して行った。

3．結果および考察

Table 1に、オスについての離乳時および臓器の摘出時における個体数および平均体重をまとめた。授乳期から亜鉛を欠乏させたマウスでは、著しい成長障害や脱毛症状が認められたほか、離乳後からは多数の死亡例が見られた。

各臓器・組織について、前述した 11 元素についての分析結果を Table 2～6にまとめた。なお、Ca については、骨においてのみ定量することができた。

Fig. 1に、本研究において分析対象とした各臓器・組織への Zn の濃度分布を表した。これに見られるように、亜鉛欠乏マウスのすい臓(PC)および骨(BN)において、その濃度が著しく低下していた。この傾向は、成獣マウス(オス、8週齢)に対して行った3週間の亜鉛欠乏実験でも認められた傾向ではあった[1,2]。しかしながら、対照マウスに対する亜鉛欠乏マウスの骨中亜鉛濃度の低下の割合は、成獣の場合と大きく異なっていた。8週齢のＩＣＲマウス(オス)を1、3、6、13 週間亜鉛欠乏餌で飼育した場合の骨中亜鉛濃度の対照マウスのそれに対する低下率は、それぞれ、17、20、24、37 %であったのに対し、本研究での授乳期から6週間にわたって亜鉛を欠乏させたマウスでは 78 %であった。成獣についての骨中亜鉛濃度の低下は、食餌中の亜鉛の欠乏により体内の各臓器中の亜鉛含有量が低下し、それを補うために骨から亜鉛が供給されているものと考えることができる。しかし、授乳期から亜鉛を欠乏させたマウスでは、もともと骨中には骨以外の臓器および組織へ供給できる充分な亜鉛の備蓄がなく、さらに母乳中および食餌中の亜鉛が欠乏したため、対照マウスの骨中濃度との間に著しい差が生じたものと思われる。また、多数の死亡例があったことから、この 20.8 ± 2.6 μg/g という骨中亜鉛濃度は、マウスがその生命を維持することができる限界の濃度なのではないかと考えている。現在、授乳期のみの亜鉛欠乏、離乳直後からの亜鉛欠乏など、いくつかの飼育条件

Table 1. Number of survival and mean weight of male mice

	Zinc-def. mouse		Control mouse	
	Number	Mean weight, g	Number	Mean weight, g
At weaning*	44		22	
At sacrificing**	20	7.9 ± 1.9	22	30.1 ± 6.4

* 3 weeks after birth.
** 6 weeks after birth.

Table 2. Elemental concentrations in livers of Zn-def. mice and control mice (means ± SD in μg/g wet weight*)

Element	Zinc-def. mouse	Control mouse
Na*	0.879 ± 0.116 (19)**	0.756 ± 0.060 (10)
Mg*	0.241 ± 0.053 (19)	0.240 ± 0.051 (10)
Cl*	1.26 ± 0.13 (19)	1.03 ± 0.06 (10)
K*	4.03 ± 0.34 (19)	3.39 ± 0.23 (10)
Ca	–	–
Mn	2.00 ± 0.55 (19)	0.57 ± 0.30 (10)
Fe	690 ± 173 (19)	260 ± 60 (10)
Co	0.316 ± 0.092 (19)	0.085 ± 0.009 (10)
Zn	26.9 ± 8.1 (19)	29.4 ± 3.1 (10)
Se	0.958 ± 0.163 (19)	1.07 ± 0.12 (9)
Rb	7.38 ± 0.69 (19)	6.77 ± 0.38 (10)

* Concentrations of Na, Mg, Cl and K are expressed in mg/g.
** Values in parentheses indicate the numbers of determination.

Table 3. Elemental concentrations in kidneys of Zn-def. mice and control mice (means ± SD in μg/g wet weight*)

Element	Zinc-def. mouse	Control mouse
Na*	1.81 ± 0.16 (11)**	1.39 ± 0.16 (10)
Mg*	0.269 ± 0.081 (8)	0.214 ± 0.047 (9)
Cl*	2.80 ± 0.33 (11)	1.67 ± 0.06 (10)
K*	3.31 ± 0.34 (11)	3.00 ± 0.34 (10)
Ca	–	–
Mn	1.49 ± 0.22 (11)	1.37 ± 0.30 (10)
Fe	91.9 ± 33.2 (11)	78.8 ± 10.2 (10)
Co	0.304 ± 0.035 (11)	0.065 ± 0.007 (10)
Zn	18.5 ± 1.0 (11)	21.2 ± 1.1 (10)
Se	1.23 ± 0.14 (11)	0.93 ± 0.07 (10)
Rb	5.62 ± 1.09 (11)	4.54 ± 0.42 (10)

* Concentrations of Na, Mg, Cl and K are expressed in mg/g.
** Values in parentheses indicate the numbers of determination.

Table 4. Elemental concentrations in pancreases of Zn-def. mice and control mice (means ± SD in μg/g wet weight*)

Element	Zinc-def. mouse	Control mouse
Na*	1.01 ± 0.22 (11)**	0.85 ± 0.06 (9)
Mg*	0.435 ± 0.115 (8)	0.336 ± 0.058 (9)
Cl*	2.09 ± 0.33 (11)	1.71 ± 0.17 (9)
K*	4.84 ± 0.44 (11)	4.93 ± 0.80 (9)
Ca	–	–
Mn	1.99 ± 0.23 (11)	1.42 ± 0.27 (9)
Fe	42.7 ± 9.3 (8)	24.9 ± 8.1 (9)
Co	0.159 ± 0.026 (11)	0.037 ± 0.010 (9)
Zn	20.8 ± 3.0 (11)	38.5 ± 9.3 (9)
Se	0.440 ± 0.142 (10)	0.432 ± 0.107 (8)
Rb	7.07 ± 0.74 (11)	6.27 ± 1.43 (9)

* Concentrations of Na, Mg, Cl and K are expressed in mg/g.
** Values in parentheses indicate the numbers of determination.

Table 5. Elemental concentrations in bones of Zn-def. mice and control mice (means ± SD in μg/g wet weight*)

Element	Zinc-def. mouse	Control mouse
Na*	2.98 ± 0.21 (11)**	3.29 ± 0.20 (10)
Mg*	1.08 ± 0.19 (11)	1.40 ± 0.22 (10)
Cl*	1.86 ± 0.24 (11)	1.25 ± 0.15 (10)
K*	3.23 ± 0.39 (11)	2.28 ± 0.29 (10)
Ca*	73.3 ± 7.9 (11)	96.5 ± 7.6 (10)
Mn	0.717 ± 0.134 (11)	0.456 ± 0.118 (10)
Fe	54.0 ± 15.7 (11)	42.2 ± 8.2 (10)
Co	0.137 ± 0.051 (11)	0.044 ± 0.009 (10)
Zn	20.8 ± 2.6 (11)	94.6 ± 11.5 (10)
Se	0.275 ± 0.079 (9)	0.242 ± 0.055 (8)
Rb	3.80 ± 0.53 (11)	2.53 ± 0.42 (9)

* Concentrations of Na, Mg, Cl, K and Ca are expressed in mg/g.
** Values in parentheses indicate the numbers of determination.

Table 6. Elemental concentrations in testes of Zn-def. mice and control mice(means ± SD in μg/g wet weight*)

Element	Zinc-def. mouse	Control mouse
Na*	1.30 ± 0.47 (11)**	1.10 ± 0.07 (10)
Mg*	–	0.158 ± 0.055 (8)
Cl*	2.79 ± 0.52 (11)	2.45 ± 0.11 (10)
K*	5.52 ± 1.39 (10)	4.17 ± 0.26 (10)
Ca	–	–
Mn	0.886 ± 0.149 (10)	0.396 ± 0.073 (10)
Fe	46.0 ± 11.8 (7)	19.7 ± 2.3 (9)
Co	0.108 ± 0.022 (10)	0.021 ± 0.004 (10)
Zn	25.4 ± 2.1 (10)	23.7 ± 1.1 (10)
Se	0.605 ± 0.195 (9)	0.716 ± 0.056 (10)
Rb	7.84 ± 1.17 (10)	5.28 ± 0.49 (10)

* Concentrations of Na, Mg, Cl and K are expressed in mg/g.
** Values in parentheses indicate the numbers of determination.

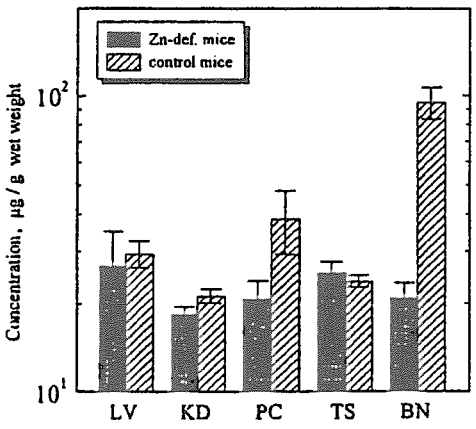

Fig. 1. Concentration of Zn in several organs of Zn-def. mice and control mice; LV – liver, KD – kidney, PC – pancreas, TS – testis, BN – bone

のマウスについての分析に着手しているが、死亡例が見られるほどの条件下で飼育したマウスの骨中の亜鉛濃度については、この値と一致する定量値が得られつつある。

Table 2～6に見られるように、分析した全ての臓器および組織で、亜鉛欠乏マウスでは、コバルト濃度が上昇していた。この亜鉛欠乏マウスの全臓器でコバルト濃度が上昇する傾向は以前に行った成獣マウスの場合でも認められていた[1,2]。しかしながら、成獣での亜鉛欠乏実験では見ることのできなかった傾向を、授乳期から6週間亜鉛欠乏餌を与えたマウス肝臓において認めることができた。Fig. 2に、本研究で定量した亜鉛欠乏マウスおよび対照マウスの肝臓中の亜鉛濃度とコバルト濃度との関係をプロットした。これに見られるように、亜鉛欠乏マウスの肝臓中の亜鉛濃度とコバルト濃度は、ともに広範囲に分布し、さらに両者の間には正の相関が認められるようである。図中の"A"は、ある1頭の母マウスから生まれた仔マウスについての定量値であり、この相関には母マウスに対する依存性はなく、また、体重あるいは肝臓重量とも無関係のようであった。このことは、亜鉛が積極的に肝臓に取り込まれると、コバルトも同時に肝臓に取り込まれることを示しているものと思われる。肝臓のみではなく、全ての臓器および組織でコバルト濃度が高まる傾向については、亜鉛タンパク質中の亜鉛とコバルトが置換可能で、活性を保つことを考えれば、一つの可能性として、亜鉛欠乏時においては、生体中で亜鉛とコバルトが置換することが考えられる。しかしながら、体内の亜鉛濃度とコバルトの濃度の差は大きく、単純な金属置換ということで説明することは難しい。また、肝臓で見られたような、亜鉛濃度とコバルト濃度の正の相関を考慮すると、亜鉛の移動に伴ってコバルトが移動することも考えられるが、骨やすい臓においては亜鉛濃度が著しく低下しているにもかかわらずコバルト濃度は増加しており、これは相反することである。この問題については、今後検討していく予定である。

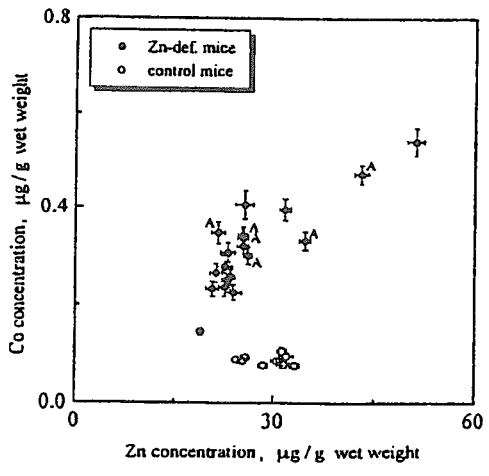

Fig. 2. Relationship between Zn concentration and Co concentration in livers of Zn-def. mice and control mice

亜鉛欠乏マウスの腎臓以外の臓器・組織では、マンガンのおよび鉄の濃度も有意に上昇していた(Table 2～6)。これまでに行ってきた実験結果より、骨中およびすい臓中の亜鉛濃度の低下、また、全臓器・組織におけるコバルト濃度の上昇という現象が、亜鉛欠乏餌を与えると速やかに起こるのに対し、マンガンおよび鉄の濃度の上昇は過酷な亜鉛欠乏状態において検知されている。したがって、これら元素の濃度上昇は、亜鉛欠乏にともなう代謝異常なのであろうが、コバルトとは異なり亜鉛欠乏による2次的な現象なのではないかと考えている。

4．まとめ

多元素同時定量法である原子炉熱中性子照射による放射化分析法を利用して、成長期あるいは成獣になってから、亜鉛欠乏餌を一定期間与えて飼育したマウスの主な臓器および組織中の亜鉛および他の微量元素の定量を行った。その結果、生命維持に関わる骨中の亜鉛濃度、亜鉛欠乏マウスにおけるコバルト濃度の上昇、肝臓中亜鉛濃度とコバルト濃度との正の相関、マンガンおよび鉄濃度の上昇といった興味あるデータを得ることができた。

今後は、亜鉛および亜鉛欠乏時にその濃度が変化した微量金属がどのような化学状態で存在しているかに注目して本研究を進めていく予定である。その第一段階として、まず、各臓器、

特に肝臓について、組織細胞内の金属元素の濃度分布および濃度変化をこの多元素同時定量法である中性子放射化分析法を利用して調べることとする。

参考文献

1 M. Yanaga, M. Iwama, K. Takiguchi, M. Noguchi and T. Omori, *J. Radioanal. Nucl. Chem.*, 231, 187 (1998).
2 M. Yanaga, M. Iwama, K. Shinotsuka, K. Takiguchi, M. Noguchi and T. Omori, *J. Radioanal. Nucl. Chem.*, 243, 661 (2000).

成果の公表

学会発表

1 岩間基訓、若狭 仁、大山拓也、吉田 努、矢永誠人、野口基子、大森 巍、「機器中性子放射化分析法による亜鉛欠乏マウス体内における微量元素の定量」、第42回放射化学討論会（1998年9月）.
2 吉田 努、若狭 仁、大山拓也、岩間基訓、矢永誠人、野口基子、大森 巍、「成長期に亜鉛を欠乏させたマウスにおける各臓器中の微量元素の定量」、理研シンポジウム "生体微量元素 '99"（1999年3月）.
3 吉田 努、釜谷恵実、若狭 仁、大山拓也、岩間基訓、矢永誠人、野口基子、大森 巍、「成長期における亜鉛の欠乏が他の微量元素の挙動に与える影響（2）」、第43回放射化学討論会（1999年10月）.
4 吉田 努、釜谷恵実、若狭 仁、大山拓也、岩間基訓、矢永誠人、野口基子、大森 巍、「成長期に亜鉛を欠乏させたマウスにおける各臓器中の微量元素の定量（2）」、理研シンポジウム "生体微量元素 '99.12"（1999年12月）.

Publications

1 M. Yanaga, H. Wakasa, T. Yoshida, M. Iwama, K. Shinotsuka, M. Noguchi and T. Omori, "Effects of zinc deficiency during the growing period on behavior of trace elements in mouse", *J. Radioanal. Nucl. Chem.*, 245, 255 (2000).

4-16 金属材料中の極微量元素の分析法の開発（Ⅱ）

Development of neutron activation analysis for ultra-trace elements in high purity materials (Ⅱ)

岡田往子、鈴木章悟、平井昭司 ： Yukiko Okada, Shogo Suzuki, Shoji Hirai

武蔵工業大学 エネルギー基礎工学科 :Department of Energy Science and Engineering Musashi Institute of Technology

1 緒言

鉄鋼の材質には不純物元素の含有量が大きな影響を与えることから,不純物元素の低減する高純度化が進められている.鉄鋼の物性研究や新機能性材料開発においては,超高純度鉄を得るための精錬技術が必要になるとともに,高純度鉄中の微量な不純物元素を定量できる分析技術が要求される.鉄鋼中に含まれるMoは鉄の精製過程で除去することが難しいため,含有量が高純度鉄の純度の指標にもなる.微量Moの定量法としては,誘導結合プラズマ発行分析法（ICP-AES）,ICP質量分析法（ICP-MS）及び機器中性子放射化分析法（INAA）等があるが,高純度鉄中のMoの定量下限値は数百 ppb 程度である.本研究では定量下限値を更に低減させるために,中性子照射した後の試料に化学操作を加える放射化学中性子放射化分析法（RNAA）を検討した.試料は,新日本製鉄製標準高純度鉄（SIN 試料）及び高純度鉄標準物質であるJSS003-4,JSS001-3及びJSS001-4を用いて検討を行った.

2 実験

2・1 熱中性子照射

熱中性子照射は、日本原子力研究所東海研究所の改造3号炉（JRR-3M）の水力ラビット1号（HR-1,熱中性子束密度：$1.0\times10^{14}n\cdot cm^{-2}\cdot sec^{-1}$）を利用した.ＳＩＮ試料又はＪＳＳ試料約0.1gを合成石英管に封入して,比較標準試料と同時に6時間照射した.比較標準試料は,1000ppmのMoの原子吸光用標準溶液を用いた. JRR-3M 照射では 5μl を合成石英管に分取後蒸発乾固して作製した.

2・2 化学分離操作

Mo 定量のための化学分離操作は水酸化鉄分離法,陽イオン交換クロマトグラフィー及びリンモリブデン酸アンモニウム沈殿法を行った.Fig.1に操作手順を示す.

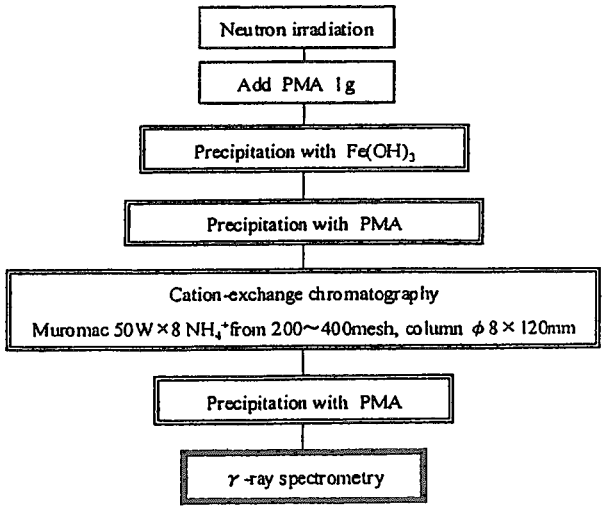

Fig.1 Scheme of radiochemical neutron activation analysis for Mo in high purity iron

Facilities and Instruments	Research field
JRR-3M(HR-1,2)	Neutron activation analysis

中性子照射後、高純度鉄試料は表面の不純物を除去するために希 HCl でエッチングを行った.その後、反応を促進のために $NiCl_2$ の HCl 溶液（Ni：10%）を HCl 10ml に対して 1ml 添加した 6MHCl 10ml で温水加熱して溶解した.その際、価数調整のため 30% H_2O_2 1ml を添加及び保持担体としてリンモリブデン酸アンモニウム〔$(NH_4)_3PO_4 \cdot 12MoO_3 \cdot 3H_2O$：PMA〕1g を添加した.次に水酸化鉄沈殿を生成するために,7.5MNH_4OH 15ml を添加しかくはんした.沈殿を熟成させるため,1 時間温水加熱を行い,自然冷却した.次に遠心分離を行い,上澄みを回収した.残った沈殿は再度 3MHCl 10ml にて温水加熱により溶解した.7.5MNH_4OH 10ml を添加しかくはんし,沈殿熟成の後,遠心分離を行い上澄みを回収した.その上澄みに含まれるわずかな水酸化鉄沈殿を吸引ろ過でフィルターに捕集し,ろ液を回収した.そのろ液に PMA 0.5g を添加し、その後かくはんしながら 6MHNO_3 10ml を添加し,PMA の沈殿を生成させた.1 時間ほど沈殿を熟成させ,吸引ろ過でメンブランフィルター（孔径 0.45μm）に捕集した.捕集した沈殿は 7.5MNH_4OH 5ml で溶解し、陽イオン交換樹脂（ムロマック樹脂　50W×8,NH_4^+ 型,200～400 メッシュ,10ml）に流し,7.5MNH_4OH 5ml により溶出液を回収した.その溶出液に再度 PMA 0.5g を添加し,かくはんしながら 6MHNO_3 10ml を添加し,PMA の沈殿を生成させた.1 時間ほど沈殿を熟成させ,吸引ろ過にてメンブランフィルター（孔径 0.45μm）に捕集した.捕集した沈殿をポリエチレン袋に封入しγ線測定サンプルとした.

2・3　γ線測定

γ線測定は高純度 Ge 半導体検出器（分解能 1332keV で 1.87keV,相対計数効率 48%）及び 4096 マルチチャンネル波高分析器（GAMA システム）を用いて行った.解析は解析プログラム（GAMA98）を用いてパーソナルコンピュータにより行った.

Mo の定量には天然存在比 24.13%の ^{98}Mo (n,γ) 反応で生成する ^{99}Mo（半減期 2.8 日）とその娘核種の半減期 6 時間の ^{99m}Tc とが放射平衡にある場合に最大の放出率を持つ 140.5keV のγ線を用い,試料と比較標準試料との計数率の比較から行った.

3　結果及び考察

3・1　^{99}Mo-^{99m}Tc の放射平衡の検証

140.5keVγ線によって ^{99}Mo を測定するには,半減期 6 時間の娘核種 ^{99m}Tc との放射平衡が成立していなくてはならない.^{99}Mo のβ壊変では,そのほとんど（約 99.65%）が ^{99m}Tc を経由して 140.5keV のγ線を放出するが,約 1.35%の割合で ^{99m}Tc を経由しないで ^{99}Mo のβ壊変の直後に 140.5keV のγ線を放出するモードが存在する.また,^{99m}Tc の半減期が短いため中性子照射中にかなりの ^{99m}Tc が蓄積されるので,照射直後でも強く 140.5keV のγ線が観測できる.しかしながら、放射平衡が成立しているわけではない.従って,INAA においては照射終了後,RNAA においは化学分離終了後,^{99m}Tc の半減期の 10 倍程度経過してから測定することが望ましいが、その冷却時間は ^{99}Mo の半減期に相当するため、検出

感度を1/2以下に低下してしまう.本研究の化学分離はマトリックスの鉄（及びその放射化生成物）からをMo分離し、回収するためのものであるため,Tcの挙動については明確ではない.そこで,放射平衡が成立するために必要な化学分離後の冷却時間について,140.5keVγ線の強度変化を追跡して検討した.その結果、化学分離によってすべての ^{99m}Tcが除去されたとしても,40時間の冷却時間後では,計算上97%の放射平衡に達していることになった.そこで本研究では,化学分離操作を終了してから40時間後に140.5keVγ線を測定することとした.

3･2　トレーサー実験結果

SIN試料に照射したMo標準溶液を添加したトレーサー実験から,各々の化学分離操作前後のγ線強度から求める ^{99}Moの回収率をTable1に示す.水酸化鉄分離法,陽イオン交換クロマトグラフィー及びリンモリブデン酸アンモニウム共沈法のそれぞれの操作の回収率は92～100%であり,全体の操作の回収率は84±2%（n=5）であることが分かった.このことより,実試料では測定値をこの84%の回収率で補正した値を定量値とすることとした.

Table 1　Recovery of ^{99}Mo

n=5

Separation method (99Mo fraction)	recovery,%
Precipitation with $Fe(OH)_3$ (Supernatant liquic	100±1
Cation-exchange chromatography (Eluate)	100±1
Precipitation with PMA (Precipitation with PM	92±2
Overall rec	84±2

PMA:$(NH_4)_3PO_4 \cdot 12MoO_3 \cdot 3H_2O$

3･3　JRR-3Mを用いたRNAAによるMoの定量値と定量下限値

Table 2に3種類の試料（JSS003-4,JSS001-3,JSS001-4）を日本原子力研究所JRR-3MのHR-1照射孔で6時間照射し,Fig.1に従ってRNAAで定量したときのMoの定量値と定量下限値を示す.3種類の高純度鉄ともMoは微量（JSS001-3及びJSS001-4のMo含有量は0.3ppm以下のため認証値は求められていない.JRR-3Mでは3種類の試料すべてでMoが定量でき,JSS003-4では670±12ppb（参考値0.7ppm）,JSS001-3では8.4±0.3ppb,JSS001-4では11.0±0.5ppbを得た.定量下限値は同様に測定時間を50000秒間に換算して算出した.JSS001-4のMo定量下限値は,立教炉と比べ約1/10になった.これらの試料の中で最も低い定量下限値は,JSS003-4の0.4ppbであった.このことにより pptレベルのMoの分析の可能性を示した.又,定量は3回の繰り返し分析の結果,5%以内の精度で求められた.

Table2　Analytical results of Mo in JSS003-4, JSS001-3 andJSS001-4 by RNAA

Sample name	Concentration, ppb	Lower limit of determination,ppb
JSS003-4 ①	660	0.4
JSS003-4 ②	660	0.9
JSS003-4 ③	680	1.2
Average670±12		
JSS001-3 ①	8.2	1.9
JSS001-3 ②	8.2	1.1
JSS001-3 ③	8.7	1.7
Average8.4±0.3		
JSS001-4 ①	10.6	2.1
JSS001-4 ②	11.3	2.3
Average11.0±0.5		

Lower limit of determination is reduced on assume the countir for 50000s. Irradiated for 6h in JRR-3M

5. ＲＩの製造

5. Production of Radio Isotopes

This is a blank page.

研究テーマ：超アクチノイド元素の核化学的研究
表　　題：原研における Rf の溶液化学

5-1 原研における Rf の溶液化学

羽場宏光，塚田和明，西中一朗，浅井雅人，平田 勝，市川進一，永目諭一郎，横山明彦[1]，豊嶋厚史[1]，正司 譲[1]，篠原 厚[1]，後藤真一[2]，金子哲也[2]，工藤久昭[2]，阪間 稔[3]，大浦泰嗣[3]，M. Schädel[4]
日本原子力研究所先端基礎研究センター
[1] *大阪大学大学院理学研究科*
[2] *新潟大学大学院自然科学研究科*
[3] *東京都立大学大学院理学研究科*
[4] *Gesellschaft für Schwerionenforschung*

超アクチノイド元素の化学的性質に関する研究は，それら元素の周期表上における位置を確認しつつ電子軌道に対する相対論効果を検証していくという点で基本的ではあるが非常に興味深い研究テーマである．我々の研究グループでは，これまで GSI 並びに Mainz 大との協力研究の下，GSI-UNILAC 並びに PSI-Philips Cyclotron を用いて特に硝酸－フッ酸系における Rf と Sg の溶液化学実験に参加してきた[1]．これとともに，原研タンデム加速器を用いて塩酸や硝酸等の単純な溶液系で Rf のイオン交換実験を行う準備を進めている．

1. 迅速化学分離装置の開発

最近我々のグループでは，^{248}Cm(^{18}O,5n)反応によって日本で初めて ^{261}Rf の合成に成功した．生成した ^{261}Rf は，He/KCl ガスジェットシステムによって数秒のうちに照射室から化学実験室へ輸送される．我々の実験条件（ビーム強度：200pnA，標的厚：0.59mg/cm^2，反応断面積：5nb）では，2 分間に 1 個の割合で ^{261}Rf を製造できるが，^{261}Rf の半減期（78s）を考えると 1 回の化学実験には僅か 1 個の Rf 原子しか取り扱えない．ここでは質量作用の法則は適用できず，クロマトグラフ法を多数回繰り返す実験が必要である．我々は，GSI が開発した Automated Rapid Chemistry Apparatus（ARCA）[2]を改良し，迅速で繰り返し実験が可能な液体クロマトグラフの装置を製作した．この装置は 20 連のイオン交換用マイクロカラム（1.6mmϕ ×8mm）を 2 カートリッジ装備し，Rf の溶液化からイオン交換分離までの一連の作業をコンピュータ制御で迅速に行う．^{261}Rf を模擬した ARCA のオンラインテストとしては，^{89}Y(p,n)並びに ^{152}Gd(^{18}O,5n)反応でそれぞれ生成される同族元素 ^{89m}Zr（4.18m）並びに ^{165}Hf（76s）を用い，硝酸－フッ酸，塩酸並びに硝酸系において溶液化効率やイオン交換の分配係数（K_d 値）等の基礎データを蓄積している．

2. Rf の同族元素の挙動

4 族元素 Rf の化学的性質をその同族元素である Hf 並びに Zr あるいは擬 4 族元素である Th のそれと比較することは，Rf の電子状態に関する情報を引き出し相対論効果を検証していく上で非常に重要である．我々は ^{88}Zr，^{175,181}Hf 並びに ^{234}Th の放射性トレーサを製造し，Rf の溶液化学実験に向けて様々な基礎データをオフラインで蓄積している．^{88}Zr 並びに ^{175}Hf に関しては，原研タンデム加速器から得られる p ビーム用いてそれぞれ ^{89}Y(p,2n)並びに ^{175}Lu(p,n)反応によって製造した．^{181}Hf は市販の硝酸ハフニウムを JRR-3M（PN-3）で中性子照射して製造した．一方，^{234}Th は天然放射性同位元素 ^{238}U と放射平衡にあり，市販の硝酸ウラニル 6 水和物から化学分離した．これらのトレーサを用いて，ARCA マイクロカラム充填用陰イオン並びに陽イオン交換樹脂（三菱化学 MCI GEL CA08Y，CK08Y）の硝酸（1-14M）並びに塩酸（1-11M）系における K_d 値をバッチ法により測定した．特に陰イオン交換挙動が興味深く，8M 硝酸系では Th の K_d 値（540ml/g）は Zr（8.4ml/g）並びに Hf（14ml/g）の K_d 値に比べて 1 桁以上大きく，また 9M 塩酸系では Th，Hf，Zr の順に 1.1，16，140ml/g と K_d 値は 1 桁ずつ大きくなる．今後この両系で Rf の K_d 値を測定し，同族元素の結果と比較することから Rf の化学形やイオン半径に関する重要な情報を引き出せるものと期待している．

参考文献

1) 塚田ほか，第 43 回放射化学討論会講演予稿集，1A03，(1999)，p. 55.
2) M. Schädel *et al.*, Radiochim. Acta **48** (1989) 171.

原子炉：JRR-3M　　装置：気送管　　分野：RI の製造（トレーサー用）

This is a blank page.

6. 原子炉材料照射試験

6. Irradiation Test of Reactor Materials

This is a blank page.

研究テーマ：原子力材料の照射効果の研究
表題：原子炉照射下における絶縁セラミックスの電気絶縁劣化特性試験

6-1 Cr添加Al_2O_3単結晶の中性子照射下電気伝導度「その場」測定

谷藤 隆昭　片野 吉男　中沢 哲也　實川 資朗

日本原子力研究所　物質科学部　材料照射解析研究グループ

（目的）

酸化アルミナ(Al_2O_3)や酸化マグネシウム(MgO)など多くの絶縁材料が核融合炉で使用される．これら絶縁材料は核融合炉内において高エネルギー中性子に曝されるため本来持っている電気絶縁性能の低下が懸念されている．そのため、中性子照射によって引き起こされる照射誘起電気伝導現象(RIC)や照射誘起絶縁劣化(RIED)を解明し、核融合炉環境におけるセラミック絶縁材料の絶縁性能劣化を評価することは重要であ。そこで、典型的な絶縁性セラミックスである酸化アルミナなどの各種放射線下における電気絶縁特性挙動を調べる実験を進めている（1）。

（実験）

図１には、日本原子力研究所の原子炉(JRR-3)における中性子照射下での1mol%のCrを添加したAl_2O_3単結晶の電気特性変化を示した。JRR-3の出力が20MWまで上昇する間に電気伝導度は$1x10^{-9}$から$1x10^{-6}$ (S/m)まで増加した。照射下での絶縁物の電気伝導度の増加、σは、$\sigma=\sigma_0\gamma^{\delta}$で表される。$\gamma$は照射線量率、$\sigma 0$, δは定数である。これまでの実験から電気絶縁材料であるMgO単結晶等のセラミックスでは，δの値としてはほぼ１に近い値がほとんどの放射線場で得られている。

Cr添加Al_2O_3単結晶の電気伝導度の変化からもとめたδは第1サイクルから第2サイクルへと照射を重ねることによって0.80と0.73へと減少している。高純度Al_2O_3単結晶についても同様の実験を行いδを求めた。第1及び第2サイクルにおける高純度Al_2O_3単結晶のδは0.76と0.75であった。照射を重ねることによるδの変化は観察されなかった。線量率に依存する定数δは照射による禁制帯中の不純物準位の濃度変化や照射によって導入された欠陥の状態及び濃度変化などによって変化する。Cr添加Al_2O_3単結晶に対して観察されたδの減少は中性子との核反応によって生成した^{51}Cr（半減期：27.8day）や添加したCrに起因した照射欠陥・照射誘起偏析などが原因と考えられる。Crなどの不純物元素は照射下におけるセラミックス絶縁材料の電気特性に大きな影響を及ぼすものと考えられる。

(1) J.Nucl.Mater. 253(1998)156-166

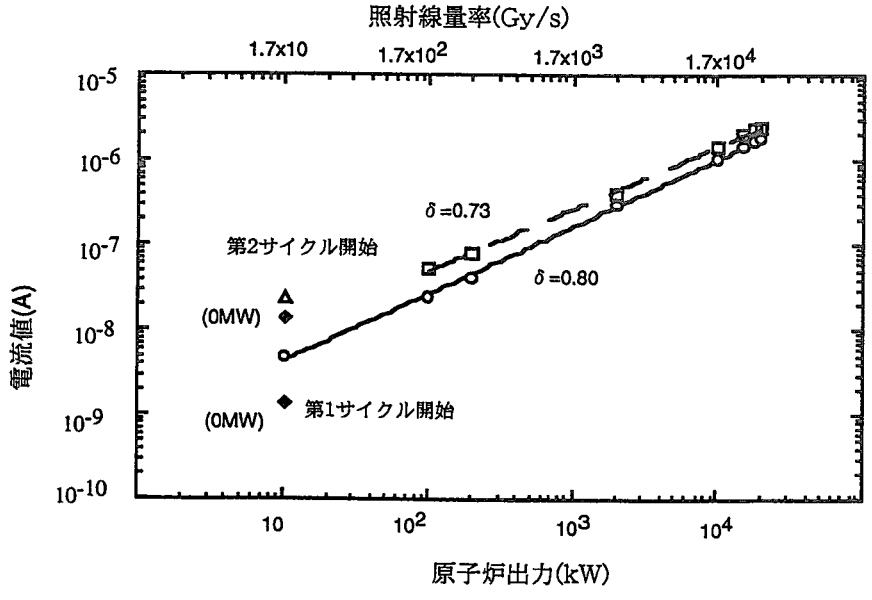

図１　中性子照射下における1mol%Cr_2O_3添加Al_2O_3単結晶の電気伝導度の変化

原子炉：JRR-3M　装置：ＢＲ-2　分野：原子炉燃料・材料（核融合炉）

研究テーマ；原子力材料の照射効果の研究
表　　題：固体増殖材からのトリチウム放出挙動

6-2　酸化リチウム焼結体からのトリチウム放出：気孔率依存性

谷藤 隆昭　　八巻大樹　　高橋正　　岩本昭

日本原子力研究所　　物質科学部　材料照射解析研究グループ

（はじめに）

多孔性のセラミック固体増殖材からのトリチウム放出挙動は内部に存在する閉気孔、開気孔、連結開気孔などの影響を大きく受けるため、気孔内トリチウムの移行挙動　　が重要な課題となる。特に連結気孔および閉気孔内から焼結体表面のパージ個所までの移行挙動が重要である。この移行過程はHTO　などが連結開気孔内壁への吸着、脱離を繰り返しながら焼結体表面までの移行する過程およびトリチウムの連結開気孔内の気相拡散などが、が複合していると考えられる。この場合、連結開気孔の屈曲度および細孔径が重要な役割をになってくる。さらに、トリチウム移行挙動は気孔分布、結晶粒径　などの影響を受けるものと考えられる。

（気孔率依存性）

ﾋﾟｰｸA領域(71%TD-86%TD)：2K/minの昇温速度で加熱したときの、71％ＴＤ、76％ＴＤ、81％ＴＤ，83％ＴＤおよび86％ＴＤ焼結体からのトリチウム放出速度を温度の関数として図1に示す。この範囲の焼結体の開気孔率は71％ＴＤで25％から86％ＴＤで11％であり、一方、閉気孔率は71％ＴＤで3.5％から86％ＴＤで3％である。また焼結体の平均粒径は71％ＴＤで9.5μｍから86％ＴＤで24μｍと変化している。にもかかわらず、トリチウム放出ﾋﾟｰｸはこの気孔率の範囲では約570Ｋとほぼ一定である。これはこの領域での開気孔率と閉気孔率の比が1.4-2.7であり開気孔率が大きいため、連結開気孔の通過が律速にはならず、また、閉気孔の影響も無視できることを意味している。

ﾋﾟｰｸB領域(87%TD-89%TD)；2K/minの昇温速度で加熱したときの、87％ＴＤ，88％ＴＤおよび89％ＴＤ焼結体からのトリチウム放出速度を温度の関数として図2に示す。この範囲の焼結体の開気孔率は87％ＴＤで8.3％から89％ＴＤで4％であり、一方、閉気孔率は87％ＴＤで4.7％から89％ＴＤで7.0％である。また焼結体の平均粒径は71％ＴＤで25μｍから86％ＴＤで29μｍと変化している。この領域でのトリチウム放出ﾋﾟｰｸは約620Ｋの単一ﾋﾟｰｸである。このことはこの領域での開気孔率と閉気孔率の比が0.57-1.8であり開気孔率と閉気孔率がほぼ同程度の範囲であり連結開気孔の通過および連結開気孔の気相拡散が律速している。すなわち、HTO　などが開気孔内壁への吸着、脱離を繰り返しながら焼結体表面まで移行する過程とトリチウムの連結開気孔内の気相拡散、が複合しているものと考えられる

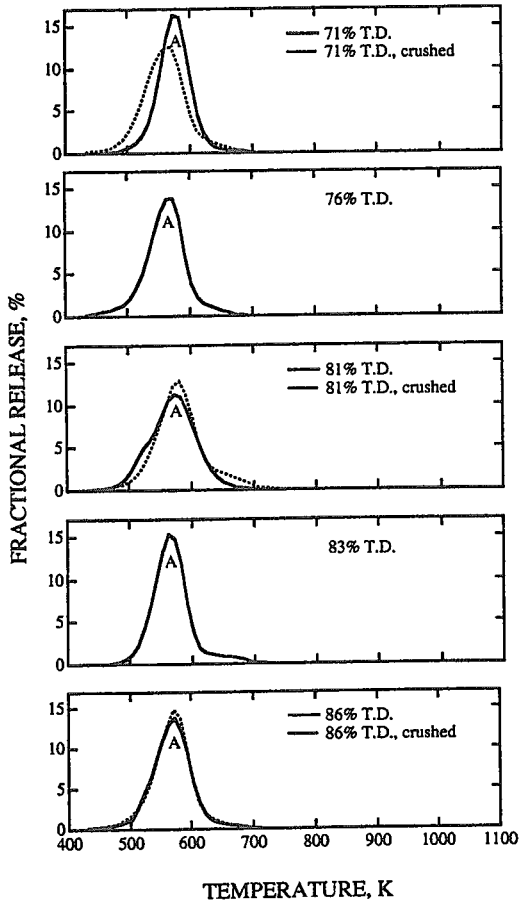

図.1　71%-86％ＴＤ焼結体からの等速昇温時（2K/min)のトリチウム放出挙動

原子炉：JRR-4　装置：Sパイプ　分野：原子炉燃料・材料（核融合炉）

ﾋﾟｰｸC,D,E 領域(90%TD-92.5%TD)；2K/minの昇温速度で加熱したときの、90%ＴＤ，91%ＴＤおよび92.5ＴＤ焼結体からのトリチウム放出速度を温度の関数として図3に示す。この範囲の焼結体の開気孔率は90%ＴＤで2.8%から92.5%ＴＤで1.5%であり、一方、閉気孔率は90%ＴＤで7.2%から92.5%ＴＤで6.0.%である。また焼結体の平均粒径は90%ＴＤで30μmから92.5%ＴＤで60μmと変化している。この領域でのトリチウム放出ﾋﾟｰｸは大別して約700K、830Kおよび約1000Kの三個となる。このことはこの領域での開気孔率と閉気孔率の比が2.6-4.0であり閉気孔率が主流を占める範囲であり閉気孔に捕捉されていたトリチウムが加熱によりデトラップされることにより放出されるものと考えられる。

ここで注目すべきことは焼結体のみかけ密度が89%ＴＤから90%ＴＤとわずか1%増したためにトリチウム放出ﾋﾟｰｸは620Kの単一ﾋﾟｰｸから620Kおよび700Kと二個のﾋﾟｰｸが現れるようになり、強い気孔率依存性を示している。

98.5%ＴＤ試料からの放出挙動；2K/min の昇温速度で加熱したときの、98.5%ＴＤ焼結体からのトリチウム放出速度を温度の関数として図3下段に示す。

この焼結体の開気孔率は約0.4%であり、一方、閉気孔率は約1.1%程度である。また焼結体の粒径は60μmから100μmと広く分布している。この焼結体のトリチウム放出ﾋﾟｰｸは700K前後で平たんである。このような高密度焼結体からの放出過程は単結晶の場合と同様に体積拡散を含んでいると考えられる。

（昇温速度依存性）

71%ＴＤから86%ＴＤ焼結体（放出ﾋﾟｰｸA領域）のトリチウム放出過程を明らかにするために代表例としてかさ密度81%TD焼結体の昇温速度1,2,5,10,20,40K/min と変えて、トリチウム放出ﾋﾟｰｸの昇温速度依存性を調べ、その放出のみかけ活性化エネルギーを求めた。

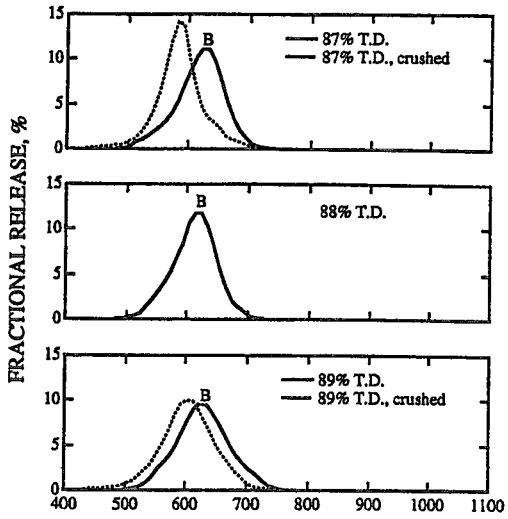

図.2 87%-89%ＴＤ焼結体からの
等速昇温時（2K/min)のトリチウム放出挙動

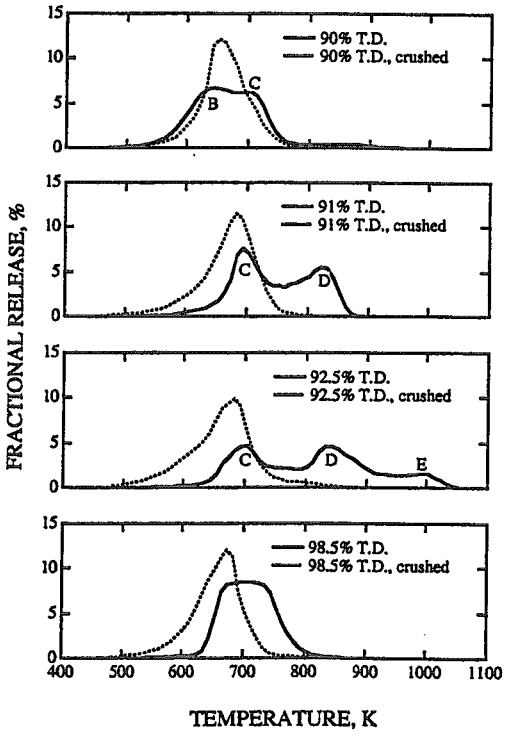

図.3 90%-98.5%ＴＤ焼結体からの
等速昇温時（2K/min)のトリチウム放出挙動

昇温速度、aとトリチウム放出ピーク、T_p の関係は

$$a/(T_p)^2 = C\exp(-E_0/kT_p)$$

となる関係がある。

$a/(T_p)^2$ に対する1/Tpの関係を図4に示す。これより、トリチウム放出のみかけ活性化エネルギーは約129 k J/mol と求まった。この結果はESRを用いた照射欠陥（F+ center ）の回復の活性化エネルギー135 k J/mol と良く一致している。
これらのことから、このピークA領域の放出過程は照射欠陥にトラップされていたトリチウムがトラップ・サイトの回復とともに放出されるものと考えられる。

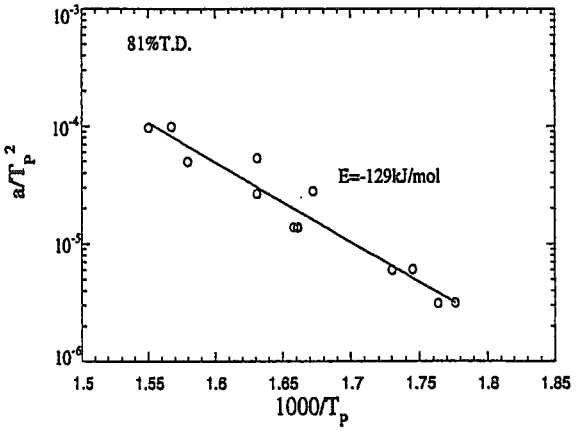

図.4　81％ＴＤ焼結体からの
トリチウム放出の昇温速度依存性

（結論）

かさ密度71％ＴＤから98.5％ＴＤの種々気孔率をもつLi2O 焼結体からのトリチウム放出挙動を2K/min の等速昇温により調べた。その結果、71％ＴＤから86％ＴＤのあいだでは気孔率依存性は全くないが、87％ＴＤ以上の焼結体では強い気孔率依存性を示すことがわかった。また、トリチウム放出過程には大別して、次の三段階があることが判明した。すなわち

1. 放出ピークA領域（約670Ｋ）；照射欠陥にトラップされたトリチウムが欠陥の回復に伴い、デトラップされトリチウムが放出される。すなわち、照射欠陥の回復が律速過程である。

2. 放出ピークＢ領域（約670Ｋ）：連結開気孔を通じて、開気孔内壁への吸着、開気孔内壁からの脱離、開気孔内の気相拡散のサイクルを繰り返しながら表面層まで移行してくるのが律速過程である。

3. 放出ピークＣ、Ｄ、Ｅ領域： 閉気孔からの逃散がトリチウム放出の律速過程 となり、閉気孔の分布に従って、おもに700K,830K,および1000Ｋの三個の放出ピークがある。

トリチウム放出挙動は気孔率のわずかな変化に非常に鋭敏である。すなわち、86%TDから87%TD と気孔率がわずか1％変化しただけで、放出ピークは約40Ｋ高温側に移行する。また、かさ密度89%TDと90%TDの間でも、89%TDでは放出ピークは630Ｋ付近の単一放出ピークをしめすが90%TDでは630Ｋおよび700Ｋの二個の放出ピークを示すようになり、トリチウム放出挙動が大幅に変化する。

Li_2O焼結体からのトリチウム放出の律速過程は体積拡散律速でもなく、また試料表面からの脱離律速過程でもないことを示唆している。今後、気孔分布、細孔径などの気孔ネット・ワークが良く調べられた試料からのトリチウム放出実験が重要となる。

参考文献 ：J..Nucl..Mater. to be published

7. その他

7. Others

This is a blank page.

研究テーマ：
表　題　：ＪＲＲ－３ＳＩ－１孔の特性測定

7-1　ＪＲＲ－３ＭＳＩ－１孔の特性測定

熊井敏夫　圷　長[1]
研究炉部研究炉利用課
[1]（財）放射線利用振興協会

１．概要

ＪＲＲ－３は平成１１年度第６サイクルより今までのアルミナイド燃料からシリサイド燃料に変更した。これにともない、シリコンを主に照射しているＳＩ孔の特性を把握するため、金箔及びコバルトを用いて軸方向の中性子束分布測定、及び照射量を監視するＳＰＮＤ積算値と照射場の中性子照射量との相関関係を把握するため、照射量（目標抵抗値）をパラメータにしてシリコンの試験照射を行った。

２．軸方向中性子束分布測定

コバルトの放射化法による中性子束測定では、平成１１年１１月１０日及び６サイクル運転中の１２月１７日にいずれも原子炉出力２０ＭＷで１時間の照射を行った。また、金箔による測定では、平成１１年１１月１６日に原子炉出力１０ＫＷで１時間の照射を行なった。中性子測定結果を下図に、アルミナイド燃料時の中性子束分布とともに示す。シリサイド燃料に変更後の中性子束は、アルミナイド燃料時より約２割減少していたが、中性子束分布は大きく変わらなかった。

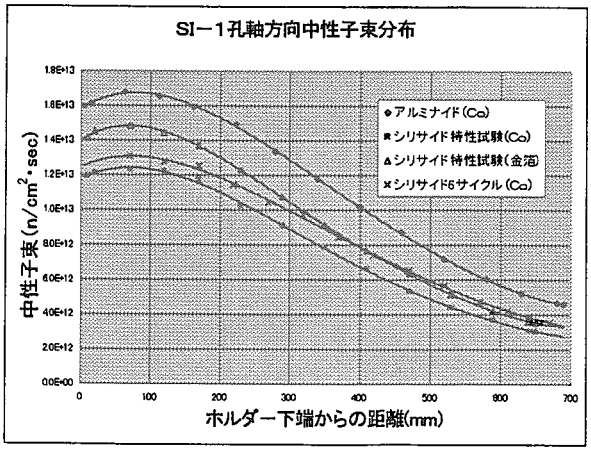

３．シリコン試験照射

試験照射は、第６サイクルに５インチシリコンについて目標抵抗値が６５０、２５０，２００，１０５，７０，６０，５３，４５及び３３オーム・ｃｍの９パラメータについて、６インチは７５０と１０６オーム・ｃｍについて行った。また、試験照射は、照射量とＳＰＮＤ積算値を監視しながら照射時間の微調整を行い進めた。

最終的には、下記に示すように上・下端での軸方向、径方向の均一度が３％以内に収まるような結果を得た。

４．まとめ

アルミナイド燃料からシリサイド燃料への変更により中性子束は大幅に減少したが、中性子束分布は大きく変わらなかった。従って、ＳＰＮＤ積算値と照射量の相関関係も大きく変わらずシリコンの照射が可能であることが判った。

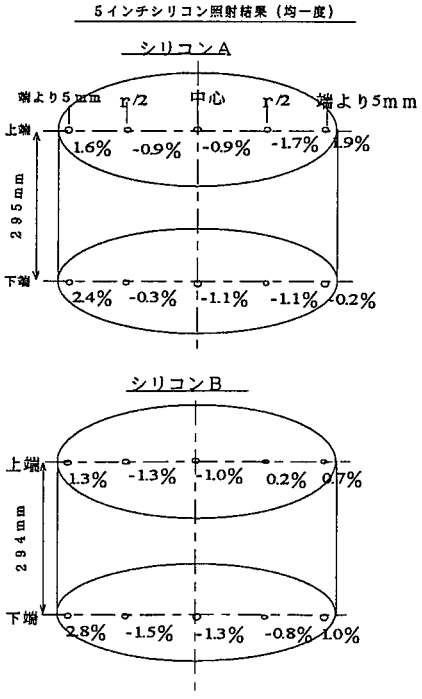

原子炉：ＪＲＲ－３　　装置：均一照射装置

分野：その他（半導体）

研究テーマ：
表　　題　：ＪＲＲ－４Ｎパイプ中性子束測定

7-2　ＪＲＲ－４Ｎパイプ中性子束測定

高田　準太郎　　圷　長[1]
研究炉部研究炉利用課
[1]（財）放射線利用振興協会

１．概要

ＪＲＲ－４は平成８年度から燃料ウランの低濃縮化を行なうとともに、利用設備についても口径１５ｃｍのＮパイプを設置するなど利用設備の改造を行ない、平成１１年１月から利用運転を開始した。Ｎパイプでシリコンを照射するため、当設備の中性子束測定などの特性測定を平成１０年度に行ない、中性子束の照射の均一性や垂直分布を等を確認している。シリコン照射を本格的に開始するにあたって照射孔内の照射位置変更による中性子束の分布状況及びＳＰＮＤ計測値と照射量の相関関係を把握するため、Ｃｏモニタを用いて試験を行なった。

２．結　果

Ｃｏモニタによる中性子束の測定は、平成１２年１月２６、２７日に原子炉出力３．５ＭＷで３時間と５時間の照射を行なった。その結果を下図－１に示す。図には平成１０年度に行なった試験（テストＥ）の中性子束分布も示してある。また、照射量とＳＰＮＤの関係を図－２に示す。図には実験から求めた関係式を合わせて示す。今後は、これらの結果を基に実シリコンの照射を行ない、最適照射条件を構築し、実用照射を開始する予定である。

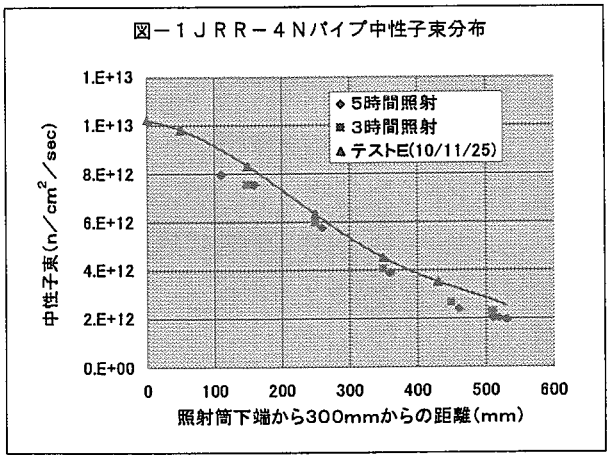

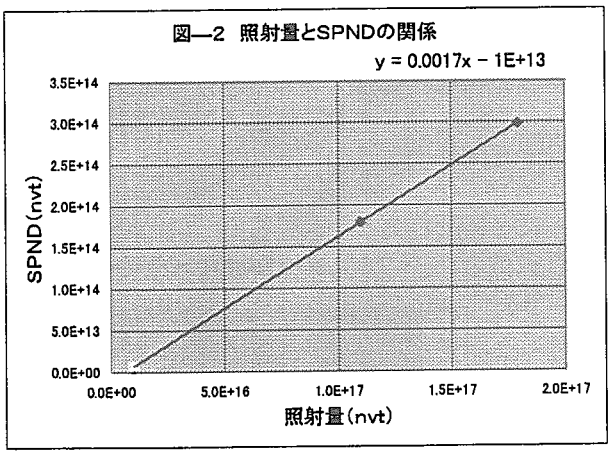

原子炉：ＪＲＲ－４　　装置：Ｎパイプ　　分野：その他（半導体）

研究テーマ:研究炉利用高度化の技術開発
表　　題:JRR-4 中性子ビーム設備の特性試験

7-3 腫瘍細胞を用いたJRR-4 中性子ビームの評価
Evaluation of JRR-4 Neutron Beam Using Tumor Cells in *in vitro*

山本和喜、鳥居義也、岸敏明、熊田博明、高田準太郎、大竹真一、山本哲哉[1]、松村明[1]、能勢忠男[1]
Kazuyoshi Yamamoto, Yoshiya Torii, Toshiaki Kishi, Hiroaki Kumada, Juntaro Takada, Shinich Ohtake、Tetsuya Yamamoto, Akira Matsumura, Tadao Nose
日本原子力研究所・研究炉部：茨城県東海村白方白根 2-4
1：筑波大学・臨床医学系：つくば市天王台 1-1-1

ホウ素中性子捕捉療法(BNCT)の照射計画を組む上で最終的に細胞に及ぼす効果を適切に評価する必要があり、RBE 等の重み付けを用いなければならない。線量評価システムで計算される物理線量に対して、各モードによる線質変化のみならず細胞種による重み付けを適切に行うことにより、より正確な線量計画を組むことができる。JRR-4 の中性子ビームに対する生物学的効果を観察するために、筑波大学と協力して、放射線感受性の異なる 2 種類の腫瘍細胞を用いた細胞照射実験（*in vitro*）を実施した。

キーワード：　医療照射、BNCT、細胞実験、JRR-4、*in vitro*

【目的】JRR-4 中性子ビーム設備は重水タンクの重水層厚さ変更及び Cd シャッタ開閉により中性子スペクトルに変化を与えることができる。熱外中性子モード(熱外中性子)、熱中性子モードⅠ(熱中性子＋熱外中性子)、熱中性子モードⅡ(熱中性子)の 3 モードを医療照射用の基本モードとして設定している。これら 3 モードの中性子ビームに対して人間の頭を模擬した頭部水ファントム中の実験腫瘍細胞に対し、最大熱中性子フルエンスが同程度になるよう照射を行った。これら実験細胞を培養し、生存率曲線を求めることによりビームの特性を生物学的見地から評価を行った。
【方法】ウェルプレートに培養したラットグリオーマ細胞懸濁液を充填し、水を満たしたアクリル製の頭部ファントム（φ18.6cm×L24cm）内にセットした。使用する実験細胞はラットグリオーマ細胞であり、感受性の異なる 2 種類の腫瘍細胞（9L gliosarcoma、C6 glioma）を用いた。BNCT では患部にホウ素化合物を添加することから、実験細胞の培養液中にホウ素化合物（ Sodium Borocaptate; BSH）をそれぞれ 0, 5, 15ppm の濃度で添加し、最大熱中性子フルエンスが 5×10^{12}n/cm^{2}程度になるよう照射を行なった。照射した細胞は培養用のシャーレに移し、CO2 インキュベータで 1 週間培養を行った。照射後 1 週間後に固定し、コロニー形成検査（Colony Formation Assay）にて生存率を調べた。
【結果と結論】ウェルプレートと呼ばれる容器を用いることにより、一度の照射で細かい生存率分布が観察することができた。JRR-4 の各中性子ビームに対しても BSH を添加しない細胞群では最低生存率が約 0.1 となるが、BSH を 15ppm 添加した場合、細胞生存率が大きく低下することが確認された。熱外中性子モード及び熱中性子モードⅠにおいてその効果は顕著で、最低生存率が 0.001 程度まで下がることが分かった。熱中性子成分を含む熱中性子モードⅠ及びⅡでは表面近傍に最低生存率があるのに対して、熱外中性子ビームでは深さ約 2cm のところに最低生存率を示すことが観察された（Fig.1 参照）。これは熱外中性子が減速されて生じる熱中性子のピークによるもので、熱中性子束分布に対応して細胞が死滅していることを示している。JRR-4 の各中性子ビームに対する腫瘍細胞（9L、C6）の生存率曲線を得ることができ、これらデータを用いて JRR-4 の中性子ビームに対する腫瘍細胞の RBE 等の評価を行う。

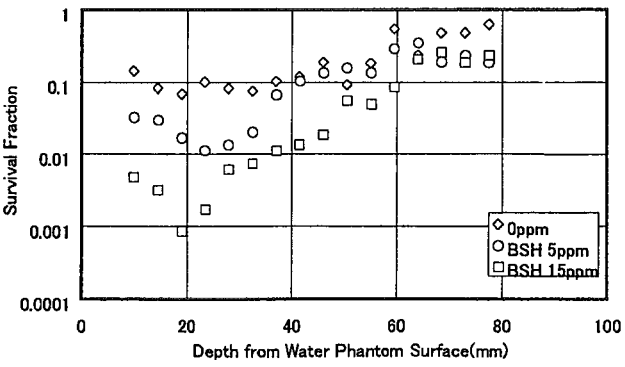

Fig.1 ファントム表面からの深さに対する C6 glioma 細胞の生存率曲線（感度曲線）、深さ約 20mm の所に最低生存率を示す。

研究テーマ：研究炉利用高度化の技術開発
標　　題：JRR-4 中性子ビーム設備の特性試験

7-4 BNCTのための頭部内熱中性子束分布測定
Measurement of Thermal Neutron Distribution in Patient Head for BNCT

熊田博明、山本和喜、鳥居義也、岸敏明、高田準太郎、大竹真一
Hiroaki KUMADA, Kazuyoshi YAMAMOTO, Yoshiya TORII,
Toshiaki KISHI, Juntaro TAKADA, Shinichi OHTAKE
日本原子力研究所　研究炉部研究炉利用課：茨城県那珂郡東海村白方白根 2-4

JRR - 4 に整備した中性子ビーム設備においてBNCT を実施するために、頭部水ファントムを用いて内部に金線を放射状に配置して、頭部内熱中性子束の 2 次元分布測定を実施した。また Void の有無による熱中性子束分布の変化も測定し比較を行った。

実験方法：　JRR－4 中性子ビーム設備は、重水厚さを変化できる重水タンクと開閉可能な Cd シャッタにより、ビーム・スペクトルを変更することができる。組合せは自在であるが、代表的な照射ビームとして、熱外中性子モード、熱中性子モードⅠ、熱中性子モードⅡの 3 種類の中性子スペクトルのビームモードを設定している。この 3 つの照射モードとコリメータ直径 10、15ｃｍそれぞれに対し、熱中性子束分布の測定実験を行った。実験には外径 18.6cm、厚さ 3mm のアクリル製の頭部水ファントムを使用し、図に示すように金線を配置してファントム照射実験を実施した。得られた測定データを 2 次元補間し、ファントム内熱中性子束の 2 次元分布を求めた。また実際の開頭 BNCT 照射では、深部の患部ターゲットに治療線量を与えるため Void を挿入して照射を行う。この Void による効果を確認するため、ファントム内に発泡スチロール製の Void を取付け、Void の有無による熱中性子束分布の変化を測定し、比較した。

実験結果：　Void を設定した場合、Void 周辺において、熱中性子束の高い領域ができることが分かった。熱外中性子モードによる Void 実験では、Void 直径 40mm の場合はターゲット領域内の熱中性子束分布が平坦化し、より深部まで高い照射線量を得られることが分かった（Fig.1 参照）。

結　論：　これらの実験による熱中性子束分布測定を踏まえ 1999 年 10 月に JRR－4 中性子ビーム設備を用いた最初の BNCT が実施された。このファントム実験データと実際の開頭 BNCT から得られたデータは、今後開頭による BNCT 実施のための基礎データとして用いるとともに、現在原研で開発を行っている BNCT 線量評価システムの検証にも使用し、より精度の高いシステム開発を行う予定である。

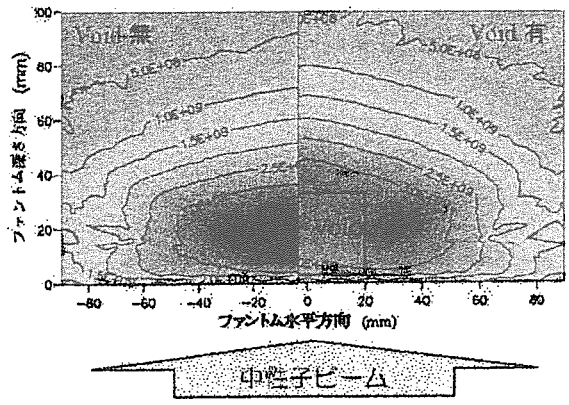

Fig.1 熱外中性子ビームモードにおける Void の有無によるファントム内熱中性子束分布の比較

原子炉：JRR-4　　装置：中性子ビーム設備　　分野：その他

研究テーマ：研究炉利用高度化の技術開発
表　　題：JRR-4 中性子ビームの特性試験

7-5

A Quantitative Approach to the Characterization of Neutron Beam for Boron Neutron Capture Therapy (BNCT) Using *In Vitro* Cell Survival

Tetsuya Yamamoto, Akira Matsumura, Tadao Nose, Kazuyoshi Yamamoto[1], Hiroaki Kumada[1], Koji Ono[2], Yoshinori Sakurai[2], Toru Kobayashi[2]

Department of Neurosurgery, Institute of Clinical Medicine, University of Tsukuba
Department of Research Reactor, Tokai Research Establishment, JAERI[1]
Kyoto University Research Reactor Institute[2]

Radiobiological response is generally predictable by invoking the physical dose and the relative biological effectiveness (RBE) of a certain endpoint. However, in boron neutron capture therapy (BNCT), this way to determine the effective dose is a most unsatisfactory procedure because RBE values are highly dependent on the precise circumstances surrounding the determination [1]. The uncertainties of the effective dose in this way are large because it is impossible to measure all RBE values for the physical doses of a mixed radiation field and for the whole of a neutron spectrum.

The aim of this study is to resolve this problem by evaluating the in-phantom characteristics of ENB, TNB-I, and the epithermal beam of the Kyoto University Research Reactor (KUR) in combination with a clonogenic cell survival assay and dosimetry to estimate the effective dose without invoking RBE values.

Irradiations of cells and dosimeters were carried out in a 186 mm-diameter cylinder PMMA phantom filled with distilled water by using ENB, TNB-I, and the KUR epithermal beam. Activation of gold wires and foils were counted with a simultaneous β - γ coincidence counting device, then thermal neutron fluence was calculated by the foil activation method. Gamma ray dose was measured with a TLD covered with quartz glass (Panasonic 170LS). V79 cells in the stage of exponential cell growth were preincubated for 1h in Minimum Essential Medium (Sigma Chemical Co.), supplemented with 10% fetal bovine serum with boric acid (5 μ g^{10}B/ml) or without boric acid. A 384-well plate was filled with conditioned medium and cells in suspension, and then irradiation was performed with each neutron beam for the colony formation assay. Thermal neutron fluence for each beam was set to

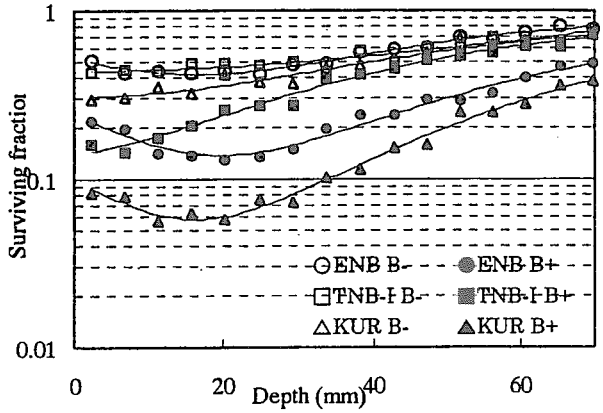

Fig.1 Depth-response curve of cells irradiated with ENB, TNB-I and the KUR epithermal beam

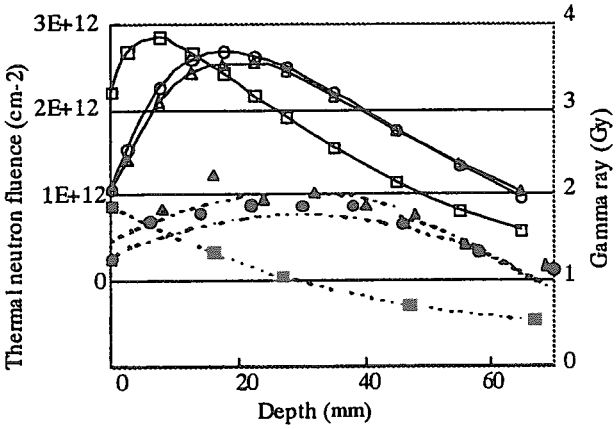

Fig.2 Thermal neutron fluence and gamma dose distribution for ENB(○,●), TNB-I(□,■) and the KUR(△,▲) epithermal beam

approximately 2.5E+12 cm^{-2} as the maximum value. Both the cell survival assay and dosimetry were repeated at least three times.

The clonogenic cell survival data were analyzed to estimate the effective dose of radiation components under the following assumptions:(a) Total response of the irradiated cells is expressed as the product of independent responses from each radiation component ($\Lambda_{total} = \Lambda_1 \times \Lambda_2 \ldots$), which are

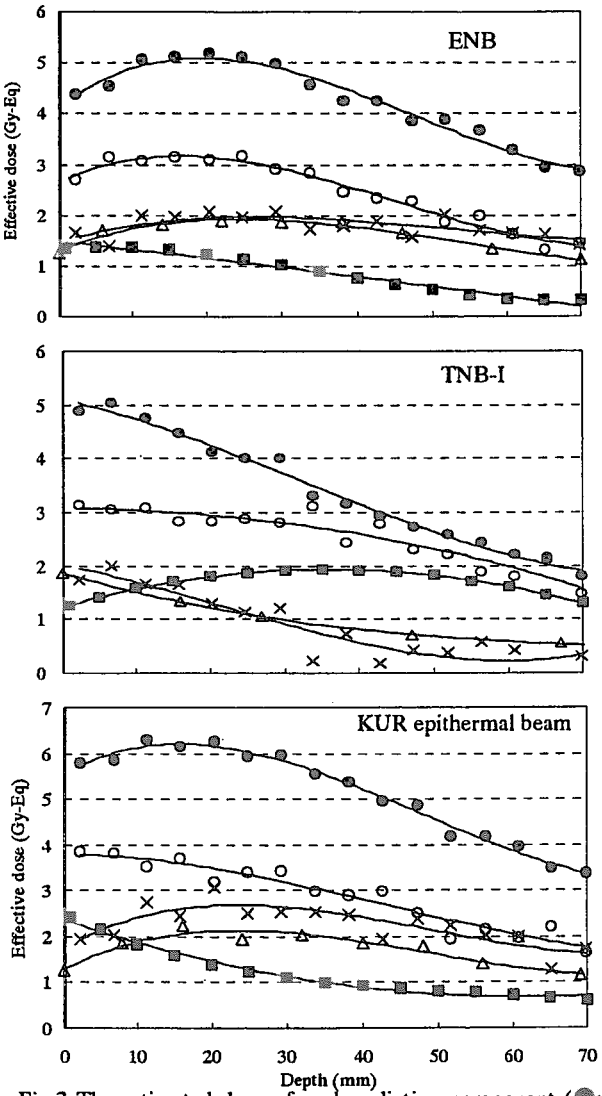

Fig.3 The estimated dose of each radiation component (●: Total dose, ○: Background dose, ×: B-10 dose, Δ: Gamma dose, ■: Combined proton dose) for ENB (upper), TNB-I (middle) and the KUR epithermal beam (lower).

derived from the B-10 dose from $^{10}B(n, \alpha)^{7}Li$; gamma dose; combined proton dose from $^{14}N(n, p)^{14}C$ and $^{1}H(n, n')p$ reactions. (b) The responses of cells to gamma photons derived from neutron irradiation and from a ^{137}Cs unit are identical [1,2].

Depth-response of irradiated cells to ENB showed a U-shape with or without ^{10}B, while that to TNB-I was linear. With ^{10}B, ENB was less effective than TNB-I beneath the phantom surface, though it was more effective at 10 mm or deeper. Without ^{10}B, there was no great difference in cell survival between ENB and TNB-I (Fig.1). The neutron fluences for ENB and TNB-I reached the maximum level at a depth of approximately 20 and 8 mm, respectively (Fig.2).

Irradiation with and without ^{10}B for ENB was less effective than that of the KUR epithermal beam. The difference between the cell survivals after irradiation by these beams tended to be prominent close to the phantom surface. The KUR epithermal beam showed a linear depth-response when irradiation was performed without ^{10}B. Contrary to the results of cell survival data, only a minor difference was seen in thermal neutron fluence and gamma ray dose between these types of beams (Fig.1, 2).

The effective dose estimation is shown in Fig.3. The maximum value of the B-10 dose for ENB and that for TNB-I were near the level of approximately 2.0 Gy-Eq. Both total and background doses of ENB were less than those of the KUR epithermal beam based on less combined proton dose.

This study described a direct method for in-phantom determination of the separated effective doses without invoking RBE values.

The difference in combined proton dose was prominent, particularly at 0 to 10mm depth, suggesting relatively less contamination of exponentially decaying fast neutrons in ENB. These data agree with more thermalized feature of ENB in free beam data, whereby fast neutron contamination per epithermal neutron is 3.1E-11 cGy-$n^{-1}cm^{-2}$, in comparison with epithermal beams at HFR or BMRR [3].

Based on the noted characteristics of ENB, further investigation should focus on the dose simulation for the clinical application of ENB to IOBNCT.

References

1. Bond VP, Laster BH and Wielopolski L, The equal effectiveness ratio: A quantitative approach to the evaluation of compounds for boron neutron capture therapy, *Radiat Res* 141, (1995), pp.287-293
2. Coderre JA, Makar MS, et al., Derivations of relative RBE for the high-LET radiations produced during boron neutron capture irradiations of the 9L rat gliosarcoma *in vitro* and *in vivo*, *Int J Radiat Oncl Biol Phys*, 28, (1993), pp.1121-1129
3. Liu HB, Brugger RM, et al., Enhancement of the epithermal neutron beam used for boron neutron capture therapy, *Int J Radiat Oncl Biol Phys*, 28, (1994), pp.1149-1156

原子炉：JRR-4　　装置：中性子ビーム設備　　分野：医療

研究テーマ：研究炉利用高度化の技術開発
表　　題：JRR-4 中性子ビームの BNCT 用新薬開発への応用

7-6

Improved *In Vitro* Cytocidal Effect in Boron Neutron Capture Therapy (BNCT) Using Boronated Mn-Metalloporphyrins

Tetsuya Yamamoto, Akira Matsumura, Tadao Nose, Kazuyoshi Yamamoto[1], Hiroaki Kumada[1]

Department of Neurosurgery, Institute of Clinical Medicine, University of Tsukuba
Department of Research Reactor, Tokai Research Establishment, JAERI[1]

Boron neutron capture therapy (BNCT) is based on the nuclear reaction between stable isotope of boron (^{10}B) and thermal neutrons which have insufficient energy to damage tissue to release high-linear energy transfer (LET) α and ^{7}Li particles trough ^{10}B(n, α) ^{7}Li reaction. In principle, BNCT allows destruction of preferentially ^{10}B-loaded tumor while normal tissue without ^{10}B is spared.

The biological problems concerning sufficient boron accumulation in tumors as well as development of neutron beam technologies are the key of successful BNCT. However, only two drugs have been employed in the recent clinical trials for BNCT: BSH and BPA[1,2].

Certain porphyrin derivatives have affinity for malignant tumors. Among the porphyrins, manganese-metalloporpphyrins were developed as low-molecular weight tumor-localizing agents with potential applications for tumor diagnosis and treatment [3]. The purpose of this study was to test the boronated manganese-metalloporphyrins as boron carriors, by determining the clonogenic *in vitro* cell survival fraction after neutron irradiation with the manganese- metalloporphyrins, and by comparing that with boric acid, BSH and BPA.

V79 cells in the stage of exponential cell growth were preincubated for 24h in Minimum Essential Medium (Sigma Chemical Co.) containing various concentrations (0, 10, 20, 30, 40 ^{10}Bμg/ml) of boron compounds, supplemented with 10% fetal bovine serum at 37 ℃ in a humidified atmosphere containing 5% CO_2. Boric acid, BSH, BPA and boronated

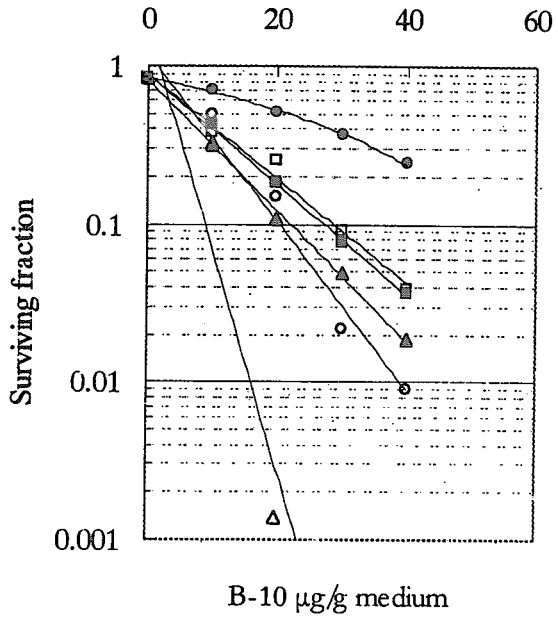

Fig.1 Clonogenic surviving fraction at a various boron levels using boric acid (-■-), BSH (-●-), BPA (-▲-), STA-BX900 (-□-), STA-BX909 (-○-) and STA-BX929 (-△-).

manganese- metalloporphyrins (STA-BX900, STA-BX909, STA-BX929) were used as the boron compounds. Samples containing 5 x 10^3 log phase cells suspended in 1ml of the conditioned medium were irradiated in polyethylene tubes for 30 minutes using the rotating irradiator at JRR-4. Thermalized beam that was generated by heavy water thickness of 33 cm and off condition of the cadmium shutter was used for the measurement: Thermal neutron beam mode II (TNB-II). After the irradiation, 200 to 400 irradiated cells were replated into each of four 6cm diameter plastic dishes for control and irradiated samples for the colony formation assay.

Clonogenic surviving fraction following the irradiation with various boron (^{10}B) levels from boron compounds was shown in Fig. 1. STA-BX929 showed the strongest effect among the compounds tested. STA-BX900 was more effective than BSH, and showed a similar level of surviving fraction with boric acid. STA-BX-909 and BPA were more effective than STA-BX900 and boric acid.

The boronated manganese-metalloporphyrins were effective as boron carriers for BNCT. In this study, the surviving fraction curves for STA-BX series showed more steeper than that of BSH (Fig.1).

ATN-10, a non-boronated type of manganese- metalloporphyrin, has the characteristics of a selectively localizing material that were confirmed by ICP-AES method and the enhancement effect on the serial magnetic resonance (MR) images in an *in vivo* experimental brain tumor model [3]. STA-BX900 was also reported as a tumor-specific contrast agent for MR imaging based on its T1 shortening effect of tissue [4]. The results of *in vivo* tissue uptake study for STA-BX909 agree with the strong cytocidal effect in the *in vitro* study [5].

BOPP, a boronated porphyrin with four boron cages in one molecular unit, achieved high boron levels in the rat brain tumor model. However, BOPP has phototoxic character and a long half-life: The animals or patients should be kept in the dark for a long period [5]. Contrary, STA-BX series have a manganese atom in the center porphyrin structure that eliminates the phototoxicity. From the clinical standpoint, the lack of the phototoxicity is of great advantage for treatment quality.

The use of boronated manganese-metalloporphyrins such as the STA-BX series may present a new opportunity for successful BNCT of brain tumors. Based on this study, further investigation for the application of the STA-BX series in IOBNCT seems to be reasonable.

References

1. Chanana AD, Capala J, Chadha M, *et al.,* Boron neutron capture therapy for glioblastoma multiforme: Interim results from the Phase I/II dose-escalation studies, *Neurosurgery,* 44, (1999), pp.1182-1193
2. Raaijmakers CPJ, Konijnenberg MW, Verhagen HW, *et al.*, Determination of dose components in phantom irradiated with an epithermal neutron beam for boron neutron capture therapy, *Med Phys* 22, (1995), 321-329
3. Yamamoto T, Matsumura A, Shibata Y, *et al.,* Mn-Metalloporphyrin (ATN-10) as a Tumor-localizing agent-MRI and ICP-AES study in experimental brain tumor, *Neurosurgery,* 45, (1998), pp.1332-1338
4. Yamamoto T, Matsumura A, Shibata Y, *et al.*, Incidence of apoptosis in neutron capture therapy using boron-porphyrin compound (STA-BX909), Recent Progress of Photodynamic Therapy. Proceedings of the 7th Annual Conference of JCIPA, Ionics, Tokyo, (1997), pp.131-135
5. Matsumura A, Shibata Y, Yamamoto T, *et al.*, A new boronated porphyrin (STA-BX909) for neutron capture therapy: An in vitro survival assay and in vivo tissue uptake study. Cancer Letters 141, (1999), pp. 203-209

7-7 INTRAOPERATIVE BORON NETURON CAPTURE THERAPY FOR MALIGNANT GLIOMAS: FIRST CLINICAL RESULTS OF TSUKUBA PHASE I/II TRIAL USING JAERI MIXED THERMAL-EPITHERMAL BEAM

A.Matsumura[1], T. Yamamoto[1], Y. Shibata[1], H. Akutsu[1], S. Yasuda[1], A. Matsushita[1], K. Nakai[1], T. Yamada[1], S.Takano[1], T.Mizutani[2], H.Takahashi[2], H.Toyooka[2], K. Yamamoto[4], H. Kumada[4], Y. Torii[4], K.Ohara[3], Y. Nakagawa[5], K. Ono [6], T. Nose[1]

Department of Neurosurgery[1], Anesthesiology[2] and Radiation Oncology[3], University of Tsukuba, Japan Atomic Energy Research Institute[4], National Kagawa Children's Hospital[5], Kyoto University Research Reactor Institute[6], Japan

ABSTRACT: Since October 1999, a clinical trial of intraoperative boron neutron capture therapy (IOBNCT) is in progress at JRR-4 in Japan Atomic Energy Research Institute (JAERI) using mixed thermal-epithermal beam (thermal neutron beam I: TNB-I). Compared to pure thermal beam (thermal neutron II: TNB-II), TNB-I has an improved neutron delivery into the deep region than TNB-II. The clinical protocol and the preliminary results will be discussed.

KEYWORDS: boron neutron capture therapy, mixed epithermal-thermal beam, intraoperative radiation therapy, JRR-4

INTRODUCTION: Boron neutron capture therapy (BNCT) is a bimodal therapy, which induce an irradiation damage to the tumor cells incorporating boron compounds. In the past, BNCT using pure thermal neutron has been applicated to over 130 patients in Japan (1). The clinical results were favorable in glioblastoma patients within 4 cm from the surface (2,3), but not better than conventional therapy (4) in patients with deeper region (3). Therefore, epithermal neutron has been developed in several institutions in the world (5,6) as well as in Japan. At JAERI, the JRR-4 was rebuilt to a research reactor which can provide pure thermal neutron beam (thermal mode II: TNB-II), mixed thermal-epithermal neutron beam (thermal mode I: TNB-I) and epithermal neutron beam (ENB). The usage of epithermal neutron can improve the thermal neutron distribution in the deeper region, which may result in better therapeutic efficacy of BNCT. After having obtained the basic beam performance data, we have initiated a clinical trial using TNB-I as a neutron source of IOBNCT. Although, the follow up period is short and the patient number treated is small, the design of the clinical trial (7) and the current preliminary results including the survival and complications will be discussed.

MATERIAL AND METHODS: Since October 1999, a new BNCT trial has been started at JRR-4 medical irradiation facility using TNB-I with intraoperative neutron irradiation. For the intraoperative radiation therapy, a fully equipped operating room, cardiorespiratory monitor and anesthetetic apparatus have been installed. For patient care during BNCT, a remote anesthetic system and cardiorespiratory monitoring have been developed and applied to the patients.

Until May 2000, five patients were entered to this clinical trial. The histological diagnosis was 3 glioblastomas (grade4) and 2 anaplastic astrocytomas (grade3). There were 1 male and 4 female and the age ranged from 20 to 66 years old (mean 45.4). The tumor was nearly totally removed in 2 cases and subtotal in 3 case.

Since, the safety margin is not yet determined by using the TNB-I, a phase I/II trial has been designed to determine the safety of IOBNCT using TNB-I. Because the dose planning system has not been completed at JAERI yet, the maximum dose at the brain surface was obtained from the measurement of gold wire which was withdrawn from the operative field 15 min. after reaching the steady power of the nuclear reactor.

The dose was calculated based on the vascular dose, which multiplies 0.33 as a weighting factor to the dose calculated from the thermal neutron fluence and the blood boron concentration. The peak B(n,α) dose was planned to 10.4Gy in normal brain the first group and dose escalation of 10% up to 13Gy is planned (n=3, for each dose) when no serious side effect is seen.

At the first tumor debulking operation, the patients were given 1 g BSH dissolved in 100ml drip infusion bottle 13 hours before the tumor debulking procedure and the blood samples were collected according to the planned time schedule. This data is used as a reference to calculate the blood boron concentration during the BNCT. The tumor sample is also obtained and maintained for boron concentration analysis.

For IOBNCT, the patients were given 100mg/kg Sodium Borocaptate (BSH) 13 hours prior to expected irradiation starting time. BSH was dissolved in 500 ml drip infusion bottle and was given intravenously for 1

hour. During the infusion, the occurrence of an allergic reaction and other adverse effects were observed.

On the day of BNCT, patients were transferred to JRR-4 and an open craniotomy under general anesthesia was performed. The irradiation angle relative to the beam port and patient's position were previously planned using simple simulation panel and phantom head based on the postoperative 3 dimensional MRI.

The irradiation time is calculated from the estimated blood boron concentration, which uses the decay curve of the 1g BSH study and the blood boron concentration directly prior to the start of neutron irradiation. The mean boron concentration during the irradiation time was used for dose calculation.

RESULTS AND DISCUSSION:

All patients are alive within the observation period from 6 to 13 months after BNCT without obvious tumor recurrence except in one case of distant recurrence (Tab.1). The postoperative MRI of case 2 is shown on Fig.1

The peak B(n,α) dose calculated from the withdrawn gold wire and prompt gamma analysis during the irradiation ranged from 9.8 to 11.4 (mean 10.5±0.58 Gy) as vascular dose of the normal brain.

In all patients, post BNCT chemotherapy was given. The protocol for chemotherapy were either ACNU + interferon or combination of ACNU, Procarbazine, Vincristine+ interferon. Follow up MRI was taken every one to two months after BNCT.

There has been one case of radiation injury that received higher dose due to the shift of the peak fluence in the margin of the target area. In other two cases, mild transient neurological damages (cranial nerve palsy in 1 case and dystharthria in 1 case) were observed. All patients, except one case are ambulant performing full activity of daily life.

From our very limited and preliminary results of IOBNCT using TNB-I, we have observed radiation effect by means of BNCT in all patients. The protocol seems to be optimal if the planned dose is kept. However, due to some technical issues, we feel that careful dose escalation should be planned because of the stronger penetrance of neutron in TNB-I and occurrence of secondary gamma in comparison to pure thermal beam mode, which has been used at JRR-2 (7). The development of the treatment planning system linked to IOBNCT is also essential in improving the clinical trial of TNB-I and ENB in the future.

In conclusions, IOBNCT using TNB-I is an effective treatment modality against malignant gliomas. Future clinical application of ENB with IOBNCT may be superior to TNB-I due to the homogeneous and better penetration of thermalized neutron around the tumor cavity (Nakai, presented at 9th ISNCT). The advantage of IOBNCT is that it can provide higher treatment dose to the lesion due to the skin reflection and void effect as compared to external irradiation of ENB(5,6).

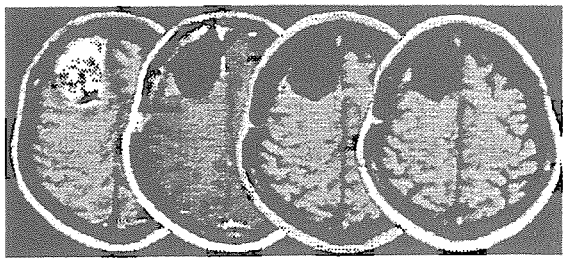

Fig.1: Pre and post BNCT MRI in a patient of glioblastoma of the right frontal lobe. Left: Preoperative MRI, Second image from left: MRI just before BNCT Third image: 4 months post-BNCT Fourtth image: 7 months post-BNCT demonstrating no recurrent tumor.

REFERENCES:

1. Hatanaka H, Nakagawa Y: Clinical Results of Long-surviving Brain Tumor Patients Who Underwent Boron Neutron Capture Therapy. Int J Radiation Oncology Biol Phys 28: 1061-1066, 1994
2. Laramore GE, Spence AM: Boron neutron capture therapy (BNCT) for high-grade gliomas of the brain: A cautionary note. Int J Radiat Oncol Biol Phys 36: 241-246, 1996
3. Ono K, Ueda S, Oda Y et al.: Boron neutron capture therapy for malignant glioma at Kyoto University reactor. Advances in Neutron Capture Therapy. Vol. I, Larsson B, Crawford J, Weinrich R eds, Elsevier, Amsterdam, pp39-45, 1997
4. The Committee of Brain Tumor Registry of Japan: Report of brain tumor registry of Japan (1969-1993) 10th edition. Neurol Med Chir , Suppl 40: 2000
5. Chanana AD, Capala J, Chadha M et al.: Boron Neutron Capture Therapy for Glioblastoma Multiforme: Interim results from the PhaseI/II Dose-Escalation Studies. Neurosurgery 44: 1182-1193, 1999.
6. Sauerwein W: The clinical project at HFR Petten – a status report. Advances in Neutron Capture Therapy. Vol. I, Larsson B, Crawford J, Weinrich R eds, Elsevier, Amsterdam, pp77-82, 1997.
7. Matsumura A, Shibata Y, Yamamoto T et al.: The University of Tsukuba BNCT research group: first

clinical experiences at JAERI. Advances in Neutron Capture Therapy. Vol. I, Larsson B, Crawford J, Weinrich R eds, Elsevier, Amsterdam, pp46-50, 1997

Table.1 Summary of cases with boron neutrona capture therapy at JRR-4 using mixed beam

Case	Age/	Diagnosis	Peak B (n,a)	Response	KPS /	outcome	FU
O.T.	55 F	GBM	10.4 Gy	CR	60→30	no rec	13M
Y.T.	46 F	GBM	10.4Gy	NT	70→100	no rec	11M
K.H.	66 M	AA	10.4Gy	PR	70 →90	remote rec	8M
M.A.	20 F	AA	11.7GY	NT	100→100	no rec	8M
I.S.	38 F	GBM	11.7 Gy	NT	90→100	no rec	6M

GBM: Glioblastoma, AA: Anaplastic Astrocytoma (Nov..2000)

Peak B (n,a): peak physical dose to normal brain

CR: Complete reponse, PR: Partial response, NT: No residual tumor

Rec: recurrence

KPS: Karnofsky Performance Scale

FU: Follow up period (months)

7-8
熱外中性子を用いた中性子捕捉療法のための基礎的・臨床的研究

Basic and Clinical Studies for Application of Epithermal Neutron Beam for Neutron Capture Therapy

筑波大学臨床医学系脳神経外科　能勢忠男、松村　明、山本哲哉、柴田　靖、吉田文代、阿久津博義、
安田　貢、松下　明、中井　啓、山田　隆、高野晋吾、
同麻酔科　水谷太郎、髙橋　宏、豊岡秀訓
同放射線科　大原　潔
日本原子力研究所研究炉利用課　山本和喜、熊田博明、鳥居義也
国立香川小児病院　中川義信
京都大学原子炉実験所　小野公二

T. Nose[1], A.Matsumura[1], T. Yamamoto[1], Y. Shibata[1], H. Akutsu[1], S. Yasuda[1], A. Matsushita[1], K. Nakai[1], T. Yamada[1], S.Takano[1], T.Mizutani[2], H.Takahashi[2], H.Toyooka[2], K. Yamamoto[4], H. Kumada[4], Y. Torii[4], K.Ohara[3], Y. Nakagawa[5], K. Ono[6],

Department of Neurosurgery[1], Anesthesiology[2] and Radiation Oncology[3], University of Tsukuba, Japan Atomic Energy Research Institute[4], National Kagawa Children's Hospital[5], Kyoto University Research Reactor Institute[6], Japan

1. OBJECTIVE OF THE PROJECT

The purpose of this study was to develop a new system for boron neutron capture threpay at JRR-4.

J RR-4 is a newly developed research reactor which can provide thermal beam (Thermal beam mode II: TNB-II), mixed thermal and epithermal beam (Thermal beam mode I: TNB-I) and eptithermal beam (Epithermal beam mode: ENB).

By using this facility, basic physical and biological character of each beam mode should be obtained. Based on these data, clinical trial was initiated.

Other related projects, such as boron concentration measurement, development of dose planning system and patient positioning system is under developement.

2. BASIC RADIOBIOLOGICAL STUDY OF VARIOUS NEUTRON MODES AT JRR-4

2.1. INTRODUCTION

In 1998, a medical irradiation facility including exclusive hospital-type operating room for intraoperative BNCT (IOBNCT) was installed in Japan Research Reactor No.4 (JRR-4) which simultaneously became capable of epithermal (epithermal neutron beam mode: ENB) and mixed thermal-epithermal (thermal neutron beam mode I: TNB-I) beams in addition to pure thermal beam. In this study, in-phantom characteristics of ENB, TNB-I and epithermal beam of Kyoto University Research Reactor (KUR) were evaluated in combination with clonogenic cell survival assay and dosimetry.

2.2. MATERIAL AND METHODS

Irradiations of cells and dosimeters were carried out in a 186 mm-diameter cylinder polymethyl-methacrylate (PMMA) phantom filled with distilled water using ENB, TNB-I and KUR epithermal beam. Activation of gold wires and foils were counted with a simultaneous β-γ coincidence counting device (γ detector: 3 x 3 in NaI (Tl) scintillator, β detector: 2 x 0.118 in plastic scintillator) then thermal neutron fluence was calculated by foil activation method. Gamma ray dose was measured with thermoluminescent dosimeter (TLD) covered with quartz glass (Panasonic 170LS). V79 cells in exponential cell growth were preincubated for 1h in Modified Eagle's Medium (Sigma Chemical Co.), supplemented with 10% fetal bovine serum with (5 μ g ^{10}B/ml) or without boric acid. A 384-well plate was filled with conditioned medium and cells in suspension, and followed by irradiation with each neutron beam for the colony formation assay. Thermal neutron fluence for each beam was aimed to be 2.5E+12 cm^{-2} in the maximum value. Both the cell survival assay and dosimetry were repeated at lest three times.

The clonogenic cell survival data were analyzed to estimate effective dose of radiation components under the following assumptions:(a) Total response of the irradiated cells are derived from B-10 dose from ^{10}B(n, α)^{7}Li, gamma dose, nitrogen (N) dose from ^{14}N(n, p)^{14}C, fast neutron dose from ^{1}H(n, n')p and expressed as multiplication of independent response from each

radiation component. (b) The responses of cells to gamma photons derived from neutron irradiation and from a ^{137}Cs unit are identical[1,2].

2.3. RESULTS AND DISCUSSION

Depth-response of irradiated cells to ENB showed U-shape regardless of with or without ^{10}B, while those to TNB-I was linear. With ^{10}B, ENB was less effective than TNB-I beneath the phantom surface, and was more effective at 10 mm or deeper. Without ^{10}B, there was no great difference in cell survival between ENB and TNB-I (Fig.1). The neutron fluence for ENB and TNB-I reached the maximum level at a depth of approximately 20 and 8 mm, respectively. The maximum thermal neutron flux for ENB and TNB-I were 1.13 and 1.61E+9$cm^{-2}sec^{-1}MW^{-1}$, respectively. The maximum gamma doses rate for ENB and TNB-I were 3.51 and 5.03 Gy $h^{-1}MW^{-1}$, respectively (Fig.2).

Irradiation with and without ^{10}B for ENB was less effective than that of KUR epithermal beam. Difference between the cell survival in these beams tended to be prominent as close to the phantom surface. KUR epithermal beam showed linear depth-response when irradiation was performed without ^{10}B. (Fig.1). Contrary to the results of cell surviving data, only a minor difference was seen in thermal neutron fluence and gamma ray dose in both beams (Fig.2).

The effective dose estimation was shown in Fig.3. The maximum value of B-10 dose for ENB and TNB-I were near level of approximately 2.0 Gy-Eq, respectively. Difference in total dose at deep portion between ENB and TNB-I mainly comprised of B-10 dose and gamma dose. Both total and background doses of ENB were less than those of KUR epithermal beam based on the less N plus fast neutron dose compared to KUR epithermal beam. Difference in this dose was prominent especially at 0 to 10mm depth suggesting the relatively less contamination of exponentially decaying fast neutron in ENB. These data agree with rather thermalized feature of ENB in free beam data whereby fast neutron contamination per epithermal neutron is 3.1E-11 $cGy\text{-}n^{-1}cm^{-2}$ compared to epithermal beams at HFR or BMRR[3]. For facilitating neutron penetration to deep-seated lesion, skin reflection and craniotomy are accompanied to the usage of "void" within the post-surgical cavity in the current procedure of IOBNCT with mixed thermal-epithermal beam.

In conclusion, ENB can compensate for relative insufficient delivery of thermal neutrons in deep-seated lesion minimizing excessive fast neutron dose at the phantom surface. Based on such characteristics of ENB, further investigation should focus on the clinical dose simulation for the application of ENB to IOBNCT.

2.4. REFERENCES

1. Bond VP, Laster BH and Wielopolski L, *Radiat Res*, 141 (1995) 287-293.
2. Coderre JA, Makar MS, et al., *Int J Radiat Oncl Biol Phys*, 28 (1993) 1121-1129.
3. Liu HB, Brugger RM, et al., *Int J Radiat Oncl Biol Phys*, 28 (1994) 1149-1156.

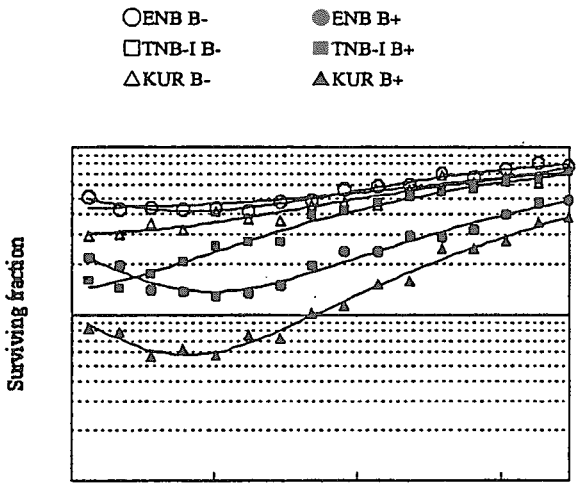

Fig.1 Depth-response curve of cells irradiated with ENB, TNB-I and KUR epithermal beam

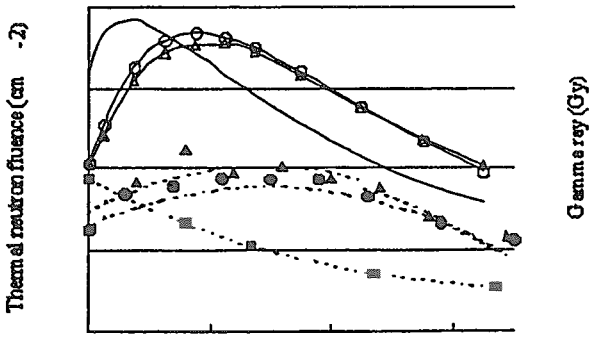

Fig.2 Thermal neutron fluence and gamma dose distribution for ENB(○, ●), TNB-I(△, ▲) and KUR(□, ■) epithermal beam

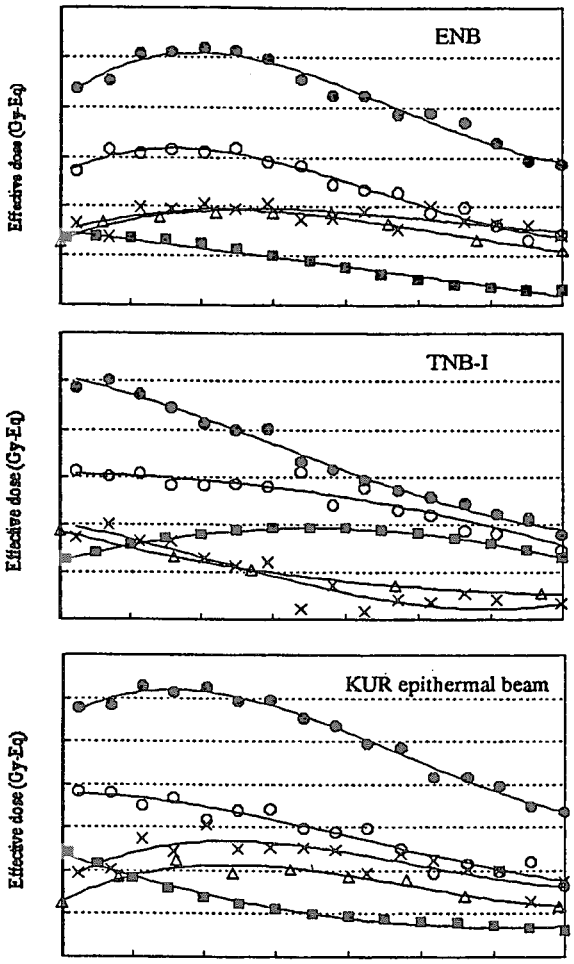

Fig.3 Estimated dose of each radiation component (●: Total dose, ○: Background dose, ×: B-10 dose, △: Gamma dose, ■: N plus fast neutron dose) for ENB (upper), TNB-I (middle) and KUR epithermal beam (lower).

3. PHASE I/II STUDY OF INTRAOPERATIVE BORON NEUTRON CAPTURE THERAPY USING MIXED THERMAL AND EPITHERMAL BEAM AT JRR-4

3.1. INTRODUCTION

Boron neutron capture therapy (BNCT) is a bimodal therapy, which induce an irradiation damage to the tumor cells incorporating boron compounds. In the past, BNCT using pure thermal neutron has been applicated to over 130 patients in Japan (1). The clinical results were favorable in glioblastoma patients within 4 cm from the surface (2,3), but not better than conventional therapy (4) in patients with deeper region (3). Therefore, epithermal neutron has been developed in several institutions in the world (5,6) as well as in Japan. At JAERI, the JRR-4 was rebuilt to a research reactor which can provide pure thermal neutron beam (thermal mode II: TNB-II), mixed thermal-epithermal neutron beam (thermal mode I: TNB-I) and epithermal neutron beam (ENB). The usage of epithermal neutron can improve the thermal neutron distribution in the deeper region, which may result in better therapeutic efficacy of BNCT. After having obtained the basic beam performance data, we have initiated a clinical trial using TNB-I as a neutron source of IOBNCT. Although, the follow up period is short and the patient number treated is small, the design of the clinical trial (7) and the current preliminary results including the survival and complications will be discussed.

3.2.MATERIAL AND METHODS

Since October 1999, a new BNCT trial has been started at JRR-4 medical irradiation facility using TNB-I with intraoperative neutron irradiation. For the intraoperative radiation therapy, a fully equipped operating room, cardiorespiratory monitor and anesthetetic apparatus have been installed. For patient care during BNCT, a remote anesthetic system and cardiorespiratory monitoring have been developed and applied to the patients.

Until May 2000, five patients were entered to this clinical trial. The histological diagnosis was 3 glioblastomas (grade4) and 2 anaplastic astrocytomas (grade3). There were 1 male and 4 female and the age ranged from 20 to 66 years old (mean 45.4). The tumor was nearly totally removed in 2 cases and subtotal in 3 case.

Since, the safety margin is not yet determined by using the TNB-I, a phase I/II trial has been designed to determine the safety of IOBNCT using TNB-I. Because the dose planning system has not been completed at JAERI yet, the maximum dose at the brain surface was obtained from the measurement of gold wire, which was withdrawn from the operative field 15 min. after reaching the steady power of the nuclear reactor.

The dose was calculated based on the vascular dose, which multiplies 0.32 as a weighting factor to the dose calculated from the thermal neutron fluence and the blood boron concentration. The peak $B(n,\alpha)$ dose was planned to 10.4Gy in normal brain the first group and dose escalation of 10% up to 13Gy is planned (n=3, for each dose) when no serious side effect is seen.

At the first tumor debulking operation, the patients were given 1 g BSH dissolved in 100ml drip infusion bottle 13 hours before the tumor debulking procedure and the

blood samples were collected according to the planned time schedule. This data is used as a reference to calculate the blood boron concentration during the BNCT. The tumor sample is also obtained and maintained for boron concentration analysis.

For IOBNCT, the patients were given 100mg/kg Sodium Borocaptate (BSH) 13 hours prior to expected irradiation starting time. BSH was dissolved in 500 ml drip infusion bottle and was given intravenously for 1 hour. During the infusion, the occurrence of an allergic reaction and other adverse effects were observed.

On the day of BNCT, patients were transferred to JRR-4 and an open craniotomy under general anesthesia was performed. The irradiation angle relative to the beam port and patient's position were previously planned using simple simulation panel and phantom head based on the postoperative 3 dimensional MRI.

The irradiation time is calculated from the estimated blood boron concentration, which uses the decay curve of the 1g BSH study and the blood boron concentration directly prior to the start of neutron irradiation. The mean boron concentration during the irradiation time was used for dose calculation.

3.3. RESULTS AND DISCUSSION

All patients are alive within the observation period from 3 to 9 months after BNCT without obvious tumor recurrence (Fig.4).

The peak B(n,α) dose calculated from the withdrawn gold wire and prompt gamma analysis during the irradiation ranged from 9.8 to 11.4 (mean 10.5±0.58 Gy) as vascular dose of the normal brain.

In all patients, post BNCT chemotherapy was given. The protocol for chemotherapy were either ACNU + interferon or combination of ACNU, Procarbazine, Vincristine+ interferon. Follow up MRI was taken every one to two months after BNCT.

There has been one case of radiation injury that received higher dose due to the shift of the peak fluence in the margin of the target area. In other two cases, mild transient neurological damages (cranial nerve palsy in 1 case and dystharthria in 1 case) were observed. All patients, except one case are ambulant performing full activity of daily life.

From our very limited and preliminary results of IOBNCT using TNB-I, we have observed radiation effect by means of BNCT in all patients. The protocol seems to be optimal if the planned dose is kept. However, due to some technical issues, we feel that careful dose escalation should be planned because of the stronger penetrance of neutron in TNB-I and occurrence of secondary gamma in comparison to pure thermal beam mode, which has been used at JRR-2 (7). The development of the treatment planning system linked to IOBNCT is also essential in improving the clinical trial of TNB-I and ENB in the future.

In conclusions, IOBNCT using TNB-I is an effective treatment modality against malignant gliomas. Future clinical application of ENB with IOBNCT may be superior to TNB-I due to the homogeneous and better penetration of thermalized neutron around the tumor cavity (Yamamoto, in preparation). The advantage of IOBNCT is that it can provide higher treatment dose to the lesion due to the skin reflection and void effect as compared to external irradiation of ENB(5,6).

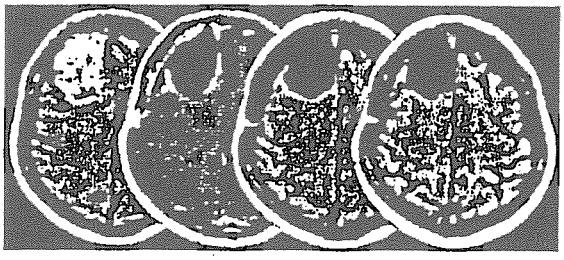

Fig.4: Pre and post BNCT MRI in a patient of glioblastoma of the right frontal lobe. Left: Preoperative MRI, second image from left: MRI just before BNCT and the remaining images are follow up MRI post-BNCT demonstrating no residual or recurrent tumor at the time of examination up to 7months.

3.4. REFERENCES

1. Hatanaka H, Nakagawa Y: Clinical Results of Long- surviving Brain Tumor Patients Who Underwent Boron Neutron Capture Therapy. Int J Radiation Oncology Biol Phys 28: 1061-1066, 1994
2. Laramore GE, Spence AM: Boron neutron capture therapy (BNCT) for high-grade gliomas of the brain: A cautionary note. Int J Radiat Oncol Biol Phys 36: 241-246, 1996
3. Ono K, Ueda S, Oda Y et al.: Boron neutron capture therapy for malignant glioma at Kyoto University reactor. Advances in Neutron Capture Therapy. Vol. I, Larsson B, Crawford J, Weinrich R eds, Elsevier, Amsterdam, pp39-45, 1997
4. The Committee of Brain Tumor Registry of Japan: Report of brain tumor registry of Japan (1969-1993)

10th edition. Neurol Med Chir , Suppl 40: 2000

5. Chanana AD, Capala J, Chadha M et al.: Boron Neutron Capture Therapy for Glioblastoma Multiforme: Interim results from the Phasel/II Dose-Escalation Studies. Neurosurgery 44: 1182-1193, 1999.
6. Sauerwein W: The clinical project at HFR Petten – a status report. Advances in Neutron Capture Therapy. Vol. I, Larsson B, Crawford J, Weinrich R eds, Elsevier, Amsterdam, pp77-82, 1997.
7. Matsumura A, Shibata Y, Yamamoto T et al.: The University of Tsukuba BNCT research group: first clinical experiences at JAERI. Advances in Neutron Capture Therapy. Vol. I, Larsson B, Crawford J, Weinrich R eds, Elsevier, Amsterdam, pp46-50, 1997

4. FUTURE PLAN

Based on the basic experiments, we have initiated a clinical trial of intraoperative boron neutron capture therapy at JRR-4 using mixed thermal and epithermal beam. The response to treatment are well and the patients are being observed for long term.

In the future project, it is planned to use epithermal beam for intraoperative boron neutron capture therapy, which will require completion of the JAERI computer dosimetry system for the treatment planning. The patient setting system has to be also completed to obtain correct position and angle towards the beam port for optimum dose distribution. This project should be continued in collaboration of JAERI group as well as other group involved in this research.

5. ACKNOWLEDGMENT

The authors would like to express their gratitude to Research Center for Nuclear Science and Technology, University of Tokyo, especially to Prof. Y.Itoh who always has supported this research project.

This project has been supported in part by The Inter-University Program for the Common Use of JAERI Facilities, by the Tsukuba University Research Project A and Grant-in-Aid for University and Society Collaboration from the Ministry of Education, Scince, Sports and Culture (11794021).

LIST OF PUBLICATIONS

1. Matsumura A, Shibata Y, Yamamoto T, Yoshida F, Isobe T, Nakai K, Hayakawa Y, Kiriya M, Shimojo N, Ono K, Sakata I, Nakajima S, Okumura M, Nose T: A new boronated porphyrin (STA-BX909) for neutron capture therapy: An in vitro survival assay and in vivo tissue uptake study. Cancer Letters 141: 203-209, 1999.
2. Matsumura A, Shibata Y, Yamamoto T, Yoshida F, Nakai K, Nose T, Sakata I, Nakajima S, Miwa N: Development of new boronated porphyrins for neutron capture therapy. Porphyrins 7: 150-157, 1998
3. Shibata Y, Matsumura A, Yamamoto T, Nakagawa K, Yoshii Y, Nose T, Sakata I, Nakajima S, Hayakawa Y, Ono K: Neutron Capture Therapy with a new boron compound in the rat 9L glioma model. J Exp Clin Cancer Res 17: 285-289, 1998.
4. Shibata Y, Matsumura A, Yoshida F, Yamamoto T, Nakai K, Nose T, Sakata I, Nakajima S: Cell cycle dependency of Porphyrin uptake in glioma cell line: Flow cytometry analysis. Cancer Letters 129: 77-85, 1998.
5. Yamamoto T, Matsumura A, Shibata Y, Fujimori H, Nakai K, Yoshida F, Nose T, Sakata I, Nakajima S, Miwa N: Manganese-metalloporphyrin (ATN-10) as a Tumor-localizing Agent: Magnetic Resonance Imaging and Inductively Coupled Plasma Atomic Emission Spectroscopy Study with Experimental Brain Tumors. Neurosurgery 42: 1332-1338, 1998
6. 松村　明、能勢忠男：中性子捕捉現象を利用した癌細胞選択的治療法。注目される中性子反応化合物を利用した手法。化学と生物：35: 336-338, 1997.
7. 松村　明、能勢忠男：中性子捕捉療法の現状と将来展望。ISOTOPE NEWS 9 月号, 7-11, 1997
8. Matsumura A, Shibata Y, Yamamoto T, Yamada T, Fujimori H, Nakai K, Nakagawa Y, Hayakawa Y, Isshiki M, Nose T: The University of Tsukuba BNCT research group: first clinical experiences at JAERI. Advances in Neutron Capture Therapy. Larsson B, Crawford J, Weinrich R eds.: Vol.1 Elsevier, Amsterdam, pp46-50, 1997
9. Matsumura A, Shibata Y, Yamamoto T, Fujimori H, Nakai K, Sakata I, Miwa N, Nakajima S, Nose T: Pharmacokinetic study of boronated metalloporphyrin (STA-BX900) and BSH in the 9L rat glioma model. Advances in Neutron Capture Therapy. Larsson B, Crawford J, Weinrich R eds.: Vol.II. Elsevier, Amsterdam, pp158-162, 1997
10. Shibata Y, Matsumura A, Yamamoto A, Nakagawa K, Yoshii Y, Nose T, Sakata I, Nakajima S, Hayakawa H, Ono K: Histologic changes in the rat 9L glioma after BNCT with a BSH-porphyrin compound. Advances in Neutron Capture Therapy. Larsson B, Crawford J, Weinrich R eds.: Vol.II, Elsevier, Amsterdam, pp. 501-506 , 1997
11. Yamamoto T, Matsumura A, Shibata Y, Yoshizawa T, Fujimori H, Nakagawa K, Nakai K, Yoshii Y, Nose T, Sakata I, Nakajima S: MR imaging using boronated Mn-metalloporphyrin (STA-BX900) for BNCT. Advances in Neutron Capture Therapy. Larsson B, Crawford J, Weinrich R eds.: Vol.II Elsevier, Amsterdam, pp267-270, 1997
12. Fujimori H, Matsumura A, Yamamoto T, Shibata Y, Yoshizawa T, Nakagwa K, Yoshii Y, Nose T, Sakata I, Nakajima S: Tumor Specific Contrast Enhancement Study of Mn-Metalloporphyrin (ATN-10). Comparison of Rat Brain Tumor Model, Cytotoxic and Vasogenic Models. Acta Neurochir (1997) [Suppl] 70: pp167-169, 1997.
13. Matsumura A, Shibata Y, Yamamoto T, Yoshida F, Nakai K, Kiriya M, Shimojo N, Hayakawa Y, Nose T, Nakajima S, Sakata I, Miwa N, Itoh Y: Radiobiological Effects of Boronated porphyrin (STA-BX909) as a

compound for neutron capture therapy. An In vitro study. Recent Progress of Photodynamic Therapy. Proceedings of the 7th Annual Conference of JCIPA. Ionics, Tokyo, pp125-130, 1997.

14. Yamamoto T, Matsumura A, Shibata Y, Yoshida F, Nakai K, Nose T, Hayakawa Y, Horiguchi Y, Aizawa M, Nakajima S, Sakata I, Miwa N: Incidence of Apoptosis in Neutron Capture Therapy Using Boron-Porphyrin Compound (STA-BX909). Recent Progress of Photodynamic Therapy.Proceedings of the 7th Annual Conference of JCIPA. Ionics, Tokyo, pp131-135, 1997.

15. Matsumura A, Shibata Y, Nakagawa K, Yamamoto T, Yoshizawa T, Yoshii Y, Nose T Sakata I, Nakajima S, Miwa N: Gadolinium-, Boron-Porphyrin Derivatives for Neutron Capture Therapy. MRI and ICP Study Using 9L Rat Model. Cancer Neutron capture Therapy. Mishima Y ed. Plenum Press, New York, 1996, pp245-250

16. Shibata Y, Matsumura A, Nakagawa K, Yamamoto T, Yoshii Y, Nose T Sakata I, Nakajima S: The Measurement of Gadolinium Concentration in Rat Brain Tumor with NMR Analyzer for Neutron Capture Therapy. Cancer Neutron capture Therapy. Mishima Y ed. Plenum Press, New York, 1996, pp251-255

PRESENTATION

1. 松村　明、山本哲哉、柴田　靖、中井　啓、高野晋吾、阿久津博義、能勢忠男、桜井文雄、早川吉則：新しい中性子源（熱外中性子）を用いた中性子捕捉療法の臨床応用に向けての展望。第 58 回日本脳神経外科学会総会、1999 年 10 月、東京。
2. 山本哲哉、松村　明、柴田　靖、中井　啓、能勢忠男、岸　敏明、熊田博明、鳥居義也、山本和喜：JRR-4 熱外中性子ビームの線量分布および in vitro 中性子捕捉療法(BNCT)での細胞殺傷効果。第 58 回日本脳神経外科学会総会、1999 年 10 月、東京。
3. 山本和喜、鳥居義也、熊田博明、岸　敏明、高田準太郎、大竹真一、山本哲哉、松村　明、能勢忠男：悪性脳腫瘍治療における JRR-4 中性子ビーム設備におけるファントム内熱中性子分布。第 58 回日本脳神経外科学会総会、1999 年 10 月、東京。
4. 柴田　靖、松村　明、山本哲哉、中井　啓、吉田文代、阿久津博義、能勢忠男、阪田　功、中島　進：脳腫瘍細胞への porphyrin と LDL の取り込みの解析。第 58 回日本脳神経外科学会総会、1999 年 10 月、東京。
5. 松村　明、柴田　靖、山本哲哉、中井　啓、高野晋吾、坪井康次、能勢忠男、山田　隆、阿久津博義：新しい医療用原子炉を用いた悪性神経膠腫に対する中性子捕捉療法。第 21 回茨城医学会脳神経外科分科会（第 46 回茨城県脳神経外科集談会)、1999 年 10 月、水戸。
6. 松村　明、山本哲哉、柴田　靖、中井　啓、高野晋吾、阿久津博義、能勢忠男、水谷太郎、高橋宏、豊岡秀訓：悪性グリオーマに対する中性子捕捉療法。選択的腫瘍照射および 1 回照射による QOL 改善の試み。第 18 回ニューロオンコロジーの会、1999 年 12 月、東京。
7. Matsumura A, Sakurai F, Shibata Y, Yamamoto T, Nakai K, Torii Y, Yokoo K, Horiguchi Y, Nakagawa Y, Nose T: Planning of BNCT using a new medical irradiation facility at JRR4. XI Scandinavian Congress of Clinical Physiology, III Nordic Congress of Nuclear Medicine and Post-Congress Symposium on Clnical Physics, Helsinki, Finnland. 1998
8. Matsumura A, Shibata Y, Yamamoto T, Hayakawa Y, Nakai K, Nakagawa Y, Sakurai F, Torii Y, Yokoo K, Akine Y, NoseT : Clinical protocol using new neutron irradiation facility (JRR4) at JAERI. Eighth International

Symposium on Neutron Capture Therapy for Cancer. San Diego. 1998

9. Matsumura A, Shibata Y, Yamamoto T,Yoshida F, Hatyakawa Y, Isobe T, Nakai K, Sakata I, Nakajima S, Miwa N, Ono K, NoseT : Radiobiological effects of boronated porphyrin (STA-BX909) compared to BSH in cultured glioma cell line. Eighth International Symposium on Neutron Capture Therapy for Cancer. San Diego. 1998

10. Matsumura A, Shibata Y, Yamamoto T,Yoshida F, Nakai K, Sakata I, Nakajima S, Miwa N, NoseT : In vivo and In vitro pharmacokinetics of boronated porphyrins for neutron capture therapy. Eighth International Symposium on Neutron Capture Therapy for Cancer. San Diego. 1998

11. Shibata Y, Matsumura A, Yoshida F, Yamamoto T, Nakai K, Nose T, Sakata I, Nakajima S: Porphyrin uptake in glioma cell line: Cell cycle analysis using flowcytometry. Eighth International Symposium on Neutron Capture Therapy for Cancer. 13-18 Sep.1998, San Diego.

12. Shibata Y, Matsumura A, Yoshida F, Yamamoto T, Nakai K, Nose T, Sakata I, Nakajima S: Cell cycle changes of 9L glioma cell after in vitro boron neutron capture therapy. Eighth International Symposium on Neutron Capture Therapy for Cancer. 13-18 Sep.1998, San Diego.

13. Kumada H, Torii Y, Saito K, Yamaguchi Y, Matsumura A, Nakagawa Y, Sakurai F: A development of computation dosimetry system for BNCT at JRR-4. Eighth International Symposium on Neutron Capture Therapy for Cancer. 13-18 Sep.1998, San Diego.

14. Yamamoto T, Matsumura A, Shibata Y, Yoshida F, Nakai K, NoseT, Horiguchi Y, , Aizawa M, Nakajima S, Sakata I: Incidence of apoptosis in tumor neutron capture therapy. Eighth International Symposium on Neutron Capture Therapy for Cancer. 13-18 Sep.1998, San Diego.

15. Matsumura A, Sakurai F, Shibata Y, Yamamoto T, Nakai K, Torii Y, Yokoo K, Horiguchi Y, Nakagawa Y, Nose T: Planning of BNCT using a new medical irradiation facility at JRR4. XI Scandinavian Congress of Clinical Physiology, III Nordic Congress of Nuclear Medicine and Post-Congress Symposium on Clnical Physics, 12.June, 1998, Helsinki, Finnland.

16. 松村 明、柴田 靖、山本哲哉、吉田文代、中井 啓、磯辺智範、小野公二、能勢忠男：熱外中性子による中性子捕捉療法のための基礎的検討。第57回日本脳神経外科学会総会、1998年10月16日、札幌

17. 柴田 靖、松村 明、山本哲哉、中井 啓、吉田文代、能勢忠男、阪田功、中島 進、小野公二：中性子捕捉療法(BNCT) による in vitro 脳腫瘍細胞の細胞周期変化（第 2 報）熱外中性子による効果。第57回日本脳神経外科学会総会、1998年10月15日、札幌。

18. 松村 明、柴田 靖、山本哲哉、吉田文代、中井 啓、高野晋吾、増永慎一朗、小野公二、能勢忠男：悪性脳腫瘍に対する中性子捕捉療法の放射線生物学的な基礎検討。第 7 回日本脳腫瘍カンファレンス、1998年11月9日、金沢。

19. 柴田 靖、松村 明、山本哲哉、中井 啓、吉田文代、能勢忠男、阪田 功、中島 進：脳腫瘍細胞に対する中性子捕捉療法の細胞周期変化の検討。第 7 回日本脳腫瘍カンファレンス、1998 年 11 月9日、金沢。

20. 松村 明、柴田 靖、山本哲哉、吉田文代、中井 啓、磯辺智範、小野公二、能勢忠男：新しいボロン化合物を用いた中性子捕捉による放射線生物学的効果の検討。日本放射線腫瘍学会第 11 回学術大会、1998年11月22日。

21. 中井 啓、松村 明、柴田 靖、山本哲哉、高野晋吾、能勢忠男、稲留征典、野口雅之：脳腫瘍症例検討；ボロン中性子捕捉療法を施行した Glioblastoma 剖検例の検討。 日本放射線腫瘍学会第 11

回学術大会、1998年11月22日。

２２．　松村　明：9L グリオザルコーマ培養細胞系に対する熱および熱外中性子の放射線生物学的効果。京都大学原子炉実験所平成９年度専門研究会「加速器と原子炉を組み合わせた中性子捕捉療法用照射場の最適化」京都大学原子炉実験所、大阪、1998

２３．　松村　明、柴田　靖、山本哲哉、中井　啓、能勢忠男、吉田文代、阪田　功、中島　進、三輪直人：ボロンポルフィリン化合物を用いた中性子捕捉療法の 9L gliosarcoma 細胞系に対する放射線生物学的の検討。加速器と原子炉を組み合わせた中性子捕捉療法用照射場の最適化専門研究会。大阪、1997

２４．　Matsumura A, Yasushi Shibata, Tetsuya Yamamoto, Takashi Yamada , Hiroyuki Fujimori, Kei Nakai, Yoshinobu Nakagawa , Yoshinori Hayakawa , Masahiko Isshiki, Tadao Nose: The University of Tsukuba BNCT Research Group. First Clinical Experiences at JAERI.7th Interenational Symposium on Neutron Capture Therapy for Cancer. Zurich, Switzerland, Sep, 1996

２５．　Matsumura A, Shibata Y, Yamamoto T , Fujimori H, Nakai K, Sakata I, Miwa N, Nakajima S, Nose T: Pharmacokinetic Study of STA-BX900 and BSH in the 9L Rat Glioma Model. 7th Interenational Symposium on Neutron Capture Therapy for Cancer. Zurich, Switzerland. Sep, 1996

２６．　Fujimori H, Matsumura A, Shibata Y,Yamamoto T,Nakagawa K, Hayakawa Y, Isshiki M, Yoshii Y, Nose T:The distribution of neutron fluxes of the rat brain tumor model :A basic study. 7th Interenational Symposium on Neutron Capture Therapy for Cancer. Sep.1996, Zurich, Switzerland.

２７．　T.Yamamoto, A. Matsumura, Y. Shibata, T. Yoshizawa, H. Fujimori, K. Nakagawa, K.Nakai, Y.Yoshii, T. Nose, I. Sakata, S. Nakajima: MR Imaging Using Mn-Metalloporphyrin (STA-BX900) as A Tumor Localizing Agent for Boron Neutron Capture Therapy. 7th Interenational Symposium on Neutron Capture Therapy for Cancer. Sep.1996, Zurich, Switzerland.

２８．　Y. Shibata, A. Matsumura, T. Yamamoto, K. Nakagawa, Y. Yoshii, T. Nose, I. Sakata , S. Nakajima, Y. Hayakawa, K. Ono : Histological changes of the rat 9L glioma model after neutron capture therapy with Boron-porphyrin compound. 7th Interenational Symposium on Neutron Capture Therapy for Cancer. Sep.1996, Zurich, Switzerland.

２９．　Fujimori H, Matsumura A, Yamamoto T, Shibata Y, Yoshizawa T, Nakagawa K, Yoshii Y, Nose T, Sakata I, Nakajima S: Tumor specific contrast enhancement study of metalloporphyrin (ATN-10). Comparison of rat brain tumor model, cytotoxic and vasogenic edema model. Brain Edema IX. 20.10.-22.10.1996, San Diego, USA.

３０．　松村　明、柴田　靖、山本哲哉、中井　啓、木村　泰、吉井與志彦、能勢忠男、中島　進、阪田　功、三輪直人: 中性子捕捉療法のためのボロンポルフィリン化合物の開発。STA-BX909, 910 の MRI 画像および組織内濃度の検討。第６回国際光化学治療学会日本支部例会、１９９６年１１月９日，岡山。

３１．　山本哲哉、松村　明、柴田　靖、藤森広幸、能勢忠男、中島　進、阪田　功：実験脳腫瘍での Mn-Metalloporphyrin (ATN-10)による増強 MRI。第６回国際光化学治療学会日本支部例会、１９９６年１１月９日，岡山。

３２．　班会議平成７年度重点研究（１）小野班第２回班会議：松村　明、柴田　靖、山本哲哉、中井　啓、能勢忠男、早川吉則、阪田　功、中島　進、三輪直人、小野公二：５ボロン－ポルフィリン化合物を用いた中性子捕捉療法の基礎的検討。１９９６年２月２日。KKR 京都くに荘、京都。

PRESENTATIONS (SYMPOSIUM&INVITED)

1．松村　明：熱外中性子による新しい中性子捕捉療法の展開。第 23 回日本脳神経 CI 学会総会シンポジウム：21 世紀の Radiosurgery の行方。横浜、2000 年 1 月

2．Matsumura A: Basic study for application of epithennal neutron capture therapy. - In vitro cell study and physical dosimetry -. Joint Research Center of European Comission at Petten, Netherland, Dec 6, 1999

3．Matsumura A: Medical Set Up and Basic Dosimetry for Neutron Capture Therapy. VTT and Helsinki University, Dec 8, 1999.

4．山本哲哉、松村　明、柴田　靖、中井　啓、能勢忠男、岸　敏明、熊田博明、鳥居義也、山本和喜：ホウ素中性子捕捉療法(BNCT)における熱外中性子ビーム導入と開頭術中照射のためのファントム内熱中性子２次元分布測定。日本放射線腫瘍学会第 12 回学術大会、1999 年 11 月、横浜。（要望演題）

5．松村　明、柴田　靖、山本哲哉、吉田文代、高野晋吾、中井　啓、能勢忠男、大原　潔、桜井文雄、熊田博明、岸　敏明、鳥居義也、早川吉則：熱外中性子を用いた新しい粒子線治療の基礎的・臨床的研究。“ワークショップ 11 ：粒子線を用いた新しい癌治療”第 37 回日本癌治療学会総会、1999 年 10 月、岐阜。

6．山本哲哉、松村　明、能勢忠男、柴田　靖、中井　啓、岸　敏明、熊田博明、山本和喜、高柳政二 、鳥居義也、桜井文雄：JRR-4 各ビームを用いたファントム内 In vitro 照射での Depth-Response Curve.第２回 BNCT セミナー。1999 年 8 月、仙台。

7．Yamamoto T, Matsumura A, Nose T, Shibata Y, Nakai K, Sakurai F, Kishi T, Kumada T, Yamamoto K, Torii Y: Medical Set up of BNCT for malignant glioma at JRR-4. Technical comittee meeting (TCM) on research Reactor Utilization for Neutron Capture Therapy. International Atomic Energy Agency (IAEA). June,1999, Vienna.

8．Matsumura A, Shibata Y, Yamamoto T, Nakai K, Nose T, Sakata I, Nakajima S, Miwa N: Symposium: Recent Progress in Basic Research in Photodynamic Therapy.Development of boronated porphyrin for neutron capture therapy. The 4th International Symposium-Heme Symposium Oct.2.1998, Yonago, Japan

9．松村　明、能勢忠男、柴田　靖、山本哲哉、中井　啓、吉井與志彦、高野晋吾、早川吉則、秋根康之、一色正彦、桜井文雄、中川義信：医療用原子炉を用いた悪性脳腫瘍に対する粒子線治療の近未来展望。第 56 回日本脳神経外科学会総会、特別ワークショップ関連演題、1997

１０．　松村　明、能勢忠男：パネルデイスカッション。研究用原子炉を用いた研究の動向と新展開。ホウ素中性子捕捉療法。第３４回理工学における同位素元素研究発表会講演要旨集、p229-230,1997

１１．　Matsumura A: Panel Discussant "Summary, Round Table Discussion amd General Debate" at 7th Interenational Symposium on Neutron Capture Therapy for Cancer. Zurich, Switzerland. Sep., 1996

7-9 放射化による金属フラーレンの研究

Study of metallofullerenes with neutron activation

末木啓介、佐藤渉、秋山和彦、趙宇亮、菊地耕一、片田元己、中原弘道
Keisuke Sueki, Wataru Sato, Kazuhiko Akiyama, Yulang Zhao, Koichi Kikuchi, Motomi Katada, Hiromichi Nakahara
東京都立大学理学研究科
Graduate School of Science, Tokyo Metropolitan University

研究の目的

金属フラーレンを中性子放射化することによって高感度で定量性が高い実験が行われることを立教大学原子力研究所のTRIGA Mark II実験炉で証明してきた。原研の研究炉を用いて比放射能の高い放射性金属フラーレンを得ることにより核分光を用いた応用研究や極少量しか生成しない新規金属フラーレンの探索に有効であると考えてこの研究課題は進められた。

1. TDPACによるCe内包フラーレンの動的及び電気的性質

^{140}Laがβ壊変して^{140}Ceになる過程でカスケードγ線の放出によりγ-γ角相関が測定できる。中間準位は4+で半減期が3.45 nsと短いがA_{22}が-0.14と大きく摂動角相関の情報が得られるものと期待された。Laを内包する金属フラーレンはフラーレン研究の当初から注目されて多くの報告がなされており、その主要に生成する分子種La@C_{82}, La_2@C_{80}はその単離方法などが既に確立していた。アーク放電法を用いて得られたススから1,2,4トリクロロベンゼンなどを用いて溶媒にフラーレンと金属内包フラーレンを抽出した。それを2段階のHPLCによって単離した。この精製試料約1mgを石英管中に減圧封入した後、JRR3MのHRで8時間から30時間照射した。この試料を都立大学のRI研究施設においてCS_2溶媒に溶かして、放射線効果等によって生成する不純物をHPLC展開で除いた。精製した放射性Laフラーレンは TDPAC用の試料管に入れて測定を行った。La@C_{82}については10Kから298Kまで固体状態とオルトジクロロベンゼン中に溶解した試料について4本のBaF_2検出器で測定した。La_2@C_{80}については10Kから423Kまで固体状態で測定した。室温までは今回の共同利用を利用して行われ、室温以上については京都大学原子炉実験所において成し遂げられた。

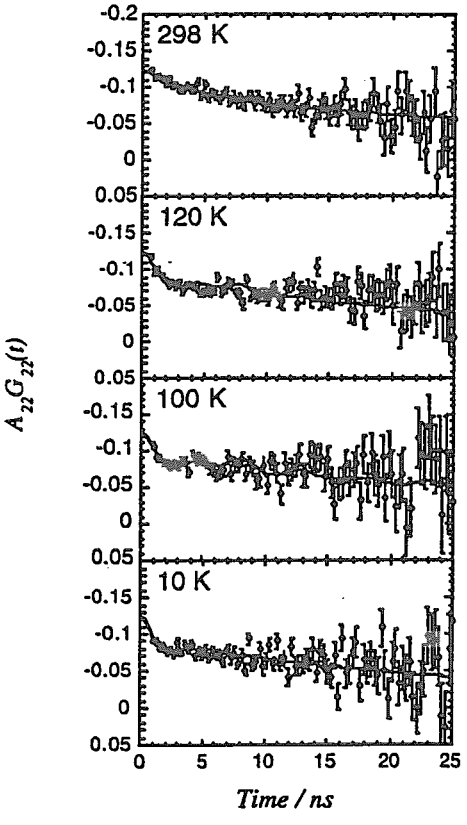

Fig. 1 TDPAC spectra of ^{140}Ce in Ce@C_{82}. The temperature-variant data for solid Ce@C_{82}.

原研装置	研究分野
JRR3M, JRR4	放射化学

$La@C_{82}$について得られた特徴的なTDPACスペクトルを図1に示す。測定温度によってスペクトルが大きく変わっていることが分かる。室温では動的摂動を受けた特徴的なスペクトルが得られた。これに対して10Kでは動的な摂動だけではなく静的摂動も含むスペクトルに変化しており、この変化は100-150K辺りで起こっていることが温度依存性から確認された。また、スペクトルの解析を進めていく中で2種類の状態が存在していることが分かった。図2に2成分それぞれの緩和定数の温度依存性を示した。この2種類の状態はβ壊変による原子核の反跳現象が大きく関わっていることが推定された。なぜならば10Kから100Kの温度範囲で片方の状態は動的摂動を観測されるが、それには温度依存性がなかった。この事から反跳現象によって金属原子がフラーレンケージとの間の結合を切る為に起こると結論された。

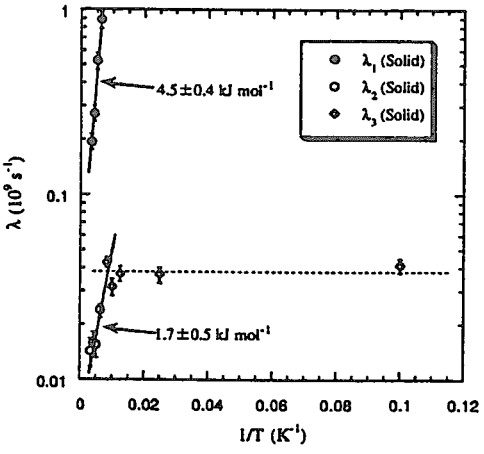

Fig. 2 Temperature dependence of the attenuation coefficent

$La_2@C_{80}$はNMR等の研究でその内包される2つの金属が全くの等価な状態で存在していることが既に分かっている分子である。TDPACスペクトルは$La@C_{82}$と類似したものが得られたが、今回は2成分の内の低温で静的摂動を示す成分が減少していることが明らかになった。この事などから、Laの2つの原子はフラーレンケージ内で常に動いている可能性を示した。この事は、Laが等価な状態でいるNMRの結果を支持するものと考えている。

2. 新規金属フラーレンの探索 (Hf, Ta)

今までに多くの研究グループによって様々な金属フラーレンの研究がなされSc, Y, Laとランタニドおよびアルカリ土類について多くの報告がなされている。また、貴ガス内包フラーレンの報告も多く存在する。ところが4族以上の金属に関しては多くの試みがなされているが既存の方法では思うように見いだせていない。この原因はこれらの金属原子が内包されるフラーレンの生成量が希土類に比べれとかなり小さいためであると考えられる。これらはマルチトレーサーを用いた研究で明らかにしたが、4族のZr, Hfと5族のNb, Taにおいて生成される可能性が示された。そこで、我々はHfとTaについて金属フラーレンの合成とその生成物の確認と単離を試みた。

Hfについては酸化物と炭素粉末を混合して作られた炭素棒を陽極にしてアーク放電法によって合成をした。この時に、生成条件などの確認のためにLaを含む炭素棒を用いる場合もある。生成されたススから1,2,4トリクロロベンゼンを用いて抽出物を得た。この抽出物を放射化してHfの挙動をγ線でトレースして実験を進めたところ、HfはLa等の希土類に比べて抽出物に含まれる金属量が1/10以下である結果が得られた。このために、今までのように抽出物をそのままHPLCの溶離挙動を調べることが困難であった。そこで、放射化の前に5PBB/CS_2系でHPLC展開を行い、大半のC_{60}と半分ぐらいのC_{70}を除いた試料を作った。この試料をJRR4で8時間照射した後にCS_2に可溶な成分を基にして、5PBB/TolueneとBuckyprep/Tolueneでの^{181}Hfの溶離挙動を検討した。図3にHPLC溶離挙動を示した。この方法で確認されたHfを含む金属フラーレンは2種類有り、主に生成した$Hf_2@C_{80}$とその1/10程度生成した$Hf@C_{84}$をTOF-MSを用いて確認することが出来た。さらに、$Hf_2@C_{80}$についてはUV/vis/NIRの吸収スペクトルなどを得ることが出来た。

Taについても同様な検討を行った。TaはHfよりもさらに生成量が少ないとの結果が出た。この場合に最も重要な現象としてはTaが蒸発せずに陽極表面に金属層として析出している。これはTaの沸点が非常に高いことに起因していると考えられる。放射化したク

ルード及びC_{60}, C_{70}を除いた試料にしても、CS_2に可溶な成分中に^{182}Taの放射能が非常に少なくHPLCでの溶離挙動を追うことが出来ていない。従って、Taに関して金属内包フラーレンの生成についてはまだ確認されていない。

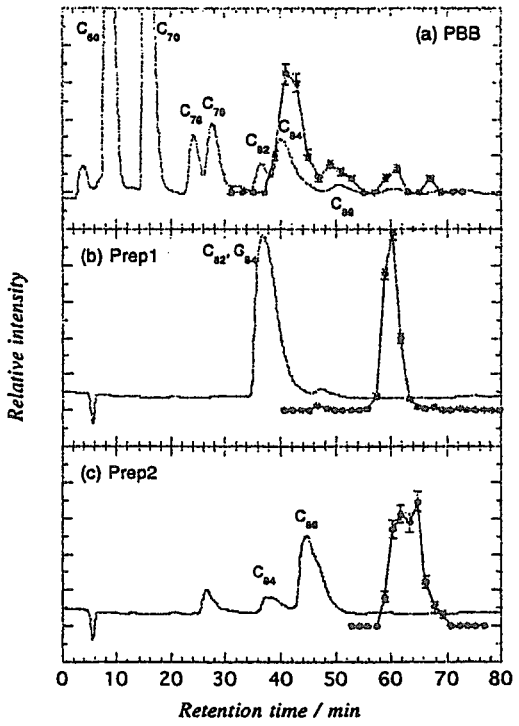

Fig. 3 The elution curves of the radioactive Hf fullerenes sample. The elution curve of empty fullerenes monitored by UV absorption is shown by the solid line. a) The elution from a 5PBB column. Two kinds of fraction samples collected within the retention time of 35-45 min and within 45-55 min were each injected into a Buckyprep column for a second column separation. The results are shown (b) and (c).

今後は新規金属内包フラーレンの研究を更に進めていくとともに、^{181}TaはTDPAC核として有望であり、現在までにHfフラーレンについての研究が進んでいることを含めて中性子放射化した$Hf_2@C_{80}$を用いてTDPAC分光法などの研究に発展させていく予定である。

研究の公表

1. W. Sato, K. Sueki, K. Kikuchi, K. Kobayashi, S. Suzuki, Y. Achiba, H. Nakahara, Y. Ohkubo, F. Ambe, K. Asai, "Novel Dynamic Behavior of $Ce@C_{82}$ at Low Temperature" *Phys. Rev. Lett* 80 (1998) 133-136.
2. W. Sato, K. Sueki, K. Kikuchi, S. Suzuki, Y. Achiba, H. Nakahara, Y. Ohkubo, K. Asai, , F. Ambe, "Molecular and intramolecular dynamics of a C_{80} dimetallofullenene" *Phys. Rev. B* 58 (1998) 10850-10856.
3. W. Sato, K. Sueki, K. Kikuchi, K. Kobayashi, S. Suzuki, Y. Achiba, H. Nakahara, Y. Ohkubo, F. Ambe, K. Asai, "Electronic state of $Ce@C_{82}$" *J. Radioanal. Nucl. Chem.* 239 (1999) 187-190.
4. K. Akiyama, K. Sueki, T. Kodama, K. Kikuchi, Y. Takigawa, H. Nakahara, I. Ikemoto, M. Katada, "New fullerenes of a group IV element: Hf metallofullerenes" *Chem. Phys. Lett.* 317 (2000) 490-496.

7-10 メスバウアー分光法による無機化合物の研究（III）

Mössbauer Spectroscopic Studies on Inorganic Compounds Part III

高橋 正，竹田 満洲雄，北澤 孝史，王 軍虎，石黒 淳，前田 正樹，岩崎 洋
（東邦大学理学部）
伊藤 泰男，澤幡浩之
（東京大学原子力研究総合センター）
M. Takahashi, M. Takeda, T. Kitazawa, J. Wang, A. Ishiguro, M. Maeda and H. Iwasaki
Department of Chemistry, Faculty of Science, Toho University
Y. Ito and H. Sawahata
Research Center for Nulcear Science and Technology, The University of Tokyo

メスバウアー効果は45元素，91核種について観測されるが，鉄，スズおよびユウロピウム以外の元素については，市販の線源がないことや低温での測定が必要なため，化学的には有益な情報を与えると期待されても，測定に用いられることが少ない．この研究は，そういった余りなじみがない元素のメスバウアー分光法を用いて，結合や構造に関する情報を得ることを目的として，進めてきた．この3年間にわたる研究では，次の研究をおこなった．①新たに^{155}Gdメスバウアー線源（^{155}Eu/$SmPd_3$）を作成し，酸化物および金属錯体の構造と電子状態の研究を進めた，②前の研究課題で確立した^{166}Erメスバウアー分光法を用いて，金属錯体の常磁性緩和についての研究を発展させた，③以前からおこなってきた^{127}Iおよび^{197}Auメスバウアー分光法により，有機金属化合物の電子状態について検討を加えた．以下にこの期間に得られた主な研究成果について報告する．

I ^{155}Gdメスバウアー分光法

中希土元素の一つGdにはハロゲン化物クラスターが多数知られており，それらの電子状態に興味をもったので，測定ができるようにすることにした．Gdにはいくつかのメスバウアー核が知られているが，化学的な応用に適している^{155}Gdの86.54 keVの遷移を用いることにした．

[実験]

線源の作成：$^{154}Sm_2O_3$を出発物質として，ギ酸サマリウム（III）を経て，$^{154}SmPd_3$とした．$^{154}SmPd_3$ 312 mgをJRR-3M HR-1で67時間中性子照射して，^{155}Eu/$SmPd_3$線源（231 MBq，半減期 1.81 y）を得た．

メスバウアースペクトルの測定：線源および吸収体の両方を冷凍機を用いて12 Kに冷却して測定した．測定には，Wissel社製 MDU-1200, DFG-1200, MVT-1000およびMVC-450を用いた．メスバウアーパラメータは，$I_g = 3/2$と$I_e = 5/2$間の遷移をsum-of-Lorentian近似で解析して得た．

[研究成果]

a. 線源の評価

Fig. 1に$GdPd_3$と立方晶系Gd_2O_3（c-Gd_2O_3）の^{155}Gdメスバウアースペクトルを示す．これらは，いずれも線源の評価のために測定したものである．$GdPd_3$は線源化合物の$SmPd_3$と同形の化合物で，シ

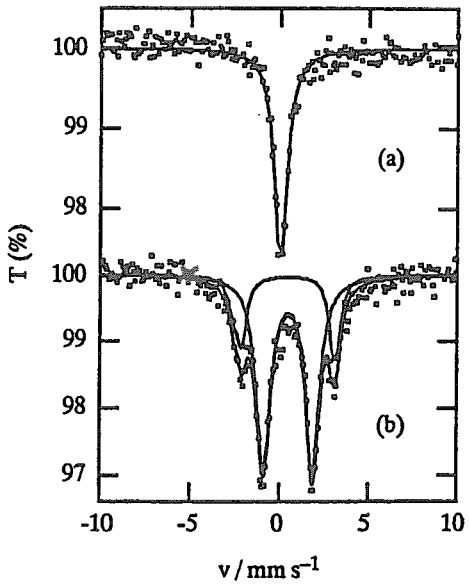

Fig. 1 ^{155}Gd Mössbauer spectra for $GdPd_3$ (a) and c-Gd_2O_3 (b)

研究施設・装置：JRR-3M（HR-1，BR-1，PN-2）JRR-4（T-パイプ），モニタリングケーブ，低温メスバウアー分光器
研究分野：メスバウアー分光法，無機固体化学，錯体化学，有機金属化学，構造化学

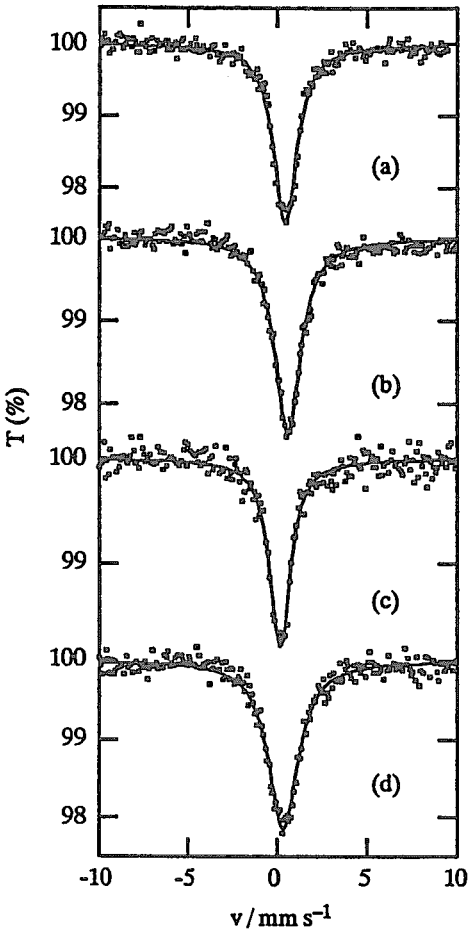

Fig. 2 ^{155}Gd Mössbauer spectra for $GdAl_2$ (a), $GdAl_3$ (b), GdAg (c) and $Gd_{14}Ag_{51}$ (d) at 12 K

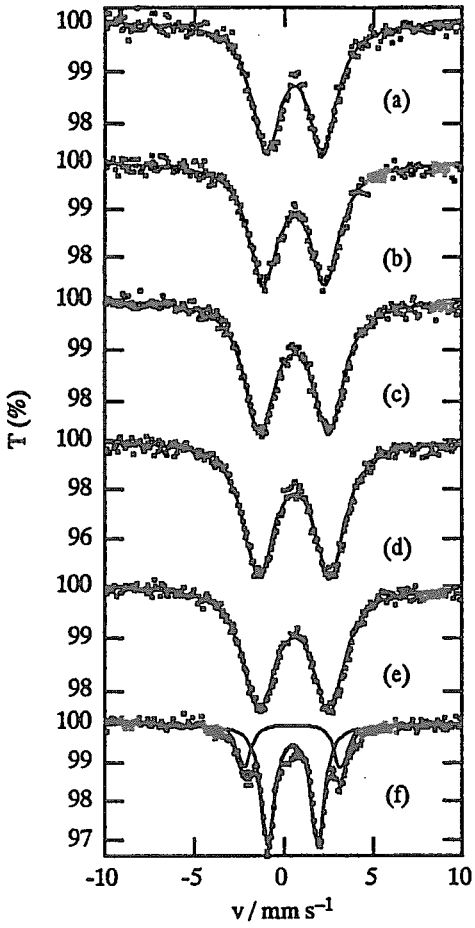

Fig. 3 ^{155}Gd Mössbauer spectra for $Zr_{1-x}Gd_xO_{2-x/2}$ at 12 K. x = 0.35 (a), 0.40 (b), 0.45 (c), 0.50 (d), 0.55 (e), 1.00 (f)

ングルラインであることがわかっている．得られたスペクトルは確かにe^2qQ = 0 mm s^{-1}と解析でき，線幅（Γ_{exp}）は0.89 mm s^{-1}であり，自然幅の2倍が0.47 mm s^{-1}であるから，満足できる線幅である．c-Gd_2O_3は2組の四極ダブレットによる吸収を与えた．これはc-Gd_2O_3のGdサイトに2種類あることに対応している．以上のことから，今回作成した線源が，良質な線源であることが確認できた．

b. Gd金属間化合物

Gdの金属間化合物はこれまでにも多くのメスバウアースペクトルが報告されている．我々は異性体シフト（δ）が金属によってどのように変化するかに興味をもっているが，δの値は線源基準で与えれていることが多く，異なる研究者間のデータの比較には問題が生じることがある．そこで手始めとして，$GdAl_2$，$GdAl_3$，GdAgおよび$Gd_{14}Ag_{51}$について，測定をおこなった．

東北大金研の宍戸助教授と福田教授の協力でアーク炉で作成した試料を粉砕して，メスバウアー測定に用いた．Fig. 2に得られた12 Kでのスペクトルを示す．磁気的相互作用を無視して，解析をおこない，GdAg，$Gd_{14}Ag_{51}$，$GdAl_2$および$GdAl_3$についてδ（線源基準）がそれぞれ，0.16 (2)，0.35 (1)，0.45 (1)，0.60 (1) mm s^{-1}と求まった．先に測定した$GdPd_3$の値が0.03 (1) mm s^{-1}であったから，δは金属原子の種類と配位構造に敏感であることがわかる．測定に用いているメスバウアー遷移では，$\Delta R/R$は負であるから，Gd核位置でのs電子密度が$GdPd_3$ > GdAg > $Gd_{14}Ag_{51}$ > $GdAl_2$ > $GdAl_3$の順に減少することがわかる．この傾向の詳細な説明は，今後の課題である．クラスターモデルの分子軌道計算をこれから行う予定である．

$GdRh_3B$と$GdRh_3B_{0.706}$のメスバウアースペクトル

もシングルラインの吸収を与えた．線幅は 1.0 mm s^{-1} 前後であるが，δ はそれぞれ 0.11 (1) と 0.08 (1) mm s^{-1} であった．若干ではあるが，ホウ素欠損があるとδが増加する傾向がある．これはホウ素が金属隙間に単に入るのではなく，ガドリニウムとの間に結合的な相互作用があることを示唆している．

c. $Zr_{1-x}Gd_xO_{2-x/2}$ 固溶体

ジルコニアのＺｒの一部をＧｄで置換した $Zr_{1-x}Gd_xO_{2-x/2}$ 固溶体は，置換量に応じてホタル石型構造，パイロクロア型構造，立方晶型構造をとる．x が小さいときホタル石型構造であるが，x が 0.5 近傍のときはパイロクロア型構造をとる．この構造では Gd^{3+} は 8 配位であるが，Zr^{4+} は 6 配位となり，酸素空孔が Zr^{4+} の周りに集まっている．この系の相図については，$0.18 \leqq x < 0.45$ でホタル石型，$0.45 \leqq x \leqq 0.55$ でパイロクロア型という報告と，$x = 0.50$ のときのみパイロクロア型で $0.33 < x < 0.62$ でホタル石型とパイロクロア型が共存しているという報告がある．EXAFSなどからは，ホタル石型とパイロクロア型では，Gd^{3+} 周りの構造が類似していると報告もある．この研究はメスバウアー分光法から，結晶構造や Gd^{3+} まわりの配位構造についての知見を得る目的で，おこなった．

$x = 0.21$, 0.26, 0.30 の試料は単結晶を粉砕して測定した．それ以外の x の試料は溶液から共沈させてのち，1500℃で16時間焼成して作成した多結晶粉末である．

Fig. 3に x=0.35から0.55までと c-Gd_2O_3 (x =1.00 に相当）の12 Kでのスペクトルを示す．c-Gd_2O_3 が2サイト明瞭に観測されるのに対して，これらの固溶体は1サイトしか観測されなかった．

異性体シフト（δ）は固溶量 x によらず，ほぼ0.55 mm s^{-1} で変化しない．この値は2サイトとも6配位であることがわかっている c-Gd_2O_3 に比べると大きな値である．x = 0.50 のときはパイロクロア型の $Zr_2Gd_2O_7$ みであるが，このとき Gd^{3+} は8配位である．他の x のときも $x = 0.50$ のときと同じδの値を示すということは，固溶量によらずGd原子の配位環境には大きな違いはなく，Gd^{3+} は8配位であることを示している．このことは，EXAFSなどの結果とも一致している．

四極結合定数 (e^2qQ) は，x の増大とともに増加する傾向があり，$x = 0.50$ で最大の 7.35 mm s^{-1} となる．このことは $x = 0.50$ のとき，Gd^{3+} 周りの電場勾配が最大であり，配位構造の歪みが大きいことを示

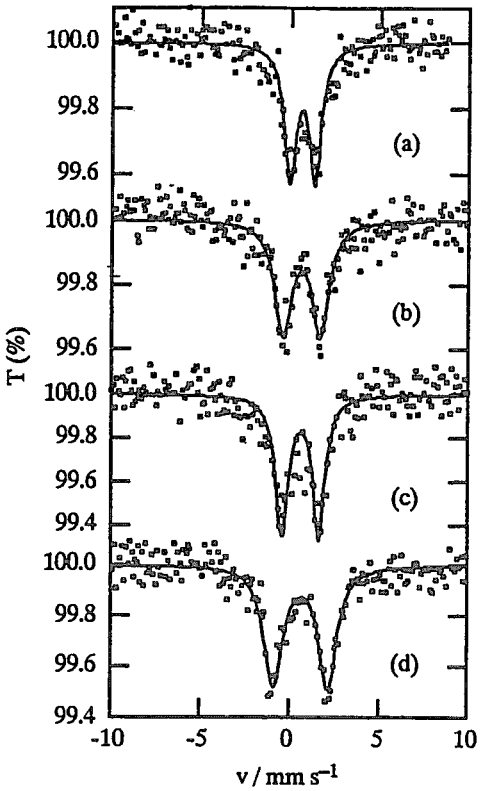

Fig. 4 ^{155}Gd Mössbauer spectra for tris-(β–diketonato) gadolinium(III) complexes. a: $Gd(bfa)_3 \cdot 2H_2O$, b: $Gd(bza)_3 \cdot 2H_2O$, c: $Gd(taa)_3 \cdot 2H_2O$, d:$Gd_2(dpm)_6$

している．完全なパイロクロア型の $Zr_2Gd_2O_7$ では，Gd^{3+} 周りの８個の酸素原子の理想的なホタル石型の位置からのずれは最も大きくなるはずなので，x = 0.50 のときパイロクロア型になると報告と一致する．線幅 (Γ_{exp}) は x の増加とともに大きくなる傾向があり，c-Gd_2O_3 に比べるとかなり大きい．固溶体の結晶性，酸素空孔位置の違いによる複数サイトの混在の可能性などがあげられる．また多結晶試料は，単結晶試料よりも広くなる傾向があり，結晶性の違いは明らかに線幅に影響を与えている．

d. 金属錯体

Gd錯体の^{155}Gdメスバウアースペクトルの報告は，見当たらないようである．我々は，^{155}Gd メスバウアー分光法の錯体化学的応用の可能性－配位構造や配位原子，錯体間の相互作用などの知見を得ることができるかどうかーを検討するため，これまでにβ－ジケトナト錯体，EDTA錯体およびCN架橋の集積型錯体などのメスバウアースペクトルを測定した．この研究で測定した錯体のメスバウアーパラメータを Table 1 にまとめた．

Table 1 ^{155}Gd Mössbauer parameters for Gd(III) complexes at 12 K

Complex	δ	e^2qQ	Γ_{exp}
	mm s^{-1}	mm s^{-1}	mm s^{-1}
$Gd_2(dpm)_6$	0.65	6.49	1.15
$Gd(bfa)_3 \cdot 2H_2O$	0.63	3.09	1.28
$Gd(taa)_3 \cdot 2H_2O$	0.58	4.47	1.27
$Gd(bza)_3 \cdot 2H_2O$	0.64	4.43	1.11
$NaGd(edta) \cdot 8H_2O$	0.62	4.72	1.25
$NH_4Gd(edta) \cdot 6H2O$	0.60	3.62	1.68
$GdFe(CN)_6 \cdot 4H_2O$	0.61	4.24	0.80
$GdCo(CN)_6 \cdot 4H_2O$	0.58	4.19	1.94
$KGdFe(CN)_6 \cdot 3H_2O$	0.54	4.49	0.98
$KGdRu(CN)_6 \cdot 3H_2O$	0.61	4.71	1.10

*relative to ^{155}Eu/$SmPd_3$ source

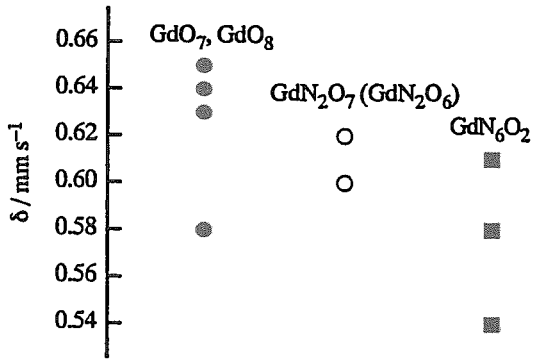

Fig. 5 Relationship between δ and coordinating atoms in Gd(III) complexes

β－ジケトナト錯体のスペクトルをFig. 4に示す（配位子の略号は右参照）．bfa錯体，bza錯体，taa錯体は$GdL_3 \cdot 2H_2O$（L = β-diketone）の8配位錯体である．これに対してdpm錯体は$Gd_2(dpm)_6$の組成を持つ2量体錯体で7配位錯体である．δの値は7配位錯体と8配位錯体とでは明瞭な違いはないが，e^2qQは7配位錯体の$Gd_2(dpm)_6$の方が8配位錯体$GdL_3 \cdot 2H_2O$よりも明らかに大きい．これはGd^{3+}まわりの電荷分布の歪み（球対称性からのずれ）は7配位錯体の方が8配位錯体よりも大きいことを示しているが，明らかに配位構造の対称性の違いを反映している．EDTA錯体については，Na塩は水が配位しているのでGdN_2O_7型の9配位構造であり，NH_4塩は結晶構造は明らかではないがGdN_2O_6型の8配位もしくは9配位と考えられる．これらの錯体のe^2qQの値は，8配位のβ－ジケトナト錯体と大きく変わらず，9配位錯体のGd^{3+}まわりの電荷分布は8配位錯体とそれほど違わないことがわかる．

$[M(CN)_6]^{n-}$ (M = Fe^{II}, Fe^{III}, Co^{III}, Ru^{II}) ユニットがGd^{3+}をCNで架橋した集積型錯体$GdM(CN)_6 \cdot 4H_2O$ (M = Fe^{III}, Co^{III}) と$KGdM(CN)_6 \cdot 3H_2O$ (M = Fe^{II}, Ru^{II}) はいずれもGd^{3+}は8配位である．e^2qQの値は，β－ジケトナト錯体で見られた値の範囲にある．δの値は，MがFe^{III}とFe^{II}のときを比較すると明らかに異なっており，架橋CNを通して遷移金属状態の違いがGd^{3+}の電子状態の違いとして現れていることがわかる．

Fig. 5は，δの値を配位構造の類型別に分類して示したものである．δの値は，GdO_7，GdO_8 > GdN_2O_7 (, GdN_2O_6) > GdN_6O_2の順に小さくなる傾向がある．窒素原子配位の配位子が増えるとδが小さくなる傾向がみられ，電子状態の違いがδに反映されることを示唆している．今後の研究で，このことを明らかにしたい．

II ^{166}Er メスバウアー分光法

これまでの研究で，^{166}Erスペクトルでは測定温度の12 Kにおいてしばしば常磁性緩和が観測された．そこで常磁性緩和について系統的に研究する目的で，EDTA錯体と種々の置換基を持つβ－ジケトナト錯体を取り上げた．

[実験]

β－ジケトナト錯体は文献の方法によって合成し，減圧昇華もしくはメタノールから再結晶して測定に用いた．無水錯体のスペクトルの測定においては，測

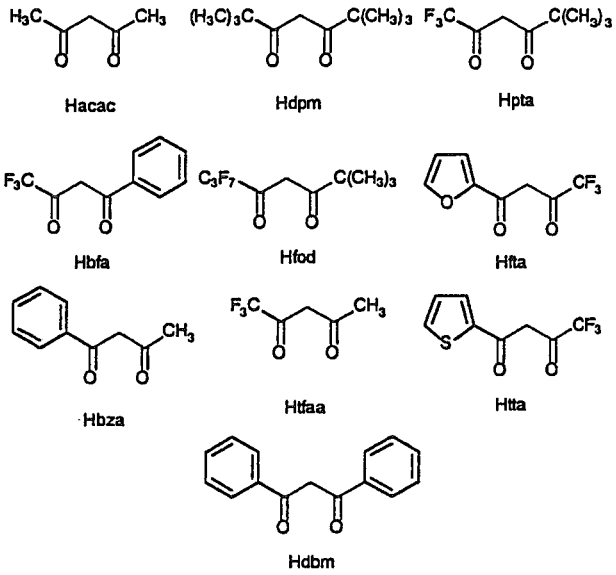

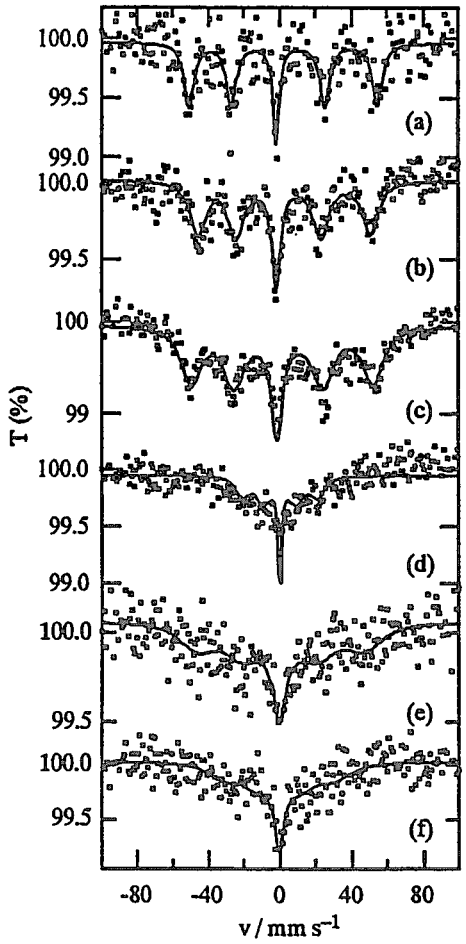

Fig. 6 ^{166}Er Mössbauer spectra for Er(III)-β-diketonato monohydrate complexes at 12 K. a: $Er(fod)_3.H_2O$, b: $Er(pta)_3.H_2O$, c: $Er(dpm)_3.H_2O$, d: $Er(dbm)_3.H_2O$, e: $Er(acac)_3.H_2O$, f: $Er(bfa)_3.H_2O$

定直前に試料を乾燥させからおこなった.

^{166}Er メスバウアー線源 $^{166}Ho/Ho_{0.4}Y_{0.6}H_2$ (1.4 GBq, 半減期 26.8 h) は, 高純度アルミニウム箔中に密封した約 50 mg の $Ho_{0.4}Y_{0.6}H_2$ を JRR-3M PN-2で8～10分中性子照射して作成した. メスバウアースペクトルの測定は, ^{155}Gd と同じようにして, 12 K でおこなった. β－ジケトナト錯体の無反跳分率は低温でも小さいので, 測定に際しては1日以上の十分な時間の積算を行った.

[研究成果]

Fig. 6 に $ErL_3.H_2O$ の ^{166}Er メスバウアースペクトルを示す. この図に示すように, いずれの錯体も常磁性緩和による線幅が広がった分裂したスペクトルを与えた. スペクトルは Nowick-Wickman model を用いて解析し, 緩和時間 τ を得た. Table 2 には得られたメスバウアーパラメーターをまとめた. 常磁性

Table 2 ^{166}Er Mössbauer parameters for te Er(III) –β-diketonato complexes at 12 K

complex	e^2qQ / mm s^{-1}	Γ_{exp} / mm s^{-1}	τ / ns	H_{eff} / T
$Er(dpm)_3$	0.1	8.0*	0.4	525
$Er(fta)_3$	–2.4	8.3	0.2	640
$Er_2(pta)_6$	3.6	8.4	0.1	621
$Er(fod)_3.H_2O$	6.1	4.1	1.0	711
$Er(pta)_3.H_2O$	7.0	5.6	0.5	654
$Er(dpm)_3.H_2O$	4.3	8.0*	0.4	690
$Er(dbm)_3.H_2O$	–0.1	8.0*	0.3	294†
$Er(acac)_3.H_2O$	–2.7	7.5	0.2	598
$Er(tta)_3.2H_2O$	1.8	8.0*	0.2	316†
$Er(bfa)_3.H_2O$	1.0	7.0	0.1	651
$Er(tfaa)_3.H_2O$	2.0	6.8	0.1	582
$Er(bza)_3.2H_2O$	–4.0	5.7	0.1	433†

* fixed value, † rather uncertain value

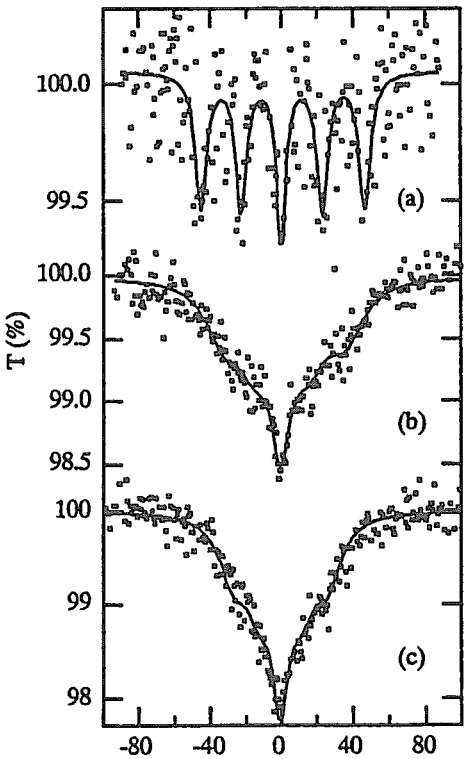

Fig. 7 ^{166}Er Mössbauer spectra for Er(III) – EDTA complexes at 12 K.
a: $Na[Er(edta)(H_2O)_3].2H_2O$, b: $NH_4[Er(edta)-(H_2O)_2].4H_2O$, c: $K[Er(edta)(H_2O)].H_2O$

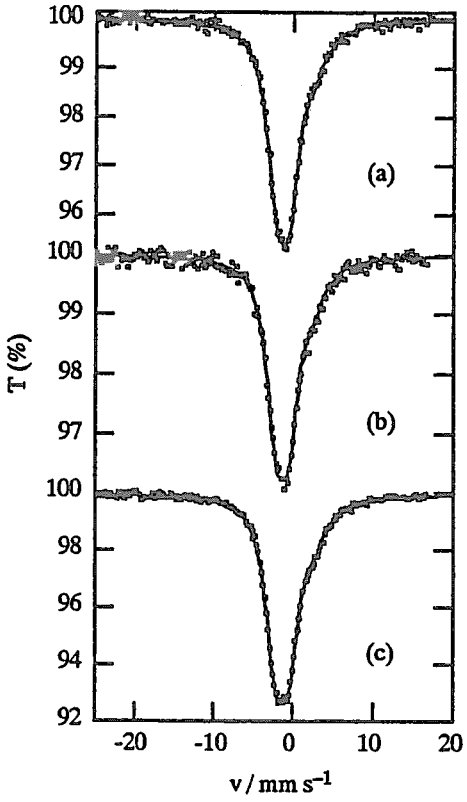

Fig. 8 ^{127}I Mössbauer spectra for seven-coordinate carbonyl complexes at 20 K. a: $[MoI_2(CO)_3(SbPh_3)(PPh_3)]$, b: $[MoI_2(CO)_3(SbPh_3)(AsPh_3)]$, c: $[NBu_4][MoI_3(CO)_3(SbPh_3)]$

緩和によりスペクトルが分裂するため，四極結合定数が求めやすくなっている．配位構造とe^2qQのはっきりとした関係は認められないが，fod錯体やpta錯体では大きな値となっている．$Er(dpm)_3$は三方プリズム錯体であることが結晶構造解析から明らかになっているが，小さなe^2qQの値は分子構造の反映と見ることができる．

結晶構造解析をおこない結晶中のEr－Erの最短距離を求めたところ，$Er(dpm)_3 \cdot H_2O$で5.58 Å，$Er(pta) \cdot H_2O$で5.87 Å，$Er_2(pta)_6$で3.82 Åであった．これらの7配位の錯体について得られた緩和時間を比べてみると，Er—Er距離が長くなると緩和時間が長くなることがわかる．しかしながら6配位の$Er(dpm)_3$はEr－Erは9.98 Åと長いにもかかわらず，τは0.4 nsである．これは，結晶場も緩和時間に影響を与えることを示唆している．同じことは，EDTA錯体についても見られた．

$Er(dpm)_3 \cdot H_2O$と$Er(pta)_3 \cdot H_2O$の分子構造が類似しているので，同様の7配位構造をとると推定される

Table 3 ^{127}I Mössbauer parameters at 20 K, valence electron populations and charge number on the iodine atom

compound	δ* / mm s^{-1}	e^2qQ / MHz	N_s	N_z	Z_I
$[MoI_2(CO)_3(SbPh_3)(PPh_3)]$	–0.10	–829	1.97	1.64	–0.61
$[WI_2(CO)_3(SbPh_3)(PPh_3)]$	–0.10	–896	1.97	1.61	–0.58
$[MoI_2(CO)_3(SbPh_3)(AsPh_3)]$	–0.10	–833	1.97	1.64	–0.61
$[WI_2(CO)_3(SbPh_3)(AsPh_3)]$	–0.10	–881	1.97	1.62	–0.58
$[NBu_4][MoI_3(CO)_3(SbPh_3)]$	–0.11	–879	1.97	1.62	–0.59
$[NBu_4][WI_3(CO)_3(SbPh_3)]$	–0.08	–873	1.96	1.62	–0.58

* relative to KI at 20 K

一水和物について，メスバウアースペクトルの緩和時間を比較してみると，β－ジケトンの置換基が大きいほど緩和時間が長くなる傾向が見られる．これは置換基が大きくなると，Er^{3+}のスピン間の距離が長くなるためと考えられる．ところで，Fig. 6で$Er(dbm)_3 \cdot H_2O$だけ著しく異なったスペクトルを与えている．この錯体はC_3対称性を持つ単面冠八面体で，他の7配位錯体とは構造が異なり，それにしたがって電子状態が他の錯体と異なるためと理解でき，再び結晶場の効果が常磁性緩和に影響を与えることが確認できる．

EDTA錯体のメスバウアースペクトルをFig. 7に示す．いずれの錯体も常磁性緩和により5本に分裂したスペクトルをとなっている．Na塩は三つの水が配位した単面冠正方ねじれプリズム型9配位構造であるのに対して，NH_4塩は二つの水が配位した正方ねじれプリズム型8配位構造である．K塩も水と隣接錯体のカルボキシル基が配位した正方ねじれプリズム型8配位構造である．τはNa塩で1.7 ns，NH_4塩で0.1_7 ns，K塩で0.1_9 nsと見積もられる．結晶構造解析から明らかになった，Er－Er原子間の距離は，Na塩で6.081 Å，K塩で5.782 Å，NH_4塩で5.886 Åであり，いずれの塩でも余り差がない．τの違いはむしろ配位構造の違いに由来する結晶場の効果を反映していると考えられる．

III ^{127}I メスバウアー分光法

最近，重いpブロック元素と遷移金属との結合に興味が集まっている．我々は$[M(CO)_n(SbR_3)]$(M = Fe, Ru; n =4, M = Cr, Mo, W; n =5, R = Me, Ph) のM－Sb結合を^{121}Sbスペクトルから研究した．この研究を発展させる目的で，7配位錯体$[MI_2(CO)_3(SbPh_3)L]$お

および$[MI_3(CO)_3(SbPh_3)]$(M = Mo, W; L = PPh_3, $AsPh_3$)について，遷移金属とヨウ素の結合を研究するために^{127}Iメスバウアースペクトルを測定した．

[実験]

錯体は，文献記載の方法で合成した．メスバウアー線源$^{127m}Te/Mg_3TeO_6$ (1.4 GBq；半減期109 d) は，^{126}Teから調製した$Mg_3{}^{126}TeO_6$ (170 mg) をJRR-3M BR-1で1サイクル照射，2ヶ月クーリング後Al箔を用いて密封して作成した．メスバウアースペクトルの測定は，大学開放研の低温メスバウアー測定装置を用いておこない，線源，吸収体とも20 Kに冷却して測定した．

[研究成果]

スペクトルをFig．8に，得られたパラメータをTable 3に示す．得られたスペクトルはいずれも負のe^2qQを示し，I⁻がMとσ結合していることを示している．Townes-DaileyとPerlow-Perlowの扱いをしてメスバウアーパラメータから見積もったヨウ素原子の価電子のポピュレーションとヨウ素原子上の電荷も，表に合せてまとめた．なお価電子のポピュレーションを見積もる際には，σ結合性なので$N_x = N_y = 2.0$と仮定した．ヨウ素の5s軌道のポピュレーションは1.96から1.97であり，本質的に5s軌道は結合に関与していないことがわかる．これはこれまでに調べてきた多くのヨウ素化合物の場合と一致している．一方，$5p_z$軌道のポピュレーションは1.61－1.64であり，I⁻から遷移金属に0.36－0.39個の電子が移動したことを示している．この値は，同じ錯体について^{121}Sbメスバウアーパラメータから見積もった$SbPh_3$から遷移金属への移動量0.44 － 0.55電子よりも少なく，M—I結合はM–$SbPh_3$に比べるとイオン結合性であることを示唆している．移動量を詳細に検討してみると，Mo錯体よりもW錯体の方が大きいが，これは$SbPh_3$からMへの移動量もWの方が大きいこととよく対応している．

e^2qQの値を他のヨード錯体と比べてみると，$[CuI(PPh_3)_3]$(e^2qQ = −470 MHz)よりは大きく，*cis*-$[PtI_2(EPh_3)_2]$ (E = P, As；e^2qQ = −981 － −1040 MHz)や$[PtI_2(L\text{-}L)]$ (L-L = ジホスフィン，ジアルシン；e^2qQ = −1100 － −1220 MHz) よりは小さい．このことはM－Iの結合は金属によって異なり，我々の錯体はCu(I)－ホスフィン錯体よりも共有結合的であるが，Pt－ホスフィン錯体ほどではないことを示している．

Table 4 ^{197}Au Mössbauer parameters for dinuclear gold complexes at 12 K

compound		δ* mm s^{-1}	ΔE_q mm s^{-1}	Γ_1 mm s^{-1}	Γ_2 mm s^{-1}
1		4.67	9.81	2.14	2.05
2		3.60	6.39	2.25	2.40
3	Au^{I}	2.87	7.26	2.27	2.27
	Au^{III}	4.42	6.06	1.85	1.85
4	Au^{III} in ring	4.26	5.87	2.24	2.24
	Au^{III} terminal	1.90	2.79	2.19	2.19

* relative to ^{197}Pt/Pt source

IV ^{197}Auメスバウアー分光法

通常の金化合物の酸化数は+1または+3であるが，少数ながら+2のものも知られている．^{197}Auメスバウアー分光法は，金化合物の酸化数の決定に非常に有用であり，既に我々も環状Au(II)化合物の^{197}Auメスバウアースペクトルを報告した．このことを応用して，次のスキームに示す環状金化合物の反応生成物1～4について，その原子価状態をメスバウアースペクトルから明らかにした．

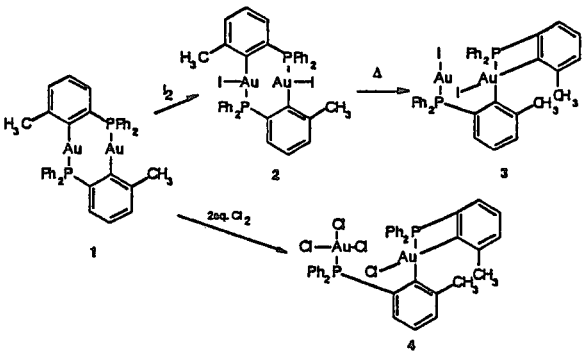

[実験]

^{196}Pt板（100 mg）をJRR-4 T_Bパイプで1時間照射して，^{197}Pt/Ptメスバウアー線源（360 MBq，半減期18.3 h）を得た．メスバウアースペクトルの測定は，^{155}Gdスペクトルと同様にして，12 Kでおこなった．

[結果]

得られたスペクトルをFig.8に，またメスバウアーパラメータをTable 4にまとめた．出発物質の1のスペクトルは大きな四極分裂を持つ一組のダブレット

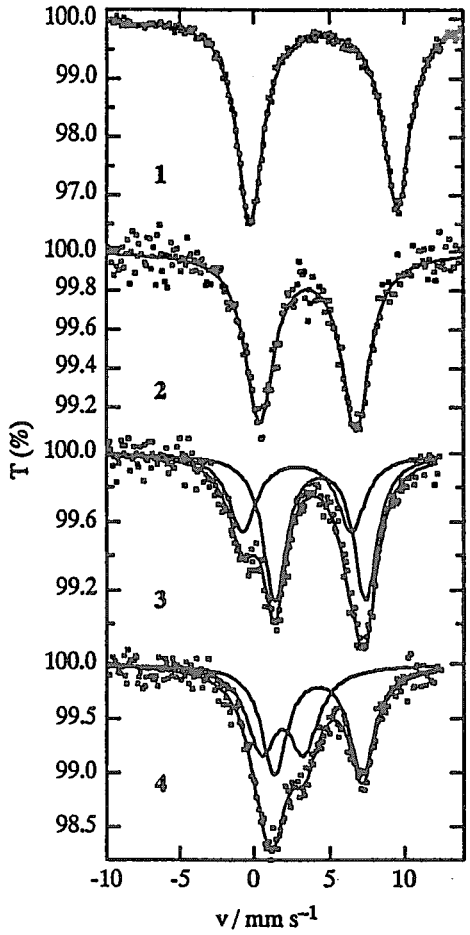

Fig. 8 ^{197}Au Mössbauer spectra for dinuclear gold complexes at 12 K

であり，パラメータからAu(I)錯体であることが確認できた．1を低温でヨウ素で穏やかに酸化して得られる2も一組のダブレットとして観測されるが，四極分裂（ΔE_q）が1よりも小さい．メスバウアーパラメータからこれは，Au(II)錯体があることが確認できた．1および2のメスバウアーパラメータの値は，先に報告した環状金化合物の値に非常に近い値である．

2は-20℃以上で3に異性化する．そのスペクトルは二組のダブレットから成りたっており，二つの異なる金のサイトがあることがわかる．解析の結果，それらは，Au(I)のサイトとAu(III)のサイトであると帰属できた．メスバウアーパラメータのδとΔE_qの関係から，Au(I)サイトには比較的ハードな配位原子が存在すること，Au(III)サイトにはソフトな配位子が存在することが推定でき，スキームに示した構造であることが確認できた．

1を塩素で酸化して得られる4のスペクトルも二つの異なる金のサイトが存在することを示している．解析の結果，それらはいずれもAu(III)の酸化状態であることがわかった．再びδとΔE_qの関係を検討してみると，二つのAu(III)サイトはかなり化学的な環境が異なっており，一つはソフトな配位子が結合し，他方はハードな配位子が結合していることが示唆された．その結果スキームに示す分子構造が確定でき，前者が環を構成するAu(III)で，後者が末端のAu(III)と帰属できた．3や4のような原子価や配位環境が異なる複核金錯体は珍しいが，このような複雑な系においてもその化学的環境を知るうえに^{197}Au メスバウアー分光法が非常に有用であることが，この研究で示すことができた．

成果の公表

学術雑誌

1. E. Bräu, A. Zickgraf, M. Dräger, E. Mocellin, M. Maeda, M. Takahashi, M. Takeda and C. Mealli, *Polyhedron*, 17, 2655 – 2668 (1998): Heterocyclic systems containing antimony(III) VIII Hypervalency by intramolecular 1,5-chelation Sb···N in rings RSb[$(CH_2)_3$]$_2$NR' (R' = NMe, NBz, NBu^t) and comparison to analogous compounds of As^{III}, Bi^{III}, Ge^{IV} and Sn^{IV}.
2. A. Ishiguro, M. Takahashi and M. Takeda, *J. Organomet. Chem.*, in press: ^{121}Sb, ^{57}Fe and ^{127}I Mössbauer spectroscopic study on antimony-transition metal bond in metal carbonyl derivatives of tertiary stibines.
3. S. K. Bhargava F. Mohr, M. Takahashi and M. Takeda, in preparation: Oxidative addition reacations of methyl substituted binuclear gold complexes studied by ^{197}Au Mössbauer spectroscopy.

学会講演

1. 竹田満洲雄，第2回ヨウ素利用研究シンポジウム，千葉（1999.10）：超原子価ヨウ素化合物の^{127}I メスバウアースペクトル（招待講演）．
2. 高橋　正，竹田満洲雄，日本化学会第76春季年会，横浜（1999.3）：メスバウアースペクトルから見たインターエレメント結合（依頼講演）．
3. M. Takeda, Symposium on Actinide Chemistry, Tokyo (Oct. 1997): ^{166}Er Mössbauer spectra of erbium compounds.
4. 王　軍虎，高橋　正，竹田満洲雄，第41回放射化学討論会，熊本（1997.10）：エルビウム－β－ジケトン錯体の^{166}Er メスバウアースペクトル．
5. 竹田満洲雄，王　軍虎，高橋　正，宍戸統悦，

吉川 彰，福田承生，第42回人工結晶討論会，仙台（1997.11）：Er－Rh－B系の^{166}Erメスバウアースペクトル.

6. 王 軍虎，高橋 正，竹田満洲雄，日本化学会第74春季年会，京田辺（1998.3）：Er(pta)$_3$ [H(pta) = 1,1,1-trifluoro-5,5-dimethyl-2,4-hexane-dione] の結晶構造と^{166}Erメスバウアースペクトル.
7. 高橋 正，根本 裕，野本裕子，王 軍虎，竹田満洲雄，日本化学会第74春季年会，京田辺（1998.3）：Er(III)-EDTA錯体の結晶構造とエルビウム－166メスバウアースペクトル.
8. 王 軍虎，高橋 正，竹田満洲雄，第42回放射化学討論会，仙台（1998.9）：エルビウム（Ⅲ）のアセチルアセトン誘導体錯体の結晶構造と^{166}Erメスバウアースペクトル.
9. 王 軍虎，高橋 正，宍戸統悦，吉川 彰，福田承生，竹田満洲雄，第42回放射化学討論会，仙台（1998.9）：エルビウムの複酸化物と蟻酸塩の^{166}Erメスバウアースペクトル.
10. 高橋 正，岩崎 洋，竹田満洲雄，澤幡浩之，伊藤泰男，第42回放射化学討論会，仙台（1998.9）：ヨウ素－炭素二重結合を持つ超原子価ヨウ素（Ⅲ）化合物の^{127}Iメスバウアースペクトル.
11. 王 軍虎，高橋 正，竹田満洲雄，音部治幹，正木信行，中田正美，中村彰夫，日本原子力学会1999年度春の年会，広島（1999.3）：$Zr_{1-x}Gd_xO_{2-x/2}$固溶体の^{155}Gdメスバウアースペクトル.
12. 王 軍虎，斎藤貴史，高橋 正，宍戸統悦，福田承生，八木栄一，竹田満洲雄，日本化学会第76春季年会，横浜（1999.3）：^{155}Gdメスバウアースペクトルの測定.
13. 王 軍虎，高橋 正，竹田満洲雄，第36回理工学における同位元素研究発表会，東京（1999.7）：ガドリニウムの^{155}Gdメスバウアースペクトル.
14. 王 軍虎，音部治幹，中村彰夫，竹田満洲雄，第43回放射化学討論会，つくば（1999.10）：$Zr_{1-x}Gd_xO_{2-x/2}$(0.35≦x≦0.55) 固溶体の^{155}Gdメスバウアー分光法による研究.
15. 石黒 淳，高橋 正，竹田満洲雄，第43回放射化学討論会，つくば（1999.10）：7配位金属カルボニル[$MI_2(CO)_3(SbPh_3)L$]および[$MI_3(CO)_3(SbPh_3)$]$^-$ (M = Mo, W; L = PPh_3, $AsPh_3$) の^{121}Sbおよび^{127}Iメスバウアースペクトル.
16. 王 軍虎，野本裕子，高橋 正，竹田満洲雄，第43回放射化学討論会，つくば（1999.10）：Gd－EDTA錯体の^{155}Gdメスバウアースペクトルと結晶構造.
17. 竹田満洲雄，京都大学原子炉実験所専門委員会「放射線と原子核をプローブとした物性研究の新展開」，熊取（1999.12）：^{155}Gdおよび^{166}Erメスバウアー分光法による無機化合物の研究.
18. 王 軍虎，北澤孝史，高橋 正，竹田満洲雄，宍戸統悦，福田承生，日本化学会第78春季年会，船橋（2000.3）：Gd-AgおよびGd-Alの金属間化合物の^{155}Gdメスバウアースペクトル.

7-11 長鎖β-ジケトンと中性二座配位アミンによるランタノイド(Ⅲ)の協同効果抽出

Synergistic Extraction of Lanthanoids(Ⅲ) with β-Diketones having Long Chain and Neutral Bidentate Amines

東北大学素材工学研究所、八戸工業高等専門学校* 武井 周一、中村 重人*、秋葉 健一

Institute for Advanced Materials Processing, Tohoku University,
Hachinohe National College of Technology*
Shuichi TAKEI, Shigeto NAKMURA*, Kenichi AKIBA

1. 緒 言

ランタノイドは、ランタン(La)からルテチウム(Lu)までの 15 元素からなり、科学技術の発達に伴い様々な分野で用いられている重要な元素群である。しかし、それらの化学的性質は類似しているため、個々の元素を分離精製するのが容易ではなく、長い時間とコストがかかる。各元素間のわずかな違いを利用して、それを何度も繰り返す多段分離が用いられているが、元々の分離係数を向上させれば、多段分離の回数を減らすことができ、省エネルギー、省コストにつながると考えられる。

溶媒(液-液)抽出法は、希薄溶液から高濃度の溶液にわたり金属イオンの分離に利用可能である。ランタノイドは水溶液中では通常 3 価の陽イオンとして存在し硬い（ハードな）酸に分類されるので、O,O 配位を有するβ-ジケトンのような酸性抽出試薬を用いることにより有機相に容易に抽出される。さらに、中性配位子を同時に用いると、金属はさらに親有機性の高い付加錯体を生成し、抽出が向上する。このような金属の抽出が増大する現象を協同効果（Synergism, Synergistic effect）という。しかし、協同効果は抽出の向上をもたらすが、逆に金属間の分離係数を低下させるといわれている。一方、中性二座配位子を用いると、大きな協同効果をもたらすだけではなく、さらに金属間の分離係数が向上する場合のあることが分かってきたが、その例は少なく抽出平衡の詳細な検討は未だ不十分である。

本研究では、工業的な使用において、より親有機性のため水相への溶解ロスのすくない長鎖β-ジケトンである LIX 54 および LIX 51 を用い、中性配位子として複素環式二座配位アミンである 2,2'-bipyridine(bpy)、1,10-phenanthroline (phen) および 2,9-dimethyl-1,10-phenanthorine (dmp) を用いて、ランタノイドの協同効果抽出を行い、抽出平衡を検討して抽出定数や付加錯体生成定数を求め、その変化について検討した。

2. 実 験

2.1 試 薬

酸性抽出試薬(HR)として長鎖β-ジケトンの LIX 54 (Henkel Corporation; 主成分 1-フェニル-3-イソヘプチル-1, 3-プロパンジオン) および LIX 51 (Henkel Corporation; 主成分 1,1,1-トリフルオロ-4-ドデシルフェニル-2,4-ブタンジオン) を用いた。Fig. 1 に構造式を示す。

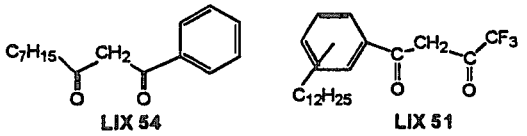

Fig. 1 Structures of β-diketones

中性二座配位子 (S) として複素環式二座アミンである bpy、phen および dmp を用いた。Fig. 2 に構造式を示す。

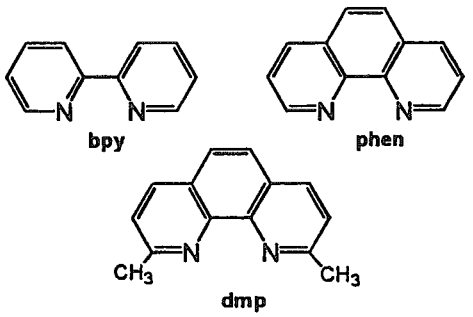

Fig. 2 Structures of bidentate heterocyclic amines

JRR-4 S-パイプまたは JRR-3 HR-2、 トレーサー製造，分離化学、溶媒抽出

また溶媒はトルエンを用いた。ランタノイド溶液（Ln^{3+}）は原子吸光用の標準試料溶液（和光純薬）を硝酸溶液に希釈して用いた。

2.2 RIの製造

La、Ce、Tb、TmおよびLuの各酸化物を、日本原子力研究所のJRR-4あるいはJRR-3において中性子を照射し、^{140}La（$t_{1/2}$＝40.2 h）、^{141}Ce($t_{1/2}$＝32.5 d)、^{160}Tb（$t_{1/2}$＝72.4 d）、^{170}Tm（$t_{1/2}$＝128.6 d）および^{177}Lu（$t_{1/2}$＝6.7 d）を製造した。照射後、硝酸に溶解し、トレーサー溶液として液-液抽出に用いた。

2.3 中性二座配位子の液-液分配

本研究で用いた中性二座配位子の水相－有機相間の分配挙動を検討した。中性二座配位子単独、またはLIX 54およびLIX 51を共存させたトルエン溶液10 cm^{3}と、0.1 M硝酸ナトリウムを含む等容の水相を25℃で1時間振とうした。水相を取り出し、水酸化ナトリウム溶液を加えて十分アルカリ性とした後、新しいトルエン10 cm^{3}と振とうして中性二座配位子をトルエン相に抽出し、次に0.1 M塩酸溶液に逆抽出した。有機相中の中性二座配位子についても0.1 M塩酸溶液に逆抽出した。それぞれの水溶液中の中性二座配位子濃度を吸光光度法により求めて，有機相－水相間の分配比を算出した。

2.4 ランタノイド(Ⅲ)の液－液抽出

抽出試薬を含むトルエン溶液4 cm^{3}と、RIでラベルした10^{-5} Mのランタノイドを含む水相4 cm^{3}を共栓付遠沈管に入れ、25℃の恒温室内で1時間振とうした。遠心分離後、各相から2 cm^{3}を分取し、γ-放射能を井戸型NaI(Tl)シンチレーションカウンターで測定してランタノイドの分配比を求めた。また、水相の平衡pHをガラス電極により測定した。トレーサーを用いない場合は、10^{-5} Mのランタノイドを含む水相 10 cm^3 と試薬を含むトルエン溶液10 cm^{3}を共栓付遠沈管に入れ、25℃ の恒温室内で1時間振とうした後、水相を取り出しICP発光分光装置で金属濃度を測定した。有機相は 8 cm^{3}を取り出し、0.1 M 硝酸溶液 10 cm^{3}に逆抽出し、ICPで金属濃度を測定した。両相の金属濃度より分配比を算出した。いずれの場合も水相のイオン強度は硝酸ナトリウムにより0.1とし、pH緩衝溶液として10^{-3} M酢酸、または5×10^{-3} Mピペラジン-1,4-ビス(2-エタンスルホン酸)（PIPES）の水酸化ナトリウム溶液を用いた。

3. 結果と考察

3.1 中性二座配位子の分配平衡

bpy、phenおよびdmpの分配比D_Sを求め、pHに対して$\log D_S$をプロットしFig. 3に示す。いずれの系でもpHとともに勾配1の直線に沿って$\log D_S$は増加し、やがて一定値となった。また、β-ジケトンを共存させてもほぼ同じ曲線となることから、中性二座配位子とβ-ジケトンとの相互作用はないと考えられる。中性二座配位子の有機相－水相間の分配比は、式(1)により表される。

$$D_S = \frac{[S]_{org}}{[S]_{aq}+[HS^+]_{aq}} = \frac{P_S}{1+[H^+]_{aq}/K_{HS}} \qquad (1)$$

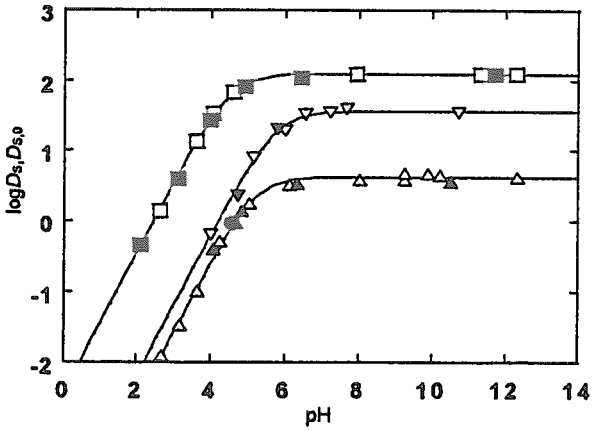

Fig. 3 Distribution of bidentate ligands in the absence and the presence of β-diketones
□ bpy alone, ■ bpy in the presence of 0.1 M LIX 54,
▽ phen alone, ▼ phen in the presence of 0.1 M LIX54,
△ dmp alone , ▲ dmp in the presence of 0.1 M LIX54,
● phen in the presence of 0.01 M LIX 51.

ここでP_Sは中性二座配位子の分配係数、K_{HS}はプロトン化した中性二座配位子の酸解離定数、下付のaqは水相、orgは有機相中の化学種であることを示す。この式を用いて実験値から最小自乗法によりP_Sと

K_{HS}を求め、その値をTable 1に示す。

Table. 1 P_S and K_{HS} of bidentate ligands

Bidentate ligands	logK_{HS}	logP_S
bpy	-4.53	2.00
phen	-5.25	0.66
dmp	-5.76	1.56

3.2 ランタノイド(III)の抽出

0.01 M LIX 51による抽出における、pHに対するLaの分配比DをFig. 4に示す。キレート試薬単独の場合と比べ、中性二座配位子が共存する場合に抽出が増大し、協同効果の起こっていることがわかる。また、いずれの場合もプロットの勾配は約3となった。LIX 51濃度に対する分配比の変化をFig. 5に示す。中性二座配位子が共存する場合においてプロットの勾配は約3となることから抽出化学種中に3分子のβ-ジケトンがあることを示している。

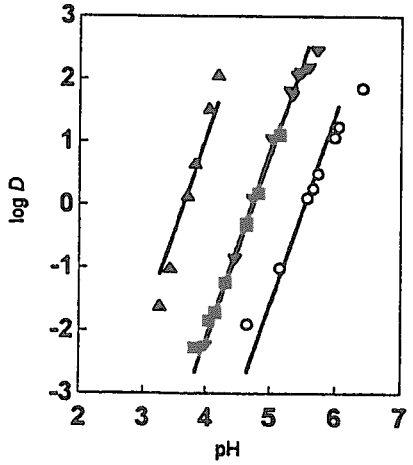

Fig. 4 Distribution ratios of La as a function of pH in the extraction with 0.01 M LIX 51.
○ LIX 51 alone ; ■ 0.01 M bpy ; ▼ 0.01 M dmp ; ▲ 0.01 M phen.

従って、Ln^{3+}の抽出平衡はLIX 51単独の場合、

$$Ln^{3+}_{aq} + 3\,HR_{org} \rightleftarrows LnR_{3,org} + 3\,H^{+}_{aq} \quad (2)$$

となり、協同効果抽出の場合は、

$$Ln^{3+}_{aq} + 3\,LnR_{org} + n\,S_{org} \rightleftarrows LnR_3S_{n,org} + 3\,H^{+}_{aq} \quad (3)$$

となると考えられる。ここで、それぞれの抽出定数をK_{ex}、K_{exs}とする。協同効果の増大分は、HRのみによる抽出におけるLn^{3+}の分配比D_0、およびHR

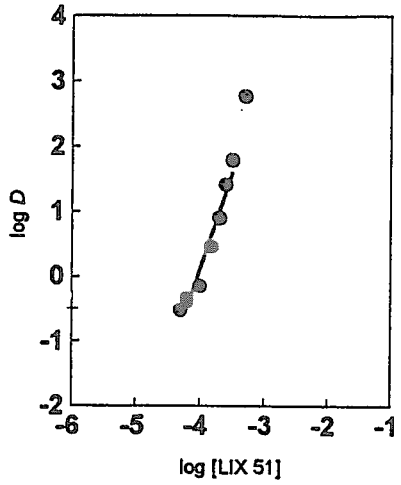

Fig. 5 Distribution ratios of Tb as a function of the LIX 51concentration. ● 0.01 M phen at pH 4.36 .

とSの協同効果抽出における分配比Dを用いて以下の式で表される。

$$D/D_0 = 1 + \sum \beta_{s,n}[S]^n_{org} \quad (4)$$

ここで、$\beta_{s,n}$は付加錯体生成定数であり、次の平衡式の平衡定数である。

$$LnR_{3,org} + n\,S_{org} \rightleftarrows LnR_3S_{n,org} \quad (5)$$

この式から、有機相中にLnR_3S_nの付加錯体が主に存在するとき、D/D_0は中性配位子濃度のn次に比例することが予想される。中性二座配位子濃度の対数に対してlog D/D_0をプロットした図をFig.6に示す。実線はn=1と仮定して(4)式を用いて最小自乗法により求めた計算値を示す。bpyではほぼ傾き1の直線となり、中性二座配位子が金属キレートに1分子

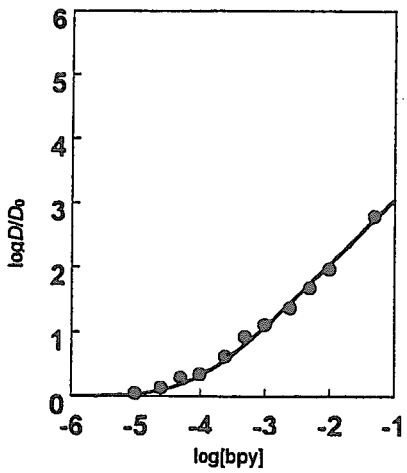

Fig. 6 Effect of the concentration of bpy on the synergistic extraction of La with 0.01 M LIX 51.

付加していると考えられる。以上から協同効果抽出における抽出化学種は LnR_3S であることがわかった。

3. 3 協同効果における各平衡定数の比較

一連のランタノイド元素について関係する平衡定数を求め、Fig. 7 から 10 に示す。K_{ex} および $K_{exs,1}$ は、原子番号の増加と共に増大していく。β-ジケトン単独においては、LIX 51 の方が LIX 54 に比べ大きな抽出が得られた。これは電子吸引性のフルオロアルキル基を持つ LIX 51 の酸解離定数が大きいので、酸解離型陰イオンが多く生成するためと考えられる。$\beta_{S,1}$ は、LIX 51 の方が LIX 54 より大きい値となった。これも LIX 51 の方が中心金属への電子

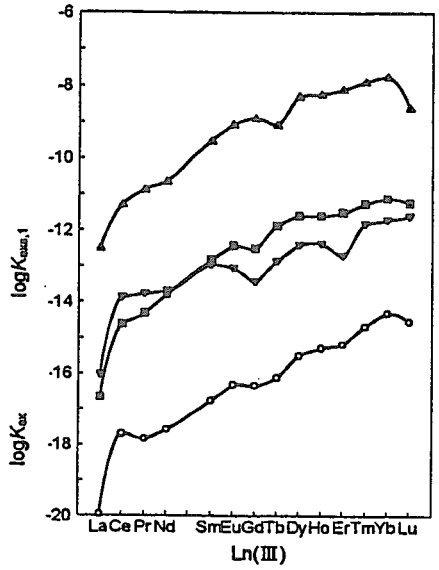

Fig. 7 Variation in extraction constants in the LIX 54 system.
○ LIX 54 alone ; ■ bpy ; ▼ dmp ; ▲ phen.

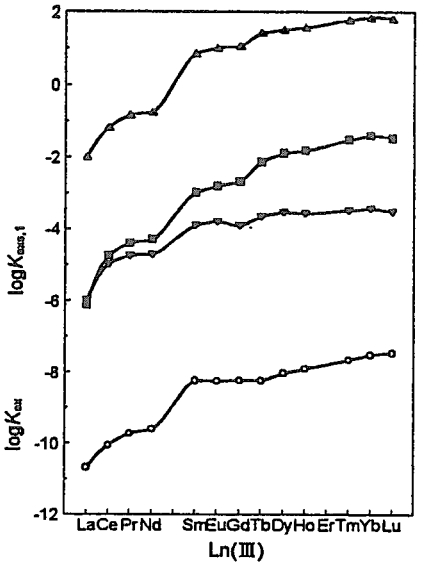

Fig. 9 Variation in extraction constants in the LIX 51 system. ○ LIX 51 alone ; ■ bpy ; ▼ dmp ; ▲ phen.

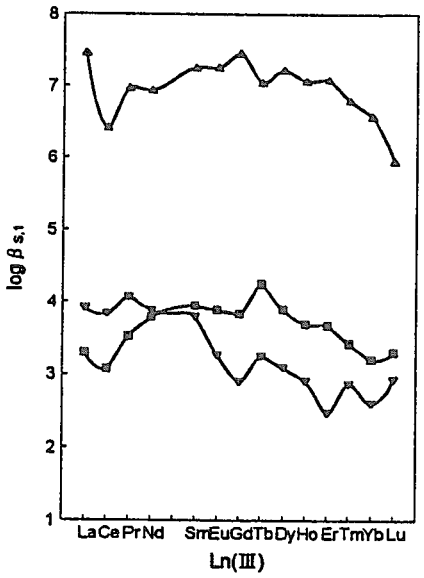

Fig. 8 Variation in adduct formation constants in the LIX 54 system. ■ bpy ; ▼ dmp ; ▲ phen.

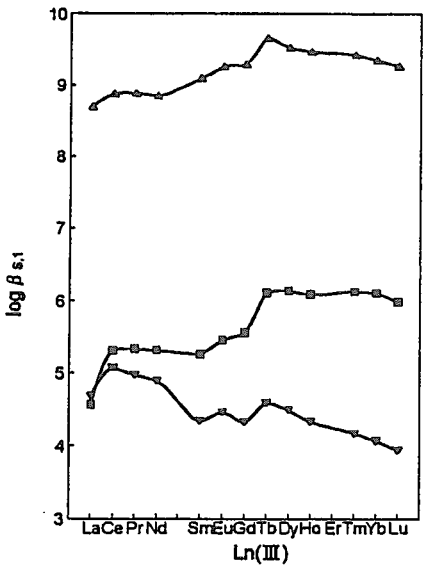

Fig. 10 Variation in adduct formation constants in the LIX 51 system. ■ bpy ; ▼ dmp ; ▲ phen.

供与が小さいため、次に結合する中性配位子が電子供与し易いため安定な付加錯体が生成するものと考えられる。$\beta_{s,1}$は、軽いランタノイド以外では、dmp < bpy < phen の順に大きくなり、特に phen で大きな値が得られている。これは、phen の酸解離定数が小さくてより塩基性であるためと考えられる。dmp の$\beta_{s,1}$が原子番号の大きいランタノイドで小さいのは、2,9 位のメチル基による立体障害がイオン半径の小さなランタノイドほど影響が大きいためと考えられる。ばらつきが大きいが、全体的な傾向として bpy および phen では、原子番号が大きくなるにつれて$\beta_{s,1}$は増加し、Tb 以降は減少するように見える。この傾向は LIX 51 の方が、増加が明瞭であり、また Tb 以降の減少は少ない。

一方、以前の研究から、phen や bpy による協同効果において、アセチルアセトン(Hacac)やベンゾイルアセトン(Hba)のような酸解離定数の大きいβ-ジケトンでは、$\beta_{s,1}$は原子番号とともに減少傾向を示し、2-テノイルトリフルオロアセトン(Htta)のようなフルオロメチル基を持つ酸解離定数の小さいものでは、$\beta_{s,1}$は原子番号とともに増大する傾向を示した。LIX54 は Hacac や Hba に、LIX51 は Htta に相当する長鎖のβ-ジケトンと考えられたが、$\beta_{s,1}$は原子番号に対して一様に変化していない。特に、LIX 51 において Tb 以降に減少する傾向が見られるのは、やはり長鎖をもつβ-ジケトンのために立体的な障害が起こりやすくなっているためとも考えられる。

4. 結 論

中性二座配位アミンは、塩基性の大きさ、二座配位による配位能の強さから、キレート錯体と安定な付加錯体を生成している。bpy および phen においては、軽いランタノイドから中程のランタノイドまで原子番号が大きくなるにつれ$\beta_{s,1}$が増加することから、協同効果により、抽出が増大するだけでなく、分離係数も向上することがわかった。一方、分子量の小さいβ-ジケトンの場合よりも、長鎖β-ジケトンの方が$\beta_{s,1}$の変化が小さく、酸性抽出試薬の長鎖化は協同効果における分離係数の変化に影響を与えることがわかった。

[成果の公表]

1) LIX 54 と中性二座配位子によるランタノイド(Ⅲ)の協同効果抽出，JAERI-Review 99-007
2) ランタノイド(Ⅲ)ー長鎖β-ジケトン抽出系における中性二座配アミンの協同効果，武井　周一，中村　重人，秋葉　健一，日本分析化学会第 47 年会
3) 含フッ素長鎖β-ジケトンと中性二座配位子によるランタノイド(Ⅲ)の抽出における協同効果，武井　周一，中村　重人，秋葉　健一，日本分析化学会第 48 年会

7-12 ＥＣ壊変を用いたＸ線状態分析（Ⅲ）

X-ray State Analysis by Means of Electron Capture Decay

玉木 洋一（宮城教育大学）
Yoichi TAMAKI （Miyagi University of Education ）

^{71}Ｇｅ標識化合物についてＥＣ壊変によるＫＸ線を波長分散法及びエネルギー分散法で測定した。^{71}Ｇｅ標識化合物とＧａ化合物との差は明確ではなかったが、ＧａＫ線はＸ線励起ではピークエネルギー、半値幅にケミカルシフトが見られた。また、Ｋβ／Ｋα強度比はその変化が小さく、Ｇａ化合物、^{71}Ｇｅ標識化合物とも有為の差を見いだせなかった。

１．はじめに

ＥＣ壊変による内殻電離はＸ線照射、電子線衝撃等と比べ多重イオン化や外殻軌道電子の励起の少ない方法である。内殻の空孔生成後、発生する特性Ｘ線は外殻電子の存在状態を反映し、そのスペクトルはわずかではあるが変化し、対象元素の酸化状態や内殻電離方法の違いを知ることができる。実験では、波長分散法を用いてＸ線を精度良く測定することにより、また、測定が比較的簡便なエネルギー分散法によるＫβ／Ｋα強度比の測定によってもケミカルシフト等の知見が得られる。

これまでの波長分散法による ^{51}Ｃｒ標識化合物の研究ではＶＫα、Ｋβ線ともケミカルシフトが測定され、状態分析が可能であることが確かめられた。その結果、壊変後の娘核は親核種の化学状態を反映していることが明らかになってきた。[1] また、ＥＣ壊変による内殻電離と、Ｘ線照射による内殻電離では、特性Ｘ線のピークエネルギーが異なり、ＥＣ壊変の方が低エネルギーであることも明らかになり、内殻電離の方法によって、その後の励起解消過程に違いが生じるという興味ある結果が得られている。^{55}Ｆｅ、^{71}ＧｅからのＭｎＫα、ＧａＫα線についてはケミカルシフトは明確ではないものの、ＥＣ壊変とＸ線照射の違いが見られた。[2]

一方、エネルギー分散法では分解能は不十分なものの、Ｋβ線とＫαの強度比を取ることによって、対応する軌道からの遷移確率の変化を精度良く求めることができる。この方法は ^{51}Ｃｒ標識化合物等に用いられており、状態分析がおこなわれてきている。しかし、^{71}Ｇｅ標識化合物及びＧａ化合物についてはまだ測定結果は報告されていない。

本研究では、ＥＣ壊変核種として^{71}Ｇｅを用い、また、Ｘ線スペクトル測定には、波長走査を必要としない位置敏感型検出器を使用した波長分散法と半導体検出器によるエネルギー分散法の両方の測定を行い、これまでに得られた ^{51}Ｃｒ，^{55}Ｆｅとの比較検討を行った。

２．実験

２．１ ^{71}Ｇｅ標識化合物の調製

測定に用いたＥＣ壊変核種はＧｅ金属、GeO_2をそれぞれ、JRR-3Mで５０または１００時間照射し、(n,γ) 反応で^{71}Ｇｅ標識化合物を得た。生成放射能は３７～７４MBq であった。

研究設備　JRR-3M 水力照射設備　　研究分野　放射化学、分析化学

2.2波長分散法による測定

波長分散型のX線スペクトル測定装置は、ゴニオメーターの中心にローランド半径３００mmのヨハンソン型LiF（２００）湾曲結晶を、集光点に位置敏感型検出器を取り付けたものである。[3)]

測定はKα線について１回約３日間の連続測定を行った。また、ＥＣ壊変による内殻電離と比較するため、測定装置を同じ光学系に保って、対応する元素であるＧａ化合物の蛍光X線を測定した。X線対陰極にはロジウムを用いた。

得られたX線スペクトルは、プロファイル関数にpseudo-Voigt関数を用いて、非線形最小自乗法により、$K\alpha_1$、$K\alpha_2$線に分離した。また、ピークエネルギーについて温度補正を行った。

2.3エネルギー分散法による測定

^{71}Ｇｅ標識化合物については約３７kBq用い、対応するＧａ化合物の測定は励起に加速エネルギー２５keVの電子線を用い、Si(Li)半導体検出器によってＫX線領域のスペクトルを測定した。測定は統計誤差を少なくするためKα線ピークで2×10^4カウント以上となるように、それぞれ６回以上繰り返し行った。スペクトルのピークはガウス関数を用いて解析し、自己吸収補正を行ってKβ／Kα強度比を求めた。測定試料を表１に示す。

表１　測定試料

試料番号	化合物	電離法
1	^{71}Ge metal	EC decay
2	$^{71}Ge_2O_3$	〃
3	Ga metal	X-ray
4	$(NH_4)_3[GaF_6]$	〃
5	$Ga_2(SO_4)_3$	〃
6	GaF_3	〃
7	Ga_2O_3	〃
8	GaAs	〃
9	GaOOH	〃
１０	$(NH_4)_3[Ga(C_2O_4)_3]$	〃

３．結果

3.1波長分散法による測定結果

測定結果の例を図１に示す。

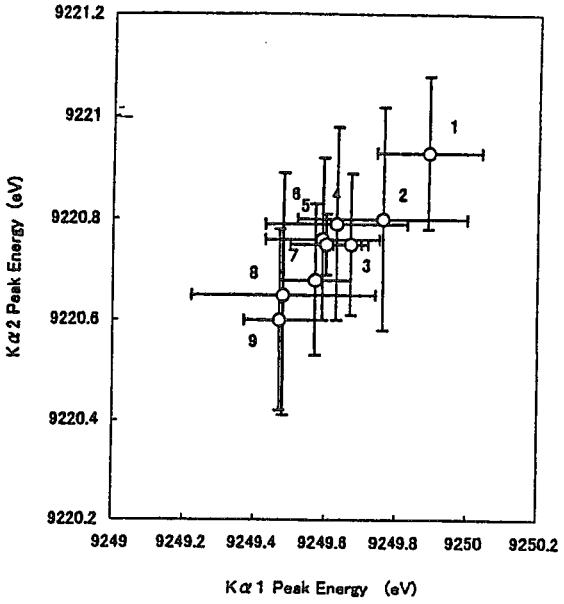

図１　GaKα$_1$線とGaKα$_2$線のピークエネルギーの関係

図中の番号は表１の試料番号であり、誤差は標準偏差で示した。

白丸で示したX線励起では$K\alpha_1$線と$K\alpha_2$線のエネルギーは化合物により違いがあり、最大0.4 eVのケミカルシフトがみられた。しかし、金属以外の３価の化合物では$K\alpha_1$線と$K\alpha_2$線に相関はあるものの、そのシフトは小さく誤差範囲が重なり、ケミカルシフトは明確とは言えない。Ｇａは第４周期典型元素であり、最外殻は閉殻構造を取っているため、結合相手の元素の影響は少ないと考えられる。

ＥＣ壊変の結果は（図中黒丸で示した）$K\alpha_1$線、$K\alpha_2$線ともピークエネルギーは誤差範囲内であり、有為の差は見いだせなかった。しかし、その値は対応するＧａ化合物（Ga metal, Ga_2O_3）のX線励起より、わずかに小さい値となった。この傾向はこれまでに得られた^{51}Ｃｒ、^{55}Ｆｅの結果と対応しており、[4)] ^{71}Ｇｅにおいても内殻電離の方法による違いを測定できる可

能性を示している。

Ｇａ化合物のＸ線励起では、Ｋα₁線の半値幅はそのピークエネルギーの増加と共に減少する結果が得られ、半値幅にもケミカルシフトが観測された。しかし、ＥＣ壊変では誤差が大きく、有為の差はみられなかった。

3.2エネルギー分散法による測定結果

Ｋβ／Ｋα強度比の測定結果を図２に示す。試料番号１，２はＥＣ壊変によるもの（^{71}Ge metal, $^{71}Ge_2O_3$）、他はＧａ化合物のＸ線励起による結果である。

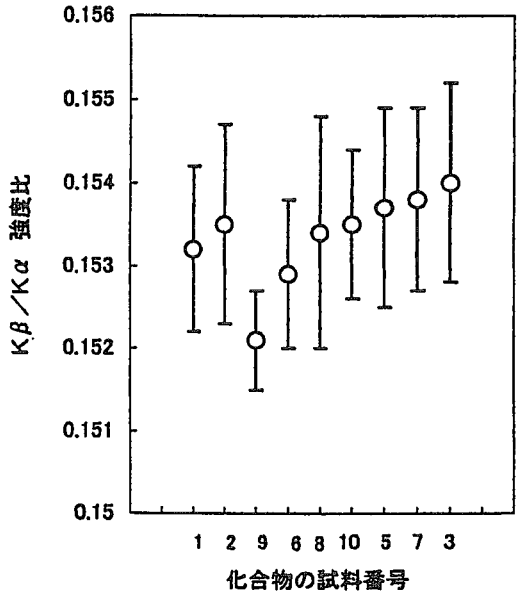

図２ ^{71}Ge標識化合物とGa化合物のＫβ/Ｋα強度比

図にみられるように、Ｇａ化合物についてはＫβ／Ｋα強度比の値に違いがみられるが、誤差範囲が重なり有為の差は得られなかった。３ｄ遷移元素の化合物では、同じ酸化数であっても配位子によってＫβ／Ｋα強度比は異なり、同じ立体配置の錯体では配位子の分光化学系列と良く対応する結果を得ている。しかし、Ｇａではその影響は小さく、化合物の違いによる変化が小さいものと考えられる。また、波長分散法で得られたＫα₁、Ｋα₂線のエネルギーシフトとの相関も明確ではなかった。

４．まとめと今後の課題

今回の研究では、^{71}Ｇｅ標識化合物とＧａ化合物について、そのＫＸ線の変化による化学状態に関する知見を得ることを目的としたが、スペクトル変化は小さく、誤差範囲内に含まれてしまい明確な結果は得られなかった。しかし、波長分散法によるＧａ化合物のＸ線励起のＫβ線測定ではＫα線より大きいケミカルシフトを得ており、今後の^{71}Ｇｅ標識化合物のＫβ線測定により、その変化を測定できる可能性がある。また、ＥＣ壊変核種として^{65}Ｚｎを対象にした実験では、壊変後のＣｕＫＸ線を測定することにより、より高分解能のスペクトルを得ることができ、今後更に研究を進める予定である。

文献

１）玉木洋一：ＥＣ壊変によるＸ線発光スペクトルを用いた化学状態の分析（ミニレビュー），RADIOISOTOPES, 45（1996）823-824.

２）玉木洋一“^{55}Ｆｅ、^{71}Ｇｅ標識化合物のＥＣ壊変によるＫα線スペクトル”、第３１回Ｘ線分析討論会（1995年11月）

３）玉木：原研施設共同利用研究成果報告書 平成６年度，５２－５３頁

４）玉木：原研施設共同利用研究成果報告書 平成８年度，８－１１頁

成果発表

Ｘ線分析の進歩，32,(2000)に「^{71}Ｇｅ標識化合物のＥＣ壊変によるＫＸ線スペクトル変化」の標題で投稿準備中である。

7-13 原子炉生産短半減期核種による放射性医薬品の製造法の確立

The Production of Radiopharmaceuticals with short lived Radionuclides produced by Reactor

金沢大学医学部

安東 醇，大石茂雄，安東逸子

School of Medicine, Kanazawa University

Atsushi Ando, Shigeo Oishi, Itsuko Ando

目的

核医学の領域においては放射性同位元素（RI）またはその化合物を投与して，これを悪性腫瘍等の病巣に集積させ，このRIから放射されるβ⁻線等によってその病巣を照射し，悪性腫瘍等を治療する方法が重要になってきた．この目的に適した核種として^{105}Rhを“Rh-105の製造と放射性医薬品への利用”[1]において製造することに成功した．^{105}Rhは物理学的半減期35.4時間，247（30%）と560（70%）keVのβ⁻線を放射すると同時に306(5%)と319（19%）keVのγ線も放射する．今，多くの核医学者の関心を集めている転移性骨腫瘍に起因する疼痛の緩和剤を創る目的で，^{105}Rh-EDTMPを製造し，この化合物の疼痛緩和剤としての有効性を調べたので報告する．

実験材料及び方法

ロジウム-105（^{105}Rh）の製造：既に報告した方法[1]，即ち天然ルテニウム金属粉をJRR-3Mで熱中性子照射し，^{104}Ru (n, γ)^{105}Ru $\xrightarrow[4.4\ h]{\beta^-}$ ^{105}Rhの反応で，核種純度99.4%以上の^{105}Rhを20.2MBq得た．これを0.1NHClに溶かして^{105}Rh-EDTMPの製造に使用した．EDTMP（Ethylenediamine-tetra-methylene phosphonic acid）は（株）同仁化学研究所（熊本県益域町）から購入した．

^{105}Rh-EDTMP：^{105}Rhの0.1NHCl溶液（0.45ml, 20MBq）に0.1NNaOH溶液に溶かしたEDTMP（10mg/ml）0.6mlを加え，pH8.4～8.6に調整後，沸騰水浴中で30分間加熱した．^{105}Rh-EDTMPの放射化学的純度はアセトン：メタノール：水（2：2：1）を展開溶媒とするミニペーパークロマトグラフィ[2]で調べた．^{105}Rh-EDTMPの安定性に関しては製造5日後まで同じ方法で観察を続けた．

^{105}Rh-EDTMPのマウス体内分布実験：マウス1匹あたり^{105}Rh-EDTMP注射液0.2ml（1mlは0.1～0.8MBqの^{105}Rhと0.3mgのEDTMPを含む）を正常なddYマウス（体重31.2g±2.2g）に静注し，静注1，3，24，48，96時間後に屠殺し，大腿骨，頭頂骨，血液，筋肉等（Table 1に示す）の一部を摘出し，直ちに重量と放射能を測定した．測定値から^{105}Rh-EDTMPの投与量を100%とした場合の臓器組織1gあたりへの取込率（% ID/g）を求めた．マウスの体重のバラツキなどを補正し，同一基準で比較するために，“% ID/g×マウスの体重g／100g”の式でマウスの体重を100gに基準化してTable 1に示した．

骨集積がよく知られている^{99m}Tc-MDPを^{105}Rh-

研究施設・装置

ＪＲＲ－３Ｍ

研究分野名

生物に対する放射線効果

EDTMPと比較のために^{105}Rh-EDTMPの場合と同様にマウスに投与して実験を行った．^{99m}Tc-MDP注射液はマウス1匹あたり0.2ml（1mlあたり約4MBqの^{99m}Tcと167μgのMDPを含む）を静注し，24時間後まで観察した．

結果及び考察

^{105}Rh-EDTMPの合成：Fig.1にペーパークロマトグラフィのアクチグラムとオートラジオグラムを示した．この図のごとく，^{105}Rh-EDTMPは原点に残り，^{105}Rh-chlorideはRf値0.42～0.48であった．^{105}RhとEDTMPとの反応液には^{105}Rh-EDTMP以外は存在せず，合成収率は99％以上であった．また，製造5日後においても分解物は認められなかった．このことから，^{105}Rh-EDTMPは容易に合成でき，かつ非常に安定であることがわかった．

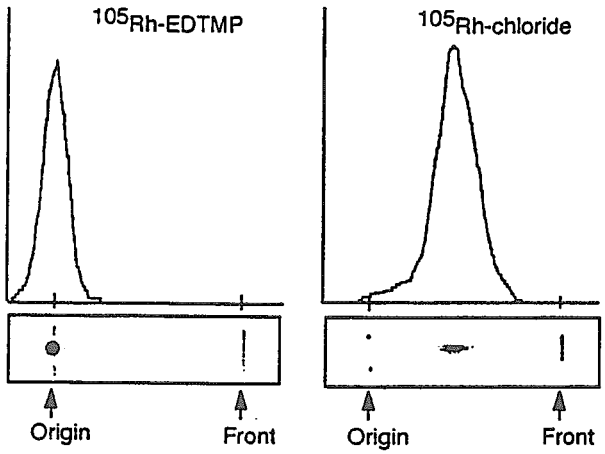

Fig.1 Actigram and autoradiogram for miniature paperchromatography with ^{105}Rh-EDTMP and ^{105}Rh-chloride Solvent system; acetone : methanol : water (2 : 2 : 1)

^{105}Rh-EDTMPの骨集積性：^{105}Rh-EDTMPのマウスにおける骨集積性についてはTable 1に示した．^{105}Rh-EDTMPの大部分が骨に集積しており，その取込率は投与1時間後に大腿骨へは4.59％ID/g，頭頂骨へは3.13％ ID/gであり，経時的にゆっくりと減少した．腎臓への取込率は投与1時間及び3時間後で各々0.348％ ID/g，0.337％ ID/gであり，以後経時的に減少した．骨取込率と比較した場合に，他の臓器組織への取込率は無視できるほど小さかった．投与1時間後までと3時間後までの尿中への排泄率は各々57.5±10.3％と61.0±5.9％であった．

^{105}Rh-EDTMPの骨取込率と他の臓器組織への取込率の比を求め，Fig. 2に示した．転移性骨腫瘍に起因する疼痛緩和剤としてはこの値の大きいほど優れた化合物と言える．大腿骨／血液一比は138～6327，大腿骨／筋肉一比は429～1311，大腿骨／肝臓一比は206～3517，大腿骨／脾臓一比は429～571，大腿骨／腎臓一比は14～64，大腿骨／肺一比は118～651であった．比較のために行った^{99m}Tc-MDPの骨及び臓器取込率をTable2に示した．^{99m}Tc-MDPの大腿骨及び頭頂骨への取込率は^{105}Rh-EDTMPのそれよりもやや大きかったが，他の軟組織への取込率も^{105}Rh-EDTMPのそれよりも大きかった．^{99m}Tc-MDPの場合の大腿骨／各臓器取込一比をFig. 2に示した．これから解るように，^{99m}Tc-MDPの場合は^{105}Rh-EDTMPの場合よりも大腿骨／各臓器取込一比がはるかに小さかった．

これらの結果は^{105}Rh-EDTMPは骨に特異的に集積し，血液及び軟組織への集積は極めて少ないことを示すものであった．

まとめ

^{105}Rh-EDTMPは^{105}Rh-chlorideとEDTMPから容易に合成でき，かつ放射化学的に非常に安定であった．マウスによる動物実験の結果，^{105}Rh-EDTMPは骨に特異的に集積し，血液及び軟組織への集積は極めて少ないことから，転移性骨腫瘍に起因する疼痛の緩和剤として非常に優れた生物学的性質を持つことが明かとなった．さらに^{105}Rhの核物理学的性質を考慮すると^{105}Rh-EDTMPは上記の疼痛緩和の

ための優れた放射性医薬品となると考えられた.

Table 1 Biodistribution of ^{105}Rh-EDTMP

	1 hour	3 hours	24 hours	48 hours	96 hours
Blood	0.034 ± 0.006	0.009 ± 0.001	0.001 ± 0.0001	0.0008 ± 0.0002	0.0005 ± 0.0001
Muscle	0.011 ± 0.003	0.007 ± 0.001	0.004 ± 0.001	0.003 ± 0.0005	0.003 ± 0.0006
Liver	0.023 ± 0.003	0.020 ± 0.003	0.015 ± 0.001	0.011 ± 0.001	0.011 ± 0.002
Spleen	0.011 ± 0.003	0.008 ± 0.003	0.009 ± 0.002	0.008 ± 0.001	0.008 ± 0.002
Kidney	0.348 ± 0.089	0.337 ± 0.156	0.132 ± 0.025	0.093 ± 0.010	0.053 ± 0.012
Lung	0.040 ± 0.006	0.021 ± 0.005	0.008 ± 0.003	0.006 ± 0.001	0.005 ± 0.002
Stomach	0.020 ± 0.004	0.013 ± 0.004	0.005 ± 0.001	0.004 ± 0.001	0.003 ± 0.001
Pancreas	0.009 ± 0.002	0.006 ± 0.003	0.003 ± 0.001	0.003 ± 0.001	0.003 ± 0.001
Heart	0.012 ± 0.002	0.011 ± 0.002	0.003 ± 0.001	0.004 ± 0.001	0.003 ± 0.001
Small intestine	0.019 ± 0.008	0.008 ± 0.001	0.006 ± 0.003	0.005 ± 0.001	0.005 ± 0.001
Brain	0.003 ± 0.001	0.002 ± 0.001	0.0003 ± 0.0001	0.0006 ± 0.0002	0.0004 ± 0.0002
Testis	0.013 ± 0.004	0.010 ± 0.001	0.007 ± 0.002	0.005 ± 0.001	0.005 ± 0.001
Parietal bone	3.13 ± 0.35	3.10 ± 0.24	2.82 ± 0.66	2.28 ± 0.20	2.03 ± 0.57
Femur	4.59 ± 0.24	4.20 ± 0.24	3.75 ± 0.64	3.75 ± .0.32	3.23 ± 0.58

Uptake rates in various tissues are expressed as % of administered dose per gram tissue weight.
Tissues are normalized to a body weight (BW) of 100 g by multiplying by BW/100.
Values represent the mean ± S.D. of five animals.

Table 2 Biodistribution of ^{99m}Tc-MDP

	1 hour	3 hours	24 hours
Blood	0.117 ± 0.016	0.078 ± 0.017	0.021 ± 0.003
Muscle	0.032 ± 0.006	0.022 ± 0.005	0.008 ± 0.001
Liver	0.716 ± 0.177	0.373 ± 0.117	0.131 ± 0.015
Spleen	0.245 ± 0.113	0.698 ± 0.225	0.702 ± 0.228
Kidney	2.87 ± 1.56	1.36 ± 0.76	0.201 ± 0.035
Lung	0.122 ± 0.025	0.245 ± 0.096	0.062 ± 0.019
Parietal bone	3.89 ± 0.29	4.68 ± 1.08	3.30 ± 0.33
Femur	4.91 ± 0.32	6.24 ± 1.24	5.37 ± 0.48

Uptake rates in various tissues are expressed as % of administered dose per gram tissue weight.
Tissues are normalized to a body weight (BW) of 100 g by multiplying by BW/100.
Values represent the mean ± S.D. of five animals.

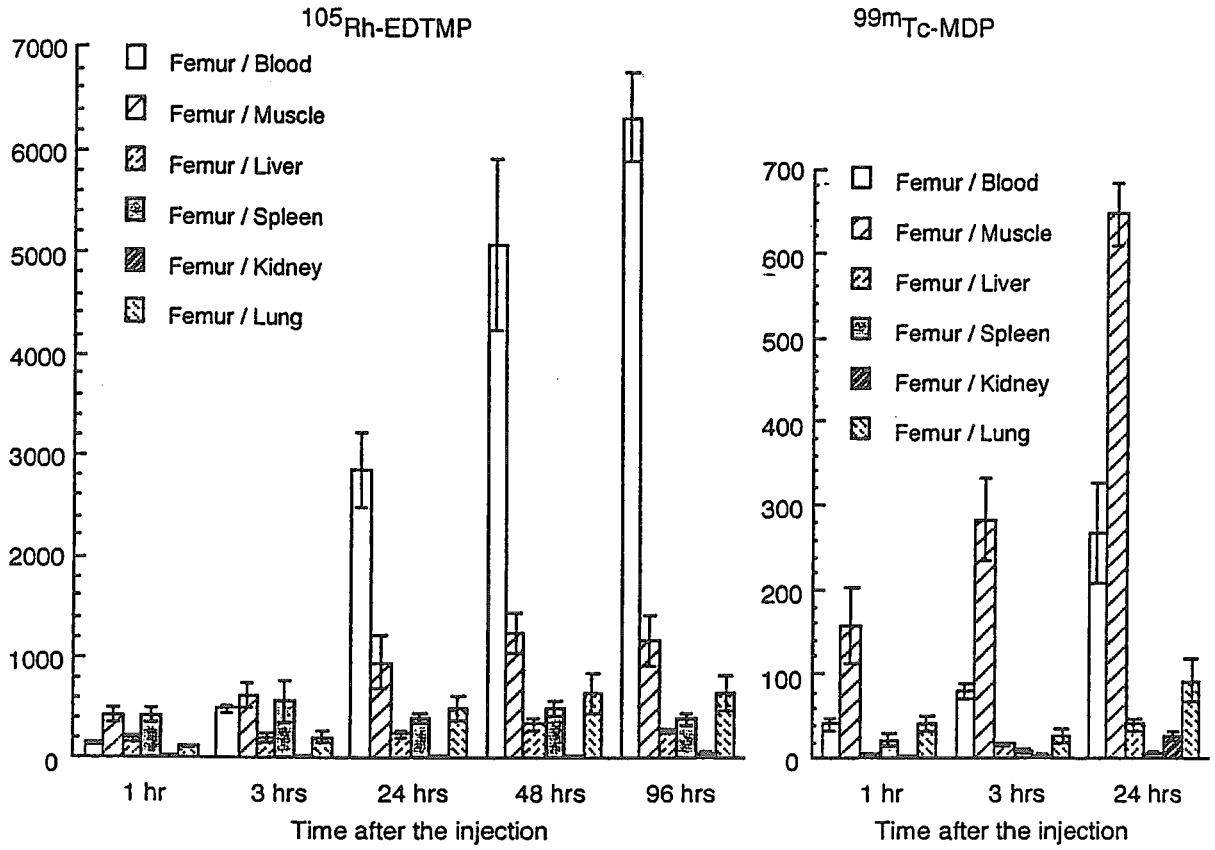

Fig. 2 Femur-to-organ uptake ratios of ^{105}Rh-EDTMP and ^{99m}Tc-MDP

成果の公表

Atsushi Ando, Itsuko Ando, Norihisa Tonami, Seigo Kinuya, Natsuko Okamoto, Masami Sugimoto, Naoko Fukuda, Satomi Matsumoto: Production of ^{105}Rh-EDTMP and its bone accumulation. Applied Radiation and Isotopes, 52, 211-215, 2000

文献

1）安東醇，真田 茂，安東逸子：Rh-105 の製造と放射性医薬品への利用，原研施設利用共同研究成果報告書平成６年度（UTRCN-G-23），p.288-29, 1994.

2）Sanada, S., Ando, A., Ando, I., Hiraki, T., Hisada, K.: A single-strip mini-paperchromatographic method for rapid purity-control of ^{99m}Tc-labeled radiopharmaceuticals. Eur. J. Nucl. Med., 12,390-393, 1986.

謝　辞

本報告書の発刊にあたり、多くの皆様から多大なご協力を頂きました。編集に際し、ご協力頂いた、東京大学物性研究所加倉井和久氏、東京大学原子力研究総合センター高野正美氏、研究炉部長高柳政二氏、研究炉利用課長堀口洋二氏、研究炉利用課市村茂樹氏、本田由里恵さん、また本報告書の査読を頂いたＪＲＲ－４管理課長桜井文雄氏に深く感謝致します。

付　録 (1)

Appendix (1)

This is a blank page.

付 録(1)

事情により、研究炉利用の成果・連絡票のみの提出となった利用者について、その内容をここに示す。

研究テーマ「表題」	所属 担当者	利用原子炉及び装置名	報告書等	利用分野
青森県における表層土壌の分配係数	（財）環境科学技術研究所 塚田 祥文	JRR-4 PN	本研究テーマでは放射化分析により土壌、農作物等の環境試料中ハロゲン元素濃度を測定し、環境移行パラメータについての知見を得ることを目的としています。なお本研究は、科学技術庁からの依託により行われており、平成11年度の成果については額の確定が未完了のため報告できません。	放射化分析
中性子放射化分析法による元素分析（依頼分析）	（財）放射線利用振興協会 照沼 久寿男	JRR-3M HR-1,2 PN-1,2,3 JRR-4 T,S,D- pipe PN	放射線利用振興協会では、諸機関等から依頼分析を受けた試料について、原子炉を利用した放射化分析業務を行っている。得られた分析結果は依頼元の研究開発等で活用されているが、機密保持が契約条件であるため成果報告の提出ができない。	放射化分析
高温酸化物超伝導材料の照射改質方法の検討及び基礎試験（1）	高温照射研究室 林 君夫	JRR-3M BR-2	現在、照射済試料を評価解析中であり成果の報告はできない。	原子炉燃料・材料
中性子イメージング検出法の研究	パルス中性子イメージング研究グループ 片桐 政樹	JRR-3M 7R	現在、実験結果を整理し特許に申請するための原稿を作成中であり、特許申請後今年度の研究成果と併せて次年度に成果として報告する予定です。	中性子ラジオグラフィ

This is a blank page.

付　録 (2)

Appendix (2)

This is a blank page.

付 録(2)

原研研究炉の利用設備一覧

１．ＪＲＲ－３Ｍ

１）実験設備

実　験　孔	実　　験　　装　　置
１Ｇ	高分解能粉末中性子回折装置（ＨＲＰＤ）
１Ｇ－Ａ	生体高分子結晶構造解析用中性子回折計（ＢＩＸ－Ｉ）
２Ｇ	三軸型中性子分光器（ＴＡＳ－１）
３Ｇ	中性子トポグラフィ・精密光学実験装置（ＰＮＯ）
４Ｇ	汎用三軸型中性子分光器（ＧＰＴＡＳ）
５Ｇ	偏極中性子散乱装置（ＰＯＮＴＡ）
６Ｇ	東北大学中性子散乱分光器（ＴＯＰＡＮ）
７Ｒ	中性子ラジオグラフィ装置（ＴＮＲＦ）
Ｔ１－１	中性子偏極回折装置（ＨＱＲ）
Ｔ１－２	単結晶中性子回折装置（ＫＳＤ）
Ｔ１－３	粉末中性子回折装置（ＨＥＲＭＥＳ） （ＫＰＤ）
Ｔ１－４－１	即発ガンマ線分析装置（ＰＧＡ）
Ｔ１－４－１Ａ	化学反応実験装置
Ｔ１－４－３	ＴＯＦ型中性子反射率計（ＴＯＦ）
Ｔ１－４－４	生物微細構造中性子回折装置
Ｔ２－１	残留応力測定用中性子回折装置（ＲＥＳＡ）
Ｔ２－２	四軸回折装置（ＦＯＮＤＥＲ）
Ｔ２－３	中性子ｲﾒｰｼﾞﾝｸﾞﾌﾟﾚｰﾄ付生体物質中性子回折計（ＢＩＸ－II）
Ｔ２－４	高分解能三軸型中性子分光器（ＴＡＳ－２）
Ｃ１－１	高エネルギー分解能三軸型中性子分光器（ＨＥＲ）
Ｃ１－２	二次元位置測定小角散乱装置（ＳＡＮＳ－Ｕ）
Ｃ１－３	超高分解能後方散乱装置（ＵＬＳ）
Ｃ２－１	冷中性子散乱実験デバイス開発装置（ＬＴＡＳ）
Ｃ２－２	中性子スペクトル変調・時間分析装置（ＮＳＭ） 中性子スピンエコー分光器（ＮＳＥ）
Ｃ２－３－１	冷中性子ラジオグラフィ装置（ＣＮＲＦ）
Ｃ２－３－２	即発ガンマ線分析装置（ＰＧＡ）
Ｃ２－３－２Ａ	化学反応実験装置
Ｃ２－３－４	ＴＯＦ型中性子反射率計（ＴＯＦ）
Ｃ２－３－５	生物微細構造中性子回折装置
Ｃ２－３－６	中性子寿命測定装置
Ｃ２－３－７	パルス中性子機器開発装置
Ｃ３－１－１	高分解能パルス冷中性子分光器（ＡＧＮＥＳ）
Ｃ３－１－２	多層膜中性子干渉計／反射率計（ＭＩＮＥ）
Ｃ３－２	中性子小角散乱装置（ＳＡＮＳ－Ｊ）

2）照射設備

水力照射設備	HR－1，2
気送照射設備	PN－1，2
放射化分析用照射設備	PN－3
均一照射設備	SI－1
回転照射設備	DR－1
垂直照射設備	VT－1，RG－1～4 BR－1～4，SH－1

2．JRR－4

1）実験設備

プール
中性子ビーム設備
散乱実験設備
冷却水循環ループ
医療照射設備（BNCT）
即発ガンマ線分析装置

2）照射設備

簡易照射筒	Tパイプ（水力）
	Sパイプ
	Dパイプ
	Nパイプ
気送管照射設備	PN

国際単位系 (SI) と換算表

表1　SI基本単位および補助単位

量	名称	記号
長さ	メートル	m
質量	キログラム	kg
時間	秒	s
電流	アンペア	A
熱力学温度	ケルビン	K
物質量	モル	mol
光度	カンデラ	cd
平面角	ラジアン	rad
立体角	ステラジアン	sr

表2　SIと併用される単位

名称	記号
分，時，日	min，h，d
度，分，秒	°，′，″
リットル	l，L
トン	t
電子ボルト	eV
原子質量単位	u

1 eV＝1.60218×10^{-19} J

1 u＝1.66054×10^{-27} kg

表5　SI接頭語

倍数	接頭語	記号
10^{18}	エクサ	E
10^{15}	ペタ	P
10^{12}	テラ	T
10^{9}	ギガ	G
10^{6}	メガ	M
10^{3}	キロ	k
10^{2}	ヘクト	h
10^{1}	デカ	da
10^{-1}	デシ	d
10^{-2}	センチ	c
10^{-3}	ミリ	m
10^{-6}	マイクロ	μ
10^{-9}	ナノ	n
10^{-12}	ピコ	p
10^{-15}	フェムト	f
10^{-18}	アト	a

表3　固有の名称をもつSI組立単位

量	名称	記号	他のSI単位による表現
周波数	ヘルツ	Hz	s^{-1}
力	ニュートン	N	m·kg/s^2
圧力，応力	パスカル	Pa	N/m^2
エネルギー，仕事，熱量	ジュール	J	N·m
工率，放射束	ワット	W	J/s
電気量，電荷	クーロン	C	A·s
電位，電圧，起電力	ボルト	V	W/A
静電容量	ファラド	F	C/V
電気抵抗	オーム	Ω	V/A
コンダクタンス	ジーメンス	S	A/V
磁束	ウェーバ	Wb	V·s
磁束密度	テスラ	T	Wb/m^2
インダクタンス	ヘンリー	H	Wb/A
セルシウス温度	セルシウス度	℃	
光束	ルーメン	lm	cd·sr
照度	ルクス	lx	lm/m^2
放射能	ベクレル	Bq	s^{-1}
吸収線量	グレイ	Gy	J/kg
線量当量	シーベルト	Sv	J/kg

表4　SIと共に暫定的に維持される単位

名称	記号
オングストローム	Å
バーン	b
バール	bar
ガル	Gal
キュリー	Ci
レントゲン	R
ラド	rad
レム	rem

1 Å＝0.1 nm＝10^{-10} m

1 b＝100 fm^2＝10^{-28} m^2

1 bar＝0.1 MPa＝10^5 Pa

1 Gal＝1 cm/s^2＝10^{-2} m/s^2

1 Ci＝3.7×10^{10} Bq

1 R＝2.58×10^{-4} C/kg

1 rad＝1 cGy＝10^{-2} Gy

1 rem＝1 cSv＝10^{-2} Sv

（注）

1. 表1－5は「国際単位系」第5版，国際度量衡局 1985年刊行による。ただし，1 eVおよび1 uの値はCODATAの1986年推奨値によった。
2. 表4には海里，ノット，アール，ヘクタールも含まれているが日常の単位なのでここでは省略した。
3. barは，JISでは流体の圧力を表わす場合に限り表2のカテゴリーに分類されている。
4. EC閣僚理事会指令ではbar，barnおよび「血圧の単位」mmHgを表2のカテゴリーに入れている。

換算表

力	N(=10^5 dyn)	kgf	lbf
	1	0.101972	0.224809
	9.80665	1	2.20462
	4.44822	0.453592	1

粘度　1 Pa·s(N·s/m^2)＝10 P(ポアズ)(g/(cm·s))

動粘度　1 m^2/s＝10^4 St(ストークス)(cm^2/s)

圧力	MPa(=10 bar)	kgf/cm^2	atm	mmHg(Torr)	lbf/in^2(psi)
	1	10.1972	9.86923	7.50062×10^3	145.038
	0.0980665	1	0.967841	735.559	14.2233
	0.101325	1.03323	1	760	14.6959
	1.33322×10^{-4}	1.35951×10^{-3}	1.31579×10^{-3}	1	1.93368×10^{-2}
	6.89476×10^{-3}	7.03070×10^{-2}	6.80460×10^{-2}	51.7149	1

エネルギー・仕事・熱量	J(=10^7 erg)	kgf·m	kW·h	cal(計量法)	Btu	ft·lbf	eV
	1	0.101972	2.77778×10^{-7}	0.238889	9.47813×10^{-4}	0.737562	6.24150×10^{18}
	9.80665	1	2.72407×10^{-6}	2.34270	9.29487×10^{-3}	7.23301	6.12082×10^{19}
	3.6×10^6	3.67098×10^5	1	8.59999×10^5	3412.13	2.65522×10^6	2.24694×10^{25}
	4.18605	0.426858	1.16279×10^{-6}	1	3.96759×10^{-3}	3.08747	2.61272×10^{19}
	1055.06	107.586	2.93072×10^{-4}	252.042	1	778.172	6.58515×10^{21}
	1.35582	0.138255	3.76616×10^{-7}	0.323890	1.28506×10^{-3}	1	8.46233×10^{18}
	1.60218×10^{-19}	1.63377×10^{-20}	4.45050×10^{-26}	3.82743×10^{-20}	1.51857×10^{-22}	1.18171×10^{-19}	1

1 cal＝4.18605 J(計量法)

＝4.184 J (熱化学)

＝4.1855 J (15 °C)

＝4.1868 J(国際蒸気表)

仕事率　1 PS(仏馬力)

＝75 kgf·m/s

＝735.499 W

放射能	Bq	Ci
	1	2.70270×10^{-11}
	3.7×10^{10}	1

吸収線量	Gy	rad
	1	100
	0.01	1

照射線量	C/kg	R
	1	3876
	2.58×10^{-4}	1

線量当量	Sv	rem
	1	100
	0.01	1

(86年12月26日現在)

研究炉利用における研究成果集（平成11年度）